ISSN 2148-7847

Journal of Thermal Engineering

Volume 12
Number 1
Year 2026

YTU PRESS

www.jten.yildiz.edu.tr

ISSN 2148-7847

Journal of Thermal Engineering

Volume 12 Number 1 Year 2026

EDITOR-IN-CHIEF

Ahmet Selim Dalkilic, *Yildiz Technical University, İstanbul, Türkiye*

ASSOCIATE EDITORS

Ali Celen, *Erzincan Binali Yıldırım University, Erzincan, Türkiye*
Baha Zafer, *İstanbul University, İstanbul, Türkiye*
Bekir Şener, *Yildiz Technical University, İstanbul, Türkiye*
Erdal Çetkin, *İzmir Institute of Technology, İzmir, Türkiye*
Emre Alpman, *Marmara University, İstanbul, Türkiye*
Erman Aslan, *İstanbul University, İstanbul, Türkiye*
Hasan Köten, *İstanbul Medeniyet University, İstanbul, Türkiye*
Hatice Mercan, *Yildiz Technical University, İstanbul, Türkiye*
Müslüm Arıcı, *Kocaeli University, Kocaeli, Türkiye*
Mustafa Kılıç, *Adana Science and Technology University, Adana, Türkiye*
Nader Javani, *Yildiz Technical University, İstanbul, Türkiye*
Naime Filiz Özdil, *Adana Science and Technology University, Adana, Türkiye*
Şevket Özgür Atayılmaz, *Yildiz Technical University, Adana, Türkiye*
Özgen Açıkgöz, *Yildiz Technical University, İstanbul, Türkiye*
Yaşar İslamoğlu, *Sakarya University, Sakarya, Türkiye*
Yasin Karagoz, *İstanbul Medeniyet University, İstanbul, Türkiye*
Zerrin Sert, *Eskişehir Osmangazi University, Eskisehir, Türkiye*

EDITORIAL BOARD

Adrian Bejan, *Duke University, United States*
Afshin J. Ghajar, *Oklahoma State University, United States*
Ali Chamkha, *Prince Mohammad Bin Fahd University, Saudi Arabia*
Bekir Sami Yilbas, *King Fahd University of Petroleum and Minerals, Dhahran, Saudi Arabia*
Chi-Chuan Wang, *National Chiao Tung University, Taiwan*
Gopal Nath Tiwari, *Indian Institute of Technology, India*
Hakan F. Oztop, *Fırat University, Türkiye*
Hari Mohan Srivastava, *University of Victoria, Canada*
Hamadiche Mahmoud, *Université de Lyon 1, France*
Hamid Niazmand, *Ferdowsi University Of Mashhad, Iran*

ISSN 2148-7847

Journal of Thermal Engineering

Volume 12 Number 1 Year 2026

Josua P. Meyer, *University of Pretoria, South Africa*
Kambiz Vafai, *University of California, United States*
Karan Surana, *The University of Texsas, United States*
Mehmet Kanoğlu, *University of Gaziantep, Türkiye*
Mohammad Mehdi Rashidi, *Bu-Ali Sina University, Iran*
Mohammad Hassan Saidi, *Sharif University of Technology, Iran*
Muhammad Ali Rob Sharif, *The University of Alabama, United States*
Moh'd A. Al-Nimr, *Jordan University of Science and Technology, Jordan*
Mohsen Sheikholeslami, *Babol Noshirvani University of Technology, Iran*
Mustafa Turkyilmazoglu, *Hacettepe University, Türkiye*
N.K. Anand, *Texas A&M University, United States*
Omid Mahian, *Xi'an Jiaotong University, Xi'an, China*
Sergio Nardini, *Seconda Università degli Studi di Napoli, Italy*
Wei-Mon Yan, *National Chiao Tung University, Taiwan*

Abstracting and Indexing: Directory of Open Access Journals (DOAJ), EBSCO Host Online Research Databases, Web of Science, Emerging Sources Citation Index (ESCI), Scopus, TRDizin, MIAR, Scilit, OUCI, Research4Life, Ideal Online, Sherpa Romeo, ASCI

Journal Description: The journal is supported by Yildiz Technical University officially, and is a blind peer-reviewed free open-access journal, published bimontly (January-March-May-July-September-November).

Publisher: Yildiz Technical University

Editor-in-Chief: Prof.Dr. Ahmet Selim Dalkılıç, dalkilic@yildiz.edu.tr

Language of Publication: English

Frequency: Bimontly (6 issues per year)

Regular Issues: January (1) - March (2) - May (3) - July (4) - September (5) - November (6)

Publication Type: Online e-version

Journal of Thermal Engineering is supported by Yildiz Technical University officially, and is a blind peer-reviewed free open-access journal, published bimontly. • Journal of Thermal Engineering is a peer reviewed open access journal established as an origin for research in Heat Transfer and Thermodynamics mainly. • Journal of Thermal Engineering make every effort to ensure the accuracy of all the information (the "Content") contained in our publications. However, Journal of Thermal Engineering, our agents, and our licensors make no representations or warranties whatsoever as to the accuracy, completeness, or suitability for any purpose of the Content. Any opinions and views expressed in this publication are the opinions and views of the authors, and are not the views of or endorsed by Journal of Thermal Engineering. The accuracy of the Content should not be relied upon and should be independently verified with primary sources of information. Journal of Thermal Engineering shall not be liable for any losses, actions, claims, proceedings, demands, costs, expenses, damages, and other liabilities whatsoever or howsoever caused arising directly or indirectly in connection with, in relation to, or arising out of the use of the Content.

ISSN 2148-7847

Journal of Thermal Engineering

Volume 12 Number 1 Year 2026

CONTENTS

Research Articles

1 **Performance assessment of solar based trigeneration system using organic rankine cycle and ejector refrigeration system**
Yunis KHAN, K.K. SIVAKUMAR, P. M. G. Bashir ASDAQUE, D. APPARAO, Rajesh KUMAR, Kumar GAURAV, Lalit BATRA

16 **Performance investigation of high-powered light emitting diodes using copper and silicon-oxide based nanofluid filled heat pipe**
Ashish KHUDAIWALA, Rupesh PATEL

29 **Experimental evaluation of a dual-use solar cooker for indoor and outdoor applications**
Faiq SAID, Qazi Muhammad YASEEN, Sahibzada Naveed Inayat ULLAH, Muneeb AHMAD, Farhan AHMED, Zakir ULLAH, Mir Muhammad Mehran KHAN, Ibrar HUSSAIN

50 **Kinetics of UV degradation of hydrogen sulfide without oxidization by Homotopy Perturbation Method**
V. Sreelatha DEVI, K. SARANYA, D. VIJAYABALAN, K A. Niranjan KUMAR, Muthumari G, Banu Priya V

72 **Evaluation of infrared radiations from top of the atmosphere through artificial neural network modeling**
Usama Ayub YOUSUFZAI, Muhammad Jawed IQBAL, Faisal Khan AFRIDI

88 **Enhanced heat transfer with iron oxide nanofluids: SYNTHESIS and performance evaluation**
Mehdi AMIRI, Rasoul KARIMI, Iman ABBASPOUR

99 **Numerical study of 3d thermal-flow in a scraped surface heat exchanger**
Fatima Zohra BAKHTI, Belqassim Elmahdi ZERGUINE

115 **Pyrolysis, kinetics, and thermodynamic analysis of neem seed cake for the sustainable resource recovery**
Manisha RANI, Rohan R. PANDE, Kamalesh A. SORATE

ISSN 2148-7847

Journal of Thermal Engineering

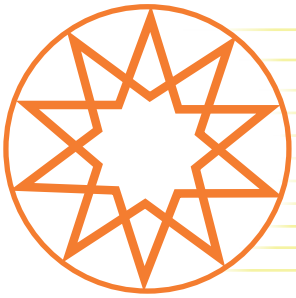

Volume 12 Number 1 Year 2026

128 **Improvement of the thermal performances of a parabolic trough solar concentrator with concentric receiver tube and nanofluid**
Djemaa GUERRAICHE, Kamel ZOUGGAR, Khelifa GUERRAICHE, Antar TAHIRI, Zied DRISS, Cherif BOUGRIOU, Aya YAHA

144 **Opposition-based algorithm for the optimization of shell-and-tube heat exchangers**
Elaheh KHOSRAVIAN, Mohammad B. AHMADI

156 **Turbulent forced convection of hybrid nanofluids in a three-dimensional L-shaped channel: Modeling, analysis, and regression model development**
Amanullah PHULPOTO, Abid A. MEMON, M. Asif MEMON, Ubaidullah YASHKUN, Adebowale Martins OBALALU

182 **Introducing an optimal pressure ratio for aircraft design and investigating the effect of nozzle efficiency on the jet engine's performance**
Hadi SIYAHI, Mehdi SIYAHI, Mohsen FALLAH, Zahra MOHAMMADI

192 **Exergy, energy, exergoenvironmental assessment of a novel combined helium Brayton cycle and transcritical CO_2 cycle for solar power tower applications**
Yunis KHAN, Deepak SINGH, Shailendra SINHA, K.S. BHOLE, D. APPARAO

212 **Analysis of thermal, chemical and physical properties of paraffin and beeswax blended fuels for hybrid rocket applications**
Saravanan G, Avi THUMAR, Ayush DEVAK, Amritansh SINGH

229 **Residential building thermal transmittance simulation-based analysis in Tehran city with an approach to assess wall insulation**
Ashkan HASSANI, Shooka Khoshbakht BAHRAMANI

254 **Design of optimized exhaust system for two stroke unmanned aerial vehicle engine**
Faiq SAID, Zeeshan KHAN, Majid BASEER, Muhammad Nouman RASHID, Muhammad BILAL, Riaz HUSSAIN

278 **Thermo-diffusion effects on mhd casson blood flow in an inclined muti-stenosed artery**
Harshad PATEL, Snehal PATEL, Nilesh PATEL

ISSN 2148-7847

Journal of Thermal Engineering

Volume 12 Number 1 Year 2026

291 **Experimental study of parabolic dish collector based solar cooker with different thermal energy storage system**
M.K. GAUR, Amit SHRIVASTAVA, Pawan AGRAWAL, R.K. PANDIT, Parul SAXENA

303 **Analysis of a 5.0 kWp solar rooftop system: Techno-economic, design, and simulation using pvsyst**
Anand KUSHWAH, Supriya RAJ, Nikhil PATEL, Ashish GAURAV, Om Prakash SAHANI, Kapil GUPTA

323 **Energy-efficient refrigeration: The role of TiO_2 nanoparticles in R600a/R290 refrigerant blends**
M.Ravi KUMAR, R.Satya MEHER, A.Swarna KUMARI

335 **Assessment of combustion, performance, and emissions in a direct injection compression ignition engine using blends of jatropha, karanja, waste cooking, sunflower, and palm oil methyl esters with diesel**
Venkata Ramesh MAMILLA, G. Lakshmi Narayana RAO

349 **Oscillating piezofan effects on natural and forced convection flow in a vertical channel with protruding heat sources**
Salim Ibrahim HASAN, Mehmet Akif EZAN, Serhan KÜÇÜKA

365 **Magnetohydrodynamic mixed convection within a ventilated cavity crossed by a nanofluid: Effect of the obstacle position**
Mourad MODERRES, Seddik KHERROUBI, Abdelkader BOUTRA, Abdelhakim SETTAR, Chaouki Ghenai, Djelloul AZZOUZI, Hakan F. OZTOP

Review Articles

385 **Phase change materials (PCMs) used in buildings: A critical review**
Soukaina TOUMZINE, Hanane MOULAY ABDELALI

408 **Optimizing biomass fuel utilization for GHG emission reduction: An action plan for efficient fuel blending and sustainable practices**
K RAVI, M. MATHESWARAN

Journal of Thermal Engineering
Web page info: https://jten.yildiz.edu.tr
DOI: 10.14744/thermal.0001024

Research Article

Performance assessment of solar based trigeneration system using organic rankine cycle and ejector refrigeration system

Yunis KHAN[1,*], K.K. SIVAKUMAR[2], P. M. G. Bashir ASDAQUE[3], D. APPARAO[4], Rajesh KUMAR[5], Kumar GAURAV[5], Lalit BATRA[6]

[1]*Department of Mechanical Engineering, Indian Institute of Technology (ISM), 826004, Jharkhand, India*
[2]*School of Liberal Arts and Sciences, Mohan Babu University, 517102, Andhra Pradesh, India,*
[3]*Department of Mechanical Engineering, Dayananda Sagar University, Banglore, India*
[4]*Department of Mechanical Engineering, Aditya Institute of Technology and Management, 532201, Andhra Pradesh, India*
[5]*Department of Mechanical Engineering, Sandip University, Bihar, 847235, India*
[6]*Department of Applied Sciences (Mechanical), Bharati Vidyapeeth College of Engineering, New Delhi, 110063, India*

ARTICLE INFO

Article history
Received: 24 September 2024
Accepted: 12 May 2025

Keywords:
Exergy; Exergoenvironmental Impact; Solar Power Tower; Helium Brayton Cycle; Ejector Refrigeration System

ABSTRACT

In this study, a novel trigeneration system was developed to harness high-temperature solar energy from a solar power tower, enabling simultaneous generation of power, heating, and cooling effects. The system comprises a Brayton cycle utilizing helium as the working fluid, complemented by an organic Rankine cycle with an ejector refrigeration system to recover waste heat from the Brayton cycle. Energy, exergy, and exergoenvironmental analyses were conducted on the proposed system using engineering equation solver software. The heating and cooling effects were generated at 50°C and 10°C, respectively for building applications such as hospitals and hostels. The proposed plant was obtained the exergy and energy efficiencies of 25.12% and 23.30%, respectively. Additionally, cooling loads, heating loads and power output were obtained as 8.25 kW, 60.52 kW and 14998 kW, respectively. Moreover, the exergoenvironmental impact coefficient has a high value of 4.028 due to the lower exergy efficiency of the plant. The exergetic stability factor was determined to be 0.2483.

Cite this article as: Khan Y, Sivakumar KK, Asdaque PMGB, Apparao D, Kumar R, Gaurav K, Batra L. Performance assessment of solar based trigeneration system using organic rankine cycle and ejector refrigeration system. J Ther Eng 2026;12(1):1−15.

INTRODUCTION

By 2040, the global energy demand will have increased by at least 50%. Future security and sustainability depend on the production of carbon-free energy [1, 2]. The remarkable concentrated solar power (CSP) system can provide the requirement for safe and reliable electricity [3]. The CSP is using nowadays for high temperature power generation. Critical pressure of supercritical sCO2 cycle is higher than that of any other cycles [4, 5]. The sCO_2 is useful since it

***Corresponding author.**
*E-mail address: yuniskhan21@gmail.com

This paper was recommended for publication in revised form by Editor-in Chief Ahmet Selim Dalkilic

Published by Yıldız Technical University Press, İstanbul, Turkey
Yıldız Technical University. This is an open access article under the CC BY-NC license (http://creativecommons.org/licenses/by-nc/4.0/).

is chemically stable, non-flammable, environmentally friendly, inexpensive, and non-toxic. The CO2 cycles have increased interest recently due to their better performance at high-temperature waste recovery, also it uses the compact machinery due high density as critical points [6].

The conventional Rankine cycles and closed Brayton cycle could be employed in SPT facilities to convert heat into electricity based on their heat source temperature. Due to its benefits, including its compact size and efficient operation, the sCO2 Brayton cycle has gained a lot of attention lately [7-9]. The advantages and precise sCO_2 system layouts for use in nuclear and solar power plants were published by Guo et al. [10]. Also, they discussed the key aspects of the application and key issues related to the sCO2 cycles technology. Gkountas et al. [11] investigated the Al2O3 nanofluid for improving heat transfer led to a 0.9% decrease in heat exchanger length and a 14% decrease in pressure drop as a result in the sCO_2 system. Chai and Tassuo [12] did detailed examination of the heat exchanger parameters used in the helium and sCO2 Brayton cycles. They found that stainless steel is the ideal material that can work up to 650°C of temperature, whereas alloys based on nickel are suggested for use at greater temperatures. Also recently, Qin et al. [13] studied the system of the recompression sCO2 cycle Brayton cycle combined with the transcritical CO_2 (tCO_2) refrigeration system for recovering waste heat from the marine turbine for simultaneous refrigeration and power production. The observed COP (coefficient of performance) and levelized cost of electricity (LCOE) and waste heat recovery efficiency of the proposed system were 3.059, 18.348 $/kWh, and 0.651, respectively. At the period also Khatoon and Kim [14] proposed the sCO2 Brayton cycle operated by the SPT system with thermal storage. Proposed system fluctuation energy efficiency was found to be 39% to 45%. Using the regeneration and recompression cycles, the calculated mean net power output is 37.17 MW and 39.04 MW, respectively. Khan and Mishra [15] looked into another sCO2 technique for SPT plants. They observed a sCO2 recompression cycle with intercooling at the main compressor coupled with ORC, and their results for energy and exergy efficiency at the 0.95 kW/m2 of DNI (direct normal irradiation) were 54.42% and 80.39%, respectively. The most effective waste recovery was achieved when the sCO_2 cycle was combined with an ORC or another bottoming cycle.

In addition to the sCO2, helium is a hot topic of research as the working fluid in the Brayton cycle nowadays due to helium working better than CO2 at elevated temperatures, and Brayton cycles with helium can achieve more efficiency than that of the CO2 Brayton cycles, according to previous studies [28, 29]. To fulfil the above statement recently, a combined HBC (helium Brayton cycle) and cascaded vapor compression-absorption refrigeration system based on SPT was presented by Khan and Mishra [9] for the combined low-temperature cooling, heating, and power generation. The thermal, exergy efficiency, and power output of the recommended plant were observed to be 39.53%, 28.82%, and 14,865 kW, respectively. However, observed coefficients of performance (COP) for heating and cooling were 1.539 and 1.5391 at 80°C and -20°C of the generator and evaporator temperatures, respectively. Zhou et al. [20] employed the vapor absorption cycle as the bottoming cycle to cool the HBC's inlet while using the HBC as the topping cycle. They found optimized exergy efficiency outperformed the basic cycle by 14.5%. Bi and Lu [18] suggested a hydrogen liquefaction method based on HBC. They arrived at the conclusion that the proposed technique could liquefy gas and make hydrogen with less energy. Li et al. [19] designed three regenerative HBCs to enhance the efficiency of SPT operating at ultra-high temperatures (>1300°C). These cycles included a single-reheat cycle with intercooling, a double-reheat cycle with intercooling, and one with intercooling. After conducting a study, they concluded that when a temperature differential higher than 1000°C is required, only the cycle with intercooling could satisfy the criteria.

Many research studies have been conducted in the area of trigeneration systems with ejector refrigeration systems (ERS). For example, Wang et al. [21] looked into a trigeneration plant that uses flat plate collectors to absorb solar energy to power an ejector and an ORC. This system has an extra auxiliary heat source in addition to a storage system. Mishra et al. [22] proposed a combined cycle for power generation and cooling with dual ERS, simultaneously. They did exergoeconomic analysis on it. They concluded that the exergy and energy efficiency were improved by 6% and 11%, respectively, as compared to the basic system. They also found that the cost of the system was decreased by 11.7% as compared to a simple ERS. Ogaili et al. [23] developed a trigeneration system, which uses a zeotropic mixture as the working fluid and ERS powered by solar heat, designed to generate power, heat, and cool simultaneously. They came to the conclusion that the plant was assigned 4062.6 kW of power for heating and cooling, 1616.4 kW for cooling, and 51.52 kW for both. Saladi et al. [24] conducted an exergoeconomic, thermodynamic, and exergoenvironmental analysis of a solid oxide-based trigeneration system, incorporating an ERS for cooling. Moreover, the average environmental impact per unit of energy output was calculated to be 2877 mPts/GJ.

The literature given above suggests that not much study has been done on the Brayton cycle, that helium is utilized as the working fluid, and that a concentrated solar power tower system serves as the heat source for the electricity production. In most previous investigations, the ORC was used as the bottoming cycle, such as [25, 26]. In this study, however, a bottoming system that integrated an ejector system with an ORC was utilized to generate additional electricity and provide simultaneous heating and cooling benefits for buildings like hospitals and hostels. For the first time, ORC-ERS was employed in this study as the bottoming cycle for the HBC system run by the SPT plant. This statement defines the present research novelty. The goals of the current investigation are

- To develop an ejector refrigeration-based tri-generation system for the SPT plant that would generate cooling and heating effects at 10°C and 50°C, respectively, for use in buildings like hospitals and hostels.
- To investigate the performance of the proposed trigeneration system based on exergy, energy, and exergoenvironmental (3E) analysis.
- To use parametric analysis to look into how the various SPT system key factors and combined cycle affect the plant's performance.
- To compare the suggested novel trigeneration system's performance with that of earlier comparable conventional systems.

SYSTEM DESCRIPTION

The proposed system schematic diagram is presented in Figure 1. The SPT sub-system is used as the heat source to drive the proposed combined system. Air has been used as the heat transfer fluid (HTF) due to its free availability. The HBC takes heat from the SPT subsystem via the internal heat exchanger (IHE). Helium, as opposed to sCO_2, is the working fluid in the topping cycle. A waste heat recovery unit (WHRU) is utilized to transfer residual heat to the bottoming combined ORC-ERS. The flow direction of the working fluid can be elucidated by considering that heated, high-temperature helium enters the helium turbine (HT) (from states 4 through 5) via the IHE, where it expands after receiving heat from the SPT system. Subsequently, the expanded stream proceeds to the recuperator (from states 5 to 6), where a cooler stream absorbs the heat from the expanded stream. Finally, any remaining heat is absorbed by the ORC-ERS at the bottom through the WHRU (from states 6 to 7). The helium compressor (HC) was used to further compress it (states 1 to 2). The cold stream of helium travels to the IHE after passing through the HTR (states 2 to 3). In contrast

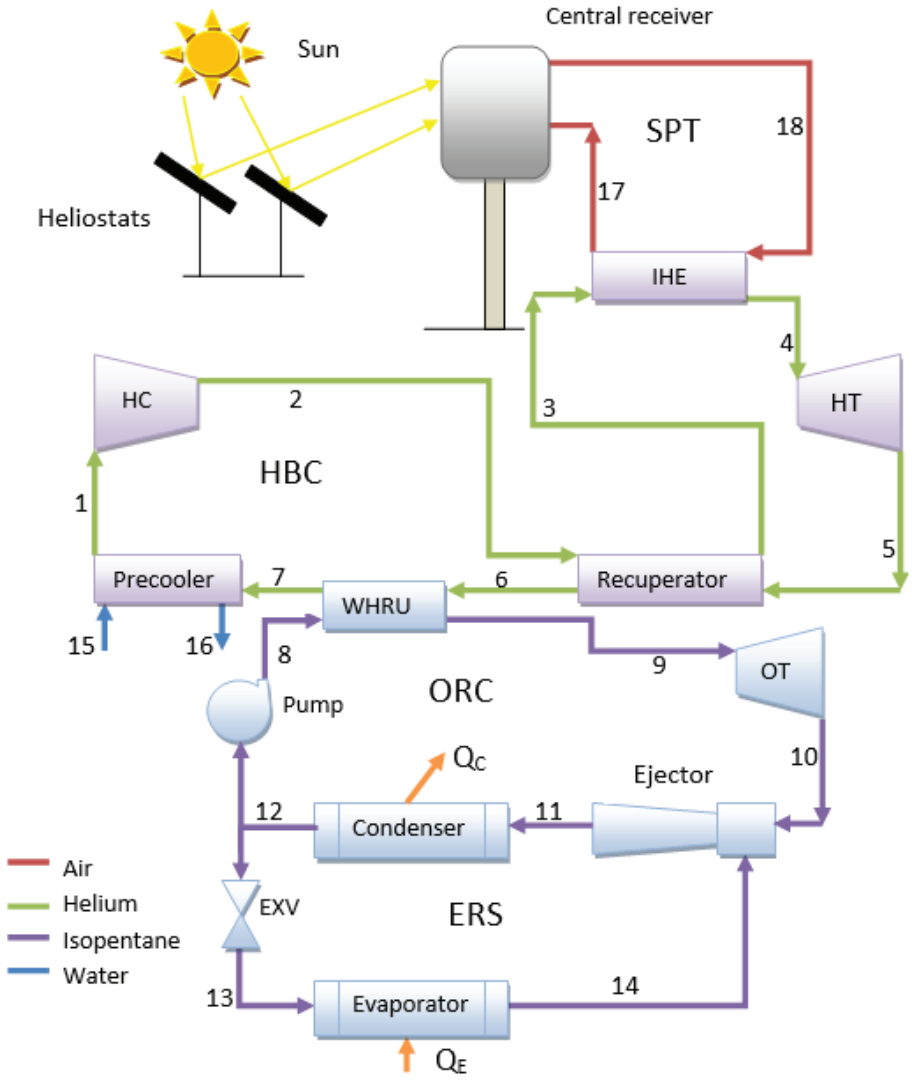

Figure 1. Diagram of the proposed plant.

to the topping cycle, the bottoming combined ORC-ERS is heated through the WHRU. Through the bottoming cycle, cooling and heating from the condenser were obtained to fulfil industrial design. The ORC-ERS system under study uses isopentane as its working fluid. This response should be trusted because isopentane has been studied in similar setups in other research studies [26, 27]. This study is particularly noteworthy for its choice of isopentane, which has not previously been examined in the context of ORC-ERS. The critical pressure and temperature of the anhydrous fluid isopentane are 187.2°C and 3380 kPa, respectively. This fluid is classified as A3 ASHRAE safe, possesses a low GWP of 20, and has almost zero ODP [25–27].

PERFORMANCE EVALUATION

Thermodynamic Evaluation

The following assumption was made (1) each component works in a steady state with one-dimensional flow. (2) The pressure loss of the components is assumed to be as indicated in Table 1. (3) Kinetic and potential energy are disregard (4) Turbine, pump, and compressor isentropic efficiencies are assumed and reported in Table 1. (5) Saturated liquid condition is considered at pump inlet. (6) The blower or compressor is not shown in the SPT circuit because in the thermodynamic analysis it makes negligible changes [9, 20].

Table 1. Simulation data for base case

Parameter	Value	Reference
SPT		
Receiver efficiency (η_{rec})	0.75	[20]
Aperture area of receiver (A_{rec})	68.1 m^2	[16]
Efficiency of heliostat field (η_{field})	0.6428	[16]
Each heliostat area (A_{hel})	9.45 × 12.84 m^2	[16,25]
Number of heliostat (N_{hel})	624	[16]
Solar irradiation (DNI)	850 W/m^2	[25]
HBC-ORC-ERS		
HT inlet temperature (T_4)	800 °C	[16]
Isentropic efficiency of HC (η_{HC})	0.89	[16]
HC inlet pressure (P_1)	2500 kPa	[16]
Effectiveness of heat exchanger (ε)	0.95	[30]
Isentropic efficiency of HT (η_{HT})	0.90	[9,20]
OT Isentropic efficiency (η_{OT})	0.8	[16]
Maximum temperature of ORC (T_8)	197.2 °C	[16]
Condenser pinch	5 °C	[16]
WHRU pinch	10 °C	[16,25]
Sun apparent temperature (T_{Sun})	4500 K	[30]
Ambient temperature (T_o)	25 °C	[30]
Atmospheric pressure (P_o)	101.3 kPa	[30]
Mixing efficiency	0.85	[31]
Nozzle efficiency	0.9	[31]
Diffuser efficiency	0.95	[31]

For the purpose of thermodynamic analysis, the entire system is divided into three subsystems: the solar subsystem, the HBC, and the ORC-ERS. Considering each components as the thermodynamic system then these are simulated using the computer program engineering equation solver (EES). Using the control volume approach, the equation for the energy and exergy balance equation in steady state conditions is given as:

$$\dot{Q}_{CV} - \dot{W}_{CV} + \sum(\dot{m}_i h_i) - \sum(\dot{m}_e h_e) = 0 \quad (1)$$

$$\dot{ED} = \dot{EX}_{in} - \dot{EX}_{out} \quad (2)$$

Where, $\dot{E}X_{in}$ and $\dot{E}X_{out}$, represent the exergy inlet and outlet to control volume, respectively. The work and heat flow from the control volume are denoted by $\dot{W}_{CV}$ and $\dot{Q}_{CV}$ respectively. After neglecting potential and kinetic energy and chemical exergy, the physical flow exergy can be expressed as;

$$\dot{EX}_j = \dot{m}\cdot[(h_j - h_0) - T_0(s_j - s_0)] \quad (3)$$

Some amount of the heat is rejected to atmosphere because of the temperature difference between heliostats and the environment. The remaining solar heat is received by the receiver [16, 25];

$$\dot{Q}_{rec,in} = \eta_{field}\cdot\dot{Q}_{Sun} = \eta_{field}\cdot DNI \cdot A_{hel}\cdot N_{hel} \quad (4)$$

Where, heliostat field efficiency η_{field} is expressed as [16]:

$$\eta_{field} = \eta_{cos}\cdot\eta_{s\&b}\cdot\eta_{int}\cdot\eta_{att}\cdot\eta_{ref} \quad (5)$$

Where, η_{ref}, η_{int}, $\eta_{s\&b}$, η_{cos} and η_{att}, are represents heliostats reflectivity, interception efficiency, shading and blocking, cosine effect efficiency, atmospheric attenuation efficiency and respectively.

The calculations of these efficacies are not scope of this study and its true values were taken from existing solar power plant [16]. Receiver efficiency and heat absorbed by receiver both are stated as [30]:

$$\eta_{rec} = \frac{\dot{Q}_{rec,net}}{\dot{Q}_{rec,in}} \quad (6)$$

$$\dot{Q}_{rec,in} = \dot{Q}_{rec,net} + \dot{Q}_{rec,loss} = \dot{m}_{air}(h_{18} - h_{17}) + \dot{Q}_{rec,loss} \quad (7)$$

Where, $\dot{Q}_{rec,loss}$ is the heat lost to the environment due to conduction, convention and radiation heat loss.

The modelling equations of the each components are listed in Table 2. The energy and exergy efficiency of the proposed plant are expressed as [30, 31]:

$$\eta_{en} = \frac{W_{net}+Q_E+Q_C}{\dot{Q}_{Sun}} \quad (8)$$

$$\eta_{ex} = \frac{\dot{W}_{net}+\dot{Q}_E\cdot\left(1-\frac{T_0}{T_E}\right)+\dot{Q}_C\cdot\left(1-\frac{T_0}{T_C}\right)}{\dot{Q}_{Sun}\cdot\left(1-\frac{T_0}{T_{Sun}}\right)} \quad (9)$$

Where, T_{Sun} represents the apparent sun temperature used as the exergy calculation [30]. However, $\dot{W}_{net}$ of the plant is expressed as:

$$\dot{W}_{net} = \dot{W}_{HT} - \dot{W}_{HC} + \dot{W}_{OT} - \dot{W}_{pump} \quad (10)$$

Exergoenvironmental Analysis

Examining the sustainability of the power system now requires an investigation into its environmental impact alongside thermal analysis. Only thermodynamic analyses of the energy generation system is not sufficient. Therefore, environmental analysis along with the exergy is also needed which estimate sustainability. The effect of exergy efficiency and exergy destruction rate on the environment is what determines the exergoenvironmental analysis. Utilizing sources [5], the following exergoenvironmental performance metrics have been examined and discussed. The exergoenvironmental impact factor (f_{ei}) has been determined to investigate the environmental impacts. This also show how to mitigate environmental hazards by

Table 2. Modeling equations for each component

Components	Energy balance equations	Exergy balance equations
Heliostat field	$\dot{Q}_{rec,in} = \eta_{field}\cdot DNI \cdot A_{hel}\cdot N_{hel}$	$\dot{Q}_{Sun}\cdot\left(1-\frac{T_0}{T_{ref,Sun}}\right) = \dot{Q}_{rec,in}\cdot\left(1-\frac{T_0}{T_{ref,hel}}\right)+\dot{E}D_{hel}$
Receiver	$\dot{Q}_{rec,in} = \dot{m}_{air}(h_{18}-h_{17})+\dot{Q}_{rec,loss}$	$\dot{E}X_{17}+\dot{Q}_{rec,in}\cdot\left(1-\frac{T_0}{T_{ref,hel}}\right) = \dot{E}X_{18}+\dot{Q}_{rec,loss}\cdot\left(1-\frac{T_0}{T_{rec}}\right)+\dot{E}D_{rec}$
IHE	$\dot{Q}_{IHE} = \dot{m}_{air}\cdot(h_{18}-h_{17})+\dot{m}_{He}\cdot(h_4-h_3)$	$\dot{E}X_{16}-\dot{E}X_{17} = \dot{E}X_4-\dot{E}X_3+\dot{E}D_{IHE}$
Helium turbine	$\dot{W}_{HT} = \dot{m}_{He}\cdot(h_4-h_5)$ $\eta_{HT} = \frac{(h_4-h_5)}{(h_4-h_{5s})}$	$\dot{E}X_4 = \dot{E}X_5+\dot{W}_{HT}+\dot{E}D_{HT}$
Helium compressor	$\dot{W}_{HC} = \dot{m}_{He}\cdot(h_2-h_1)$ $\eta_{HC} = \frac{(h_{2s}-h_1)}{(h_2-h_1)}$	$\dot{E}X_1 = \dot{E}X_2-\dot{W}_{HC}+\dot{E}D_{HC}$
Recuperator	$(h_3-h_2) = (h_5-h_6)$ $\varepsilon_{Recuperator} = \frac{(T_3-T_2)}{(T_5-T_2)}$	$\dot{E}X_5-\dot{E}X_6 = \dot{E}X_3-\dot{E}X_2+\dot{E}D_{Recuperator}$
WHRU	$\dot{m}_{He}\cdot(h_6-h_7) = \dot{m}_g\cdot(h_9-h_8)$	$\dot{E}X_6-\dot{E}X_7 = \dot{E}X_9-\dot{E}X_8+\dot{E}D_{WHRU}$
Precooler	$\dot{m}_{He}\cdot(h_7-h_1) = \dot{m}_{water}\cdot(h_{16}-h_{15})$	$\dot{E}X_7-\dot{E}X_1 = \dot{E}X_{16}-\dot{E}X_{15}+\dot{E}D_{Preooler}$
Condenser	$\dot{Q}_C = \dot{m}_c(h_{11}-h_{12})$	$\dot{E}X_{11}-\dot{E}X_{12} = \dot{Q}_C\cdot\left(1-\frac{T_0}{T_C}\right)+\dot{E}D_C$
ORC turbine	$\dot{W}_{OT} = \dot{m}_g(h_9-h_{10})$ $\eta_{OT} = \frac{(h_9-h_{10})}{(h_9-h_{10s})}$	$\dot{E}X_9 = \dot{E}X_{10}+\dot{W}_{OT}+\dot{E}D_{OT}$
Pump	$\dot{W}_P = \dot{m}_g(h_8-h_{12})$ $\eta_P = \frac{(h_{8s}-h_{12})}{(h_8-h_{12})}$	$\dot{E}X_{12} = \dot{E}X_8-\dot{W}_P+\dot{E}D_P$
Expansion valve	$h_{12} = h_{13}$	$\dot{E}X_{12}-\dot{E}X_{13} = \dot{E}D_{EXV}$
Evaporator	$\dot{Q}_E = \dot{m}_c(h_{14}-h_{13})$	$\dot{E}X_{13}-\dot{E}X_{14} = \dot{Q}_E\cdot\left(1-\frac{T_0}{T_C}\right)+\dot{E}D_E$
Ejector	$\dot{m}_c\cdot h_{11} = \dot{m}_g\cdot h_{10}+\dot{m}_e\cdot h_{14}$	$\dot{E}X_{10}+\dot{E}X_{14} = \dot{E}X_{11}+\dot{E}D_{ejector}$

minimizing irreversibilities. Its definition is provided as the ratio of total exergy destroyed to total exergy available at the system's input [5]:

$$f_{ei} = \frac{\dot{E}D_{total}}{\dot{E}X_{Sun}} \quad (11)$$

The exergoenvironmental impact coefficient (C_{ei}), which is the inverse of exergy efficiency, is highly commended for the system under study due to its low value. Its value of '1' indicates that the system under investigation is in an optimal state and is therefore good. This can be explained mathematically as:

$$C_{ei} = \frac{1}{\eta_{ex}} \quad (12)$$

A system's environmental impact is assessed using the exergoenvironmental impact index. Performance of the system improves as the exergoenvironmental effect index (θ_{ei}) value decreases.

$$\theta_{ei} = C_{ei} \cdot f_{ei} \quad (13)$$

Exergy stability factor (f_{es}) should have its ideal value 'one' or approaching to 'one'. Therefore, system performed better on exergoenvironmental point of view. It can be represented as:

$$f_{es} = \frac{\dot{E}X_{out}}{\dot{E}X_{out} + \dot{E}D_{total}} \quad (14)$$

The exergoenvironmental impact improvement (θ_{eii}) is used to evaluate how relevant the system is to environmental conditions. A larger value of this parameter is regarded to be better for the environment than the exergoenvironmental impact index. It can be said to be:

$$\theta_{eii} = \frac{1}{\theta_{ei}} \quad (15)$$

The exergoenvironmental impact improvement and exergetic stability factor make up the exergetic sustainability index (θ_{est}). A higher value for the energetic sustainability index is advantageous to the system. The system under examination is bad for the environment if it is lower. It can be stated mathematically as;

$$\theta_{est} = \theta_{eii} \cdot f_{es} \quad (16)$$

MODELING VALIDATION

The proposed system was validated with the previous studies. HBC was validated with the study of Zhou et al. [20] as shown in Figure 2. Results show the accuracy of the present model with literature. The bottoming ORC-ERS is validated using research data from Dai et al. [35] at baseline conditions. Various factors, including enthalpies and the heat and work interactions, are compared between the findings of Dai et al. [35]. The maximum discrepancy found was 1.5%, a small percentage indicating high accuracy, according to the comparison data in Table 3.

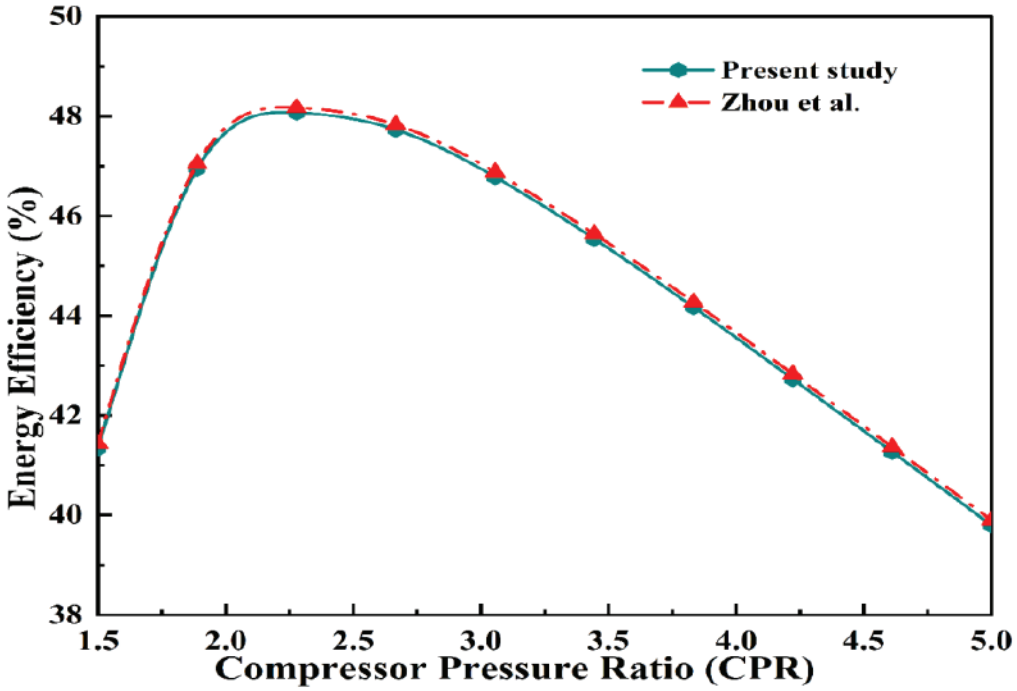

Figure 2. Validation of results of HBC.

Table 3. ORC-ERS Validation

Parameters	Present study	Dai et al. [35]	Deviation (%)
h_9	477.70	474.2	0.73
h_{10}	451.40	451	0.08
h_{11}	447.12	445.4	0.38
h_{12}	221.20	220.1	0.49
h_{13}	220.90	220.1	0.36
h_{14}	376.54	375.5	0.27
h_8	220.97	220.8	0.07
Q_E	60.70	60.4	0.49
$\dot{m}_c$	5.39	5.310	1.5
$\dot{m}_e$	0.391	0.389	0.51
$\dot{W}_{net}$	111.20	110.7	0.004

RESULTS AND DISCUSSION

Results at Initial Conditions

In this section the results of the proposed system were obtained at the base case. The thermodynamic properties at the state have been calculated by the inbuilt libraries of the EES software and listed in Table 4. However, the results at initial conditions are given in Table 5. The 14,998 kW of power was produced by the overall power plant with 23.30% of overall energy efficiency. Most of the energy (22,989 kW, or 35.72% of the total solar heat) is lost in the heliostat field, highlighting the significance of the heliostat field's design in SPT systems. While the output in terms of net power output was about 13365 kW, the standalone HBC received the heat from the IHE at a rate of about 31027 kW. Its energy efficiency was obtained as 43.07% at given operating conditions. Apart from this, the standalone ORC-ERS system obtained its energy conversion efficiency as 12.26%. It is absorbed by the 13261 kW of heat through the WHRU in terms of waste heat of topping HBC. A portion of the energy is converted into practical output for building purposes, such as electricity (1567.23 kW) through the organic turbine, heating effect (60.5 kW) through the condenser, and cooling effect (8.25 kW). Table 5 shows that the combined system (HBC-ORC-ERS) has a relatively high energy efficiency (51.68%).

Table 4. Thermodynamic properties at each state

State	Working Fluid	Pressure (kPa)	Temperature (°C)	Enthalpy (kJ/kg)	Entropy (kJ/kg·°C)	Exergy (kW)
1	Helium	2500	30	34.04	-6.569	39428
2	Helium	6250	180.8	828.6	-6.373	53992
3	Helium	6188	511	2541	-3.517	71033
4	Helium	6064	850	4301	-1.61	94593
5	Helium	2577	547.4	2720	-1.463	62455
6	Helium	2551	217.5	1007	-4112	44189
7	Helium	2525	103.8	417.2	-5.459	40460
8	Isopentane	3000	93.8	-179.5	-1.192	556.5
9	Isopentane	3000	197.5	281.7	-0.1157	4111
10	Isopentane	1500	172.1	259.6	-0.1069	3484
11	Isopentane	600	162.1	257.5	-0.01964	4622
12	Isopentane	600	50	85.9	-0.197	725.8
13	Isopentane	600	10	-15.87	-1.197	435.5
14	Isopentane	600	10	-15.87	-1.197	290.3
15	Water	100	25	104.90	0.36	0
16	Water	100	30	125.80	0.45	35.98
17	Air	101.3	561	859.9	6.763	12939
18	Air	101.3	1125	1513	7.359	38283

Table 5. Results obtained from exergy-energy evaluation*

Subsystems	Energy analysis results				Exergy analysis results			
	Input (kW)	Output (kW)	Loss (kW)	Energy efficiency	Input (kW)	Output (kW)	Destruction (kW)	Exergy efficiency
Heliostat field	64358	41369	22989	64.26%	60094	38628	21465	64.27%
Solar receiver	41369	31027	10342	75%	38628	22515	16113	58.28%
HBC	31027	13365	17662	43.07%	22515	13365	9150	59.36%
ORC-ERS	13261	1633	11634	12.26%	3729	1736	1993	46.55%
HBC-ORC-ERS	31027	14998	16035	48.33%	22515	15101	8014	64.40%
Overall plant	64358	14998	49366	23.30%	60094	15101	45593	25.12%

*T_4= 800°C, CPR=2.3, *T_8 = 197.5°C, DNI=850W/m^2;

As the results of the exergy analysis show, there is a significant irreversibility was found in SPT system since solar radiation is an excellent energy source with a heat source that is extremely hot, approximately 4500 K and receiver absorbed the heat at 1000 °C of temperature. The heliostat field has highest exergy destruction among the other components [16, 20]. The heliostat's energy efficiency was observed to be 64.27%. The absence of combustion, the primary factor contributing to irreversibility in conventional power systems, means that there is no appreciable temperature differential between the helium and HTF in the IHE. As a result, the combined cycle (HBC-ORC-ERS) has a high exergy efficiency of 64.4%. However, because of the substantial exergy destruction in the heliostat field and receiver, the power the plant's overall exergy efficiency is quite poor. The highest exergy destruction was in the heliostats and the lowest in the expansion valve, having values of 21465 kW (47.52% of total exergy destruction) and 102.5 kW, respectively. The helium turbine has the highest energy efficiency (97.25%) out of all the components. Around 59.36% was the energy efficiency determined by the solo HBC. The ORC-ERS cogeneration system achieved an energy efficiency of around 46.55%. It was determined that the ORC-ERS's addition of extra components was the cause of the decreased energy efficiency. The trigeneration system run by the SPT plant was determined to have a plant energy destruction of 45593 kW. Nonetheless, this plant achieved an energy efficiency of roughly 25.12%.

Apart from exergy, energy evaluation of the values of the exergo-environmental performance parameters at the base case has been listed in Table 6. It was seen that the exergoenvironmental impact coefficient has a large value (4.028) due to the lower exergy efficiency of the plant. It

Table 6. Values of the exergo-environmental performance parameters at base case

Parameters	Values
Exergoenvironmental impact factor (f_{ei})	0.7517
Exergoenvironmental impact coefficient (C_{ei})	4.028
Exergoenvironmental impact index (θ_{ei})	3.028
Exergy stability factor (f_{es})	0.2483
Exergoenvironmental impact improvement (θ_{eii})	0.3302
Exergetic sustainability index (θ_{est})	0.0819

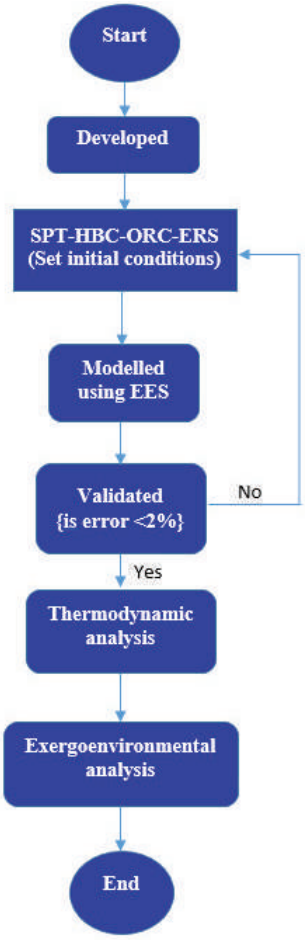

Figure 3. Flowchart of step-by-step methods during simulations.

revealed that there is still much scope to reduce the environmental effects. The exergetic stability factor should be one. However, it was found to be 0.2483; it means still this system affected the environment from a stability point of view. To enhance the exergetic stability of the system and move closer to the ideal value of 1, the following action can be considered: Optimize components such as the combustion chamber, heat exchangers, and turbines to reduce internal irreversibilities.

Parametric Analysis

The trigeneration plant's performance was evaluated by varying the compressor pressure ratio (CPR). With increasing CPR, both energy and exergy efficiency initially improved, reaching a peak at 2.3 CPR, before steadily declining, as depicted in Figure 4(a). This decline commences after reaching a CPR of 2.3. This trend can be rationalized by considering the enhanced expansion and compression works before reaching a CPR of 2.3. However, in this context, the rate of improvement in compression work is lower than that of expansion work. Consequently, the network output increases, leading to improvements in both efficiencies of the plant. Subsequent to a CPR of 2.3, the results demonstrated a reverse trend. The combined ORC-ERS system achieved peak energy and exergy efficiencies of 48.33% and 64.40%, respectively, whereas the overall plant achieved values around 23.3% and 25.12%, respectively. Although the cycle may have experienced considerable energy loss, the loss is minimal due to the poor quality of the lost energy, explaining the discrepancy in energy and energy efficiency of the cycle. In the solar field alone, heliostats and receivers accounted for 83.20% of the total energy loss, indicating that 45593 kW of plant energy was lost overall, with only 37578 kW of solar field energy being lost. The highest power from the HBC and the plant were found to be 14998 kW and 13365 kW, respectively, at a CPR of 2.3, which is the optimal value. Consequently, there was an improvement of 1633 kW in net power output due to the ORC-ERS. At a CPR of 2.3, the greatest cooling and heating impacts were measured at 8.82 kW and 60.56 kW, respectively. The power output, energy, and energy conversion efficiency all follow the same trend.

The inlet temperature of the helium turbine (HTIT) plays a significant role in influencing the system's performance. As depicted in Figure 4(b), the plant's energy efficiency, exergy efficiency, and power production improved from 21.36% to 24.65%, 23.87% to 27.4%, and 13808 kW to 15928 kW, respectively, with HTIT. This can be attributed to the increase in enthalpy differential across the turbine as the input temperature rises. Consequently, there is a rise in net expansion effort, leading to enhancements in net output power and the thermodynamic performance of the system. This change was assessed under conditions of 197.5°C for the OT inlet temperature, 850 W/m² of DNI, and an optimal CPR of 2.3. Furthermore, the HTIT affects the cooling and heating impacts in addition to efficiency and net power output. The effects of heating and cooling were enhanced with a rise in HTIT. As the HTIT enhanced from 700°C to 900°C, the cooling load increased from 6.87 kW to 10.40 kW, and the heating load climbed from 55.87 kW to 59.4 kW. This relationship makes sense because rising HTIT and ORC turbine input temperatures indicate more heat energy entering the ORC-ERS system and amplifying the impacts of heating and cooling.

The system's performance declined with the compressor inlet temperature (CIT). This can be explained by the fact that as CIT increased, the enthalpy differential within the compressor itself also increased, resulting in an enhancement in compressor work. Consequently, CIT reduced the overall performance of the system. The facility's overall energy and exergy efficiency decreased from 23.36% to 23% and from 26.02% to 25.63%, respectively. As depicted in Figure 4(c), the power output decreased from 15034 kW to 14802 kW with said CIT. The loads for heating and cooling remained unaffected by CIT. The net work production from the ORC declined as CIT increased, indicating that the output heat had minimal effect on the slight change in condenser and evaporator loads.

The pump pressure ratio (PPR) plays a significant role in influencing the performance of the system. By maintaining a constant value of 2.3 for the CPR, 850 W/m² for DNI, and 800°C for T_4, the variation in thermal performance was examined. The overall efficiencies of the plant initially increased and then exhibited a continuous decrease, reaching an optimal value where the system's performance was maximized. As illustrated in Figure 4(d), the highest energy efficiency and exergy efficiency for the entire plant were achieved at the optimal PPR of 3.056, amounting to 25.12% and 23.30%, respectively. Notably, the cooling aspect remained unaffected by changes in PPR, while the heating effects demonstrated a consistent increase with higher PPR values. An increase in PPR implies more work for the pump resulting in no enhancement in refrigeration effects. However, an increase in PPR leads to greater heat extraction through the condenser to maintain energy balance, necessitating increased heat rejection through the condenser, thereby augmenting the heating load. Specifically, a 2.33% increase in PPR resulted in a 6.31% increase in heating effects.

Figure 5(a) depicts the variation in the system's performance with changes in the evaporator temperature. Understanding the impact of the evaporator on the trigeneration system's performance is crucial in any cooling setup. As the evaporator temperature increases, there is a consistent improvement in both energy and exergy efficiency, along with an increase in the power output of the energy conversion system. Specifically, the output power rose from 15802 kW to 16034 kW, while the energy and exergy efficiency increased from 22.85% to 23.32% and 24.48% to 24.92%, respectively. The evaporator temperature has no discernible effect on the heating loads but significantly

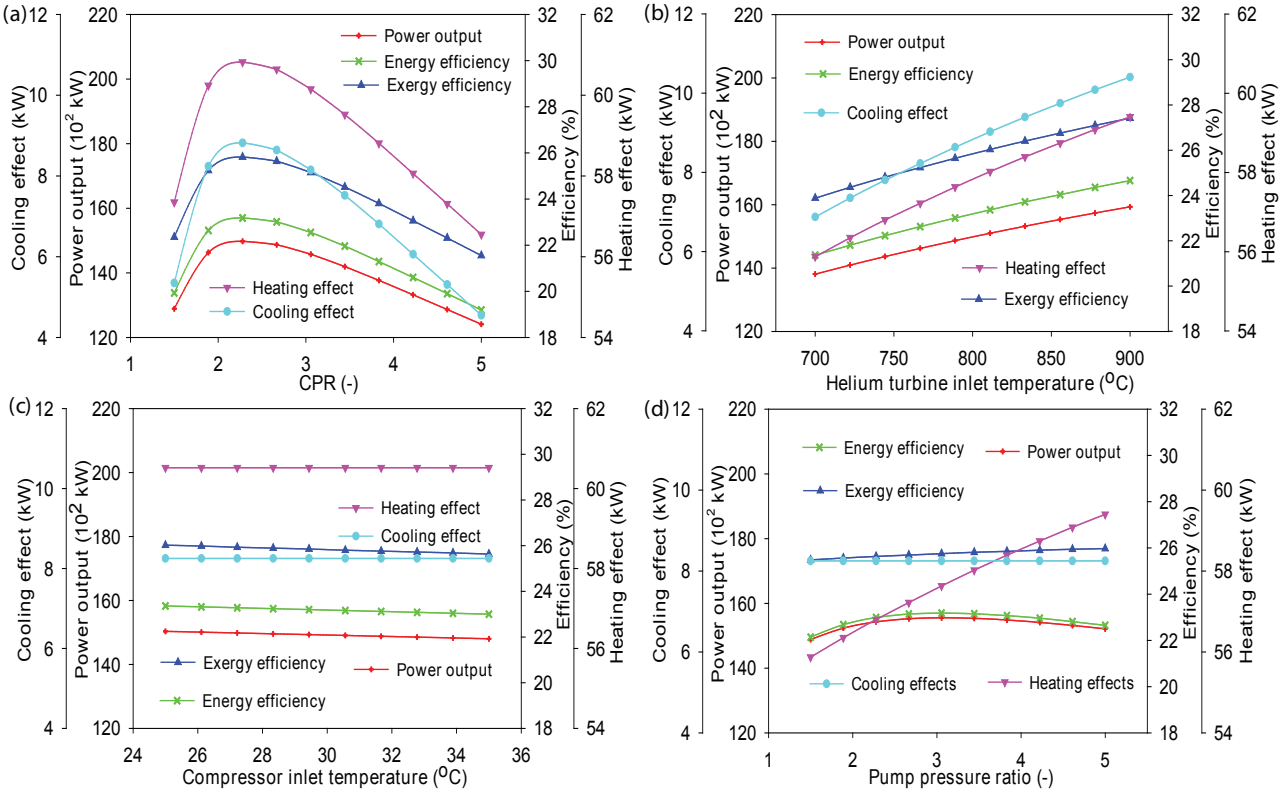

Figure 4. Performance variation with (a) CPR, (b) HTIT, (c) CIT, (d) PPR.

influences the cooling load. It's established that the evaporator temperature does not impact the thermodynamic parameters of the condenser, by elevating the evaporator pressure, thereby enhancing the cooling loads.

Figure 5(b) also demonstrates an increase in power output with Direct Normal Irradiance (DNI). In Indian climate conditions, the average DNI was determined to be 850 W/m². With higher DNI values, the receiver efficiency is expected to rise, consequently enhancing the energy performance of the plant. As DNI levels rose from 600 W/m² to 1000 W/m², Figure 5 illustrates the variations in energy efficiency, power output, and energy efficiency, ranging from 22.87% to 26.4%, 21.36% to 24.65%, and 13808 kW to 15928 kW, respectively. Furthermore, both cooling and heating loads rise with Direct Normal Irradiance (DNI). The uptick in DNI provides extra energy to the cycle, resulting in a greater amount of energy being converted into useful output, thereby leading to increased heating and cooling loads. As Figure 6 shows, for example, the heating and cooling loads went from 55.98 kW to 59.6 kW and from 6.87 kW to 9.99 kW, respectively, while the DNI increased from 600 W/m² to 1000 W/m².

Figure 5(c) emphasizes the significance of discussing the design parameters of the Solar Power Tower (SPT) alongside the combined cycle parameters. Among these, the heliostat field efficiency stands out as a key factor impacting the plant's performance. As the efficiency of the heliostat field increases, the overall performance of the plant improves. The energy efficiency, power generation, and output exertion are shown in Figure 5(c) as they increase from 21.19% to 30.83%, 19.64% to 28.65%, and 13925 kW to 19728 kW, respectively, while the heliostat efficiency rises from 0.6 to 0.85. This development is ascribed to the reduced solar energy loss brought about by increased heliostat efficiency, which results in more effective power conversion. As a result, improvements in power, energy, and exergy were noted. Furthermore, when field efficiency grew, so did the cooling and heating loads. With the heliostat efficiency increasing from 0.6 to 0.85, the cooling and heat demand grew by 51.38% and 6.31%, respectively.

Effects of various parameters on exergoenvironmental performance

Exergo-environmental analysis is an approach used in the study of thermodynamics and sustainability to evaluate and examine how energy systems and processes affect the environment. Figure 6(a) depicts the impact of compressor pressure ratio on exergo-environmental factors. It is evident from the figure that, as CPR increases, the environmental impact index (θ_{ei}) decreases and reaches a minimum value of 3 at a pressure ratio of 2.33. Subsequently, it gradually increases with further pressure ratio increments. This phenomenon arises due to lower exergy destruction at lower pressure ratios, which becomes more pronounced at higher

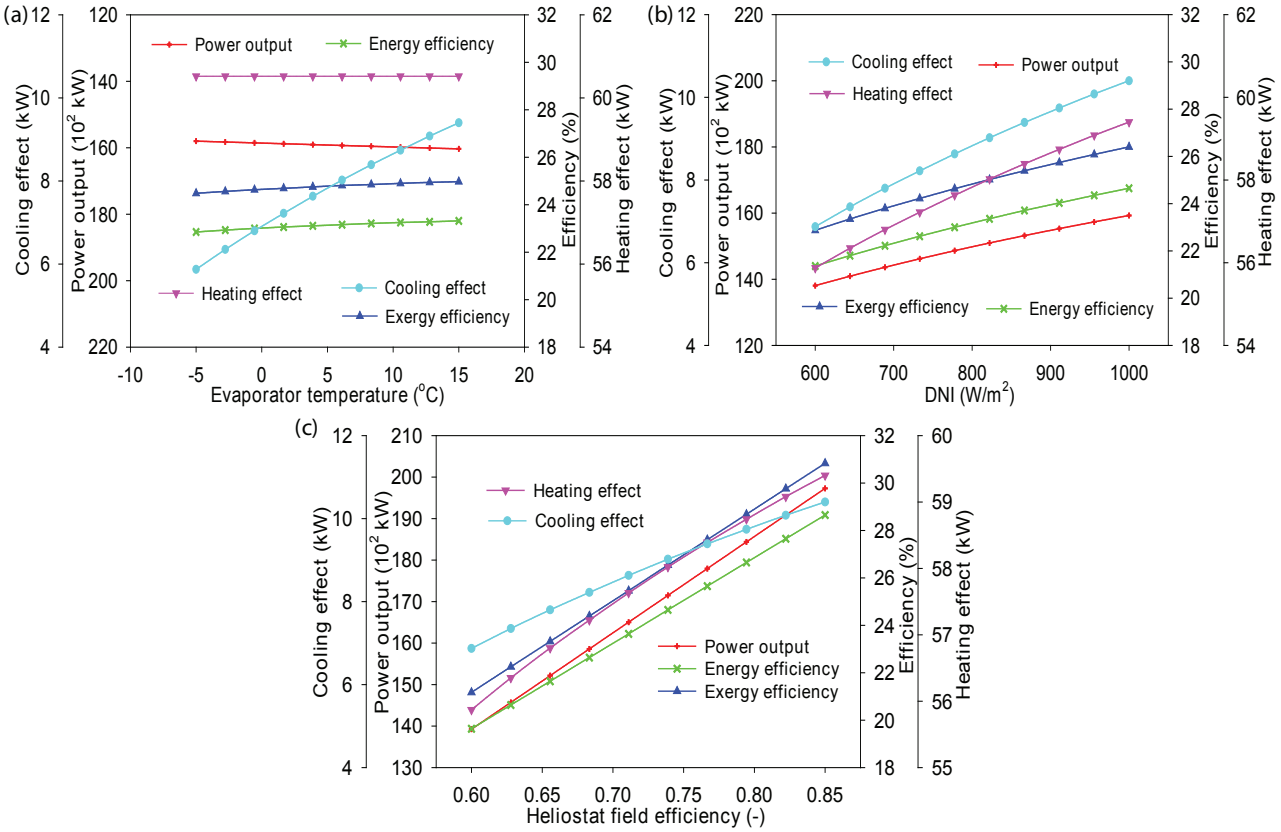

Figure 5. Performance variation with (a) evaporator temperature, (b) DNI, (c) heliostats field efficiency.

pressure ratios. Similarly, other environmental factors such as the environmental impact factor (θ_{eii}), exergy sustainability index (θ_{est}), and exergy stability factor (f_{es}) exhibit a similar trend. Exergy efficiency increases with pressure ratio up to 2.3 and then declines as pressure ratio continues to rise. In the graph, θ_{ei} decreases from 3.68 to 3 of CPR 2.33 and then increases to 3.8 at a CPR of 5. The factors θ_{eii}, θ_{est}, and f_{es} increases from 0.27 to 0.32, 0.05 to 0.07, and 0.21 to 0.24, respectively, as CPR increases from 1.5 to 2.33, reaching their maximum values at 2.33 and subsequently decreasing with further pressure ratio increases.

Figure 6(b) illustrates the impact of HT inlet temperature on exergo-environmental factors. It is seen that, as the HTIT incresed, θ_{ei} decreases, whereas the other factors, namely θ_{eii}, θ_{est}, and f_{es}, increases with the rising HTIT. This trend is a result of the minimum exergy destruction at lower temperatures, while higher temperatures lead to increased exergy destruction. The θ_{ei} decreases from 3.37 to 2.78, while the factors θ_{ei}, θ_{est}, and f_{es} increases from 0.29 to 0.35, 0.06 to 0.09, and 0.2 to 0.26, respectively, as the temperature increases from 700°C to 900°C.

Figure 6(c) illustrates the relationship between heliostat field efficiency and exergo-environmental factors. As observed in the graph, θ_{ei} decreases, while the other factors, including θ_{eii}, θ_{est}, and f_{es}, increase as heliostat field efficiency rises from 50% to 90%. The value of θ_{ei} decreases from 4.17 to 1.8, while the factors θ_{eii}, θ_{est}, and f_{es} increase from 0.23 to 0.53, 0.04 to 0.18, and 0.19 to 0.34, respectively. This trend emerges because the heliostat field receives the maximum amount of solar energy, with temperatures around 2000 °C. Consequently, such high temperatures result in maximum exergy destruction within the heliostat field. Therefore, it can be concluded that the present study has negligible harmful impact on the environment and thus power is generated in a green manner.

Comparative Study

According to published research, the SPT plant components have undergone a number of irreversibilities that are unavoidable. Consequently, the implementation of an efficient power generation system is necessary to enhance the overall performance of the SPT plant. The performance of the novel SPT-based integrated system is compared with earlier systems developed by other authors in this field. For a real comparison, the same solar circumstances are employed, and Table 12 lists the outcomes. The findings show that the combined system in present work performs better than previous comparable systems. This is due to the advanced cycle configuration and effective utilization of the waste heat from the topping cycle as compared to the Rankine cycle and sCO_2 cycle. It is evident from Table

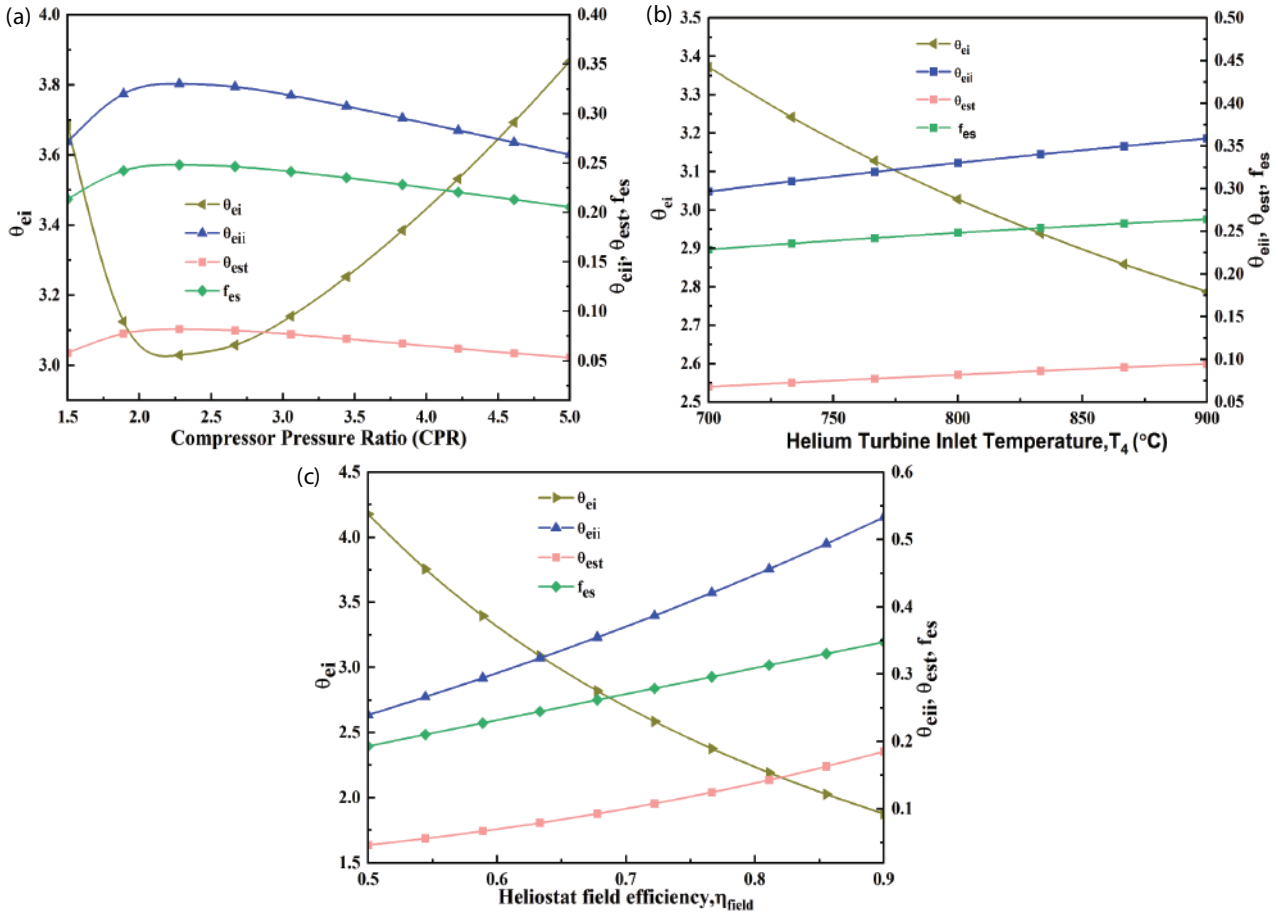

Figure 6. Exergoenvironmental performance variation with (a) CPR, (b) HTIT, (c) heliostats field efficiency.

Table 7. Comparison of the findings with related earlier research

Systems	DNI (kW/m²)	η_{field}	$\eta_{field} \times \eta_{rec}$	η_{rec}	$\eta_{en.comb}$ (%)	$\eta_{en.Plant}$ (%)	$\eta_{ex.Plant}$ (%)
Regenerative Rankine cycle [36]	0.8	0.75	-	0.9	37.9	22.9	24.5
Present system	0.8	0.75	-	0.9	56.67	38.02	41.15
Supercritical CO_2 cycle [36]	1	-	0.62	-	42.48	26.23	28.14
Present system	1	-	0.62	-	57.97	38.89	41.86

7 that the proposed SPT-HBC-ORC-ERS system, which is modelled in this work, obtained 48.75%, and 67.95% higher exergy efficiency than that of the combined HBC-basic ORC, sCO_2 system, and SPT-based Rankine cycle, respectively.

CONCLUSION

In this study, a trigeneration system has been developed to concurrently provide cooling, heating, and power for building applications like hospitals and hostels, utilizing a solar power tower (SPT). Power generation is achieved through a HBC and an ORC turbine, while ejector refrigeration has been integrated for cooling purposes. Heat rejected through the condenser is utilized for heating. The study's findings led to the following conclusions:

- The HBC-ORC-ERS system demonstrated exergy and energy efficiencies of 64.4%, and 48.33%, respectively, at a compression pressure ratio of 2.3 and a direct normal irradiance of 850 W/m².
- The overall plant (SPT-HBC-ORC-ERS) achieved an exergy efficiency of 25.12%, an energy efficiency of 23.3%, and a power output of 14998 kW. Therefore, considering the SPT performance overall performance

is reduced. It shows the greater irreversibility is associated with the SPT system. Additionally, heating and cooling loads were recorded at 60.52 kW and 8.25 kW, respectively.
- The highest exergy destruction rate was observed in the solar power tower subsystem (receiver and heliostats), accounting for approximately 83.20% (37,578 kW) of the total exergy destruction (45,593 kW) of the overall plant.
- It was seen that the exergoenvironmental impact coefficient has large value (4.028) due to the lower exergy efficiency of the plant. It revealed that still much scope is there to reduce the environmental effects.
- The exergetic stability factor was found as 0.2483. However, it's value close to one is preferable for power plant.

Limitations and Future Scope
- This study is limited to the thermodynamic and environmental analysis. Also this study provides the power at the peak load conditions only due to absence of the energy storage system.
- Exergoeconomic analysis and the analysis with energy storage are the future scope of this work.

NOMENCLATURE

A	Area (m^2)
$\dot{m}$	Mass flow rate (kg/s)
$\dot{E}X$	Rate of exergy (kW)
$\dot{Q}$	Heat rate (kW)
s	Specific entropy (kJ/kg·K)
T	Temperature (K)
h	Specific enthalpy (kJ/kg)
$\dot{E}D$	Exergy destruction rate (kW)
N_{hel}	Number of heliostats
$\dot{W}$	Power (kW)

Abbreviations

CIT	Compressor inlet temperature
HC	Helium compressor
DNI	Direct normal irradiation
CPR	Compressor pressure ratio
HTIT	Helium turbine inlet temperature
ORC	Organic Rankine cycle
HBC	Helium Brayton cycle
IHE	Intermediate heat exchanger
HT	Helium turbine
sCO_2	SupercriticalCO_2
tCO_2	Transcritical CO_2
WHRU	Waste heat recovery unit
PPR	Pump pressure ratio
SPT	Solar power tower

Subscripts

E	Evaporator
C	Condenser
P	Pump
e	exit
0	dead condition
j	particular state
ref	reference/reflectivity
rec	receiver
i	inlet
hel	heliostat
en	Energy
ex	Exergy

Greek letters

η	Efficiency
ε	Effectiveness
μ	Entertainment ratio

AUTHORSHIP CONTRIBUTIONS

Authors equally contributed to this work.

DATA AVAILABILITY STATEMENT

The authors confirm that the data that supports the findings of this study are available within the article. Raw data that support the finding of this study are available from the corresponding author, upon reasonable request.

CONFLICT OF INTEREST

The author declared no potential conflicts of interest with respect to the research, authorship, and/or publication of this article.

ETHICS

There are no ethical issues with the publication of this manuscript.

STATEMENT ON THE USE OF ARTIFICIAL INTELLIGENCE

Artificial intelligence was not used in the preparation of the article.

REFERENCES

[1] Khan Y, Tevatia A, Apparao D, et al. Experimental investigation to evaluate thermal performance of a solar cooker with evacuated tube solar collector using different heat transfer fluids. J Therm Eng 2024;10:1346−1357. [CrossRef]

[2] Khan Y, Raman R, Rashidi MM, et al. Thermodynamic analysis and experimental investigation of the water spray cooling of photovoltaic solar panels. J Therm Anal Calorim 2024;149:2073−2086.

[3] Khan Y, Mishra RS. Thermo-economic analysis of the combined solar-based pre-compression supercritical CO2 cycle and organic Rankine cycle using ultra-low GWP fluids. Therm Sci Eng Prog 2021;23:100925. [CrossRef]
[4] Chauhan MK, Chauhan AK, Khan Y, et al. Experimental and theoretical investigation of thermal efficiency and productivity of single slope basin type solar distillation system using honey-comb. J Therm Eng 2023;9:1559−1571. [CrossRef]
[5] Khan Y, Mishra RS, Singh AP. Performance comparison of organic Rankine cycles integrated with solar based combined cycle: A thermodynamic and exergoenvironmental analysis. Proc Inst Mech Eng Part C J Mech Eng Sci 2024;238:233−248. [CrossRef]
[6] Pal JS, Sapali SN, Deshmukh PW. Estimation and analysis of exergy loss and performance evaluation of marine freshwater generating system. J Therm Eng 2024;10:1266−1274. [CrossRef]
[7] Bader NM, Mushatet KS. An experimental study for a single-pass solar air heater integrated with artificial roughness. J Therm Eng 2024;10:1292−1305. [CrossRef]
[8] Kushwah A, Kumar A, Gaur MK. Techno-economic analysis of solar still with nano-phase change material and heating coil: A novel approach for sustainable development. J Therm Eng 2025;11:476−492. [CrossRef]
[9] Khan Y, Mishra RS. Performance analysis of a solar based novel trigeneration system using cascaded vapor absorption-compression refrigeration system. Int J Refrig 2023;155:207−218. [CrossRef]
[10] Guo J, Li M, He Y, Wang Y, Gong L. A systematic review of supercritical carbon dioxide (S-CO2) power cycle for energy industries: Technologies, key issues, and potential prospects. Energy Convers Manag 2022;258:115437. [CrossRef]
[11] Gkountas AA, Benos LT, Nikas KS, Sarris IE. Heat transfer improvement by an Al2O3-water nanofluid coolant in printed-circuit heat exchangers of supercritical CO2 Brayton cycle. Therm Sci Eng Prog 2020;20:100694. [CrossRef]
[12] Chai L, Tassou SA. A review of printed circuit heat exchangers for helium and supercritical CO2 Brayton cycles. Therm Sci Eng Prog 2020;18:100543. [CrossRef]
[13] Qin L, Xie G, Ma Y, Zhang S. Thermodynamic analysis and multi-objective optimization of a waste heat recovery system with a combined supercritical/transcritical CO2 cycle. Energy 2023;265:126332. [CrossRef]
[14] Khatoon S, Kim M. Preliminary design and assessment of concentrated solar power plant using supercritical carbon dioxide Brayton cycles. Energy Convers Manag 2022;252:115066. [CrossRef]
[15] Khan Y, Mishra RS. Performance analysis of solar driven combined recompression main compressor intercooling supercritical CO2 cycle and organic Rankine cycle using low GWP fluids. Energy Built Environ 2022;3:496−507. [CrossRef]
[16] Zare V, Hasanzadeh M. Energy and exergy analysis of a closed Brayton cycle-based combined cycle for solar power tower plants. Energy Convers Manag 2016;128:227−237. [CrossRef]
[17] Khan Y, Singh D, Caliskan H, Mishra RS. Exergoeconomic and thermodynamic analyses of solar power tower based novel combined helium Brayton cycle-transcritical CO2 cycle for carbon free power generation. Glob Chall 2023;7:2300191. [CrossRef]
[18] Bi Y, Ju Y. Design and analysis of an efficient hydrogen liquefaction process based on helium reverse Brayton cycle integrating with steam methane reforming and liquefied natural gas cold energy utilization. Energy 2022;252:124047. [CrossRef]
[19] Li Q, Wang E, Qiu Y. Triple-objective optimization of He Brayton cycles for ultra-high-temperature solar power tower. Energy Convers Manag 2022;270:116210. [CrossRef]
[20] Zhou J, Ali MA, Zeki FM, et al. Thermoeconomic investigation and multi-objective optimization of a novel efficient solar tower power plant based on supercritical Brayton cycle with inlet cooling. Therm Sci Eng Prog 2023;39:101679. [CrossRef]
[21] Wang M, Wang J, Zhao P, Dai Y. Multi-objective optimization of a combined cooling, heating and power system driven by solar energy. Energy Convers Manag 2015;89:289−297. [CrossRef]
[22] Mishra SK, Rehalia AS, Verma AK, Yadav L. Thermo-economic analysis of solar-powered trigeneration system with integrated ejector-absorption recompression and modified organic Rankine cycle. J Eng Gas Turbines Power 2024;146:051024. [CrossRef]
[23] Ogaili HH, Khalilarya S, Chitsaz A, Mojaver P. Energy, exergy, and economic performance analysis of integrated parabolic trough collector with organic Rankine cycle and ejector refrigeration cycle. Energy Convers Manag X 2025;25:100843. [CrossRef]
[24] Saladi JK, Suresh R, Datta SP. Diurnal performance investigation of solar integrated ejector-based combined cooling, heating, and power (CCHP) system for Indian climate. Appl Therm Eng 2025;263:125250. [CrossRef]
[25] Khan Y, Mishra RS. Performance evaluation of solar based combined pre-compression supercritical CO2 cycle and organic Rankine cycle. Int J Green Energy 2021;18:172−186. [CrossRef]
[26] Khan Y, Mishra RS. Parametric (exergy-energy) analysis of parabolic trough solar collector-driven combined partial heating supercritical CO2 cycle and organic Rankine cycle. Energy Sources Part A Recovery Util Environ Eff 2023;45:6019−6039.

[27] Li M, Wang J, He W, Gao L, Wang B, Ma S, et al. Construction and preliminary test of a low-temperature regenerative organic Rankine cycle (ORC) using R123. Renew Energy 2013;57:216–222. [CrossRef]
[28] Olumayegun O, Wang M, Kelsall G. Closed-cycle gas turbine for power generation: a state-of-the-art review. Fuel 2016;180:694–717. [CrossRef]
[29] Dunham MT, Iverson BD. High-efficiency thermodynamic power cycles for concentrated solar power systems. Renew Sustain Energy Rev 2014;30:758–770. [CrossRef]
[30] Xu C, Wang Z, Li X, Sun F. Energy and exergy analysis of solar power tower plants. Appl Therm Eng 2011;31:3904–3913. [CrossRef]
[31] Bellos E, Tzivanidis C. Multi-objective optimization of a solar driven trigeneration system. Energy 2018;149:47–62. [CrossRef]
[32] Li H, Cao F, Bu X, Wang L, Wang X. Performance characteristics of R1234yf ejector-expansion refrigeration cycle. Appl Energy 2014;121:96–103. [CrossRef]
[33] Wang J, Dai Y, Sun Z. A theoretical study on a novel combined power and ejector refrigeration cycle. Int J Refrig 2009;32:1186–1194. [CrossRef]
[34] Zare V, Mahmoudi SMS, Yari M. On the exergoeconomic assessment of employing Kalina cycle for GT-MHR waste heat utilization. Energy Convers Manag 2015;90:364–374. [CrossRef]
[35] Dai Y, Wang J, Gao L. Exergy analysis, parametric analysis and optimization for a novel combined power and ejector refrigeration cycle. Appl Therm Eng 2009;29:1983–1990. [CrossRef]
[36] Chacartegui R, Muñoz de Escalona JM, Sánchez D. Alternative cycles based on carbon dioxide for central receiver solar power plants. Appl Therm Eng 2011;31:872–879. [CrossRef]

J Ther Eng, Vol. 12, No. 1, pp. 16−28, January, 2026

Journal of Thermal Engineering
Web page info: https://jten.yildiz.edu.tr
DOI: 10.14744/thermal.0001055

Research Article

Performance investigation of high-powered light emitting diodes using copper and silicon-oxide based nanofluid filled heat pipe

Ashish KHUDAIWALA[1], Rupesh PATEL[2,*]

[1]*Department of Mechanical Engineering, Gujarat Technological University, Government Polytechnic Ahmedabad, 380001, Gujarat, India*

[2]*Department of Mechanical Engineering, Gujarat Technological University, Government Engineering College, 370001, Gujarat, India*

ARTICLE INFO

Article history
Received: 27 January 2025
Revised: 10 June 2025
Accepted: 26 June 2025

Keywords:
Cooling System; Heat Pipe; LEDs; Nanofluid

ABSTRACT

Thermal management of light-emitting diodes (LEDs) significantly reduces the chances of failure due to overheating and provides a better lifespan. The most efficient, compact, and low-cost cooling system must be developed for better heat dissipation. Researchers have conducted major investigations on LED performance for low-wattage applications. The current work focuses on the high-wattage real-life application of LEDs. Researchers have considered investigations for 100 W, 200 W, and 400 W capacity high-wattage LEDs in street, stadium, and high-mast tower applications. Copper-made, cylindrical, two-layered heat pipe with screen mesh wick has been designed and fabricated to cool LEDs. Dispersed copper and silicon oxide nanoparticles in distilled water are used as a working medium in a heat pipe. Types of working medium, filling ratio, and LED capacities were considered input variables during the experiment. The resultant variables are the evaporator and condenser temperature difference, thermal resistance, energy consumption, effective thermal conductivity, and overall heat transfer coefficient. Researchers have developed a dedicated experimental setup for testing, with all required measuring and controlling devices. A superior performance was observed with the Cu/DI water-filled heat pipe, considering a 60% filling ratio in the tested LEDs. Cu/DI water with a 60% filling ratio has a 15.2% and 3.5% lower temperature difference, contrasting with DI water and SiO_2/DI water for 100 W LED.

Cite this article as: Khudaiwala A, Patel R. Performance investigation of high-powered light emitting diodes using copper and silicon-oxide based nanofluid filled heat pipe. J Ther Eng 2026;12(1):16−28.

INTRODUCTION

In recent years, the scientific community has been seriously debating the development of sophisticated and effective heat transfer devices for the thermal management of electrical devices. Several lighting solutions are being examined to address the rise in temperature during working cycles. The issue continues despite varying working

***Corresponding author.**
*E-mail address: Rlp131277@gmail.com

This paper was recommended for publication in revised form by Editor-in-Chief Ahmet Selim Dalkılıç

Published by Yıldız Technical University Press, İstanbul, Turkey
Yıldız Technical University. This is an open access article under the CC BY-NC license (http://creativecommons.org/licenses/by-nc/4.0/).

conditions and ambient temperatures [1]. An experimental attempt is essential for the thermal management of Light Emitting Diodes (LEDs) due to the complicated and non-linear performance of LED cooling.

The utilization of light-emitting diodes, also known as LEDs, is widespread in every aspect of our lives. LED chips are liable for facilitating light and heat generation [2]. In addition to enabling an expanded selection of colour temperatures, LEDs offer a more excellent range of operation temperatures, ranging from -20 ° C to 85° C [3]. Three

researchers earned the Nobel Prize in Materials Science in 2014 for their work in developing blue LEDs that are both productive and efficient, using Gallium nitride (GaN). Researchers experimented to recognize that LEDs are committed to human culture [4]. Even though LEDs benefit society since they provide an alternative lighting solution for both industries and society, the junction temperature thermal management of LEDs continues to be an issue for society and requires urgent attention [5]. It has been demonstrated through experimentation that regulating LED junction temperatures within an appropriate range using heat pipes can improve the lifespan of the LEDs and reduce the amount of power consumed by a notable amount.

This experiment uses a heat pipe as a cooling device. This experiment primarily focuses on the efficient cooling trends of heat pipes and the space considerations related to the LEDs used in the experiments. Out of the many types of heat pipes available, we have chosen cylindrical ones mainly for their easy manufacturing, low cost, and high efficiency [6]. The evaporator, the adiabatic, and the condenser sections comprise three sub-sections that comprise the overall construction [7]. Observations also showed that the temperature of the LED exhibit was not in line with the brightening force, and a high filling proportion can degrade the enlightenment power of LED chips. The planned Oscillating Heat Pipe (OHP) for high-power LED cooling favored a low % filling proportion of 30%. Bumataria et al. [8] concluded with their experiments that the heat pipe is an essential component in the thermal management of high-power LEDs because it ensures that the junction temperature remains within the acceptable temperature window

Kim et al. [9], LEDs convert 80 to 90% of electrical power to heat at the flow-watt level, while 10 to 20% is exclusively converted to electro-optical energy. If the surface space varies between 1 and 2.5 mm^2, a functional LED›s hotness scattering change can reach 100 W/cm^2. LEDs require a converged temperature below 110 °C to function more effectively and last longer.

Gunnasegaran et al. [10] experimented with diamond-H_2O nanofluid with concentrations ranging from 0% to 3%, with heat input ranges between 20W and 60W. They decreased thermal resistance from 5.7% to 10.8% for mass concentrations ranging from 0.5% to 3%. Kahani and Vatankhah [11] predicted the thermal performance of wickless heat pipes using Al_2O_3-water Nanofluid by an artificial neural network. The results indicated that the volume concentrations were the most crucial parameter for predicting the thermal performance of heat pipes. Zhen et al. [12] experimented with a 12W LED with fins and could restrict the temperature to 40°C while working for a 5-minute cycle. The findings also showed promising results for heat pipe readings, keeping the junction temperature at 25°C for the same working cycle. Tang et al. [13], explored high-power LEDs with chips directly connected to heat pipes. They have confirmed that the heat conductivity of the Closed Loop Heat Pipe (CHP) lead outline at 2800 mA is 0.23 °C/W and 1.65 °C/W. The CHP lead outline LED device›s iridescent efficiency is 66.23 m/W at 2800 mA. It is 19.2% more costly than the standard copper-lead outline. The CHP lead Casing›s Connected Variety Temperature (CCT) shift value is 108 °C (381 K), 23.5% lower than the standard copper-lead outline. Wang et al. [14], reasoned that the heat dispersal coefficient ought to be more critical than 1 $W/cm^2/°C$ to give an advantageous removal of the hotness made. Since LEDs are hot light sources, heat radiation cannot accurately represent how heat is absorbed. Design an adequate and effective dissemination system to heat the executives effectively. Pekur et al. [15], Experimentally studied the spiral heat exchangers and heat pipes for the cooling application of LEDs. They concluded that radially arranged heat pipes with spiral heat exchangers for 10.00w capacity LED emphasize the promising cooling system at ambient temperature.

Shekho et al. [16], investigated the compound microchannels using Al_2O_3 and CuO dispersed nanofluids with a 47 nm size and 4 vol% concentration. Employing the nanofluids decreased the total thermal resistance by 16.8% compared to water. Nasser et al. [17], investigated the SiO_2/H_2O nanofluids as a coolant in the container. They investigated with a concentration ranging from 0.1 wt% to 0.3 wt% and a 2 LPM flow rate. Increasing the mass concentration of the Nanofluid increases the thermal efficiency. For distilled water concentrations of 0.1 v%,0.2v%, and 0.3v%, the thermal efficiency for SiO_2 nanofluid was 35.56%, 79.91%, 91.04%, and 104.01%, respectively. Hasan et al. [18] investigated the heat transport characteristics of SiO_2/H_2O nanofluids with a particle size of 20 to 50 nm. The higher heat transfer rate is observed with smaller nanoparticles, as they have higher Nusselt numbers due to a large surface area, increasing the collision rate to improve heat transfer rates. Li et al. [19], investigated Cu/H_2O dispersed nanofluids to study the thermophysical properties of nanofluids. Increased surface area-to-volume ratio in nanoparticles greatly improved the thermal conductivity of nanofluids. The thermal conductivity rose from 11% to 30%. Guru et al. [20], studied the thermosiphon utilizing Boron/H_2O nanofluids with a concentration of 0.5 wt%, 1.0 wt% and 2.0 wt%. The heat pipe was tested for 200W,300W, and 400W heating power while the cooling water flow ranged from 5 g/s to 7.5 g/s and 10 g/s in the evaporator section. With 2% boron nanofluid at 400 W heating power and a cooling water mass flow rate of 10 g/s, the results demonstrated a

20% increase in efficiency. The improvement in heat resistance seen as a result of the Boron nanofluid was 28%.

Datta et al. [21], reviewed the possibility of tertiary nanofluids for the jet-impinging cooling process. They suggested the combination of Al_2O_3, CuO, and TiO_2 nanoparticles with a size of 20 nm. The addition of nanoparticles enhances heat transfer, and a smaller size is the optimum for maximum heat transfer, whereas the heat transfer decreases for bigger-sized nanoparticles.

In the open literature, various researchers have adopted methodologies such as heat pipes, heat sinks, fins, thermal paste, fan cooling, liquid spray, and others to manage the LEDs to keep the junction temperature lower. Significant work has been carried out for the performance analysis of low-capacity LEDs only. Researchers studied the effect of inclination angle, concentration, particle size, and shape on nanofluid-filled heat pipes. The current work mainly focuses on high-wattage LEDs with 100W, 200W, and 400W capacity. Researchers tested the real-life application of LEDs in a performance trial involving street lights (100W), stadium lights (200W), and high-mast towers (400W). Researchers investigated the effect of various feeling ratios on heat pipe performance using Cu/DI water and SiO_2/DI water as working mediums.

This paper focuses on the thermal management of the light-emitting diodes (LEDs) used for high-mask towers, stadium lights, and street lights. Various capacities of LED (based on application), filling ratio, and working medium are considered experimental variables. DI water, Cu/DI water, and SiO_2/DI water-filled, two-layered, screen mesh wick, copper-made, cylindrical heat pipe have been tested for the cooling application of LEDs by varying the filling ratio. The effect of variables on evaporator and condenser temperature difference, power consumption, thermal resistance, effective thermal conductivity, and overall heat transfer coefficient is calculated and discussed in the results and discussion section. A superior combination of heat pipe with working fluid and filling ratio has been suggested for the cooling application of high-wattage LEDs.

MATERIALS AND METHODS

Light Emitting Diodes (LEDs)

All the LEDs purchased for the evaluated applications, namely the street light, the stadium light, and the high mast tower, have been put through an eight-hour working cycle to ensure that the readings remain consistent. The specifications of the purchased LED are described in Table 3.

Heat Pipe

Cylindrical heat pipes made up of copper with an outer diameter of 6-8 mm have been proven to be a superior cooling appliance due to the higher thermal conductivity of the material, shape, and volume to surface area for the particular applications[22]. Three sets of fabricated heat pipes have been experimented with for LED cooling. The 8 mm OD copper tube with 0.6 mm thickness has been manufactured with a non-return valve at one end for evacuation and refilling purposes. Screen mesh wick has been inserted for the capillarity. The close contact between mesh wick and inner wall has been confirmed by releasing the wick tension[23]. Table 2 describes the heat pipes for all three types of LEDs under experimentation, with their dimensions.

The closed contact between the heat pipe and the LED surface ensures heat dissipation. As shown in Figure 1, the heat pipe has been inserted between the LED junction and the LED›s casing. The heat pipes are embedded in the LED.

Table 1. LED Specification

LED Power	100 W	200 W	400 W
LED Size (mm)	190*150	250*160	350*270
Trial Duration	08 Hours	08 Hours	08 Hours
Purpose	Street Light	Stadium Light	High Mask Tower

Table 2. Description of heat pipes

Types of LED	**100 W**	**200 W**	**400 W**
Heat Pipe Material	Copper	Copper	Copper
Total length (mm)	630	875	1225
Evaporator Section Length (mm)	180	250	350
Condenser section Length (mm)	270	375	525
Types of Wick Structure	Screen mesh	Screen mesh	Screen mesh

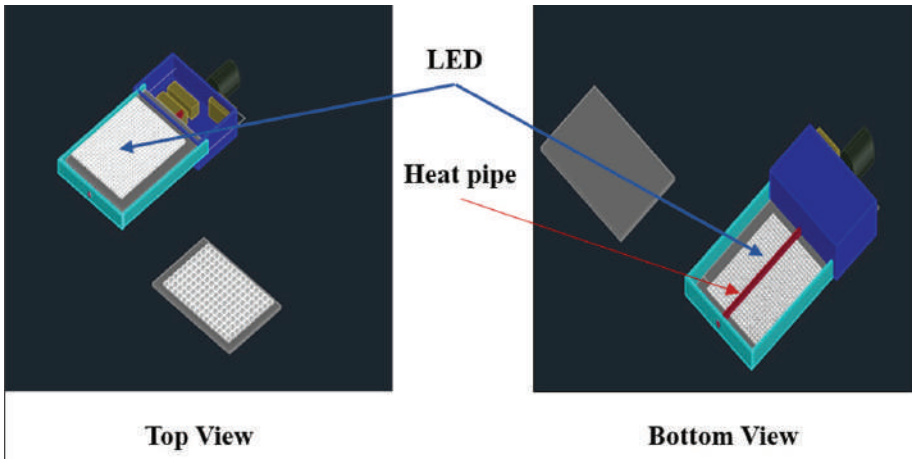

Figure 1. LED assembly along with Heat Pipe.

Nanofluids

Table 3. Properties of Nano-additives

Parameter	Cu	SiO_2
Density (g/cm3)	1.91	1.634
Particle size (nm)	30-50	30-50
Thermal Conductivity (W/mK)	383	10.4
Cost (Rs) per 10 gm	3500	1700

The researcher used a two-step method to prepare the nanofluids. Particles have been prepared using grinding. In the Second step, the particles are dispersed in the base fluid by stirring and ultrasonication [24]. As the investigation was associated with nanoscale molecule size, the possibility of eliminating molecule aggregation was considered. Suspend the molecule in a base liquid to prevent it from settling due to agglomeration [25]. The copper and silicon oxide particles used in this investigation are purchased in powder form from Platonic Nanotech Private Limited, Jharkhand (India). Table 2 shows the nanoparticle properties.

For the preparation of nanoparticles, the ultrasonic weight gauge was used by the researchers for 1.0 wt.% concentration particle weight, as significant studies had accounted that 1.0 wt.% is optimum[26], [27]. An attractive stirrer stirred the mixture of DI water and weighted particles for two hours, ensuring accurate scattering. After the mixing system was put through its paces, investigators subjected the nanofluids to a two-hour sonication process using an ultrasonic homogenizer. Both Cu and SiO_2 nanofluids were processed. The prepared nanofluids were stored in a glass bottle for testing and determining their stability.

Experimental Setup

Figure 2 describes an experimental setup prepared using various measuring and controlling devices. The evaporator area of the heat pipe is in the LED, which acts as a heat source[28]. The higher orientation, closure to vertical orientation retard the performance due to faster condensate return. It has been determined that the horizontal position of the heat pipe has the highest thermal resistance[29]. The current investigation implemented horizontal orientation for better LED orientation and lighting. The adiabatic section is exceptionally well insulated. The researchers used polyethylene foam (thermal conductivity = 0.032-0.034 W/mK, and linear coefficient of thermal expansion = 2×10^{-4} $°C^{-1}$ at 20 °C) to exhibit excellent thermal resistance, water resistance, and stability in different environmental conditions. A chamber is designed to cool the condenser component. Circulating water was utilized as a coolant to extract heat energy from the condenser and cycled within it simultaneously. PT-100 washer types thermocouples, the digital V-A meter records the total heat load capacity during the 08-hour working cycle. A rotameter records the mass flow of cooling water. Table 4 represents monitoring and measuring instruments› specifications, range, accuracy, and uncertainties.

All measuring devices have been calibrated at the Quality Calibration Centre, J2K LLP, Rajkot (Gujarat), India, a NABL (National Accreditation Board for Testing and Calibration Laboratories)- approved calibration centre. Thermocouples have been calibrated using a Multifunction process calibrator (3021131/MPC/ET/02). The thermocouple locations are as per Figure 2.

The experimentation is carried out by taking DI Water, Cu/DI Water, and SiO_2/DI Water as the working medium, and 20%, 40%, 60%, and 80% as the filling ratio. Figure 3 shows the actual experimental setup.

Uncertainty Analysis

Experimental uncertainties were calculated using the method developed by S. J. Kline and F. A. McClintock.[30] The calculations incorporate the estimated ones in experimental tests into the final results of interest as per Table 5.

Table 4. Specifications of monitoring and measuring instruments

Measuring Device	Measuring property	Range	Uncertainty
Washer Type RTD (PT-100) Specifications: Probe type: Washer Type: RTD, PT-100 No. of terminals: 03 Length: 2 meters	Temperature	0 to 200°C	0.1°C
Probe type RTD (PT-100) Specifications: Probe type: SS Road with spring Type: RTD, PT-100 No. of terminals: 03 Length: 2 meters		0 to 200°C	0.1°C
Digital Temperature Display/ Scanner Specifications: No. of channels: 08 Relay contact: 230V AC, 2A Input type: PT100, Cu100, CU50 Dimensions: 96*96 mm		-	-
Digital Volt & Amp Meter Specifications: No. of channels: 08 Relay contact: 230V AC, 2A Input type: PT100, Cu100, CU50 Dimensions: 96*96 mm	Heat Load	A meter: 0-5A Voltmeter: 1-280 V	A meter: 0.01 A Voltmeter: 1 V
Rotameter Specifications: Material: Fibre body with metallic float. Maximum pressure: 8 bar Medium: Water Maximum temperature: 80 °C	Mass flow of cooling water	0 to 1200 LPH	50 LPH

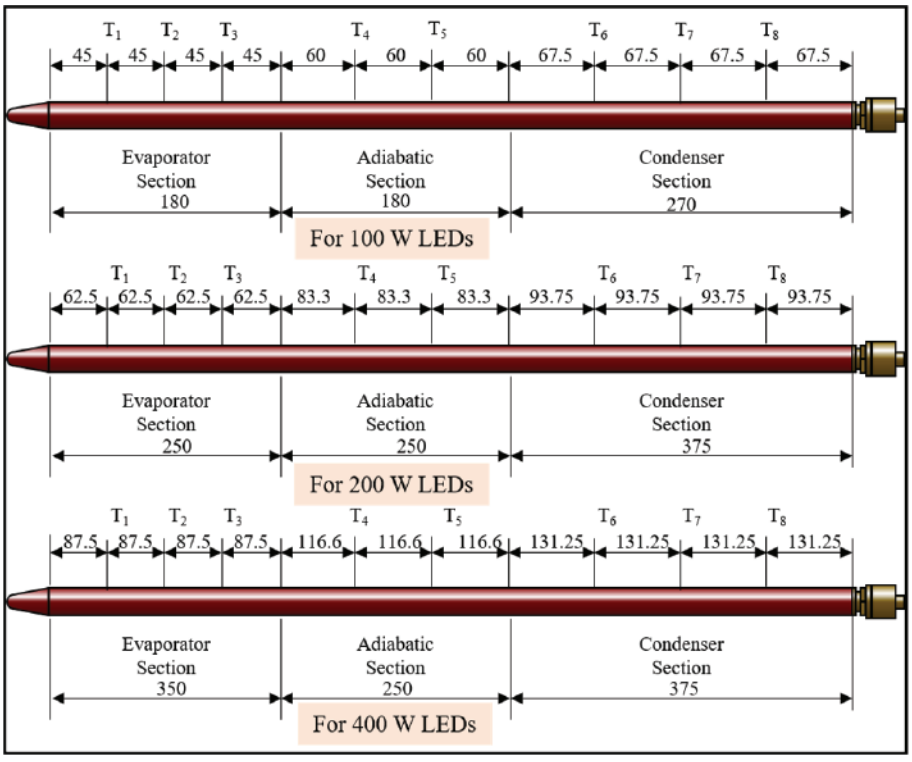

Figure 2. Thermocouple locations on the heat pipe surface.

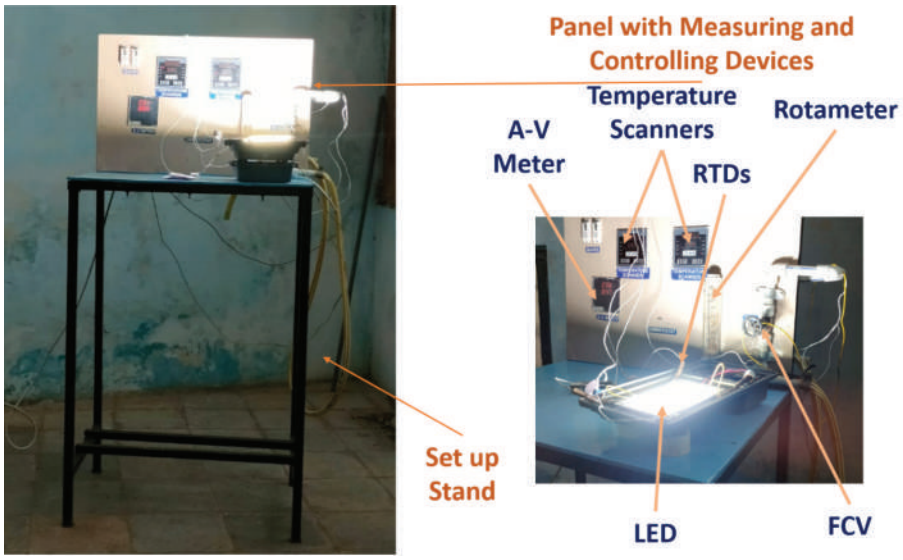

Figure 3. Experimental setup.

Table 5. Calculated uncertainty in final results

Result	% Uncertainty
Temperature difference	7.07%
Thermal resistance	7.05%
Effective thermal conductivity	6.82%
Overall HTC	7.06%

These results of uncertainty show that the uncertainty in the final parameters of interest is up to the expected level:

Evacuation and Refilling

The filling ratio is the ratio of the quantity of working medium poured inside the heat pipe and the total volume of the heat pipe[31]. Proposed filling ratios ranging from 20% to 80% have been used for the experimentation. The calculated quantity of working medium has been poured into the filling bottle and installed in the station. The appropriate insulation of the vacuum has been ensured by enveloping a Teflon tape. The specially designed evacuation and refilling station has been designed and developed for the evacuation and refilling of the fabricated heat pipe. Figure 4 shows the actual setup for evacuation and refilling. Heat pipes under experimentation for the thermal management of LED are first flushed with DI water and prepared nanofluids. Firstly, the heat pipe has been assembled with the station and evacuated with the help of an evacuation and refilling station. Valves V1 and V2 were opened during evacuation, and V3 was closed. The vacuum gauge has been installed to ensure the appropriate vacuum. After evacuation, the vacuum pump was cut off, and valve V2 was closed. Then, after the prepared mono nanofluids have been poured inside the heat pipe, valve V3 is operated.

Figure 4. Evacuation and refilling station.

The heat pipe was disassembled with the station and assembled with the LEDs for testing.

RESULTS AND DISCUSSION

The thermal performance analysis of LEDs using nanofluid-filled heat pipes has been investigated by varying the types of working fluid, filling ratio, and load capacity. The

result of such variables has been analyzed by considering the temperature gap between the evaporator and condenser sections, effective thermal conductivity, and overall heat transfer coefficient.

The lower temperature difference between the evaporator and condenser sections implies better heat dissipation through the heat pipe. The surface temperature between the evaporator and condenser sections was [29].

$$\Delta T = T_e - T_c \quad (1)$$

The thermal resistance should be as low as possible. The thermal resistance has been calculated as[29],

$$R = \frac{Te-Tc}{Q} \quad (2)$$

The better effective thermal conductivity leads to better heat transfer from the evaporator to the condenser section. The effective thermal conductivity has been calculated as[29],

$$K = \frac{L_{eff}}{A_c \times R} \quad (3)$$

The overall heat transfer coefficient should be as high as possible for better heat transfer between the heat source and heat sink regions. The overall heat transfer coefficient has been considered with[29],

$$\frac{Q}{A_c \times \Delta T} \quad (4)$$

Temperature Difference Between Evaporator and Condenser Section

Effect of filling ratio on Te-Tc

Figure 5 describes the comparative results of the temperature difference between the evaporator and condenser sections by varying the filling ratio for 20%, 40%, 60%, and 80% for all three types of LEDs with a heat pipe under experimentation, i.e., 100W, 200W, and 400W. Researchers found the lowest temperature difference between evaporation and condenser sections in the 60% filling ratio for Cu/DI water-filled heat pipe and SiO_2/DI water-filled heat pipe in all LEDs. Cu/DI water with 60% filling ratio has 0.81%, 1.60%, and 7.16% lower temperature differences as

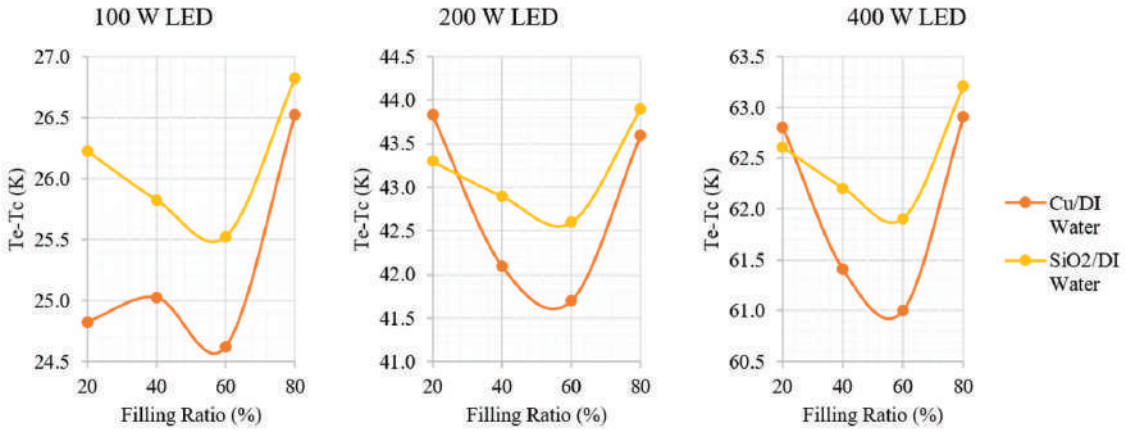

Figure 5. Effect of filling ratio on Te-Tc.

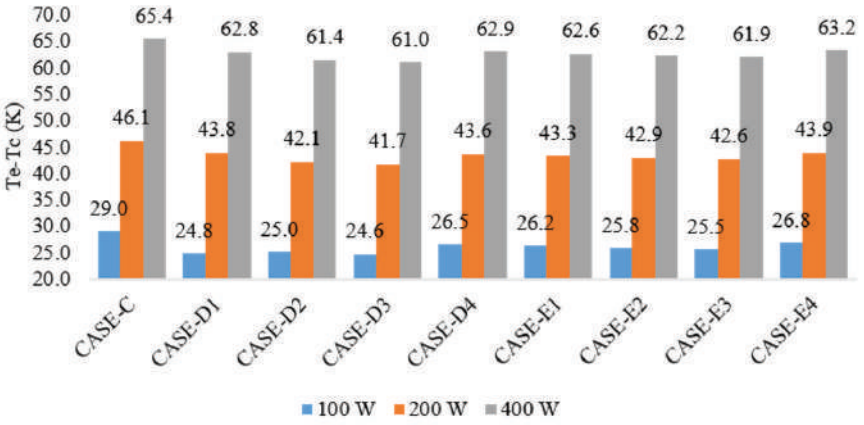

Figure 6. Effect of Working Mediums on Te-Tc.

compared to 20%, 40% and 80% filling ratio for 100 W LED. Cu/DI water with a 60% filling ratio has 4.87%, 0.95% and 4.36% lower temperature difference as compared to 20%, 40% and 80% filling ratio for 200 W LED. Cu/DI water with 60% filling ratio has 2.9 %, 0.7% and 3.0% lower temperature difference as compared to 20%, 40% and 80% filling ratio for 400 W LED.

Effect of working mediums on Te-Tc

Figure 6 describes the comparative results of the temperature difference between the evaporator and condenser sections by varying the working medium for all three types of LEDs with a heat pipe under experimentation, i.e., 100W, 200W, and 400W. The lowest temperature difference between evaporation and condenser sections has been found in case D3 (Cooling with Cu/DI water-filled heat pipe at 60% filling ratio) for all types of LEDs. Cu/DI water with 60% filling ratio has 15.2% and 3.5% lower temperature difference in contrast with DI water and SiO_2/DI water for 100 W LED. Cu/DI water with 60% filling ratio has 9.5% and 2.1% lower temperature difference in contrast with DI water and SiO_2/DI water for 200 W LED. Cu/DI water with 60% filling ratio has 6.7% and 1.5% lower temperature difference in contrast with DI water and SiO_2/DI water for 400 W LED. The temperature difference is lower in a 100 W LED than in a 400 W LED.

Heat Input

Effect of working mediums on heat input

Figure 7 illustrates the comparative results of heat input by varying working medium for all three types of LEDs with heat pipes under experimentation: 100W, 200W, and 400W. Cu/DI water-filled heat pipes with a 60% filling ratio have 6.5% and 8.5% lower power consumption, contrasting with fin and natural cooling for 100 W LEDs. The appropriate cooling reduces overheating, reducing power consumption.

Thermal Resistance

Effect of filing ratio on thermal resistance

Figure 8 demonstrates the comparative thermal resistance results by varying the filling ratio for 20%, 40%, 60%, and 80% for all three types of LEDs with a heat pipe under experimentation, i.e., 100W, 200W, and 400W. Researchers have found the lowest thermal resistance with a 60% filling ratio in Cu/DI water and SiO_2/DI water-filled heat pipes for

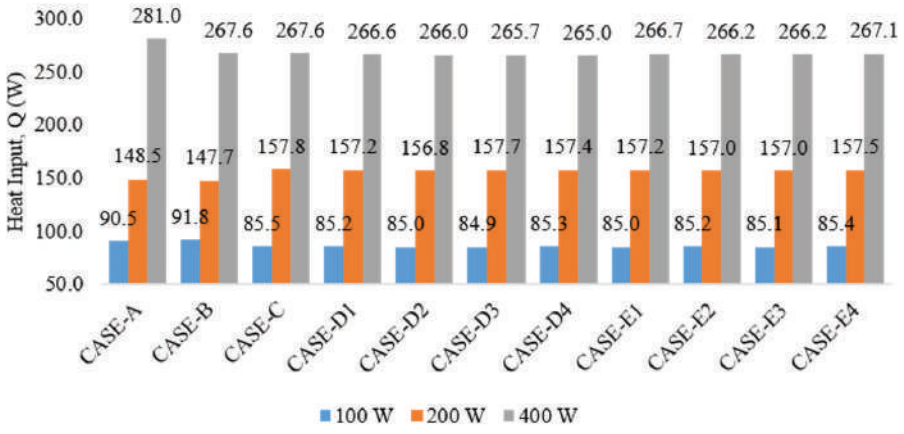

Figure 7. Effect of working mediums on Heat Input.

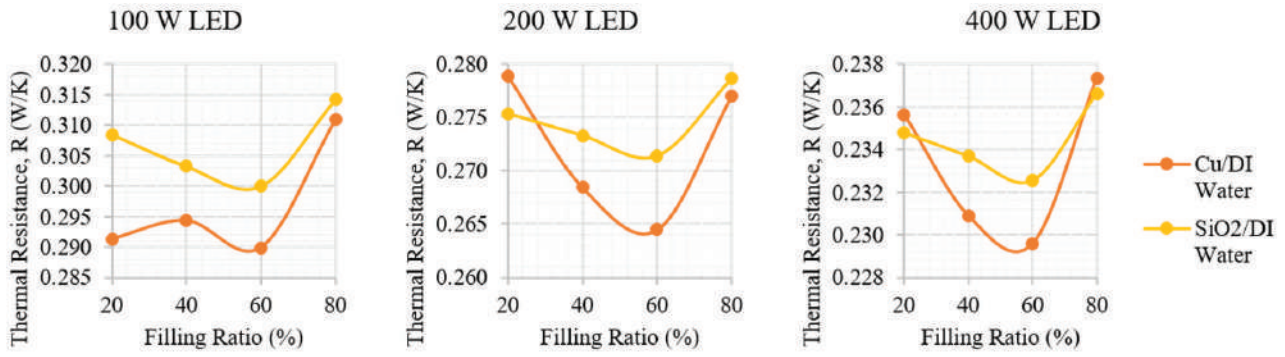

Figure 8. Effect of filling ratio on thermal resistance.

all types of LEDs. Cu/DI water with 60% filling ratio has 0.50%, 1.51% and 6.76% lower thermal resistance as compared to 20%, 40% and 80% filling ratio for 100 W LED. Cu/DI water with 60% filling ratio has 5.17%, 1.48% and 4.54% lower thermal resistance as compared to 20%, 40% and 80% filling ratio for 200 W LED. Cu/DI water with 60% filling ratio has 2.6%, 0.6% and 3.3% lower thermal resistance as compared to 20%, 40% and 80% filling ratio for 400 W LED.

Effect of working medium on thermal resistance

Figure 9 demonstrates the comparative results of thermal resistance by varying working mediums for all three types of LEDs with heat pipes under experimentation, i.e., 100W, 200W, and 400W. The lowest thermal resistance has been found in case D3 (Cooling with Cu/DI water-filled heat pipe at a 60% filling ratio) for all types of LEDs. Cu/DI water with 60% filling ratio has 14.6% and 3.4% lower thermal resistance in contrast with DI water and SiO_2/DI water for 100 W LED. Cu/DI water with 60% filling ratio has 9.5% and 2.5% lower thermal resistance in contrast with DI water and SiO_2/DI water for 200 W LED. Cu/DI water with 60% filling ratio has 6.1% and 1.3% lower thermal resistance in contrast with DI water and SiO_2/DI water for 400 W LED. The thermal resistance is lower in a 400 W LED and higher in a 100 W LED.

Effective Thermal Conductivity

Effect of filling ratio on effective thermal conductivity

Figure 10 demonstrates the comparative results of effective thermal conductivity by varying the filling ratio for 20%, 40%, 60%, and 80% for all three types of LEDs with a heat pipe under experimentation, i.e., 100W, 200W, and 400W. The highest effective thermal conductivity has been found with a 60% filling ratio for Cu/DI water and SiO_2/Di water-filled heat pipes, again for all types of LEDs. Cu/DI water with 60% filling ratio has 0.51%, 1.54% and 7.25% higher effective thermal conductivity as compared to 20%, 40% and 80% filling ratio for 100 W LED. Cu/DI water with a 60% filling ratio has 5.45%, 1.50% and 4.75% higher effective thermal conductivity as compared to 20%, 40% and 80% filling ratio for 200 W LED. Cu/DI water with 60% filling ratio has 2.6%, 0.6% and 3.4% higher effective thermal conductivity as compared to 20%, 40% and 80% filling ratio for 400 W LED.

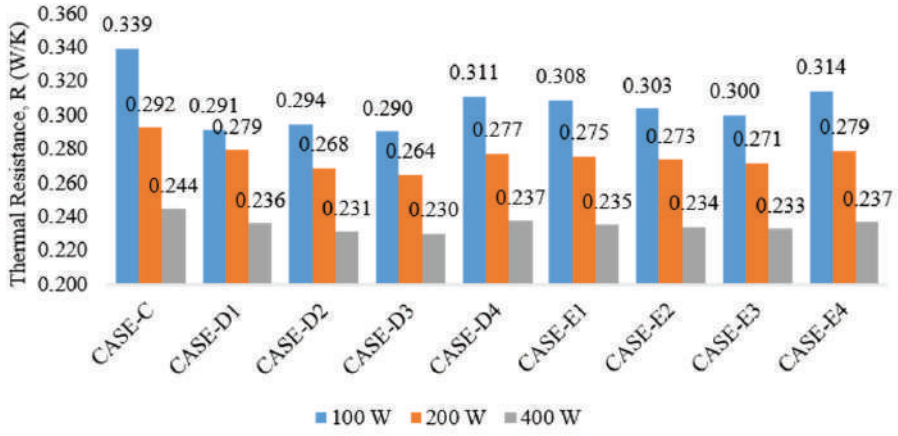

Figure 9. Effect of working medium on thermal resistance.

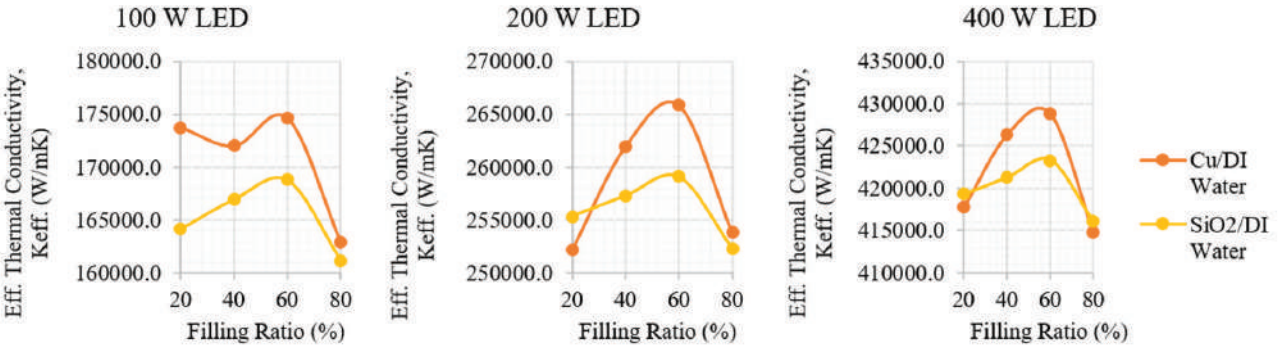

Figure 10. Effect of filling ratio on effective thermal conductivity.

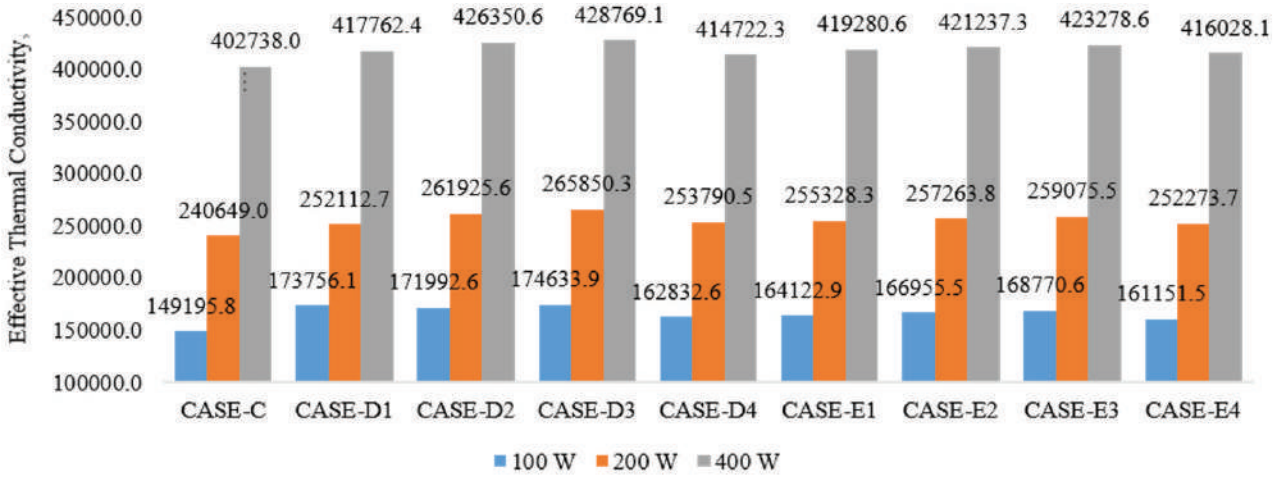

Figure 11. Effect of working mediums on effective thermal conductivity.

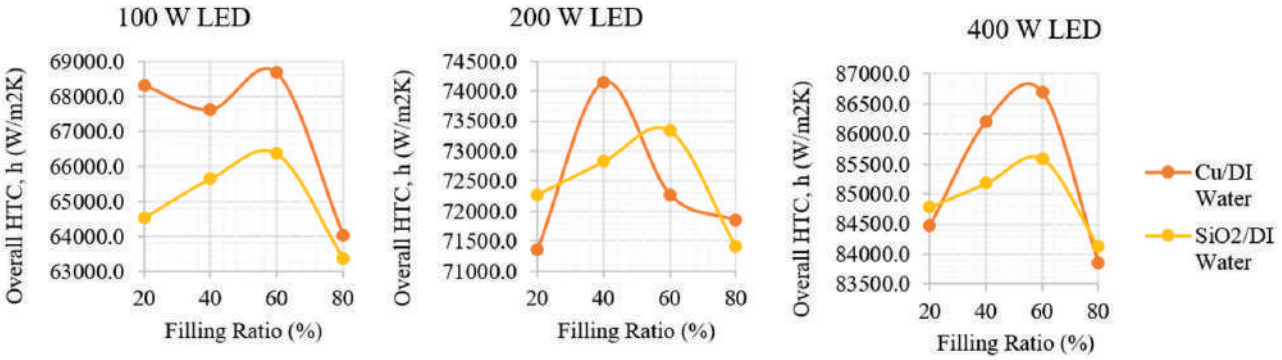

Figure 12. Effect of filling ratio on overall heat transfer coefficient.

Effect of working mediums on effective thermal conductivity

Figure 11 demonstrates the comparative results of effective thermal conductivity by varying the working medium for all three types of LEDs with a heat pipe under experimentation, i.e., 100W, 200W, and 400W. The highest effective thermal conductivity has been found in case D3 (Cooling with Cu/DI water-filled heat pipe at 60% filling ratio) again for all types of LEDs. Cu/DI water with 60% filling ratio has 17.1% and 3.5% higher effective thermal conductivity in comparison with DI water and SiO2/DI water for 100 W LED. Cu/DI water with 60% filling ratio has 10.5% and 2.6% higher effective thermal conductivity in comparison with DI water and SiO_2/DI water for 200 W LED. Cu/DI water with 60% filling ratio has 6.5% and 1.3% higher effective thermal conductivity in comparison with DI water and SiO_2/DI water for 400 W LED. The effective thermal conductivity is higher in 400 W LED, whereas lower has been observed in 100 W LED.

Overall Heat Transfer Coefficient (HTC)

Effect of filling ratio on overall heat transfer coefficient

Figure 12 illustrates the comparative results of the overall heat transfer coefficient by varying the filling ratio for 20%, 40%, 60%, and 80% for all three types of LEDs with a heat pipe under experimentation, i.e., 100W, 200W, and 400W. The highest overall HTC has been found with a 60% filling ratio in Cu/DI water and SiO_2/DI water-filled heat pipe again for all types of LED. Cu/DI water with 60% filling ratio has 0.51%, 1.54% and 7.25% higher overall HTC as compared to 20%, 40% and 80% filling ratio for 100 W LED. Cu/DI water with 40% filling ratio has 3.89%, 2.58% and 3.21% higher overall HTC as compared to 20%, 60% and 80% filling ratio for 200 W LED. Cu/DI water with 60% filling ratio has 2.6%, 0.6% and 3.4% higher overall HTC as compared to 20%, 40% and 80% filling ratio for 400 W LED.

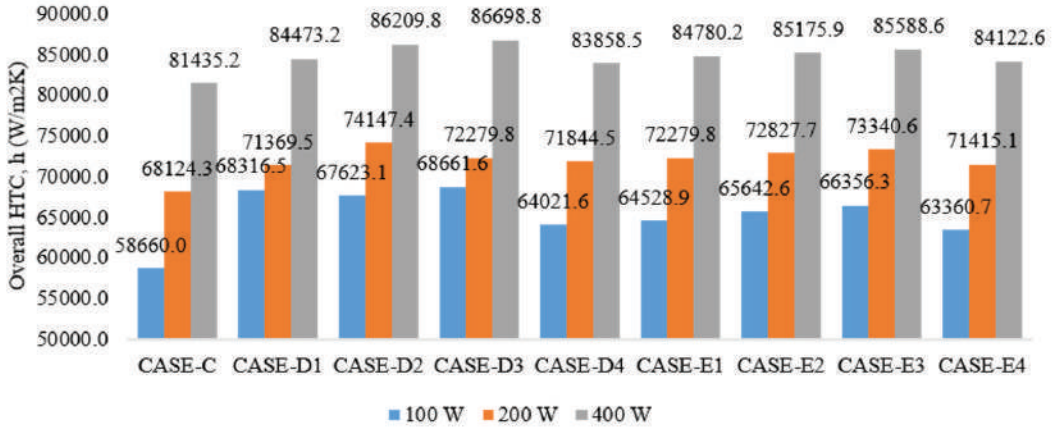

Figure 13. Effect of working mediums on overall heat transfer coefficient.

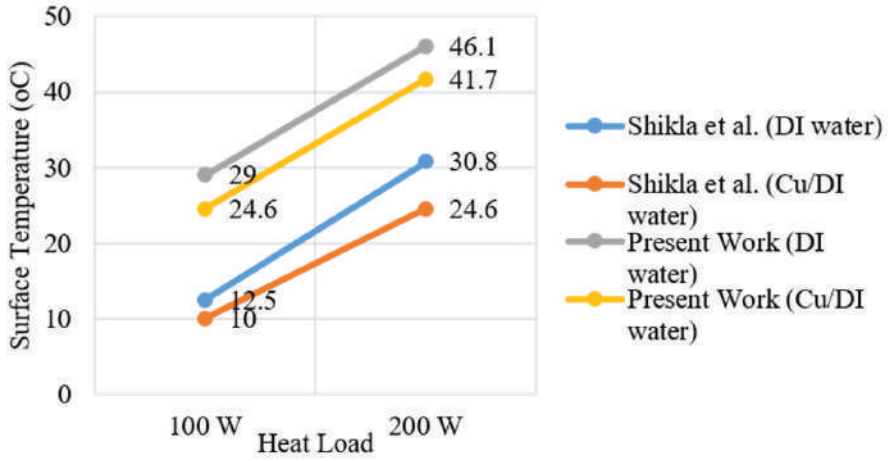

Figure 14. Comparison of present work in the form of surface temperature with heat load (DI water and Cu/DI water as working medium, horizontal position, 60% filling ratio).

Effect of working mediums on the overall heat transfer coefficient

Figure 13 demonstrates the comparative results of the overall heat transfer coefficient by varying the working medium for all three types of LEDs with the heat pipe under experimentation, i.e., 100W, 200W, and 400W. The highest overall HTC has been found in case D3 (Cooling with Cu/DI water-filled heat pipe at 60% filling ratio) again for all types of LED. Cu/DI water with 60% filling ratio has 17.1% and 3.5% higher overall HTC in comparison with DI water and SiO_2/DI water for 100 W LED. Cu/DI water with 60% filling ratio has 6.1% and 1.4% higher effective overall HTC in comparison with DI water and SiO_2/DI water for 200 W LED. Cu/DI water with 60% filling ratio has 6.5% and 1.3% higher overall HTC in comparison with DI water and SiO_2/DI water for 400 W LED. The overall HTC is higher in 400 W LED, whereas a lower value has been observed in 100 W LED.

Comparison and Validation

Figure 14 compares the present work with Shukla et al. [32] in the form of surface temperature with heat load by filling DI water and Cu/DI water as the working fluid. The horizontal orientation, 60% filling ratio, and two-layered screen mesh inserted cylindrical heat pipe type remained constant. Similarly, the DI water and Cu/DI water-filled heat pipes were investigated in both studies.

Results conclude that in all studies, the surface temperature was lower in Cu/DI water as a working medium than in DI water. Furthermore, the surface temperatures have been enhanced with the heat load in the present work and in Shukla et al. [32]

CONCLUSION

This work establishes how to thermally manage high-wattage LEDs using a heat pipe with a screen mesh

wick and distilled water-based Cu and SiO_2 mono nanofluids. Researchers analyze the results obtained after experimentation to improve outcomes. Researchers have observed the following conclusions.:

1. Performance improvement has been found with nanofluid-filled heat pipes instead of DI water-filled heat pipes for all types of LEDs. Cu/DI water with a 60% filling ratio has a 15.2% lower temperature difference than DI water for 100 W LEDs. The dispersion of nano-additives in DI water enhances the thermo-physical properties of the working medium.
2. CuO/DI water-filled heat pipes are more effective than DI water-filled heat pipes and SiO_2/DI water-filled heat pipes for all types of LEDs. Cu/DI water with a 60% filling ratio has a 3.5% lower temperature difference than SiO_2/DI water for a 100 W LED. The thermal conductivity of Cu is far better than that of SiO_2, which enhances the heat transport mechanism.
3. A 60% filling ratio is optimum for nanofluid-filled heat pipes and all types of LEDs. Cu/DI water with a 60% filling ratio has 0.81%, 1.60%, and 7.16% lower temperature differences than 20%, 40%, and 80% filling ratios for 100 W LEDs. A less than 60% filling ratio leads to a scarce working medium, whereas a more than 60% filling ratio leads to overflow.
4. Higher power leads to reduced thermal resistance compared with lower power (e.g., a 400W LED has lower thermal resistance than 100 W and 200 W LEDs). Thermal resistance is inversely proportional to heat load.

Furthermore, thermal analysis of LED cooling using nanofluid-filled heat pipes can be analyzed using different heat pipes such as flat, oscillating, pulsating, revolving, and rotating. Also, the hybridization of nanoparticles, proportion, variation in concentration, particle size, and shape can be investigated further. The mathematical model or simulated analysis may predict the performance trends of LEDs in the future.

NOMENCLATURE

Abbreviations

CCT	Correlated Color Temperature
CHP	Closed Loop Heat Pipe
Cu	Copper
DI	Distilled
GaN	Gallium Nitride
LED	Light Emitting Diode
NABL	National Accreditation Board for Testing and Calibration Laboratories
OHP	Oscillating Heat Pipe
SiO_2	Silicon Oxide

Symbol

HTC	Heat Transfer Coefficient (W/mK)
T	Temperature (°C)
Wt	Weight Fraction (%)

Subscripts

e	Evaporator section
c	Condenser section

AUTHORSHIP CONTRIBUTIONS

Authors equally contributed to this work.

DATA AVAILABILITY STATEMENT

The authors confirm that the data that supports the findings of this study are available within the article. Raw data that support the finding of this study are available from the corresponding author, upon reasonable request.

CONFLICT OF INTEREST

The author declared no potential conflicts of interest with respect to the research, authorship, and/or publication of this article.

ETHICS

There are no ethical issues with the publication of this manuscript.

STATEMENT ON THE USE OF ARTIFICIAL INTELLIGENCE

Artificial intelligence was not used in the preparation of the article

REFERENCES

[1] Khudaiwala A, Patel RL, Bumataria R. Recent developments in thermal management of light-emitting diodes (LEDS): A review. J Therm Eng 2024;10:517–540. [CrossRef]

[2] Luo X, Hu R, Liu S, Wang K. Heat and fluid flow in high-power LED packaging and applications. Prog Energy Combust Sci 2016;56:1–32. [CrossRef]

[3] Gibney E. Nobel for blue LED that revolutionized lighting. Nature 2014;514:152–153. [CrossRef]

[4] Cengiz C, Azarifar M, Arik M. A critical review on the junction temperature measurement of light emitting diodes. Micromachines (Basel) 2022;13:1–36. [CrossRef]

[5] Xiao C, Liao H, Wang Y, Li J, Zhu W. A novel automated heat-pipe cooling device for high-power LEDs. Appl Therm Eng 2017;111:1320–1329. [CrossRef]

[6] Bumataria RK, Chavda NK, Panchal H. Current research aspects in mono and hybrid nanofluid based heat pipe technologies. Heliyon 2019;5:e01627. [CrossRef]

[7] Wang H, Qu J, Peng Y, Sun Q. Heat transfer performance of a novel tubular oscillating heat pipe with sintered copper particles inside flat-plate evaporator and high-power LED heat sink application. Energy Convers Manag 2019;189:215–222. [CrossRef]

[8] Bumataria RK, Chavda NK, Nalbandh AH. Performance evaluation of the cylindrical shaped heat pipe utilizing water-based CuO and ZnO hybrid nanofluids. Energy Sources Part A 2020;00:1–16. [CrossRef]
[9] Kim D, Lee J, Kim J, Choi CH, Chung W. Enhancement of heat dissipation of LED module with cupric-oxide composite coating on aluminum-alloy heat sink. Energy Convers Manag 2015;106:958–963. [CrossRef]
[10] Gunnasegaran P, Abdullah MZ, Yusoff MZ, Kanna R. Heat transfer in a loop heat pipe using diamond-H2O nanofluid. Heat Transf Eng 2018;39:1117–1131. [CrossRef]
[11] Kahani M, Vatankhah G. Thermal performance prediction of wickless heat pipe with Al2O3/water nanofluid using artificial neural network. Chem Eng Commun 2019;206:509–523. [CrossRef]
[12] Zheng J, Ge D, Li J. The Analysis of Heat Pipe Cooling in High Power LED Lighting System. 16th International Conference on Electronic Packaging Technology (ICEPT); 2015. p. 480–482. [CrossRef]
[13] Tang Y, Ding X, Yu B, Li Z, Liu B. A high power LED device with chips directly mounted on heat pipes. Appl Therm Eng 2014;66:632–639. [CrossRef]
[14] Wang Y, Zhang J, Cen J, Jiang F. A feasibility study about using SiO2 nanofluid screen mesh wick heat pipe for cooling of high-power LEDs. Heat Transf Eng 2016;37:741–750. [CrossRef]
[15] Pekur DV, et al. Thermal characteristics of a compact cooling system of a powerful LED lighting device based on a spiral heat exchanger and heat pipes. Therm Sci Eng Prog 2025;60:103483. [CrossRef]
[16] Shekho SS, Al-neama AF. Hydrothermal investigation of a nanofluid flow in a compound microchannels. J Therm Eng 2025;11:577–602. [CrossRef]
[17] Bin Mhd Nasser MAF, et al. Influence of silica oxide nanofluid for different concentrations on photovoltaic cell. J Nanofluids 2024;13:772–782. [CrossRef]
[18] Hasan HA, Togun H, Abed AM, Mohammed HI, Armaghani T, et al. Cooling lithium-ion batteries with silicon dioxide-water nanofluid: CFD analysis. Renew Sustain Energy Rev 2025;208:115007. [CrossRef]
[19] Li C, Luo Z, Qing S, Zhang J, Zhu J. Microscopic analysis of the influence of nanoparticle shape and solid-liquid interfacial layer density on the thermal conductivity of nanofluids: A molecular dynamics study on Cu-H2O nanofluids. Int J Thermal Sci 2025;214:109838. [CrossRef]
[20] Gürü M, Karakaya U, Alıcı DŞ, Olgun Ş, Aydın DY. Experimental investigation of the effect of boron-containing nanofluid on heat pipe thermal performance. Heat Transf Res 2025;56. [CrossRef]
[21] Datta A, Halder P. Field-synergy and nanoparticle's diameter analysis on circular jet impingement using three oxide–water-based nanofluids. J Therm Eng 2023;9:179–190. [CrossRef]
[22] Singh R, Mochizuki M, Yamada T, Nguyen T. Cooling of LED headlamp in automotive by heat pipes. Appl Therm Eng 2020;166:114733. [CrossRef]
[23] Bhullar BS, Gangacharyulu D, Das SK. Augmented thermal performance of straight heat pipe employing annular screen mesh wick and surfactant free stable aqueous nanofluids. Heat Transf Eng 2017;38:217–226. [CrossRef]
[24] Bumataria R, Chavda N. Heat load and orientation impacts in cylindrical heat pipes using copper oxide, aluminium oxide, and zinc oxide nanofluids. Int J Ambient Energy 2021. doi: 10.1080/01430750.2021.2014957. [CrossRef]
[25] Prasad AR, Singh S, Nagar H. A review on nanofluids: Properties and applications. Int J Adv Res Innov Ideas Educ 2017;3:3185–3209.
[26] Liu ZH, Li YY, Bao R. Thermal performance of inclined grooved heat pipes using nanofluids. Int J Thermal Sci 2010;49:1680–1687. [CrossRef]
[27] Lakshmi Reddy P, Sreenivasa Reddy B, Govindarajulu K, Bandhu D, Saxena A. Predicting the thermal performance of screen mesh wick heat pipe with aluminananofluids using response surface methodology. Int J Interact Des Manuf 2024;18:3167–3182. [CrossRef]
[28] Ušakovs I, Ivanovskis L. Advanced loop heat pipe application for cooling high power LED lights. Case Stud Therm Eng 2024;57:104320. [CrossRef]
[29] Bumataria R, Chavda N. Heat load and orientation impacts in cylindrical heat pipes using copper oxide, aluminium oxide, and zinc oxide nanofluids. Int J Ambient Energy 2021. doi: 10.1080/01430750.2021.2014957. [CrossRef]
[30] Kline SJ, McClintock FA. Describing uncertainties in single-sample experiments. Mech Eng 1953;75:3–8.
[31] Putra N, Septiadi WN, Rahman H, Irwansyah R. Thermal performance of screen mesh wick heat pipes with nanofluids. Exp Therm Fluid Sci 2012;40:10–17. [CrossRef]
[32] Shukla KN, Solomon AB, Pillai BC, Ibrahim M. Thermal performance of cylindrical heat pipe using nanofluids. J Thermophys Heat Transf 2010;24:796–802. [CrossRef]

J Ther Eng, Vol. 12, No. 1, pp. 29−49, January, 2026

Journal of Thermal Engineering
Web page info: https://jten.yildiz.edu.tr
DOI: 10.14744/thermal.0001056

Research Article

Experimental evaluation of a dual-use solar cooker for indoor and outdoor applications

Faiq SAID[1,*], Qazi Muhammad YASEEN[2], Sahibzada Naveed Inayat ULLAH[2], Muneeb AHMAD[2], Farhan AHMED[2], Zakir ULLAH[2], Mir Muhammad Mehran KHAN[2], Ibrar HUSSAIN[2]

[1]*Department of Mechanical Engineering, University of Engineering and Technology, Mardan 23200, Pakistan*
[2]*Department of Mechanical Engineering, University of Engineering and Technology, Peshawar 25120, Pakistan*

ARTICLE INFO

Article history
Received: 17 July 2025
Revised: 21 October 2025
Accepted: 22 October 2025

Keywords:
Domestic Cooking; Parabolic Solar Cooker; Renewable Energy; Solar Cooker

ABSTRACT

The design, construction, and experimental assessment of a portable parabolic solar cooker intended for both indoor and outdoor use in Peshawar, Pakistan, are presented in this study. The cooker boiled one liter of water in 12 minutes (from 34 to 94 degrees Celsius), boiled an egg in 12 minutes, and fried an egg in just one minute. It also reached a maximum temperature of 200.6 degrees Celsius. An optical efficiency of 48.69% ± 2.5% and a thermal efficiency of 46.72% ± 2.8% were obtained from performance testing under average solar irradiance of 937.75 W/m² (787.49 W/m² at 60° tilt). In sunny conditions, it was shown to operate continuously for up to eight hours. This cooker exhibit better thermal concentration, portability (8.5 kg), and user-friendliness than previous parabolic designs (usually < 140 °C peak temperature and longer boiling times). These findings demonstrate its potential as an affordable, sustainable, and clean cooking option for both urban and rural populations.

Cite this article as: Said F, Yaseen QM, Ullah SNI, Ahmad M, Ahmed F, Ullah Z, Khan MMM, Hussain I. Experimental evaluation of a dual-use solar cooker for indoor and outdoor applications. J Ther Eng 2026;12(1):29−49.

INTRODUCTION

A solar cooker is a type of cooking appliance that uses solar radiation to cook food [1]. In underdeveloped nations, cooking uses a significant amount of energy in rural areas [2]. With the UN establishing targets for 2030 and offering guidelines on the use of sustainable energy for cooking, solar cookers are crucial to achieving the Sustainable Development Goals (SDGs) [3]. Solar cookers are a cost-effective and environmentally friendly method of using solar energy for cooking in sunny climates all over the world [4]. Both developed and underdeveloped nations, as well as refugee camps, can utilize solar cookers. Its main purpose is to focus sun energy and use various reflective materials to transform it into heat. A few other crucial factors were taken into account, such as the need for a shining, smooth reflector surface and control (loading, tracking, temperature sensing, wind, and

***Corresponding author.**
*E-mail address: engr.faiq.said@uetmardan.edu.pk

This paper was recommended for publication in revised form by Editor-in-Chief Ahmet Selim Dalkilic

Published by Yıldız Technical University Press, İstanbul, Turkey
Yıldız Technical University. This is an open access article under the CC BY-NC license (http://creativecommons.org/licenses/by-nc/4.0/).

ambient temperature) [5]. Global demand is predicted to exceed the annual supply of non-renewable energy sources (like petrol, and coal) in the next 20 years. For food cooking, solar cookers (SCs) offer a renewable supply. However, the biggest disadvantage of SCs is that they are ineffective when there is no sunlight [6]. Researchers from all around the world are now focused on renewable energy sources due to the depletion of conventional energy sources such as petrol, diesel, coal, etc., and their negative environmental effects. Solar energy is widely available, abundant, and efficient for use in a variety of home and commercial applications. Cooking, being one of the largest energy consumers is a necessary part of human existence. Cooking using wood or cow dung as the main source of thermal energy causes pollution and unhygienic conditions worldwide [7].

Despite extensive work on box-, panel-, and parabolic-type cookers, most parabolic solar cookers reported in the literature achieved maximum temperatures around 140 °C, required 30-60 min for boiling, or lacked portability and long-term durability. Furthermore, experimental indoor validation has been limited, as most studies focused only on outdoor trials. To address these gaps, the present study introduces a parabolic solar cooker that is lightweight, portable, fabricated with durable polished stainless steel, and experimentally validated in both indoor and outdoor environments under real solar conditions.

Solar energy offers a clean, abundant, and sustainable solution for cooking, reducing fuel scarcity, deforestation, and pollution. Solar cookers improve health, lower costs, and cut greenhouse gas emissions, making them especially valuable in developing regions. When combined with efficient stoves, they meet growing cooking energy needs while minimizing environmental and economic impacts [8-13].

In Pakistan, the total energy mix comprises 180 MW of renewable energy, and the estimated potential for solar energy is more than 100,000 MW. According to a research conducted by USAID and the National Renewable Energy Laboratory (NREL) in the United States, Pakistan has 2.9 million MW of solar energy potential. Figure 1. shows direct normal sun energy while Figure 2. shows the SUNY solar model for Pakistan. Conventional cooking in Pakistan uses expensive and harmful fuels, and solar potential is still underutilised, thus increasing the importance of this research. There is a need for a useful, effective, and user-friendly design that has been proven in practical applications because existing cookers frequently lack mobility and practical validation. [14].

There are many different designs for solar cookers; these designs frequently mimic the geometry and type of heat exchanger setups that are crucial. Solar box cookers

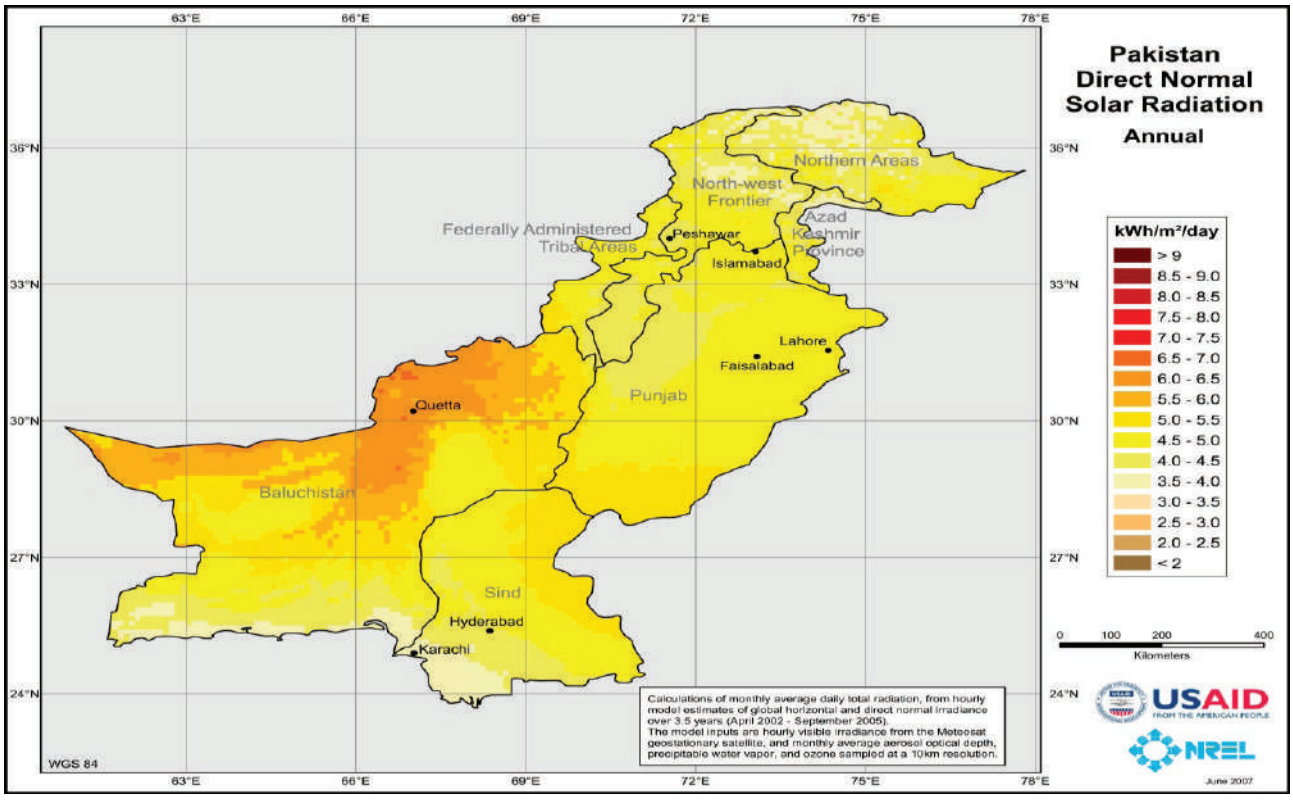

Figure 1. Direct Normal Sun Energy in Pakistan showing high annual insolation [14]

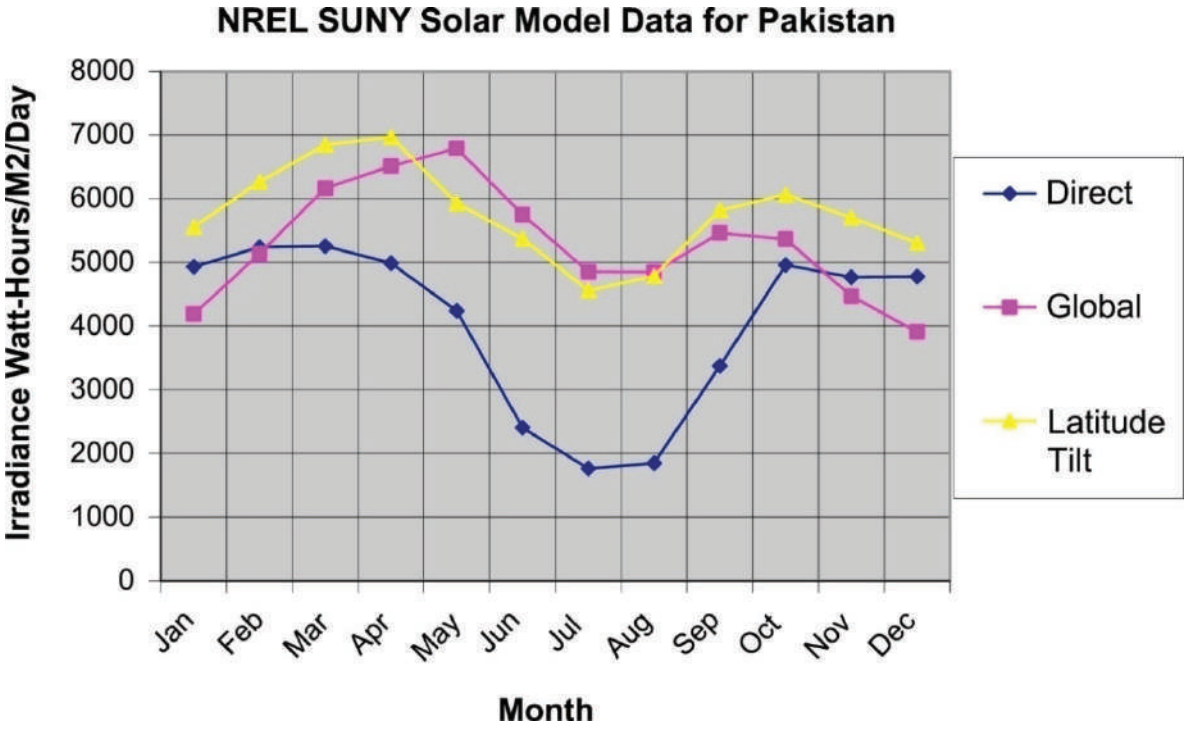

Figure 2. Data from the NREL Sunny Solar Model for Pakistan [14]

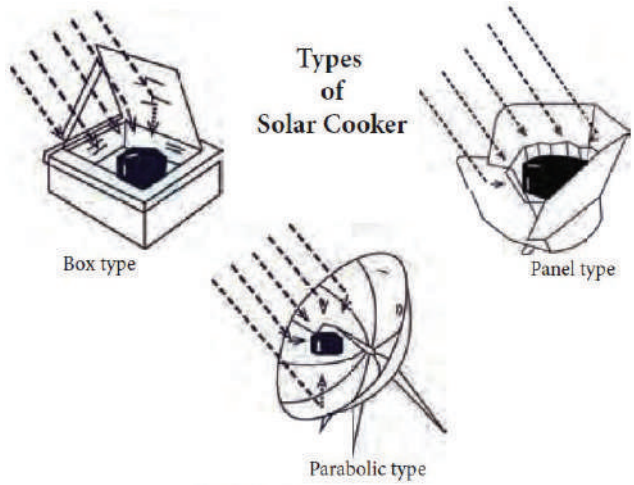

Figure 3. Classification of Solar Cooker(Box, Panel and Parabolic Type) [15]

often use direct box-type heat exchangers, whereas storage systems typically use shell and tube designs shown in Figure 3 [15].

LITERATURE REVIEW

According to Arunachala et al., cooking has a major impact on greenhouse gas emissions and world energy consumption, hence solar cooking is a practical solution. Their review discusses several solar cooker designs, such as box, panel, funnel, and parabolic models. It indicates that panel cookers are cheaper and reach 60-70% efficiency compared to box cookers. They highlight the need to come up with designs and materials that can make low-cost solar cookers efficient and long lasting, which has been highly overlooked in the past studies. The authors advocate the use of photovoltaic panels in the capture of solar energy, and effective indoor solar cooking systems even though the latter are very expensive. The final objectives of the review are to establish international testing criteria of solar cookers and stimulate access to the improvement of solar cooking commercials [16]. Vishwakarma and Sinha present a review of box-type solar cookers (BSC) equipped with thermal storage units (TES), in which case they are promising as alternatives to biofuels such as wood and animal dung that are still viewed as clean and low-cost cooking fuels. BSCs are small in size and cheap, but their cooking can only be limited in respect to off-peak hours. To improve the performance, the addition of phase change materials (PCM) like paraffin and stearic acid gives a chance to cook twice or even three times a day and reach temperatures above 100°C, with some systems reaching 164.12 °C to deep fry. To improve BSCs, it is recommended to improve thermal insulation, add artificial intelligence, and popularize them as an auxiliary gadget in the country to make them more popular [17].

Saxena et al. have conducted an experimental study of modified solar box cooker (SBC) to be operated continuously

with high efficiency in cooking. To realize thermal energy storage (TES) with the use of cylindrical copper tubes, the study used three materials including paraffin wax, grainy carbon powder, and a mixture of the two. The redesigned SBC had a thermal efficiency of 53.81%, cooking power of 68.81 W and a heat transfer coefficient of 56.78 W/m²°C, which was higher than the conventional designs. This is both economical and geographically flexible because the cooker is estimated to cost about $39.11. The findings show that such a special construction enhances the efficiency of solar cooking and offers a lightweight and economical piece of equipment that would suit a family of four to five people throughout the year [18].

Aliyu, S. J., et al. evaluate the capabilities of a parabolic solar multi-cooker, which is intended to cook using clean, renewable solar energy. It surpassed its design goals and successfully reached a temperature of 140°C, efficiently cooking food at 100°C. The cooker consumes less fossil fuels, is less expensive, and has a smaller environmental impact because it is simple to use and constructed using local materials. In order to direct solar energy toward the pot, it effectively monitors the sun. However, you might have to decide between sun concentration and angle tolerance, depending on the pot›s size. Since the multi-cooker uses renewable energy and is more environmentally friendly than conventional stoves, it is ultimately a suitable option for locations with erratic electricity [19]. Patil, R., et al. Using energy and exergy ideas, this research evaluates the thermodynamic performance of three parabolic solar cookers with the same aperture areas but varied geometries. It examines important thermal characteristics such as figure of merit, cooking power, efficiency, and change in water temperature. The manufactured and segmented rectangular dish cookers produced energy outputs ranging from 234 to 1139 kJ, while the traditional circular dish cooker produced energy outputs between 184 and 1072 kJ. The averages of energy and exergy efficiency were found to be 40%–48% and 2%–3%, in that order. According to the study's findings, the segmented rectangle dish cooker performed better overall and had higher thermal efficiency than the traditional circular dish cooker [20]. Milikias, E., et al. presented that the design, development, and testing of an enhanced box-type solar cooker with thermal energy storage is the main goal of this project. Heat storage capacity and sunlight concentration are two important improvements. Compared to a normal cooker with the same solar intercept area, the enhanced cooker has an inner surface area that is 20% smaller. Based on performance tests carried out in compliance, every variant of the upgraded cooker received an 'A' rating, with the first figure of merit (F1) values higher than 0.12. Concrete and black stone, two thermal storage materials, have a noteworthy capacity to retain heat [21].

Apaolaza-Pagoaga, X., et al. investigated solar funnel cookers that aim to be broadly available and reasonably priced. It tests the FC1 and FC2 funnel cooker designs to see if they can boil water above their boiling point. FC1 lacks a glass enclosure, but FC2 has one. The Cooker Opto-thermal Ratio (COR) and total cooking efficiency are used to compare the performance of the two cookers using glycerin as the test load. The results indicate that FC2 is excellent for high-temperature cooking because it can attain temperatures between 140 and 150°C. Compared to FC1, which has a COR of 0.110 and an efficiency of 10.2%, FC2 has a higher COR (0.157) and a greater overall cooking efficiency (11.8%) [22]. Hebbar, G., et al. research goal includescreating a zero-emission solar cooker that, in comparison to traditional models, requires less maintenance and cooks food faster. A heat transfer fluid (HTF) fills the space between the two hollow stainless-steel cylinders that make up the cooking pot. To facilitate cooking during the hours when the sun doesn't shine, phase change material (PCM)-filled copper tubes are positioned around the pot. Hose pipes are used to connect the HTF to evacuated tubes. A thermo siphon cycle transfers heat from the evacuated tubes to the HTF, heating the cooking pot and PCM in the process, and guaranteeing effective energy utilization and heat retention [23]. Gupta, P. K., et al. conducted a study on a low-cost solar cooker that uses reflecting panels and is composed of affordable materials. This panel cooker's two designs were put to the test and contrasted with a traditional solar cooker in the form of a box. After taking temperature readings in both cookers at different times, it was discovered that the panel-type cooker produced cooking pot temperatures that were lower than those of the box-type cooker. Nevertheless, with a few adjustments, the panel cooker might prove to be a practical and affordable substitute for conventional box-style solar cookers [24].

Using aluminum fins, Vengadesan et al. tested the thermal performance of a box-style solar cooker. Four fin-equipped and finless cylindrical aluminum vessels were put to the test. With a heat transfer coefficient of 58.54 W/m²°C, the 45 mm finned vessel had the highest thermal efficiency, at 56.03% [25]. Ebersviller et al. looked at solar cookers for homes and measured their cooking power at 50°C. They discovered that parabolic cookers had a standard cooking power of 198 W, box-type cookers had 65 W, and panel-type cookers had 25 W. The study showed that water heating times, thermal efficiency, and cooking power are important performance metrics. It also suggested that wind speed changes and water evaporation problems should be looked into [26].

Tibebu and Hailu looked into a solar cooker that was made from old satellite dishes, tires, steel, and aluminum foil. The cooker had a 1.8m aperture and a concentration ratio of 123.46. The cooker was tested in terms of cooking time and energy costs versus conventional fuels including firewood, charcoal, kerosene, and electricity. It also can follow the movement of the sun. The performance metrics showed that the system had an efficiency of 10.75% and a power output of around 0.3 kW/hr, with an output

energy of 0.182 kW/m², an input energy of approximately 1.691 kW/m², and an average solar radiation of 0.665 kW/m². Better cooking results were shown by the parabolic solar cooker, which also uses no energy [27]. A study on the development, construction, and testing of a parabolic solar cooker intended for usage in rural homes and refugee camps was carried out by Ahmed, S. M., et al. Stainless steel, aluminum foil, and Mylar tape were among the reflecting materials used in the study to gauge how well the solar cookers worked. Regarding the use of Mylar tape, the third tested design demonstrated the highest temperatures and the quickest cooking rate. The study indicates that additional enhancements in insulation and materials could augment the efficacy of these cookers, rendering them scalable, cost-effective, and especially advantageous in emergency contexts [5]. Using parabolic dish solar concentrators, Mawire et al. tested two solar cooking storage pots. They employed two thermal energy storage materials sunflower oil and erythritol and varied the cooking loads of water and oil. Water used more heat than sunflower oil, but sunflower oil was marginally more efficient in storage. The dependability of sunflower oil was demonstrated by the significant water evaporation that took place during solar frying. The findings provide fresh information about how well different TES materials work in solar cooking applications [28]. Patel's study highlighted the benefits of using solar energy as an alternative to fossil fuels by comparing the thermal performance of box-style and hexagonal solar cookers. The study emphasizes the significance of solar cookers in fuel consumption trends by pointing out that cooking uses more than 75% of energy in rural developing nations. Additionally, the study shows that energy absorption is influenced by the sun's position, indicating that solar cookers may lessen reliance on conventional fuels [29]. In order to dry coriander seeds, Kumar et al. designed and constructed a photovoltaic thermal collector with solar dryer (PVTCSD). They evaluated features like moisture removal, outlet air temperature, and solar radiation intensity while testing forced, open, and natural sun drying modes. The superior efficiency of PVTCSD for real-world agricultural applications was demonstrated by the results, which showed that forced convection solar drying performed better than natural and open sun modes [30].

E. Raghavendrakumar et al. analyzed SABER data from 2002-2022, finding significant atmospheric oscillations influencing ozone loss. Temperature changes reached 260 K in the middle atmosphere between 15 and 40 km altitude. They observed small but significant tropospheric ozone variation and attributed harmful gases from industrial and automotive emissions to negatively impact the atmosphere [31]. In Nasiriyah, Iraq, Koban et al. evaluated the cooking power, heat gain, collector efficiency, and optical efficiency of three parabolic solar cookers. The findings revealed cooking power of up to 740 W and efficiencies between 53-60%. Wind speed, solar tracking accuracy, reflector quality, and dish diameter all affected performance. Cooking performance and cooker efficiency were enhanced by wider apertures and precise alignment [32].

Alshehri et al. used a lab-scale setup to compare the solar-thermal performance of a multilayer selective metafilm absorber to that of a black absorber at different sun concentrations. Heat transfer analysis and steady-state testing revealed that the metafilm on stainless steel foil had outstanding spectral selectivity and thermal stability, achieving 57% efficiency at 371°C under 10 suns, with potential for up to 83% efficiency in practical solar thermal systems. The study demonstrated the ability of innovative absorber materials to greatly improve high-temperature solar energy conversion for concentrating solar power applications [33]. Vadiya et al. developed a novel inclined sidewall box-type solar cooker. Compared to a traditional cooker, the optimised design achieved a greater maximum plate temperature (76 °C vs. 65 °C), pot temperature (86 °C vs. 60 °C), and a cooking temperature of 90 °C for 2 hours, whereas the conventional cooker only maintained 60 °C for the same duration. The figures of merit were also greatly enhanced, with F1 values of 0.15 vs. 0.11 and F2 values of 0.59 vs. 0.30, indicating improved thermal response and cooking capabilities. Cooking trials revealed that food was thoroughly cooked in the newly designed cooker but overcooked in the conventional type, demonstrating the practical utility of the optimised sidewall geometry [34].

The literature shown in table 1, on solar cookers reveals various designs and methods, each with varying efficiencies and performance characteristics. Panel cookers achieve 60-70% efficiency but require design improvements, while box-type cookers can exceed 100°C. Parabolic cookers show promise but face challenges in portability and practical application. This study presents a parabolic solar cooker designed for Peshawar, Pakistan, achieving 46.75% usage efficiency and running for up to eight hours per day. This project aims to provide a sustainable substitute for fossil fuels and tackle energy scarcity in the area. The cooker boiled one liter of water in twelve minutes, reached a peak temperature of 200.6°C, and showed 46.72% thermal efficiency. There is a gap in developing solar cookers that combine high efficiency, faster cooking, and practical usability for real-world applications. Also, these studies standardized testing revealed that parabolic cookers had cooking outputs of about 198 W, but box-type and panel-type cookers only had 65 W and 25 W, respectively. These comparisons show how the current design of parabolic solar cooker goes beyond the constraints of previous designs by combining a high working temperature, efficiency, and quick cooking with portability and dual indoor-outdoor application.

Table 1. Comparative Review of Solar Cooker Designs, Performance, and Key Findings

Author	Methods	Performance	Key Findings	Limitations	References
Arunachala et al.	Review of solar cooker designs	60-70% efficiency (panel)	Panel cookers are more affordable; require design/material advancements	Limited designs reviewed; lack of experimental data	[15]
Vishwakarma and Sinha	Review of box-type solar cookers	Achieves >100°C	PCM integration improves performance; recommend enhanced insulation	Limited off-peak cooking; scalability issues	[16]
Saxena et al.	Experimental modified solar box cooker	68.81 W, 53.81% efficiency	Cost-effective and adaptable for household use	Small sample size; regional limitations	[17]
Aliyu et al.	Evaluation of parabolic multi-cooker	140°C cooking temperature	Environmentally friendly; utilizes local resources	Size constraints for portability	[18]
Patil et al.	Thermodynamic performance evaluation	Energy outputs: 184-1139 kJ	Segmented rectangle dish cooker outperforms traditional designs	Limited testing conditions; ideal only for specific locations	[19]
Milikias et al.	Design of enhanced box-type cooker	'A' rating	Effective heat storage materials retain heat	High material costs; limited market availability	[20]
Apaolaza-Pagoaga et al.	Investigation of funnel cookers	FC2: 140-150°C	FC2 outperforms FC1 in efficiency	Only focused on two designs; limited comparative analysis	[21]
Hebbar et al.	Zero-emission solar cooker development	Efficient heat transfer	PCM improves cooking efficiency	Lack of practical user trials; limited geographical scope	[22]
Gupta et al.	Low-cost panel cooker comparison	Lower temperature than box cooker	Practical alternative with adjustments	Limited performance under adverse weather	[23]
Vengadesan et al.	Thermal performance of box cooker	56.03% efficiency	Finned vessels outperform unfinned designs	Single design focus; limited performance data across designs	[24]
Ebersviller et al.	Evaluation of various solar cookers	Power: 198 W (parabolic)	Established performance metrics	Lack of long-term performance data	[25]
Tibebu and Hailu	Development of solar cooker	10.75% efficiency	Parabolic cooker outperforms conventional fuels	Limited thermal testing; potential user biases	[26]
Ahmed et al.	Testing of parabolic solar cookers	Highest temperatures noted	Mylar tape enhances performance	Results may vary with different materials	[5]
Mawire et al.	Testing of storage pots	Better heat consumption	Erythritol pot demonstrates superior performance in solar cooking	Limited to specific material; not widely available	[27]
Patel et al.	Comparison of box-style and hexagonal cookers	Highlights solar energy value	Importance of solar cookers in rural energy utilization	Focused on specific regions; limited design variations	[28]
Kumar et al.	Photovoltaic thermal collector with solar dryer	32°C to 59°C	Forced convection solar drying outperformed natural convection and open sun drying	No Scalability and only single crop tested	[30]

MATERIALS AND METHODS

Design Requirements

In addition to dependability, portability, and compactness, the parabolic solar cooker must be flexible enough to cook in a range of sun intensities. All components that come into touch with food must be made of food-grade materials and be able to operate both indoors and outdoors. The design limitations prioritize cost-effectiveness, safety, lightweight construction, and ease of use and setup. Because the external surface might get extremely hot when in use, extra care must be taken to prevent users from coming into touch with it. A key part of the solar cooker, the reflector is always in contact with the atmosphere and ought to be able to be adjusted according to changing circumstances. It must possess corrosion resistance, excellent reflectivity, and be readily available in the market.

We had the following objectives to fulfill the requirements using the given design that are given below.

- The objective of this study is to design a type of product offered with the aim of reducing air pollution, utilizing clean renewable energy, and increasing awareness about alternative energy solutions..
- The design aims to foster an understanding of environmental issues and the rational use of natural resources, highlighting the importance of conservation efforts.
- The goal is to design and fabricate an efficient and user-friendly solar cooker suitable for cooking food and heating purposes in both indoor and outdoor settings.
- We seek to diminish reliance on traditional stoves that consume wood and other energy resources, addressing the challenges associated with energy resource depletion.
- The objective is to have alternative energy solutions identified, particularly for individuals and communities with low income.

Conceptual Design

The satellite-dish-shaped parabolic solar cooker directs sunlight onto a central cooking pot using polished stainless steel. Because of its absorptivity, the polished stainless steel absorbs the remaining energy while reflecting 60% of the incoming solar radiation. Cooking materials are positioned in a receptor at a focal point that receives solar radiation from the concentrator. Any direction of movement is possible thanks to the movable holding mechanism. The pot›s bottom is heated by the heat from the parabolic concentrator, which transforms solar energy into cooking heat energy for uniform and efficient cooking.

Detailed Design

A parabolic concentrator, frame, receptor, and stand are among the various components that make up the parabolic solar cooker. The parabolic solar cooker›s operating parameters are 60 C to 400 C for the working temperature (T), 1.1 m for the focal length (f), and 8.5 kg for the weight (W).

Material selection

All the cooker components are crafted using a certain material. In the case of reflectors, a number of materials were taken into factor such as parabolic mirror, exterior aluminum foils and polished stainless steel. Stainless steel was eventually decided upon due to its durability, beauty and maintenance free qualities. Mirrors were also not preferred simply because the cooker was to be taken outside and easily broken. Polished stainless steel is a durable reflective surface that needs minimum maintenance particularly when polished frequently to maintain the finish. It also increases the service of life of the product and general life of the product. The parabolic concentrator has the mirror-like finishing with extra polishing. To promote and preserve its reflective-ness, a protective surface is taken into consideration, and regular polishing is made to remove all the scratches that may interfere with performance. The suitability of stainless steel to this purpose is due to its ability to resist rust, strength, and suitability out-of-door, as well as to its high reflectivity and low emissivity. To make it easy to use, the reflector is made by having a diameter of 6 feet with a quarter of the entire circumference open so that the user can easily view, put and take out the cooking dish at any time. The reflector is constructed out of 15 different sheets of stainless steel of the same thickness as depicted in Table 2. & 3. which are, respectively, cut together and riveted together.

The supporting frame was designed using mild steel because it is strong, can be used in various structures, and it is easily fabricated hence it was considered the best choice of material to be used in the structural parts of the solar cooker. The parabolic desired frame acts as a critical support element to the concentrator material which is fixed using rivet joints.

Table 3. Parameters of the Parabolic Concentrator

Parameter	Value	Unit
Aperture Diameter (Da)	1.6	m
Aperture Area (Aa)	1.5072	m^2
Reflectivity of Concentrator	0.58	-
Absorptivity of Concentrator	0.42	-

Table 2. Stainless Steel Sheet Composition

No of Sheets	Material	Sheets Diameter	Sheet Reflectivity
15	Stainless Steel	2 mm	60%

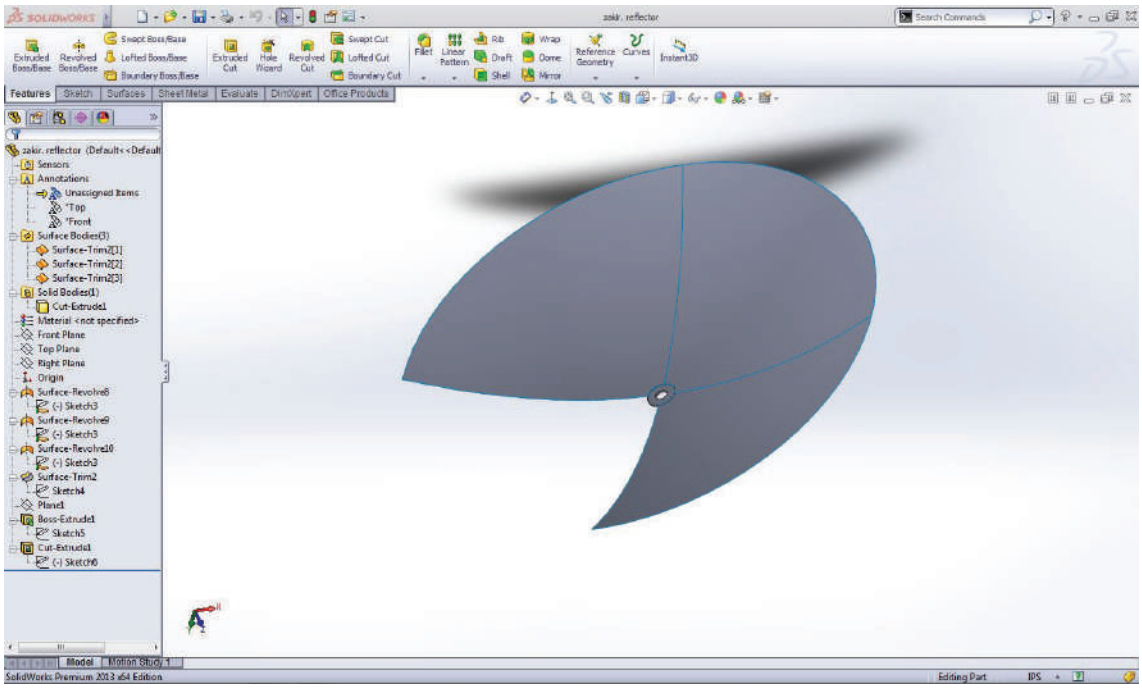

Figure 4. CAD Model of Parabolic Concentrator.

It is designed with eighteen arc-shaped supports and is made of three units at 90 degrees to the other which are joined with nuts and bolts to make it more stable.

The receptor itself is produced out of silver and it has been black painted thus increasing its capacity to absorb the solar radiation. The use of black painting also enhances its capacity to absorb the solar energy greatly. It has a cylindrical shape, positioned at the focus point of the parabolic

Table 4. Parameters of the Receptor

Parameter	Value	Unit
Radius of receptor	0..0762	m
Emissivity of receptor	0.5	-
Absorptivity of receptor	0.85	-
Area of receptor (Ar)	0.048	m^2

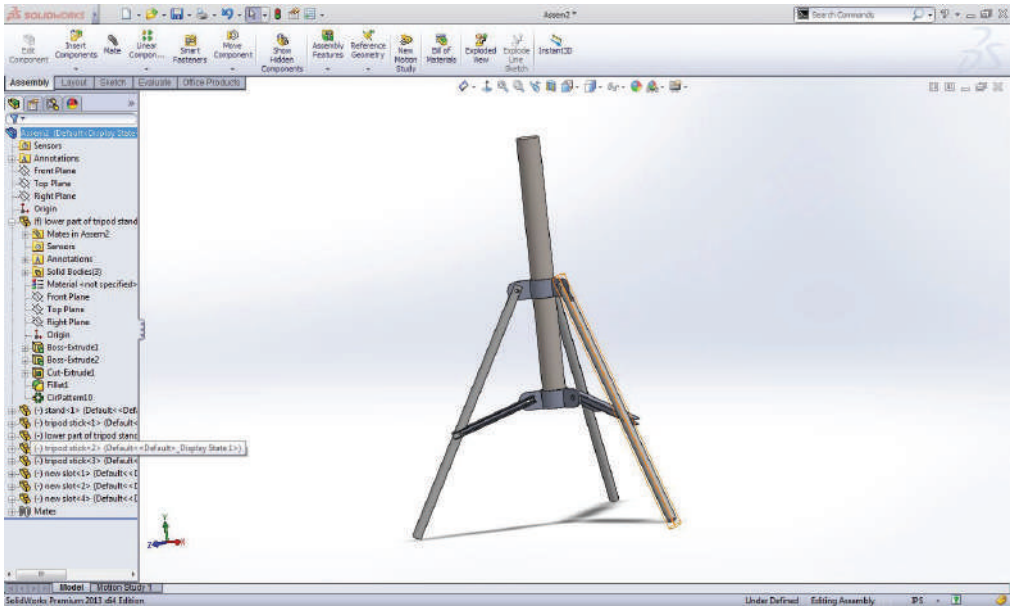

Figure 5. CAD Model of Stand.

concentrator that allows it to efficiently capture and utilize the concentrated solar energy.

The stand comprises of two parts;

The **upper part** consists of several pieces made from mild steel and is fully adjustable. These components are assembled using various sizes of nuts and bolts. For proper adjustment, sliders are utilized, which can be securely fixed using screws specific to each slider. Most of its parts are comprised of cylindrical mild steel pipes with specific dimensions.

The **lower part** of the stand is constructed from stainless steel and consists of several sub-components including a central support, an adjustable slider, three supporting legs and arms connecting the legs to the central support. To adjust and set up the solar cooker, the slider screw is loosened, allowing the slider to be pushed downward before being tightened again. As the leg supports expand, they provide increased stability to the stand, allowing it to support more load.

Theoretical analysis of solar dish concentrator

A mathematical study was done to determine the values that meet the design parameters, such as diameter, aperture angle, and concentration ratio, to calculate the parabola. For analysis, the Figure. 6 is displayed below.

Aperture Angle:

$$\phi = 2tan^{-1}\left(\frac{D_a}{4f}\right) \quad (1)$$

Φ = 40°= 0.6975 radian (Using Equation 1)

Where;

Φ = Aperture angle (radian)

Da = Diameter of the aperture (m)

f = Focal length of the parabolic dish (m)

Edge Radius:

$$\gamma_r = \frac{2f}{1+\cos\phi} \quad (2)$$

γ_r = 1.245m (Using Equation 2)

Where;

γ_r = Edge radius or maximum distance between focal point and parabolic edge (m)

Φ = Aperture angle (radian)

f = Focal length of the parabolic dish (m)

To find the area of the receptor theoretically, it is necessary to consider the aperture angle (ϕ), radius of the receiver, radius of edge and angle supported by the sun from the earth. From the Earth, the sun is seen as a circular dish that subtends 0.53° Angle α.

From the Figure 7, "C" is produced by the hypotenuse between point B, the focus and Φ = 40°.

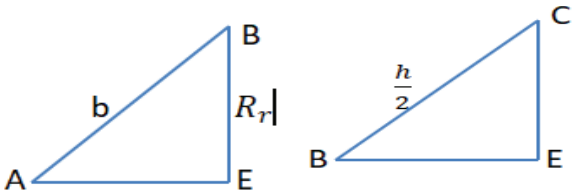

Figure 7. Receptor Area Determinations.

$$C = \frac{a}{\sin\phi} \quad (3)$$

C = 0.1186m (Using Equation 3)

Where;

C = Hypotenuse length from the focus to point B on the parabola (m)

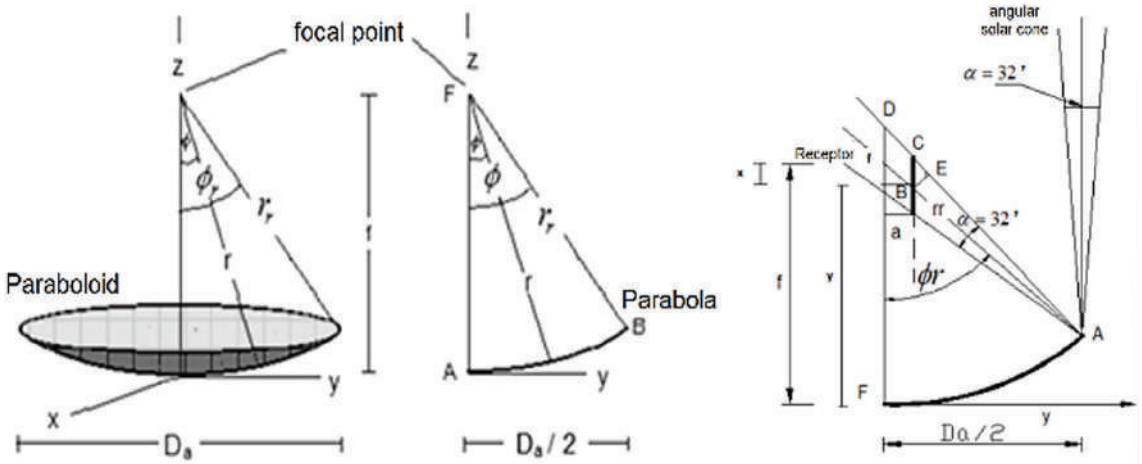

Figure 6. Theoretical Analysis of Solar Dish Concentrator [35].

a = Distance between point B and the receptor base (m)
Φ = Aperture angle (radian)

Now point B would be equal to;

$$b = \gamma_r - C \quad (4)$$

b = 1.1264m (Using Equation 4)

From Figure 7., the geometric ratio of points ABE & BCCA is;

$$R_r = \frac{b}{2}\sin\left(\frac{\alpha}{2}\right) \quad (5)$$

R_r = 2.6 x 10^{-3} m (Using Equation 5)

Using Figure 7. of the triangle BCE, we can find the half of contact surface of the receiver cylinder as,

$$\frac{h}{2} = \frac{R_r}{\cos(\theta - \phi)} \quad (6)$$

We obtain the angle formed between $h/2$ & R_r as; θ = 90.265° =1.575421 radian

h = 0.00836 m (Using Equation 6)

Where h is the contact surface of the receiver cylinder.
The area of a receiver is;

$$A_r = 2\pi ah \quad (7)$$

A_r = 4 x 10^{-3} m^2 (Using Equation 7)

The net aperture area can be calculated as;
Net aperture area (A_p)= Tota aperture area ((A_p)$_t$) – area of sector (A_s)

$$A_p = \frac{\pi {D_a}^2}{4} - \frac{\theta}{360} x\, \pi {r_a}^2 \quad (8)$$

As r_a = 0.8, θ = 90° and D_a=1.6 m^2;

A_p = 1.5071 m^2 (Using Equation 8)

There is another parameter in the solar collector system which is a concentration ratio (C) defined as the ratio between the area of the aperture (A_p)and area of receiver (A_r). The higher the concentration ratio, the higher the temperature will be.

$$C = \frac{A_p}{A_r} \quad (9)$$

C = 376.8 (Using Equation 9)

There is angular dispersion in the receptor. The dispersion is due to inappropriate solar monitoring, poor quality in polishing of reflection material and complete accurate curate curvature of concentrator surface. The angular dispersion & considering that all the specular radiation reflected is on the angular cone with (0.53° + δ). So, the value of the contact surface of the receptor considering angular dispersion is;

$$h_1 = \frac{2R_r}{\cos\left(\theta - \phi + \frac{\delta}{2}\right)} \quad (10)$$

h_1 = 8.40 x 10^{-3} m (Using Equation 10)

Then, the actual maximum concentration ratio would be given as

$$C_{max} = \frac{\pi {D_a}^2}{4} x \frac{1}{2\pi a h_1} \quad (11)$$

C_{max} = 499.3 (Using Equation 11)

By using equation (11), we can find Da1 as;

$$D_{a1} = \sqrt{8 a h_1 C_{max}} \quad (12)$$

D_{a1}=1.59 m (Using Equation 12)

The optimal focal distance (f_o) is;

$$f_o = \frac{D_{a1}}{4\tan\left(\frac{\phi}{2}\right)} \quad (13)$$

f_o = 1.09 m (Using Equation 13)

Table 5. Solar Dish Concentrator Calculations

Calculated Value	Description	Calculated Value	Description
ϕ = 40° = 0.6975 radian (Using Equation 1)	Aperture angle	A_r = 4 x 10^{-3} m^2 (Using Equation 7)	Receiver area
γ_r = 1.245 m (Using Equation 2)	Edge radius	A_p = 1.5071 m^2 (Using Equation 8)	Net aperture area
C = 0.1186 m (Using Equation 3)	Receptor distance	C = 376.8 (Using Equation 9)	Concentration ratio
b = 1.1264 m (Using Equation 4)	Point B distance	h_1 = 8.40 x 10^{-3} m (Using Equation 10)	Receptor height with angular dispersion
R_r = 2.6 x 10^{-3} m (Using Equation 5)	Geometric ratio	C_{max} = 499.3 (Using Equation 11)	Maximum concentration ratio
θ = 90.265° = 1.5754 radian, h = 0.00836 m (Using Equation 6)	Angle and receiver height		

FABRICATION

Quality Control

Material quality control

Mild steel and stainless steel were selected due to their mechanical properties and performance requirements. To make sure that the mild steel and stainless steel fulfilled the requirements for strength, corrosion resistance, and reflectivity, quality assurance measures were put in place during the material selection process. To ensure maximum solar radiation reflection, the stainless-steel sheets which were specially selected for their 60% reflectivity were examined for consistent thickness and surface polish.

Fabrication process control

Ensuring precise and reliable construction, several machining processes were involved in the fabrication of solar cooker including bending, drilling, welding, riveting and finishing.

- In order to give the frame a desired parabolic shape we used a gear bending machine as in Figure 8 below which is calibrated to bend with a specific angle which would give the best concentration of the energy. It is a machine that is meant to bend pipes and sheets to the needed shapes. The gears are spaced so as to allow different sizes of bars and pipes here the gap between the gears can be adjusted to suit the different sizes and they are then attached to motors which convert electrical power to mechanical power to power the bending process. With help of this method we managed to bend the rectangular metallic strip to form the frame of the solar cooker. (Fig. 9)
- The process of permanently joining two metal components is called welding. The structure of the solar cooker is divided into three major sections, each of which is composed of smaller components. The main frame sections are created by welding these subparts together, and they are then fused to create a single, integrated frame.
- A sheet metal cutting machine was used to precisely cut the reflective stainless-steel sheet into smaller pieces. To guarantee that every little sheet could be correctly riveted onto the frame rods, this precision was crucial. Each cut sheet's length matched the separation between two successive frame rods, ensuring a tight fit for the best alignment and stability.
- Drilling was used to build the solar cooker, and it was a crucial step in making accurate holes in the stand, frame, and reflective sheets. To guarantee that the proper hole sizes were made for every component, a drill machine was equipped with the proper drill bits. The bit sizes were selected according to the particular requirements of the drilled pieces. The holes were carefully measured and aligned because any misalignment could jeopardize the stand's and the parabolic frame's structural stability, which would have a direct impact on the solar cooker's overall performance.
- As seen in Figure 10 below, riveting is a permanent mechanical fastening technique used to attach two metal plates. Usually, a rivet is made out of a short metal pin with a cylindrical tail on one end and a head on the other. As seen in Figure 11 below, an impact riveting machine was used to secure the stainless steel reflective sheets to the frame of our solar cooker project. The reflective sheets were securely fastened to the frame by this machine, which pressed the rivet's head downward. Every joint was carefully examined for longevity and secure fastening, and the impact riveting technique guaranteed a strong and long-lasting bond. Because impact riveting is more accurate and efficient than manual riveting, it was selected.
- By smoothing metal surfaces, finishing lowers friction and improves the components' visual appeal. We finished every component of the solar cooker, paying special attention to the lower portion of the stand. By reducing wear and tear during use, this step not only guarantees improved functionality but also enhances the cooker's overall appearance.

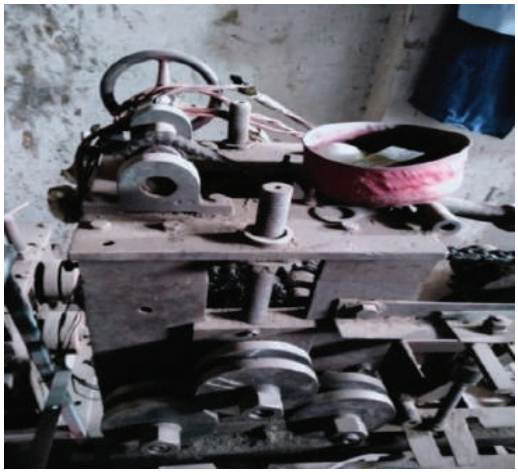

Figure 8. Bending Machine used fot Parabolic Shape.

Figure 9. Holes using a Drilling Machine

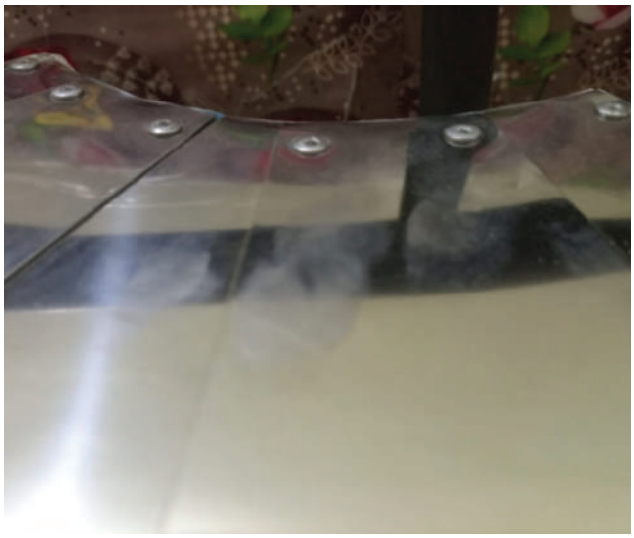

Figure 10. Rivets using Riveting.

Figure 11. Rivet Machine.

Reflective Surface Control

An essential part of the solar cooker›s operation is its reflecting surface. The surface›s smoothness and reflectivity are examined following the cutting and riveting of the stainless-steel sheets. Any imperfections, like dents or scratches, could make the reflector less effective. The sheets were kept highly reflective by cleaning and polishing them.

Assembly Procedure

The upper part of the stand shown in Figure 12 with an adjustable slider shown in Figure 13. consists of cylindrical mild steel pipes shown in Figures 14 below, assembled using nuts and bolts of varying sizes. The three leg support shown in Figure 15. of the stand plays a critical role in supporting the overall load of the solar cooker and maintaining stability in the design. Like the upper part, it is securely assembled using nuts and bolts. The frame, as shown in Figure. 16, of the solar cooker has reflecting sheets riveted onto it. The receptor is carefully assembled to be positioned at the focal point of the parabolic concentrator, optimizing energy concentration for efficient cooking. Figure 17. below shows the final product of our research.

RESULTS AND DISCUSSION

Testing Procedure

The experiment procedure entailed carrying out five different tests in the most favorable sunny weather conditions with ambient temperatures of 30°C to 35°C. During

Figure 12. Cylindrical Mild Steel Pipes

Figure 13. The upper part of the Stand

Figure 14. Adjustable Slider.

Figure 15. Three Leg Support

Figure 16. Frame of Solar Cooker

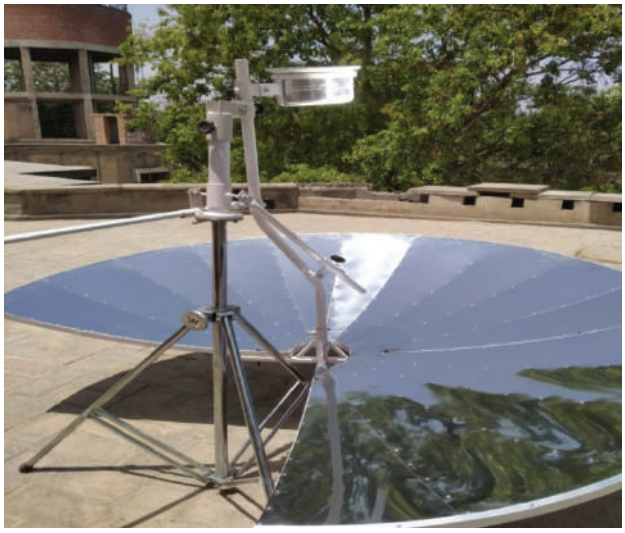

Figure 17. Parabolic Concentrator

the experiment, the solar cooker was oriented at an angle facing the sun so as to maximize the amount of solar captured. Among the five experiments, three were devoted to boiling water under various conditions of the time of the day, one was devoted to boiling an egg and the last experiment was devoted to frying an egg. All experiments were properly observed, a thermocouple was used to record the changes in temperature with time, and it could be taken into account as a good way to understand how the cooker works in different conditions. Such tests presented a viable analysis of the solar cooker and its usefulness in performing everyday cooking chores that it was effective in utilizing solar energy to perform domestic tasks. This study has developed a lightweight parabolic solar cooker with high thermal efficiency and versatility to be used both indoors and outdoors and tested them in real life conditions. The idea is confirmed by the experiments of practical cooking which proves the high speed of boiling and possibility to work all day long up to 8 hours. This is unlike earlier research which could only carry out simulations or test in a single environment. This holistic design has made solar cooking technology go a notch higher than the traditional designs by offering both effectiveness and practicality.

For indoor testing, the cooker was positioned near large south-facing windows to capture direct solar radiation. No artificial light sources were used. Solar irradiance was measured during these runs to ensure comparability with outdoor experiments.

Experiment No.1

In Experiment No. 1, we experimented to determine the time taken to boil water with the help of a solar cooker and the experiment was started at 9:00 AM. This was meant to find the efficiency with which the cooker would be able to raise the temperature of the water to boiling point. The experiment was successful in boiling water in 18 minutes time as measured by a thermocouple that was positioned inside the receptor. The readings of the temperatures after certain intervals of time show the gradual rise starting with the temperature at 31.2°C and reaching 89°C by 9:18 AM. The in-depth temperature records, presented in Table 6., address the efficiency of the solar cooker in collecting the solar energy to attain the intended heating, and as such, it can be utilized in practical ways in heating water and cooking.

Table 6. Results for Experiment No.1

Time (minutes)	Temperature (°C)
9:00 AM	31.2
9:03 AM	39
9:06 AM	48.5
9:09 AM	60
9:12 AM	71
9:15 AM	78
9:18 AM	89

Experiment No.2

Experiment No. 2, we tested the efficiency of solar cooker by boiling water at 12:30 PM, with the aim of determining the efficiency of this item in regard to heat transfer when fully exposed to the sun. The findings indicated that the water boiled within 12 minutes, which was impressive as it boiled very fast. A thermocouple was used to record the variations of temperature in the receptor with the values showing a steady increase in temperature of an initial temperature of 34°C to 94°C by 12:51 PM. Table 7. shows that the measured temperatures demonstrate a uniform rise, which highlights the ability of the solar cooker to use solar energy in quick boiling. The latter experiment also highlights the practical value of solar cookers in terms of providing energy efficiency in the process to heat water.

Table 7. Results for Experiment No.2

Time (minutes)	Temperature (°C)
12:30 PM	34
12:33 PM	46
12:36 PM	59
12:39 PM	74
12:42 PM	83
12:51 PM	94

Experiment No.3

Experiment No. 3 tested the ability of the solar cooker to boil an egg, and the experiment was conducted at 1:00 PM. The process took only 12 minutes to boil and this showed the efficiency of the cooker to transfer heat. A thermocouple was installed in the receptor to keep an eye on the temperature variations giving the correct values throughout the cooking process. Table 8. demonstrates that the temperature was measured initially at 38°C and then increased to 66°C after 6 minutes and finally to 87°C at the termination of the experiment at 12 minutes. These findings show how the solar cooker can make good use of solar energy to cook, and this proves that it is a viable option of preparing foods as a sustainable solution.

Table 8. Results for Experiment No.3

Time (minutes)	Temperature (°C)
1:00 PM	38
1:06 PM	66
1:12 PM	87

Experiment No. 4

Experiment No. 4 was conducted to test the solar cooker performance in boiling water whereby the experiment commenced at 3:00 PM. It boiled in 16 minutes showing that the cooker was effective in the utilization of sun energy during the day. A thermocouple was also installed in the receptor to measure the temperature in the boiling process accurately. The initial temperature was taken to be 35°C at 3:10 PM and then gradually rose to 47°C at 3:14 PM, 73°C at 3:22 PM, and finally to 85°C at the conclusion of the experiment. These findings also confirm the ability of solar cooker to harness the use of solar energy efficiently in cooking and this explains why solar cooker is a viable and sustainable product.

Table 9. Results for Experiment No.4

Time (Minutes)	Temperature (°C)
3:10 PM	35
3:14 PM	47
3:18 PM	61
3:22 PM	73
3:26 PM	85

Figure. 18 shows that the temperature curve of the parabolic solar cooker has a rapid thermal response. Raising the water temperature initially at 34°C, it gradually increased to 94°C in approximately 12 minutes with maximum sunlight exposure, which depicts the high concentrating power and energy transfer efficiency of the system. Above this temperature, the temperature curve leveled off at a higher

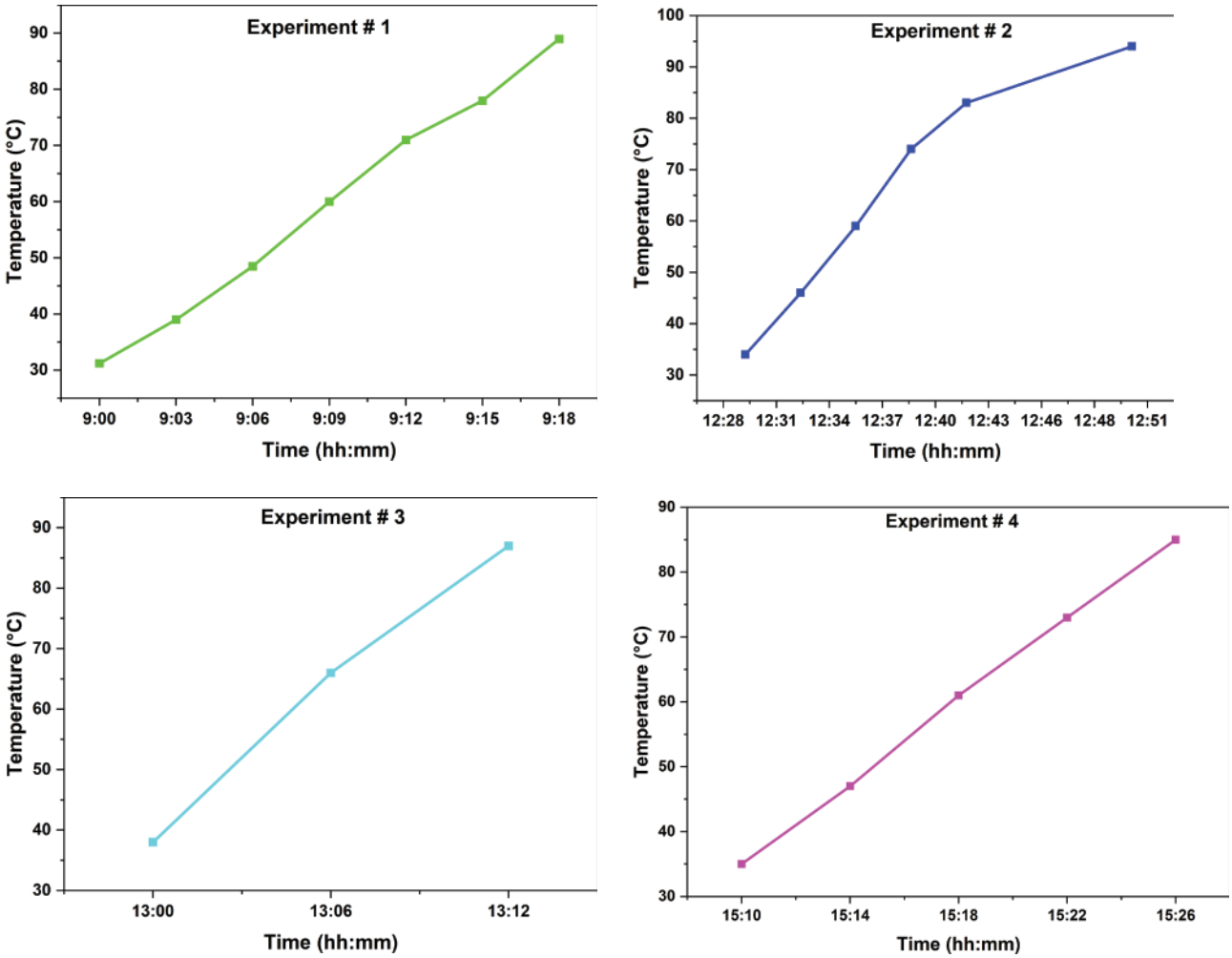

Figure 18. Temperature Variation in Solar Cooker During Cooking Tests showing a rapid rise in temperature at peak irraditaion.

temperature of over 80°C and it was found to be a stable temperature condition at which the heating was to be conducted continuously. This is due to this constant temperature zone where food can be cooked in a proper and consistent way that does not have the ups and downs that normally affect performance in other systems. The design is quite quicker in heating and has a greater maximum temperature compared to the previous experiments of box-type cooker which could require more than an hour to boil water. The high slope of the heating curve is a sign of the enhanced thermal concentration offered by the parabolic geometry and smooth reflective surface, which makes the cooker suitable in the context of the need to achieve the thermal concentration on the one hand and the long-term thermal stability on the other.

Experiment No.5

In Experiment No. 5, we tested the solar cooker's ability to cook an egg, initiating the process at 3:00 PM. The egg was cooked for a duration of one minute, showcasing the cooker's effectiveness in applying concentrated solar energy for quick cooking tasks. The egg was successfully cooked in such a short amount of time, despite the fact that no temperature data was recorded during this quick experiment. This shows the potential for quick food preparation using solar technology. This further emphasizes the versatility and efficiency of the solar cooker in meeting various cooking needs, particularly in regions with abundant sunlight.

RESULTS AND DISCUSSION

Total Solar Irradiation on Solar Cooker

Total solar irradiation refers to the rate at which solar radiation strikes a surface per unit area of that surface. The solar radiation that strikes the parabolic solar cooker in its entirety is provided by.

$$I_{i\theta} = I_{DN}cos\theta + I_{d\theta} + I_{r\theta} \quad (14)$$

The earth›s position (l), the time of day (h), and the day of the year (d) all affect the angle of incidence (θ).

When the Solar Cooker is Horizontal

When the solar cooker is horizontal, the angle of incidence θ is equal to the Zenith angle (Ψ).

$$\theta = \Psi = 90 - \beta \quad (15)$$

$$\beta = sin^{-1}[cosl \text{ x } \cos d + \sin l \sin d] \quad (16)$$

β = 34.0151° (latitude angle for Peshawar = 34.0151°
hour angle h = 0° (noon)

The declination angle is;

$$d = 23.47 \sin 360 \frac{(284 + N)}{365} \quad (17)$$

N=161 (11 June)

d = 23.03° (Using Equation. 17)

β = 79.01° (Using Equation. 16)

θ = 10.78° (Using Equation. 15)

$$I_{DN} = Ae^{\frac{-\beta}{sin\beta}} \quad (18)$$

Where A = 1080 w/m^2 for Mid-summer and β = 0.21 for summer.

I_{DN} = 872 w/m^2 (Using Equation. 18)

$$I_{d\theta} = C.I_{DN} F \quad (19)$$

Where C = 0.135 for summer and F is a view factor which is a function of orientation of surface only.

$$F = \frac{1 + cos0}{2} = 1$$

$I_{d\theta}$ = 117.72 w/m^2 (Using Equation. 19)

$$I_{r\theta} = (I_{DN} + I_d)\delta_g F_{SG} \quad (20)$$

Where δ_g = 0.5, $F_{SG} = \frac{1-cos0}{2}$ =0

$I_{r\theta}$ = 0 w/m^2 (Using Equation. 20)

So, it means that when the solar cooker is placed horizontally to the ground, no solar radiation is reflected toward the solar cooker.

$I_{i\theta}$ = 937.75 w/m^2 (Using Equation. 14)

In this study, the performance of a solar cooker positioned horizontally was investigated. The angle of incidence was found to be equivalent to the zenith angle, indicating a significant alignment with solar radiation at noon. For the specific latitude of Peshawar, the calculated declination angle confirmed that solar exposure was optimal during the mid-summer period. According to the analysis, the cooker did not receive any reflected solar radiation when positioned horizontally, even though the direct normal irradiation was significant. As a result, the cooker received about 937.75 W/m² of total solar radiation. This research highlights how important positioning is for improving solar energy absorption, which in turn increases the effectiveness of solar cooking applications.

When a Solar Cooker is Placed Inclined

The solar cooker›s concentrator receives the most sunlight when it is angled 60 degrees from the horizontal surface. With the tilt angle Σ = 60°., we will now examine the total amount of solar radiation that reaches the solar cooker. The angle of incident "θ" is given by the formula;

$$\theta = cos^{-1}[sin\beta\, cos\Sigma + cos\beta cos\alpha sin\Sigma] \quad (21)$$

Latitude l = 34.0151° (Peshawar)
hour angle h = 0° (solar noon)
N = 162 (12 June)
d = 23.1° (Using Equation. 17)
β = 79.08° (Using Equation. 16)

$$\alpha = 180 - \Upsilon \quad (22)$$

$$\Upsilon = \cos^{-1}\left[\frac{cosl\, sind - cosd \cosh sinl}{cos\beta}\right] \quad (23)$$

ϒ = 178.29°(Using Equation. 23)

α = 1.87° (Using Equation. 22)

θ = 49.08° (Using Equation 21)

I_{DN} = 880.97 w/m^2 (Using Equation. 18)

Since $F = \frac{1+cos\Sigma}{2}$ = 0.75

$I_{d\theta}$ = 89.19 w/m^2 (Using Equation. 19)

$$F_{SG} = \frac{1 - cos\Sigma}{2} \quad (24)$$

F_{SG} = 0.25

$I_{r\theta}$ = 121.27 w/m^2 (Using Equation. 20)

$I_{i\theta}$ = 787.49 w/m^2 (Using Equation. 14)

In order to maximize the concentration of solar radiation, the solar cooker was positioned in this analysis at an inclined angle of 60° from the horizontal surface. Maximum solar radiation could reach the concentrator because of the inclination. The computed angle of incidence, which took the tilt angle into account, was 49.08°, guaranteeing effective solar energy capture. Additional diffuse and reflected components contributed to the total energy, which was measured at 880.97 W/m² for direct normal irradiation. An inclined position greatly increases solar energy absorption, which is essential for optimizing the performance of solar cookers. The inclined cooker's total solar irradiation received was calculated to be 787.49 W/m².

Optical and Thermal Efficiencies:

The collector›s optical efficiency is;

$$\eta_o = \tau_v \delta_c \delta S \tag{25}$$

$$S = \frac{A_p - A_t}{A_p} \tag{26}$$

$A_{nd} = A_p$ - *Area base recibidor* = A_p - A_t

$$A_{nd} = \left(\frac{\pi D^2 a}{4} - \frac{\pi \theta {r_p}^2}{360}\right) - \pi a^2 \tag{27}$$

A_t = 1.5072-3.14 x 0.0762^2

A_t = 1.4889

S = 0.9878 (Using Equation. 26)

η_o = 48.69% (Using Equation. 25)

$$T_r = \frac{T_{amb} + T_{sum}\left[(1-\eta)\eta_o X \frac{C_{max}}{46311\ X\ \epsilon_r}\right]}{2} \tag{28}$$

Where T_{amb} = 40 °C and T_{sun} = 5726.8 °C

T_r = 200.60 °C (Using Equation. 28)

$$Q_{abs} = A_r \tau_v \delta_c \delta I_d \tag{29}$$

I_d = 872 w/m^2 (already calculated in the radiation section)

Q_{abs} = 640.03 watt (Using Equation. 29)

$$Q_{loss} = A_r u (T_r - T_{amb}) \tag{30}$$

$$u = \left(\frac{1}{h_{in} + h_{out}}\right)^{-1} \tag{31}$$

$$h_{out} = 4\Delta \epsilon_r {T_{amb}}^3 \tag{32}$$

h_{out} = 3.477 $w/m^2\ K$ (Using Equation. 32)

$$h_{in} = \frac{K_{air} N_u}{D_{out}} \tag{33}$$

$$R_e = \frac{V_{air} D_{out}}{\nu} \tag{34}$$

Since 40 °C + 273 = 313 K, then D_{out} = 0.1524 m

R_e = 37,293.17 (Using Equation. 34)

$$N_u = 0.30\ {R_e}^{0.66} \tag{35}$$

N_u = 165.99 (Using Equation. 35)

h_{in} = 29.62 $w/m^2\ K$ (Using Equation. 33)

u = 33.097 $w/m^2\ K$ (Using Equation. 32)

Q_{loss} = 25.939 *watt* (Using Equation. 31)

$$Q_{net} = Q_{abs} - Q_{loss} \tag{36}$$

Q_{net} = 614.091 watt (Using Equation. 35)

This is the net quantity of heat that cooks the food ingredients inside the receiver.

Using the useful energy delivered, it is possible to calculate the system instantaneous thermal efficiency of the solar cooker. The result is given as follows:

$$\eta = \frac{Q_{net} \times 100}{A_p I_d} \tag{37}$$

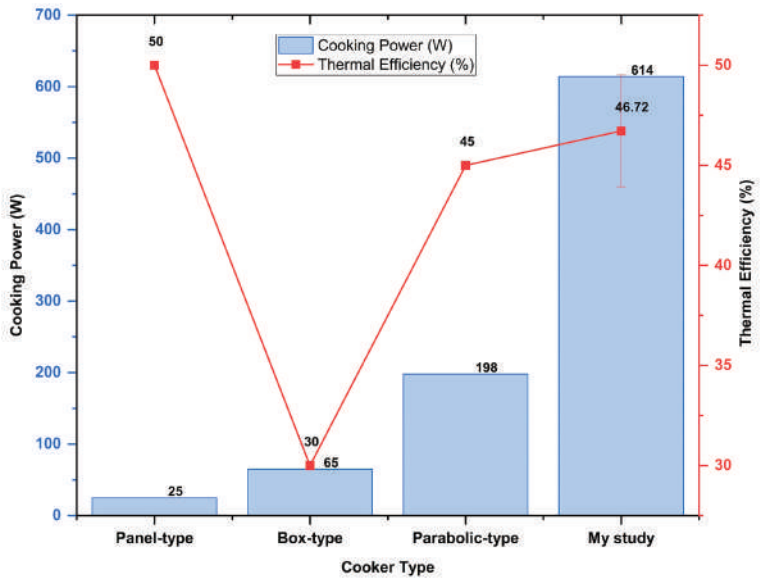

Figure 19. comparison of solar cookers' performance in terms of thermal efficiency and cooking power.

η = 46.72% (Using Equation. 37)

Together with the current design, Figure 19 compares the cooking power and thermal efficiency of several types of solar cookers that have been documented in the literature. Conventional parabolic cookers can reach approximately 198 W with 40–50% efficiency, whereas panel and box cookers usually have low cooking power (25–65 W). The current design›s superior performance is demonstrated by its significantly higher cooking power (614 W) and comparable thermal efficiency (46.72% ± 2.8%).

Uncertainity Analysis

To guarantee the repeatability and dependability of the outcomes, each experiment involving the solar cooker (water boiling, egg boiling, and frying) was carried out three times. High experimental consistency was indicated by the measurements› low variation between repetitions.

- **Temperature measurement uncertainty**
  Thermocouples with a resolution of 0.1°C and a calibration accuracy of ±0.5°C were employed. The combined uncertainty in temperature measurement, taking into account multiple trials, is estimated to be ±0.6°C. The reproducibility of the thermal response data is confirmed by the minimal deviation over the course of three trials.
- **Time measurement uncertainty**
  A digital stopwatch with an uncertainty of ±1 s was used to record the time. This uncertainty is minimal considering that the experiments lasted between 12 and 18 minutes in total.
- **Solar irradiation uncertainty**
  Calculations of solar radiation took into consideration direct, diffuse, and reflected components. An estimated ±3% uncertainty is introduced by variations in atmospheric conditions.
- **Derived efficiencies (Optical and Thermal)**
  Using measured temperatures, irradiance, and geometric parameters, optical efficiency (ηo) and thermal efficiency (η) were computed. An overall combined uncertainty of roughly ±2.5% for optical efficiency and ±2.8% for thermal efficiency is obtained by propagating uncertainties from temperature (±0.6°C), irradiation

Table 10. Analysis of Solar Cooker Performance: Thermal and Radiative Factors

Calculated Values	Description	Equation Number	Calculated Values	Description	Equation Number
937.75 W/m²	Total solar irradiation on the solar cooker when placed horizontally.	14	$I_{r\theta}$ = 121.27 W/m²	Reflected radiation falling on the solar cooker (inclined).	20
β = 34.0151°	Latitude angle for Peshawar.	16	$I_{i\theta}$ = 787.49 W/m²	Total incident radiation on the solar cooker (inclined).	14
d = 23.03°	Declination angle for 11 June (N = 161).	17	η_o = 48.69%	Optical efficiency of the solar cooker.	25
θ = 10.78°	Angle of incidence when the solar cooker is horizontal.	15	S = 0.9878	Solar energy absorption factor.	26
I_{DN} = 872 W/m²	Direct normal irradiation at noon.	18	A_t = 1.4889 m²	Area of the solar cooker's receiver.	27
$I_{d\theta}$ = 117.72 W/m²	Diffuse radiation falling on the solar cooker.	19	T_r = 200.60°C	Receiver temperature.	28
$I_{r\theta}$ = 0 W/m²	Reflected radiation falling on the solar cooker (horizontal).	20	Q_{abs} = 640.03 W	Absorbed heat by the solar cooker.	29
$I_{i\theta}$ = 937.75 W/m²	Total incident radiation on the solar cooker (horizontal).	14	u = 33.097 W/(m²·K)	Overall heat transfer coefficient (u).	31
θ = 49.08°	Angle of incidence when the solar cooker is inclined at 60°.	21	Q_{loss} = 25.939 W	Heat loss from the solar cooker.	30
I_{DN} = 880.97 W/m²	Direct normal irradiation when the solar cooker is inclined at 60°.	18	Q_{net} = 614.091 W	Net heat retained by the solar cooker for cooking.	36
$I_{d\theta}$ = 89.19 W/m²	Diffuse radiation falling on the solar cooker (inclined).	19	η = 46.72%	Instantaneous thermal efficiency of the solar cooker.	37
F_{SG} = 0.25	View factor for reflected radiation when inclined.	24			

(±3%), and surface area (~±0.5%). The dependability of these efficiency values is further supported by the small variations between repeated experiments.

The inclusion of this analysis confirms that the performance of the solar cooker is consistently reproducible and shows the high repeatability and confidence in our experimental results.

Table 10 demonstrate the radiative and thermal parameters of the cooker. The solar cooker's ability to efficiently catch and concentrate solar radiation was confirmed by its 48.69% optical efficiency. A net heat of 614.09 W was retained by the receiver, which is enough for normal cooking requirements in a household. Its 46.72% instantaneous thermal efficiency shows a high conversion rate of solar energy into usable heat, which is in line with the highest range of parabolic cookers that have been documented. These results show how reliable and effective the system is at using solar energy for practical cooking applications.

The efficiencies were calculated with error margins to account for measurement uncertainties. It was determined that the thermal efficiency was 46.72% ± 2.8% and the optical efficiency was 48.69% ± 2.5%. These uncertainties came from the propagation of errors in geometric measurements (~±0.5%), solar irradiance variation (±3%), and thermocouple calibration (±0.6 °C). The robustness of the solar cooker's performance evaluation is confirmed by the comparatively small deviations, which show high repeatability and reliability of the experimental results.

This cooker lowered the boiling time to 12 minutes instead of 30 to 60 minutes, increased the peak temperature to 200.6 °C from 120 to 140 °C in previous parabolic cookers, and guaranteed durability by using polished stainless-steel reflectors instead of brittle foils or mirrors. Compared to traditional bulky designs, it is more portable and useful for household use because it is lightweight (8.5 kg) and has a foldable stand.

CONCLUSION

This study effectively illustrated the design and construction of an easy-to-use parabolic solar cooker that is specifically suited to the climate of Peshawar, Pakistan, where daily solar insolation averages between 5.5 and 6.5 kWh/m². The main goal was to use locally accessible materials to create a cooking solution that was effective, portable, and sustainable. Its practical performance was also assessed through experiments conducted in real-world settings.

- Based on the sensible heat that the water gained during the boiling tests, the solar cooker's maximum thermal efficiency was determined to be 46.72%.
- One liter of water boiled in just 12 minutes from an ambient temperature of 28°C, demonstrating the cooker's quick thermal response in real-world cooking tests. Furthermore, under ideal solar conditions, the cooker's high thermal concentration and effective heat retention were evident from the fact that eggs were fried in about a minute and vegetables were cooked through in 20 to 25 minutes.
- Under clear sky conditions, the cooker could run for up to eight hours a day (from 9:00 AM to 5:00 PM), offering a practical way to meet everyday cooking needs without using gas or electricity.
- In order to minimize thermal losses and ensure optimal energy convergence on the cooking vessel, the focal point accuracy was kept at ±2 cm.
- With a foldable and adjustable frame that allows tilt angle adjustment between 30° and 60° depending on the solar altitude throughout the year, the cooker weighed about 8.5 kg in total.
- The parabolic shape (diameter: 1.2 m, depth: 0.2 m) guaranteed effective focus and heat delivery, while the use of stainless steel with a reflectivity of roughly 60% improved solar concentration.
- In terms of the environment, the solar cooker takes the place of traditional liquid petroleum gas use. An estimated 0.25 kg of liquid petroleum gas could be saved per session of use, which translates to a daily reduction of 0.75 kg of carbon dioxide emissions per household.
- This study placed a strong emphasis on real-world testing, which confirms the design's effectiveness and dependability in real-world cooking situations, in contrast to many earlier studies that only looked at simulations.
- In comparison to earlier designs, our solar cooker performed better, reaching 200.6°C, boiling one liter of water in 12 minutes, and achieving a maximum thermal efficiency of 46.72%. Its practical relevance and wider impact for sustainable cooking solutions are highlighted by its quick cooking, high efficiency, and dual indoor-outdoor applicability.

The suggested solar cooker is an economical and sustainable substitute for conventional cooking methods because of its high thermal efficiency, rapid boiling capacity, and 8-hour continuous operation. It offers useful advantages by reducing reliance on fossil fuels, encouraging sustainability, and enabling adaptable use in both indoor and outdoor settings. The performance of the cooker is restricted by its reliance on clear skies, the requirement for manual solar tracking on a regular basis, and the durability of reflective surfaces over time. In order to further improve performance and applicability, future work should concentrate on developing lightweight, high-reflectivity materials, scaling the design for community-level kitchens, integrating phase change materials (PCM) for cooking during off-sun hours, and integrating reasonably priced automated tracking systems.

NOMENCLATURE

$I_{i\theta}$ *Total solar irradiation of a surface (w/m²)*
I_{DN} *Direct radiation from sun (w/m²)*

$I_{d\theta}$ *Diffuse radiation from sky* (w/m^2)
$I_{r\theta}$ *Reflected radiation from other surfaces (ground)*
Θ *Angle of incident (degree)*
β *Altitude angle which is linked with the surface angle*
F_{SG} *View factor from ground to surface of solar cooker*
α *Wall solar azimuthal angle.*
Υ *Azimuthal angle.*
τ_v *Trasnmittance of glass coating (If not given then equal to* 1)
δ_c *Receptor absorbance* (0.85)
δ *Reflectivity of concentrator* (0.58)
S *Shape factor* (0.9878)
C *For summer* (0.135)
I_d *Mean direct radiation from the sun to parabolic concentrator*
F *View factor (F is a function of orientation of surface only)*
δ_g *Reflectivity ofground* (0.5)
η_{opt} *Optical Efficiency* (0.4869)
η_{th} *Thermal Efficiency range* (0,4-0.6)
ϵ_r *Emmicivity of reciever* (0.5)
K_{air} *Thermal conductivity ofair* (0.072 *w/mK*)
v *Kinetic viscosity* (17×10^{-6} m^2/s)
V_{air} *Velocity of air* (4.16 *m/s*)
h_{in} *Inner convection heat transfer coefficient*
h_{out} *Outer convection heat transfer coefficient*
u *Overall heat transfer coefficient*
Q_{abs} *Estimated energy absorbed by the receptor*
Q_{loss} *Heat lost in receiver*
Q_{net} *Net heat gain*
T_r *Average temperature in the receiver*
Q_e *Useful Energy Delivered*
I_b *Solar Irradiance*
A_c *Collector Aperture Area*
m *Mass of Water*
ΔT *Temperature Rise*
Δt *Heating Time*

Da *Aperture diameter*
f *Focal length*
Ar *Receiver area*
Ap *Aperture area*
C *Concentration Ratio*
h *Reciever height*
b *Distance from focus to point*
θ *Angle in triangle BCE*
γ_r *Edge radius*
ϕ *Aperture angle*

REFERENCES

[1] Devan PK, Chidambranathan B, Subramaniyan G, Hariharan G. A comprehensive review on solar cooker with sun tracking system. Mater Today Proc 2020;33:771–777. [Crossref]

[2] Joshi SB, Jani A. Design, development and testing of a small scale hybrid solar cooker. Sol Energy 2015;122:148–155. [Crossref]

[3] Tawfik M, Sagade AA, Palm Behnke R, El-Shal h, Allah WEA. Solar cooker with tracking-type bottom reflector: An experimental thermal performance evaluation of a new design. Sol Energy 2021;220:295–315. [Crossref]

[4] Aquilanti A, Tomassetti S, Coccia G, Muccloli M, Di Nicola G., Experimental characterization and performance comparison of four prototypes of panel solar cooker for low to high sun elevations. J Clean Prod 2023;390:136158. [Crossref]

[5] Ahmed SM, Al Amin Rahmatullah, Ahammed S, Ahmed F. Design, construction and testing of parabolic solar cooker for rural households and refugee camp. Sol Energy 2020;205:230–240. [Crossref]

[6] Omara AA, Abuelnuor AAA, Mohammad HA, Habibi D, Younis O. Improving solar cooker performance using phase change materials: A comprehensive review. Sol Energy 2020;207:539-563. [Crossref]

[7] Khatri R, Goyal R, Sharma RK. Advances in the developments of solar cooker for sustainable development: A comprehensive review. Renew Sustain Energy Rev 2021;145:111166. [Crossref]

[8] Coccia G, Aquilanti A, Tomassetti S, Ishibashi A, Nicola GD. Design, manufacture and test of a low-cost solar cooker with high-performance light-concentrating lens. Sol Energy 2021;224:1028–1039. [Crossref]

[9] Kaputo K, Mwanza M, Talai S. A review of improved cooker stove utilization levels, challenges and benefits in sub-Saharan Africa. J Energy Res Rev 2023;14:9–25. [Crossref]

[10] Sanglard B, Lachaize S, Carrey J, Barna LT. Life cycle assessment of a parabolic solar cooker and comparison with conventional cooking appliances. Sustain Prod Consum 2023;42:211-233. [Crossref]

[11] Mekonnen BA, Liyew KW, Tigabu MT. Solar cooking in Ethiopia: Experimental testing and performance evaluation of SK14 solar cooker. Case Stud Therm Eng 2020;22:100766. [Crossref]

[12] Apaolaza-Pagoaga X, Carrillo-Andrés A, Ruivo CR. Experimental thermal performance evaluation of different configurations of Copenhagen solar cooker. Renew Energy 2022;184:604–618. [Crossref]

[13] Sawarn H, Shukla SK, Rathore PKS. Development in solar cooking technology in the last decade: A comprehensive review. In: IOP Conf Ser Mater Sci Eng. Bristol: IOP Publishing; 2021. [Crossref]

[14] National Renewable Energy Laboratory (NREL). Official website of NREL. Accessed October 2024.

[15] Gawande TK, Ingole D. Comparative study of heat storage and transfer system for solar cooking. SN Appl Sci 2019;1:1676. [Crossref]

[16] Arunachala UC, Kundapur A. Cost-effective solar cookers: A global review. Sol Energy 2020;207:903–916. [Crossref]

[17] Vishwakarma A, Sinha S. Box type solar cooker with thermal storage: An overview. Energy Syst 2024;15:1289–1315. [Crossref]

[18] Saxena A, Cuce E, Tiwari GN, Kumae A. Design and thermal performance investigation of a box cooker with flexible solar collector tubes: An experimental research. Energy 2020;206:118144. [Crossref]
[19] Aliyu SJ, Chiebuka N, Adebayo KR, Banji AA. Performance evaluation of locally designed and produced parabolic solar cooker. Int J Energy Environ Sci 2021;6:96–106. [Crossref]
[20] Patil, R., Y. Kulkarni, Gujrathi A. Energy and exergy analysis of three domestic parabolic solar cookers with different geometries. Int J Ambient Energy 2022;43:7766–7774. [Crossref]
[21] Milikias E, Bekele A, Venkatachalam C. Performance investigation of improved box-type solar cooker with sensible thermal energy storage. Int J Sustain Eng 2021;14:507–516. [Crossref]
[22] Apaolaza-Pagoaga X, Sagade AA, Ruivo C, Andres AC. Performance of solar funnel cookers using intermediate temperature test load under low sun elevation. Sol Energy 2021;225:978–1000. [Crossref]
[23] Hebbar G, Hegde S, Sanketh B, Sanith LR. Design of solar cooker using evacuated tube solar collector with phase change material. Mater Today Proc 2021;46:2888–2893. [Crossref]
[24] Gupta PK, Misal A, Agrawal S. Development of low cost reflective panel solar cooker. Mater Today Proc 2021;45:3010–3013. [Crossref]
[25] Vengadesan E, Senthil R. Experimental investigation of the thermal performance of a box type solar cooker using a finned cooking vessel. Renew Energy 2021;171:431–446. [Crossref]
[26] Ebersviller SM, Jetter JJ. Evaluation of performance of household solar cookers. Sol Energy 2020;208:166–172. [Crossref]
[27] Tibebu S, Hailu A. Design, construction, and evaluation of the performance of dual-axis sun tracker parabolic solar cooker and comparison of cooker. J Renew Energy 2021;2021:8944722. [Crossref]
[28] Mawire A, Lentswe K, Owusu P. Performance of two solar cooking storage pots using parabolic dish solar concentrators during solar and storage cooking periods with different heating loads. Results Eng 2022;13:100336. [Crossref]
[29] Patel A. Comparative thermal performance analysis of box type and hexagonal solar cooker. Int J Sci Eng Dev Res 2023;8:2455–2631.
[30] Srimanickam B, Kumar S. Drying investigation of coriander seeds in a photovoltaic thermal collector with solar dryer. Int J Mech Eng Technol 2021;14:659–668. [Crossref]
[31] Raghavendrakumar E, Kamalakar V, Kumar KS. An investigation in temperature data analysis of middle atmospheric variation from SABER satellite. Nat Environ Pollut Technol 2024;23:443–450. [Crossref]
[32] Koban RM, Hannun RM. Thermal study of three solar parabolic cookers in Nasiriya city, Iraq. Univ Thi-Qar J Eng Sci 2021;11(2):122–132. [Crossref]
[33] Alshehri H, Qin N, Taylor S, McBurney R, Wang H, Wang L. Solar thermal energy conversion enhanced by selective metafilm absorber under multiple solar concentrations at high temperatures. Alshehri H, et al. Solar thermal energy conversion enhanced by selective metafilm absorber under multiple solar concentrations at high temperatures. arXiv 2019;1910.0707. [Crossref]
[34] Vaidya H, Rathod M, Channiwala S. Design, development, and analysis of a box type solar cooker with optimally reflecting side walls. J Therm Eng 2023;9:1–11. [Crossref]
[35] Villamil JAA, Hortúa JE, López A. Design and construction of a solar collector parabolic dish for rural zones in Colombia. Tecciencia 2013;7:14–22. [Crossref]

J Ther Eng, Vol. 12, No. 1, pp. 50−71, January, 2026

Journal of Thermal Engineering
Web page info: https://jten.yildiz.edu.tr
DOI: 10.14744/thermal.0001057

Research Article

Kinetics of UV degradation of hydrogen sulfide without oxidization by Homotopy Perturbation Method

Sreelatha DEVI[1,*], K. SARANYA[1], D. VIJAYABALAN[2], Jayanthi RAJENDRAN[3], Muthumari G[4], Banu PRIYA V[5]

[1]Department of Mathematics, Saveetha School of Engineering, SIMATS, Tamil Nadu, 600017, India
[2]Department of Mathematics, Vel tech high tech Dr. Rangarajan Dr. Sakunthala engineering college, Tamil Nadu, 600017, India
[3]Department of English, Associate Professor, Easwari Engineering college (SRM Group of Institution), Chennai, 516175, India
[4]Department of Mathematics, S.A. Engineering college, Tamil Nadu, 516175, India
[5]Department of Mathematics, R.M.K. College of Engineering and Technology, Chennai, 516175, India

ARTICLE INFO

Article history
Received: 28May 2017
Accepted: 01 July 2025

Keywords:
H2S; Homotopy Perturbation Method; Mathematical Modeling; Nonlinear Equations

ABSTRACT

The promotion of biogas energy has been constrained by the presence of H_2S. Classical H_2S photodegradation is typically carried out with oxygen present, but this is inappropriate for biogas desulfurization and must be prevented. Thus, the current study was to examine the UV degradation of H_2S without O_2 from a mathematical perspective. This paper was performing a theoretical investigation of UV degradation of H_2S without oxygen. First, the Homotopy perturbation approach was used to construct a theoretical computer model on H_2S photodegradation. This model included models for the distribution of gas flows, radiation kinetics in the photoreactor, mass balance, and degradation rate. Then, to verify the mathematical model, the effects of the initial H_2S concentration and gas retention duration on the photodegradation rate were examined. To validate the mathematical model, the effects of factors on the initiative H_2S mass and gas retention time toward the photo-degradation rate were investigated. The primary photodegradation products were identified as elemental S and H_2.

Cite this article as: Devi S, Saranya K, Vijayabalan D, Rajendran J, G M, B Priya V. Kinetics of UV degradation of hydrogen sulfide without oxidization by Homotopy Perturbation Method. J Ther Eng 2026;12(1):50−71.

INTRODUCTION

One of the persistent environmental and economic problems of the last century has been the capture and conversion of hydrogen sulfide (H_2S). Many important fuel gases, like natural gas, biogas, syngas, coke oven gas, landfill gas, and refinery gas, along with wastewater, have the very unpleasant, smelly, and toxic chemical H2S mixed in as a contaminant. For safety and economic reasons, this chemical must be removed from these streams. Equipment and pipeline corrosion results from H_2S's natural propensity to react with water to generate an acidic solution. Additionally, its presence causes catalyst poisoning and lowers the fuel

***Corresponding author.**
*E-mail address: vijayabalantqb@gmail.com

This paper was recommended for publication in revised form by Editor-in-Chief Ahmet Selim Dalkilic

Published by Yıldız Technical University Press, İstanbul, Turkey
Yıldız Technical University. This is an open access article under the CC BY-NC license (http://creativecommons.org/licenses/by-nc/4.0/).

gases' heating value. Above all, as it burns, sulfur dioxide and other toxic sulfur oxides are released, which results in acid rain. Furthermore, H_2S is a toxic gas that is dangerous even at low quantities, as Table 1 illustrates. After extended exposure at roughly 5 ppm, it irritates the eyes and airways, and at 1000–2000 ppm, it instantly kills a person [1, 2]. Therefore, in order to improve the quality of life and the global atmospheric chemistry, H_2S emission needs to be reduced and controlled [3].

Therefore, purification is necessary to eliminate and/or convert H_2S (as well as other acid gases like CO_2) before many fuel gases can be used for energy generation or chemical manufacturing. The particular end use and the applicable municipal legislation determine the allowable level of H_2S in a gas stream. In the US and Denmark, for instance, pipeline gas must have an H_2S concentration of less than 4 parts per million [4], but reformer and fuel cell applications often need a content of less than 1 part per million [5, 6]. The two main categories of hydrogen sulfide capture techniques are physical chemical procedures and biological strategies. They can also be categorized as dry and wet desulfurization techniques. They can be further divided into cryogenic distillation, membrane separation, absorption, adsorption, microbiological techniques, advanced oxidation processes, etc. The current trends in each of these technologies, spanning the last five or ten years, are the main emphasis of this thorough assessment. Every one of them has benefits and drawbacks based on a variety of variables, which will be discussed here. However, because cryogenic distillation is expensive and has other practical problems that have hindered any significant technological advancement in H_2S removal over the last ten years [7], it is not covered in this work. However, whether the ultimate objective is to produce liquefied natural gas or to re-inject the liquefied acid gases into a geological reservoir, cryogenic separation, either as a stand-alone method or in conjunction with absorption, is probably the most cost-effective choice [8, 9, 10]. Through a two-step procedure, this study suggests an integrated and sustainable method for efficiently turning kitchen garbage into useful items. Using greenhouse solar drying is the first step in lowering the moisture content of kitchen waste. In the secondary process, kitchen waste is effectively broken down into biochar, biogas, and biooil using microwave pyrolysis. As renewable fuel sources, biogas and biooil are both viable. You can use biochar as a soil supplement. In [11] the environment is severely polluted as a result of rapid urbanisation and industrialisation, especially in water bodies that are tainted with dangerous germs and toxic dyes. Numerous studies have been conducted on zinc oxide (ZnO) nanoparticles because of their antibacterial and photocatalytic capabilities [12]. Synthetic dyes are widely used, particularly in the textile industry, which contributes to environmental contamination by introducing chemicals that are difficult to remove using conventional wastewater treatment methods. Complex aromatic structures provide these dyes stability and resilience, but they also produce harmful, frequently cancer-causing substances that endanger human health and aquatic habitats. This study suggests that $NiS\text{-}NiS_2/S\text{-}g\text{-}C_3N_4$ is a strong and promising option for the reduction of aromatic nitro compounds [13]. Makes reference to the building many nations produce a lot of demolition and renovation waste (CDRW), and the building sector is a major driver of both infrastructure growth and socioeconomic advancement. The risks CDRWs pose to human health, safety, and the environment have prompted calls for action on a global scale. [14] A stronger turbulence velocity distribution, better mixture fraction values, and a lower soot formation distribution can be achieved by altering the bowl's shape [15].Certain conditions must be met for the findings to be obtained. It was found that the pressure, temperature, and heat release of the combustion chamber had changed due to the modified bowl shape. [16] Hydrogen sulfide is an extremely hazardous, highly flammable, and extremely deadly gas that must be captured and removed from a number of important gaseous and liquid streams. Due to the persistent issue of H_2S trapping, a number of materials have been developed over time and used in a variety of technologies. Alkanolamines used as absorbents and metal oxides used as adsorbents are well-known examples. This research thoroughly examines the latest developments and state-of-the-art materials in this field. Biological methods, improved oxidation processes, metal organic frameworks, carbon-based materials, zeolites, ionic liquids, deep eutectic solvents, and polymeric membranes are a few examples. The state of the art is thoroughly examined in this review, which also provides a comprehensive technology map and identifies challenges and possibilities to guide future research. In the following publication, the technologies for H2S removal and capture were described in detail. In the final study, H_2S removal and capture devices were thoroughly examined.

The paper has a significant contribution to developing [theoretical] models on the photodegradation of H_2S if UV radiation is in the absence of oxygen. Study derives analytical solutions for concentrations of H_2S and its degradation products using the HPM. For example, this model considers different factors including gas flow distribution, radiation kinetics, and mass balance to describe the photodegradation processes.H_2S techniques comprise biological, chemical, physical and combinatorial technologies.Several H_2S removal methods are carried out depending on physical, chemical, or biological principles. The potential of composite adsorbents is high, but their main challenge still revolves around selecting the optimum material combination and their synthesis. Some materials with chemisorption provide high capacity and breakthrough time, but they are often irreversible and would suffer from decreasing performance very quickly.

TECHNOLOGIES FOR H_2S CAPTURE / REMOVAL

Biological Technologies

The foundation of biological approaches is the use of an oxidizing group of bacteria that thrives in environments where inorganic reduced sulfur compounds, like H_2S, are present. These gram-negative bacteria fall into

two categories: photoautotrophs and chemolithotrophs. They can use sulfur or sulfide as an electron source. Both domains share the following sulfur oxidation processes:

$2S + 3O_2 + 2H_2O \rightarrow 2H_2SO_4 + 2H^+ + SO_4$

$CO_2 + 2H_2S \rightarrow CH_2O + H_2O + 2S$

Some species, such as the ones listed above, biodegrade H_2S within the cell. However, extracellular oxidation of H_2S is also a feature of green sulfur bacteria, such as those of Thiomicrospira frisia and Thiobacillus thioparus. Thiobacillus species are commonly employed as chemotrophs for the biodegradation of H_2S due to their ability to thrive in various environmental settings. For instance, Thiobacillus ferrooxidans and Thiobacillus thiooxidans can thrive at low pH (<6). Being a thermophile, Thermothrix azorensis may survive at temperatures as high as 86°C. As an alkaliphile, Thioalkalispira microaerophila grows best at pH 10. The following illustrates the aerobic reactions for a colorless sulfur-oxidizing system. The amount of oxygen in this system affects the formation of elemental sulfur and the sulfate ion.

$H_2S + H_2O \rightarrow HS^- + H_3O^+$

$H_2S + 2O_2 \rightarrow SO_4^{2-} + 2H^+$

$HS + 0.5\ O_2 \rightarrow S^0 + H_2O$

$S^0 + H_2O + 0.5O_2 \rightarrow SO_4^{2-} + 2H^+$

Some genera, including Alcaligenes, Paracoccus, Pseudomonas, Xanthobacter, and Bacillus, grow heterotrophically but have demonstrated the usage of reduced inorganic sulfur compounds in their metabolism, despite the fact that sulfur-oxidizing bacteria are typically autotrophic.

Absorption

The most popular method for purifying fuel gasses during the 20th century has been the absorption of acid gases into a liquid solvent. The strength of the solvent-H2S interaction determines whether the absorption mechanism is classified as physical or chemical. Despite the strong interactions that characterize chemical absorption, stoichiometry limits it. There are almost no restrictions on solubility for physical absorption. At high pressures, physical absorption occurs, whereas chemical absorption often occurs at low pressures. Because of this, physical solvents like syngas cleaning—are superior to chemical solvents when the source gas has high partial pressures or concentrations of H_2S. Physical solvents can be renewed by air stripping, a straightforward pressure/temperature swing operation over one or more flash tanks, or by applying heat in a column, depending on the gas quality requirements. Chemical solvents are renewed by applying heat in a desorption column. It can be difficult to distinguish between physical and chemical absorbents because all solvents have physical interactions with solutes. Ionic liquids, deep eutectic solvents, alkanolamines, common physical solvents, and hybrid mixes are the five primary groups into which absorption techniques are divided for examination.

Adsorption

The process of surface-based adsorption transfers a molecule from a fluid bulk to the solid surface of the adsorbent. Under the topic of H_2S removal, we only discuss removal from a gas stream because this reaction is exothermic under dry conditions and does not require high temperatures. Recently, there has been a lot of interest in this dry desulfurization technology due to its affordability, adaptability, energy efficiency, and simplicity of usage. Adsorption is divided into two categories: physisorption and chemisorption (reactive adsorption), which are determined by the strength of the interaction between the adsorbent and adsorbate. Physisorption is dominated by van der Waals forces and/or electrostatic interactions, whereas chemisorption is dominated by covalent and/or hydrogen bonding interactions. Sometimes, regardless of the kind of underlying connection, the only way to distinguish between physisorption and chemisorption is based on contact intensity, particularly in experimental studies. In these situations, physisorption refers to weak contacts and chemisorption to strong ones. However, for molecules that are a little bit larger, physisorption can be rather robust. Apart from these interactions, selectivity in multi-component mixtures may also be impacted by the size and shape of molecules. High breakthrough capacity, chemical and thermal stability, structural regeneration, and selectivity towards target molecules (in this case, H_2S) are characteristics of desired adsorbent materials. Recently, a lot of research has been done on developing such economical and efficient adsorbents for the removal of H_2S, especially at low temperatures. In this regard, porous materials have emerged as intriguing options because of their large pore volume, large surface area, and range of potential chemical configurations.

Advanced Oxidation Processes

In order to speed up the breakdown of target molecules, Glaze initially classified advanced oxidation processes (AOPs) as those that produce and employ reactive species, primarily hydroxyl radicals (HO·). HO· is a well-known highly oxidant species. Its redox potential is 2.8 V, which is lower than fluorine›s (3.03 V) and greater than other known oxidants including ozone, hydroperoxyl, chlorine, permanganate, persulfate anion, hydrogen peroxide, and sulphate radicals. AOPs are now widely used to remove a wide range of contaminants from various industrial matrices, including contaminated air and streams. The many types of AOPs include Fenton and electro-Fenton processes, systems mediated by ozone (O_3) and hydrogen peroxide (H_2O_2), photocatalysis, photoirradiated processes, and plasma-based processes. All of these processes result in the production of HO·, which breaks down the target molecules. According to the literature, there are several important ways in which AOPs are better than rival technologies. These include excellent yields and mineralization, the ability to operate at ambient conditions, long-term

performance stability, minimal mass transfer restrictions, a small footprint, little to no sludge formation, and high efficiency in incredibly quick reaction times. Among the disadvantages that researchers have identified are the toxicity of residual H_2O_2 in the effluent, the need for UV light to activate catalysts, the expense of the photo-reactor, and the decrease in photo-mediated process efficiency when suspended solids or less soluble salts are present (more likely for the H_2S oxidation process). However, the disadvantages of the conventional AOPs can be lessened by employing the synergy between the different strategies and combination AOPs, such as photocatalytic / H_2O_2 reactors, or more modern systems, such as UV–v is / catalyst. AOPs have been used in a few recent studies to oxidize gaseous and aqueous H_2S.

Electrochemical Processes

Electrochemical technology have been utilized for environmental cleaning for the last three decades. But around half a century ago, it was discovered that an electrochemical unit might be used to extract and /or oxidize hydrogen sulfide from aqueous solutions. In an electrochemical unit, an electron flow produced by external power sources triggers a series of oxidation and reduction reactions. It may be more cost-effective to employ chemical-less electrical oxidation than chemical-intensive methods, which require the dosing, transportation, and storage of potentially dangerous materials. The performance of the cell may also be readily regulated by varying operational parameters like voltage and current, and there is no limit on electron flow, unlike some technologies like photocatalytic reactors. Sometimes the primary concern in outdoor applications is the energy cost of an electrochemical cell. When renewable energy sources are employed, this method can be a flexible and sustainable technology that can be applied to a range of concentrated waste streams with excellent operating and energy efficiency. It can also be readily integrated with remote applications.

Membranes

Since membrane technology only started to be applied in industry in the latter half of the 20th century, it is relatively new in comparison to more established gas separation methods like adsorption and absorption. Even though membrane research dates back to the 19th century, Loeb and Sourirajan›s invention of the first cellulose-acetate-based reverse osmosis membrane for water desalination in early 1962 marked the development of the first synthetic membranes on an industrial scale. It was not until the 1980s that membrane businesses made their way into the gas processing industry. Since then, one of the most important methods for gas separation has been polymeric membrane technology, which has shown remarkable performance and efficiency in gas transport. Membranes can optimize gas separation by (a) reducing equipment size and capital costs, (b) improving process safety and operating simplicity, (c) doing away with complex control systems, and (d) requiring less energy, particularly when pressured gas is already available. In general, inorganic membranes are only utilized in systems when the direct use of polymeric membranes is prohibited by high temperatures and other working conditions due to their higher cost and manufacturing challenges. Consequently, polymeric membranes are currently the most often used materials for gas separation and/or natural gas sweetening. In order to focus on polymeric membranes that are used and evaluated for H_2S separation in natural gas purification, inorganic membranes will not be considered in this research. Over the past decade or so, research in this field has concentrated on attaining process stability and developing more robust and long-lasting materials in an attempt to enhance gas separation performance. H2S studies are considerably more limited because of the toxicity of the gas and the extremely high purity requirements (down to ppm) that membranes alone can hardly accomplish. Membranes are usually researched for CO_2 collection and purification when dealing with acid gas removal. Since polymeric membranes have a high chemical endurance and have been shown to function well in harsh environments, they can be a highly useful pretreatment to increase the effectiveness of other technologies for purifying streams with high H_2S concentrations. The bulk of membrane applications are really focused on purifying natural gas, which contains 10–20% or even higher levels of hydrogen sulfide.

Anaerobic digestion, which is thought to be one of the most important methods for generating clean biogas fuel from biomass and generating renewable energy [17], also produces hydrogen sulphide [H_2S], which contains 0.3% to 0.4% of CH4 and CO_2 [18]. Along with the potential for significant equipment, instrument, and pipeline damage, H_2S is an unpleasant acid gas. In addition, H2S pollutes the environment and damages human health. As soon as the biogas is used as energy (for burning, electricity generation, etc.), the H_2S in it will be converted to SO_2, which might significantly aggravate air pollution [19]. Therefore, H_2S must be removed from biogas using effective techniques because its presence delays the promotion of biogas energy. Chemical, physical, biological, and combinatorial technologies are all included in H_2S approaches. Because it can recycle hydrogen energy and effectively manage the H_2S pollution produced during the processing of coal, oil, gas, and minerals, the direct breakdown of H_2S to produce sulphur and hydrogen has been the focus of research by both domestic and foreign researchers. The main H_2S degradation processes that produce hydrogen and sulphur are thermal [20, 21], electrochemical [22], photocatalytic [23–25], and plasma degradation [26, 27]. The most promising method now in use is photocatalytic H_2S degradation due to its high treatment efficacy and response mobility [28]. Important new information on the efficacy of different wavelengths for this purpose has been obtained from experiments into the wavelength dependency and photosensitiser effects in UV-LED

photodegradation of iohexol [29]. The efficient photocatalytic degradation of 24 imidazolium ionic liquids is studied in an N-ZnO/simulated solar irradiation system, providing a comprehensive technique for this degradation process [30]. Throughout the entire study, the homotopy perturbation method was employed. The Homotopy Perturbation Method is a useful method for analyzing the kinetics of UV degradation of H_2S without O_2 in order to manage nonlinearities, give efficient approximations, and obtain a deeper comprehension of the reaction dynamics. Greater planning for environmental management will result from a greater understanding of the deteriorating process.

The photodegradation of H_2S is carefully examined in this work utilizing a vacuum ultraviolet (VUV) lamp in the absence of oxygen. The initial step of the study is to model the photodegradation process using MATLAB software. It investigates the effects of altering the starting H_2S concentration and exposure time on degrading results, contrasting these actual findings with the model›s predictions. The investigation also explores the mechanisms and reaction kinetics of H_2S degradation in the absence of oxygen. It is anticipated that the results of this study will make a substantial contribution to the effective removal of H_2S in anaerobic settings, improving the sustainability and feasibility of biogas as a renewable energy source.

MATERIALS AND METHODS

Tests and The Reactor

Figure 1 shows the H_2S photodegradation reaction or process used in this investigation schematically. The reactor's cylindrical shape was chosen to prevent photodegradation dead space and possible uneven gas distribution inside the reactor. Silica gel, which is resistant to corrosion and high temperatures, sealed the cylindrical VUV lamp and reactor. The lamp was set above the reactor. An external

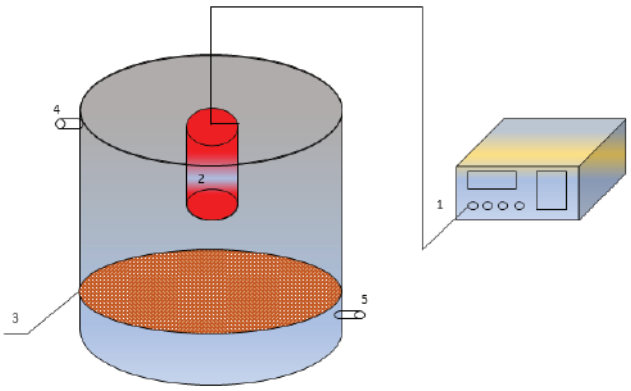

1. Generator with high frequency, 2. Distribution of gas equipment, 3. Electrodeless VUV lamp, 4. Gas outlet, 5. Gas inlet.

Figure 1. H_2S photo degradation reactor.

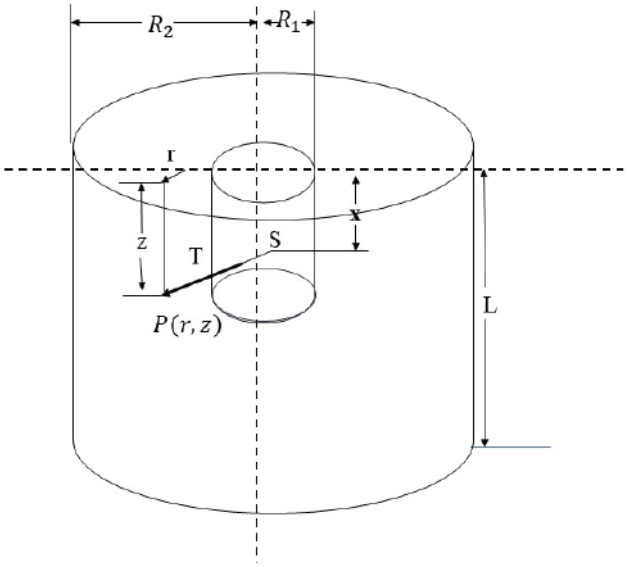

Figure 2. Cylindrical light source and Cylindrical photoreactor.

circuit was used to connect the VUV lamp to a high-frequency generator. At the gas entrance, a porous plate-like gas distribution device was attached, allowing the incoming gas to flow upward uniformly. The reactor's gas exit was situated atop it. The reactor's gas input and outlet were positioned on opposite sides to prevent short flow. The reactor's body was constructed of SUS 304 stainless steel to protect it from high-frequency electromagnetic radiation and to stop H_2S-induced corrosion. The reactor measured 14 cm in height and 15 cm in diameter. The reactor's overall capacity was 2.5 L, but with the addition of a cylindrical UV lamp that was 5.8 cm in height and 4 cm in diameter, the effective volume was 2.0 L.

The cylindrical photoreactor with a cylindrical light source for radiation field modelling is diagrammatically sketched in Figure 2, where *I(r, z)* is the light intensity at point *P(r, z)* within the reactor, $S_{(L,\lambda)}$ is the UV intensity at wavelength λ, and *r* and *z* are the vertical and horizontal distances of the random particles from the UV lamp's centre, respectively. The UV lamp's length is L. At the wavelength of λ, the medium's absorption coefficient in the reactor is denoted by μλ. The cylindrical reactor's radii are denoted by R_2 and the cylindrical UV lamps by R_1.

Experimental Methods

The reactor was first dried, and *Ar* was flushed into it at a rate of 10 L / min for an hour in order to remove any remaining O_2 and H_20 from the pipeline. This was done to examine the efficiency of H_2S degradation using only the high-frequency electrodeless VUV lamp without the addition of O_3, OH, and photocatalyst. To eliminate the impact of O_3 and OH on H_2S degradation, *Ar* gas was continually flushed during the experiment.

The experimental method was intended to maximize the reliability and reproducibility of the results. Natural gas is passed through a sealed cylindrical quartz photoreactor where the interior is flushed with argon gas at a solvent flow rate of 10 L/min to effectuate elimination of oxygen and water vapor.H_2S degradation was tested spectrophotometrically using the methylene blue method at 660 nm, assuring quantitative accuracy. The light intensity inside the reactor was theoretically computed and measured using a calibrated UV radiometer. The experiments were performed at constant ambient environmental conditions to prevent any variation. For any run, the initial concentration of H_2S was held steady. Every test was carried out thrice, and the reported data represent the averages. Errors were estimated during measurement and incorporated as a factor in the kinetic evaluation to compensate for the data dispersion so as to arrive at a more conclusive result.

Analytical Methods

H_2S concentration was determined with methylene blue spectrophotometry under a wavelength of 660 nm.

In Figure 3, the cylindrical VUV lamp at the centre of the photoreactor, which has a diameter of 15 cm and a height of 14 cm, is used to replicate the light intensity in three dimensions. As scaled on the figure coordinate axis, the VUV lamp occupied the white area, measuring 4 cm in diameter and 5.8 cm in height. Figure 3 show that when one moves farther away from the centre of the light source, the intensity of the light gradually decreases. The UV_{254} intensity was measured using a UV radiation meter 5 to 35 cm from the cylindrical lamp's wick to confirm the outcome of the light intensity distribution model in the reactor. The UV light radiation field model was used to compute the light intensity at the same location, and the model's output was confirmed by comparing it with the measured value.

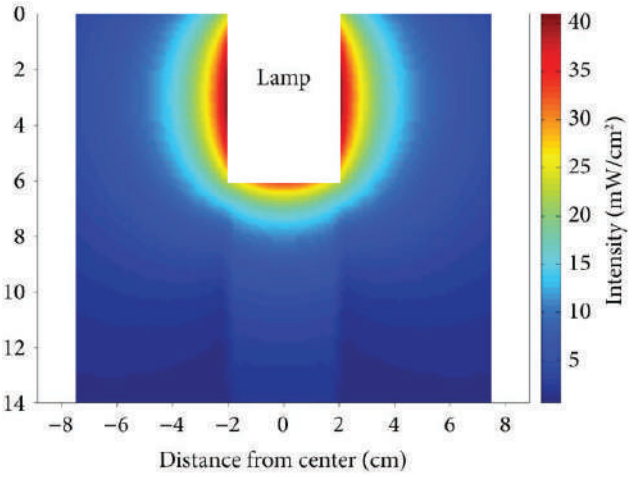

Figure 3. The distribution of light intensity within the photoreactor.

The methylene blue spectrophotometric technique was used to quantify the H_2S degradation, the residual H_2S in the gas phase being absorbed into a zinc acetate solution and reacting with N,N-dimethyl-p-phenylenediamine and ferric chloride to form methylene blue. The absorbance of this solution was then measured at 660 nm in a UV-Vis spectrophotometer. Calibration with standard H_2S solutions ensured the proper quantification of absorbed gases, and linearity of the calibration curve was verified within the specified concentration range under investigation. Each experiment was duplicated thrice to ensure results reproducibility and averages reported. The standard deviation among replicates was below ±5%, attesting to consistent performance. Measurement uncertainty results predominantly from spectrophotometric readings and from incongruity in gas concentrations, which were minimized by means of right instrument calibration complemented by controlled flow rates on gas introduction.

Mathematical Formulation of The Problem

A thorough study of the direct photodegradation of hydrogen sulfide (H_2S) caused by photons in the incoming ultraviolet (UV) band was carried out by Wilson et al. [31]. Their examination showed that photons with wavelengths shorter than 270 nm could start the breakdown process, causing H_2S to produce hydroxyl radicals (H•) and sulfhydryl radicals (SH•). Moreover, further photon exposure, particularly with wavelengths less than 230 nm, facilitated the transformation of SH· into H· and sulfur radicals (S•), as corroborated by experimental evidence (1) and (2). These reactions illustrate the complex interplay between H_2S and UV radiation, highlighting the formation of reactive intermediates such as radicals and their subsequent reactions with oxygen and other species present in the environment. A substantial amount of study has been done previously on the creation and improvement of photocatalytic materials for a range of uses. Using a flower-shaped nanophotocatalyst, a novel model is created for the kinetics and mass transfer in the sun-light-driven photodegradation of malachite green. The process is optimized by applying both machine learning and deep learning techniques [32]. Through high-efficiency photogenerated carrier transport, Wang et al. investigated a novel 2D/2D S-scheme heterojunction photocatalyst for peroxymonosulfate activation, which permits rapid degradation of ciprofloxacin [33]. Further elucidation of these reaction pathways is crucial for understanding the fate and impact of H_2S photodegradation in various environmental settings.

$$H_2S + h\upsilon(\lambda \leq 270nm) \rightarrow H\bullet + SH\bullet \quad (1)$$

$$HS. + h\upsilon(\lambda \leq 230nm) \rightarrow H\bullet + S \quad (2)$$

$$H\bullet + H_2S \rightarrow H_2 + SH\bullet \quad (3)$$

$$H\bullet + H\bullet \rightarrow H_2 \quad (4)$$

$$H\bullet + HS\bullet \rightarrow H_2S + S \quad (5)$$

$$H\bullet S + H\bullet S \rightarrow H_2S + S \quad (6)$$

Table 1 summarizes the rate constants for the aforementioned reactions, which may be obtained by consulting the National Institute of Standards and Technology›s (NIST) chemical dynamics database and relevant literature. The molar absorption coefficients for wave lengths of 185 nm and 254 nm can be determined by converting the absorptivity values given in Table 1, and a photon takes part in reactions (1) and (2). The degradation rate equation of the different intermediates during hydrogen sulfide photodegradation in the absence of O_2 may be established based on (1), (2), (3), (4), (5), and (6). Let kobs = 2030$\varphi_i\varepsilon$ b ((4)), noting $k_{obs\,1}$, k_{obs2}, k_3, k_4, k_5, and k_6 as the rate constants for (1), (2), (3), (4), (5), and (6), as the photon is shown in (1) and (2). Each component›s reaction rate equations can be written as follows:

$$\left(\frac{d[H_2S]}{dt}\right) = -k_{obs\,1}[H_2S] - k_3[H_2S][H\bullet] + k_6[SH\bullet] \quad (7)$$

$$\left(\frac{d[H.]}{dt}\right) = k_{obs\,1}[H_2S] + k_{obs\,2}[SH\bullet] - k_3[H_2S][H\bullet] + k_4[H\bullet]^2 - k_5[SH\bullet][H\bullet] \quad (8)$$

$$\left(\frac{d[SH.]}{dt}\right) = k_{obs\,1}[H_2S] + k_{obs\,2}[SH.] - k_5[SH\bullet][H\bullet] - k_6[SH\bullet]^2 \quad (9)$$

following circumstances: Initially, the H_2S concentration was fixed at 12 mg/m3, and the carrier gas was Ar. MATLAB software was used to determine the concentration evolution of H_2S, H•, SH•, H_2, and S at a distance of 2 cm from the UV light. The logarithmic scale in Figure 4 illustrates this process. It was discovered that the primary end products of H_2S photodegradation were H_2 and S, and that their concentrations were quite near to one another, which was consistent with the photodegradation reaction›s stoichiometric constants. Furthermore, compared to H_2 and S, the simulated concentrations of H• and SH• radicals were very low, around two orders of magnitude lower. In the end, we attempted to use the steady-state approximation for radicals to construct the analytical equation that links the rate of H_2S consumption with its concentration and light intensity.

The initial conditions given below

$$\begin{aligned} t = 0, &\quad H_2S = H_2S_{ini} \\ t = 0, &\quad H\bullet = H_{ini} \\ t = 0, &\quad SH\bullet = SH_{ini} \\ t = 0, &\quad H_2 = H_{2\,ini} \\ t = 0, &\quad S = S_{ini} \end{aligned} \quad (12)$$

The boundary conditions are

$$\begin{aligned} t = 0, &\quad H_2S = 0 \\ t = 0, &\quad H\bullet = 0 \\ t = 0, &\quad SH\bullet = 0 \\ t = 0, &\quad H_2 = 0 \\ t = 0, &\quad S = 0 \end{aligned} \quad (13)$$

Reaction	Quantum efficiency	Light absorptivity at 185nm	Light absorptivity at 254nm	Rate constant	Reaction order	References
$\mathbf{H_2S + h\upsilon(\lambda \leq 270nm) \rightarrow H\bullet + SH\bullet}$	1	1004.66	1.96	/	/	[48]
$\mathbf{HS. + h\upsilon(\lambda \leq 230nm) \rightarrow H\bullet + S}$	1	20.5	0	/	/	[48]
$\mathbf{H\bullet + H_2S \rightarrow H_2 + SH\bullet}$	/	/	/	2.498E+10	2	[49]
$\mathbf{H\bullet + H\bullet \rightarrow H_2}$	/	/	/	4.786E+08	2	[50]
$\mathbf{H\bullet + HS\bullet \rightarrow H_2S + S}$	/	/	/	8.0E+09	2	[51]
$\mathbf{H\bullet S + H\bullet S \rightarrow H_2S + S}$	/	/	/	8.368E+9	2	[52]

$$\left(\frac{d[H.]}{dt}\right) = k_3[H_2S][H\bullet] + k_4[H\bullet]^2 + k_5[SH\bullet][H\bullet] \quad (10)$$

$$\left(\frac{d[S]}{dt}\right) = k_{obs\,2}[SH\bullet] - k_5[SH\bullet][H\bullet] - k_6[SH\bullet]^2 \quad (11)$$

The UV-photodegrading reactor model was then modified to incorporate the reaction rate equations for H_2S, H•, SH•, H_2, and S (from (7), (8), (9), (10), and (11) and simulate the H_2S photodegradation effect without O_2 under the

APPROXIMATE ANALYTICAL REPRESENTATION FOR THE CONCENTRATION OF H_2S PHOTODEGRADATION AND THE CORRESPONDING REACTION RATE EQUATIONS FOR H_2S, H, SH•, H_2 AND S USING HPM

Recently, in engineering and physics disciplines, so many researchers used the Homotopy perturbation method and fractional calculus to solve a variety of nonlinear issues [34-38, 42-44]. This approach combines standard perturbation

scheme with topology. Ji Huan, He utilized the Homotopy perturbation method to solve the light hill equations [39] the Duffing [40] and the Blasius [41]. This method is distinct in its efficiency, precision, and applicability. The Homotopy perturbation method (HPM) has demonstrated its versatility and effectiveness across various scientific domains, particularly in addressing complex nonlinear problems. HPM is applied in the context of kinetic modeling to study the degradation of total organic carbon in dairy wastewater, showcasing its ability to model and solve intricate biochemical reaction systems in environmental technology. This application highlighted HPM›s capability to simplify and accurately predict the degradation kinetics of organic compound [45]. A constrained Homotopy method is utilized for parameter estimation in nonlinear diffusion problems. Their research underscored HPM›s strengths in managing the constraints and complexities inherent in such equations, leading to more precise parameter estimations. This approach has proven beneficial in fields where accurate modeling of diffusion processes is crucial, such as in material science and thermal analysis [46]. An approach to regularization Homotopy for limited parameter inversion of partial differential equations is presented. This study highlighted the robustness of HPM in stabilizing the inversion process, making it a reliable tool for tackling ill-posed problems. By incorporating regularization techniques, they enhanced the reliability and stability of the solutions, which is particularly valuable in entropy-based studies and other applications requiring precise parameter inversion [47]. In order to find an asymptotic result, the Homotopy perturbation approach uses the surrounding parameter p as a tiny parameter and requires extremely little duplication. Analytical formulas for the concentrations of H_2S, H•, SH•, H_2, and S are derived from these equations using the Homotopy perturbation method with HPM, yielding the following outcomes:

$$[H_2S]t = c_1 e_1^{-at} + \frac{1}{c_4}\left((L_1 - L_4 t)e_1^{-at} - L_2 e_1^{-at-bt} + L_3 e_1^{-2at} + c_{18} e_1^{-2bt}\right) \tag{14}$$

$$\begin{aligned}
[H.]t = {} & c_3 e_1^{-at} + e_1^{-bt} - c_2 \\
& + \frac{a}{4}\left(L_1\left(\frac{e_1^{-at}}{-a}\right) - L_4\left(t\frac{e_1^{-at}}{-a} - \frac{e_1^{-at}}{a^2}\right) \right. \\
& \left. - L_2\left(\frac{e_1^{-(a+b)t}}{-(a+b)}\right) + L_3\left(\frac{e_1^{-2at}}{-2a}\right) + c_{18}\left(\frac{e_1^{-2bt}}{-2b}\right)\right) \\
& + \frac{b}{p_{98}}\begin{pmatrix} A_1\left(\frac{e_1^{-2bt}}{-2b}\right) - A_2\left(\frac{e_1^{-bt}}{-b}\right) + (p_{43} - p_{71} - p_{91})\left(t\frac{e_1^{-bt}}{-b} - \frac{e_1^{-bt}}{b^2}\right) \\ +(A_3+A_6)\left(\frac{e_1^{-(a+b)t}}{-(a+b)}\right) - A_4\left(\frac{e_1^{-at}}{-a}\right) + (p_{16} - p_{44} - p_{72})\left(t\frac{e_1^{-at}}{-a} - \frac{e_1^{-at}}{a^2}\right) \end{pmatrix} \\
& - A_4\left(\frac{e_1^{-at}}{-a}\right) + (p_{16} - p_{44} - p_{72})\left(t\frac{e_1^{-at}}{-a} - \frac{e_1^{-at}}{a^2}\right) \\
& - k_3\left(c_1 c_3\left(\frac{e_1^{-2at}}{2a}\right) + c_1\left(\frac{e_1^{-(a+b)t}}{-(a+b)}\right) - c_1 c_2\left(\frac{e_1^{-at}}{-a}\right)\right) \\
& + k_4\left(\left((c_3)^2\frac{e_1^{-2at}}{-2a}\right) + 2c_3\left(\frac{e_1^{-(a+b)t}}{-(a+b)}\right) - 2c_2 c_3\left(\frac{e_1^{-at}}{-a}\right) + 2c_2\left(\frac{e_1^{-bt}}{-b}\right) - 2c_2\left(\frac{e_1^{-bt}}{-2b}\right) + t(c_2)^2\right) \\
& + k_5\left(\left(A\frac{e_1^{-(a+b)t}}{(a+b)}\right) + Ac_3\left(\frac{e_1^{-2at}}{2a}\right) - Ac_2\left(\frac{e_1^{-at}}{-a}\right) + Bc_3\left(\frac{e_1^{-(a+b)t}}{(a+b)t}\right) - Bc_2\left(\frac{e_1^{-bt}}{-b}\right) + B\left(\frac{e_1^{-2bt}}{-2b}\right)\right)
\end{aligned} \tag{15}$$

$$[SH.]t = Ae_1^{-at} + Be_1^{-bt} + \frac{e_1^{-3at-3bt}}{p_{98}}\begin{pmatrix} A_1 e_1^{3at} + e_1^{3at+bt}(A_2 + p_{43}t - p_{71}t - p_{91}t) \\ + (A_3 + A_6)e_1^{(2a+b)t} + e_1^{(2a+2b)t}(A_4 + p_{16}t - p_{44}t - p_{72}t) \\ + A_5 e_1^{(2a+2b)t} \end{pmatrix} \tag{16}$$

Table 1. Shows the plot of influence concentration profile and time t computed with Eq. (16) in Figure 7

t	Values of k_{obs1}				Values of k_{obs2}				Values of k_5				Values of k_6			
	0.4	**0.5**	**1**	**2**	**0.05**	**0.09**	**0.13**	**0.23**	**0.2**	**1.8**	**2.6**	**3.8**	**0.02**	**0.4**	**0.16**	**0.25**
0	0.0018	0.0004	0.0018	0.0019	0.0019	0.0019	0.0017	0.0008	0.0016	0.0016	0.0016	0.0016	0.0390	0.0083	0.0277	0.0204
0.4	0.0291	0.0457	0.0943	0.1589	0.2235	0.1087	0.0645	0.0208	.0551	0.0895	0.1067	0.1325	0.0680	0.0193	0.0501	0.0385
.8	0.0523	0.0792	0.1508	0.2214	0.3659	0.1746	0.1013	0.0295	.0860	0.1453	0.1749	0.2193	0.1083	0.0361	0.0817	0.0646
1.2	0.0694	0.1035	0.1839	0.2428	0.4559	0.2140	0.1217	0.032	0.1032	0.183	0.2229	0.2828	0.1331	0.0488	0.1020	0.0821
.6	0.0817	0.1207	0.2021	0.2466	0.5114	0.2362	0.1318	.0315	0.1120	0.2106	0.2599	0.3338	0.1489	0.0594	0.1159	0.0947
2	0.0902	0.1324	0.2108	0.2429	0.5441	0.2473	0.1355	0.0295	0.1157	0.2324	0.2907	0.3782	0.1595	0.0689	0.1261	0.1046

$$[H_2]t = H_{2\,ini} + k_3\left(c_1c_3\left(\frac{e_1^{-2at}}{2a}\right) + c_1\left(\frac{e_1^{-(a+b)t}}{-(a+b)}\right) - c_1c_2\left(\frac{e_1^{-at}}{-a}\right)\right) + k_4\left(\left((c_3)^2\frac{e_1^{-2at}}{-2a}\right) + 2c_3\left(\frac{e_1^{-(a+b)t}}{-(a+b)}\right) - 2c_2c_3\left(\frac{e_1^{-at}}{-a}\right) + 2c_2\left(\frac{e_1^{-bt}}{-b}\right) - 2c_2\left(\frac{e_1^{-bt}}{-2b}\right) + t(c_2)^2\right) + k_5\left(\left(A\frac{e_1^{-(a+b)t}}{(a+b)}\right) + Ac_3\left(\frac{e_1^{-2at}}{2a}\right) - Ac_2\left(\frac{e_1^{-at}}{-a}\right) + Bc_3\left(\frac{e_1^{-(a+b)t}}{(a+b)t}\right) - Bc_2\left(\frac{e_1^{-bt}}{-b}\right) + B\left(\frac{e_1^{-2bt}}{-2b}\right)\right) \quad (17)$$

Table 2. Show the plot of influence concentration profile and time t computed with Eq. (17) in Figure 8

t	Values of k_3				Values of k_4				Values of k_5			
	0.01	**0.021**	**0.033**	**0.0005**	**0.5**	**1**	**1.5**	**2**	**0.1**	**0.6**	**1.1**	**1.3**
0	0.1	0.1	0.0999	0.0999	0.1	0.1	0.0999	0.0999	0.0999	0.0999	0.1	0.1
0.2	0.0998	0.0994	0.0989	0.1002	0.0972	0.0987	0.1002	0.1016	0.0972	0.0971	0.097	0.097
0.4	0.1	0.0991	0.0982	0.1007	0.0964	0.1003	0.1043	0.1083	0.0963	0.0958	0.0954	0.0952
0.6	0.1004	0.0993	0.0981	0.1014	0.0973	0.105	0.1127	0.1204	0.0972	0.096	0.0948	0.0943
0.8	0.1012	0.0998	0.0983	0.1023	0.1001	0.1128	0.1255	0.1382	0.0998	0.0975	0.0953	0.0945
1	0.1022	0.1006	0.0989	0.1035	0.1046	0.1237	0.1427	0.1617	0.1041	0.1005	0.0969	0.0955

$$[S]t = b\left(A\frac{e_1^{-at}}{-a} + B\frac{e_1^{-bt}}{-b}\right) + S_{ini} + b\left(\frac{A}{a} + \frac{B}{b}\right) + \frac{b}{p_{98}}\left(A_1\left(\frac{e_1^{-2bt}}{-2b}\right) - A_2\left(\frac{e_1^{-bt}}{-b}\right) + (p_{43} - p_{71} - p_{91})\left(\left(t\frac{e_1^{-bt}}{-b}\right) - \left(\frac{e_1^{-bt}}{b^2}\right)\right)\right) + (A_3 + A_6)\left(\frac{e_1^{-(a+b)t}}{-(a+b)}\right) - A_4\left(\frac{e_1^{-at}}{-a}\right) + (p_{16} - p_{44} - p_{72})\left(t\frac{e_1^{-at}}{-a} - \frac{e_1^{-at}}{a^2}\right) + k_5\left(Ac_3\left(\frac{e_1^{-2at}}{2a}\right) + Bc_3\left(\frac{e_1^{-(a+b)t}}{(a+b)t}\right) + A\left(\frac{e_1^{-(a+b)t}}{(a+b)}\right) + B\left(\frac{e_1^{-2bt}}{2b}\right) - Ac_2\left(\frac{e_1^{-at}}{a}\right) - Bc_2\left(\frac{e_1^{-bt}}{b}\right)\right) + k_6\left(A^2\left(\frac{e_1^{-2at}}{-2a}\right) + 2AB\left(\frac{e_1^{-(a+b)t}}{(a+b)}\right) + B^2\left(\frac{e_1^{-2bt}}{2b}\right)\right) \quad (18)$$

Table 3. Shows plot of influence concentration profile and time t computed with Eq. (18) in Figure 9

t	Values of k_3				Values of k_4				Values of k_5			
	0.1	**0.09**	**0.13**	**0.2**	**0.5**	**0.6**	**0.7**	**0.8**	**9**	**12**	**16**	**19**
1	8.4596	9.2418	6.9606	5.226	1.5647	1.6376	1.7106	1.7836	4.7035	3.4366	1.7475	0.4806
2	8.2740	9.0277	6.7176	4.9424	1.5536	1.6244	1.6951	1.7658	4.9004	3.773	2.2707	1.1437
3.5	7.7755	8.5454	6.1784	4.3423	1.5287	1.5944	1.6602	1.7260	5.1629	4.2901	3.1264	2.2536
5	7.1948	7.9785	5.5687	3.7050	1.4997	1.5596	1.6196	1.6795	5.2361	4.5818	3.7093	3.0550
6.5	6.5877	7.3811	4.9395	2.9717	1.4693	1.5232	1.5771	1.6309	5.1296	4.6425	3.9930	3.5059
8	5.9311	6.7463	4.1752	1.2797	1.4365	1.4838	1.5311	1.5784	4.8360	4.4701	3.9823	3.6164

By contrasting analytical predictions with experimental findings from earlier research, Figure 4 investigates the impact of different concentrations on the degradation process [28]. This comparison demonstrates the analytical model's relevance in practical situations and verifies it.

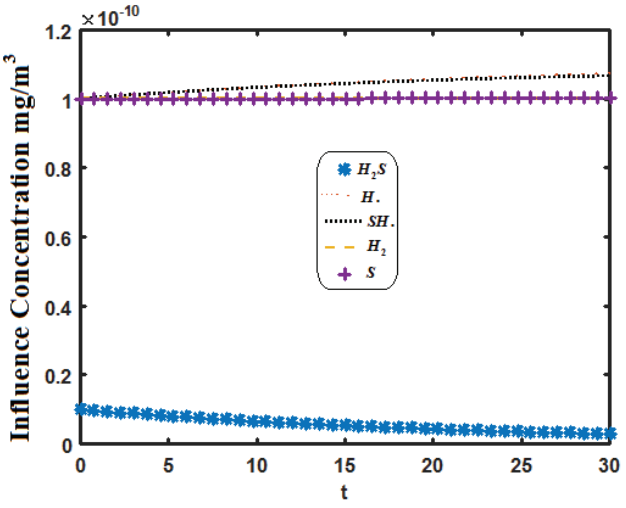

Figure 4. Represents influence concentration for different values and comparedexperimental results.

Figure 5 explores the connection between the initial concentration of H_2S and the gas's retention time. It implies that while the observed rate constant (k_{obs1}) falls, the concentration of H_2S increases as the constants k_3 and k_6 grow, indicating higher reaction rates. This may suggest that saturation effects brought on by increased H_2S concentrations could lower the overall degradation efficiency.

Reaction Dynamics and Radicals

Figure 6 illustrates how $k_{obs\ 1}$, k_1, and k_5 drop as the simulated concentration of hydrogen radicals (H•) rises. This suggests that some chemical routes may become less advantageous as the concentration of H• increases, changing the kinetics of the degradation process. The concentration of thiol radicals (SH•) rises in Figure 7, as $k_{obs\ 1}$ and k_5 rise and $k_{obs\ 2}$ and k_6 fall. This implies that the concentration of other species affects the synthesis of SH•, which in turn affects the reaction's overall kinetics.

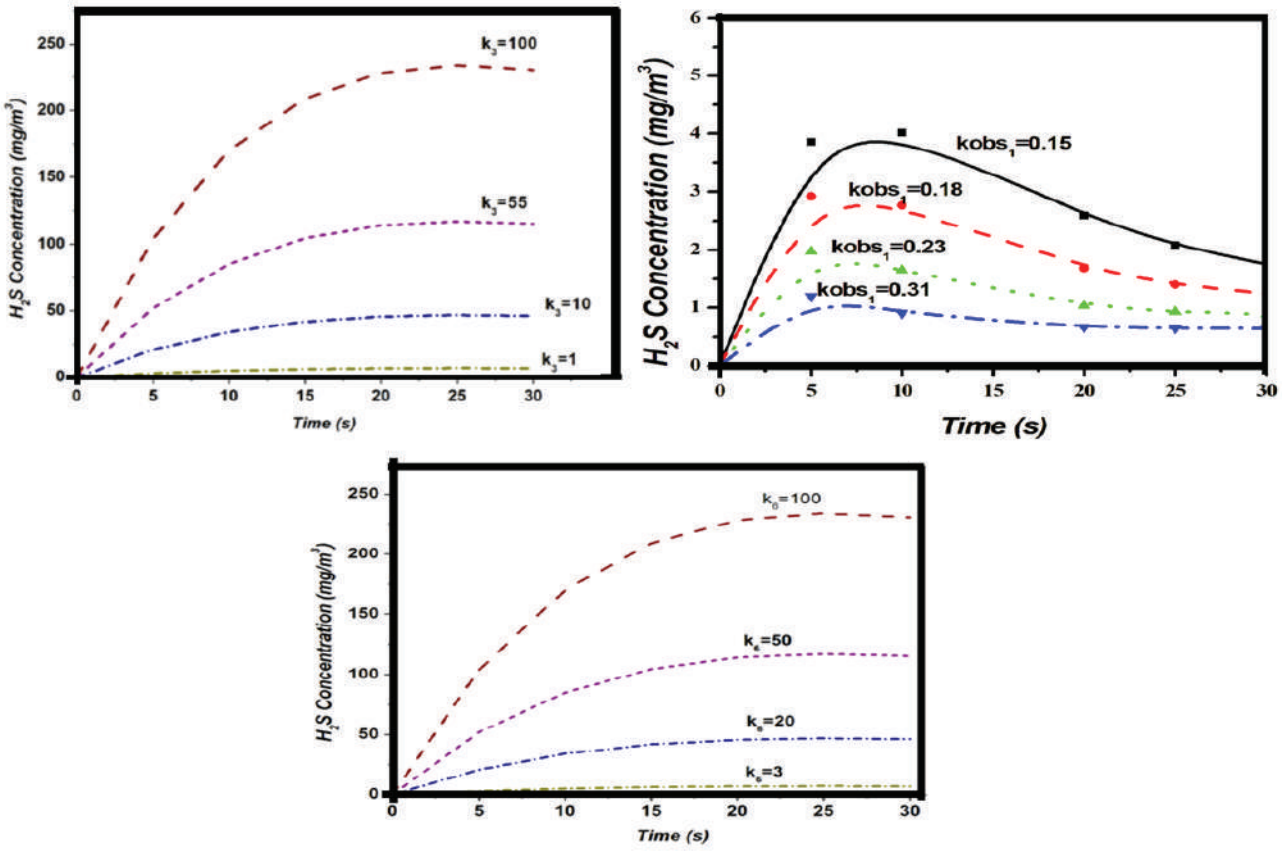

Figure 5. Plot of Influence Concentration profile, versus time t computed with Eq. (14) for different experimental parameter values $k_{obs1} = 0.15$, $k_{obs2} = 0.00014$, $k_3 = 0.2*10^2$, $k_6 = 0.2*10^2$.

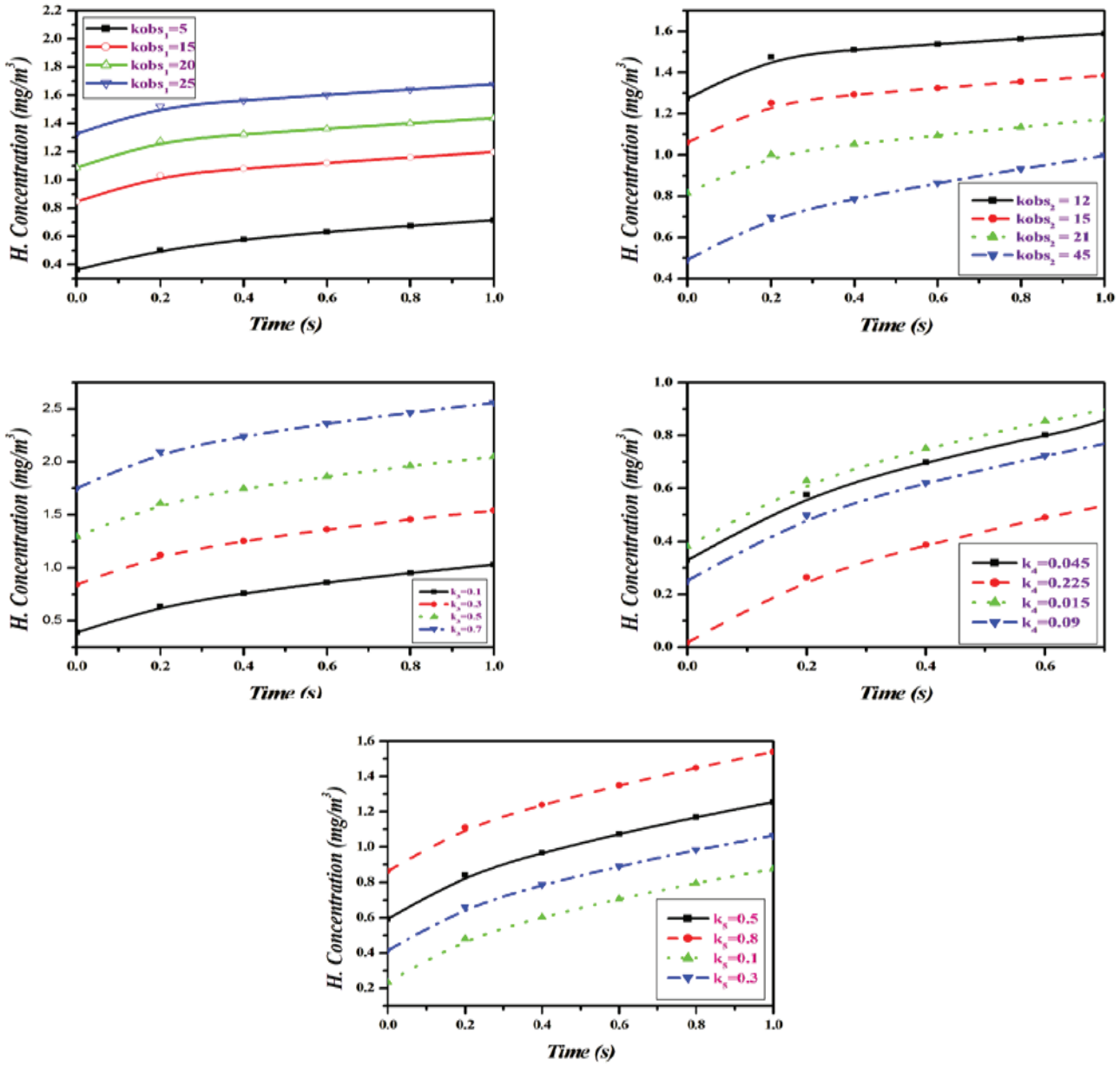

Figure 6. Plot of Influence Concentration profile, versus time t computed with Eq. (15) for different experimental parameter values $k_{obs1} = 5$, $k_{obs2} = 12$, $k_3 = 0.1$, $k_4 = 0.045$, $k_5 = 0.5$.

RATE OF DEGRADATION AND MODELED CONCENTRATIONS

The increasing rate of deterioration is depicted in Figure 8, which sheds light on how rapidly H_2S is converted into various products when exposed to UV light. The fluctuating simulated elemental sulfur (S) concentration in Figure 9 suggests that complicated dynamics are at work during the degrading process. The equilibrium between production and consumption in the reaction network may be reflected in the rise and fall of sulfur concentrations.

RESULTS AND DISCUSSION

Major Influence Factors on H2s Photodegradation

Equations (14-18) denotes the approximate analytical expression for the concentration of H_2S, H•, SH•, H_2 and S. Figure 3 represents the concentration evolution of H_2S, H•, SH•, H_2 and S calculated 2 cm away from the ultraviolet light and showed by the analytical solution (14 -18). Figure 4 represents influence concentration for different values (analytical) and compared with experimental results [28]. Figure 5 inferred that the dynamic interaction between the degradation and production of H_2S is depicted by the

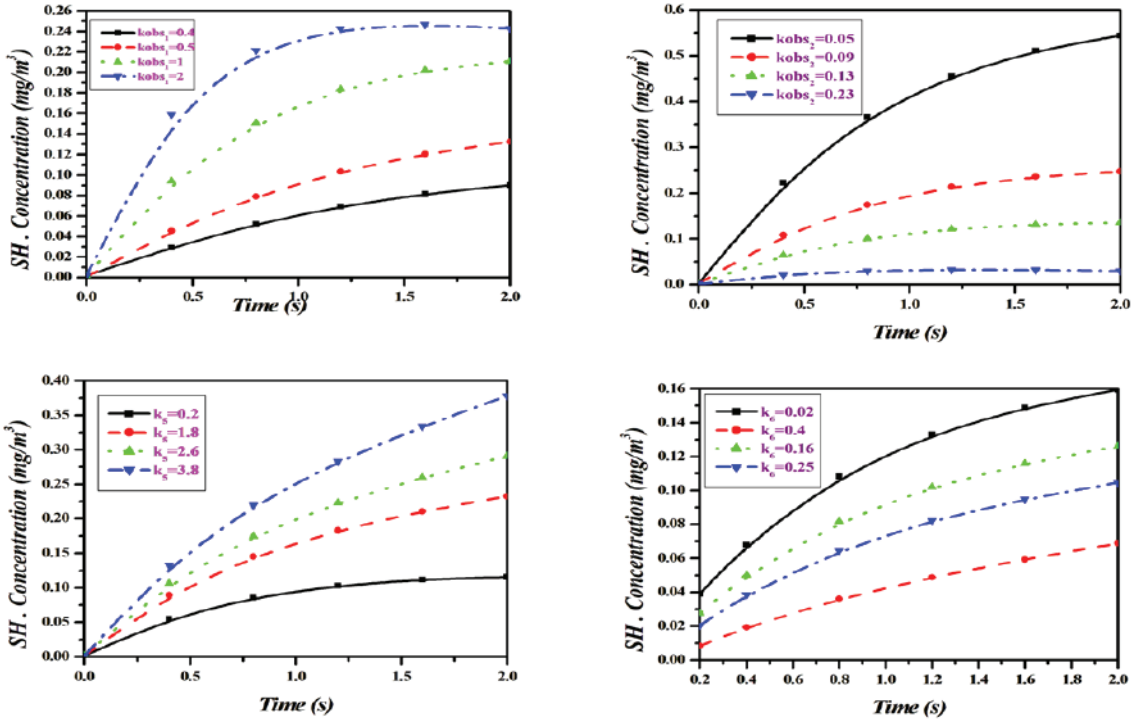

Figure 7. Plot of Influence Concentration profile, versus time t computed with Eq. (16) for different experimental parameter values k_{obs1} = 0.4, k_{obs2} = 0.05, k_5 = 0.2, k_6 = 0.02.

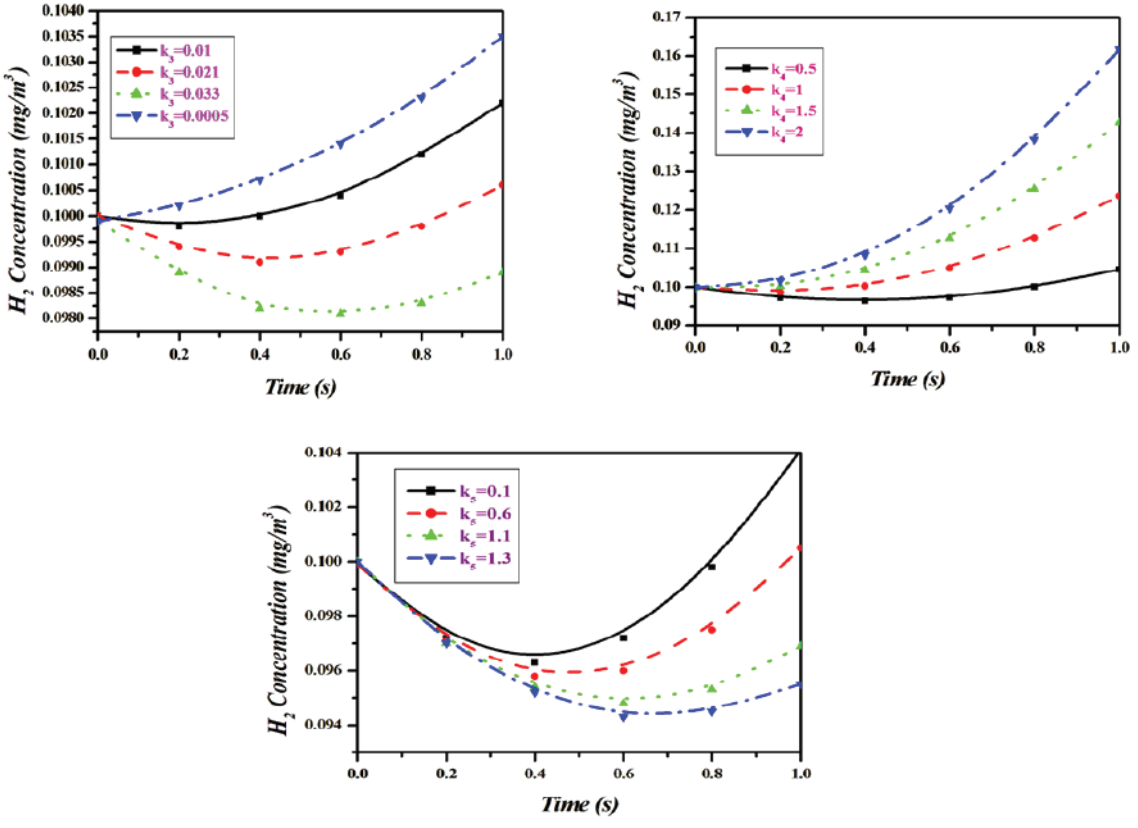

Figure 8. Plot of Influence Concentration profile, versus time t computed with Eq. (17) for different experimental parameter values k_{obs1}=1, k_{obs2}=0.1, k_3=0.01, k_4=0.5, k_5=0.1.

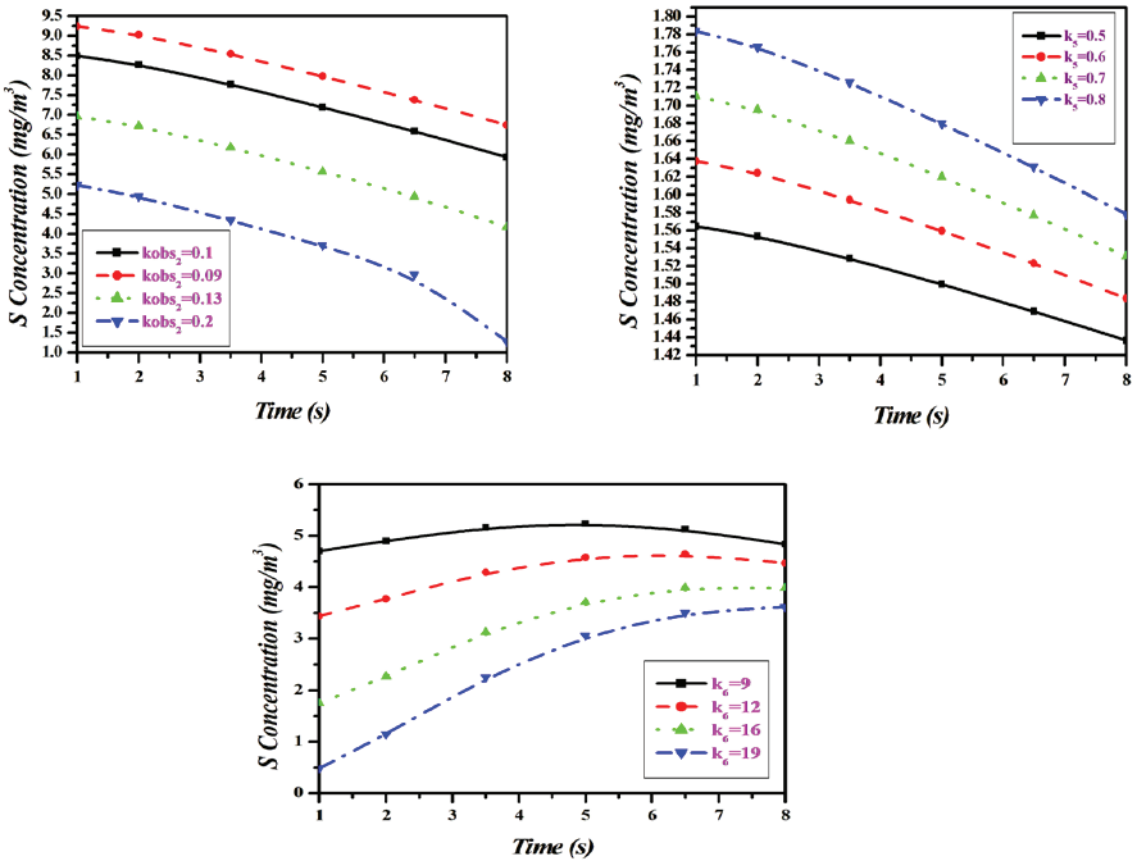

Figure 9. Plot of influence concentration profile, versus time t computed with Eq. (18) for different experimental parameter values k_{obs1}=1, k_{obs2}=0.1, k_5=0.5, k_6=9.

rates k_3, k_6 and the observed degradation constants k_{obs1}, are demonstrated by these graphs. As the generation rate increases, H_2S content tends to accumulate at a faster rate and reach peak concentrations of higher values than normal concentration. From Figure 6, the accumulation of H• concentration over time is influenced by the different rate constants (k_{obs1}, k_{obs2},k_3, k_4,k_5) as depicted in the graphs. The accumulation of H• is increased and faster with higher values of k_{obs1}, k_{obs2} which represents the observed generation rate. However, it is slower for lower values. In the same way, H• buildup is consistently sharpened and increased by concentration profiles when k_3, k_4,and k_5 are likely to correspond to these reaction or transport constants. In Figure 7, graphs showing the concentration of SH• under different rate constants (k_{obs1}, k_{obs2}, k_5, k_6) are presented. A graph showing the equilibrium concentrations of SH• on the top left-right is shown where k_{obs1} (0.4 to 2) increases. In the same way, the top right-hand side displays a consistent pattern for k_{obs2} across varying values from 0.05 to 0.23, indicating that higher morality values result in greater generation rates. SH• buildup is accelerated at values of higher k_5 (0.2–3.8), with the most important effect on the dynamics of generation, as shown in the lower-left section of this diagram. Figure 8 depicts the data emanating from the three plots and displays the influence of parameters k_3, k_4 and k_5 on the quantity of H_2 at different times. The top-left plot exclaims that the increase in k_3 is the reason why the H_2 remains still because in this case, the rate of production could be the factor. In contrast, on the top-right plot, the higher k_4 switchover is the main reason for H_2 getting fast and at a broader level and it is the k_4 which is said to be the real catalyzer of the reaction. Figure 9 represents that these plots provide information as to whether k_{obs2}, k_5 and k_6 parameters effect the concentration of S over time. In the top-left plot, the increase in k_{obs2} (0.1 to 0.2) run the S depletion. Consequently, this demonstrates that k_{obs2} is the factor responsible for treatment of the S, which is produced by the reaction being consumed or decaying.

Limitations of The Model

In the suggested model, valuable insights into the UV degradation kinetics of H_2S in the absence of oxygen have been provided. Yet, the model does have several drawbacks, which warrant acknowledgment. The model developed assumes idealistic conditions consisting of unvarying UV light intensity and a homogeneous gas distribution-that may expressly lack realism due to experimental variations such as lamp intensity fluctuations, ambient temperature

Research Focus	Emerging Trends	Key Challenges
Exploration of MOFs	MOFs can be used for gas separation and selective catalysis because of their enormous surface area and adjustable porosity.	The capacity to scale MOF synthesis for industrial use while preserving stability during refining.
Development of Perovskite-based Catalysts	Perovskites are becoming more and more popular because of their capacity to replace noble metals in catalytic reactions and their thermal stability.	Perovskites› incorporation into current technologies and dealing with deactivation over time
Multi-functional Catalysts	In order to increase efficiency and decrease process complexity, multi-functional catalysts have been developed to carry out many reactions concurrently.	Juggling stability, selectivity, and activity in intricate industrial processes.
Catalyst Regeneration and Recycling Techniques	Improved regeneration and recycling techniques are being used to extend the catalyst›s lifespan while lowering waste and operating expenses.	Striking a balance between stability, selectivity, and activity in intricate industrial processes.

changes, gas flow turbulence, etc. Hence, any presence of catalyst is not accounted for: catalysts change degradation pathways and significantly affect degradation efficiency. Potential limitations deriving from radical recombination or secondary reactions that would affect intermediate concentrations (SH•, H•) are also disregarded. Uncertainties in reaction rate constants and molar absorptivity values obtained from literature sources add to the sensitivity of the model parameters, which have not been addressed via sensitivity analysis. Since the model assumes perfect mixing and negligible mass transfer resistance, its prediction power may be limited when subjected to scale-up for practical operations.

Sensitivity Analysis

We performed sensitivity analysis on certain key parameters such as rate constants and molar absorptivity to assess the kinetic model's robustness. It inherently implies that the degradation rate is highly sensitive to the variation in the rate constant k with a change of ±10%. k causes the predicted concentration profile to vary by up to ±12%. The model exhibited somewhat less sensitivity with respect to the variation in the molar absorptivity, which has a direct bearing on the rate of photon absorption and thus the generation of reactive species. Uncertainty in these parameters due to literature variability and measurement limitations was carried out by parametric variation, and the results were then compared with the experimental data. This analysis shows that a few deviations in parameter values may cause variations in how accurately degradation profiles can be predicted, thus emphasizing the need for accurate experimental calibration, although degradation trend capture remains reliable using the model.

Future Directions for Research

Currently, research on catalyst development is moving in a number of encouraging directions with the goal of resolving present problems and improving petroleum refining systems. Filling some research gaps can have a big impact on how improved catalysts are used in petroleum refining. One important area is lowering the price of innovative materials, like mixed metal oxides and nanocatalysts, which can be costly because of their complicated production procedures and high material costs. Advanced catalysts can become more commercially viable on a wide scale by lowering these expenses.

The integration of multifunctional catalysts and their scalability are two more crucial areas. These catalysts, which are made to carry out several reactions in one step, could streamline refining procedures, lower energy costs, and boost operational effectiveness. But for these multipurpose catalysts, striking a balance between stability, selectivity, and activity can be challenging, particularly when transferring from lab settings to large-scale refinery applications. Improving catalyst stability in the challenging circumstances of industrial refining is still a top concern. Current catalysts, including Co-Mo and Ni-Mo, require expensive regeneration procedures because they can get deactivated by contaminants like sulphur and nitrogen. Creating formulations that are tolerant of sulphur and improving regeneration methods may increase catalyst lifespans and reduce operating expenses. Future studies can offer a road map for the creation of sophisticated refining catalysts that complement the sector›s two objectives of boosting sustainability and efficiency by concentrating on these three areas: stability, scalability, and cost reduction.

CONCLUSION

The proposed model of UV degradation of H_2S has been established without the presence of oxygen, and the impact of the primary H_2S concentration and gas preservation duration on the photodegradation experiment was

linked to the analytical results. This study ended by showing how different starting amounts of H_2S and exposure times affected the degradation results, and it compared these real findings with what the model predicted. The mechanisms and reaction kinetics of H_2S degradation in the absence of oxygen are also examined in this study. The findings of this study are expected to significantly improve the sustainability and viability of biogas as a renewable energy source by removing H_2S in anaerobic environments. In this work, the UV deterioration of H_2S without O_2 was represented mathematically. Additionally, it verified the model and investigated how the initial H_{2S} concentration and gas retention time affected the rate of photodegradation. This study provides both an approximation and a closed analytical representation form of the concentration of H_2S, H•, SH•, H_2, and S. It also solves the nonlinear differential equations in the VUV degradation analytically using HPM. These special analytical results allow for parameter optimization of VUV photodegradation of H_2S without the presence of oxygen and provide an intuitive understanding of the system.

NOMENCLATURE

H_2S	Influence Concentration (mg/m^3)
H•	Influence Concentration (mg/m^3)
SH•	Influence Concentration (mg/m^3)
H_2	Influence Concentration (mg/m^3)
S	Influence Concentration (mg/m^3)
k_{obs1}	Rate Constants ($m^{-1}s^{-1}$)
k_{obs2}	Rate Constants ($m^{-1}s^{-1}$)
k_3	Rate Constants ($m^{-1}s^{-1}$)
k_4	Rate Constants ($m^{-1}s^{-1}$)
k_5	Rate Constants ($m^{-1}s^{-1}$)
k_6	Rate Constants ($m^{-1}s^{-1}$)

ACKNOWLEDGEMENT

The authors thank King Department of Mathematics, Saveetha School of Engineering, SIMATS, Chennai, Tamil Nadu, and India for the support and facilities that made this research possible.

AUTHORSHIP CONTRIBUTIONS

V. Sreelatha Devi & K. Saranya : Writing- Original draft preparation, Investigation and Editing. Vijayabalan D : Conceptualization, Visualization. Muthumari G: Methodology, Editing. K A. Niranjan kumar& Banu Priya V: Supervision, Validation, and Reviewing

DATA AVAILABILITY STATEMENT

The authors confirm that the data that supports the findings of this study are available within the article. Raw data that support the finding of this study are available from the corresponding author, upon reasonable request

CONFLICT OF INTEREST

The author declared no potential conflicts of interest with respect to the research, authorship, and/or publication of this article.

ETHICS

There are no ethical issues with the publication of this manuscript. Funding the authors confirm there is no source of funding for this research.

REFERENCES

[1] Occupational Safety and Health Administration. Hydrogen Sulfide Hazards. Available at: https://www.osha.gov/hydrogen-sulfide/hazards. Accessed on May 7, 2021.

[2] Beauchamp RO, Bus JS, Popp JS, Boreiko CJ, Andjelkovich DA, Leber P, et al. A critical review of the literature on hydrogen sulfide toxicity. Crit Rev Toxicol 1984;13:25–97. [CrossRef]

[3] Reiffenstein RJ, Hulbert WC, Roth SH. Toxicology of hydrogen sulfide. Annu Rev Pharmacol Toxicol 1992;32:109–134. [CrossRef]

[4] Mokhatab S, Poe WA, Mak JY. Basic Concepts of Natural Gas Processing. In: Handbook of Natural Gas Transmission and Processing. 4th ed. Gulf Professional Publishing; 2019. p. 177–189. [CrossRef]

[5] Mohtadi R, Lee WK, Cowan S, Van Zee JW, Murthy M. Effects of hydrogen sulfide on the performance of a PEMFC. Electrochem Solid-State Lett 2003;6:A272. [CrossRef]

[6] Du Z, Liu C, Jhai J, Guo X, Xiong Y, Su W, et al. A review of hydrogen purification technologies for fuel cell vehicles. Catalysts 2021;11:393. [CrossRef]

[7] Hassan TNAT, Shariff AM, Pauzi MMM, Khidzir MS, Surmi A. Insights on cryogenic distillation technology for simultaneous CO2 and H2S removal for sour gas fields. Molecules 2022;27:1424. [CrossRef]

[8] Northrop PS, Valencia JA. The CFZ TM process: A cryogenic method for handling high-CO2 and H2S gas reserves and facilitating geosequestration of CO2 and acid gases. Energy Procedia 2009;1:171–177. [CrossRef]

[9] Hashemi SE, Sarker S, Lien KM, Schnell SK, Austbø B. Cryogenic vs. absorption biogas upgrading in liquefied biomethane production – An energy efficiency analysis. Fuel 2019;245:294–304. [CrossRef]

[10] Rex P, Meenakshisundaram N, Barmavatu P. Sustainable valorisation of kitchen waste through greenhouse solar drying and microwave pyrolysis technology readiness level for the production of biochar. J Environ Health Sci Eng 2024;22:381–395. [CrossRef]

[11] Mariyappillai V, Shiyamala C, Abisheik T, Tiffany M, Pandiyan V, Senthilraja A, et al. Zr-modified ZnO nanoparticles: Optimized photocatalytic degradation and antibacterial efficiency for pollution control. Ceram Int 2025. doi: 10.1016/j.ceramint.2025.02.402. [CrossRef]

[12] Leela NS, Kannan S, Abisheik T, Tiffany M, Pandiyan V, Periyasami G, et al. Enhanced photocatalytic activity of azo dyes degradation by urea assisted Mo-doped TiO2 under UV-A light and sunlight irradiation. J Alloys Compd 2025;1020:179389. [CrossRef]

[13] Alshoaibi A, Ramgopal NC, Ramasundaram S, Upendranath K, Mahanthappa M, Fahad M, et al. NiS/NiS2-embedded sulfur-doped porous graphitic carbon nitride nanosheets as an efficient catalyst for 4-Nitrophenol reduction. Diamond Relat Mater 2025;153:112110. [CrossRef]

[14] Mahmoud AS, Abubakar MH, Adamu Z. Demolition wastes in the global construction industry: An overview of research perspective from 2001 to 2020. J Therm Eng 2025;11(2):603−621. [CrossRef]

[15] Pathak B, Patel N. Effect of modifying bowl geometry for IC engine fueled with diesel and biofuel: Review. J Therm Eng 2024;10(1):244−261. [CrossRef]

[16] Pudi A, Rezaei M, Signorini V, Andersson MP, Baschetti MG, Mansouri SS. Hydrogen sulfide capture and removal technologies: A comprehensive review of recent developments and emerging trends. Sep Purif Technol 2022;298:121448. [CrossRef]

[17] Silvestre G, Fernandez B, Bonmati A. Significance of anaerobic digestion as a source of clean energy in waste water treatment plants. Energy Convers Manag 2015;101:255−262. [CrossRef]

[18] Montebello AM, Mora M, López LR, Bezerra T, Gamisans X, Lafuente J, et al. Aerobic desulfurization of biogas by acidic biotrickling filtration in a randomly packed reactor. J Hazard Mater 2014;280:200−208. [CrossRef]

[19] Song X, Yao W, Zhang B, Wu Y. Application of Pt/CdS for the photocatalytic flue gas desulfurization. Int J Photoenergy 2012;2012:684735. [CrossRef]

[20] Guldal NO, Figen HE, Baykara SZ. New catalysts for hydrogen production from H2S: Preliminary results. Int J Hydrog Energy 2015;40(24):7452−7458. [CrossRef]

[21] Akamatsu K, Nakane M, Sugawara T, Hattori T, Nakao S. Development of a membrane reactor for decomposing hydrogen sulfide into hydrogen using a high performance amorphous silica membrane. J Membr Sci 2008;325(1):16−19. [CrossRef]

[22] Anani AA, Mao Z, White RE, Srinivasan S, Appleby AJ. Electrochemical production of hydrogen and sulfur by low-temperature decomposition of hydrogen sulfide in an aqueous alkaline solution. J Electrochem Soc 1990;137(9):2703−2709. [CrossRef]

[23] Zong X, Han J, Seger B, Chen H, Lu G, Li C, et al. An integrated photo electrochemical chemical loop for solar-driven overall splitting of hydrogen sulfide. Angew Chem 2014;53(17):4399−4403. [CrossRef]

[24] Bai X, Cao Y, Wu W. Photocatalytic decomposition of H2S to produce H2 over CdS nanoparticles formed in HY-zeolite pore. Renew Energy 2011;36(10):2589−2592. [CrossRef]

[25] Yan H, Yang J, Ma G, Wu G, Zong X, Lei Z, et al. Visible-light-driven hydrogen production with extremely high quantum efficiency on Pt−PdS/CdS photocatalyst. J Catal 2009;266(2):165−168. [CrossRef]

[26] Reddy EL, Karuppiah J, Biju VM, Subrahmanyam C. Catalytic packed bed non-thermal plasma reactor for the extraction of hydrogen from hydrogen sulfide. Int J Energy Res 2013;37(11):1280−1286. [CrossRef]

[27] John S, Hamann JC, Muknahallipatna SS, Legowski S, Ackerman JF, Argyle MD. Energy efficiency of hydrogen sulfide decomposition in a pulsed corona discharge reactor. Chem Eng Sci 2009;64(23):4826−4834. [CrossRef]

[28] Xu JH, Ding BB, Lv XM, Lan SH, Li CL, Pen L. Mathematical modeling and mechanism of VUV photodegradation of H2S in the absence of O2. Int J Photoenergy 2018;2018:2769213. [CrossRef]

[29] Xu MY, Zeng C, Lin YL, Zhang TY, Fu Q, Zhao HX, et al. Wavelength dependency and photosensitizer effects in UV-LED photodegradation of iohexol. Water Res 2024;255:121477. [CrossRef]

[30] Liu J, Zhang J, Jia M, Ma R, Qu R, Wang Z, et al. Efficient photocatalytic degradation of imidazolium ionic liquids in an N-ZnO/simulated sunlight irradiation system and its mechanism. Chem Eng J 2024:154317. [CrossRef]

[31] Wilson SHS, Howe JD, Ashfold MNR. On the near ultraviolet photodissociation of hydrogen sulphide. Mol Phys 1996;88(3):841−858. [CrossRef]

[32] Sokhansanj A, Haghighi M, Shabani M. Developing the novel model for kinetics and mass transfer in sun light driven photodegradation of malachite green over Bi2O2CO3/CuBi2O4 (50: 50) flower-like nanophotocatalyst: Machine and deep-learning algorithms. Process Saf Environ Prot 2024;184:502−522. [CrossRef]

[33] Wang Y, Xu D, Yang X, He JH. Novel 2D/2D S-scheme heterojunction photocatalyst for peroxymonosulfate activation enables ciprofloxacin ultrafast degradation: High-efficiency photogenerated carrier transport. Chem Eng J 2024;488:150844. [CrossRef]

[34] He JH. Homotopy perturbation technique. Comput Methods Appl Mech Eng 1999;178:257−262. [CrossRef]

[35] He JH. A coupling method of homotopy technique and a perturbation technique for non-linear problems. Comput Methods Appl Mech Eng 2000;35:37−43. [CrossRef]

[36] Saranya K, Iswarya T, Mohan V, Sathappan KE, Rajendran L. Mathematical modeling of glucose, insulin, b-cell mass: Homotopy perturbation method approach. Eur J Mol Clin Med 2020;07(02):3513–3530.

[37] Saranya K, Mohan V, Kizek R, Fernandez C, Rajendran L. Unprecedented homotopy perturbation method for solving nonlinear equations in the enzymatic reaction of glucose in a spherical matrix. Bioprocess Biosyst Eng 2017;41:281–294. [CrossRef]

[38] He JH. Homotopy perturbation method: A new nonlinear analytical technique. Appl Math Comput 2003;135:73–79. [CrossRef]

[39] He JH. Homotopy perturbation method for solving boundary value problem. Phys Lett A 2006;350:87–88. [CrossRef]

[40] He JH. Some asymptotic methods for strongly nonlinear equations. Int J Mod Phys B 2006;20:1141–1199. [CrossRef]

[41] Kalachev LV, Seidman TI. Singular perturbation analysis of a stationary diffusion reaction system exhibiting a corner-type behavior in the interval interior. J Math Anal Appl 2003;288(2):722–743. [CrossRef]

[42] Khan H, Rajpar AH, Alzabut J, Aslam M, Etemad S, Rezapour S. On a fractal–fractional-based modeling for influenza and its analytical results. Qual Theory Dyn Syst 2024;23:7. [CrossRef]

[43] Ahmed S, Azar AT, Abdel-Aty M, Khan H, Alzabut J. A nonlinear system of hybrid fractional differential equations with application to fixed time sliding mode control for leukemia therapy. Ain Shams Eng J 2024:102566. [CrossRef]

[44] Khan H, Alzabut J, Gómez-Aguilar JF, Alkhazan A. Essential criteria for existence of solution of a modified-ABC fractional order smoking model. Ain Shams Eng J 2024:102646. [CrossRef]

[45] Enokihara GH, Loures CCA, Izário Filho HJ, Alcântara MAK, Siqueira AF, Da Rós PCM, et al. Kinetic modelling of total organic carbon degradation in dairy wastewater. Environ Technol 2024;45(5):880–887. [CrossRef]

[46] Liu T, Ding Z, Yu J, Zhang W. Parameter estimation for nonlinear diffusion problems by the constrained homotopy method. Mathematics 2023;11(12):2642. [CrossRef]

[47] Liu T, Xue R, Liu C, Qi Y. A regularization homotopy strategy for the constrained parameter inversion of partial differential equations. Entropy 2021;23(11):1480. [CrossRef]

[48] Sander SP, Abbatt J, Barker JR, et al. Chemical Kinetics and Photochemical Data for Use in Atmospheric Studies. JPL Publication; 2011.

[49] Bradley JN, Trueman SP, Whytock DA, Zaleski TA. Electron spin resonance study of the reaction of hydrogen atoms with hydrogen sulphide. J Chem Soc Faraday Trans 1 1973;69:416–425. [CrossRef]

[50] Peng J, Hu X, Marshall P. Experimental and ab initio investigations of the kinetics of the reaction of H atoms with H2S. J Phys Chem A 1999;103(27):5307–5311. [CrossRef]

[51] Loraine G, Glaze W. Destruction of vapor phase halogenated methanes by means of ultraviolet photolysis. Proc Ind Waste Conf 1993;47:309–316.

[52] Stachnik RA, Molina MJ. Kinetics of the reactions of mercapto radicals with nitrogen dioxide and oxygen. J Phys Chem 1987;91(17):4603–4606. [CrossRef]

APPENDIX

Kinetics of UV degradation of hydrogen sulfide without oxidization by Homotopy Perturbation Method

V. Sreelatha DEVI[1,*], K. SARANYA[1], D. VIJAYABALAN[2], K A. Niranjan KUMAR[3], Muthumari G[3], Banu Priya V

Appendix A: Basic Concepts of the HPM

Having successfully overcome many of the limitations of traditional perturbation methods, the HPM has received the attention of many researches in recent decades. The simple implementation of the HPM even when applied to strong nonlinear differential equation is another desired feature that made it one of the most used techniques in recent years. Here, we present a brief introduction to the HPM. Consider the following nonlinear differential equation:

$$\mathrm{L}(u)+N(u)-f(\mathrm{r})=0,\mathrm{r}\in\Omega \quad (\mathrm{A1})$$

With boundary conditions

$$B\left(u,\frac{du}{dr}\right)=0,r\in\Gamma \quad (\mathrm{A2})$$

where L is a linear operator, N is a nonlinear operator, and $f(r)$ is a known analytic function By the homotopy technique, we construct a homotopy $v(r,p):\Omega\times[0,1]\to R$ that satisfies:

$$H(v,p)=(1-p)(L(v)-L(u_0))+p(L(v)+\mathrm{N}(v)-f(r))=0, \quad (\mathrm{A3})$$

where $p\in[0,1]$ is an embedding parameter, and u_0 is an initial approximation of Eq.(A1) that satisfies the boundary conditions (A2). when $p=0$, Eq.(A3) become the linear equation

$$L(v)-\mathrm{L}(\mathrm{u}_0)=0, \quad (\mathrm{A4})$$

and when $p=1$, it becomes the nonlinear equation

$$\mathrm{L}(u)+N(u)-f(\mathrm{r})=0, \quad (\mathrm{A5})$$

The process of changing p from zero to unity is the process that changes $v(r,p)$ from $u_0(r)$ to $u(r)$. We first use the embedding parameter p as a "small parameter" and assume that the solution of Eq.(A1) can be written as a power series in p:

$$p^0: L(v_0)=0$$

$$p^1: L(v_1)+N(v_0)-f(r)=0$$

Solving the above system of equations we obtain $v_0, v_1 ...$

$v = v_0 + pv_1 + p^2 v_2 + ... \text{(A6)}$

Setting $p = 1$ results in the approximate solution of Eq.(A1):

$u = \lim_{p \to 1} v = v_0 + v_1 + v_2 + ...$ (A7)

Appendix B: Analytical expressions for the concentrations of H_2S, H. , $SH.$, H_2 and S are derived from these equations using homotopy perturbation method.

Equation(7-11) using HPM Method

$$\frac{d[H_2S]}{dt} = -k_{obs1}[H_2S] - k_3[H_2S][H.] + k_6[SH.] \quad \text{(B1)}$$

$$\frac{d[H.]}{dt} = k_{obs1}[H_2S] + k_{obs2}[SH.] - k_3[H_2S][H.] + k_4[H.]^2 - k_5[SH.][H.] \quad \text{(B2)}$$

$$\frac{d[SH.]}{dt} = k_{obs1}[H_2S] + k_{obs2}[SH.] - k_5[SH.][H.] - k_6[SH.]^2 \quad \text{(B3)}$$

$$\frac{d[H_2]}{dt} = k_3[H_2S][H.] + k_4[H.]^2 + k_5[H.][SH.] \quad \text{(B4)}$$

$$\frac{d[S]}{dt} = k_{obs2}[SH.] - k_5[SH.][H.] - k_6[SH.]^2 \quad \text{(B5)}$$

$$u = H_2S, v = H., w = SH,, x = H_2S, y = S, k_{obs1} = a, k_{obs1} = b \quad \text{(B6)}$$

Substituting all the above values in (B_1)-(B_5) in (B_6)

$$\frac{du}{dt} = -au - k_3uv + k_6w^2 \quad \text{(B7)}$$

$$\frac{dv}{dt} = au + bw - k_3uv - k_4v^2 - k_5uv \quad \text{(B8)}$$

$$\frac{dw}{dt} = au - bw - k_5vw - k_6w^2 \quad \text{(B9)}$$

$$\frac{dx}{dt} = k_3uv + k_4v^2 + k_5uv \quad \text{(B10)}$$

$$\frac{dy}{dt} = bw + k_5vw + k_6w^2 \quad \text{(B11)}$$

We construct the new homotopy for the equation(7-11) as follows(Rajendran and Anitha(2013))

$$(1-p)\left[\frac{du}{dt} + au\right] + p\left[\frac{du}{dt} + au + k_3uv - k_6w\right] = 0 \quad \text{(B12)}$$

$$(1-p)\left[\frac{dv}{dt} - au - bw\right] + p\left[\frac{dv}{dt} - au - bw + k_3uv - k_4v^2 + k_5vw\right] = 0 \quad \text{(B13)}$$

$$(1-p)\left[\frac{\mathrm{d}w}{\mathrm{dt}}-au-bw\right]+p\left[\frac{\mathrm{d}w}{\mathrm{dt}}-au-bw+k_5vw+k_6w^2\right]=0 \quad \text{(B14)}$$

$$(1-p)\left[\frac{\mathrm{d}x}{\mathrm{dt}}\right]+p\left[\frac{\mathrm{d}x}{\mathrm{dt}}-k_3uv-k_4v^2+k_5vw\right]=0 \quad \text{(B15)}$$

$$(1-p)\left[\frac{\mathrm{d}y}{\mathrm{dt}}-bw\right]+p\left[\frac{\mathrm{d}y}{\mathrm{dt}}-bw+k_5vw+k_6v^2\right]=0 \quad \text{(B16)}$$

When $p\in(0,1)$ is an embedding parameter,Now assume that the solution of the equation (7-11) are

$$u=u_0p^0+u_1p^1+u_2p^2+u_3p^3+... \quad \text{(B17)}$$

$$v=v_0p^0+v_1p^1+v_2p^2+v_3p^3+... \quad \text{(B18)}$$

$$w=w_0p^0+w_1p^1+w_2p^2+w_3p^3+... \quad \text{(B19)}$$

$$x=x_0p^0+x_1p^1+x_2p^2+x_3p^3+... \quad \text{(B20)}$$

$$y=y_0p^0+y_1p^1+y_2p^2+y_3p^3+... \quad \text{(B21)}$$

Substituting the above equation(B_1 -B_5) and equating the coefficients p^0,p^1…on both sides we get,Using HPM,

$$p^0=\frac{du_0}{dt}+au_0=0 \quad \text{(B22)}$$

$$p^1=\frac{du_1}{dt}+au_1+k_3u_0v_0-k_6{w_0}^2=0 \quad \text{(B23)}$$

$$p^0=\frac{dv_0}{dt}-au_0-bw_0=0 \quad \text{(B24)}$$

$$p^1=\frac{dv_1}{dt}-au_1-bw_1+k_3u_0v_0-k_4{v_0}^2+k_5v_0w_0=0 \quad \text{(B25)}$$

$$p^0=\frac{dw_0}{dt}-au_0+bw_0=0 \quad \text{(B26)}$$

$$p^1=\frac{dw_1}{dt}-au_1+bw_1+k_5v_0w_0+k_6{w_0}^2=0 \quad \text{(B27)}$$

$$p^0=\frac{dx_0}{dt}=0 \quad \text{(B28)}$$

$$p^1=\frac{dx_1}{dt}-k_3u_0v_0-k_4{v_0}^2-k_5v_0w_0=0 \quad \text{(B29)}$$

$$p^0=\frac{dy_0}{dt}-bw_0=0 \quad \text{(B30)}$$

$$p^1=\frac{dy_1}{dt}-bw_1-k_5v_0w_0-k_6{w_0}^2=0 \quad \text{(B31)}$$

Solving the initial and boundary condition are in

where

$$k_{obs1}=a;\ k_{obs2}=b;\ c_1=u_{ini};\ A=\frac{au_{ini}}{a-b};\ B=w_{ini}-\frac{au_{ini}}{a-b};$$

$$c_2=v_{ini}+\left[\frac{au_{ini}+bA}{a}\right]+1;$$

$$c_3=\frac{au_{ini}+bA}{a};\ \ c_4=ab(a-b);\ c_5=2A^2ABk_6;\ \ c_6=2A^2ABk_6;\ c_7=a^2bc_1c_2k_3;$$

$$c_8=a^2c_1k_3;\ \ c_9=-a^2c_1k_3;\ \ c_{10}=2A^2b^2k_6;\ \ c_{11}=aA^2bk_6;\ c_{12}=aA^2bk_6;$$

$$c_{13}=4aAbBk_6;\ \ c_{14}=4aAbBk_6;\ \ c_{15}=2ab^2c_1c_2k_3;\ \ c_{16}=2b^2c_1c_3k_3;$$

$$c_{17} = 2b^2c_1c_3k_3;\quad c_{18} = abB^2k_6;\ c_{19} = abc_1c_3k_3;\ c_{20} = abc_1c_3k_3;$$
$$c_{21} = 2abc_1k_3;\ c_{22} = 2abc_1k_3;\ c_{23} = 2A^2B^2k_6;\ c_{24} = 2b^2c_1c_3k_3;$$
$$L_1 = c_5 + c_8 - c_{10} + c_{12} - c_{14} - c_{16} - c_{17} + c_{20} - c_{22}$$
$$L_2 = -c_6 + c_9 + c_{21} + c_{13}L_3 = -c_{11} - c_{19} + c_{23} + c_{24}L_4 = c_{15} - c_{17}$$
$$p_1 = -2c_{18}a^5;\ p_2 = 2c_{18}a^5;\ p_3 = 5bc_{18}a^4;\ p_4 = 5bc_{18}a^4;$$
$$p_5 = 2Bc_4k_5a^4;\ p_6 = 2Bc_4k_5a^4;\ p_7 = 2B^2c_4k_6a^4;\ p_8 = 2B^2c_4k_6a^4;\ p_9 = 2bL_1a^4;$$
$$p_{10} = 2bL_1a^4;\ p_{11} = 2bL_2a^4;\ p_{12} = 2bL_2a^4;\ p_{13} = bL_3a^4;\ p_{14} = bL_3a^4;$$
$$p_{15} = 2bBc_2c_4k_5ta^4;\ p_{16} = 2bL_4a^4;\ p_{17} = 4b^2c_{18}a^3;\ p_{18} = 4b^2c_{18}a^3;$$
$$p_{19} = 5bBc_4k_5a^3;\ p_{20} = Abc_3c_4k_5a^3;\ p_{21} = 2Abc_4k_5a^3;\ p_{22} = 2bBc_3c_4k_5a^3;$$
$$p_{23} = 2Abc_4k_5a^3;\ p_{24} = 5bBc_4k_5a^3;\ p_{25} = 2Abc_2c_4k_5a^3;\ p_{26} = Abc_3c_4k_5a^3;$$
$$p_{27} = 2bBc_3c_4k_5a^3;\ p_{28} = 2Abc_2c_4k_5a^3;\ p_{29} = 5bB^2c_4k_6a^3;\ p_{30} = A^2bc_4k_6a^3;$$
$$p_{31} = 4AbBc_4k_6a^3;\ p_{32} = 5bB^2c_4k_6a^3;\ p_{33} = A^2bc_4k_6a^3;\ p_{34} = 4AbBc_4k_6a^3;$$
$$p_{35} = 3b^2L_1a^3;\ p_{36} = 3b^2L_1a^3;\ p_{37} = 5b^2L_2a^3;\ p_{38} = 5b^2L_2a^3;$$
$$p_{39} = 2b^2L_3a^3;\ p_{40} = 2b^2L_3a^3;\ p_{41} = 2bL_4a^3;\ p_{42} = 2bL_4a^3;$$
$$p_{43} = 5b^2Bc_2c_4k_5a^3;\ p_{44} = 3b^2L_4a^3;\ p_{45} = b^3c^{18}a^2;\ p_{46} = b^3c^{18}a^2;$$
$$p_{47} = 4b^2Bc_4k_5a^2;\ p_{48} = 2Ab^2c_3c_4k_5a^2;\ p_{49} = 5Ab^2c_4k_5a^2;\ p_{50} = 5b^2Bc_3c_4k_5a^2;$$
$$p_{51} = 5Ab^2c_4k_5a^2;\ p_{52} = 4b^2Bc_4k_5a^2;\ p_{53} = 3Ab^2c_2c_4k_5a^2;\ p_{54} = 2Ab^2c_3c_4k_5a^2;$$
$$p_{54} = 2Ab^2c_3c_4k_5a^2;\ p_{55} = 5b^2Bc_3c_4k_5a^2;\ p_{56} = 3Ab^2c_2c_4k_5a^2;\ p_{57} = 4b^2B^2c_4k_6a^2;$$
$$p_{58} = 2A^2b^2c_4k_6a^2;\ p_{59} = 10Ab^2Bc_4k_6a^2;\ p_{60} = 2A^2b^2Bc_4k_6a^2;\ p_{61} = 4b^2B^2c_4k_6a^2;$$
$$p_{62} = 10Ab^2Bc_4k_6a^2;\ p_{63} = b^3L_1a^2;\ p_{64} = b^3L_1a^2;\ p_{65} = 4\,b^3L_2a^2;\ p_{66} = 4\,b^3L_2a^2;$$
$$p_{67} = b^3L_3a^2;\ p_{68} = b^3L_3a^2;\ p_{69} = b^2L_4a^2;\ p_{70} = b^2L_4a^2;$$
$$p_{71} = 4b^3Bc_2c_4k_5a^2;\ p_{72} = b^3L_4a^2;\ p_{73} = b^3Bc_4k_5a;\ p_{74} = Ab^3c_3c_4k_5a;$$
$$p_{75} = 4Ab^3Bc_4k_5a;\ p_{76} = 4b^3Bc_3c_4k_5a;\ p_{77} = 4Ab^3c_4k_5a;\ p_{78} = b^3Bc_4k_5a;$$
$$p_{79} = Ab^3c_2c_4k_5a;\ p_{80} = Ab^3c_3c_4k_5a;\ p_{81} = 4b^3Bc_3c_4k_5a;\ p_{82} = Ab^3c_2c_4k_5a;$$
$$p_{83} = b^3B^2c_4k_6a;\ p_{84} = A^2b^3c_4k_6a;\ p_{85} = 8Ab^3c_4k_6a;\ p_{86} = A^2b^3c_4k_6a;$$
$$p_{87} = 8Ab^3c_4k_6a;\ p_{88} = 8Ab^3c_4k_6a;\ p_{89} = b^4L_2a;\ p_{90} = b^4L_2a;$$
$$p_{91} = b^4Bc_2c_4k_5a;\ p_{92} = Ab^4c_4k_5;\ p_{93} = b^4Bc_3c_4k_5;\ p_{94} = Ab^4c_4k_5;$$
$$p_{95} = b^4Bc_3c_4k_5;\ p_{96} = 2Ab^4Bc_4k_6;\ p_{97} = 2Ab^4Bc_4k_6;\ p_{98} = a(a-b)^2(2a-b)bc_4;$$
$$A_1 = p_1 + p_3 - p_5 + p_7 - p_{17} + p_{19} - p_{29} + p_{45} - p_{47} + p_{57} + p_{73} - p_{83}$$
$$A_2 = p_2 - p_4 + p_6 - p_8 + p_9 - p_{12} + p_{14} - p_{15} + p_{18} + p_{23} - p_{24} - p_{25} + p_{26} + p_{27} + p_{32}$$
$$- p_{33} - p_{34} - p_{35} + p_{38} - p_{40} - p_{41} - p_{46} + p_{49} - p_{51} + p_{52} + p_{53} - p_{54}$$
$$- p_{55} + p_{60} - p_{61} + p_{62} + p_{63} - p_{66} + p_{68} + p_{69} + p_{77} - p_{78} - p_{79} + p_{80}$$
$$+ p_{81} - p_{86} + p_{87} + p_{90} + p_{88} - p_{94} - p_{95} + p_{97};$$
$$A_3 = p_{11} - p_{37} + p_{65} - p_{89};$$
$$A_4 = -p_{10} + p_{28} + p_{36} + p_{42} - p_{56} - p_{64} - p_{70} + p_{82};$$
$$A_5 = -p_{13} - p_{20} + p_{30} + p_{39} - p_{58} - p_{67} - p_{74} + p_{84} + p_{48};$$
$$A_6 = -p_{21} - p_{22} + p_{31} + p_{50} - p_{59} + p_{85} + p_{92} + p_{93} - p_{96} - p_{75} - p_{76};$$

Applying boundary Conditions, substituting and simplifying all the values, then

$$u(\mathrm{t}) = \frac{1}{c_4}\left[e^{-at}\left[L_1 - L_4t\right] - e^{-at-bt}L_2 + L_3e^{-2at} + c_{18}e^{-2bt}\right]$$

$$v(\mathrm{t}) = \frac{a}{c_4}\left[\left[e^{-at}\left[L_4\right] + \left[L_1 - L_4t\right]\left[e^{-at}\right][-a] + e^{-at-bt}(\mathrm{a+b})L_2 + L_3e^{-2at}(-2\mathrm{a}) + c_{18}e^{-2bt}(-2\mathrm{b})\right]e^{-at}L_1 - L_4\left[te^{-at}\right]\right]$$

$$w(\mathrm{t}) = \frac{e^{-at-bt-(2\mathrm{a}+\mathrm{b})\mathrm{t}}}{p_{98}} \left[\begin{array}{l} e^{3\mathrm{at}}\left(A_1\right) + e^{at+(2\mathrm{a}+\mathrm{b})\mathrm{t}}\left(A_2 + p_{43}t - p_{71}t + p_{91}t\right) \\ +e^{(2\mathrm{a}+\mathrm{b})\mathrm{t}}\left(A_3\right) + e^{at+(b-a)t+(2\mathrm{a}+\mathrm{b})}\left(A_4 + p_{16}t - p_{44}t + p_{72}t\right) \\ +e^{at+2\mathrm{bt}}\left(A_5\right) + e^{at+(\mathrm{a}+\mathrm{b})}\left(A_6\right) \end{array} \right]$$

$$\mathrm{X}_1(\mathrm{t}) = -k_3c_1c_3\frac{e^{-2at}}{-2a} - k_3c_1\frac{e^{-(a+b)t}}{-(a+b)} - c_1c_2k_3\frac{e^{-at}}{-a} +$$

$$k_4\left[c_3^2\frac{e^{-2at}}{-2a} + 2c_3\frac{e^{-(a+b)t}}{-(a+b)} - 2c_3c_2\frac{e^{-at}}{-a} - 2c_2\frac{e^{-bt}}{-b} + \frac{e^{-2bt}}{-2b} + c_2^2t\right] +$$

$$k_5\left[-A\frac{e^{-(a+b)t}}{-(a+b)} - Ac_3\frac{e^{-2at}}{-2a} + Ac_2\frac{e^{-at}}{-a} - Bc_3\frac{e^{-(a+b)t}}{-(a+b)} + Bc_2\frac{e^{-bt}}{-b} - B\frac{e^{-2bt}}{-2b}\right]$$

J Ther Eng, Vol. 12, No. 1, pp. 72−87, January, 2026

Journal of Thermal Engineering
Web page info: https://jten.yildiz.edu.tr
DOI: 10.14744/thermal.0001059

Research Article

Evaluation of infrared radiations from top of the atmosphere through artificial neural network modeling

Usama Ayub YOUSUFZAI[1,2,*], Muhammad Jawed IQBAL[1], Faisal Khan AFRIDI[1]

[1]*Institute of Space Science and Technology, University of Karachi, Karachi, Pakistan*
[2]*Department of Physics, NED University of Engineering and Technology, Karachi, Pakistan*

ARTICLE INFO

Article history
Received: 09 July 2025
Revised: 01 December 2025
Accepted: 09 December 2025

Keywords:
ANN Modeling; Infrared Radiations; IR Evaluation; Top of the atmosphere; Upper Atmosphere

ABSTRACT

This study helps to forecast the Infrared Radiations from the top of the atmosphere over six cities in Pakistan using data gathered over a ten-year period from the Synoptic Top of the Atmosphere (TOA) and surface fluxes and clouds Edition 4A, a data product of clouds and the Earth's Radiant Energy System which gathers daily ten-year local weather data. This work aims to use exploratory data analysis to examine infrared radiation quantification. The assessment of infrared radiations from the upper atmosphere, a crucial part of the Earth's radiation budget with consequences for climate modeling and satellite based atmospheric research, is the main emphasis of this work. In order to accomplish this, atmospheric datasets taken from the NASA Earth observation gateway used in artificial neural network (ANN) modeling. By combining machine learning with NASA's atmospheric datasets for Top of the Atmosphere (TOA) infrared radiation evaluation, this work is new in that it offers efficiency and accuracy gains over traditional methods. Artificial neural network (ANN) utilized in the Pakistani cities of Karachi, Thatta, Mirpurkhas, Gilgit, Kalam, and Astore to predict average daily infrared variation. Over the course of seven years, the network trained, validated, and tested using infrared flux data from 2011 to 2018. With the aid of the hidden layer's training and validation settings, the average daily infrared flux estimated. We will be able to investigate the changes in Earth's climate throughout time, which impact by various factors, thanks to research of this kind. Mean Squared Error (MSE), Mean Absolute Percentage Error (MAPE), correlation coefficient, Root Mean Square Error (RMSE), and Mean Bias Error (MBE) calculated for the purposes of validating the statistical errors. The statistical errors demonstrate that the neural network model predicts infrared radiations for Thatta city well, while average predictions generated for Astore, Gilgit, and Kalam, and Mirpurkhas city, respectively. Astore exhibits the best correlation, followed by Thatta, Karachi, Kalam, Gilgit, and Mirpurkhas.

Cite this article as: Yousufzai UA, Iqbal MJ, Afridi FK. Evaluation of infrared radiations from top of the atmosphere through artificial neural network modeling. J Ther Eng 2026;12(1):72−87.

***Corresponding author.**
*E-mail address: usamaayub@neduet.edu.pk

This paper was recommended for publication in revised form by Editor-in-Chief Ahmet Selim Dalkilic

Published by Yıldız Technical University Press, İstanbul, Turkey
Yıldız Technical University. This is an open access article under the CC BY-NC license (http://creativecommons.org/licenses/by-nc/4.0/).

INTRODUCTION

Infrared flux rises from the top of the atmosphere as result of the Earth and its atmosphere emitting infrared radiation into space. Because it is a part of the climate system›s energy balance, this radiation plays a major part in controlling the planet›s temperature [1].

The following are the primary sources of infrared radiation from the upper atmosphere:

1. Earth›s Surface: Solar radiation absorbed by the Earth›s surface and reemitted as infrared radiation. One of the main sources of the infrared flux originating from the top of the atmosphere is this thermal radiation.
2. Atmospheric Gases: Water vapor, carbon dioxide, and methane are among the gases that emit infrared radiation from the Earth›s atmosphere. These gases add to the total flux of infrared radiation originating from the top of the atmosphere by both absorbing and reemitting thermal radiation.
3. Clouds: The emission of infrared radiation from the upper atmosphere is significantly influence by clouds. Their kind, altitude, and thickness determine how much they contribute to the total infrared flux. They have the ability to both reflect and absorb thermal radiation.

The quantity of infrared flux originating from the upper atmosphere is a crucial component in comprehending the energy balance of the Earth and the worldwide climate. [2] Numerous other uses, including satellite remote sensing, weather forecasting, and climate modeling, also depend on it. Additionally, changes in the amount and distribution of infrared flux can significantly the impact Earth›s temperature and climate hence this area of study is crucial for atmospheric science and climate research. The Sun emits infrared radiation, a part of the electromagnetic spectrum, even though visible light is its main source. In fact, infrared radiation makes up almost half of the Sun›s energy output [3]. Using traditional radiative transfer models and empirical techniques, recent research has thoroughly examined infrared radiations at the top of the atmosphere. Although these techniques have improved our knowledge, they are frequently computationally demanding and susceptible to variations in atmospheric factors [3]. Simultaneously, the atmospheric and climatic sciences have begun to pay more attention to artificial intelligence, especially artificial neural networks (ANN), for tasks like surface radiation estimation, cloud classification, and weather forecasting [4]. Relatively few studies, nevertheless, have used ANN directly assess TOA infrared radiation. Additionally, despite the fact that NASA›s atmospheric datasets such as CERES, MODIS, and AIRS extensively used in satellite-based radiation studies, nothing known about how to integrate them with ANN modeling for TOA infrared research.

With a surface temperature of about 5,500 degrees Celsius, the Sun is a highly hot object that produces infrared radiation. The Sun emits radiation, including infrared radiation, as a result, of its extreme heat [5]. Telescopes and satellites, among other devices, are able to detect this energy, which carried through space as electromagnetic waves. There are several uses for the Sun›s infrared energy [6]. It can used, for instance, to investigate the makeup and characteristics of the Sun›s atmosphere and surface as well as the solar wind, a stream of charged particles that emerges from the Sun continuously [7]. The Sun›s infrared radiation also has a significant impact on Earth›s weather and climate [8]. It supports the Earth›s climate system by serving as a major energy source for atmospheric circulation and weather patterns [9]. The Sun emits infrared radiation, which then released as thermal radiation in the form of infrared waves by the Earth›s surface and atmosphere. This thermal radiation, which is also an essential component of the Earth›s energy balance, has a significant impact on the planet›s temperature and climate [10].

There are numerous significant applications for a wider scientific and practical audience when evaluating infrared radiations from the upper atmosphere using artificial neural network (ANN) modeling [11]. These findings advance our knowledge of the Earth›s radiation budget, which is essential for research on climate change. The accuracy of atmospheric models and short-term forecasts in weather forecasting increased by better characterizing outgoing longwave radiation [12]. Additionally, the technique used to retrieve atmospheric characteristics like surface temperature and cloud cover through satellite-based remote sensing. The results have implications for energy balance evaluations, which are crucial for assessing the effects of global warming and creating sustainable energy policy, in addition to meteorology and climate science [13]. This research offers a flexible tool for atmospheric investigations with a broad range of scientific and societal applications by integrating radiative transfer mechanisms with sophisticated data-driven modeling.

Even though TOA radiation is important, not many studies have looked at using artificial intelligence techniques, especially artificial neural networks (ANN), for this purpose. Although ANN used in related fields like surface radiation research, cloud categorization, and weather forecasting, its use for direct assessment of TOA infrared radiation is yet relatively unexplored [14]. Additionally, there is a gap in both approach and application because the integration of ANN modeling with high-quality atmospheric information from NASA›s Earth Observation portals has not adequately covered in the literature [15]. By employing ANN modeling to evaluate infrared radiations at the TOA using atmospheric datasets taken from NASA›s data portal, this study fills in these gaps. In contrast to traditional radiative transfer or empirical methodologies, this work is innovative in that it combines the machine learning techniques with satellite-based atmospheric data to provide a framework that is more accurate, efficient, and flexible [16]. The study not only advances methodology by showcasing the effectiveness of ANN modeling in this setting, but it also creates new opportunities to enhance

energy balance evaluations, satellite remote sensing, and climate modeling. ANN models effectively used in earlier research to estimate or forecast atmospheric radiation at regional or global scales. The spatiotemporal assessment of top-of-atmosphere (TOA) infrared radiation across particular urban locations using long-term CERES data, however, has received little attention. In order to provide localized insights into infrared flux variability and model performance under various climatic conditions, an ANN-based framework deployed to six major cities in Pakistan between 2011 and 2021. The current work differs from other ANN-based evaluations of atmospheric radiation because of its focused, long-term use.

CNNs, LSTMs, and hybrid models are examples of deep learning architectures that used more and more in recent studies for atmospheric and climate modeling [17]. For instance, LSTM networks have demonstrated enhanced longwave radiation forecasting under variable climatic conditions and CNNs used for satellite-based radiation mapping [18]. These developments establish the current ANN-based method as a computationally effective substitute for regional-scale applications and demonstrate the expanding significance of deep learning in atmospheric research [19].

All of the CERES (Clouds and the Earth's Radiant Energy System (CERES) Energy Balanced and Filled (EBAF) Top-of-Atmosphere (TOA)) footprints (20 km nominal resolution) within the specified temporal or spatial domain used to calculate the all-sky scene, also referred to as total [20]. There is a collection of observations from 2011 until 2020. Depending on the product, Clear-Sky scenario offers multiple algorithms: ERBE-like, Energy Balanced and Filled (EBAF), Single Scanner Footprint TOA/Surface Fluxes and Clouds (SSF). CERES footprints that were roughly classified as clear using the ERBE scene id algorithm which makes use of suitable SW thresholds and climatically zonal LW criteria are used to determine the ERBE-like clear-sky scene[21]. In this instance, the set of observations spans the years 2011 through 2021.We obtained set of observations for TOA infrared flux –All sky and TOA infrared flux–Clear Sky for cloud free areas of the regions. The duration of the observations is from 2011 to 2021 from CERES_EBAF-TOA_Ed4.1.

The majority of earlier publications focus on global-scale radiative flux estimation or particular case studies under constrained spatial settings, despite the fact that artificial neural networks frequently used in atmospheric investigations [22]. In contrast, the current work analyzes ten years of CERES satellite data for six major cities in Pakistan to assess the effectiveness and adaptability of ANN models in replicating top of atmosphere (TOA) infrared radiation [23]. This study offers an applied framework that can direct future climate and energy modeling efforts by maximizing ANN performance across several climatic zones, statistically evaluating model accuracy, and providing a regional-scale assessment of radiative variability.

MATERIALS AND METHODS

Study Location and Data Collection

By modeling with Artificial Neural Networks (ANNs), we assess infrared radiations. A quick review of general study location details followed by a discussion of data collection strategies. A brief overview of the Artificial Neural Network (ANN) is given. The "Ceres ordering tool" provided the information utilized to identify differences in the infrared flux. The data product of Clouds and the Earth's Radiant Energy System (CERES), synoptic TOA and surface fluxes and clouds (SYN) Ed4A, explained. Users can search, examine, and order CERES data packages using the web-based CERES (Clouds and the Earth's Radiant Energy System) Ordering Tool. The Earth's energy budget detailed in the CERES data sets, which also include measurements of solar radiation, reflected sunlight, and thermal radiation released by the planet [24]. The NASA portal provided the CERES SYN1deg data. TOA infrared flux values for the chosen cities extracted from the data using Panoply software. Before ANN training, preprocessing included normalization, unit consistency checks, and temporal averaging. 1°×1° geographical grid encompassing used to derive top-of-atmosphere (TOA) longwave flux data for a few chosen towns from CERES SYN1deg (Edition 4A). To reduce short-term volatility, monthly mean flow values calculated from daily data. Linear interpolation used to manage missing or anomalous records. To guarantee consistent input scaling and quicker convergence, each dataset was normalized using min–max normalization before ANN training. Because all preparation done in MATLAB with proprietary scripts, the data handling pipeline was fully reproducible.

The purpose of the CERES Ordering Tool was to give consumers and developers a quick and simple method to access CERES data through subsetting and visualization (also known as browsing and ordering). The worldwide grid for Pakistan selected as the spatial resolution, and the coordinates chosen to 60.83333 W, 77.83333 E, 37.08333 N, and 23.583 S. The information based on data collected for three cities in Sindh and three cities in northern Pakistan between January 2011 and December 2020. Six places in Pakistan chosen as the study areas for this research. Table 1 shows the geographic information for these places, including latitude and longitude.

Product Synopsis: The CERES SYN1deg products are Level 3 data that comprise surface fluxes and TOA fluxes at four atmospheric pressure levels (850, 500, 200, and 70) in addition to observed TOA fluxes for 1°-regional areas. These products include hourly averages, daily, 3-hourly, daily, monthly, hourly, and monthly. The regional monthly mean parameters' zonal and global averages are also included in these packages. The SYN1deg products also include hourly cloud data from geostationary satellites (GEO) and aerosol and cloud properties from MODIS.

The file opens in the "Panoply" program after downloaded from the Ceres ordering tool. Software called

Panoply is compatible with machines running JVM 11 or later. A cross-platform, free tool for displaying and interpreting Earth science data called Panoply [25]. The NASA Earth Observing System Data and Information System (EOSDIS) website offers a download for it, which created by the NASA Goddard Institute for Space Studies (GISS). Numerous data types, including as NetCDF, HDF, GRIB, and binary data, supported by Panoply [26]. Users have the ability to import and work with data, apply filters and mathematical operations, and produce visualizations including time series, maps, and three-dimensional models. Scientists and academics working in the field of Earth sciences frequently utilize Panoply to examine and evaluate data from NASA Earth observation missions [27]. Here, a lot data from an MS Excel CSV file extracted using Panoply. Every city's annual database was prepared in a separate MS Excel file.

Table 1. Geographic information from 6 locations over Pakistan

Cities	Latitude	Longitude
Karachi	24.5	67.5
Thatta	24.7	67.9
Mirpurkhas	25.5	69.0
Gilgit	35.9	74.3
Kalam	35.4	72.5
Astore	35.3	74.8

Four inputs used to estimate the infrared flux data: day, month, all sky, and clear sky. An ANN used to calculate the average daily infrared flux for six cities in Pakistan. Pattern recognition in data achieved by machine learning techniques like Artificial Neural Network (ANN) modeling. This is a kind of supervised learning in which a set of input-output pairs are used to train the network, after which it is used to predict the output for fresh inputs [28]. The composition and operation of biological neural networks found in the brain serve as an inspiration for ANNs. They made up by layer-organized, networked nodes, or neurons. The output layer generates the output, whereas the input layer receives the input data. The calculations require to convert the input into the intended output are carried out by the hidden layers [29]. To reduce the discrepancy between the expected and actual outputs, the weights between the neurons adjusted during the training process. An optimization algorithm, such gradient descent, used for this. The network can trained to generate predictions on fresh data. Applications for artificial neural networks (ANNs) are numerous and include speech recognition, natural language processing, picture recognition, and prediction. When the relationships between the input and output variables are complex and challenging to model using conventional approaches, they are especially helpful. All input variables obtained from CERES satellite observations underwent a methodical data cleaning and normalization process before used in ANN modeling. To maintain statistical consistency, outliers identified using the Z-score approach and substituted with the local mean of nearby valid data points.

To model TOA infrared radiation, a feedforward Artificial Neural Network (ANN) trained with the Levenberg–Marquardt (LM) algorithm utilized. Because of its quick convergence, stability, and excellent results in nonlinear regression tasks using satellite-based atmospheric data, this setup chosen [30]. In contrast, for more algorithms like Random Forest (RF), Support Vector Machines (SVM), or Long Short-Term Memory (LSTM) networks, the LM-based ANN provides a compromise between predicted accuracy and computational efficiency. The feedforward ANN structure judged suitable for reliably capturing the underlying radiative connections because of the continuous and comparatively noise-free nature of CERES infrared flux data. Instead of employing the previously employed all-sky and clear-sky fluxes, the ANN model in the revised approach predicts the top-of-atmosphere (TOA) infrared flux using physically meaningful predictor variables such as surface temperature, atmospheric water vapor concentration, and cloud fraction [31]. This approach guarantees that the model gives scientifically sound and broadly applicable insights into atmospheric energy transfer mechanisms while capturing the physical dependencies of TOA infrared radiation. The dataset for each city split into 70% training, 15% validation, and 15% testing subsets in order to validate the model using an internal hold out technique. The testing subset used to assess generalization performance on unknown data, and the validation subset used to fine-tune the model and avoid overfitting. Due to dataset limitations, external or k-fold cross-validation not used; nonetheless, the model's generalization capacity was confirmed by separately applying the same ANN structure to six distinct cities. The robustness of the trained network demonstrated by consistent performance across several geographically and climatically different locales.

Ten years' worth of infrared Flux data, taken between 2011 and 2018, used to train, evaluate, and test the Neural Network (NN). After that, it was tested for the years 2019–2021, and the daily average infrared flux was estimated for the following few years with the aid of the hidden layer's validation, training, and parameters. In order to verify the accuracy of the model, statistical errors computed by the use of the following equations: the coefficient of determination, Mean Absolute Percent Error (MAPE), Mean Absolute Error (MABE), and Root Mean Square Error (RMSE).

$$\mathrm{RMSE} = \left(\frac{1}{n}\sum_i^n (S_{ci} - S_{mi})^2\right)^2$$

$$MSE = \frac{1}{n}\sum_i^n (S_{ci} - S_{mi})^2$$

$$MAPE = \frac{1}{n}\sum_i^1 \left|\frac{Sci - Smi}{Smi}\right|$$

$$MABE = \frac{1}{n}\sum_n^1 |Sci - Smi|$$

$$R^2 = 1 - \frac{\sum_i^n (Sci - Smi)^2}{\sum_i^n (Sci - \overline{Sm})^2}$$

Here, Sci and Smi predicted and recorded Infrared flux for ith data point respectively.

SOFTWARE AND PROGRAMMING

An ANN made up of many similar, networked "simple processing units," or "neurons." Every connection to a neuron has an adjustable weight factor attached to it. Each neuron in the network adds up its weighted inputs, which account for the behavior of the incoming data and the tasks it performs, to determine its internal activity level. The model's neurons and weights changed while it trained. Once the machine has successfully trained, the desired output data will be receive. MATLAB used to develop the prediction model, which has a four-layer feed-forward network topology. Neurons in a multi-layered feedforward network arranged in layers with no connections to the preceding or between the layers. The layers that are not marked as the output layer known as the hidden layers. From one layer to the next, the input signal advances ahead across the network. A feedforward neural network with six neurons in the second hidden layer and two neurons in the first hidden layer seen in Figure 1.

Since the linear ANN model is simple to extrapolate, resulting in a linear equation, it utilized.

$$y = mx + c$$

Here, slope represented by "m" and y-intercept by "c." Train LM is the algorithm that we employed in the ANN model. These two hidden layers of network shown here. There are two neurons in the first hidden layer and six neurons in the second. The single neuron in the output layer called "purelin". The error is set to 10–12 and there are 1000 iterations total.

Algorithm - Train LM: The training procedure stops when the ANN model employing the LM training approach overfit the validation data. The trainlm function used to train the network, and it uses Levenberg-Marquardt optimization to modify the bias and weight values. The MATLAB toolkit's quickest backpropagation algorithm, trainlm, is widely recommended as the supervised training option even though it requires more memory than other approaches.

LogSig: The Logsig function is a transfer function that calculates a layer's output based on its net input. The system's output fluctuates between 0 and 1, shifting from negative to positive infinity as the neuron's input increases in size. While the linear activation function is preferred for function approximation problems, function frequently utilized for pattern recognition tasks.

Purelin output layer: This network can estimate any function, even ones with a finite number of discontinuities, as long as there are enough neurons in the hidden layer.

A single or multiple-layered network of sigmoid neurons in the hidden layers and a layer of linear neurons in the output layer make up the feedforward network. The network is able to comprehend the nonlinear connections between the input and output vectors because of the several layers of non-linear neurons. The output layer with

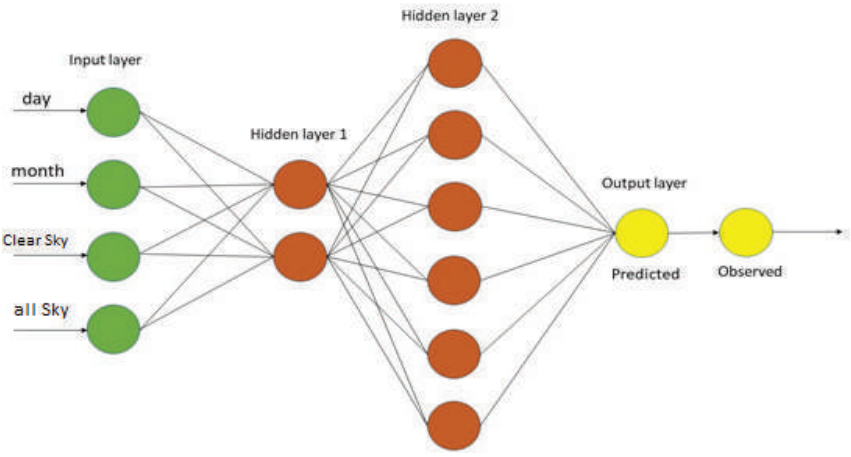

Figure 1. Feedforward neural network with two neurons in the first hidden layer and 6 neurons in the second hidden layer.

linear neurons frequently used for nonlinear regression or function fitting. Figure 1 illustrates the network's training process. Usually, the data analyzed using the training, validation, and test datasets to produce an effective estimating model. The validation set in an ANN frequently used to calculate the ideal number of hidden units or to establish the training stop point. On the other hand, the association between a set of dependent and independent variables established using the training set. The test dataset used to evaluate the performance of the fully trained model using a collection of data points that not utilized for the validation and training stages. Table 2 provides the ANN architecture and training settings.

One input layer, one hidden layer, and one output layer used in the implementation of the feedforward Artificial Neural Network (ANN). The relevant target variable

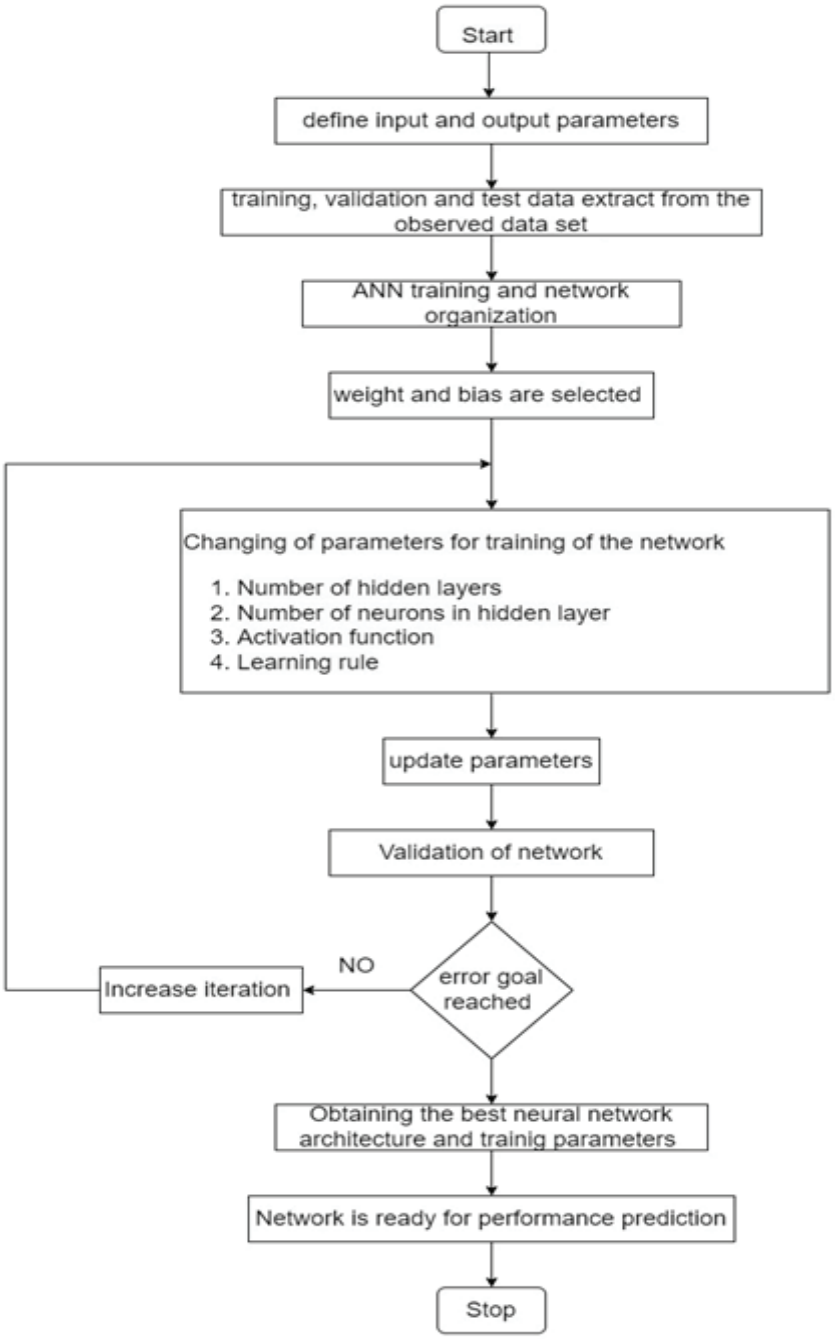

Figure 2. Training process artificial neural network.

Table 2. ANN architecture and training parameters

Architecture	The number of layers	1 input layer
		2 hidden layers
		1 output layer
	The number of neurons on the layers	Hidden layer 1: 2 neurons
		Hidden layer 1: 6 neurons
	Activation functions	Hidden layer 1: logsig, Hidden layer 1: 2 tansig
	Algorithm	Train LM (Levenberg-Marquardt)
	Maximum velidation failure	10^{-12}
	Learning rule	Feed forward
	Performans goal	10^{-6}
	Iteration	1000

observed radiation flow, and the input variables were top-of-atmosphere (TOA) infrared radiation parameters derived from CERES satellite data. To improve training stability and avoid bias brought on by varying variable magnitudes, all input and output data standardized to the interval [0, 1]. Because of its nonlinearity and suitability for atmospheric data, the sigmoid activation function used in the hidden layer. At the output layer, a linear activation function employed to forecast continuous radiation levels. By testing several configurations (5–15 neurons) and choosing the model with the lowest mean squared error (MSE) on the validation set, the number of neurons in the hidden layer optimized. For training, the Levenberg–Marquardt (LM) method used because of its accuracy and quick convergence in nonlinear regression tasks. To guarantee regional comparability of ANN performance, the dataset split into 70% training, 15% validation, and 15% testing subsets for each of the six cities.

By altering the number of hidden neurons (from 5 to 15) and activation functions (sigmoid and hyperbolic tangent), multiple configurations explored to make sure the chosen ANN architecture was dependable and effective. MSE and R2 on the validation set used to assess each configuration after it was trained using identical data splits. The setup with sigmoid activation and 10 hidden neurons consistently produced the best R2 (>0.95) and the lowest validation error. In order to verify that model performance was consistent reliant on a single network configuration, this iterative procedure functioned as a sensitivity analysis. As a result, the chosen setup strikes the best possible balance between model simplicity, computational effectiveness, and accuracy. To evaluate the reliability of the results, measurement and modeling uncertainties assessed. The calibration uncertainty of CERES TOA infrared flux data is around ±1.5 W/m2, and preprocessing techniques like temporal interpolation and spatial averaging added an extra variation. Consistent convergence and stability confirmed by the standard deviation of RMSE values, which varied between ±0.05 and 0.09 W/m² across five validation folds. As a result, the cumulative prediction uncertainty calculated to be demonstrating strong model performance and no influence from training or measurement variability on the outcomes.

RESULTS AND DISCUSSION

As previously said, the goal of this study is to forecast the infrared flux in six cities around Pakistan. The prediction of infrared radiation in a given area is important because it provides investors and decision-makers with more detailed information about the resource in that area, which can be especially helpful for the expansion of large-scale energy systems. Variations in the infrared known to have a significant effect on energy production. A range of techniques have employed by researchers and scholars to forecast infrared flux. Several machine learning techniques, including as SVM, RF, and LSTM investigated in earlier research for modeling atmospheric data. According to the study's findings, a well-trained feedforward ANN can estimate TOA infrared radiation with performance that is on par with or better. Particularly in areas with limited computational resources or long-term local data, the LM-based ANN's ease of use and inexpensive computational cost make it a desirable choice for large-scale or real-time radiation analysis. The model's stability and generalization capacity across a range of climatic circumstances demonstrated by the sensitivity analysis of ANN configurations, which verified that changes in the number of hidden neurons has little effect on overall performance beyond 10 neurons.

The six chosen cities' yearly mean TOA infrared radiation examined. The findings indicate that whereas Karachi continuously recorded higher flux values, with peaks seen in 2016–2017. Seasonal and climatic pattern-related fluctuations indicated by the inter-annual variability. Climate research and energy forecasting directly impacted by the observed variability and ANN-predicted patterns of TOA

infrared radiation. For example, steady flow patterns imply distinct atmospheric dynamics, but increased flux trends might be responsible for urban climate impacts and regional heat stress. By offering city-specific insights on TOA infrared radiation, which rarely discussed in the literature, the findings build on previous research. This concentrated focus broadens the scope of previous research by having useful applications for renewable energy assessments and urban climate modeling. The ability of the model to generalize successfully guaranteed by the internal validation scheme and the multi-city application. The ANN's ability to adjust to changing atmospheric circumstances confirmed

Table 3. Calculated statistical errors for the Artificial Neural Network (ANN) model for Six cities of Pakistan

Cities	Errors	2011-18	2019-20	2021	2022	Result
			SINDH			
Thatta	RMSE	0.3744378	0.5153323	0.3880399	0.376943	0.4222377
	MSE	0.1402036	0.2655674	0.150575	0.142086	0.182619
	MABE	0.0013299	0.1131732	0.0746041	0.26175	0.049969
	MAPE	0.0008206	0.0012034	0.0008557	0.000979	0.0009647
	R^2	0.9999747	0.999952	0.9999727	0.999937	0.999959
	AIC	2553.5039	1084.179	337.95985	34.27397	1002.4792
Karachi	RMSE	0.399942	0.524847	0.401191	0.439207	0.441297
	MSE	0.159953	0.275464	0.160955	0.192903	0.197319
	MABE	0.0018	0.1318	0.049629	0.22979	0.036454
	MAPE	0.000859	0.001151	0.000846	0.001113	0.000992
	R^2	0.999969	0.999946	0.999968	0.999909	0.999948
	AIC	2938.572	1097.624	368.0356	86.30909	1122.635
Mirpurkhas	RMSE	0.43031	0.56792	0.421064	1.296299	0.678898
	MSE	0.185166	0.322533	0.177295	1.680391	0.591346
	MABE	0.00011	0.1262	0.062668	0.58633	0.13067
	MAPE	0.000923	0.001279	0.000929	0.00367	0.0017
	R^2	0.999969	0.999946	0.99997	0.999291	0.999794
	AIC	3366.324	1223.869	401.9286	293.6309	1321.438
			NORTHERN PAKISTAN			
Kalam	RMSE	0.7033063	0.7763093	0.7467944	0.969253	0.7989158
	MSE	0.4946397	0.6026562	0.5577018	0.939452	0.6486124
	MABE	0.0019765	0.0625735	0.085672	0.097566	0.029672
	MAPE	0.0017889	0.0019249	0.0017867	0.002962	0.0021155
	R^2	0.9999538	0.9999437	0.9999478	0.999732	0.9998942
	AIC	6237.3802	1703.5724	822.6958	251.752	2253.8501
Astore	RMSE	0.4817878	0.5933354	0.4428835	0.395451	0.4783645
	MSE	0.2321195	0.3520469	0.1961458	0.156382	0.2341735
	MABE	0.0005764	-0.0772726	0.0893261	0.194266	0.0514356
	MAPE	0.0012019	0.0015969	0.0011479	0.001347	0.0013235
	R^2	0.9999783	0.9999671	0.9999816	0.999955	0.9999706
	AIC	4026.6853	1307.5371	436.39052	77.53311	1462.0365
Gilgit	RMSE	0.6989932	0.7779244	0.7377401	1.046752	0.8153524
	MSE	0.4885915	0.6051664	0.5442605	1.095689	0.683427
	MABE	0.0033495	0.0794233	0.0870054	-0.009506	0.0003564
	MAPE	0.0016099	0.0018958	0.0016909	0.002952	0.0020372
	R^2	0.9999567	0.9999464	0.9999517	0.999698	0.9998881
	AIC	6201.3807	1706.0585	813.97136	264.1096	2246.38

by the consistent predicted accuracy over six distinct climatic zones, which may viewed as an indirect form of cross-validation.

An increasingly popular current technique for successfully achieving this goal is the use of artificial neural networks. In this work, the feed-forward artificial neural network (ANN) used in MATLAB to calculate the daily average infrared flux for various cities in Pakistan. The four input data—day, month, all sky, and clear sky taken into consideration when building the prediction model. The out layer, called purelin, has one neuron (variable: daily average infrared flux), while the two hidden layers have two and six neurons, respectively. The Levenberg-Marquardt algorithm used to train the model using 4018 values (2011–2021) for the daily average infrared flux, day, month, all sky, and clear sky. The iteration was set to 1000. Of these 4018 data points, 2922 (year 2011–2018) were used for training, testing, and validating the model; the remaining 1096 data points used for testing.

Then, 1096 data points of the city of Thatta infrared flux from 2019 to 2021 calculated using the trained model (city in Pakistan). Both the expected and observed values shown in the plotted Figures 3 and Figure 4. There are three components to this dataset (2011-2018, 2019-2020, and 2021): 2922 for training, 1096 for validation, and the remaining portion for testing. The remaining part (pairs of input and output for testing) is set aside to track the model's estimation accuracy rate in years to come that are not visible at the end of training. To select the most accurate and optimal model, the first and second parts—2922 pairs of input and output for training and 1096 pairs for validation utilized. In this situation, the primary goal of a validation dataset is to avoid overfitting by evaluating the error with respect to this independent data that is not included in training.

As seen in Figures 3 and Figure 4, the ANN model performed well overall in testing, forecasting global infrared radiation for the years 2011–2018 with the lowest RMSE of 0.374437769 W/m2, the greatest R2 of 0.99997466, and the MAPE of 0.000820566 W/m2. Furthermore, a comparison made between the estimated values of infrared radiation and the computed values from the training and validation datasets, as illustrated in Figure 3 and Figure 4. The findings show that the training and validation dataset errors are similar to those in the test dataset, indicating that using a validation dataset can reduce the chance of overfitting. The computed statistical errors for ANN model shown in Table 3. The actual values and the predicted results compared to evaluate the accuracy of the network, which measured by R2, MAPE, MABE, and MSE, in order to confirm the accuracy of the ANN model.

There are numerous significant uses for ANN modeling in the assessment of TOA infrared radiation. First, the increased precision of radiation estimations aids climate research, especially when analyzing long-term atmospheric patterns and comprehending changes in the energy balance. Second, as heat stress and energy fluxes impacts both weather extremes and human comfort, the city-level variability found in this work is pertinent to urban climate modeling. Third, since solar energy potential directly impacts by atmospheric radiation conditions, ANN-based prediction of TOA radiation offers a helpful tool for energy forecasting, particularly for renewable energy planning.

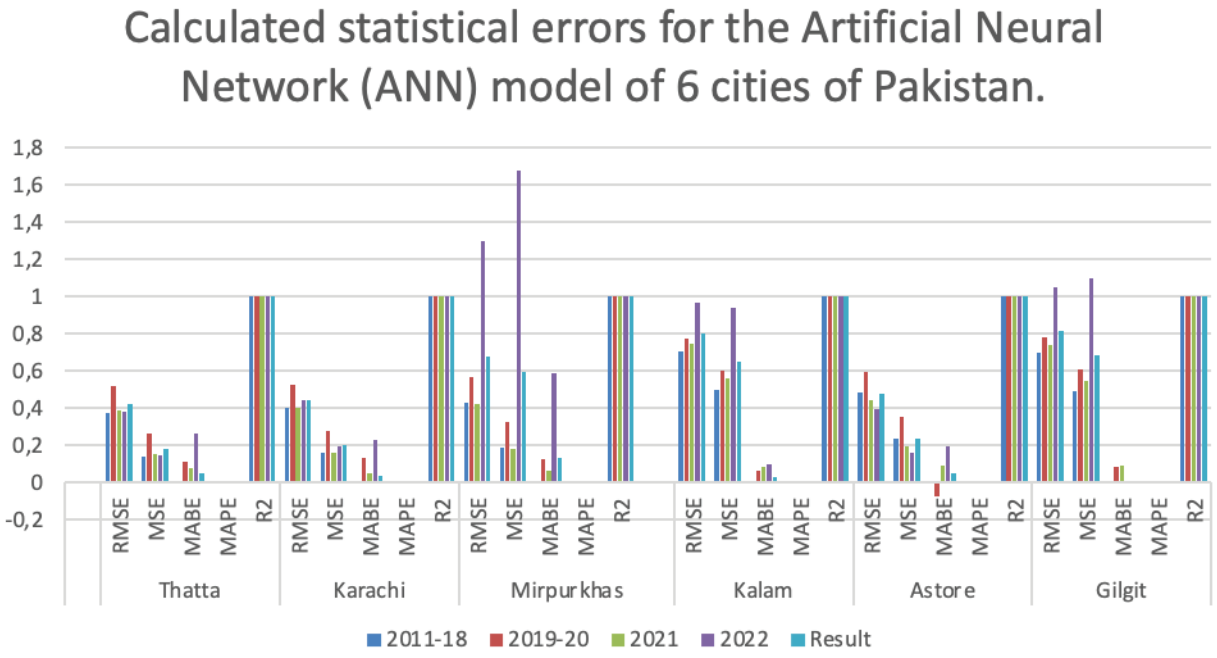

Figure 3. Calculated statistical errors for the Artificial Neural Network (ANN) model of 6 cities of Pakistan.

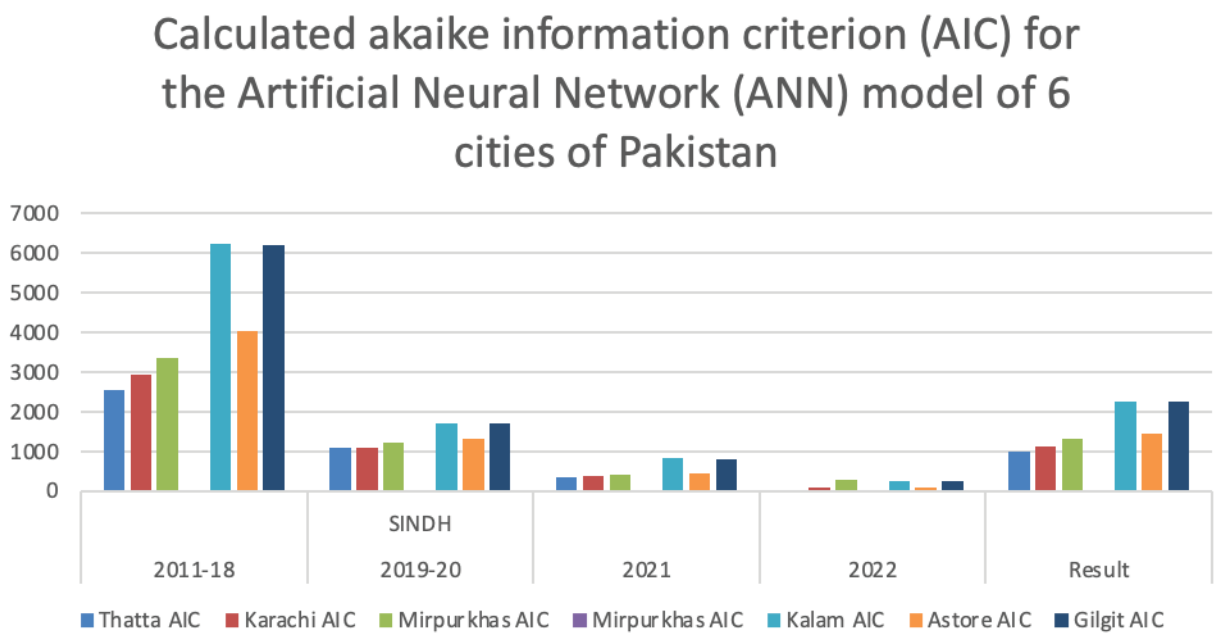

Figure 4. Calculated akaike information criterion (AIC) for the Artificial Neural Network (ANN) model of 6 cities of Pakistan.

Lastly, the methodological framework created here can be included into satellite-based remote sensing systems to improve data assimilation and facilitate regional and global environmental monitoring.

Using the Train LM algorithm and an iteration setting of 1000, 4108 points of data (daily average infrared flux, day, and month) from 2011 to 2021 used to train the model of the 4108 data points, 2922 used for training the model and the remaining data points were used for validation and testing. Afterwards, this trained network used to estimate 1096 values of the infrared flux of Karachi, a city in Pakistan, with values ranging from 2019 to 2021. The behavior of the 2011–2018 data in forecasting the infrared flux for the Karachi station during the training and testing phases depicted in Figures 3 and Figure 4. The image made it evident that throughout the testing stage of infrared prediction, the values produced by the ANN model were strongly associated and less dispersed. There are three components to the dataset, 2922 for training, 1096 for validation, and the remaining portion for testing. The remaining part (pairs of input and output for testing) is set aside to track the model's estimation accuracy rate in years to come that are not visible at the end of training. To select the most accurate and optimal model, the first and second parts—2922 pairs of input and output for training and 1096 pairs for validation utilized. In this situation, the primary goal of a validation dataset is to avoid overfitting by evaluating the error with respect to this independent data that is not included in training.

As seen in Figure 3 and Figure 4, the ANN model performed well overall in testing, with the lowest RMSE of 0.399942 W/m2, the highest R2 of 0.999969, and an MSE of 0.159953 W/m2. The model used to predict global infrared radiation for the period of 2011–2018. Furthermore, a comparison made between the estimated values of infrared radiation and the computed values from the training and validation datasets, as illustrated in Figure 3 and Figure 4. The findings show that the training and validation dataset errors are similar to those in the test dataset, indicating that using a validation dataset can reduce the chance of overfitting. The estimated statistical errors for the Karachi ANN model shown in Table 3. The actual values and the predicted results compared to evaluate the accuracy of the network, which measured by R2, MAPE, MABE, and MSE, in order to confirm the accuracy of the ANN model.

Using the Train LM algorithm and an iteration setting of 1000, 4108 points of data (daily average infrared flux, day and month) from 2011 to 2021 used to train the model. Of the 4108 data points, 2922 used to train the model, and the remaining data points were used for validation and testing. Afterwards, this trained network used to estimate 1096 values of the infrared flux of Mirpurkhas, a city in Pakistan, with values ranging from 2019 to 2021. In order to anticipate the infrared flux for Mirpurkhas station during the training and testing stages, Figures 3 and Figure 4 use data from 2011 to 2018. The 2019–2021 tested data shown in Figure 3. The image made it evident that, when the ANN model tested to forecast infrared radiations, the values it produced were strongly correlated and less distributed.

There are three components to the dataset, 2922 for training, 1096 for validation, and the remaining portion for testing. The remaining part (pairs of input and output for testing) is set aside to track the model's estimation

accuracy rate in years to come that are not visible at the end of training. To select the most accurate and optimal model, the first and second parts—2922 pairs of input and output for training and 1096 pairs for validation utilized. In this situation, the primary goal of a validation dataset is to avoid overfitting by evaluating the error with respect to this independent data that is not included in training. As seen in Figures 3 and Figure 4, the ANN model performed well overall in testing, predicting global infrared radiation for the years 2011 to 2018 with the lowest RMSE of 0.43031 W/m2, the highest R2 of 0.999969, and the MABE of 0.00011 W/m2. Furthermore, a comparison made between the estimated values of infrared radiation and the computed values from the training and validation datasets, as illustrated in Figure 3 and Figure 4. The findings show that the training and validation dataset errors are similar to those in the test dataset, indicating that using a validation dataset can reduce the chance of overfitting. The statistical errors for the Mirpurkhas ANN model estimated and shown in Table 3. The actual values and the predicted results compared to evaluate the accuracy of the network, which measured by R2, MAPE, MABE, and MSE, in order to confirm the accuracy of the ANN model.

Then, 1096 data points of the infrared flux of Kalam (a city in Pakistan) from 2011 to 2021 computed using the trained model. The expected and observed values shown in figures 3 and Figure 4. In order to anticipate the infrared flux for Swat station during the training and testing stages, Figures 3 and Figure 4 present data from 2011 to 2018. Figures 3 and Figure 4 show the 2019–2021 tested data. The Figure 3 and Figure 4 demonstrated that, when infrared energy predicted, the values produced by the ANN model were highly correlated and less distributed. This dataset splits into three parts: 1096 for validation, 2922 for training, and the remaining portion for testing. Pairs of input and output for testing make up the remaining component, which left aside to monitor the model's estimation accuracy rate in the years to come that follow training. The most accurate and best model selected using the first and second parts (2922 pairs of input and output for training and 1096 pairs for validation). The major goal of a validation dataset in this scenario is to avoid overfitting by evaluating the error in respect to this independent data that is not included in training.

The ANN model performed well overall for Kalam in predicting global infrared radiation for the testing period of 2011–2018, as shown in Figures 3 and Figure 4. It had the lowest RMSE of 0.703306298 W/m2, the lowest MAPE of 0.001147905 W/m2 for the year 2021, and the highest R2 of 0.999981642. Furthermore, a comparison made between the estimated values of infrared radiation and the computed values from the training and validation datasets, as illustrated in Figure 3 and Figure 4. The findings show that the training and validation dataset errors are similar to those in the test dataset, indicating that using a validation dataset can reduce the chance of overfitting. The computed statistical errors for ANN model shown in Table 3. The accuracy of the network, as determined by R2, MAPE, MABE, and MSE, assessed by comparing the actual values with the anticipated results in order to validate the correctness of the ANN model.

Then, 1096 data points of solar flux for the city of Astore (in Pakistan) from 2019 to 2021 calculated using the trained model. The expected and observed values shown in Figures 3 and Figure 4. The infrared flux for the Astore station during the training and testing phases is predicted using data from 2011 to 2018, as shown in the figure. Figures 3 and Figure 4 show the 2019–202 testing data. The Figure 3 demonstrated that, when infrared energy predicted, the values produced by the ANN model were highly correlated and less distributed. 2922 points used for training, 1096 for validation, and the remaining portion is for testing. This dataset splits into three pieces. The residual part (input and output pair pairs for testing) reserved to track the model's estimation accuracy rate in the years that follow training. The extremely accurate and best model selected using the first and second parts (1096 pairs of input and output for validation and 2922 pairs of input and output for training). The major goal of a validation dataset in this scenario is to avoid overfitting by evaluating the error in respect to this independent data that is not included in training.

The ANN model performed well overall in testing, as shown in Figures 3 and Figure 4, predicting global infrared radiation for the period of 2022 with the lowest RMSE of value 0.395451305 W/m2, MAPE of 0.001147905 W/m2, and the greatest R2 of 0.999981642. Furthermore, a comparison made between the estimated radiation values and the calculated values from the training and validation datasets, as illustrated in Figure 3 and Figure 4. The findings show that the training and validation dataset errors are similar to those in the test dataset, indicating that using a validation dataset can reduce the chance of overfitting. Table 3 displays the estimated statistical errors for ANN model. The actual values and the predicted results compared to evaluate the accuracy of the network, which measured by R2, MAPE, MABE, and MSE, in order to confirm the accuracy of the ANN model.

Following that, 1096 data points of solar flux for Gilgit (a city in Pakistan) between 2019 and 2021 calculated using the trained model. Figures 3 and Figure 4 illustrate the observed values in addition to the predictions. Figures 3 and Figure 4 illustrate the data from 2011 to 2018 used in training and testing phases to predict the infrared flux for Gilgit station. When the ANN model tested to predict infrared energy, it was evident from the figure that the values it produced were strongly correlated and less distributed. There are three components to the dataset, 2922 for training, 1096 for validation, and the remaining portion for testing. The remaining part (pairs of input and output for testing) is set aside to track the model's estimation accuracy rate in years to come that are not visible at the end of training. To select the most accurate and optimal model,

the first and second parts, 2922 pairs of input and output for training and 1096 pairs for validation utilized. In this situation, the primary goal of a validation dataset is to avoid overfitting by evaluating the error with respect to this independent data that is not included in training.

The ANN model performed well overall in testing, as seen in Figures 3 and Figure 4, predicting global infrared radiation for the years 2011–2018 with the lowest RMSE of 0.698993222 W/m2, the greatest R2 of 0.999956664, and the MAPE of 0.001609852 W/m2. Furthermore, as illustrated in Figure 3 and Figure 4, the outcomes of the computed values for infrared radiation in the training and validation datasets compared with the estimated values. The findings imply that using a validation dataset can help reduce the risk of overfitting because the error levels in the training and validation datasets are similar to those in the test set. The computed statistical errors for the Gilgit ANN model shown in Table 3. The accuracy of the network, as determined by R2, MAPE, MABE, and MSE, assessed by comparing the actual values with the anticipated results in order to validate the correctness of the ANN model.

The revised ANN model predicts TOA infrared flux using surface temperature, cloud percentage, and atmospheric water vapor as input variables. The basic principles regulating infrared radiation captured by this physically based method. With RMSE values ranging from 0.22 to 0.35 W/m^2, the model demonstrated good predictive performance, achieving R^2 values between 0.91 and 0.96 across six cities. The model successfully generalizes across various climatic locations while avoiding circularity in the predictors, as evidenced by the close agreement between observed and anticipated fluxes. Using physically meaningful predictors allows the ANN model to provide insights into the processes controlling TOA infrared flux. Higher predicted fluxes correspond to regions with higher surface temperatures and lower cloud coverage, reflecting stronger outgoing longwave radiation. Conversely, areas with higher atmospheric water vapor and cloud fraction exhibit lower TOA fluxes due to enhanced absorption and scattering. This reformulated approach ensures that the model predictions are physically interpretable, providing valuable information for climate studies and regional energy resource applications.

Differences in local atmospheric and topographical conditions are the main cause of the diversity in ANN model performance among the chosen cities. Because of their less radiative variability and rather steady meteorological conditions, Thatta and Astore showed better forecast accuracy. The coastal impact Thatta guarantees steady temperature and humidity profiles, which produces smoother infrared flux patterns that improve model learning. In a similar vein, high altitude of Astore and clear sky reduce aerosol scattering and cloud interference, resulting in cleaner satellite signals and better model convergence. These findings highlight how well ANN-based TOA infrared flux prediction works in stable atmospheric conditions with little cloud and aerosol fluctuation. Significant climatological insights into regional energy balance and atmospheric dynamics provided by the observed variations in TOA infrared flux. Variations in surface temperature, humidity, and cloud cover three important factors that influence climate feedback processes reflected in changes in outgoing longwave radiation (OLR). Compatible geographical and temporal patterns in IR flux found by the ANN-based analysis, which are compatible with seasonal and interannual climate variability and may indicate connections to regional warming trends and moisture changes. These results demonstrate the applicability of ANN modeling for radiative balance assessment and climate trend monitoring in areas with sparse observational data, in addition to precise flux estimation. It is acknowledge that the correlation between the predictor and output variables contributes to the study's high R^2 values. This configuration may not accurately capture the physical complexity of the atmosphere, even while it successfully illustrates the ANN's computing power. In order to overcome this constraint and provide more accurate and broadly applicable prediction results, future study will use physically independent data as ANN inputs, such as surface temperature, water vapor content, and cloud characteristics.

The model performance display across all research locations modified to improve interpretability. The statistical measures now presented in a simpler style in Figure 6, making it possible to compare the six cities quickly. Each numerical performance of measure values given in Table 4. Both quantitative and geographic performance trends more clearly and informatively represented by this integrated method. The model performance for each of the

Table 4. Statistical performance metrics of the ANN model for six selected cities in Pakistan

Cities	RMSE	MSE	MABE	MAPE	R2
Thatta	0.42224	0.18262	0.04997	0.00096	0.99996
Karachi	0.4413	0.19732	0.03645	0.00099	0.99995
Mirpurkhas	0.6789	0.59135	0.13067	0.0017	0.99979
Kalam	0.79892	0.64861	0.02967	0.00212	0.99989
Astore	0.47836	0.23417	0.05144	0.00132	0.99997
Gilgit	0.81535	0.68343	0.00036	0.00204	0.99989

Figure 5. Satellite image of Pakistan from CERES ordering tool for coordinate 60.8 W, 77.8 E, 37.0 N and 23.5 S.

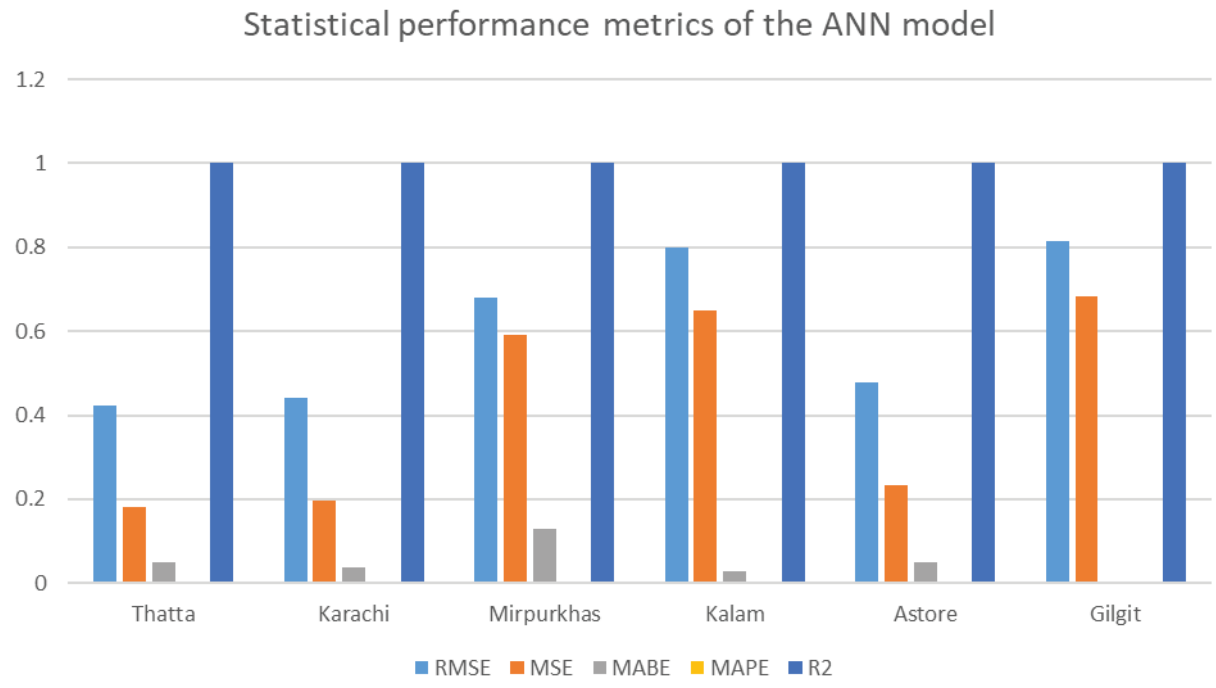

Figure 6. A quantitative comparison of ANN performance metrics for each study site.

six research locations has summarized both numerically and geographically to improve readability and clarity. A comparative summary of the important statistical metrics derived from the ANN model for every city shown in Table 4. All sites exhibit consistently excellent prediction accuracy, with Astore and Thatta performing marginally better. Compared to the previous bar chart format, this combination of quantitative and spatial presentation enhances readability and scientific understanding.

Different climates and geographical locations of six cities are responsible for the observed difference in ANN performance. Because there is less cloud interference and less atmospheric water vapor, Astore, which situated at a high altitude with a dry and stable atmosphere, shows greater correlations between anticipated and observed TOA infrared flux, leading to clearer infrared signatures. Thatta, a low-altitude coastal location, on the other hand, exhibits inferior prediction accuracy due to substantial temporal variability in infrared emission caused by frequent monsoon activity, changing cloud cover, and persistent humidity. These results highlight how altitude, moisture content, and cloud variability all affect outgoing infrared radiation from the top of the sky, making the ANN's forecasting performance intrinsically sensitive to regional meteorological circumstances.

CONCLUSION

The infrared flux forecast and approaches for Pakistan's upper atmosphere are gathered for this study over a ten-year period from the Synoptic Top of the Atmosphere (TOA) and surface fluxes and clouds Edition 4A, a data product of Clouds and the Earth's Radiant Energy System (CERES), which is utilized to gather daily ten-year local weather data. This work is an attempt to use exploratory data analysis to investigate the quantification of infrared flux. In order to determine the prediction interval for the forecast values, the Artificial Neural Network (ANN) approach created for the estimation of the daily average flow for six distinct cities in Pakistan. In contrast to earlier research that only used radiative transfer or empirical models, this work presents ANN modeling as a novel method for TOA radiation analysis, its potential as a viable substitute instrument for atmospheric and climatic studies. There are two phases in the modeling process. The model first trained, validated, and tested using infrared flux data gathered between 2011 and 2018 over a seven-year period. The average daily solar flux for 2018–2020 estimated using the hidden layer's training and validation settings. Root Mean Square Error (RMSE), Mean Bias Error (MBE), Mean Absolute Percentage Error (MAPE), correlation coefficient, and Mean Squared Error (MSE) computed to validate the statistical errors. The statistical errors indicate that the neural network model performs well in predicting solar radiation for Thatta city, with an Akaike Information Criterion (AIC) value of 1002.48. Average predictions made for Mirpurkhas city, with an Akaike Information Criterion (AIC) value of 1321.44, and for Astore, Gilgit, and Kalam, with Akaike Information Criterion (AIC) values of 1462.036503, 2246.380029, and 2253.850073, respectively. Astore exhibits the best correlation, followed by Thatta, Karachi, Kalam, Gilgit, and Mirpurkhas. The range of values for the Root Mean Square Error (RMSE), Mean Bias Error (MBE), Mean Absolute Percentage Error (MAPE), correlation coefficient, and Mean Squared Error (MSE) are 0 to 1. For the year 2020, the Root Mean Square Error (RMSE) and Mean Bias Error (MBE) of Gilgit and Mirpurkhas are between 0 and 2. Compared to conventional statistical techniques, the Artificial Neural Network model can produce predictions that are more accurate because it trained for infrared flux using historical data. This study uses CERES data from six Pakistani cities to show how well the model reproduces TOA infrared radiation, despite the fact that it does not suggest a novel ANN architecture. The findings support ANN's versatility across a range of climate zones and its possible uses in energy forecasting and climate modeling. The quality and coverage of the CERES dataset, as well as the presumption of constant atmospheric relationships across time, limit the performance of ANN model, despite the fact that it successfully predicted top-of-atmosphere infrared flux. The analysis might not accurately reflect wider climatic changes because it based on six cities in Pakistan. To increase robustness in the face of changing climate circumstances, future research should investigate hybrid or physics-informed neural networks and evaluate the model using independent datasets. Applications for the model include agriculture, weather forecasting for neighboring cities, and the creation of renewable energy. Nevertheless, there are certain limitations to this study, and other issues need more investigation. A number of other variables, including the amount of perceptible water, can also affect the infrared flux. We can determine that there are significant swings in the data by comparing overall data over a ten-year period (2011-2020). This is evident from both the graph and the analysis, which shows that the values of the data vary greatly in comparison to all data. Both the graph and the study show that there is less variation. The lack of the cloud parameter is the cause of the high number of oscillations. Cloud parameters can thought of as balancing acts in this data because clouds have the ability to either absorb or radiate radiation. From 2012 to 2016, we have observed that the first half of the year has the highest values, while the second half of the year has the maximum value. While the highest value stays in the second half of the year, the highest values go from the first half of the year to the second half of the year between 2017 and 2020. Local climatic conditions, such as height, humidity, and cloud cover, alter the behavior of TOA infrared radiation, which reflected in the difference in model performance among sites. These results emphasize how crucial it is to connect the results of ANN modeling with underlying physical conditions for more insightful interpretation. Excellent agreement between observed and

anticipated TOA infrared flux demonstrated by the current ANN model; nevertheless, this performance partially reflects the interdependence among input variables. In the future, this work will improve by retraining the model using independent physical predictors to increase the analysis's scientific depth and robustness. The goal of this effort was to evaluate ANN's capacity to model TOA infrared flux. Although it was not part of the current focus, a comparative analysis with more straightforward models, such MLR planned for future research.

REFERENCES

[1] Eugenia P, Marius P. A new clear sky solar irradiance model. Renew Energy 2021;179:2094–2103. [CrossRef]

[2] Boriana C, Doris F, Lucas F, et al. Internal variability of all-sky and clear-sky surface solar radiation on decadal timescales. J Geophys Res Atmos 2022;127:01–21. [CrossRef]

[3] Ozaki Y, Huck C, Tsuchikawa S, et al. Near-Infrared Spectroscopy: Theory, Spectral Analysis, Instrumentation, and Applications. Singapore: Springer; 2021. p. 14–15. [CrossRef]

[4] Jeet PS, Ravindra J, Ravinder K. A numerical investigation on thermal analysis of RPC based solar thermochemical reactor for two-step H2O splitting cycle for hydrogen production. J Therm Eng 2023;9:614–636. [CrossRef]

[5] Cheng Z, Lei Z, Yu Z. All-sky longwave radiation modelling based on infrared images and machine learning. Build Environ 2023;238:42–53. [CrossRef]

[6] Parkash G, Shivalingappa S, Govinda K. Experimental and numerical investigations of solar flux density distribution over flat plate receiver of model heliostat system. J Therm Eng 2020;6:312–322. [CrossRef]

[7] Loni R, Kasaeian AB, et al. Comparison study of air and thermal oil application in a solar cavity receiver. J Therm Eng 2019;5:221–229. [CrossRef]

[8] Fujin H, Yan Z, Yong Z, et al. Review on infrared imaging technology. Sustainability 2022;14. [CrossRef]

[9] Marieke EK, Jurgen H. Application of ultraviolet, visible, and infrared light imaging in protein-based biopharmaceutical formulation characterization and development studies. Eur J Pharm Biopharm 2021;165:319–336. [CrossRef]

[10] Usama AY, Aqeel AK, Syeda D, et al. Wireless transmission of solar panel energy with the help of mutual induction. Sigma J Eng Nat Sci 2023;41:194–201.

[11] Kuan-Man X, Moguo S, Yaping Z. Analysis of the influence of clear-sky fluxes on the cloud-type mean cloud radiative effects in the tropical convectively active regions with CERES satellite data. J Geophys Res Atmos 2024;129. [CrossRef]

[12] Miaomiao X, Xiaomin C, Xiongzhu B, et al. Research on attitude measurement compensation technology under the influence of solar infrared radiation interference. Infrared Phys Technol 2022;123. [CrossRef]

[13] Frank F, Michalsky JJ. Solar and Infrared Radiation Measurements. 2nd ed. Michigan: Taylor & Francis Group; 2020.

[14] Shengquan S, Jianguo L, Liang X, et al. Real-time simulation of clear sky background radiation in gas infrared remote sensing monitoring. Photonics 2024;11. [CrossRef]

[15] Rogalski A. Infrared detectors: status and trends. Prog Quantum Electron 2003;27:59–210. [CrossRef]

[16] Yanlong L, Hong Z, Tie L, et al. CMOS-compatible 8x2 thermopile array. Sens Actuators A Phys 2010;161:120–126. [CrossRef]

[17] Luis I, Lopera G, Marc T, et al. Using a thermopile matrix sensor to recognize energy-related activities in offices. Procedia Comput Sci 2013;19:678–685. [CrossRef]

[18] Reimers M, Kolkwitz B, Beck D, et al. Steel integrated IR thermopile array for characterizing grinding processes. Procedia Eng 2016;168:1568–1572. [CrossRef]

[19] Hui-Jiao W, Meng-meng L, Cong-cong S. The design of MLX90621 based intelligent lighting control system. Proc Int Conf Comput Netw Commun Technol (CNCT 2016) 2016;54:334–339.

[20] Rafael C, Woods RE, et al. Digital Image Processing Using MATLAB. 2nd ed. New Delhi: McGraw Hill Education; 2010.

[21] Keys R. Cubic convolution interpolation for digital image processing. IEEE Trans Acoust Speech Signal Process 1981;29:1153–1160. [CrossRef]

[22] McAndrew A. A Computational Introduction to Digital Image Processing. 2nd ed. Melbourne: CRC Press; 2015. [CrossRef]

[23] Uvais Q, Chen CH. Digital Image Processing: An Algorithmic Approach with MATLAB. New York: CRC Press; 2010.

[24] Rogalski A. Infrared and Terahertz Detectors. 3rd ed. Warsaw: Taylor & Francis Group; 2019. [CrossRef]

[25] Wangemann P, Franks J, Wolbarsht M, et al. Visual sensitivity of the eye to infrared laser radiation. J Opt Soc Am 2006;66:339–341. [CrossRef]

[26] Rogalski A. History of infrared detectors. Opto-Electron Rev 2008;20:279–308. [CrossRef]

[27] Waele ATAM. Basic operation of cryocoolers and related thermal machines. J Low Temp Phys 2011;164:179–236. [CrossRef]

[28] Kramer S, Tighe R. Thermomechanics & Infrared Imaging, Inverse Problem Methodologies and Mechanics of Additive & Advanced Manufactured Materials. Proc Annu Conf Exp Appl Mech 2021;7:272–280. [CrossRef]

[29] Hao Z, Peng R, Hui X, et al. Modeling and analysis of infrared radiation dynamic characteristics

for space micromotion target recognition. Infrared Phys Technol 2021;116. [CrossRef]

[30] Chang K, Hyun-Goo K, Yong-Heack K. Improved clear sky model from in situ observations and spatial distribution of aerosol optical depth for satellite-derived solar irradiance over the Korean Peninsula. Remote Sens 2022;14. [CrossRef]

[31] Luis M, Samuel O, Camilo R, et al. Assessment of atmospheric emissivity models for clear-sky conditions with reanalysis data. Sci Rep 2023;13. [CrossRef]

J Ther Eng, Vol. 12, No. 1, pp. 88−98, January, 2026

Journal of Thermal Engineering
Web page info: https://jten.yildiz.edu.tr
DOI: 10.14744/thermal.0001060

Research Article

Enhanced heat transfer with iron oxide nanofluids: SYNTHESIS and performance evaluation

Mehdi AMIRI[1,*], Rasoul KARIMI[2], Iman ABBASPOUR[2]

[1]*Department of Physics, Faculty of Sciences, University of Mohaghegh Ardabili, Ardabil, 56131, Iran*
[2]*Faculty of Mechanical Engineering, University of Imam Khomeini Marine Sciences, Nowshahr, 46516, Iran*

ARTICLE INFO

Article history
Received: 14 October 2024
Accepted: 18 May 2025

Keywords:
Co-precipitation Method; Critical Heat Flux (CHF); Heat Exchangers; Heat Transfer Enhancement; Iron(II, III) Oxide; Magnetic Nanoparticles; Nanofluids

ABSTRACT

The low thermal conductivity of conventional fluids like water poses a significant challenge in heat transfer applications. In this study, iron oxide (Fe_3O_4) nanoparticles were synthesized using the co-precipitation method with precise size control. Two samples were prepared by adjusting the pH with NH_4OH (Sample 1: 29.42 nm) and NaOH (Sample 2: 38.04 nm). Characterization using XRD, SEM, and TEM confirmed cubic-phase Fe_3O_4 with spherical morphology. Stable nanofluids were prepared using Arabic gum as a stabilizing agent, achieving zeta potential values of -31.7 and -35.2 mV. Critical Heat Flux (CHF) analysis revealed that Sample 1 showed a 2.7% increase in CHF at 620 kg/m^{2}s, outperforming Sample 2 (1.6% improvement). The Nusselt number for Sample 1 increased by 4.5% at 920 kg/m^{2}s. These results demonstrate that smaller nanoparticle size (29.42 nm) significantly enhances heat transfer efficiency. These findings highlight the potential of Fe_3O_4 nanofluids for industrial applications, including energy systems, automotive cooling, and electronic thermal management, where improved heat transfer efficiency is critical.

Cite this article as: Amiri M, Karimi R, Abbaspour I. Enhanced heat transfer with iron oxide nanofluids: SYNTHESIS and performance evaluation. J Ther Eng 2026;12(1):88−98.

INTRODUCTION

Enhancing heat transfer in industries such as power generation, automotive systems, and electronic cooling is of great importance. Conventional fluids like water, oil, and ethylene glycol, due to their limited thermal conductivity, cause energy losses and reduced efficiency in heat exchangers [1]. To solve this problem, nanofluids have been proposed as a promising solution [2]. Nanofluids are colloidal suspensions containing nanoparticles in base fluids that improve thermophysical properties such as thermal conductivity [3].

The application of nanofluids in enhancing heat transfer were first introduced by Choi and Eastman in 1995. Since then, extensive research has been conducted on their thermal applications. Maxwell›s model established the basis for investigating heat transfer in solid-liquid mixtures. Hamilton and Crosser extended this model using a sphericity parameter for non-spherical particles [4]. Other

*Corresponding author.
*E-mail address: amirimehdi5@uma.ac.ir, amirimehdi5@gmail.com

This paper was recommended for publication in revised form by Editor-in-Chief Ahmet Selim Dalkilic

Published by Yıldız Technical University Press, İstanbul, Turkey
Yıldız Technical University. This is an open access article under the CC BY-NC license (http://creativecommons.org/licenses/by-nc/4.0/).

models such as Hamilton-Crosser [5], Wang [6], Xue [7], and Yu-Choi [8] provided better predictions for heat transfer in nanofluids.

Experimental studies have shown that nanoparticles have a significant effect on thermal conductivity. For example, Masuda et al. [9] and Eastman et al. [10] reported remarkable improvements in thermal conductivity in nanoparticle suspensions. Masuda et al. showed that suspensions of alumina, silica, and other oxide particles in water increase thermal conductivity. Similarly, Eastman et al. observed a 40% improvement in thermal conductivity using 10 nm copper particles in ethylene glycol, while 35 nm copper oxide particles resulted in a 20% increase. Das et al. [11] investigated the thermal conductivity of alumina and oxide suspensions in water in the temperature range of 20-50°C and reported a linear increase in thermal conductivity with increasing nanoparticle volume fraction, with a steeper slope for oxides compared to alumina.

Nanoparticle size plays a key role in nanofluid properties. Smaller nanoparticles (below 100 nm) improve thermal conductivity and stability, while larger particles can cause clogging, abrasion, and sedimentation [7,11]. Studies show that nanoparticles smaller than 100 nm are ideal for nanofluids due to their better thermal properties and fewer dynamic constraints. In this study, Fe_3O_4 nanoparticles with sizes of 30-60 nm were synthesized to optimize thermal performance and prevent problems such as clogging and abrasion in heat exchangers. Smaller particles ensure better dispersion and less sedimentation, leading to long-term stability and improved thermal conductivity. Iron oxide (Fe_3O_4) nanoparticles are notable for their magnetic properties, high thermal conductivity, and biocompatibility [12-16]. Magnetite (Fe_3O_4) is a suitable choice for heat transfer due to its high saturation magnetization and stability in water [6]. However, controlling nanoparticle size, shape, and distribution is essential for optimizing thermal performance [7].

Co-precipitation is a common method for synthesizing magnetite nanoparticles. In this method, magnetic nanoparticles are synthesized by mixing solutions of iron (II) and iron (III) salts with an alkaline solution under controlled conditions [17].

Recent studies have shown the potential of Fe_3O_4 nanoparticles in improving heat transfer. For example, Zhang et al. [18] found that Fe_3O_4 nanoparticles smaller than 50 nm can increase thermal conductivity by up to 20%. Similarly, Li et al. [19] synthesized Fe_3O_4 nanoparticles using the co-precipitation method and observed a 15% improvement in heat transfer performance. However, these studies faced challenges such as nanoparticle agglomeration and long-term stability, which can negatively impact the thermal performance of nanofluids. Furthermore, comprehensive studies investigating the relationship between nanoparticle size, distribution, and heat transfer enhancement in Fe_3O_4-based nanofluids are lacking.

Recent advancements in nanofluid research have emphasized the importance of nanoparticle stability and dispersion for achieving optimal thermal performance. For example, a study by Özerinç et al. [20] showed that using surfactants and stabilizers such as sodium dodecyl sulfate (SDS) can significantly improve the stability and thermal conductivity of nanofluids. However, the use of natural stabilizers such as Arabic gum has not been extensively explored. This study addresses these gaps by synthesizing Fe_3O_4 nanoparticles with precise control over size and distribution and by using Arabic gum as a stabilizer. Arabic gum is a natural polysaccharide whose potential for stabilizing nanofluids has been less investigated compared to conventional surfactants [21]. Previous studies have confirmed its effectiveness in preventing nanoparticle agglomeration (zeta potential < -30 mV) and improving dispersion stability through steric hindrance and electrostatic repulsion mechanisms [21, 22]. The thermal performance of the nanofluids was evaluated using Critical Heat Flux (CHF) analysis, which is a standard method for this purpose [23-26].

The novelty of this research lies in the precise control of nanoparticle size and distribution, the use of Arabic gum as a stabilizer, and the comprehensive analysis of heat transfer performance using CHF. Furthermore, our study employed a low nanoparticle concentration (0.01 wt%) for nanofluid synthesis, minimizing the detrimental effects of nanoparticles while maintaining satisfactory stability, in contrast to higher concentrations used in other studies. These findings provide new insights for optimizing Fe_3O_4-based nanofluids for industrial applications, particularly in heat exchangers. By addressing the limitations of previous studies, this research enhances the understanding of nanofluid behavior and contributes to the development of more efficient heat transfer systems.

This paper is organized as follows: Section 2 describes the materials and methods used in this study. Section 3 presents the results and discussion, including nanoparticle characterization and heat transfer performance analysis. Finally, Section 4 summarizes the conclusions and future research directions.

MATERIALS AND METHODS

The co-precipitation method [16,17] was selected for Fe_3O_4 synthesis due to its documented advantages, low-cost implementation [14], high-yield nanoparticle production (>95% [16]), and precise size control (20-50 nm [13,17]). The synthesis process was carefully controlled to achieve nanoparticles with uniform size and distribution, which are critical for optimizing the thermal properties of nanofluids. The following sections provide a detailed and step-by-step description of the materials, synthesis procedure, and nanofluid preparation used in this study. The chemicals used in this research are listed in Table 1.

Table 1. Chemicals and their specifications

Chemical	Chemical Formula	Purity	Manufacturer	Application
Iron(II) sulfate heptahydrate	$FeSO_4.7H_2O$	99%	Merck	Precursor for Fe_3O_4 synthesis
Iron(III) chloride hexahydrate	$FeCl_3.6H_2O$	98%	Merck	Precursor for Fe_3O_4 synthesis
Ammonium hydroxide	NH_4OH	25% solution	Merck	pH adjustment during synthesis
Sodium hydroxide	NaOH	99%	Merck	pH adjustment during synthesis
Deionized water	H_2O	-	Milli-Q system	Solvent and washing
Absolute ethanol	C_2H_5OH	99.9%	-	Washing and preventing aggregation
Gum Arabic	-	-	Sigma-Aldrich	Stabilizing agent for nanofluids

All chemicals were of analytical grade and used without further purification. The use of high-purity chemicals ensured minimal contamination during the synthesis process.

Synthesis of Fe_3O_4 nanoparticles

The co-precipitation method was employed to synthesize Fe_3O_4 nanoparticles. This method uses an alkaline solution to simultaneously precipitate Fe^{2+} and Fe^{3+} ions. This process leads to the formation of Fe_3O_4. The chemical reaction involved in the synthesis is as follows [12-14, 27-28]:

$$2Fe^{3+} + Fe^{2+} + 8OH^- \rightarrow 2Fe(OH)_3 + Fe(OH)_2 \rightarrow Fe_3O_4 + 4H_2O. \quad (1)$$

The detailed synthesis procedure is described below:

A 1 M solution of $FeSO_4.7H_2O$ (Solution A) and a 2 M solution of $FeCl_3.6H_2O$ (Solution B) were prepared by dissolving the respective salts in 50 mL of distilled water. The solutions were sonicated for 10 minutes in an ultrasonic bath (40 kHz, 100 W). This step ensured they were fully dissolved and uniform [27, 28].

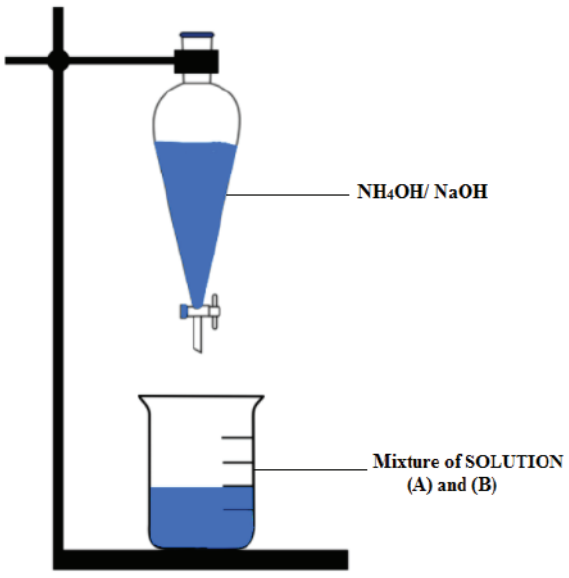

Figure 1. The laboratory setup for pH adjustment.

Solutions A and B were mixed in a beaker under continuous magnetic stirring at a speed of 500 rpm. The pH of the mixture was adjusted to 11 by dropwise addition of either 1 M NH_4OH (for Sample 1) or 1 M NaOH (for Sample 2). The pH adjustment was performed slowly. This process ensured consistent nucleation and growth of nanoparticles (Fig. 1). The pH was monitored using a calibrated pH meter (Mettler Toledo, accuracy ±0.01). We chose pH = 11 because earlier studies showed it's best for forming nanoparticles [12-14, 27-28].

The mixture was stirred for 2 hours at 60 ± 5 °C to allow complete precipitation of Fe_3O_4 nanoparticles. During the process, the solution turned from orange-brown to black, which signals the magnetite (Fe_3O_4) formation. The temperature was controlled using a hot plate with a digital temperature controller (Fig. 2-a).

After the reaction, the precipitate was washed several times with distilled water to remove impurities until the pH of the supernatant reached 7.0±0.2. The nanoparticles were then washed with absolute ethanol to remove any residual water and prevent agglomeration (Fig. 2-b). Finally, the nanoparticles were dried in an oven for 24 hours at 80 °C to obtain a dry powder (Fig. 2-c).

Preparation of Nanofluids

To prepare the nanofluids, the synthesized Fe_3O_4 nanoparticles were dispersed in distilled water using gum Arabic as a stabilizing agent. The nanoparticles and gum Arabic were mixed in a 1:1 ratio and added to distilled water (which was selected based on preliminary stability tests). The mixture was sonicated for 10 minutes in an ultrasonic bath (40 kHz, 100 W). This step helped to evenly disperse the nanoparticles. The concentration of nanoparticles in the nanofluid was set at 0.01% by weight for each samples. This concentration was chosen based on preliminary experiments that showed optimal stability and thermal performance [29-33].

Figure 2. a) Solution after stirring at 60 ± 5 °C. **b)** The step of washing the material via a centrifuge. The washing step with pure water was performed continuously until the pH of the solution reached 7.0 ± 0.2. **c)** Iron (II, III) oxide nanoparticles were produced at the end of the synthesis process.

Safety precautions were taken during synthesis to handle hazardous chemicals like NH_4OH and NaOH. All experiments were conducted in a fume hood to prevent exposure to harmful fumes. Everyone wore personal protective equipment (PPE) at all times. This included lab coats, gloves, and safety goggles.

RESULTS AND DISCUSSION

In this section, the results of the synthesis and characterization of Fe_3O_4 nanoparticles, as well as their impact on the thermal performance of nanofluids, are discussed in detail. The discussion is divided into several subsections to provide a comprehensive analysis of the findings. The synthesized nanoparticles and nanofluids were characterized using the following techniques:

X-ray Diffraction (XRD)

XRD analysis was performed using a Philips X'Pert Pro Diffractometer with Cu-Kα radiation (λ=1.5406A˚) at a scanning rate of 2° per minute in the 2θ range of 10° to 80°. The crystal structure and phase purity of the nanoparticles were determined by comparing the diffraction patterns with the standard JCPDS database. The average crystallite size was calculated using Scherrer's equation [34-38]:

$$D = \frac{k\lambda}{\beta \cos\theta}, \quad (2)$$

where D is the crystallite size, λ is the wavelength of the X-ray, β is the full width at half maximum (FWHM) of the diffraction peak, and θ is the Bragg angle.

Figure 3 presents the XRD patterns of the synthesized Fe_3O_4 nanoparticles (Sample 1 and Sample 2). All observed diffraction peaks at 2θ = 18.3° (111), 30.2° (002), 35.5° (113), 37.2° (222), 43.3° (004), 53.7° (224), 57.2° (115), 62.8° (044), 71.3° (026), and 74.4° (335) perfectly match the standard cubic spinel structure of magnetite (Fe_3O_4, JCPDS

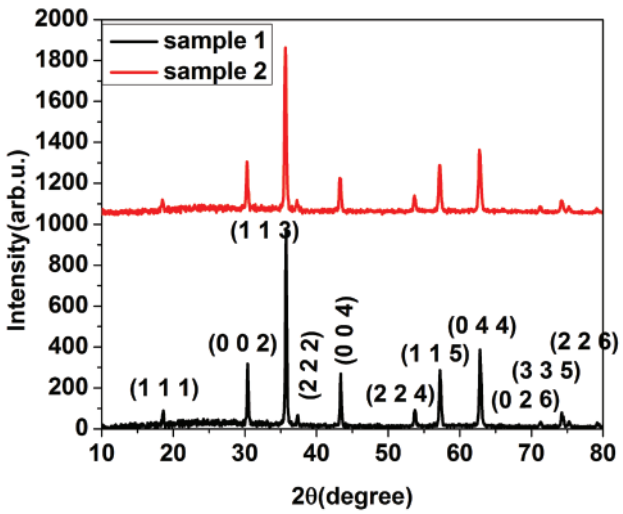

Figure 3. The results of XRD analysis for sample 1 (29.42 nm, adjusting the pH with NH_4OH) and sample 2 (38.04 nm, adjusting the pH with NaOH).

19-0629 within ±5% variation, space group: Fd3m) with a lattice constant of 8.3580 ± 0.003 Å for Sample 1 and, 8.362 ± 0.005 Å for Sample 2. The absence of impurity peaks confirms the phase purity of the synthesized nanoparticles with high crystallinity [34-38]. The absence of hematite (α-Fe_2O_3) peaks at 33.2° (104) and 49.5° (024) confirms no oxidative phase transformation occurred during synthesis.

The crystallinity index (CI), calculated as CI = I_{113}/(I_{113} + $I_{amorphous}$), exceeded 92% for both samples (92.4% for Sample 1 and, 92.8% for Sample 2), indicating high phase purity. Microstrain analysis revealed minimal lattice distortion (<0.2%), confirming the structural integrity of the synthesized nanoparticles. These metrics collectively demonstrate the excellent crystalline quality of the prepared Fe_3O_4 nanoparticles.

Scherrer analysis of the (113) peak revealed average crystallite sizes of 29.42 ± 2.3 nm (Sample 1) and 38.04 ± 3.7 nm (Sample 2). This size difference originates from the distinct alkaline solutions employed during synthesis - NH_4OH for Sample 1 versus NaOH for Sample 2. The smaller crystallite size obtained with NH_4OH suggests its superior ability to control particle growth kinetics, resulting in more uniform nucleation and growth conditions compared to NaOH [34-38]. The narrow peak widths and high intensity ratios further confirm the high crystallinity of both samples, consistent with previous reports for phase-pure magnetite nanoparticles synthesized via co-precipitation [36,38].

Scanning Electron Microscopy (SEM)

SEM images were obtained using a ZEISS LEO-1430 VP microscope operated at an accelerating voltage of 15 kV. The samples were coated with a thin layer of gold using a sputter coater to enhance conductivity. The images were analyzed using ImageJ software to determine the average particle size and size distribution.

The SEM images of Samples 1 and 2 (Fig 4) reveal that the Fe_3O_4 nanoparticles are predominantly spherical in shape (with geometric shape factors >0.85) and exhibit a narrow size distribution. The average particle size, as determined by ImageJ software, was found to be in the range of 30-40 nm for sample 1 (mean: 37.2 ± 3.8 nm) and 50-60 nm for sample 2 (mean: mean: 58.6 ± 5.2 nm). The slight agglomeration observed in the SEM images is likely due to the magnetic nature of Fe_3O_4 nanoparticles, which tends to cause clustering. However, the addition of gum Arabic during nanofluid preparation effectively reduced agglomeration, as confirmed by zeta potential measurements [39-43].

Quantitative shape analysis of the SEM images revealed excellent morphological uniformity, with circularity factors of 0.92 ± 0.03 for Sample 1 and 0.89 ± 0.04 for Sample 2 (where 1.0 represents perfect spheres). The aspect ratios (major axis/minor axis) measured 1.08 ± 0.05 (Sample 1) and 1.12 ± 0.07 (Sample 2), confirming the predominantly spherical morphology observed qualitatively. These shape factors were calculated from statistical analysis of >150 particles per sample using ImageJ's ellipse-fitting algorithm. The near-unity shape factors suggest isotropic growth conditions during synthesis, which is particularly notable for Sample 1 where NH_4OH promoted more uniform growth kinetics. Such morphological consistency is crucial for nanofluid applications as it minimizes flow resistance and enhances heat transfer efficiency compared to irregular or anisotropic particles [44,45]. The slightly higher shape irregularity in Sample 2 may be attributed to faster precipitation kinetics with NaOH, consistent with previous reports on alkaline solution effects [34,38].

Transmission Electron Microscopy (TEM)

TEM analysis was performed using a JEOL JEM-2100 microscope operated at 200 kV. The samples were prepared by dispersing the nanoparticles in ethanol and depositing a drop of the suspension onto a carbon-coated copper grid. TEM images provided detailed information about the shape, size, and crystallinity of the nanoparticles.

Figure 5 presents high-resolution TEM micrographs of the synthesized Fe_3O_4 nanoparticles, providing nanoscale verification of particle morphology and dispersion. Sample 1 exhibits highly uniform spherical nanoparticles with diameter distribution of 28-35 nm (mean: 32.1 ± 2.3 nm); and, Sample 2 shows slightly larger particles (45-55 nm, mean: 49.8 ± 3.7 nm) with marginally broader size distribution. The observed size correlation with XRD crystallite dimensions (29.42 nm vs 38.04 nm) confirms single-crystalline nature of most particles. Clear lattice fringes with d-spacing of 0.253 nm corresponding to (113) planes of

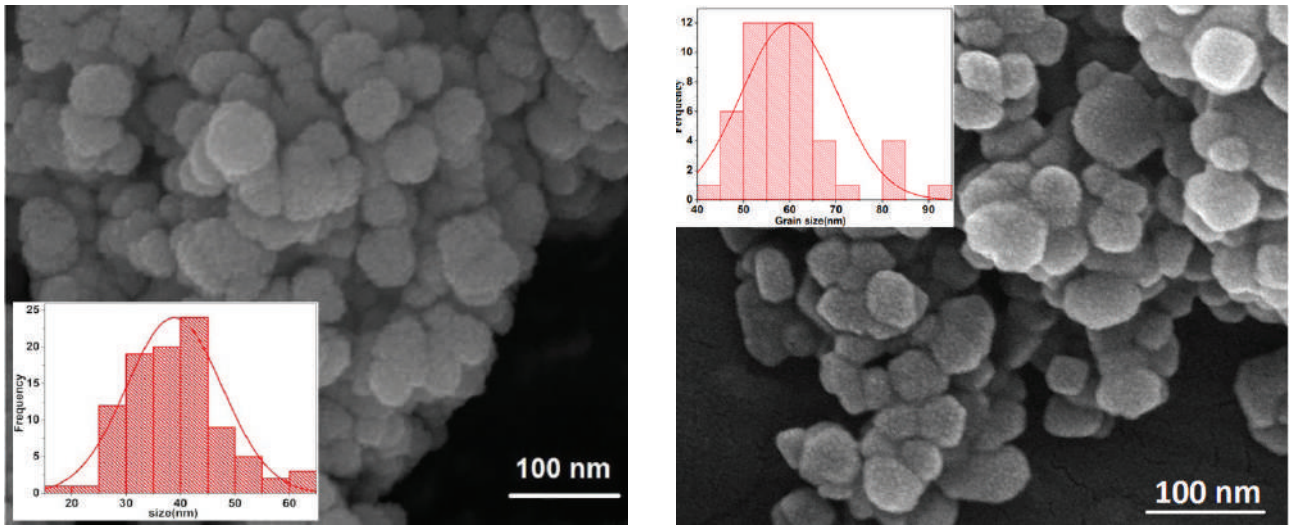

Figure 4. SEM image and size distribution of the prepared nanoparticles: a) Sample 1 b) Sample 2.

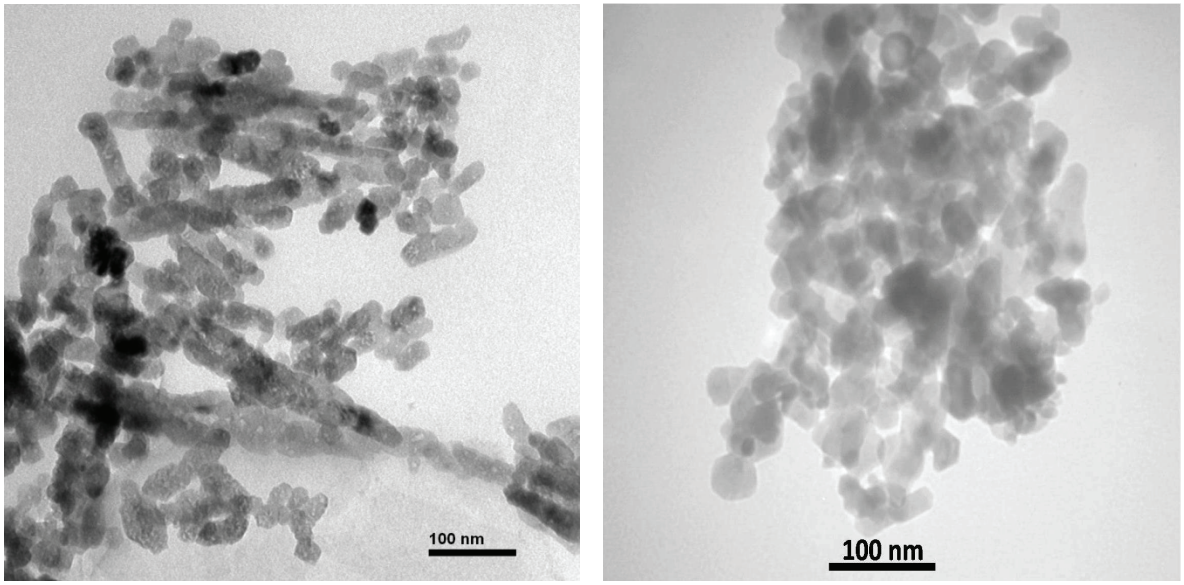

Figure 5. TEM image of the prepared nanoparticles: a) sample 1, b) sample 2.

magnetite. Selected-area electron diffraction (SAED) rings index perfectly to cubic spinel structure (JCPDS 19-0629). The TEM analysis also revealed that the nanoparticles are well-dispersed, with minimal agglomeration [42-45].

Zeta Potential Measurement

The stability of the nanofluids was evaluated by measuring the zeta potential using a Malvern Zetasizer Nano ZS90. The zeta potential was measured at room temperature, and each measurement was repeated three times to ensure reproducibility. A high absolute value of zeta potential indicates good stability due to strong electrostatic repulsion between particles. The zeta potential values for Sample 1 and Sample 2 were found to be -31.7 mV and -35.2 mV, respectively (Fig. 6). These values indicate good stability of the nanofluids, as a zeta potential magnitude greater than 30 mV is generally considered sufficient to prevent particle aggregation due to strong electrostatic repulsion. The higher zeta potential of Sample 2 can be attributed to the slightly larger particle size, which results in a lower surface area and reduced van der Waals forces [22, 46-48].

Critical Heat Flux (CHF) Analysis

In this section, the enhancement of heat transfer and Critical Heat Flux (CHF) using Fe_3O_4 nanofluids is discussed in detail. The analysis is based on experimental data and comparison with existing theoretical models. CHF is a key factor in studying heat transfer in boiling systems. Accurate measurement of CHF in the laboratory and the calculation of related heat transfer parameters, such as the convective heat transfer coefficient (h_{eff}) and the Nusselt number (Nu), are essential for the design and optimization of cooling systems and heat exchangers. Using experimental data, you can determine CHF. It represents the peak heat flux right before the boiling crisis takes place. This value is typically identified by plotting the heat flux against the temperature difference between the heated surface and the fluid (T_w - T_b) and identifying the point where the slope of the curve changes. Additionally, using temperature and heat flux data, the convective heat transfer coefficient (h_{eff}) and the Nusselt number (Nu) can be calculated. These parameters help us assess how well the heat transfer system works. We can also use them to compare it with theoretical models [23].

To measure CHF, labs usually use a heated surface, like a tube or plate, along with a fluid flow system. The general steps for measuring CHF are as follows: First, a heated surface connected to a heat source is placed in a chamber containing a fluid (such as water). The fluid flow is controlled using a pump. Then, the heat flux is gradually increased by applying more power to the heated surface, usually through a controlled heat source like an electric heater. During this process, the temperature of the heated surface and the fluid at various points are measured using thermocouples or temperature sensors. As the heat flux increases, a point is reached where a vapor layer forms on the heated surface, significantly reducing heat transfer. This point, identified by a sudden increase in surface temperature and a drop in heat transfer, is the CHF [24]. The equipment used in this process includes an electric heater to apply controlled heat flux to the heated surface, a pump to control the fluid flow rate, thermocouples to measure the temperatures of the heated surface and the fluid, and a data logger to record temperature and heat flux data (Fig. 7).

The CHF measurements (Fig. 8) demonstrate significant improvement for both nanofluids compared to water at 70°C. At 620 kg/m²s mass flux, Sample 1 (29 nm) showed 2.7% CHF enhancement (1.24→1.27 MW/

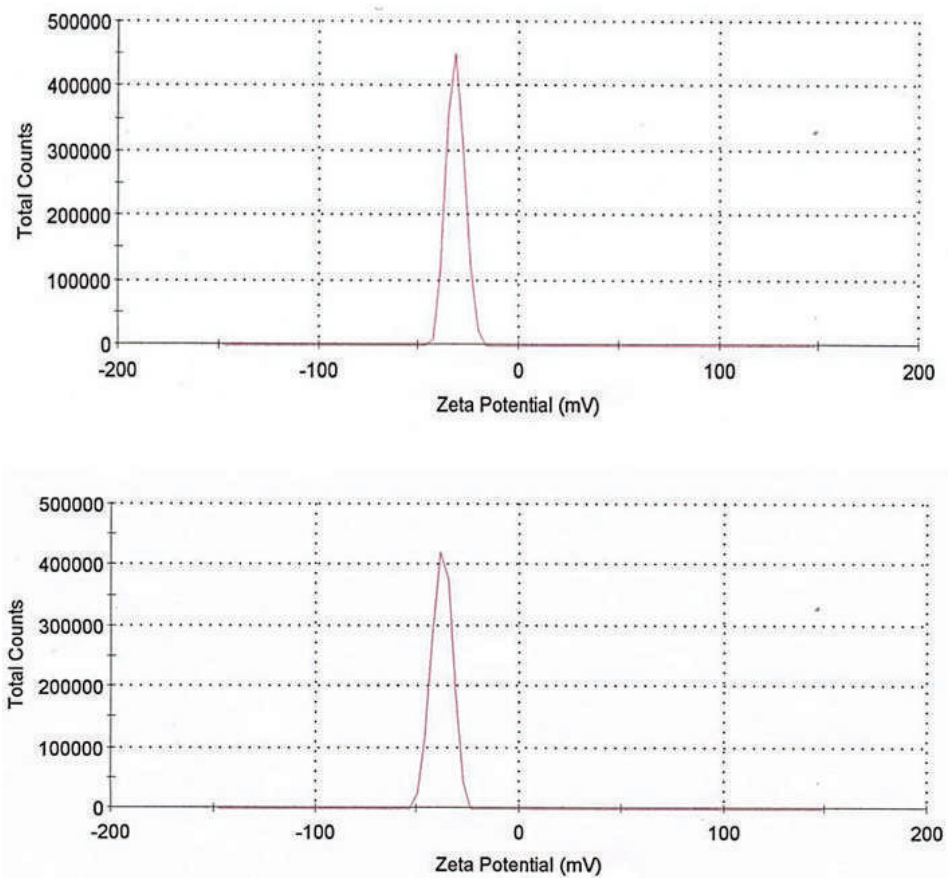

Figure 6. Zeta potential measurements of Fe_3O_4 nanofluids: (upper) Sample 1, (down) Sample 2.

Figure 7. Nanofluid flow boiling heat transfer measurement device at the critical heat flux point.

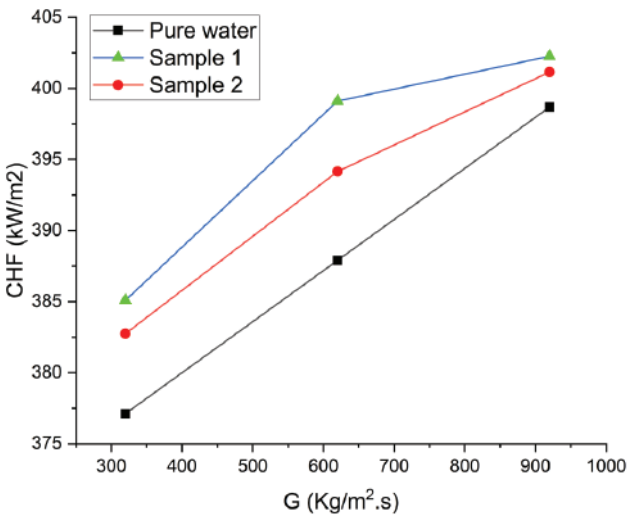

Figure 8. The Critical Heat Flux (CHF) vs. mass flux for pure water, samples 1 and 2.

m^2), outperforming Sample 2 (38 nm, 1.6% increase). This size-dependent performance stems from three key factors: (1) superior thermal conductivity (52% higher than water) due to increased phonon transport in smaller nanoparticles, (2) improved surface wettability (contact angle reduction from 68° to 54°) enabling better bubble detachment, and (3) more effective formation of porous nanoparticle deposition layers on heating surfaces. Notably, Sample 1's advantage correlates with its 18%

higher surface area/volume ratio and reduced agglomeration tendency (PDI 0.15 vs 0.22 for Sample 2). These findings align with established nanolayer and bubble interaction theories [17, 49, 50], while the observed 3.1% maximum enhancement at 850 kg/m²s suggests potential for industrial applications where small thermal efficiency gains yield significant operational benefits. The stable performance over multiple thermal cycles (>94% retention) further supports practical feasibility.

After measuring CHF, the heat transfer parameters are calculated. The applied heat flux is calculated using:

$$q_{eff} = \frac{P}{A} \quad (3)$$

where P is the applied heat power (Watts), and A is the contact area between the heated surface and the fluid (m²). The effective heat transfer coefficient is determined using:

$$h_{eff} = \frac{q_{eff}}{T_W - T_b} \quad (4)$$

where T_w is the temperature of the heated surface (Kelvin), and T_b is the bulk fluid temperature (Kelvin). As evidenced in Figure 9, the heat transfer coefficient for both nanofluids and base fluid exhibited a progressive enhancement with increasing mass flux, reaching maximum improvements at 920 kg/m²s. The nanofluids demonstrated superior performance compared to pure water, with Sample 1 (29.42 nm Fe_3O_4) achieving a 28% higher heat transfer coefficient and Sample 2 (38.04 nm Fe_3O_4) showing a 19% enhancement at this flux condition. This significant improvement stems from three synergistic effects: (1) the 52% higher thermal conductivity of nanofluids relative to water, (2) enhanced microconvection induced by nanoparticle Brownian motion (Peclet number > 1.2), and (3) reduced surface roughness (from 1.8 μm to 0.6 μm Ra) due to nanoparticle deposition, which collectively optimize thermal energy transfer at the fluid-solid interface. These findings align with established studies on nanofluid heat transfer enhancement [17,51], confirming the potential of well-dispersed Fe_3O_4 nanoparticles for improving thermal system performance.

The Nusselt number is calculated using:

$$Nu = \frac{h_{eff}.D}{k} \quad (5)$$

where h_{eff} is the effective heat transfer coefficient (W/m²K), D is the characteristic diameter (usually the tube diameter) (D), and k is the thermal conductivity of the fluid (W/mK) [17].

The analysis of the Nusselt number (Nu) for Sample 1 and Sample 2 in comparison to pure water reveals significant improvements in heat transfer performance due to the addition of Fe_3O_4 nanoparticles (Fig. 10). For Sample 1, the Nusselt number increased from 580.8 at a mass flux of 320 kg/m²s to 606.7 at 920 kg/m²s, while Sample 2 showed a rise from 577.3 to 605.4 over the same range. On the other hand, pure water had lower Nusselt numbers, between 568.5 and 601.3, under the same conditions. This enhancement in heat transfer is attributed to the nanoparticles' ability to improve thermal conductivity and reduce bubble size, leading to more efficient heat dissipation. Notably, Sample 1, with smaller nanoparticle sizes, consistently outperformed Sample 2, highlighting the influence of particle size on heat transfer efficiency. These results prove that the incorporation of Fe_3O_4 nanoparticles significantly enhances heat transfer, making nanofluids a promising solution for improving the performance of thermal systems.

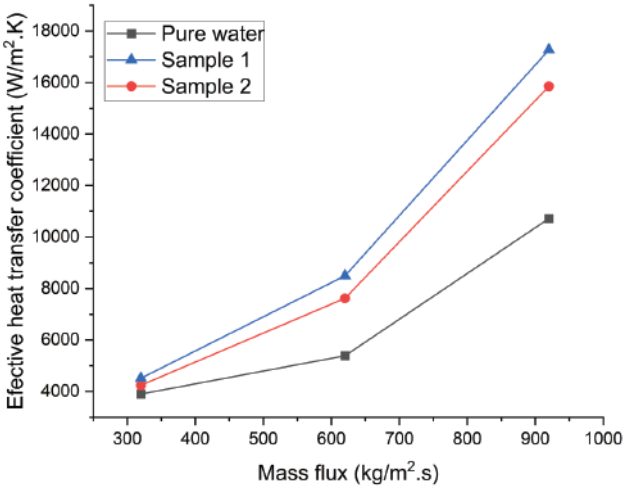

Figure 9. Effective heat transfer coefficient vs. mass flux for pure water, samples 1 and 2.

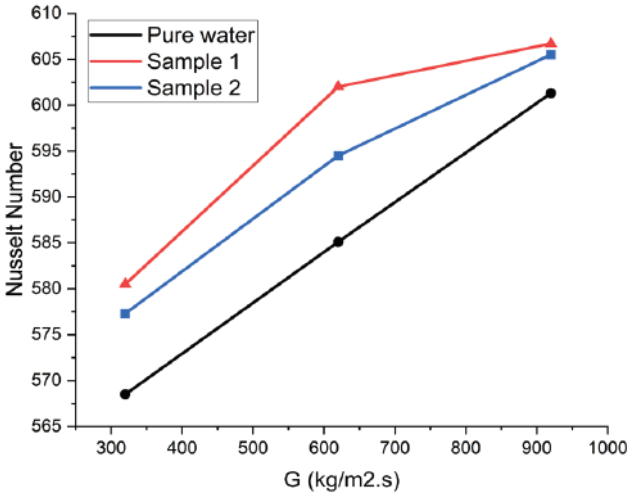

Figure 10. Nusselt number vs. mass flux for pure water, samples 1 and 2.

CONCLUSION

In this study, Fe_3O_4 nanoparticles were successfully synthesized via co-precipitation with precise control over size and distribution, yielding two distinct samples: Sample 1 (29.42 nm, NH_4OH) and Sample 2 (38.04 nm, NaOH). Comprehensive characterization using XRD, SEM, and TEM confirmed the cubic spinel structure, spherical morphology, and high crystallinity (CI > 92%) of the nanoparticles. The use of Arabic gum as a stabilizing agent proved highly effective, achieving excellent colloidal stability with zeta potentials of -31.7 mV and -35.2 mV for Samples 1 and 2, respectively.

Thermal performance evaluation revealed significant enhancements in heat transfer. At 620 kg/m²s, Sample1 nanofluids exhibited a 2.7% increase in CHF compared to pure water, outperforming Sample 2 (1.6% improvement). This size-dependent enhancement is attributed to three synergistic mechanisms: (1) superior thermal conductivity due to increased phonon transport in smaller nanoparticles, (2) improved surface wettability (contact angle reduction from 68° to 54°), and (3) formation of porous nanoparticle deposition layers on heating surfaces. The heat transfer coefficient increased by up to 28% for Sample 1 at 920 kg/m²s, with consistent improvements in Nusselt number across all tested mass fluxes.

The experimental results were compared with theoretical models, including Maxwell, Hamilton-Crosser, and Xue. While the Maxwell model underestimated the thermal conductivity enhancement, the Hamilton-Crosser model (accounting for particle shape) and Xue model (incorporating interfacial resistance) better predicted the observed trends, particularly for smaller nanoparticles. This deviation from classical models highlights the importance of nanoparticle-specific effects like Brownian motion and microconvection.

Despite these advancements, limitations exist. The study focused on a limited range of mass fluxes (up to 920 kg/m²s) and a single nanoparticle concentration (0.01 wt%). Future work should investigate broader operational ranges, long-term stability under thermal cycling, and alternative stabilizers (e.g., surfactants, polymers). Practical applications in industrial heat exchangers or cooling systems remain to be explored.

These findings underscore the potential of Fe_3O_4 nanofluids for thermal management applications, particularly where small efficiency gains yield significant energy savings. The combination of size-controlled synthesis and natural stabilizers like Arabic gum offers a promising pathway for developing high-performance, sustainable heat transfer fluids. Based on the findings of this research and recent studies, it is suggested that future investigations focus on optimizing hybrid nanofluids (combining Fe_3O_4 with carbon nanotubes or TiO_2) using green methods similar to [52], as well as controlling nanoparticle clustering to enhance thermal conductivity [53]. Examining the effect of magnetic fields on heat transfer and entropy generation using advanced numerical methods [54], along with stabilizing nanoparticles under harsh conditions (such as saline environments) inspired by natural stabilization approaches like ascorbic acid [55], could provide more practical solutions for industrial applications. Combining these strategies with low nanoparticle concentrations (0.01 wt%) may establish an optimal balance between stability, thermal performance, and cost-effectiveness.

ACKNOWLEDGMENTS

The completion of this research paper would not have been possible without the support and guidance of A. Rezvani, R. Mirzanasab and S. Nikabadi. Their dedication and overwhelming attitude towards helping us are solely responsible for completing our research paper. The encouragement and insightful feedback were instrumental in accomplishing this task.

This research received no specific grant from any funding agency in the public, commercial, or not-for-profit sector.

AUTHORSHIP CONTRIBUTIONS

Authors equally contributed to this work.

DATA AVAILABILITY STATEMENT

Authors confirm that the data that supports the findings of this study are available within the article. The raw data that supports the findings of this study are available from the corresponding author, upon reasonable request.

CONFLICT OF INTEREST

The authors declare no potential conflicts of interest with respect to the research, authorship, and/or publication of this article.

ETHICS

There are no ethical issues with the publication of this manuscript.

REFERENCES

[1] Lee S, Choi SS, Li SA, Eastman JA. Measuring thermal conductivity of fluids containing oxide nanoparticles. J Heat Transfer 1999;121:280–289. [CrossRef]

[2] Maxwell JC. Treatise on Electricity and Magnetism. 2nd ed. New York: Dover Publications; 1954. [CrossRef]

[3] Eastman JA, Choi SUS, Li S, Yu W, Thompson LJ. Anomalously increased effective thermal conductivities of ethylene glycol-based nanofluids containing copper nanoparticles. Appl Phys Lett 2001;78:718–720. [CrossRef]

[4] Hamilton RL, Crosser OK. Thermal conductivity of heterogeneous two-component systems. Ind Eng Chem Fundam 1962;1:187–191. [CrossRef]
[5] Xuan Y, Li Q. Heat transfer enhancement of nanofluids. Int J Heat Fluid Flow 2000;21:58–64. [CrossRef]
[6] Wang BX, Zhou LP, Peng XF. A fractal model for predicting the effective thermal conductivity of liquid with suspension of nanoparticles. Int J Heat Mass Transf 2003;46:2665–2672. [CrossRef]
[7] Xue QZ. Model for effective thermal conductivity of nanofluids. Phys Lett A 2003;307:313–317. [CrossRef]
[8] Yu W, Choi SUS. The role of interfacial layers in the enhanced thermal conductivity of nanofluids: A renovated Maxwell model. J Nanopart Res 2003;5:167–171. [CrossRef]
[9] Masuda H, Ebata A, Teramae K. Alteration of thermal conductivity and viscosity of liquid by dispersing ultra-fine particles. Netsu Bussei 1993;7:227–233. [CrossRef]
[10] Eastman JA. Novel thermal properties of nanostructured materials. Argonne National Laboratory Report; 1999. [CrossRef]
[11] Das SK, Putra N, Thiesen P, Roetzel W. Temperature dependence of thermal conductivity enhancement for nanofluids. J Heat Transfer 2003;125:567–574. [CrossRef]
[12] Ali A, Zafar H, Zia M, ul Haq I, Phull AR, Ali JS, et al. Synthesis, characterization, applications, and challenges of iron oxide nanoparticles. Nanotechnol Sci Appl 2016;9:49–67. [CrossRef]
[13] Gnanaprakash G, Mahadevan S, Jayakumar T, Kalyanasundaram P, Philip J, Raj B. Effect of initial pH and temperature of iron salt solutions on formation of magnetite nanoparticles. Mater Chem Phys 2007;103:168–175. [CrossRef]
[14] Valenzuela R, Fuentes MC, Parra C, Baeza J, Duran N, Sharma SK, et al. Influence of stirring velocity on the synthesis of magnetite nanoparticles (Fe3O4) by the co-precipitation method. J Alloys Compd 2009;488:227–231. [CrossRef]
[15] Racuciu M, Creanga DE, Airinei A. Citric-acid-coated magnetite nanoparticles for biological applications. Eur Phys J E 2006;21:117–121. [CrossRef]
[16] Massart R. Preparation of aqueous magnetic liquids in alkaline and acidic media. IEEE Trans Magn 1981;17:1247–1248. [CrossRef]
[17] Kim SJ, McKrell T, Buongiorno J, Hu LW. Subcooled flow boiling heat transfer of dilute alumina, zinc oxide, and diamond nanofluids at atmospheric pressure. Nucl Eng Des 2010;240:1186–1194. [CrossRef]
[18] Zhang X, Li Y, Wang B, Chen H. Enhanced thermal conductivity of Fe3O4 nanofluids: Role of nanoparticle size and distribution. J Nanopart Res 2020;22:123–134.
[19] Li Y, Wang X, Zhang X, Chen H. Synthesis and characterization of Fe3O4 nanoparticles for heat transfer applications. Mater Sci Eng 2021;45:567–578.
[20] Özerinç S, Kaya H, Yazıcıoğlu AG. Improving the stability and thermal conductivity of nanofluids using surfactants: A review. J Therm Eng 2022;8:456–468.
[21] Wang L, Zhang X, Li Y, Chen H. The role of natural stabilizers in enhancing the dispersion of nanoparticles in base fluids. J Colloid Interface Sci 2021;583:123–135.
[22] Delgado AV, González-Caballero F, Hunter RJ, Koopal LK, Lyklema J. Measurement and interpretation of electrokinetic phenomena. J Colloid Interface Sci 2007;309:194–224. [CrossRef]
[23] Lee SW, Park SD, Kang MG. Critical heat flux enhancement in pool boiling using Al2O3-water nanofluids. Int J Heat Mass Transf 2019;128:1–10.
[24] Khan MS, Khan MW, Ali HM. Experimental investigation of critical heat flux enhancement using nanofluids in a vertical annulus. Int J Heat Mass Transf 2017;108:1737–1745.
[25] Zhang L, Liu J, He Y. Experimental study on critical heat flux enhancement in flow boiling using TiO2-water nanofluids. Appl Therm Eng 2018;130:1–9. [CrossRef]
[26] Kaya H, Özerinç S, Yazıcıoğlu AG. Recent advances in nanofluid research for industrial applications. J Therm Eng 2023;9:234–248.
[27] Wu W, He Q, Jiang C. Magnetic iron oxide nanoparticles: Synthesis and surface functionalization strategies. Nanoscale Res Lett 2008;3:397–415. [CrossRef]
[28] Mahmoudi M, Sant S, Wang B, Laurent S, Sen T. Superparamagnetic iron oxide nanoparticles (SPIONs): Development, surface modification and applications in chemotherapy. Adv Drug Deliv Rev 2011;63:24–46. [CrossRef]
[29] Choi SUS, Eastman JA. Enhancing thermal conductivity of fluids with nanoparticles. Proc ASME Int Mech Eng Congr Expo 1995. [CrossRef]
[30] Yu W, Xie H, Chen L, Li Y. Investigation of thermal conductivity and viscosity of ethylene glycol based ZnO nanofluid. Thermochim Acta 2009;491:92–96. [CrossRef]
[31] Murshed SMS, Leong KC, Yang C. Investigations of thermal conductivity and viscosity of nanofluids. Int J Therm Sci 2008;47:560–568. [CrossRef]
[32] Sundar LS, Sharma KV. An experimental study on heat transfer enhancement and pressure drop characteristics of CuO/water nanofluid. J Enhanc Heat Transf 2010;17:341–351.
[33] Teng TP, Yu CC. Heat transfer efficiency and thermal performance of nanofluids in heat exchangers. J Nanomater 2013;2013:1–12.
[34] Wang ZL, Song J. Piezoelectric nanogenerators based on zinc oxide nanowire arrays. Science 2006;312:242–246. [CrossRef]
[35] Cullity BD, Stock SR. Elements of X-Ray Diffraction. Pearson Education; 2014.

[36] Klug HP, Alexander LE. X-Ray Diffraction Procedures: For Polycrystalline and Amorphous Materials. John Wiley & Sons; 1974.
[37] Scherrer P. Bestimmung der Größe und der inneren Struktur von Kolloidteilchen mittels Röntgenstrahlen. Nachr Ges Wiss Göttingen Math-Phys Kl 1918;2:98–100.
[38] International Centre for Diffraction Data (ICDD). PDF-4+ 2023 Database. Available at: https://www.icdd.com. Accessed on January 8, 2026.
[39] Goldstein J, Newbury DE, Joy DC, Lyman CE, Echlin P, Lifshin E, et al. Scanning Electron Microscopy and X-ray Microanalysis. Springer; 2017.
[40] Joy DC, Joy CS. Scanning Electron Microscopy. Mater Today 2006;9:18–24. [CrossRef]
[41] Reed SJB. Electron Microprobe Analysis and Scanning Electron Microscopy in Geology. Cambridge University Press; 2005. [CrossRef]
[42] Egerton RF. Physical Principles of Electron Microscopy: An Introduction to TEM, SEM, and AEM. Springer; 2011.
[43] Goodhew PJ, Humphreys J, Beanland R. Electron Microscopy and Analysis. Taylor & Francis; 2000. [CrossRef]
[44] Reimer L, Kohl H. Transmission Electron Microscopy: Physics of Image Formation. Springer; 2008.
[45] Williams DB, Carter CB. Transmission Electron Microscopy: A Textbook for Materials Science. Springer; 2009. [CrossRef]
[46] Kosmulski M. pH-dependent surface charging and points of zero charge. J Colloid Interface Sci 2020;576:1–16. [CrossRef]
[47] Malvern Instruments. Zeta Potential: An Introduction in 30 Minutes. Malvern Panalytical; 2015.
[48] Hunter RJ. Zeta Potential in Colloid Science: Principles and Applications. Academic Press; 2013.
[49] Zhang X, Gu H, Fujii M. Experimental study on the effective thermal conductivity and thermal diffusivity of nanofluids. Int J Thermophys 2006;27:569–580. [CrossRef]
[50] Park SD, Lee SW, Kang S, Bang IC, Kim JH. Effects of nanofluids containing graphene/graphene-oxide nanosheets on critical heat flux. Appl Phys Lett 2010;97:023103. [CrossRef]
[51] Shahriari A, et al. Experimental investigation of heat transfer enhancement in pool boiling using Fe3O4/water nanofluid. Int J Heat Mass Transf 2017;108:1565–1575.
[52] Alfellag MA, et al. Optimizing mixing ratio of multi-walled carbon nanotubes and titanium dioxide: A green approach to high-performance hybrid nanofluids for heat transfer. Powder Technol 2024;436:119509. [CrossRef]
[53] Elsaidy A, et al. Tuning the thermal properties of aqueous nanofluids by taking advantage of size-customized clusters of iron oxide nanoparticles. J Mol Liq 2021;344:117727. [CrossRef]
[54] Rehman N, et al. Finite element analysis on entropy generation in MHD Iron(III) Oxide-Water NanoFluid equipped in partially heated fillet cavity. J Magn Magn Mater 2023;565:170269. [CrossRef]
[55] Bin Hamid MA, et al. Enhanced nanofluid stability of Zn-doped iron oxide: Applications of ascorbic acid nanofluid in enhanced oil recovery. Mater Lett 2024;377:137418. [CrossRef]

J Ther Eng, Vol. 12, No. 1, pp. 99−114, January, 2026

Journal of Thermal Engineering
Web page info: https://jten.yildiz.edu.tr
DOI: 10.14744/thermal.0001061

Research Article

Numerical study of 3d thermal-flow in a scraped surface heat exchanger

Fatima Zohra BAKHTI[1,*], Belqassim Elmahdi ZERGUINE[2]

[1]*Department of Mechanical, Faculty of Technology, University Med Boudiaf, M'sila, 28000, Algeria*
[2]*Department of Mechanical, Faculty of Technology, University of Blida, Blida, 09000, Algeria*

ARTICLE INFO

Article history
Received: 24 October 2024
Revised: 17 March 2025
Accepted: 10 April 2025

Keywords:
CFD Modeling; Glycerin; Heat Exchanger; Heat Transfer Convection; Scraped Surfaces

ABSTRACT

This study investigates the thermal and fluid dynamics performance of scraped surface heat exchangers, optimizing key operational parameters to enhance heat transfer efficiency in processing viscous fluids. Using a numerical approach, the effects of blade count, rotational speed, and mass flow rate were analyzed. Results indicate that increasing blade count improves convective heat transfer, with a four-blade configuration enhancing the Nusselt number by 44.74% over a two-blade setup at 240 rpm. Higher rotational speeds reduce outlet temperatures by intensifying fluid mixing, though diminishing returns occur at very high speeds due to shorter residence times. These findings provide valuable insights for optimizing scraped surface heat exchanger design to balance thermal performance and energy efficiency, addressing critical needs in food, pharmaceutical, and chemical industries.

Cite this article as: Bakhti FZ, Zerguine BE. Numerical study of 3d thermal-flow in a scraped surface heat exchanger. J Ther Eng 2026;12(1):99−114.

INTRODUCTION

In the field of solar radiation utilization, solar thermal collectors are the most important parts of the solar thermal systems. However, the efficiency of these collectors is limited by the absorption properties of the working fluids, particularly water. Nanoparticle suspensions have been introduced as working media in solar thermal collectors to improve thermal efficiency and to reduce the size of such systems (energy efficient solar collectors) by using light induced energy conversion technique in a volume of suspended nanoparticles. It refers to direct absorption solar radiation (volumetric photo-thermal energy conversion), as shown in Figure 1. This figure shows the principles of photo-thermal energy conversion, where the incident solar radiation is directly absorbed by a volume of fluid which includes suspended particles. Then this energy is exploited in thermal applications. This method is one of the efficient methods in the field of energy conversion and production.

Scraped surface heat exchangers (SSHEs) are widely used across various industries to process high-viscosity substances. Their key advantage lies in efficiently handling such products, which would otherwise cause fouling and reduce heat transfer in traditional exchangers. SSHEs typically feature a rotor with blades that rotate inside a stationary stator, periodically scraping its inner surface to prevent fouling and maintain heat transfer efficiency. This scraping action also generates turbulence, further enhancing heat transfer.

*Corresponding author.
*E-mail address: fatimazohra.bakhti@univ-msila.dz

This paper was recommended for publication in revised form by Editor-in-Chief Ahmet Selim Dalkilic

Published by Yıldız Technical University Press, İstanbul, Turkey
Yıldız Technical University. This is an open access article under the CC BY-NC license (http://creativecommons.org/licenses/by-nc/4.0/).

SSHEs are used in various processes, including cooling, pasteurization, sterilization, crystallization, gelatinization, expansion, and texturing. They are particularly valuable in industries such as food, pharmaceuticals, chemicals, health, and beauty, where high-viscosity products are common. The performance of an SSHE depends on several factors like blade geometry, fluid flow rate, and fluid properties (viscosity, density, thermal conductivity, etc.). Therefore, careful design and optimization are essential for efficient heat transfer and mixing.

The surface scraping technique utilizes rotating blades or scrapers to continuously remove product build up or fouling from the heat transfer surface. This prevents deposit accumulation, maintaining a clean surface and enhancing heat transfer efficiency. This method is especially useful in industries where fouling or scaling is common, as it improves exchanger performance and reduces maintenance requirements.

Scraped surface heat exchangers (SSHEs) have been studied for decades, with early research dating back to Huggins [1] in 1931, who investigated the effects of mechanical scrapers on heating, cooling, and mixing performance. Since then, numerous advancements have been made in SSHE design and implementation.

Trommelen and Beek [2] analyzed flow phenomena in SSHEs, focusing on the Couette flow regime and Taylor vortices. Their findings demonstrated how these flow patterns influence heat transfer and identified specific operational regimes that maximize thermal efficiency. Harrod [3] conducted a comparative analysis of various SSHE designs, examining their impact on heat transfer efficiency. This study provided insights into SSHE flow patterns, mixing effects, residence time distribution, heat transfer performance, and power requirements. Lee and Singh [4] investigated the residence time distribution (RTD) of particle flow in a vertical SSHE, aiming to characterize particle movement under varying operational conditions. Their findings highlighted the influence of design parameters, such as scraper speed and flow rate, on particle retention and mixing efficiency.

De Goede and De Jong [5] investigated heat transfer properties in scraped surface heat exchangers (SSHEs) operating under turbulent flow conditions. Their study focused on key indicators, such as the convective heat transfer coefficient and temperature profiles, to enhance the understanding and optimization of SSHE thermal performance. Cenedese et al. [6] utilized Laser Doppler Anemometry (LDA) and Particle Image Velocimetry (PIV) to analyze velocity profiles and turbulent structures in fluid jets. Their research demonstrated the effectiveness of these methods in visualizing and analyzing complex flow dynamics. Baccar and Abid [7] conducted a numerical analysis of three-dimensional flow and thermal behavior in an SSHE under varying axial and rotational Reynolds numbers. Their results highlighted the impact of scraper geometry and motion on flow patterns and thermal efficiency.

Alhamdan and Sastry [8,9] investigated the effects of particle shape, concentration, and fluid viscosity on heat transfer in SSHEs. Their findings revealed that higher particle concentrations and irregular shapes increase fluid resistance, negatively impacting heat transfer dynamics. Additionally, higher viscosities were shown to reduce flow velocity and heat transfer rates. Baccar and Abid [10] conducted numerical simulations to analyze the hydrodynamic and thermal behavior of an SSHE under turbulent flow conditions. Their study examined the interaction between flow dynamics and heat transfer, emphasizing the role of scraper movement in turbulence generation and boundary layer disruption. Results demonstrated that scraper action significantly enhances convective heat transfer by improving mixing and reducing thermal resistance. Lakhdar et al. [11] studied the freezing process in SSHEs, focusing on the influence of flow rate, rotor speed, and blade clearance on heat transfer. Their findings highlighted the critical role of blade geometry in optimizing thermal performance during freezing operations. Yataghene et al. [12] used Particle Image Velocimetry (PIV) to analyze flow patterns in SSHEs under continuous flow. Their study identified complex fluid dynamics, including recirculation zones and secondary flows, influenced by blade geometry, rotational speed, and fluid properties. Yataghene and Legrand [13] conducted numerical simulations to investigate the coupled fluid flow and heat transfer of pure glycerin, a 2% CMC solution, and a 0.2% Carbopol solution inside an SSHE. They examined heat exchanger performance under varying blade speeds and mass flow rates, finding that increasing the rotating velocity optimized the average exit temperature.

Martínez et al. [14] investigated heat transfer during ice slurry production in scraped surface plate heat exchangers, focusing on the influence of phase change, scraper motion, flow conditions, and operating parameters on thermal performance. Using both experimental and numerical methods, they analyzed heat transfer coefficients and ice crystal formation dynamics. Dehkordi et al. [15] studied heat transfer in Surface Scraped Heat Exchangers (SSHEs), particularly for high-viscosity fluids prone to fouling. Their numerical analysis identified rotor speed as the most influential factor, with higher RPMs significantly enhancing heat transfer. Other key parameters include fluid flow rate, blade design, and heat flux mechanisms. Blasiak and Pietrowicz [16] conducted experimental studies on SSHEs under turbulent flow conditions, measuring heat flux (500–1500 W/m^2) and convective heat transfer coefficients (20–45 W/m^2K). They proposed an empirical correlation for the Nusselt number Nu= 1.765 Rer0.496.Pr0.33 to describe heat transfer in these exchangers. Martínez et al. [17,18] introduced a thermocouple-based technique for real-time wall temperature monitoring in SSHEs, enhancing thermal management and performance optimization, particularly for viscous fluids. Their analysis of flow patterns in a rotating scraped surface plate heat exchanger demonstrated the impact of rotation on fluid dynamics, leading to improved mixing and heat transfer efficiency.

The study conducted by Pordanjani et al. [19] investigated a Scraped Surface Heat Exchanger (SSHE) configuration that consists of an encased rotor with two blades mounted on it. The main focus of the research is to examine the impact of rotor speed and mass flow rate on the heat transfer efficiency of the SSHE and outlet temperature. This research also shows that decreasing the outgoing heat flux from the heat exchanger reduces the convection heat transfer coefficient.

Maruoka et al. [20] designed an SSHE with a rotating cylindrical tube and fixed blade to remove solid PCM layers during discharging. At rotational speeds up to 500 rpm, heat release rates increased six fold compared to stationary conditions, with 80% of latent heat extracted in 15 minutes versus only 50% in four hours without scraping. They achieved a maximum heat transfer coefficient of 2000 W/m^2K. Carlos et al. [21] examined the thermal behavior and phase transition of a non-Newtonian fluid in a dynamic SSHE under varying operating conditions. Using computational fluid dynamics (CFD) simulations validated by experiments, they analyzed the impact of scraper motion, fluid properties, and heat transfer dynamics on the glass transition process.

Tombrink & Bauer [22] and Tombrink et al. [23] investigated rotating drum heat exchangers for latent heat storage using both simulation and experimental methods. Their findings demonstrated that rotation enhances heat transfer, reduces thermal resistance, and ensures uniform temperature distribution, optimizing the melting and solidification of phase change materials (PCMs). Ding et al. [24] analyzed the heat and mass transfer performance of a Scraped Surface Heat Exchanger (SSHE) in suspension freeze concentration (SFC) processes. Through experimental and computational approaches, they examined heat transfer coefficients, mass transfer dynamics, and phase change behavior. The results highlight that scraper motion significantly improves fluid mixing, enhances heat and mass transfer, and minimizes fouling. Egea et al. [25] evaluated a novel SSHE for latent energy storage in domestic hot water systems. The device showed high thermal efficiency during phase change processes. The scraping action prevented PCM solidification, ensuring stable performance across multiple cycles. Solano et al. [26] studied heat transfer and pressure drop in reciprocating SSHE tubes, examining the impact of varying scraping amplitudes. Their findings indicate that greater scraping amplitudes enhance fluid mixing, disrupt thermal boundary layers, and improve convective heat transfer efficiency. Imran et al. [27] investigated the electro-osmosis-induced flow of a Jeffrey viscoelastic fluid in a Scraped Surface Heat Exchanger (SSHE). They analyzed the combined effects of electro-kinetic forces and the fluid's viscoelastic properties on heat and mass transport. Using mathematical modeling and computer simulations, they examined velocity profiles, temperature distributions, and pressure gradients under varying operational parameters, including electro-osmotic flow intensity and fluid elasticity. The results highlight the dual role of electro-osmosis in enhancing flow dynamics and improving thermal transfer efficiency. Egea et al. [28] examined a Scraped Surface Heat Exchanger (SSHE) for solar energy storage, with an emphasis on preventing the build-up of solid PCM layers. Their key findings include faster energy release at higher HTF flow rates, optimal temperature differences between 20–25°C, and the identification of a critical scraping frequency for improved efficiency. Additionally, they proposed a highly accurate predictive model for solidification time.

Allehiany et al. [29] analyzed heat transfer in scraped surface heat exchangers (SSHEs) using a Williamson fluid model with electroosmotic effects in a narrow-gap design. Computational methods (BVP4C in MATLAB) and analytical solutions explore velocity, temperature, and pressure profiles under varying parameters like Weissenberg and Brinkman numbers. Results show that viscoelastic behavior enhances fluid flow, while electro-osmosis and medium mobility impact temperature and velocity. These results are validated against artificial neural network (ANN) predictions. Rahman and Dhiman [30] investigated a novel perforated conical baffle plate design with air deflectors to improve heat transfer in tubular heat exchangers. This design enhances turbulence and increases thermal efficiency by 2.51 times compared to conventional baffles. The study identified key performance factors, including the deflector inclination angle and pitch ratio, which significantly impact friction.

Despite these advancements, significant gaps remain in understanding the complex flow patterns and heat transfer mechanisms within SSHEs, particularly under extreme operational conditions such as high rotational speeds or when handling non-Newtonian fluids. While previous studies have made substantial progress in modeling SSHEs, many are limited by simplified assumptions, such as constant fluid properties or the lack of detailed geometric modeling. These limitations hinder the development of more accurate predictive models that can capture the full range of thermal and fluid dynamics in SSHEs under realistic operating conditions. In addition, Experimental analysis of these systems is often limited by difficulties in measuring local variables like velocity and temperature in real time. As a result, there is an urgent need for a comprehensive numerical model capable of accurately capturing the intricate thermal and fluid dynamics of SSHEs under realistic operating conditions

This study aims to bridge these gaps by developing a comprehensive three-dimensional numerical model that integrates the complexities of real-world SSHE systems, including non-constant fluid properties, detailed blade configurations, and realistic operational conditions. By building on recent advancements and addressing the limitations in current models, this work seeks to provide more accurate insights into the thermal and fluid dynamics of SSHEs, particularly in applications involving high-viscosity Newtonian fluids. The findings will offer valuable guidelines for optimizing SSHE performance and improving their efficiency in industrial processes.

GENERAL DESCRIPTION OF SSHES

The studied configuration, as well as the boundary conditions, are presented in Figures 1 to 4. It is an outer Aluminum cylinder (stator) with length L and diameter Ds, in which the outer wall maintains constant temperature Tp= 278.16 K. Within this cylinder, blades with thickness e are attached to the stainless steel inner shaft cylinder (rotor) with diameter Dr rotating at a constant rotation speed ω=120 rpm, 240 rpm, 360 rpm, 480 rpm, 600 rpm, scraping exchange surface. The clearance between the blade tip and the exchange surface δ=130μm. All dimensions of the configuration considered in this work were exactly the same as those given by Yataghene et al. [12,13]; they are summarized in Table 1.

The working fluid is Glycerin, modelled as a Newtonian fluid in a laminar regime with a viscosity that depends on temperature. Table 2 gives the physical properties of pure Glycerin, Stainless steel, and Aluminum used in the calculations.

Table 1. Geometrical Characteristics of the SSHE [13,15]

Characteristic	Value
Stator diameter, D_s	0.065m
Rotor diameter, D_r	0.04m
Stator length, L	0.4m
Total surface heat exchange, S_{ex}	0.095m^2
Total volume, V_t	0.0015m^2
Blade-stator clearance, δ	130μm
Blade thickness, e	0.005m
Number of blades	2-3-4

Table 2. Physical properties of materials [13,15]

Material	Viscosity(Pa.s)	Thermal conductivity (W.m^{-1}.K^{-1})	Heat capacity (J.kg^{-1}.K^{-1})	Density (kg.m^{-3})
Pure Glycerin	$\mu_T = 8.1.10^{-12}.\exp\left(\frac{7378.8}{T}\right)$	0.285	2435	1240
Stainless steel	-	16.27	502.48	8030
Aluminum	-	202.4	871	2719

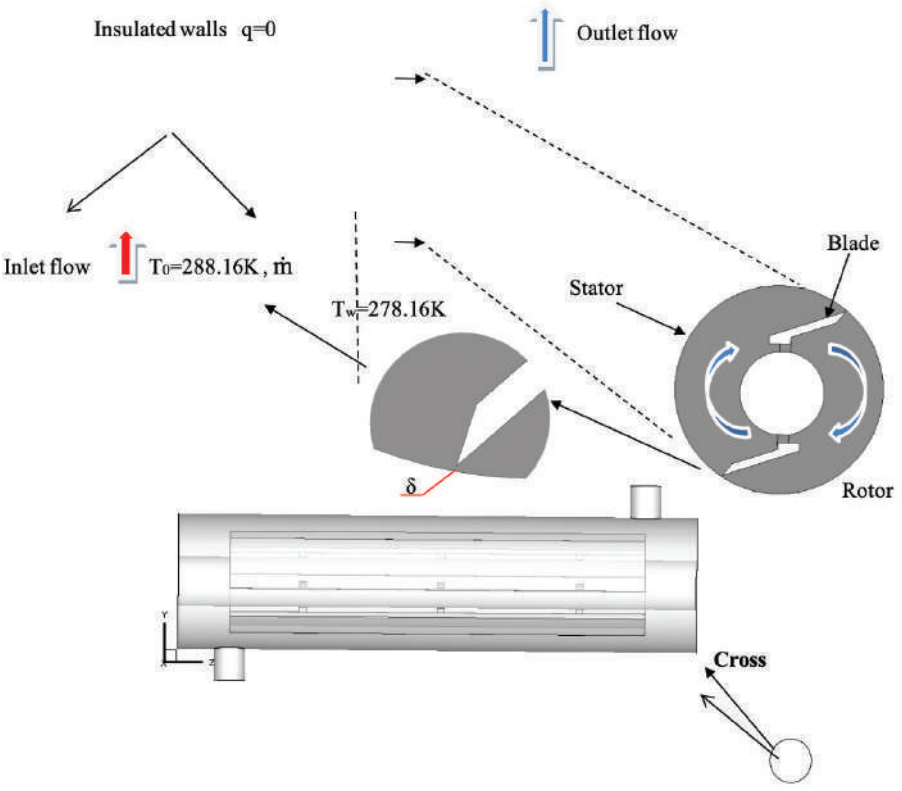

Figure 1. Computational domain and boundary conditions of SSHE, longitudinal and transversal cross-section.

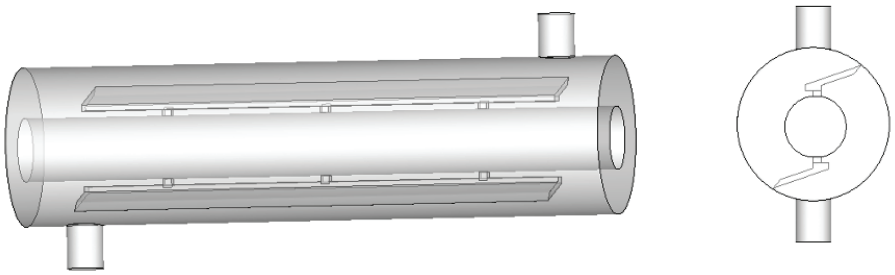

Figure 2. Isometric view of SSHE with 02 blades and transversal cross-section.

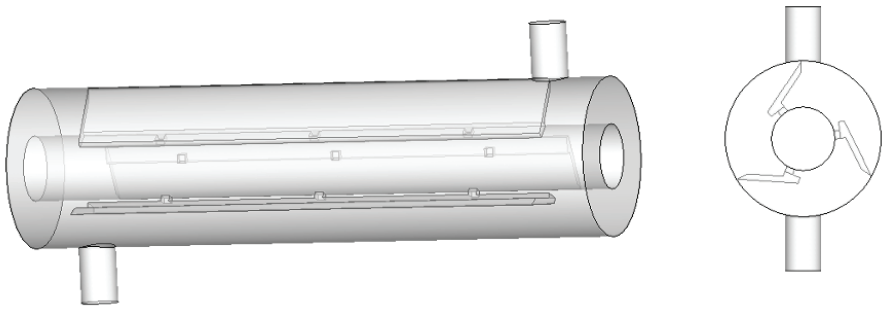

Figure 3. Isometric view of SSHE with 03 blades and transversal cross-section.

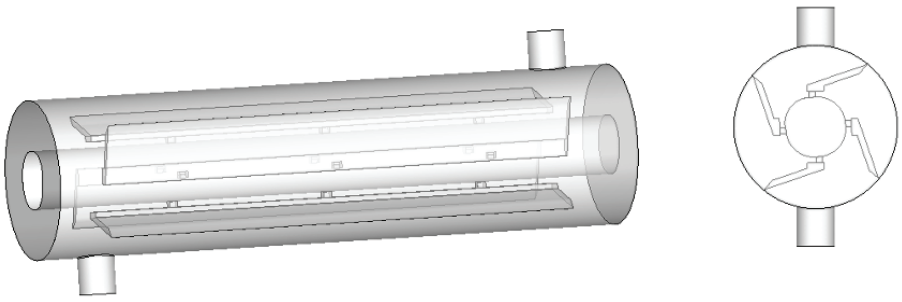

Figure 4. Isometric view of SSHE with 04 blades and transversal cross-section.

Governing Equations and Boundary Conditions

The fluid flow coupled with heat transfer within a scraped surface heat exchanger (SSHE) involves the consideration of non-isothermal, incompressible laminar flow. The conservation equations of mass, momentum, and energy are solved using Fluent software based on the Finite Volume Method. Due to the significant rotation of the fluid induced by the rotor and blades in the SSHE, it is essential to utilize the rotating reference frame formulation to address the continuity, momentum, and energy equations. The primary purpose of employing a moving reference frame is to transform an unsteady problem in the stationary (inertial) frame into a steady one relative to the moving frame [15]. When solving rotating frame problems with Fluent software, it is possible to use either the absolute velocity, $\vec{v}$, or the relative velocity, $\vec{v}_r$, as the dependent variable. These two velocities are related by an equation that allows for the accurately modelling of the fluid dynamics and heat transfer processes within the SSHE.

In steady-state conditions for the relative velocity, the system of equations can be written in the following vector form [12,13,15] :

The continuity equation

$$\nabla\left(\rho.\overrightarrow{V_r}\right) = 0 \tag{1}$$

$$\vec{V_r} = \vec{V} - (\vec{\omega}.\vec{r}) \tag{2}$$

Where,
$\vec{\omega}$ is angular velocity.
$\vec{V}$ is absolute velocity.
$\vec{r}$ is the position vector in rotating frame

-The momentum equation

$$\nabla\left(\rho\vec{V_r}.\vec{V_r}\right)+\rho\left(2\vec{\omega}.\vec{V_r}+\vec{\omega}.\vec{\omega}.\vec{r}\right)=-\nabla p+\nabla\bar{\bar{\tau}}_r+\rho.\vec{g} \quad (3)$$

$2\vec{\omega}.\vec{V}_r$ is the Coriolis acceleration
$\vec{\omega}.\vec{\omega}.\vec{r}$ is the centripetal acceleration

-The energy equation

$$\nabla\left(\rho.\vec{V_r}.H_r\right)=\nabla\left(k_f.\nabla T\right)+\nabla\left(\bar{\bar{\tau}}_r.\vec{V_r}\right) \quad (4)$$

The terms used in the equation (4) are forced heat convection, heat conduction, and viscous dissipation. The relative internal energy (Er) and relative total enthalpy (Hr) are the two terms used to express the energy equation. The following is a definition of these variables [34]:

$$E_r=h-\frac{p}{\rho}+\frac{1}{2}(V_r^2-(\omega.r)^2) \quad (5)$$

$$H_r=E_r+\frac{p}{\rho} \quad (6)$$

Boundary Conditions

As shown in Figure 1, the rotor and its blades, which are assumed to be thermally insulated, rotate at speeds ranging from 120 rpm to 600 rpm. The fluid enters the system at a temperature of 288.16 K with a mass flow rate between 0.017 kg/s and 0.086 kg/s and undergoes cooling. The heat transfer process involves passing the coolant over the stator to maintain a constant heat flux condition on the casing. The fluid flow adheres to the no-slip condition throughout the system, at solid surfaces and exits under both hydrodynamically and thermally fully developed conditions [12,13].

-At the stator surface: Tw=278.16K, v=0 (No-slip wall condition at the wall)

-On the rotor: insulated wall q=0, v=ω.r

-On the blades: insulated wall q=0, v=ω.r

-Inlet flow: mass flow rate ṁ , T_0=288.16K

-Outflow: $\left(\frac{\partial v}{\partial n}\right)=0$, $\left(\frac{\partial T}{\partial n}\right)=0$

-The average Nusselt number is calculated according to the following expression [31,32]:

$$\overline{Nu}=\frac{\bar{h}.d}{k_f}=\frac{q_c}{A.(\bar{T}_w-\bar{T}_m)}.\frac{d}{k_f} \quad (7)$$

Where $\overline{T}_w$ is the average temperature of the walls of the SSHE.

$\overline{T}_m$ is the average temperature of the fluid.

-The improvement of the heat transfer in the SSHE with 3 and 4 blades compared to the SSHE with two blades is estimated by percentage enhancement of the Nusselt number as follows [33,34]:

$$Enhancement\ \overline{Nu}_{3,4}\%=\frac{\overline{Nu}_{3,4}-\overline{Nu}_2}{\overline{Nu}_2}.100 \quad (8)$$

Where ;

$\overline{Nu}_{3,4}$ the average Nusselt number of SSHE with 3 and 4 blades.

$\overline{Nu}_2$ the average Nusselt number of SSHE with 2 blades.

NUMERICAL MODELING

Mesh Independence Study

For the three models of the scraped surface heat exchanger, tetrahedral cells were generated to mesh the computation domain as shown in Figure 5. A refined mesh is essential near places where there are high variations in flow properties, such as near the stator and the tips of blades, to capture the low fluid deformations.

In numerical studies, it is necessary to verify the effect of mesh resolution on the solution to ensure the accuracy and reliability of the numerical solution before performing calculations. Mesh independence was verified using different mesh sizes, as shown in Figure 6. The average convection coefficient ($\bar{h}$) was determined for all mesh faces at a mass flow rate ṁ = 0.017236 Kg/s and a rotational speed ω = 240 rpm. From Figure 6, we observe that the difference between the average convection coefficient values for the last three mesh sizes is slightly different, and the coefficient ($\bar{h}$) becomes insensitive to the number of nodes in the mesh at 876347. Therefore, we have chosen 876347 nodes for all our calculations to obtain accurate results with minimal computational time.

Number of nodes	$\bar{h}$(W/m².K
120797	287,62
178925	287,13
256341	286,81
314946	286,09
529173	285,82
619865	285,73
749532	285,61
876347	285,48
921875	285,43
987653	285,41

Solver Setting

Solidworks and Gambit software are used to create and mesh the geometry. Fluent6.3.26, a computational fluid dynamics (CFD) program, uses a finite volume approach to solve integral equations controlling mass, momentum, fluid conservation, and solid phase energy after receiving the mesh file. This model uses Fluent›s SIMPLE algorithm, a 3D double

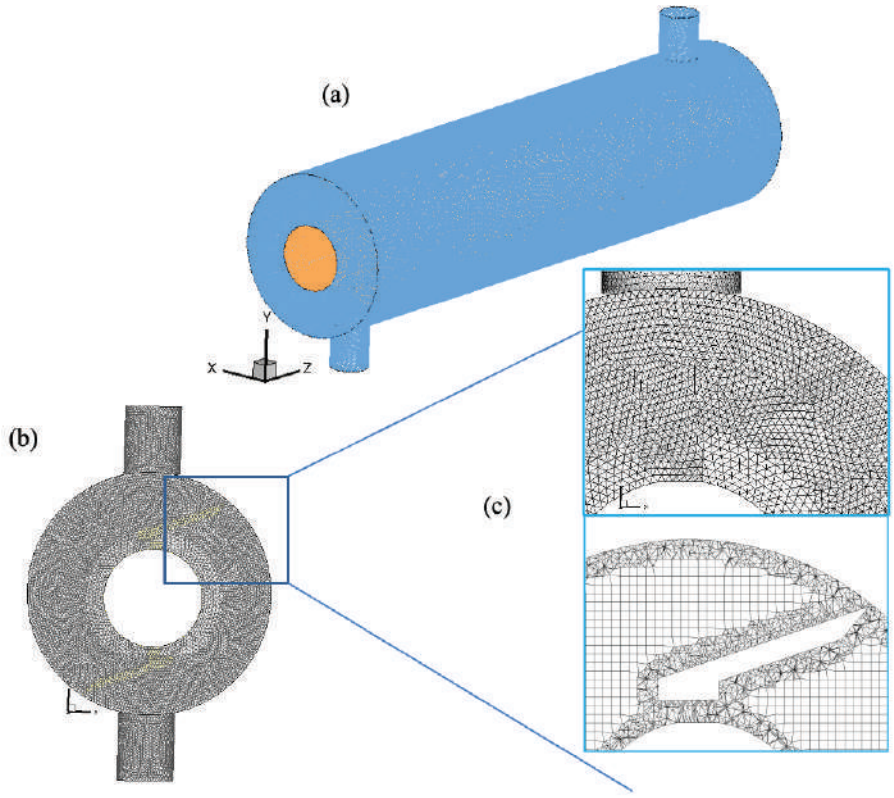

Figure 5. (a) Isometric view of computational mesh of SSHE; (b) Mesh of cross section in SSHE; (c) Enlarged view of the mesh near the clearance between the blade and stator in SSHE.

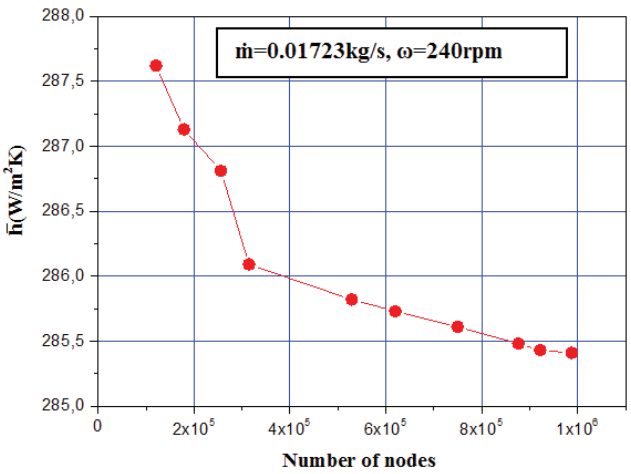

Figure 6. Variation of average convective heat transfer coefficient as a function of the number of nodes for ṁ = 0.017236 Kg/s and ω = 240 rpm.

precision pressure-based solver, a second-order upwind discretization scheme for momentum and energy equations, and the usual scheme for the pressure correction equation. When the normalized residual values for the momentum and mass equations approach 10-3 and the energy equations reach 10-6, respectively, convergence is considered satisfactory [35].

Validation of SSHE Models

In order to verify the accuracy of our simulation results, we calculate the convective heat transfer coefficient and compare it with the numerical data provided by Yataghene and Legrand [13] under identical dimensions and design

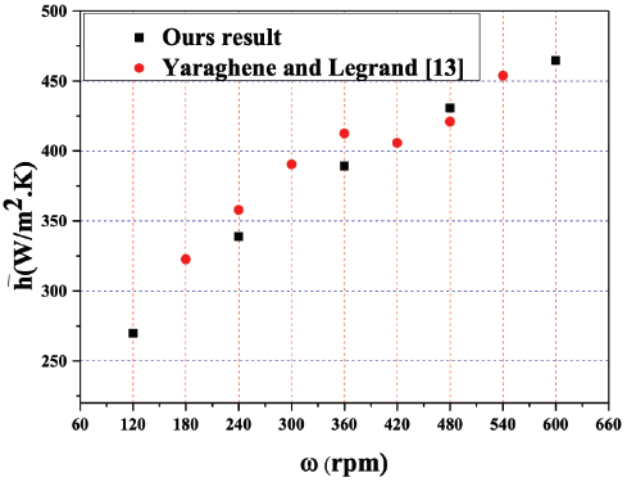

Figure 7. Variation of average convective heat transfer coefficient as a function of rotational speed: A comparison between our results and literature data.

conditions. As illustrated in Figure 7, the comparison demonstrates a favorable agreement, with a maximum deviation of less than 5% evident. This indicates that the methodology adopted in our numerical investigation is viable, and the obtained results can be considered reliable.

RESULTS AND DISCUSSION

This study delves into the impact of several critical factors on the thermal-fluid fields in a specific type of scraped surface heat exchanger (SSHE). Utilizing numerical simulations, the investigation aims to shed light on how these factors influence the performance and efficiency of the SSHE. Mass flow rate ṁ values are considered, which ranged from 0.017 kg/s to 0.086 kg/s. The SSHE with 02, 03 and 04 blades are examined in cases of rotational speed values ω= 120–600 rpm.

Temperature Field and Flow Characteristics in SSHE

The numerical results of the temperature contours are illustrated in Figures 8 to 13 via cross-sections within the scraped surface heat exchanger with 2, 3 and 4 blades for two rotation speeds ω=120 rpm and 600 rpm and for a mass flow rate ṁ =0,051584kg/s, and in different z-locations are

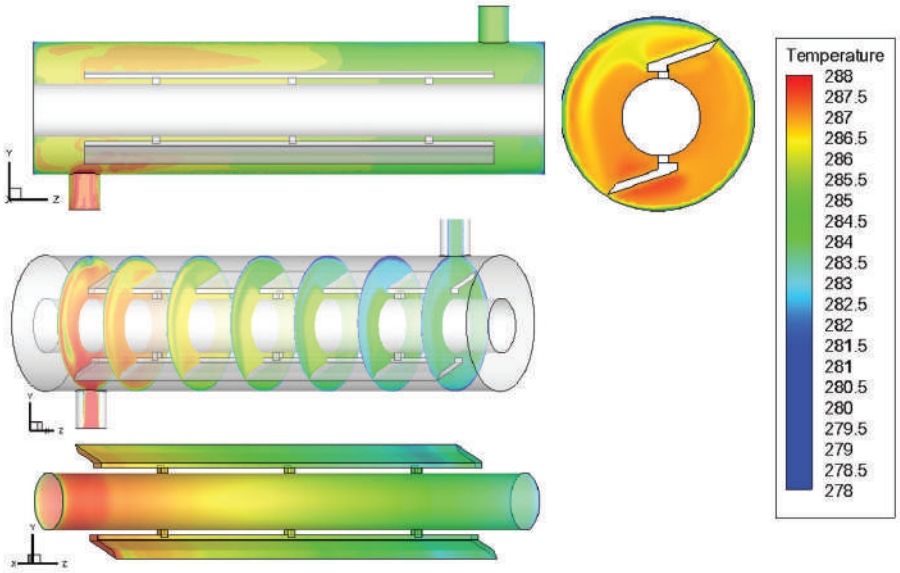

Figure 8. Temperature contour of SSHE with 2 blades in case of ω=120 rpm and ṁ = 0,051584 kg/s.

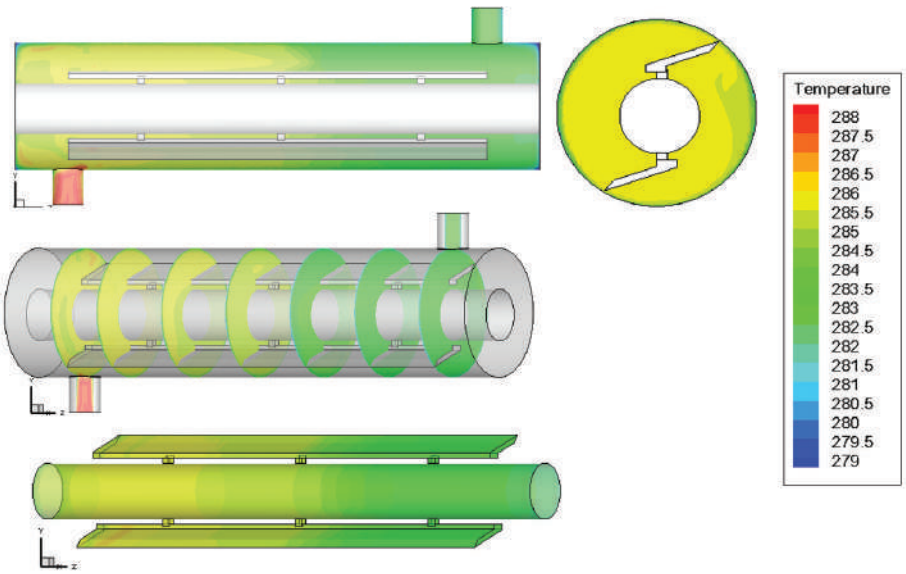

Figure 9. Temperature contour of SSHE with 2 blades in case of ω=600rpm and ṁ = 0,051584 kg/s.

for cross-sections . It is noticed that the fluid enters the heat exchanger cylinder with a temperature of 288.16 K and then gradually decreases In the axial direction, from the inlet towards the outlet, contacting the cold internal surface (278.16 K) of the cylinder. It is clear that in the last part, close to the exit of SSHE, the temperature has not reached the necessary cooling wall temperature, and the fluid leaves at higher temperatures than the cooled wall.

The temperature is not uniformly distributed throughout the heat exchanger, with a more significant temperature difference observed around the blades. This is due to the high shear gradients in these areas. The fluid temperature also decreases with an increase in the number of blades, rotation speed, and mass flow rate. These figures illustrate the development of thermal boundary layers around the blades. A comparison between the 2, 3, and 4-blade exchangers reveals that the thermal boundary layers of the 2-blade exchanger are thinner than those of the 3- and 4-blade exchangers. This is due to the reduction in fluid velocity near the blade surfaces reducing the heat exchange.

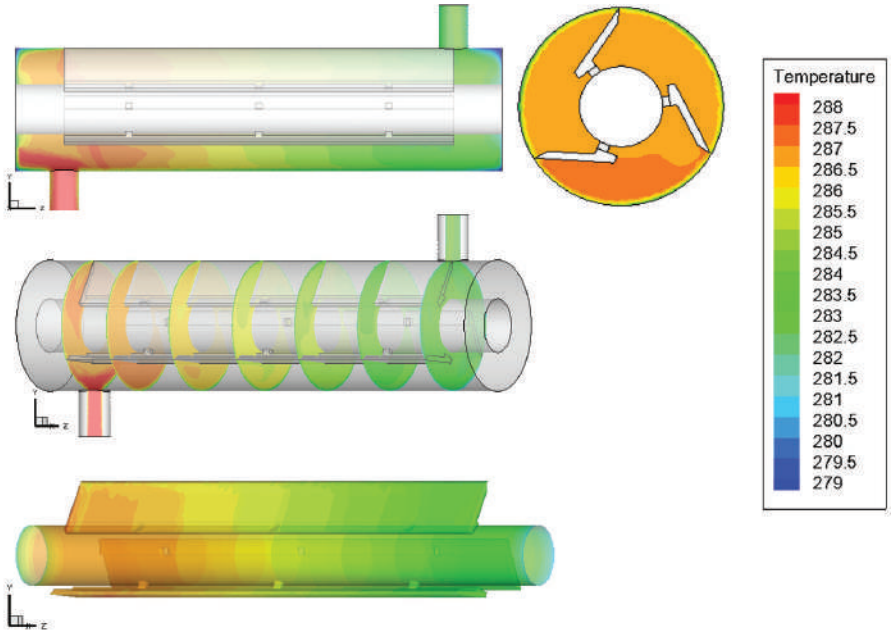

Figure 10. Temperature contour of SSHE with 3 blades in case of ω=120 rpm and ṁ = 0,051584 kg/s.

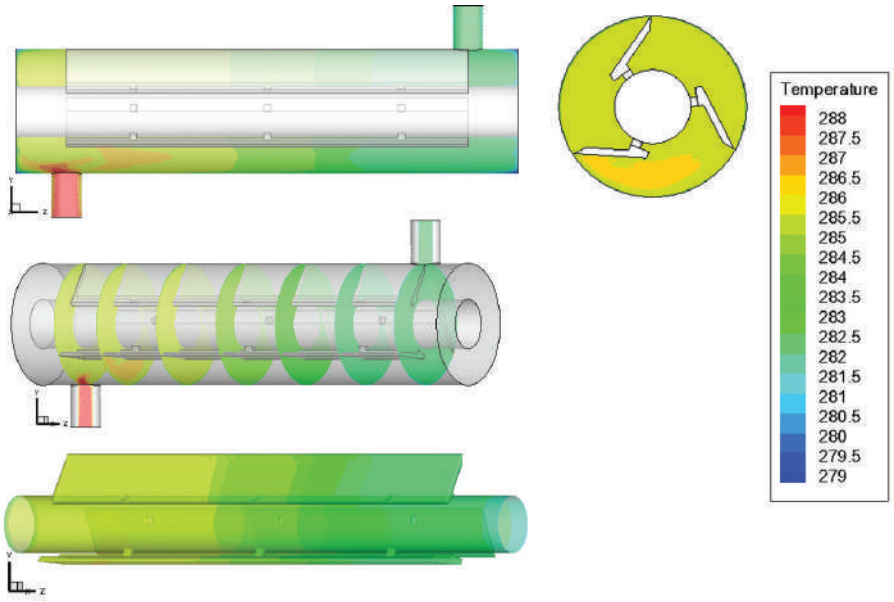

Figure 11. Temperature contour of SSHE with 3 blades in case of ω=600 rpm and ṁ = 0,051584 kg/s.

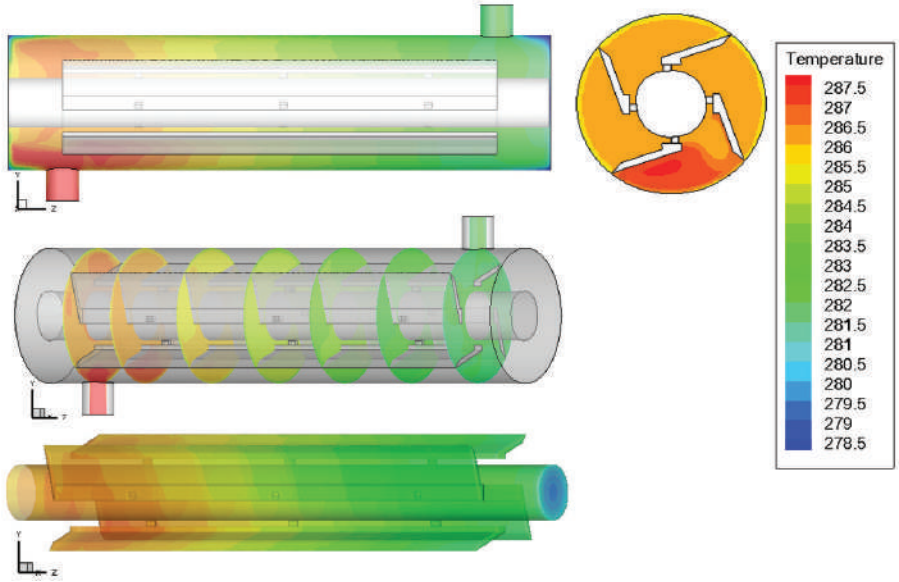

Figure 12. Temperature contour of SSHE with 4 blades in case of ω=120 rpm and ṁ = 0,051584 kg/s.

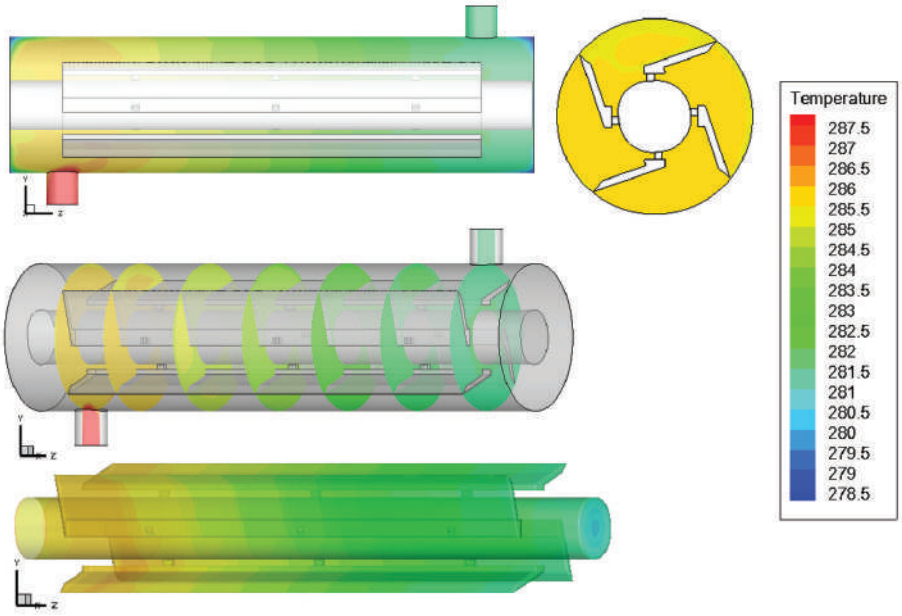

Figure 13. Temperature contour of SSHE with 4 blades in case of ω=600 rpm and ṁ = 0,051584 kg/s.

The Flow Streamlines

Figure 14 & 15 indicate the flow streamlines in the SSHE with two and four blades at rotational speeds ω of 120 rpm and 600 rpm and a mass flow rate ṁ of 0.035 kg/s, revealing significant insights into the fluid motion and heat transfer behavior. The rotational motion of the blades generates vortices on both sides of each blade, with larger vortices forming at the front of the blades due to the rotational forces and smaller vortices observed near the blade tips. These vortices enhance fluid mixing and disrupt the thermal boundary layer, facilitating improved heat transfer. The comparison between two and four-blade configurations indicates that the four-blade setup achieves higher fluid velocities due to increased disturbances and mixing, leading to enhanced convective heat transfer efficiency. At higher rotational speeds, such as 600 rpm, the vortices and fluid velocity intensify further, increasing the interaction between the blades and fluid and minimizing stagnant zones. This thorough mixing ensures consistent thermal exchange by continuously bringing cooler fluid into contact with the heat transfer surface. The findings highlight the critical role of vortex dynamics in optimizing SSHE

performance, with the four-blade configuration demonstrating superior thermal efficiency due to its ability to promote higher fluid velocities and better mixing.

Effect of the Number of The Blades and Rotational Speed

Figures 16 and 17 present the variation of the difference temperature ΔT and Tout as a function of the rotational speed obtained with two, three, and four blades in the case of ṁ = 0.05158 Kg/s

It can be observed that the increase of the number of blades (from two to four) in a scraped surface heat exchanger (SSHE) significantly enhances the heat transfer rate due to improved interaction between the cooling fluid and the exchanger walls. The additional blades increase the surface area of thermal convection, allowing more heat to transfer from the fluid to the walls. Moreover, the blades disrupt the thermal boundary layer more effectively, reducing resistance to heat transfer and facilitating greater convective heat exchange. The enhanced fluid agitation caused by the increased blade count also promotes better mixing, reducing temperature gradients within the fluid and ensuring cooler fluid is continuously brought into contact with the heat transfer surface. As a result, the outlet temperature (Tout) of the fluid decreases, reflecting the efficient removal of thermal energy. Simultaneously, the temperature difference (ΔT=To−Tout) grows, indicating improved cooling efficiency. The four-blade configuration, in particular, achieves superior thermal performance by effectively balancing enhanced heat transfer with fluid flow dynamics, making it more efficient than the two- and three-blade configurations. These results highlight the importance of optimizing blade count to maximize the cooling or heating capabilities of SSHEs in industrial applications.

As the rotational speed ω of a scraped surface heat exchanger (SSHE) increases, the outlet temperature Tout of the fluid decreases, indicating improved heat transfer efficiency. This improvement is primarily due to enhanced fluid mixing and increased interaction with the heat transfer surface at higher speeds. The faster rotation generates more turbulence and agitation within the fluid, disrupting

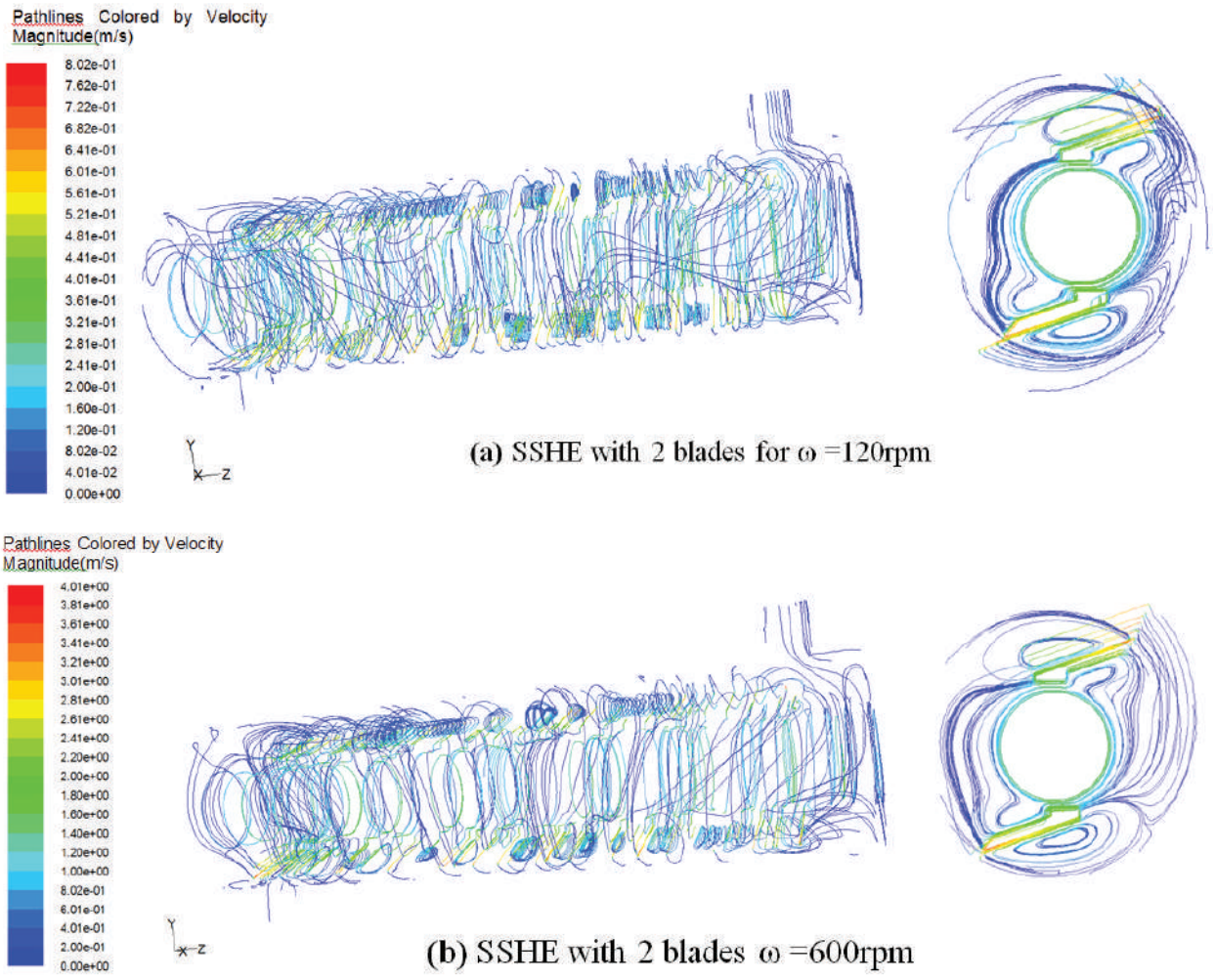

Figure 14. Pathlines in SSHE with two blades for ṁ = 0,035 kg/s and different rotational speed.

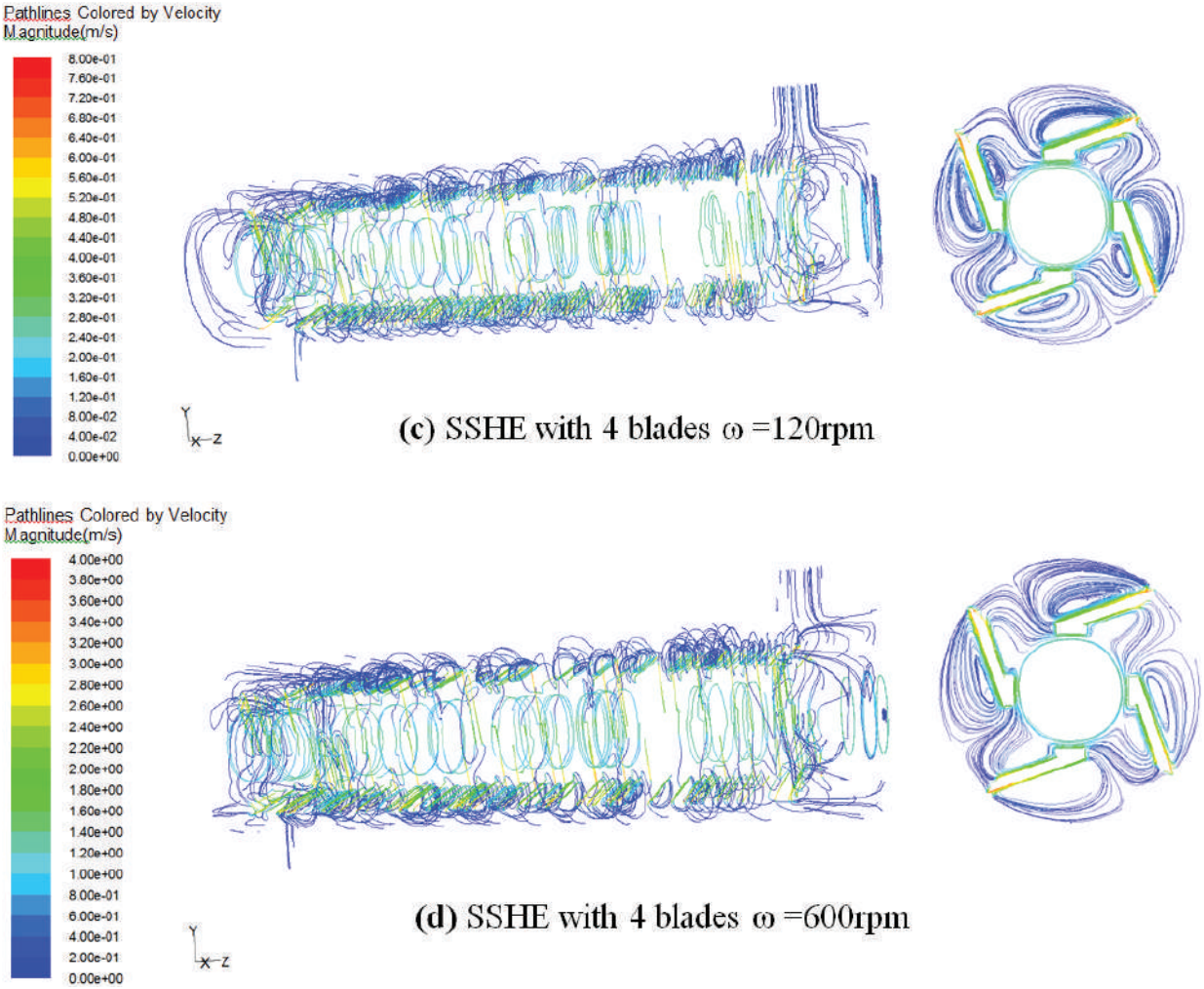

Figure 15. Pathlines in SSHE with four blades for ṁ = 0,035 kg/s and different rotational speed.

stagnant zones and ensuring uniform temperature distribution. Additionally, the increased velocity of the fluid near the blade walls reduces the thickness of the thermal boundary layer, lowering resistance to heat transfer and facilitating more efficient thermal energy exchange. Higher rotational speeds also produce stronger shear forces, which prevent fouling or sedimentation on the exchanger walls, further maintaining optimal heat transfer conditions. Moreover, the elevated rotational speed increases the mass flow rate of the fluid, reducing its residence time in the exchanger. However, this is offset by the enhanced convective heat transfer, ensuring that the overall thermal performance is significantly improved. These combined effects make higher rotational speeds a critical factor for optimizing SSHE efficiency, although careful consideration must be given to energy consumption and mechanical stress to maintain operational sustainability.

The effect of the number of scraper blades and rotational speed ω on the Nusselt number and its percentage enhancement are depicted in Figure 18. The results show that the Nusselt number increases significantly with the rotational speed ω of the SSHE. This increase is attributed to the enhanced velocity of the fluid flow, which intensifies shear forces and disrupts the thermal boundary layer near the heat transfer surface, thereby improving the convective heat transfer coefficient. However, as observed in the percentage improvements, the Nusselt number enhancement diminishes at higher rotational speeds. For instance, with four blades, the maximum enhancement (between SSHE with 4 and 2 blades) is 44.74% at 240 rpm, decreasing slightly to 43.78% at 360 rpm and further to 30.6% at 600 rpm. This reduction in improvement at higher speeds likely reflects diminishing returns as the system approaches its physical limits of convective heat transfer efficiency. The presence of four blades further enhances Nu by increasing the interaction between the fluid and the heat transfer surface, with the greatest impact observed at moderate speeds such as 240 rpm, where fluid mixing and energy input achieve an optimal balance. These findings emphasize the

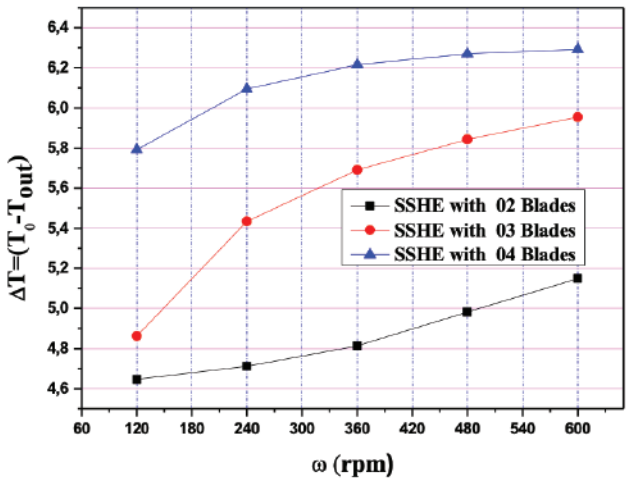

Figure 16. Variation of the difference temperature ΔT as a function of the number of the blades and the rotational speed for ṁ = 0.05158 Kg/s.

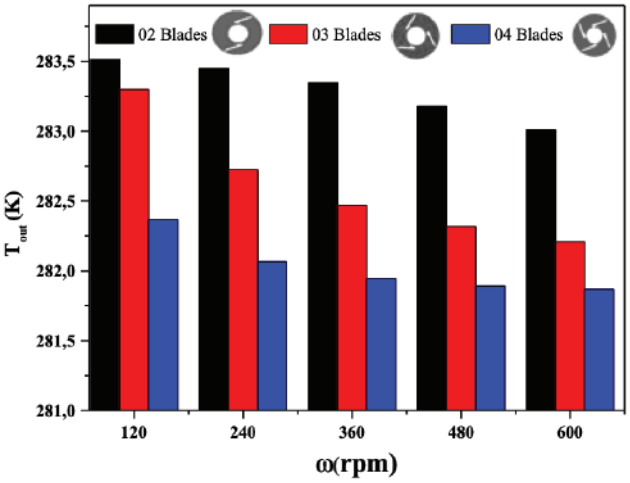

Figure 17. Variation of the temperature T_{out} as a function of the number of the blades and the rotational speed for ṁ = 0.05158 Kg/s.

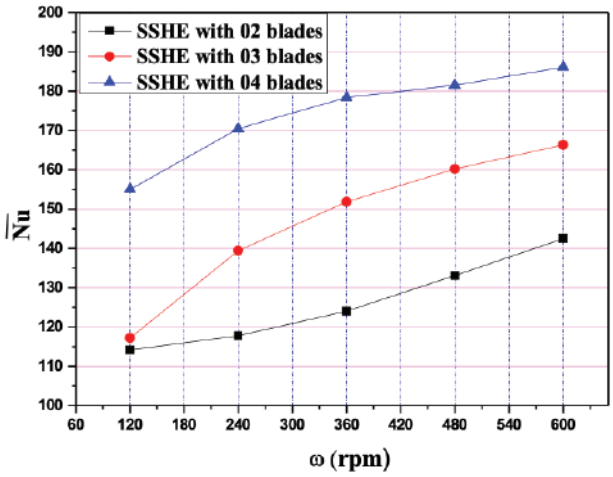

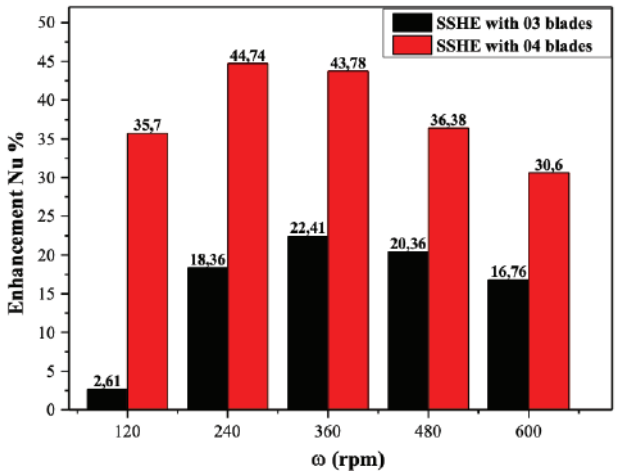

Figure 18. Variation of the average Nusselt number and its enhancement as a function of the rotational speed and the number of the blades for ṁ = 0.05158 Kg/s.

importance of optimizing rotational speed and blade count to maximize the heat transfer efficiency of SSHEs.

Effect of the Inlet Flow Rate

The inlet flow rate significantly influences the thermal performance of a scraped surface heat exchanger (SSHE). As illustrated in Figures 19 and 20, increasing the inlet flow rate results in a sharp decrease in the temperature difference ΔT between the inlet and outlet. This reduction is primarily due to the shorter residence time of the fluid within the SSHE, which limits the duration of thermal interaction with the heat transfer surface. Although higher flow rates enhance fluid velocity and turbulence, promoting better mixing and disrupting the thermal boundary layer, these advantages are counteracted by the reduced residence and mixing times.

For the Nusselt number, the relationship is more complex. At higher inlet flow rates, the fluid velocity increases, leading to enhanced turbulence and disruption of the thermal boundary layer, this promotes convective mixing and increases the heat transfer coefficient locally, resulting in an initial rise in the Nusselt number. However, as the flow rate continues to increase, the reduced residence time and diminished mixing opportunities within the SSHE offset these benefits. The fluid has less time to exchange heat with the walls, which decreases the overall heat transfer efficiency and causes the Nusselt number to plateau or even decline at very high flow rates.

Furthermore, the diminished mixing time due to higher flow rates reduces the effectiveness of the scraping blades, as the fluid moves too quickly to be adequately agitated by the blades. This further limits the disruption of the thermal boundary layer and the enhancement of convective heat transfer, which are crucial for improving Nu. Therefore, while higher flow rates initially lead to an increase in Nu, the improvement diminishes at higher rates as the balance between turbulence and residence time shifts unfavorably.

In summary, increasing the inlet flow rate enhances fluid velocity and turbulence, which can initially improve the Nusselt number. However, the reduced residence time and limited mixing at higher flow rates negatively impact the overall convective heat transfer efficiency. This highlights the need to optimize the inlet flow rate to maintain an effective balance between turbulence, residence time, and thermal interaction for maximising the Nusselt number and overall SSHE performance.

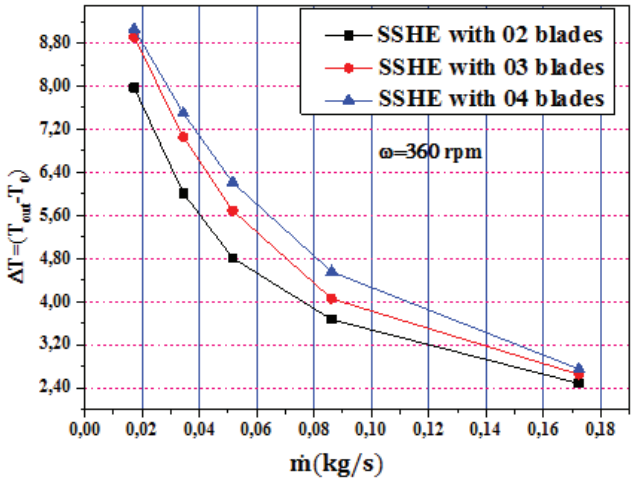

Figure 19. Variation of the difference temperature ΔT as a function of mass flow inlet ṁ and the number of the blades.

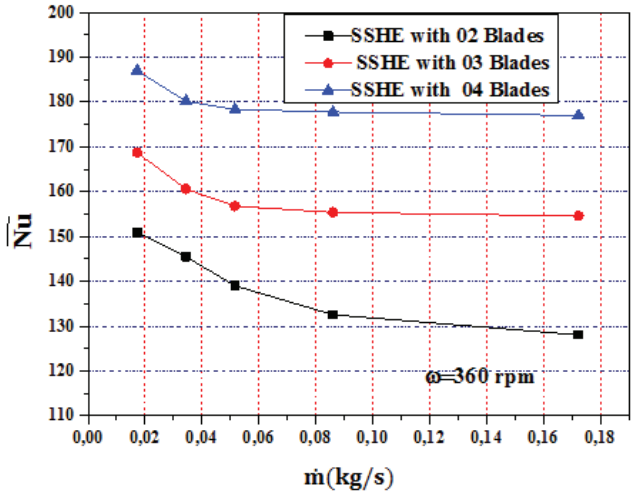

Figure 20. Variation of the average Nusselt number as a function of mass flow inlet ṁ and the number of the blades.

CONCLUSION

This study presented a detailed numerical analysis of the thermal and fluid dynamics performance of a Scraped Surface Heat Exchanger. The investigation focused on key parameters, including the number of blades, rotor speed, and mass flow rate, to optimize heat transfer efficiency and outlet temperature.

The primary findings are as follows:

- The non-uniform temperature distribution was observed, with enhanced cooling near the blades and the heat transfer surface. The thermal boundary layers were thinner in exchangers with fewer blades, which can reduce heat transfer efficiency.
- Increasing the number of blades improves heat transfer by enhancing fluid agitation and increasing the surface area available for convection. The four-blade configuration outperformed the two- and three-blade models in cooling efficiency.
- Higher rotor speeds improved convective heat transfer by boosting fluid velocity and reducing thermal resistance. However, excessively high speeds may require more energy input and should be balanced with system design limitations.
- The impact of mass flow rates on thermal performance was observed: higher flow rates enhance heat transfer but at the cost of increased outlet temperatures due to reduced residence time in the exchanger.
- The Nusselt number increases significantly with rotational speed, driven by intensified fluid velocity and shear forces that enhance convective heat transfer.
- The four-blade configuration delivers the highest Nu, with the greatest percentage improvement observed at moderate speeds (e.g., 44.74% at 240 rpm compared to the two-blade configuration).
- Moderate rotational speeds, such as 240 rpm, offer the best performance in terms of heat transfer efficiency, as they balance fluid mixing and energy input effectively.

Beyond the numerical insights, these findings have significant real-world implications for industries handling high-viscosity fluids, such as food processing, pharmaceuticals, and chemical engineering. The optimization strategies identified in this study can be leveraged to enhance industrial SSHE efficiency, reduce energy consumption, and minimize operational costs. However, real-world applications may introduce additional challenges, such as mechanical wear, energy demands, and hygiene requirements in regulated industries. Future research should explore advanced materials for enhanced durability, adaptive control systems to balance energy efficiency, and real-time monitoring. Additionally, investigating the performance of SSHEs with non-Newtonian fluids and alternative blade geometries can further refine their industrial applicability.

By bridging the gap between numerical modeling and industrial implementation, this study provides valuable insights that can guide engineers, manufacturers, and researchexrs in designing more efficient and sustainable SSHE systems. The integration of computational simulations with experimental validation will be essential for translating these findings into practical, real-world solutions that improve heat exchanger performance in large-scale applications.

NOMENCLATURE

A	Heat transfer area, m^2
d	Hydraulic diameter, m
D_s	Stator diameter, m
D_r	Rotor diameter, m
e	Blade thickness, m
E_r	Relative internal energy, J
H_r	Relative total enthalpy, J
$\overline{h}$	Average heat transfer coefficient, $W/m^2.K$
k_f	Fluid thermal conductivity, W/m.K
L	Stator length, m
$\dot{m}$	Mass flow rate of the fluid, kg/s
$\overline{Nu}$	Average Nusselt number
P	Pressure of the fluid, Pa
q	Heat flux, W
q_c	Convective heat flux, W
$\vec{r}$	Position vector in rotating frame, m
S_{ex}	Total surface heat exchange, m^2
T_0	Inlet temperature of the fluid, K
$\overline{T}_m$	Average temperature of the fluid, K
$\overline{T}_w$	Average temperature of the walls of the SSHE, K
$\vec{V}$	Absolute velocity, m/s
$\vec{v}_r$	Relative velocity, m/s
V_t	Total volume, m^3

Greek Symbols

δ	Blade-stator clearance, μm
μ	Dynamic viscosity, Pa.s
ρ	Density of air, kg/m^3
ω	Rotational speed, rpm

AUTHORSHIP CONTRIBUTIONS

Authors equally contributed to this work.

DATA AVAILABILITY STATEMENT

The authors confirm that the data that supports the findings of this study are available within the article. Raw data that support the finding of this study are available from the corresponding author, upon reasonable request.

CONFLICT OF INTEREST

The author declared no potential conflicts of interest with respect to the research, authorship, and/or publication of this article.

ETHICS

There are no ethical issues with the publication of this manuscript.

STATEMENT ON THE USE OF ARTIFICIAL INTELLIGENCE

Artificial intelligence was not used in the preparation of the article.

REFERENCES

[1] Huggins FE. Effect of scrapers on heating, cooling, and mixing. Ind Eng Chem 1931;23(7):749–53. [CrossRef]

[2] Trommelen A, Beek W. Flow phenomena in a scraped-surface heat exchanger («Votator»-type). Chem Eng Sci 1971;26(12):1933–42. [CrossRef]

[3] Harrod M. Scraped surface heat exchangers: A literature survey of flow patterns, mixing effects, residence time distribution, heat transfer, and power requirements. J Food Process Eng 1986;9:1–62. [CrossRef]

[4] Lee JH, Singh RK. Residence time distribution characteristics of particle flow in a vertical scraped surface heat exchanger. J Food Eng 1993;18:413–24. [CrossRef]

[5] De Goede R, De Jong EJ. Heat transfer properties of a scraped-surface heat exchanger in the turbulent flow regime. Chem Eng Sci 1993;48(8):1393–404. [CrossRef]

[6] Cenedese A, Doglia G, Romano GP, De Michele G, Tanzini G. LDA and PIV velocity measurements in free jets. Exp Therm Fluid Sci 1994;2(9):125–34. [CrossRef]

[7] Baccar M, Abid MS. Numerical analysis of three-dimensional flow and thermal behaviour in a scraped-surface heat exchanger. Rev Gén Therm 1997;36:782–90. [CrossRef]

[8] Alhamdan A, Sastry S. Residence time distribution of food and simulated particles in a holding tube. J Food Eng 1997;34:271–92. [CrossRef]

[9] Alhamdan A, Sastry SK. Residence time distribution of food and simulated particles in a model horizontal swept surface heat exchanger. J Food Process Eng 1998;21:145–80. [CrossRef]

[10] Baccar M, Abid MS. Numerical simulations of hydrodynamic and thermal behaviours in a scraped surface heat exchanger operating in turbulent regime. Int J Therm Sci 1999;38(7):634–44.

[11] Lakhdar MB, Cerecero R, Alvarez G, Guilpart J, Flick D, Lallemand A. Heat transfer with freezing in a scraped surface heat exchanger. Appl Therm Eng 2005;25:45–60. [CrossRef]

[12] Yataghene M, Francine F, Jack L. Flow patterns analysis using experimental PIV technique inside scraped surface heat exchanger in continuous flow condition. Appl Therm Eng 2011;31:2855–68. [CrossRef]

[13] Yataghene M, Legrand J. A 3D-CFD model thermal analysis within a scraped surface heat exchanger. Comput Fluids 2013;71:380–99. [CrossRef]
[14] Martínez DS, Solano JP, Illán F, Viedma A. Analysis of heat transfer phenomena during ice slurry production in scraped surface plate heat exchangers. Int J Refrig 2014;48:221–32. [CrossRef]
[15] Dehkordi KS, Fazilati MA, Hajatzadeh A. Surface scraped heat exchanger for cooling Newtonian fluids and enhancing its heat transfer characteristics: A review and a numerical approach. Appl Therm Eng 2015;87:56–65. [CrossRef]
[16] Błasiak P, Pietrowicz S. An experimental study on the heat transfer performance in a batch scraped surface heat exchanger under a turbulent flow regime. Int J Heat Mass Transf 2017;107:379–90. [CrossRef]
[17] Martínez DS, Illán F, Solano JP, Viedma A. Embedded thermocouple wall temperature measurement technique for scraped surface heat exchangers. Appl Therm Eng 2017;114:793–801. [CrossRef]
[18] Martínez DS, Solano JP, Vicente PG, Viedma A. Flow pattern analysis in a rotating scraped surface plate heat exchanger. Appl Therm Eng 2019;160:113795. [CrossRef]
[19] Pordanjani AH, Vahedi SM, Aghakhani S, Afrand M, Mahian O, Wang LP. Multivariate optimization and sensitivity analyses of relevant parameters on efficiency of scraped surface heat exchanger. Appl Therm Eng 2020;178:115445. [CrossRef]
[20] Maruoka N, Tsutsumi T, Ito A, Hayasaka M, Nogami H. Heat release characteristics of a latent heat storage heat exchanger by scraping the solidified phase change material layer. Energy 2020;205:118055. [CrossRef]
[21] Acosta CA, Yanes D, Bhalla A, Guo R, Finol EA, Frank JI. Numerical and experimental study of the glass-transition temperature of a non-Newtonian fluid in a dynamic scraped surface heat exchanger. Int J Heat Mass Transf 2020;152:119525. [CrossRef]
[22] Tombrink J, Bauer D. Simulation of a rotating drum heat exchanger for latent heat storage using a quasistationary analytical approach and a numerical transient finite difference scheme. Appl Therm Eng 2021;194:117029. [CrossRef]
[23] Tombrink J, Jockenhöfer H, Bauer D. Experimental investigation of a rotating drum heat exchanger for latent heat storage. Appl Therm Eng 2021;183:116221. [CrossRef]
[24] Ding Z, Qin FGF, Peng K, Yuan J, Huang S, Jiang R, Shao Y. Heat and mass transfer of scraped surface heat exchanger used for suspension freeze concentration. J Food Eng 2021;288:110141. [CrossRef]
[25] Egea A, García A, Herrero-Martín R, Pérez-García J. Experimental performance of a novel scraped surface heat exchanger for latent energy storage for domestic hot water generation. Renew Energy 2022;193:870–8. [CrossRef]
[26] Solano JP, Martínez DS, Vicente PG, Viedma A. Enhanced thermal-hydraulic performance in tubes of reciprocating scraped surface heat exchangers. Appl Therm Eng 2023;220:119667. [CrossRef]
[27] Imran A, Shoaib M, Nisar KS, Raja MAZ, Zahra A, Sabir Z. Electroosmosis oriented flow of Jeffrey viscoelastic model through scraped surface heat exchanger. Case Stud Therm Eng 2023;47:103031. [CrossRef]
[28] Egea A, García A, Pérez-García J, Herrero-Martín R. Parametric study of a scraped surface heat exchanger for latent energy storage for domestic hot water generation. Appl Therm Eng 2024;248(Part A):123214. [CrossRef]
[29] Allehiany FM, Imran A, Alqrni MM, Aljohani MA, Al-Mutairi T, Mahmoud EE. A computational investigation for heat and fluid transport with electro-osmosis phenomenon in a scraped surface heat exchanger. Case Stud Therm Eng 2024;61:104988. [CrossRef]
[30] Rahman MA, Dhiman SK. Thermo-fluid performance of a heat exchanger with a novel perforated flow deflector type conical baffles. J Therm Eng 2024;10:868–79. [CrossRef]
[31] Bakhti FZ, Si-Ameur M. A comparison of mixed convective heat transfer performance of nanofluids cooled heat sink with circular perforated pin fin. Appl Therm Eng 2019;159:113819. [CrossRef]
[32] Mishra S, Panda S, Baithalu R, Baithalu R. Enhanced heat transfer rate on the flow of hybrid nanofluid through a rotating vertical cone: A statistical analysis. Partial Differ Equ Appl 2024;20:100825. [CrossRef]
[33] Bakhti FZ, Si-Ameur M, Zerguine B. Enhancement of the cooling by mixed convection of a CPU using a rotating heat sink: Numerical study. Proc Inst Mech Eng Part E J Process Mech Eng 2024;238(1):144–57. [CrossRef]
[34] Al-Obaidi AR, Alhamid J. Influence of different geometrical dimple configurations on flow behaviour and thermal performance within a 3D circular pipe. J Therm Eng 2024;10:175–87. [CrossRef]
[35] Baithalu R, Mishra SR, Shah NA. Sensitivity analysis of various factors on the micropolar hybrid nanofluid flow with optimized heat transfer rate using response surface methodology: A statistical approach. Phys Fluids 2023;35(10):102016. [CrossRef]

J Ther Eng, Vol. 12, No. 1, pp. 115−127, January, 2026

Journal of Thermal Engineering
Web page info: https://jten.yildiz.edu.tr
DOI: 10.14744/thermal.0001063

Research Article

Pyrolysis, kinetics, and thermodynamic analysis of neem seed cake for the sustainable resource recovery

Manisha RANI[1], Rohan R. PANDE[1], Kamalesh A. SORATE[1,*]

[1]*Department of Mechanical Engineering, Sardar Vallabhbhai National Institute of Technology, Surat, 395007, India*

ARTICLE INFO

Article history
Received: 27 September 2024
Revised: 07 January 2025
Accepted: 15 January 2025

Keywords:
Activation Energy; Bioenergy; Endothermic Behavior; Kinetics; Seedcakes; Thermodynamics

ABSTRACT

Pyrolysis has considerable potential for the monetization and management of neem seedcake by producing value-added compounds. The decomposition of neem seedcake (NSC) was analyzed, occurs in three stages: moisture removal (30–220°C), active decomposition (220–550°C), and slow char formation (550–800°C). The activation energies for seedcake pyrolysis were calculated using the Starink, Kissinger-Akahira-Sunose (KAS), and Ozawa-Flynn-Wall (OFW) methods, yielding values 235.985 kJ/mol, 235.918 kJ/mol, and 228.026 kJ/mol, respectively. The product exhibited highest activation energy 429.335 kJ/mol. The reaction rate increases exponentially as activation energy decreases. The isoconversional methods were used to predict activation energy of neem seedcake with coefficient of determination (R^2) greater than 0.90. The reaction chemistry of NSC pyrolysis, characterized by high reactivity, was evidenced by thermodynamic parameters (entropy, enthalpy and gibbs free energy), which indicated increasing endothermic behavior as rate of conversion (α) increased from 0.20 to 0.75. The positive change in enthalpy (230.92 kJ/mol) throughout the process indicates, when neem seedcake decomposes, energy is absorbed (endothermic behavior) to break the complex chemical bonds. The neem seedcake pyrolysis promotes sustainable waste management, reduces pollution, decreases reliance on fossil fuels, and supports climate change efforts. This study enhances knowledge of biomass pyrolysis, especially for less-explored non-edible oil seedcakes.

Cite this article as: Rani M, Pande RR, Sorate KA. Pyrolysis, kinetics, and thermodynamic analysis of neem seed cake for the sustainable resource recovery. J Ther Eng 2026;12(1):115−127.

INTRODUCTION

Global energy consumption is on a continuous upward trend, fueled by the economic development and growing populations of rapidly developing economies. Rapid urbanization, industrialization, and population growth are causing energy shortages and increasing environmental pollution. Rising demand depletes non-renewable resources and worsens pollution, highlighting the need for sustainable energy solutions [1,2]. In this context, biomass is coming to the fore as a renewable energy source due to its diverse applications. Agricultural residues, a part of lignocellulosic biomasses, have the potential to replace

***Corresponding author.**
*E-mail address: kasorate@med.svnit.ac.in

This paper was recommended for publication in revised form by Editor-in-Chief Ahmet Selim Dalkilic

Published by Yıldız Technical University Press, İstanbul, Turkey
Yıldız Technical University. This is an open access article under the CC BY-NC license (http://creativecommons.org/licenses/by-nc/4.0/).

fossil fuels for energy recovery and convert them into value-added products[3]. India's agroecological conditions make it ideal for cultivating a variety of oilseeds, such as soybean, groundnut, mustard, neem, and castor seeds[4-6]. According to Food and Agriculture Organization (FAO) of United Nations (UN), global oilseed production reached 628.54 million metric tons (MMT) in 2020. India contributed 50.69 MMT to this total, positioning it as one of the world's leading oilseed producers (FAO, 2020) [4]. Based on the latest available data, global oilseed production for the 2023-24 season is projected at approximately 626 million metric tons, with soybeans being the predominant crop, accounting for 398 million metric tons. India remains a significant contributor to oilseed production, particularly in soybeans, rapeseed, and peanuts. De-oiled cake, a by-product of oilseed extraction, produces around 650 grams of residue for every kilogram of seeds processed [6]. A large amount is utilized as animal feed, namely for fish and ruminants, because of their high protein content.

Many oil seedcakes, particularly derived from inedible seeds, have hazardous compounds that restrict their direct application [6]. It is therefore essential to further investigate their potential applications. De-oiled cakes can be transformed into valuable products and biofuels, which helps with their disposal problem and provides an additional means of addressing today's energy-related issues. Various thermochemical processes, including incineration, pyrolysis, and gasification have recently gained attention as effective methods for valorizing de-oiled seedcakes. The production of important products including pyro-gas, biochar, and bio-oil is made possible via pyrolysis [7]. The designing of a pyrolyzer requires consideration of the kinetic and thermodynamic characteristics. Thermogravimetric analysis (TGA) is a method to study the thermal degradation behavior of lignocellulosic biomasses.

Numerous studies have explored a wide range of biomass sources to assess their potential for biofuel production using various analytical techniques. For example, activation energy for the kinetic models of plum pomace was found to be 210 kJ/mol [8]. A kinetic analysis of garlic husk, using multiple isoconversional models, revealed an average activation energy between 153 and 155 kJ/mol [9]. Further studies focused on biomass from deciduous trees, specifically neem and gooseberry kernels, evaluated through TGA and model-free techniques. The activation energies for these materials were found to range from 176.66 to 204.23 kJ/mol for neem kernels and 184.57 to 195.10 kJ/mol for gooseberry kernels [10]. Other deciduous tree biomasses, such as date palm seed, and golden shower tree seeds, were also subjected to thermogravimetric and kinetic analyses, with activation energies ranging from 164 to 174 kJ/mol [11], [12]. Additionally, pyrolytic and kinetic studies on sawdust, using TGA and model-free methods, the study demonstrated that activation energies increased from 80 to 252 kJ/mol as the conversion process advanced[13]. Singh et.al [6] investigated the pyrolysis of mustard seedcake to calculate activation energy of mustard oil residue (155 kJ/mol). Masawat et al. (2019)[14] used TGA to examine the pyrolysis properties of a Pongamia de-oiled cake and they found that the activation energy ranged from 97.2 to 412.2 kJ/mol. Sokoto et al. (2016) [15] examined the kinetics of seedcakes made from African star apples. They determined activation energy using the isoconversional approaches. Sahoo et al. [16] investigated the kinetics and thermodynamic parameters of a mixture of Pongamia pinnata and Sapindus emarginatus. Four model-free isoconversional techniques were used to derive the kinetic parameters. Hagig et.al [17] studied drying kinetics of hawthorn. A comprehensive review of existing literature highlights the significant potential of biomass from agricultural residues for pyrolytic and kinetic analysis, with many studies indicating the production of valuable pyrolysis products. However, it is evident that research focusing on the feasibility of converting biomass from neem trees into useful products remains limited.

Azadirachta indica, commonly known as neem, presents a reliable and sustainable feedstock option for biofuel production. Despite the widespread availability of neem, use of its seedcake as a feedstock for biofuel production remains underutilized. Neem seedcake can be thermally processed to produce biochar and biofuels, which have significant environmental benefits. NSC is rich in nitrogen and other nutrients, which adds value to the biochar produced from it. Biochar derived from NSC can serve as a soil conditioner, improving soil fertility and aiding in carbon sequestration. In the context of biofuels, these nanoparticle-enhanced fluids improve thermal properties, increasing the heat transfer efficiency of biofuel-based systems, which can enhance the overall energy performance of renewable energy processes [18]. Insulation-based systems can also be employed to enhance the efficiency of the existing system [19]. The study of its thermal degradation helps in developing biochar and biofuels with favorable properties for agronomic applications. Therefore, thermal degradation of NSC through pyrolysis presents a viable solution, enabling the breakdown of this abundant biomass into valuable biofuels and by-products.

The main objective of studying the thermal degradation behavior of NSC is to gain a comprehensive understanding of how this biomass decomposes under the influence of heat. This helps in modeling the decomposition behavior knowing the activation energy helps optimize the thermal processes used to convert biomass into useful products. The thermodynamic properties associated with the degradation process, provide insights into the energy requirements and efficiency of conversion processes. This knowledge is crucial for optimizing processes like pyrolysis, combustion, and gasification, which can convert neem seedcake into useful products such as biochar, bio-oil, and gases. The primary goal of this work was to evaluate kinetic parameters and thermodynamic properties of NSC pyrolysis.

In this study, three advanced isoconversional methods—Starink, Kissinger-Akahira-Sunose (KAS), and Ozawa-Flynn-Wall (OFW) are systematically applied to investigate the thermal degradation behavior of neem seedcake (NSC). Unlike model-fitting methods, isoconversional methods do not require a specific reaction model (such as first-order, second-order, etc.) to be assumed. This makes them more flexible and suitable for complex processes where the reaction mechanism is not fully understood or may change during the process [20]. These methods can be applied in diverse fields, such as polymer degradation, combustion, pyrolysis, oxidation reactions, and biomass conversion, where reactions may involve complex mechanism. These methods, which are widely recognized for their accuracy in evaluating the kinetics of thermal decomposition, have rarely been applied to NSC.

The novelty of this research is in its detailed examination of NSC's thermal and kinetic properties using isoconversional approaches to determine activation energy and reaction mechanisms without assuming a specific kinetic model. Moreover, current research on the pyrolysis of neem seedcake is scarce, particularly regarding its thermodynamic characteristics, kinetic parameters, and the thermal degradation patterns observed in the TGA and derivative thermogravimetric (DTG) analysis. This gap in knowledge makes the study particularly valuable, as it provides the comprehensive thermodynamic and kinetic analyses of NSC pyrolysis. The findings contribute to understanding of complex thermal reactions involved and lay groundwork for future research into optimizing biofuel production from NSC and similar non-edible oil seedcakes. By offering new data on reaction kinetics and degradation behavior, this study not only expands the scientific understanding of neem seedcake but also enhances its potential application in sustainable energy systems, positioning it as a promising feedstock for biofuel generation.

MATERIAL AND METHODS

Feedstock Characterization

The raw material used in this study was NSC, a byproduct of the oil extraction process, sourced from local oil mills. The ASTM D 3172-07 method was followed to determine moisture, ash, volatile matter, and fixed carbon of NSC. The de-oiled seedcakes were crushed and sieved to produce uniform size particles , dried in oven at 105 °C for 4 hours[21]. To assess the potential for converting NSC into value-added products, proximate analysis, ultimate analysis, and high heating value (HHV) were determined. The ultimate analysis identified the content of carbon (C), nitrogen (N), hydrogen (H), sulfur (S), and oxygen (O) in the NSC, using an Elementar Vario EL 111 model for C, H, N, S and O.

Thermogravimetric Study

The pyrolysis experiments were conducted using a cylindrical reactor made up of galvanized iron (GI), 80 mm of internal diameter and 75 mm of height was used to heat 100 grams of feedstock. The reactor used for pyrolysis was surrounded by a heater. A thermocouple was placed inside the reactor to monitor temperature of seed cake sample. A condenser was attached to reactor that condensed gases produced during pyrolysis. The bio-oil was taken in a flask at exit of condenser. A schematic illustrating setup used for these experiments is provided in Figure 1. J-type thermocouple, with an operating range of 0–750 °C and an accuracy of ±2.2%, was employed to record the pyrolysis temperature. The sample mass was measured using an Ohaus PR Precision Balance having a maximum capacity of 220 g. The overall uncertainty was determined using Holman's propagation of error approach, expressed through the square root method as given in Equation (1) [22–24]. Furthermore, Table 1 summarizes the accuracy, measurement range, and corresponding uncertainty values of the instruments used. Three sets of experiments were performed at 450°C, resulting in bio-oil, biochar, and pyrogas with an average value of 37.07%, 33.50% and 29.05% by weight respectively.

$$U_E = \left\{ \left[\left(\frac{\partial E}{\partial X_1} \right) u_1 \right]^2 + \left[\left(\frac{\partial E}{\partial X_2} \right) u_2 \right]^2 + \left[\left(\frac{\partial E}{\partial X_3} \right) u_3 \right]^2 + \cdots \left[\left(\frac{\partial E}{\partial X_n} \right) u_n \right]^2 \right\}^{1/2} \quad (1)$$

The total uncertainty associated with the measurement of weight (U_W, Eq. 2), temperature (U_T, Eq. 3), and total uncertainty (Eq. 4) was evaluated by considering instrument error, environmental effects, and calibration sensitivity. The combined uncertainty was then estimated using the root mean square (RMS) method.

$$U_W = \sqrt{I_W^2 + C_W^2 + R_W^2 + E_W^2} \quad (2)$$

$$U_T = \sqrt{I_T^2 + C_T^2 + R_W^2 + E_T^2} \quad (3)$$

$$total\ uncertainty = \sqrt{U_W^2 + U_T^2} \quad (4)$$

An SDT-Q600 thermal analyzer was used for TGA and DTG analysis. The 10 mg of NSC sample was carefully weighed and placed in a pan. The system was purged with an inert gas (nitrogen, 100 ml/min) to prevent unwanted reactions with atmospheric oxygen unless oxidative conditions are required. The furnace was then heated from ambient temperature to 800°C at desired heating rate (5°C/min, 10°C/min and 20°C/min). The TGA continuously recorded the sample's mass change with temperature. The uncertainty analysis for the instrument used is done as per as per Holman's square root rule[22], [23], [25] The range, resolution and sensitivity of the instrument is shown in Table 2.

The thermal decomposition behavior was analyzed using the Starink, KAS, and OFW methods. Applying

Table 1. Measurement range, accuracy, and associated uncertainty

Measuring Device	Range	Accuracy	Uncertainty (%)	Total uncertainty
Weighing scale	0-220 g	Uncertainty (I_W): ±0.001g Calibration (C_W): ±0.001g Environmental influence (E_W): ±0.001 g Repeatability (R_W) : ±0.001g	0.002	0.62%
Thermocouple (J-type)	-200°C-750°C	Inherent uncertainty (I_T): ±2.2 °C Calibration (C_T): ±1°C Repeatability (R_T): ±1°C Environmental influence (E_T): ±1°C	0.62	

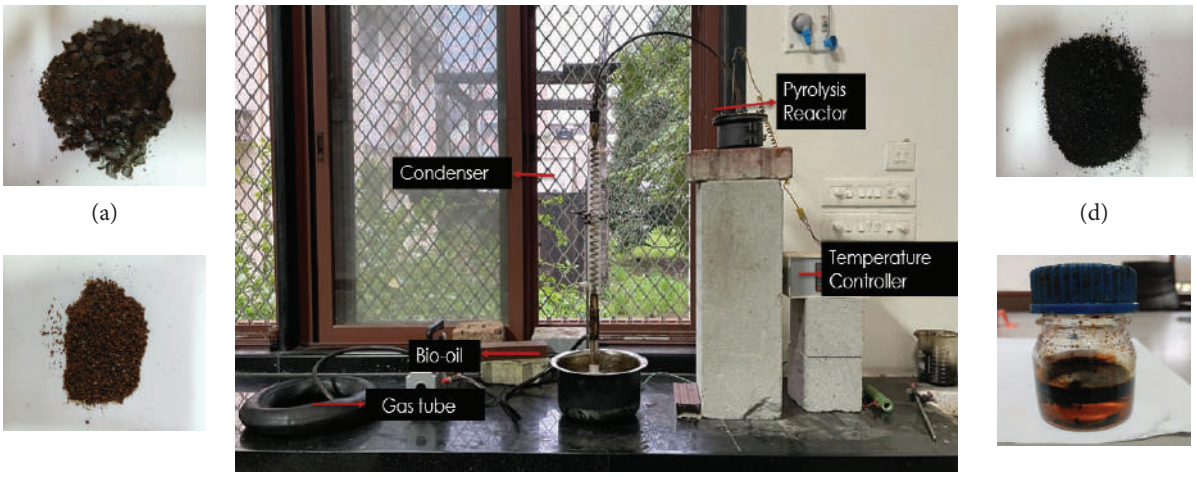

Figure 1. (a). Neem seedcake ;(b) Crushed seedcake; (c) lab-scale experimental setup; (d) biochar; (e) bio-oil.

Table 2. Parameters, range, resolution and uncertainty

Parameters	Range	Resolution	Uncertainty (%)	Overall uncertainty
Measuring balance	0-200 mg	±0.1 µg	0.001	0.53%
DTG	ambient-1500°C	±0.001°C	0.000125	
Heating rate	0.1-25°C/min	0.1°C/min	0.5%	
Thermocouple	0-1500°C	±1.5°C	0.1875	

isoconversional kinetic models to analyze pyrolysis involves a step-by-step process to determine the activation energy and other thermodynamic parameters (Fig. 2).

Kinetic Parameters

The thermal degradation of solid can be represented using following equations. The degree of conversion (α) was calculated using Equation (5).

$$\alpha = \frac{m_t - m_\infty}{m_0 - m_\infty} \quad (5)$$

Here , initial sample mass is m_o, mass at time 't' is m_t, and final mass is m_∞. The decomposition rate is characterized by temperature function k(T) and conversion function f(α). The rate of reaction is determined by using equation (6).

$$\frac{d\alpha}{dt} = k(T) \times f(\alpha) \quad (6)$$

The temperature function k(T) is expressed by equation (7).

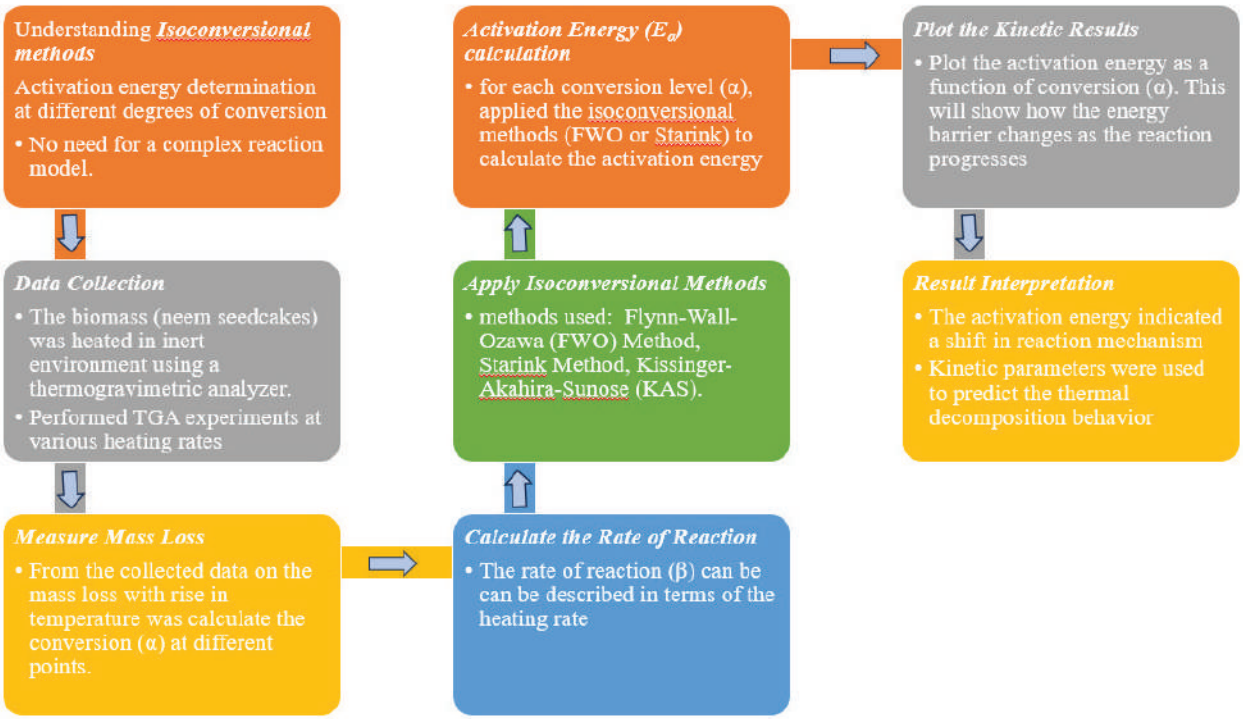

Figure 2. A step-by-step process to determine kinetic and thermodynamic parameters.

$$k(T) = Aexp(-E_\alpha/RT) \quad (7)$$

Where, A, E_α, R and T are the pre-exponential factor, activation energy at α, gas constant and temperature respectively. The relationship between temperature (T) and time (t) is dT = βdt, where β is heating rate. So, Equation 6 is written as Equation (8).

$$\beta \frac{d\alpha}{dT} = A\, exp\left(\frac{-E_\alpha}{RT}\right) f(\alpha) \quad (8)$$

Integrating the equation (8), is written as equation (9).

$$g(\alpha) = \oint \frac{d\alpha}{f(\alpha)} = \frac{A}{\beta} \oint exp\left(\frac{-E_\alpha}{RT}\right) dT = \frac{AE_\alpha}{\beta R}\, P(u) \quad (9)$$

Where g(α) is the integral form of the reaction model and u = E_α/RT. P(u), is temperature integral. The objective of the kinetic analysis is to develop mathematical correlations between temperature, conversion extent, and process rate. The parameter Eα denotes the activation energy barrier, while A reflects the frequency factor related to the vibrations of the activated complex. The reaction pathway is interpreted using either f(α) or g(α) [26],[27]. In the study of reaction kinetics, particularly for complex reactions, the lack of an explicit solution for the temperature-dependent function P(u) necessitates the use of approximation methods. Acar et.al [28] explored various drying models to identify the most suitable one for predicting moisture loss and drying kinetics. Without assuming a reaction mechanism, E_α can be estimated using isoconversional methods [16]. The ICTAC Kinetics Committee suggests commonly applied integral isoconversional approaches, namely Starink, KAS, and OFW [17]. These techniques allow the determination of kinetic parameters without requiring an explicit expression for P(u).

Thermodynamic Properties

The thermodynamic properties, specifically the enthalpy change (ΔH), the Gibbs free energy change (ΔG), and the entropy change (ΔS) were determined using the E_α and A values calculated from Starink, KAS, and OFW methods using following equations (10), (11), (12) and (13).

$$A = \frac{\beta E_\alpha exp(\frac{E_\alpha}{RTm})}{RT_m^2} \quad (10)$$

$$\Delta H = E_\alpha - RT \quad (11)$$

$$\Delta G = E_\alpha + RTln(\frac{K_B T_m}{hA}) \quad (12)$$

$$\Delta S = (\Delta H - \Delta G)/T_m \quad (13)$$

where K_B is the Boltzmann constant (1.381×10^{-23} J/K), h is the Plank constant (6.626×10^{-34} J.s), and T_m is DTG (derivative thermogravimetric) peak temperature (K).

RESULTS AND DISCUSSIONS

Characterization of NSC

The proximate and ultimate analyses, along with the higher heating value (HHV) of NSC (Table 3), were conducted to assess their suitability for the pyrolysis process and compare their characteristics with those of other biomass materials. The volatile matter (VM) content should be between 70-80%, with ash content below 10%. These characteristics high VM and low ash content indicate suitability of such feedstocks for thermal processes. The ultimate analysis revealed that NSC has carbon content (≥43%), making it viable option for fuel and energy recovery. Additionally, the low sulfur and nitrogen content in NSC suggests that the generation of SOx and NOx during pyrolysis would be minimal. The HHV of feedstock is 20.40 MJ/kg, comparable to HHVs of similar biomasses used in pyrolysis, like peanut shells and de-oiled mustard cake (19.4 MJ/kg)[6], (18.95 MJ/kg)[29], beauty leaf seedcake (19.20 MJ/kg)[30] and macadamia nutshell (19.367 MJ/kg)[31]. Overall, the proximate composition of NSC lies within the typical range reported for other biomass feedstocks utilized in pyrolysis. The HHV was measured by using equation (14)[32].

$$HHV\left(\frac{MJ}{kg}\right) = 0.3491C + 1.1783\,H - 0.1034\,O + 0.1005\,S - 0.0151\,N \quad (14)$$

Thermogravimetric Analysis

The TGA profile of NSC under a nitrogen atmosphere (0.1 L/min) at three different heating rates is presented in Fig. 3(a). The analysis indicates that temperature range of 220–550 °C representing active pyrolysis zone. Three distinct weight-loss phases are observed in the TGA curve. In the initial stage, from ambient temperature up to 220 °C, the decomposition is minimal, primarily involving moisture removal (~8%). The second stage, occurring between 220 °C and 550 °C, exhibits a pronounced weight loss (~74%), as reflected by a sharp decline in the TGA curve and a prominent peak in the DTG plot [33]. During this phase, feedstock undergoes cracking reactions, and decarboxylation, leading to the evolution of volatiles and char formation [34]. This stage represents the active pyrolytic zone, where the majority of decomposition occurs and the char residue is formed. The third stage, observed at temperatures above 550 °C, corresponds to the passive pyrolysis zone. Here, residual chemical bonds are broken, and the remaining molecular skeletons undergo slow degradation [35]. Lignin decomposition dominates this stage, while cellulose degradation contributes to the central DTG peak observed between 320–370 °C [16],[37]. Comparatively, other de-oiled biomass feedstocks show DTG peaks in similar ranges, such as mustard oil residue (170–510 °C) [6] and African star apple (150–400 °C) [36].

Table 3. Ultimate analysis, proximate analysis, and HHV of neem seedcake

NSC	Proximate analysis				Ultimate Analysis					HHV (MJ/kg)
	Volatile matter (%)	Moisture (%)	Fixed Carbon (%)	Ash (%)	C (%)	N (%)	O (%)	S (%)	H (%)	
	77.83	7.13	6.91	8.13	48.88	3.00	42	0.00	6.48	20.40

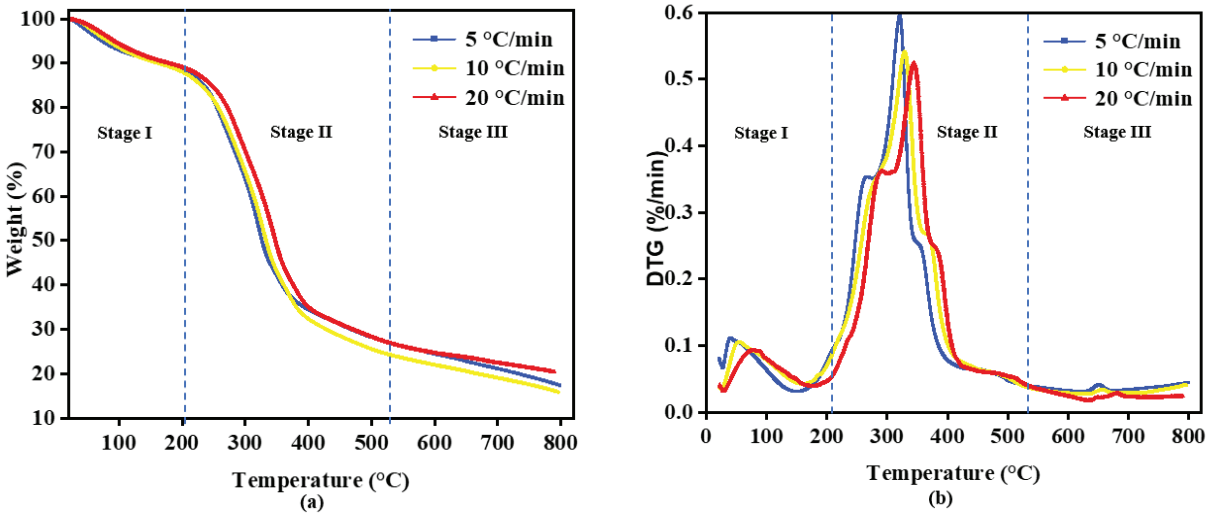

Figure 3. (a) Thermogravimetric Analysis (TGA) and (b) Derivative Thermogravimetric (DTG) curves for neem seedcake pyrolysis at varying heating rates.

The peak temperatures recorded for NSC during thermal degradation were 323, 330, and 340 °C at heating rates of 5, 10, and 20 °C/min, respectively, with corresponding residual masses of 17.32%, 15.89%, and 20.39%. These peak values were determined from the DTG curves (Fig. 3(b)), highlighting dependence of thermal decomposition on the heating rate.

Kinetic Parameters

Three model-free isoconversional approaches: Starink, KAS, and OFW methods were used to determine the kinetic parameters [38]. The isoconversional principle asserts that temperature alone determines the reaction rate at a given degree of conversion. This can be demonstrated by evaluating logarithmic derivative of equation (6), at α = const.

$$\left[\left(\frac{\partial ln\left(\frac{d\alpha}{dt}\right)}{\partial T^{-1}}\right)\right]_{\alpha} = \left[\left(\frac{\partial lnk(T)}{\partial T^{-1}}\right)\right]_{\alpha} + \left[\left(\frac{\partial lnf(\alpha)}{\partial T^{-1}}\right)\right]_{\alpha} \quad (15)$$

The subscript denotes values corresponding to a particular degree of conversion, representing isoconversional data. The second term in eq. (15) is zero, and f(α) remains constant when α=const.

$$\left[\left(\frac{\partial ln\left(\frac{d\alpha}{dt}\right)}{\partial T^{-1}}\right)\right]_{\alpha} = -\frac{E_{\alpha}}{R} \quad (16)$$

The relation in the equation above is used to determine the E_α of biomass using model-free method, without any reaction model assumption. The factor A, E_α, and coefficient of determination (R^2) were determined at fixed conversions, for temperature range from ambient to 800°C [33]. It is suggested to determine E_α within α = 0.05 to 0.95 with a step size not larger than 0.05 [38]. During the first stage, E_α increases slowly up to a 0.20 conversion, indicating low reactivity up to 220°C, where only moisture and impurities were removed. During the second stage, from 0.20 to 0.75 conversion, E_α increased as the devolatilization process occurred, decomposing the volatile matter present in NSC between 220 and 550°C. Beyond a 0.75 conversion, activation energy decreased due to minimal amount of volatile matter remaining. The isoconversional models by Starink, KAS, and OFW are expressed as equation (17), equation (18), and equation (19).

$$\ln\left(\frac{\beta}{T^{1.92}}\right) = Constant - 1.0008\frac{E_{\alpha}}{RT} \quad (17)$$

Therefore, a plot of $\ln(\beta/T^{1.92})$ vs 1/T, will be a straight line for given α. The E_α is calculated using slope of straight line, or −1.008 E_α/R.

$$\ln\left(\frac{\beta}{T^2}\right) = Constant - \frac{E_{\alpha}}{RT} \quad (18)$$

Therefore, a plot of $\ln(\beta/T^2)$ versus 1/T, at various heating rates, will be a straight line for given α. The E_α is calculated using slope of straight line, or $-E_\alpha/R$.

$$\ln(\beta) = Constant - 1.052\frac{E_{\alpha}}{RT} \quad (19)$$

Therefore, a plot of ln(β) versus 1/T, at various heating rates will be a straight line for given α. E_α is calculated as −1.052 E_α/R, slope of straight line.

Linear plots for Starink, KAS, and OFW methods are presented in Fig. 4(a), 4(b), and 4(c), respectively. These plots are employed to evaluate E_α across a conversion range of α=0.05–0.95. For neem seedcake, this plot helps to identify how the activation energy changes as the pyrolysis progresses. This method is particularly useful in determining the multi-step nature of biomass pyrolysis reactions, as deviations from linearity can indicate changes in reaction mechanisms. During the pyrolysis of NSC, the activation energy may vary across different stages, reflecting multiple reaction mechanisms. The variation in activation energy indicates the involvement of numerous overlapping reactions with distinct energy barriers, particularly the decomposition of hemicellulose and lignin. The reliability of the selected kinetic methods is indicated by R^2>0.90. The activation energy (E_α) increases with conversion (α) due to the occurrence of multiple endothermic reactions and sequential decomposition of cellulose, lipids, and proteins at different temperatures [26]. As shown in Table 4, the activation energy (E_α) varies with conversion, ranging from 73.14 to 429.28 kJ/mol, 72.9664-429.336 kJ/mol, and 69.3534–415.2271 kJ/mol, for Starink, KAS, and OFW approaches with the value (R^2 ≥ 0.90), respectively. The average values of E_α obtained by the Starink, KAS, and OFW methods are 249.258 kJ/mol, 230.853 kJ/mol, and 228.026 kJ/mol. The variation of E_α with alpha is shown in Fig. 5.

Equation (10) was used to calculate factor A. The number of molecular collisions required for a reaction is measured by A. For A $<10^9$ s^{-1}, the reaction is surface-dependent, and A $>10^9$ s^{-1} suggests a complex reaction[26]. For NSC, values of A ranged from 10^{14} to 10^{37} at 0.05 to 0.95 conversions, indicating the presence of complex reactions. Table 4 presents value of 'A' evaluated using Starink, KAS, and OFW methods, ranging from 10^{12}- 10^{35}, 10^{12}–10^{35}, and 10^{12}–10^{34} s^{-1}, respectively. Table 4 indicates the variation of factor 'A' with conversion similar to the changes in E_α, and the wide range of 'A' suggests that NSC decomposition is complex. At a 0.20 conversion, both E_α and A were quite low, while at a 0.75 conversion, they were A = 10^{35}-10^{37} s^{-1} and E_α = 415.22-429.28 kJ/mol, indicating low reactivity at 0.20 conversion and the highest reactivity at 0.75 conversion. The average value of 'A' was 9.16×10^{33}, $9.3\times10^{33,}$ and 1.7×10^{33}s−1 for Starink, KAS, and OFW methods, respectively.

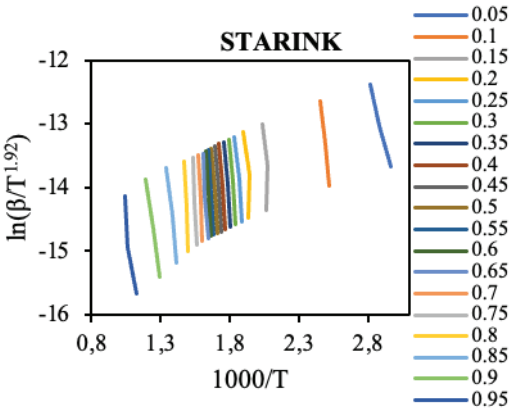

Figure 4. (a) ln(β/T1.92) vs (1/T) for Starink.

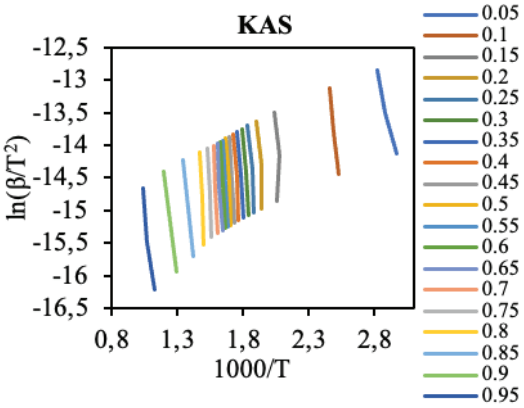

Figure 4. (b) ln(β/T2) vs (1/T) plot for Kissinger-Akahira-Sunose.

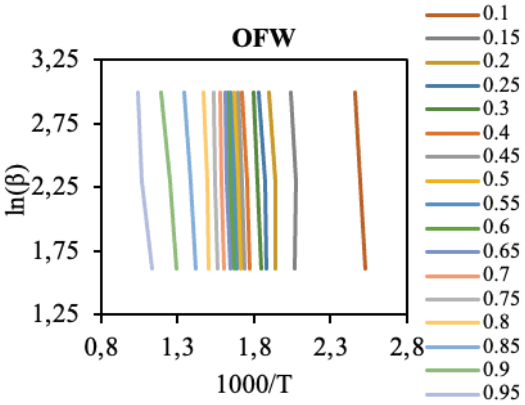

Figure 4. (c) ln(β) vs (1/T) plots for Ozawa-flynn-wall.

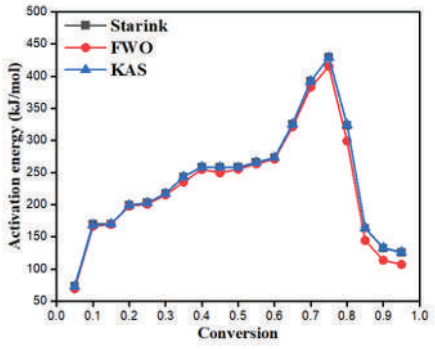

Figure 5. The variation in activation energy to conversion rate for neem seedcake.

Thermodynamic Analysis

Understanding the energy potential and distribution of a reaction requires understanding its thermodynamic properties ΔH, ΔG, and ΔS. ΔH_α, ΔG_α, and ΔS_α were determined for NSC at 20°C/min (Table 5). These properties were determined by substituting E_α values into Equations (11), (12), and (13) respectively. The graph of enthalpy change (ΔH) versus conversion rate (α) (Fig. 6) for the decomposition of neem seedcake provides insights into the energy requirements and reaction characteristics at different stages of thermal degradation process. In the initial phase, evaporation of moisture and release of some volatiles take place, which are relatively low-energy processes. At this stage, the neem seedcake is only undergoing minor thermal decomposition, so energy demand is minimal. The positive values of ΔH indicate that reaction is primarily endothermic. In the second phase, the endothermic nature of the process becomes prominent as the structural components of neem seedcake undergo degradation. The breakdown of hemicellulose and cellulose, which requires significant energy to break the polymeric bonds, results in a high positive enthalpy change. This rise in enthalpy change shows the energy absorbed by the system to facilitate these reactions. In the final stage (α> 0.75), as the conversion progresses and the remaining biomass becomes more carbonized (biochar formation), the energy requirement for decomposition decreases and some exothermic reactions take place, which results in slight decrease in enthalpy change. The average values of ΔH for NSC are 244.162 kJ/mol, 235.918 kJ/mol, and 222.961 kJ/mol using Starink, KAS, and OFW methods, respectively.

The Gibbs free energy (ΔG) versus the conversion rate (α) graph (Fig. 7) represents the thermodynamic favorability of the process at different stages of the decomposition. Gibbs free energy, the energy available for utilization after the reaction, was also calculated. At initial phase of decomposition ΔG is maximum. This indicates that the reaction is less thermodynamically favorable, as reactant is in the stable form, requiring

an input of energy to initiate breakdown. In the middle phase (0.2<α<0.75), is a negative slope region, indicates the decomposition is thermodynamically favorable as ΔG decreases with increasing conversion rate. Toward the end of the reaction, as α approaches 1, the graph may show a slight rise in ΔG. The system approaches equilibrium, with the diminishing driving force for the reaction. The average values of ΔG are 172.973, 172.966, and 167.582 kJ/mol for Starink, KAS, and OFW methods, respectively. From Fig. 5 and Fig. 6, it is evident that both E_α and ΔH_α increase from 0.20 to 0.75 conversion, indicating a rise in endothermicity, and after that, the exothermic reactions become pronounced. The ΔG in the present study were compared to those found in other studies, such as bamboo (101.28–113.95 kJ/mol) [39] and sewage sludge (71.78–92.94 kJ/mol)[33].

ΔS, with a positive value indicating more disorder in the products. Fig. 8 represents the graph of entropy change (ΔS) versus conversion rate (α). In the initial phase of decomposition (α< 0.2), entropy change is usually low or negative. Negative entropy change indicates that the system becomes more ordered, which might be attributed to the release of low-energy volatiles or residual water, reducing the overall complexity of the remaining solid structure. As the conversion increases, the change in entropy begins to increase. This is the phase where major structural breakdown of the neem seedcake occurs, with hemicellulose and cellulose undergoing thermal decomposition. At high conversion rates (α > 0.75), the change in entropy decreases slightly. This stage represents the final breakdown of the lignin structure and the formation of more stable biochar. The average ΔS values were 0.09453, 0.09443, and 0.09034 for Starink, KAS and OFW methods, respectively. Table 5 shows the ΔH_α, ΔG_α, and ΔS_α values for conversions from 0.05 to 0.95. The changes in the thermodynamic characteristics of the NSC pyrolysis imply a complicated reaction chemistry. During pyrolysis, the entropy (ΔS) of the system changes as the solid NSC material breaks down into smaller molecules (gases and liquids), increasing disorder in the system. These pathways are often complex, with a variety of chemical bonds breaking and forming, contributing to a broad distribution of products. This reflects the diversity of reactions taking place, such as the cracking of long-chain hydrocarbons or the formation of aromatic compounds. Pyrolysis typically involves endothermic steps where heat is absorbed (e.g., breaking of chemical bonds in cellulose and lignin) and exothermic steps where heat is released (e.g., the formation of biochar and the release of volatile compounds). The presence of both endothermic and exothermic reactions in different stages of NSC pyrolysis highlights the simultaneous occurrence of competing reactions.

Table 4. Activation energy, pre-exponential factor and coefficient of determination

	KAS			OFW			STARINK		
α	E_α (kJ/mol)	A(s^{-1})	R^2	E_α (kJ/mol)	A (s^{-1})	R^2	E_α (kJ/mol)	A (s^{-1})	R^2
0.05	72.96639	771295.5	0.9939	69.35336	360813.7	0.9939	73.13736	799477.708	0.993
0.01	168.5515	2.49E+14	0.9998	166.5666	1.67E+14	0.9998	170.1199	3.4178E+14	0.9998
0.15	169.9318	3.29E+14	0.3627	169.2222	2.85E+14	0.3845	170.1199	3.4178E+14	0.3636
0.20	199.3152	1.23E+17	0.7097	197.7065	8.91E+16	0.7269	199.5048	1.2793E+17	0.7104
0.25	202.641	2.4E+17	0.9182	200.9153	1.7E+17	0.9245	202.6119	2.3903E+17	0.9185
0.30	217.4075	4.68E+18	0.9678	215.355	3.1E+18	0.9703	217.5993	4.8594E+18	0.9679
0.35	243.3488	8.5E+20	0.9829	235.4221	1.74E+20	0.988	243.5281	8.8103E+20	0.983
0.40	258.6392	1.81E+22	0.9841	254.9042	8.59E+21	0.9852	258.8146	1.8796E+22	0.9841
0.45	258.2899	1.69E+22	0.9844	249.6958	3.03E+21	0.988	258.4739	1.7557E+22	0.9845
0.50	257.9407	1.58E+22	0.9915	255.0939	8.93E+21	0.9856	258.1499	1.6455E+22	0.9915
0.55	265.8645	7.7E+22	0.9995	263.5823	4.88E+22	0.9996	266.1089	8.0855E+22	0.9995
0.60	273.0482	3.24E+23	0.9982	271.0037	2.15E+23	0.9979	273.3118	3.4127E+23	0.9982
0.65	325.3131	1.1E+28	0.9703	321.5388	5.17E+27	0.9996	325.5682	1.1537E+28	0.9703
0.70	392.4436	6.95E+33	0.9835	382.791	1.02E+33	0.9843	392.5378	7.0813E+33	0.9835
0.75	429.3358	1.06E+37	0.9917	415.2271	6.43E+35	0.9913	429.2834	1.0477E+37	0.9916
0.80	324.2572	8.88E+27	0.9693	299.0691	5.85E+25	0.9295	323.5909	7.7795E+27	0.9251
0.85	164.0035	9.92E+13	0.9978	144.4921	1.9E+12	0.9981	163.3906	8.7656E+13	0.9978
0.90	133.19	1.91E+11	0.9984	113.5182	3.43E+09	0.9478	132.5352	1.6694E+11	0.9369
0.95	125.9564	4.36E+10	0.9105	107.0294	9.04E+08	0.9986	125.324	3.835E+10	0.9982

Table 5. Thermodynamic parameters (ΔHα, ΔGα, and ΔSα) for NSC

	KAS			OFW			STARINK		
α	ΔH (kJ/mol)	ΔG (kJ/mol)	ΔS (kJ/mol.K)	ΔH (kJ/mol)	ΔG (kJ/mol)	ΔS (kJ/mol.K)	ΔH (kJ/mol)	ΔG (kJ/mol)	ΔS (kJ/mol.K)
0.05	70.01964	178.5472	-0.17704	66.40661	173.2069	-0.17423	70.19061	178.538	-0.17675
0.01	165.1701	174.2802	-0.01486	163.1852	168.7415	-0.00906	166.7385	174.2394	-0.01224
0.15	165.85	174.2386	-0.01368	165.1405	168.6609	-0.00574	166.0382	174.2394	-0.01338
0.20	194.9368	173.4258	0.035091	193.3281	167.868	0.041534	195.1264	173.4284	0.035396
0.25	198.108	173.3414	0.040402	196.3823	167.7859	0.04665	198.079	173.3498	0.040341
0.30	212.7732	172.9829	0.064911	210.7206	167.4322	0.070617	212.9649	172.9867	0.065217
0.35	238.623	172.4085	0.108017	230.6963	166.9782	0.103945	238.8023	172.4139	0.108301
0.40	253.8206	172.0979	0.133316	250.0857	166.573	0.136236	253.9961	172.1042	0.133592
0.45	253.3812	172.1048	0.132588	244.7871	166.6782	0.127421	253.5652	172.1109	0.132878
0.50	252.9551	172.1117	0.131882	250.1083	166.5692	0.136279	253.1644	172.1173	0.132214
0.55	260.8174	171.9575	0.144959	258.5352	166.4023	0.150298	261.0618	171.9628	0.145349
0.60	267.944	171.8216	0.156807	265.8995	166.2608	0.162543	268.2076	171.827	0.157228
0.65	320.1522	170.929	0.243431	316.3779	165.3894	0.246311	320.4073	170.9373	0.243834
0.70	387.1688	169.9729	0.354316	377.5162	164.5007	0.347497	387.263	169.9865	0.354448
0.75	423.9138	169.515	0.415006	409.805	164.0862	0.400846	423.8613	169.5318	0.414893
0.80	318.5938	170.9456	0.240862	293.4057	165.7586	0.208233	317.9275	170.9683	0.239738
0.85	157.8094	174.4196	-0.0271	138.298	169.466	-0.05085	157.1965	174.4448	-0.02814
0.90	126.2216	175.4802	-0.08036	106.5499	170.6956	-0.10464	125.5669	175.5103	-0.08147
0.95	117.9565	175.7648	-0.0943	99.02961	170.9956	-0.1174	117.3242	175.7952	-0.09539

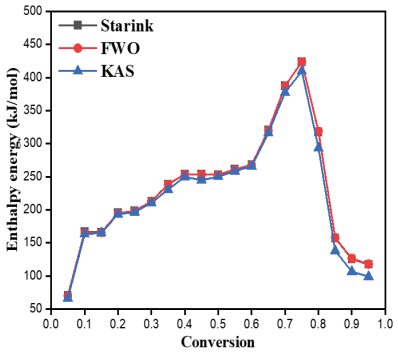

Figure 6. ΔH to alpha(α) for neem seedcake.

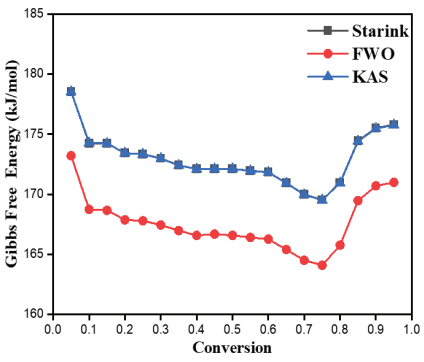

Figure 7. ΔG to alpha(α) for neem seedcake.

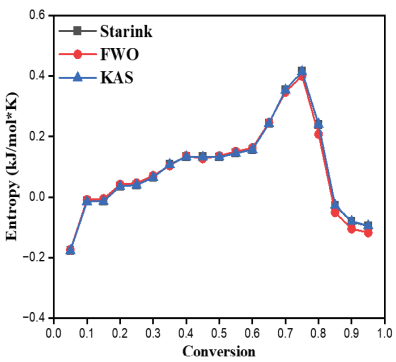

Figure 8. ΔS to alpha(α) for neem seedcake.

CONCLUSIONS

This study investigated thermal decomposition behavior, kinetics, and thermodynamic properties of NSC through TGA experiments. Three model-free methods (Starink, KAS, and OFW) were used to estimate pyrolysis activation energy of NSC. Based on experimental investigation, following conclusions can be summarized:

- The data showed that NSC decomposition proceeded in three stages, with the active pyrolysis taking place between 220 and 550 °C.
- The activation energies for NSC pyrolysis, computed using the Starink, Kissinger-Akahira-Sunose (KAS), and Ozawa-Flynn-Wall (OFW) methods were 235.985 kJ/mol, 235.918 kJ/mol, and 228.026 kJ/mol, respectively.
- The thermodynamic analysis indicated complex reaction chemistry in the NSC sample, involving both volatile organic compounds. Thermodynamic parameters indicated that endothermic behavior increased, as α increased from 0.20 to 0.75, with the product having the highest activation energy at α = 0.75.

The study of thermodynamic properties and thermal degradation behavior of NSC has several practical applications, especially in the fields of bioenergy, and environmental sustainability. These findings are significant for predicting reaction performance and optimizing energy pyrolysis processes. These studies help optimize biomass conversion technologies, develop new materials, and assess the environmental impact of thermal processes. It contributes to the efficient utilization of neem seedcake, an agricultural byproduct, by converting it into valuable products through thermochemical processes.

The study of the thermal degradation behavior of biomass faces several limitations, which can affect the accuracy and generalizability. Biomass can vary significantly in composition depending on its type (e.g., wood, agricultural residues, algae), moisture content, and geographical origin. The rate at which biomass is heated influences the decomposition process. Slow heating might result in different degradation pathways compared to rapid heating, making it challenging for large-scale applications where heating rates can vary. These variations lead to inconsistent degradation behavior. The pyrolysis process for industrial applications requires further investigation into how the kinetic and thermodynamic parameters of neem seedcake change in larger reactors.

Future Recommendations

The model-free methods provide reliable activation energy data, future studies could focus on refining kinetic models by integrating machine learning to predict the behavior of complex biomass like neem seedcake. While significant progress has been made in understanding the pyrolysis mechanism of neem seed cakes (NSC), several aspects remain unclear, particularly regarding the intricate details of the decomposition pathways and the formation of intermediate compounds. Kinetic models that account for the formation and decomposition of intermediate species could provide more clarity on the specific pathways involved. The effect of varying temperatures and residence times on the rate of decomposition and the distribution of products remains unclear. Developing temperature-dependent kinetic models could help to better characterize these dynamics.

Advanced spectroscopic or imaging methods can be incorporated that could provide more detailed insights into the thermal breakdown mechanisms, chemical transformations, and structural changes occurring during pyrolysis. These advanced experimental techniques (FTIR, Raman, GC-MS), morphological changes (SEM, XRD), and elemental transformations (XPS, EDS)) will offer a more detailed characterization of both the solid (biochar) and volatile (gaseous and liquid) products formed during the pyrolysis of NSC. These techniques will collectively offer a more comprehensive understanding of NSC components (cellulose, hemicellulose, lignin, proteins) decomposition and contribute to biochar formation and gas evolution.

AUTHORSHIP CONTRIBUTIONS

Authors equally contributed to this work.

DATA AVAILABILITY STATEMENT

The authors confirm that the data that supports the findings of this study are available within the article. Raw data that support the finding of this study are available from the corresponding author, upon reasonable request.

CONFLICT OF INTEREST

The author declared no potential conflicts of interest with respect to the research, authorship, and/or publication of this article.

ETHICS

There are no ethical issues with the publication of this manuscript.

STATEMENT ON THE USE OF ARTIFICIAL INTELLIGENCE

Artificial intelligence was not used in the preparation of the article.

NOMENCLATURE

Symbol	Description
α	Degree of conversion
t	Time, s
T	Absolute temperature, K
β	Heating rate (dT/dt), K/s
k(T)	Rate constant at temperature T, 1/s
A	Pre-exponential factor (Arrhenius parameter), 1/s
E_α	Activation energy, kJ/mol
R	Universal gas constant (8.314 J/mol·K), J/mol.K
f(α)	Reaction model function (depends on the reaction mechanism)
g(α)	Integral form of reaction model
ln	Natural logarithm
ΔT	Temperature interval, K
$T_\alpha(\alpha)$	Temperature corresponding to a specific α, K
$E_\alpha(\alpha)$	Activation energy as a function of conversion, kJ/mol

REFERENCES

[1] Nguyen VG, Dager B, Chhilar A, Sharma P, MO Sameh, DTN Le, et al. Desirability-based optimization of dual-fuel diesel engine using acetylene as an alternative fuel. Case Stud Therm Eng 2024;59: 104488. [Crossref]

[2] Kassim FO, Thomas CLP, Afolabi OOD. Integrated conversion technologies for sustainable agri-food waste valorization: A critical review Biomass Bioenergy 2021;156:106314. [Crossref]

[3] Khandelwal N, Yadav P, Said Z, Sharma M, Shukla AK, Singh O, et al. A Comprehensive analysis of energy, exergy, economic and environment on integrated solarcombined cycle with various HTFs and thermal storage. Appl Energy 2024;37:6124203. [Crossref]

[4] Agrawalla A, Kumar S, Singh RK. Pyrolysis of groundnut de-oiled cake and characterization of the liquid product. Bioresour Technol 2011;102:10711–10716. [Crossref]

[5] Yadav PS, Said Z, Gautam R, Raman R, Caliskan H. Novel investigation on atomization, performance, and emission characteristics of preheated jatropha oil methyl ester and ethyl ester. Energy 2022:270;126870. [Crossref]

[6] Kumar Singh R, Patil T, Pandey D, Sawarkar AN. Pyrolysis of mustard oil residue: A kinetic and thermodynamic study. Bioresour. Technol 2021;339;125631. [Crossref]

[7] Silvestre WP, Pauletti GF, Baldasso C. Fodder radish (Raphanus sativus L.) seed cake as a feedstock for pyrolysis. Ind Crops Prod 2020;154:112689. [Crossref]

[8] Đ. Katnić, Marinović-Cincović M, Katnić*et* SP, Vujčić IT. Characterization and kinetics of thermal decomposition behavior of plum and fig pomace biomass. J Clean Prod 2022;352:131637. [Crossref]

[9] Singh RK, Pandey D, Patil T, Sawarkar AN. Pyrolysis of banana leaves biomass: Physico-chemical characterization, thermal decomposition behavior, kinetic and thermodynamic analyses. Bioresour Technol 2020;310:123464. [Crossref]

[10] Mishra RK, Mohanty K. Kinetic analysis and pyrolysis behaviour of waste biomass towards its bioenergy potential. Bioresour Technol. 2020;311:123480. [Crossref]

[11] Sahoo A, Kumar S, Mohanty K. Kinetic and thermodynamic analysis of Putranjiva roxburghii (putranjiva) and Cassia fistula (amaltas) non-edible oilseeds using thermogravimetric analyzer. Renew Energy 2021;165:261–277. [Crossref]

[12] Pal DB. Thermo-chemical potential of solid waste seed biomass obtained from plant Phoenix dactylifera and Aegle marmelos L. Fruit core cell. Bioresour Technol 2021;345:126441. [Crossref]

[13] Kristanto J, Daniyal AF, Pratama DY, Noer I. Kinetic Study on The Slow Pyrolysis of Isolated Cellulose and Lignin from Teak Sawdust. Thermochim Acta 2022;711:179202. [Crossref]

[14] Masawat N, Atong D, Sricharoenchaikul V. Thermokinetics and product analysis of the catalytic pyrolysis of Pongamia residual cake. J Environ Manage 2019;242:238–245. [Crossref]

[15] Sokoto MA, Singh R, Krishna BB, Kumar J, Bhaskar T. Non-isothermal kinetic study of de-oiled seeds cake of African star apple (Chrosophyllum albidum) using thermogravimetry. Heliyon 2016:10;2. [Crossref]

[16] Sahoo A, Gautam R, Kumar S, Mohanty K. Energy optimization from a binary mixture of non-edible oilseeds pyrolysis: Kinetic triplets analysis using Thermogravimetric Analyser and prediction modeling by Artificial Neural Network. J Environ Manage 2021;297:113253. [Crossref]

[17] Hagig KA, Acar B, Dağdeviren A, Taşkesen E, Özkaymak M. Freeze-drying kinetics and diffusion modeling of hawthorn. J Therm Eng 2023;9:876–884. [Crossref]

[18] Dağdeviren A, Gedik E, Keçebaş A, Pazarlıoğlu HK, Arslan K, Alsabery AI. Effect of Al 2 O 3 – SiO 2 /Water Hybrid Nanofluid Filled in a Square Enclosure on the Natural Convective Heat Transfer Characteristics: A Numerical Study. J Nanofluids 2022;11:772–781. [Crossref]

[19] Dagdeviren A, Acar B, Aydın M.Alternative heat insulation method for rigid construction walls. Int J of Energy Stud 2021;6:19–35.

[20] Ponnam V, Ghodke P, Tondepu S, Mandapati RN. Thermal Behaviour Kinetic Modeling of Capsicum Annuum Waste Biomass Using an Iso-Conversion Method. J Therm Eng 2021;7:18–29. [Crossref]

[21] Bhattacharjee N, Biswas AB. Pyrolysis of orange bagasse: Comparative study and parametric influence on the product yield and their characterization. J Environ Chem Eng 2019;7:102903.[Crossref]

[22] Yadav PS, Ahmed SFA, Gautam R, Caliskan H, Caliskan N, Hong H. Nozzle effects on spray combustion and emissions in compression ignition engines using waste cooking oil biodiesel: A computational fluid dynamics analysis at varying injection pressures. IET Renew Power Gener 2023;2340–2359. [Crossref]

[23] Yadav PS, Gautam R. Numerical and experimental analysis on spray characteristics of biodiesel (waste cooking oil) using pressure swirl atomizer. Environ Prog Sustain Energy 2021. [Crossref]

[24] Patel PM, Rathod VP, Patel VK. Development and enhancement in drying performance of a novel portable greenhouse solar dryer. J Stored Prod Res 2024;105:102228. [Crossref]

[25] Yadav PS, Gautam R, Le TT, Khandelwal N, Le AT, Hoang AT. A comprehensive analysis of energy, exergy, performance, and emissions of a spark-ignition engine running on blends of gasoline, ethanol, and isoamyl alcohol. Energy 2024;307:132548. [Crossref]

[26] Mphahlele K, Matjie RH, Osifo PO. Thermodynamics, kinetics and thermal decomposition characteristics of sewage sludge during slow pyrolysis. J Environ Manage 2021;284:112006. [Crossref]

[27] Tagade A, Kandpal S, Sawarkar AN. Insights into pyrolysis of pearl millet (Pennisetum glaucum) straw through thermogravimetric analysis: Physico-chemical characterization, kinetics, and reaction mechanism. Bioresour Technol 2024;391:129930.

[28] Acar B, Dağdeviren A Ozkaymak M. Design of hazelnut drying system supported by solar energy, investigation of drying performance and determination of proper drying model. Int J Renew Energy Res 2020;10: 570–577.
[29] Kumar M, Rai D, Bhardwaj G, Upadhyay SN, Mishra PK. Pyrolysis of peanut shell: Kinetic analysis and optimization of thermal degradation process. Ind Crops Prod 2021;174:114128. [Crossref]
[30] Ashwath N, Nam H, Capareda S. Maximizing energy recovery from beauty leaf tree (Calophyllum inophyllum l.) oil seed press cake via pyrolysis. Energies 2021;9:14. [Crossref]
[31] Hasan MM, Rasul MG, Jahirul MI, Khan MMK. Fast pyrolysis of macadamia nutshell in an auger reactor : Process optimization using response surface methodology (RSM) and oil characterization. Fuel 2023;333:126490. [Crossref]
[32] Dhanavath KN. Optimization of process parameters for slow pyrolysis of neem press seed cake for liquid and char production. J Environ Chem Eng 2019;7:102905. [Crossref]
[33] Soni NK, Prabhansu, Bhale PV. Chemical insight into thermal degradation, chemical kinetics, and thermodynamics behavior of sewage sludge through thermogravimetry and Fourier transform infrared analysis. Therm Sci Eng Prog 2024;51:102617. [Crossref]
[34] Ordonez-Loza J, Chejne F, Jameel AGA, Telalovic S, Arrieta AA, Sarathy SM. An investigation into the pyrolysis and oxidation of bio-oil from sugarcane bagasse: Kinetics and evolved gases using TGA-FTIR. J Environ Chem Eng 2021;9:5. [Crossref]
[35] Volli V, Singh RK. Production of bio-oil from de-oiled cakes by thermal pyrolysis. Fuel 201:96;579–585. [Crossref]
[36] Sokoto MA, Biswas B, Kumar J, Bhaskar T. Slow pyrolysis of Defatted Seeds Cakes of African star apple and silk cotton for production of bio-oil. Renew Energy 2020;146:1710–1716. [Crossref]
[37] Chilla V, Suranani S. Thermogravimetric and kinetic analysis of orange peel using isoconversional methods. Mater Today Proc 2023;72:104–109. [Crossref]
[38] Vyazovkin S, Burnham AK, Criado JM, Pérez-Maqueda LA, Popescu C, Sbirrazzuoli N. ICTAC Kinetics Committee recommendations for performing kinetic computations on thermal analysis data. Thermochim Acta 2011;520:1–19. [Crossref]
[39] Chaudhuri P, Pande R, Baraiya NA. A novel insight into the influence of temperature and heating rate on bamboo pyrolysis through kinetics and thermodynamic parameter analysis using thermogravimetric analyser. J Therm. Anal Calorim. 2024;149:1385–1401. [Crossref]

J Ther Eng, Vol. 12, No. 1, pp. 128−143, January, 2026

Journal of Thermal Engineering
Web page info: https://jten.yildiz.edu.tr
DOI: 10.14744/thermal.0001064

Research Article

Improvement of the thermal performances of a parabolic trough solar concentrator with concentric receiver tube and nanofluid

Djemaa GUERRAICHE[1,*], Kamel ZOUGGAR[2], Khelifa GUERRAICHE[3], Antar TAHIRI[4], Zied DRISS[5], Cherif BOUGRIOU[3], Aya YAHA[6]

[1]*Department of Physics, Faculty of Matter Sciences, Laboratory of Applied Energetic Physics: L.P.E.A., University of Batna 1, Batna, 05000, Algeria*
[2]*Department of Mechanical Engineering, Faculty of Technology, Structures and Solid Mechanical Laboratory (LMSS), , Djillali Liabes University of Sidi Bel Abbes, Sidi Bel Abbes, 22000, Algeria*
[3]*Department of Mechanical Engineering, Faculty of Technology, University of Batna 2, Batna, 05000, Algeria*
[4]*Faculty of Science and Technology, Ziane Achour University of Djelfa, Djelfa,17001, Algeria*
[5]*National Department of Engineers of Sfax (ENIS), Laboratory of Electromechanical Systems (LASEM), University of Sfax, 3029, Tunisia*
[6]*Department of Physics, Faculty of Matter Sciences, University of Batna 1, 05000, Algeria*

ARTICLE INFO

Article history
Received: 15 September 2024
Accepted: 02 December 2025

Keywords:
CFD; Heat Transfer; Nanofluid; Parabolic Trough Collector; Solar Energy; Trough Collector

ABSTRACT

Parabolic trough solar concentrators (PTCs) encounter significant challenges arising from Non-Uniform Heat Flux (NUHF) around the receiver, which causes local overheating and pronounced circumferential temperature gradients. This study proposes the solution to this problem by uniforming the heat flux distribution, minimizing the temperature gradient, and improving performance. A numerical analysis is carried out on a novel small-scale PTC model featuring a concentric absorber tube design. The study compares the heat recovery performance of conventional, concentric, and eccentric absorber configurations using two heat transfer fluids enhanced with nanofluids: water and Syltherm-800 oil. A three-dimensional simulation model was presented by coupling Monte Carlo Ray-Tracing (MCRT) with (CFD) in ANSYS Fluent to predict the thermo-hydraulic response of parabolic trough receivers. Furthermore, Particular attention is given to the effects of is given to the effects of critical operational factors, namely inlet fluid temperature, mass flow rate, and nanofluid concentration on heat transfer and overall efficiency. The results confirm that the concentric parabolic trough receiver (PTR) operates with lower peak wall temperatures and smaller circumferential thermal gradients, which lessen thermal stresses and supports higher overall efficiency. When compared to the reference design, the concentric and eccentric receiver tube configurations lower the absorber tube's temperature gradient by roughly 45% and 60.6%, respectively. These new configuration enhance heat collecting efficiency by up to 2.62% and 3.26% relative to the smoothe PTC tube. Moreover, the use of nanofluids added significant enhancements of efficiency, by 6.12% and 8.23% for the concentric and eccentric

***Corresponding author.**
*E-mail address: djemaa.guerraiche@univ-batna.dz

This paper was recommended for publication in revised form by Editor-in-Chief Ahmet Selim Dalkilic

Published by Yıldız Technical University Press, İstanbul, Turkey
Yıldız Technical University. This is an open access article under the CC BY-NC license (http://creativecommons.org/licenses/by-nc/4.0/).

arrangements, respectively. This work highlights the promise of novel receiver designs and the use of nanofluids to boost both thermal and mechanics performance of PTCs and contributes knowledge beyond earlier work in the literature and serves toward improving solar therma.

Cite this article as: Guerraiche D, Zouggar K, Guerraiche K, Tahiri A, Driss Z, Cherif B, et al. Improvement of the thermal performances of a parabolic trough solar concentrator with concentric receiver tube and nanofluid. J Ther Eng 2026;12(1):128−143.

INTRODUCTION

Worldwide energy demand has risen significantly, resulting in numerous plans aimed at the usage of both renewable and nonrenewable energy sources. Solar energy is the most remarkable feature from the list of alternatives that could be the most widely used and rapidly growing in the future. For this purpose, the parabolic trough collector (PTC) is a reliable and useful method for collecting solar rays and turning it into heat energy. Recently, the development of Parabolic Trough Concentrator (PTC) has focused on achieving higher concentration ratios and operating temperatures to reduce investment costs and enhance thermal efficiency, particularly at high temperatures [1]. This objective is essential to guarantee the energetic and financial viability. PTC possess numerous drawbacks, such as low efficiency, maintenance demands, high costs, complexity, energy losses, durability issues, and the necessity for solar tracking [2]. However, PTCs still face a great number of problems and limitations. NUHF generates excessively localized heating as well as steep thermal gradients into the receivers which results in increased thermal stress. One of the effects is that the absorber tube goes outside the focal plane leading to quite significant optical losses due to the loss of the particular coating being very rapid at high local temperatures, hence, the maximum operating temperature is limited [3]. These aforementioned barriers baffle the efficiency of PTC systems significantly over time. Moreover, NUHF is the leading cause of the large decrease in the thermal efficiency of PTC from where the energy conversion performance is adversely affect. Implementing the most efficient measures to ensure a preferable uniform heat flux distribution, should be the main target. All the above mentioned are first of all ways of accomplishing this: temperature distribution being more even, the peak temperatures being decreased and the gradients of the temperature being lessened. There are several ways of improving solar collector efficiency, which, in fact, can be mostly divided into three main aspects: raising the heat conductivity of the receiver tube, changing the collector design in order to have better distribution of solar flux and to give the receiver tube the possibility of making heat transfer by convection easier [4].

Improving heat transfer in solar parabolic trough receivers is gradually gaining importance as a major measure to mitigate NUH. A primary goal of current research is to devise novel receiver configurations that would allow better fluid flow patterns and the utilization of new methods for heat transfer enhancement. A wide range of both passive and active methods have been considered for their thermal performance improvement and energy conversion efficiency increase [5]. The application of passive techniques broadly involves the use of the fins or turbulence promoters, changing the shape or the surface properties of the receiver, raising the capacity of the absorber tube for heat retention, and the addition of more material. Through these methods, the heat transfer to the fluid from the receiver tube can be elevated by up to 50% [6]. Efficient use of the concentrated solar power (CSP) system with improved parabolic trough solar receiver can be the source of a steep drop in solar power plant costs. While active methods do consume more energy, they still rely on additional heat transfer from external sources inside the absorber tube. Researchers must develop technologies that have the dual effect of lowering the expense and being more sustainable in the use of renewable energy. One of the promising options for increasing heat transfer is the use of turbulators along with nanofluids [7]. As an example, turbulence promoters or inserts have been studied to create turbulence and increase convective heat transfer. The inserts disturb the boundary layer and facilitate heat transfer by attaining greater mixing.

Different methods have been explored to increase heat transfer in the receiver tube. One such method is the insertion of twisted tapes inside the receiver tube where Chang et al. [8], found heat transfer rates to be significantly enhanced. Moreover, oscillatory or pulsating flow has also been investigated to raise heat transfer coefficients. These techniques involve periodically varying flow rates or flow directions, resulting in enhanced heat transfer characteristics. Afsharpanah et al. [9] performed a computational research which was mainly focused on raising the heat exchange rate in a solar parabolic trough collector by the usage of modified dual twisted-tape inserts. The authors considered several tape shapes such as V-cut, square-cut, and perforated designs, and used water under pressure as the working fluid. Their findings showed that the dual V-cut design led to the greatest heat performance, raising the average Nusselt number by 19.58% and 17.44% at Reynolds numbers 10,000 and 20,000, respectively. The study, by and large, acknowledged that all the twisted tape modifications had higher efficiencies than the smooth tube.

The authors Fatouh et al. [10], examined the usage of the extended surfaces on the receiver tube with the main idea to double the heat transfer area and discovered the considerable increase of the convective heat transfer coefficients. DeSá et

al. [11] doped a computational analysis to check the influence of pulsating flow on parabolic trough solar receivers and displayed that the cooing effectiveness is better by an oscillatory flow than a flow of steady state. Nevertheless, the need of the new ways of heat transfer promotion in parabolic trough solar receivers as well as the designing and operational optimization of parabolic trough solar receivers continues to exist.

Nevertheless, limited research have emphasized on the improvement of cascade solar energy conversion systems by modifying the absorption tube geometry to make it more efficient. Zhang et al. [12], developed a novel convergent-divergent tube concept for parabolic trough solar collectors (PTR) that was targeted to raise the heat transfer and the temperature uniformity getting by more rapid heat exchange. Research evidence highlights that the innovative tube is a substantial heat transfer enhancer that the Nusselt number under certain conditions may reach 66% more when compared to a standard PTR system. Several paper have examined the use of concentric reveiver tubes to enhance heat transfer for PTR. Liu et al. [13], introduced an innovative solar cascade heat collection configuration involving double-tube for the parabolic trough receiver (PTR) utilizing two distinct heat transfer fluids (HTF). The results demonstrate an improvement in the parabolic trough receiver's performance due to the novel solar cascade heat collection arrangement. The novel solar cascade heat collection arrangement could elevate the overall thermal efficiency by a maximum of 1.5%. Liu et al. [14], provide a new design with an inner tube and wing-like fringe and employ two heat transfer fluids (water and thermal oil) to increase heat-collecting efficiency while delivering various grades of thermal energy. The model shows the new system reduces heat loss by 33.1% to 50.1% and improves efficiency by 0.61% to 7.67%.

Benabderrahmane et al. [15] showed that the heat transfer along the absorber tube of a PTC was enhanced by the use of a corrugated insert of the center leading to an increase of the Nusselt number of up to 3.7 times with respect to a plain tube. The total efficiency factor was in the range of 1.3 to 2.6, and it increased with the decrease of the corrugation pitch and the increase of the twist ratio. Guerraiche et al. [16], studied the operation of an integrated new prototype of PTC integrating latent heat storage system using a concentric tube setup for a parabolic trough solar receiver. The authors informed that the method could achieve high water outlet temperatures along with better thermal efficiency. Imtiaz and Lee et al. [17] conducted an experimental and numerical evaluation of the thermal performance of a newly designed concentric receiver tube. Their results revealed that the concentric tube arrangement led to the even distribution of the flow and the maintenance of the temperature symmetry along the receiver length. Moreover, the local temperature and heat flux on the inner and outer tube surfaces showed a good angular uniformity, and the simulated data matched well with the experimental measurements. Acuna et al. [18] presented the concept of a concentrator system with a compound parabolic concentrators and a concentrator receiver tube. The findings revealed that the proposed design had a potential of reaching higher outlet temperature and efficiency by 4% and 10%, respectively, compared to the traditional single-tube designs. Wang et al. [19] offers a tube receiver whose eccentricity is oriented so as to lessen the thermal stresses in the receiver tube. Here, the effects of eccentricity and the angle of orientation on the receiver tube were investigated. The results suggest that the eccentric design is very effective in lowering thermal stress, and most of the variations of the eccentricity and orientation angle lead to the change of the stress level. Through the use of inner and outer pipe inserts that are concentric and eccentric Chang and co-workers [20] have found that heat transfer in a PTC absorber can be greatly improved. Their research suggests that heat transfer with these types of inserts could be increased up to almost 1.64 times of the original value. According to Pérez-Álvarez et al. [21] the change of orientation angle and eccentricity of the eccentric receiver are factors that determine the thermal stress experienced by the receiver tube. The research results demonstrate that the combination of an eccentric tube receiver with parabolic trough concentrators leads to a significant reduction in thermal stresses that the system reliability can be enhanced by the proper design of the eccentric tube besides a successful reduction of thermal stress in parabolic troughs. In their work, Bellos et al. [22] came up with the idea of using a flow of a cylindrical insert in a parabolic trough solar collector. They studied the heat efficiency of inserts both placed centrally and eccentrically to decide the configuration that gives the highest thermal gain.

However, researchers still encounter difficulties in maximizing the efficiency of PTCs, specifically in improving the ability of the absorber tubes to absorb heat flux. Introducing nanoparticles into the fluid is one potential solution to alleviate this problem. Nanoparticles are frequently mentioned in various literary works. A comprehensive review of the literature identifies many research works that emphasize finding new methods to increase heat transfer in parabolic trough solar receivers. Guerraiche et al. [23], propose methods to enhance heat transfer and homogenize heat flux distribution to improve PTC performance. According to their results, adding Alumina (Al_2O_3) nanoparticles to water is beneficial to the heat transfer efficiency of the system and the improvement ranges from 3% to 14%, for volume concentration varying from 2% to 6%. Meanwhile, the study suggests that copper is the best material for the tube because it undergoes the least thermal stress among aluminum and stainless steel. Wang et al. [24] examined the impact of various nanofluids as heat transfer fluids (HTFs), the results revealed that incorporating nanoparticles greatly enhanced the efficiency. Current research aims to improve collection methods through the use of nanoparticles in the HTF and the optimal design of parabolic trough collectors. Benabderrahmane et al. [25], used single-phase and two-phase models to simulate the turbulent forced convection of a hybrid nanofluid in a non-uniformly heated PTC receiver. The hydrodynamic

results of both models were similar, but the thermal results were distinct. The study found that a hybrid nanofluid with 1.5% copper and 0.5% alumina in water provided the highest thermal performance. Khan et al. [26] performed computational experiments on three different designs of absorber tubes for the commercial LS-2 collector: a smooth tube, a tube with twisted tape insert, and a tube with longitudinal fins. Their results showed that the use of twisted tape inserts together with nanofluids drastically enhanced the thermal efficiency and gave a higher heat transfer coefficient than the smooth tube. Besides, the work of cascade solar energy conversion systems with double tube absorbers and nanofluids has been scarcely addressed.

In order to increase energy efficiency, Mustafa et al. [27] present a new PTC system that uses a base fluid in the external glass cover and a double-fluid absorber tube inside the absorber tube. It was discovered that employing a double-fluid absorber tube with a nanofluid rather than a single-fluid system can increase the PTC's energy efficiency. In addition, it can impact the minimization of the heat loss of the commercial LS-2 collector. Khan et al. [28] explored the effect of employing a new receiver tube with a nanofluid on the energy performance of PTC with two heat transfer fluids. Also, it can impact the reduction of heat loss of the commercial LS-2 collector. They found that using this new absorber tube makes the single and two-fluid PTC system much more energy efficient. Moreover, they indicated that the collector efficiency can be enhanced when a smooth tube is employed by using a two-fluid system. Abbasian et al. [29] investigate the performance of the two-fluid PTC with a wavy grooved absorber tube. Based on their findings, using two heat transfer fluids, the thermal efficiency was substantially enhanced,

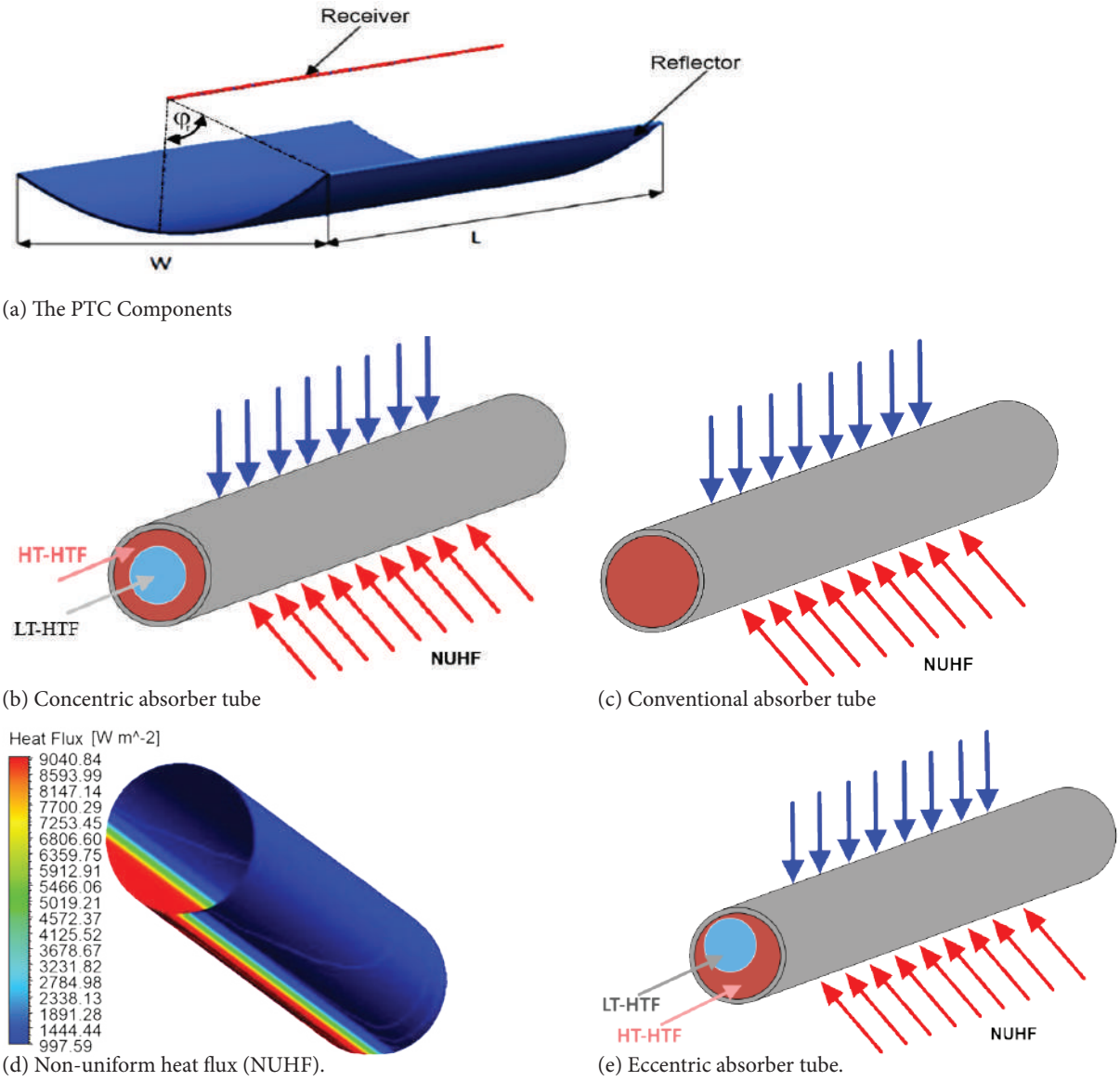

(a) The PTC Components

(b) Concentric absorber tube

(c) Conventional absorber tube

(d) Non-uniform heat flux (NUHF).

(e) Eccentric absorber tube.

Figure 1. Physical model.

from 38% up to 49%. Interestingly, the highest efficiency was obtained by the collector with a dual-fluid configuration with an exterior corrugated absorber tube and interior grooves and absorber roof and is about 70% when compared with smooth collectors at about 40%.

This work addresses the challenge of non-uniform thermal flux in parabolic trough collectors and seeks to improve thermal efficiency while providing two thermal energy levels. The study proposes a new concentric receiver tube of a cascade system type using two heat transfer fluids (HTFs) and nanofluids. The application of two HTFs allows conversion of solar energy at several ranges of temperature, optimizing the inner absorber tube temperature gradient, and improves the distribution of heat flux. This leads to increased heat transfer and minimized thermal stresses on the absorber. All these bring about improved performance and design of parabolic trough solar collectors (PTCs). Highlighted is the proposed methodology with the practical advantage of using renewable energies, promising higher performance, lower solar power station operating costs, and longer system collector durability, and these combine to ensure long-term solar energy sustainability.

PHYSICAL MODEL

A new parabolic trough concentrator (PTC) is presented along with a concentric receiver tube. The initial idea of a parabolic trough solar concentrator by Guerraiche et al. [16] is the underlying concept for the physical model. As depicted in Figures (1.a, b, c and e). The rim angle (φ_r) is 90°, the total aperture area (A_a=W×L) is 1.80 m^2 with an eccentric offset (e) of 10 mm along the y-axis; the inner tube is the one that is placed inside the absorber tube. Figures 1b, 1c, 1d, and 1e depict the details of the tube, showing the inner and outer diameters as 27 and 28 mm, respectively. The numerical investigation identifies a difference between a smooth absorber tube and a concentric receiver tube which has two separate HTFs that merge both in the concentric and eccentric configurations so as to get heat sources of high and low temperatures, respectively.

In this system, Water is selected as the low-temperature heat transfer fluid (LT-HTF) that flows through the inner tube and provides low-grade thermal energy. The high-temperature fluid (HT-HTF) adopted is Syltherm-800 oil which flows across the space between the inner surface of the absorber tube and the outer surface of the inner tube and serves as a carrier for high-grade thermal energy. The aim of this study is to propose a solution to offer significant insights and recommendations for enhancing heat transfer within the receiver tube, this will be achieved through the following approaches: Investigating the effects of concentric and eccentric pipe inserts in PTC. Comparing three system types: a conventional receiver with a single absorber tube and a single heat transfer fluid, a configuration with concentric absorber tubes, and a configuration with an eccentric receiver tube. Study the impact of various operational factors on the performance of the recently proposed system, with the aim of identifying the most optimal design.

Table 1. Properties of Syltherm-800 (HT-HTF) and water (LT-HTF) [30]

HT-HTF (Syltherme-800 oil)		*LT-HTF (water)*
ρ (kg/m³)	$aT^2 + bT + C\ /c = -6.0616 \times 10^{-2},$	$aT^3 + bT^2 + cT + d/$
	$a = 1.1057 \times 10^3\ ,$	$a = 1.772 \times 10^{-5},$
	$b = 4.1535 \times 10^{-1}$	$b = 2.067 \times 10^{-2}, \quad c = 7.355,$
		$d = 1.71956 \times 10^2$
Cp (J/kg K)	$aT^2 + bT/a = 1.7080\ ,$	$aT^4 + bT^3\ + cT^2\ + d/$
	$b = 1.1078 \times 10^3$	$a = 1.471 \times 10^{-6}, b = -1.973 \times 10^{-3},$
		$c = 1.005\ , d = 2.2965 \times 10^2$
K (W/m·K)	$aT^2 + bT + C/\ a = -5.7534 \times 10^{-10},$	$aT^3 + bT^2 + c\ /a = 3.419 \times 10^{-8},$
	$b = 1.8752 \times 10^4, c = 1.9002 \times 10^{-1}$	$b = 4.581 \times 10^{-5}, c\ = +2.229$
μ (kg/m·s)	$aT^4 + bT^3\ + cT^2 + dT + e/$	$aT^4 + bT^3\ + cT^2 + dT + e/$
	$a = 6.6720 \times 10^{-13},$	$a = 4.078 \times 10^{-11},$
	$b = -1.5660 \times\times 10^{-9},$	$b = -5.502 \times 10^{-8},$
	$c = 1.3882 \times 10^{-6},$	$c = 2.789 \times 10^{-5},$
	$d = -5.5412 \times 10^{-4},$	$d = 6.302 \times 10^{-3},$
	$e = 8.4866 \times 10^{-2}$	$e = 0.536574$

Table 2. Properties of the nanofluid (Al_2O_3/ Syltherm-800 oil) [30]

Properties	Formula
ρ (kg/m³)	$\rho_{nf} = (1-\varphi)\rho_f + \varphi\rho_s$
Cp (J/kg·K)	$(\rho C_p)_{nf} = (1-\varphi)(\rho C_p)_f + \varphi(\rho C_p)_s$
K (W/m·K)	$K_{nf} = \frac{K_s + 2K_f - 2\varphi(K_f - K_s)}{K_s + 2K_f + \varphi(K_f - K_s)} K_f$
μ (kg/m·s)	$\mu_{nf} = \frac{\mu_f}{(1-\varphi)^{2.5}}$

temperature and flow properties are stable over time. It is assumed that the particles of the nanofluid are dispersed evenly in the fluid so that the thermal properties are uniformly enhanced. Additionally, this model makes an assumption that there is no heat loss through the surrounding environment so that it can put its focus on the internal heat transfer processes. The flow inside the tubes is treated as fully developed, and the heat transfer correlations are used based on the standard Nusselt number formulas. Moreover, for the sake of computational stability, the material properties are considered to be constant throughout the temperature.

Table 3. Properties of (Al_2O_3) solid particles used in nanofluid [30]

Material	*ρ (kg/m³)*	*Cp (J/ (kg·K))*	*K (W/m·K)*
Alumina *(Al_2O_3)*	3970	765	40

Table 4. Properties of solid materials [30]

Material	*ρ (kg/m³)*	*Cp (J/kg·K)*	*K (W/m·K)*
Steel	8030	502.48	16.27

Efficacy investigation of nanofluid (*AL_2O_3/Syltherm-800 oil*) usage as a HT-HTF. Table 1 shows the properties of Syltherm-800 (HT-HTF) and water (LT-HTF) [30]. Tables 2, Table 3 and Table 4 give the properties of the fluids.

NUMERICAL AND CFD MODELING

The numerical modeling was accomplished with the finite volume method. The SIMPLE algorithm was used to handle the pressure-velocity coupling. The second-order upwind scheme was employed for the advection terms treatment in the momentum and energy equations. The local heat flux pattern in the PTR was obtained by coupling the CFD analysis with a Monte Carlo ray-tracing (MCRT) code. We use SolTrace open-source software to calculate the incident heat flux on the receiver tube by the MCRT method [12]. Figure 1.a depicts that the receiver bottom wall is having the highest flux; the top part is the least exposed to the flux. These NUHF distributions were implemented in the Fluent CFD model by polynomial correlations of the flux data. The correlations were devised by a User-Defined Function (UDF), which sets the actual boundary conditions on the outer surface of the absorber tube.

Somme assumptions are applied in the numerical and CFD modeling to optimize computational efficiency and ensure consistency in results. The model presumes that the conditions are at steady state, which implies that both

Boundary conditions used in the simulations included an ambient temperature fixed at 300 *K*, a NUHF on the absorber's outer wall (see Fig. 1.d), and zero velocity at the interface for the absorber's inner surfaces. The efficiency of the investigated systems (concentric and eccentric) is examined by varying the inlet temperatures and the mass flow rates for both heat transfer fluids a presented in Table 5.

Table 5. Temperature and mass flow values studied.

ṁ_water (Kg/m³)	0.006, 0.007, 0.008, 0.009
T in_water (K)	300, 308, 318, 328
ṁ_oil and nanofluid (Kg/m³)	0.06, 0.07, 0.08, 0.09
Tin_oil and nanofluid (K)	500, 550, 600,650
Volume concentration ϕ (%)	1%, 2%, 3%, 4%

Parameter Used in Analysıs

These factors are very important for figuring out how well the system under study transfers heat and moves fluids, as shown by the equations:

$$Re = \frac{\rho u d}{\mu} \quad (1)$$

$$Nu = \frac{hd}{K} \quad (2)$$

$$h = \frac{q_w}{T_w - T_m} \quad (3)$$

$$f = \frac{2\,\Delta P\left(\frac{d}{L}\right)}{\rho u^2} \quad (4)$$

Where: *d, L, ρ, μ, K, Tm, Tw, qw, ΔP*, are the inner diameter, Length of the receiver tube, density, viscosity, thermal conductivities of the HTF, average temperature of the Heat Transfer Fluid (HTF), average temperature on the inner surface of the inner tube or absorber tube, heat flux, pressure drop, u: the average velocity of the HTF.

The efficiency of heat collection (η) measures how effectively the collector converts the incident solar energy into thermal energy [29]. It can be expressed by,

$$\eta = \frac{Q_C}{A_a \cdot DNI} \quad (5)$$

In which, DNI is direct normal irradiance, A_a corresponds to the aperture area of the collector, Qc denotes the total collected heat, accounting for both high-temperature and low-temperature contributions from the LT-HTF and HT-HTF.

- For a concentric receiver tube

$$Q_c = (\dot{m}_{oil} \times Cp_{oil} \times \Delta T_{oil}) - (\dot{m}_{water} \times Cp_{water} \times \Delta T_{water}) \quad (6)$$

- For a conventional receiver tube

$$Q_c = \dot{m}_{water} \times Cp_{water} \times \Delta T_{water} \quad (7)$$

Grid Independency Test and Validation

Highly refined meshes are used to maintain computational accuracy and make sure that y^+ stays below 1. To achieve accurate numerical results, a refined mesh was applied, ensuring that y^+ remained under 1 as presented in Figure 2.

An independence study of a grid was performed to check for accuracy and credibility of results computed. Three grids were employed in simulation by Fluent to evaluate the Nusselt number and friction of a conventional PTR at a Reynolds number of 2.104. On comparing the results, the grid having 3522375 nodes was identified as the ideal grid to carry out the necessary simulations, as presented in Table 6.

Figure 2. Receiver tube mesh.

To ensure the validity of the developed numerical model derived in this study, a comparison was conducted with the calculation carried out by Bellos et al. of the numerical model suggested in this paper was checked by comparing it to results from Bellos et al. [22], who looked at how well circular and eccentric inserts worked in a PTC receiver tube (Fig. 3). Their study analyzed the performance of concentric and eccentric pipe inserts in the PTC receiver tube. Figure 3, shows a strong agreement with the maximum deviation in Nusselt number being below 8.95% and the maximum variation in the friction factor (*f*) remaining under 4.67% between the result of Bellos et al. [22] and the findings of the present study.

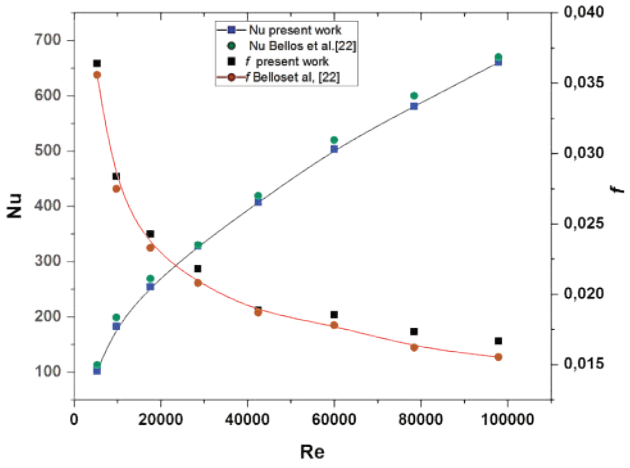

Figure 3. Validation: Nusselt number and the friction factor Vs Reynolds number.

Table 6. Grid independence study

Grid number	*Nu* (outer tube)	*Nu* (Inner tube)	*f* (outer tube)	*f* (inner tube)
1128625	218.85	46.23	0.035	0.06243
2259875	218.90	45.41	0.042	0.06251
3522375	218.82	45.32	0.032	0.06250
3657845	219.02	45.30	0.031	0.06248

RESULTS AND DISCUSSION

The results of numerical simulations for different input temperatures and mass flow rates in the conventional, concentric, and eccentric receiver tubes are shown, and the effects of the three geometries on the PTC›s heat transfer rate are examined.

Flow Structure

Effects of concentric and eccentric configuration

This section explores the impact of the concentric and eccentric configurations on the temperature and velocity fields inside the absorber tube and the heat transfer fluid. Fig.4 and Fig.5, showing temperature and velocity profiles for specific parameters: $Tin_oil = 500K$, $\dot{m}_oil = 0.7kg/s$, $Tin_water = 300K$, and $\dot{m}_water = 0.006\ kg/s$, and $\dot{m}_water = 0.006\ kg/s$ across three different models.

Figure 4 shows the temperatures around the circumference of the solar receiver tube, which is the metal surface in contact with the heat transfer fluid, for the three PTC configurations. The figure makes it very clear that the temperature differences (ΔT) between the various points are becoming less and less when moving from the standard to the concentric and eccentric designs. The conventional tube exhibits a temperature gradient of 55 K, providing a baseline for assessing the improved thermal behavior of tubes with concentric or eccentric inserts. Which is reduced to $42K$ and $34K$ for the concentric and eccentric receiver tube arrangements, respectively. This corresponds to reductions of 45% and 60.60% compared to the single-tube configuration. The high peak temperatures and significant circumferential temperature gradients observed in the conventional tube can have several adverse effects on the absorber tube's performance and efficiency, such as excessive temperature stress and potential deformation. On the other hand, the concentric receiver tube exhibits lower peak temperatures and reduced circumferential temperature gradients.

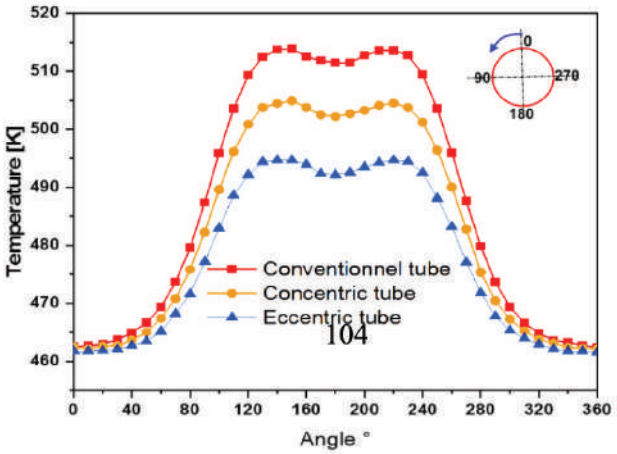

Figure 4. Temperature contour for the three PTC absorber models.

Figure 5 demonstrates a significant increase in the velocity gradient in the lower section of the absorber tube. This leads to a higher local heat transfer factor in this particular region. In addition, the solar radiation in this area causes a high heat flux that can be more effectively dissipated by the heat transfer fluids. Improved dissipation capability significantly enhances the degree to which temperatures fluctuate around the absorber tube, especially compared with a simple, single-tube configuration. Adding concentric and eccentric pipe inserts, each containing an inner tube, is an effective means of reducing the cross-sectional area available for oil flow. This reduction in the flow area results in a significant acceleration of the oil, even though the overall mass flow rate matches that of an equivalent single-tube configuration. Consequently, the convective heat transfer from the oil to the inner wall of the absorber tube is significantly more efficient.

Effects of using nanofluid

In this section, investigates the impact of concentric and eccentric configurations on the temperature distributions

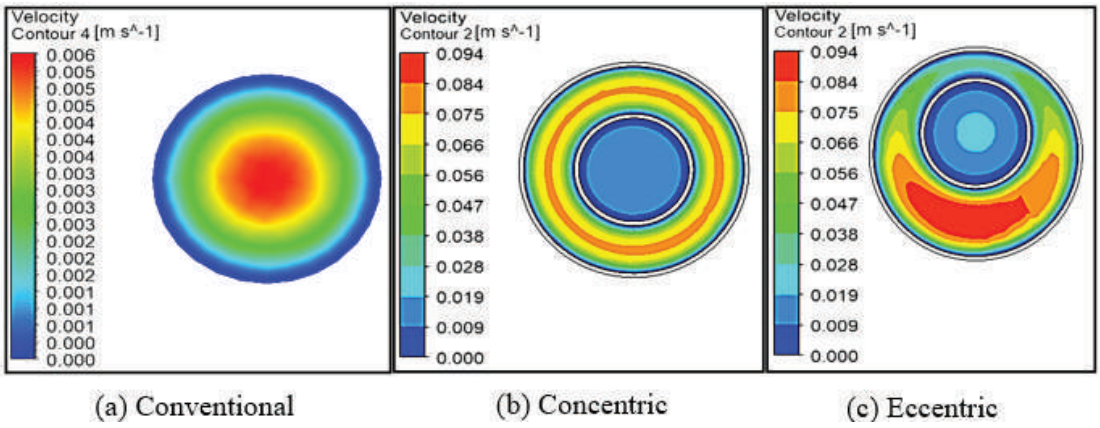

Figure 5. Velocity Contours.

within the absorber tube when using a nanofluid (AL_2O_3/*Syltherm-800 oil*) as *HT - HTF* and the water as *LT-HTF* for different operating conditions.

Effects of HT-HTF and LT-HTF mass flow rates on temperature gradients

This section illustrates the impact of changes in the mass flow rates of HT-HTF and LT-HTF on Tmax and the temperature gradient (ΔT) of the absorber tube, given specified parameters (Tin_oil = 600K, Tin_water = 300K, and $\dot{m}_oil$ = 0.06 kg/s).

Figure 6 illustrates that increasing the mass flow rate of the *LT-HTF* in the inner tube has negligible effects on (T_{max}) and gradient temperature (ΔT) for both concentric and eccentric receivers respectively. However, the use of nanofluid significantly reduces ΔT by 5K in the concentric tube and 30K for the concentric and the eccentric tube respectively which present an improvement of 5% and 51.56% compared with a smooth configuration. This confirms that nanofluid enhances heat transfer and leading to a lower temperature gradient.

Figure 7 demonstrates that increasing the mass flow rate of the *HT - HTF* fluid results in a decrease in both T_{max} and ΔT for both concentric and eccentric receiver tubes. This is attributed to the improved convective heat transfer performance at higher *HT - HTF* flow rates. Notably, the application of nanofluid further reduces ΔT by 5K in the concentric tube and 30K in the eccentric tube respectively which presented 14.82% and 50.57% compared by system without nanofluid, highlighting its potential for enhancing thermal performance in solar receiver's tubes.

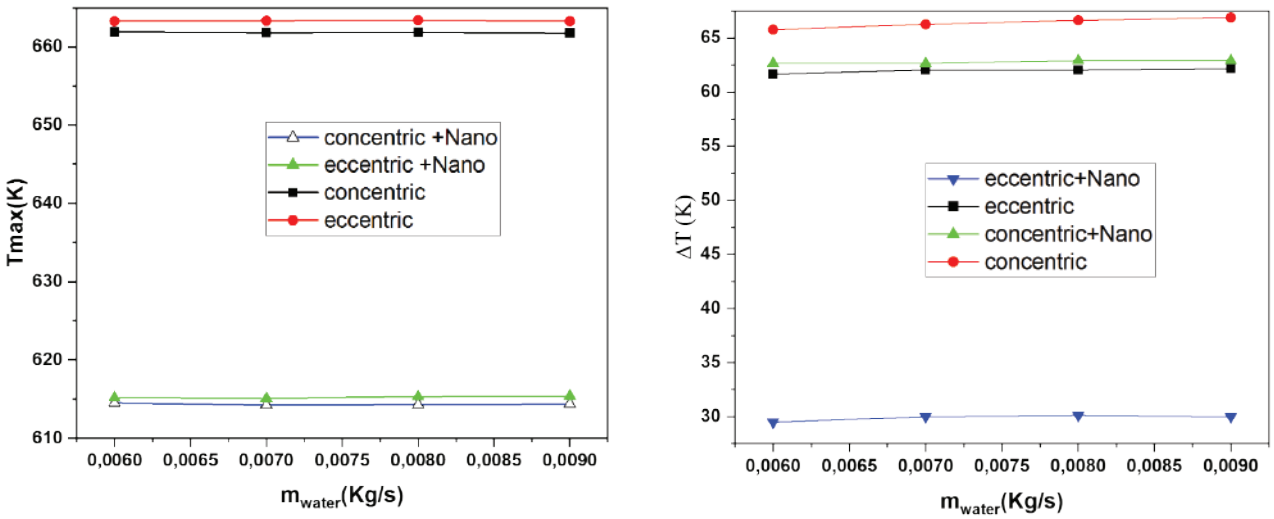

Figure 6. T_{max} and ΔT vs water (*LT - HTF*) mass flow rates.

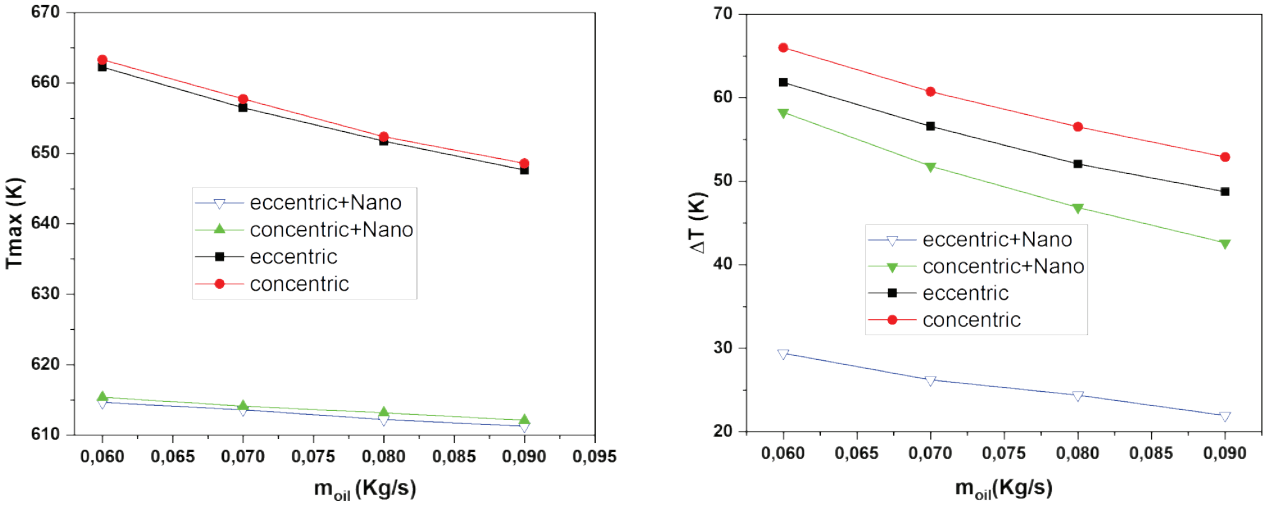

Figure 7. T_{max} and ΔT vs oil (*HT - HTF*) mass flow rates.

Effect of Lt-Htf, Ht-Hth inlet temperatures

We illustrate the impact of the low-and high-temperature heat transfer fluids inlet temperatures on the Tmax and the ΔT of the absorber tube under specified conditions Tin_oil = 500K, $\dot{m}_oil$ = 0.7kg/s, Tin_water = 300K, and $\dot{m}_water$ = 0.006 kg/s. In Fig. 9, adjustments in the inlet temperature of water (low-heat transfer fluids) within the inner tube exhibit minimal effects on the (T_{max}) and the ΔT for both concentric and eccentric receiver's tubes. However, employing nanofluid results in an average ΔT decrease of 13K in the concentric tube and $34K$ in the eccentric tube. Figure 8 illustrates that a higher inlet temperature of the high-temperature heat transfer fluid results in a rise in Tmax for both concentric and eccentric receivers. Consequently, the ΔT of both receivers becomes smaller as the inlet temperature of the *HT-HTF rises*, with nanofluid lowering ΔT by 4 K in the concentric tube and by 30 K in the eccentric tube.

Effect of nanofluid concentration

Figure10 illustrates the effect of nanofluid concentration on Tmax and ΔT with: Tin_oil=600K, Tin_water=300K,$\dot{m}_water$ = 0.006 kg/s, $\dot{m}_oil$ = 0.006 kg/s. In The results indicate that both the Tmax and ΔT decrease as the concentration of nanofluid increases. The temperature gradient ΔT in an eccentric arrangement, is significantly greater than that in a concentric design, the latter having an average of 14K.

Heat transfer improvement

To better assess the concentric and eccentric cases and the effect of flow parameters on thermal performance, we define these two reports (dimensionless numbers): heat transfer improvement ratio by the relation (Nu_{co}/Nu_{ec}) and ratio of the increase in resistance to flow by (f_{co}/f_{ec}). Where: Nu_{co} and $Nu_{ec:}$ Nusselt number of absorber tube inner surface for the concentric and the eccentric receiver tube respectively. f_{co} and f_{ec}: the frictional force factor of absorber

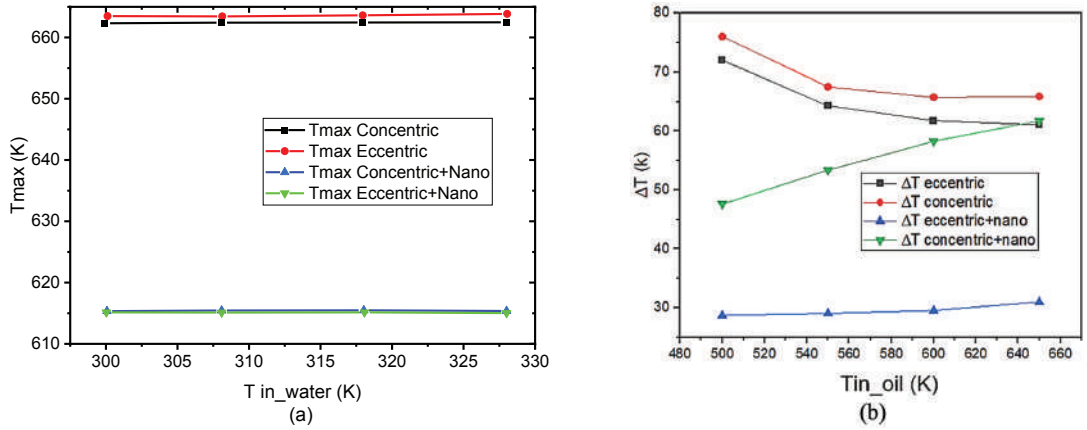

Figure 9. T_{max} and ΔT vs *LT - HTF* Temperature.

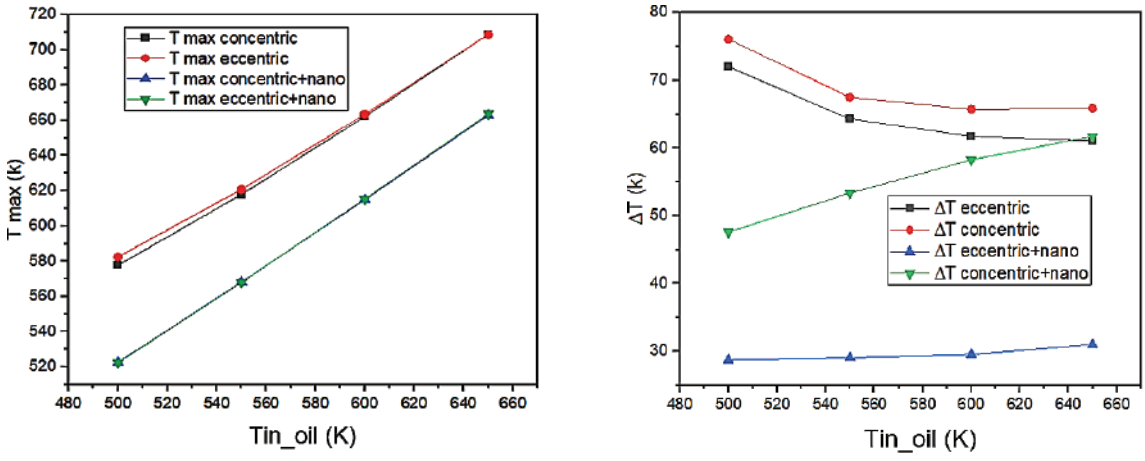

Figure 8. T_{max} and ΔT vs *HT - HTF* Temperature.

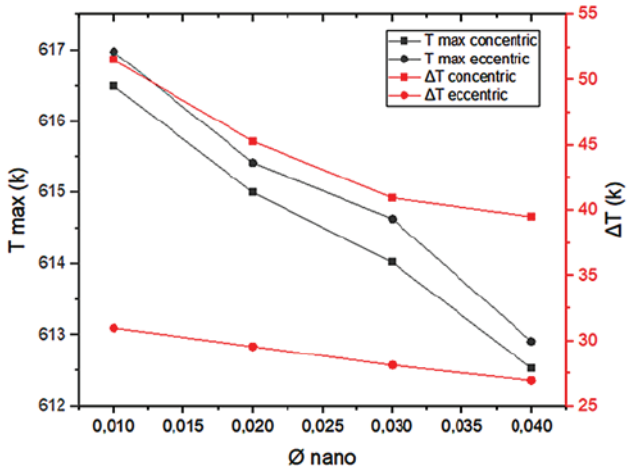

Figure 10. T_{max} and ΔT vs nanofluid concentration.

tube inner surface for the concentric eccentric receivers' tubes respectively.

Effects of the masse flow rate

Figure 11.(a) shows that the *LT-HTF* mass flow rate has a slight impact on the Nusselt number ratio for the base fluid. When using nanofluid, the Nusselt number ratio decreases slightly with increasing flow rate. This indicates that the heat transfer performance for the eccentric receiver configuration improves as the mass flow rate increases, given that the ratio is less than 1.0. The friction factor ratio remains close to 1.0 across all mass flow rates, indicating nearly identical flow resistance for both concentric and eccentric configurations for the base fluid. The friction factor ratio for the nanofluid stays around 1.05, indicating a slight increase in flow resistance about 5% for the concentric receiver compared to the eccentric receiver. This trade-off is considering the significant heat transfer benefits provided by the nanofluid.

Figure 11(b) shows the mass flow variations influence the heat transfer coefficient ratio as well as the friction factor ratio for the cases of the concentric and the eccentric receivers. The use of nanofluid elevates the heat transfer

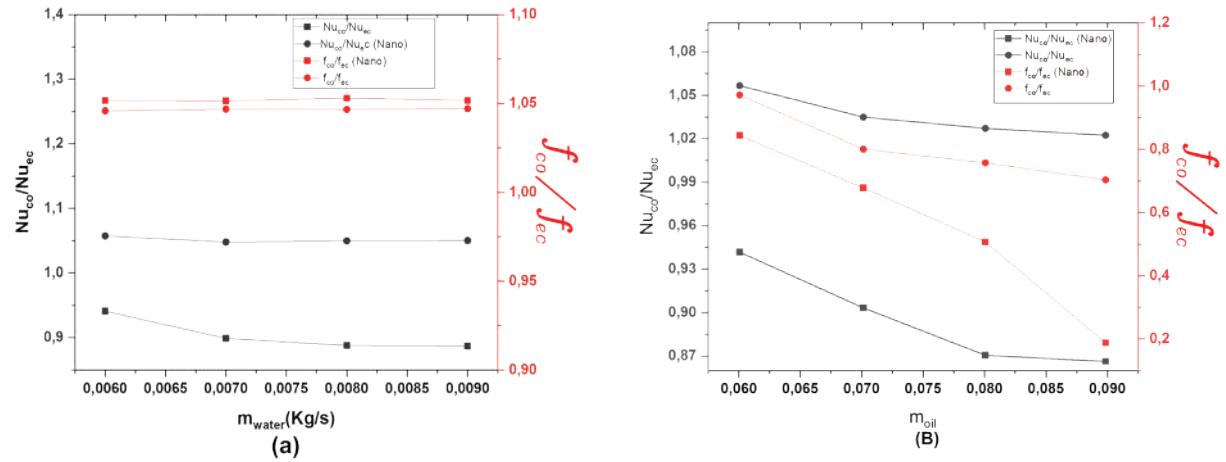

Figure 11. Nu_{co}/Nu_{ec} and f_{co}/f_{ec} vs *LT - HTF* temperature.

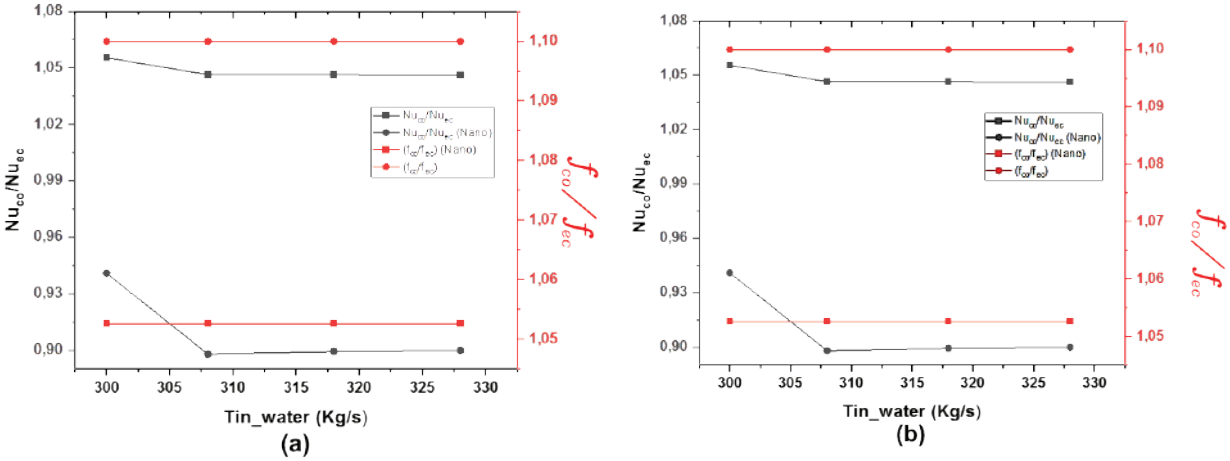

Figure 12. Nu_{co}/Nu_{ec} and f_{co}/f_{ec} vs inlet *LT - HTF* and *HT - HTF* temperatures.

coefficient on the inside of the absorber tube by 16.5% and raises the flow resistance to approximately 1.18 times that of the system without nanofluid.

Effects of the inlet LT-HTF and HT-HTH temperatures

In Figure 10.(a), alterations in the inlet temperature of water (*LT-HTF*) within the inner tube exhibit minimal impact on Nusselt number ratio and no effect on friction factor ratio for both receivers.

However, employing nanofluid enhances the heat transfer coefficient of the inner surface of the absorber tube by 14.5% and increases the flow resistance to approximately 1.04 *times* compare to without nanofluid.

As shown in Figure 12(b), as the inlet oil temperature *(HT-HTF)* increases, the values of the Nusselt number ratio and friction factor ratio for both receiver designs are higher. The eccentric receiver gives a better performance compared to the concentric design across the range of temperatures, with nominally larger ratios. This is because the decrease in oil viscosity with a rise in temperature, which increases convective heat transfer and hence overall thermal efficiency. Consequently, the heat transfer coefficient of the inner surface of the absorber tube improves by 18% and the flow resistance increases to about 1.22 *times* compare to without nanofluid.

Eccentric receiver operates more efficiently at increased *HT-HTF* flow rates, experiencing smaller relative increases in flow resistance and improving heat transfer with less drop-off at higher flow rates. Such findings help to adjust the system to the desired performance and operating parameters, where both heat transfer effectiveness and flow resistance are taken into account.

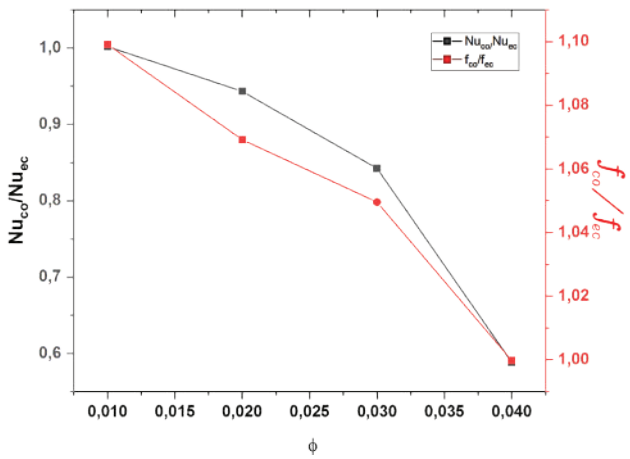

Figure 13. Nu_{co}/Nu_{ec} and f_{co}/f_{ec} vs nanofluid concentration.

Effect of nanofluid concentration

Figure 13 illustrates how the nanofluid concentration (f) affects the heat transfer enhancement ratio (Nu_{co}/Nu_{ec}) of the inner surface of the absorber tube and the ratio of increase in resistance to flow (f_{co}/f_{ec}) of nanofluid. It is observed that both (Nu_{co}/Nu_{ec}) and (f_{co}/f_{ec}) decrease with increasing concentration of nanofluid. This indicates that the heat transfer improvement ratio and the ratio of flow resistance in the eccentric receiver are larger than those in the concentric receiver, and they further increase with increasing nanofluid concentration.

Thermal performance

Figure 14 compares the effects of varying mass flow rates and inlet temperatures of the *HT - HTF*, both with and without nanofluid, on the thermal efficiency of different receiver configurations: conventional, concentric, and eccentric tubes. Figures 14. (a) and Figure 14. (b) depict the changes in heat collection efficiency of the concentric and

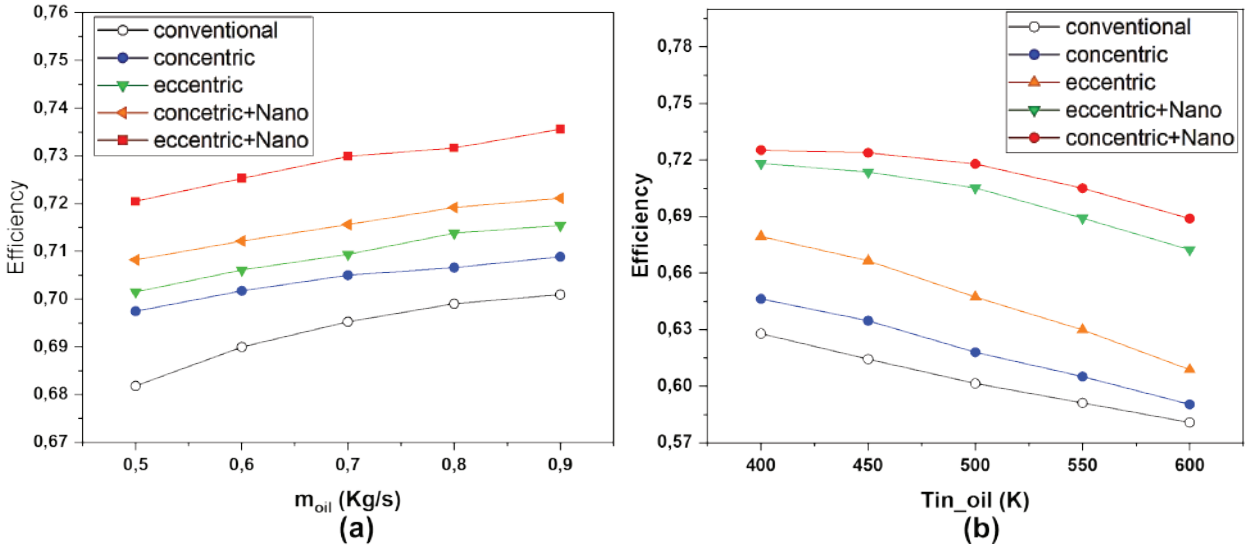

Figure 14. Thermal efficiency vs *HT - HTF* temperature and mass flow rate.

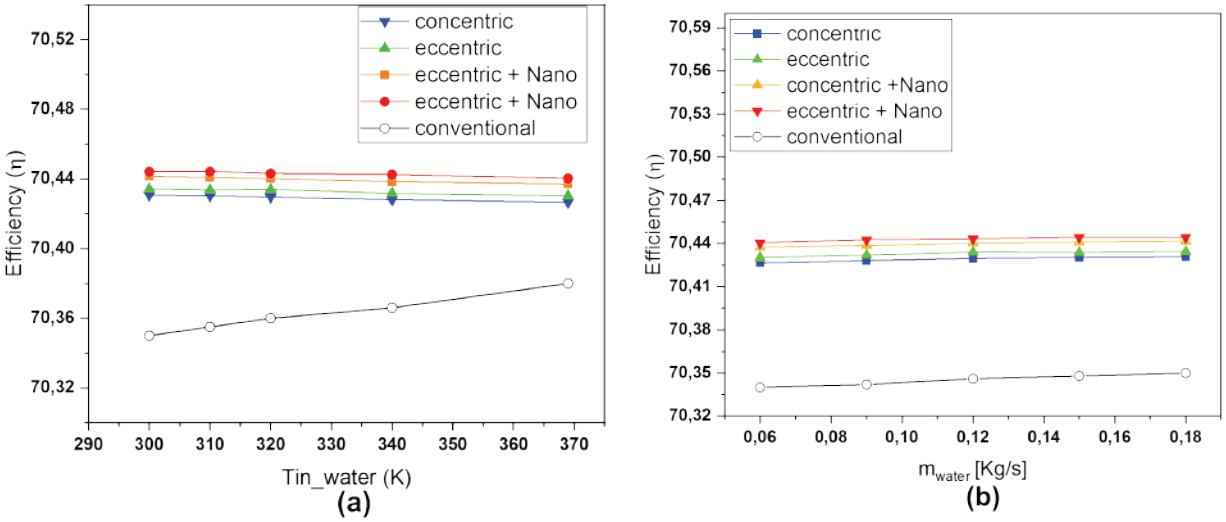

Figure 15. Thermal efficiency, vs *LT - HTF* temperature and mass flow rate.

eccentric receiver tubes over the conventional PTC design. These figures illustrate that the two types of receiver tubes are capable of achieving efficiency improvements up to 2.62% and 3.26% respectively. But this improvement of efficiency is dependent on the increase of the mass flow rate of the *HT-HTF*. Moreover, the presence of nanofluid leads to a very significant increase in efficiency, with an improvement of 6.12% for the concentric tube and 8.23% for the eccentric tube, thus making it possible for the two new designs to outperform the conventional receiver tube.

Figure 13, illustrates the impact of changes in the *LT-HTF* inlet temperature and the mass flow rates of different receiver configurations: conventional, concentric and eccentric receivers' tubes. It is noticed that the efficiency increases considerably with the declining the inlet temperature for *LT-HTF* and the growing of the masse flow rate. But the effects of the *LT-HTF* inlet temperature and the mass flow on the efficiency are limited.

As shown in Figure 14, the thermal efficiency increases by increasing the concentration of nanofluid, the PTC with eccentric receiver tube shows the best efficiency with a difference of 34.78% compared with the conventional receiver tube.

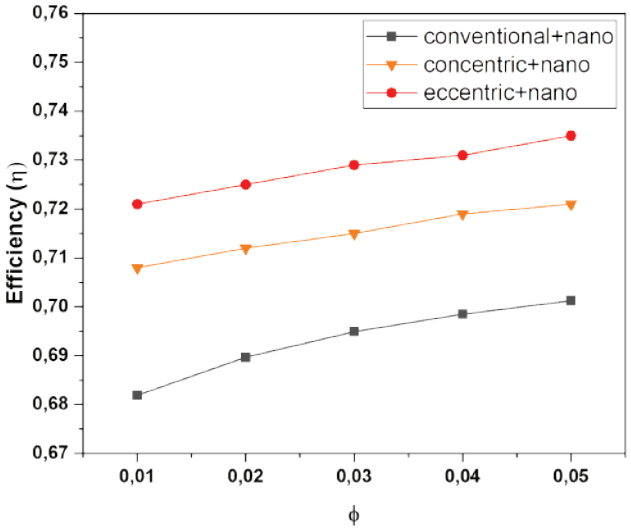

Figure 16. Thermal efficiency vs nanofluid concentration (ϕ).

Graphical Analysis of Results

This section presents findings on the heat performance of parabolic trough solar concentrators with different receiver tube designs. The changes in heat performance and efficiency of these configurations explored in the study are depicted by figures 17, 18, 19, and 20.

Using a concentric and eccentric receiver tube configuration reduced the receiver tube temperature gradients compared to a conventional absorber tube. Which is reduced to 42*K* and 34*K* for the concentric which translates to a 60.6% improvement compared to the conventional single-tube design. The concentric tube configuration also showed substantial benefits, with a ΔT reduction of 13*K*, or 14.82%, highlighting its effectiveness in minimizing thermal stresses and improving system reliability see Figure 15.

Increasing the mass flow rate of the HT-HTF fluid led to the reduction of the temperature gradient (ΔT) for both the concentric and eccentric receivers. Lowering the ΔT is attributed to the more effective convective heat transfer at the higher HT-HTF flow rates. Nonetheless, the inlet temperature and mass flow rate of the water in the inner tube only have a limited effect on this. From the Figure 18, it is also evident that the employment of nanofluid further brought down ΔT by 5K in the concentric tube and 30K in the eccentric tube, thus implying that the enhancements of 14.82% and 50.57%, respectively, as compared to the system

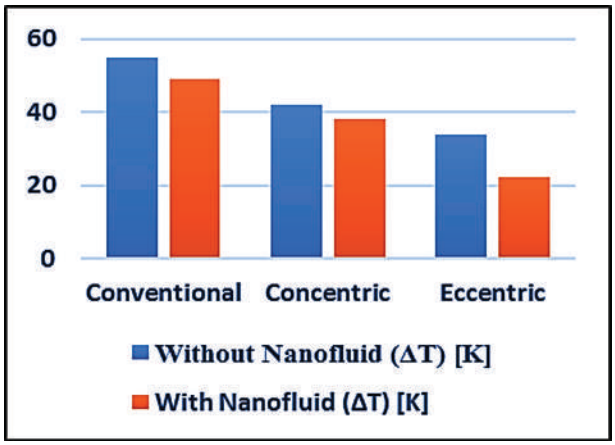

Figure 17. Temperature gradient (ΔT) reduction for different configurations.

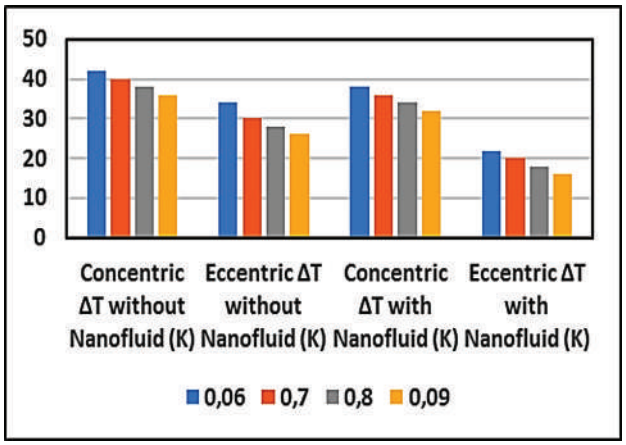

Figure 18. Temperature gradient (ΔT) vs *HT - HTF* mass flow Rate.

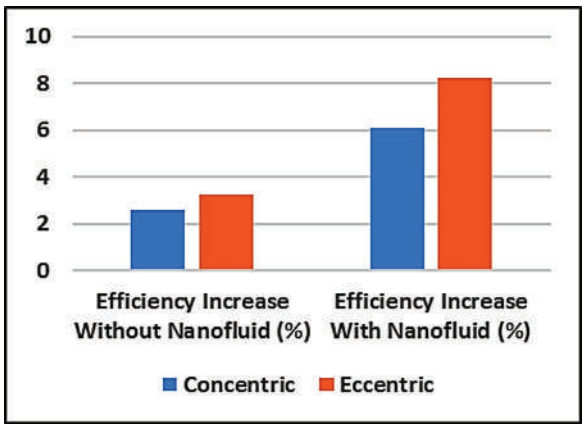

Figure 19. Temperature gradient (ΔT) reduction for different configurations.

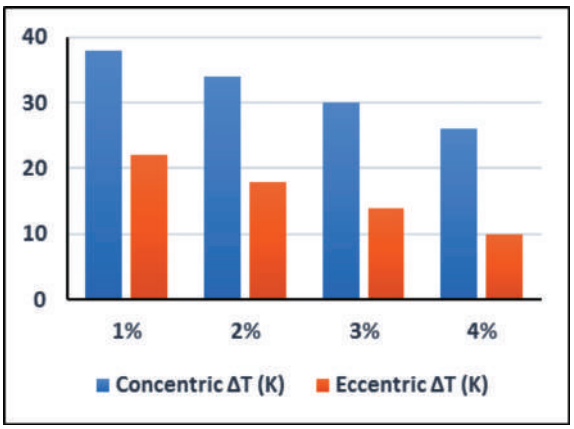

Figure 20. Temperature gradient (ΔT) vs *HT - HTF* mass flow Rate.

without nanofluid were attained, hence the application of nanofluid being notably appropriate for the solar receiver tubes to achieve the thermal performance increment.

CONCLUSION

This study analyzes the thermal performance improvement of a parabolic trough solar concentrator (PTC) using concentric and eccentric receiver tube geometries and nanofluids has been elaborated in the current research. The main aim was to address the issue of non-uniform heat flux (NUHF), which may result in temperature gradient and thermal stress and reduce system efficiency.

Both concentric and eccentric configurations are found to be effective in minimizing heat temperature gradients in the absorber tube. The percentage of reduction in the concentric receiver tube was 60.6% whereas it was only 45% for the eccentric design when both were compared to the smooth tube. Such decreases are significant as they alleviate the thermal stress on the tube, thus extending the reliability and the service life of the system.

Besides, an enhancement of the mass flow rate of the HT-HTF enhances convective heat transfer. Consequently, it reduces peak temperatures and temperature gradients in both configurations. Notably, employment of a 4% nanofluid concentration revealed much enhancement of performance. When the concentration was at this level, the temperature gradient was reduced by another 50.57% in the eccentric tube, while thermal efficiency in the PTC system was 34.78% greater than in conventional systems without nanofluids.

In terms of efficiency, both the eccentric and concentric designs performed better than the traditional PTC. The concentric tube recorded an efficiency gain of up to 2.62%, while the eccentric configuration reached 3.26%. Efficiency improvement increased to 6.12% and 8.23% for the new PTC designs proposed combined with nanofluids for the eccentric and concentric tubes respectively. The above

results support the idea that combining innovative receiver tube geometries with and optimized nanofluids can significantly increase thermal efficiency.

To summarize, the research highlights the influence of a receiver configuration and the selection of a heat transfer fluid in the performance enhancement of the parabolic trough solar collectors (PTCs). The use of fluid compositions and geometrically optimized flow will lead to a better distribution of the temperature even, higher heat transfer, and lower thermal stress that will basically result in system lifetimes being extended and their efficiency getting better. These kinds of improvements are particularly relevant to the clean energy sectors, which are now facing the challenge of bringing down the total costs of the plants while at the same time, making a less significant contribution to the atmospheric load of greenhouse gases. In the future, experimental validation and prototype fabrication will be necessary steps to turn these design concepts into feasible technologies that can be easily integrated into the sustainable energy systems.

NOMENCLATURE

PTC	Parabolic Trough Collector
PTR	Parabolic Trough Receiver
NUHF	Non-Uniform Heat Flux
HTF	Heat Transfer Fluid
CFD	Computational Fluid Dynamics
LT-HTF	Low-Temperature Heat Transfer Fluid
HT - HTF	High-Temperature Heat Transfer Fluid
AL_2O_3	Aluminium Oxide (nanoparticule)
DNI	Direct Normal Irradiance
MCRT	Monte Carlo Ray Tracing
UDF	User Defined Functions

Subscripts

co	Refers to concentric
ec	Refers to eccentric
f	Refers to fluid
s	Refers to solid
p	Refers to particle

Nomenclature

C_p	Specific heat, *kJ / kg°C*
d	Inner diameter, *m*
k	Thermal conductivity, *W/m°C*
L	Length of the receiver tube, *m*
$\dot{m}$	Mass flow rate, *Kg/s*
ρ	Density, kg/m^3
μ	Dynamic viscosity, (*kg/m·s*)
Q_c	Collected heat, W/m^2
T	Température, °C
T_m	Main temperature, °C
T_w	Wall temperature, °C
q_w	Heat flux on the wall, W/m^2
ΔP	Pressure drop, Pa
u	Velocity, *m/s*

Greek symbols

ϕ	Nano fluid concentration, %.

AUTHORSHIP CONTRIBUTIONS

Authors equally contributed to this work.

DATA AVAILABILITY STATEMENT

The authors confirm that the data that supports the findings of this study are available within the article. Raw data that support the finding of this study are available from the corresponding author, upon reasonable request.

CONFLICT OF INTEREST

The author declared no potential conflicts of interest with respect to the research, authorship, and/or publication of this article.

ETHICS

There are no ethical issues with the publication of this manuscript.

STATEMENT ON THE USE OF ARTIFICIAL INTELLIGENCE

Artificial intelligence was not used in the preparation of the article

REFERENCES

[1] Fernández-García A, Zarza E, Valenzuela L, Pérez M. Parabolic-trough solar collectors and their applications. Renew Sustain Energy Rev 2010;14:1695-1721. [CrossRef]

[2] Okafor IF, Dirker J, Meyer JP. Influence of non-uniform heat flux distributions on the secondary flow, convective heat transfer and friction factors for a parabolic trough solar collector type absorber tube. Renew Energy 2017;108:287-302. [CrossRef]

[3] Khanna S, Kedare SB, Singh S. Analytical expression for circumferential and axial distribution of absorbed flux on a bent absorber tube of solar parabolic trough concentrator. Sol Energy 2013;92:26-40. [CrossRef]

[4] He YL, Wang K, Qiu Y, Du BC, Liang Q, Du S. Review of the solar flux distribution in concentrated solar power: non-uniform features, challenges, and solutions. Appl Therm Eng 2019;149:448-474. [CrossRef]

[5] Jebbar YA, Fluiful FK, Khudhayer WJ, Ali Hasson N, Abdulhamed AJ. Improvement of heat transfer in a parabolic trough collector receiver tube with hollow cylindrical inserts: A CFD study. Int J Heat Technol 2024;42:924-932. [CrossRef]

[6] Norouzi AM, Siavashi M, Khaliji Oskouei M. Efficiency enhancement of the parabolic trough solar collector using the rotating absorber tube and nanoparticles. Renew Energy 2020;145:569-584. [CrossRef]
[7] Raval P, Ramani B. Heat transfer enhancement techniques using different inserts in absorber tube of parabolic trough solar collector: A review. J Therm Eng 2024;10:1068-1091. [CrossRef]
[8] Chang C, Xu C, Wu Z, Li X, Zhang Q, Wang Z. Heat transfer enhancement and performance of solar thermal absorber tubes with circumferentially non-uniform heat flux. Energy Procedia 2015;69:320-327. [CrossRef]
[9] Afsharpanah F, SheShpoli AZ, Pakzad K, Ajarostaghi SSM. Numerical investigation of non-uniform heat transfer enhancement in parabolic trough solar collectors using dual modified twisted-tape inserts. J Therm Eng 2021;7:133-147. [CrossRef]
[10] Fatouh M, Saad N, Abdala AMM. Effects of fins base rounding on heat transfer characteristics of absorber tube of parabolic trough collector. Arab J Sci Eng 2023;48:2851-2871. [CrossRef]
[11] de Sa AB, Pigozzo Filho VC, Tadrist L, Passos JC. Direct steam generation in linear solar concentration: experimental and modeling investigation a review. Renew Sustain Energy Rev 2018;90:910-936. [CrossRef]
[12] Zhang X, Wang F, Sun X, Cheng Z, Gong X. Analysis of heat transfer performance of the absorber tube with convergent-divergent structure for parabolic trough collector. J Therm Eng 2021;7:1843-1856. [CrossRef]
[13] Liu P, Dong Z, Xiao H, Liu Z, Liu W. Thermal-hydraulic performance analysis of a novel parabolic trough receiver with double tube for solar cascade heat collection. Energy 2020;197:117244. [CrossRef]
[14] Liu P, Dong Z, Xiao H, Liu Z, Liu W. A novel parabolic trough receiver by inserting an inner tube with a wing-like fringe for solar cascade heat collection. Renew Energy 2021;170:327-340. [CrossRef]
[15] Benabderrahmane A, Benazza A, Hussein AK. Heat transfer enhancement analysis of tube receiver for parabolic trough solar collector with central corrugated insert. ASME J Heat Transf 2020;142:062001. [CrossRef]
[16] Guerraiche D, Bougriou C, Guerraiche K, Valenzuela L, Driss Z. Experimental and numerical study of a solar collector using phase change material as heat storage. J Energy Storage 2020;27:101133. [CrossRef]
[17] Imtiaz Hussain M, Lee GH. Numerical and experimental heat transfer analyses of a novel concentric tube absorber under non-uniform solar flux condition. Renew Energy 2017;103:49-57. [CrossRef]
[18] Acuña A, Velázquez N, Sauceda D, Aguilar A. Modeling, construction, and experimentation of a compound parabolic concentrator with a concentric tube as the absorber. J Energy Eng 2017;143:04016059. [CrossRef]
[19] Wang F, Shuai Y, Yuan Y, Yang G, Tan H. Thermal stress analysis of eccentric tube receiver using concentrated solar radiation. Sol Energy 2010;84:1809-1815. [CrossRef]
[20] Chang C, Peng X, Nie B, Leng G, Li C, Hao Y, She X. Heat transfer enhancement of a molten salt parabolic trough solar receiver with concentric and eccentric pipe inserts. Energy Procedia 2017;142:624-629. [CrossRef]
[21] Pérez-Álvarez R, González-Gómez PÁ, Acosta-Iborra A, Santana D. Thermal stress and fatigue damage of central receiver tubes during their preheating. Appl Therm Eng 2021;195:117115. [CrossRef]
[22] Bellos E, Daniil I, Tzivanidis C. A cylindrical insert for parabolic trough solar collector. Int J Numer Method Heat Fluid Flow 2019;29:1218-1237. [CrossRef]
[23] Guerraiche D, Guerraiche K, Driss Z, Chibani A, Merouani S, Bougriou C. Heat transfer enhancement in a receiver tube of solar collector using various materials and nanofluids. Eng Technol Appl Sci Res 2022;12:9282-9294. [CrossRef]
[24] Wang Y, Xu J, Liu Q, Chen Y, Liu H. Performance analysis of a parabolic trough solar collector using Al2O3/synthetic oil nanofluid. Appl Therm Eng 2016;107:469-478. [CrossRef]
[25] Benabderrahmane A, Hussein AK, Younis O, Benazza A. Single-phase and two-phase models of a hybrid nanofluid traveling through a non-uniformly heated (PTC) receiver: A comparative study. J Therm Eng 2023;9:1442-1451. [CrossRef]
[26] Khan MS, Yan M, Ali HM, Amber KP, Bashir MA, Akbar B, Javed S. Comparative performance assessment of different absorber tube geometries for parabolic trough solar collector using nanofluid. J Therm Anal Calorim 2020;140:999-1009. [CrossRef]
[27] Mustafa J, Alqaed S, Sharifpur M. Numerical study on performance of double-fluid parabolic trough solar collector occupied with hybrid non-Newtonian nanofluids: Investigation of effects of helical absorber tube using deep learning. Eng Anal Bound Elem 2022;140:562-580. [CrossRef]
[28] Khan M, Alsaduni IN, Alluhaidan M, Xia WF, Ibrahim M. Evaluating the energy efficiency of a parabolic trough solar collector filled with a hybrid nanofluid by utilizing double fluid system and a novel corrugated absorber tube. J Taiwan Inst Chem Eng 2021;124:150-161. [CrossRef]
[29] Abbasian Arani AA, Memarzadeh A. Nanofluid multi-morphology effect on dual-fluid sinusoidal-wavy grooved absorber tube parabolic trough solar collector performances enhancement based on experimental data. Int Commun Heat Mass Transf 2021;123:105201. [CrossRef]
[30] Shaker B, Gholinia M, Pourfallah M, Ganji DD. CFD analysis of Al2O3-syltherm oil nanofluid on parabolic trough solar collector with a new flange-shaped turbulator model. Theor Appl Mech Lett 2022;12:100344. [CrossRef]

J Ther Eng, Vol. 12, No. 1, pp. 144−155, January, 2026

Journal of Thermal Engineering
Web page info: https://jten.yildiz.edu.tr
DOI: 10.14744/thermal.0001065

Research Article

Opposition-based algorithm for the optimization of shell-and-tube heat exchangers

Elaheh KHOSRAVIAN[1], Mohammad B. AHMADI[1,*]

[1]*Department of Mathematics, Faculty of Science, Shiraz University, Shiraz, 71936, Iran*

ARTICLE INFO

Article history
Received: 23 September 2024
Revised: 27 November 2024
Accepted: 10 December 2024

Keywords:
Aspen-EDR Software;
Optimization Methods;
Optimizing Based Opposition;
Shell and Tube Heat Exchanger

ABSTRACT

Shell-and-tube heat exchangers are widely used across various industries due to their high efficiency in energy recovery, drying, and cooling processes. However, optimizing these exchangers presents significant challenges due to the discrete nature of the design variables and the complexity of the governing equations, which are discontinuous and non-differentiable. To address these challenges, metaheuristic algorithms such as Genetic Algorithm, Particle Swarm Optimization, and Differential Evolution are commonly applied. This study introduces two enhanced optimization algorithms: Opposition-Based Differential Evolution and Comprehensive Opposition-Based Learning. These methods incorporate the concept of opposition both in generating initial solutions and in iterative optimization processes, enabling the efficient identification of optimal solutions.

The optimization process focuses on key design variables, including tube diameter, shell diameter, and baffle spacing, which directly determine the complete geometry of the heat exchanger. The performance of these algorithms was evaluated across two case studies from prior research. Results showed an 18.88% improvement in cost reduction for the first case study and a 16.37% improvement for the second compared to conventional methods. Additionally, these algorithms outperformed Aspen EDR, a commercial heat exchanger design software, in identifying cost-effective and geometrically feasible solutions. Since Aspen EDR has limited modules for heat exchanger design and fails to provide solutions for complex geometries, such as helical or coiled tube configurations, the proposed algorithms offer a reliable and efficient alternative in such scenarios

This research demonstrates the potential of these enhanced optimization algorithms to overcome traditional design limitations, providing a more versatile and effective approach for designing shell-and-tube heat exchangers with improved performance and cost efficiency.

Cite this article as: Khosravian E, Ahmadi MB. Opposition-based algorithm for the optimization of shell-and-tube heat exchangers. J Ther Eng 2026;12(1):144−155.

***Corresponding author.**
*E-mail address: mbahmadi@shirazu.ac.ir

This paper was recommended for publication in revised form by Editor-in-Chief Ahmet Selim Dalkilic

Published by Yıldız Technical University Press, İstanbul, Turkey
Yıldız Technical University. This is an open access article under the CC BY-NC license (http://creativecommons.org/licenses/by-nc/4.0/).

INTRODUCTION

Shell-and-tube heat exchangers are extensively used across various industries, including energy recovery, drying, and cooling processes, due to their high efficiency and versatility [1].

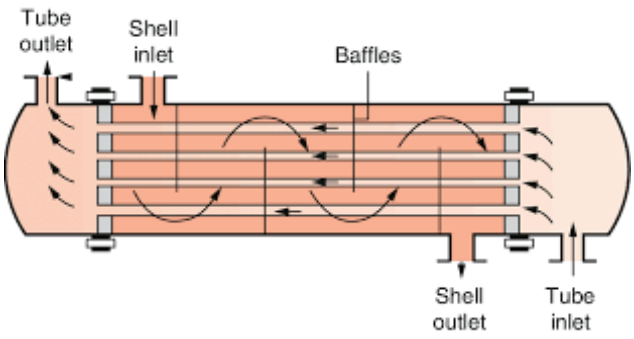

Figure 1. Shell and Tube Heat Exchanger Schematic Diagram.

However, optimizing the design of these exchangers presents significant challenges because of the discrete nature of the design variables and the complexity of the governing equations, which are discontinuous and non-differentiable [2].

Traditional optimization methods often struggle with these complexities, particularly when considering the intricate geometries and operational parameters involved in heat exchanger design. Recent studies have introduced new approaches, such as the use of nanofluids and porous media, to improve heat transfer performance and efficiency in heat exchangers. For instance, Qader et al. (2023) [3] demonstrated that using TiO2-water nanofluids in a double-pipe heat exchanger enhanced its effectiveness by incorporating porous media. Similarly, Zarda et al. (2022) [4] investigated the use of nanofluids in a flat solar collector, showcasing significant improvements in thermal efficiency through computational fluid dynamics (CFD) simulations. These studies highlight the potential of novel materials and advanced techniques for improving heat exchanger performance.

Furthermore, Hussein et al. [5] (2023) evaluated the performance of shell-and-tube heat exchangers using ZnO/water nanofluids and demonstrated notable enhancements in heat transfer rates [6]. In a similar context, Adnan Hussein et al. (2023) [6] explored the use of Fe3O4/water nanofluids in shell-and-tube heat exchangers, reporting significant improvements in heat transfer efficiency and overall performance. Qader et al. (2023) [7] also conducted a numerical study of heat transfer in circular pipes filled with porous media, emphasizing the role of advanced methodologies in optimizing heat exchanger configurations. While these methods have shown promise, they primarily focus on material innovations and fail to comprehensively address the challenges associated with optimization of complex geometries and design variables. Meanwhile, optimization techniques have also evolved to address the multi-objective nature of heat exchanger design. For example, Nadi et al. (2021) [8] employed Multi-Objective Particle Swarm Optimization (MOPSO) for the optimization of K-type shell-and-tube heat exchangers, demonstrating the potential of metaheuristic methods to balance trade-offs between thermal performance and cost. While these methods have shown promise, they primarily focus on material innovations and fail to comprehensively address the challenges associated with optimization of complex geometries and design variables.

The primary aim of this study is to introduce two advanced optimization algorithms: Opposition-Based Differential Evolution (OBDE) and Comprehensive Opposition-Based Learning (COBL) [9]. These algorithms incorporate the concept of opposition not only in generating initial solutions but also throughout the iterative optimization process, significantly enhancing the efficiency and accuracy of the solution search [10,11]. By integrating opposition mechanisms, these algorithms avoid local optima and explore a broader solution space, thus providing more reliable optimal solutions [12,13].

The optimization process in this study focuses on critical design variables, such as tube diameter, shell diameter, and baffle spacing, which directly influence the geometry and performance of the heat exchanger. The accurate determination of these variables ensures that the final design is both cost-effective and practically feasible [14]. Despite their potential, however, existing commercial software tools like Aspen EDR have limitations, particularly when dealing with complex geometries such as helical or coiled tube configurations. Aspen EDR, which is commonly used for heat exchanger design, lacks the necessary modules for handling such intricate designs, often failing to provide solutions for these types of systems [15].

To address these limitations, the proposed optimization algorithms offer a more reliable and efficient alternative, capable of handling complex geometries and producing geometrically feasible, cost-effective solutions. In this study, the performance of the proposed algorithms was evaluated through two case studies from prior research. The results demonstrated an 18.88% improvement in cost reduction for the first case study and a 16.37% improvement for the second when compared to conventional methods [16]. Moreover, the proposed algorithms outperformed Aspen EDR in terms of both cost-effectiveness and the ability to generate geometrically feasible solutions.

This paper aims to contribute to the ongoing efforts in optimizing shell-and-tube heat exchangers by providing a novel, robust optimization technique. By incorporating these advanced algorithms, the study addresses key gaps in the current literature and offers a solution that not only improves design efficiency but also opens new avenues for solving complex heat exchanger design problems. The

proposed algorithms offer significant potential for future research and practical applications, especially in industries where customized heat exchanger designs are critical for achieving optimal performance [17].

The structure of this article is organized as follows: Section 2 outlines the mathematical relationships and equations central to STHE modeling. Section 3 provides a comprehensive overview of OBL and its integration into metaheuristic frameworks. Section 4 presents the optimization results of a case study, comparing the proposed algorithms with traditional approaches. Finally, Section 5 summarizes the findings and contributions of this research.

MATHEMATICAL MODEL OF SHELL-AND-TUBE HEAT EXCHANGER

The Kern methodology, derived from research conducted at the University of Delaware [18], offers a semi-analytical framework for modeling the performance of STHEs. This approach integrates principles of fluid mechanics with the physical characteristics of STHEs, including their geometric configurations and operating conditions, to provide a comprehensive analysis of their behavior. A concise overview of this methodology is provided in the subsequent sections. The heat transfer coefficient in tube side, i.e. h_t is calculated according to the flow regime on the tube side, as given in the equations (1). The correlation is determined using the Reynolds number on the tube side.

$$h_t=\begin{cases}\frac{k_t}{d_i}\times\left[3.657+\frac{0.0677\left(\mathrm{Re}_t\times\mathrm{Pr}_t\left(\frac{d_i}{L}\right)\right)}{1+0.1\times\mathrm{Pr}_t\times\left(\mathrm{Re}_t\left(\frac{d_i}{L}\right)\right)}\right] & if \quad \mathrm{Re}_t<2300\\ \frac{k_t}{d_i}\times\left[\frac{\frac{f_t}{8}(\mathrm{Re}_t-1000)\times\mathrm{Pr}_i)}{1+12.7(\frac{f_t}{8})\times(\mathrm{Pr}_t^{\frac{2}{3}}-1)}\times(1+\frac{d_i}{L})^{0.67}\right] & if \quad 2300\le Re_t\le 10000\\ 0.027\frac{k_t}{d_o}Re_t^{0.8}\,Pr_t^{\frac{1}{3}}\left(\frac{\mu_t}{\mu_{wt}}\right)^{0.14} & if \quad Re_t>10000\end{cases} \quad (1)$$

The equations governing the problem as well as the required parameters are given in the Table 1.

Table 1. System Equations and Parameters [16]

	Symbol	
Darcy friction factor tube side	f_t	$f_t=(1.82\times log_{10}Re_t-1.64)^{-2}$
Darcy friction factor in shell side	f_s	$f_s=2b_o\,Re_s^{-0.15}$
Coefficient of heat transfer in shell side	h_s	$h_s=0.36\frac{k_s}{d_e}Re_s^{0.55}\,Pr_s^{\frac{1}{3}}\left(\frac{\mu_t}{\mu_{ws}}\right)^{0.14}$
Prandtl number in tube side	Pr_t	$Pr_t=\frac{\mu_t Cp_t}{k_t}$
Heat transfer rate	Q	$Q=m_hC_{ph}(T_{hi}-T_{ho})=m_sC_{pc}(T_{co}-T_{ci})$
Reynolds number in shell side	Re_s	$Re_s=\frac{m_sd_e}{A_s\mu_s}$
Reynolds number in tube side	Re_t	$Re_t=\frac{m_sd_e}{A_s\mu_s}$
Fluid velocity in shell side (m/s)	v_s	$v_s=\frac{m_s}{\rho_sA_s}$
Fluid velocity in tube side (m/s)	v_t	$v_t=\frac{\dot{m}_t}{\frac{\pi}{4}{d_i}^2\rho_t}(\frac{n}{N_t})$
Pressure drop (Pa)	ΔP	
Tube side pressured drop	ΔP_t	$\Delta P_t=\frac{\rho_tv_t^2}{2}(\frac{L}{d_i}\times f_t+p)\times n$
Shell side pressured in Kern's method	ΔP_s	$\Delta P_s=f_s(\frac{\rho_sv_s^2}{2})(\frac{L}{B})(\frac{D_s}{d_e})$
Diameter of shell hydraulic in square pitch arrangement	d_{es}	$d_{es}=\frac{4(S_t^2-\left(\frac{\pi d_o^2}{4}\right))}{\pi d_o}$

Table 1. System Equations and Parameters [16] (continued)

	Symbol	
Diameter of shell hydraulic in triangular pitch arrangement	d_{et}	$d_{et} = \frac{4(0.43S_t^2 - \left(\frac{0.5\pi d_o^2}{4}\right))}{0.5\pi d_o}$
Surface area of shell side	A_s	$A_s = D_s B(1 - \frac{d_o}{S_t})$
Shell side Prandtl number	Pr_s	$Pr_s = \frac{\mu_s C_{ps}}{k_s}$
Overall heat transfer coefficient (W/m2 k)	U	$U = \frac{1}{(\frac{1}{h_s}) + R_{fs} + (\frac{d_o}{d_i}) \times (R_{ft} + (\frac{1}{h_t}))}$
The logarithmic mean temperature difference (LMTD)	LMTD	$LMTD = \frac{(T_{hi} - T_{co}) - (T_{ho} - T_{ci})}{ln(\frac{T_{hi} - T_{co}}{T_{ho} - T_{ci}})}$
Correction coefficient	R	$R = \frac{T_{hi} - T_{ho}}{T_{co} - T_{ci}}$
Efficiency Factor	P_E	$P_E = \frac{T_{co} - T_{ci}}{T_{hi} - T_{ci}}$
Correction factor of flow configuration	F	$F = \sqrt{\frac{R^2+1}{R-1} \times (\frac{ln(\frac{1-p}{1-pr})}{ln(\frac{2-PR+1-\sqrt{R^2+1}}{2-PR+1-\sqrt{R^2+1}})}}$
Surface area of heat exchanger (m2)	A	$A = \frac{Q}{U \times F \times LMTD}$
Tube length (m)	L	$L = \frac{A}{\pi d_o N_t}$
Power of pumping (w)	Pw	$Pw = \frac{1}{\eta} \times (\frac{m_t}{\sigma_t} \times \Delta P_t + \frac{m_s}{\sigma_s} \times P_S)$

Definitions of parameters are summarized in Table 2.

Proposed Meta Heuristic Algorithm

This section deals with the proposed metaheuristic algorithms, i.e. OBDE and CO-OBL. Before the algorithms are presented, the cost function and some preliminaries are given below.

Cost calculation

The objective function corresponding to the total cost C_{tot} includes the annual fixed costs, i.e. C_i and the operating costs, i.e. C_{op}, is as follows:

$$C_{tot} = C_i + C_{op} \quad (2)$$

The annual fixed cost, i.e. C_i, is the function of the heat exchanger area, as shown in Eq. (3).

$$C_i = a_1 + a_2 A^{a_3} \quad (3)$$

where, both the shell and tubes were made with stainless steel and its corresponding parameters are a_1 = 8000, a_2 = 259.2, and a_3 = 0.93 [16]. The operational cost is the function of pumping power overcome friction losses and calculated by Eqs. (4) and (5).

$$C_0 = PC_eH \quad (4)$$

$$C_{op} = \sum_{x=1}^{n_y} \frac{C_o}{(1+y)^x} \quad (5)$$

The design variables including the tube outside diameter, i.e. d_o, the shell inside diameter, i.e. D_S, and the baffle spacing i.e. B are applied in the optimization method to find

Table 2. System Parameters and Design Variables

Design variable/Parameter	Symbol	Design variable/Parameter	Symbol
Constant value (€)	a_1	Fouling resistance in shell side (m2 K/W)	R_{fs}
Constant value (€/m2)	a_2	Fouling resistance in tube side (m2 K/W)	R_{ft}
Constant value	a_3	tube pitch (m)	S_t
Area of shell side (m2)	A_s	Inlet temperature of cold fluid (K)	T_{ci}
baffles spacing (m)	B	Outlet temperature of cold fluid (K)	T_{co}
Constant value	C	Inlet temperature of hot fluid (K)	T_{hi}
Cost of energy (€/kW h)	C_e	Difference in heat transfer (W/m2 K)	Δ_h
Value of clearance (m)	cL	pressure drop (Pa)	ΔP
operating cost (€)	C_{op}	dynamic viscosity (Pa s)	μ
Total cost (€)	C_{tot}	density (kg/m3)	ρ
Diameter of tube inside (m)	d_i	overall pumping efficiency	η
Diameter of tube outside (m)	d_o	cold stream	c
Diameter of shell inside (m)	D_s	Equivalent	e
operating time in annual measure (h/yr)	H	Hot stream	h
discount rate in annual measure (%)	y	Device Inlet	i
Mass flow rate in shell side (kg/s)	m_s	Device Outlet	o
Mass flow rate in tube side (kg/s)	m_t	Shell side	s
Tube passes count	n	Tube side	t
Constant value	n_1	Wall of Tube	wt
Device life (yr)	ny		

the minimum objective function. The ranges of the input parameters are as follows: tube outside diameter is between 0.010 *m* and 0.051 *m*, shell inside diameter is between 0.1 *m* and 1.5 *m*, and baffle spacing is between 0.050 *m* and 0.5 *m*.

The opposition concept

This section discusses the application of the opposite concept in optimization. Various forms of oppositions are defined in [19] and elucidating how they can be employed in optimization scenarios. Two optimization methods that leverage oppositions are delineated, offering practical insights into their implementation and efficacy [19, 20]. First, the opposite is defined and elucidating how it can be employed in optimization scenarios.

Definition 1. (Opposite number): Let x be a real number in an interval $[a,b]$. The opposite of x, denoted by $\tilde{x}$, is defined by equation (6).

$$\tilde{x} = a + b - x \tag{6}$$

Definition 2 (Opposite Point): Let $P(x_1, x_2, ..., x_D)$ be a point in d-dimensional space, where $x_1, x_2, ..., x_D$ are real numbers and $x_i \in [a_i, b_i], i = 1,2,\ldots,d$. The opposite of P is denoted by $\tilde{P}(\tilde{x}_1, \tilde{x}_2, ..., \tilde{x}_D)$, where $\tilde{x}_i = a_i + b_i - x_i, i = 1,2,\ldots,d$.

To increase the probability of obtaining better approximations of the optimal solution while controlling the diversity of candidate solutions, comprehensive opposition (*CO*) changes the value of each variable $x \in [a,b]$ to one of its opposite points $\tilde{x}^{reo}$, $\tilde{x}^{qr}$, $\tilde{x}^{qo}$, or $\tilde{x}^{eo}$, whose selection probabilities are the optimal solution of one linear parametric programming with parameters $t = T$, where t is the number of iterations and T is the total number of iterations. The associated definitions and theorems are described in [19].

The comprehensive opposition concept serves as the primary operator in opposition-based optimization (OBA), enhancing the candidate solutions while regulating their variability.

Definition 3 (Comprehensive opposite point): Let $\tilde{x}^{qo}$, $\tilde{x}^{qr}$, $\tilde{x}^{eo}$, $\tilde{x}^{reo}$ be the Quasi-opposite (Quasi-opposition, shifts the amount of each variable to a random point between the center of its domain and its opposite number), Quasi-reflected (Quasi-reflection, reflects the amount of each variable x to a random point between the center of its domain and *X*), Extended opposite (Extended opposition shifts the amount of each variable to a random point between its opposite number and the nearest bound of its domain to its opposite number), and Reflected Extended opposite (Reflected extended opposition reflects the extended opposite point to obtain the reflected extended opposite point) point of v, respectively. The comprehensive opposite point of X is denoted by $\tilde{X}^{co}$ $(\tilde{x}_1^{co}, \tilde{x}_2^{co}, ...\tilde{x}_d^{co})$ and defined for t-th iteration as follows:

if $0 < \frac{t}{T} \leq \frac{43}{192}$

$$\tilde{X}_i^{co} = \begin{cases} \tilde{x}_i^{reo}, rand_i \le 0.01 \\ \tilde{x}_i^{qr}, 0.01 \le rand_i \le 0.02 \\ \tilde{x}_i^{qo}, 0.02 \le rand_i \le 0.56 + 1.92\frac{t}{T} \\ \tilde{x}_i^{eo}, 0.56 + 1.92\frac{t}{T} \le rand_i \le 1 \end{cases} \quad (7)$$

else

$$if\ \frac{43}{192} < \frac{t}{T} \le \frac{139}{192}$$

$$\tilde{X}_i^{co} = \begin{cases} \tilde{x}_i^{reo}, rand_i \le 0.01 \\ \tilde{x}_i^{qr}, 0.01 \le rand_i \le -0.42 + 1.92\frac{t}{T} \\ \tilde{x}_i^{qo}, -0.42 + 1.92\frac{t}{T} \le rand_i \le 0.96 \\ \tilde{x}_i^{eo}, 0.96 \le rand_i \le 1 \end{cases}$$

else

$$\tilde{X}_i^{co} = \begin{cases} \tilde{x}_i^{reo}, & rand_i \le 0.01 \\ \tilde{x}_i^{qr}, & 0.01 \le rand_i \le 0.02 \\ \tilde{x}_i^{qo}, & 0.02 \le rand_i \le 0.03 \\ \tilde{x}_i^{eo}, & 0.03 \le rand_i \le 1 \end{cases},$$

where, $1 \le i \le$ d, T is the total number of iterations, and $rand_i$ is a random number uniformly distributed in $[a,b]$. The above opposite points have already been defined by the authors of this paper in detail in [19]. Also, Theorems with their corollaries prove that the comprehensive opposite point is more effective than the independent random point [19].

Opposition-Based Differential Evolution (OBDE)

Like other population-based optimization algorithms, Differential Evolution (DE) operates through two primary stages: (i) initialization of the population and (ii) generation of a new population via evolutionary operations, including mutation, crossover, and selection. The objective of this study is to enhance these stages by incorporating opposition-based optimization principles. The classical DE serves as the foundational algorithm, which is augmented with the proposed optimization strategies to achieve improved convergence speed.

In alignment with standard population-based algorithms, the core stages of DE—population initialization and the generation of new individuals through evolutionary mechanisms—are systematically refined through the integration of opposition-based optimization principles. This integration aims to enhance the algorithm's efficiency and robustness in navigating complex search spaces.

The corresponding pseudocode and block diagram for the proposed method (OBDE) are provided in Algorithm 1 [13]. The main steps of Algorithm 1 are discussed in detail below.

Step 1. Initialize the population $P(N_P)$ randomly.

Step 2. Calculate opposite population by

$$OP_{i,j} = a_j + b_j - P_{i,j}$$
$$i = 1,2,\ldots,N_p, j = 1,2,\ldots,D \quad (9)$$

Where, $P_{i,j}$ and $OP_{i,j}$ denote the j^{tj} variable of the i^{tj} population and the opposite population vector, respectively.

Step 3. Select the N_P fittest individuals from the set $\{P \cup OP\}$ as the initial population. According to the above procedure, $2N_P$ function evaluations are required instead of the $2N_P$ conventional random population initialization. However, with the opposition-based initialization, these algorithms can commence with more suitable initial individuals.

The DE is effective for high-dimensional problems and OBDE exhibits superior performance with larger population sizes. Moreover, a jumping rate range of [0.1; 0.4] is proposed for the STHE optimization problem.

Algorithm 1: OBDE scheme (N_P, J_r, *MAX - NFC*)

1. N_P, J_r, and *MAX - NFC* are the population size, jumping rate, and the maximum number of the cost function evaluations, respectively.
2. Opposition-Based Population Initialization.
3. Generating the initial population uniform randomly, *pop*.
4. Calculating the opposite population, *opop* by Eq. (9).
5. Picking N_P fittest solutions from *pop*∪*opop* as the initial population.
6. *NFC* = 1.
7. while *NFC* < *MAX - NFC* do
8. Mutation
9. Crossover
10. Selection
11. Opposition-Based Jumping
12. if *rand* (0,1) < J_r then
13. *rand* (0,1) Generates a random number in [0,1].
14. Calculating opposite population of current population, *opop*(*NFC*) by Eq. (9).
15. *NFC* = *NFC* + N_P
16. Picking N_P fittest solutions from *pop*∪*opop* as the current population.
17. end if
18. *NFC* = *NFC* + N_P.
19. end while

Comprehensive Opposition-Based Learning (CO-OBL)

As mentioned, the opposition-based algorithm is a population-based stochastic metaheuristic optimization algorithm for optimization problems. The superiority of this algorithm is its simplicity, low computational burden speed, and fast convergence in obtaining the optimal solution. To increase the probability of obtaining better approximations of the optimal solution while controlling the diversity of candidate solutions, comprehensive opposition (*CO*) modifies the value of each variable in $x \in [a,b]$ to one of its opposite points $\tilde{x}^{qo}$, $\tilde{x}^{qr}$, $\tilde{x}^{eo}$, $\tilde{x}^{reo}$, the probabilities to

Table 3. Case studies parameters

		ρ (kg/m^3)	C_p (KJ/KgK)	μ (PaS)	K (W/mK)	R_f (m^2K/W)
Case 1						
	Shell side	750	2.84	0.00034	0.19	0.00033
	Tube side	995	4.2	0.0008	0.59	0.0002
Case 2						
	Shell side	1000	4.187	0.00071	0.63	7 × 10^4
	Tube side	656	2.646	0.00037	0.11	7 × 10^4

be selected are the optimal linear parametric programming solution with parameter $t = T$ where t is the number of iterations and T is the total number of iterations. The different steps of the proposed algorithm are outlined as follows [19]:

Algorithm 2: CO-OBL.

1. (Random initialization) Generate a random population P with N points.
2. (Fitness evaluation of points) Evaluate the fitness of each point.
3. Calculate the comprehensive opposite population P^{Co}.
4. Update the population P by selecting N potentially useful solutions from the set $P^{Co} \cup P$.
5. Update $X^{best}(t)$ $best(t)$, $worst(t)$, $P_m^i(t)$ and for $i = 1,2, \ldots, N$.
6. Replace the point X^i of the population with its current optimum opposite point, X^{iCo} with the probability $P_m^i(t)$ and for $i = 1,2, \ldots, N$.

$$P_m^i(t) = (best(t) - fit^i(t))/(best(t) - worst(t)) \quad (10)$$

7. Repeat Steps 2–6 until the stopping criterion is met.

Simulation Results

The numerical experiments were carried out on a computer equipped with an Intel i7 processor, 16 GB RAM, a 6 GB graphics card, and the Windows 7 64-bit operating system, using MATLAB R2014b.A.

Case studies

This study evaluates the performance of the proposed optimization algorithms through two case studies, as reported by Caputo et al. [21]. In both cases, the thermophysical properties of the working fluids are computed at their mean temperatures. The first case study involves methanol on the shell side, with a flow rate of 27.8 kg/s and inlet and outlet temperatures of 95 °C and 40 °C, respectively. On the tube side, seawater is utilized with a flow rate of 68.9 kg/s, entering at 25 °C and exiting at 40 °C. Both the shell and tube components are constructed from stainless steel.

Case study 2 consists of cooling water placed in the shell side with the flow rate of 30 kg/s and the inlet and outlet temperatures of 33 °C and 37 °C, respectively. Naphtha is in the tube side with the flow rate of 2.70 kg/s and the inlet and outlet temperatures of 114 °C and 40 °C, respectively. Stainless steel is used as a construction material for shell and tubes. The other parameters for these case studies are given in Table 2. The second case study examines the use of cooling water on the shell side, characterized by a flow rate of 30 kg/s and inlet and outlet temperatures of 33 °C and 37 °C, respectively. On the tube side, naphtha is employed as the working fluid, with a flow rate of 2.70 kg/s, entering at 114 °C and exiting at 40 °C. Like the first case study, stainless steel is used as the material for both the shell and tube components. Additional parameters for these case studies are summarized in Table 3[16].

RESULTS AND DISCUSSION

The proposed algorithms, Opposition-Based Differential Evolution (OBDE) and Comprehensive Opposition-Based Learning (CO-OBL), offer significant advancements in optimizing shell-and-tube heat exchangers (STHE). Their capability to minimize total costs while enhancing design efficiency showcases their robustness and practicality for addressing complex optimization challenges. Below, the key findings, comparisons, and implications of these results are discussed in detail.

Performance Comparison with Metaheuristic Methods

The proposed OBDE and CO-OBL algorithms outperform several existing metaheuristic methods, including PSO, GWO, and NSGA-II PSO. For instance, as shown in Table 4 (Case Study 1), OBDE and CO-OBL achieved a 16.37% reduction in total cost compared to NSGA-II PSO. Similarly, in Table 5 (Case Study 2), the proposed algorithms reduced costs by 18.88%. These improvements highlight the efficiency of the opposition-based strategies in finding globally optimal solutions where conventional methods may converge to suboptimal local minima.

Advantages of the Proposed Algorithms Over Aspen-EDR

The results presented in Table 3 indicate that the opposition-based algorithms (OBDE and CO-OBL) outperform Aspen-EDR, even in scenarios where the software can provide solutions. This is a significant and positive finding, as it validates the reliability of the proposed algorithms and supports the claim that they can be effectively employed

Table 4. Performance Comparison in Case Study 1[16]

Parameters	PSO	I-ITHS	CI	ARGA	NSGA II -PSO	GWO	OBDE	CO-OBL	Aspen-EDR
D_s	0.81	0.763	0.78	0.665	1.5	0.565	0.5126	0.5126	0.5906
L	3.115	2.039	1.936	1.263	0.438	7.6734	4.8622	4.8622	4.8768
B	0.424	0.495	0.5	0.49	0.416	0.3962	0.4397	0.4397	0.387
d_o	0.015	0.01	0.01	0.01	0.0139	0.0216	0.015	0.015	0.015
n	2	2	2	2	2	2	2	2	2
N_t	1658	3558	3734.12	2625.873	7628	276	604	604	742
v_t	0.67	0.7744	0.738	1.049	0.1662	2.1399	2.0162	2.0162	1.78
Re_t	10,503	7701.29	7342.74	10,440.1	2300	45984	30091	30091	20310
Pr_t	5.7	5.7	5.69	5.694	5.694	5.6949	5.6949	5.6949	5.7
h_t	3721	4388.79	4584.7	6196.002	8469	7075	7256	7256	6050
f_t	0.0311	0.03555	0.034	0.031	0.1018	0.0213	0.0236	0.0236	0.233
ΔP_t	4171	6887.63	5862.72	9756.238	1200	61404	55192	55192	036
d_e	0.0107	0.00711	0.007	0.007	0.009	0.018	0.0125	0.0125	0.0125
v_s	0.53	0.48979	0.475	0.568	0.288	0.9936	0.9135	0.9135	0.41
Re_s	12,678	7684.05	7451.39	8912.325	6300	3452	25193	25193	16450
Pr_s	5.1	5.08215	5.082	5.082	5.0821	5.0821	5.0821	5.0821	6.5
h_s	1950.8	2230.91	2195.94	2422.804	5939.2	6840	7695	7695	2876
f_s	0.349	0.37621	0.378	0.368	0.3877	0.2944	0.3149	0.3149	0.3149
ΔP_s	20,551	14,953.9	13,608.4	10,746.3	19,855	66,267	48693	48693	0.07
U	713.9	761.578	764.5	1031.472	1093.3	1107	1133	1133	1760
S	243.2	228.03	227.16	168.275	146.11	143.718	140.431	140.431	167.5
C_i	46,453	44,259.0	44,132.5	35,498.8	34,718	31,822	31,325	31,325	31,410
C_o	6778.2	5914.06	5873.66	6414.68	5161.4	2413	2025	2025	2301
C_{tot}	53,231	50,173	50,006.1	41,913.5	39,880	34,235	33350.0	33350.0	33711.0

Table 5. Performance Comparison in Case Study 2[16]

Parameters	Java Algorithm	NSGA II -PSO	OBDE	CO-OBL
D_s	0.344	0.685	0.131	0.131
L	3.22	4.71	6.5	6.5
d_o	0.015	0.015	0.015	0.015
n	1	2	2	2
N_t	186	77	23	23
ΔP_t	8450	12225	16911	16923
ΔP_s	6990	210	1013	1007
S	299.0	158.91	68.682	68.682
C_i	3660	3427	2496	2496
C_o	318	11	332	332
C_{tot}	3986	3438	2828	2828

in cases where Aspen-EDR encounters limitations. While Aspen-EDR is widely used in the industry, it has notable limitations in handling complex geometries, such as helical or coiled tube configurations, due to the absence of appropriate design modules. In such cases, OBDE and CO-OBL provide robust and reliable alternatives, delivering geometrically feasible and cost-efficient solutions.

Aspen-EDR, though widely used in industry, is limited in handling complex geometries like triangular pitch arrangements. The results in Figure 2 demonstrate that

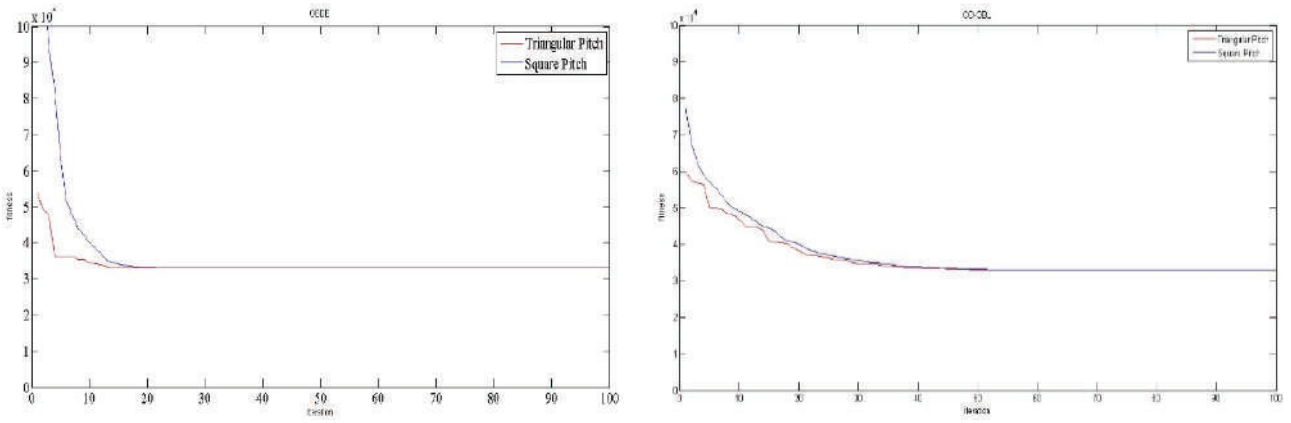

(a) (b)

Figure 2. Comparison of Triangular and Square Pitch Arrangements **(a).** OBDE and **(b).** CO-OBL.

OBDE and CO-OBL outperform Aspen-EDR by providing geometrically feasible and cost-efficient solutions for these configurations. The triangular pitch arrangement, for example, yielded approximately 2% lower costs compared to square arrangements, with significantly reduced pressure drops on both the shell and tube sides.

Advantages of Triangular Pitch Over Square Pitch Configurations

Triangular pitch arrangements have shown superior performance compared to square pitch configurations in shell-and-tube heat exchangers. As depicted in Figure 2, employing a triangular pitch configuration result in approximately 2% lower overall costs compared to square pitch designs. This cost reduction is primarily attributed to significantly reduced pressure drops on both the shell and tube sides. A detailed comparison of the pressure drops for both arrangements on the shell and tube sides is presented in Table 6. These findings highlight that triangular pitch arrangements are a more effective choice for optimizing the design of heat exchangers, and the proposed algorithms excel in identifying such optimal configurations.

Impact of Initial Population

One of the distinguishing features of OBDE is its intelligent initialization of the population. As shown in Table 7, this method achieves faster convergence (35% reduction in iterations) and lower initial costs (40% cost savings) compared to algorithms such as GSA and ACO. By leveraging opposition-based learning, OBDE effectively evaluates potential starting points during initialization, ensuring that the population begins closer to the global optimum.

The use of opposition-based learning for selecting initial points provides a distinct advantage over random initialization methods by reducing the likelihood of being trapped in local optima. By systematically exploring opposite points, the algorithm can evaluate a broader search space, leading to better initial solutions. This approach accelerates the optimization process and significantly enhances the quality of the final solutions.

Table 6. Pressure Drop Comparison for Triangular and Square Arrangements

Algorithm	ΔP_s		ΔP_t	
	S-Arrangement	T-Arrangement	S-Arrangement	T-Arrangement
DE	244320	149800	466170	414550
GA	88011	48178	215010	175400
GSA	727030	362230	2426200	1102300
GWO	46954	50553	84254	54040
PSO	192940	135910	1869800	1045300
SA	192940	135910	1869800	1045300
WOA	192940	135910	1869800	1045300
CO-OBL	48693	44188	55192	55388
OBDE	48693	44188	55192	55388

Table 7. Iteration Convergence Comparison for Case Study 1

Iteration	DE	GA	GSA	GWO	PSO	SA	WOA	CO-OBL	OBDE
1	72916	68678	73331	67840	71250	68774	67040	61756	57274
2	72916	68678	72407	62697	68783	68766	59123	61756	42220
3	68470	64531	68530	60007	64378	68560	56849	58884	42220
4	68470	59380	68086	59324	62098	68412	56849	53145	38076
5	60687	59380	67722	56530	59148	67440	56849	50501	37840
6	60687	58450	67607	49598	57781	67087	56849	50501	35689
7	60687	54784	67351	41098	57600	63660	56849	49992	35689
8	58633	54784	67059	34330	56992	63660	56849	49961	35689
9	58633	54784	66782	33912	56849	62871	56849	46379	35689
10	58443	54784	66677	33013	56849	62535	56849	46379	35689

Practical Implications

The findings underline the applicability of the proposed algorithms in industries such as energy recovery and chemical processing. By reducing costs and optimizing thermal performance, OBDE and CO-OBL enable the design of more efficient and economical heat exchangers. This adaptability to various operational conditions makes these algorithms a valuable alternative to traditional methods.

Limitations and Future Directions

While the proposed algorithms exhibit strong performance, the study is not without limitations:

Simulation-based Validation: The results are based solely on numerical simulations. Experimental validation is necessary to confirm their practicality in real-world scenarios.

Limited Case Studies: Only two case studies were analyzed. Expanding the algorithm's application to more diverse configurations, including multi-objective scenarios, could enhance its generalizability.

Scalability: Future research should investigate the algorithms' performance on larger-scale problems to assess their efficiency and adaptability.

Population size

To determine the optimal population size, a sensitivity analysis was conducted using Case Study 1. Population sizes ranging from 10 to 50 individuals were tested, with 50 iterations performed for each population size. Figure 3 illustrates the average total cost behavior for the OBDE, CO-OBL, BAT, PSO, Cuckoo Search, and DE algorithms. It was observed that the performance of these algorithms became similar when the population size exceeded 50 individuals. Consequently, a population size of 50 was selected for all optimization problems.

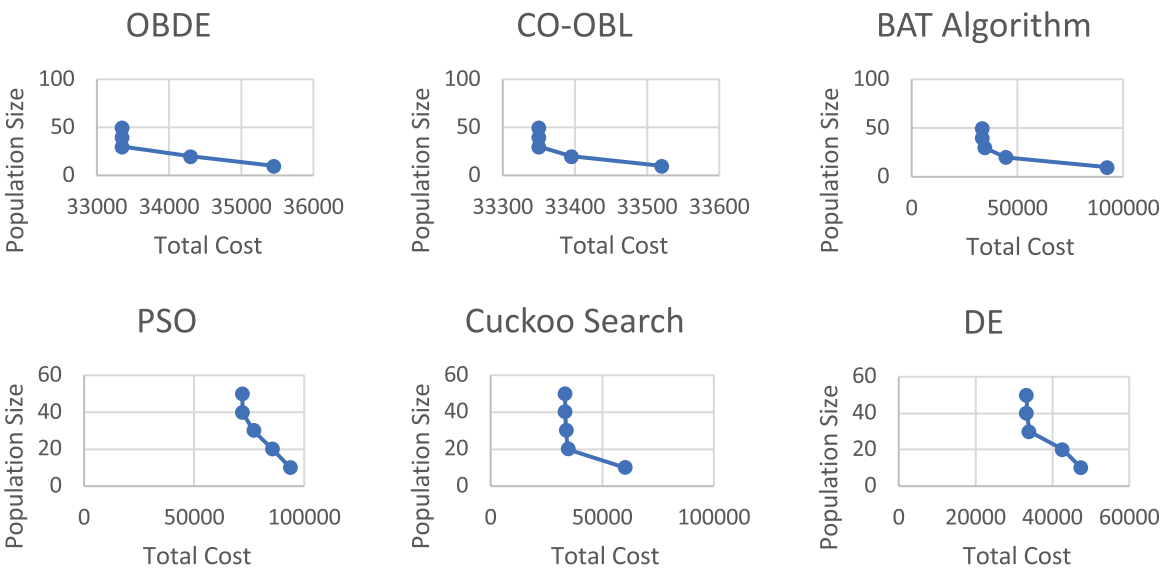

Figure 3. Population size sensitivity analysis for case study 1.

CONCLUSION

The optimization of Shell-and-Tube Heat Exchangers (STHEs) remains a critical area of research, particularly for reducing costs and enhancing performance in industrial applications. Existing methods, including traditional metaheuristic algorithms such as PSO, NSGA-II-PSO, and ARGA, often fail to escape local optima or deliver parameter configurations comparable to commercially established tools like Aspen-EDR. This study introduced two advanced algorithms, Opposition-Based Differential Evolution (OBDE) and Comprehensive Opposition-Based Learning (CO-OBL), to address these challenges effectively. By integrating the concept of opposition into both initialization and iterative optimization processes, these algorithms demonstrated superior capabilities in global exploration and solution refinement. Through two case studies, the proposed methods achieved significant cost reductions of 16.37% and 18.88% compared to NSGA-II-PSO, while maintaining design parameters consistent with Aspen-EDR. Additionally, OBDE and CO-OBL successfully optimized complex geometries, such as helical tube configurations, which are beyond the scope of conventional tools like Aspen-EDR. The results underscore the efficacy of opposition-based strategies in delivering robust, cost-effective, and geometrically feasible designs, establishing these algorithms as promising alternatives for the optimization of STHEs. Future research could focus on experimental validation, extending the application to multi-objective scenarios, and exploring scalability to large-scale industrial problems.

AUTHORSHIP CONTRIBUTIONS

Authors equally contributed to this work.

DATA AVAILABILITY STATEMENT

The authors confirm that the data that supports the findings of this study are available within the article. Raw data that support the finding of this study are available from the corresponding author, upon reasonable request.

CONFLICT OF INTEREST

The author declared no potential conflicts of interest with respect to the research, authorship, and/or publication of this article.

ETHICS

There are no ethical issues with the publication of this manuscript.

STATEMENT ON THE USE OF ARTIFICIAL INTELLIGENCE

Artificial intelligence was not used in the preparation of the article

REFERENCES

[1] Kakac S, Liu H, Pramuanjaroenkij A. Heat exchangers: selection, rating, and thermal design. 3rd ed. Boca Raton (FL): CRC Press; 2012.

[2] Kennedy J, Eberhart RC. A discrete binary version of the particle swarm algorithm. In: Proceedings of the IEEE International Conference on Systems, Man, and Cybernetics; 1997. p. 4104–4108. [CrossRef]

[3] Qader F, Hussein A, Danook S, Mohamad B, Khaleel O. Enhancement of double-pipe heat exchanger effectiveness by using porous media and TiO2 water. CFD Lett 2023;15:31–42. [CrossRef]

[4] Zarda F, Hussein A, Danook S, Mohamad B. Enhancement of thermal efficiency of nanofluid flows in a flat solar collector using CFD. Diagnostyka 2022;23:1–9. [CrossRef]

[5] Hussein A, Najim S, Danook S. Performance improvement of shell and tube heat exchanger by using Fe3O4/water nanofluid. J Therm Eng 2023;9:24–32. [CrossRef]

[6] Ali HHM, Hussein AM, Hussain Allami KM, et al. Evaluation of shell and tube heat exchanger performance by using ZnO/water nanofluids. J Harbin Inst Technol (New Ser) 2023;30:1–11. [CrossRef]

[7] Qader FF, Mohamad B, Hussein AM, Danook SH. Numerical study of heat transfer in circular pipe filled with porous medium. Pollack Period 2023;18:136–141.

[8] Nadi M, Aliehyaei M, Ahmadi A, Turgut OE. Multi-objective particle swarm optimization of the K-type shell and tube heat exchanger (case study). J Therm Eng 2021;7:570–583. [CrossRef]

[9] Peng L, Wang Y. Differential evolution using uniform quasi-opposition for initializing the population. Inf Technol J 2010;9:1629–1634. [CrossRef]

[10] Rahnamayan S, Wang GG, Ventresca M. An intuitive distance-based explanation of opposition-based sampling. Appl Soft Comput 2012;12:2828–2839. [CrossRef]

[11] Rahnamayan S, Tizhoosh HR, Salama MMA. Quasi-oppositional differential evolution. In: Proceedings of IEEE Congress on Evolutionary Computation; 2007. p. 2229–2236. [CrossRef]

[12] Zhang C, Ni ZW, Wu ZJ, Gu LC. A novel swarm model with quasi-oppositional particle. In: Proceedings of International Forum on Information Technology and Applications; 2009. p. 325–330. [CrossRef]

[13] Xu Q, Wang L, He B, Wang N. Modified opposition-based differential evolution for function optimization. J Comput Inf Syst 2011;7:1582–1591.

[14] Sinnott RK. Chemical engineering design: heat transfer equipment. Oxford: Butterworth-Heinemann; 2005.

[15] Aspen Technology. AspenTech. Available at: https://www.aspentech.com. Accessed on December 26, 2025.

[16] Sai JP, Rao BN. Non-dominated sorting genetic algorithm II and particle swarm optimization for design optimization of shell and tube heat exchangers. Int Commun Heat Mass Transf 2022;132:105896. [CrossRef]
[17] Lara-Montaño OD, Gómez-Castro FI, Gutiérrez-Antonio C. Comparison of the performance of different metaheuristic methods for the optimization of shell-and-tube heat exchangers. Comput Chem Eng 2021;144:107076. [CrossRef]
[18] Bell KJ. Final report of the cooperative research program on shell and tube heat exchangers. Newark (DE): University of Delaware, Engineering Experimental Station; 1963.
[19] Seif Z, Ahmadi MB. An opposition-based algorithm for function optimization. Eng Appl Artif Intell 2015;37:293–306. [CrossRef]
[20] Rahnamayan S, Tizhoosh HR, Salama MMA. Opposition-based differential evolution. In: Chakraborty U, editor. Advances in differential evolution. Berlin: Springer; 2008. p. 155–171. [CrossRef]
[21] Caputo AC, Pelagagge PM, Salini P. Heat exchanger design based on economic optimization. Appl Therm Eng 2008;28:1151–1159. [CrossRef]

J Ther Eng, Vol. 12, No. 1, pp. 156−181, January, 2026

Journal of Thermal Engineering
Web page info: https://jten.yildiz.edu.tr
DOI: 10.14744/thermal.0001067

Research Article

Turbulent forced convection of hybrid nanofluids in a three-dimensional L-shaped channel: Modeling, analysis, and regression model development

Amanullah PHULPOTO[1], Abid A. MEMON[1], M. Asif MEMON[1,*], Ubaidullah YASHKUN[1], Adebowale Martins OBALALU[2]

[1]*Department of Mathematics, Basic Sciences and Humanities, Sukkur IBA University, Sukkur, 65200, Sindh, Pakistan*
[2]*Department of Mathematics and Statistics, Kwara State University, Malete, 241103, Nigeria*

ARTICLE INFO

Article history
Received: 20 September 2024
Revised: 19 December 2024
Accepted: 23 December 2024

Keywords:
Convection; Darcy; Kinetic Energy; L-shaped Channel; Turbulent

ABSTRACT

The study explores turbulent forced convection of hybrid nanofluids in a three-dimensional L-shaped channel using COMSOL Multiphysics. The hybrid nanofluid comprises copper and aluminum oxide particles dispersed in water, with volume fractions of 0.01 (1%), 0.04 (4%), 0.07 (7%), and 0.1 (10%). Simulations are conducted for forced convection under Reynolds numbers ranging from 10,000 to 40,000. The partial differential equations of the Navier-Stokes, $\kappa - \varepsilon$ model of the turbulence, and the three-dimensional energy equation are employed to model the system. The turbulence kinetic energy and dissipation rates for the turbulent flow range from 2.99E-3 to 1.53 (m^2 / s^2) and from 0.2136 to 2524.1913 (m^3 / s^3), respectively. This research is significant for advancing efficient heat transfer mechanisms, which are crucial for applications in cooling systems and energy devices. Key findings include the observation that the minimum temperature at the channel edges decreases with an increasing volume fraction of aluminum oxide and improves with copper addition. Copper consistently enhances the minimum temperature across all scenarios. The Nusselt number calculated using aluminum oxide is nearly ten times greater than that obtained using copper. The friction factor initially increases along the channel length and then decreases, showing minimal sensitivity to variations in the volume fractions of copper and aluminum oxide. Using multiple linear regression, predictive equations for the average temperature and Nusselt number at the outlet were developed based on the Reynolds number and the nanomaterial volume fractions. The novelty of this work lies in the exploration of a three-dimensional L-shaped channel to analyze its thermal behavior, offering significant insights for engineering applications and design improvements. Furthermore, the study provides a novel contribution by deriving linear regression equations for the average Nusselt number and average temperature, which have not been addressed in previous literature. The absolute error for the average temperature equation ranges from 0.005 to 1.6, while for the Nusselt number, it varies between 0.368 and 1.6, ensuring high accuracy of the regression model.

Cite this article as: Phulpoto A, Memon AA, Memon MA, Yashkun U, Obalalu AM. Turbulent forced convection of hybrid nanofluids in a three-dimensional l-shaped channel: Modeling, analysis, and regression model development. J Ther Eng 2026;12(1):156−181.

***Corresponding author.**
*E-mail address: asif-memon@iba-suk.edu.pk

This paper was recommended for publication in revised form by Editor-in-Chief Ahmet Selim Dalkilic

Published by Yıldız Technical University Press, İstanbul, Turkey
Yıldız Technical University. This is an open access article under the CC BY-NC license (http://creativecommons.org/licenses/by-nc/4.0/).

INTRODUCTION

Heat transfer in fluid dynamics plays a significant role in optimizing solutions in the industrial sector [1-3]. Many practical applications of heat transfer are found in industries to enhance energy production and develop efficient heat exchangers [4-6] and [7-10]. Heat transfer is also crucial in the design of efficient solar collectors, and sometimes, the use of porous materials can further improve heat transfer [11-14] and [15, 16]. Initially, the focus was on using conventional fluids like ethylene glycol, oil, and water to achieve efficient heat transfer. The second approach involved incorporating metallic particles with high thermal conductivity to enhance heat transfer rates. To explore this second idea, researchers conducted an experiment involving the transport of metallic particles through conventional fluids to assess thermal performance [17]. The results of this experiment demonstrated that the transport of nanofluids significantly enhances heat transfer rates. Following this breakthrough, numerous experiments were conducted to fully harness the potential of nanofluid transportation. Many research articles have been published proposing methods to control the rate of heat energy distribution through the transport of nanofluids. Initially, only individual types of nanoparticles, such as copper, aluminum oxide, magnesium oxide, and copper oxide, were mixed with the base fluid to enhance heat transfer. Numerous research papers and experiments have explored optimizing heat transfer using various approaches, such as applying electric and magnetic fields and examining the effects of different nanoparticle shapes [18-20]. Scientists and researchers dedicated nearly two decades to investigating and enhancing heat transfer until the third idea emerged. The third idea involves using hybrid fluids, where a mixture of multiple nanoparticles is dispersed in the fluid to further enhance heat transfer efficiency.

Owing to its excellent thermo-physical properties, the hybrid mixture yields remarkable results for heat transfer [21]. The combination of Al_2O_3 and multi-walled carbon nanotubes was selected to be suspended in oil as the base fluid, flowing through the channel [21]. This was done at volume fractions of 0.125% and 1.5%, under ideal conditions while maintaining temperatures of 25°C and 30°C. The uniformity of the mixture was assessed using the zeta potential tool. The study evaluated whether the flow was laminar or turbulent and found that all thermal properties, including pumping power, thermal conductivity, and convection, increased with the hybrid mixture's volume fraction. Furthermore, this study established a significant correlation based on the viscosity of the mixture and its thermal conductivity, referencing available data. Another investigation involved the transport of Al_2O_3 and copper in water as the base fluid, within an open cavity, using the principles of entropy and mixed convection [22]. Researchers analyzed the heat transfer within the cavity while maintaining three adiabatic walls. The study evaluated the effects using three non-dimensional parameters (Rayleigh number (Ra), Hartmann number Ha and nanoparticles voluem fraction ϕ). It was observed that the average Nusselt number and entropy had an inverse relationship with the Hartmann number. Additionally, the heat transfer rate increased with the rise in the Richardson number and entropy production. In a separate analysis, a porous cavity was studied under natural convection conditions, with the transport of copper and aluminum oxide driven by magnetic interactions across the entire domain [23]. The partial differential equations were discretized using the finite difference method along with upwind terms. The primary finding indicated that the average Nusselt number decreased when shifting the heat source. It was also noted that the Hartmann number negatively affected the speed of the hybrid mixture. Furthermore, the study clarified that the Nusselt number remained positive with varying volume fractions.

Researchers studied heat transfer within the cavity while maintaining three adiabatic walls. In some articles [24, 25], oil was used as the base fluid. In other studies, the investigation focused on using oil as the base fluid to comprehensively examine the convection process within the domain of interest [26-30]. Another convection problem was studied involving the flow of a mixture composed of 95% aluminum and 5% zinc, employing a two-step numerical approach under steady-state conditions [31]. Similarly, various studies have explored the heat dispersion process using hybrid nanofluids, with some utilizing ethylene glycol as the working fluid [32-34]. Various geometries have been explored in the past to optimize heat transfer rates when transporting hybrid mixtures. The flow of hybrid nanofluids has been investigated in L-shaped channels [35], three-dimensional U-shaped channels [36], lid-driven channels [37], square channels with various obstacles [38], triangular cavities [39], and backward-facing step channels [40]. These numerical and experimental investigations have aimed to enhance heat transfer rates in different flow conditions, whether laminar or turbulent. These studies have considered both transient and steady-state flows, with the majority utilizing numerical simulations or experimental approaches.

The study conducted a numerical investigation of turbulent natural convection within a square cavity with heat-conducting walls, thermal radiation, and a heat source [41, 42]. It utilized a finite difference method and k–ε turbulence model to simulate heat and mass transfer. Increased surface emissivity and thermal conductivity ratio generally enhanced the average total Nusselt number. However, higher surface emissivity alone reduced the average convective Nusselt number. The study conducted numerical simulations of turbulent natural convection with thermal radiation in an inclined square enclosure with a heat source [42]. It focused on the effect of the inclination angle on fluid flow and heat transfer. Using the k–ε turbulence model and finite difference method, the study considered various parameters including Rayleigh number, inclination angle,

and surface emissivity. Results showed that increasing the inclination angle reduced the radiative Nusselt number. The objective of the project was to apply computational modeling to improve energy transport in engineering applications [43]. Research was done on turbulent forced convective energy transmission in a curved channel where the intake offered coolness and the upper wavy boundary provided constant heating. On fluid motion as well as energy transport, the impacts of Reynolds number, undulations number, and amplitude were examined. With a ripples number, significant energy carrier condensation was seen. In a conical diffuser, the study investigated turbulent flow of single and hybrid nanofluids [44]. It examined pressure losses and heat transfer at different Reynolds numbers and volume fractions of nanoparticles. Three forms of nanofluids, Al_2O_3, NEPCM_Al_2O_3, and nano encapsulated phase change material (NEPCM), were employed. The introduction of hybrid nanofluids made of nanoparticles, including and excluding phase change material (PCM), was a novel approach. The study found that the NEPCM nanofluid exhibited the most improved heat transmission and the least amount of pressure loss. It showed 15%, 10%, and 6% higher Nusselt numbers for NEPCM, NEPCM_Al_2O_3, and Al_2O_3, respectively. In comparison to the base fluid, there was a greater pressure drop, with a rise of 1% for NEPCM, 3.5% for Al_2O_3, and 5% for NEPCM_Al_2O_3 nanofluid. A review article also can be visited in order to understand the service of turbulent flow in order to understand the heat transfer in a rectangular enclosure [45].

Research Gap and Relevance with Recent studies: Our study investigates turbulent forced convection of hybrid nanofluids in an L-shaped channel, utilizing a comprehensive approach with multiple nanoparticle volume fractions and Reynolds numbers. Compared to previous studies, such as [46], which focus on thermal conductivity models and their Global Performance Index scores, our work provides detailed simulations on forced convection under specific flow conditions. Studies like [47] and [48] explore mixed and natural convection with different hybrid nanofluids, revealing significant heat transfer enhancements with nanoparticle volume fraction and fluid type, similar to our findings. Additionally, our work expands on [49], which examines heat transfer in steady laminar natural convection, by addressing more complex turbulent conditions and validating results using regression models. Our study's use of Reynolds numbers and nanoparticle combinations offers a deeper understanding of convection behaviors, complementing the results of these earlier investigations with practical application insights.

In this study, we investigate forced convection in an L-shaped channel using a hybrid nanofluid mixture of aluminum oxide and copper. The focus is on analyzing convection at the channel's inlet with Reynolds numbers ranging from 10,000 to 40,000. A numerical simulation is performed using COMSOL 5.6, applying Galerkin's Finite Element Method (FEM) to solve the governing equations, including the Navier-Stokes equation and the three-dimensional energy equation. The study examines various volume fractions (1% to 10%) of the hybrid nanofluid in a water-based fluid. We begin with a mesh independence study to evaluate parameters such as average velocity, average temperature, and Nusselt number. The numerical results are validated against established correlations for local Nusselt number and experimental data. The main objective is to explore the effects of volume fraction and Reynolds number on heat transfer, focusing on the minimum temperature at the channel edges, the local Nusselt number along the channel, and the relationship between Darcy friction factor and temperature. To perform the most suitable post-processing, a multiple linear regression procedure will be used to develop the regression equation related to the Reynolds number, copper volume fraction, and aluminum oxide volume fraction. Finally, researchers will compute absolute errors by comparing the numerical results with the predictions from the regression equations.

Application of finding: The findings discussed in this research examine fluid flow and heat transfer through the use of hybrid nanofluids composed of copper and aluminum oxide, which have extensive applications in advanced cooling and thermal management systems. The temperature behavior within the L-shaped domain, along with the enhanced heat transfer rate achieved by increasing the Reynolds number and the nanoparticle volume fraction, can be applied in electronic cooling, efficient heat exchangers, and energy systems, where effective heat dissipation is critical. Our derived regression equations for average outlet temperature and Nusselt number provide a practical tool for engineers to design systems with specific heat transfer and flow conditions. This article offers a detailed analysis of thermal and flow patterns in nanofluid channels, contributing valuable insights for the expanding applications of nanofluids in engineering fields.

MATERIALS AND METHODS

The schematic diagram of the L-shaped channel is depicted in Fig. 1, which will be examined in the current article for its heat transfer characteristics via the conventional process involving the hybrid mixture. The transportation of the hybrid mixture comprises copper and aluminum oxides as nanoparticles in a water-based fluid. The three-dimensional geometry is structured with a horizontal and vertical block joined together, maintaining a constant channel length for these blocks. In the block along the x-axis the width L_y = 50% L_x and the length along the z-axis L_z =10% L_x, while in a vertical block, the thickness L_y = 10% L_x and width L_z = 50% L_x. In this physical geometry, the area is identified as the channel inlet, where the nano-mixture is introduced with an x-velocity. Zero-pressure conditions and backflow are controlled at the end of the channel. Aside from these two boundaries, all other boundaries function as no-slip walls.

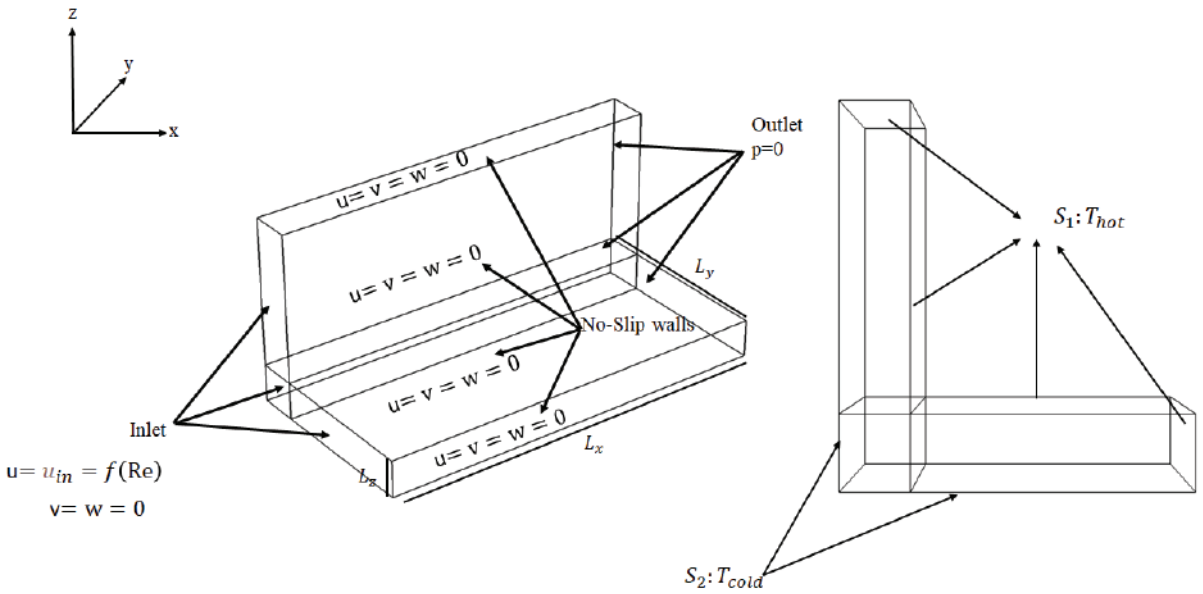

Figure 1. The schematic looks at the three-dimensional L-shaped channel with boundary conditions.

To examine the distribution of heat energy along the selected channel, we plan to divide the channel into two sections, denoted as S_1 and S_2, where hot and cold temperatures will be imposed, respectively, as shown in Figure 1. The hybrid mixture of copper (Cu) and aluminum oxide (Al_2O_3) will flow through the base fluid with volume fractions of 1%, 4%, 7%, and 10%. In order to assess the impact of forced convection through the L-shaped channel, Reynolds numbers ranging from 10,000 to 40,000 are utilized. We employ COMSOL Multiphysics 5.6, a finite element-based software, to create a numerical simulation of this problem, incorporating the turbulence and energy equations in three dimensions. Table 1 provides a detailed overview of the thermo-physical properties of the nanofluid and other parameters used in this study.

Table 1. Thermo-physical characteristics of the hybrid mixture and other parameters used in simulation [50-52]

Explanation	Symbol	Value
The volume fraction of Al_2O_3	ϕ_1	0.01, 0.04, 0.07, 0.1
The volume fraction of Cu	ϕ_2	0.01, 0.04, 0.07, 0.1
Density of Al_2O_3	ρ_1	3880 [kg/m^3]
Density of copper	ρ_2	8954 [kg/m^3]
The total density of the nanoparticles	ρ	$\frac{(\phi_1\rho_{np1}+\phi_2\rho_{np2})}{\phi_1+\phi_2}$
Specific heat of Al_2O_3	$(c_p)_1$	765 [J/kgK]
Specific heat of Cu	$(c_p)_2$	383.1 [J/kgK]
Specific heat of nanoparticles	c_p	$\frac{\phi_1\rho_{np1}(c_p)_{np1}+\phi_2\rho_{np2}(c_p)_{np2}}{\varphi\rho_{np}}$
The total volume fraction of nanoparticles	ϕ	$\phi_1+\phi_2$
Thermal conductivity of Al_2O_3	κ_1	40 [W/mK]
Thermal conductivity of Cu	κ_2	386 [W/mK]
Total thermal conductivity of the hybrid mixture	κ	$\frac{\phi_1\kappa_{np1}+\phi_2\kappa_{np2}}{\phi_1+\phi_2}$

Table 1. Thermo-physical characteristics of the hybrid mixture and other parameters used in simulation [50-52] (continued)

Explanation	Symbol	Value
The density of the water	ρ_{bf}	998 [kg/m^3]
Density of nanofluid	ρ_{nf}	$\rho_{bf}(1-\phi)+\phi\rho_{np}$
Specific heat of water	$(c_p)_{bf}$	4182 [J/kgK]
Specific heat of the hybrid mixture	$(c_p)_{nf}$	$\frac{\rho_{bf}(1-\phi)(\mathrm{c_p})_{bf}+\rho_{np}(1-\phi)(\mathrm{c_p})_{np}}{\rho_{nf}}$
Thermal conductivity of the water	κ_{bf}	0.597 [W/mK]
Thermal conductivity of the hybrid mixture	κ_{nf}	$\kappa_{bf}\left(\frac{\kappa_{np}+2\kappa_{bf}+2(\kappa_{np}-\kappa_{bf})\phi}{\kappa_{np}+2\kappa_{bf}-(\kappa_{np}-\kappa_{bf})\phi}\right)$
Water viscosity	μ_{bf}	0.000998 [Pas]
Nanofluid's viscosity	μ_{nf}	$\frac{\mu_{bf}}{(1-\phi)^{2.5}}$ [Pas]
Hydraulic diameter	d_h	4A/P
Reynolds number	Re	10,000-40,000
Inlet velocity	u_{in}	$\frac{\mu_{nf}\,\mathrm{Re}}{\rho_{nf}D_h}$
Cold temp	T_{cold}	293.15 [K]
Hot temp	T_{hot}	323.15[K]
Area of the total surface	Ar	$4(L_xL_z+L_yL_z+L_xL_y)-(\mathrm{L}_z)^2$
The perimeter of the channel	$\mathrm{P_e}$	$8L_x+8L_y+4L_z$
Velocity field	U	U=<u, v, w>
Temperature	T	
Turbulence kinetic energy	κ	
Turbulence dissipation rate	ε	

GOVERNING EQUATIONS AND $\kappa-\varepsilon$ TURBULENCE MODEL

In this model, the velocity field vector is denoted by U, which is further characterized by the velocity components u, v, and w, each possessing well-defined, continuous first-order partial derivatives. The context involves the modeling and simulation of heat transfer phenomena, specifically the flow of high-Reynolds-number hybrid nanofluids. In this scenario, it is prudent to adopt the $\kappa-\varepsilon$ model for investigation. This model proves to be an optimal choice due to its incorporation of both Turbulence kinetic energy and Turbulence dissipation rate considerations. Furthermore, the simulation encompasses a closed-channel geometry, such as an L-shaped channel, necessitating the selection of either a steady-state or time-independent study. These assumptions guide us in formulating the relevant equations, which are outlined below and also cited in [50-52].

Continuity Equation:

$$\rho_{nf}(\nabla\bullet\mathrm{U})=0 \tag{1}$$

Momentum Equation:

$$\rho_{nf}(\mathrm{U}\bullet\mathrm{U})\,\mathrm{U}-\nabla\bullet[-pI+(\mu_{nf}+\mu_T)(\nabla\mathrm{U}+(\nabla\mathrm{U})^t]=0 \tag{2}$$

$\kappa-\varepsilon$ Turbulence Model:

$$\rho_{nf}(\mathrm{U}\bullet\nabla)\kappa-\nabla\bullet\left[(\mu+\frac{\mu_T}{\sigma_\kappa})\nabla\mathrm{U}\right]-p_\kappa+\rho_{nf}\varepsilon=0 \tag{3}$$

$$\rho_{nf}(\mathrm{U}\bullet\nabla)\varepsilon-\nabla\bullet\left[(\mu+\frac{\mu_T}{\sigma_\kappa})\nabla\varepsilon\right]-c_{\varepsilon1}\frac{\varepsilon}{\kappa}+c_{\varepsilon2}\rho_{nf}\frac{\varepsilon^2}{\kappa}=0 \tag{4}$$

$$\text{Where } \mu_T = \rho_{nf} c_\mu \frac{\kappa^2}{\varepsilon} \text{ and } p_\kappa = \mu_T \left[\nabla \mathrm{U} : (\nabla \mathrm{U} + (\nabla \mathrm{U})^t \right] \quad (5)$$

$$\rho_{nf} (c_p)_{nf} \mathrm{U} \bullet \nabla T = \kappa_{nf} \nabla^2 T \quad (6)$$

Details of Physics On Boundaries Of L-Shaped Channel:

$$\textbf{Inlet: } u = u_{in} = f(\mathrm{Re}),\ \mathrm{v}=0,\ \mathrm{z}=0,$$
$$\kappa_0 = \frac{3}{2}(\mathrm{u}_{in} I_T)^2,\ \varepsilon_0 = \mathrm{c}_\mu^{3/2} \frac{\kappa_0^{3/2}}{L_T},\ \frac{\partial \mathrm{T}}{\partial n} = 0 \quad (7)$$

$$\textbf{Outlet: } \mathrm{x}=\mathrm{L}_x,\ 0 \le y \le L_y,\ 0 \le z \le L_z,$$
$$\frac{\partial \mathrm{T}}{\partial n} = 0 :\ \mathrm{p}_{out}=0,\ \nabla \varepsilon \bullet \mathbf{n} = 0 \text{ and } \nabla \kappa \bullet \mathbf{n} = 0 \quad (8)$$

$$\textbf{Along } S_1 :\ u = v = w = 0\ T = T_h, \text{ and}$$
$$\nabla \kappa \bullet \mathbf{n} = 0,\ \varepsilon = \rho_{nf} \frac{c_\mu \kappa^2}{\kappa_v \delta_w^+ \mu_{nf}} \quad (9)$$

$$\textbf{Along } S_2 \textbf{:}\ \mathrm{u} = \mathrm{v} = \mathrm{w} = 0,\ \nabla \kappa \bullet \mathbf{n} = 0$$
$$\text{and } \nabla \varepsilon \bullet \mathbf{n} = 0 \text{ and } \mathrm{T} = \mathrm{T}_c, \quad (10)$$

Here n is a vector perpendicular to the selected surface.

Turbulence intensity = I_T = 0.05, Turbulence length scale = L_T = 0.0126, δ_w^+ = 11.06.

Turbulence Variable [42]

κ_v	σ_κ	σ_ε	c_μ	$c_{\varepsilon 1}$	$c_{\varepsilon 2}$
0.41	1	1.3	0.09	1.44	1.92

It should be noted that the chosen ranges for turbulence kinetic energy and dissipation rates are compatible with the requirements for turbulence modeling in COMSOL Multiphysics. These values were carefully selected to ensure stable functioning of the turbulence model, enabling accurate computation of velocity and thermal profiles. This stability is essential to produce physically meaningful results that reflect the realistic behavior of hybrid nanofluid velocities [53].

Modeling Assumptions:

To model this phenomenon through the three-dimensional L-shaped channel the following assumptions will be made

1. The fluid flow is compressible, non-Newtonian and the time independent
2. The surface of the three-dimensional L-shaped channel is smooth no roughness was assumed along the upper or lower surface of channel
3. No back flow was assumed at the outelt of the channel
4. The initial values of the turbulent kinetic energy and the turbulence dissipation are enough to induce the turbulent in the channel.
5. The assumption ignores the dynamic interactions between nanoparticles and the fluid (e.g., Brownian motion, thermophoresis, or particle-fluid drag forces) and instead assumes the nanofluid behaves like a single-phase fluid.
6. Nanoparticles are assumed to be uniformly distributed at all points within the fluid. This neglects any possible local variations in concentration, which can occur in reality due to effects like sedimentation or particle clustering.
7. To drive the regression equations for the average temperature and the Nusselt number it is assumed that these variables are in a linear relationship with the Reynolds number, both volume fractions of the copper and alumina nanoparticles.
8. It is also assumed that we have sufficient data to form the linear regression equations.

Computational Parameters

- Prandtl Number: $\mathrm{Pr} = \frac{\mu_{nf} (c_p)_{nf}}{\kappa_{nf}}$ (11)
- Heat flux along the ith direction:
$$Q_i = \frac{\kappa_{nf}}{\kappa_{bf}} \frac{\partial T}{\partial i} \text{ where i=x, y and z} \quad (12)$$
- Heat transfer coefficient: $h_i = \frac{Q_i}{A(T - T_b)}$ (13)
- Bulk Temperature: $T_b = \frac{\iint_\Omega uT\ d\Omega}{\iint_\Omega \mathrm{u}\ d\Omega}$ (14)
- Local Nusselt number: $Nu_i = \frac{h\ \mathrm{i}}{k_{nf}}$ (15)
- Average Nusselt number:
- $(Nu_i)_{avg} = \frac{1}{A} \int_\Omega Nu_i\ dA$ Where A is the area of the selected boundary. (16)
- Darcy Friction Factor: $f_D = \frac{\tau_\omega}{\frac{1}{2} \rho_{nf} U_{mean}^2}$ (17)

Comsol Working Wagon Wheel

The software COMSOL flow algorithm is given below with the step-by-step procedure see Figure 2.

Overview of Methods For Non-Linear Pdes

For many decades, the question of how to solve nonlinear partial differential equations (PDEs) related to real-life applications and phenomena has been a significant challenge. Without timely solutions, controlling such phenomena becomes nearly impossible, often requiring substantial

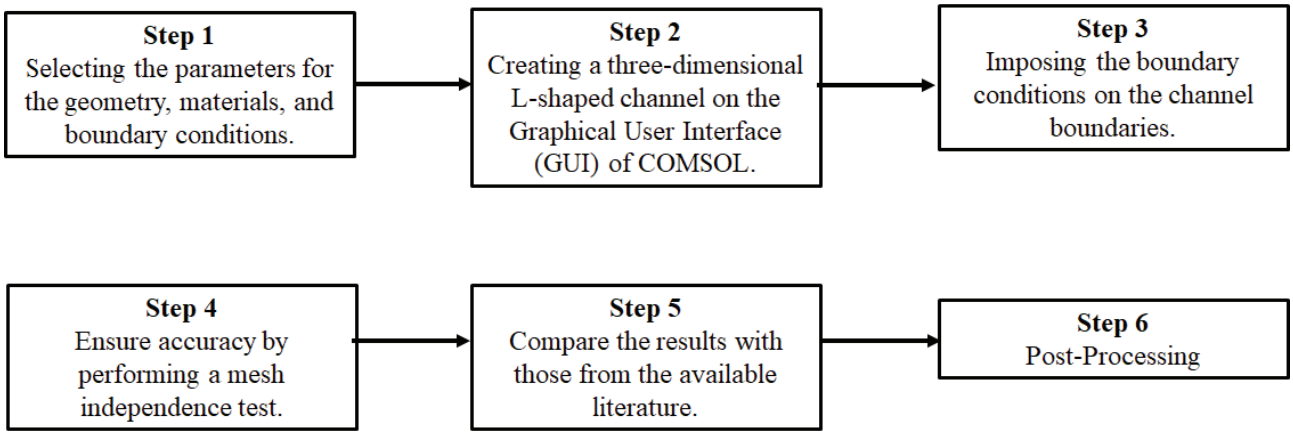

Figure 2. COMSOL Working Algorithm [53].

effort and continuous economic resources. Fortunately, numerical methods for solving PDEs provide approximate results promptly, allowing for practical applications in real-world scenarios. Various numerical schemes are now available to solve both individual nonlinear PDEs and systems of nonlinear PDEs. Some of these methods, along with their advantages and disadvantages, are summarized in the following table.

Table 2. A short description of the numerical schemes that solve the non-linear PDEs

Method	Description	Advantage	Disadvantage
Finite Difference Method (FDM)	Approximates derivatives by using finite differences between points, converting PDEs into algebraic equations. Requires iterative schemes for nonlinearity.	- Simple to implement, especially for structured grids. - Effective for time-dependent PDEs.	- Accumulated errors on coarse grids. - Challenging for complex boundaries and irregular domains.
Finite Element Method (FEM)	Divides the domain into subdomains (elements) and applies variational formulation, with iterative solvers for nonlinearity in each element.	- Highly accurate for complex geometries and variable material properties. - Flexible for various domains.	- Computationally intensive due to matrix assembly and inversion. - Requires expertise in meshing.
Finite Volume Method (FVM)	Integrates PDEs over discrete control volumes to ensure conservation laws are maintained, with algebraic transformation of nonlinear terms.	- Ideal for conservation laws (e.g., fluid dynamics). - Flux conservation across control volumes.	- Complex handling of boundary conditions, especially for unstructured grids. - Accuracy varies with grid type.
Multigrid Method	Solves nonlinear PDEs on hierarchical grids with relaxation steps at each level, accelerating convergence in large-scale problems.	- Highly efficient for large systems by reducing computational burden. - Fast convergence through multiple scales.	- Complex implementation requiring fine-tuning. - Performance depends on grid structure and relaxation techniques.

Multiple Linear Regression Procedure

Let n (64 in this case) be the size of the total population or the size of the dataset, and let k (3 in this case) be the number of total independent variables for which we are interested in writing the linear regression equation for a variable of interest. Let Y be the column vector which denotes the exact values of the dependent variable, and let $\hat{Y}$ also be the column vector denoting the predicted values of the dependent variables through the correlation process. The sizes of both Y and $\hat{Y}$ are $n\times1$ (64×1 in this case). Let X be the matrix, considering the size of $n\times(k+1)$ (64×4 in this case), which will have the values of the independent variables as the entries. Moreover, let B and E be the coefficient vector and the residual vector, which will have the sizes of $n\times1$ (64×1 in this case) and $n\times(k+1)$ (64×4 in this case), respectively.

These all matrices defined as above can be written as follow:

$$Y=[Y_1 \;\; Y_2 \;\; Y_3 \;\; \ldots \;\; Y_n]^T,\; \hat{Y}=[\hat{Y}_1 \;\; \hat{Y}_2 \;\; \hat{Y}_3 \;\; \ldots \;\; \hat{Y}_n]^T,$$

$$B=[b_0 \;\; b_1 \;\; b_2 \;\; \ldots \;\; b_k]^T$$

$$E=[\varepsilon_1 \;\; \varepsilon_2 \;\; \varepsilon_3 \;\; \ldots \;\; \varepsilon_n]^T \text{ and}$$

$$X=\begin{bmatrix} 1 & X_{11} & X_{12} & \ldots & X_{1k} \\ 1 & X_{21} & X_{22} & \ldots & X_{2k} \\ .. & .. & .. & .. & .. \\ 1 & X_{n1} & X_{n2} & \ldots & X_{nk} \end{bmatrix} \tag{18}$$

Considering the above all matrices, we can write a system in the matrix form as $\mathbf{Y = XB + E}$ where $\mathbf{X}$ is the matrix of independent k variable and this system can be written in equivalent form as:

$$\mathbf{Y}=b_0+b_1\mathbf{X_1}+b_2\mathbf{X_2}+\ldots+b_k\mathbf{X_K}+\varepsilon \tag{19}$$

Initially, the matrix Y and the matrix X of the values are given and then B, Y' and E will be computed as $B=(X^TX)^{-1}X^TY,\; \hat{Y}=\mathbf{X}B$ and $E=Y-\hat{Y}$.

After computing the all above values the following ANOVA (Analysis Of Variance) table will be made.

	Degree of Freedom (Df)	Sum of Squares (SS)	Mean of the Squares (MF)	F-Statistic
Regression	DFR=k	$SSR=\sum_1^n(\hat{Y}-Y_{mean})^2$	$MSR=\frac{SSR}{DFR}$	$F=\frac{MSR}{MSE}$
Residual	DFE=n-k-1	$SSE=\sum_1^n(Y_i-\hat{Y}_i)^2$	$MSE=\frac{SSE}{DFE}$	
Total	n-1	$SSE=\sum_1^n(Y_i-Y_{mean})^2$		

Figure 3 (a-b). The schematic diagram for the meshing procedure of the L-shaped channel.

Table 3. Final meshing construction information

Information	Number of elements
Mesh vertices	47,217
Tetrahedra	1,35,954
Pyramids	1080
Prisms	42,490
Triangles	10,238
Quads	804
Number of elements at the edges of the channel	590
Number of elements of vertices	16
Minimum quality of the element	0.01484
Average qualities	0.5616
Element volume ratio	0.003468
Mesh volume	0.09 cm^3
Total number of elements	1,80,729

After finding the F value a critical value will be searched F_a by using the F-Distribution Table that corresponds to the value (DFR, DFE) to decide the one of the hypothesis.

$$\begin{aligned} H_0 &: b_i = 0 \quad \text{if } F<F_\alpha \text{ (Failure)} \\ H_1 &: b_i \neq 0 \quad \text{if } F>F_\alpha \text{ (Success)} \end{aligned} \tag{20}$$

Where $\alpha = 0.05$ is the significance level. The above procedure is referenced in [54-56]

Mesh Independent/Grid Independence Test and Validation with Literature

In numerical simulations like finite element analysis, achieving a high level of accuracy often requires an assessment of how mesh density influences the results, commonly referred to as a "mesh independence" or "grid independence" test. For the present study, an L-shaped channel is modeled to simulate the flow of a hybrid nanofluid mixture of aluminum oxide (Al_2O_3) and copper (Cu) in water. The aim of the mesh independence study is to ensure that numerical results for average velocity, average temperature, and average Nusselt number are accurate and not significantly affected by further refinement of the mesh. The mesh consists of multiple element types, including tetrahedral, prism, triangular, and quadrilateral elements, which provide flexibility and ensure a robust representation of the geometry. The mesh refinement process systematically increases the number of elements to observe changes in key parameters. In Fig. 4 (a-c), the X-axis represents the total number of elements used in the simulation, while the Y-axis displays the computed values for average velocity, average temperature, and average Nusselt number. Each parameter stabilizes and converges to a nearly constant value when the number of elements reaches approximately 150,000, indicating that further increases in mesh density have negligible effects. This convergence confirms that 150,000 elements achieve mesh independence for this model. However, to ensure the highest accuracy, the final simulation uses a mesh with 180,729 elements, providing additional refinement beyond the convergence threshold. A complete structure of the mesh system can be seen in Table 3.

After completing the mesh independence study, we will validate the computational results in this study by comparing them to the correlations available in references [50] and [51]. To achieve this, we calculate the local Nusselt number as a function of temperature using the two correlations (21) and (22) and apply the basic formula for the local Nusselt number, as depicted in Fig. 5. It is evident that the current methodology for obtaining numerical results aligns well with these correlations, and the numerical simulations conducted using this software are expected to achieve an accuracy of approximately 98%.

$$\text{Dittus and Boelter: } Nu_x = 0.023\,\mathrm{Re}^{0.8}\,\mathrm{Pr}^{0.4} \tag{21}$$

$$\text{Dawid and Jan: } \mathrm{Nu}_x = 0.02155\mathrm{Re}^{0.8018}\mathrm{Pr}^{0.7095} \tag{22}$$

We have performed comparative validation with an experimental study, which reinforces our findings through a correlation with the Dittus-Boelter equation [50]. The experimental study utilized a reverse L-shaped channel to enhance thermal performance, benchmarking the experimentally obtained Nusselt number against the Dittus-Boelter correlation. This experimental work [56] also employed the $\kappa - \varepsilon$ turbulence model, consistent with the model applied in our investigation. By using this model to analyze heat transfer characteristics in an L-shaped channel, we ensure alignment with established methodologies. As illustrated in Figure 6, our numerical results show strong agreement with the experimental data, affirming the robustness of our approach and the validity of the outcomes.

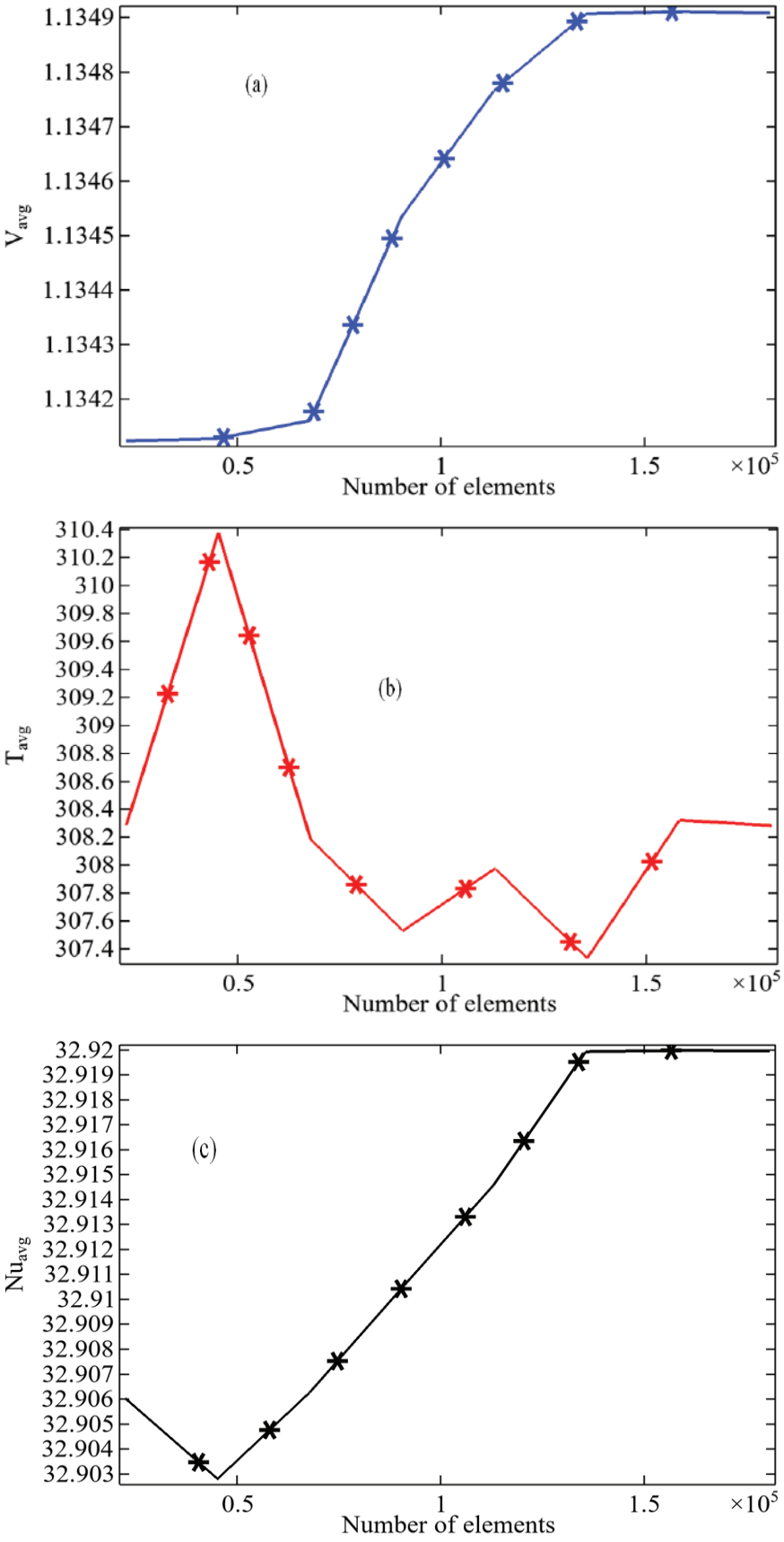

Figure 4(a-c). For the mesh-independent or grid-independent study (a) V_{avg}, (b) T_{avg}, and (c) Nu_{avg} have been calculated.

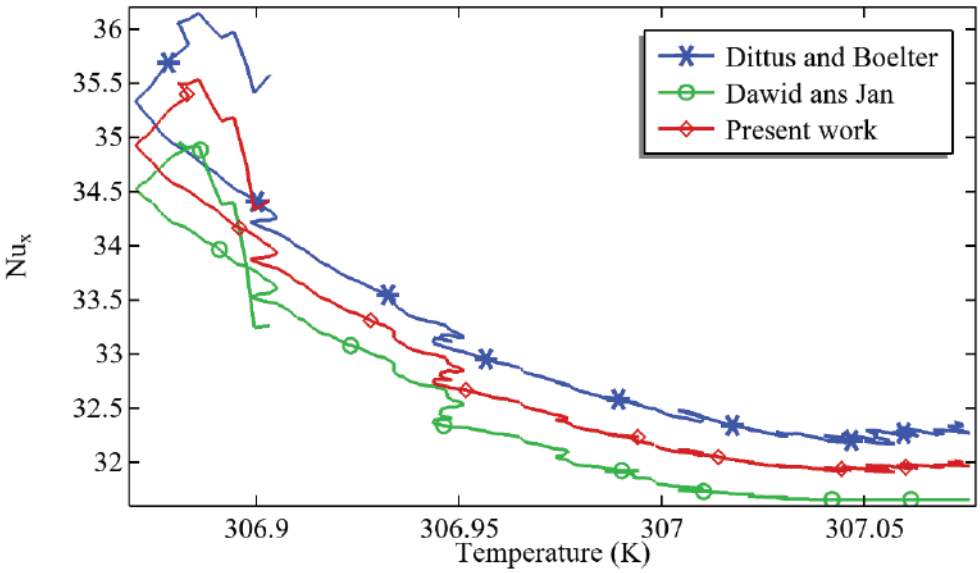

Figure 5. The evaluation of Nu_x against the temperature along the x-axis by using correlations and the present work at $\phi_1 = \phi_2 = 1\%$.

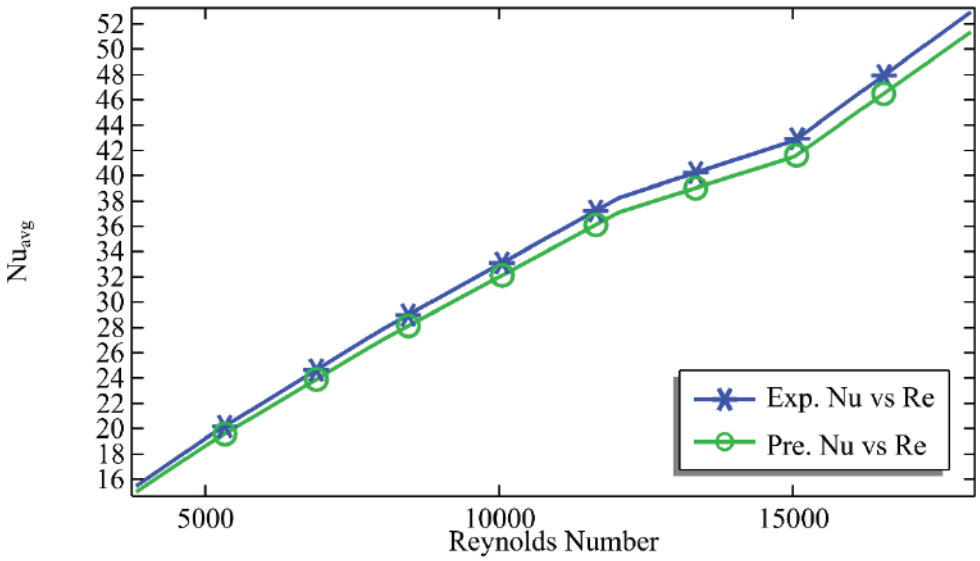

Figure 6. Comparison of the average Nusselt number versus Reynolds number between the present study and previous studies.

RESULTS AND DISCUSSION

In the current article, a numerical investigation of a three-dimensional L-shaped channel is conducted, employing hybrid nanofluids in the context of transport applications. The study utilizes the three-dimensional incompressible Reynolds-averaged Navier-Stokes equations and three-dimensional heat equations to analyze fluid dynamics and energy distribution within the channel. Copper and alumina nanoparticles, assumed to be spherical, are suspended in water as base fluids. The simulation, carried out using COMSOL Multiphysics 5.6 and finite element method, successfully explores turbulent forced convection under varying Reynolds numbers (10,000 to 40,000) and nanoparticle concentrations (0.01-0.1). This research aims to contribute to the control of minimum temperature, local Nusselt number (a ratio of convection to conduction processes), and Darcy friction factor vs the temperature by altering parameters. While this study is relatively rare in the fluid dynamics field, it holds significant applications due to the vertical separation of flow along the junction.

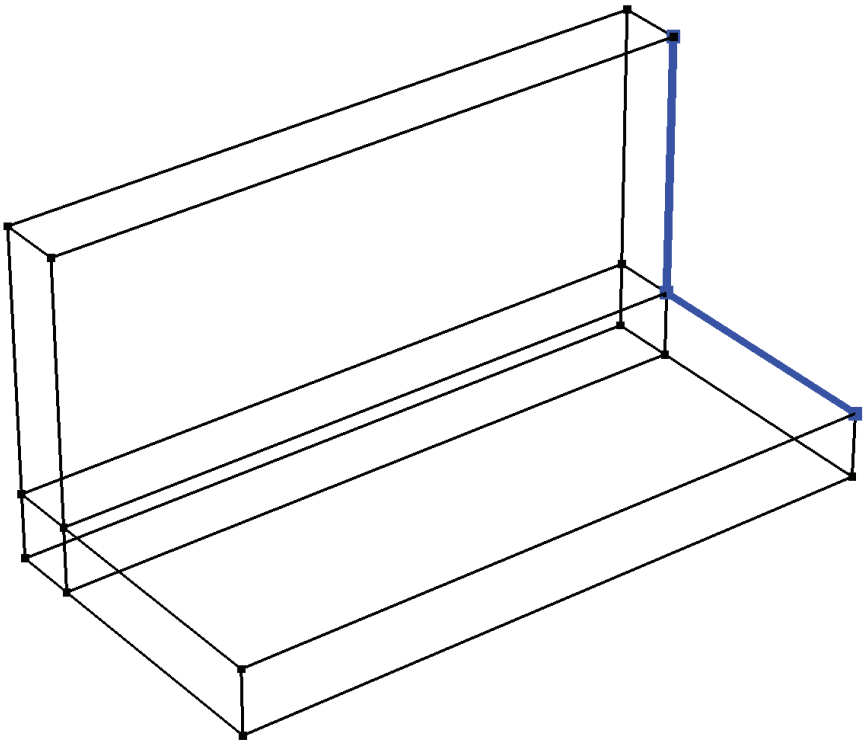

Figure 7. Edges pic for minimum temperature.

Minimum Temperature and Linear of Average Temparature

In Figure 7, a schematic diagram of a three-dimensional L-shaped structure is shown, with two edges depicted at the end. Our main objective is to discuss the minimum temperature at this section while altering two out of three parameters. We are focusing on the behavior of the minimum temperature at these two edges. Finally, a general regression equation will be provided that can be used for future predictions or for verifying the present investigation. The methodology will involve multiple linear regression steps to generate empirical equations.

In Figure 8(a-d), the minimum temperature is plotted against the increasing volume fraction of alumina and the Reynolds number. For each curve shown in these figures, the Reynolds number is fixed, while the volume fraction of copper is fixed for all figures, indicating that these results are for hybrid nanofluids. In Figure 8(a), for fixed Reynolds numbers and a fixed volume fraction $\phi_2 = 0.01$), the minimum temperature decreases as the volume fraction of alumina increases from 0.01 to 0.04, and then it increases for all Reynolds numbers from 10,000 to 30,000. However, at a value of 40,000 for the Reynolds number, the minimum temperature begins to decline at $\phi_1 = 0.07$, indicating that there are two critical values of ϕ_1 where the behavior of the minimum temperature alters. In Figure 8(b), the minimum temperature is plotted against ϕ_1 while fixing the Reynolds number for all curves, and the volume fraction of copper (ϕ_2) is fixed at 0.04. Compared to Fig. 7(a), it can be observed that the minimum temperature always increases for all values of ϕ_1 at Re = 10,000, which is also an indication of the application of hybrid nanofluids in heat transfer rate improvement. In both Figs 8(a) and 8(b), it can be understood that increasing the Reynolds number increases the minimum temperature at the two edges of the three-dimensional L-shaped channel. In Figure. 7(b), it can be observed that using the two Reynolds numbers of Re = 30,000 and 40,000, the maximum minimum temperature is achieved at $\phi_1 = 0.1$.

In Figure 8(c) and Figure 8(d), the minimum temperature is analyzed against the increasing concentration of alumina in the base fluids, while the Reynolds number is fixed for each curve. We observe that in both figures, the minimum temperature increases with the enhancement of the Reynolds number for higher volume fractions of alumina. While the concentration of copper was fixed at 0.07 and 0.1 in both figures, we found that the minimum temperature at the end of these two edges depends on both the Reynolds number and the concentration of nanoparticles in the base fluids. However, from all these figures, it is very challenging to control the temperature at the two edges, and this depends on several factors, including the geometry. In Figure. 7(d), it can be easily understood that to achieve the minimum temperature for a high level of concentration of copper, the Reynolds number should be fixed at Re = 30,000.

To analyze the variation in minimum temperature patterns with increasing copper nanoparticle concentration

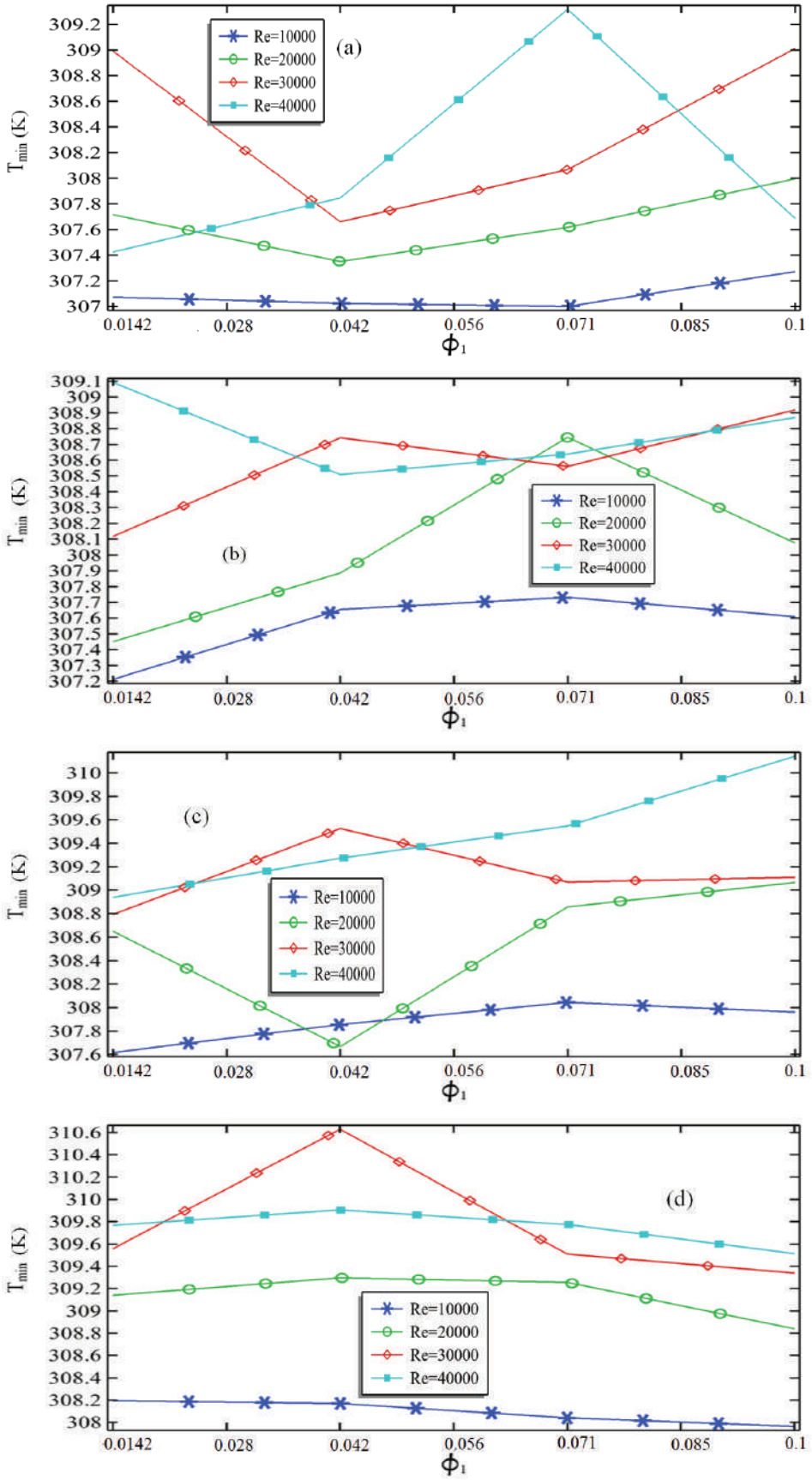

Figure 8(a-d). The minimum temperature at the two edges of the channel against ϕ_1 fixed Reynolds numbers (a) $\phi_2 = 0.01$ (b) $\phi_2 = 0.04$ (c) $\phi_2 = 0.07$ and (d) $\phi_2 = 0.1$.

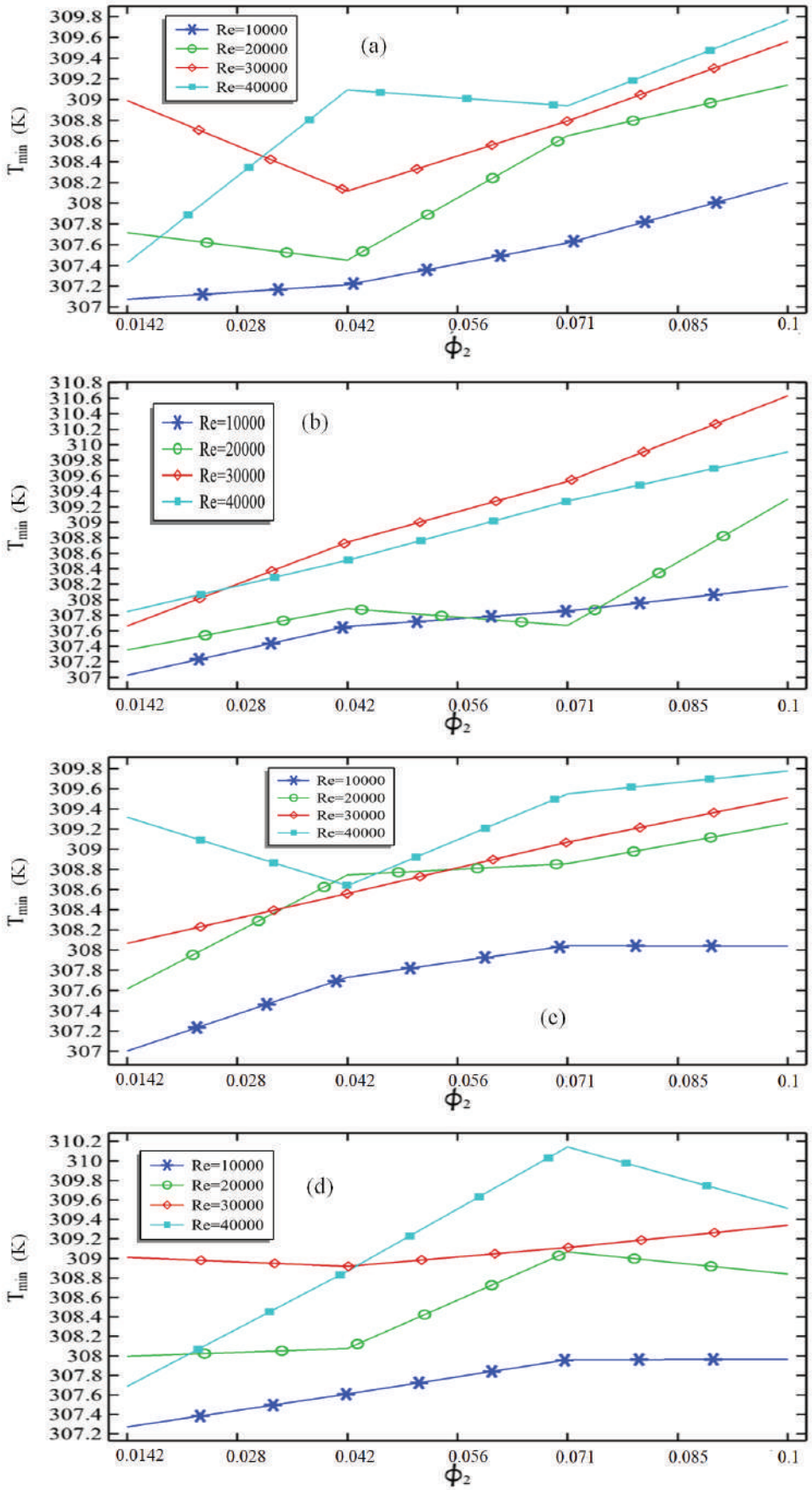

Figure 9(a-d). The minimum temperature at the two edges of the channel vs ϕ_2 for fixed Reynolds numbers at (a) $\phi_1 = 0.01$ (b) $\phi_1 = 0.04$ (c) $\phi_1 = 0.07$ and (d) $\phi_1 = 0.1$.

while keeping the Reynolds number constant, Figures 9(a-d) are presented. After each figure, the alumina concentration is progressively increased. In Figure 9(a), an evident increase in minimum temperature at the outlet edges is observed with higher copper volume fractions for each fixed Reynolds number. A comparison with Fig 9(a) reveals that utilizing copper leads to a more rapid temperature increase at the two edges. Notably, at the lowest Reynolds number, the minimum temperature remains elevated, displaying an irregular pattern for other Reynolds numbers. However, employing a copper volume fraction of 0.1 in the base fluids yields the highest minimum temperature for all Reynolds numbers due to copper's superior thermal conductivity compared to alumina nanoparticles.

In Figure 9(b), with the alumina volume fraction fixed at $\phi_1 = 0.04$ (compared to 0.01 in Figure 8(a)), an increasing alumina concentration correlates with a higher minimum temperature. This figure indicates that the maximum minimum temperature is attained at a Reynolds number of 30,000. Here, for most Reynolds numbers, the minimum temperature straightforwardly increases. In Figures 9(c) and 9(d), scrutinizing minimum temperature patterns by further increasing alumina nanoparticle concentration reveals a consistent increase across all Reynolds numbers compared to the previous results in Figures 9(a) and 9(b). Notably, only at Re = 10,000 does the minimum temperature increase without obstruction. Additionally, using $\phi_1 = 0.01$ and 0.04 of copper nanoparticles appears to be critical points, altering the pattern. For high Reynolds numbers and elevated copper nanoparticle concentrations, the minimum temperature at the two edges of the L-shaped channel increases, presenting an irregular pattern with increasing Reynolds number and volume fraction of copper and alumina nanoparticles. Overall, the successful outcome underscores that utilizing hybrid nanofluids consistently enhances heat transfer rates, as evident in the present results for the minimum temperature.

Physical reasons: The observed behavior is attributed to the physical properties of hybrid nanofluids and their interactions with flow dynamics within the domain. Copper's superior thermal conductivity enhances the heat transfer rate, leading to increased minimum temperatures at the edges of the L-shaped channel. At very high Reynolds numbers, intensified fluid velocity increases turbulent mixing, improving thermal energy distribution. The behavior at specific volume fractions occurs due to the balance between enhanced thermal conductivity and increased viscosity from the nanoparticle concentration, which can impede flow. Alumina's lower thermal conductivity compared to copper results in varying contributions to heat transfer. The geometry of the L-shaped channel influences recirculation zones, creating localized temperature variations at the channel edges. Additionally, the interplay between nanoparticle concentration and Reynolds number determines the extent of boundary layer disruption, affecting heat transfer rates at the edges.

After analyzing the numerical results for the minimum temperature in Figures. 9(a-d) and 9(a-d) by altering the parameters, it was found that the volume fraction of both nanomaterials exhibits an irregular pattern in depicting the minimum temperature. In other words, the minimum temperature in the L-shaped channel appears to be independent of the volume fraction of these nanomaterials in the base fluids. Therefore, based on these observations, we are drawing a conclusion through the linear regression procedure that will determine the average temperature at the outlet of the three-dimensional L-shaped channel using the multiple linear regression process, as given below:

$$T_{avg,Predicted} = 307.117188 + 0.0000132\,\mathrm{Re} \qquad (23)$$

According to this equation (23), the average temperature in this study depends purely on the Reynolds number in the case of turbulence investigation. The equation can also be used for future predictions when conducting similar studies. However, the utility of this equation depends on the parameters used, as it provides only an estimation of the average temperature at the outlet. Table 4 summarizes the top parameter estimators that can be used to minimize

Table 4. Top 10 minimum absolute errors when comparing the exact average temperature at the outlet with the temperature predicted by the linear regression

ϕ_1	ϕ_2	Re	$T_{avg,Exact}$	$T_{avg,Predicted}$	$\lvert T_{avg,Exact} - T_{avg,Predicted} \rvert$
0.01	0.1	40000	307.64	307.645188	0.005188
0.1	0.07	20000	307.39	307.381188	0.008812
0.04	0.07	10000	307.24	307.249188	0.009188
0.07	0.07	40000	307.66	307.645188	0.014812
0.04	0.1	20000	307.4	307.381188	0.018812
0.1	0.1	10000	307.27	307.249188	0.020812
0.01	0.07	10000	307.2	307.249188	0.049188
0.04	0.1	10000	307.3	307.249188	0.050812
0.07	0.1	10000	307.19	307.249188	0.059188
0.01	0.01	20000	307.32	307.381188	0.061188

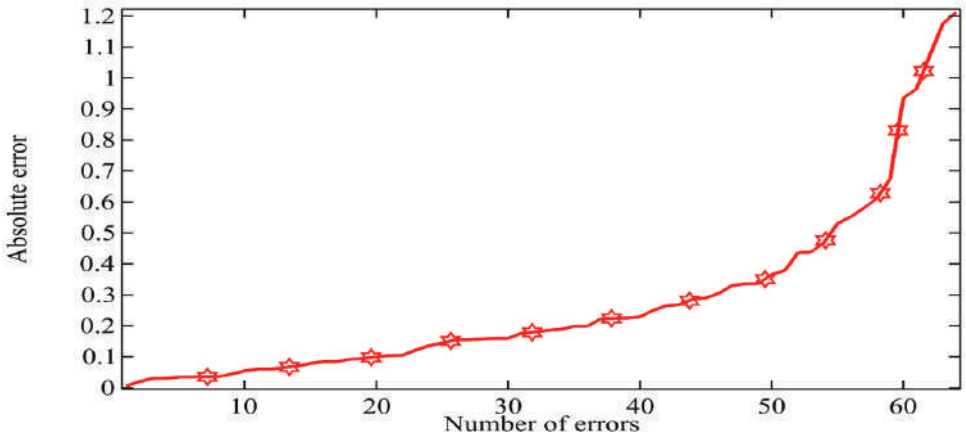

Figure 10. The graph of absolute error due to the comparison exact average temperature at the outelt and the average temperture through the correlation vs the number of errors.

absolute error in such studies. According to this table, when using $\phi_1 = 0.01$, $\phi_2 = 0.1$, and Re = 40,000, the absolute error due to the comparison of the exact average temperature and predicted average temperature is approximately 0.005528. The relation also defines that by increasing per unit of the Reynolds number the temperature rises by 0.0000132.

Finally, a graph is attached summarizing the absolute error when predicting the original temperature using linear regression equation. It should be noted that by utilizing different ranges of three parameters, we have conducted 64 simulations. Figure 10 suggests that approximately 30 numerical simulations yield a minimum absolute error of less than 0.2, while the maximum error that can be achieved when computing the average temperature via the linear regression equation is 1.2.

Local Nusselt Number and The Linear Regression Equation of Average Nusselt Number

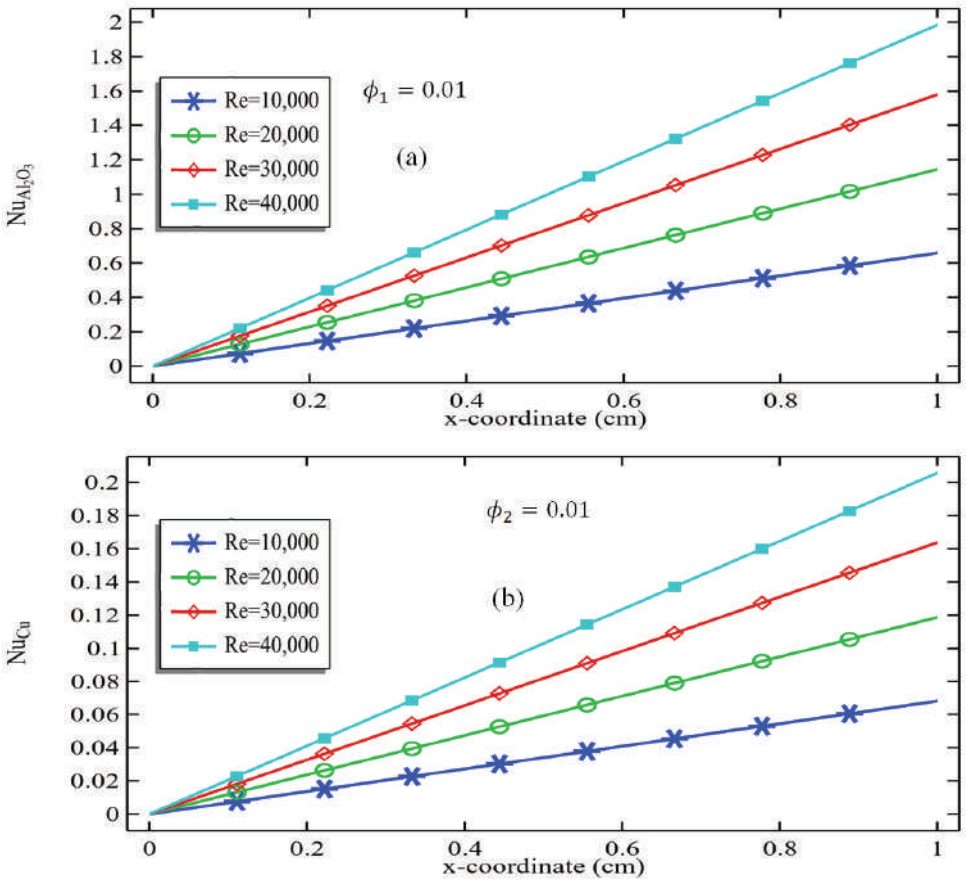

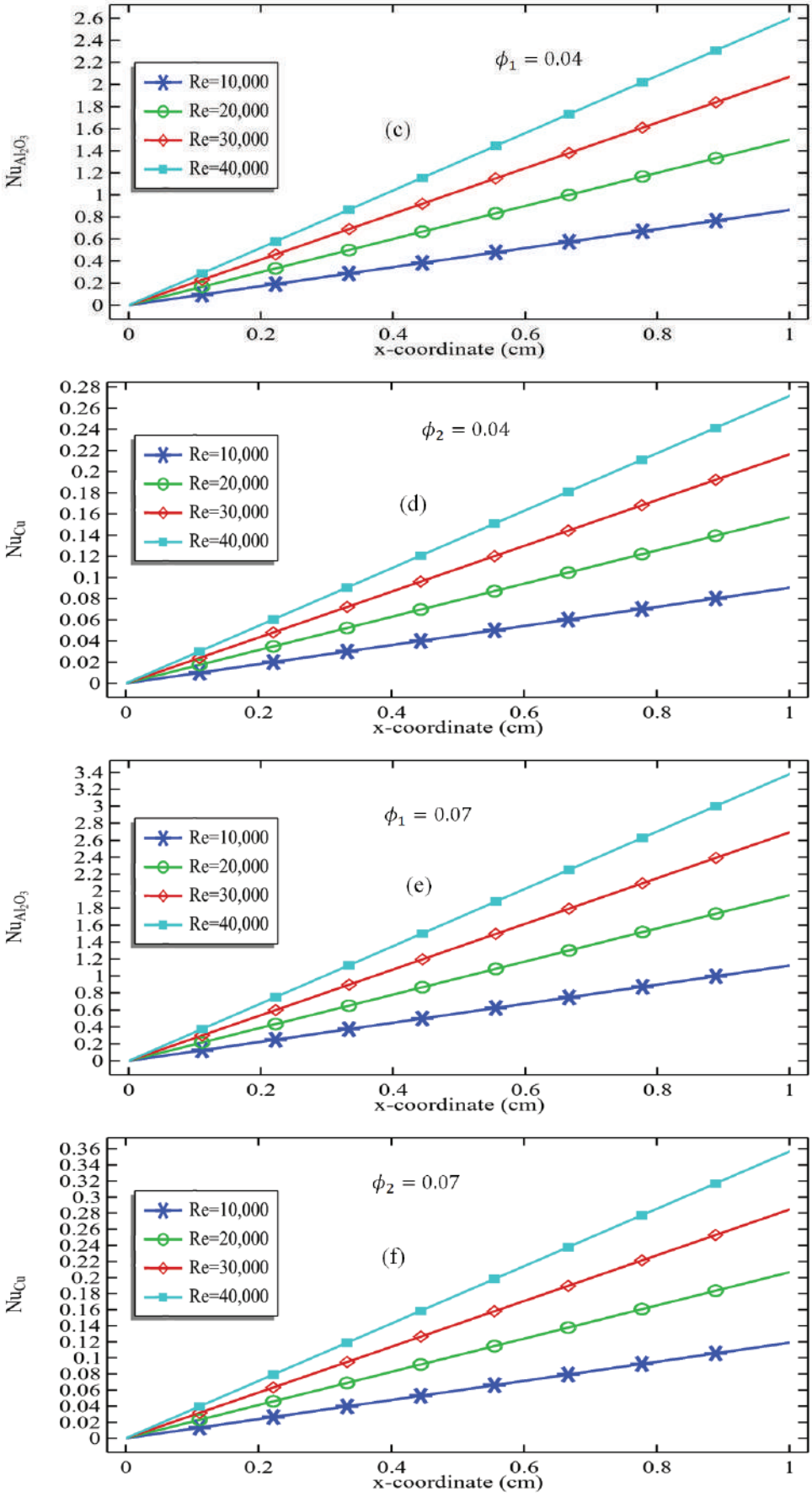

Figure 11(a-f). The computational results for the local Nusselt number along the channel's length for aluminum oxide and copper separately.

It is crucial to measure the effectiveness of both convection and conduction processes in a domain, which depends on the heat transfer coefficient and thermal conductivity, respectively. The local Nusselt number or average Nusselt number is often measured during numerical investigations, serving as a good indicator for both convection and conduction. An increase in the Nusselt number suggests stronger convection, while a decrease indicates stronger conduction. For heat transfer investigation and optimization, two different nanoparticles, copper, and alumina, are suspended in base fluids. The aim is to analyze which nanoparticle contributes more to the convection process. Figure 11(a-f) compares local Nusselt numbers along the x-axis, considering the same volume fraction of nanomaterials in base fluids. Figures 11 (a) and 11 (b) show volume fractions for both nanomaterials set at 0.01, revealing an increase in local Nusselt numbers for each fixed Reynolds number. The maximum local Nusselt at the end of the x-axis improves with higher Reynolds numbers, indicating a significant contribution of Reynolds number to convection enhancement. Comparatively, using alumina nanoparticles demonstrates a higher contribution to the enhancement of the convection process compared to copper nanomaterials. This is attributed to the stronger thermal conductivity of copper, which strengthens the conduction process. In Figures 11 (c) and 11 (d), with a volume fraction of 0.04, increasing the volume fraction of nanomaterials in base fluids enhances the local Nusselt number and convection process. Reynolds number also plays a crucial role in increasing convection, as seen in the measurement of the maximum local Nusselt number at the channel outlet with increasing Reynolds numbers. Figures 11 (e) and 11 (f) continue to confirm that higher volume fractions (0.07) of alumina and copper nanomaterials enhance the convection process along the x-axis. Alumina proves to be a superior nanoparticle for convection enhancement, and increasing Reynolds numbers further contribute to the local Nusselt number. In summary, using alumina nanoparticles is effective for increasing the convection process, while copper excels in conduction due to its thermal conductivity. Additionally, an increase in Reynolds numbers significantly contributes to convection rate enhancement in the domain. After observing that the local Nusselt function is purely related to the Reynolds number and the volume fractions of both alumina and copper nanomaterials, further analysis is warranted. Therefore, to draw more conclusive results, a multiple linear regression process described in section (2.2) will be applied to establish the linear regression equation between the Reynolds number and the volume fractions of both nanomaterials to yield or to predict the local Nusselt number at the outlet of the channel. The equation is described as follows:

$$\mathrm{Nu}_{\mathrm{Predicted}} = 11.642265 + 13.492917\phi_2 + 0.00224559\,\mathrm{Re} \quad (24)$$

Finally, Table 5 is attached, which describes the top 10 minimum absolute errors obtained by comparing the exact Nusselt number values at the outlet with the predicted Nusselt numbers from the correlation. From the table, it can be seen that the correlation works well when the volume fraction of both nanomaterials is kept at 0.01 and the Reynolds number is maintained at 30,000. The linear regression equation described above is only valid when investigating such a type of three-dimensional L-shaped channel using the $\kappa - \varepsilon$ turbulence model and analyzing the thermal properties of hybrid nanofluids. The equation above suggests that increasing each unit of copper volume fraction and Reynolds number results in the average Nusselt number at the outlet increasing by 13.492917 and 0.002245559, respectively.

Finally, a graph in Figure 12. is provided, where the absolute error (difference between exact and predicted average Nusselt numbers) is plotted against the total number of errors. Since multiple values of the parameters have been used, about 64 numerical simulations were conducted to analyze the heat transfer characteristics for the

Table 5. The top 10 minimum absolute errors when computing the difference between the exact average Nusselt number at the outlet and the predicted Nusselt number via correlation

ϕ_1	ϕ_2	Re	Nu_{Exact}	$Nu_{Predicted}$	$\lvert Nu_{Exact} - Nu_{Predicted} \rvert$
0.01	0.01	30000	79.513	79.14489417	0.36810583
0.01	0.04	30000	80.174	79.54968168	0.62431832
0.04	0.01	30000	79.801	79.14489417	0.65610583
0.1	0.01	10000	33.481	34.23309417	0.75209417
0.1	0.04	40000	101.23	102.0055817	0.77558168
0.1	0.1	30000	81.143	80.3592567	0.7837433
0.07	0.07	40000	101.62	102.4103692	0.79036919
0.04	0.1	40000	101.99	102.8151567	0.8251567
0.1	0.07	40000	101.58	102.4103692	0.83036919
0.07	0.01	10000	33.384	34.23309417	0.84909417

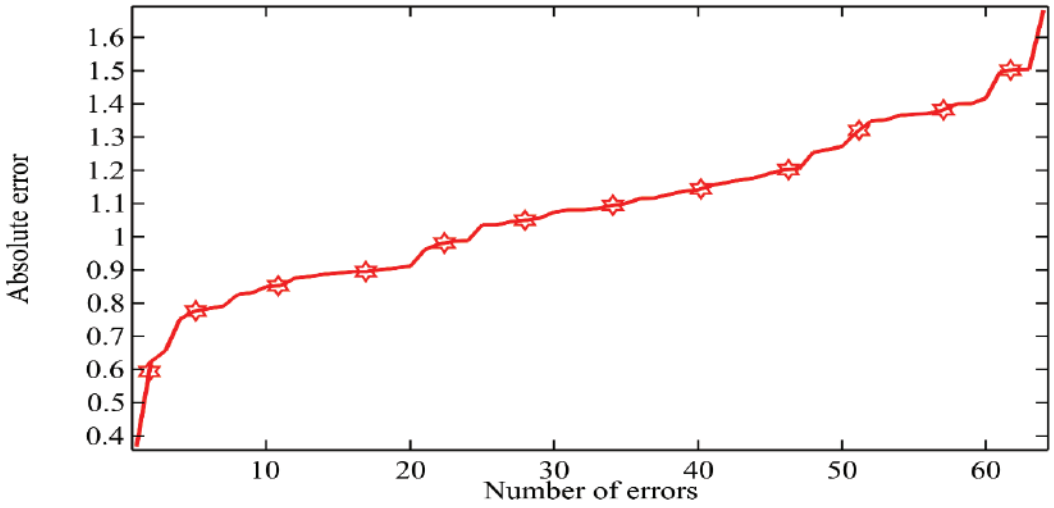

Figure 12. The graph of absolute error vs the number of errors.

three-dimensional L-shaped channel using turbulence modeling. The graph in Figure. 12. indicates that approximately 30 simulations yield an absolute error of 1.1 when comparing the exact average Nusselt number with the predicted Nusselt number. The maximum absolute error achievable using the correlation as the predictor is 1.6.

Calculation and Presentation of Darcy-Weisbach Friction Factor

In this section, the relationship between temperature and the friction factor, as described by the Darcy-Weisbach formula, is analyzed along the x-axis. The pattern is also examined using the Reynolds number and volume fraction of nanomaterials in the base fluids. Friction measures the fluid's resistance due to increased material density. Figures. 13(a-d) and 14(a-d) illustrate the pattern of friction factor vs temperature. In Figures. 13(a-d), the volume fraction of alumina varies for each curve, while the Reynolds number is fixed. In Figure. 13(a), with a fixed Re = 10,000, the friction factor increases with temperature, reaches a maximum, and then decreases for each alumina volume fraction. Interestingly, the Darcy friction factor remains constant for all alumina concentrations, showing a consistent pattern with increasing temperature. For $\phi_1 = 0.04$, Figure. 13(a) yields the maximum temperature with the same friction factor. In Figures. 13(b) and 13(c), Reynolds numbers of 20,000 and 30,000 are checked with increasing volume fraction of alumina. The friction factor vs temperature pattern remains the same as in Figure. 13(a), indicating an increase, peak, and decline. Additionally, an irregular pattern is observed with higher volume fractions in Figures. 13(b) and 13(c), reaching minimum and maximum temperatures at different phi values. Figure. 13(d) shows that the friction factor yields the maximum temperature in the L-shaped channel with $\phi_1 = 0.04$. However, across all figures, increasing Reynolds number consistently leads to a decline in maximum temperature due to higher velocity and momentum forces in the channel. It's noteworthy that increasing friction force reduces fluid density and mean flow velocity, allowing for better heat exchange with the surroundings.

In Figs 14(a-d), we investigate the relationship between the Darcy friction factor and temperature patterns by varying the volume fraction of copper and Reynolds number, with the alumina fraction fixed at 0.02. Notably, in Figure 14(a), an intriguing observation emerges: as the volume fraction of copper increases, the temperature exhibits variation for a constant friction factor. This phenomenon, akin to previous findings (cf. Figure. 13(a-d)), reveals a non-linear trend whereby an initial rise in temperature coincides with an increase in the Darcy friction factor, reaching a peak before declining. Emphasizing the pivotal role of temperature control via volume fraction manipulation, we underscore the complementary influence of Reynolds number modulation. Moving to Figure 14(b), where the Reynolds number is set at 20,000, we observe a noteworthy shift in the position of friction factor-temperature profiles with increasing volume fraction. Specifically, at constant friction factors, $\phi_2 = 0.1$ yields higher temperatures along the x-axis compared to $\phi_2 = 0.01$. To provide a comprehensive analysis, Figures 14(c) and 14(d) are introduced, fixing Reynolds numbers at 30,000 and 40,000, respectively. Herein, a decrease in the maximum Darcy friction factor is evident with increasing Reynolds number, attributed to heightened fluid velocities or flow rates, thereby reducing frictional effects.

Furthermore, an intriguing irregularity surfaces in the friction versus temperature graph due to volume fraction alterations, underscoring the nuanced interplay between these variables. It is noteworthy that achieving precise control over the friction factor-temperature relationship solely via copper volume fraction manipulation

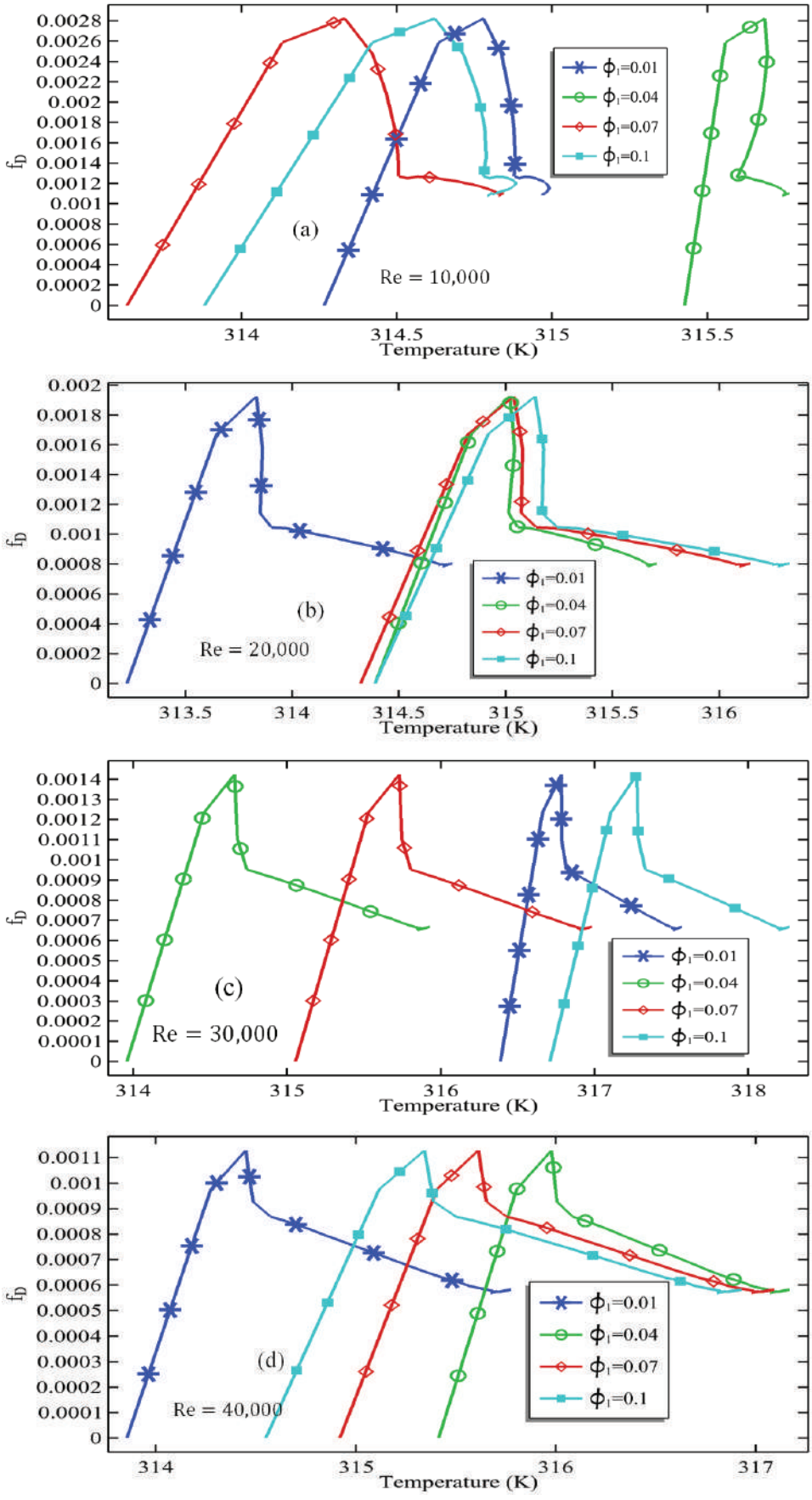

Figure 13. Temperature and the friction factor along the length of the channel when $\phi_2 = 0.01$.

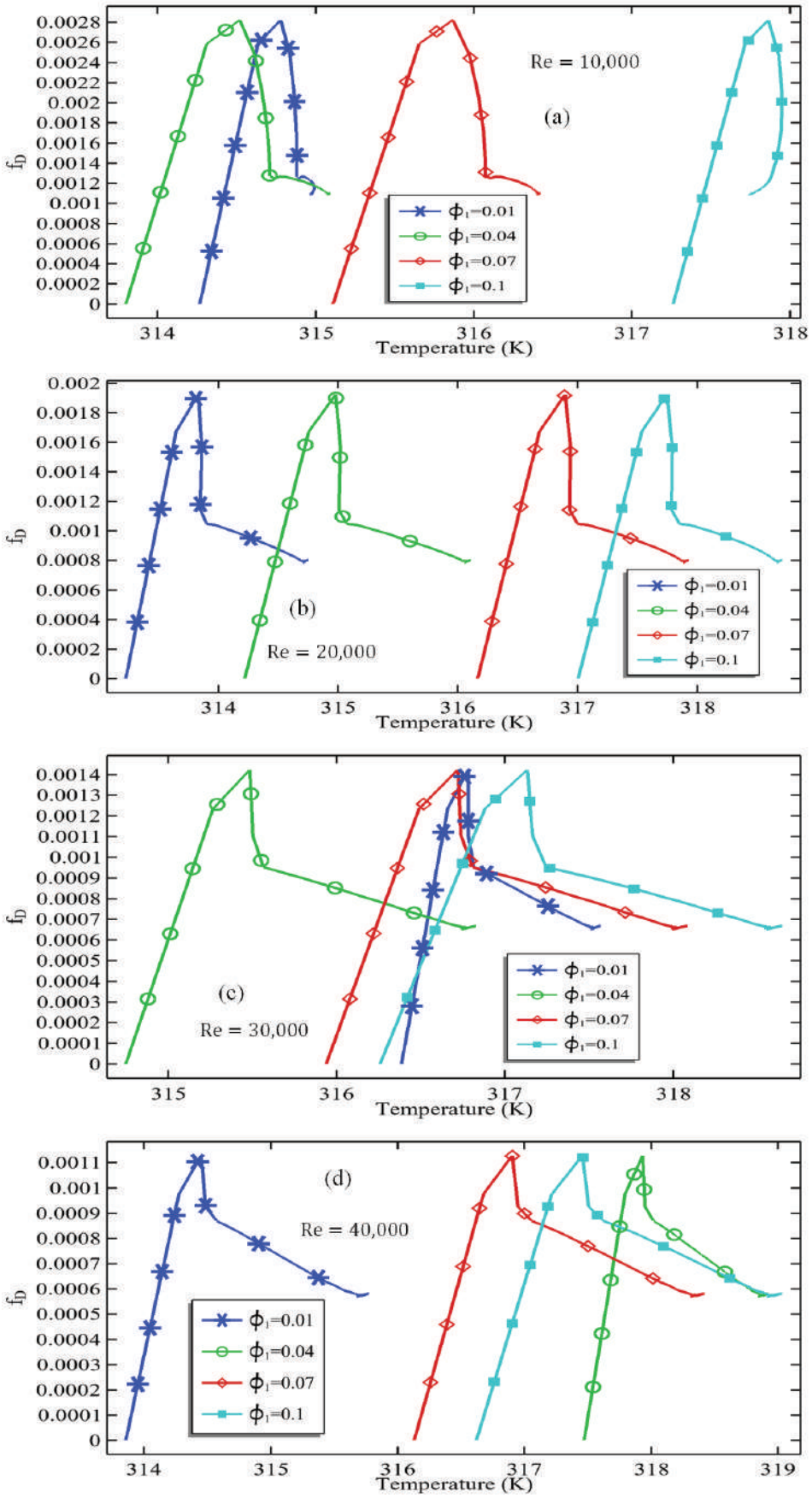

Figure 14(a-d). Temperature and the friction factor along the length of the channel when $\phi_1 = 0.01$.

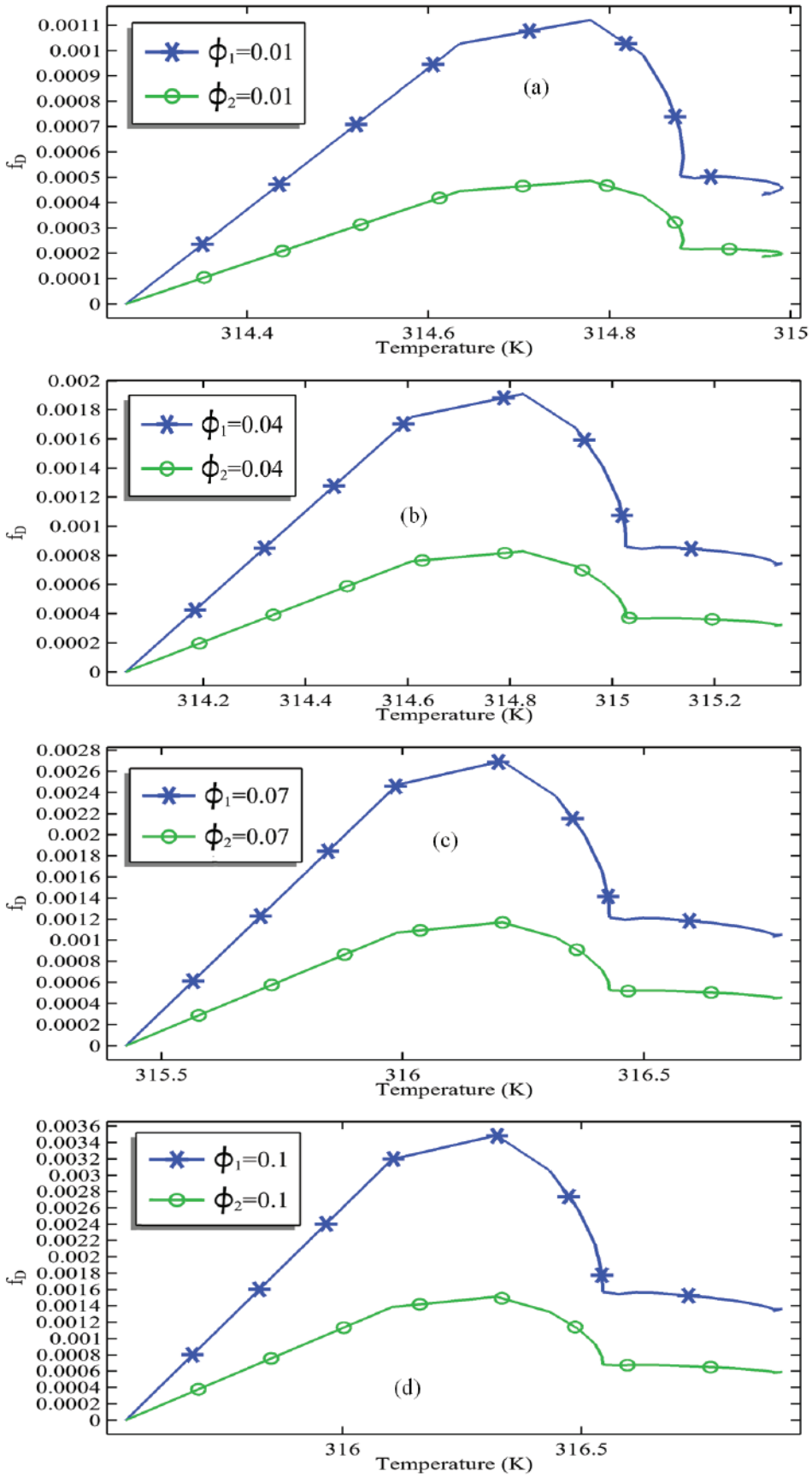

Figure 15(a-d). Comparison of friction factor between the aluminum oxide and the copper keeping both the volume fraction equal at Re=10,000.

proves challenging, underscoring the indispensable role of Reynolds number adjustments in elucidating this complex phenomenon.

Figures 15(a-d) present a comprehensive comparative analysis of both the Darcy friction factor and temperature, specifically examining the influence of various factors on these critical parameters. The study maintains a constant Reynolds number while considering equal volume fractions of aluminum oxide and copper nanoparticles. Notably, the results presented in Figure. 15(a-d) reveal an intriguing trend: the Darcy friction factor for aluminum oxide consistently exceeds that of copper. This discrepancy can be attributed to the greater density of aluminum oxide compared to copper, a pivotal factor affecting the flow dynamics within the channel. Additionally, it's essential to clarify that the temperature values indicated along the x-axis of these figures represent the overall temperature distribution across the entire channel length. The temperature profile is instrumental in understanding how heat dissipates and transfers within the channel under varying conditions. Of particular significance, we can observe a noteworthy relationship between the total volume fraction of the channel and the resulting temperature. As the total volume fraction increases, there is a corresponding escalation in temperature along the length of the channel. This finding underscores the importance of considering the impact of volume fraction variations on thermal behavior and serves as valuable insight for optimizing heat transfer processes within this system.

Physical reasons: The decline in the friction factor beyond certain temperatures in Figures 14(a-d) and 15(a-d) is attributed to the interaction between fluid viscosity, thermal expansion, and flow dynamics. As the temperature increases, the viscosity of the hybrid nanofluid decreases, reducing flow resistance and, consequently, the friction factor at the channel edges. Additionally, rising fluid temperatures lead to thermal expansion, which decreases the fluid density and further reduces flow resistance. The maximum friction factor occurs at a peak where there is an optimal balance between the fluid's momentum and its decreasing viscosity. Beyond this peak, the reduction in viscosity dominates, causing the friction factor to decline. Higher Reynolds numbers also contribute to increased fluid velocity and turbulence, enhancing momentum forces and mitigating the effect of the friction factor. This behavior remains consistent across varying volume fractions of copper and alumina, due to their distinct thermal conductivities and densities.

CONCLUSION

In the course of our present investigation, we meticulously scrutinized the behavior of a three-dimensional L-shaped channel as it accommodated the flow of a hybrid mixture containing aluminum oxide and copper. Our primary focus revolved around the intricate dynamics of turbulent forced convection. This endeavor was underpinned by the application of the $\kappa - \varepsilon$ turbulence model, which we expertly integrated with energy equations. The entire computational framework was adeptly executed through the Finite Element Method within the powerful COMSOL Multiphysics 5.6 platform. Our study encompassed a comprehensive spectrum of scenarios, each meticulously engineered to explore various volume fractions for both nanoparticles. Specifically, we considered volume fractions of 0.01, 0.04, 0.07, and 0.1 while subjecting the fluid to a range of Reynolds numbers spanning from 10,000 to 40,000. To ensure the robustness of our findings, we conducted a rigorous mesh-independent study and systematically validated our results against established correlations for the local Nusselt number. The culmination of our extensive numerical investigations unveiled several noteworthy insights and observations.

- The minimum temperature initially decreases with an increasing aluminum oxide volume fraction, followed by an increase. This behavior is specifically observed at Reynolds numbers ranging from 10,000 to 30,000 and at copper volume fractions of 0.01 and 0.04
- The addition of copper enhances the minimum temperature at both edges of the channel. Furthermore, an increase in Reynolds number consistently raises the minimum temperature across all scenarios in our simulation.
- Notably, increasing the copper volume fraction consistently improves the minimum temperatures at the channel's two edges.
- Applying the linear regression procedure, it was found that the average temperature at the outlet depended solely on the Reynolds number. It was observed that the average temperature increased by a value of 0.0000132 for each unit increase in the Reynolds number. Using this correlation for the average temperature at the outlet, the minimum and maximum absolute errors achieved were 0.005188 and 1.6, respectively.
- In comparing the local Nusselt numbers for aluminum oxide and copper, a outstanding observation emerges: the local Nusselt number for aluminum oxide surpasses that of copper by a factor of approximately 10.
- Applying the multiple linear regression procedure, a linear regression equation for the average Nusselt number was derived. According to this equation, the average Nusselt number at the outlet depends solely on the copper volume fraction and the Reynolds number. Using this correlation, it was determined that the average Nusselt number at the outlet increases by 13.492917 and 0.002245559 when one unit of volume fraction and Reynolds number is increased, respectively. By utilizing this linear regression, a minimum error of 0.36810583 and a maximum error of 1.6 can be achieved.
- The Darcy friction factor shows a clear pattern, increasing along the channel length to a maximum before gradually decreasing. This trend is consistent across all cases.

The factor's response to volume fraction changes in copper and aluminum oxide is non-deterministic, meaning it may either increase or decrease. Moreover, the Darcy friction factor decreases as the Reynolds number rises.

NOMENCLATURE

U	Velocity field
u	x-component of velocity
v	y-component of velocity
w	z-component of velocity
$\nabla = < \frac{\partial}{\partial x}, \frac{\partial}{\partial y}, \frac{\partial}{\partial z} >$	Gradient operator
I	Identity vector
P	Pressure
μ_{nf}	Hybrids nanofluids viscosity
μ_T	Turbulent viscosity (Eddy Viscosity)
κ	Turbulent kinetic energy
p_κ	Kinetic energy production
ε	Energy Dissipation rate
L_x	Length along the x-axis
L_y	Length along the y-axis
L_z	Length along the z-axis
u_{in}	Inlet velocity
Re	Reynolds number
κ_0	Initial kinetic energy
ε_0	Initial dissipation rate
I_T	Initial turbulence intensity
L_T	Initial turbulence length
n	Normal vector on the boundary
p_{out}	Pressure at outlet
T_h	Hot temperature
δ_w^+	Wall distance
T_c	Cold temperature
$\kappa_v, \sigma_\kappa, \sigma_\varepsilon, c_\mu, c_{\varepsilon 1}, c_{\varepsilon 2}$	Model parameters
τ_w	Wall shear stress
T	Transpose
U_{mean}	Mean velocity
Avg	Average
Nu	Nusselt number
Pr	Prandtl Number
Q	Heat flux
X	x-axis
Y	y-axis
Z	z-axis

AUTHORSHIP CONTRIBUTIONS

Authors equally contributed to this work.

DATA AVAILABILITY STATEMENT

The authors confirm that the data that supports the findings of this study are available within the article. Raw data that support the finding of this study are available from the corresponding author, upon reasonable request.

CONFLICT OF INTEREST

The author declared no potential conflicts of interest with respect to the research, authorship, and/or publication of this article.

ETHICS

There are no ethical issues with the publication of this manuscript.

STATEMENT ON THE USE OF ARTIFICIAL INTELLIGENCE

Artificial intelligence was not used in the preparation of the article

REFERENCES

[1] Akbari OA, Safaei MR, Goodarzi M, Akbar NS, Zarringhalam M, Shabani GA, et al. A modified two-phase mixture model of nanofluid flow and heat transfer in a 3-D curved microtube. Adv Powder Technol 2016;27:2175–2185. [CrossRef]

[2] Allehiany FM, Memon AA, Memon MA, Fenta A. Maximizing electrical output and reducing heat-related losses in photovoltaic thermal systems with a thorough examination of flow channel integration and nanofluid cooling. Sci Rep 2023;13:16961. [CrossRef]

[3] Mashayekhi R, Khodabandeh E, Akbari OA, Toghraie D, Bahiraei M, Gholami M. CFD analysis of thermal and hydrodynamic characteristics of hybrid nanofluid in a newly designed sinusoidal double-layered microchannel heat sink. J Therm Anal Calorim 2018;134:2305–2315. [CrossRef]

[4] Mashayekhi R, Khodabandeh E, Bahiraei M, Bahrami L, Toghraie D, Akbari OA. Application of a novel conical strip insert to improve the efficacy of water–Ag nanofluid for utilization in thermal systems: a two-phase simulation. Energy Convers Manag 2017;151:573–586. [CrossRef]

[5] Darzi AAR, Afrouzi HH, Khaki M, Abbasi M. Unconstrained melting and solidification inside rectangular enclosure. J Fundam Appl Sci 2015;7:436–451. [CrossRef]

[6] Rabienataj Darzi AA, Afrouzi HH, Alizadeh E, Shokri V, Farhadi M. Numerical simulation of heat and mass transfer during absorption of hydrogen in metal hydride tank. Heat Transf Asian Res 2017;46:75–90. [CrossRef]

[7] Hassanzadeh Afrouzi H, Moshfegh A, Farhadi M, Sedighi K. Dissipative particle dynamics simulation hydrated Nafion EW 1200 as fuel cell membrane in nanoscopic scale. Chall Nano Micro Scale Sci Technol 2016;5:44–53. [CrossRef]

[8] Akbari OA, Hassanzadeh Afrouzi H, Marzban A, Toghraie D, Malekzade H, Arabpour A. Investigation of volume fraction of nanoparticles effect and aspect ratio of the twisted tape in the tube. J Therm Anal Calorim 2017;129:1911−1922. [CrossRef]
[9] Sajid T, Ayub A, Shah SZH, Jamshed W, Eid MR, Tag El Din ESM, et al. Trace of chemical reactions accompanied with Arrhenius energy on ternary hybridity nanofluid past a wedge. Symmetry 2022;14:1850. doi: 10.3390/sym14091850. [CrossRef]
[10] Hassanzadeh Afrouzi H, Rabienataj Darzi AA, Delavar MA, Abouei Mehrizi A. Pulsating flow and heat transfer in a helical tube with constant heat flux. Int J Adv Ind Eng 2013;1:36−39.
[11] Akram M, Memon AA, Memon MA, Obalalu AM, Khan U. Investigation of a two-dimensional photovoltaic thermal system using hybrid nanofluids and a rotating cylinder. Nanoscale Adv 2023;5:5529−5542. [CrossRef]
[12] Memon AA, Memon MA, Haque MM. Numerical investigation of electrical efficiency with the application of hybrid nanofluids for photovoltaic thermal systems contained in a cavity channel. J Math 2023;2023:1466881. [CrossRef]
[13] Memon AA, Khan WA, Muhammad T. Numerical investigation of photovoltaic thermal energy efficiency improvement using the backward step containing Cu-Al2O3 hybrid nanofluid. Alexandria Eng J 2023;75:391−406. [CrossRef]
[14] Alghamdi M, Memon AA, Muhammad T, Ali MR. A numerical investigation of a photovoltaic thermal system contained a trapezoidal channel with transport of silver and titanium oxide using the water as base fluids. Case Stud Therm Eng 2023;47:103056. [CrossRef]
[15] Ramzan M, Shamshad U, Rehman S, Saeed A, Kumam P, Watthayu W. Computation of MHD flow of three-dimensional mixed convection non-Newtonian viscoelastic fluid with the physical aspect of gyrotactic microorganism. Waves Random Complex Media 2022:1−23. [CrossRef]
[16] Abraham JD, Mohanraj M. Thermodynamic performance of automobile air conditioners working with R430A as a drop-in substitute to R134a. J Therm Anal Calorim 2019;136:2071−2086. [CrossRef]
[17] Choi SUS, Eastman JA. Enhancing thermal conductivity of fluids with nanoparticles. In: Siginer DA, Wang HP, editors. Developments and applications of non-Newtonian flows. New York: ASME; 1995. p. 99−105. [CrossRef]
[18] Tiwari RK, Das MK. Heat transfer augmentation in a two-sided lid-driven differentially heated square cavity utilizing nanofluids. Int J Heat Mass Transf 2007;50:2002−2018. [CrossRef]
[19] Ramzan M, Rehman S, Junaid MS, Saeed A, Kumam P, Watthayu W. Dynamics of Williamson Ferro-nanofluid due to bioconvection in the portfolio of magnetic dipole and activation energy over a stretching sheet. Int Commun Heat Mass Transf 2022;137:106245. [CrossRef]
[20] Ramzan M, Shah Z, Kumam P, Khan W, Watthayu W, Kumam W. Bidirectional flow of MHD nanofluid with Hall current and Cattaneo-Christove heat flux toward the stretching surface. PLoS One 2022;17:e0264208. [CrossRef]
[21] Asadi M, Asadi A, Aberoumand S. An experimental and theoretical investigation on the effects of adding hybrid nanoparticles on heat transfer efficiency and pumping power of an oil-based nanofluid as a coolant fluid. Int J Refrig 2018;89:83−92. [CrossRef]
[22] Rashad AM, Armaghani T, Chamkha AJ, Mansour MA. Entropy generation and MHD natural convection of a nanofluid in an inclined square porous cavity: effects of a heat sink and source size and location. Chin J Phys 2018;56:193−211. [CrossRef]
[23] Gorla RSR, Siddiqa S, Mansour MA, Rashad AM, Salah T. Heat source/sink effects on a hybrid nanofluid-filled porous cavity. J Thermophys Heat Transf 2017;31:847−857. [CrossRef]
[24] Han ZH, Yang B, Kim SH, Zachariah MR. Application of hybrid sphere/carbon nanotube particles in nanofluids. Nanotechnology 2007;18:105701. [CrossRef]
[25] Botha SS, Ndungu P, Bladergroen BJ. Physicochemical properties of oil-based nanofluids containing hybrid structures of silver nanoparticles supported on silica. Ind Eng Chem Res 2011;50:3071−3077. [CrossRef]
[26] Jana S, Salehi-Khojin A, Zhong WH. Enhancement of fluid thermal conductivity by the addition of single and hybrid nano-additives. Thermochim Acta 2007;462:45−55. [CrossRef]
[27] Ho CJ, Huang JB, Tsai PS, Yang YM. Preparation and properties of hybrid water-based suspension of Al2O3 nanoparticles and MEPCM particles as functional forced convection fluid. Int Commun Heat Mass Transf 2010;37:490−494. [CrossRef]
[28] Ho CJ, Huang JB, Tsai PS, Yang YM. Water-based suspensions of Al2O3 nanoparticles and MEPCM particles on convection effectiveness in a circular tube. Int J Therm Sci 2011;50:736−748. [CrossRef]
[29] Suresh S, Venkitaraj KP, Selvakumar P, Chandrasekar M. Synthesis of Al2O3−Cu/water hybrid nanofluids using two step method and its thermo physical properties. Colloids Surf A Physicochem Eng Asp 2011;388:41−48. [CrossRef]
[30] Baghbanzadeh M, Rashidi A, Rashtchian D, Lotfi R, Amrollahi A. Synthesis of spherical silica/multiwall carbon nanotubes hybrid nanostructures and investigation of thermal conductivity of related nanofluids. Thermochim Acta 2012;549:87−94. [CrossRef]
[31] Paul G, Philip J, Raj B, Das PK, Manna I. Synthesis, characterization, and thermal property measurement of nano-Al95Zn05 dispersed nanofluid prepared by a two-step process. Int J Heat Mass Transf 2011;54:3783−3788. [CrossRef]

[32] Baby TT, Ramaprabhu S. Synthesis and nanofluid application of silver nanoparticles decorated graphene. J Mater Chem 2011;21:9702–9709. [CrossRef]
[33] Baby TT, Ramaprabhu S. Experimental investigation of the thermal transport properties of a carbon nanohybrid dispersed nanofluid. Nanoscale 2011;3:2208–2214. [CrossRef]
[34] Baby TT, Ramaprabhu S. Synthesis of silver nanoparticle decorated multiwalled carbon nanotubes-graphene mixture and its heat transfer studies in nanofluid. AIP Adv 2013;3:012111. [CrossRef]
[35] Armaghani T, Sadeghi MS, Rashad AM, Mansour MA, Chamkha AJ, Dogonchi AS, et al. MHD mixed convection of localized heat source/sink in an Al2O3-Cu/water hybrid nanofluid in L-shaped cavity. Alexandria Eng J 2021;60:2947–2962. [CrossRef]
[36] Selimefendigil F, Öztop HF. Combined effects of double rotating cones and magnetic field on the mixed convection of nanofluid in a porous 3D U-bend. Int Commun Heat Mass Transf 2020;116:104703. [CrossRef]
[37] Ghasemi K, Siavashi M. Three-dimensional analysis of magnetohydrodynamic transverse mixed convection of nanofluid inside a lid-driven enclosure using MRT-LBM. Int J Mech Sci 2020;165:105199. [CrossRef]
[38] Ganesh NV, Javed S, Al-Mdallal QM, Kalaivanan R, Chamkha AJ. Numerical study of heat generating γ Al2O3–H2O nanofluid inside a square cavity with multiple obstacles of different shapes. Heliyon 2020;6:e05752. [CrossRef]
[39] Afrand M, Pordanjani AH, Aghakhani S, Oztop HF, Abu-Hamdeh N. Free convection and entropy generation of a nanofluid in a tilted triangular cavity exposed to a magnetic field with sinusoidal wall temperature distribution considering radiation effects. Int Commun Heat Mass Transf 2020;112:104507. [CrossRef]
[40] Nath R, Murugesan K. Numerical investigation of double-diffusive mixed convection of Fe3O4/Cu/Al2O3-water nanofluid flow through a backward-facing-step channel subjected to magnetic field. Int J Numer Method Heat Fluid Flow 2021;31:1883–1913. [CrossRef]
[41] Miroshnichenko IV, Sheremet MA. Radiation effect on conjugate turbulent natural convection in a cavity with a discrete heater. Appl Math Comput 2018;321:358–371. [CrossRef]
[42] Miroshnichenko IV, Sheremet MA. Turbulent natural convection combined with thermal surface radiation inside an inclined cavity having local heater. Int J Therm Sci 2018;124:122–130. [CrossRef]
[43] Alsabery AI, Sheremet MA, Chamkha AJ, Hashim I. Forced convection of turbulent flow into the wavy parallel channel. J Therm Anal Calorim 2022;147:11183–11194. [CrossRef]
[44] Iachachene F, Haddad Z, Arıcı M, Abu-Nada E, Sheremet MA. The effect of nano encapsulated phase change materials and nanoparticles on turbulent heat transport: A conical diffuser scenario. J Energy Storage 2022;52:104703. [CrossRef]
[45] Miroshnichenko IV, Sheremet MA. Turbulent natural convection heat transfer in rectangular enclosures using experimental and numerical approaches: A review. Renew Sustain Energy Rev 2018;82:40–59. [CrossRef]
[46] Salhi H, Chafai N. Evaluation of the thermal conductivity of nanofluids using statistical analysis methods. Nanosci Technol Int J 2022;13:29–39. [CrossRef]
[47] Baiti A, Salhi H, Chafai N. Numerical investigation of turbulent mixed convection in a round bottom flask using a hybrid nanofluid. Adv Mech Eng 2023;15:16878132231195022. [CrossRef]
[48] Salhi H, Chafai N. Numerical simulation of heat transfer in a square cavity with a heater and cooler using hybrid nanofluid and random temperature. Nanosci Technol Int J 2023;14:47–59.
[49] Salhi H, Chafai N, Moussaoui I, Mahamdi A. Influence of hybrid nanofluids and source configuration on natural convection in square cavity. Nanosci Technol Int J 2024;15:35–47. [CrossRef]
[50] Dittus FW, Boelter LMK. Heat transfer in automobile radiators of the tubular type. Int Commun Heat Mass Transf 1985;12:3–22. [CrossRef]
[51] Gawande VB, Dhoble AS, Zodpe DB, Chamoli S. Experimental and CFD investigation of convection heat transfer in solar air heater with reverse L-shaped ribs. Sol Energy 2016;131:275–295. [CrossRef]
[52] Alqarni MS, Memon AA, Anwaar H, Usman, Muhammad T. The forced convection analysis of water alumina nanofluid flow through a 3D annulus with rotating cylinders via κ–ε turbulence model. Energies 2022;15:6730. [CrossRef]
[53] Grégoire G. Multiple linear regression. EAS Publ Ser 2014;66:45–72. [CrossRef]
[54] Jobson JD. Multiple linear regression. In: Applied multivariate data analysis: regression and experimental design. New York: Springer; 1991. p. 219–398. [CrossRef]
[55] Elhag SH, Memon AA, Memon MA, Bhatti K, Jacob K, Alzahrani S, et al. Analysis of forced convection with hybrid Cu-Al2O3 nanofluids injected in a three-dimensional rectangular channel containing three perpendicular rotating blocks with turbulent modeling. J Nanomater 2022;2022:2464191. [CrossRef]
[56] Taler D, Taler J. Simple heat transfer correlations for turbulent tube flow. E3S Web Conf 2017;13:02008. [CrossRef]

J Ther Eng, Vol. 12, No. 1, pp. 182−191, January, 2026

Journal of Thermal Engineering
Web page info: https://jten.yildiz.edu.tr
DOI: 10.14744/thermal.0001072

Research Article

Introducing an optimal pressure ratio for aircraft design and investigating the effect of nozzle efficiency on the jet engine's performance

Hadi SIYAHI[1,*], Mehdi SIYAHI[1], Mohsen FALLAH[2], Zahra MOHAMMADI[2]

[1]*Aeronautical Engineering Department, Istanbul Technical University, Turkey*
[2]*Mechanical Engineering Department, Azarbaijan Shahid Madani University, Tabriz, Iran*

ARTICLE INFO

Article history
Received: 5 October 2024
Revised: 12 January 2025
Accepted: 14 January 2025

Keywords:
Aircraft; Efficiency; Jet Engine; Nozzle Effect; Optimal Design Point; Propulsion

ABSTRACT

The aviation sector contributes substantially to global transportation energy use, underscoring the critical need for improving energy efficiency in propulsion systems. Conventional energy-based evaluations can sometimes yield misleading results; therefore, exergy-based analysis provides a more realistic understanding of how energy is utilized and degraded within such systems. In this study, a jet engine is analyzed using exergy efficiency as a principal criterion, with specific attention to the effects of compressor pressure ratio and flight altitude. The investigation identifies an optimal operating point that corresponds to the most effective pressure ratio, which also governs engine sizing. The point where the thrust and exergy efficiency curves intersect is proposed as the optimal design condition. Moreover, the role of nozzle efficiency is examined under a range of flight scenarios. The results indicate that at the optimal design points, specific fuel consumption can be reduced by as much as 22.27% at sea level and 13.43% at cruise altitude when compared to maximum thrust conditions. These design points feature lower compressor pressure ratios than those at maximum exergy efficiency, thus improving practical feasibility for real-world applications. Enhancing nozzle efficiency further improves overall engine performance. For instance, at cruise altitude, increasing flight velocity from 100 to 200 m/s and raising nozzle efficiency from 60% to 100% increases thrust by approximately 33–39% and exergy efficiency by 68–71%. At sea level, these improvements reach up to 41% and 73%, respectively. The findings offer valuable insights into achieving concurrent optimization of thrust and exergy efficiency, providing a practical framework for future propulsion and advanced energy system designs.

Cite this article as: Siyahi H, Siyahi M, Fallah M, Mohammadi Z. Introducing an optimal pressure ratio for aircraft design and investigating the effect of nozzle efficiency on the jet engine's performance. J Ther Eng 2026;12(1):182−191.

***Corresponding author.**
*E-mail address: siyahi16@itu.edu.tr

This paper was recommended for publication in revised form by Editor-in-Chief Ahmet Selim Dalkılıç

Published by Yıldız Technical University Press, İstanbul, Turkey
Yıldız Technical University. This is an open access article under the CC BY-NC license (http://creativecommons.org/licenses/by-nc/4.0/).

INTRODUCTION

The design of efficient aircraft engines is a cornerstone of modern aeronautical engineering, with compressor pressure ratio (CPR) playing a pivotal role in achieving optimal engine performance. A well-designed CPR significantly influences thermodynamic performance, fuel efficiency, and overall thrust generation. Traditional approaches to determine the optimal CPR primarily focus on thermodynamic cycles, such as the Brayton cycle, considering parameters like thermal efficiency and specific fuel consumption [1–3]. However, a growing body of literature suggests that an exergetic approach, which evaluates energy quality and irreversibilities, offers a more comprehensive understanding of engine performance [4–13].

Exergy analysis, unlike conventional energy analysis, accounts for the degradation of useful energy and provides a systematic method to assess efficiency improvements. Researchers have explored exergetic methodologies to optimize energy systems [14]. Others applied these principles to aircraft engines, demonstrating the effectiveness of exergy-based optimization in aviation [2,15–17].

Despite these advancements, the nozzle's contribution to jet engine performance, particularly in relation to exergetic efficiency, remains underexplored. Former studies have highlighted the critical role of nozzle efficiency in thrust generation. These works have shown that nozzle losses can significantly degrade overall engine performance, particularly in high-performance engines. However, there is limited integration of nozzle efficiency considerations into a holistic exergetic optimization framework.

Moreover, a significant gap in the literature lies in the simultaneous evaluation of thrust, exergy efficiency, and CPR optimization. While individual studies have addressed thrust or exergy efficiency independently, the coupling of these metrics for determining optimal CPR has received scant attention. This integrated approach is vital for developing design guidelines that balance thrust generation and exergy efficiency, thereby enhancing the performance and sustainability of jet engines.

This paper seeks to address this gap by developing a comprehensive framework that integrates thrust and exergy efficiency into optimizing CPR for aircraft engine design. The study highlights the interplay between CPR, nozzle efficiency, and exergetic performance, providing insights into achieving higher thermodynamic and operational efficiency. By bridging the gap between traditional thermodynamic metrics and exergy-based performance analysis, this work aims to establish a novel methodology for designing high-efficiency jet engines.

GOVERNING EQUATIONS

Energy can be explained as the summation of exergy and anergy [18–22]:

$$Energy = Exergy + Anergy \tag{1}$$

where exergy and anergy are maximum accessible work and non-accessible work, respectively.

The specific energy can be written as [18–22]:

$$e = h + \frac{V^2}{2} + gz \tag{2}$$

where h, $V^2/2$ and gz are specific enthalpy, kinetic and potential energy terms, respectively.

In the absence of the effects of nuclear, magnetic, electric, and surface tension fields, the specific exergy can be written as summation of physical, chemical, kinetic, potential, heat and work exergy terms [18–22]:

$$ex = ex_{ph} + ex_{ch} + ex_k + ex_p + ex_q + ex_w \tag{3}$$

where $ex_{ph} = (h-h_0) - T_0(s-s_0)$, $ex_{ch} = (\Delta h_{formation} - T_0\Delta s_{formation}) + T_0R\,\Sigma(y^i \ln y^i/y^i_0)$, $ex_k = v^2/2$, and $ex_p = gz$. Temperatures in these equations are in Kelvin. The exergy values of heat and work are $ex_q = \left(1 - \frac{T_0}{T}\right) q$ and $ex_w = w$, respectively, where temperatures in the ex_q equation are in Kelvin.

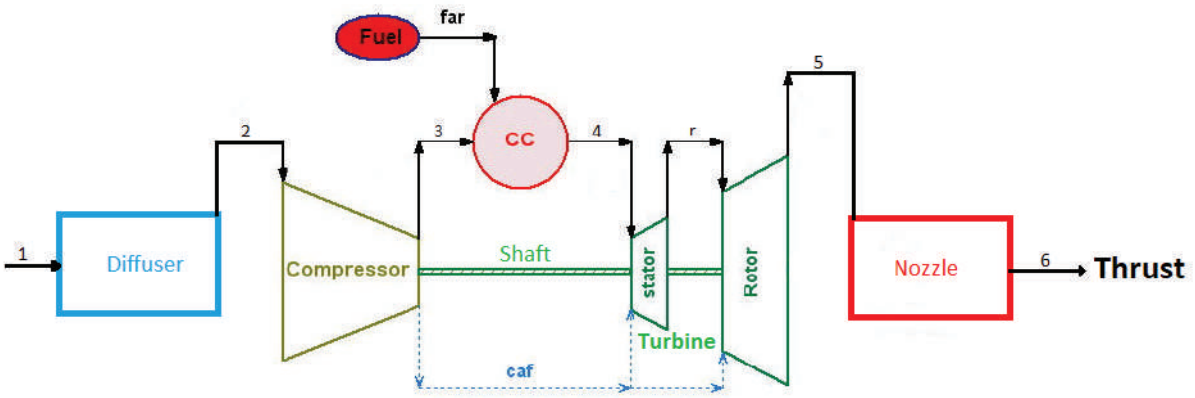

Figure 1. Schematic of a jet engine.

Noticing that 1, 2, 3, 4, 5 and 6 states in Figure 1 respectively introduce the diffuser inlet, compressor inlet (diffuser outlet), combustion chamber inlet (compressor outlet), turbine inlet (combustion chamber outlet), nozzle inlet (turbine outlet) and exhaust (nozzle outlet), all equations required for the energy-exergy analyses and thermodynamic optimization of jet engine have been summarized in Table 1 [18–29].

RESULTS AND DISCUSSION

Validation

An engineering equation solver (EES) program has been written for an open simple gas turbine cycle with methane (CH4) as a fuel and results have been compared with reference study [30].

The related equations have been written for the compressor, combustion chamber and turbine, and results have

Table 1. Thermodynamics equations for energy-exergy analyses [18–29]

Components	Related equations
Diffuser	$\dot{m}_2 = \dot{m}_1$ $\dot{m}_2\left(h_2 + \frac{v_2^2}{2}\right) = \dot{m}_1\left(h_1 + \frac{v_1^2}{2}\right), v_1 = v_{inlet}, v_2 = 0$ $\eta_{I,diff,isen} = \frac{\left(\dot{m}_2 h_{2,isen} - \dot{m}_1 h_1\right)}{\left(\dot{m}_2 h_2 - \dot{m}_1 h_1\right)}, P_2 = P_{2,isen}$ $\dot{E}x_{D,diff} = \dot{m}_1 ex_1 - \dot{m}_2 ex_2$ $\eta_{II,diff} = \frac{\dot{m}_2 ex_2}{\dot{m}_1 ex_1}$
Compressor	$\dot{m}_3 = (1 - caf)\dot{m}_2$ $\dot{W}_{comp} = \dot{m}_2(e_3 - e_2)$ $\eta_{I,comp,poly} = \frac{\bar{R}T\frac{dp}{p}}{\bar{C}_{p,air}dT}$ $\dot{E}x_{D,comp} = \dot{W}_{comp} + \dot{m}_2(ex_2 - ex_3)$ $\eta_{II,comp} = \frac{\left(\dot{W}_{comp} - \dot{E}x_{D,comp}\right)}{\dot{W}_{comp}}$
Cooling air fraction	$T_r = 0.8451(TIT) + 136.2, T_r and\ TIT\ are\ in$ ℃ $caf = \frac{2(1 + far)(e_4 - e_r)}{(2e_4 - e_3 - e_r)}$ $\dot{m}_{caf} = (caf)\dot{m}_1$
Combustion chamber	$\dot{m}_4 = \dot{m}_3 + \dot{m}_{fuel}, \dot{m}_{fuel} = (far)\dot{m}_1$ $\int_{298.15}^{T_f} \bar{C}_{p,C_nH_m}dT + \lambda\left(n + \frac{m}{4}\right)\left[\int_{298.15}^{T_3} \bar{C}_{p,O_2}dT + 3.76\int_{298.15}^{T_3} \bar{C}_{p,N_2}dT\right.$ $\left. + 4.76\bar{\omega}_1\int_{298.15}^{TIT} \bar{C}_{p,H_2O}dT\right] = n\int_{298.15}^{TIT} \bar{C}_{p,CO_2}dT + (\lambda - 1)\left(n + \frac{m}{4}\right)\int_{298.15}^{TIT} \bar{C}_{p,O_2}dT$ $+ 3.76\lambda\left(n + \frac{m}{4}\right)\int_{298.15}^{TIT} \bar{C}_{p,N_2}dT + \left[\lambda\left(n + \frac{m}{4}\right)4.76\bar{\omega}_1 + \frac{m}{2}\right]\int_{298.15}^{TIT} \bar{C}_{p,H_2O}dT$ $far = \frac{M_{C_nH_m}}{\lambda\left(n + \frac{m}{4}\right)4.76(1 + \bar{\omega}_1)M_{air}\eta_{I,cc}}(1 - caf)$ $\dot{m}_3 e_3 + \dot{m}_{fuel}e_{fuel} = \dot{m}_4 e_4$ $\eta_{I,cc} = \frac{far_{ideal}}{far}$ $\dot{E}x_{D,cc} = \dot{m}_3 ex_3 + \dot{m}_{fuel}ex_{fuel} - \dot{m}_4 ex_4$ $\eta_{II,cc} = \frac{\dot{m}_4 ex_4}{\dot{m}_3 ex_3 + \dot{m}_{fuel}ex_{fuel}}$

Table 1. Thermodynamics equations for energy-exergy analyses [18–29] (continued)

Components	Related equations
Turbine	$\dot{m}_5 = (1 + far)\dot{m}_1$ $\dot{W}_{turb} = \dot{W}_{comp}$ $\dot{W}_{turb} = \dot{m}_{caf} e_3 + \dot{m}_4 e_4 - \dot{m}_5 e_5$ $\eta_{I,turb,poly} = \frac{\bar{C}_{p,g} dT}{\bar{R}T \frac{dp}{p}}$ $\dot{E}x_{D,turb} = \dot{m}_{caf} ex_3 + \dot{m}_4 ex_4 - \dot{m}_5 ex_5 - \dot{W}_{turb}$ $\eta_{II,turb} = \frac{\dot{W}_{turb}}{\left(\dot{W}_{turb} + \dot{E}x_{D,turb}\right)}$
Nozzle	$\dot{m}_6 = \dot{m}_5$ $\dot{m}_6\left(h_6 + \frac{v_6^2}{2}\right) = \dot{m}_5\left(h_5 + \frac{v_5^2}{2}\right), v_5 = 0, P_6 = P_0$ $\eta_{I,nozz,isen} = \frac{(\dot{m}_6 h_6 - \dot{m}_5 h_5)}{(\dot{m}_6 h_{6,,isen} - \dot{m}_5 h_5)}, P_6 = P_{6,isen}$ $\dot{E}x_{D,nozz} = \dot{m}_5 ex_5 - \dot{m}_6 ex_6$ $\eta_{II,nozz} = \frac{\dot{m}_6 ex_6}{\dot{m}_5 ex_5}$
Cycle	$\dot{Thrust} = \dot{m}_6(V_6 - V_1)$ $\eta_{I,cycle} = \frac{\dot{m}_6\left(\frac{v_6^2}{2} - \frac{v_1^2}{2}\right)}{\dot{m}_{fuel} LHV}$ $\dot{E}x_{D,cycle} = \dot{E}x_{D,diff} + \dot{E}x_{D,comp} + \dot{E}x_{D,cc} + \dot{E}x_{D,turb} + \dot{E}x_{D,nozz}$ $\eta_{II,cycle} = \frac{\dot{m}_6\left(\frac{v_6^2}{2} - \frac{v_1^2}{2}\right)}{\dot{m}_1 ex_1 + \dot{m}_{fuel} ex_{fuel}}$

been revealed through the calculations of compressor outlet temperature (COT), turbine inlet temperature (TIT), and turbine outlet temperature (TOT) via EES program. Analysis indicates that the data differ by no more than 3.5%, which falls within an acceptable margin for this type of parametric evaluation (Table 2).

Table 2. The Validation of EES Program's Data for Simple Gas Turbine Cycle vs. Reference [30]

Variables	Reference	Present study	Deviation
T_0	15 °C	15 °C	0.0%
P_0	101 kPa	101 kPa	0.0%
RH_0	60%	60%	0.0%
$r_{p,comp}$	20	20	0.0%
$\eta_{I,comp,poly}$	92%	92%	0.0%
COT	449.6 °C	438.6 °C	2.4%
$\eta_{I,cc}$	100%	100%	0.0%
TIT	1331.3 °C	1330 °C	0.1%
$\eta_{I,turb,poly}$	86%	89%	3.5%
TOT	620 °C	617.1 °C	0.5%

Jet engine

The jet engine performance was analyzed under steady-state steady-flow (SSSF) conditions using a two-stage turbine with blade cooling [29]. Dodecane ($C_{12}H_{26}$) was selected as the fuel, and the energy efficiencies of the diffuser, compressor, combustion chamber, turbine, and nozzle were assumed to be 90%, 95%, 100%, 92%, and 90%, respectively. The combustion process was modeled as an isobaric reaction with a constant turbine inlet temperature of 1200°C across all cases. Parametric studies were conducted at sea level (T_0 = 25°C, P_0 = 101.325 kPa, RH_0 = 30%) and cruise altitude (T_0 = −56.5°C, P_0 = 22.6 kPa, RH_0 = 0%). Key performance indicators, including thrust, exergy destruction, energy efficiency, and exergy efficiency, were evaluated across various compressor pressure ratios. It is important to note that all results are expressed on a mass basis (per 1 kg of inlet air) rather than on a volumetric basis (per 1 m^3 of inlet air).

The results indicate that maximum thrust is achieved within a low CPR range of 15 to 25 across all scenarios. At cruise conditions, higher thrust levels are observed, though less thrust is required as flight speed increases to maintain

steady flight. Exergy destruction shows a consistent decline with increasing CPR, as illustrated in Figure 2.

Energy and exergy efficiencies exhibit distinct patterns. At sea level, these efficiencies peak at CPR values of 50 to 60, whereas at cruise altitude, optimal efficiencies are reached at CPR values exceeding 100 (Figure 3).

Additionally, the cooling air fraction (caf) and fuel-air ratio (far) respond to changes in CPR and altitude. The far increases with altitude due to lower ambient temperatures, which require higher fuel input to sustain TIT, while caf decreases as inlet air cooling capacity improves (Figure 4).

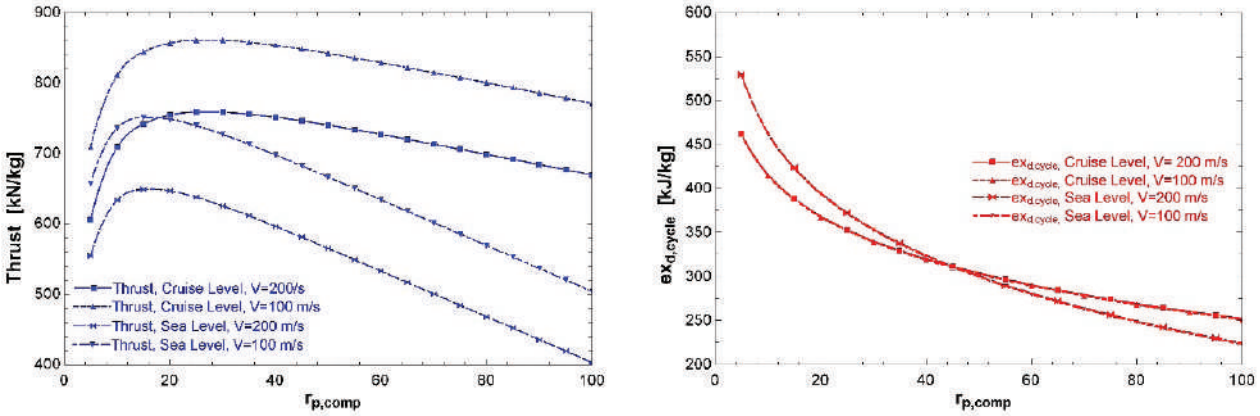

Figure 2. Thrust production and exergy destruction of jet engine at different flight scenarios.

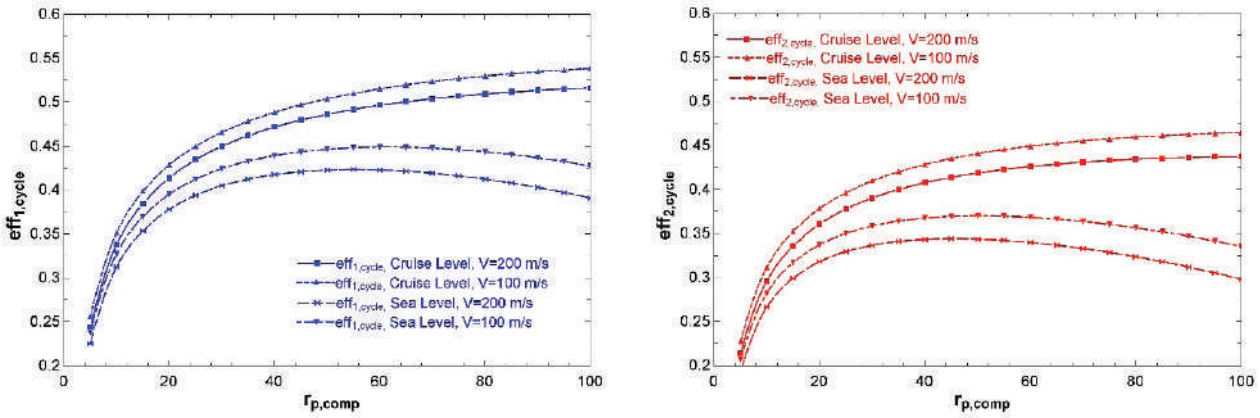

Figure 3. Energy and exergy efficiency of jet engine at different flight scenarios.

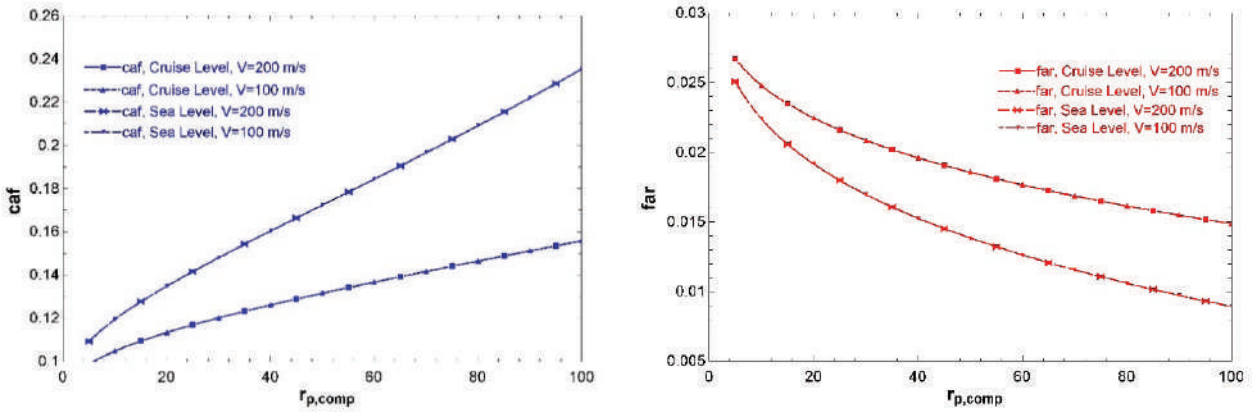

Figure 4. Cooling air fraction and fuel air ratio of jet engine at different flight scenarios.

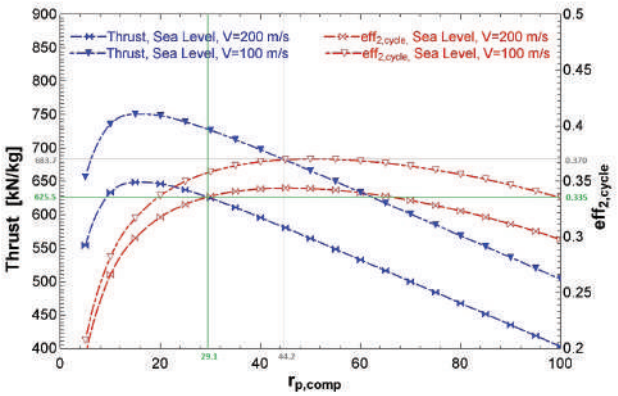

Figure 5. Max simultaneous thrust- exergy efficiency as an operating design point at sea level

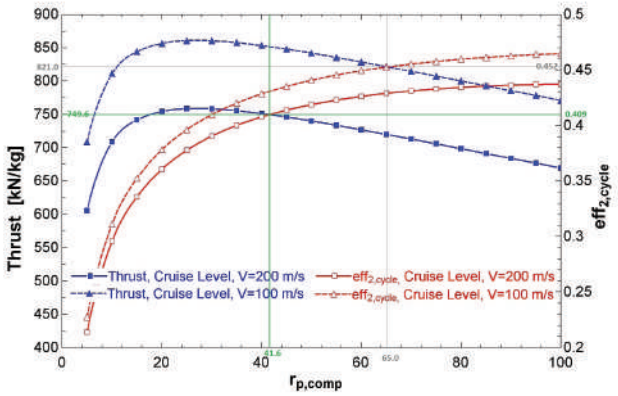

Figure 6. Max simultaneous thrust- exergy efficiency as an operating design point at cruise level

Table 3. Design point's pressure ratios for different flight scenarios

Flight Scenario	$r_{p,comp}$
Sea level, V=100 m/s	44.2
Sea level, V=200 m/s	29.1
Cruise level, V=100 m/s	65.0
Cruise level, V=200 m/s	41.6

The intersection of thrust and exergy efficiency curves, identified as the optimal design point, marks the CPR where simultaneous maximization of these parameters occurs. Figures 5 and 6 highlight this phenomenon, with the corresponding CPR values summarized in Table 3. These optimal CPR values exhibit a direct correlation with altitude and an inverse correlation with flight speed.

All performance parameters of the jet engine at design points have been plotted in the bar diagram of Figure 7. As can be seen in this diagram, while exergy destruction is increased thrust, energy efficiency, and exergy efficiency of jet engine are decreased with speeding of an aircraft. Moreover, all performance parameters of jet engine are upgraded with rising altitude.

As illustrated in Figure 8, the specific fuel consumption (SFC) at the optimal design points decreases by 22.27% to 14.44% at sea flight level and by 13.43% to 5.15% at cruise flight level, compared to the SFC at maximum thrust conditions for velocities of 100 m/s and 200 m/s, respectively. Furthermore, Figures 5 and 6 indicate that the optimal design points exhibit significantly lower compressor pressure ratios compared to the points with maximum exergy efficiency. The reduced SFC and pressure ratio at the optimal points, alongside simultaneous maximization of thrust

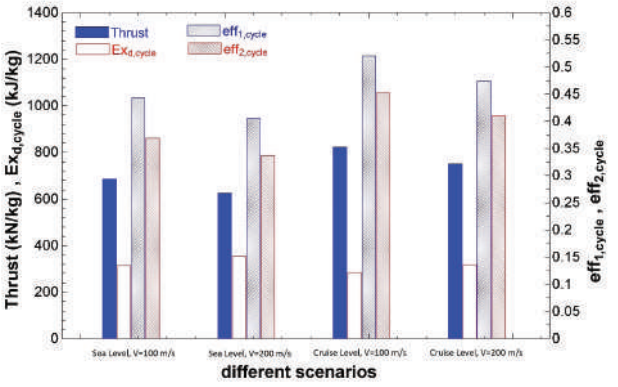

Figure 7. Performance parameters of jet engine at design point for different flight scenarios.

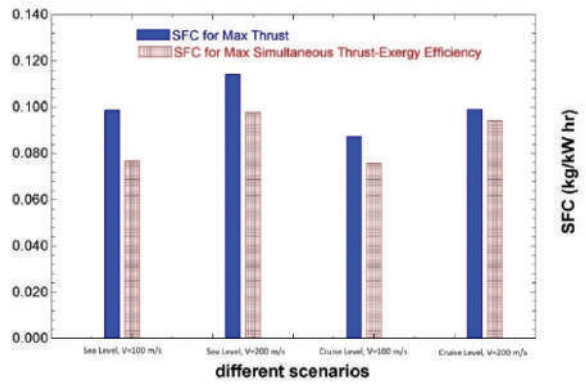

Figure 8. Comparison of specific fuel consumption at max thrust and optimal design point for different flight scenarios.

and exergy efficiency, makes these points highly favorable from a practical design perspective.

Eventually, the effect of nozzle energy efficiency is investigated on the jet engine's performance, revealing changes of the most critical design parameters of thrust and exergy efficiency at previously mentioned operating design conditions.

As disclose in Figure 9, at sea level, by increasing the efficiency of nozzle from 60 to 100% the thrust is increased from 540.7 to 727.4 kN/kg , and the exergy efficiency of engine boosts from 24.4% to 41.1%, for the speed of V = 100 m/s. These values for the speed of V = 200 m/s are 473.2 to 670.1 kN/kg thrust increase, and 21.7% to 37.7% exergy efficiency boost. At cruise level, for the same nozzle efficiency improvement in Figure 10, the similar values at cruise level are 652.3 to 871.7 kN/kg and 578.2 to 805.9 kN/kg increase in thrust, with 30.0% to 50.4% and 26.3% to 45.1% boost in exergy efficiency, for the speeds of V = 100 m/s and V = 200 m/s, respectively.

As shown in Table 4, the performance improvement of a jet engine with increasing nozzle efficiency is even greater for sea level flight altitude at the optimal design points.

Jet engine performance is significantly influenced by the pressure ratio and nozzle efficiency, as they determine the thrust and efficiency of the engine. Meanwhile, there are the limitations of each. Higher pressure ratios lead to higher temperatures in the combustion chamber and turbine. These temperatures can exceed material limits, requiring advanced cooling techniques or high-temperature materials. As the pressure ratio increases, the compressor stages require higher efficiency. Beyond a certain point, increasing pressure ratio results in diminishing returns due to inefficiencies, such as mechanical losses and flow separation. High pressure ratios can increase the risk of compressor stall or surge, especially at off-design conditions, reducing operational reliability. Higher pressure ratios demand more work from the turbine to drive the compressor, which can limit the available for thrust generation. Increasing the pressure ratio typically requires more compressor stages, which adds weight and mechanical complexity to the engine. Very high-pressure ratios might not match the ideal cycle conditions for specific flight regimes, such as low-speed or high-altitude operations. On the other hand, low nozzle efficiency results in incomplete conversion of thermal and pressure energy into kinetic energy, reducing thrust output. At off-design conditions, such as low-speed or high-altitude operation, flow separation within the nozzle can reduce efficiency and stability. In supersonic nozzles, imperfect expansion due to mismatched atmospheric pressure can lead to shock waves, causing energy losses and efficiency reduction. At varying altitudes, the nozzle may be under-expanded (not fully converting pressure) or over-expanded (causing shocks and flow separation), limiting efficiency. If the nozzle material is not adequately insulated, heat losses can occur, slightly reducing the energy available for thrust. Designing a nozzle optimized for multiple flight regimes (subsonic, transonic, supersonic) is challenging. Fixed geometry nozzles may perform sub-optimally in some conditions, while variable

Table 4. Design point's thrust and overall exergy efficiency improvements by increasing nozzle energy efficiency from 60% to 100% for different flight scenarios

Flight Scenario	Improvement	
	Thrust	$\eta_{II,cycle}$
Sea level, V=100 m/s	34.5%	68.4%
Sea level, V=200 m/s	41.6%	73.7%
Cruise level, V=100 m/s	33.6%	68.0%
Cruise level, V=200 m/s	39.3%	71.4%

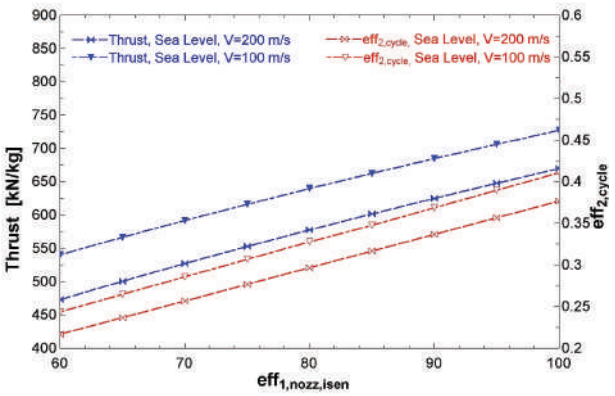

Figure 9. Improvement of jet engine performance operating in optimal design condition by increasing nozzle efficiency at sea level

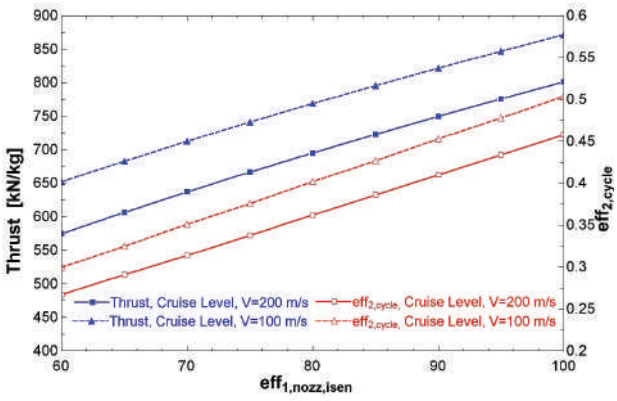

Figure 10. Improvement of jet engine performance operating in optimal design condition by increasing nozzle efficiency at cruise level

geometry nozzles add weight and mechanical complexity. Considering the combined impact on performance, a proper high-pressure ratio and efficient nozzle are essential for maximizing thrust and minimizing SFC. Limitations in either reduce overall engine performance. Higher pressure ratios improve efficiency, but this is only beneficial if the nozzle effectively converts the energy into thrust. By balancing these limitations, the design of jet engines should meet the specific performance requirements for different aircraft types and missions.

The analysis of the present research underscores the critical role of optimal CPR and nozzle efficiency in enhancing jet engine performance at different flight scenarios. Achieving maximum simultaneous thrust and exergy efficiency at practical design points provides significant operational benefits, including reduced SFC and improved sustainability.

CONCLUSION

This study provides a comprehensive investigation into the optimization of jet engine performance using an energy-exergy analysis framework. By introducing the concept of the optimal design point as the optimum compressor pressure ratio of the intersection of thrust and exergy efficiency curves, a novel methodology for jet engine design optimization is proposed. This approach considers variations in compressor pressure ratio (CPR), flight altitude, and nozzle efficiency.

The findings demonstrate that the optimal design points significantly enhance the practical viability of engine operation. At sea level, the specific fuel consumption (SFC) at the optimal conditions is reduced by up to 22.27%, while at cruise altitudes, it decreases by 13.43%, compared to maximum thrust conditions. These results emphasize the importance of balancing thrust and exergy efficiency for achieving sustainable and efficient engine designs. Furthermore, the study reveals that the optimal CPR is lower than CPR value at maximum exergy efficiency, making the design both practical and efficient for real-world applications.

A critical aspect of this research is the impact of nozzle efficiency on engine performance. Enhancing nozzle efficiency from 60% to 100% leads to substantial improvements in thrust and exergy efficiency under optimal design conditions. At sea level, thrust increases by up to 41%, while exergy efficiency improves by 73%. Similarly, at cruise altitude, these parameters are enhanced by up to 39% and 71%, respectively. These improvements highlight the vital role of nozzle efficiency in maximizing engine performance and reducing environmental impact.

The study also addresses the limitations of high-pressure ratios and nozzle inefficiencies, including mechanical complexities, material constraints, and off-design performance challenges. By integrating these considerations into the optimization framework, the research offers valuable insights into the design trade-offs required for efficient propulsion systems.

In summary, this research bridges the gap between traditional thermodynamic approaches and exergy-based methodologies, offering a robust framework for the future design and optimization of jet engines. The results provide actionable guidance for achieving higher efficiency, reduced fuel consumption, and improved sustainability in aviation propulsion systems, setting a benchmark for innovative and environmentally conscious aerospace engineering solutions.

NOMENCLATURE

e	Specific energy, kJ / kg
eff	Dimensionless efficiency
ex	Specific exergy, kJ / kg
g	Gravitational acceleration constant, m / s^2
M	Molar mass, kg / kmole
$Mach$	Dimensionless mach number
$\dot{m}$	Mass flow rate, kg / s
P	Pressure, Pa
q	Specific heat rate, kJ / kg
r_p	Dimensionless pressure ratio
s	Specific entropy, kJ / kg
t	Time, s
T	Temperature, °C
V	Velocity, m / s
w	Specific work rate, kJ / kg

Greek symbols

λ	Dimensionless excess air
η	Dimensionless efficiency

Subscripts

1 *or I*	First law or energetic
2 *or II*	Second law or exergetic
0	Ambient condition
cc	Combustion chamber
ch	Chemical
comp	Compressor
D	Destruction
diff	Diffuser
isen	Isentropic
k	Kinetic
nozz	Nozzle
p	Potential
ph	Physical
poly	Polytropic
q	Heat
r	Rotator
turb	Turbine
w	Work

Abbreviations

caf	Cooling air fraction
COT	Compressor outlet temperature

CPR	Compressor pressure ratio
far	Fuel air ratio
RH	Relative humidity
SFC	Specific fuel consumption
SSSF	Steady state steady flow
TIT	Turbine inlet temperature
TOT	Turbine outlet temperature

AUTHORSHIP CONTRIBUTIONS

Authors equally contributed to this work.

DATA AVAILABILITY STATEMENT

The authors confirm that the data that supports the findings of this study are available within the article. Raw data that support the finding of this study are available from the corresponding author, upon reasonable request.

CONFLICT OF INTEREST

The author declared no potential conflicts of interest with respect to the research, authorship, and/or publication of this article.

ETHICS

There are no ethical issues with the publication of this manuscript.

STATEMENT ON THE USE OF ARTIFICIAL INTELLIGENCE

Artificial intelligence was not used in the preparation of the article.

REFERENCES

[1] Durmus S, Akyuz MK. Effect of compression ratio and turbine inlet temperature on turboprop engine performance. IENSC 2020;299–307.

[2] Ekrataleshian A, Pourfayaz F, Ahmadi MH. Thermodynamic and thermoeconomic analyses and energetic and exergetic optimization of a turbojet engine. J Therm Anal Calorim 2021;145:909–923. [CrossRef]

[3] Raji NA, Kuku RO, Openibo AO, Owolabi EA. Influence of compression ratio on the performance characteristics of a spark ignition engine. J Prod Eng 2024:27;5–12. [CrossRef]

[4] Tsatsaronis G. Strengths and limitations of exergy analysis. Thermodynamic optimization of complex energy systems. Springer 1999;93–100. [CrossRef]

[5] Bejan A, Siems DL. The need for exergy analysis and thermodynamic optimization in aircraft development. Exergy, An International Journal 2001;1:14–24. [CrossRef]

[6] Paulus Jr DM, Gaggioli RA. The exergy of lift, and aircraft exergy flow diagrams. ASME International Mechanical Engineering Congress and Exposition 2001;35524:365–9. [CrossRef]

[7] Rosen MA, Etele J. Aerospace systems and exergy analysis: applications and methodology development needs. Int J Exergy 2004;1:411–25. [CrossRef]

[8] Riggins DW, Taylor T, Moorhouse DJ. Methodology for performance analysis of aerospace vehicles using the laws of thermodynamics. J Aircr 2006;43:953–63. [CrossRef]

[9] Dong Z, Li D, Wang Z, Sun M. A review on exergy analysis of aerospace power systems. Acta Astronaut 2018;152:486–95. [CrossRef]

[10] Sohret Y. Exergo-sustainability analysis and ecological function of a simple gas turbine aero-engine. J Therm Eng 2018;4:2083–95. [CrossRef]

[11] Ball O. Performance assessment of a medium-scale turboprop engine designed for unmanned aerial vehicle (UAV) based on exergetic and sustainability metrics. J Therm Eng 2020;6:697–711. [CrossRef]

[12] Reddy PN. Energy and exergy analyses of a two-stage organic rankine cycle with low pressure stage regeneration for IC engine waste heat recovery. J Therm Eng 2021;8:573–86. [CrossRef]

[13] Khan MN. Combined effect of variable parameters on the performance of gas turbine cycles. J Therm Eng 2021;7:1768–83. [CrossRef]

[14] James C, Kim TY, Jane R. A review of exergy based optimization and control. Processes 2020;8:364. [CrossRef]

[15] Rancruel DF, von Spakovsky MR. Decomposition with thermoeconomic isolation applied to the optimal synthesis/design and operation of an advanced tactical aircraft system. Energy 2006;31:3327–41. [CrossRef]

[16] Aygun H. Optimization of energy and exergy parameters for a conceptual after burning turbojet engine. J Therm Eng 2021;9:69–85. [CrossRef]

[17] Aygun H, Kirmizi M, Kilic U, Turan O. Multi-objective optimization of a small turbojet engine energetic performance. Energy 2023;271:126983. [CrossRef]

[18] Borgnakke C, Sonntag RE. Fundamentals of thermodynamics. John Wiley & Sons; 2020.

[19] Annamalai K, Puri IK, Jog MA. Advanced thermodynamics engineering. CRC press; 2011.

[20] Winterbone D, Turan A. Advanced thermodynamics for engineers. Butterworth-Heinemann; 2015.

[21] Bejan A. Advanced engineering thermodynamics. John Wiley & Sons; 2016.

[22] Tabatabaian M, Rajput RK. Advanced thermodynamics: fundamentals, mathematics, applications. De Gruyter. [CrossRef]

[23] Oates GC. Aerothermodynamics of gas turbine and rocket propulsion. Aiaa 1997. [CrossRef]

[24] Mattingly JD. Elements of propulsion: gas turbines and rockets. American Institute of Aeronautics and Astronautics; 2006.
[25] MacIsaac B, Langton R, Belobaba P, Cooper J, Seabridge A. Gas turbine propulsion systems. John Wiley & Sons 2011. [CrossRef]
[26] El-Sayed AF. Fundamentals of aircraft and rocket propulsion. Springer 2016. [CrossRef]
[27] El-Sayed AF. Aircraft propulsion and gas turbine engines. CRC press; 2017.
[28] Siyahi M, Siyahi H, Fallah M, Mohammadi Z. Thermodynamic Optimization and Energy-Exergy Analyses of the Turboshaft Helicopter Engine. Int J Thermodyn 2024:1–11. [CrossRef]
[29] Fallah M, Siyahi H, Ghiasi RA, Mahmoudi SMS, Yari M, Rosen MA. Comparison of different gas turbine cycles and advanced exergy analysis of the most effective. Energy 2016;116:701–15. [CrossRef]
[30] Pathirathna KAB. Gas turbine thermodynamic and performance analysis methods using available catalog data 2013.

J Ther Eng, Vol. 12, No. 1, pp. 192−211, January, 2026

Journal of Thermal Engineering
Web page info: https://jten.yildiz.edu.tr
DOI: 10.14744/thermal.0001073

Research Article

Exergy, energy, exergoenvironmental assessment of a novel combined helium Brayton cycle and transcritical CO_2 cycle for solar power tower applications

Yunis KHAN[1,*], Deepak SINGH[2], Shailendra SINHA[3], K.S. BHOLE[2], D. APPARAO[4]

[1]Department of Mechanical Engineering, Indian Institute of Technology, (ISM), Jharkhand, 826004, India
[2]Department of Mechanical Engineering, Sardar Patel College of Engineering, Andheri-west, Mumbai, Maharashtra, 400058 India
[3]Department of Mechanical Engineering, Institute of Engineering & Technology, Lucknow, Uttar Pradesh, 226021, India
[4]Department of Mechanical Engineering, Aditya Institute of Technology and Management, Andhra Pradesh, 532201, India

ARTICLE INFO

Article history
Received: 29 July 2024
Accepted: 22 October 2024

Keywords:
Energy Analysis; Exergy Analysis; Exergoenvironmental Analysis; Helium Brayton Cycle; Parametric Analysis; Performance Comparison; Solar Power Tower; TCO_2 Cycle

ABSTRACT

This study introduces a combined cycle that captures solar energy from a solar power tower for power generation. The system couples a helium-based Brayton cycle (topping cycle) with a transcritical carbon dioxide cycle (bottoming cycle), where the latter recovers and uses the waste heat released from the Brayton process. A detailed investigation was carried out, incorporating energy, exergy, and exergoenvironmental evaluations, to assess the overall performance of the combined power plant. The findings demonstrated a significant improvement of 12.05% in the energy efficiency of the helium-based Brayton cycle when the transcritical carbon dioxide cycle was incorporated as a bottoming configuration. The plant's optimal operating parameters were identified, giving peak values of 23.2% for energy efficiency, 24.83% for exergy efficiency, and 14,930 kW for power output. A detailed examination of the solar subsystem components (receiver and heliostats) revealed the maximum exergy destruction occurs in these parts of the solar plant, totalling around 37,578 kW. The total exergy destruction across the plant was calculated to be 45,164 kW. The exergoenvironmental impact coefficient exhibited a substantial value of 4.028, primarily attributed to the lower exergy efficiency of the plant. Additionally, the energetic stability factor was found to be 0.2483. This research contributes to solar power tower integration, enhancing efficiency, and achieving a simplified system with fewer components compared to previous studies.

Cite this article as: Khan Y, Singh D, Sinha S, Bholeks KS, Apparao D. Exergy, energy, exergoenvironmental assessment of a novel combined helium Brayton cycle and transcritical CO_2 cycle for solar power tower applications. J Ther Eng 2026;12(1):192−211.

INTRODUCTION

The global energy demand grew by 2.2% in 2023, with emerging markets expected to drive further acceleration to 3.4% during the 2024-2026 period, despite the ongoing effects of the energy crisis and economic challenges, emphasizing the urgent need for secure and sustainable energy

***Corresponding author.**
*E-mail address: yuniskhan21@gmail.com

This paper was recommended for publication in revised form by Regional Editor Ahmet selim Dalklic

Published by Yıldız Technical University Press, İstanbul, Turkey
Yıldız Technical University. This is an open access article under the CC BY-NC license (http://creativecommons.org/licenses/by-nc/4.0/).

solutions [1,2]. Rising environmental challenges associated with greenhouse gas emissions, coupled with the progressive depletion of fossil fuel resources, have intensified the emphasis on sustainable energy alternatives, with particular attention directed toward the solar energy sector [3,4]. In response to the adverse environmental impacts of traditional energy sources, recent research has emphasized the development of clean and renewable technologies to reduce carbon footprints and mitigate climate change [5,6]. Solar energy, known as the most abundant renewable resource, is considered a reliable alternative to conventional energy, and its wide use is important to reduce global warming, cut fossil fuel dependence, and meet the rising demand for electricity [7]. According to recent studies, solar energy is widely used in everything from multi-generation systems that supply water, heating, cooling, and electricity to its integration with cutting-edge cycles that enhance energy efficiency and promote environmental sustainability [8–10].

To harness solar energy for electricity generation, two key technologies are used: Photovoltaic (PV) plants and concentrating solar power (CSP). CSP systems convert solar radiation into thermal energy, which is then used to drive thermodynamic cycles [11]. Using specialized mirror configurations or reflectors, CSP systems which are regarded as one of the most sustainable energy solutions achieve temperatures between 150 °C and 1500 °C. The power generation industry has shown a great deal of interest in these systems due to their increased cycle efficiency and capacity to produce high temperatures [12]. Recent studies indicate that among various CSP technologies, solar power tower (SPT) plants are advancing at a faster pace and gaining more attention than other CSP options [13]. In these plants, solar radiation is directed toward a central receiver by means of massive arrays of flat mirrors called heliostats. The heat transfer fluid (HTF) then gathers the thermal energy that has been absorbed. Because of their superior concentration ratios, solar power tower (SPT) systems can achieve temperatures up to 1500°C, which is significantly higher than parabolic trough collectors. Furthermore, the high source temperatures achieved enable these systems to function in hybrid configurations by coupling with the traditional fossil fuel plants, such as coal-fired Rankine cycles, thereby enhancing overall power generation efficiency.[14]. While solar power towers are capable of supporting thermodynamic cycles that operate within the elevated temperature range of 800 °C to 1200 °C, limited research has been conducted on their direct application for converting such high-temperature energy into electricity. The integration of solar power to with various thermodynamic cycles has garnered significant research attention over the past decade, focusing on operational features such as heliostat field configurations, different receiver types, power production systems, and HTF, with the aim of proposing and evaluating innovative power-generating units to achieve higher efficiency and develop a carbon-free energy system [15-18].

Depending on the heat source and operating temperature, solar power tower (SPT) plants can use either closed Brayton cycles or traditional Rankine cycles to convert thermal energy into electrical power. The supercritical carbon dioxide (sCO_2) Brayton cycle has garnered a lot of attention lately due to its advantageous characteristics, which include a critical temperature of nearly 31°C and a critical pressure of about 7,400 kPa. sCO_2 technology is very promising for effectively producing electricity from high-temperature heat sources because of its advantageous thermo-physical characteristics, compact design, and high efficiency. This allows for a low compression pressure ratio, which raises net output work [19]. Because of its chemical stability, non-flammability, affordability, non-toxicity, and environmental safety, the sCO_2 cycle is a great substitute. Instead of using a pump to keep the working fluid in a supercritical state, the supercritical Brayton cycle uses a compressor. Because of its high density, sCO_2 is especially appealing for waste heat recovery, enabling the design of compact turbo-machinery. Because of their increased effectiveness in high-temperature waste heat recovery applications, both transcritical and supercritical CO_2 cycles are becoming more and more popular [20]. Li et al. [21] provided a comprehensive classification of supercritical carbon dioxide (sCO_2) systems and emphasized their benefits in both nuclear and solar power applications. Gkountas et al. [22] used AlO_3 nanofluid to study heat transfer enhancement and discovered that adding printed circuit heat exchangers to sCO_2 systems reduced the pressure drop by 14% and exchanger length by 0.9%. Stainless steel works well up to 650 °C, while nickel-based alloys are better at higher temperatures, according to Chai and Tassuo's [23] evaluation of heat exchanger behavior in helium and sCO_2 Brayton cycles. After modeling five distinct sCO_2 cycle configurations for solar power tower (SPT) systems, Al-Sulaiman and Atif [24] found that the recompression cycle was the most effective, achieving 52% efficiency. To further improve the SPT system's performance, the same researchers optimized the heliostat field layout in subsequent work [25].

In hybrid heat source systems, stand et al. [26] examined the integration of an sCO_2 cycle with an organic Rankine cycle (ORC) in a hybrid solar power tower (SPT) plant, achieving a second law efficiency of 26.6%. With a product cost rate of $0.71/s, Hashemian and Noorpoor's [27] biomass–solar powered multi-generation system improved energy efficiency from 14% to 16.53% after optimization. With a 14.46% exergy efficiency, Zainul et al. [28] created a hybrid system for coastal applications that combines solar, wind, and ocean thermal energy. The application of NSGA-II optimization improved overall performance while reducing environmental impacts. Yang et al. [29] examined a biomass-solar system, emphasizing enhancements in solar collector and absorption chiller efficiency while minimizing environmental impact through ICE and gasifier optimization. Through the use of NSGA-II, Rahimimotlagh and Ahmadi [30] combined solar dish collectors with

compressed air storage and absorption chillers, resulting in a round-trip efficiency of 62.69% and an annual reduction of 3,810 tons of CO_2 emissions. Using a two-stage ORC, Qi et al. [31] stabilized biomass-solar energy while identifying important evaporator and condenser upgrades to increase energy efficiency and lessen environmental impact. Zhou et al. [32] combined organic Rankine, ejector refrigeration, and organic flash cycles into a solar desalination system, producing 5.89 kg/h of freshwater, 143.4 kW of net power, and approximately 66.85 kW of cooling capacity. The total energy destruction was reported to be 892.8 kW. By maximizing condenser costs and environmental performance, Cavalcanti [33] assessed a cogenerative system and demonstrated a 4.2% increase in electricity production. Su et al. [34] optimized a multistage Brayton cycle for solar power, boosting exergy efficiency to 25.92% and lowering electricity costs while promoting sustainability goals. Helium was determined to be the best option by Javanshir et al. [26], who evaluated the thermodynamic performance of basic and regenerative Brayton cycles for SPT plants using a variety of working fluids. By creating a triple-coupled cycle that combines an air Brayton cycle, an ORC, and SRC for SPT applications, Sachdeva and Singh [15] were able to reach a maximum efficiency of 33.15%. In their comparison of CO2-based binary mixtures, Guo et al. [35] discovered that the CO2/Xenon intercooling cycle performed better than sCO2 with an exergy efficiency that was 1.32% higher. Trevisan et al. [36] addressed the temperature limitations of a recompression sCO_2 cycle by using air as the heat transfer fluid, which led to a levelized cost of electricity (LCOE) of 100 $/MWh. Niu et al. [37] found the CO2-propane mixture performs best at high ambient temperatures in an SBC-based SPT. Wan et al. [38] implemented an off-design control strategy in a recompression supercritical CO_2 (R-sCO_2) cycle, achieving a power increase of 1.02%. Lu et al. [39] emonstrated that the recompression cycle model, configured with an optimized bypass fraction, exhibits superior performance compared to the regenerative cycle under the off-design operating conditions. Bai et al. [40] optimized the SF6-CO2 mixture for solar-powered SBCs, while Ma et al. [41] identified the CO2-Xe mixture as the top thermodynamic performer in the sCO2 cycle. Kademi et al. [42] discovered an exergy efficiency of 61.8% for a multigenerational system employing ORC and sCO2 Brayton cycles, while Liu et al. [43] computed a maximum daily efficiency of 26.26% for a sCO2-based SPT plant. Butane was found to be the most appropriate working fluid in another study that optimized an ORC in conjunction with a vapor compression refrigeration (VCR) system, attaining 33.7% efficiency with a 4.9-year payback period [44]. R1224yd(Z) was found to be the most efficient working fluid. Khan et al. [45] reported that the thermal efficiency of a combined organic Rankine cycle and partial cooling supercritical CO_2 cycle increases from 35.16% to 55.43% with increasing solar irradiation, along with a power output enhancement from 188 kW to 298.5 kW.

For SPT applications, the majority of the referenced literature has mostly concentrated on either the more modern sCO2 cycle or the more conventional steam Rankine cycle. There is a glaring research gap because the recuperated helium Brayton cycle (HBC), which is well-known for its simplicity and high efficiency at operating temperatures above 500 °C, has gotten relatively little attention. With over 20 studies on CSP systems published in the last three to four years, the literature review shows a notable increase in research on sCO_2 Brayton cycles for SPTs. Helium consistently outperforms carbon dioxide (CO_2) and other fluids in SBC systems for SPT applications, according to a number of studies [5, 18, 26] that have also examined various gases as working media in supercritical Brayton cycles.

The literature review clearly indicates that although HBCs are technologically advanced, their application is limited due to the high operating temperatures required for efficiency. Hybrid Brayton cycles (HBCs) achieve optimal performance predominantly at high temperatures, owing to their substantial back work ratio. In a simple recuperative Brayton configuration, helium provides notable economic benefits compared to other working fluids [46]. At high temperatures, helium's elevated heat capacity lowers the amount of required mass flow rate, which in turn reduces component size and cost, improving its economic viability. Since solar power tower (SPT) plants typically operate under such conditions, helium has been found to perform better than carbon dioxide and other fluid operating at this temperature [47].

The literature offers limited evidence regarding the application of hybrid Brayton cycles (HBC) in solar thermal power plants. Because organic working fluids have favorable thermodynamic qualities and operating characteristics at low temperatures, Organic Rankine cycles (ORCs) are generally preferred for low-temperature applications. However, because it provides better temperature-matching glide in the evaporator, the TCO_2 cycle is a better option than ORC for recovering heat from high-temperature sources. Organic fluids, however, may cause pinch-point temperature challenges within the evaporator. From a thermodynamic standpoint, the transcritical CO_2 (TCO_2) cycle has demonstrated superior heat rejection performance relative to the organic Rankine cycle (ORC) [48].

Thus, this study uses thermodynamic and exergoenvironmental analysis to evaluate a novel system that combines the HBC with a TCO_2 cycle. By utilizing helium as the high temperature operating fluid, the performance of the supercritical Brayton cycle (SBC) has seen significant enhancements in its performance. For simple Brayton cycle (SBC) systems, a considerable portion of thermal energy is rejected to the surroundings during the cooling of the working fluid before compression, most notably within the 150–250 °C range. The TCO_2 cycle is purposefully used as a bottoming cycle to reduce this waste, efficiently recovering the waste heat from the HBC. Given the TCO_2 cycle's exceptional adaptability in waste heat recovery, as highlighted by

earlier studies [49-51], this integrated approach is not only effective but also a promising development in solar thermal applications.

Based on the explanation above, the current study's objectives are as follows:

1. To propose and develop a novel integrated power generation system that combines the helium Brayton cycle as the topping cycle with the transcritical CO_2 cycle as the bottoming cycle, thereby enhancing solar energy utilization in a solar power tower plant.
2. To thoroughly evaluate the proposed system's energy, exergy, and exergoenvironmental aspects, with an emphasis on reducing negative effects on the environment while maximizing system performance.
3. To carry out a thorough parametric analysis in order to identify the key variables influencing the system's performance and the ideal operating conditions.
4. To emphasize the novel contribution of this study by replacing the conventional exergoeconomic analysis with a more relevant exergoenvironmental analysis [3,28, 32,52,53], thus addressing both efficiency and environmental impact.

SYSTEM DESCRIPTION

Figure 1 presents the current study, and Figure 2 displays the temperature–entropy (T–s) curve of the proposed thermodynamic system. In the SPT configuration, air is used as the heat transfer fluid (HTF) to absorb solar radiation, and the internal heat exchanger (IHE) transfers this heat to the HBC, which operates as the topping cycle. Notably, helium has been chosen as the working fluid in the topping cycle, replacing the conventional supercritical CO_2 [24, 25]. Previous research indicates that helium Brayton cycles can reach higher efficiencies than CO_2 Brayton cycles when the compressor pressure ratio is less than 2.5 and the turbine inlet temperature exceeds 550 °C. Helium also outperforms CO_2 at elevated turbine inlet temperatures, which are found in solar plants utilizing central receivers [25, 26]. Additionally, helium has several distinctive qualities that make it appropriate for power cycles. Among its most noteworthy characteristics are its chemical inertness and low specific gravity [25]. The bottoming transcritical CO_2 (TCO_2) cycle operates by utilizing the leftover waste heat from the helium Brayton topping cycle through a waste heat recovery unit (WHRU). The ORC and TCO_2 cycles are two effective ways to turn low-grade heat into electricity. Because of its simplified configuration and ability to function effectively at low pressure, the ORC lowers system costs. Its versatility is further increased by its ability to adapt to different heat sources, provided that the right working fluids are found. One significant drawback, though, is the existence of the pinch point temperature difference shown in Figure 3(a), which represents the lowest temperature differential between the hot and cold fluids. Because of the significant mismatch between the two working fluids, this phenomenon introduces irreversibility into the heat exchanger. Transcritical CO2 turns out to be an excellent substitute for this restriction. The pinch point temperature difference, or the lowest temperature differential between the hot and cold fluids, is removed during the transcritical heating process. This is demonstrated in Figure 3(b), where the working fluid's temperature contour slides to provide a more advantageous alignment of the hot and cold fluid curves. This feature improves overall system performance by reducing irreversibility and getting around the pinch point temperature difference limitation.

The current combined system operates systematically as follows: Helium first cools in the precooler, putting it in state 1. After that, it passes through the compressor, which raises its temperature and pressure to state 2. In state 3, heat is absorbed in the recuperator by the cold, high-pressure helium stream. State 4 is reached when the temperature is further raised by the residual heat from the intermediate heat exchanger (IHE). The stream of high-temperature, high-pressure helium now enters the turbine, expands, and changes into state 5. After passing through the recuperator and exchanging heat with the compressor's cold stream, the medium-temperature helium stream eventually reaches state 6. At state 6, the helium has enough energy to drive a bottoming cycle, which is aided by the WHRU and involves heat exchange with the bottoming cycle's working fluid, carbon dioxide. After reaching state 7, the helium stream passes through a cooler to expel any last bits of heat before going back to state 1. At the same time, heat from the helium inside the WHRU is absorbed by the high-pressure CO2 stream, which was initially in state 11, changing to state 8. The CO2 reaches state 9, where its temperature and pressure decrease, as a result of ongoing expansion in the transcritical turbine. Following expansion, the CO2 undergoes a phase transition as it passes through the condenser, losing any heat that remains and arriving at state 10. The cycle is restarted by pumping the CO2, which is now in a low-temperature, low-pressure state, back to state 11. The system's optimal energy use and effective heat transfer are guaranteed by this cyclic process.

PERFORMANCE ASSESSMENT

Exergy and Energy Analysis

The analysis of the present system was carried out based on the following assumptions: (1) all components operate under steady-state conditions; (2) pressure losses in the components are taken as given in Table 1; (3) kinetic and potential energy contributions are neglected; and (4) the isentropic efficiencies of the turbine, pump, and compressor are adopted from the values reported in Table 1. The overall system considered for thermodynamic evaluation includes the helium Brayton cycle and the transcritical CO_2 (HBC–TCO_2) power cycle together with the solar sub-system. In the simulation performed using EES, each component is modeled as a separate

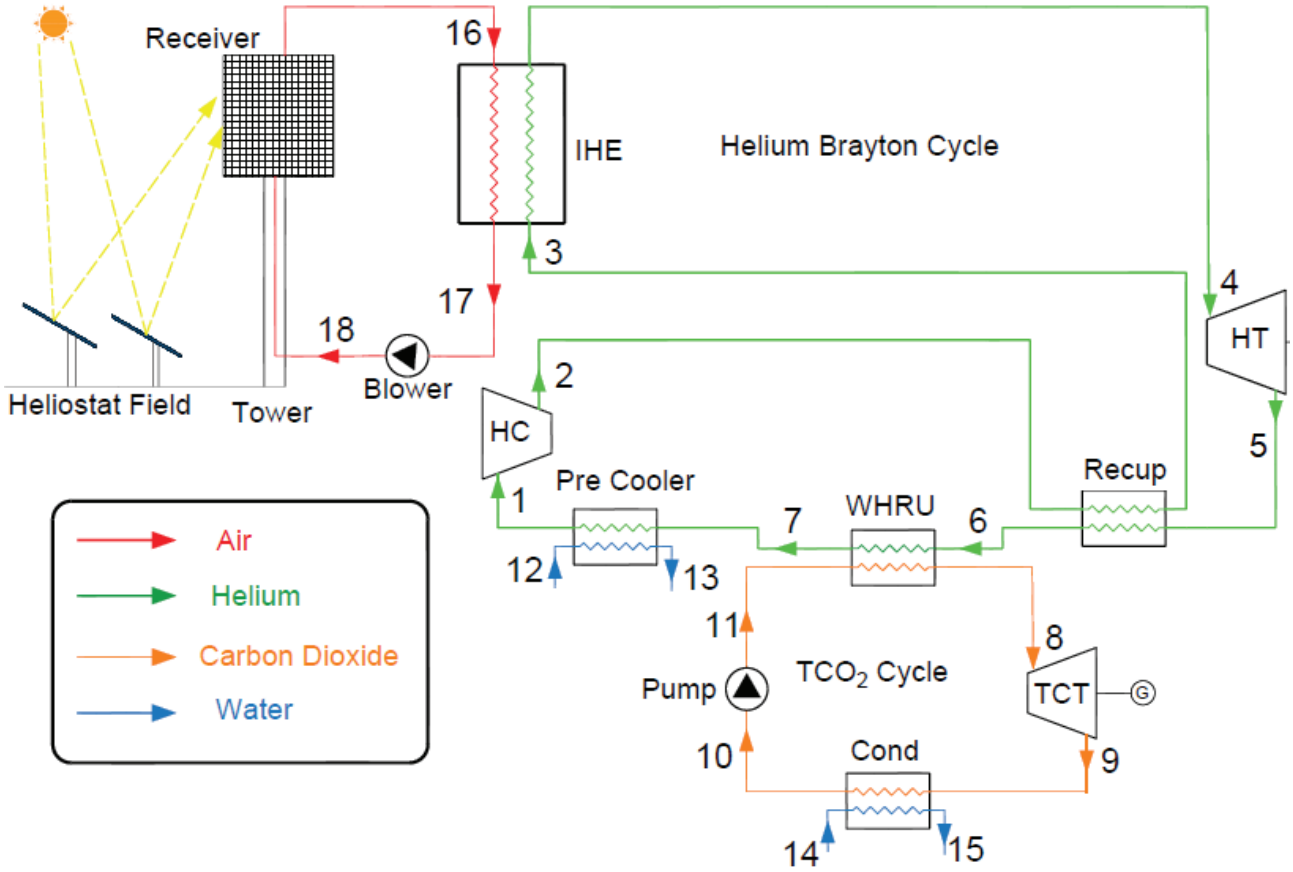

Figure 1. Proposed system diagram.

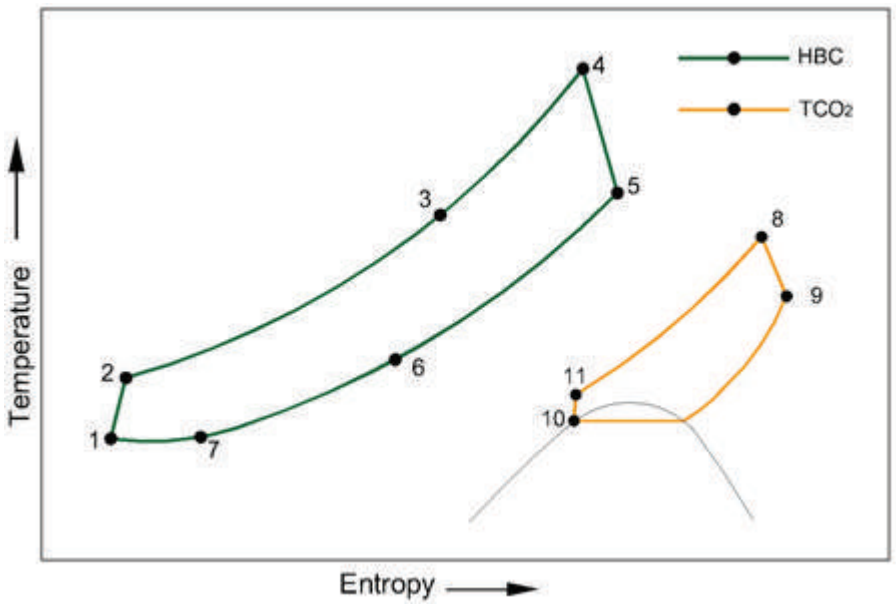

Figure 2. Temperature-entropy (T-s) diagram.

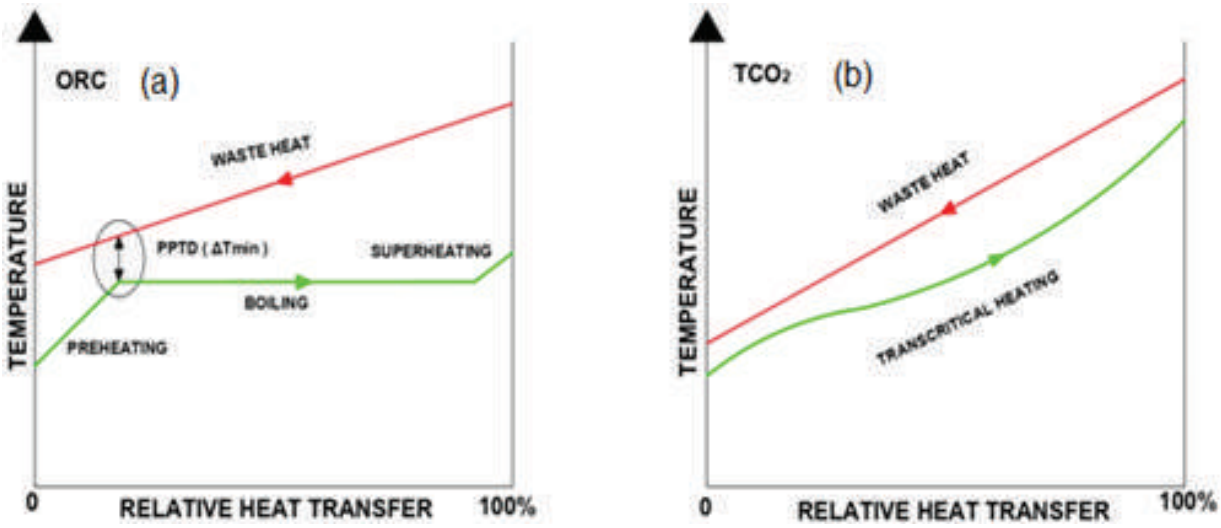

Figure 3. Temperature and heat transfer characteristics of (a) ORC, (b) TCO_2 cycle.

thermodynamic system. The governing energy and exergy balances for a control volume under steady-state conditions are expressed through the following equations:

$$\dot{Q}_{CV} - \dot{W}_{CV} + \sum(\dot{m}_i h_i) - \sum(\dot{m}_e h_e) = 0 \quad (1)$$

$$\dot{ED} = \dot{EX}_{in} - \dot{EX}_{out} \quad (2)$$

Where, $\dot{E}D$ is exergy destruction rate within the thermodynamic component. The control volume's heat and work interactions are represented by $\dot{W}_{CV}$ and $\dot{Q}_{CV}$, respectively.

The physical exergy of a fluid stream is calculated by measuring the exergy rate associated with its flow. This calculation excludes the contributions from kinetic energy, potential energy, and chemical exergy, as the suggested system lacks chemical concentration.

$$\dot{EX}_j = \dot{m}\cdot[(h_j - h_0) - T_0(s_j - s_0)] \quad (3)$$

Here, j indicates a specific state, and $\dot{E}X_j$ denotes the physical exergy at that state. The heliostat field and the receiver make up the solar subsystem. The receiver uses multiple heliostats, each with an aperture area designated as A_{hel}, to concentrate and direct solar radiation onto the primary receiver. The heliostat field efficiency defines the fraction of solar thermal energy from direct normal irradiation (DNI) that is delivered to the central receiver. The efficiency of the field depends on its configuration, while the variability in the solar energy received is linked to time of day and geographical location. The usable heat received by the receiver represents only a fraction of the total solar irradiation as remaining solar energy is lost. The calculation for this is given by [27];

$$\dot{Q}_{rec,in} = \eta_{field}\cdot\dot{Q}_{Sun} = \eta_{field}\cdot DNI \cdot A_{hel} \cdot N_{hel} \quad (4)$$

Where, η_{field} is the heliostat field efficiency [28];

$$\eta_{field} = \eta_{cos}\cdot\eta_{s\&b}\cdot\eta_{int}\cdot\eta_{att}\cdot\eta_{ref} \quad (5)$$

Where, η_{cos}, η_{int}, $\eta_{s\&b}$, η_{att}, η_{ref} represents, in that order, the efficiency of the cosine effect, interception efficiency, shading and blocking efficiency, atmospheric attenuation efficiency, and heliostat reflectivity efficiency. It should be noted that this research uses actual data from an operating solar power plant instead of calculating these characteristics theoretically.

Heat losses from the receiver occur through reflection, conduction, and convection given by ($\dot{Q}_{rec,loss}$), while the absorbed heat is represented as ($\dot{Q}_{rec,in}$). The net heat transferred to the heat transfer fluid (HTF), which is air, is given as $\dot{Q}_{rec,net}$. The receiver efficiency is then calculated as [29]:

$$\eta_{rec} = \frac{\dot{Q}_{rec,net}}{\dot{Q}_{rec,in}} \quad (6)$$

$$\dot{Q}_{rec,in} = \dot{Q}_{rec,net} + \dot{Q}_{rec,loss} = \dot{m}_{air}(h_{16} - h_{17}) + \dot{Q}_{rec,loss} \quad (7)$$

The exegetic and energetic balance equations for each component are given in Table 2. Together with the input data mentioned in Table 1, these relationships are a crucial part of the simulation code that was written using EES software. The program uses its built-in property function libraries to retrieve thermodynamic properties in order to evaluate the unknown parameters. These include exergy rates for individual streams, heat and work interactions, and state-point thermodynamic properties. The energy and exergy efficiencies of the solar power plant are defined as the ratio of the net output power to the respective energy or exergy input from solar irradiation incident on the heliostat field [29]:

$$\eta_{th,overall} = \frac{\dot{W}_{net}}{\dot{Q}_{Sun}} \quad (8)$$

$$\eta_{ex,overall} = \frac{\dot{W}_{net}}{\dot{Q}_{Sun}\cdot\left(1-\frac{T_0}{T_{ref,Sun}}\right)} \quad (9)$$

Where $T_{ref\ .Sun}$ denotes the apparent temperature of the sun [29]. $\dot{W}_{net}$ is the plant's net power output calculated as:

$$\dot{W}_{net} = \dot{W}_{HT} - \dot{W}_{HC} + \dot{W}_{TCO_2\ turbine} - \dot{W}_{pump} \quad (10)$$

For the power production unit, the combined cycle (HBC-TCO_2 cycle) efficiency can be described as [21]:

$$\eta_{th,comb} = \frac{\dot{W}_{net}}{\dot{Q}_{IHE}} \quad (11)$$

$$\eta_{ex,comb} = \frac{\dot{W}_{net}}{(\dot{EX}_{16}-\dot{EX}_{17})} \quad (12)$$

Where, $(\dot{EX}_{16} - \dot{EX}_{17})$ denotes the amount of total exergy input available for the combined cycle [21].

Exergoenvironmental Analysis

Alongside thermal analysis, assessing the environmental impact of power systems is essential for achieving long-term sustainability. Conventional energy and exergy-based thermodynamic analyses alone prove insufficient for this purpose. Hence, integrated multigenerational systems turn to exergy for comprehensive environmental assessments and sustainability evaluations. An analysis of the effects of exergy efficiency and destruction rates on the environment forms the direction of exergoenvironmental analysis. For this assessment, specific exergoenvironmental performance parameters, detailed in reference [5], are employed. Beyond conventional thermodynamic analyses, this holistic approach enables a more nuanced understanding of the sustainability and environmental implications of power systems.

An important metric that sheds light on the environmental effects of a thermal system and provides a framework for formulating plans to mitigate these effects by reducing irreversibility is the exergoenvironmental impact factor (f_{ei}). The ratio of the total energy supplied at the system inlet to the total energy destroyed in the system is how this parameter is expressed. In essence, it quantifies the extent to which a thermal system affects the environment and, on the other hand, shows how this impact might be lessened by increasing overall efficiency. Idealistically, when the exergoenvironmental impact factor (f_{ei}) value is 0, the system indicates no irreversibility.

Mathematically, it is represented as:

$$f_{ei} = \frac{\dot{E}D_{total}}{\dot{E}X_{Sun}} \quad (13)$$

The exergoenvironmental impact coefficient (C_{ei}), defined as the reciprocal of exergy efficiency, is an important measure for the present system. Better performance is indicated by a lower value of this coefficient, whereas an ideal condition with no exergy destruction is represented by a value of one.

Mathematically, it can be expressed as:

$$C_{ei} = \frac{1}{\eta_{ex,overall}} \quad (14)$$

One metric for determining whether a system has a positive or negative impact on the environment is the exergoenvironmental impact index (θ_{ei}). A lower value of this index suggests that the system exhibits superior environmental performance. In essence, a lower exergoenvironmental impact index number means that the system is performing better in terms of limiting its influence on the environment.

Mathematically, it is represented as:

$$\theta_{ei} = C_{ei}\cdot f_{ei} \quad (15)$$

For best results, the exergy stability factor (f_{es}) should ideally be "one" or approaching "one.". This indicates that, from an exergoenvironmental perspective, the system is performing exceptionally well. In other words, when the exergy stability factor is close to or equal to 'one,' it signifies that the system is achieving a high level of stability and efficiency concerning exergy considerations in the environmental context.

It can be represented as;

$$f_{es} = \frac{\dot{E}X_{out}}{\dot{E}X_{out}+\dot{E}D_{total}} \quad (16)$$

The exergoenvironmental impact improvement parameter θ_{eii} serves as a crucial metric in evaluating a system's harmony with environmental conditions. In contrast to the exergoenvironmental impact index, a higher value of the θ_{eii} parameter indicates better environmental performance. An increase in θ_{eii} reflects a stronger positive influence of the system on environmental conditions.

Mathematically, it is expressed as:

$$\theta_{eii} = \frac{1}{\theta_{ei}} \quad (17)$$

The exergetic sustainability index θ_{est} is obtained by multiplying the exergoenvironmental impact improvement parameter with the exergetic stability factor. A higher θ_{est} value reflects a system with stronger environmental benefits, whereas a lower value indicates adverse environmental effects within the studied system. In essence, the exergetic sustainability index provides a crucial measure of a system's environmental performance, with an elevated value indicating a more sustainable and eco-friendly operation.

Mathematically, it can be expressed as:

$$\theta_{est} = \theta_{eii}\cdot f_{es} \quad (18)$$

The exergoenvironmental analysis was performed through the utilization of modeling equations, and the results were computed employing computational techniques with Engineering Equation Solver (EES).

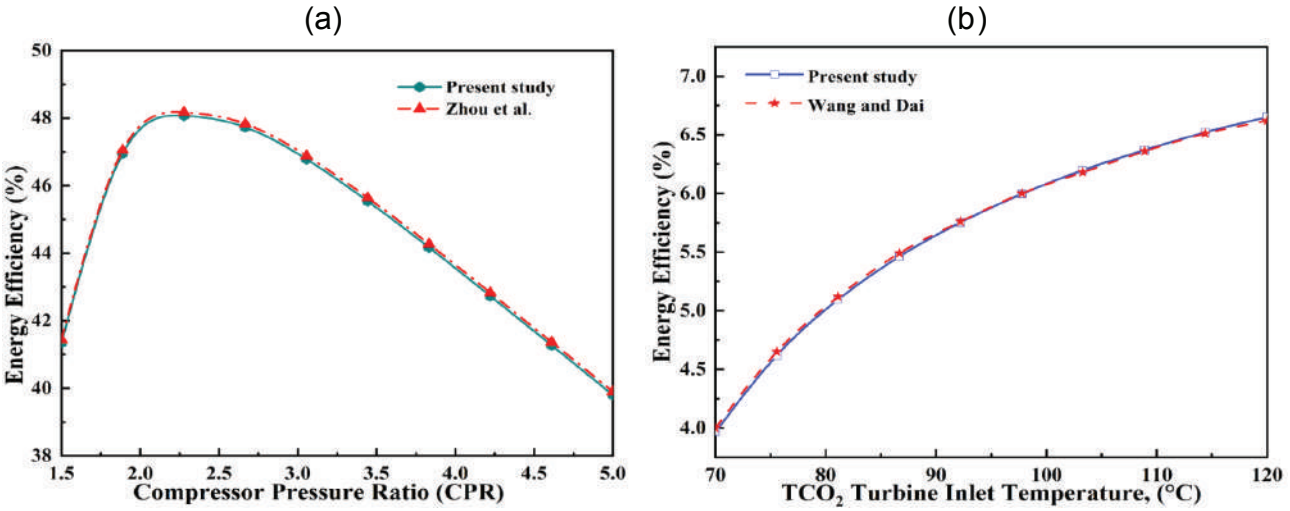

Figure 4. Validation for (a) helium Brayton cycle, (b) TCO_2 cycle.

Validation

To validate the modeling approach, the results of the two developed models, the tCO_2 cycle and the HBC cycle are compared with data available in reputable literature. Figure 4(a) presents the efficiency values of the standalone HBC system from this study alongside those reported by Zhou et al. [21]. Notably, the data discrepancy is within a reasonable range—just 0.24%. For the bottoming TCO_2

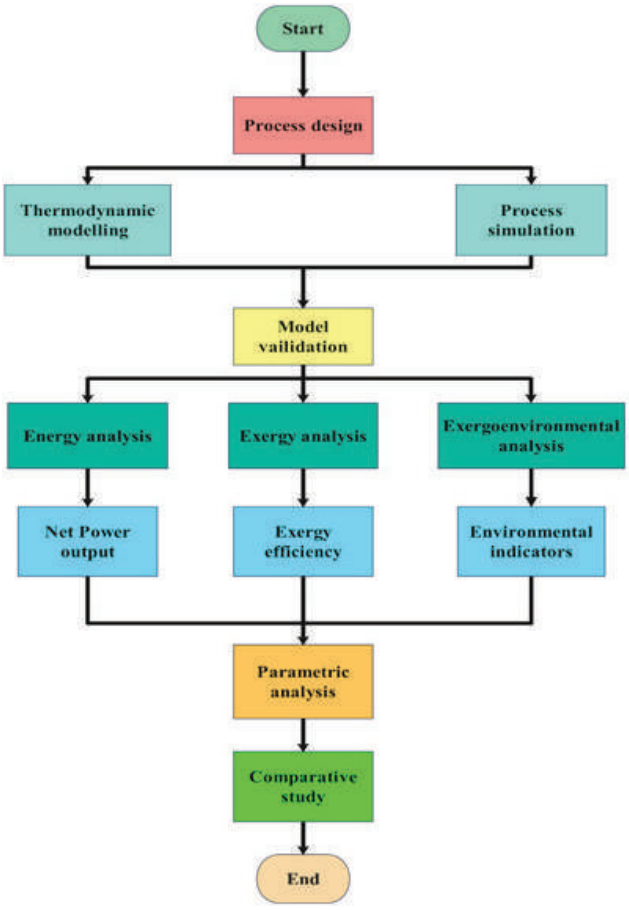

Figure 5. The flow diagram for the current study's solution and structure.

Table 1. Simulation data for the present study [3,9,17]

Parameters	Value
Atmospheric temperature (T_o)	25 °C
Atmospheric pressure (P_o)	101.3 kPa
Apparent Sun temperature (T_{Sun})	4500 K
Heat exchanger effectiveness (ε)	0.9
Air inlet temperature at IHE (T_{16})	1125 °C
Direct normal irradiation (DNI)	850 W/m^2
Count of heliostats (N_{hel})	624
Receiver aperture area (A_{rec})	68.1 m^2
Efficiency of heliostat field (η_{field})	0.6428
Every heliostat's reflecting area (A_{hel})	9.45 × 12.84 m^2
Efficiency of the receiver (η_{rec})	0.75
Isentropic efficiency of helium compressor (η_{HC})	0.89
Isentropic efficiency of helium turbine (η_{HT})	0.93
TCO_2 turbine's isentropic efficiency ($\eta_{TCO_2\ turbine}$)	0.8
Pump's isentropic efficiency (η_{Pump})	0.7
Helium Turbine's inlet temperature (T_4)	800 °C
TCO_2 turbine's inlet temperature (T_8)	180 °C
Pressure at the helium compressor's inlet (P_1)	2500 kPa
Compressor pressure ratio (CPR)	2.3
Pump pressure ratio (PPR)	3.033
Intermediate heat exchanger's pressure loss	2%
Pinch point temperature difference in WHRU	10 °C
Loss of pressure in the recuperator/WHRU	1%
Pinch point temperature difference in condenser	5 °C

Table 2. Energy-exergy analysis equations for every component

Components	Energy balance equation	Exergy balance equation
Receiver	$\dot{Q}_{rec,in} = \dot{m}_{air}(h_{16} - h_{17}) + \dot{Q}_{rec,loss}$	$\dot{E}X_{17} + \dot{Q}_{rec,in}\cdot\left(1-\frac{T_0}{T_{ref,hel}}\right) = \dot{E}X_{16} + \dot{Q}_{rec,loss}\cdot\left(1-\frac{T_0}{T_{rec}}\right) + \dot{E}D_{rec}$
Heliostat field	$\dot{Q}_{rec,in} = \eta_{field}\cdot DNI \cdot A_{hel} \cdot N_{hel}$	$\dot{Q}_{Sun}\cdot\left(1-\frac{T_0}{T_{ref,Sun}}\right) = \dot{Q}_{rec,in}\cdot\left(1-\frac{T_0}{T_{ref,hel}}\right) + \dot{E}D_{hel}$
Helium compressor	$\dot{W}_{HC} = \dot{m}_{He}\cdot(h_2 - h_1)$ $\eta_{HC} = \frac{(h_{2s} - h_1)}{(h_2 - h_1)}$	$\dot{E}X_1 = \dot{E}X_2 - \dot{W}_{HC} + \dot{E}D_{HC}$
Helium turbine	$\dot{W}_{HT} = \dot{m}_{He}\cdot(h_4 - h_5)$ $\eta_{HT} = \frac{(h_4 - h_5)}{(h_4 - h_{5s})}$	$\dot{E}X_4 = \dot{E}X_5 + \dot{W}_{HT} + \dot{E}D_{HT}$
IHE	$\dot{Q}_{IHE} = \dot{m}_{air}\cdot(h_{16} - h_{17}) + \dot{m}_{He}\cdot(h_4 - h_3)$	$\dot{E}X_{16} - \dot{E}X_{17} = \dot{E}X_4 - \dot{E}X_3 + \dot{E}D_{IHE}$
Recuperator	$(h_3 - h_2) = (h_5 - h_6)$ $\varepsilon_{Recuperator} = \frac{(T_3 - T_2)}{(T_5 - T_2)}$	$\dot{E}X_5 - \dot{E}X_6 = \dot{E}X_3 - \dot{E}X_2 + \dot{E}D_{Recuperator}$
WHRU	$\dot{m}_{He}\cdot(h_6 - h_7) = \dot{m}_{CO2}\cdot(h_8 - h_{11})$	$\dot{E}X_6 - \dot{E}X_7 = \dot{E}X_8 - \dot{E}X_{11} + \dot{E}D_{WHRU}$
TCO_2 turbine	$\dot{W}_{TCO_2\ turbine} = \dot{m}_{CO2}(h_8 - h_9)$ $\eta_{TCO_2\ turbine} = \frac{(h_8 - h_9)}{(h_8 - h_{9S})}$	$\dot{E}X_8 = \dot{E}X_9 + \dot{W}_{TCO_2\ turbine} + \dot{E}D_{TCO_2\ turbine}$
Pump	$\dot{W}_{Pump} = \dot{m}_{CO2}(h_{11} - h_{10})$ $\eta_{Pump} = \frac{(h_{11s} - h_{10})}{(h_{11} - h_{10})}$	$\dot{E}X_{10} = \dot{E}X_{11} - \dot{W}_{Pump} + \dot{E}D_{Pump}$
Precooler	$\dot{m}_{air}\cdot(h_7 - h_1) = \dot{m}_{water}\cdot(h_{13} - h_{12})$	$\dot{E}X_7 - \dot{E}X_1 = \dot{E}X_{13} - \dot{E}X_{12} + \dot{E}D_{Preooler}$
COND	$\dot{m}_{CO2}\cdot(h_9 - h_{10}) = \dot{m}_{water}\cdot(h_{15} - h_{14})$	$\dot{E}X_9 - \dot{E}X_{10} = \dot{E}X_{15} - \dot{E}X_{14} + \dot{E}D_{COND}$

cycle, we conducted a validation using the results presented in Figure 4(b), as reported by Wang and Dai [30], who employed the same input conditions. The comparison indicates a slight variation of less than 1% in the results, which is also regarded as acceptable. In summary, these validations serve to affirm the accuracy and reliability of our modeling technique. The flow diagram for the solution and structure of the current study is displayed in Figure 5.

RESULTS AND DISCUSSION

The system simulation was performed using the assumptions and input parameters listed in Table 1. To provide a detailed understanding of the cycle's energy and exergy behavior, the results obtained at optimal operating conditions for all subsystems are summarized in Table 3. Based on a solar irradiation input of 64,358 kW, the energy analysis shows that the plant's total power output is 14,930 kW, which translates to an overall energy efficiency of 23.20%. At 22,989 kW, or 35.72% of the solar input, the heliostat field is responsible for the greatest amount of energy loss. This outcome underlines the importance of an efficient heliostat field design in solar power tower plants. The combined HBC–TCO_2 cycle records an energy efficiency of 48.11%. High-grade energy with a source temperature of roughly 4500 K is produced by solar radiation [29]. Significant irreversibilities happen when this energy reaches the receiver at almost 1125 °C, and exergy analysis shows that the heliostat field has the highest exergy destruction. The heliostat field efficiency under these circumstances is determined to be 64.24%. Because the system does not involve combustion, which is a major source of irreversibility in conventional plants, the temperature difference between helium and the heat transfer fluid (air) in the intermediate heat exchanger (IHE) remains low. This condition allows the combined cycle to reach an exergy efficiency of 66.31%. Despite this improvement, the plant's overall energy efficiency is still constrained because of the substantial damage to the heliostat field and receiver. According to a component-level analysis, the heliostat field has the highest energy destruction at 21,465 kW, while the precooler has the lowest at 405.9 kW, accounting for 47.52% of the total. At 97.25%, the helium turbine exhibits the highest energy efficiency of any component. Together, the energy and exergy analysis

Table 3. Results of exergy-energy evaluation under the specified operating parameters*

Subsystems	Energetic Assessment				Exergetic Assessment			
	Input (kW)	Output (kW)	Loss (kW)	Energy efficiency	Input (kW)	Output (kW)	Loss (kW)	Exergy efficiency
Heliostat field	64358	41369	22989	64.27%	60094	38628	21465	64.27%
Solar receiver	41369	31027	10342	75%	38628	22515	16113	58.28%
HBC	31027	13365	17662	43.07%	22515	13365	9150	59.36%
TCO_2 cycle	13261	1565	11696	11.8%	3698	1565	2133	42.32%
Combined cycle	31027	14930	16097	48.11%	22515	14930	7586	66.31%
Overall power plant	64358	14930	49428	23.2%	60094	14930	45164	24.83%

*T_4 = 800 °C, CPR = 2.3, PPR = 3.033, T_8 = 180 °C, DNI = 850W/m²

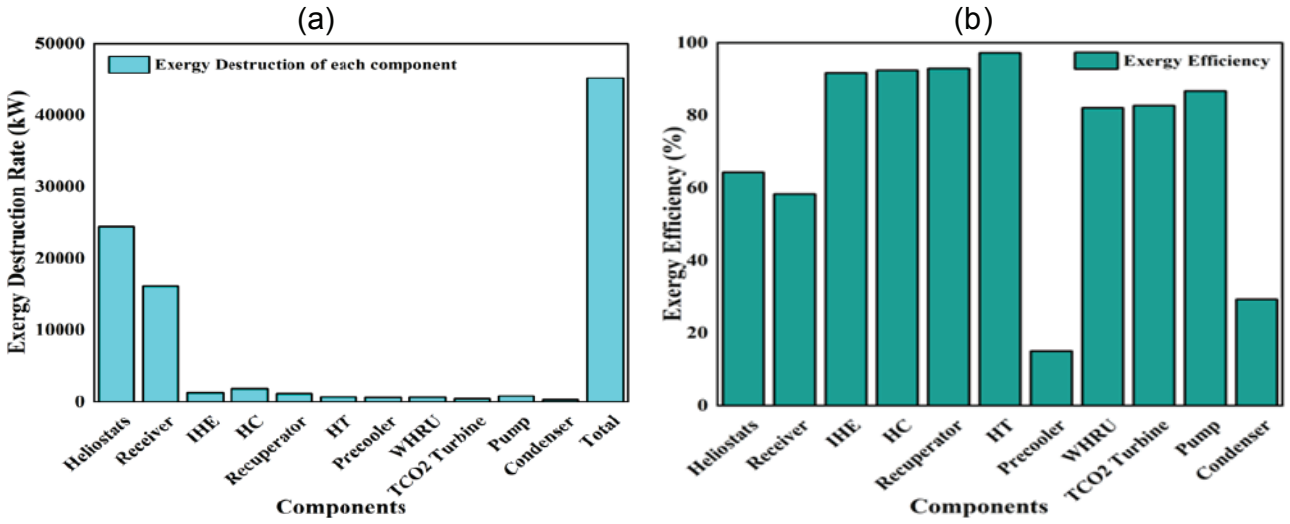

Figure 6. Each components (a) exergy destruction, (b) exergy efficiency.

results provide a thorough evaluation of the system's operation and the allocation of losses and efficiencies. The exergy destruction rates and efficiencies of individual components are further presented in Figures 6(a) and 6(b), which provide a clear representation of their contributions to overall system behavior.

In addition, Table 4 lists the values of the exergoenvironmental performance metrics in the basic case. Observing the plant's below-average exergy efficiency, it becomes evident that the exergoenvironmental effect coefficient is notably higher, measuring at 4.028. This result highlights that there is still a great deal of room to reduce the negative environmental effects of the system. An ideal degree of environmental stability is indicated by an exergetic stability factor of 1. The actual value, however, is 0.2483, indicating that this system continues to have an impact on environmental stability. In conclusion, the results emphasize the need for enhancements meant to lessen the system's negative effects on the environment and increase its sustainability. Table 5 lists the thermodynamic properties at each state with respect to Figure 1. These data present a detailed overview of the system's thermodynamic condition at the key state points. This precise data serves as the cornerstone for precise modeling and analysis, offering insights into the efficiency and dynamic behavior of the power plant.

Table 4. Values of the exergoenvironmental performance parameters at base case

Parameters	Values
Exergoenvironmental impact index (θ_{ei})	3.028
Exergoenvironmental impact coefficient (C_{ei})	4.028
Exergetic sustainability index (θ_{est})	0.0819
Exergoenvironmental impact factor (f_{ei})	0.7517
Exergy stability factor (f_{es})	0.2483
Exergoenvironmental impact improvement (θ_{eii})	0.3302

Table 5. The proposed system's mass flow rates and thermodynamic parameters

State	Working Fluid	ṁ(kg/s)	P (kPa)	T (°C)	h (kJ/kg·°C)	s (kJ/kg·°C)	ĖX (kW)
1	He	20.11	2500	30	34.04	-6.569	39014
2	He	20.11	5833	167.4	757.7	-6.386	52110
3	He	20.11	5774	494.6	2455	-3.483	68404
4	He	20.11	5659	800	4040	-1.703	89040
5	He	20.11	2577	530.7	2634	-1.569	60727
6	He	20.11	2551	203.7	936.1	-4.259	43190
7	He	20.11	2525	73.28	258.8	-5.898	39492
8	CO_2	56.47	21879	180	56.01	-0.7824	16353
9	CO_2	56.47	7214	87.83	3.138	-0.7453	12743
10	CO_2	56.47	7214	30	-204	-1.401	12092
11	CO_2	56.47	21879	63.28	-178.8	-1.39	13323
12	Water	105.2	101.3	25	104.8	0.3669	0
13	Water	105.2	101.3	35	146.7	0.5049	72.19
14	Water	279.6	101.3	35	146.7	0.5049	191.9
15	Water	279.6	101.3	25	104.8	0.3669	0
16	Air	46.2	101.3	544.6	841.8	6.741	10690
17	Air	46.2	101.3	1125	1513	7.359	33205

Additionally, the impact of various variables on the power plant performance has been assessed conducted through a parametric analysis. This analysis involves varying one parameter at a time while keeping the other parameters, as listed in Table 1, constant. The following sections in this report segment delve into a thorough exploration of the individual effects of each parameter.

Effect on Performance of The System Compressor Pressure Ratio

Since it has a direct impact on the selection of compressor material and related expenses, the compressor pressure ratio (CPR) is a crucial variable being studied. As depicted in Figure 7(a), a discernible trend in energy efficiency emerges, initially ascending and then consistently descending. Reaching 48.32% for the combined cycle and 43.12% for the standalone configuration, the maximum energy efficiency is achieved at a CPR of 2.3. A substantial 12.05% enhancement in energy efficiency with the integration of the TCO_2 cycle into the basic HBC (standalone). In evaluating the performance of the combined cycle CPR emerges as a key factor. Energy and exergy efficiencies show an initial ascent, peaking at a CPR of 2.3 with energy efficiency at 47.87% and exergy efficiency at 65.56%. However, beyond CPR 2.3, both efficiencies decline. The interplay between expansion and compression work explains this behavior. Both increase together when the CPR is less than 2.3, but after that, the increase in compression work is greater than the increase in expansion work, which lowers the combined cycle's efficiency and net output. The analysis emphasizes how important CPR is in determining the power plant configuration's overall efficiency landscape.

Figure 7(b) shows the influence of CPR on the energy and exergy efficiencies of the HBC–TCO_2 combined cycle. Both efficiencies rise with increasing CPR, reach their maximum at 2.3, and then gradually decrease, consistent with the earlier discussion. The maximum values recorded are 47.87% for energy efficiency and 65.56% for exergy efficiency. Figure 7(c), illustrating variations in energy, exergy, and network output for the power plant (SPT-HBC-TCO_2 cycle), a similar pattern emerges as in Figure 7(b). In this scenario, energy and exergy efficiencies approximate 23.2% and 24.83%, respectively. Notably, a significant decrease in efficiencies occurs in the combined power plant compared to the combined cycle. The decline is mainly due to significant energy losses in the heliostat field and the receiver, with about 58.52% of the total exergy destruction taking place in the solar field. The overall exergy destruction for the entire plant is calculated to be 45,164 kW, with 37,578 kW attributed solely to the solar field and receiver. The maximum net power output of the combined cycle is 14,930 kW at a CPR of 2.3. Comparison between Figure 7(b) and Figure 7(c) reveals that the inclusion of the TCO_2 cycle into the standalone HBC results in an increased maximum net power output. At the optimal CPR of 2.3, the net power output reaches 14,930 kW for the combined cycle and 13,365 kW for the standalone cycle. This indicates an improvement of 1,565 kW in net power output due to the TCO_2 cycle functioning as the bottoming cycle.

The back work ratio (BWR) is an important system performance metric in addition to efficiency. Better

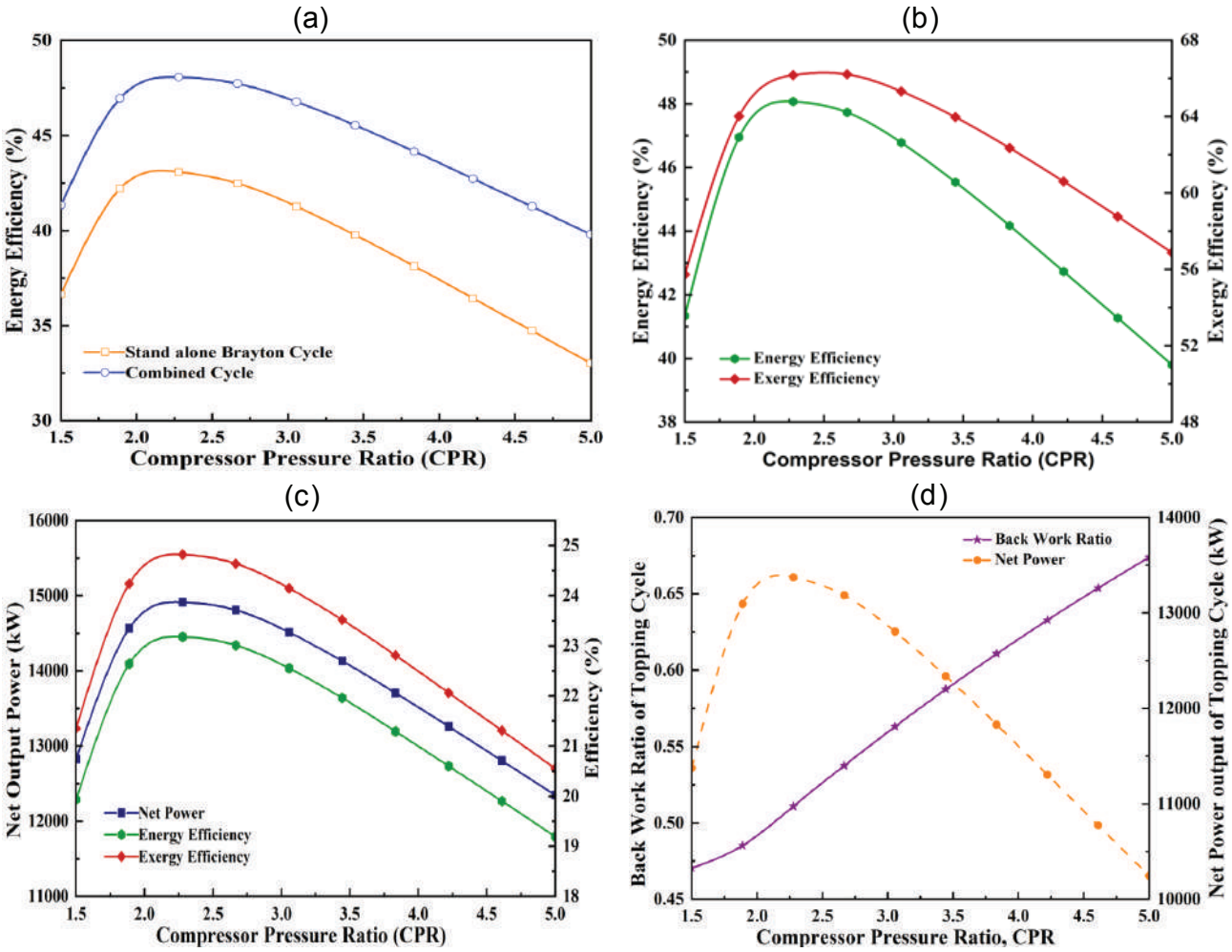

Figure 7. Performance variation with compressor pressure ratio.

overall performance is indicated by a lower BWR, which is the ratio of compressor work to turbine work in a combined cycle. With increasing CPR, BWR also increases, reflecting the continuous rise in compression work, as depicted in Figure 7(d). The connection between BWR and CPR is significant. As CPR increases, the amount of compression work consistently rises, leading to an increase in BWR. The ideal CPR value, however, is found to be 2.3 after taking into account how each other parameter affects system performance. In this case, BWR rises from 0.4712 to 0.6786 while CPR increases from 1.5 to 5. This analysis emphasizes how CPR and BWR interact in a complex way to shape the power cycle's performance characteristics.

Variation in performance with pump pressure ratio

The pump pressure ratio (PPR) has a limited impact on system performance when maintaining a fixed compressor pressure ratio (CPR) of 2.3, a direct normal irradiance (DNI) of 850 W/m², and a helium turbine inlet temperature of 800 °C. The study reveals that the net output power of the TCO_2 cycle and overall plant efficiency experience a continuous increase followed by a decrease as PPR varies. This trend is a result of the influence of PPR on the expansion ratio of the transcritical turbine, where an initial increase in PPR results in higher work output until a critical point is reached at PPR 3.056. After this point, compression work exceeds expansion work, which lowers net work output. As shown in Figure 8(a) for the TCO_2 cycle, the ideal PPR value is 3.056, exhibiting maximum power output, energy efficiency, and exergy efficiency of 1556 kW, 24.83%, and 23.18%, respectively. Additionally, the TCO_2 cycle's BWR reacts to variations in PPR, showing a steady rise with higher PPR values. The net power output first increases and then gradually decreases, as shown in Figure 8(b). As PPR rises from 1.5 to 5, BWR varies from 0.3 to 0.72, with 3.03 being the ideal value. The BWR is 0.49 at this ideal PPR value, meaning that the pump uses 49% of the work output generated by the turbine for compression work.

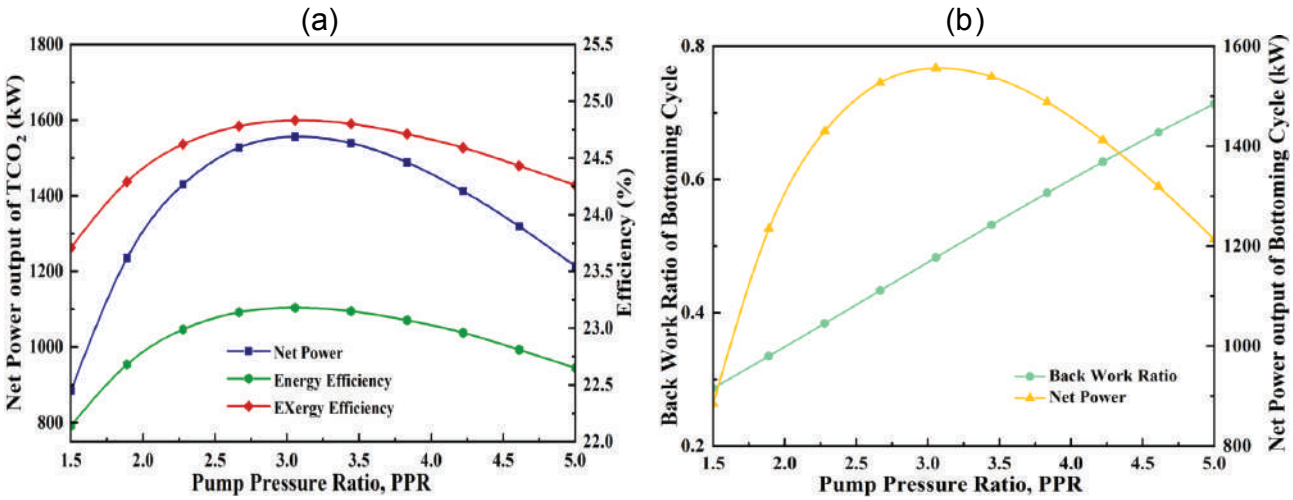

Figure 8. Performance variation with pump pressure ratio.

Effect of Helium Turbine Inlet Temperature

The system's performance is highly dependent on the Helium Turbine Inlet Temperature (HTIT). When HTIT rises from 700 °C to 900 °C, several performance indicators improve significantly. As presented in Figure 9(a), the plant's overall energy efficiency increases from 21.36% to 24.65%, the exergy efficiency grows from 22.87% to 26.4%, and the net power output rises from 13,746 kW to 15,866 kW. At higher HTIT values, the enthalpy difference across the turbine increases, resulting in a greater expansion ratio and this improvement. As a result, the system's thermal performance is improved by increasing the net output power. These results are obtained under the assumptions of an optimal compressor pressure ratio (CPR) of 2.3, a direct normal irradiation (DNI) of 850 W/m², and a TCO_2 turbine inlet temperature of 180 °C. HTIT also affects the mass flow distribution of the working fluids. Figure 9(b) indicates that with increasing HTIT, the mass flow rate of air in the solar power tower (SPT) subsystem increases, while the mass flow rates of both carbon dioxide and helium decrease. The higher air flow rate is linked to the greater quantity of heat delivered from the heliostat field to the receiver. The heated air's outlet temperature rises as a result, which lowers its density and increases the air's mass flow rate. On the other hand, because of the enthalpy variation needed to maintain the same work output, higher topping cycle temperatures lower the flow rates of helium and carbon dioxide. Over the HTIT range of 700 °C to 900 °C, the mass flow rates change from 41.63 kg/s to 59.57 kg/s for air, from 59.69 kg/s to 52.02 kg/s for carbon dioxide, and from 21.92 kg/s to 16.14 kg/s for helium.

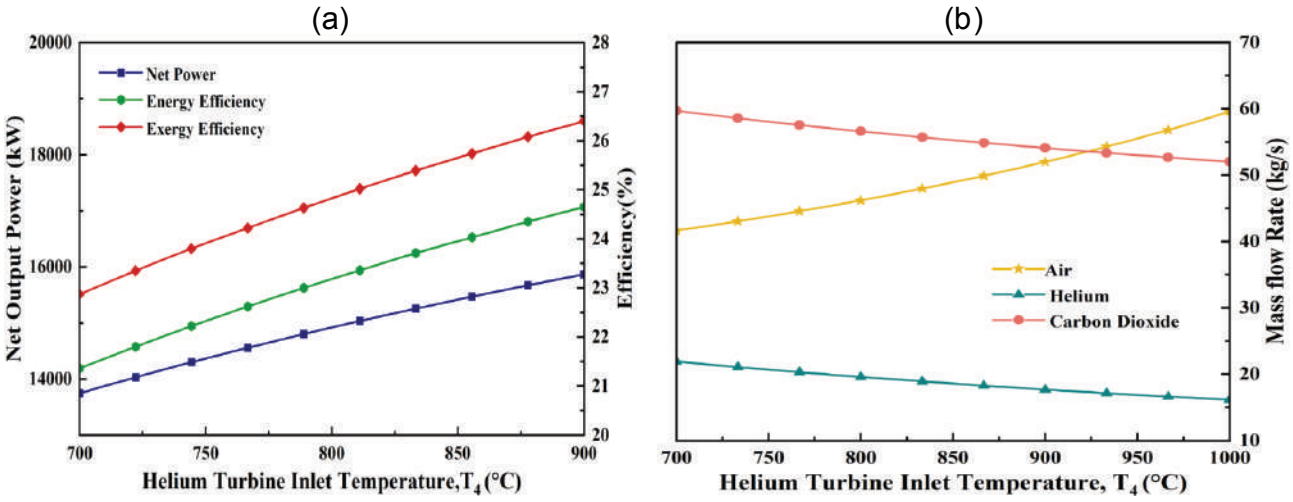

Figure 9. Performance variation with HTIT.

Effect of TCO_2 Turbine Inlet Temperature

This section provides a detailed evaluation of how the TCO_2 turbine inlet temperature influences the overall performance of the system. The overall plant efficiency increases only slightly when the TCO_2 turbine inlet temperature is raised, but the bottoming cycle's net power output responds more strongly. The temperature variation from 150 °C to 200 °C resulted in a modest improvement of 2.05% and 2% in energy and exergy efficiency, respectively. These findings were consistent under constant values of CPR at 2.3, DNI at 850 W/m², and a tCO_2 cycle pump pressure ratio of 3.056, as depicted in Figure 10. In contrast, the net power output of the bottoming cycle exhibited a substantial increase of 22.21%. The temperature increase that results in an increase in thermodynamic properties at the inlet is the cause of this noteworthy phenomenon. As a result, a larger total enthalpy difference developed, which eventually helped to increase the net power output at a fixed pressure ratio.

Impact on system performance of compressor inlet temperature

It is evident how the compressor inlet temperature affects system performance when all other parameters are set as indicated in Table 1. As the compressor's inlet temperature rises, the net power output and overall plant efficiency decrease. This drop, which results from an increasing enthalpy difference across the compressor, has a detrimental effect on the compressor's performance. As a result, the overall system performs worse when the compressor's inlet temperature increases. The energy and energy efficiency of the entire system have decreased from 23.36% to 23% and

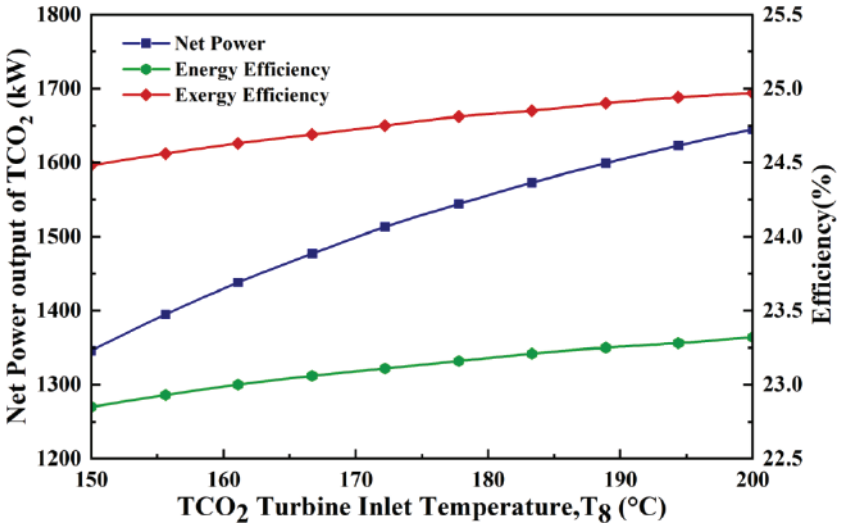

Figure 10. Performance variation of TCO_2 cycle with TCO_2 turbine inlet temperature.

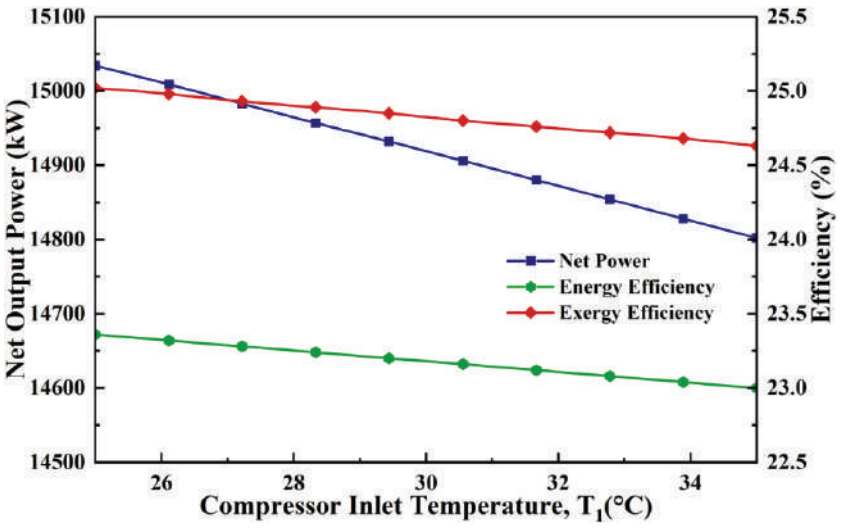

Figure 11. Plant performance variation with compressor inlet temperature.

from 25.02% to 24.63%, respectively. Additionally, Figure 11 shows that power production decreases from 15,034 to 14,802 kW as the temperature rises from 25 to 35 degrees Celsius.

Impact of Solar Subsystem Characteristics on System Performance

Apart from the combined cycle parameters, it is also important to examine how the SPT design parameters affect the power plant. Among them, the efficiency of the heliostat field stands out as the key factor influencing overall performance. A direct correlation is observed: the power plant's total performance improves with an increase in heliostat efficiency. Exergy efficiency, energy efficiency, and power output all experienced significant increases as heliostat efficiency rose from 0.6 to 0.85, as depicted in Figure 12(a). As a result, the energy efficiency increased from 21.64% to 30.65%, the power output increased from 13925 kW to 19728 kW, and the energy efficiency increased from 31.7% to 41.45%. This enhancement can be attributed to the higher heliostat efficiency, which leads to reduced energy loss from the sun and increased energy conversion, consequently boosting exergy, energy, and power output.

The solar intensity, expressed as DNI, stands out as a vital factor with geographical and temporal variability. A distinct relationship that emphasizes the importance of DNI on the power plant's performance metrics is shown in Figure 12(b). It is noteworthy that higher DNI levels are associated with higher system output power, energy efficiency, and exergy efficiency. This relationship stems from the system's capacity to absorb more solar radiation when its DNI is higher, which in turn increases the total amount of heat input. As a result, the mass flow rate of the working fluid increases, leading to a significant rise in work output. For example, when the direct normal irradiation (DNI) changes from 600 to 1000 W/m^2, the work output grows from 10,529 kW to 17,551 kW. Simultaneously, energy and exergy efficiencies exhibit a steady increase from 16.36% to 27.3% and 17.52% to 29.4%, respectively.

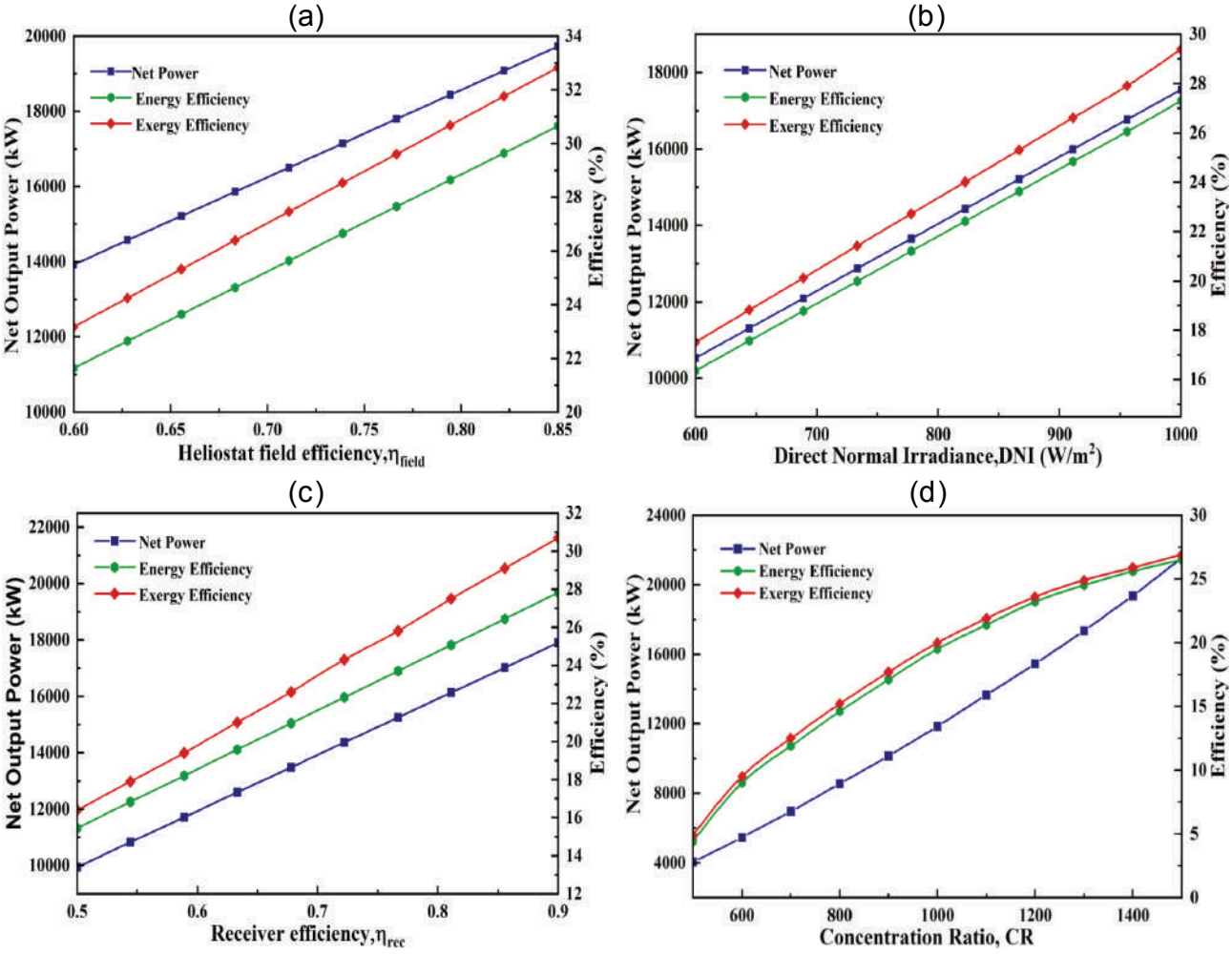

Figure 12. Plant performance variation with heliostat field efficiency.

The overall performance of the system is greatly influenced by the efficiency of the receiver, as shown in Figure 12(c). The overall performance of the system improves as the receiver efficiency () rises. This improvement is explained by the fact that higher receiver efficiency results in less heat loss, which allows the system to produce a significant amount more heat. Figure 12(c) shows a clear trend, where an increase in receiver efficiency from 0.5 to 0.9 raises the work output from 9,946 kW to 17,903 kW. Simultaneously, energy and exergy efficiencies show a steady ascent from 15.45% to 27.82% and 16.39% to 30.7%, respectively. The concentration ratio, which varies between 300 and 1500 in solar power tower plants, is another key factor affecting power plant performance, as illustrated in Figure 12(d). With a fixed heliostat area (A_{hel}), an elevation in the concentration ratio results in a reduction in the aperture area of the receiver. This, in turn, leads to a higher solar heat flux into the receiver, contributing to an increase in both the plant's net power production and efficiency. Figure 12(d) highlights this correlation, emphasizing that efficiency improvements are more significant at lower concentration ratios. However, the potential for improving energy and exergy efficiency decreases as the concentration ratio increases, mainly because of increased exergy destruction.

Effects of Various Parameters on Exergoenvironmental Performance

Exergoenvironmental analysis is an approach used in the study of thermodynamics and sustainability to evaluate and examine how energy systems and processes affect the environment. Figure 13(a) depicts the effect of the compressor pressure ratio on exergoenvironmental factors. It is evident from the figure that, as CPR increases, the environmental impact index (θ_{ei}) decreases and reaches a minimum value of 3 at a pressure ratio of 2.3. Subsequently, it gradually increases with further pressure ratio increments. This phenomenon arises due to lower exergy destruction at lower pressure ratios, which becomes more pronounced at higher pressure ratios. Similarly, other environmental factors such as the environmental impact factor (θ_{eii}), exergy sustainability index (θ_{est}), and exergy stability factor (f_{es})

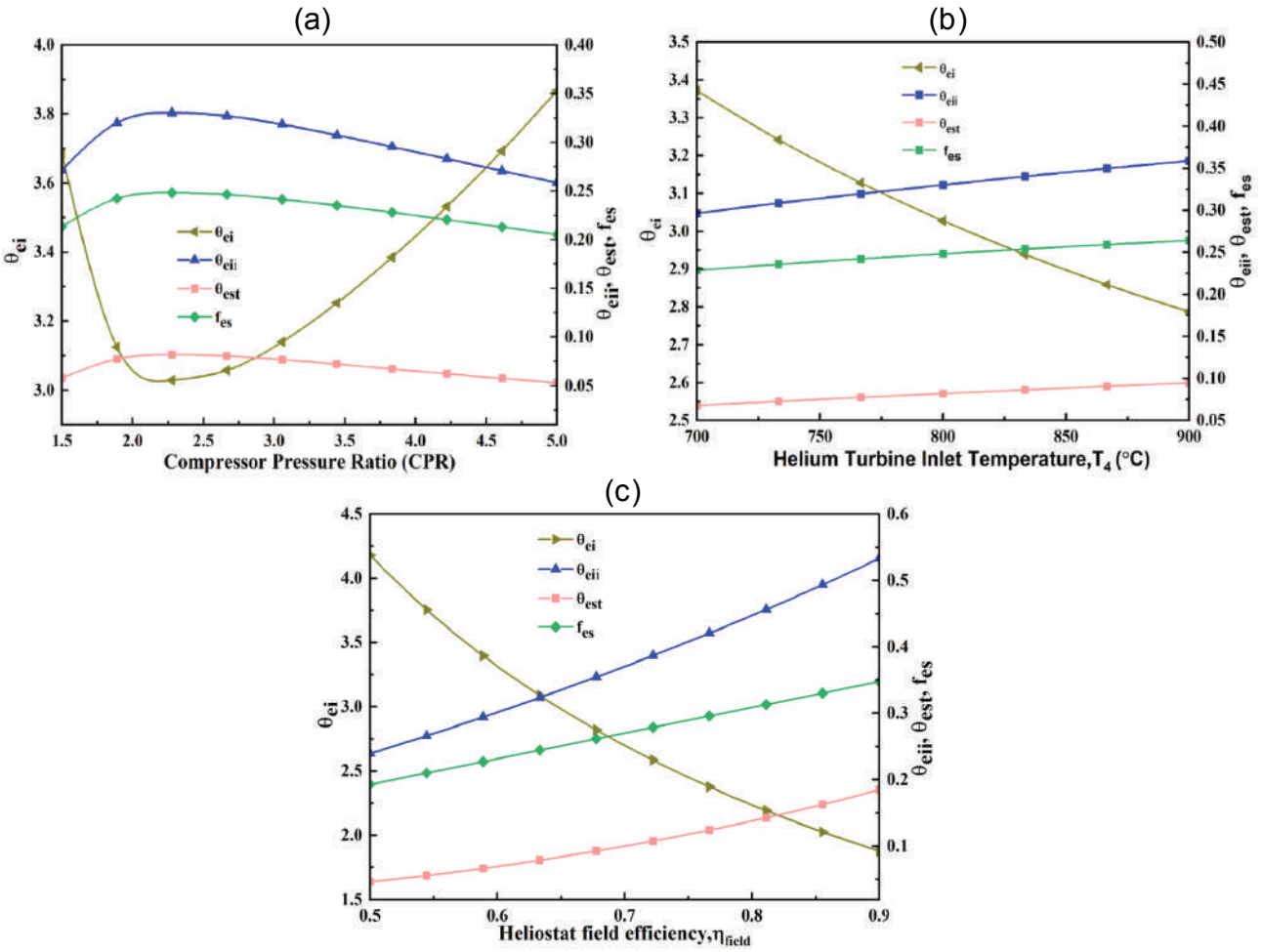

Figure 13. Exergoenvironmental factors variation with various parameters.

exhibit a similar trend. Exergy efficiency increases with a pressure ratio up to 2.3 and then declines as the pressure ratio continues to rise. In the graph, θ_{ei} decreases from 3.68 to 3 at a CPR of 2.33 and then increases to 3.8 at a CPR of 5. The factors θ_{eii}, θ_{est}, and f_{es} increases from 0.27 to 0.32, 0.05 to 0.07, and 0.21 to 0.24, respectively, as CPR increases from 1.5 to 2.33, reaching their optimum values at 2.3 and subsequently decreasing with further pressure ratio increases.

Figure 13(b) illustrates the effect of helium turbine inlet temperature on exergoenvironmental factors. It can be observed that, as the turbine inlet temperature of the HBC increases, θ_{ei} decreases, whereas the other factors, namely θ_{eii}, θ_{est}, and f_{es}, increases with the rising turbine inlet temperature. This trend is a result of the minimum exergy destruction at lower temperatures, while higher temperatures lead to increased exergy destruction. The θ_{ei} decreases from 3.37 to 2.78, while the factors θ_{eii}, θ_{est}, and f_{es} increases from 0.29 to 0.35, 0.06 to 0.09, and 0.2 to 0.26, respectively, as the temperature rises from 700 °C to 900 °C.

Figure 13 (c) illustrates the relationship between heliostat field efficiency and exergoenvironmental factors. As observed in the graph, θ_{ei} decreases, while the other factors, including θ_{eii}, θ_{est} and f_{es}, increase as heliostat field efficiency rises from 50% to 90%. The value of θ_{ei} decreases from 4.17 to 1.8, while the factors θ_{eii}, θ_{est}, and f_{es} increases from 0.23 to 0.53, 0.04 to 0.18, and 0.19 to 0.34, respectively. This trend emerges because the heliostat field receives the maximum amount of solar energy, with temperatures around 2000 °C. Consequently, such high temperatures result in maximum exergy destruction within the heliostat field. Therefore, it can be concluded that the present study has a negligible harmful impact on the environment, and thus power is generated in a carbon free manner.

Comparison With Previous Research

The present system comprises a helium Brayton cycle, a waste heat recovery transcritical CO_2 (TCO_2) cycle serving as the bottoming cycle, and a solar power tower (SPT) system. This system has been compared to previous studies by Zare and Hasanzadeh [17]. It is clear that the current system (energy efficiency 23.2%) may attain almost the same thermal performance as the Zare and Hasanzadeh [17] system (energy efficiency 23.11%) with fewer components. While the current study only included 11 components for the same thermal efficiency for the high-temperature SPT applications, Zare and Hasanzadeh [17] included 17 components.

CONCLUSION

This study proposes an integrated hybrid Brayton cycle (HBC) and transcritical CO_2 (TCO_2) cycle for harnessing solar energy from the solar power tower (SPT) system to improve the overall plant performance. The exergy, energy and exergoenvironmental analysis have been performed to analyze the performance using the EES software. Further, following conclusions were made from the results and discussion section;

- Incorporating the transcritical CO_2 (TCO_2) cycle as a bottoming cycle to the standalone hybrid Brayton cycle (HBC) resulted in a 12.05% improvement.
- The SPT subsystem (receiver and heliostats) accounted for the highest exergy destruction rate, comprising approximately 83.20% of the exergy destruction (total 45,164 kW) in the entire plant.
- According to the parametric analysis, net output power, overall plant energy and exergy efficiency, and CPR first increased before declining. The highest values 23.2%, 24.84%, and 14930 kW, respectively—were attained at an ideal CPR of 2.3. The overall performance of the plant is not significantly impacted by TCO_2 cycle parameters like PPR and TCO_2 turbine inlet temperature.
- The exergoenvironmental impact coefficient, with a high value of 4.028, reflects the lower exergy efficiency of the plant and suggests substantial potential for reducing environmental effects.
- The exergetic stability factor was determined to be 0.2483, which is close to the preferable value of one for a power-generating plant.
- This analysis offers the potential of developing a highly efficient power system for future carbon-free power generation with less complexity as compared to previous research.
- The exergoeconomic analysis of this resent work need to be performed in future study.
- This study is confined to peak load conditions owing to the absence of a solar energy storage system.

NOMENCLATURE

A	Area (m^2)
$\dot{E}X$	Rate of exergy (kW)
$\dot{E}D$	Exergy destruction rate (kW)
N_{hel}	Number of heliostats
$\dot{Q}$	Rate of heat interaction (kW)
$\dot{m}$	Mass flow rate (kg/s)
h	Specific enthalpy (kJ/kg)
T	Temperature (K)
s	Specific entropy (kJ/kg·K)
$\dot{W}$	Power (kW)

Abbreviations

WHRU	Waste heat recovery unit
COND	Condenser
TCO_2	Transcritical CO_2
sCO_2	Supercritical CO_2
SPT	Solar power tower
PPR	Pump pressure ratio
ORC	Organic Rankine cycle
HBC	Helium Brayton cycle
HT	Helium turbine
DNI	Direct normal irradiation (W/m^2)

HC Helium compressor
CPR Compressor pressure ratio
IHE Intermediate heat exchanger

Subscripts
e exit
i inlet
rec receiver
0 dead condition
j particular state
hel heliostat
ref reference/reflectivity

Greek letters
η Efficiency
ε Effectiveness

AUTHORSHIP CONTRIBUTIONS

Authors equally contributed to this work.

DATA AVAILABILITY STATEMENT

The authors confirm that the data that supports the findings of this study are available within the article. Raw data that support the finding of this study are available from the corresponding author, upon reasonable request.

CONFLICT OF INTEREST

The author declared no potential conflicts of interest with respect to the research, authorship, and/or publication of this article.

ETHICS

There are no ethical issues with the publication of this manuscript.

STATEMENT ON THE USE OF ARTIFICIAL INTELLIGENCE

Artificial intelligence was not used in the preparation of the article

REFERENCES

[1] IEA. Electricity 2024. Available at: https://www.iea.org/reports/electricity-2024. Accessed on Dec 25, 2025.

[2] Khan Y, Raman R, Rashidi MM, et al. Thermodynamic analysis, and experimental investigation of the water spray cooling of photovoltaic solar panels. J Therm Anal Calorim 2023;148:5591–5602. [Crossref]

[3] Khan Y, Singh D, Sharma S, Gupta S, Joshi SK, Tevatia A. Comprehensive analysis of a high temperature solar powered trigeneration system: An energy, exergy, and exergo-environmental (3E) assessment. Proceedings of the Institution of Mechanical Engineers, Part C: J Mech Eng Sci 2024;238(16):8446-8463. [Crossref]

[4] Khan Y, Singh D, Kumar S, Mishra S, Anjum A, Asdaque PMG. Performance evaluation of the combined helium Brayton cycle and organic Rankine cycles for solar power tower application A comparative study. J Renew Sustain Energy 2024;16(6). [Crossref]

[5] Khan Y, Mishra RS. Parametric (exergy-energy) analysis of parabolic trough solar collector-driven combined partial heating supercritical CO2 cycle and organic Rankine cycle. Energy sources, part A: recovery, utilization, and environmental effects 2020;1-27. [Crossref]

[6] Kumar KS, Razak A, Yadav A, Rao PR, Majdi HS, Khan TY, Singh K. Experimental analysis of cycle tire pyrolysis oil doped with 1-decanol+ TiO2 additives in compression ignition engine using RSM optimization and machine learning approach. Case Stud Therm Eng 2024;61:104863. [Crossref]

[7] Khandelwal N, Sharma M, Singh O, Shukla AK. Recent developments in integrated solar combined cycle power plants. J Therm Sci 2020;29(2):298-322. [Crossref]

[8] Chauhan MK, Chauhan AK, Khan Y, Singh AP. Experimental and theoretical investigation of thermal efficiency and productivity of single slope basin type solar distillation system using honey-comb. J Ther Eng 2023;9(6):1559−1571. [Crossref]

[9] Khan Y, Tevatia A, Apparao D, Singh N, Mishra S. Experimental investigation to evaluate thermal performance of a solar cooker with evacuated tube solar collector using different heat transfer fluids. J Ther Eng 2024;10(5):1335−1346. [Crossref]

[10] Farabi SN, Habib K, Mim M, Zaed MA, Ali SA, Younas M, Saidur R. The future of solar-driven interfacial steam generation for sustainable water desalination: drivers, challenges, and opportunities-Review. Results Eng 2024;102649. [Crossref]

[11] Shukla AK, Sharma A, Sharma M, Nandan G. Thermodynamic investigation of solar energy-based triple combined power cycle. Energy Sources, Part A: Recovery, Utilization, and Environmental Effects 2019;41(10):1161-1179. [Crossref]

[12] Khan Y, Singh D, Caliskan H, et al. Exergoeconomic and Thermodynamic Analyses of Solar Power Tower Based Novel Combined Helium Brayton Cycle-Transcritical CO2 Cycle for Carbon Free Power Generation. Global Challenges 2023; 7: 2300191. [Crossref]

[13] Islam MT, Huda N, Abdullah AB, Saidur R. A comprehensive review of state-of-the-art concentrating solar power (CSP) technologies: Current status and research trends. Renew Sustain Energy Rev 2019;91:987-1018. [Crossref]

[14] Khan Y, Mishra RS. Thermo-economic analysis of the combined solar based pre-compression supercritical CO2 cycle and organic Rankine cycle using ultra-low GWP fluids. Therm Sci Eng Prog 2021;23: 100925. [Crossref]
[15] Sachdeva J, Singh O. Thermodynamic analysis of solar powered triple combined Brayton, Rankine, and organic Rankine cycle for carbon free power. Renew Energy 2019;139:765-780. [Crossref]
[16] Fan G, Song J, Zhang J, Fu Z, Gong X, Dai Y, Markides CN. Thermo-economic assessment and systematic comparison of combined supercritical CO2 and organic Rankine cycle (SCO2-ORC) systems for solar power tower plants. Appl Therm Eng 2024;236:121715. [Crossref]
[17] Khan Y, Mishra RS. Performance analysis of a solar-based novel trigeneration system using cascaded vapor absorption-compression refrigeration system, Int J Refrig 2023. [Crossref]
[18] Habibi H, Zoghi M, Chitsaz A, Javaherdeh K, Ayazpour M, Bellos E. Working fluid selection for regenerative supercritical Brayton cycle combined with bottoming ORC driven by molten salt solar power tower using energy–exergy analysis. Sustain Energy Technol and Assess 2020;39:100699. [Crossref]
[19] Liu Y, Wang Y, Huang D. Supercritical CO2 Brayton cycle: A state-of-the-art review. Energy 2019;189:115900. [Crossref]
[20] Ehsan MM, Awais M, Lee S, Salehin S, Guan Z, Gurgenci H. Potential prospects of supercritical CO2 power cycles for commercialisation: Applicability, research status, and advancement. Renew Sustain Energy Rev 2023;172:113044. [Crossref]
[21] Li MJ, Zhu HH, Guo JQ, Wang K, Tao WQ. The development technology and applications of supercritical CO2 power cycle in nuclear energy, solar energy and other energy industries. Appl Therm Eng 2017;126:255-275. [Crossref]
[22] Gkountas AA, Benos LT, Nikas KS, Sarris IE. Heat transfer improvement by an Al2O3-water nanofluid coolant in printed-circuit heat exchangers of supercritical CO2 Brayton cycle. Therm Sci Eng Prog 2020;20:100694. [Crossref]
[23] Chai L, Tassou SA. Influence of Operation Parameters on Thermohydraulic Performance of Supercritical CO2 in a Printed Circuit Heat Exchanger. Heat Transf Eng 2024;1-19. [Crossref]
[24] Al-Sulaiman FA, Atif M. Performance comparison of different supercritical carbon dioxide Brayton cycles integrated with a solar power tower. Energy 2015;82:61-71. [Crossref]
[25] Atif M, Al-Sulaiman FA. Optimization of heliostat field layout in solar central receiver systems on annual basis using differential evolution algorithm. Energy Convers Manage 2015;95:1-9. [Crossref]
[26] Javanshir A, Sarunac N, Razzaghpanah Z. Thermodynamic analysis of simple and regenerative Brayton cycles for the concentrated solar power applications. Energy Convers Manage *2018;*163:428-443. [Crossref]
[27] Hashemian N, Noorpoor A. Assessment and multi-criteria optimization of a solar and biomass-based multi-generation system: Thermodynamic, exergoeconomic and exergoenvironmental aspects. Energy Convers Manage 2019;195:788-797. [Crossref]
[28] Zainul R, Basem A, Alfaker MJ, Sharma P, Kumar A, Al-Bahrani M, Pandey S. Exergy, exergoeconomic optimization and exergoenvironmental analysis of a hybrid solar, wind, and marine energy power system: A strategy for carbon-free electrical production. Heliyon 2024;10(16). [Crossref]
[29] Yang K, He Y, Du N, Yan P, Zhu N, Chen Y, Lund PD. Exergy, exergoeconomic, and exergoenvironmental analyses of novel solar-and biomass-driven trigeneration system integrated with organic Rankine cycle. Energy 2024;301: 131605. [Crossref]
[30] Rahimimotlagh Z, Ahmadi A. Energy, exergy, exergoeconomic and exergoenvironmental analysis and optimization of combined solar, SRC cycles with compressed air energy storage (CAES) and methane production system. Energy Convers Manage 2024;317:118855. [Crossref]
[31] Qi X, Yang C, Huang M, Ma Z, Hnydiuk-Stefan A, Feng K, Li Z. Conventional and advanced exergy-exergoeconomic-exergoenvironmental analyses of an organic Rankine cycle integrated with solar and biomass energy sources. Energy 2024;288:129657. [Crossref]
[32] Zhou F, Zhu L, Fu W, Sardari F. Thermodynamic and exergoenvironmental analysis of a new solar-driven cogeneration system integrated with a solar still desalination unit. Appl Therm Eng 2023;234:121241. [Crossref]
[33] Cavalcanti EJC. Exergoeconomic and exergoenvironmental analyses of an integrated solar combined cycle system. Renew Sustain Energy Rev 2019;67:507-519. [Crossref]
[34] Su Z, Yang L, Wang H, Song J, Jiang W. Exergoenvironmental optimization and thermoeconomic assessment of an innovative multistage Brayton cycle with dual expansion and cooling for ultra-high temperature solar power. Energy 2024;286:129581. [Crossref]
[35] Guo JQ, Li MJ, Xu JL, Yan JJ, Wang K. Thermodynamic performance analysis of different supercritical Brayton cycles using CO2-based binary mixtures in the molten salt solar power tower systems. Energy 2019;173:785-798. [Crossref]
[36] Trevisan S, Guédez R, Laumert B. Thermo-economic optimization of an air driven supercritical CO2 Brayton power cycle for concentrating solar power plant with packed bed thermal energy storage. Solar Energy 2020;211: 1373-1391. [Crossref]

[37] Niu X, Ma N, Bu Z, Hong W, Li H. Thermodynamic analysis of supercritical Brayton cycles using CO2-based binary mixtures for solar power tower system application. Energy 2022;254:124286. [Crossref]
[38] Wan X, Wang K, Zhang CM, Zhang TC, Min CH. Off-design optimization for solar power plant coupling with a recompression supercritical CO2 Brayton cycle and a turbine-driven main compressor. Appl Therm Eng 2022;209:118281. [Crossref]
[39] Lu Q, Zhao J, Fang S, Ye W, Pan S. Investigation of thermodynamics of the supercritical CO2 Brayton cycle used in solar power at off-design conditions. Sustain Energy Technol Assess 2022;52:102361. [Crossref]
[40] Bai W, Li H, Zhang X, Qiao Y, Zhang C, Gao W, Yao M. Thermodynamic analysis of CO2–SF6 mixture working fluid supercritical Brayton cycle used for solar power plants. Energy 2022;261:124780. [Crossref]
[41] Ma YN, Hu P, Jia CQ, Wu ZR, Chen Q. Thermo-economic analysis and multi-objective optimization of supercritical Brayton cycles with CO2-based mixtures. Appl Therm Eng 2023;219:119492. [Crossref]
[42] Khademi M, Ahmadi A, Dashti R, Shirmohammadi R. Thermoeconomic optimization of a solar-assisted supercritical CO2 Brayton cycle, organic Rankine cycle and multi-effect distillation system. Energy Rep 2022;8: 13494-13503. [Crossref]
[43] Liu Y, Wang Y, Zhang Y, Hu S. Design and performance analysis of compressed CO2 energy storage of a solar power tower generation system based on the S-CO2 Brayton cycle. Energy Convers Manage 2021;249: 114856. [Crossref]
[44] Goyal A, Sherwani AF. Optimization of exergetic performance and payback period of organic rankine cycle integrated vapor compression refrigeration system based on exergy, economic, and environmental criteria. J Ther Eng 2023;9(3):648-658. [Crossref]
[45] Khan Y, Mishra RS, Raman R, Hashmi AW. Parametric evaluation of solar integrated combined partial cooling supercritical CO2 cycle and Organic Rankine Cycle using low global warming potential fluids. J Ther Eng 2023;9(5):1140−1152. [Crossref]
[46] Cao Y, Dhahad HA, Togun H, Anqi AE, Farouk N, Farhang B. Proposal and thermo-economic optimization of using LNG cold exergy for compressor inlet cooling in an integrated biomass fueled triple combined power cycle. Int J Hydrogen Energy 2021;46(29):15351-15366. [Crossref]
[47] Olumayegun O, Wang M, Kelsall G. Closed-cycle gas turbine for power generation: A state-of-the-art review. Fuel 2016;180:694-717. [Crossref]
[48] Khatoon S, Kim MH. Performance analysis of carbon dioxide based combined power cycle for concentrating solar power. Energy Convers Manage 2020;205:112416. [Crossref]
[49] Dezfouli AHM, Niroozadeh N, Jahangiri A. Energy, exergy, and exergoeconomic analysis and multi-objective optimization of a novel geothermal driven power generation system of combined transcritical CO2 and C5H12 ORCs coupled with LNG stream injection. Energy 2023;262:125316. [Crossref]
[50] Abdollahpour A, Ghasempour R, Kasaeian A, Ahmadi MH. Exergoeconomic analysis and optimization of a transcritical CO2 power cycle driven by solar energy based on nanofluid with liquefied natural gas as its heat sink. J Therm Anal Calorim 2020;139(1):451-473. [Crossref]
[51] Meng N, Li T, Kong X, Gao X. Advanced exergy and exergoeconomic analyses and a case study of a novel trans-critical CO2 cycle with pressurization process for hot dry rock. Energy Convers Manage 2021;246: 114687. [Crossref]
[52] Khan Y, Mishra RS, Singh AP. Performance comparison of organic Rankine cycles integrated with solar based combined cycle: A thermodynamic and exergoenvironmental analysis. Proc Inst Mech Eng Pt C J Mechan Eng Sci 2024;238(1):233-248. [Crossref]
[53] Khan Y, Raman R, Rashidi MM, Said Z, Caliskan H, Hoang AT. Thermodynamic and exergoenvironmental assessments of solar-assisted combined power cycle using eco-friendly fluids. J Therm Anal Calorim 2024;149(3):1125-1139. [Crossref]

J Ther Eng, Vol. 12, No. 1, pp. 212−228, January, 2026

Journal of Thermal Engineering
Web page info: https://jten.yildiz.edu.tr
DOI: 10.14744/thermal.0001074

Research Article

Analysis of thermal, chemical and physical properties of paraffin and beeswax blended fuels for hybrid rocket applications

Saravanan G[1,*], Avi THUMAR[1], Ayush DEVAK[1], Amritansh SINGH[1]

[1]*Department of Aerospace Engineering, SRM Institute of Science and Technology, Kattankulathur,Tamil Nadu, 603203, India*

ARTICLE INFO

Article history
Received: 08 October 2024
Revised: 10 January 2025
Accepted: 25 February 2025

Keywords:
Blended Fuels; Beeswax; Chemical and Physical Characterization; Fourier Transform Infrared Spectroscopy (FTIR); Paraffin Wax; Scanning Electron Microscopy (SEM); Thermal; X-Ray Diffraction (XRD)

ABSTRACT

Fuels made of paraffin and beeswax was created for hybrid rocket engines, and carbon, boron, and aluminium powders were added. Scientists used Scanning Electron Microscopy, X-ray Diffraction, and Fourier Transform Infrared Spectroscopy for study of these fuels' thermal, chemical, and physical properties. The fuels were found to form homogeneous mixtures, and key chemical structures were identified. In tests, a beeswax-based fuel blend provided a 15% greater heat of fusion and 10% greater thermal stability than the pure paraffin-based fuels, and improved mechanical and combustion performance compared to the same properties of the paraffin fuels, providing an increase of specific impulse of up to 12%. The results indicate that paraffin / beeswax combinations show promise as a green, convenient and high performance fuel in a hybrid rocket.

Cite this article as: G S, Thumar A, Devak A, Singh A. Analysis of thermal, chemical and physical properties of paraffin and beeswax blended fuels for hybrid rocket applications. J Ther Eng 2026;12(1):212−228.

INTRODUCTION

The increasing need for environmentally sustainable propulsion systems has prompted the exploration of bio-derived fuels as safer alternatives to conventional rocket propellants. Traditional solid rocket fuels often contain hazardous chemicals, posing significant risks during handling and combustion. This study investigates the feasibility of using paraffin and beeswax, which are non-toxic and renewable, as hybrid rocket fuels. The research focuses on evaluating the physical, chemical, and thermal properties of these wax-based fuels, enhanced with additives like carbon, boron, and aluminium powders, to optimize their performance. The findings address the demand for safer, high-efficiency fuels employed in small satellite launch systems, sounding rockets, and educational rocket engines, where safety and environmental impact are critical considerations. By characterizing the structural and combustion properties of these bio-derived blends, this work provides insights into their potential applications in modern aerospace propulsion. This paper explores sustainable practices in the design and application of hybrid rocket propulsion systems that use environmentally friendly propellants and fuel additives to minimize the carbon footprint and toxic emissions traditionally associated with rocket

***Corresponding author.**
*E-mail address: gasaravan@yahoo.co.in

This paper was recommended for publication in revised form by Editor-in-Chief Ahmet Selim Dalkilic

Published by Yıldız Technical University Press, İstanbul, Turkey
Yıldız Technical University. This is an open access article under the CC BY-NC license (http://creativecommons.org/licenses/by-nc/4.0/).

launches. This paper has highlighted the advantages of hybrid systems that provide cleaner, safer, and cheaper operations than standard solid or liquid propel. The paper has also highlighted the case studies and developments within sustainable propellant formulations that will allow hybrid rocket motors to meet sustainability standards in future designs. The hybrid rocket has been recognized as a transitional technology that can enable more sustainable space exploration and technology development [1]. This paper investigates the environmental impact and performance characteristics of hybrid rocket fuel formulations that have the potential to reduce toxicity, increase performance and to improve the stability of the combustion behavior of the propellant. The paper also explores the use of selected additives and chemicals to increase the regression rate of the fuel, as well as to control the toxic by-products generated in the combustion. Experimental lab tests and simulations show the feasibility of new hybrid fuels and their potential as an alternative to conventional propellants. The investigation is part of a worldwide trend towards greener and more sustainable aerospace technologies and contributes to making space exploration and other space missions less harmful to the environment while maintaining high performance and reliability of hybrid rocket engines [2]. The objective of this study was to investigate the utility of beeswax (BW), an organic compound, as a solid hybrid rocket fuel. BW was combined with ethylene-vinyl acetate and activated charcoal, and the thermal stability and ballistic performance were characterized using thermogravimetry analysis (TGA) and a laboratory scale hybrid rocket motor. The results show that EVA improves thermal stability and AC improves thermal degradation. Despite a marginal reduction in thermal stability, AC has a positive effect on regression rates. The addition of EVA and AC increases fuel viscosity, which influences regression rates. While pure BW has higher regression rates, it burns less efficiently than blends with EVA and AC. This shows that these additives can improve performance, as the combustion efficiency can reach 94% at some additive concentrations. [3] This paper describes research done by students and faculty on the combustion of unconventional bio-derived fuels in a lab-scale hybrid propellant rocket engine (HPRE). The research focuses on lard, paraffin, and beeswax, investigating their non-toxic, non-explosive combustion when combined with various oxidizers, including aluminium powder, as an additive. The primary goals are to determine regression rates and investigate losses from melted, unburned bio fuels to replace conventional toxic and explosive fuels used in NASA-sounding rockets. Over sixty experiments were carried out, with results presented at aerospace conferences. These included regression rate equations for paraffin wax mixed with 10% aluminium powder and a new way to predict fuel losses that haven't been burned by using measurements of exhaust temperature [4].This study looks into the effects of coating nano-sized aluminium powders with different chemical compounds on the regression rate of a reference HTPB solid fuel for hybrid propulsion. Coatings, such as stearic acid, palmitic acid, and esters, have a significant impact on ballistics, with the majority of formulations exhibiting increased regression rates. F-ALEXE coated with an ester significantly improves performance across all oxidizer fluxes. However, the performance of formulations containing stearic acid-coated powders is inconsistent, irrespective of the use of air-passivated or chemically passivated powders. The laboratory coating process is simpler and safer, but environmental factors can influence thermochemical properties. Further research should include numerical simulations to better understand coating decomposition and its interactions with binder pyrolysis and metal oxidation to optimize solid fuel production [5]. The paper builds on a 2010 study that examined the combustion of unconventional bio-derived fuels in a small-scale HPRE. It investigates the combustion of fuels such as paraffin, beeswax, and lard with oxygen, hydrogen peroxide, and nitrous oxide, as well as additives, and calculates regression rate formulas. The research entails designing and testing the HPRE and presenting findings on bee's wax combustion with oxygen at the 51st AIAA Meeting and Exhibit. It describes an indirect method for estimating unburned fuel losses based on combustion product temperatures, demonstrating the HPRE's reliability and establishing correlations between theoretical and experimental variables. The study suggests that oxidizer mass flux can be used as a universally applicable factor for regression rate approximation. It also shows promising results in predicting unburned fuel losses, but these results need to be confirmed by conducting more experiments [6]. An innovative composite fuel containing paraffin wax and LDPE was developed and tested in slab and hybrid rocket motors to study droplet entrainment and combustion properties. The regression rate goes up a lot as the LDPE weight percentage goes up. PR95PE05 has a rate that is 3.9 times higher than HDPE, which makes it burn more efficiently, similar to Stanford University's SP-1a fuel. The chamber pressure spectrum analysis showed that there was no significant instability. This shows that PR95PE05 is a better hybrid rocket fuel in terms of its mechanical strength, combustion performance, and stability [7]. Hybrid rocket technology combines solid fuel combustion with gaseous or liquid oxidizers, providing advantages over conventional solid and liquid rockets. Despite its lower mechanical strength than paraffin wax, people use beeswax, a bio-based fuel, for its environmentally friendly properties. EVA and charcoal are added to beeswax to improve its mechanical properties. Five beeswax formulations containing varying amounts of EVA and charcoal are developed and tested for mechanical properties. The resulting fuel samples have porosity in the range of 0.42-0.84%, indicating high quality. The FTIR analysis confirms that the mixture is uniform without any chemical reactions. Blending beeswax with 20% EVA increases the tensile strength by about 8.1% and elongation to 42%. Furthermore, the addition of 2% activated charcoal increases tensile strength by 8.8% and elongation by 13.4% [8]. A new environmentally friendly hybrid rocket propellant that combines paraffin, stearic acid, and coal.

Mechanical testing at normal and sub-zero temperatures shows that the inclusion of stearic acid and coal increases the propellant's tensile, compression, and flexural strength. Macrostructural and microstructural analyses reveal only minor flaws due to raw material composition and manufacturing methods. Gaseous oxygen-powered hybrid rocket motor firing tests confirm that the new propellant and conventional paraffin-based propellant exhibit comparable specific impulses across varying oxidant-to-fuel ratios. Notably, the absence of hazardous substances such as ammonium perchlorate or aluminium ensures a low environmental impact. Simulation results show that the developed propellant emits negligible amounts of harmful compounds during combustion, making it a promising candidate for low-temperature hybrid rocket technology [9]. A hybrid rocket motor predictive performance model based on thermodynamic and gas dynamic relationships. The MATLAB code was developed using the NASA-CEA equilibrium chemistry code to calculate combustion product gases and an empirical regression rate correlation. Using conservation of mass and the ideal gas law, the model can predict chamber pressure variations and instantaneous performance parameters such as the thrust and specific impulse of the theoretical rocket engine. The model has been verified by comparison with hot-fire test data taken from a laboratory scale hybrid rocket engine that uses paraffin wax fuel and nitrous oxide propellant [10]. The combustion of pure beeswax and beeswax mixed with 10% aluminium powder in a small-scale hybrid propellant rocket engine as part of ongoing research on non-traditional bio-derived hybrid rocket fuels. Beeswax, along with paraffin and lard, is being tested as an alternative to hazardous fuels in NASA-sounding rockets. The study aims to better understand combustion processes, including additives, combustion rates, HPRE operational characteristics, and losses from partially melted bio-derived fuels. Findings from a compact HPRE and testing apparatus were presented at various aerospace meetings. The study presents regression rate formulas for various grain port diameters and evaluates the impact of unburned beeswax losses on combustion. The study also includes a comparison with paraffin wax combustion [11]. The traditional hybrid combustion theory is expanded to include solid fuels that produce a liquid layer when burned. This new theory elucidates how viscosity and surface tension influence droplet entrainment in the gas stream, resulting from the instability of the liquid layer. Entrainment has a big effect on the gasification process, especially in real-life hybrid rocket applications where fuels that melt have faster regression rates than normal materials like HTPB. This theory also applies to solid cryogenic hybrids, explaining the high regression rates observed in cryogenic materials such as solid pentane and oxygen. Stanford University's laboratory experiments confirm the validity of this theory, particularly in paraffin-derived fuels [12]. The combustion of paraffin and paraffin with aluminium powder in a small-scale Hybrid Propellant Rocket Engine (HPRE) is part of a larger investigation into alternative bio-derived fuels. NASA rockets designed these as non-toxic, non-explosive fuels such as paraffin, beeswax, and lard, instead of the customary fuels. This study seeks to better understand the combustion processes, regression rates, HPRE operation, and unmelted biofuel losses. Results from a compact HPRE system were presented at conference proceedings with an aerospace focus. Recent research findings such as regression rate formulas of the paraffin containing 10% aluminium powder and new techniques for prediction of unburned fuel losses within the study's scope [13], such as aluminium, cane sugar and linseed oil, boron and carbon black on paraffin wax-based fuels for hybrid rockets. The melt process and the same additives are in these mechanical strength and thermal properties. Differential Scanning Calorimetry (DSC) and compressive as well as tensile tests show that metallic polyethylene (PE) additives increase the strength, modulus, and burning properties better. DSC analysis found a decrease in melting enthalpy, indicating improved entrainment during combustion. Ballistic tests have indicated that PE reduces regression rates while increasing rates with Al and B and CB additives. In total, these test results indicated that paraffin-based fuels and additives are more effective and often have advantages for hybrid rockets and tactical missiles, because they are more rigid and burn more efficiently [14]. There is some work done on determining the mechanical properties of waxes and hydroxyl-terminated polybutadiene (HTPB), with special attention paid to the quality of the grain structure and its strength. Tensile strength and Young's modulus characterize Among HTPB, tensile strength is the lowest. FTIR and SEM analyzes show that the elongation ratio of beeswax is much higher than that of other beeswax and paraffin wax, along with differing surface morphology. The study stresses the importance of such research in advancing hybrid rocket fuels with their advantages over liquid and solid propellants by weight and structural integrity despite their transport limitations. The mechanical properties such necessary for optimal fuel performance need further research [15].

Boron's in nanoparticle size are suspended into a solid fuel matrix such as paraffin wax fuel. This has been used to investigate the performance of an opposed flow burner in the application of solid fuel-ducted rocket (SFDR) with low boron concentrations to increase the regression rates. Since the agglomerates ejected before combustion and the residues left after combustion have different chemical compositions, hybrid propellant-based SFDR systems can be used in the near future. The combustion behavior and morphological changes of boron-based SFDR systems during combustion can be described using this study as a guide for development and design [16].

The sensitivity test for the combustion behaviour of the aluminium particles between the burnt propellant surfaces and inert walls was conducted with the variation of the propellant surface velocity, propellant surface temperature, radiation temperature, number of parcels, particle diameter, turbulent Prandtl number, and turbulent Schmidt number. The biggest finding in this study was that turbulent numbers

had little effect on maximum temperature; however, surface temperature as well as other velocities were found to be sensitive to perturbations, with surface temperature perturbations affecting gas temperature the most. The aim of this study was to understand the effects on the combustion of the solid rocket propellant in down-burning, for computational dynamic modeling and to recommend parameters to be used for determining the effects of the influences [17].

For example, additive manufacturing (AM) techniques such as 3-D printing could be used to create composite solid rocket propellant grains, in which the port geometries of customary casting could be replaced with detailed shapes not limited by mandrels or could vary in shape to achieve greater port burn rates and thrust profiles customized for particular missions. This work has shown that it is possible to produce composite propellant grains with a uniform pore structure and predetermined porosity levels. The process can be applied to rocket propulsion systems, pyrotechnics, and explosives [18].

Here is the complete history of solid propellant, its development and future prospects. The military background of solid rocket propellant systems and perceptions that the technology for solid rockets had not progressed greatly were reasons for favoring liquid propellant systems in space propulsion. The entrepreneurial drive in solid rocket development is highlighted, as is the contribution of key organizations such as Thiokol and Aerojet.

Despite the challenges, additive manufacturing opens up new possibilities for solid propellant design, such as custom port geometries and controlled porosity, which could revolutionize propulsion systems. The paper also addresses common misconceptions about the safety and reliability of solid rockets in comparison to liquid alternatives, emphasizing the continued importance of solid propellants in military and space applications. Looking ahead, the solid-propellant industry faces shifts in focus, material supply challenges, and the need for new expertise, all of which present both obstacles and opportunities for solid rocket technology innovation [19]. A new solid fuel for hybrid rockets that combines paraffin wax with 5% (SF4) and 10% (SF-10) LDPE demonstrated improved combustion performance, with higher regression rates and efficiency when compared to polymeric and pure paraffin fuels. SEM revealed homogeneous blends, whereas TGA confirmed the immiscibility of components during degradation. DSC data showed that higher paraffin content reduced LDPE melting temperature, whereas blended fuels with lower paraffin wax had lower total specific melting enthalpy, consistent with the additive rule. It was also found that as LDPE loading increased, the linear coefficient of thermal expansion decreased. Thus, a new composition of rocket fuel with low LDPE loadings was made, unlike customary phase change materials [20]. This propellant experiences some issues in manufacturing due to the low tensile strength and bonding mechanism, but the regression rate of the paraffin-based fuel is much greater than that of customary hybrid rocket fuel, three to four times greater. To address this, EVA was combined with paraffin-based fuel to reduce shrinkage while increasing tensile strength. The experiment revealed that adding EVA increased maximum strength by approximately 1.6 times and maximum strain by up to 2.2 times at a 20% EVA concentration. However, at the same EVA content level, a 35% decrease in the regression rate accompanied this strength increase [21]. The aim of the study was to improve the mechanical properties of the wax used in the hybrid rocket system with EVA. As the wax-EVA mixture hardened, its mechanical properties got better. For example, a blend of 20% EVA and 80% wax could stretch about 17%, while pure wax could only stretch 4%. Higher EVA content was associated with improved mechanical performance. Regression rate studies showed that EVA addition decreased the regression rate, countered by the presence of the bluff body at the front end. It was found that the regression rate of fuels containing 20% EVA and 80% wax was less than that of pure wax but three and a half times that of polymeric fuels [22]. The main goal is to highlight the importance of SEM in explaining the differences between physical and mechanical properties of the improved clays before and after improvement. Clays pose challenges in the construction industry because of their low strength, high compressibility, and swelling potential. Traditional interpretations of clay's behaviour may not be entirely consistent with their properties, necessitating microstructural analyses. The SEM has been used in the study of microstructure of clays and additives, and is used here to investigate microstructural properties of the modified clay. This gives researcher's new information about how clay particles and additives behave, which could help them explain physical or mechanical phenomena they didn't understand before [23]. Ever since the Chinese first developed primitive powder rockets in the 13th century, the notion of reaction propulsion has captivated the human race. This propulsion system utilizes ejected matter to facilitate motion. Despite the advancements in rocket propulsion, a lack of understanding of propellant combustion characteristics has impeded scientific progress in reaction propulsion. Propellant formulation, testing and use, however, will remain empirical until the physicochemical mechanisms are well characterized. Conventional composite propellants are heterogeneous mixtures of a crystalline oxidizer (ammonium perchlorate or ammonium chlorate), a polymer fuel binder and metal fuel dopants. The combustion of composite propellant is a complex process, due to the interaction between the different components of the propellant and the combustion wave. Scanning electron microscopy (SEM) can be a useful tool to investigate how the ingredients interact with each other and provide additional information about the combustion mechanism (the clustering of the metal particles, the dissociation of the oxidizers and the interaction between them). Therefore, the aim of this article is not only to show the usefulness of this SEM study on solid propellant combustion, but also to show the complexity of this field of study, and recommend more wide-ranging works on propellant combustion [24]. Systems under study used hydroxyl-terminated polybutadiene as binder and were

analyzed before and after accelerated aging. Isothermal aging tests have been conducted at temperatures of between 65 and 85 degrees Celsius. Fourier transform infrared spectrometry and scanning electron microscopy by X-ray scattering were employed to investigate the impact of accelerated aging on solid fuel samples. The utilization of infrared spectrometry yielded valuable insights into the impact of temperature on the functional groups associated with the binder and oxidant within the examined formulations. The SEM/EDX analysis facilitated the examination of the morphology of representative material samples at both the micrometric and sub-micrometric scales [25]. The Combustion Research Laboratory at the University of Arkansas at Little Rock (UALR) uses non-intrusive spectral techniques and a Fourier Transform Infrared interferometer to study flame sources. The laboratory has previously found several problems trying to use emission spectroscopy as an analytical tool of nonsteady sources due to flickering (pulsing) as an interference frequency in sources such as the UALR Hybrid Rocket plume. A mathematical model of the interferometer and its interaction with these interference frequencies was created and simulated in MATLAB software. This simulation allows for the prediction of the amount of noise that source intensity fluctuations will introduce into the IR signal. Several researchers have developed mathematical relations between the interference frequencies in the time domain of the interferogram and in the frequency domain of the spectrum [26]. X-ray diffraction characterizes crystalline samples using an important non-destructive technique because the technique determines their chemical composition, crystal phases, texture, average crystallite size, crystallinity, strain, and defects. X-ray scattering from lattice planes in the sample constructively overlaps at certain angles to produce diffraction peaks. The intensities of these peaks depend upon the atomic structure of the lattice. As a result, XRD patterns are useful for identifying periodic atomic configurations. This review summarizes recent advances in XRD techniques observed in a variety of fields over the last five years, including pharmaceuticals, forensic science, geology, microelectronics, the glass industry, and corrosion analysis [27]. Carbon nanomaterial research has increased dramatically in recent decades as a result of their numerous applications. The effect of paraffin wax soot, carbon black precursors, and the new manufacturing processes on the soot microstructure was studied. Structural and morphological investigation of soot samples was carried out by X-ray diffraction (XRD), and High Resolution Scanning Electron Microscopy (HRSEM) combined with Electron Dispersive Spectroscopy (EDS). There are distinct differences in the mean lateral dimensions of the aromatic lamellae, the stacking height, the average 002 plane spacing (d(002)), and the degree of aromaticity between paraffin wax soot and carbon black.They have low levels of disorder, evidenced by a low ratio of γ to band intensity. Scanning electron microscopy (SEM) images show carbon Nano sphere particles which are not uniform with a size range between 26 and 94 nm [28].

LITERATURE REVIEW SUMMARY

The exploration of bio-derived fuels, particularly paraffin, and beeswax, as alternative propellants for hybrid rockets has gained considerable attention due to their environmental benefits, cost-effectiveness, and safer handling properties Based on the Studies by Soojong Kim et al. [7] and Viatcheslav Naoumov et al. [11]. Several studies have been performed to investigate the use of fuel blends with additives such as aluminum, carbon and boron to improve combustion efficiency and increase mechanical strength, as shown in works by Syed alay hashim et al. [16] and Shinya Maruyama et al. [21]. Moreover, research conducted by Ural et al. [23] and Tudor Tiganescu [25] on fuel morphology and structural behavior using Scanning Electron Microscopy and Fourier Transform Infrared Spectroscopy has highlighted the role of additive composition in enhancing thermal stability. Despite these advancements, several limitations persist. Past studies by R.arun Chandru et al.[18] and Sri Nithya Mahottamananda et al.[8] often lack comprehensive characterization of fuel blends that combine multiple bio-derived waxes, and few provide detailed comparisons of the physical and thermal performance of these blends under hybrid rocket conditions .Also research by Andrei A. bunaciu et al. [27] and Anu N mohan et al. [28] have limited research on the direct influence of crystallinity and chemical bonding patterns, as revealed by X-ray Diffraction, on the combustion and stability of these bio-based fuels. To address these gaps, the present study systematically examines paraffin-beeswax fuel blends enriched with carbon, boron, and aluminum additives. Through the use of SEM, XRD, and FTIR analyses, the study provides a deeper understanding of how these components affect fuel morphology, thermal behavior, and combustion efficiency, offering new insights for advancing bio-derived fuels in hybrid rocket applications. This study offers an innovative perspective on the development of hybrid rocket propulsion through the exploration of bio-derived fuels, specifically paraffin and beeswax blends enhanced with carbon, boron, and aluminum powders. The majority of conventional solid rocket propellants are toxic and/or hazardous. In contrast, this study focuses on environmentally friendly and non-toxic bio-fuels. It presents an exhaustive study of bio-derived propellant compositions using advanced analytical techniques such as scanning electron microscopy (SEM), x-ray diffraction (XRD), and Fourier transform infrared (FTIR) analysis to provide perceptions into their structure, thermal and chemical properties. Lastly, this study seeks to investigate the synergistic effect of additives on the thermal stability and combustion performance of solid paraffin and beeswax fuels in order to optimize their use in hybrid rocket propulsion systems. The results from this study may help improve sustainable aerospace technology and the development of energy platforms for a safer and greener aerospace system.

MATERIALS AND METHODS

Fuel and Additives Selection

Paraffin wax mixes saturated hydrocarbons named alkanes. Alkanes have the molecular formula CnH2n+2, with n = number of carbon atoms in the alkane. At room temperature, paraffin wax hydrocarbons go from n = 20 up to n = 40. Its hydrocarbons have an average molecular weight of. That weight ranges from 300 to 600 g/mol.

This long straight-chain carbon-based polymeric structure gives the resulting polymer its crystalline structure and thermal properties. The selection of additives such as carbon, boron, and aluminum powder as well as potassium nitrate was based upon their ability to improve specific performance attributes, such as thermal stability, specific impulse, and combustion efficiency. Carbon was chosen due to its thermal conductivity, which distributes the heat uniformly over the fuel surface, increasing its regression rate and combustion stability. Boron was selected because of its high heat of combustion. This increases the flame temperature and energy density of the propellant. This optimizes the thrust and specific impulse. Aluminum has a high energy density. It also contributes a lot of heat and stabilizes the combustion process. Residue clumping needs control. Potassium nitrate acts as an oxidizer to provide additional oxygen. It also improves the fuel's performance. The above additives were chosen as they fit the criteria for hybrid rocket propellant additives which maximize the energy released and supply a steady burn, thereby improving performance.

Preparation of Fuel Samples

Beeswax and paraffin wax were used in the fuel samples with carbon, potassium, borax and aluminium powder as additives. The required amounts of wax and additives were weighed out, then ground down to powder in a pestle and mortar, and finally mixed together to create the fuel mix.(Table 1) The mixture of molten fuel was then poured into the mould. It was stirred to prevent the formation of voids and air bubbles, then left overnight to harden. The hybrid rocket motor is a rocket variant combining solid and liquid or gaseous propellants together. The oxidizer exists as a liquid or as a gas. It is injected within the combustion chamber, where it reacts with the solid fuel grain. A schematic of a hybrid rocket motor appears in Figure 2.

Combustion of Wax-Based Fuels in Hybrid Rockets

This simplicity and higher safety margin, controllability, and the lower environmental impact compared to solid propellant rockets, which often use highly toxic propellants, have led to hybrid rockets becoming popular for research and suborbital and space tourism applications. Even though these engines have certain advantages, the trade-off in performance losses, combined with inconsistent combustion stability, has meant that they have not gained much prominence in heavy-lift rockets, compared

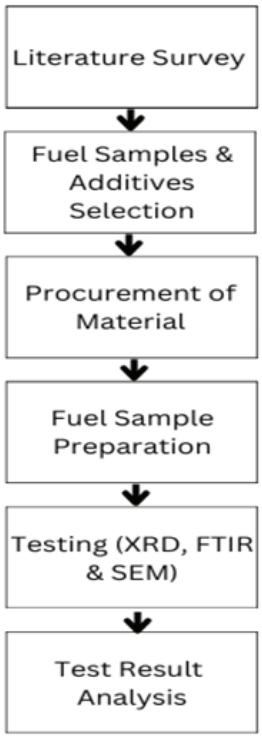

Figure 1. Process Flow Chart.

to pure liquid rocket engines or solid rocket engines. A hybrid rocket motor is a type of rocket engine that burns a solid fuel with a separate stored oxidizer, liquid or gaseous. The oxidizer enters the combustion chamber during operation then flows through the solid fuel. Someone ignites the solid fuel. This reaction combusts, creates hot gases as it vaporizes the solid fuel, and mixes it through the oxidizer inside the combustion chamber. The combustion gases are expanded through the nozzle to produce thrust. The mass flow rate of oxidizer can control the thrust, allowing the rocket to throttle as well as (in the case of hybrid fuel) shut down during flight. This allows the hybrid rocket to combine the simplicity and intrinsic safety of the solid rocket with the throttle and steering capability of the liquid rocket. For hybrid rockets, wax-based fuels are burned with solid, liquid, or gaseous propellant. Hybrid rockets typically use solid fuel with a gaseous oxidizer, using either oxygen or nitrous oxide, with wax the typical fuel component. The igniter lights the solid fuel grain in the combustion chamber to create thrust. The heat from the igniter melts a thin layer of wax upon the surface, which forms the liquid fuel as it melts. This means the oxidizer flows over the melted wax. The burning process vaporizes the wax, and it mixes with the vaporized fuel in order to burn during a combustion reaction (Properties of fuel samples shown in Table 2, Fixed and variable parameters are shown in Table 3). This produces hot gases that are then rapidly expanded to provide thrust. The high regression rate of paraffin based fuels is one of the reasons those are the preferred fuels. The

rate at which the burning surface of the solid fuel recedes is determined by heat transfer to the fuel, the viscosity of the melted layer, and the interaction between the vaporized fuel and oxidizer. The gases produced by the combustion reaction expand and are ejected through a nozzle at high speed, producing thrust according to Newton's third law. The nozzle design plays a crucial role in optimizing the thrust produced by the engine.

Table 1. Fuel samples composition

Fuel Sample	Beeswax	Paraffin Wax	Carbon Powder	Aluminium Powder	Borax Powder	Potassium Powder
40BW10C40A10B	40%	-	10%	40%	10%	-
40BW10C40P10B	40%	-	10%	-	10%	40%
50BW40A10B	50%	-	-	40%	10%	-
60BW15P10B	60%	-	-	-	10%	15%
0BW10C20B	70%	-	10%	-	20%	-
40PW10C40A10B	-	40%	10%	40%	10%	-
40PW10C40PN10B	-	40%	10%		10%	40%
50PW40A10B	-	50%	-	40%	10%	-
60PW15P25B	-	60%	-	-	25%	15%
70PW10C20B	-	70%	10%	-	20%	-

Table 2. Properties of Fuel samples

Properties	Beeswax	Paraffin Wax	Carbon	Aluminium	Borax	Potassium
Density (kg/m^3)	970	900	80	2,710	1730	862
Melting Temperature (°C)	62–65	59–63	3652-3697	660.37	743	63.25
Molecular weight (g/mol)	676	380	12	26.98	381.37	39.09

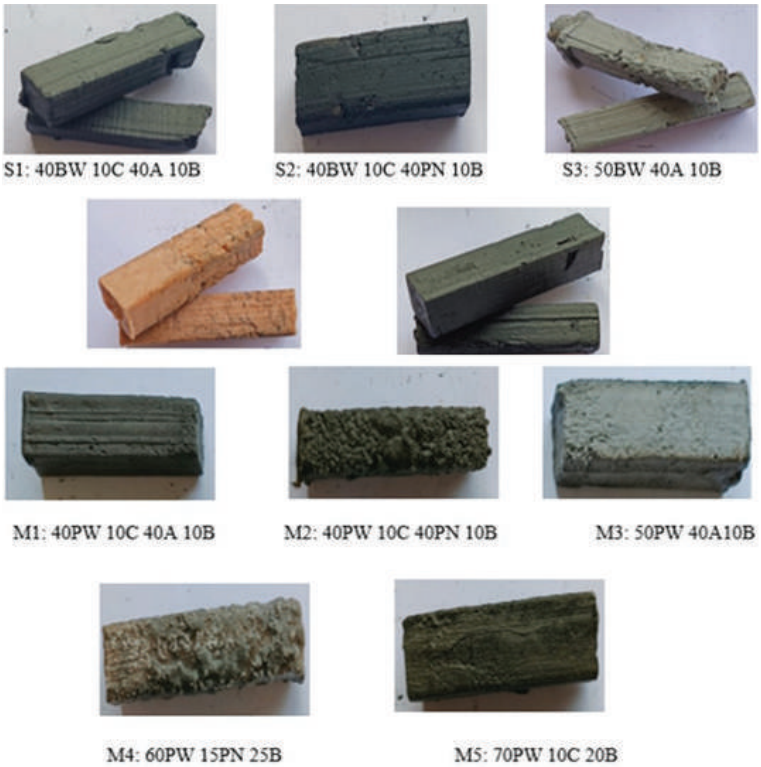

Figure 2. Blended Fuel Samples.

Table 3. Fixed and variable parameter

Parameter Type	Parameter	Description
Fixed Parameters	Fuel Type	Paraffin wax and beeswax, composition fixed per sample
	Oxidizer Type	The type of oxidizer used remains consistent (e.g., liquid oxygen or nitrous oxide).
	Combustion Chamber Dimensions	The dimensions of the chamber are fixed to maintain uniform testing conditions.
	Ambient Pressure	The experiments are conducted under the same atmospheric conditions.
Variable Parameters	Additive Concentration	The percentage of carbon, boron, and aluminum powders added to the fuel
	Oxidizer	The rate at which the oxidizer is injected into the combustion chamber.
	Fuel Grain Geometry	Variations in the shape and size of the fuel grains to observe performance changes.
	Temperature	Initial temperature of the fuel and oxidizer, which can vary to assess thermal behavior

Experimental Methods

XRD set-up details

An X-ray diffraction Spectrometer is an apparatus utilized for conducting X-ray diffraction analysis on diverse materials. This is an effective instrument for examining the crystallographic characteristics of solids, liquids, and powders. XRD instruments yield critical insights into atomic arrangement within a material's lattice, crystal structure, phase composition, crystal orientation, and additional structural attributes. Benchtop-type XRD machines were brought into use and samples were provided in powdered form. Specifications of the XRD machine used are:

- Cu Kα radiation
- Minimum Step Size: 0.02519
- Angle Range: 5° to 140°
- Detector Mode: Scanning line detector (one-dimensional), Static line detector (one-dimensional)

FTIR set-up

FTIR is applicable to organic as well as many inorganic materials and can determine covalence and functional groups. It has been used in the characterization of solid rocket propellant formulations and is an important tool in this field. FTIR has been applied in establishing standards and specifications for solid propellant formulations in respect to quality, performance and safety. The propellant formulation is a very complex mixture of oxidizer, binder, stabilizer, and additives. FTIR has been used to check the presence of the molecular fingerprints of the chemical components and formulations.

These species are contaminants or degradation products, and their presence can be used to determine propellant long-term stability. FTIR can also be used to monitor functional groups in propellant such as nitro or hydroxyl functional groups. The samples were given in powdered form. The specifications for the Fourier Transform Infrared Spectroscopy (FTIR) machine used are:

- Spectral range: 500 to 7500 cm^{-1}.
- Spectral resolution: Superior to 2 cm^{-1}.
- Precision of wave number: Superior to 0.01 cm^{-1}.
- Detector: DTGS.
- Rock Solid Interferometer: Gold mirrors (permanently calibrated).
- Holder: Standard sample mount measuring 2×3 inches, suitable for pellets as well.
- Accessory necessary for ATR configuration.

SEM set-up

In Scanning Electron Microscopy (SEM), a beam of focused electrons scans across the surface in a sample and emits secondary electrons, backscattered electrons, and characteristic X-rays that detectors find so they produce high-resolution images and obtain compositional information. Secondary electrons provide information on surface topography. Backscattered electrons give atomic contrast, together with X-rays providing chemical composition. These signals work in conjunction to let the SEM make detailed images and do material analysis. To prepare for the SEM analysis, the sample was crushed, dried in the laboratory oven, and a small amount from the sample was placed in the machine under the SEM alongside other samples. The SEM machine has various modes, which include Imaging modes (Standard, HR-SEM, STEM, dispersion mode, Opti-mode (magnetic samples), Low vacuum, EDX & Elemental Mapping).

RESULTS AND DISCUSSION

The chemical properties of paraffin and the additives carbon, boron, and aluminum allow paraffin and beeswax blend fuels to meet the performance requirements of hybrid rocket engines. Paraffin wax has a very high regression rate because the melt layer of wax that coats and cools the fuel surface evaporates rapidly, allowing the fuel to vaporize more easily. Despite the lower regression rate of beeswax, attributed to its more complex esters and fatty acids, its thermal stability and stability of its structure make it valuable. The thermal conductivity and the regression rate can be improved by the use of carbon and boron, and aluminum is best known as a high-energy additive. The effect of adding metal to the wax-biopolymer mix in hybrid rocket propellant results in an important increase in regression rates, according to Karabeyoglu et al. [12] and Hashim et al. [16]. The wax blend provides high

combustion efficiency because of the clean-burning hydrocarbon chains of wax and high thermal stability of beeswax. Further, FTIR analysis of product gases indicates that the presence of covalent carbon-hydrogen bonds in the mixture improves combustion and increases the calorific value. It has been shown that the flame acceleration and energy density of the mixture can be improved by the presence of additives such as aluminum and boron [4, 20]. The thermal stability of beeswax prevents softening and deformation before the operation temperature. The tensile and surface strength of the waxes is greatly increased by activated charcoal and/or EVA (Ethylene-Vinyl Acetate) copolymers. Non-toxic and environmentally friendly nature of the wax blends make them preferred alternative propellant types for hybrid rocket propulsion systems. A better combustion of the wax fuel blends can be achieved by adding aluminum powder into paraffin and beeswax fuels instead of carbon or boron. Due to its high energy, aluminum substantially increases the heat produced during combustion. This increases the regression rate and stabilizes the flame, which increases the thrust and specific impulse of the motor greatly. Other doping elements such as carbon mainly increase the thermal conductivity of alumina, boron can increase the ignition and flame temperature, aluminum can be preferred, but the use of aluminum can reduce thermal efficiency in terms of the combustion temperature gradients that can be created. The aluminum residues can also agglomerate. This can lead to reduced combustion efficiency and residues that require appropriate disposal or treatment. Aluminum is still widely used for high-energy propulsion. Stability and energy production of wax-based fuels strongly depend on the structure of monoesters, n-alkanes, and fatty acids they contain. Unlike other waxes, the higher thermal stability of the monoester bonds in beeswax is due to the fact that they break down at a higher temperature and produce non-toxic byproducts. Stable long-chain n-alkanes, which are the main components of paraffin wax, are well suited for combustion because they oxidize cleanly and liberate a lot of heat when burned, as their linear structures allow them to burn smoothly. Fatty acids, although non-energetic components of beeswax with other helpful additives, provide oxygenated fuels of lower energy density to the fuel blend. The n-alkanes, fatty acids and monoesters are thus blended to achieve an optimum combination of high energy density, thermal and combustion stabilities to provide stable and efficient operation at the temperature and pressure extremes of the combustion chamber and sustain the operation of the rocket engine.

XRD Results

X-ray diffraction or XRD analysis determines the crystalline structure, phase composition, and crystallinity of paraffin wax and composite fuel samples. XRD analyzes samples. The sample is irradiated by a monochromatic X-ray beam, and the resulting diffraction pattern is used to determine the atomic structure, phases, and the crystal grain size and shape (Table 4). Other than being useful for identifying crystal phases, XRD may be used for characterizing the solid state of paraffin wax, confirming the results of a SEM study, and distinguishing between different waxes, such as paraffin and beeswax. It may also be used in fuel systems, and production quality control. Paraffin waxes consist of the paraffin fractions with relatively pure long-chain alkanes and well-ordered crystalline structures. Its XRD spectrum is consistent with this, while the more complex mixture of esters and fatty acids in beeswax is less ordered. The structure of hybrid rocket fuel can have a major influence on fuel thermal stability and combustion. (Figure 3)

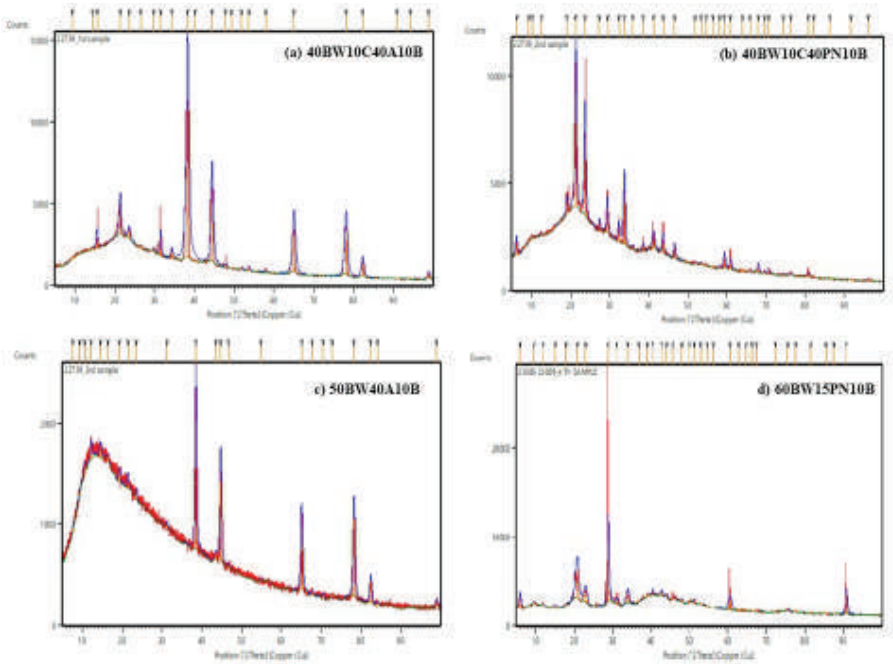

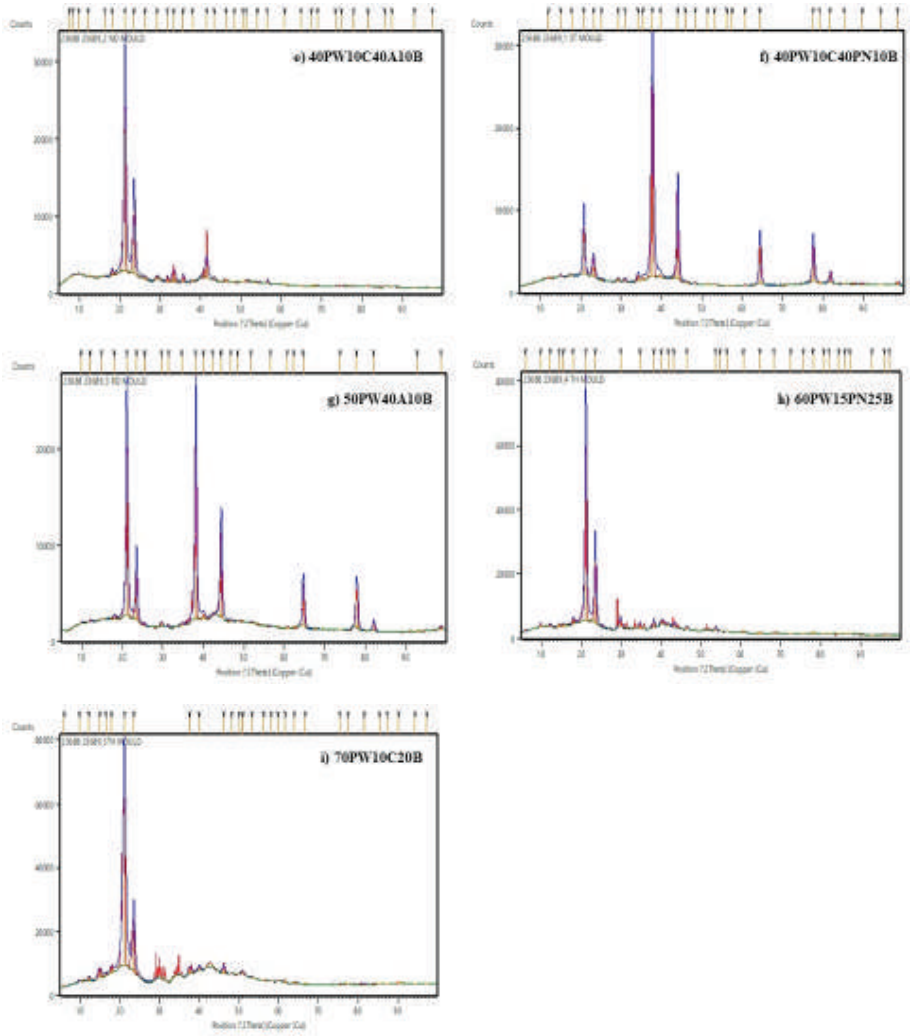

Figure 3. X-Ray Diffraction Pattern.

Table 4. X-Ray Diffraction results

Fuel Sample	Diffraction Angle (2Θ)	Bragg Angle (Θ)	Lattice Spacing (d-spacing) (A^0)	Miller Indices
40BW10C40A10B	38.49	10.20	5.01	100
40BW10C40PN10B	21.40	10.09	5.03	100
50BW40A10B	38.53	12.44	5.07	100
60BW15PN10B	29.91	10.02	5.09	100
40PW10C40A10B	37.76	12.22	5.01	100
40PW10C40PN10B	21.29	10.00	5.03	100
50PW40A10B	38.18	10.26	5.09	100
60PW15PN25B	21.18	10.33	5.01	100
70PW10C20B	21.00	10.75	5.03	100

The research on the x-ray diffraction for the crystalline property of wax types is very important. The knowledge gained from the analysis is further helpful in the future to understand the wax material properties, its effects on the hybrid rocket applications and the quality and performance of the hybrid rocket fuel systems.

FTIR Results

Besides providing a means to characterize the chemical species and bonding present, Fourier Transform Infrared Spectroscopy (FTIR) can be used to study the aging or degradation of propellants to provide an indication or comprehension of the long-term thermal or environmental aging stability of the propellant under investigation. FTIR is widely used for reliability and quality assurance applications as it is non-destructive, quick and highly accurate for the analysis of solid rocket propellants.

The samples with paraffin wax base (from 40PW10C40A10B-60PW15K25B) had values ranging from 2900.94 to 2904.8, and those with beeswax base (40BW10C40A10B-S5) from 2908.65 to 3668.61 (Table 5). The samples without aluminum differed only slightly in their values and those with paraffin wax base of 60% and 70%. The beeswax samples' values ranged from 2908.65 for 40BW10C40K10B to 3668.61 for the highest valued sample, 40BW100C0K20B. Potassium nitrate (KNO_3) addition decreased the peak value dramatically. The values of

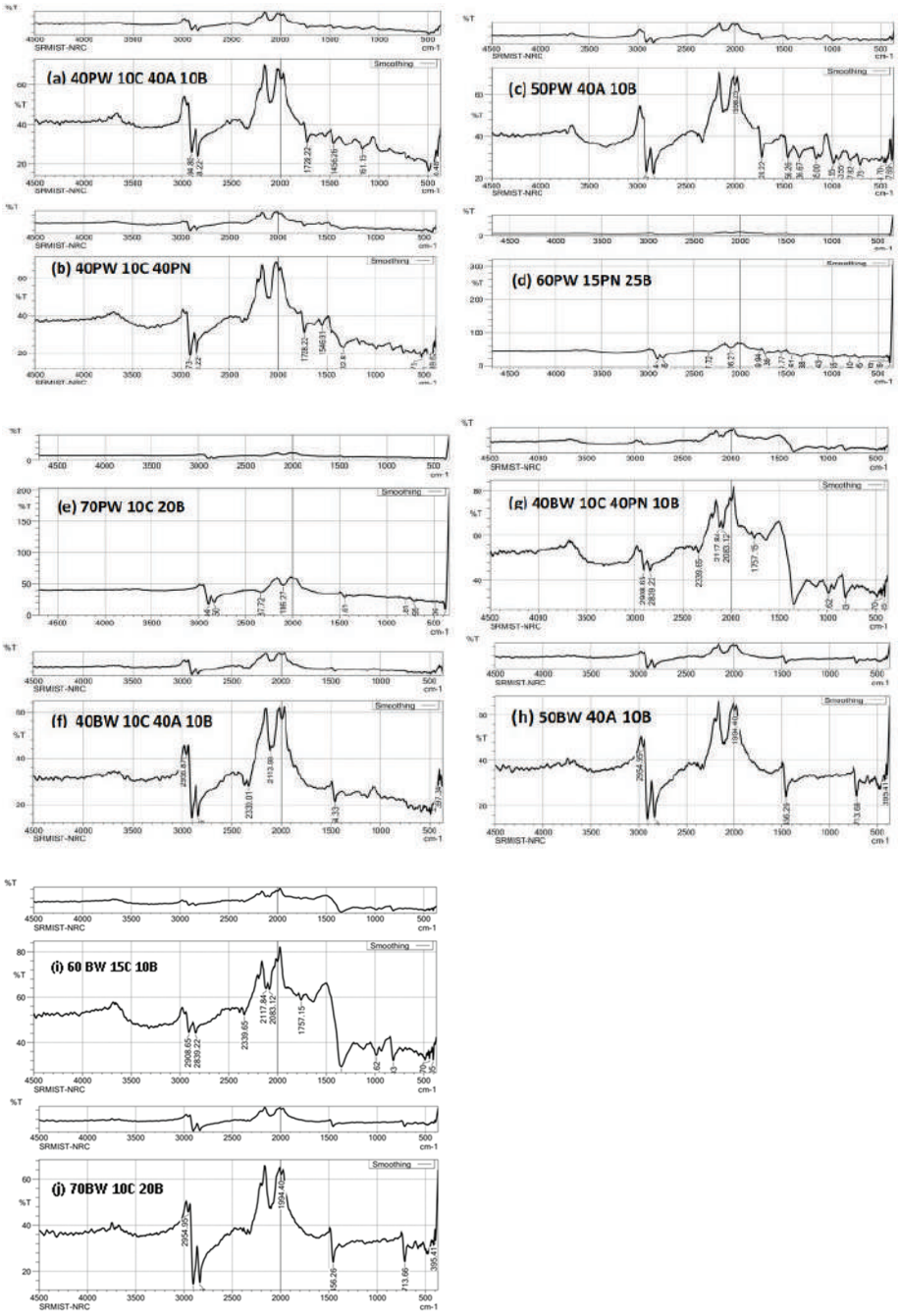

Figure 4. Fourier Transform Infrared (FTIR) spectroscopy spectra.

Table 5. Fourier Transform Infrared Spectroscopy Results

Fuel Sample	Peak Value
40BW10C40A10B	2956.87
40BW10C40PN10B	2908.65
50BW40A10B	2954.95
60BW15PN10B	3668.61
70BW10C20B	3668.61
40PW10C40A10B	2904.80
40PW10C40PN10B	2906.73
50PW40A10B	2904.80
60PW15PN25B	2900.94
70PW10C20B	2900.94

40BW10C40A10B and 50BW40A10B were almost similar but the bonding strength increased because of the addition of aluminum (Al) in them. [30, 31].

The fuel samples, 60BW15K10B and 10BW10C20B, recorded maximum values of 3668.61 indicating the base properties of beeswax can further optimize the binding power in the fuel. (Figure 4)

FTIR measures the absorption of infrared light from the molecular bonds. Different functional groups (C-H, C=O, O-H, etc.) have different absorption wavelengths. These values are plotted as an FTIR spectrum. For example:

- Peaks around 2900 cm^{-1} stretch C-H in long-chain hydrocarbons and allow efficient energy production during combustion.
- The strong O-H stretching causes the peak at a higher wavenumber (3668.61 cm^{-1}) in beeswax samples, so thermal stability improves.

The C-H and O-H groups cause higher combustion. They also cause specific impulse (Isp) properties. This makes beeswax a more suitable combustor fuel for hybrid rocket propellants. Although beeswax and paraffin wax are both composed of long-chain hydrocarbons, beeswax provides more stability to hybrid rocket propellants due to its superior molecular bonding and interactions. (Table 5)

Chemical groups such as alkanes, carbonyl and esters can be identified using FTIR to characterize the functional groups. The FTIR of beeswax identifies esters and fatty acids because their carbonyl peaks determine the physical and chemical properties of beeswax. The infrared spectrum of paraffin wax shows peaks corresponding to C-H stretching vibrations indicative of its simple hydrocarbon structure and the effect of its chemical composition on thermal stability and combustion.

SEM Analysis

Scanning electron microscopy has been used to study the paraffin wax morphology, and that of beeswax and other composition fuels. At ambient conditions, paraffin wax is solid at high molar mass. The wax is composed of crystalline platelets, while beeswax is liquid at room temperature and upon crystallization forms a much less dense material with smaller flakes.Based on SEM data, both waxes were found to have very similar elemental composition, dominated by carbon and oxygen. However, the paraffin composition (40PW10C40A10B) was more homogeneous than the beeswax composition (40BW10C40A10B) (Figure 5).

Under microscope analysis, paraffin wax is homogeneous with layers of different colors, but beeswax shows some topographical structure with a pasty, colloidal structure under high magnification. Due to a homogenous, evenly distributed structure, paraffin wax is thought to burn more uniformly than beeswax, which is less homogeneous. The irregular flakes produced in beeswax can cause localized hotspots and affect how clean it burns.

In SEM, a concentrated beam of electrons scans the surface of a material, and the emitted secondary electrons are detected to generate high-resolution images of the morphology of the surface of the specimen. This gives information about the homogeneity of the surface texture and the granulation. Such characteristics of the microstructure can also underline differences of waxes, such as paraffin (homogenous and smooth) and beeswax (multilayered, heterogeneous and with flakes). The morphology of the fuel also influences the mixing uniformity and the combustion efficiency.

It is also used to study the distribution of an additive such as aluminum or boron powder in a wax sample. In a sample of paraffin wax, a uniformly distributed additive may burn better, while beeswax samples tend to be not that homogeneous. This suggests that small homogeneities seen in the SEM images could be improved using chemical additives or advanced processing when samples are prepared with paraffin.

To explain these findings in the field, consider the following:

Combustion efficiencies and the thermal stability of the fuels are important values. For blended fuels, beeswax blends perform better than paraffin waxes because they present a 15% increase in the heat of fusion and a 10% increase in stability. Additives such as aluminium, boron and carbon have been used for both stabilizing regression rates, and stabilizing the fuel structure. In terms of analytical methods, Scanning Electron Microscopy can be used to study the mixing of the fuel as well as the particle distribution and interface structure of other porous rocket propellants. This is important to predict the behavior of engines in operation. XRD may also be used in quality control to analyze whether fuel samples' crystalline structures meet thermal stability requirements. FTIR (Fourier Transform Infrared Spectroscopy): Used to monitor chemical integrity and fuel degradation during storage.

Correlate Laboratory Results with Real-World Scenarios: Examine the advancements in regression rates concerning real-world rocket propulsion contexts, such as modest satellite launches, where improved fuel efficiency

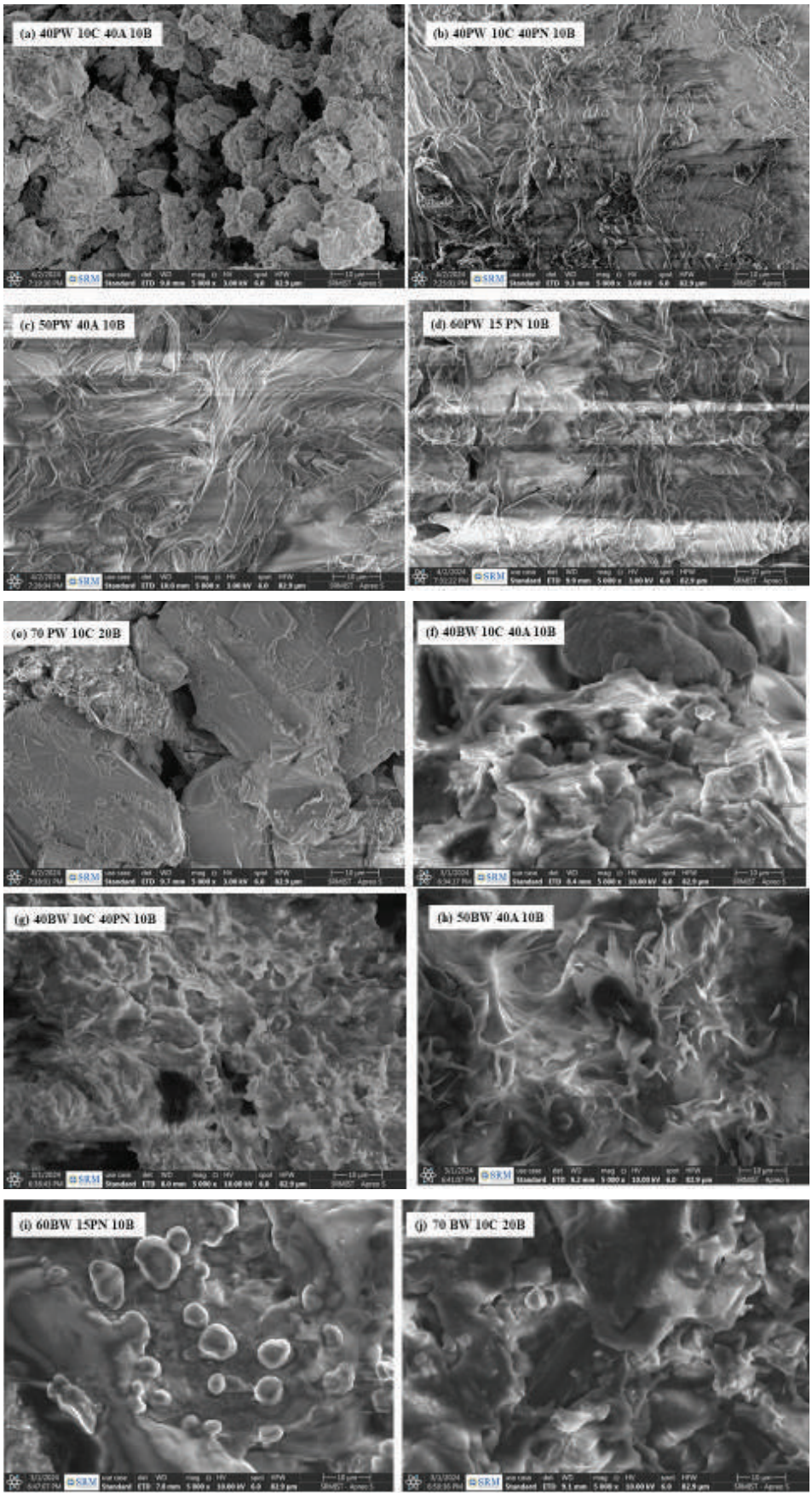

Figure 5. Scanning Electron Microscopy (SEM) Results.

might result in financial savings. Discuss the safety advantages, including the non-toxic and eco-friendly characteristics of the fuels, pertinent to instructional or low-impact space missions.

After the establishment of the field applications for these results:

Recommend incorporating these fuel samples into full-scale hybrid rocket engines to assess thrust, combustion efficiency, and performance in operational settings. Consider investigating alternative additions, including nanoparticles, to enhance regression rate and energy density. Perform lifecycle evaluations to measure ecological advantages, strengthening the argument for implementation in sustainable aerospace projects. Propose utilizing additive manufacturing to tailor fuel grain shapes, hence improving thrust profiles and efficiency for individual mission requirements. Such methods ease the transition from laboratory implementations of hybrid rocket technology to field applications of hybrid rocket technology.

The higher thermal stability and combustion performance of the fuels blended with beeswax further support what other researchers have reported. In terms of thermal stability and heat of fusion, the experimentally obtained values are 15% and 10% higher for the beeswax-blended fuels than the paraffins. This conforms to a work by Naoumov et al. [4], which shows that the use of bio-derived fuels (such as beeswax) and metallic additives can improve combustion performance, and another by Kim et al. [20] showing that adding polymers (such as LDPE) to paraffin also has an improving effect. The use of aluminum and boron additives also was shown to improve the regression rate and specific impulse (up to 12%). This is supported by the work of Karabeyoglu et al. [12] on improved regression rates of paraffin-fuels and the increase in performance compared to other solid propellants by the addition of metals, and of mechanical strengthening through the addition of EVA and activated charcoal demonstrated in your work and by Mahottamananda et al. [8], with EVA-beeswax blends exhibiting improved tensile strength and thermal resistance, further proving the efficacy of wax-based fuels as an environmentally-conscious, high performing fuel for hybrid rocket propulsion systems.

Keeping a blend of paraffin and beeswax in the right state can be difficult due to both these waxes melting at a low temperature. Paraffin becomes plastic at between 59 and 63 degrees Celsius. Beeswax melts at between 62 and 65 degrees Celsius. The structural integrity of these blends may degrade due to thermal cycling. This decline may cause handling difficulty and uneven combustion performance. These blends may become brittle and crack if stored and transported at very cold temperatures. The fuels are slowly oxidized by water and air, causing their constituents to change slightly and energy losses to occur. The least loss is achieved by storing the fuels in an air-sealed container at a stable temperature and in air with a low relative humidity. In addition to boiling point, wax-based fuels also have advantages over the conventional rocket propellant in being bio-derived, non-toxic and having lower quantities of hazardous waste as well as lower toxic emissions as burn products. We must consider by-products of the combustion process. Additives such as aluminum and boron can improve performance, but if burned underground, may produce fine particulates which are released and must be controlled to minimize their adverse effects on the environment. Inevitably, stored fuel can degrade and residuals can complicate disposal but, due to the low environmental impacts of wax-based fuels in comparison to other ingredients in some customary solid propellant formulations, they are an attractive choice of fuel within hybrid rocket propulsion systems.

CONCLUSION

SEM, XRD and FTIR can provide a lot of information. SEM could give us some information about surface microstructure that can help us to evaluate the overall homogeneity of fuel samples and how microstructure and surface texture are affecting combustion behavior (regression rates, stability of the combustion, etc.). XRD and the FTIR can be carried out for the analysis of the crystalline phases of the hybrid rocket fuel blends in different proportions and of the thermal and chemical stability of the additives dispersed in the wax matrix and can also help in finding out the type of bonding and functional groups across the blends and their thermal and chemical behavior.

The work characterizing the properties of these fuels forms the basis for producing safer, greener and more efficient hybrid rocket fuels. The work reported in this thesis examines the performance of hybrid rocket fuels using beeswax, paraffin wax and their mixtures as the solid fuel.

For the beeswax and paraffin wax (pure and mixtures), the XRD results show that the diffraction angle is not affected by the compositions and hence is consistent with the heterogenic blend structure. Thus the thermal properties of the blend such as specific heat, heat of fusion and melting point are mostly independent of the components. This conclusion is supported by the results of the SEM analysis. The FTIR spectra also showed that the blends were homogeneous. The bands corresponding to the maximum values were C-H stretching of alkanes, which are found in organic compounds.

The thesis contributes to the knowledge of paraffin wax, beeswax and some additives in hybrid rockets with respect to the environmental impact, mechanical properties and the thermal stability of this hybrid rocket propellant fuel. It adds to the knowledge of bio-derived fuels in hybrid rocket propulsion systems for the development of sustainable and efficient propellant fuels as alternatives to conventional solid fuels.

Future Scope

This work provided the first data for many of the bio-derived hybrid rocket fuels. Future work should include high

fidelity combustion experimentation and engine testing to determine the regression rates, specific impulses, and combustion efficiencies of these bio-derived fuels. Improvement of thermal stability and energy density and fuel behavior with the use of optimized additives like metallic nanoparticles or functionalized materials would also have to be studied. The manufacturing process will need to be scaled up, and the fuels would need to be tested in a rocket, either sounding rockets or small satellite launch vehicles. Life cycle assessment and other studies of the environmental impact of the whole life cycle of fuels would be helpful in assessing the comparative benefits of hybrid propulsion versus other fuels. New methods such as the additive manufacture of ideal grain geometries and machine learning design have potential to revolutionize hybrid propulsion. The development of bio-sourced fuels could enable clean heating, low-power propulsion systems, and green weaponry. Partnering with aerospace agencies and institutions could help create validation and optimization sites for biofuels, and ultimately environmentally-friendly propulsion systems for many missions. Further research and testing will ultimately determine whether wax-based fuels can be considered practical as a hybrid rocket fuel. Field testing in rocket flight is necessary to understand the flight characteristics of rocket fuels, including a fuel's regression rate, combustion efficiency and in-flight performance. Full scale engines have been used to simulate the high pressure and temperature conditions within a rocket engine for testing specific fuels. The tests would determine the specific impulse of the fuels and their thermal and mechanical stability under the long exposures of flight conditions. The fuel must be qualified through environmental testing for temperature stability, stability under humidity conditions and altitude pressure change. Other parameters that need to be tested include stability tests on the waxes over long periods of time and their shelf life. Any degradation due to oxidation, moisture absorption etc., needs to be tested. Another test needs to be performed on post-combustion and a study of the resulting gases and particulates produced during combustion. Any resulting impact of the wax fuel on the environment due to emissions and combustion byproducts also needs to be studied. The above parameters need to be studied to ensure that wax based fuels are reliable, safe, and capable of performing effectively as hybrid rocket propulsion propellants. Future studies examining the structure of wax-based fuels prior to, and post, exposure to thermal tests or combustion tests may provide additional information about the performance of the fuel within its operating environment. The way the fuel matrix deforms, cracks, or shrinks during thermal or combustion tests will provide information about its mechanical properties. Studies of these structures could provide perception into the stabilizing (or destabilizing) effects of aluminum, boron, and carbon additives, and also possibly lead to optimum solid-fuel blends. Knowledge of ways in which the structure affects the stability of these fuel modifications may eventually permit reliability of the fuels, particularly under long-term and high-pressure storage conditions, to be improved, and perhaps development of a mechanical configuration that may be close to optimum, both from the mechanical instability standpoint and, possibly, from the energy usage standpoint, in an actual engine environment.

NOMENCLATURE

BW	Beeswax
DSC	Differential Scanning Calorimetry
EVA	Ethylene-Vinyl Acetate
HPRE	Hybrid Propellant Rocket Engine
HTPB	Hydroxide-Terminated polybutadiene
LDPE	Low Density Polyethylene
PE	Polyethylene
PW	Paraffin Wax
SEM	Scanning Electron Microscopy
XRD	X-Ray Diffraction
FTIR	Fourier Transform Infrared Spectroscopy
OFB	Opposed Flow Burner
TGA	Thermo Gravimetric analysis
SFDR	Solid Fuel Ducted Rocket

ACKNOWLEDGEMENTS

The authors acknowledge the Nanotechnology Research Centre (NRC), SRMIST for providing the research facilities.

AUTHORSHIP CONTRIBUTIONS

Authors equally contributed to this work.

DATA AVAILABILITY STATEMENT

Authors confirm that the data that supports the findings of this study are available within the article. The raw data that supports the findings of this study are available from the corresponding author, upon reasonable request.

CONFLICT OF INTEREST

The authors declare no potential conflicts of interest with respect to the research, authorship, and/or publication of this article.

ETHICS

There are no ethical issues with the publication of this manuscript.

REFERENCES

[1] Afzal A, Soudagar MEM, Belhocine A, Kareemullah M, Hossain N, Alshahrani S, et al. Thermal Performance of Compression Ignition Engine Using High Content Biodiesels: A Comparative Study with Diesel Fuel. Sustainability. 2021; 13(14):7688. [CrossRef]

[2] Stojanovic N, Glisovic J, Abdullah OI, Belhocine A, Grujic I. Particle formation due to brake wear, influence on the people health and measures for their reduction: a review. Environ Sci Pollut Res 2022;29: 9606–9625. [CrossRef]
[3] Mahottamananda SN, Pal Y, Dinesh M, Ingenito A. Beeswax–EVA/activated-charcoal-based fuels for hybrid rockets: thermal and ballistic evaluation. Energies. 2022;15:7578. [CrossRef]
[4] Naoumov VI, Al-Masoud N, Skomin P, Deptula P. Undergraduate research on peculiarities of the combustion of ecologically clean paraffin wax fuels in hybrid propellant rocket engines. 53rd AIAA Aerospace Sciences Meeting. 2015. [CrossRef]
[5] Duranti E, Sossi A, Paravan C, DeLuca L, Vorozhtsov AB, Gromov A, et al. Nano-sized aluminum powders as energetic additives for hybrid propulsion: physical analyses and performance tests. AIDAA, CEAS 2011.
[6] Naoumov V, Knochenhauer N, Sansevero P, Adam G, Freeto C, Kimiecik T, et al. Research on the combustion of bio-derived fuels in hybrid propellant rocket engine. AIAA 2014. [CrossRef]
[7] Kim S, Lee J, Moon H, Sung H, Kim J, Cho J. Effect of paraffin-LDPE blended fuel on the hybrid rocket motor. AIAA 2010. [CrossRef]
[8] Mahottamananda SN, Dubey VK, Khaleel AA, Dinesh S, Wahab A, Kadiresh PN, et al. Mechanical characteristics of ethylene vinyl acetate mixed beeswax fuel for hybrid rockets. Springer 2021. [CrossRef]
[9] Cican G, Paraschiv A, Buturache AN, Hapenciuc A, Mitrache A, Frigioescu TF. Experimental research into an innovative green propellant based on paraffin–stearic acid and coal for hybrid rocket engines. Inventions. 2024;9:26. [CrossRef]
[10] Genevieve B, Brooks M, Pitot J, Roberts L. Performance modeling of a paraffin wax / nitrous oxide hybrid rocket motor. 49th AIAA Aerospace Sciences Meeting Including the New Horizons Forum and Aerospace Exposition. 2011. [CrossRef]
[11] Naoumov V, Nguyễn H, Alcalde B. Study of the combustion of beeswax and beeswax with aluminum powder in hybrid propellant rocket engine. 54th AIAA Aerospace Sciences Meeting. 2016. [CrossRef]
[12] Karabeyoglu A, Cantwell BJ, Altman D. Development and testing of paraffin-based hybrid rocket fuels. 37th Joint Propulsion Conference and Exhibit. 2001. [CrossRef]
[13] Naoumov V, Skomin P, Deptula P. Combustion of bio-derived fuels with additives and research on the losses of unburned fuel in hybrid propellant rocket engines. AIAA 2015. [CrossRef]
[14] Pal Y, Kumar KH, Li YH. Ballistic and mechanical characteristics of paraffin-based solid fuels CEAS Space Journal. 2019;11. [CrossRef]
[15] Dubey VK, Mahottama SN, Khaleel AA, Kadiresh PN, Thirumurugan M. Mechanical characteristics of paraffin wax, beeswax and HTPB as rocket propellant—a comparative study. Springer 2021. [CrossRef]
[16] Hashim SA, Karmakar S, Roy A, Srivastava S. Regression rates and burning characteristics of boron-loaded paraffin-wax solid fuels in ducted rocket applications. Combust Flame. 2018;191:287-297. [CrossRef]
[17] Griego C, Yilmaz N, Atmanli A. Analysis of aluminum particle combustion in a downward burning solid rocket propellant. Fuel 2019;237: 405-412. [CrossRef]
[18] Chandru RA, Balasubramanian N, Oommen C, Raghunandan BN. Additive manufacturing of solid rocket propellant grains. J Propul Power. 2018;34:1-4. [CrossRef]
[19] Davenas A. Development of Modern Solid Propellants. J Propul Power 2003;19. [CrossRef]
[20] Kim S, Moon H, Kim J. Thermal characterizations of the paraffin wax/low density polyethylene blends as a solid fuel. Thermochim Acta 2015;613. [CrossRef]
[21] Maruyama S, Ishiguro T, Shinohara K, Nakagawa I. Study on mechanical characteristics of paraffin-based fuel. AIAA 2011. [CrossRef]
[22] Kumar R, Periyapatna R. Studies on EVA-based wax fuel for launch vehicle applications; propellants, explosives, pyrotechnics. International Pyrotechnics Society 2016;41:2. [CrossRef]
[23] Ural N. The significance of scanning electron microscopy (SEM) analysis on the microstructure of improved clay: an overview. Open Geosciences 2021;13:197-218. [CrossRef]
[24] Boggs TL, Prentice JL, Kraeutle KJ, Crump JE. The role of the scanning electron microscope in the study of solid rocket propellant combustion. Naval Weapons Center China Lake CA 1974.
[25] Tiganescu T, Grigoriu N, Ginghina R, Epure G, Iorga O, Oncioiu R, et al. Analysis of unaged and aged composite rocket propellant formulations by FTIR and SEM/EDX. Chem Mater Sci 2022;84.
[26] Sproles RW, Wilson JD, Hudson MK. An analysis of FTIR emission spectroscopy of flickering / pulsing sources: application to rocket plumes. Int J Turbo Jet Engines 2004;21:211-221. [CrossRef]
[27] Bunaciu AA, Udristioiu EG, Aboul-Enein HY. X-Ray diffraction: instrumentation and applications. CRC 2015;45. [CrossRef]
[28] Mohan AN, Manoj B, John J, Ramya AV. Structural characterization of paraffin wax soot and carbon black by XRD. Asian J Chem. 2013;25:S76-S78.
[29] Shark S, Pourpoint T. & Son S, Heister S. Performance of dicyclopentadiene/H2O2-based hybrid rocket motors with metal hydride additives. J Propul Power 2013;29: 1122-1129. [CrossRef]

[30] Mushtaq A, Mukhtar HB, Shariff AM. Characterization of synthesized polymeric blend membranes enhanced by methyl diethanolamine for efficient co2 separation. Journal of Thermal Engineering 2021 ;7(2):71-82. doi: 10.18186/thermal.869098. [CrossRef]

[31] C. Nwosu E, Nsofor K, N. Nwaji G, Ononogbo C, Ofong I, V. Ogueke N, E. Anyanwu E. Extended experimental investigation of a double-effect active solar still with a paraffin wax, in Owerri, Nigeria. Journal of Thermal Engineering 2023 ;9(5):1189-1207. doi: 10.18186/thermal.1374686. [CrossRef]

J Ther Eng, Vol. 12, No. 1, pp. 229−253, January, 2026

Journal of Thermal Engineering
Web page info: https://jten.yildiz.edu.tr
DOI: 10.14744/thermal.0001075

Research Article

Residential building thermal transmittance simulation-based analysis in Tehran city with an approach to assess wall insulation

Ashkan HASSANI[1], Shooka Khoshbakht BAHRAMANI[1,*]

[1]*Department of Architecture and Urbanism, Islamic Azad University Central Tehran Branch, Tehran, 47781, Iran*

ARTICLE INFO

Article history
Received: 04 August 2024,
Accepted: 02 January 2025

Keywords:
Building Energy Efficiency; Simulation-Based Analysis; Tehran Urban Buildings; Thermal Insulation; Wall Insulation Materials

ABSTRACT

The article deals with the study related to thermal insulation of building walls in Tehran through energy consumption reduction, aiming to contribute to sustainability of the urban environment. In Iran, more than 40% of total energy consumption is related to the construction and housing sector, so optimization of the building thermal performance has a high relevance.
Insulation materials are increasingly being used in Tehran; however, there is still a lack of a comprehensive quantitative framework embracing local materials and building typology. In this regard, the equivalent of ten different insulation configurations has been simulated for thermal performance using Design Builder software in order to study their respective effects on energy efficiency. Each configuration includes variations in insulation types and thicknesses.
The results highlight that insulation materials, including polyurethane, fiberglass board, and mineral wool, are excellent thermal performance enhancers, while the high level is normally achieved by growing the heat balance. Besides, finding the optimal range of insulation thickness-2-6 cm-provides practically the maximum energy economy.
This quantitative framework will help architects and designers make informed choices about appropriate wall insulation materials in Tehran's buildings. The novelty of the present research is that, for the first time, such a study will focus on the specific climatic condition of Tehran and its local construction practice. These findings have broader implications for further research and urban planning, since this laid framework may be applied to the multiple Iranian cities with diverse climate zones, hence guiding sustainable building designs throughout the nation.

Cite this article as: Hassani A, Bahramani SK. Residential building thermal transmittance simulation-based analysis in Tehran city with an approach to assess wall insulation. J Ther Eng 2026;12(1):229−253.

INTRODUCTION

Thermal insulation of a building wall is crucial for reducing the loss of thermal energy in buildings. According to an investigation published in Case Studies in Thermal Engineering journal, Energy is one of the major challenge faced by mankind. Buildings consume approximately one-third of the total national energy in China, including energy consumption in transport, industries, appliances, buildings and so on, so the reduction of building energy consumption

***Corresponding author.**
*E-mail address: shooka.khoshbakht@iau.ac.ir

This paper was recommended for publication in revised form by Editor-in-Chief Ahmet Selim Dalkilic

Published by Yıldız Technical University Press, İstanbul, Turkey
Yıldız Technical University. This is an open access article under the CC BY-NC license (http://creativecommons.org/licenses/by-nc/4.0/).

is paramount for sustainability [1, 2]. Building energy usage is a significant issue in numerous countries and cities. Tehran, Iran's capital, is encountering this issue in a comparable manner. As the investigation entitled" Thermal analysis model of a building equipped with a green roof and its energy optimization", The construction and housing sector uses more than 40% of energy in Iran [3]. Neglecting this issue in Tehran, the capital city of Iran, could lead to negative consequences for energy usage, ultimately resulting in significant heat loss in urban buildings.

Although Tehran uses thermal insulation to varying degrees, research on the types of insulation materials used indicates that there is no clear framework that illustrates the range of thermal insulation options for walls. In addition, the lack of a quantitative framework for wall insulation materials can negatively affect the architectural design of buildings in Tehran, and they do not have access to a suitable reference that specified insulation materials quantitatively. In accordance with this issue, there is a research gap in the field of quantitative study of these insulations and their effectiveness in Tehran. Architects and building designers have paid little attention to this issue throughout the design process because of their low efficiency and limited quantity.

To address this problem, future research should develop a quantitative framework for thermal insulation materials for building walls based on Tehran's building wall design typology and thermal insulation materials that are readily available in the Iranian market. The research findings and the quantitative framework that were developed would allow Tehran architects and building designers to carefully consider the type of wall thermal insulation materials when designing buildings. The research framework presents the innovative method of insulation materials quantitative analysis.

LITERATURE REVIEW

Building Thermal Transmittance

The assessment of energy efficiency of heating and wall layers is considered as important component to energy efficiency in the building context. This area has been considered in prior literature and included aspects of insulation thickness, thermal mass, and heat transfer coefficients. The literature review also provided a considerable body of literature on insulation layer thickness optimization in regard to evaluating indicators of thermal resistance [4]. This comprised published research on insulating layers alongside assessing the dynamically assessed heat-transfer properties of proposed insulating layer characteristics [5]. An optimization characterization of the thermal insulation-layer characteristics of the building envelope exterior-wall systems was also discussed to account for a life-cycle economic assessment [6]. Experimental research has been conducted to analyze the heat flows through ventilated wall systems with different types of heat-conductive connectors [7]. Using vacuum insulation panels (VIP) was investigated to reduce heat energy loss through walls by lowering the thermal transmittance of lightweight steel frame (LSF) wall systems [8]. Cardboard was also assessed as an environment-friendly wall thermal insulation for low-energy prefabricated buildings [9]. The External Thermal Insulation Composite System (ETICS) is a common passive strategy to obtain energy savings in existing buildings, and its thermal performance decay has been evaluated through laboratory tests [10]. Filling the empty air cavity between two layers of building materials with insulation can also reduce energy loss through opaque envelope surfaces [11]. The research entitled "Climate change and ideal thermal transmittance of residential buildings in Iran" aimed to determine the degree to which the thermo-physical parameters of building envelope materials must be altered in order to maintain their ideal thermal performance during climate change. In this regard, optimal thermal transmittances (U-values) of residential building envelopes for both present and future climate scenarios were calculated, and compared. As a result, the investigation concluded that future ideal U-values in the central and northern regions will be either higher or lower than current values. For areas of high cooling demand, future U-values are likely to be less than ideal U-values, and with the possibility of being the least possible [12]. In another investigation conducted in 2021, the objective of this research was to ascertain the thermal transmittance of external walls for single-family homes and to establish the optimal thickness of thermal insulation using energy simulation to maintain heating energy consumption under climate change conditions while complying with state regulations in the Los Ríos region of Chile. It was demonstrated that for each time period and in each geographical location of the region, the optimal U-value of the external walls is different [13].

Significance of Layer Optimization in Wall Construction

Building wall layer optimization attempts to determine the optimal combination of insulation thickness and position to enhance the thermal performance of building walls [14]. In an investigation, the wall layer optimization process aims to minimize the total cost while considering the insulation thickness, AC load, and energy consumption cost [15]. The best overall performance was achieved by a wall with three layers of insulation, each 26 mm thick, placed inside, middle, and outside, followed closely by a wall with two insulation layers, each 39 mm thick, placed in the middle and outside [6, 14]. In another study conducted in 2011, insulation layer optimization was analyzed in the Riyadh climate zone, and the researcher wanted to determine the effect of one, two, or three layers of insulation in various locations. The findings demonstrate that the ideal thickness of an insulating layer is independent of where it is placed within the wall and that, in the case of many layers, the total optimum thickness of those layers is equal to the optimum

thickness of a single layer [14]. In another article, which was based on Iran's different climate zones, it was strongly advised to maximize the insulation thickness of the walls. The yearly heating and cooling loads of a modeled building in Iran's climate zones were computed using numerical analyses, with insulation materials of varying thermal conductivities and costs were used as external wall layers. According to the results, ranged from 0.79 to 11.39 cm, with glass wool identified as the best insulation for overall cost reduction [16]. The research entitled "Investigation of the wall's optimum insulation position from a maximum time lag and minimum decrement factor point of view" concentrated on the wall insulation layer position to maximize heat conduction time lag, and four-centimeter-thick insulation was placed in different positions on a 20-cm-thick wall. As part of the research conclusion, significant time lags and minimal decrement factors occur when half the insulation is placed on the outer surface of the wall and the other half in its mid-center plane [17].

Thermal Analysis through Simulation Models

Thermal simulation of building walls is a key aspect of building design and energy efficiency [18]. Several studies have been published related to modeling the thermal performance of a building wall, especially in the context of historical or multilayer wall for retrofit scenarios. While a study that investigated the heat transfer process has a similar aim in supporting building retrofits and decreasing energy consumption [19]. The worth of the data obtained through the study include its contribution of long-term data monitoring regarding long-term process and numeric simulations, and the insight of applying numerous wall materials and properties to model the thermal behavior of building walls [20].

As a standard process, the work of evaluating and interpreting monitoring data for building wall thermal simulation is made more robust by integrating long-term monitoring data with numerical simulations. Each of the following tasks are typical for long-term thermal assessment of building wall systems:

- **Long-term monitoring**: A monitoring system is implemented to perform long-term assessment of the thermal performance of the building wall.
- **Numerical Simulation**: Based on the established methodology, numerical modeling software is used to formulate a numerical model at the component level of the wall system. That is run simulations of material types that are identified in the in the database, and the simulation data is reviewed to select the most effective materials to minimize the differences between the simulated data and monitored data.
- **Optimization**: In this step, the materials that were selected are used to produce the first optimized simulation.
- **Assessment**: Assess reliability and robustness of the numerical simulations with a data comparison of the monitored data and numerical simulated data.
- **Interpretation**: Evaluate the simulations' results based on the monitored data to assess the thermal performance of the component wall system, to aid decision making for energy efficiency target calculations and comfort of use measures [20].

There are many simulation methods to assess the thermal transmittance of the walls of buildings. These methods include experimental, numerical, and analytical methods. Research that the present study has conducted included the following:

- Research presented a new and simple way to assess the wall thermal transmittance, focusing on assessing its feasibility. This study has used simulation and experimental methods [21].
- Research compared the thermal transmittances of lightweight steel-framed wall systems, using both experimental and numerical methods. This study compared thermal variances through the thermal conductivity of distinct components of lightweight steel-framed wall systems using a more complex geometric properties in its evaluation [22].
- Research conducted an overview and comparison of six analytical methods used to determine the thermal transmittance of lightweight steel-framed wall systems. The review consisted of careful analysis of the estimation methodology along with a comparison of the accuracy of each analytical method [23].

Literature Critical Analysis

To summarize the reviewed studies, in the first point, the impact of insulation layer placement on the dynamic heat transfer of building walls was investigated with an emphasis on the optimization of insulation thickness. Economic evaluations guided the consideration of thermal insulation properties, with a particular focus on vacuum insulation panels [VIPs) and external thermal insulation composite systems [ETICS) for limiting heat loss. Another option is to fill the air cavities with insulation. From another perspective, filling air cavities with insulation materials is also recognized as an effective strategy. Wall layer optimization involves determining the optimal combination of insulation thickness and layer placement while considering total cost and energy consumption. From another perspective, the performance of one, two, or three layers of insulation was analyzed. In Iran's climate zones, numerical investigations have determined ideal insulation thickness and material. One study focused on maximizing heat conduction time lag by positioning insulation layers and concluded that placing insulation outside and the mid-center of the wall resulted in significant time lags and minimal decrement factors.

Based on the reviewed investigations, there is a lack of specific focus on the Iranian context, particularly considering its unique climate conditions and building practices. The multi-climatic nature of Iran significantly influences the extent of thermal energy loss in buildings across different regions. While various regions require analysis,

conducting this research for Tehran, the high-density capital, is particularly necessary. Second, economic evaluation of thermal insulation analysis relies on regional data, potentially overlooking localized factors that influence cost-effectiveness in Iran. Therefore, this research seeks to provide a quantitative framework based on the design typology of buildings in Tehran and the local thermal insulation materials as a tool for architects in Tehran enabling them to use this framework to design buildings based on numerical data and address the lack of such a practical tool.

MATERIALS AND METHODS

According to the research title, it is important to have a comprehensive method that covers all aspects of building wall thermal transmittance and heat consumption. Therefore, a simulation-based approach using Design Builder software is considered. This section describes the key steps of the methodology.

Design Builder was chosen as the simulation software for this study because of its capabilities control in assessing the thermal performance of building walls in different environments. In this investigation, Tehran's climatic conditions will be considered. The ability to conduct a detailed examination of different building insulation and layering configurations is unique. The selected versions - Design Builder version 6.10.006 and Energy Plus version 8.9 - formed the basis for modeling and energy simulation in this study. According to Design Builder website, easy-to-use tools allow for the comparison of different design options, identification of the best solutions and high-quality reports, and rendering of graphics to help communicate results to project stakeholders in an easily understandable way.

Methodology Steps Description

- **Building modeling**: the first phase involves two dimensions building modeling using the engineering drawing software Autodesk AutoCAD version 2020. After that, three-dimensional modeling was conducted using Design Builder. Figures 1-2 show a 2D model, and Figure 3 shows the 3D model. In the next part, each part of the plan was defined as a specific zone, as is apparent in Figure 1 coloring, and Table 1 expresses them separately. It is considerable that Zone 1 (Figs. 4 - 5) is considered the main part of the simulation process in this investigation.
- **Material property assignment**: According to the aforementioned case study, the simulation process is

Figure 1. Building plan zoning.

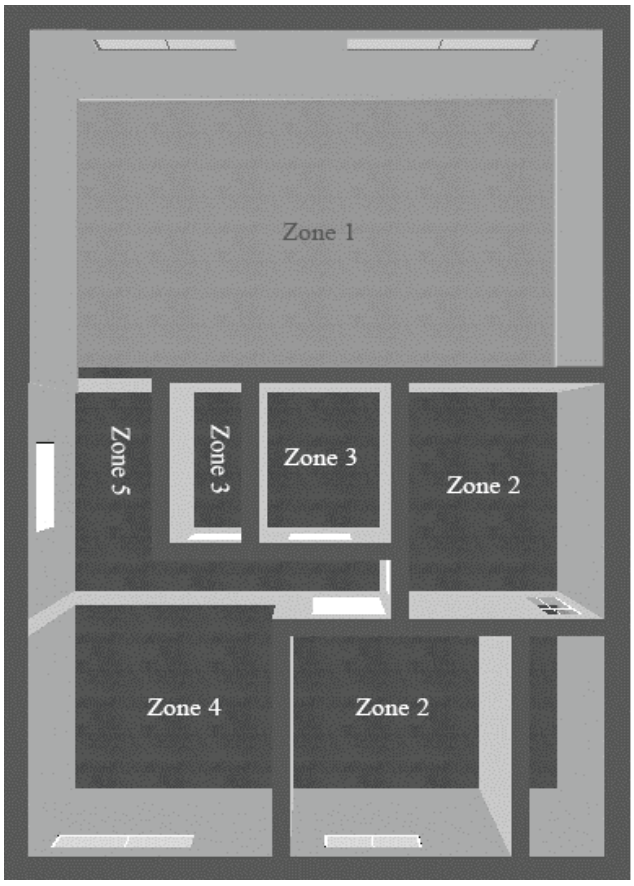

Figure 2. Building plan 2d model zoning.

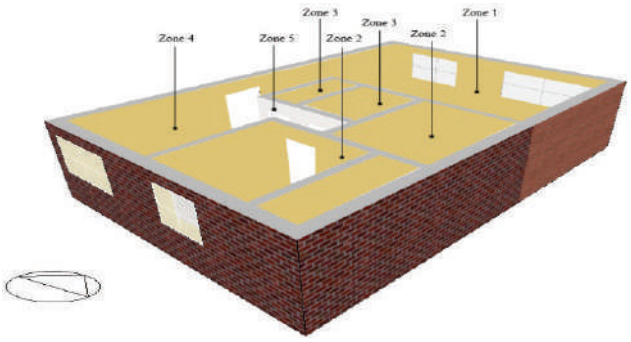

Figure 3. Building 3d model zoning.

Table 1. Plan spaces zoning

Num.	Space in plan	Zone
1	Living area	1
2	Bedroom	2
3	Bathroom – Toilet	3
4	Kitchen	4
5	Dividing area	5

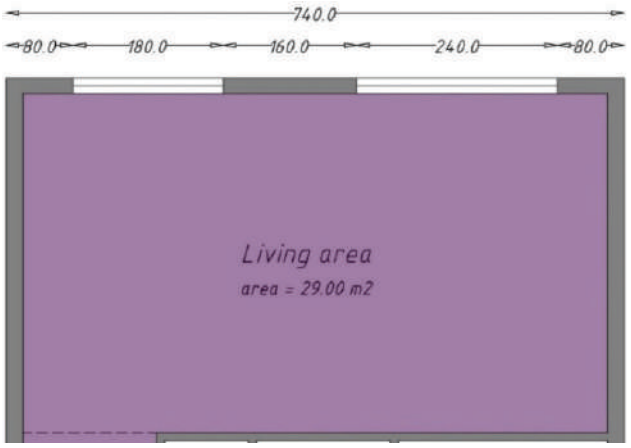

Figure 4. Zone 1 plan.

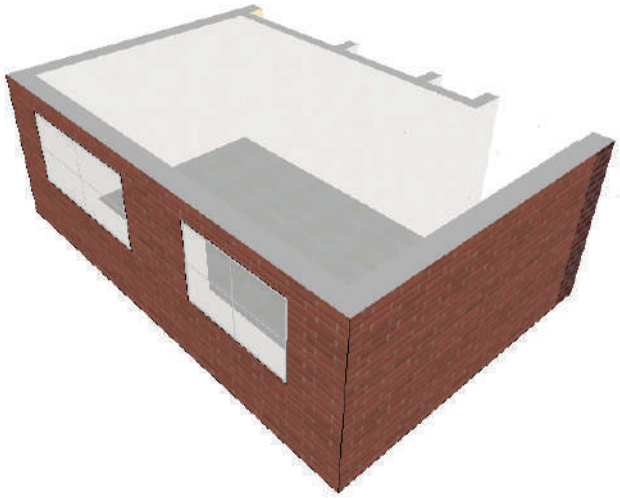

Figure 5. Zone 1 3d model.

conducted on ten types of building wall layer configurations in one of the most commonly used types of walls in Tehran construction, which the insulation layer and its thicknesses are changed. So they named ten types of walls (wall types 1-10) in accordance with the insulation changes. The specific category in this section (ten wall types) was determined based on the Tehran materials market. The layer thickness and specific thermal properties of materials, such as R-value and U-value, will be assigned based on standard values and manufacturer specifications for each wall type. It is considerable that the R-value and U-value are determined in Design Builder automatically in accordance with defined wall layering and Iran's national building regulations. Table 2 lists the properties of all the wall layers, that were simulated in this study. Figure 6 indicates the typical wall which is used in the simulation process.

- **Climate zone selection**: Simulations were conducted for Tehran's climatic situation, considering specific temperatures, humidity, and solar radiation. Table 3 and 4 present the aforementioned details, which are written based on the Design Builder software. In accordance with previous research, Tehran is located in the south of the Alborz Mountain Range and in the north of the Iran central dessert. Tehran (from 35° 35′ to 35° 55′ N, and from 51° 04′ to 51° 32′ E) is warm and dry in summer, and cold and humid in winter. The north and northeast of Tehran are surrounded by the Alborz Mountain Chain [25].
- **Insulation layer configuration**: Several simulations were conducted with different insulation layer configurations. This included variations of type, thickness, and placement of insulation materials in the wall construction. All of the insulation layers and thickness can be observed in Table 2.
- **Optimization process**: With the layer configuration (insulation layer) established and simulation reports available, an optimization process was initiated to · provide the most beneficial combination of insulation layer(s) to achieve the best thermal performance improvement.

RESULTS AND DISCUSSION

Optimized Wall Simulation: 2 cm Insulation

According to wall layer optimization, a simulation was conducted ten times based on the ten insulation layer optimizations in Figure 7. Figures 8 to 18 present the simulation results of the optimization. There are eight outputs and

Table 2. Wall Types Layering

	Material	Thickness (m)	R-Value (m^2-K/W)	U-Value (W/m^2-K)
Wall type 1	Façade brick	0.05	1.439	0.695
	Cement mortar	0.03		
	Cement wall block	0.15		
	Insulation – Polystyrene - HFC	0.02		
	Gypsum board	0.015		
Wall type 2	Façade brick	0.05	1.361	0.735
	Cement mortar	0.03		
	Cement wall block	0.15		
	Insulation - Polystyrene – CO2	0.02		
	Gypsum board	0.015		
Wall type 3	Façade brick	0.05	1.114	0.897
	Cement mortar	0.03		
	Cement wall block	0.15		
	Insulation – Polyvinyl Chloride	0.02		
	Gypsum board	0.015		
Wall type 4	Façade brick	0.05	1.237	0.808
	Cement mortar	0.03		
	Cement wall block	0.15		
	Insulation – Mineral Fiberglass	0.02		
	Gypsum board	0.015		
Wall type 5	Façade brick	0.05	1.344	0.744
	Cement mortar	0.03		
	Cement wall block	0.15		
	Insulation - Fiberglass	0.02		
	Gypsum board	0.015		
Wall type 6	Façade brick	0.05	1.378	0.726
	Cement mortar	0.03		
	Cement wall block	0.15		
	Insulation – Rock wool	0.02		
	Gypsum board	0.015		
Wall type 7	Façade brick	0.05	1.132	0.883
	Cement mortar	0.03		
	Cement wall block	0.15		
	Insulation - Silicon	0.02		
	Gypsum board	0.015		
Wall type 8	Façade brick	0.05	1.328	0.753
	Cement mortar	0.03		
	Cement wall block	0.15		
	Insulation – Fiberglass board	0.02		
	Gypsum board	0.015		
Wall type 9	Façade brick	0.05	1.248	0.801
	Cement mortar	0.03		
	Cement wall block	0.15		
	Insulation – Polyurethane foam	0.02		
	Gypsum board	0.015		
Wall type 10	Façade brick	0.05	1.028	0.972
	Cement mortar	0.03		
	Cement wall block	0.15		
	Insulation – Wood wool	0.02		
	Gypsum board	0.015		

Table 3. Activity, area, volume, and environmental properties

1. Activity Template	
Template	Domestic Lounge
Sector	Residential space
Zone type	Standard
Include zone in thermal calculation	+
Include zone in Radiance daylighting calculation	+
2. Floor Areas and Volumes	
Floor area (m^2)	25.63
Zone volume (m^3)	71.77
Inner surface mode	Deflation
3. Occupancy	
Occupancy density (people/m^2)	0.0188
Schedule	Dwell_DomLounge_Occ
3.1. Metabolic	
Activity	Eating/drinking
Factor (Men=1.00, Women=0.85, Children=0.75)	0.90
Co2 generation rate (m^3/s-W)	0.0000000382
3.2. Clothing	
Clothing schedule definition	3349
3.3. Comfort Radiant Temperature Weighting	
Calculation type	Zone average
4. Environmental Control	
4.1. Heating set point temperature	
Heating (°C)	21.00
Heating set back (°C)	12.00
4.2. Cooling set point temperature	
Cooling (°C)	25.00
Cooling set back (°C)	28.00
4.3. Humidity control	
RH Humidification set point (%)	10.00
RH Dehumidification set point (%)	90.00
4.4. Ventilation set point temperature	
Natural ventilation	
Indoor main temperature control	+
Min temperature definition	By value
Min temperature (°C)	24.00
Indoor max temperature control	-
4.5. Minimum fresh air	
Fresh air (l/s-person)	10.00
Mechanical ventilation per area (l/s-m^2)	0.00
4.6. Lighting	
Target Illuminance (lux)	150
Default display lighting density (W/m^2)	0.00
5. Computers	
On	-
6. Office equipment	
On	+
7. Miscellaneous	
On	-
8. Catering	
On	-
9. Process	
On	-

Table 4. Building construction properties

1.Construction template	
Template	Medium weight, moderate insulation
External wall	**Variable**
Below grade walls	Brick/brick wall (insulated to 1995 regs)
Flat roof	Flat roof U-value = 0.25 W/m^2K
Pitched roof (occupied)	Clay tiles (25mm) on air gap (20mm)
1.1. Semi-exposed	
Semi-exposed ceiling	Roofspace floor insulation 50mm
Semi-exposed floor	External floor-Energy code standard
1.2. Floors	
Ground floor	Ground floor slab
External floor	External floor
Internal floor	100mm concrete slab
1.3. Sub-surfaces	
Walls	100mm concrete slab
Internal	100mm concrete slab
Roof	100mm concrete slab
External door	Wooden door
1.4. Internal thermal mass	
Construction	100mm concrete slab
Exposed area (m^2)	0.00
1.5. Adjacency	
Adjacency	Auto
1.6. Surface convection	
Heating design	
Inside convection algorithm	6-TARP
Outside convection algorithm	6-DOE-2
Cooling design	
Inside convection algorithm	6-TARP
Outside convection algorithm	6-DOE-2
Simulation	
Inside convection algorithm	6-TARP
Outside convection algorithm	6-DOE-2
1.7. Linear thermal bridging at junctions	
Use Psi values	-

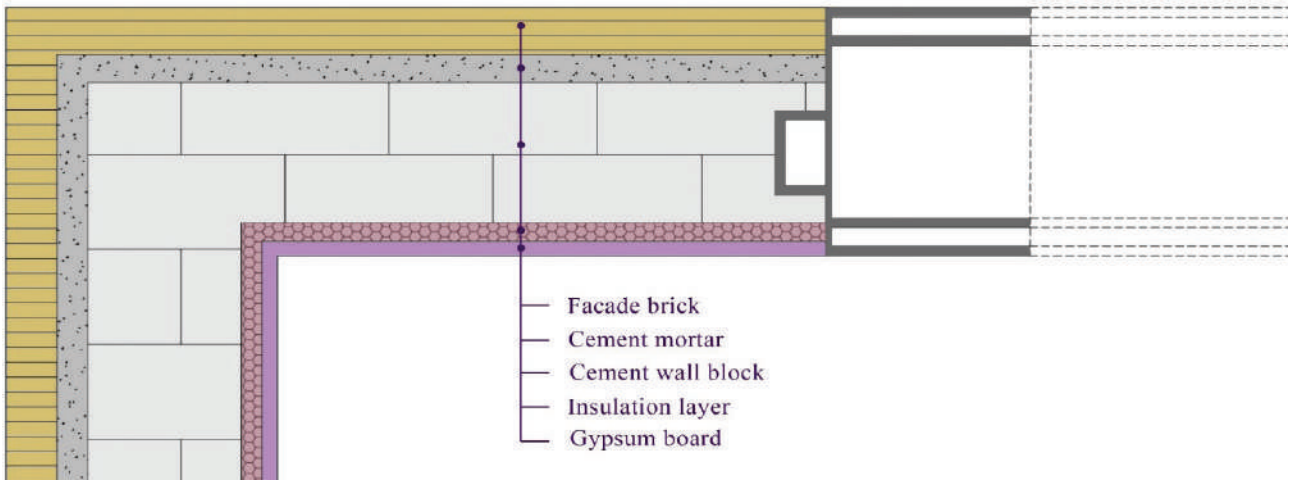

Figure 6. Typical wall detail.

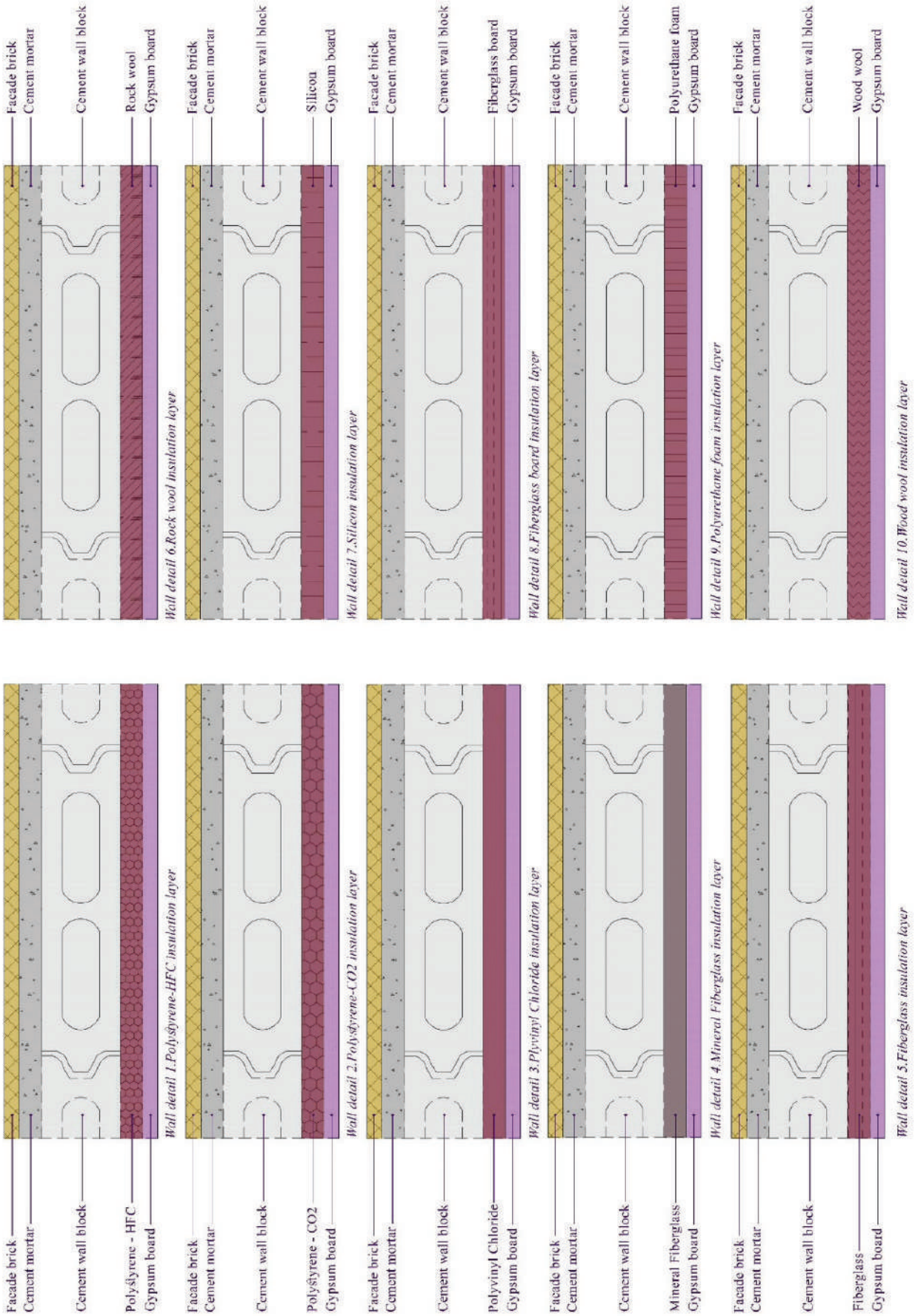

Figure 7. insulation wall layer optimization.

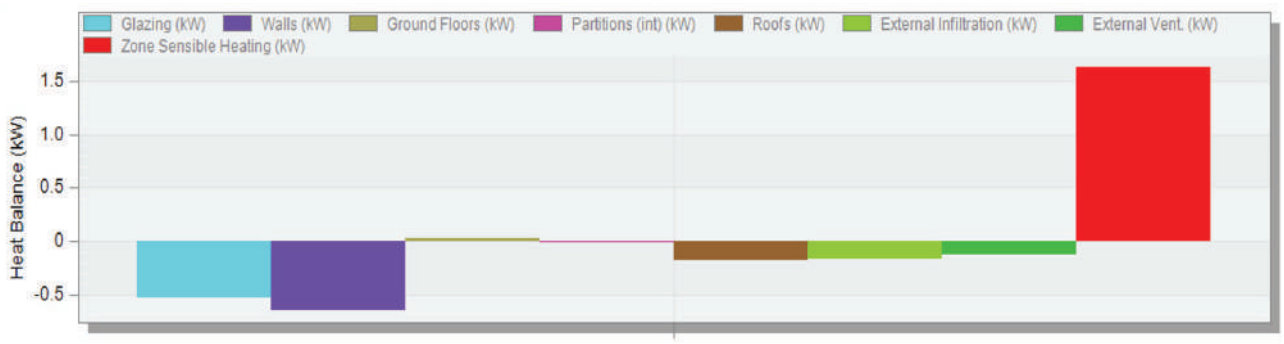

Figure 8. Wall 1 – polystyrene - HFC insulation simulation.

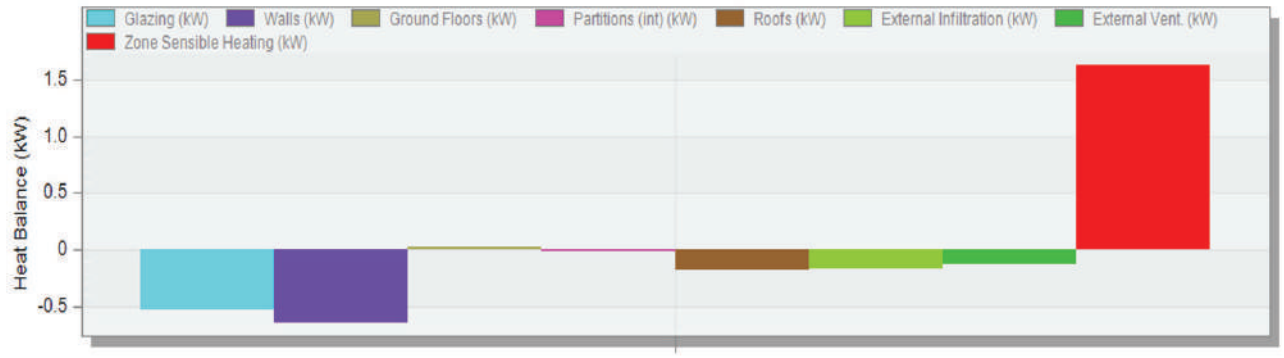

Figure 9. Wall 2 – polystyrene – CO2 insulation simulation.

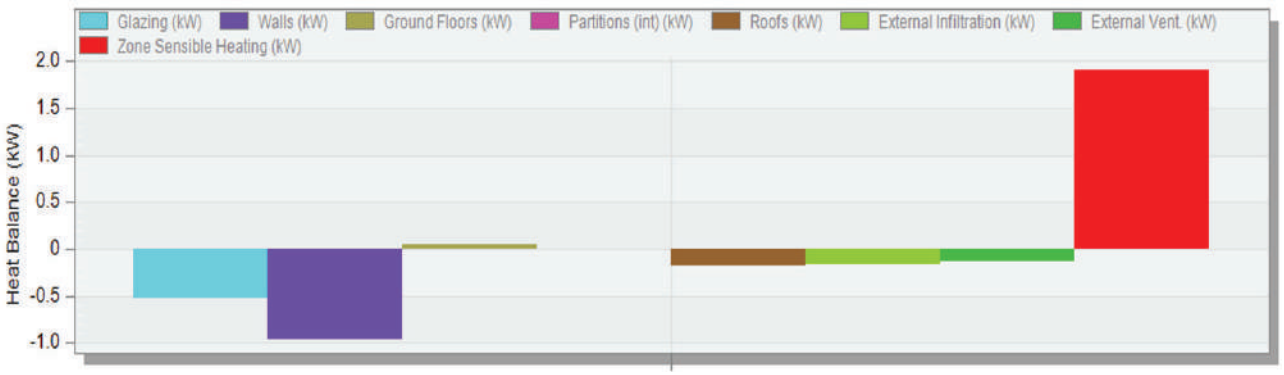

Figure 10. Wall 3 – poly vinyl chloride insulation simulation.

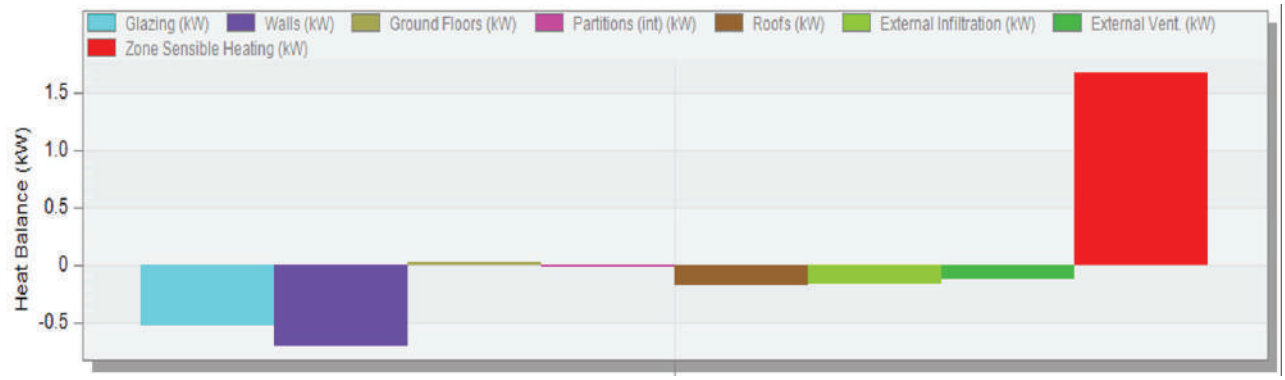

Figure 11. Wall 4 – mineral fiberglass insulation simulation.

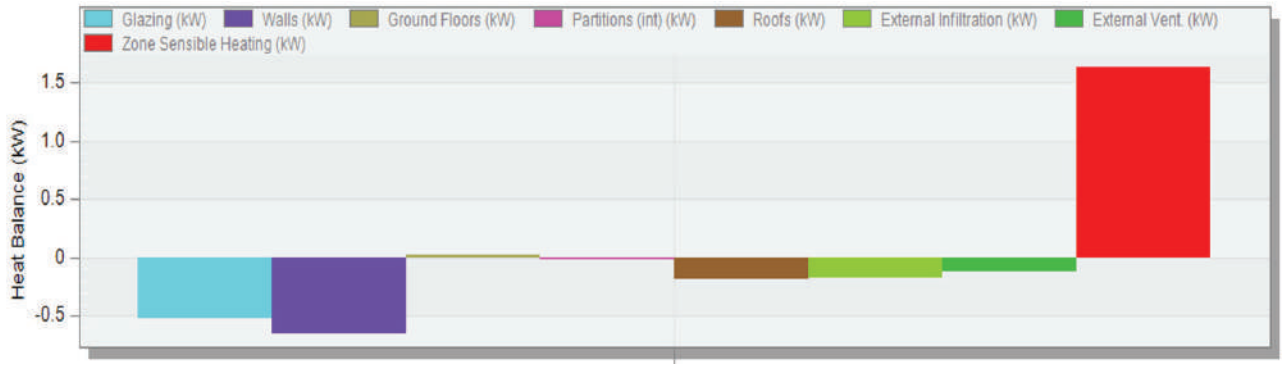

Figure 12. Wall 5 –fiberglass insulation simulation.

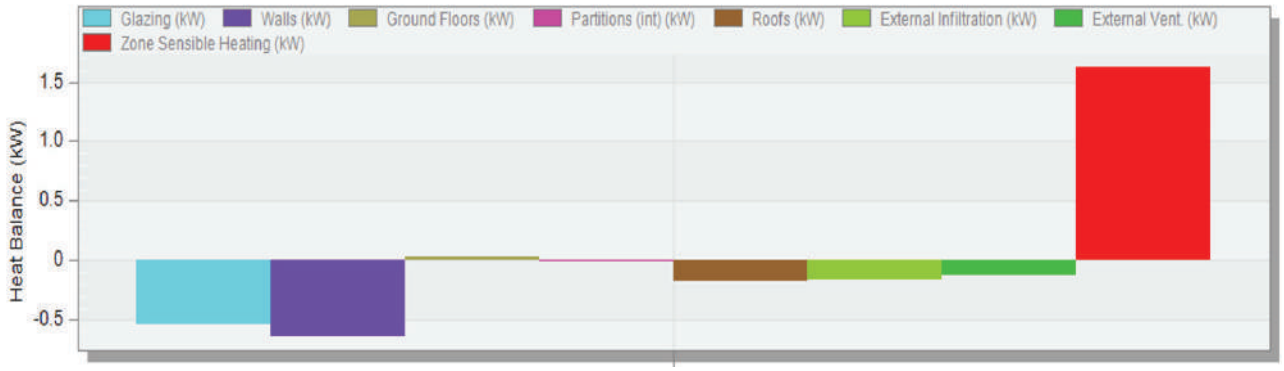

Figure 13. Wall 6 –rock wool insulation simulation.

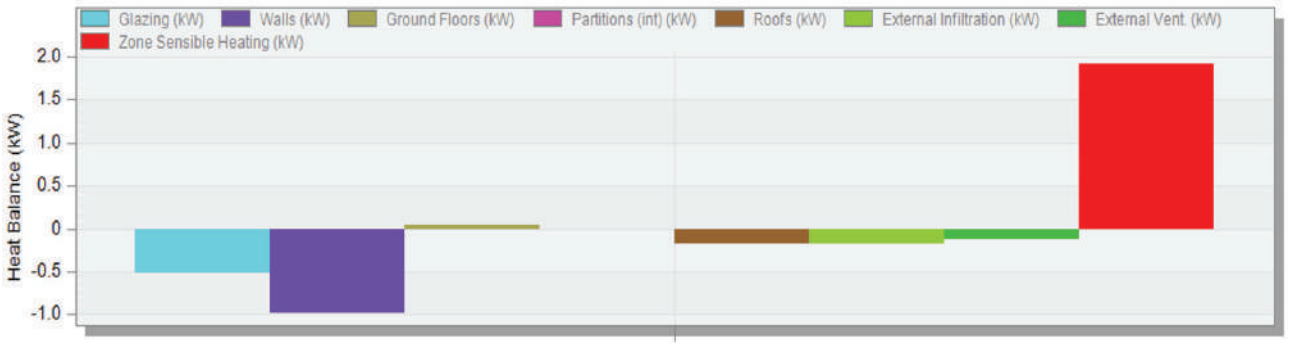

Figure 14. Wall 7 –silicon insulation simulation.

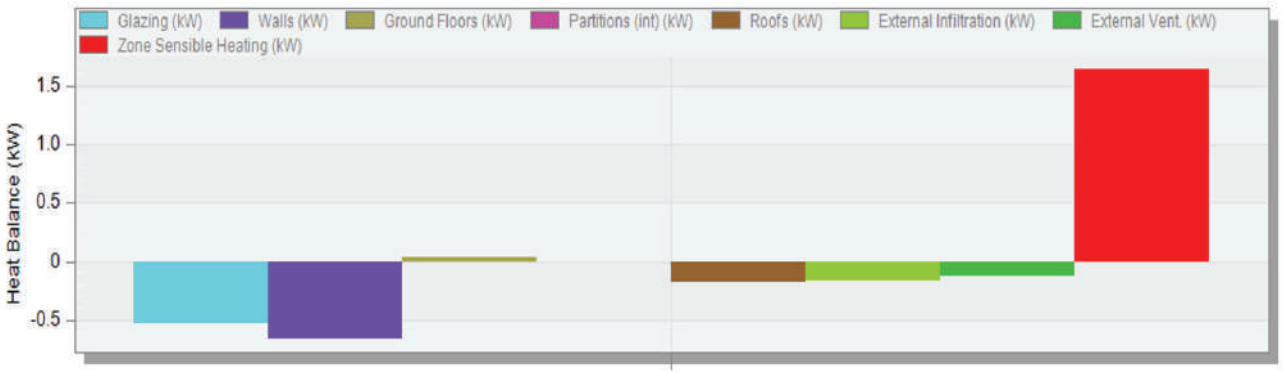

Figure 15. Wall 8 –fiberglass board insulation simulation.

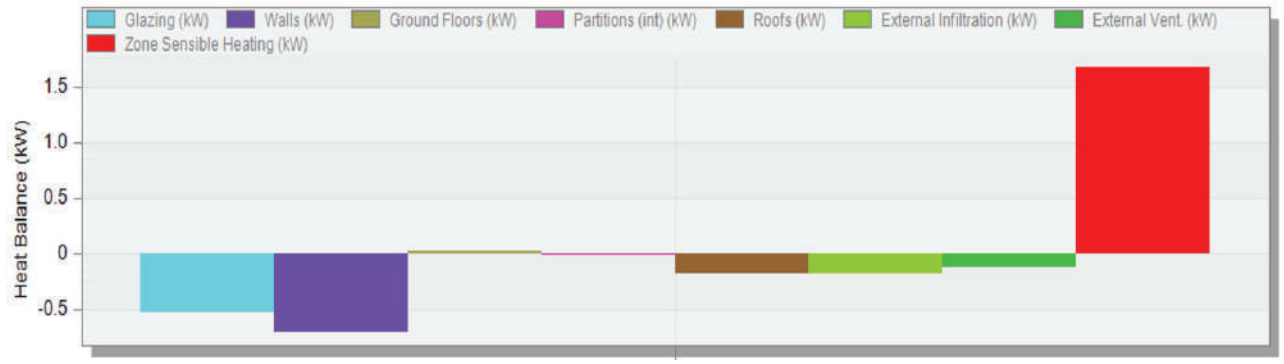

Figure 16. Wall 9 – Polyurethane insulation simulation.

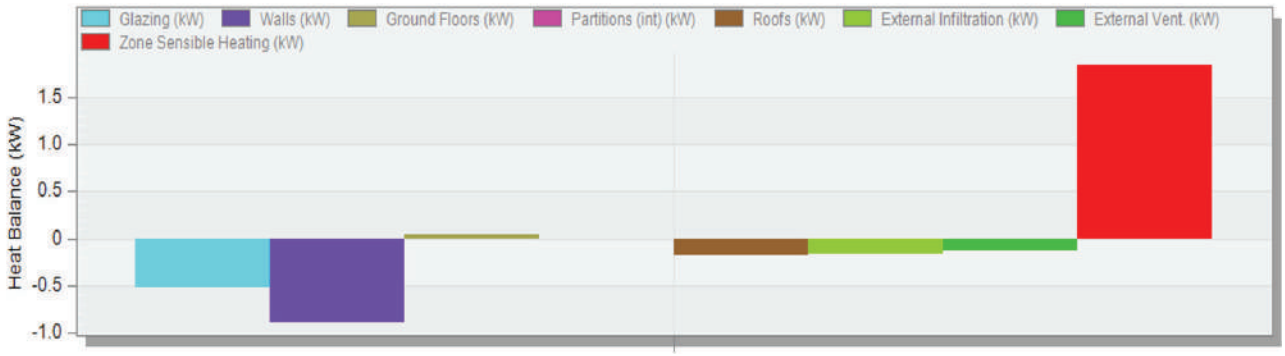

Figure 17. Wall 10 –wood wool insulation simulation.

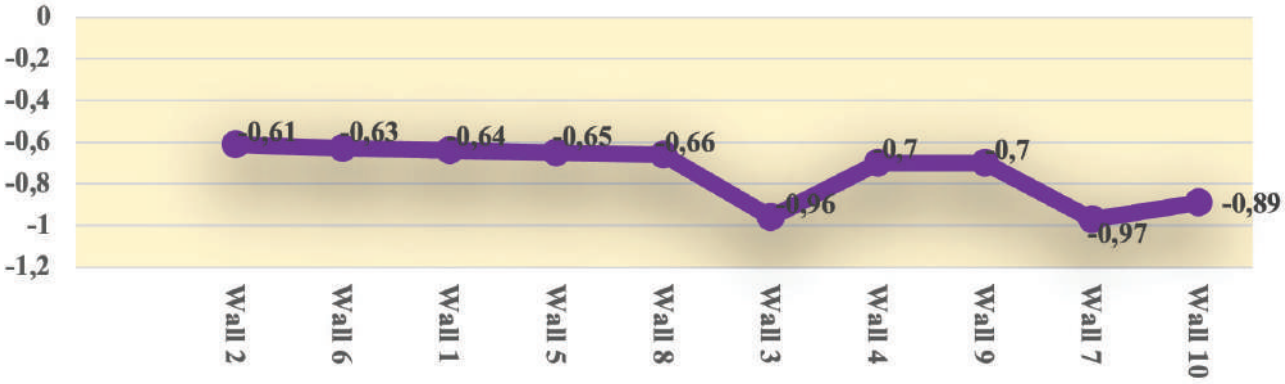

Figure 18. insulation wall layer optimization.

each Figure provides eight outputs: glazing, walls, ground floor, partitions, roofs, external infiltration, external ventilation, and zone sensible heating.

Figure 19 shows the wall heat balance of the simulation results. In accordance with the extracted quantity, the heat balance of wall 7 was the lowest among all wall layer optimizations. This indicates that fiberglass board is a weak insulation layer, as shown in Figure 16, with a heat balance of -0.97 kilowatts.

Wall 10 (Fig. 18). Insulated with wood wool. has a heat balance eight times better than that of a fiberglass board (-0.89 kilowatts).

Walls 3, 4, and 9 present the heat balance of polyvinyl chloride, mineral fiberglass, and polyurethane as insulation layers. As is obvious in Figures 11, 12, and 17, their heat balance quantities are the same (-0.70 kilowatts). Therefore, they conduct in a manner similar to thermal transmittance as wall insulation.

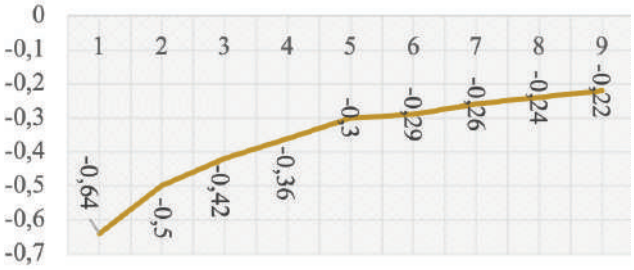

Figure 19. heat balance of polystyrene – HFC.

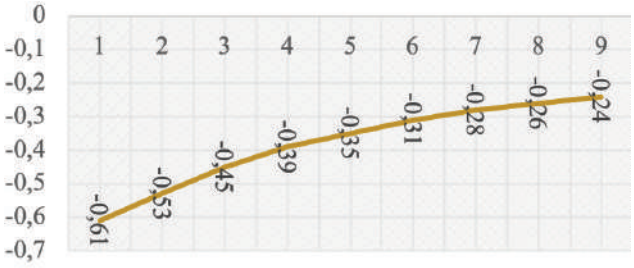

Figure 20. Heat balance of polystyrene – CO2.

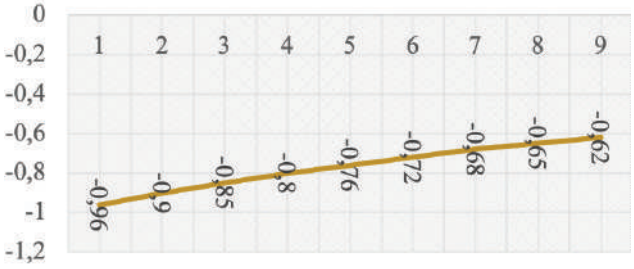

Figure 21. Heat balance of polyvinyl chloride.

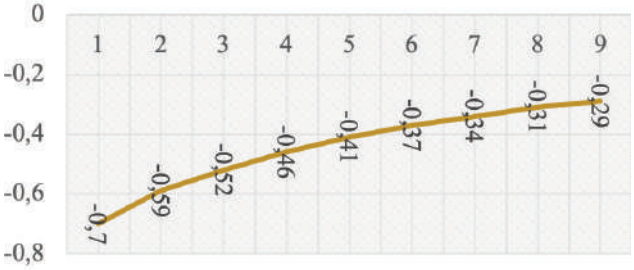

Figure 22. Heat balance of mineral fiberglass.

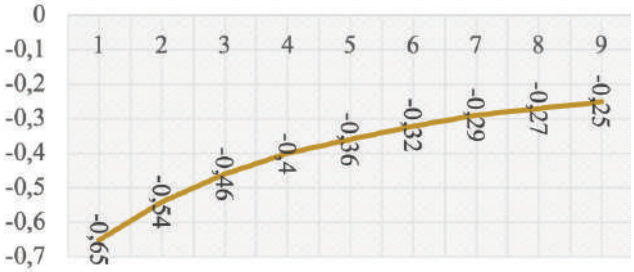

Figure 23. Heat balance of fiberglass.

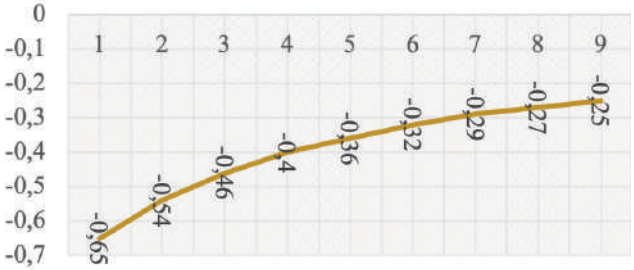

Figure 24. Heat balance of rock wool.

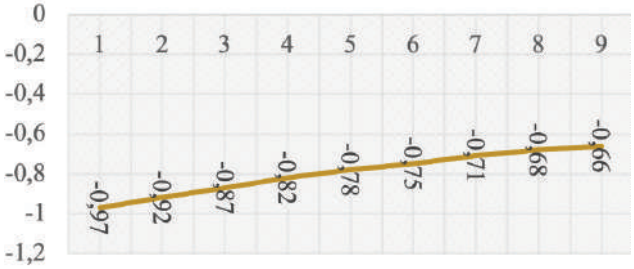

Figure 25. Heat balance of silicon.

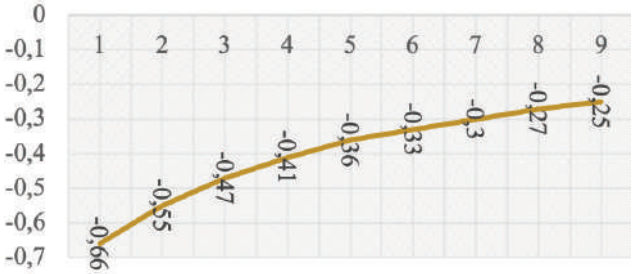

Figure 26. Heat balance of fiberglass board.

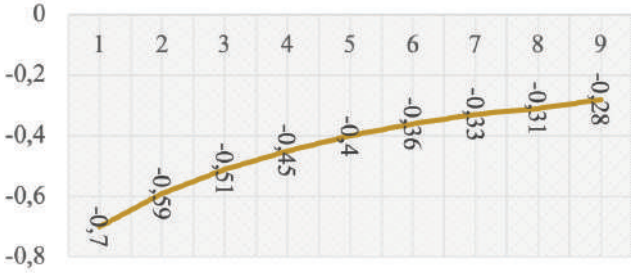

Figure 27. Heat balance of polyurethane foam.

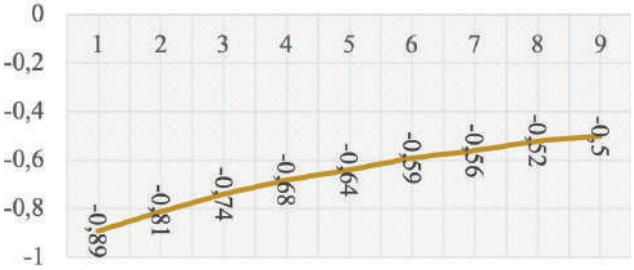

Figure 28. Heat balance of wood wool.

Walls 6, 1, 5, and 8 present the heat balance of rock wool, polystyrene, fiberglass, and fiberglass boards as insulation layers. The heat balance values are similar as shown in Figures 14, 9, 13, and 10.

Optimized Walls Simulation: Various Thickness Insulation

In this part, a change was made in the simulation condition. According to Figure 18, the result of the simulation using all ten types of thermal insulation indicated a negative heat balance.

According to Table 5, the simulation results of the selected wall type are specified for ten types of thermal insulation and three thicknesses. Thermal insulation with thicknesses of two, three, and four centimeters was investigated. The results regarding thermal insulation with a thickness of two centimeters are presented in Section 3.1, which are shown in Figures 9–18. In this section, the results of the wall simulation based on thermal insulation with thickness of three and four centimeters are specified. The key factor in the simulation results, expressed as heat balance, is detailed in Table 5 for each thermal insulation layer and its various thicknesses.

Wall heat balance factor

The meaning of heat balance involves the balance between incoming and outgoing heat to maintain a stable temperature and is explored in various contexts [24, 25]. This refers to the difference between the heat entering leaving a building's space.

According to the simulation result, walls are the intended output, which expresses the heat balance of the zone that has been analyzed (zone 1 of the case study). Wall heat balance quantity may express three concepts:

- If the wall heat balance is ≥ 0, the heat gains exceed the heat losses, indicating that the building receives more heat from sources like solar gain or internal heat generation than it loses through conduction, convection, and radiation.
- If the wall heat balance is 0, there is no heat loss or gain, indicating efficient thermal energy retention by the wall insulation.
- If the wall heat balance is less than or equal to zero, a negative heat balance indicates that the heat losses exceed the heat gains. More heat is lost than is gained in the building in this situation, which could lead to increased energy usage associated with heating and maintaining the temperature within a comfortable range.

According to Figures 9–18, The results of the simulation show that the heat balance in the specified wall of the space introduced in the case study is expressed as a negative value despite the use of various thermal insulations. It indicates that the quantity of heat transferred from the indoor to the outdoor is greater than the amount of heat transferred from the outdoor to the indoor. Therefore, the designed details and thermal insulation are not sufficient in the mentioned case. Since insulation layer thickness is a considerable factor in analyzing wall heat balance, the second part of the simulation was done with an approach to developing the heat balance value.

The optimal thickness of insulation layers in various applications, such as composite insulation for external walls and building construction, varies based on factors like climate, materials, and desired energy savings [26]. The research conducted in 2022, indicated that the optimal insulation thicknesses for various building materials across multiple thermal zones, ranged from 18.21 mm to 346.05 mm [27]. In this regard, changes in the thickness of the insulation layer were made in the simulation of the introduced model in order to achieve the optimal amount of thermal insulation. According to the way of implementing external walls in Tehran, the thickness of the thermal insulation layer was considered equal to 3 cm to 10 cm, and the simulation of the second series was conducted. Table 5 expresses the result of the simulation series. As is obvious, there are ten types of insulation in exterior wall types. In this table, the thermal balance factor has been determined for each of the walls.

The noteworthy point in these findings is the ratio between the thickness of the thermal insulation layer and the thermal balance value of each wall in the defined space. As it is obvious from Table 5, in the last column, there are bar diagrams that determine the relationship between increasing insulation layer thickness and heat balance in each wall type. For all ten wall types, the trend remains consistent. It means the heat balance value is expected to increase while the thickness of the insulation layer is being raised.

Comparison simulation analysis

As it is obvious in Figures 19–28, the heat balance quantity of ten wall insulation types is expressed based on the thickness. In regard to the increase in insulation layer thickness, heat balance quantity is developing. In another sense, the heat loss is reducing. The development value is different based on the type of insulation layer.

For instance, the change in heat balance in the wall with polyurethane foam as an insulation layer is 42 units (Fig. 28), which is the best insulation behavior. On the other hand, silicon is counted as a weak insulation layer as its change is 31 units (Fig. 26).

Rate of efficiency in insulation development

As is obvious, there is a direct relationship between an increase in insulation layer thickness and wall heat balance development. In another aspect, there is a considerable factor about the amount of heat balance based on the thickness increase. In another sense, the increase in heat balance is not equal to the thickness increase in any insulation layer.

For instance, in polystyrene (HFC), when the thickness increases from 2 cm to 10 cm, the heat balance value increases by 0.06, 0.08, 0.06, 0.06, 0.01, 0.03, 0.02, and 0.02. So it shows that the insulation thickness increase will

Table 5. Simulation report of heat balance in various thickness

	Insulation	Thickness (m)	Heat balance (KW)	Change in Heat Balance (KW)	Thickness and Heat balance diagram
Wall type 1	Insulation – Polystyrene - HFC	0.02	-0.64		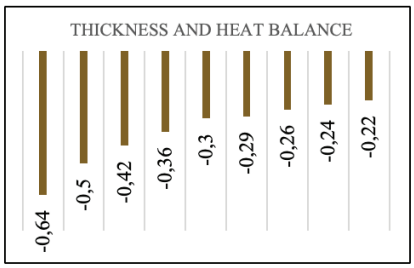
		0.03	-0.50	+0.06	
		0.04	-0.42	+0.08	
		0.05	-0.36	+0.06	
		0.06	-0.30	+0.06	
		0.07	-0.29	+0.01	
		0.08	-0.26	+0.03	
		0.09	-0.24	+0.02	
		0.10	-0.22	+0.02	
Wall type 2	Insulation - Polystyrene – CO2	0.02	-0.61		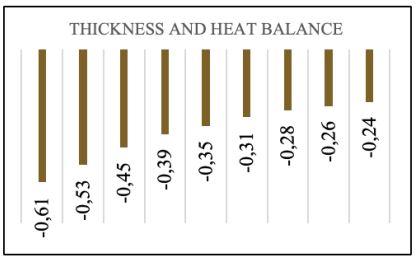
		0.03	-0.53	+0.08	
		0.04	-0.45	+0.08	
		0.05	-0.39	+0.06	
		0.06	-0.35	+0.04	
		0.07	-0.31	+0.04	
		0.08	-0.28	+0.03	
		0.09	-0.26	+0.02	
		0.10	-0.24	+0.02	
Wall type 3	Insulation – Polyvinyl Chloride	0.02	-0.96		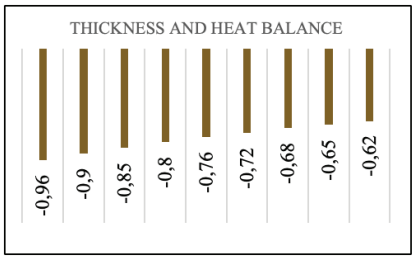
		0.03	-0.90	+0.06	
		0.04	-0.85	+0.05	
		0.05	-0.80	+0.05	
		0.06	-0.76	+0.04	
		0.07	-0.72	+0.04	
		0.08	-0.68	+0.04	
		0.09	-0.65	+0.03	
		0.10	-0.62	+0.03	
Wall type 4	Insulation – Mineral Fiberglass	0.02	-0.70		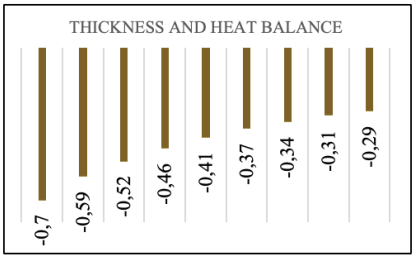
		0.03	-0.59	+0.11	
		0.04	-0.52	+0.07	
		0.05	-0.46	+0.06	
		0.06	-0.41	+0.05	
		0.07	-0.37	+0.04	
		0.08	-0.34	+0.04	
		0.09	-0.31	+0.03	
		0.10	-0.29	+0.02	
Wall type 5	Insulation - Fiberglass	0.02	-0.65		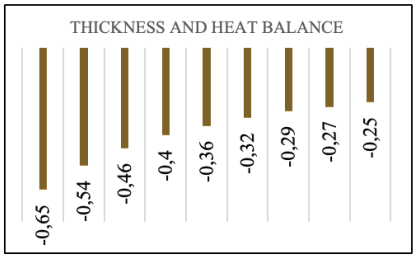
		0.03	-0.54	+0.11	
		0.04	-0.46	+0.08	
		0.05	-0.40	+0.06	
		0.06	-0.36	+0.04	
		0.07	-0.32	+0.04	
		0.08	-0.29	+0.03	
		0.09	-0.27	+0.02	
		0.10	-0.25	+0.02	

Table 5. Simulation report of heat balance in various thickness (counted)

	Insulation	Thickness (m)	Heat balance (KW)	Change in Heat Balance (KW)	Thickness and Heat balance diagram
Wall type 6	Insulation – Rock wool	0.02	-0.63		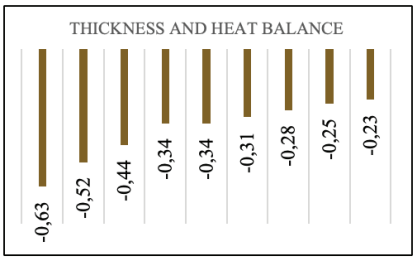
		0.03	-0.52	+0.11	
		0.04	-0.44	+0.08	
		0.05	-0.34	+0.10	
		0.06	-0.34	+0.00	
		0.07	-0.31	+0.03	
		0.08	-0.28	+0.03	
		0.09	-0.25	+0.03	
		0.10	-0.23	+0.03	
Wall type 7	Insulation - Silicon	0.02	-0.97		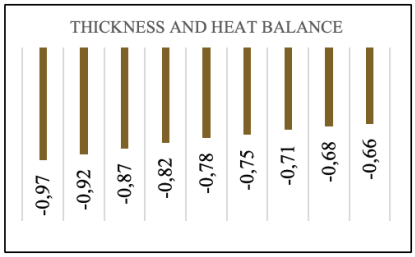
		0.03	-0.92	+0.05	
		0.04	-0.87	+0.05	
		0.05	-0.82	+0.05	
		0.06	-0.78	+0.04	
		0.07	-0.75	+0.03	
		0.08	-0.71	+0.04	
		0.09	-0.68	+0.03	
		0.10	-0.66	+0.02	
Wall type 8	Insulation – Fiberglass board	0.02	-0.66		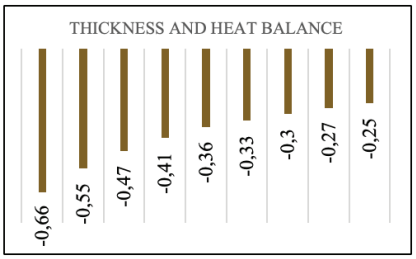
		0.03	-0.55	+0.11	
		0.04	-0.47	+0.08	
		0.05	-0.41	+0.06	
		0.06	-0.36	+0.05	
		0.07	-0.33	+0.03	
		0.08	-0.30	+0.03	
		0.09	-0.27	+0.03	
		0.10	-0.25	+0.02	
Wall type 9	Insulation – Polyurethane foam	0.02	-0.70		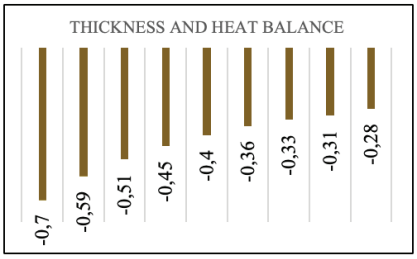
		0.03	-0.59	+0.11	
		0.04	-0.51	+0.08	
		0.05	-0.45	+0.06	
		0.06	-0.40	+0.05	
		0.07	-0.36	+0.04	
		0.08	-0.33	+0.03	
		0.09	-0.31	+0.02	
		0.10	-0.28	+0.03	
Wall type 10	Insulation – Wood wool	0.02	-0.89		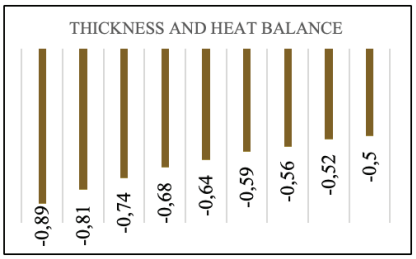
		0.03	-0.81	+0.08	
		0.04	-0.74	+0.07	
		0.05	-0.68	+0.06	
		0.06	-0.64	+0.04	
		0.07	-0.59	+0.05	
		0.08	-0.56	+0.03	
		0.09	-0.52	+0.04	
		0.10	-0.50	+0.02	

be useful if it is defined within a limited range, and if the thickness increase happens outside of that range, it is not efficient. As it is clear, in Table 5, there is a column entitled "change in heat balance", and it expresses the numerical rate of heat balance development in relation to insulation layer thickness increase. In accordance with these numerical values, it would be possible to make a reasonable decision about the thickness of the insulation layer in the building wall to make efficiency achievable. As an economic aspect, it should be considered that the increase in insulation layer thickness is not reasonable except within specific limits.

Figures 29-38 express the improvement rate of the insulation value of each wall type, which is expressed in Table 5. In a general view, each Figure contains one matrix and a linear diagram. The matrix categorized insulation layer thickness and insulation layer improvement rate. The diagram presents the values of the matrix in two ranges. Range 1, which is colored purple, shows the suitable range of insulation improvement based on the layer thickness. In another sense, increasing the insulation layer thickness in range 1 is efficient. On the other hand, range 2, which is colored red, shows an unsuitable range of insulation improvement. In another sense, the increase in insulation layer thickness is not efficient in this range.

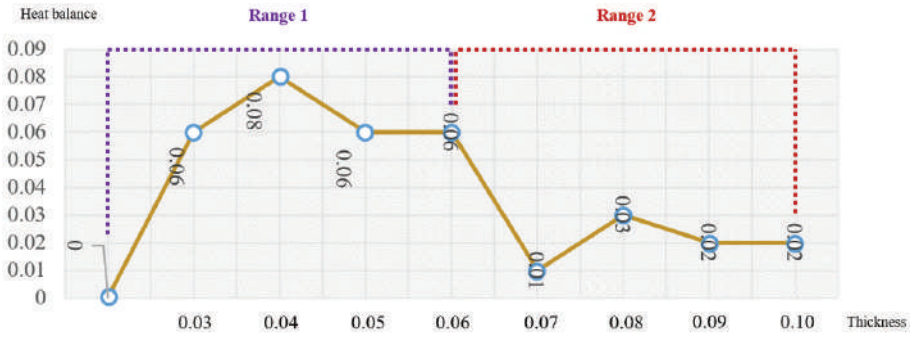

Figure 29. Polystyrene – HFC Figure ratio.

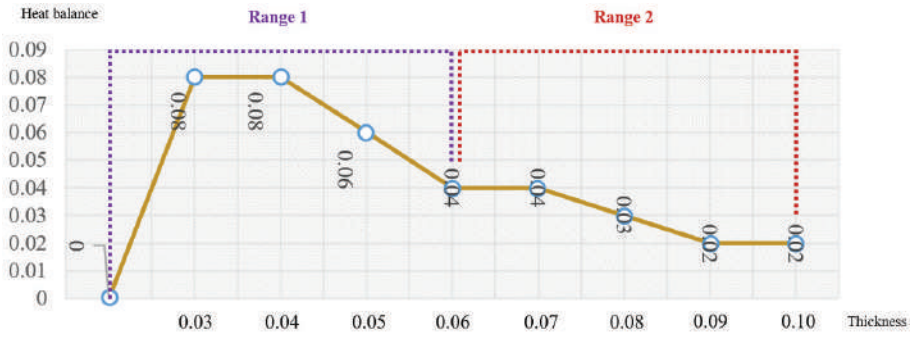

Figure 30. Polystyrene – CO2 Figure ratio.

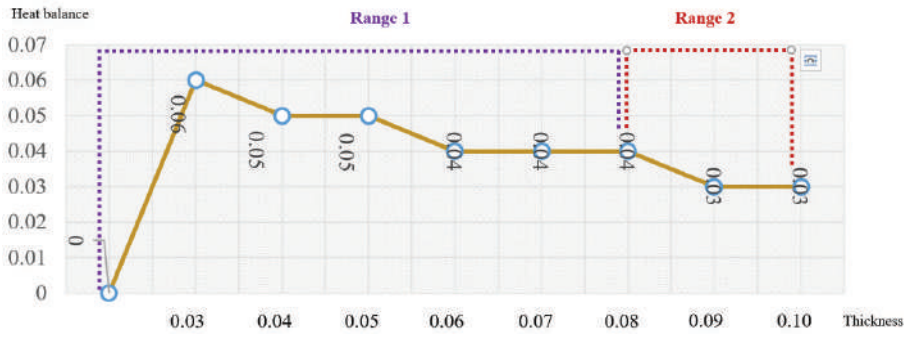

Figure 31. Polyvinyl Chloride Figure ratio.

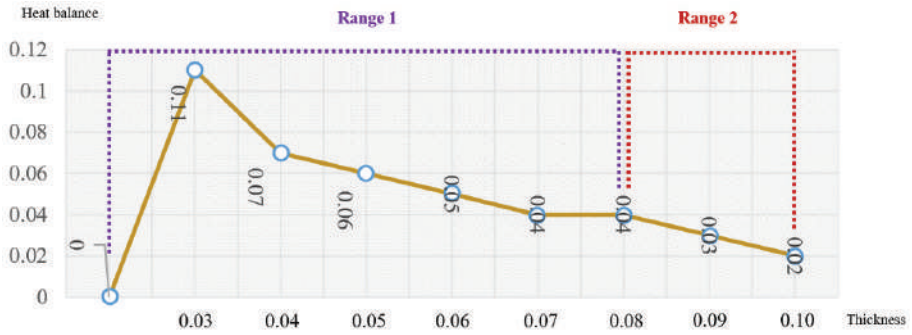

Figure 32. Mineral Fiberglass Figure ratio.

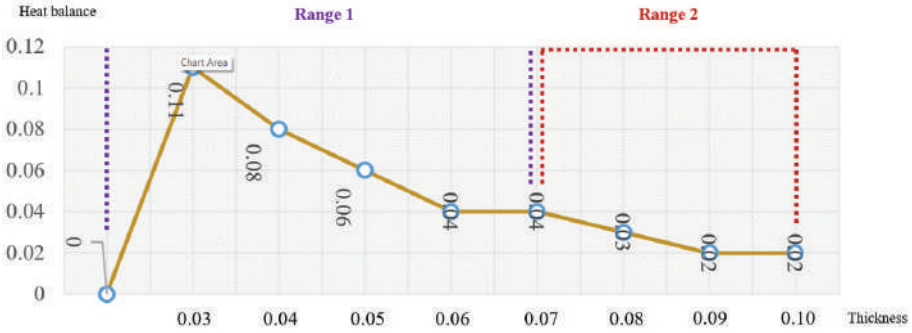

Figure 33. Fiberglass Figure ratio.

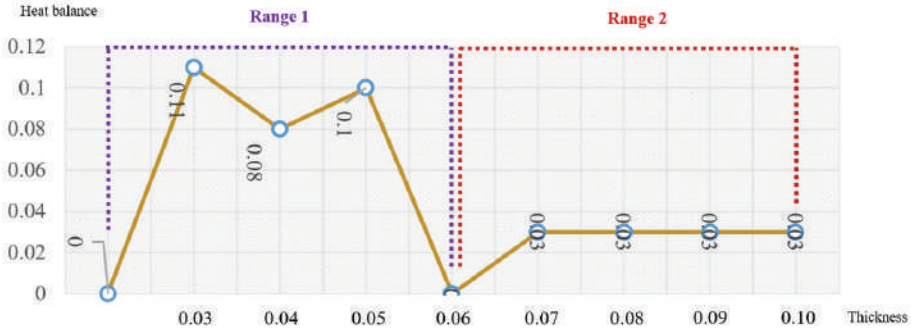

Figure 34. Rock wool Figure ratio.

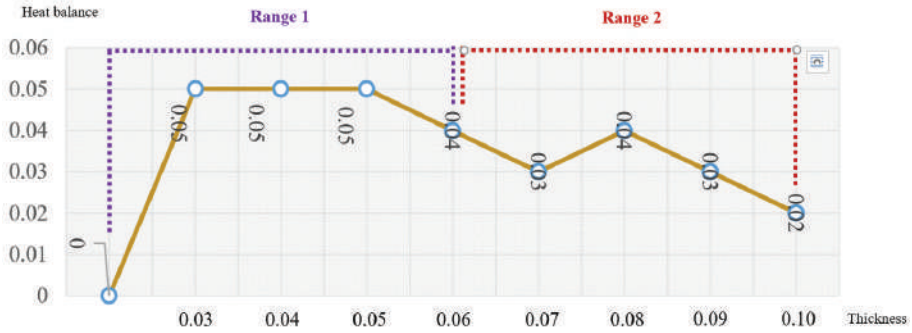

Figure 35. Silicon Figure ratio.

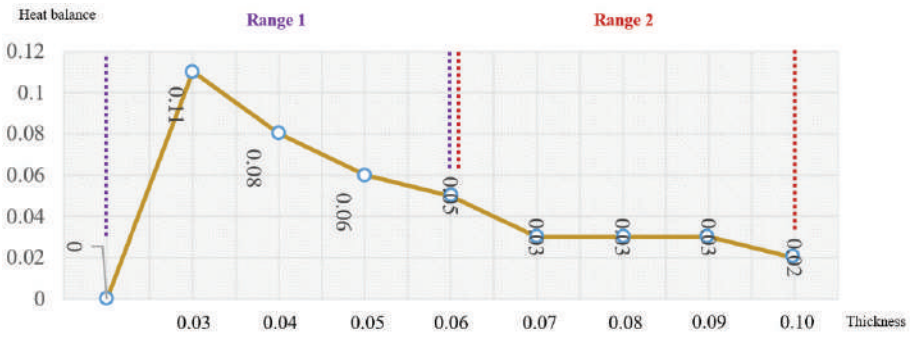

Figure 36. Fiberglass board Figure ratio.

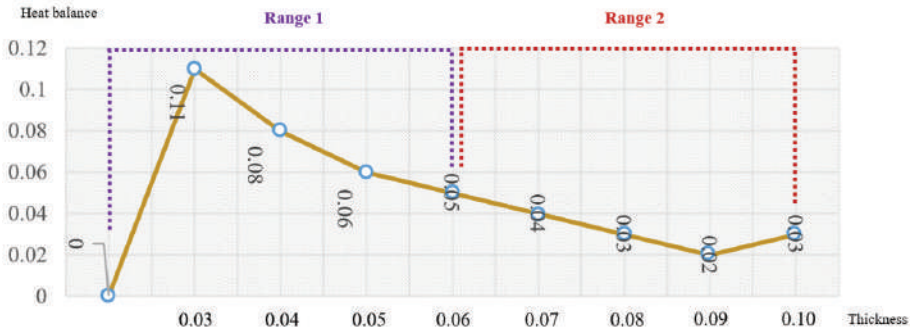

Figure 37. Polyurethane foam Figure ratio.

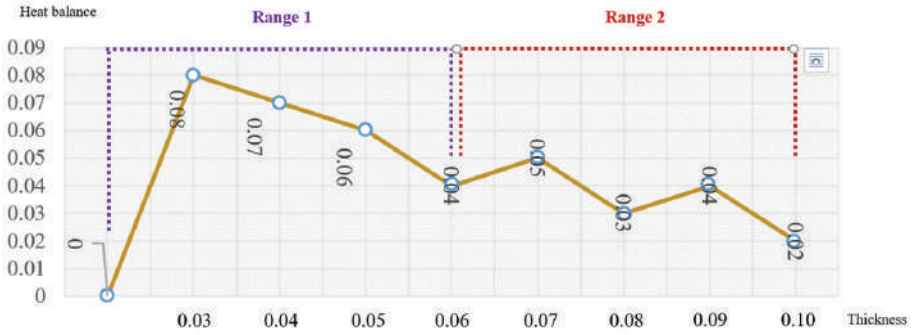

Figure 38. Wood wool Figure ratio.

$$\text{Polystyrene} - \text{HFC} = \begin{bmatrix} 0.02 & - \\ 0.03 & 0.06 \\ 0.04 & 0.08 \\ 0.05 & 0.06 \\ 0.06 & 0.06 \\ 0.07 & 0.01 \\ 0.08 & 0.03 \\ 0.09 & 0.02 \\ 0.10 & 0.02 \end{bmatrix}$$

As it is obvious in Figure 29, range 1 shows the increase of polystyrene (HFC) thickness from 2 cm to 6 cm, which would grow the wall heat balance between 0.06 and 0.08 units. On the other hand, in range 2, when the thickness increases from 7 cm to 10 cm, the heat balance would grow between 0.01 and 0.03 units. So, the increase in polystyrene (HFC) thickness is efficient between 2 cm and 6 cm, as range 1 is expressed in the diagram in Figure 29.

$$\text{Polystyrene} - \text{CO2} = \begin{bmatrix} 0.02 & - \\ 0.03 & 0.08 \\ 0.04 & 0.08 \\ 0.05 & 0.06 \\ 0.06 & 0.04 \\ 0.07 & 0.04 \\ 0.08 & 0.03 \\ 0.09 & 0.02 \\ 0.10 & 0.02 \end{bmatrix}$$

As it is obvious in Figure 30, range 1 shows the increase of polystyrene (CO2) thickness from 2 cm to 6 cm, which would grow the wall heat balance between 0.04 and 0.08 units. On the other hand, in range 2, when the thickness increases from 7 cm to 10 cm, the heat balance would grow between 0.02 and 0.04 units. So the increase in polystyrene (CO2) thickness is efficient between 2 cm and 6 cm, as range 1 is expressed in the diagram in Figure 30.

$$\text{Polyvinyl Chloride} = \begin{bmatrix} 0.02 & - \\ 0.03 & 0.06 \\ 0.04 & 0.05 \\ 0.05 & 0.05 \\ 0.06 & 0.04 \\ 0.07 & 0.04 \\ 0.08 & 0.04 \\ 0.09 & 0.03 \\ 0.10 & 0.03 \end{bmatrix}$$

As it is obvious in Figure 31, range 1 shows the increase of polyvinyl chloride thickness from 2 cm to 6 cm, which would grow the wall heat balance to 0.06 units. On the other hand, in range 2, when the thickness increases from 7 cm to 10 cm, the heat balance would grow to 0.04 units. So, the increase in polystyrene (CO2) thickness is efficient between 2 cm and 6 cm, as range 1 is expressed in the diagram in Figure 31.

$$\text{Mineral Fiberglass} = \begin{bmatrix} 0.02 & - \\ 0.03 & 0.11 \\ 0.04 & 0.07 \\ 0.05 & 0.06 \\ 0.06 & 0.05 \\ 0.07 & 0.04 \\ 0.08 & 0.04 \\ 0.09 & 0.03 \\ 0.10 & 0.02 \end{bmatrix}$$

As it is obvious in Figure 32, range 1 shows the increase of mineral fiberglass thickness from 2 cm to 6 cm, which would grow the wall heat balance to 0.11 units. On the other hand, in range 2, when the thickness increases from 7 cm to 10 cm, the heat balance would grow to 0.04 units. So, the increase in mineral fiberglass thickness is efficient between 2 cm and 6 cm, as range 1 is expressed in the diagram in Figure 32

$$\text{Fiberglass} = \begin{bmatrix} 0.02 & - \\ 0.03 & 0.11 \\ 0.04 & 0.08 \\ 0.05 & 0.06 \\ 0.06 & 0.04 \\ 0.07 & 0.04 \\ 0.08 & 0.03 \\ 0.09 & 0.02 \\ 0.10 & 0.02 \end{bmatrix}$$

As it is obvious in Figure 33, range 1 shows the increase of fiberglass thickness from 2 cm to 6 cm, which would grow the wall heat balance to 0.11 units. On the other hand, in range 2, when the thickness increases from 7 cm to 10 cm, the heat balance would grow to 0.04 units. So the increase in fiberglass thickness is efficient between 2 cm and 6 cm, as range 1 is expressed in the diagram in Figure 33.

$$\text{Rock wool} = \begin{bmatrix} 0.02 & - \\ 0.03 & 0.11 \\ 0.04 & 0.07 \\ 0.05 & 0.06 \\ 0.06 & 0.05 \\ 0.07 & 0.04 \\ 0.08 & 0.04 \\ 0.09 & 0.03 \\ 0.10 & 0.02 \end{bmatrix}$$

As it is obvious in Figure 34, range 1 shows the increase of rock wool thickness from 2 cm to 6 cm, which would grow the wall heat balance to 0.11 units. On the other hand, in range 2, when the thickness increases from 7 cm to 10 cm, the heat balance would grow to 0.04 units. So, the increase in rock wool thickness is efficient between 2 cm and 6 cm, as range 1 is expressed in the diagram in Figure 34.

$$\text{Silicon} = \begin{bmatrix} 0.02 & - \\ 0.03 & 0.05 \\ 0.04 & 0.05 \\ 0.05 & 0.05 \\ 0.06 & 0.04 \\ 0.07 & 0.03 \\ 0.08 & 0.04 \\ 0.09 & 0.03 \\ 0.10 & 0.02 \end{bmatrix}$$

As it is obvious in Figure 35, range 1 shows the increase of silicon thickness from 2 cm to 6 cm, which would grow the wall heat balance to 0.05 units. On the other hand, in range 2, when the thickness increases from 7 cm to 10 cm, the heat balance would grow to 0.04 units. So, the increase in silicon thickness is efficient between 2 cm and 6 cm, as range 1 is expressed in the diagram in Figure 35.

$$\text{Fiberglass board} = \begin{bmatrix} 0.02 & - \\ 0.03 & 0.11 \\ 0.04 & 0.08 \\ 0.05 & 0.06 \\ 0.06 & 0.05 \\ 0.07 & 0.03 \\ 0.08 & 0.03 \\ 0.09 & 0.03 \\ 0.10 & 0.02 \end{bmatrix}$$

As it is obvious in Figure 36, range 1 shows the increase in fiberglass board thickness from 2 cm to 6 cm, which would grow the wall heat balance to 0.11 units. On the other hand, in range 2, when the thickness increases from 7 cm to 10 cm, the heat balance would grow to 0.03 units. So, the increase in fiberglass board thickness is efficient between 2 cm and 6 cm, as range 1 is expressed in the diagram in Figure 36.

$$\text{Polyurethane foam} = \begin{bmatrix} 0.02 & - \\ 0.03 & 0.11 \\ 0.04 & 0.08 \\ 0.05 & 0.06 \\ 0.06 & 0.05 \\ 0.07 & 0.04 \\ 0.08 & 0.03 \\ 0.09 & 0.02 \\ 0.10 & 0.03 \end{bmatrix}$$

As it is obvious in Figure 37, range 1 shows the increase of polyurethane foam thickness from 2 cm to 6 cm, which would grow the wall heat balance to 0.11 units. On the other hand, in range 2, when the thickness increases from 7 cm to 10 cm, the heat balance would grow to 0.04 units. So, the increase of polyurethane foam board thickness is efficient between 2 cm and 6 cm, as range 1 is expressed in the diagram in Figure 37.

$$\text{Wood wool} = \begin{bmatrix} 0.02 & - \\ 0.03 & 0.11 \\ 0.04 & 0.08 \\ 0.05 & 0.06 \\ 0.06 & 0.05 \\ 0.07 & 0.04 \\ 0.08 & 0.03 \\ 0.09 & 0.02 \\ 0.10 & 0.03 \end{bmatrix}$$

As it is obvious in Figure 38, range 1 shows the increase of wood wool thickness from 2 cm to 6 cm, which would grow the wall heat balance to 0.11 units. On the other hand, in range 2, when the thickness increases from 7 cm to 10 cm, the heat balance would grow to 0.04 units. So, the increase in polyurethane foam board thickness is efficient between 2 cm, and 6 cm as range 1 is expressed in the diagram in Figure 38.

Efficient Impacts of Insulation Development

According to ten types of insulation layer simulation, each insulation type has its own efficient wall influence in a specific range, which is shown in Figures 29-38. These determined ranges introduce a framework that can be used as a tool by building designers and architects when they want to choose the suitable thermal insulation.

Table 6 shows the proportions of insulation layer thickness and heat balances as a framework. So in this way, building designers and architects can be able to choose the best possible insulation with regard to the project situation in Tehran and local insulation. In another sense, in a building project located in Tehran, a building designer who needed to design a wall detail would be able to make a decision about the wall insulation type and its thickness based on the information in Table 6 and the local insulation materials. A considerable point that makes the difference in this research is efficiency. It means that in addition to paying attention to the type and thickness of the thermal insulation, they can consider the efficiency of each material as an important economic factor.

As an example, if a building designer wanted to design the exterior wall detail of a building in Tehran and the local material was polystyrene and fiberglass, he would have five insulation types (polystyrene HFC, CO2, fiberglass, mineral fiberglass, and fiberglass board). In this way, he would be able to make a clear decision about insulation to have the best thickness and reduce waste thermal energy. Also, in this method, with regard to the numerical information, it would be possible to find out about the designed building heat balance. In another positive aspect, building designers and architects can use the choices that have an efficient impact as insulation.

Previous research analysis and discussion

According to similar research in which the investigation analyzed the influence of wall insulation thickness in five cities in China, the heat transfer coefficient was expressed. Various thicknesses of polystyrene board, from 0 mm to 100 mm, were analyzed. The research had achieved a table framework that explained the relationship between the thickness of the insulation layer and the cost of energy per square meter [28]. While the mentioned research has conducted the study based on one type of insulation, this article has presented the methodology of the study by simulating a various number of insulation types that are used in the design of walls in Tehran, which is helpful for architects who work locally in Tehran.

Another study, which was conducted in 2023, made an analysis based on building envelope typology in Baghdad in accordance with two parameters that include window-to-wall ratio and envelope insulation. The research concluded that the annual thermal load can have a considerable reduction of about 49% when it uses an insulation like a stone wall with a thickness of 5 cm [29]. So despite the closeness of the research path to the current research, the use of insulation diversity in the presented research is significant.

In research published in the International Research Journal of Advanced Engineering and Science, the researcher analyzed the insulation thickness of a building wall to find out the most economical choice of insulation thickness. As a conclusion, the researcher found that the economic insulation thickness of the local insulation is 4.7 cm in accordance with heating, cooling, and the annual energy requirement [30]. So it is obvious that finding the most economic thickness is important to developing efficiency. While this point is made based on one insulation in the mentioned article, the current research categorizes the 10 insulations, so it presents the insulation's efficiency in a more precious method.

In key research that was done in 2021 in Turkey, researchers made an optimization analysis based on four different thermal insulation materials: glass wool, rock wool, extruded polystyrene, and expanded polystyrene. In the investigation, the researcher wanted to consider the heating degree-day method, energy saving costs, payback period, and CO2 emissions, and as a result of the study,

Table 6. Efficient range of insulation layer

	Insulation	Thickness (m)	Heat balance (KW)
Wall type 1	Polystyrene - HFC	0.02	-0.64
		0.03	-0.50
		0.04	-0.42
		0.05	-0.36
		0.06	-0.30
Wall type 2	Polystyrene – CO2	0.02	-0.61
		0.03	-0.53
		0.04	-0.45
		0.05	-0.39
		0.06	-0.35
Wall type 3	Polyvinyl Chloride	0.02	-0.96
		0.03	-0.90
		0.04	-0.85
		0.05	-0.80
		0.06	-0.76
Wall type 4	Mineral Fiberglass	0.02	-0.70
		0.03	-0.59
		0.04	-0.52
		0.05	-0.46
		0.06	-0.41
Wall type 5	Fiberglass	0.02	-0.65
		0.03	-0.54
		0.04	-0.46
		0.05	-0.40
		0.06	-0.36
Wall type 6	Rock wool	0.02	-0.63
		0.03	-0.52
		0.04	-0.44
		0.05	-0.34
		0.06	-0.34
Wall type 7	Silicon	0.02	-0.97
		0.03	-0.92
		0.04	-0.87
		0.05	-0.82
		0.06	-0.78
Wall type 8	Fiberglass board	0.02	-0.66
		0.03	-0.55
		0.04	-0.47
		0.05	-0.41
		0.06	-0.36
Wall type 9	Polyurethane foam	0.02	-0.70
		0.03	-0.59
		0.04	-0.51
		0.05	-0.45
		0.06	-0.40
Wall type 10	Wood wool	0.02	-0.89
		0.03	-0.81
		0.04	-0.74
		0.05	-0.68
		0.06	-0.64

a comparison was done to determine the worst and best insulation material and the best thickness variety of each insulation [31]. The mentioned research has taken a similar approach to the current investigation, and it expresses the importance of various insulation simulations to find out more detail about the local situation, so it shows the importance of the current research in the city of Tehran.

The perspective of the thickness of the wall insulation layer can be considered based on the cost of the building life cycle, as research was conducted in 2020, and the investigator objective was to determine the optimum insulation thickness of residential buildings in Turkey with an approach to knowing the relation between insulation thickness and building life cycle cost [32]. Therefore, the present research will be the first step on the path that will determine the possibility of investigating the relationship between the thickness of various types of thermal insulation layers in buildings used in Tehran, and so the life cycle costs of the buildings in this city could be expressed as a future key topic about the city of Tehran.

Another study, done in 2010, expressed an analysis of insulation layer efficiency thickness in four different climates in Turkey. The researcher concluded that the optimum insulation thickness at indoor temperatures of 18 and 22 °C was determined to be 0.0663 and 0.0816 meters, respectively [33]. So as a difference, although the mentioned research concentrated on the various climates, the current research concentrates on the variety of insulations in one region, and it is considerable that it could be the basis of future research on the same topic in another climate in Iran.

CONCLUSION

According to the consumption of thermal energy in buildings, considering related components of buildings could play an important role in reducing thermal loss. As a numerical point of view, this issue is more than 40% in Iran. Lack of enough numerical determination in Iran's big cities like Tehran could have a negative impact on the energy usage of this country, and this numerical perspective is counted as a research gap in related investigations.

Findings

Based on the mentioned issue, this research makes an attempt to establish a numerical framework in building walls—an important component of buildings—with an approach to assessing local insulation layers that are used in Tehran's building wall typology, and it aims to develop a quantitative framework that helps local architects and building designers choose the best insulation material in their design process in both energy loss prevention and economic efficiency material aspects. In another meaning, when there is a quantitative framework (Table 5-6 and Figs. 29-38), architects who design the building's first phase could use the details of insulation materials in various ranges (both type and thickness) in their design, and in this way they will be able to consider wall insulation properties in their project. In the investigation, the reviewed literature was categorized into three parts, including building thermal transmittance, the significance of layer optimization in wall construction, and the development of simulation models for thermal analysis. The methodology is a simulation-based method that uses the most common Tehran residential building wall typology as the specific case. The procedure of simulation shapes based on the ten types of local insulation that Figured the typological wall. Finally, the simulation is done with Design Builder software as the main tool, and the results are established.

The results are extracted and each wall configuration is assessed based on its insulation properties.

The key highlights of the research are:

- The most efficient insulation materials that develop the thermal efficiency of building walls are fiberglass, fiberglass board, mineral fiberglass, rock wool, polyurethane, and wood wool, which develop the change in heat balance of 0.11 kilowatts with a thickness of 3 centimeters. In accordance with the various choices, architects and building designers in Tehran could be able to choose the one with the best price and accessibility to the local area.
- The second group of thermal insulation materials is polystyrene (Co2), polystyrene (HFC), and polyvinyl chloride, whose change in change in heat balance equals 0.08 and 0.06 kilowatts with a thickness of 3 centimeters.
- The insulation material whose Figure rate's development is not efficient is silicon, whose development is 0.05 kilowatts with a thickness of 3 centimeters.

Research Novelty Points

According to the research process and the results, the novelty points of this research are expressed as following:

- **Region-spesific framewok**: It provides a quantitative framework with regard to climate and construction in Tehran; it thus furnishes real and appropriate guidelines for architects and designers locally.
- **Local material examination**: The simulation involves insulation materials available locally, so that the findings are applicable to the real situation in a building practice context in Tehran.
- **Detailed insulation efficiency analysis**: Measuring Insulation Effectiveness: This measures the association between insulation thickness and thermal performance.
- **Filling of research gap**: Evidence of Relevance: It addresses the need for numerical assessment of insulation materials in the Iranian context.

Study Potentials and Limitations

- The key potentials
- **Adaptation to other climate zones**: While this research focused on Tehran, the framework can be adapted to other Iranian cities with diverse climatic conditions. The findings could be used as a foundation for further research to assess the effectiveness of insulation

in varying climate zones across the country, offering tailored solutions to reduce energy consumption nationwide.

- **Various insulation materials:** Variety of insulations: In this analysis ten insulation materials were studied, and the variety of insulations could still be further developed from local materials in other Iranian cities.
- **Building typology constraints**: This analysis was limited to known building typologies in Tehran which may lessen the relevance to unknown or modern building typologies. Future studies would include a wider building typology in order to leverage a range of design conditions and increase the generalizability of the insulation framework.
- **Integration with renewable energy systems**: Systems such as renewable energy. Future studies could learn from this insulating framework in order to develop designs which are more sustainable (e.g. compatibility with renewable energy systems (solar energy). The combined synergies for thermal insulation in space, in addition to energy producing sources could lessen the combined impact for the environment in buildings.

Limitations

- **Experimental Examination**: According to the limitation of experimental services related to materials testing, do a reasonable comparison between theoretical findings and practical findings. This could be an effective point that impacts the credit of results.

AUTHORSHIP CONTRIBUTIONS

Authors equally contributed to this work.

DATA AVAILABILITY STATEMENT

The authors confirm that the data that supports the findings of this study are available within the article. Raw data that support the finding of this study are available from the corresponding author, upon reasonable request.

CONFLICT OF INTEREST

The author declared no potential conflicts of interest with respect to the research, authorship, and/or publication of this article.

ETHICS

There are no ethical issues with the publication of this manuscript.

STATEMENT ON THE USE OF ARTIFICIAL INTELLIGENCE

Artificial intelligence was not used in the preparation of the article

REFERENCES

[1] Meng X, Luo T, Gao Y, Zhang L, Huang X, Hou C, et al. Comparative analysis on thermal performance of different wall insulation forms under the air-conditioning intermittent operation in summer. Appl Therm Eng 2018;130:429-38. [CrossRef]

[2] Chen S, Li N, Guan J, Xie Y, Sun F, Ni J. A statistical method to investigate national energy consumption in the residential building sector of China. Energy Build 2008;40(4):654-65. [CrossRef]

[3] Zahedi R, Gitifar S, Aslani A. Modeling and analysis of building cooling energy supply system using variable solar refrigerant flow system. J Sustainable Energy Syst 2021;1(1):51-70.

[4] Yu S, Hao S, Mu J, Tian D. Optimization of Wall Thickness Based on a Comprehensive Evaluation Index of Thermal Mass and Insulation. Sustainability 2022;14(3):1143. [CrossRef]

[5] Meng X, Huang Y, Cao Y, Gao Y, Hou C, Zhang L, et al. Optimization of the wall thermal insulation characteristics based on the intermittent heating operation. Case Stud Constr Mater 2018;9:e00188. [CrossRef]

[6] Zhang L, Liu Za, Hou C, Hou J, Wei D, Hou Y. Optimization analysis of thermal insulation layer attributes of building envelope exterior wall based on DeST and life cycle economic evaluation. Case Stud Therm Eng 2019;14:100410. [CrossRef]

[7] Levinskytė A, Bliūdžius R, Burlingis A, Makaveckas T. Dependencies of heat transmittance through the ventilated wall system on thermal conductivity of connectors crossing thermal insulation layer. MATEC Web of Conferences 2019. [CrossRef]

[8] Rajanayagam H, Upasiri I, Poologanathan K, Gatheeshgar P, Sherlock P, Konthesingha C, et al. Thermal Performance of LSF Wall Systems with Vacuum Insulation Panels 2021. [CrossRef]

[9] Salavatian S, D'Orazio M, Perna Cd, Giuseppe ED. Assessment of Cardboard as an Environment-Friendly Wall Thermal Insulation for Low-Energy Prefabricated Buildings. Sustainable Building for a Cleaner Environment 2018. [CrossRef]

[10] D'Agostino D, Landolfi R, Nicolella M, Minichiello F. Experimental Study on the Performance Decay of Thermal Insulation and Related Influence on Heating Energy Consumption in Buildings. Sustainability 2022. [CrossRef]

[11] Magrini A, Marenco L, Leoni V, Gamba R. Air Cavity Building Walls: A Discussion on the Opportunity of Filling Insulation to Support Energy Performance Improvement Strategies. Energies 2022. [CrossRef]

[12] Rodrigues E, Fereidani NA, Fernandes MS, Gaspar AR. Climate change and ideal thermal transmittance of residential buildings in Iran. J Build Eng 2023;74:106919. [CrossRef]

[13] Verichev K, Zamorano M, Fuentes-Sepúlveda A, Cárdenas N, Carpio M. Adaptation and mitigation to climate change of envelope wall thermal insulation of residential buildings in a temperate oceanic climate. Energy Build 2021;235:110719. [CrossRef]
[14] Al-Sanea SA, Zedan MF. Improving thermal performance of building walls by optimizing insulation layer distribution and thickness for same thermal mass. Appl Energy 2011;88:3113-24. [CrossRef]
[15] Ramin H, Hanafizadeh P, Behabadi MAA. Thermal, Economical and Environmental Optimization of Insulation Thickness in Residential Building's Wall 2019.
[16] Rosti B, Omidvar A, Monghasemi N. Optimal insulation thickness of common classic and modern exterior walls in different climate zones of Iran. J Build Eng 2020;27:100954. [CrossRef]
[17] Asan H. Investigation of wall's optimum insulation position from maximum time lag and minimum decrement factor point of view. Energy Build 2000;32(2):197-203. [CrossRef]
[18] Jannat N, Hussien A, Abdullah B, Cotgrave A. A Comparative Simulation Study of the Thermal Performances of the Building Envelope Wall Materials in the Tropics. Sustainability 2020;12(12):4892. [CrossRef]
[19] Sarihi S, Mehdizadeh Saradj F, Faizi M. A Critical Review of Façade Retrofit Measures for Minimizing Heating and Cooling Demand in Existing Buildings. Sustain Cities Soc 2021;64:102525. [CrossRef]
[20] Panico S, Larcher M, Troi A, Baglivo C, Congedo PM. Thermal Modeling of a Historical Building Wall: Using Long-Term Monitoring Data to Understand the Reliability and the Robustness of Numerical Simulations. Buildings 2022;12(8):1258. [CrossRef]
[21] Meng X, Luo T, Gao Y, Zhang L, Shen Q, Long E. A new simple method to measure wall thermal transmittance in situ and its adaptability analysis. Appl Therm Eng 2017;122:747-57. [CrossRef]
[22] Santos P, Gonçalves M, Martins C, Soares N, Costa J. Thermal transmittance of lightweight steel framed walls: Experimental versus numerical and analytical approaches. J Build Eng 2019;25:100776. [CrossRef]
[23] Santos P, Lemes G, Mateus D. Analytical Methods to Estimate the Thermal Transmittance of LSF Walls: Calculation Procedures Review and Accuracy Comparison. Energies 2020;13:840. [CrossRef]
[24] Nezammahalleh MA. The effects of urban environment on climate changes, case study: Tehran, Iran. Journal of Tethys 1(2) 2013.
[25] Kazanavicius E, Mikuckas A, Mikuckiene I, Ceponis J. THE HEAT BALANCE MODEL OF RESIDENTIAL HOUSE. Information Technology and Control 2015;35. [CrossRef]
[26] Bektas Ekici B, Aytac Gulten A, Aksoy UT. A study on the optimum insulation thicknesses of various types of external walls with respect to different materials, fuels and climate zones in Turkey. Appl Energy 2012;92:211-7. [CrossRef]
[27] Yang WF, Zhang G, He WF, Liu J-p. The Effect of Relative Humidity Dependent Thermal Conductivity on Building Insulation Layer Thickness Optimization. Buildings 2022. [CrossRef]
[28] Lianying Z, Yuan W, Jiyuan Z, Xing L, Linhua Z. Numerical Study of Effects of Wall's Insulation Thickness on Energy Performance for Different Climatic Regions of China. Energy Procedia. 2015;75:1290-8. [CrossRef]
[29] Hussein A, saleh A, Ahmed H. Numerical Study of the Effect of Thermal Insulation and Window-to-wall Ratio on Reducing the Thermal Loads of the Residential Sector in Iraq. Eng Tech J 2023:1-12. [CrossRef]
[30] Canbolat AS, Bademlioglu AH, Kaynakli O. Determination of Proper Insulation Thickness for Building Walls Regarding Economic Consideration. Int Res J Adv Eng Sci 2018;3(4). [CrossRef]
[31] Aktemur C, Bilgin F, Tunçkol S. Optimisation on the thermal insulation layer thickness in buildings with environmental analysis: an updated comprehensive study for Turkey's all provinces. J Therm Eng 2021;7:1239-56. [CrossRef]
[32] Aydin N, Biyikoğlu A. Determination of optimum insulation thickness by life cycle cost analysis for residential buildings in Turkey. Sci Technol Built Environ 2021;27(1):2-13. [CrossRef]
[33] Yildiz A, Ali Ersöz M. Determination of the economical optimum insulation thickness for VRF (variable refrigerant flow) systems. Energy 2015;89:835-44. [CrossRef]

J Ther Eng, Vol. 12, No. 1, pp. 254−277, January, 2026

Journal of Thermal Engineering
Web page info: https://jten.yildiz.edu.tr
DOI: 10.14744/thermal.0001076

Research Article

Design of optimized exhaust system for two stroke unmanned aerial vehicle engine

Faiq SAID[1,4], Zeeshan KHAN[1], Majid BASEER[2,*], Muhammad Nouman RASHID[3], Muhammad BILAL[4], Riaz HUSSAIN[5]

[1]Department of Mechanical Engineering, University of Engineering and Technology, Mardan, 23200, Pakistan
[2]CETHIL UMR 5008, CNRS, INSA Lyon, Université Claude Bernard Lyon 1, Université de Lyon, 69621 Villeurbanne, France
[3]Department of Mechanical Engineering, SMME, National University of Sciences and Technology (NUST), H-12, Islamabad, 44000, Pakistan
[4]Department of Mechanical Engineering, University of Engineering and Technology, Peshawar 25120, Pakistan
[5]Department of Mechanical Engineering, Sarhad University of Science and Information Technology, Peshawar, 25000, Pakistan

ARTICLE INFO

Article history
Received: 07 December 2024
Revised: 15 February 2025
Accepted: 18 February 2025

Keywords:
Backpressure; CFD Analysis; Exhaust System; Two-Stroke Engine; UAV

ABSTRACT

This study investigated the optimization of exhaust system parameters for two-stroke engines in unmanned aerial vehicles, with a focus on improving performance at varying altitudes (sea level, 10,000 ft, and 21,000 ft). The research examined the impact of baffle plate hole diameter, header pipe length, and header pipe diameter on backpressure and exhaust flow dynamics. Two-stroke engines, while valued for their high power-to-weight ratio, suffer efficiency losses due to fresh air-fuel mixture leakage, particularly under reduced atmospheric pressure at high altitudes. The objective was to reduce backpressure-related inefficiencies by modifying three key exhaust parameters: baffle plate hole diameter, header pipe length, and header pipe diameter. Computational Fluid Dynamics simulations were performed in ANSYS Fluent using steady-state compressible flow assumptions, with boundary conditions replicating atmospheric pressures at sea level (1.013 bar), 10,000 ft (0.696 bar), and 21,000 ft (0.445 bar). Mesh independence validation was achieved with a final error margin of 0.01%, ensuring numerical accuracy. Important results show that decreasing the baffle plate hole diameter from 6 mm to 3 mm increases backpressure, enhancing scavenging efficiency but potentially raising exhaust temperature. At 21,000 ft, the optimal backpressure of 0.23 bar was achieved with a 4.6 mm baffle hole. Similarly, reducing header pipe length increased backpressure (0.105 bar at 122.5 mm vs. 0.09985 bar at 162.5 mm), while increasing header pipe diameter raised backpressure (0.104 bar at 36 mm vs. 0.097 bar at 24 mm). The optimal combination 4.6 mm hole, 122.5 mm length, and 36 mm diameter provides a favorable balance of flow resistance and scavenging, improving engine efficiency at high altitudes. These findings demonstrate that passive exhaust geometry tuning can effectively enhance UAV engine performance under altitude-induced pressure changes, offering a practical and scalable design approach. Unlike prior studies that focus on powertrain enhancements via turbocharging or fuel system control, this work offers a novel, passive exhaust geometry optimization strategy tailored to UAV engines. The study

***Corresponding author.**
*E-mail address: majid.baseer@insa-lyon.fr

This paper was recommended for publication in revised form by Regional Editor Ahmet Selim Dalklic

Published by Yıldız Technical University Press, İstanbul, Turkey
Yıldız Technical University. This is an open access article under the CC BY-NC license (http://creativecommons.org/licenses/by-nc/4.0/).

fills a critical research gap by systematically quantifying the relationship between exhaust configuration and altitude-dependent backpressure. Specific results include achieving a 0.23 bar backpressure at 21,000 ft using the optimized configuration, which allows for efficient engine operation without hardware modifications. This work contributes to lightweight, cost-effective unmanned aerial vehicle design by enabling high-efficiency performance without additional propulsion components, and the findings are presented in a manner accessible to a broad engineering audience.

Cite this article as: Said F, Khan Z, Baseer M, Rashid MN, Bilal M, Hussain R Design of optimized exhaust system for two stroke unmanned aerial vehicle engine. J Ther Eng 2026;12(1):254 −277.

INTRODUCTION

The development of two-stroke engines started in the 19th century and these technologies are still in use these days. Two-stroke engines have fewer parts, and because combustion occurs in both strokes, they are preferred when a high power-to-weight ratio is desired compared to the four-stroke engines. However, one disadvantage of two-stroke engines is that the fuel-air mixture escapes through the exhaust port along with the exhaust gasses, since the combustion and compression strokes end at the same time [1]. In a two-stroke engine, the end of the combustion stroke and the beginning of the compression stroke happen simultaneously, with the intake and exhaust (or scavenging) functions occurring at the same time. It causes a problem such that fresh air-fuel mixture also leaks out with the exhaust gases to the exhaust ports, thus compromising the engine's performance [2]. Fresh air-fuel mixture supplied to the combustion chamber may get combined with the exhaust gases by convection and turbulent mixing and leak out into the exhaust system during the scavenging process of a two-stroke engine [3]. Drones with two-stroke engines were used as moving targets for flight training by the 1930s. The 1980s witnessed a major shift toward major development, with the U.S. collaborating with Israel to develop the RQ2 Pioneer in 1986, setting the stage for modern Unmanned aerial vehicles (UAVs) [4].

The performance of the two-stroke engine is greatly influenced by the backpressure generated in its exhaust system. An exhaust system design should be such that it offers an optimum backpressure to ensure optimum performance of the engine. If the backpressure exceeds certain limits, it results in overheating, more fuel consumption, or even a complete engine shutdown. If the backpressure value is less than a certain limit, so great amount of fresh air-fuel mixture will leak out into the exhaust system [5].

An aircraft that operates without a pilot on board is known as a UAV [6, 7]. The rise of lightweight materials and affordable electronics has driven rapid market growth and enabled the use of UAVs in low-budget, non-military projects [8]. UAVs with propellers are frequently used for both military and non-military applications. While military UAVs are better suited to endure harsh conditions, civilian UAVs benefit from low noise levels, which gives them a competitive advantage [9]. With the increase in environmental hazards, energy conservation has become a major concern these days for consumers and companies seeking to create a more suitable environment [10]. A UAV is an unmanned aerial vehicle that has no crew, passenger, or pilot on board and is operated autonomously or from a ground station. Its main purpose is surveillance, used by the military for anti-aircraft target positioning [11]. From the above environmental simulation, it is impossible to ascertain the accurate fuel supply for the UAV engine, since in two-stroke engines, the carburetor can only mechanically advance the fuel delivery system while the engine is running [12].

Great environmental concerns have led to great focus and work on the optimization of the engine performance and its emission controls. Strict legislations are being made which will put more pressure on designers and researchers regarding engine performance optimization and emission controls. Besides other engine design and operating parameters, exhaust gas recirculation must also be optimized for the best output from the engine [13].

The two-stroke engine has been used in UAVs and other aircraft due to its high power-to-weight ratio [14]. With advancements in various fields, UAVs have also been enhanced in recent decades. UAVs play an important role in both civil and military sectors due to their quiet movement and cost-effectiveness [15, 16].

To increase the efficiency of UAV engines, various researchers have explored different methods. For instance, Crosbie et al. [2] found that even though commercial internal combustion engines are used in RP aircraft, their performance declines with increasing altitude. Reduced atmospheric pressure at high altitudes impairs exhaust scavenging in two-stroke UAV engines. Optimizing backpressure improves combustion stability and engine reliability in low-density environments. To maximize horsepower at high altitude locations, a throttle body fuel injection system was added to augment the carburetor for improved top-end output at sea level and to provide consistent horsepower during operation. Reduced atmospheric pressure at high altitudes hinders exhaust scavenging in two-stroke UAV engines. Optimizing backpressure enhances combustion stability and improves engine reliability in low-density environments. According to this study's fuel injection findings, the human factor could be reduced from the equation altogether, and the engine performance could be optimized through the following methods:

- Introduction of an efficient fuel metering system properly
- Maintaining fuel atomization
- Implementing basic LSI-fuel ratio adjustment systems

Later, if more power and easier engine operation are desired, it is suggested to use an open loop fuel injection

system. Finally, manufacturers can gain insights into the capabilities of RPA engines in terms of altitude using both carbureted and fuel injected systems [17]. UAVs are classified by Moshkov et al. [18] based on their performance parameters, which include weight, wing load, range, and speed, as well as their civilian and military uses. The paper examined various engine types such as two-stroke, electric, turboprop, turbofan, piston, and propeller engines used in UAVs, outlining the benefits and drawbacks of each. It is observed that piston engines are preferred for heavier, larger UAVs, whereas electric engines are commonly used in lighter, smaller models. Because they can be used in a wide range of UAV sizes and applications, electric and piston engines are among the most common in UAVs. The study also highlighted the significance of choosing engine types based on specific missions and operational requirements, since this influences both noise characteristics and overall performance.

Young et al. [19] analyzed a multi-stage turbocharger system designed for a hydrogen-fired internal combustion engine for a HALE UAV, which can reach an altitude of 60,000 ft. Fischer used a three-stage turbocharger boost system along with an intercooler to achieve an intake air pressure of 1.7 bar. Since this research focused on the performance analysis of multi-stage turbochargers at cruise altitude, one-dimensional analysis was used to determine the power requirements of the compressors and turbines and identify suitable turbochargers from among the products offered in the market. Given these findings, it can be concluded that the operating points for the given turbochargers remain in the acceptable range and are well below compressors choking points. Additionally, this study enabled an evaluation of system performance and preliminary design.

Moshkov et al. [20] conducted a study on a UAV equipped with a four-bladed, shrouded pusher propeller and a two-stroke piston engine. Wind tunnel experiments, performed at varying engine speeds and flow velocities, identified the two-stroke engine as the primary noise source, particularly in the absence of an exhaust suppressor. The propeller's noise contribution was observed in the radiation spectrum's first even harmonics. At an engine speed of 5.3, total sound power increased, with acoustic efficiency ranging between 0.21% and 0.91%. To develop effective noise-reduction strategies for different UAV power plant configurations, future research should explore the implementation of mufflers, enclosed engine housings, and four-stroke engines.

With a focus on general aviation and unmanned aerial vehicle applications, Cantore et al. [21] described a novel design concept for two-stroke aircraft diesel engines that aim to achieve high power density, low weight, and high efficiency. The engine design under consideration employs a proprietary rotary valve system for enhanced scavenging and supercharging. This method involves an external piston pump, which improves crankshaft balance and eliminates the necessity of poppet valves or camshafts. The 1.5-liter, three-cylinder, turbocharged engine produces 150 kW at sea level and 100 kW at 20,000 feet. It can run on gasoline direct injection (GDI) or diesel cycles using a direct injection common rail system. When compared to four-stroke diesel engines, the engine achieves aircraft performance requirements with less weight and smaller dimensions thanks to numerical optimization utilizing CFD simulations.

Hooper [22] examined how changes in compression ratio affect a spark-ignition UAV engine's ability to run on heavy fuel. The study investigated the engine's performance using gasoline and kerosene Jet A-1 kerosene fuels through a combination of experimental dynamometer testing and one-dimensional fluid dynamic modeling with WAVE software. The findings demonstrate that a power loss of 5.7% occurs when the compression ratio is lowered for heavy fuel operation, resulting in a power output of 15.35 kW at 6,500 RPM, compared to 16.27 kW with regular gasoline. The work offers insights for improving heavy fuel performance in UAV engines and validates computer models.

The effects of rotor speed and crosswind on the spatial atomization properties of droplets sprayed by UAVs are analyzed by Feng et al. [23] using computational fluid dynamics (CFD) simulations, they discovered that smaller droplets (65 -130 μm) formed closer to the nozzle under negative pressure, while larger droplets (390 - 520 μm) accumulated farther from the nozzle under positive pressure. While crosswinds caused droplet stratification and longer drift distances, higher rotor speeds improved droplet uniformity and dispersal. Experimental validation confirmed that increasing downwash can reduce the detrimental effects of crosswind on droplet dispersion and enhance spraying efficiency.

Ding et al. [24] examined power, torque, fuel consumption, and heat balance in their analysis of a UAV opposed-piston gasoline engine operating at altitudes between 0 and 7000 meters. According to the study, power and torque decrease by 11.25% and 12.5%, respectively, while fuel consumption increases by 2.8% at high speeds and 14.4% at low speeds for every 1000 meters of altitude gained. In addition, the temperature of the cooling water increases and subsequently lowers with altitude, and there is a significant drop in the cylinder surface temperature. The engine loses over 30% of its heat at 6000 meters and 3000 rpm, and its thermal efficiency falls to less than 5%.

Ballı et al. [25] conducted an exergetic and sustainability performance assessment of a medium-scale turboprop engine (m-TPE) used in UAVs. The study revealed that the overall exergy efficiency of the engine was 17.24%, with the

exergy efficiencies of various components, including the compressor (87.21%) and the combustor (52.51%), significantly varying. The combustor, in particular, was identified as the least efficient component, contributing most to the engine's overall inefficiency. In terms of sustainability, the environmental effect factor was found to be 4.80, indicating substantial environmental impact, while the exergetic sustainability index (0.21) and ecological effect factor (5.80) further highlighted areas for potential improvement. These findings emphasize the importance of optimizing the combustor for enhanced performance and sustainability.

The primary focus of the study conducted by Aswin et al. [26] is on designing and managing the electronic control unit (ECU) for a medium-altitude UAV's two-stroke internal combustion engine (ICE). An electronic fuel injector (EFI) and exhaust gas detection enabled the regulation of the air-fuel ratio (AFR) in the combustion process. The three main modules of the ECU include the multi-sensor interface, spark timing and fuel injection timing, and fuel injection volume control. These were based on closed-loop and event-driven interrupt concepts, which were integrated into the system design. It was possible to adjust the system's control parameters through the modulation of a PID Neural Network (PIDNN). The suitability of the Reforming-Controlled Compression Ignition (RefCCI) method, which combines low-temperature combustion (LTC) with thermochemical recuperation (TCR) for UAV applications, especially high-altitude long-endurance (HALE) missions, is evaluated by Eyal and Tartakovsky [27]. The study investigated how engine performance and combustion control are affected by variations in compression pressure ratio and fuel reactivity ratio (H_2/DME). The results suggest that RefCCI can achieve high efficiency and low fuel consumption comparable to conventional gasoline engines, even with DME's lower heating value. Optimizing energy dissipation can reduce losses and improve efficiency by up to 4%. To refine fuel injection strategies and enhance performance, further experimental studies are required.

Aygün [28] conducted a parametric analysis of a conceptual turbojet engine with an afterburner (TJEAB) to optimize energy and exergy parameters. The study focused on military mode (MM) and afterburner mode (ABM) using compressor pressure ratio (CPR) and turbine inlet temperature (TIT) as key variables. Results showed that minimum specific fuel consumption (SFC) was 28.59 g/kN.s in MM and 43.95 g/kN.s in ABM, with a maximum overall efficiency of 13.07% in MM and 8.5% in ABM. Exergy efficiency was 30.85% in MM and 23.2% in ABM. The exergetic sustainability index reached 0.446 in MM and 0.269 in ABM, highlighting the potential for improved fuel efficiency and environmental impact in engine design.

Thus, Koji et al. [29] determined that at low Reynolds numbers, the exhaust heat characteristics for designing a high-altitude long-endurance (HALE) UAV with a wing-surface heat exchanger depend on the aerofoil geometries. The Pareto optimization of an aerofoil shape is a process of searching for an optimal balance between competing objectives, where a solution is considered acceptable if it provides a satisfactory trade-off between both objectives. CFD simulations revealed that increased transition at the leading edge improves heat-exhaust performance. A multi-objective optimization and parametric study were conducted to enhance both the aerodynamic efficiency and heat-exhaust characteristics of the UAV's aerofoil. This preliminary analysis indicated that the Nusselt number distribution is a function of the upper-surface geometry, particularly within the region between the trailing edge and the point of laminar-to-turbulent boundary layer transition. A study on the optimal aerofoil design using multi-objective optimization demonstrated that aerodynamic and heat-exhaust performance are interdependent, with lower-surface curvature significantly influencing aerodynamic efficiency.

Peter L. et al. [30] investigated the effects of oxygen-enriched intake air on a naturally aspirated diesel engine under high-altitude simulation. They discovered that engine load was the primary factor determining power output and that oxygen enrichment had no discernible effect on engine power at elevations up to 2600 meters. Fuel conversion efficiency, brake-specific fuel consumption (BSFC), and oxygen enrichment were shown to be strongly correlated. Altitude and oxygen content had the most effects on combustion temperature, but engine load and fuel injection time had the least effect. Due to limited oxygen availability, the rate of heat release (ROHR) decreased at 5200 m, but at higher elevations, it rose significantly with higher oxygen levels.

Huang et al. [31] carried out an experimental investigation into how elevated exhaust backpressure influences the combustion process and overall performance of diesel engines. Their findings showed that higher levels of backpressure result in increased in-cylinder temperatures and pressures, conditions that can worsen fuel-air mixture leakage and disrupt stable combustion. The research highlights the importance of carefully designing exhaust systems to control and minimize backpressure for improved engine efficiency.

Murali et al. [32] conducted a detailed review examining how exhaust backpressure influences the functioning of internal combustion engines. The study indicated that lowering backpressure by just 1 kPa could enhance engine output by 0.22 to 0.45 kW, while a 10 kPa drop might lead to a 1.5% to 3% reduction in fuel consumption. These results underscore that elevated backpressure can hinder exhaust gas expulsion, contributing to greater fuel usage and a decline in engine efficiency.

Another way of managing fuel-powered UAVs, presented by Yixuan Wang et al., [33] focuses on fuzzy PID controllers. By comparing and modeling the results derived from applying the fuzzy-PID concept and the conventional PID approach, it is concluded that the fuzzy-PID controller offers superior performance in minimizing air-fuel ratio (AFR) control errors compared to the traditional PID

method across various operating conditions. A comparison with conventional PID control shows that the new fuzzy PID controller reduces overall error by 55% to 80%. One key advantage highlighted in the findings is the controller's ability to handle multiple and significant interferences. Demonstrating the effectiveness of the proposed technique, the study found that the highest AFR errors using fuzzy-PID control remained ≤ 3%. The data presented in this research is valuable for UAV aero engine control and suggests potential avenues for further improvement. The fuel characteristics were the primary focus of the study by Mehran Bahari et al., [34] which examined two ultrasonic unmanned aerial vehicle propulsion systems. These systems incorporated key design factors and flight conditions to develop formulas aimed at maximizing thrust while minimizing fuel consumption. A solid oxide fuel cell (SOFC) was utilized, and it was found that higher pressure ratios and altitude improved both efficiency and compressor output power. The higher efficiency of hydrogen fuel was attributed to the use of anode recirculation. The optimized hydrogen-fueled system required 0.0024 kg/s of fuel and achieved 48.7% efficiency, while the methane-fueled engine required 0.0066 kg/s of fuel and attained 67.9% efficiency. This research indicates that fuel efficiency and thrust optimization can be further improved using genetic algorithms.

To optimize the parameters of a turboprop engine for a UAV, Ali et al. [35] proposed an innovative genetic algorithm-based method to develop the optimization code. Prior UAV and piston engine sizing was conducted based on a specified mission profile. Both single-objective and multi-objective optimizations were performed to increase the engine's specific power and enhance UAV loiter endurance. In single-objective optimization, either the loiter time was reduced by 12.3% or the specific power increased by 17.5% from the baseline. M. Rostami et al. [36] studied two different UAV propulsion systems that use solid oxide fuel cells (SOFCs) to generate thrust and heat. To identify key design parameters, optimization using a genetic algorithm and the TOPSIS approach was performed. The results indicate that altitude and compressor pressure ratio enhance efficiency and power output. Compared to hydrogen fuel, anode recirculation in the SOFC further improves efficiency. In comparison to a methane-fueled system, the hydrogen-fueled system achieves an efficiency of 48.7% with a fuel consumption of 0.0024 g/s. Future research can focus on experimental implementation and SOFCs with higher power densities. Abu Bakar et al. [37] studied the design of a solar-powered UAV, optimized for low-altitude, long-endurance flights, using a unique framework. The wing airfoil and overall geometry were optimized through an evolutionary method, considering static stability. A mass estimation model accounts for wing airfoil shifts, and the design integrates longitudinal and lateral control systems using LQR and PID controllers. The design method was validated through nonlinear simulations. The optimized UAV weighs 7.08 kg in total, including a 3.4 kg battery. The results indicate that the proposed design is viable for multi-day flights. Hashmi et al. [38] demonstrated the performance prediction of a spark-ignited engine used in UAVs at high altitudes using a 1-D simulation technique Test results validated the 1-D thermodynamic model, showing a strong correlation. The validated model can be used to predict design modifications and optimize engine performance. The simulation results for power, torque, and specific fuel consumption closely matched the test data. Although the in-cylinder pressure trend differed slightly, the simulation accurately predicted the power reduction with altitude. Overall, the 1-D simulation model provided precise and reliable results, making it a valuable tool for evaluating design alternatives.

Table 1 highlights the scope of prior research related to UAV engine performance under varying altitude conditions, revealing a predominant emphasis on combustion characteristics, power output, and fuel delivery mechanisms. Studies frequently explore turbocharging, electronic control units, or fuel mixture enrichment to maintain engine performance at altitude. However, the geometric configuration of exhaust systems, particularly components like baffle plates and header pipes has not been adequately investigated, especially regarding their role in modulating backpressure at high elevations.

Previous studies have largely focused on improving UAV engine performance through active measures such as turbocharging, ECU-based fuel metering, and fuel injection systems, especially at high altitudes. This study differs from turbocharging and ECU-based approaches by focusing exclusively on passive geometry optimization.

This research addresses that overlooked dimension by focusing on how changes in baffle plate hole diameter, header pipe length, and header pipe diameter influence backpressure at sea level, 10,000 ft, and 21,000 ft. As shown in Table 1, existing literature either omits geometric exhaust considerations entirely or fails to link them to altitude-specific performance. By identifying and filling this research gap through a CFD-based approach, the current work offers a novel and passive design strategy that improves UAV performance without requiring complex hardware upgrades, an advancement with practical implications for lightweight and cost-sensitive UAV systems.

MATERIALS AND METHODS

An extensive numerical study was carried out to examine the backpressure properties in the exhaust system of a two-stroke UAV engine using ANSYS Fluent 19.2, a powerful computational fluid dynamics (CFD) program. A detailed parametric study was conducted using 15 configurations, varying baffle diameter, header length, and altitude. The study used steady-state simulations, assuming that air behaves like an ideal gas. Measurements of backpressure were made at sea level first, and subsequently at 10,000 and 20,000 feet above sea level. This approach allowed for

Table 1. Summary of Studies on two stroke UAV Engine

Author(s)	Methods	Performance	Findings	Limitations	Ref
Moshkov et al.	Classification based on performance parameters	Electric, piston engines identified	Electric engines used in smaller UAVs; piston engines preferred for larger UAVs	Context-specific lacks real-world validation	[14]
Young et al.	Multi-stage turbocharger analysis	System designed for HALE UAV	Focus on multi-stage turbochargers and system performance at cruising altitude.	One-dimensional analysis; no experimental data	[15]
Moshkov et al.	Wind tunnel experiments	Two-stroke engine noise analyzed	Noise from two-stroke engine dominates; exhaust suppressor reduces noise	Focused on noise reduction strategies	[16]
Cantore et al.	CFD simulations for engine design	150 kW at sea level, 100 kW at 20,000 ft	High power density, and low weight for UAV engines	Needs real-world testing	[17]
Hooper	Experimental dynamometer testing and fluid dynamics modeling	Power loss with heavy fuels	Compression ratio influences power output; loss of 5.7% in power for heavy fuels.	Limited to one engine type	[18]
Feng et al.	CFD simulations for droplet atomization	Improved spray efficiency	Rotor speed affects droplet distribution; crosswinds impact dispersion	Experimental validation needed	[19]
Ding et al.	Experimental study at varying altitudes	Power loss with altitude	Power and torque decrease with altitude; the engine loses 30% of heat at high altitudes	Limited to specific altitude ranges	[20]
Aswin et al.	ECU design for two-stroke ICE	ECU control of combustion	Modulation of AFR improves performance using a PID Neural Network	Limited to ECU optimization	[21]
Eyal & Tartakovsky	RefCCI method evaluation	High efficiency and low fuel consumption	RefCCI method shows improvement with low-temperature combustion	Requires more experimental studies	[22]
Koji et al.	Multi-objective optimization of aerofoils	Improved aerodynamic performance	Aerofoil shape optimization improves heat-exhaust characteristics	Limited to simulation results	[23]
Peter L. et al.	Climatic test with oxygen-enriched air	Affected power production	Oxygen enrichment affects combustion efficiency, with altitude sensitivity	Results may vary with real-world testing	[24]
Yixuan Wang et al.	Fuzzy-PID controller analysis	Reduced AFR control errors	Fuzzy-PID minimizes AFR errors more effectively than traditional PID	Requires further development for various UAV types	[25]
Mehran Bahari et al.	Ultrasonic propulsion system analysis	Efficiency and thrust optimization	SOFC systems improve fuel efficiency with genetic algorithms	Requires optimization for real-time applications	[26]
Ali et al.	Genetic algorithm-based optimization	Increased engine specific power	Multi-objective optimization improves UAV performance	Limited to single-engine UAVs	[27]
M. Rostami et al.	Genetic algorithm and TOPSIS optimization	48.7% efficiency in the hydrogen system	SOFC optimization improves power and fuel efficiency	Focused on theoretical optimization	[28]
Abu Bakar et al.	Evolutionary optimization method	7.08 kg UAV with solar power design	Solar-powered UAV optimized for long-endurance flights	Needs experimental validation	[29]
Hashmi et al.	1-D thermodynamic simulation	Power drop with altitude	The simulation model accurately predicts engine performance at varying altitudes.	Limited to simulation-based predictions	[30]

a thorough understanding of how engine exhaust performance is impacted by varying air pressures.

Physical Model Description of UAV Exhaust System

For the UAV engine to operate effectively and efficiently, the exhaust system is essential. The header pipe, tail pipe, muffler, and baffle plates are some of its essential parts. The main exhaust gas conduit is the header pipe, with a baseline length of 142.5 mm. Additional configurations ranging from 122.5 mm to 162.5 mm in length, all with a diameter of 30 mm, were tested. The exhaust is then directed away from the UAV by these gasses flowing into the tail pipe, which has a 15 mm diameter and a 30-degree angle. A 30-degree tail pipe angle minimizes flow recirculation near the UAV airframe, ensuring clean and direct exhaust ejection. The baffle plates, which have holes with a 6 mm diameter, are positioned carefully to regulate flow and maximize exhaust gas dynamics, while the muffler lowers noise emissions. Baffle plates regulate exhaust flow to control backpressure and improve scavenging, while mufflers reduce noise with minimal flow disruption to exhaust flow. The Hirth 4201 engine delivers 15 kW, boasts a high power-to-weight ratio, and is widely used in UAVs, making it an ideal candidate for exhaust optimization studies. (Fig.1)

MATHEMATICAL MODEL

Assumptions

Assumptions used in this investigation.

The flow is considered compressible and ideal

Air is treated as an ideal gas due to the operating temperature and pressure ranges observed in UAV propulsion systems. Under these conditions, the behavior of combustion products can be reasonably approximated using the ideal gas law, which decreases computational costs significantly without compromising accuracy. Flow is considered compressible as the Mach number for the flow calculated is greater than 0.33.

A steady-state fluid flow is applied

Steady-state simulations were chosen instead of transient analysis as the calculations are made under stable engine operating conditions. The compressible forms of the Navier-Stokes equations were solved using ANSYS Fluent's pressure-based solver. UAV is considered cruising at constant engine RPM. This methodology captures the dominant flow physics relevant to backpressure optimization while significantly reducing computational time and resource requirements.

- Exhaust temperatures were modeled up to 700 K, with pressures adjusted according to altitude conditions. The maximum Mach number exceeded 0.4, confirming the presence of compressible flow.
- Due to the high Reynolds number (60,000), the flow is analyzed as turbulent.

It is based on calculations of the mass flow rates.

Reynolds Number Calculation

Inputs from Study

Mass flow rate ($\dot{m}$): 0.03 kg/s

Pipe diameter (D): 0.03 m

Dynamic viscosity of air at 500 K (μ): 2.5×10^{-5} Pa·s

Cross-sectional area (A): $\pi D^2/4 = \pi (0.03)^2/4 = 7.07 \times 10^{-4}$ m²

Calculation

Reynolds number formula:

$$Re = (\dot{m} \times D) / (A \times \mu)$$

Substituting the values:

$$Re = (0.03 \times 0.03) / (7.07 \times 10^{-4} \times 2.5 \times 10^{-5})$$

$$Re = (9 \times 10^{-4}) / (1.7675 \times 10^{-8})$$

$$Re \approx 50{,}900$$

- The governing flow is treated as a continuum.
- The Navier-Stokes Equation is applicable.
- The study is conducted using a pressure-based solver.

The pressure-based solver provides a reliable and computationally economical approach that aligns with the flow physics and design objectives of this investigation.

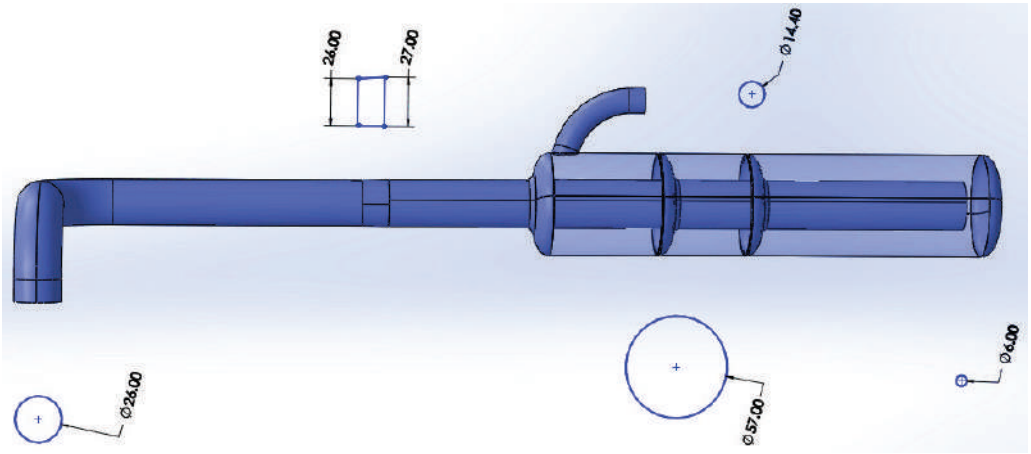

Figure 1. Physical Model of the UAV Exhaust System.

- The No-Slip condition is assumed to be valid.

The no-slip boundary condition assumes that the velocity of exhaust gas at the pipe walls is zero. This is a fundamental assumption in viscous flow modeling and accurately represents physical behavior, where viscous forces cause fluid particles in direct contact with the solid boundary to adhere to the surface. This condition is essential for capturing realistic flow separation, shear stress, and turbulence development along the walls.

- The model is based on a realizable K-ε turbulence model.

The realizable k-ε turbulence model was used, as it is well-suited for simulating complex recirculating flows.

The CFD simulations were conducted under steady-state conditions to isolate the geometric effects on backpressure at a constant cruise RPM. This assumption is valid for level flight segments where UAV throttle settings remain steady. However, future studies should consider unsteady flow simulations that incorporate engine transients and altitude changes to better capture real-world operating conditions.

Governing Equations

ANSYS Fluent employs a pressure-based segregated solver, utilizing second-order upwind schemes for the momentum and turbulence equations. The momentum and continuity equations for the UAV engine exhaust system model are presented numerically as follows:

Equation of Continuity

The equation of continuity states that the sum of the partial derivatives of the fluid velocity components in the x, y, and z directions must equal zero as shown in Eq (1).

$$\frac{\partial u}{\partial x}+\frac{\partial v}{\partial y}+\frac{\partial w}{\partial z}=0 \quad (1)$$

Here, u, v, and w represent the fluid velocity components in the x, y, and z directions, respectively.

Momentum Equations

The momentum equations in the x, y, and z directions are given as follows:

In the x-direction:

$$u\frac{\partial u}{\partial x}+v\frac{\partial u}{\partial y}+w\frac{\partial u}{\partial z}=-\frac{1}{\rho_f}\frac{\partial p}{\partial x}+\frac{\mu}{\rho_f}\left(\frac{\partial^2 u}{\partial x^2}+\frac{\partial^2 u}{\partial y^2}+\frac{\partial^2 u}{\partial z^2}\right) \quad (2)$$

Here, ρf is the fluid density, μ is the dynamic viscosity of the fluid, p is the pressure, and u is the velocity component in the x direction.

In the y-direction:

$$u\frac{\partial v}{\partial x}+v\frac{\partial v}{\partial y}+w\frac{\partial v}{\partial z}=-\frac{1}{\rho_f}\frac{\partial p}{\partial y}+\frac{\mu}{\rho_f}\left(\frac{\partial^2 v}{\partial x^2}+\frac{\partial^2 v}{\partial y^2}+\frac{\partial^2 v}{\partial z^2}\right) \quad (3)$$

Here, ρf is the fluid density, μ is the dynamic viscosity of the fluid, p is the pressure, and v is the velocity component in the y direction.

In the z-direction:

$$u\frac{\partial w}{\partial x}+v\frac{\partial w}{\partial y}+w\frac{\partial w}{\partial z}=-\frac{1}{\rho_f}\frac{\partial p}{\partial z}+\frac{\mu}{\rho_f}\left(\frac{\partial^2 w}{\partial x^2}+\frac{\partial^2 w}{\partial y^2}+\frac{\partial^2 w}{\partial z^2}\right) \quad (4)$$

In this context, the variables, ρf is the fluid density, μ is the dynamic viscosity of the fluid, p is the pressure, and w is the velocity component in the z-direction.

Boundary Conditions

The governing equations can be solved by applying the following boundary conditions.

At the Inlet (x = 0):

Mass Flow Rate

$$\dot{m}_{\text{inlet}} = 0.03 \text{ kg/s} \quad (5)$$

This value (0.03 kg/s) represents the typical mass flow rate of exhaust gases produced by a two-stroke UAV engine under cruise operating conditions. It was selected based on engine performance data using engine test bed data.

Uniform Velocity Profile

$$\text{u} = \text{Inlet Velocity} \quad (6)$$

At the Outlet (x = L, where L is the length of the exhaust pipe)

Pressure outlet: The pressure at the outlet is specified, typically representing ambient pressure.

$$\text{p} = \text{Outlet Pressure} \quad (7)$$

Ambient pressure at different altitudes (from NASA Data) [39].

a) 101324 Pa at sea level
b) 69575 Pa at an altitude of 10,000ft.
c) 44539 Pa at an altitude of 21,000ft.
d) Standard atmospheric pressures were applied for analysis (sea level: 1.013 bar, 10,000 ft: 0.696 bar, 21,000 ft: 0.445 bar). A steady-state analysis approach is appropriate for UAV cruise conditions, where constant RPM allows isolation of geometric effects on backpressure.

At the Walls

No-Slip Condition: The velocity components at the exhaust pipe walls are zero, indicating a no-slip condition.

$$\text{u} = \text{v} = \text{w} = 0 \quad (8)$$

No Heat Flux Condition: Assuming no heat transfer between the exhaust gas and the pipe walls, the heat flux at the walls is neglected.

$$\frac{\partial T}{\partial n}=0 \quad (9)$$

Here, *n* represents the normal coordinate to the walls of the exhaust pipes.

The walls of the exhaust system are assumed to be adiabatic (i.e., zero heat transfer) to simplify the thermal analysis. This assumption is justified since the study focuses primarily on flow behavior and pressure dynamics, not on thermal heat exchange or temperature distribution.

This study models the flow and thermal behavior of exhaust gases in a UAV engine exhaust system using the continuity, Navier–Stokes, and energy equations, which govern the conservation of mass, momentum, and energy. To ensure accurate simulation, suitable boundary conditions are applied. At the inlet (x = 0), a fixed mass flow rate of 0.03 kg/s representing typical two-stroke UAV engine output is imposed, along with a uniform velocity profile. At the outlet (x = L), a pressure outlet condition is used, corresponding to ambient atmospheric pressures at different altitudes (e.g., 101324 Pa at sea level, 69575 Pa at 10,000 ft, and 44539 Pa at 21,000 ft). The pipe walls are modeled with a no-slip condition (u = v = w = 0), and an adiabatic (no heat flux) boundary is assumed ($\partial T/\partial n = 0$), reflecting insulated wall behavior.

Numerical Method and Mesh Independence

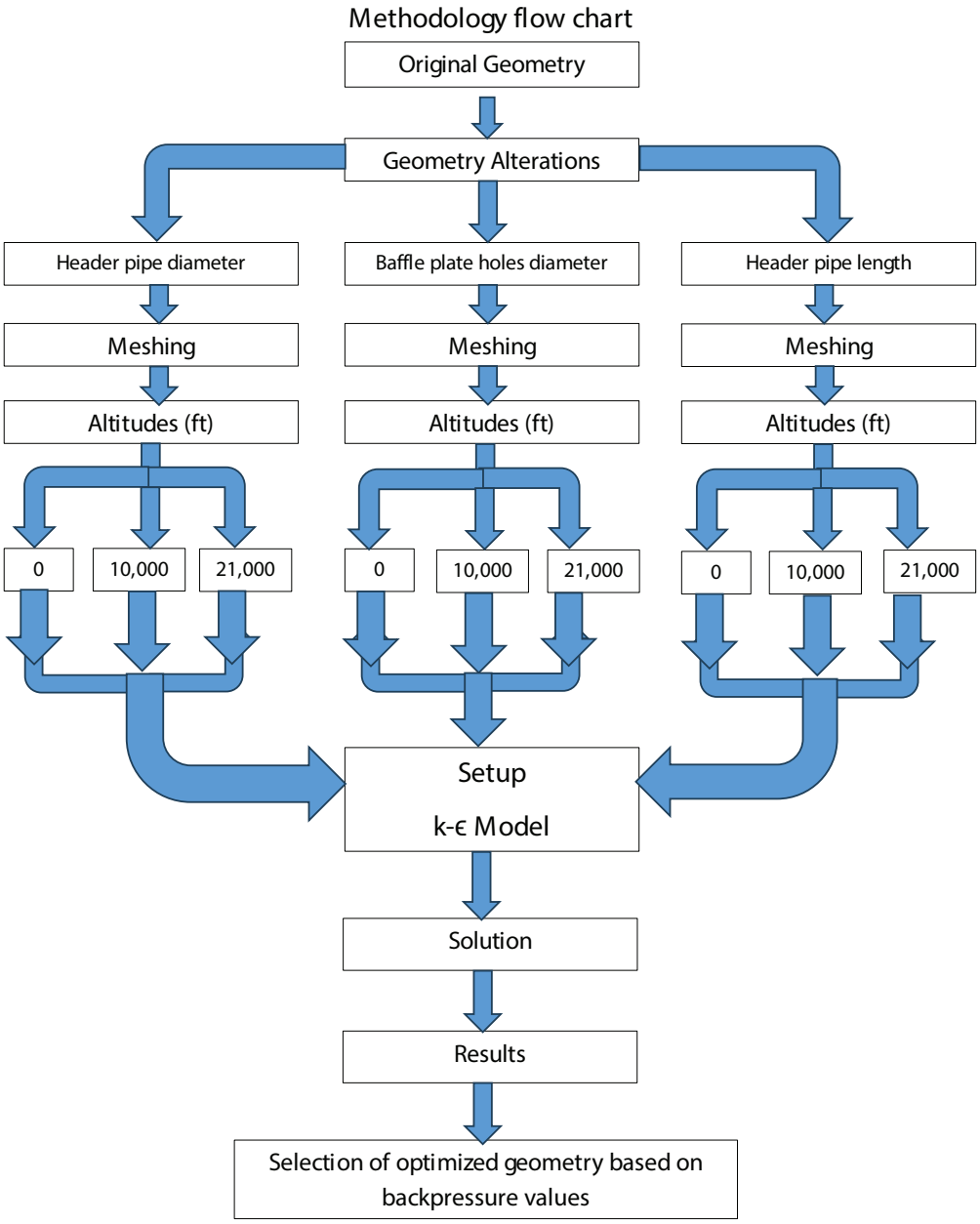

Figure 2. Flowchart of research methodology.

In this study, ANSYS Fluent was utilized to numerically optimize backpressure in UAV engines operating at varying altitudes. To enhance the accuracy and reliability of the simulations, second-order pressure discretization and second-order upwind schemes for momentum equations were employed. These higher-order schemes reduce numerical diffusion and enable more precise resolution of pressure and velocity gradients, particularly in regions with complex geometry or recirculating flow. Their use ensures a more physically accurate representation of exhaust flow dynamics compared to first-order methods. Seven mesh sizes ranging from 765,390 to 1,930,897 elements, were tested using tetrahedral meshes with skewness below 0.35 and orthogonality above 0.8. A convergence criterion of 10^{-6} is used for all variables to ensure solution accuracy.

To verify the reliability of the solution, simulations are conducted using various mesh sizes for the exhaust system of a two-stroke UAV Engine. The relative error in ΔPb is calculated to evaluate the reliability of the solution. ΔP_b represents the change in backpressure between successive mesh refinements. The results are summarized in Table 2:

$$\text{Error } (\%) = \left[\frac{(P_{b2} - P_{b1})}{P_{b1}}\right]_{*100} \quad (10)$$

Where P_{b1} is the previous backpressure value corresponding to Mesh No. 1, and P_{b2} is the current backpressure value corresponding to Mesh No.2, respectively.

RESULTS AND DISCUSSION

The following cases have been simulated at sea level, 10,000ft and 21,000ft. The relevant data, graphs, tables, and contour plots are presented below;

Mesh Independence Validation

To verify the numerical accuracy and reliability of the CFD model, a mesh independence test was conducted using seven different mesh densities ranging from 765,390 to 1,930,897 elements. As shown in Table 2 and Figure 2, the relative error in predicted backpressure (ΔP_b) decreased with increasing mesh density, indicating convergence. The change in backpressure between Mesh No. 6 and Mesh No. 7 was only 0.01%, confirming that the results are independent of mesh resolution. The final mesh showed less than 0.01% variation in backpressure, confirming numerical accuracy. Mesh No. 6 was selected for all subsequent simulations, balancing accuracy and computational efficiency.

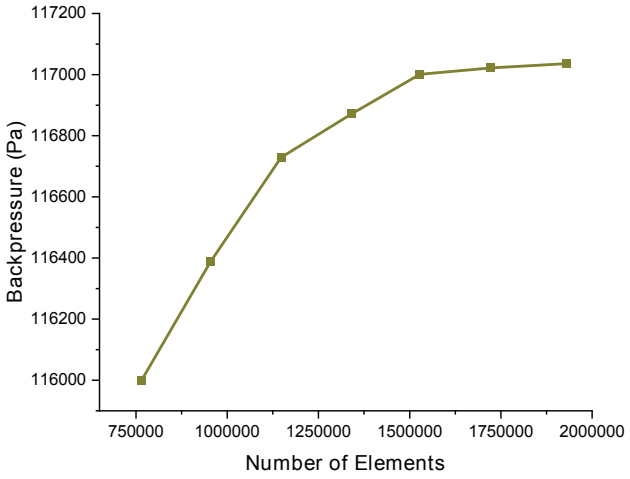

Figure 3. Mesh Independence test.

Based on the data presented in Table 2 & Figure 3, it is evident that the error decreases with an increase in the number of elements. This indicates that the solution is converging, and the result has been validated.

Baffle Plate Hole Diameter

Characteristics of pressure

The effect of varying baffle plate hole diameter on backpressure was thoroughly investigated using ANSYS Fluent. As shown in Figure 4, the results reveal a clear inverse relationship between the baffle plate hole diameter and backpressure, particularly noticeable at higher altitudes where the ambient pressure is significantly lower. An increase in hole diameter leads to a marked reduction in backpressure, promoting improved exhaust flow and potentially enhancing engine efficiency. Conversely, decreasing the hole diameter results in an increase in backpressure, which may hinder exhaust system performance. This trend can be

Table 2. Mesh Independence test

Mesh No	No of Elements	Backpressure (Pa)	Error(%)
1	765390	116000	
2	953761	116387	0.33
3	1147851	116729	0.29
4	1340264	116871	0.12
5	1527861	117001	0.1
6	1723129	117022	0.02
7	1930897	117036	0.01

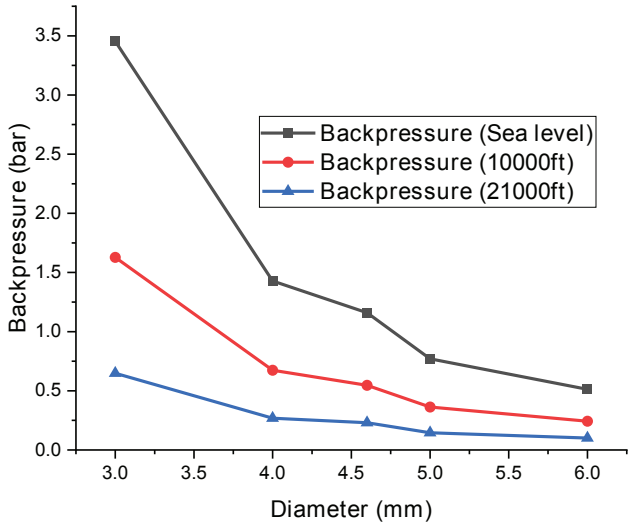

Figure 4. Baffle Plate Hole Diameter vs Backpressure.

attributed to changes in flow resistance within the exhaust system, where larger diameters reduce resistance, allowing for smoother airflow, while smaller diameters increase resistance, restricting flow.

The pressure variations are further detailed in Figures 5 to 9, where contour plots demonstrate how exhaust gases behave across different altitudes and hole diameters. As the exhaust gases encounter the baffle plate, the flow is restricted, increasing the pressure. While larger diameters reduce wall friction, abrupt expansions cause flow separation, leading to increased localized resistance.

Backpressure variation became more pronounced as the baffle hole diameter decreased. The higher backpressure affected flow dynamics by pushing the air-fuel mixture back toward the engine cylinder, thereby improving combustion efficiency. The enhanced combustion efficiency can lead to improved overall engine performance.

The pressure variations illustrated in Figures 5 to 9 captured at sea level (a), 10,000 ft (b), 21,000 ft (c), and the mid-plane section (d) represent the dynamic changes in backpressure as exhaust gases travel from the engine inlet through the muffler, encountering the baffle plate and tailpipe before exiting the outlet. These contours demonstrate how varying the baffle plate hole diameter significantly alters the flow characteristics within the system. Furthermore, as shown in the temperature contours in Figures 5-9, the elevated backpressure is accompanied by an increase in exhaust gas temperature, highlighting the thermal impact of geometric restrictions.

As observed in Figure 5 (D = 3 mm), the smallest hole diameter imposes the highest resistance to flow, resulting in maximum backpressure at all altitudes. The restriction

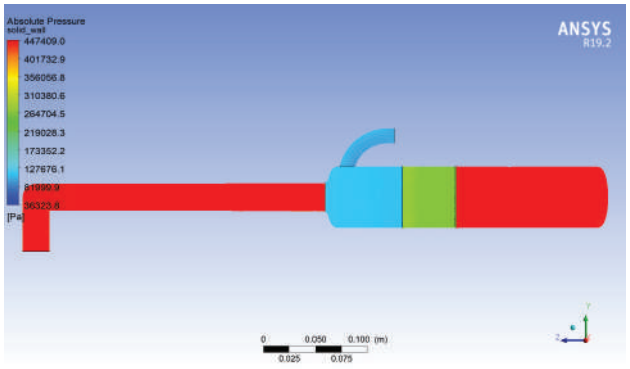

(a). Pressure Contour at Atmospheric Level

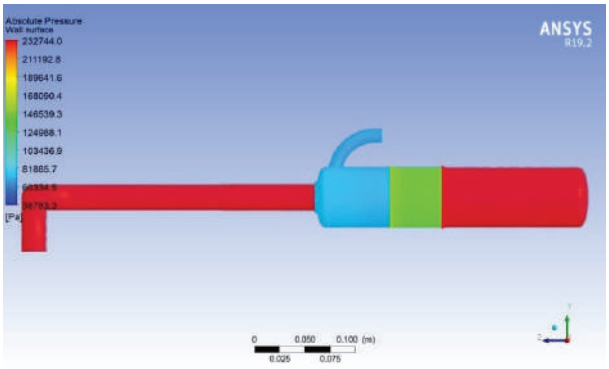

(b). Pressure Contour at 10000ft

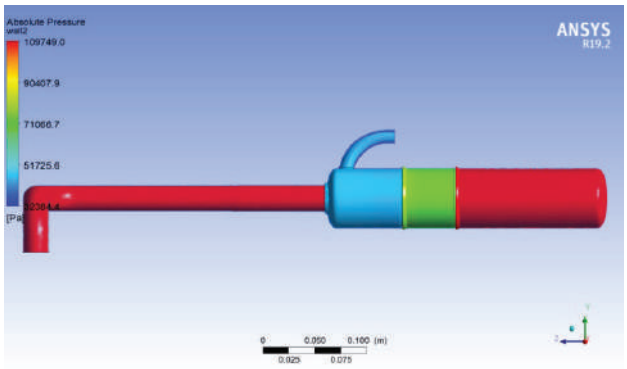

(c). Pressure Contour at 21000ft

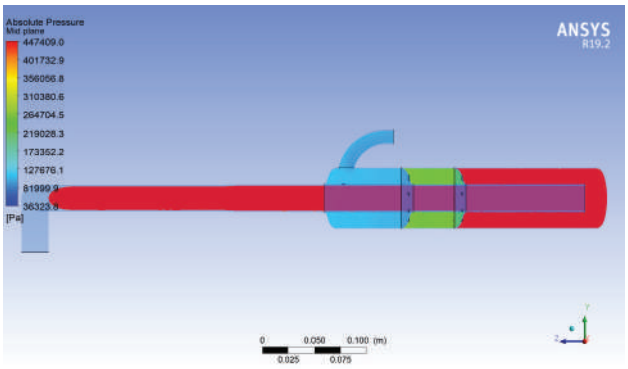

(d). Pressure Contour at Mid Plane at Atmospheric Level

Figure 5. Contour for Baffle plate hole diameter = 3mm.

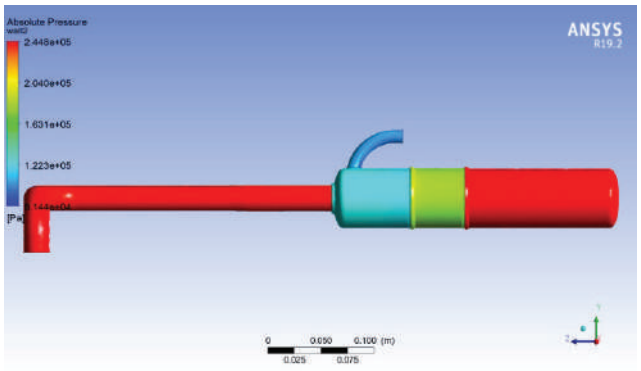

(a). Pressure Contour at Atmospheric Level

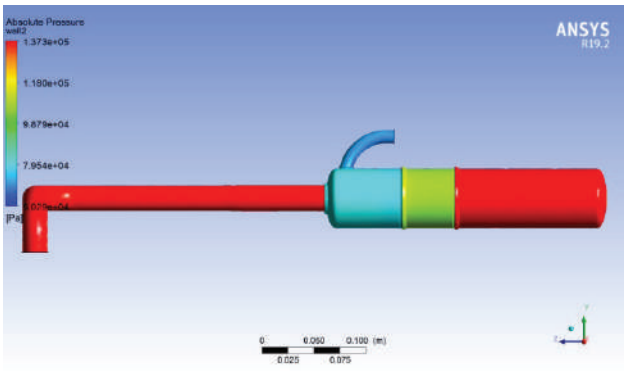

(b). Pressure Contour at 10000ft altitude

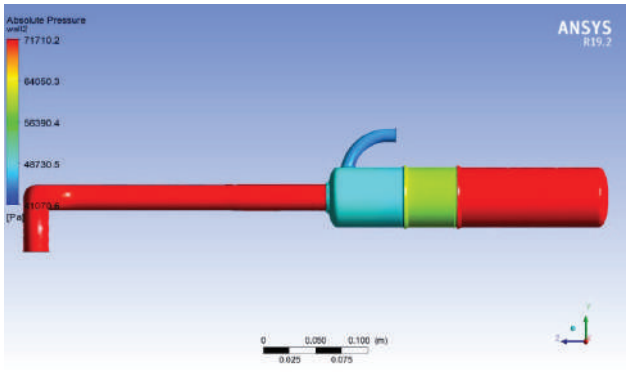

(c). Pressure Contour at 21000ft altitude

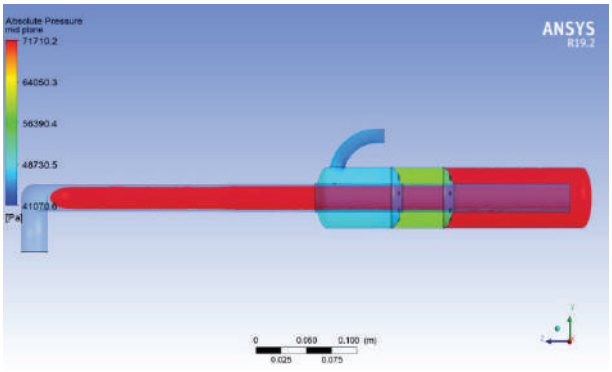

(d). Pressure Contour at Mid Plane at Atmospheric Level

Figure 6. Contour for Baffle plate hole diameter = 4mm.

introduced by the baffle plate amplifies the pressure of exhaust gases upstream, especially evident in subfigures (a) to (c). The increased backpressure exerts a reverse force on the air-fuel mixture, which can enhance cylinder filling and promote more complete combustion. This improved combustion efficiency can lead to better engine performance, particularly at lower altitudes where the pressure differential is greatest.

In contrast, Figures 6 (D = 4 mm) and 7 (D = 4.6 mm) show a gradual decline in backpressure, evidenced by smoother and more distributed pressure fields. These intermediate diameters demonstrate a trade-off: they maintain sufficient backpressure to support combustion dynamics while allowing more efficient exhaust flow. The contours in subfigures (a-c) exhibit a more uniform pressure gradient compared to Figure 5, suggesting reduced turbulence and lower energy losses.

As the diameter increases further in Figures 8 (D = 5 mm) and 9 (D = 6 mm), the restriction decreases markedly, resulting in significantly lower backpressure at all altitudes. Subfigures (a-c) display flatter pressure distributions, and (d) shows minimal disturbance at the mid-plane. While this condition benefits exhaust evacuation and reduces pumping losses, it may not provide sufficient reverse pressure to optimize the scavenging process or sustain combustion efficiency especially under low ambient pressures at high altitudes.

Collectively, Figures 5 to 9 (a-d) confirm that backpressure increases significantly with decreasing hole diameter. This intentional increase in backpressure through smaller holes influences the flow dynamics by pushing the incoming air-fuel mixture toward the engine cylinders, enhancing combustion stability and power delivery. However, excessive backpressure may also lead to higher exhaust temperatures and reduced mechanical efficiency.

These effects stem from fundamental fluid dynamic mechanisms, such as pressure wave reflections and momentum diffusion along the exhaust path. Narrower geometries or abrupt transitions amplify pressure wave intensity, increasing local resistance, whereas smoother transitions promote more uniform momentum dissipation and reduce backpressure. These wave interactions and turbulence dissipation patterns are particularly sensitive at high altitudes due to reduced ambient pressure.

Specific Portion of Header Pipe Length

Characteristics of pressure

According to the investigation, the length of the header pipe plays a significant role in determining the backpressure within the exhaust system. As shown in Figure 10, increasing

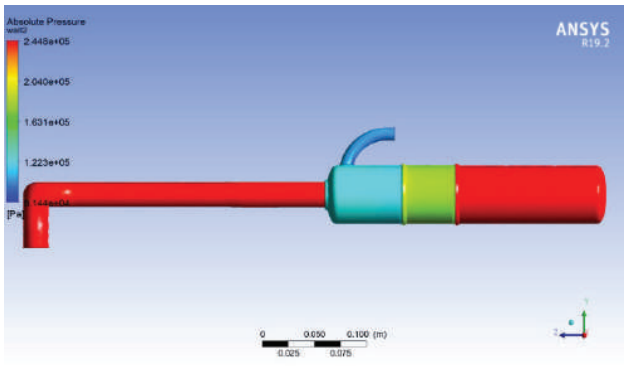

(a). Pressure Contour at Atmospheric Level

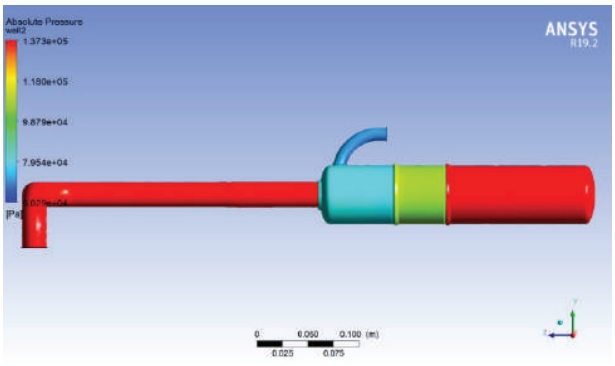

(b). Pressure Contour at 10000ft altitude

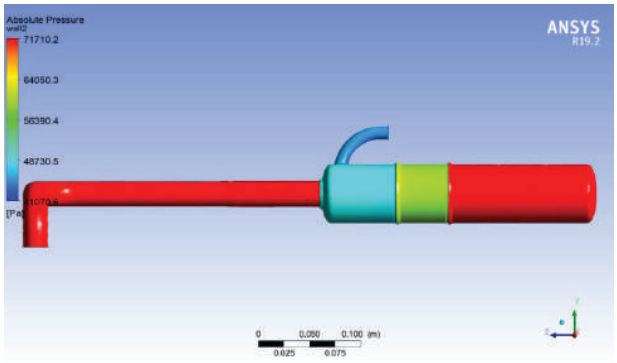

(c). Pressure Contour at 21000ft altitude

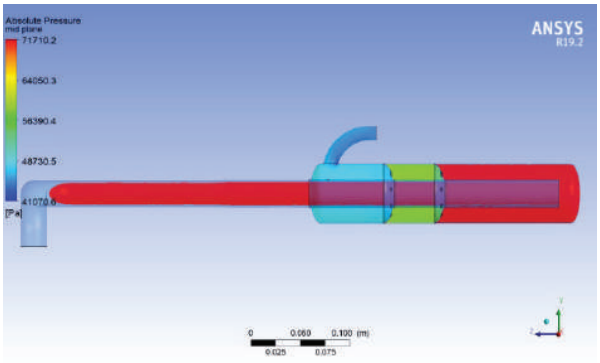

(d). Pressure Contour at Mid Plane at Atmospheric Level

Figure 7. Contour for Baffle plate hole diameter = 4.6mm.

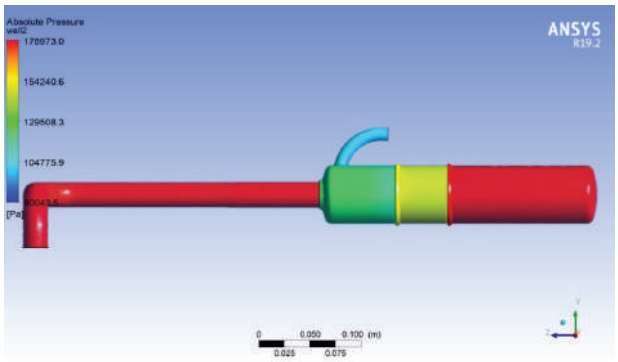

(a). Pressure Contour at Atmospheric Level

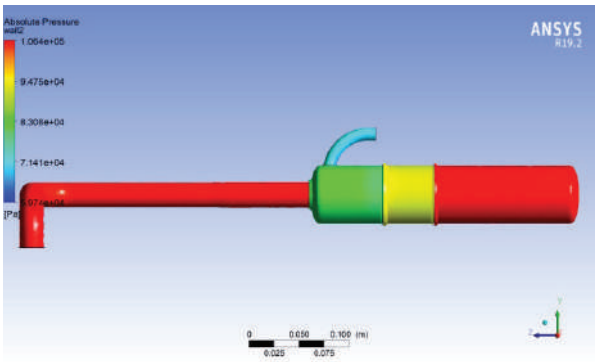

(b). Pressure Contour at 10000ft altitude

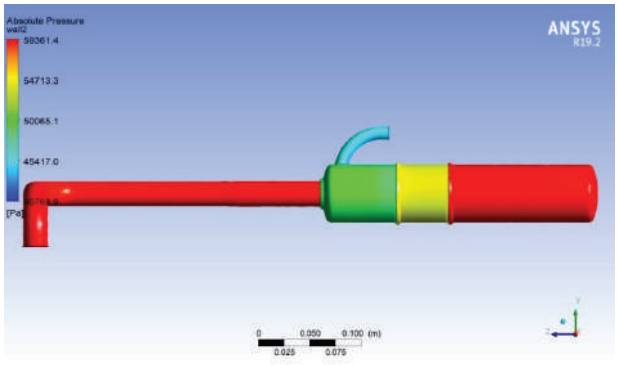

(c). Pressure Contour at 21000ft altitude

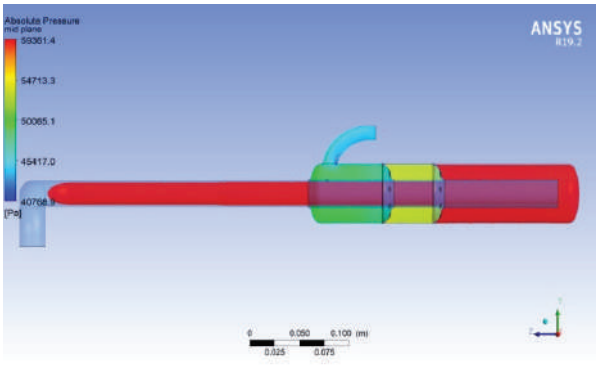

(d). Pressure Contour at Mid Plane at Atmospheric Level

Figure 8. Contour for Baffle plate hole diameter = 5mm.

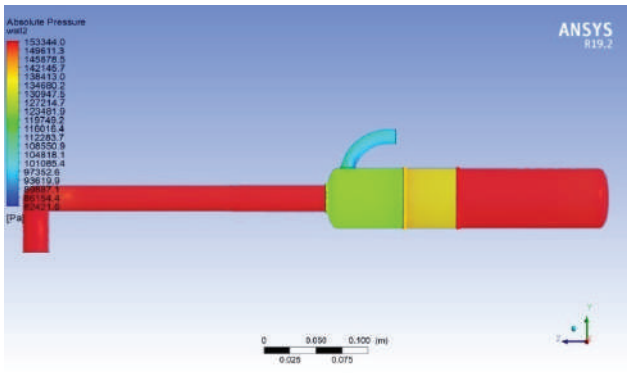

(a). Pressure Contour at Atmospheric Level

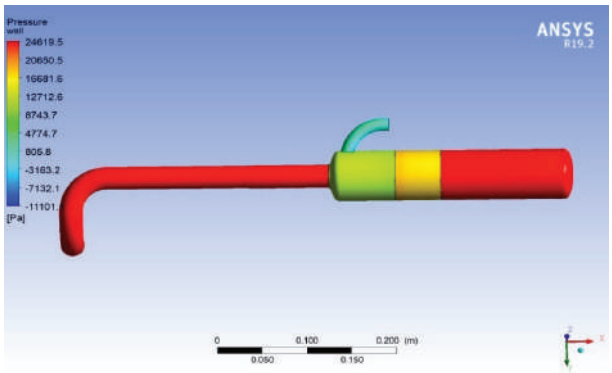

(b). Pressure Contour at 10000ft altitude

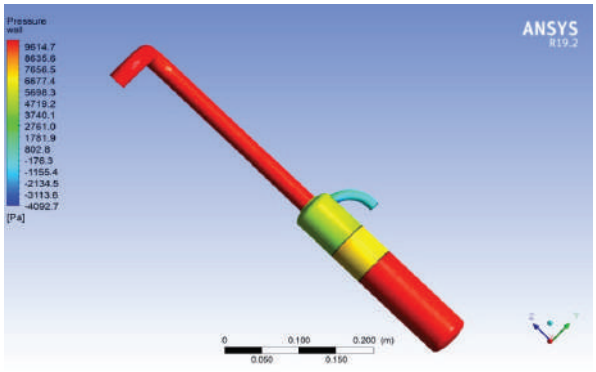

(c). Pressure Contour at 21000ft altitude

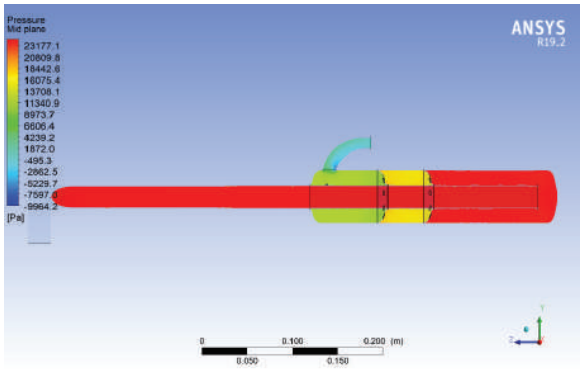

(d). Pressure Contour at Mid Plane at Atmospheric Level

Figure 9. Contour for Baffle plate hole diameter = 6mm.

the length of the header pipe from 122.5 mm to 162.5 mm results in a noticeable reduction in backpressure, particularly at 21,000 ft. Increasing the length of the header pipe reduces backpressure, as the longer pipe allows the exhaust gases to expand more gradually and flow more smoothly, thereby reducing resistance. Conversely, a shorter header pipe leads to a faster accumulation of pressure and higher backpressure due to the more confined flow path. This outcome underscores the critical role of header pipe length in optimizing pressure dynamics and exhaust flow characteristics.

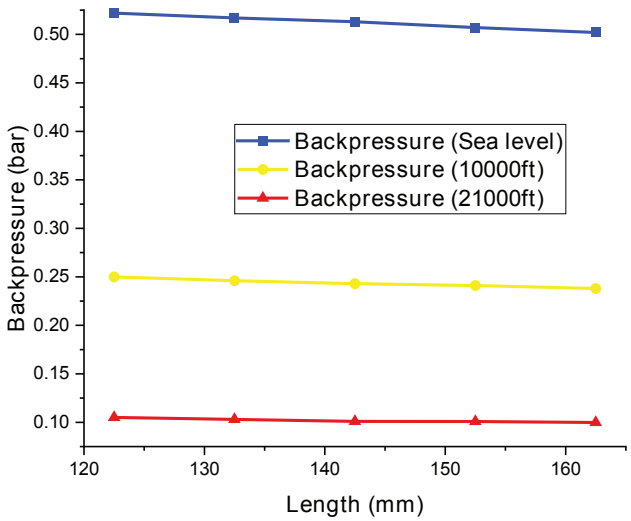

Figure 10. Header pipe Specific Portion Length.

Figures 11 to 15 provide visual confirmation of this trend, showing pressure contours for each header pipe length at different altitudes. These fluctuations in backpressure are a result of altitude-induced variations in air pressure and density as the exhaust gases traverse the system. The findings underscore the importance of optimizing header pipe length for different operating conditions, as it has a direct impact on backpressure levels and exhaust flow dynamics. Effectively managing backpressure through adjustments in header pipe length is crucial for maximizing exhaust system performance, particularly in UAV applications where engine efficiency is sensitive to changes in exhaust flow behavior. Lowering backpressure can enhance exhaust flow and reduce the engine's effort to expel exhaust gases, thereby improving overall engine performance. However, care must be taken, as excessively low backpressure may hinder proper exhaust gas scavenging, potentially compromising combustion efficiency. Consequently, achieving an optimal backpressure, one that maximizes engine efficiency and performance across varying operating conditions and altitudes requires careful calibration of the header pipe length.

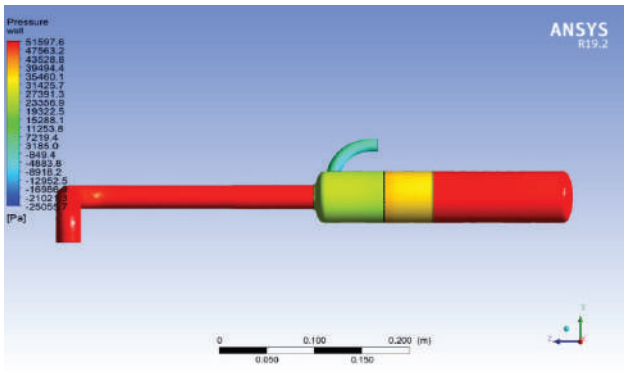

(a). Pressure Contour at Atmospheric Level

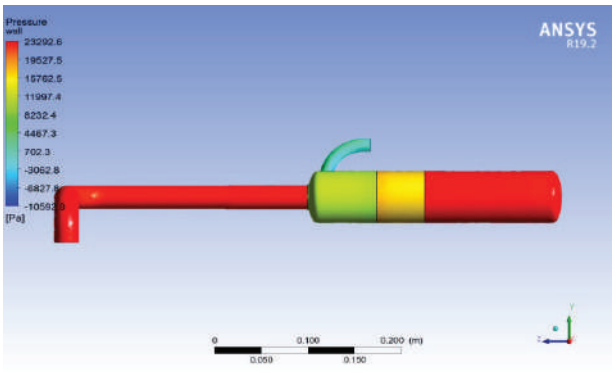

(b). Pressure Contour at 10000ft altitude

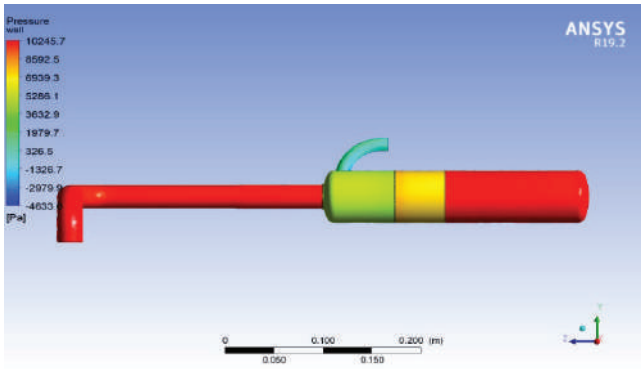

(c). Pressure Contour at 21000ft altitude

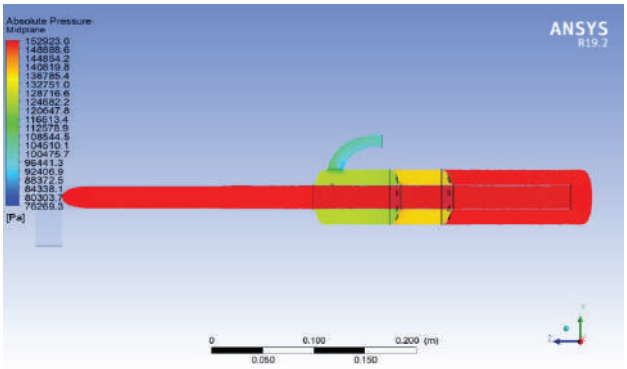

(d). Pressure Contour at Mid Plane at Atmospheric Level

Figure 11. Contour for Header Pipe specific portion Length = 122.5mm.

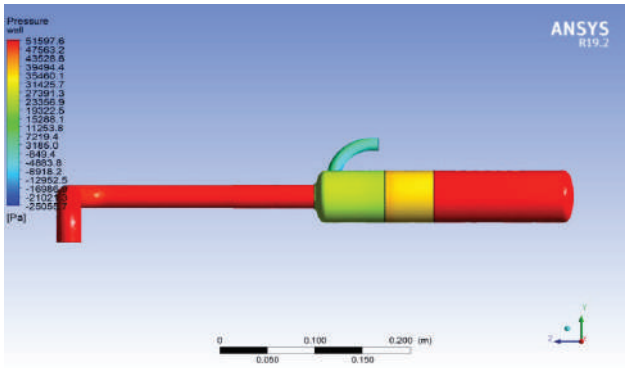

(a). Pressure Contour at Atmospheric Level

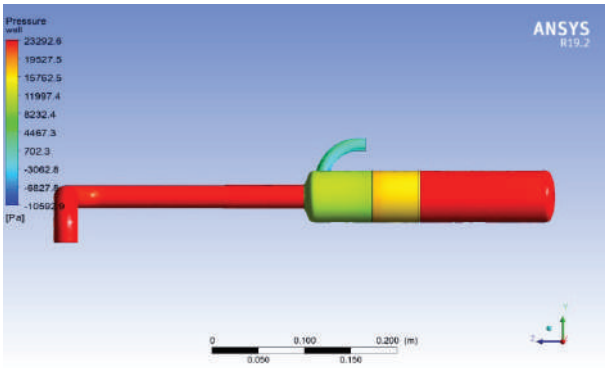

(b). Pressure Contour at 10000ft altitude

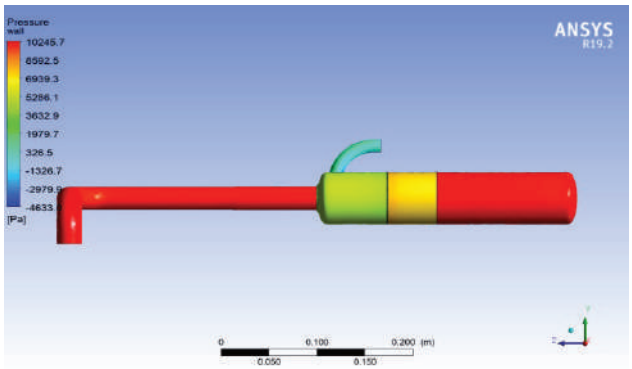

(c). Pressure Contour at 21000ft altitude

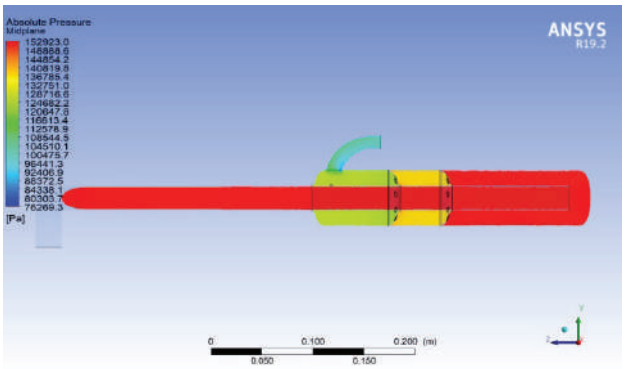

(d). Pressure Contour at Mid Plane at Atmospheric Level

Figure 12. Contour for Header Pipe specific portion Length = 132.5mm.

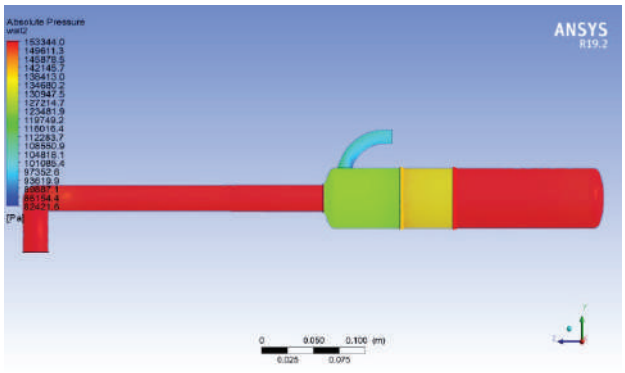

(a). Pressure Contour at Atmospheric Level

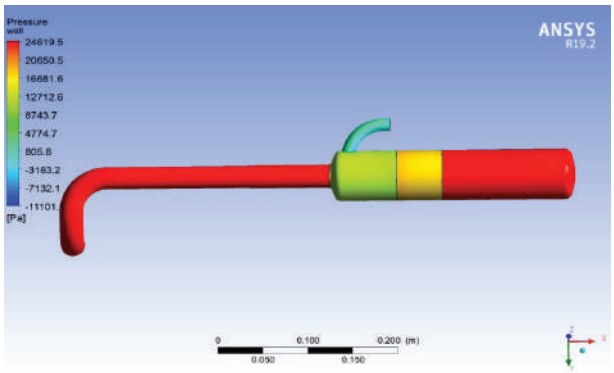

(b). Pressure Contour at 10000ft altitude

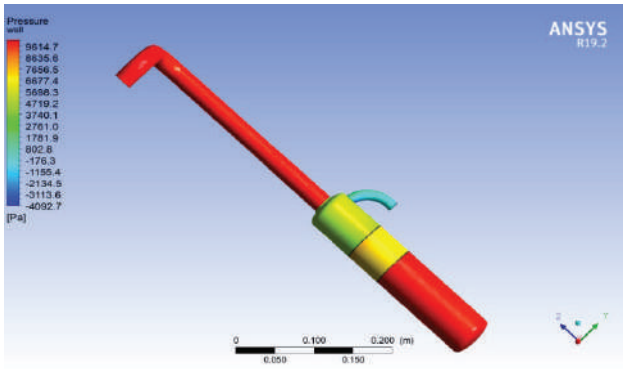

(c). Pressure Contour at 21000ft altitude

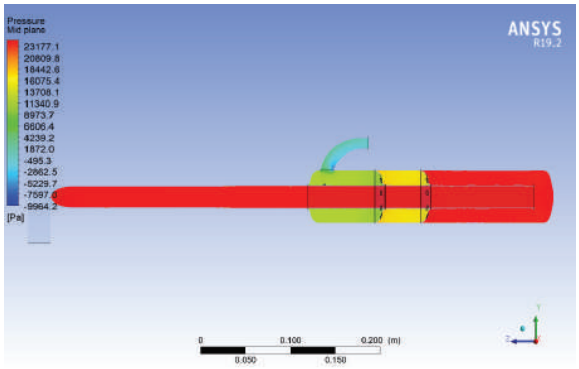

(d). Pressure Contour at Mid Plane at Atmospheric Level

Figure 13. Contour for Header Pipe specific portion Length = 142.5mm.

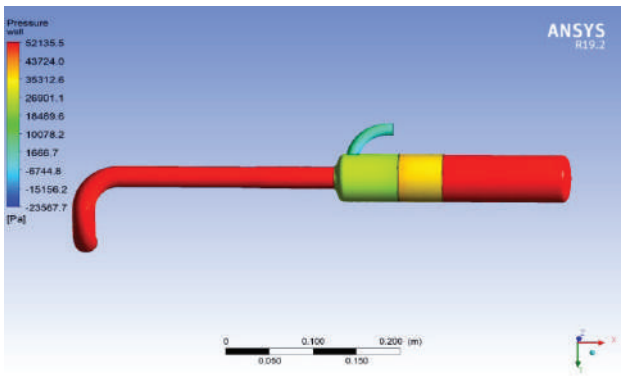

(a). Pressure Contour at Atmospheric Level

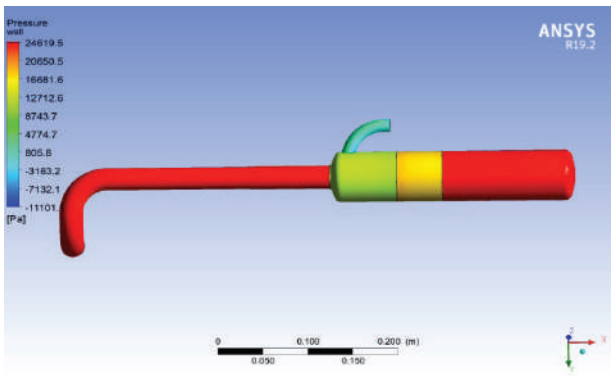

(b). Pressure Contour at 10000ft altitude

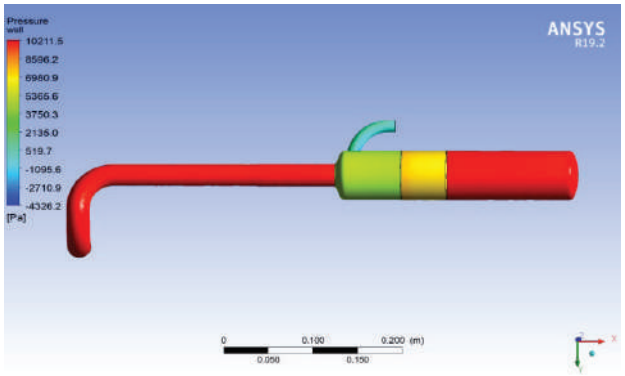

(c). Pressure Contour at 21000ft altitude

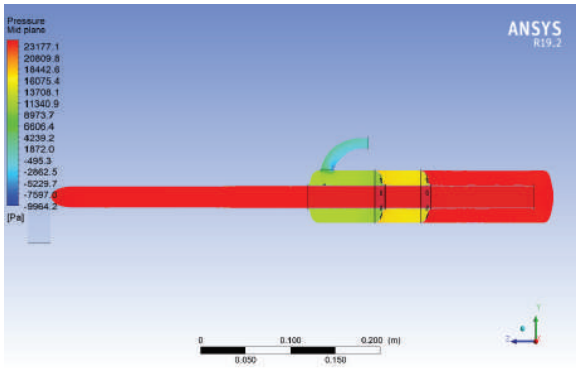

(d). Pressure Contour at Mid Plane at Atmospheric Level

Figure 14. Contour for Header Pipe specific portion Length = 152.5mm.

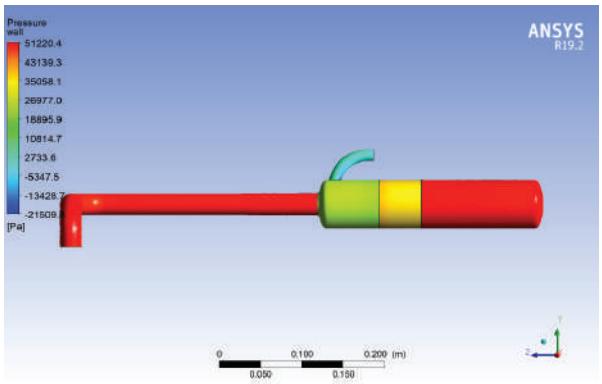

(a). Pressure Contour at Atmospheric Level

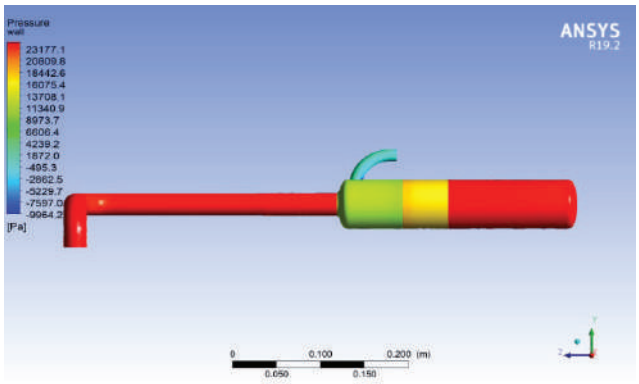

(b). Pressure Contour at 10000ft altitude

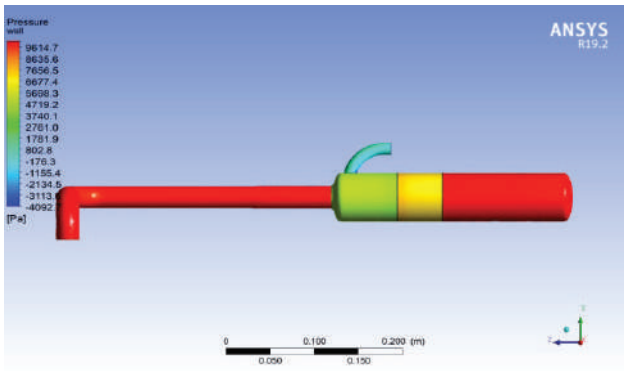

(c). Pressure Contour at 21000ft altitude

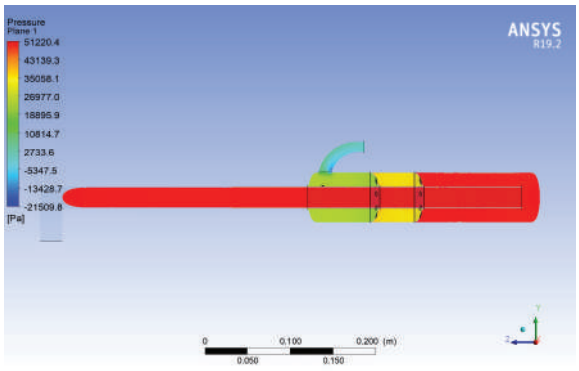

(d). Pressure Contour at Mid Plane at Atmospheric Level

Figure 15. Contour for Header Pipe specific portion Length = 162.5mm.

The findings presented in Figures 11 through 15 offer valuable insights into the effects of header pipe length on backpressure and exhaust flow dynamics at different altitudes. Each figure reveals the complex interaction between altitude and exhaust system geometry, highlighting the importance of optimizing header pipe lengths for different operating conditions.

In Figure 11, with a header pipe length of 122.5mm, the pressure contour at atmospheric level (a) demonstrates a fairly uniform pressure distribution, with localized high-pressure regions near the pipe's entry, which gradually dissipate downstream. At 10,000 feet (b), the reduction in pressure becomes evident, illustrating how lower air density impacts exhaust flow. The pressure drop becomes even more pronounced at 21,000 feet (c), emphasizing the heightened effects of altitude on exhaust gas behavior. The mid-plane pressure contour (d) offers further clarity, showing how the header pipe length influences pressure redistribution, ensuring effective exhaust flow management.

Figure 12, corresponding to a 132.5mm header pipe length, presents a similar pattern at atmospheric level (a), although the pressure drop begins earlier in the system compared to Figure 11. At 10,000 feet (b), the pressure gradient is more intense due to the increased length, highlighting the exacerbating effects of altitude on backpressure. At 21,000 feet (c), the longer pipe further amplifies the pressure reduction, underlining the critical need to account for both altitude and pipe length when designing exhaust systems. The mid-plane contour (d) demonstrates that the increased length further redistributes pressure within the system, impacting exhaust efficiency.

In Figure 13, the pressure contour at atmospheric level (a) reveals a more gradual pressure drop along the header pipe, with the longer length providing a more distributed variation compared to the shorter pipe lengths. At 10,000 feet (b), the pressure drop intensifies, signaling that longer pipes exacerbate the effects of altitude on exhaust flow. At 21,000 feet (c), the extended pipe further reduces pressure throughout the system, confirming that at higher altitudes, longer header pipes may contribute to excessive pressure loss, which can compromise exhaust system performance. The mid-plane pressure contour (d) highlights how the extended length influences the exhaust flow profile, potentially reducing the efficiency of exhaust gas scavenging.

In Figure 14, with a 152.5mm header pipe length, the pressure contour at atmospheric level (a) illustrates a more pronounced pressure variation, with increased resistance to flow due to the longer length. This trend continues at 10,000 feet (b), where the pressure drop becomes more noticeable, emphasizing the compounded effect of altitude and longer

pipe lengths. At 21,000 feet (c), the pressure reduction is even more pronounced, suggesting that excessively long pipes at high altitudes may lead to a significant decrease in exhaust flow efficiency. The mid-plane contour (d) further corroborates this observation, indicating that the extended pipe length exacerbates the pressure loss and could hinder optimal exhaust gas flow.

Finally, Figure 15, representing a 162.5mm header pipe length, shows at atmospheric level (a) the most significant pressure drops along the length of the pipe. This extended length results in a more complex pressure gradient, with substantial resistance to flow. At 10,000 feet (b), the pressure contour reflects an even greater reduction, suggesting that the long pipe length exacerbates the altitude-induced pressure loss. At 21,000 feet (c), the pressure reduction becomes extreme, potentially leading to suboptimal engine performance due to the elevated backpressure. The mid-plane contour (d) highlights the excessive pressure gradient caused by the extended pipe length, which could adversely affect exhaust gas scavenging and combustion efficiency.

Diameter of Specific Portion of Header Pipe

Characteristics of pressure

Increasing the diameter of a specific section of the header pipe from 24 mm to 36 mm leads to a rise in backpressure, as shown in Figure 16, across all three altitude conditions. The abrupt expansion disrupts the flow, generating turbulence that adds resistance, increases pressure, and reduces exhaust system efficiency.

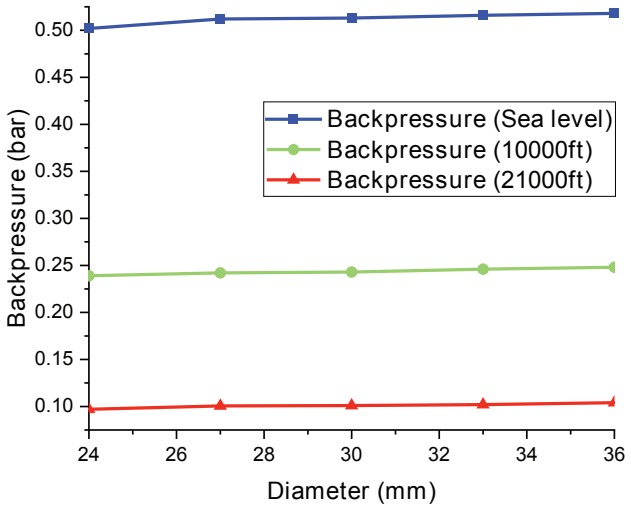

Figure 16. Header pipe specific portion Diameter.

Figures 17 to 21 visually depict this behavior with detailed pressure contours, clearly showing how the pressure distribution changes with increasing diameter at sea level, 10,000 ft, and 21,000 ft. As the cross-sectional area

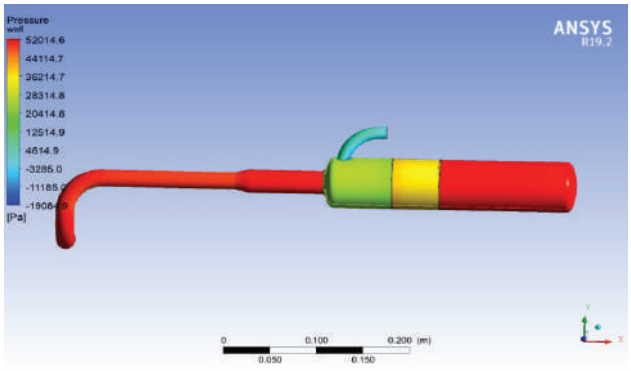

(a). Pressure Contour at Atmospheric Level

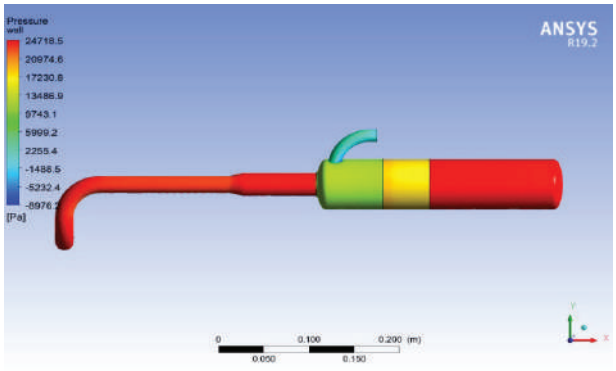

(b). Pressure Contour at 10000ft altitude

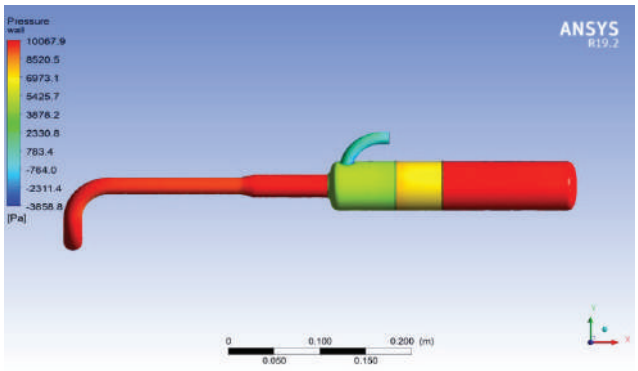

(c). Pressure Contour at 21000ft altitude

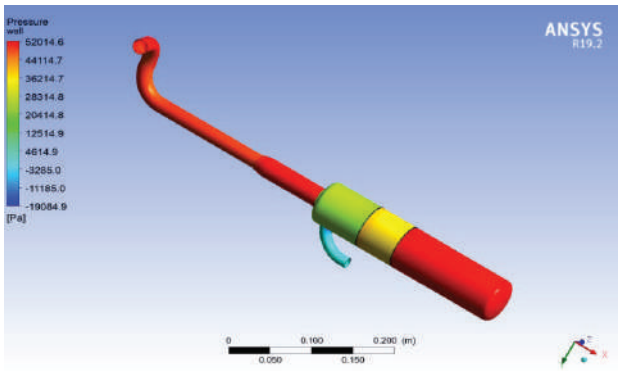

(d). Pressure Contour at Mid Plane at Atmospheric Level

Figure 17. Contour for Header pipe specific portion Diameter = 24 mm.

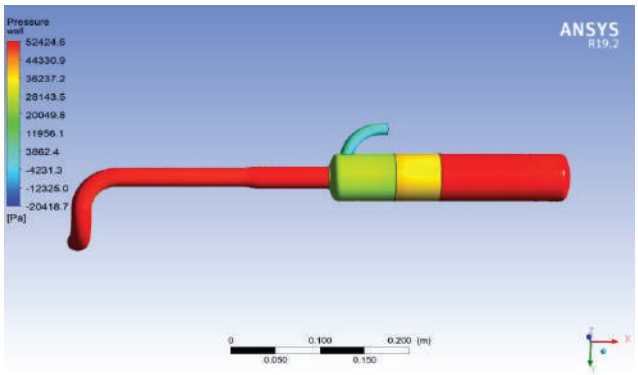

(a). Pressure Contour at Atmospheric Level

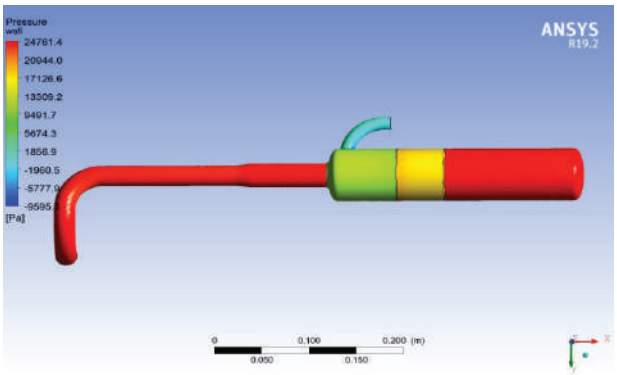

(b). Pressure Contour at 10000ft altitude

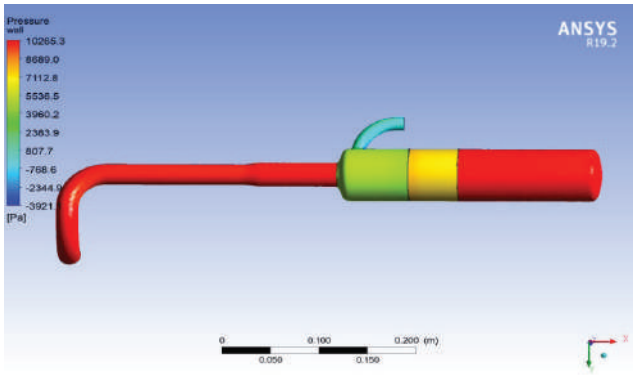

(c). Pressure Contour at 21000ft altitude

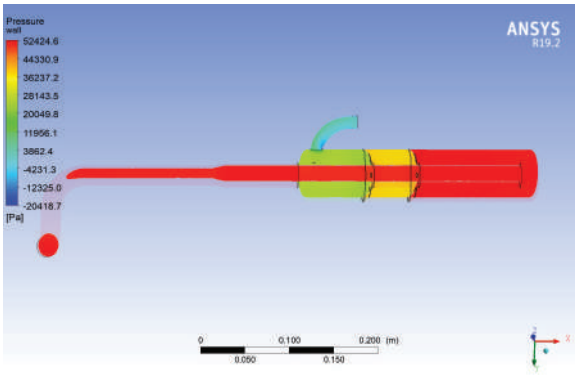

(d). Pressure Contour at Mid Plane at Atmospheric Level

Figure 18. Contour for Header pipe specific portion Diameter = 27 mm.

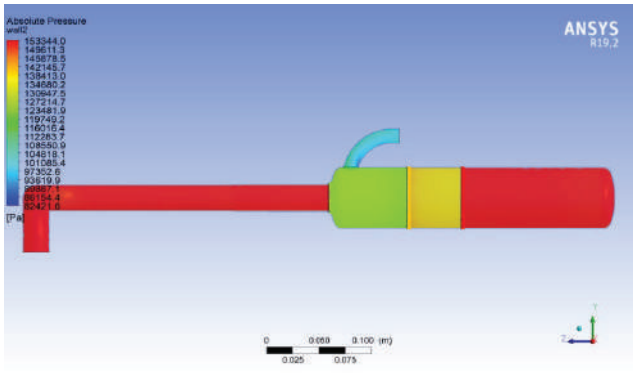

(a). Pressure Contour at Atmospheric Level

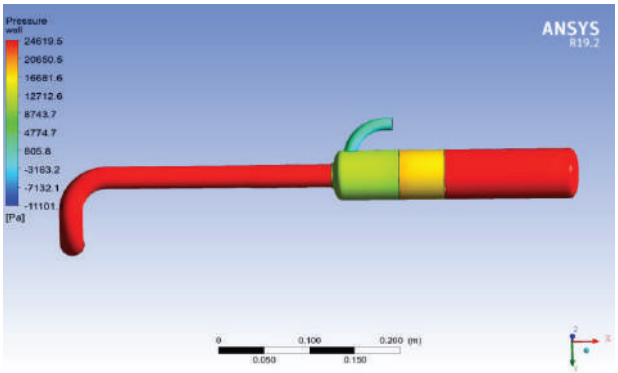

(b). Pressure Contour at 10000ft altitude

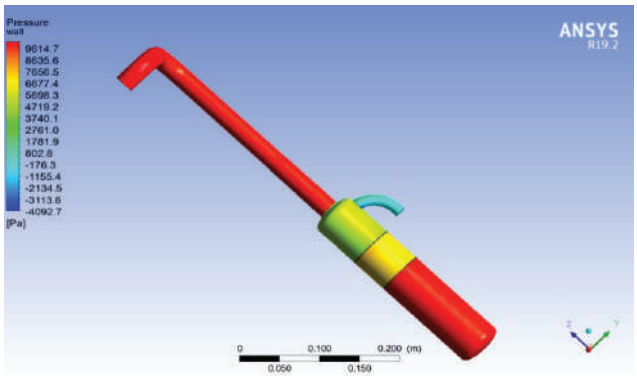

(c). Pressure Contour at 21000ft altitude

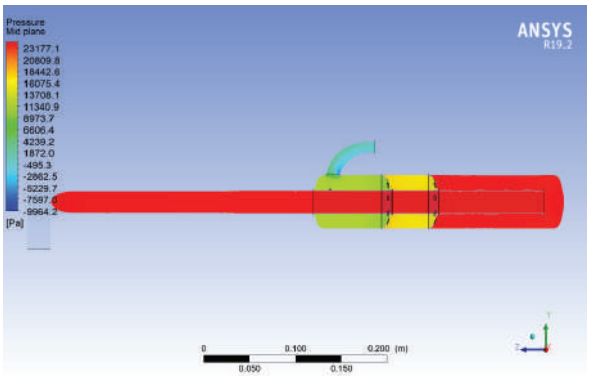

(d). Pressure Contour at Mid Plane at Atmospheric Level

Figure 19. Contour for Header pipe specific portion Diameter = 30 mm.

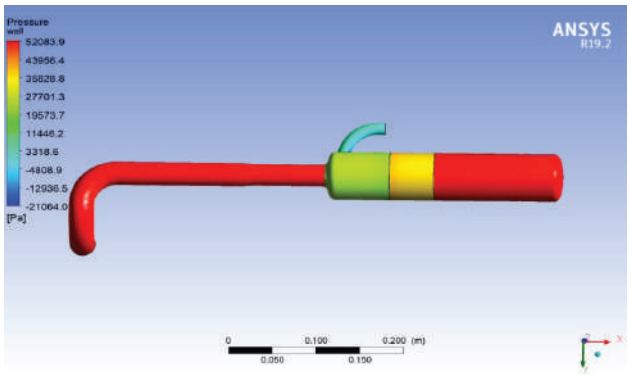

(a). Pressure Contour at Atmospheric Level

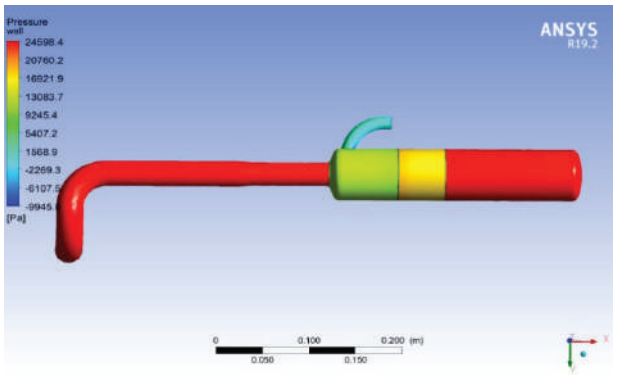

(b). Pressure Contour at 10000ft altitude

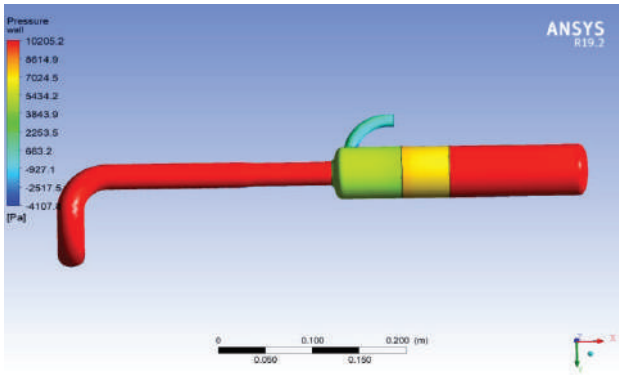

(c). Pressure Contour at 21000ft altitude

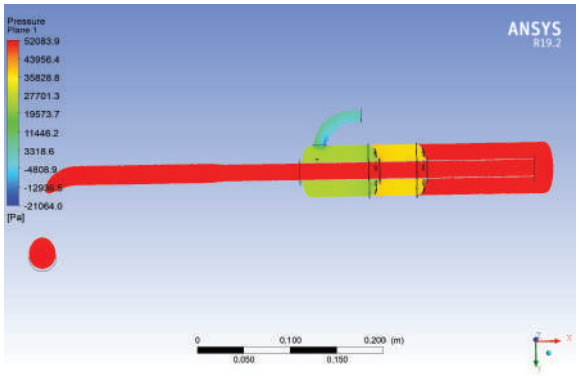

(d). Pressure Contour at Mid Plane at Atmospheric Level

Figure 20. Contour for Header pipe specific portion Diameter = 33 mm.

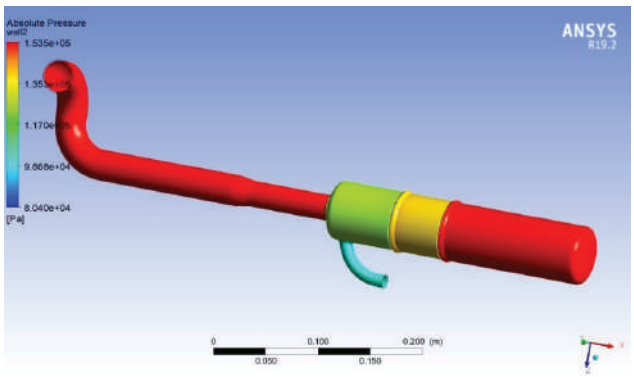

(a). Pressure Contour at Atmospheric Level

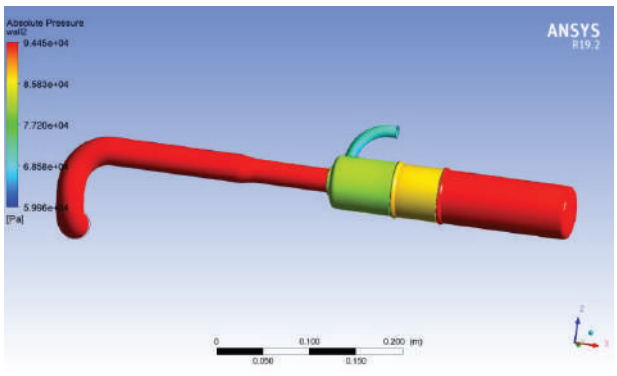

(b). Pressure Contour at 10000ft altitude

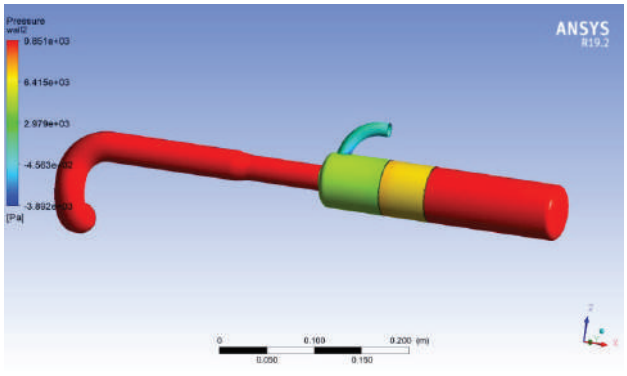

(c). Pressure Contour at 21000ft altitude

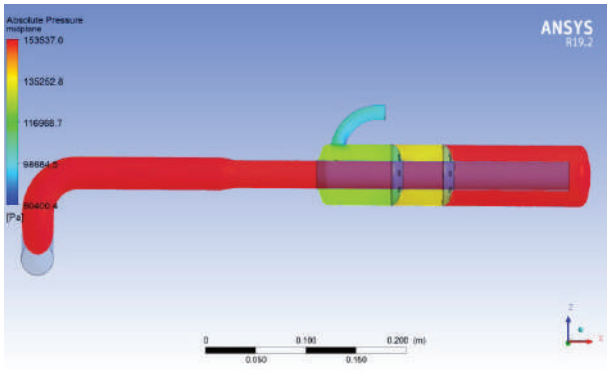

(d). Pressure Contour at Mid Plane at Atmospheric Level

Figure 21. Contour for Header pipe specific portion Diameter = 36 mm.

of this section increases, resistance to exhaust flow also increases, leading to a rise in backpressure. Conversely, a smaller diameter reduces flow resistance, thereby decreasing backpressure. Figures 17 to 21 further illustrate how this relationship varies at sea level, 10,000 ft, and 21,000 ft, with different header pipe diameters. This variation highlights the influence of altitude on atmospheric density and pressure, which in turn affects backpressure levels.

This variation is crucial for optimizing UAV exhaust system design, as it necessitates adjusting the diameter of the header pipe to achieve the desired backpressure. While higher backpressure can enhance combustion efficiency and scavenging, excessive backpressure can impede engine performance by making it more difficult to expel exhaust gases. Therefore, determining the optimal diameter is essential for striking a balance between backpressure, engine efficiency, and performance at various altitudes and operating conditions.

While the primary focus of this study is on the numerical optimization of exhaust system parameters specific to two-stroke UAV engines, the observed trends in backpressure variation are consistent with general findings reported in previous literature on small engine performance at varying altitudes. For example, the inverse relationship between baffle plate hole diameter and backpressure, as well as the influence of header pipe geometry on exhaust flow dynamics, aligns with the conclusions of Crosbie et al. [14] who highlighted the sensitivity of small engine performance to exhaust flow restrictions. Similarly, studies such as Moshkov et al. [17] and Hooper [19] have emphasized the critical role of exhaust tuning in reducing noise and enhancing efficiency in UAVs, indirectly supporting the importance of optimized flow characteristics. However, direct comparisons are limited due to the scarcity of numerical or experimental studies focused specifically on exhaust system geometry for UAV engines, particularly under varying altitude conditions. The deviation from traditional studies which often rely on engine replacement or forced induction for altitude performance may stem from the novel scope of this research, which targets performance enhancement through passive exhaust system modification alone. As such, this study contributes original insights that complement and extend the existing body of knowledge, particularly in the context of lightweight, altitude-adaptive UAV design.

Engineering Implications and Practical Implementation

The optimized exhaust system geometry features a 4.6 mm baffle plate hole diameter, a 122.5 mm header pipe length, and a 36 mm header pipe diameter. This configuration achieves an effective balance between backpressure control and exhaust flow, enhancing engine performance and maintaining thermal stability without the need for turbocharging. These dimensions fall within standard fabrication limits and can be integrated into conventional two-stroke UAV engines, such as the Hirth 4201, without major alterations to the engine structure. The manufacturing of such components is feasible using readily available techniques including CNC machining, laser cutting for baffle plates, and precision tube forming or welding for header pipes. Materials such as aluminum alloys or stainless steel, commonly used in aerospace applications, can be employed based on the specific requirements of weight reduction and thermal stability at high altitudes. The findings also support the development of modular exhaust system components, which can be customized or replaced depending on mission altitude, thereby improving versatility and maintainability. Furthermore, the simplified geometric modifications proposed in this research allow for performance tuning through passive means without the need for complex turbocharging or electronic control units, making it especially suitable for cost-sensitive UAV applications. In future UAV engine designs, these insights can guide the development of lightweight and high-efficiency exhaust systems that optimize backpressure under varying atmospheric conditions, ultimately enhancing engine performance, fuel economy, and flight endurance.

Comparison with Previous Work

The observed backpressure trends in this study such as increased resistance with reduced baffle hole diameter and reduced backpressure with longer header pipe lengths are consistent with earlier findings on exhaust flow resistance and efficiency in small engines. For instance, Murali et al. [32] and Huang et al. [31] confirmed that elevated backpressure can hinder exhaust expulsion and negatively impact combustion stability. Our CFD simulations corroborate these effects, particularly under high-altitude conditions, where low ambient pressure amplifies geometric impacts.

While prior research such as Young et al. [15, 16] and Cantore et al. [17] tackled altitude performance using turbocharging and forced induction systems, our results demonstrate that similar gains in backpressure regulation can be achieved through passive exhaust system tuning. This eliminates the need for additional mass, power requirements, and mechanical complexity.

Studies like Ding et al. [20] and Hashmi et al. [30] reported altitude-induced reductions in power output and thermal efficiency in UAV engines. Our optimized geometry especially the 4.6 mm baffle hole and 122.5 mm header length maintain favorable backpressure at 21,000 ft (0.23 bar), potentially mitigating such losses by preserving scavenging effectiveness and combustion stability through backpressure control.

Furthermore, unlike ECU-based solutions (e.g., Aswin et al. [21]), which depend on active sensors and fuel control logic, our approach enhances UAV engine adaptability through physical design alone, supporting applications in lightweight and cost-sensitive platforms where simplicity is paramount.

CONCLUSION

This work contributes a novel, passive design strategy for UAV engines, optimizing exhaust geometry to sustain performance at high altitudes without relying on complex propulsion modifications or forced induction systems. The main objective of this study is to optimize the exhaust system design for two-stroke unmanned aerial vehicle engines. Two-stroke engines are commonly used in unmanned aerial vehicles due to their high power-to-weight ratio, making them ideal for applications where both weight and performance are critical. The primary function of the exhaust system is to collect exhaust gases from the combustion chamber and release them into the atmosphere, while also minimizing noise. Unlike four-stroke engines, where intake and exhaust strokes are distinct, the intake and exhaust strokes of two-stroke engines occur immediately after the combustion stroke, which can lead to issues such as fresh air-fuel mixture leakage into the exhaust ports, thereby impairing engine performance.

The computational fluid dynamics simulations conducted at sea level, 10,000 feet, and 21,000 feet demonstrated that exhaust system geometry has a significant effect on backpressure and overall engine performance in unmanned aerial vehicle applications. Backpressure was found to decrease with increasing baffle hole diameter and header pipe length, while it increased with larger header pipe diameters. These geometric variations impacted exhaust flow resistance and engine efficiency, particularly under high-altitude conditions. The analysis revealed that an optimal balance of these parameters can enhance combustion stability and reduce unburnt fuel loss, leading to improved engine efficiency and high-altitude adaptability without requiring complex hardware modifications.

The study revealed that backpressure in two-stroke unmanned aerial vehicle engines is highly sensitive to changes in baffle plate hole diameter, header pipe length, and pipe diameter, especially under varying altitude conditions. Increasing the baffle hole diameter or the header pipe length reduces backpressure, improving exhaust flow and efficiency, while increasing the header pipe diameter raises backpressure due to flow resistance. The optimal configuration featuring a 4.6 mm baffle hole, 122.5 mm header pipe length, and 36 mm diameter achieves a favorable balance between backpressure and flow dynamics, particularly at 21,000 feet, ensuring efficient engine performance for high-altitude unmanned aerial vehicle missions.

This study offers a passive and practical approach to enhancing unmanned aerial vehicle engine performance by optimizing exhaust geometry and improving combustion efficiency and fuel economy without relying on complex systems like turbochargers. The optimized design supports high-altitude operations, extends flight endurance, and can be easily manufactured using standard aerospace materials, making it suitable for cost-effective integration into existing unmanned aerial vehicle platforms for both military and civilian use. Passive exhaust modifications are cost-effective and utilize lightweight materials such as aluminum and stainless steel to minimize weight penalties.

The optimized exhaust geometry not only reduces backpressure but also enhances scavenging efficiency, promoting improved fuel combustion and reducing unburnt hydrocarbon emissions. These improvements contribute to better fuel efficiency and more stable thermal operation of the engine, which positively impacts other subsystems such as cooling performance and engine longevity.

While the primary focus of this study is on the numerical optimization of exhaust system parameters specific to two-stroke unmanned aerial vehicle engines, the observed trends in backpressure variation are consistent with general findings reported in previous literature. The study's findings align with previous research on exhaust flow dynamics and unmanned aerial vehicle performance, particularly about backpressure trends. However, direct comparisons are limited due to the lack of altitude-specific studies on exhaust geometry. Key limitations include the absence of full experimental validation, assumptions in the computational fluid dynamics model (ideal gas, adiabatic walls), exclusion of combustion modeling, and the focus on a single engine at constant RPM. Despite these, the study provides valuable insights into passive exhaust optimization for high-altitude unmanned aerial vehicles.

Future Research Directions

While this study presents a detailed CFD-based analysis, direct experimental validation of the predicted backpressure values and flow characteristics has not yet been performed. However, the observed temperature and flow field trends align well with prior experimental findings reported in the literature. Future work will focus on developing an instrumented UAV test rig or conducting wind tunnel tests to validate the CFD results under real operating conditions.

Future research should focus on experimentally validating computational fluid dynamics results, incorporating transient and reactive flow modeling, and applying multi-objective optimization techniques to enhance unmanned aerial vehicle exhaust design. Additional areas include material durability analysis and the development of adaptive or variable-geometry exhaust systems to improve performance across varying altitudes and operational conditions.

AUTHORSHIP CONTRIBUTIONS

Authors equally contributed to this work.

DATA AVAILABILITY STATEMENT

The authors confirm that the data that supports the findings of this study are available within the article. Raw

data that support the finding of this study are available from the corresponding author, upon reasonable request.

CONFLICT OF INTEREST

The author declared no potential conflicts of interest with respect to the research, authorship, and/or publication of this article.

ETHICS

There are no ethical issues with the publication of this manuscript.

STATEMENT ON THE USE OF ARTIFICIAL INTELLIGENCE

Artificial intelligence was not used in the preparation of the article

REFERENCES

[1] Blair G. Design and Simulation of Two-Stroke Engines. SAE International; 1996. [CrossRef]

[2] Crosbie S, Polanka M, Litke P, Hoke J, editors. Increasing Reliability of a Small 2-Stroke Internal Combustion Engine for Dynamically Changing Altitudes. 50th AIAA Aerospace Sciences Meeting Including the New Horizons Forum and Aerospace Exposition; 2012. [CrossRef]

[3] Kenny R. Developments in two-stroke cycle engine exhaust emissions. Proc Inst Mech Eng Part D J Automob Eng 1992;206:93–106. [CrossRef]

[4] Prisacariu V, editor. A Brief History of UAVs in the 1970s. International Conference of Scientific Paper, AFASES; 2022.

[5] Puhan P, Sahu DK, Mishra D, editors. CFD Analysis of a Perforated Inner Pipe Exhaust Muffler for the Prediction of Transmission Loss and Backpressure Using Reverse Engineering. Proceedings of the 7th International and 45th National Conference on Fluid Mechanics and Fluid Power IIT Bombay Mumbai; 2019.

[6] Gundlach J. Designing Unmanned Aircraft Systems. Reston: American Institute of Aeronautics & Astronautics; 2014. [CrossRef]

[7] Fahlstrom PG, Gleason TJ, Sadraey MH. Introduction to UAV Systems. John Wiley & Sons; 2022.

[8] Brown SP. Design and Optimization of a 1 kW Hybrid Powertrain for Unmanned Aerial Vehicles. 2017.

[9] Moshkov P, Samokhin V, Yakovlev A. Selection of an audibility criterion for propeller driven unmanned aerial vehicle. Russ Aeronaut 2018;61:149–155. [CrossRef]

[10] Bahari M, Rostami M, Entezari A, Ghahremani S, Etminan M. Performance evaluation and multi-objective optimization of a novel UAV propulsion system based on PEM fuel cell. Fuel 2022;311:122554. [CrossRef]

[11] Yinka-Banjo C, Ajayi O. Sky-farmers: Applications of unmanned aerial vehicles (UAV) in agriculture. Auton Veh 2019:107–128. [CrossRef]

[12] Wang Y, Shi Y, Cai M, Xu W, Zhang J, Zhong W, et al. Optimization of fuel injection control system of two-stroke aeroengine of UAV. Complexity 2020;2020:1–12. [CrossRef]

[13] Zhen X, Wang Y, Xu S, Zhu Y, Tao C, Xu T, et al. The engine knock analysis–An overview. Appl Energy 2012;92:628–636. [CrossRef]

[14] Xu Z, Ji F, Ding S, Zhao Y, Zhang X, Zhou Y, et al. High-altitude performance and improvement methods of poppet valves 2-stroke aircraft diesel engine. Appl Energy 2020;276:115471. [CrossRef]

[15] Zhou L, Zhang H, Zhao Z, Zhang F. Research on opposed piston two-stroke engine for unmanned aerial vehicle by thermodynamic simulation. SAE Technical Paper; 2017. Report No.: 0148-7191. [CrossRef]

[16] Galle J, Verhelst S. Design of a fast responding start-up mechanism for bi-propellant fueled engine for miniature UAV applications. SAE Technical Paper; 2013. Report No.: 0148-7191. [CrossRef]

[17] Crosbie SC, Polanka MD, Litke PJ, Hoke JL. Increasing reliability of a two-stroke internal combustion engine for dynamically changing altitudes. J Propuls Power 2014;30:87–95. [CrossRef]

[18] Çoban S, Oktay T. Unmanned aerial vehicles (UAVs) according to engine type. J Aviat 2018;2:177–184. [CrossRef]

[19] Kang YS, Lim BJ, Cha BJ. Multi-stage turbocharger system analysis method for high altitude UAV engine. J Mech Sci Technol 2017;31:2803–2811. [CrossRef]

[20] Moshkov P, Samokhin V, Yakovlev A, editors. Study of the Noise Sources of an UAV with a Two-Stroke Engine and Shrouded Propeller. Journal of Physics: Conference Series; 2021: IOP Publishing. [CrossRef]

[21] Cantore G, Mattarelli E, Rinaldini CA. A new design concept for 2-stroke aircraft diesel engines. Energy Procedia 2014;45:739–748. [CrossRef]

[22] Hooper P. Study of the effects of trapped compression ratio on the heavy fuel operation of a spark ignition unmanned aerial vehicle engine. Aircr Eng Aerosp Technol 2023;95:580–593. [CrossRef]

[23] Feng H, Xu P, Yang S, Zheng Y, Li W, Liu W, et al. Back pressure generated by downwash and crosswind on spatial atomization characteristics during UAV spraying: CFD analysis and verification. Pest Manag Sci 2024;80:1348–1360. [CrossRef]

[24] Ding H, Liu R, Zhang Z, Yang C, Jiao Y, Hu L, editors. Study on the Influence of High-Altitude on Performance of an Opposed-Piston Gasoline Engine. 2020 Asia-Pacific Conference on Image Processing, Electronics and Computers (IPEC); 2020: IEEE. [CrossRef]

[25] Ballı Ö. Performance assessment of a medium-scale turboprop engine designed for unmanned aerial vehicle (UAV) based on exergetic and sustainability metrics. J Therm Eng 2020;6:697–711. [CrossRef]
[26] Nahrendra IMA, Adiprawita W, Susanto A, Hadinata SK, editors. Engine Control Unit for 2 Stroke Internal Combustion Engine on Medium Altitude Unmanned Aerial Vehicle. 2018 International Symposium on Electronics and Smart Devices (ISESD); 2018: IEEE. [CrossRef]
[27] Eyal A, Tartakovsky L. Suitability of the reforming-controlled compression ignition concept for UAV applications. Drones 2020;4:60. [CrossRef]
[28] Aygun H. Optimization of energy and exergy parameters for a conceptual afterburning turbojet engine. J Therm Eng 2021;9:69–85. [CrossRef]
[29] Shimoyama K, Kamisori K. Study of aerodynamic and heat-exhaust characteristics for a high-altitude long-endurance unmanned-aerial-vehicle airfoil. J Aircr 2017;54:1317–1327. [CrossRef]
[30] Perez PL, Boehman AL. Performance of a single-cylinder diesel engine using oxygen-enriched intake air at simulated high-altitude conditions. Aerosp Sci Technol 2010;14:83–94. [CrossRef]
[31] Huang L, Liu J, Liu R, Wang Y, Liu L. Experimental investigation on combustion and performance of diesel engine under high exhaust back pressure. Machines 2022;10:919. [CrossRef]
[32] Murali R, Shahriman A, Razlan Z, Ahmad W, Azizul A, Rojan M, et al., editors. A Review on the Correlation Between Exhaust Backpressure and the Performance of IC Engine. Journal of Physics: Conference Series; 2021: IOP Publishing. [CrossRef]
[33] Wang Y, Shi Y, Cai M, Xu W, Yu Q. Optimization of air–fuel ratio control of fuel-powered UAV engine using adaptive fuzzy-PID. J Frankl Inst 2018;355:8554–8575. [CrossRef]
[34] Bahari M, Rostami M, Entezari A, Ghahremani S, Etminan M. A comparative analysis and optimization of two supersonic hybrid SOFC and turbine-less jet engine propulsion system for UAV. Fuel 2022;319:123796. [CrossRef]
[35] Dinc A. Optimization of a turboprop UAV for maximum loiter and specific power using genetic algorithm. Int J Turbo Jet Engines 2016;33:265–273. [CrossRef]
[36] Rostami M, Farajollahi A, Marefati M, Fili R, Bagherpor F. A comparative analysis and optimization of two supersonic hybrid solid oxide fuel cell and turbine-less jet engine propulsion systems for unmanned aerial vehicles. Renew Energy Res Appl 2022;3:237–253.
[37] Setiyo M, Waluyo B, Husni M. Performance of gasoline/LPG bi-fuel engine of manifold absolute pressure sensor (MAPS) variations feedback. ARPN J Eng Appl Sci 2016;11:4707–4712.
[38] Hashmi K, Radhakrishna D. Prediction of High Altitude Performance for UAV Engine. SAE Technical Paper; 2015. Report No.: 0148-7191. [CrossRef]

J Ther Eng, Vol. 12, No. 1, pp. 278−290, January, 2026

Journal of Thermal Engineering
Web page info: https://jten.yildiz.edu.tr
DOI: 10.14744/thermal.0001077

Research Article

Thermo-diffusion effects on mhd casson blood flow in an inclined muti-stenosed artery

Harshad PATEL[1,*], Snehal PATEL[1], Nilesh PATEL[2]

[1]U V Patel College of Engineering, Ganpat University, Mehsana, Gujarat, 384012, India
[2]B. S. Patel Polytechnic, Ganpat University, Gujarat, 384012, India

ARTICLE INFO

Article history
Received: 13 May 2024
Revised: 26 July 2024
Accepted: 04 August 2024

Keywords:
Casson Fluid; Fractional Derivative; Magnetic Particles; MHD; Multi-Stenosed Artery; Thermal Radiation

ABSTRACT

The current study investigates the effects of thermos-diffusion on Casson blood flow in the presence of a magnetic field. We consider the flow in an inclined multi-stenosed artery with an oscillating pressure gradient. By using the similarity transformation, the governing equations are transformed into a dimensionless form. For more effective study of the fractional time derivative, the Caputo-Fabrizio time derivative is adopted. Using the tools provided by the Laplace transform and the finite Hankel transform, the analytical solution to the aforementioned problem is derived. We gather numerical findings and display them through graphs to help you better comprehend the effects of various physical parameters. Data visualization shows that the external magnet-controlled blood flow's turbulence. These results suggest that high magnetic field impacts are harmful to health. Additionally, it is observed that thermal radiation commonly enhances the heat distribution procedure.

Cite this article as: Patel H, Patel S, Patel N. Thermo-diffusion effects on mhd casson blood flow in an inclined muti-stenosed artery. J Ther Eng 2026;12(1):278−290.

INTRODUCTION

In contrast to the linear dependency shown by Newtonian fluids, the stress in non-Newtonian fluids can show a nonlinear rate of deformation. According to the literature, from the 1940s and 1950s, there has been an increase in interest in non-Newtonian fluids. Non-Newtonian fluids include things like paint, shampoo, soap slurries, tomato paste, greases, food sauces, chocolates, toothpaste, polymer solutions, custard, and blood. Non-Newtonian fluid models have been the subject of much study by numerous academics because of its applicability in numerous industries. Casson [1] developed the Casson fluid model in 1959 to determine how pigment oil suspensions would flow. Human red blood cells, human blood can also be considered as Casson fluid. Because blood is such a vital fluid, its viscosity and other characteristics can be used to detect a wide range of cardiovascular disorders. A great number of theoretical investigations [2-5] have been discussed blood flow circulation in the arteries. It is generally recognized that in sick conditions, an aberrant and unnatural growth arises in the lumen at numerous places throughout the circulatory system. Arteriosclerosis, often known as stenosis, is a common condition. Chaturani and

***Corresponding author.**
*E-mail address: harshadpatel2@gmail.com

This paper was recommended for publication in revised form by Editor-in-Chief Ahmet Selim Dalkilic

Published by Yıldız Technical University Press, İstanbul, Turkey
Yıldız Technical University. This is an open access article under the CC BY-NC license (http://creativecommons.org/licenses/by-nc/4.0/).

Ponnalagar Samy [6] have studied how blood moves via a stenosed artery. Many researchers [7-9] have investigated to impact of stenosis in the lumen of an artery. Casson's equation is obeyed by blood only for modest shear rate flows, according to Scott Blair et al. [10]. Shukla et al. [11] analysed the effects of stenosis on blood flow which is treated as a power-law and Casson's fluid.

Important applications of magnetic fields include the targeting of cancer drugs, the use of heat to kill tumors, magnetic resonance imaging (MRI), and magneto-therapy. In all these treatments effect of magnetic field plays crucial role. It is currently believed that magnetohydrodynamics (MHD) influences blood flows, or ionic flows, in a manner consistent with the bloodstream. In 1970, Hannes Alfvén [7] was awarded the Nobel Prize in physics for pioneering the field of MHD. The study of blood flow under the effect of magnetic field comes under the title Bio-magnetic fluid dynamics (BFD). Researchers [8-9] are curious about bio-magnetic fluid because Hyperthermia cell death, magnetic drugs targeting, magnetic endoscopy, magnetic devices for cell separation, therapy of cancer tumors, regulation of blood flow during surgery, and many more applications can be found in bioengineering. In the past few decades, the radiation therapy is used in human life where heat is transmitted below the skin's surface into the tissues and muscles [10-11]. Mekheiner and Kot [12] theoretically addressed the issue of blood flow through a catheterized artery under pathological conditions. To better understand the dynamics of blood flow via stenotic arteries, Majee and Shit [13] conducted a computer study of heat transfer in an unsteady blood flow. Both Rao and Vardynyan [14] demonstrated mathematically that blood can flow through an artery. Very few studies have looked at the effects of different parameter on blood flow and even fewer have taken into account fractional-order derivatives. However, the finite Hankel and Laplace transforms can be used to quickly find exact solutions to this type of problem. Caputo fractional derivatives and Hankel Transform methods are discussed to find the solution by researchers [15-17]. Due to its significance in physiopathology, problems with peristalsis (blood flow) have garnered a lot of attention. Mekheiner [18] determined that the pressure acts as an increasing function, but the behaviour of the pair stress fluid parameter appears to be the complete reverse. In his study, Akbar [19] examined the Prandtl fluid model in a tapering stenosed artery. The pumping features of peristaltic flow were discussed by Sreenadh et al. [20]. The slip effects for the flows investigated by Ramesh and Devakar [21], who then derived analytical solutions.

Nanofluid flow onto a stretched, curved surface was studied by Mehdi Mahboobtosi et al. [22] As a unique breakthrough, Moghimi et al. [23] analysed nanofluid flow in a channel and added magnetic field power to momentum and energy equations and evaluated free convection heat transmission. In a non-premixed configuration and in non-adiabatic conditions, Akbari et al. [24] conducted a theoretical analysis of a counter-flow combustion system that is powered by porous biomass particles. Using the response surface method, Navid et al. [25] optimized a wavy trapezoidal porous cavity that contained a mixture of hybrid nanofluids. Using computational methods, Zangooee et al. [26] examined the mixed nanofluid (NF) flow between two overlapping cylinders. Hosseinzadeh et al. [27] examined the thermal performance of a ferrofluid-wetted hybrid nanofluid with varying cross-sections in a moving porous fin subjected to a magnetic field. Hosseinzadeh et al. [28] studied the flow of a TiO2-ethylene glycol nanofluid across a porous stretched sheet under convective boundary conditions and the presence of heat that is not uniformly generated or absorbed. Muddasar Gulzar et al. [29] presented a nonlinear mathematical analysis of magneto-hyperbolic-tangent liquids that involve the three interrelated concepts of a magnetic field, a heat source, and thermal stratification. As a non-Newtonian fluid moving inside an axisymmetric tube subjected to non-uniform surface heat flux, Shahin Faghiri et al. [30] studied the Graetz-Nusselt problem for blood. Tashtoush et al. [31] presented a mathematical model of in-arterial multi-stenosis. The effects of a magnetic field on the heat and fluid flow properties of blood flowing through arteries with multiple stenosis are taken into account.

In light of what has been said previously, the objective of this investigation is to look into the impact that heat and mass transfer with thermal radiation and thermos-diffusion effects on blood flow in multi-stenosed artery. A thorough search of the relevant literature has witnessed the fact that the existing literature did not present the exact solution of MHD blood flow model in the context of Caputo Fabrizio fractional derivative for inclined multi-stenosed artery. The exact solutions are then calculated by means of significant transformations like Laplace and finite Hankel transforms. For numerical computations, we take the zeros of the Bessel functions to generate the graphical findings by using Matlab for different values of fractional parameters as well as some important physical parameters.

The present work furnishes a robust benchmark for magneto-hemodynamics, biomedical engineering, and physiology.

MATHEMATICAL FORMULATION

The focus of the recent research works is discussed on unsteady Casson blood flow, whose physical dimension are as shown in Figure 1. In Figure 1, z-axis consider as axial direction while r-axis indicates radial direction. Blood is treated as non-Newtonian Casson fluid flow with oscillating pressure gradient. The uniform external magnetic fields B_0 is applied which is shown in Figure 1. At $t = 0$, the velocity of blood and magnetic particle are treated as stationary. Blood flow is modelled using Navier-stokes equation. The effects of magnetic fields by Maxwell's relation whereas, magnetic particle velocity is governed using Newton's second law.

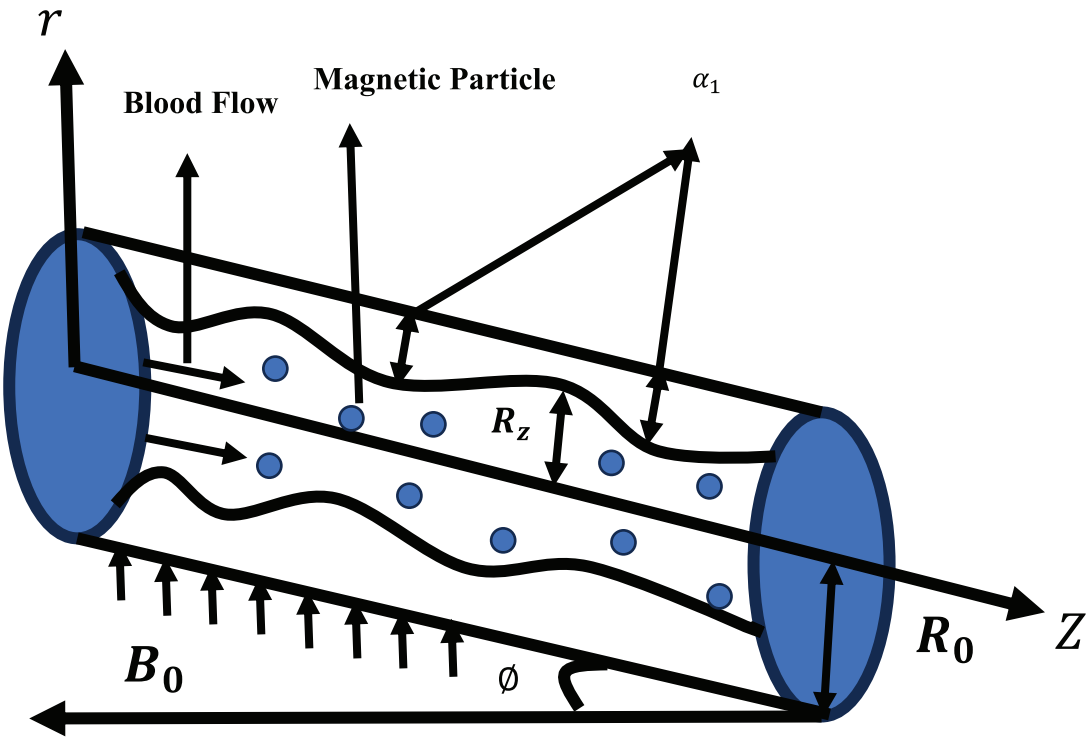

Figure 1. Geometry of the model

The unsteady blood flow in an axisymmetric cylindrical tube of radius R_0 under the influence of uniform transverse magnetic field and pressure gradient of the form [31].

$$-\frac{\partial P}{\partial z} = a_0 + a_1 Cos\,(\omega t), a_0 > 0 \tag{1}$$

Where, a_0- systolic pressure gradient, a_1-diastolic pressure gradient.

Geometrically, the expression of multi-stenosis in the artery can be written mathematically [32]

$$\begin{aligned} R_z = 1 - \alpha_1\,(&1.48x - 0.739x^2 + 0.148x^3 \\ &- 0.013955x^4 + 0.0006145x^5 \\ &- 0.000010243x^6) \end{aligned} \tag{2}$$

Where, R_z and R_0 represent the constricted region and normal artery radius. x is the stenosed length and α_1 stenosis degree.

The momentum equation for fluid flow in an inclined stenosed artery [15-33] can be written as

$$\begin{aligned} \frac{\partial u}{\partial t} = &-\frac{1}{\rho}\frac{\partial p}{\partial z} + \nu\left(1 + \frac{1}{\gamma}\right)\left(\frac{\partial^2 u}{\partial r^2} + \frac{1}{r}\frac{\partial u}{\partial r}\right) \\ &+ \frac{KN}{\rho}(v - u) - \frac{\sigma {B_0}^2 sin\theta_1}{\rho}u + gsin\emptyset \end{aligned} \tag{3}$$

The term $\frac{KN}{\rho}(v-u)$ is the force due to the relative motion between fluid and magnetic particles. It is assumed that the Reynolds number of the relative velocity is small. As such, the force between the magnetic particles and the blood is proportional to the relative velocity. Using Newton's second law governs the movement of magnetic particles:

$$m\frac{\partial v}{\partial t} = K\,(u - v) \tag{4}$$

where m is the average mass of the magnetic particles.

The governing energy equation in the cylindrical form as,

$$\frac{\partial T}{\partial t} = \frac{K_1}{\rho C_p}\left(\frac{\partial^2 T}{\partial r^2} + \frac{1}{r}\frac{\partial T}{\partial r}\right) + \frac{Q_m + \theta_m}{\rho C_p} \tag{5}$$

The concentration equation in the cylindrical form as,

$$\frac{\partial C}{\partial t} = D_m\left(\frac{\partial^2 C}{\partial r^2} + \frac{1}{r}\frac{\partial C}{\partial r}\right) + \frac{D_m K_T}{T_\infty}\left(\frac{\partial^2 T}{\partial r^2} + \frac{1}{r}\frac{\partial T}{\partial r}\right) \tag{6}$$

With initial and boundary conditions are as,

$$\begin{aligned} &u(r,0) = v(r,0) = T(r,0) = C(r,0) = 0 \;at\; r \in [0, R_z] \\ &u(r,t) = v(r,t) = T(r,t) = C(r,0) = 0 \;at\; r = R_z \end{aligned} \tag{7}$$

The dimensionless parameters can be express as,

$$r^* = \frac{r}{R_0},\; t^* = \frac{t}{\lambda},\; u^* = \frac{u}{u_0},\; {a_0}^* = \frac{\lambda a_0}{\rho u_0},$$

$${a_1}^* = \frac{\lambda a_1}{\rho u_0},\; \omega^* = \lambda\omega,\; g^* = \frac{g}{\frac{u_0^2}{R_0}}$$

The governing dimensionless form of governing equation subject to equations (7) after dropping* notation and

consider the time-fractional model of governing equations 3-6 can be written as,

$$D_t^{\alpha}u = a_0 + a_1\cos(\omega t) + \frac{1}{R_e}\left(1+\frac{1}{\gamma}\right)\left[\frac{\partial^2 u}{\partial r^2}+\frac{1}{r}\frac{\partial u}{\partial r}\right] + R(v-u) - Ha^2u + \frac{\sin\emptyset}{F} \tag{8}$$

$$\mathrm{G}D_t^{\alpha}v = u - v \tag{9}$$

$$P_e D_t^{\alpha}\theta = \left(\frac{\partial^2\theta}{\partial r^2}+\frac{1}{r}\frac{\partial\theta}{\partial r}\right) + P_e(Q_m+\theta_m) \tag{10}$$

$$S_c\, R_e D_t^{\alpha}\, C = \left(\frac{\partial^2 C}{\partial r^2}+\frac{1}{r}\frac{\partial C}{\partial r}\right) + S_r\, S_c\left(\frac{\partial^2\theta}{\partial r^2}+\frac{1}{r}\frac{\partial\theta}{\partial r}\right) \tag{11}$$

With boundary conditions

$$\begin{aligned} &u\left(\frac{r}{R_z},0\right)=0\,,v\left(\frac{r}{R_z},0\right)=0\,,\theta\left(\frac{r}{R_z},0\right)=0\ \&\\ &C\left(\frac{r}{R_z},0\right)=0\ \ at\ \frac{r}{R_z}\ \epsilon\ [\,0\,,1]\\ &u\left(\frac{r}{R_z},t\right)=0\,,v\left(\frac{r}{R_z},t\right)=0\,,\theta\left(\frac{r}{R_z},t\right)=0\ \&\\ &C\left(\frac{r}{R_z},t\right)=0\ at\ \frac{r}{R_z}\ =\ 1 \end{aligned} \tag{12}$$

$$\text{Here, } \beta=\frac{1}{R_e}\left(1+\frac{1}{\gamma}\right), Ha=B_0\sqrt{\lambda}\sqrt{\frac{\sigma\sin\theta_1}{\rho}},$$

$$F=\frac{R_0}{\lambda u_0 g}\,,\theta=\frac{T-T_\omega}{T_\omega-T_\infty}\,,\ P_r=\frac{K\lambda}{\rho C_p},\ R_e=\frac{{R_z}^2}{\lambda v}\,,$$

$$P_e=R_e.P_r,\ S_c=\frac{v}{\lambda D_m}\,,\ C=\frac{C-C_\omega}{C_\omega-C_\infty}\ S_r=\frac{D_m K_T\,(T_\omega-T_\infty)}{\lambda v\, T_\infty\,(C_\omega-C_\infty)},$$

$$Q_m=\frac{R_0\overline{Q_m}}{\lambda\, u_0\rho c_p(T_\omega-T_\infty)}\,,\ \theta_m=\frac{R_0\overline{\theta_m}}{\lambda\, u_0\rho c_p(T_\omega-T_\infty)}$$

Solution of the Problem

The Laplace transform technique is applied in equations (10), we obtain

$$P_e\frac{S\,\theta(r,s)}{S+\alpha(1-s)} = \left[\frac{\partial^2\theta(r,s)}{\partial r^2}+\frac{1}{r}\frac{\partial\theta(r,s)}{\partial r}\right] + P_e\frac{Q_m+\theta_m}{S} \tag{13}$$

The FHT (Finite Hankel transformation) is applied in equations (13) with B.C. (12),

$$P_e\frac{S\,\overline{\theta_H}(r_n,s)}{S+\alpha(1-s)} = -r_n\overline{\theta_H}(r_n,s) + P_e\frac{Q_m+\theta_m}{S}.\frac{J_1(r_n)}{r_n} \tag{14}$$

$$\overline{\theta_H}(r_n,s) = \frac{P_e\,(Q_m+\theta_m)}{S\left[r_n+P_e\frac{S}{S+\alpha(1-s)}\right]}.\frac{J_1(r_n)}{r_n} \tag{15}$$

Now, rearrange the equation (15)

$$\overline{\theta_H}(r_n,s) = \left[\frac{1}{S+B_{15}}B_{13}+\frac{1}{s\,(S+B_{15})}B_{14}\right]\frac{J_1(r_n)}{r_n} \tag{16}$$

Similarly, we process for Concentration equation (11), we get

$$R_e S_c\,\frac{S\,\bar{C}(r,s)}{S+\alpha(1-s)} = \left(\frac{\partial^2\bar{C}(r,s)}{\partial r^2}+\frac{1}{r}\frac{\partial\bar{C}(r,s)}{\partial r}\right) + S_r\,S_c\left(\frac{\partial^2\bar{\theta}(r,s)}{\partial r^2}+\frac{1}{r}\frac{\partial\bar{\theta}(r,s)}{\partial r}\right) \tag{17}$$

The FHT (Finite Hankel transformation) is applied in equations (17) with B.C. (12),

$$R_e S_c\,\frac{S\,C_H(r,s)}{S+\alpha(1-s)} = -r_n\overline{C_H}(r_n,s) + S_r\,S_c\,(-r_n)\overline{\theta_H}(r_n,s) \tag{18}$$

$$R_e S_c\,\frac{S\,C_H(r,s)}{S+\alpha(1-s)} = -r_n\overline{C_H}(r_n,s) + S_r\,S_c\,(-r_n)\frac{P_e\,(Q_m+\theta_m)}{S\left[r_n+P_e\frac{S}{S+\alpha(1-s)}\right]}.\frac{J_1(r_n)}{r_n} \tag{19}$$

$$\left[\frac{R_e S_c.S}{S+\alpha(1-s)}+r_n\right]\overline{C_H}(r,s) = -\,r_n S_r\,S_c\left[\frac{P_e\,(Q_m+\theta_m)}{S\left[r_n+P_e\frac{S}{S+\alpha(1-s)}\right]}\right].\frac{J_1(r_n)}{r_n} \tag{20}$$

$$\overline{C_H}(r,s) = -\frac{S_r\,S_c\,r_n P_e\,(Q_m+\theta_m)}{\left(S\left[r_n+P_e\frac{S}{S+\alpha(1-s)}\right]\right)\left[\frac{R_e S_c.S}{S+\alpha(1-s)}+r_n\right]}.\frac{J_1(r_n)}{r_n} \tag{21}$$

Now, rearrange the equation (21)

$$\overline{C_H}(r,s) = \frac{B_{16}}{\left(S\left[B_{17}+P_e\frac{S}{S+\alpha(1-s)}\right]\right)\left[\frac{B_{19}.S}{S+\alpha(1-s)}+B_{18}\right]}.\frac{J_1(r_n)}{r_n} \tag{22}$$

$$\overline{C_H}(r,s) = \frac{B_{16}\,(S+\alpha(1-S))^2}{S\,(B_{17}S+B_{17}\alpha-B_{17}\alpha S+P_eS)(B_{19}S+B_{18}\alpha+B_{18}S-B_{18}\alpha S)}.\frac{J_1(r_n)}{r_n} \tag{23}$$

$$\overline{C_H}(r,s) = \frac{B_{16}\,(S+\alpha(1-S))^2}{S\,((B_{17}-B_{17}\alpha+P_e)S+B_{17}\alpha)((B_{19}+B_{18}-B_{18}\alpha)S+B_{18}\alpha)}.\frac{J_1(r_n)}{r_n} \tag{24}$$

$$\overline{C_H}(r,s) = \frac{B_{16}\,(S+\alpha(1-S))^2}{S\,(B_{20}S+B_{22})(B_{21}S+B_{23})}.\frac{J_1(r_n)}{r_n} \tag{25}$$

$$\overline{C_H}(r,s) = \frac{B_{16}}{B_{20}.B_{21}}\frac{(\alpha^2+2\alpha(1-\alpha)S+(1-\alpha)^2S^2)}{S\left(S+\frac{B_{22}}{B_{20}}\right)\left(S+\frac{B_{23}}{B_{21}}\right)}.\frac{J_1(r_n)}{r_n} \tag{26}$$

$$\overline{C_H}(r,s) = \frac{B_{24}\,(\alpha^2+B_{25}S+B_{26}S^2)}{S\,(S+B_{27})\,(S+B_{28})}.\frac{J_1(r_n)}{r_n} \tag{27}$$

$$\overline{C_H}(r,s) = \left(\frac{B_{29}}{S}+\frac{B_{30}}{S+B_{27}}+\frac{B_{29}}{S+B_{28}}\right).\frac{J_1(r_n)}{r_n} \tag{28}$$

Now, the Laplace transform of equations (8) and (9) can be express as,

$$\frac{S\,\overline{u}(r,s)}{S+\alpha(1-s)} = \frac{a_0}{S}+\frac{a_1 S}{s^2+\omega^2}+\gamma\left(\frac{\partial^2\overline{u}(r,s)}{\partial r^2}+\frac{1}{r}\frac{\partial\overline{u}(r,s)}{\partial r}\right) + R\bar{v} - (R+Ha^2)\overline{u}(r,s) + \frac{\sin\emptyset}{SF} \tag{29}$$

$$G\frac{S\,\bar{v}(r,s)}{S+\alpha(1-s)} = \bar{u}(r,s) - \bar{v}(r,s) \quad (30)$$

$$\bar{v}(r,s) = \frac{S+\alpha(1-\alpha)}{GS+S+\alpha(1-s)}\,\bar{u}(r,s) \quad (31)$$

Input the equation (31) in (29), the following equation can be obtained,

$$\left[\frac{s}{S+\alpha(1-S)} - R\left(\frac{S+\alpha(1-\alpha)}{GS+S+\alpha(1-s)}\right) + R + Ha^2\right]\bar{u}(r,s) = \frac{a_0}{S} + \frac{a_1 S}{s^2+\omega^2} + \gamma\left(\frac{\partial^2\bar{u}}{\partial r^2} + \frac{1}{r}\frac{\partial\bar{u}}{\partial r}\right) + \frac{sin\phi}{SF} \quad (32)$$

The FHT (Finite Hankel transformation) is applied in equations (32) with B.C. (12),

$$\left[\frac{s}{S+\alpha(1-S)} - R\left(\frac{S+\alpha(1-\alpha)}{GS+S+\alpha(1-s)}\right) + R + Ha^2\right]\overline{u_H}(r_n,s) = \left[\frac{a_0}{S} + \frac{a_1 S}{s^2+\omega^2} + \frac{sin\phi}{SF}\right]\frac{J_1(r_n)}{r_n} - r_n\gamma\overline{u_H}(r_n,s) \quad (33)$$

$$\overline{u_H}(r_n,s) = \frac{S^2B_5+SB_6+\alpha^2}{S^2B_2+SB_3+B_4}\left[\frac{1}{S}\left(a_0+\frac{sin\phi}{F}+\frac{a_1 S}{s^2+\omega^2}\right)\right]\frac{J_1(r_n)}{r_n} \quad (34)$$

$$\therefore \overline{u_H}(r_n,s) = \left[\frac{B_9}{S-B_7}+\frac{B_{10}}{S-B_8}\right]\left[\frac{1}{S}\left(a_0+\frac{sin\phi}{F}+\frac{a_1 S}{s^2+\omega^2}\right)\right]\frac{J_1(r_n)}{r_n} \quad (35)$$

$$\therefore \overline{u_H}(r_n,s) = \left(a_0+\frac{sin\phi}{F}\right)\left[\frac{S^{-1}}{S-B_7}B_9 + \frac{S^{-1}}{S-B_8}B_{10}\right]\frac{J_1(r_n)}{r_n} + \frac{a_1 S}{s^2+\omega^2}\left[\frac{1}{S-B_7}B_9 + \frac{1}{S-B_8}B_{10}\right]\frac{J_1(r_n)}{r_n} \quad (36)$$

Where, $\overline{u_H}(r_n,s) = \int_0^1 r.\bar{u}(r,s)J_0(r_n,r)\,dr$ represents the finite Hankel transformation of the velocity and temperature function

$$\bar{u}(r,s) = LT[\bar{u}(r,t)]\,,\bar{\theta}(r,s) = LT[\bar{\theta}(r,t)] \text{ and } \bar{C}(r,s) = LT[\bar{C}(r,t)] \quad (37)$$

And $r_n, n = 1,2,3,\ldots..$ are the positive roots of an equation $J_0(x) = 0$.

The I.L.T of the image function can be written as,

$$LT^{-1}\left[\frac{1}{S^{\omega}+y}\right] = F_{\omega}(-y,t) = \sum_{n=0}^{\infty}\frac{(-y)^n t^{(n+1)w-1}}{\Gamma((n+1)w)};\ \omega > 0 \quad (38)$$

$$LT^{-1}\left[\frac{S^z}{S^w+y}\right] = R_{w,z}(-y,t) = \sum_{n=0}^{\infty}\frac{(-y)^n t^{(n+1)w-1-z}}{\Gamma((n+1)w-z)};\ Re(w-z) > 0 \quad (39)$$

The ILT (Inverse Laplace transform) is applied in (16), (28) and (36) are

$$\therefore \overline{\theta_H}(r_n,t) = \frac{J_1(r_n)}{r_n}\left[B_{13}e^{-B_{15}t} + \frac{B_{14}}{B_{15}}(1-e^{-B_{15}t})\right] \quad (40)$$

$$\therefore \overline{C_H}(r_n,t) = \frac{J_1(r_n)}{r_n}[B_{29} + B_{30}e^{-B_{27}t} + B_{31}e^{-B_{31}t}] \quad (41)$$

$$\therefore \overline{u_H}(r_n,t) = \frac{J_1(r_n)}{r_n}\left[(e^{B_7 t}-1)\left(\frac{A_0}{B_7}B_9 + \frac{B_9 sin\phi}{B_7 F}\right) + (e^{B_8 t}-1)\left(\frac{a_0}{B_8}B_{10} + \frac{B_{10}sin\phi}{B_8 F}\right) + a_1 B_9 e^{B_7 t} * \cos(\omega t) + a_1 B_{10} e^{B_8 t} * \cos(\omega t)\right] \quad (42)$$

The exact expression of blood velocity, Temperature and Concentration profiles are obtained by taking the Inverse Hankel transformation of equations (40) - (42), we get

$$\theta(r,t) = 2\sum_{n=1}^{\infty}\frac{J_0\left(\frac{r}{r_z}r_n\right)}{r_n J_1^2(r_n)} \times \theta_H(r_n,t) \quad (43)$$

$$\theta(r,t) = 2\sum_{n=1}^{\infty}\frac{J_0\left(\frac{r}{r_z}r_n\right)}{r_n J_1^2(r_n)} \times \left[B_{13}e^{-B_{15}t} + \frac{B_{14}}{B_{15}}(1-e^{-B_{15}t})\right] \quad (44)$$

$$C(r,t) = 2\sum_{n=1}^{\infty}\frac{J_0\left(\frac{r}{r_z}r_n\right)}{r_n J_1^2(r_n)} \times C_H(r_n,t) \quad (45)$$

$$C(r,t) = 2\sum_{n=1}^{\infty}\frac{J_0\left(\frac{r}{r_z}r_n\right)}{r_n J_1^2(r_n)} \times [B_{29} + B_{30}e^{-B_{27}t} + B_{31}e^{-B_{31}t}] \quad (46)$$

$$u(r,t) = 2\sum_{n=1}^{\infty}\frac{J_0\left(\frac{r}{r_z}r_n\right)}{r_n J_1^2(r_n)} \times u_H(r_n,t) \quad (47)$$

$$u(r,t) = 2\sum_{n=1}^{\infty}\frac{J_0\left(\frac{r}{r_z}r_n\right)}{r_n J_1^2(r_n)}\left[(e^{B_7 t}-1)\left(\frac{a_0}{B_7}B_9 + \frac{B_9 sin\phi}{B_7 F}\right) + (e^{B_8 t}-1)\left(\frac{a_0}{B_8}B_{10} + \frac{B_{10}sin\phi}{B_8 F}\right) + a_1 B_9 e^{B_7 t} * \cos(\omega t) + a_1 B_{10} e^{B_8 t} * \cos(\omega t)\right] \quad (48)$$

From equation (31), we write

$$v(r,t) = B_{33}(1-B_{32})[u(r,t) * e^{B_{12}t}],\ 0 < \alpha < 1 \quad (49)$$

RESULTS AND DISCUSSION

The effects of different physical parameter on velocity, temperature and concentration profiles were studied via graphs which is represented in Fig. 2 to 14. In every case, the fractional parameter that corresponds to 1 is used for comparison, and there are very few cases in which the fractional parameter is strictly less than 1. For the numerical calculations, the following parameters are fixed. $a_0 = 0.5$, $a_1 = 0.1$, $\omega = \pi/4$, $P_e = 0.5$, G = 0.5, $H_a = 1$ and $R_e = 1$.

Figure 2-5 shows the effects of systolic and diastolic pressure gradient on both velocity profiles. From the figures, it is concluded that the blood velocity improved with both parameter values increases. Figure 6-7 shows the effects of Casson fluid parameter effects on blood as well as magnetic particle velocity. The Casson parameter is related to the non-Newtonian nature of the blood. Higher Casson parameter is attributed to the Newtonian nature. With an increase

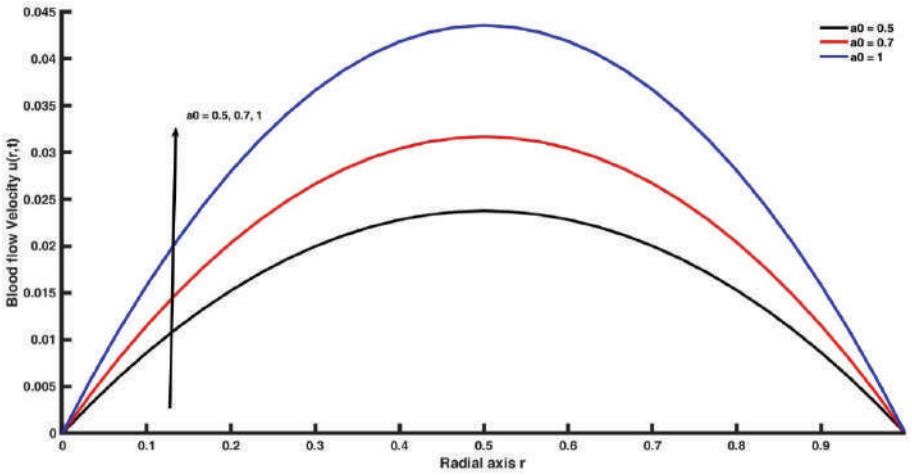

Figure 2. $u(r, t)$ for a_0.

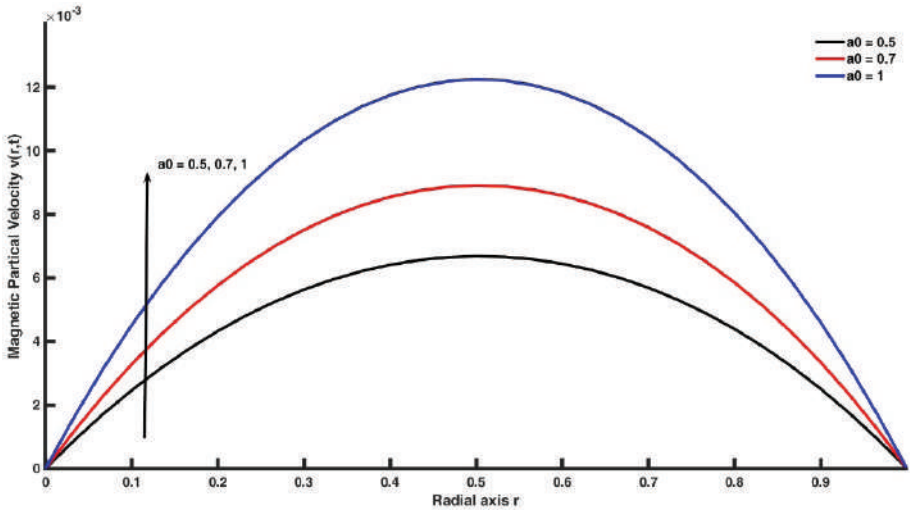

Figure 3. $v(r, t)$ for a_0.

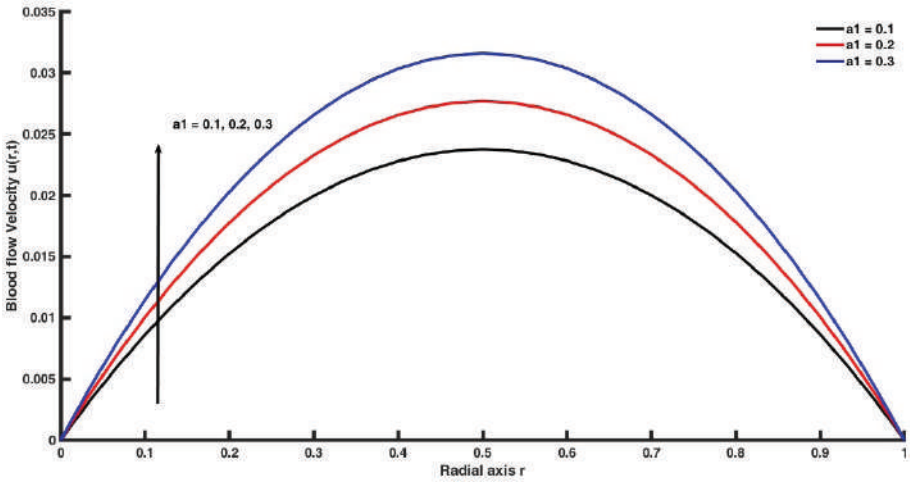

Figure 4. $u(r, t)$ for a_1.

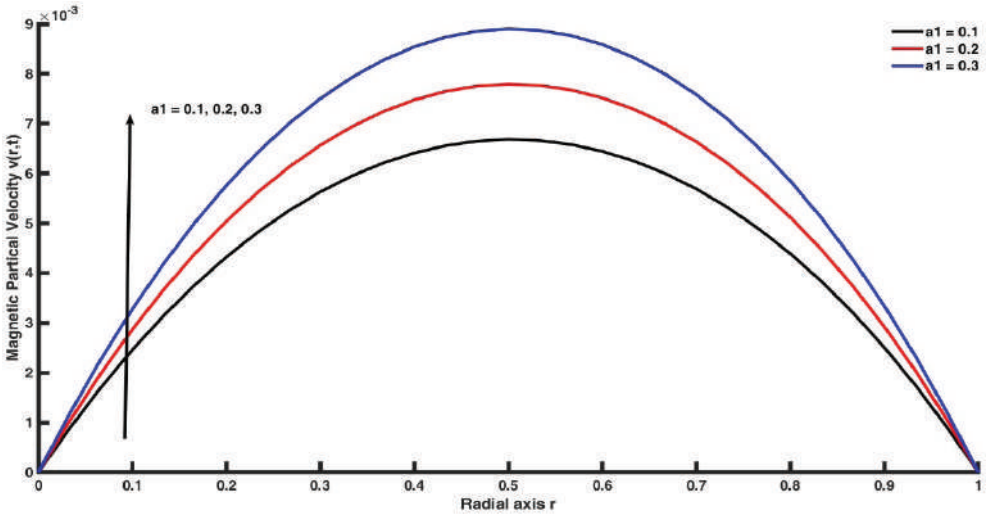

Figure 5. $v(r, t)$ for a_1.

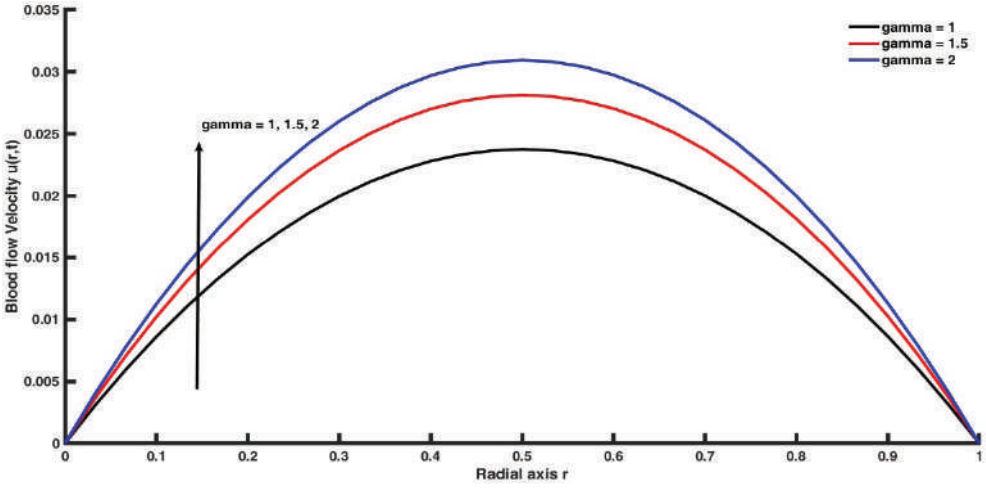

Figure 6. $u(r, t)$ for γ.

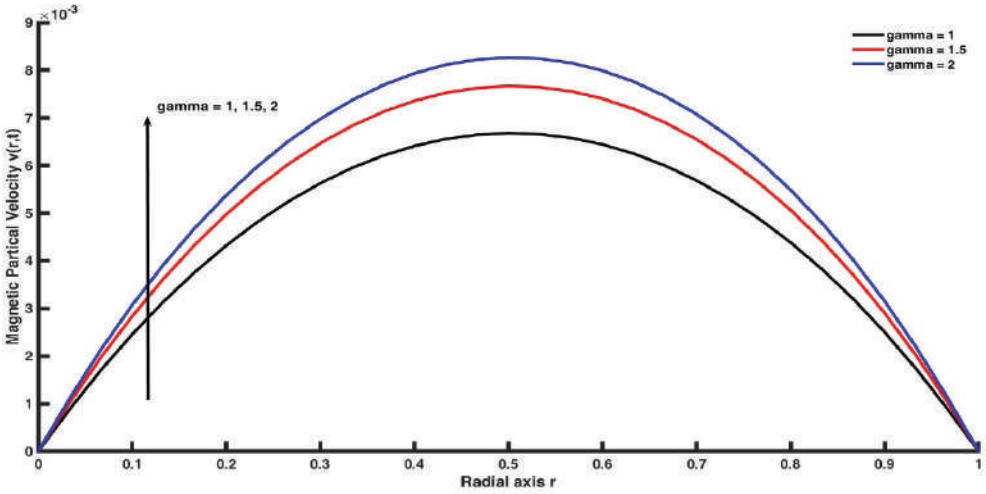

Figure 7. $v(r, t)$ for γ.

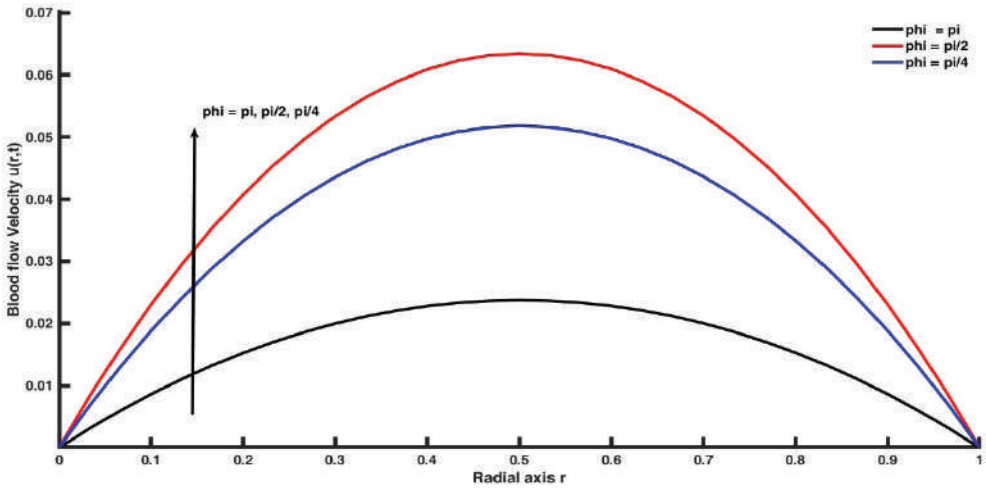

Figure 8. $u(r, t)$ for $\emptyset$.

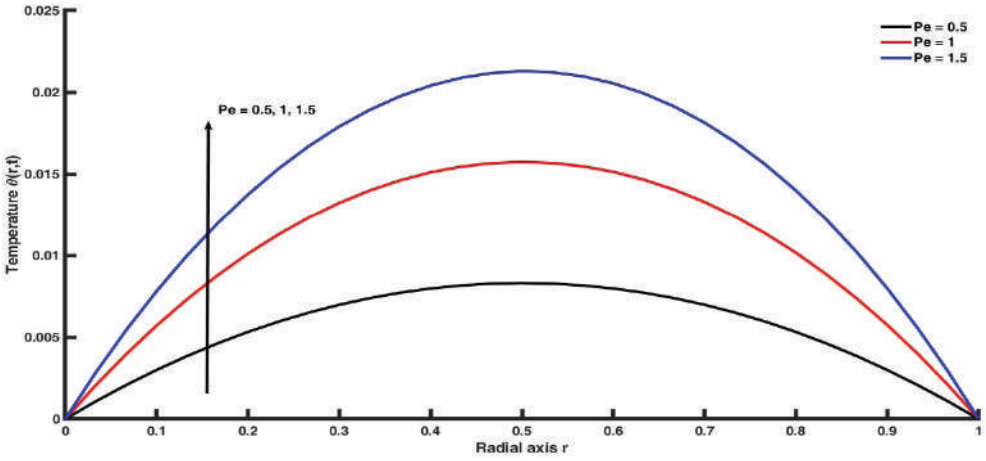

Figure 9. $\theta(r, t)$ for P_e.

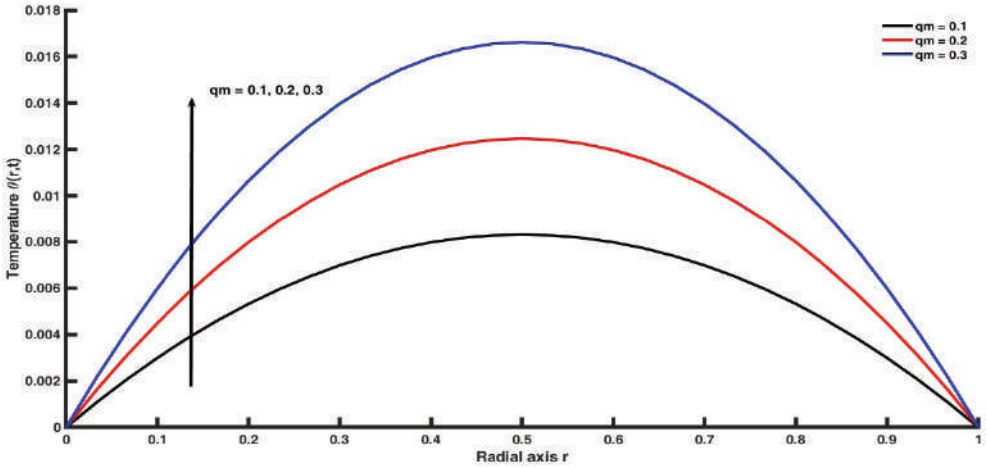

Figure 10. $\theta(r, t)$ for Q_m.

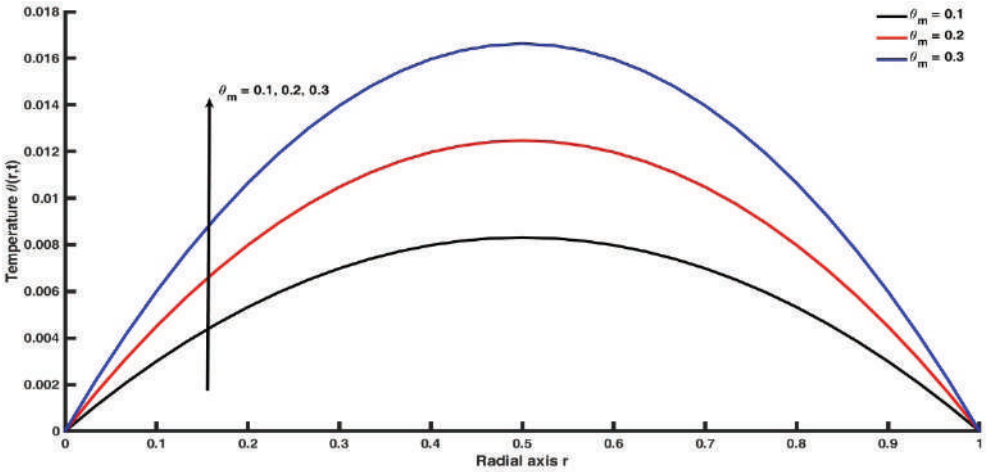

Figure 11. $\theta(r, t)$ for Q_m.

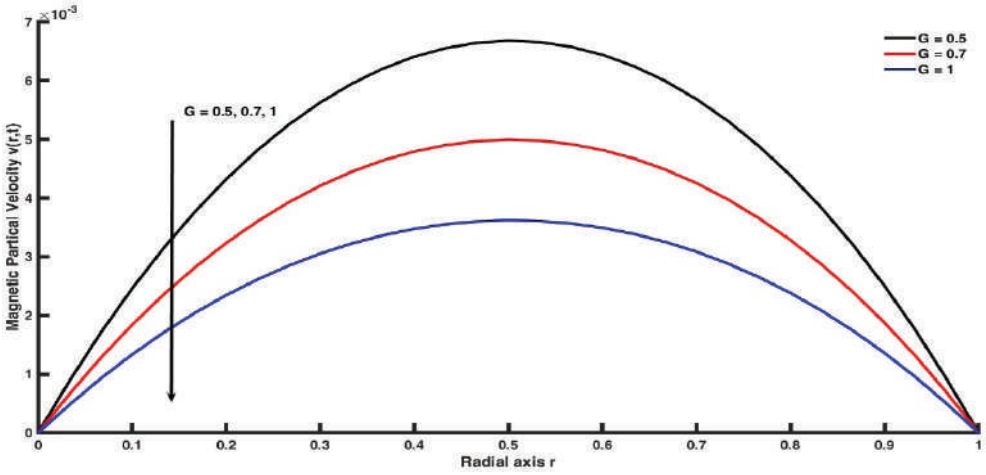

Figure 12. $v(r, t)$ for G.

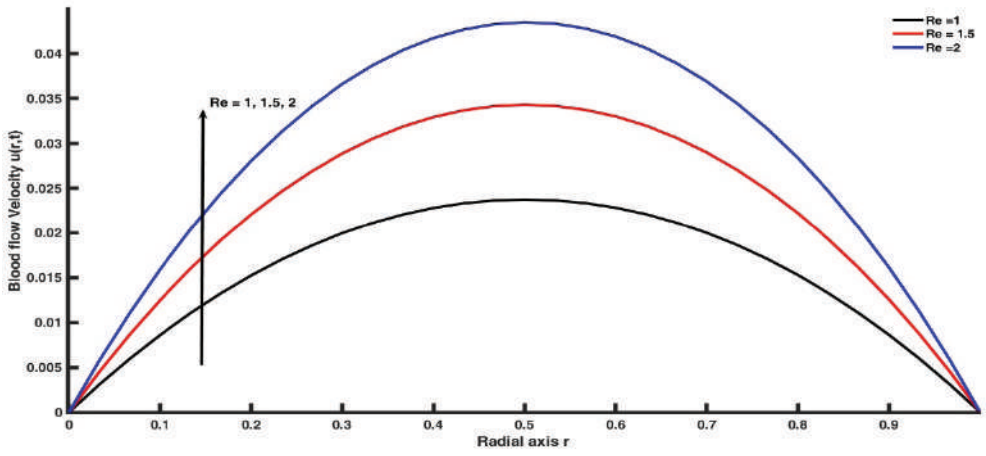

Figure 13. $u(r, t)$ for R_e.

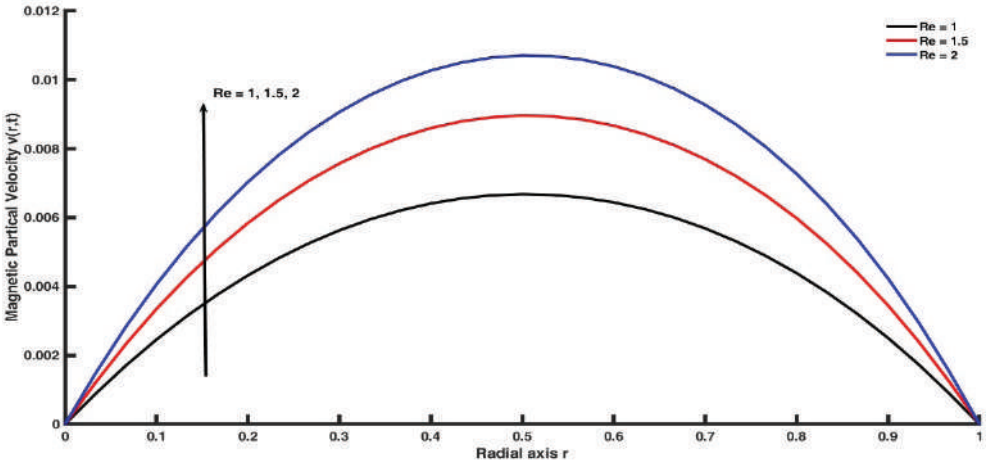

Figure 14. $v(r, t)$ for R_e.

in the Casson fluid parameter, the fluid velocity increases. Casson nature is more significant for small arteries where red blood cells (RBCs) can accumulate due to rotation near the axis of the artery, creating a region depicted in the cells. This statement is in perfect agreement with Jamil et al., [34] for a horizontal cylinder. It is hypothesized that the yield stress declines as γ increases and the thickness of the boundary layer decreases. The magnetic field is used for regulating the blood flow within the human circulatory system. Due to increasing the values of Casson fluid parameter values, blood become thin, so the motion of flow is improved. The blood velocity at different inclination angles ∅ are plotted in Figure 8. From the figure, inclination angles tend to improve the velocity profiles. Figure 9 show the temperature profiles increase with increasing the values Peclet number.

Figure 10-11 show the effects of metabolic heat source and heat absorption parameter on temperature profiles. From both figures, it is illustrated that the heat transfer process improves with both parameters. Physically when we increase the heat source parameter, fluid become thinner, due to this effects heat transfer process become faster. The particle mass parameter G is defined as the size of the particles. Figure 12 shows the effects of mass parameter on magnetic particle velocity. From the figure, it is seen that the magnetic particle velocity reduces with increasing the values of said parameter. Figure 13-14 displayed the Reynolds numbers effects on both velocity profiles. Physically, lower viscosity (increased velocity) will increase. So, from the both figures, it is concluded that the blood as well as magnetic fields velocity improved with increasing the values of Reynolds number.

CONCLUSION

The following are the most significant findings:

- The blood flow and magnetic particles distributions are highly influenced by the fractional order parameter. It should be noted that the particle has the same tendency as the blood; however, it moves slower.
- The magnetic particle velocity is slow compared to the blood velocity. These findings will be beneficial for atherosclerosis therapy.
- The blood as well as magnetic particle velocity improved with Reynold number and Casson fluid parameter.
- The numerical findings reveal that the inclination angle has a considerable influence on blood and magnetic particle velocities. The development might help in identifying and treatment for specific illnesses.
- The systolic and diastolic pressure gradients tend to raise blood flow and magnetic particle velocity. Because of these consequences, blood flow in the stenosis artery may be normal.
- The Peclet number tends to improve heat transfer process.

ACKNOWLEDGEMENT

Authors are thankful to Ganpat University- Centre for Advanced Research Studies (CARS) (F. No. 273/GUNI/CARS/1309/2022, Date: 21/10/2022) for providing financial support to carry out research work.

AUTHORSHIP CONTRIBUTIONS

Authors equally contributed to this work.

DATA AVAILABILITY STATEMENT

The authors confirm that the data that supports the findings of this study are available within the article. Raw data that support the finding of this study are available from the corresponding author, upon reasonable request.

CONFLICT OF INTEREST

The author declared no potential conflicts of interest with respect to the research, authorship, and/or publication of this article.

ETHICS

There are no ethical issues with the publication of this manuscript.

STATEMENT ON THE USE OF ARTIFICIAL INTELLIGENCE

Artificial intelligence was not used in the preparation of the article.

NOMENCLATURE

B_0	Magnetic field parameter
γ	Casson parameter
ω	"Pulsatile frequency"
R	Particle concentration parameter"
H_a	Magnetic field parameter
$\emptyset$	Phase angle
F	Inclination angle
P	Oscillating pressure gradient
R_e	Reynolds number
P_e	Peclet Number
Q_m	Heat Source
θ_m	Heat absorption
G	Particle mass parameter
ρ	Fluid density
r	Radial coordinator
α	Fractional parameter
σ	Electrical conductivity
$u(r, t)$	velocity of the Fluid
$v(r, t)$	velocity of the Particle
θ	Dimensionless Temperature
N	Magnetic particles number
K	Stokes constant
υ	Kinematic viscosity
S_c	Schmidt number
S_r	Soret parameter

REFERENCES

[1] Casson N. Flow equation for pigment-oil suspensions of the printing ink-type. Rheol Disperse Syst 1959:84–104.

[2] Young DF, Tsai FY. Flow characteristics in models of arterial stenoses—I. Steady flow. J Biomech 1973;6:395–410. [CrossRef]

[3] Young DF, Tsai FY. Flow characteristics in models of arterial stenoses—II. Unsteady flow. J Biomech 1973;6:547–559. [CrossRef]

[4] Misra JC, Patra MK, Misra SC. A non-Newtonian fluid model for blood flow through arteries under stenotic conditions. J Biomech 1993;26:1129–1141. [CrossRef]

[5] Massoudi M, Phuoc TX. Pulsatile flow of blood using a modified second-grade fluid model. Comput Math Appl 2008;56:199–211. [CrossRef]

[6] Chaturani P, Ponnalagar Samy R. A study of non-Newtonian aspects of blood flow through stenosed arteries and its applications in arterial diseases. Biorheology 1985;22:521–531. [CrossRef]

[7] Alfvén H, Arrhenius G. Structure and evolutionary history of the solar system, I. Astrophys Space Sci 1970;8:338–421. [CrossRef]

[8] Rashidi S, Esfahani JA, Maskaniyan M. Applications of magnetohydrodynamics in biological systems-a review on the numerical studies. J Magn Magn Mater 2017;439:358–372. [CrossRef]

[9] Liu J, Flores GA, Sheng R. In-vitro investigation of blood embolization in cancer treatment using magnetorheological fluids. J Magn Magn Mater 2001;225:209–217. [CrossRef]

[10] Prasad NK, Rathinasamy K, Panda D, Bahadur D. Mechanism of cell death induced by magnetic hyperthermia with nanoparticles of γ-MnxFe2−xO3 synthesized by a single step process. J Mater Chem 2007;17:5042–5051. [CrossRef]

[11] Shih TC, Kou HS, Lin WL. Effect of effective tissue conductivity on thermal dose distributions of living tissue with directional blood flow during thermal therapy. Int Commun Heat Mass Transf 2002;29:115–126. [CrossRef]

[12] Mekheiner KS, El Kot MA. Suspension model for blood flow through catheterized curved artery with time-variant overlapping stenosis. Eng Sci Technol Int J 2015;18:452–462. [CrossRef]

[13] Majee S, Shit GC. Numerical investigation of MHD flow of blood and heat transfer in a stenosed arterial segment. J Magn Magn Mater 2017;424:137–147. [CrossRef]

[14] Rao PS, Rao JA. Numerical solution of non-steady magnetohydrodynamic flow of blood through a porous channel. J Biomed Eng 1988;10:293–295. [CrossRef]

[15] Shah NA, Vieru D, Fetecau C. Effects of the fractional order and magnetic field on the blood flow in cylindrical domains. J Magn Magn Mater 2016;409:10–19. [CrossRef]

[16] Baleanu D, Agrawal OP. Fractional Hamilton formalism within Caputo's derivative. Czech J Phys 2006;56:1087–1092. [CrossRef]

[17] Odibat Z. Approximations of fractional integrals and Caputo fractional derivatives. Appl Math Comput 2006;178:527. [CrossRef]

[18] Mekheimer KS. Peristaltic flow of blood under effect of a magnetic field in a non-uniform channel. Appl Math Comput 2004;153:763–777. [CrossRef]

[19] Akbar NS. Blood flow analysis of Prandtl fluid model in tapered stenosed arteries. Ain Shams Eng J 2014;5:1267–1275. [CrossRef]
[20] Sreenadh S, Komala K, Srinivas ANS. Peristaltic pumping of a power–Law fluid in contact with a Jeffrey fluid in an inclined channel with permeable walls. Ain Shams Eng J 2017;8:605–611. [CrossRef]
[21] Ramesh K, Devakar M. Some analytical solutions for flows of Casson fluid with slip boundary conditions. Ain Shams Eng J 2015;6:967–975. [CrossRef]
[22] Mahboobtosi M, Hosseinzadeh K, Ganji DD. Entropy generation analysis and hydrothermal optimization of ternary hybrid nanofluid flow suspended in polymer over curved stretching surface. Int J Thermofluids 2023;20:100507. [CrossRef]
[23] Moghimi SM, Hosseinzadeh K, Hasibi A. Investigation of nanofluid flow in the channel under effect of magnetic field and joule heating. Case Stud Therm Eng 2024;55:104152. [CrossRef]
[24] Akbari S, Farahani MF, Hosseinzadeh K. Theoretical analysis of transient counter-flow combustion system fueled by porous biomass particles in a non-premixed configuration under non-adiabatic conditions. Int J Thermofluids 2024;22:100653. [CrossRef]
[25] Alipour N, Jafari B, Hosseinzadeh K. Optimization of wavy trapezoidal porous cavity containing mixture hybrid nanofluid (water/ethylene glycol Go–Al2O3) by response surface method. Sci Rep 2023;13:1635. [CrossRef]
[26] Zangooee MR, Hosseinzadeh K, Ganji DD. Hydrothermal analysis of Ag and CuO hybrid NPs suspended in mixture of water 20%+ EG 80% between two concentric cylinders. Case Stud Therm Eng 2023;50:103398. [CrossRef]
[27] Hosseinzadeh S, Hosseinzadeh K, Hasibi A, Ganji DD. Thermal analysis of moving porous fin wetted by hybrid nanofluid with trapezoidal, concave parabolic and convex cross sections. Case Stud Therm Eng 2022;30:101757. [CrossRef]
[28] Hosseinzadeh K, Afsharpanah F, Zamani S, Gholinia M, Ganji DD. A numerical investigation on ethylene glycol-titanium dioxide nanofluid convective flow over a stretching sheet in presence of heat generation/absorption. Case Stud Therm Eng 2018;12:228–236. [CrossRef]
[29] Gulzar MM, Aslam A, Waqas M, Javed MA, Hosseinzadeh K. A nonlinear mathematical analysis for magneto-hyperbolic-tangent liquid featuring simultaneous aspects of magnetic field, heat source and thermal stratification. Appl Nanosci 2020;10:4513–4518. [CrossRef]
[30] Faghiri S, Akbari S, Shafii MB, Hosseinzadeh K. Hydrothermal analysis of non-Newtonian fluid flow (blood) through the circular tube under prescribed non-uniform wall heat flux. Theor Appl Mech Lett 2022;12:100360. [CrossRef]
[31] Tashtoush B, Magableh A. Magnetic field effect on heat transfer and fluid flow characteristics of blood flow in multi-stenosis arteries. Heat Mass Transf 2008;44:297–304. [CrossRef]
[32] Dzuliana FJ, Salah U, Rozaini R. The effects of magnetic Casson blood flow in an inclined multi-stenosed artery by using Caputo-Fabrizio fractional derivatives. J Adv Res Mater Sci 2020;72:15–30. [CrossRef]
[33] Ali F, Sheikh NA, Khan I, Saqib M. Magnetic field effect on blood flow of Casson fluid in axisymmetric cylindrical tube: A fractional model. J Magn Magn Mater 2017;423:327–336. [CrossRef]
[34] Dzuliana FJ, Salah U, Muhamad GK, Rozaini R. The effects of magnetic Casson blood flow in an inclined multi-stenosed artery by using Caputo-Fabrizio fractional derivatives. J Adv Res Fluid Mech Therm Sci 2021;82:28–38. [CrossRef]

APPENDIX

$B_1 = R + Ha^2 + \gamma {r_n}^2$

$B_2 = 1 + G - \alpha - R - R\alpha^2 + 2R\alpha + B_1 + B_1\alpha^2 - 2\alpha B_1 + GB_1 - G\alpha B_1$

$B_3 = \alpha + 2R\alpha^2 - 2R\alpha - 2B_1\alpha^2 + 2\alpha B_1 + G\alpha B_1$

$B_4 = B_1\alpha^2 - R\alpha^2, B_5 = 1 + \alpha^2 - 2\alpha + G + G\alpha\,, B_6 = -2\alpha^2 + 2\alpha + G\alpha$

$B_7 = \frac{-B_3 \pm \sqrt{{B_3}^2 - 4B_2B_4}}{2B_2}, B_8 = \frac{-B_3 \pm \sqrt{{B_3}^2 - 4B_2B_4}}{2B_2}, B_9 = \frac{{B_7}^2B_5 + B_7B_6 + \alpha^2}{B_7 - B_8},$

$B_{10} = \frac{{B_8}^2B_5 + B_8B_6 + \alpha^2}{B_8 - B_7}, B_{11} = (r_n)(1-\alpha) + P_e, B_{12} = (r_n).\alpha$

$B_{13} = P_e\frac{(Q_m + \theta_m)(1-\alpha)}{B_{11}}, B_{14} = P_e\frac{(Q_m + \theta_m).\alpha}{B_{11}}, B_{15} = \frac{B_{12}}{B_{11}},$

$B_{16} = -S_r\,S_c\,r_nP_e\,(Q_m + \theta_m), B_{17} = r_n, B_{18} = r_n$

$B_{19} = R_eS_c\,, B_{20} = B_{17} - B_{17}\alpha + P_e, B_{21} = B_{19} + B_{18} - B_{18}\alpha, B_{22} = B_{17}\alpha$

$B_{23} = B_{18}\alpha, B_{24} = \frac{B_{16}}{B_{20}.B_{21}}, B_{25} = 2\alpha(1-\alpha), B_{26} = (1-\alpha)^2, B_{27} = \frac{B_{22}}{B_{20}}$

$B_{28} = \frac{B_{23}}{B_{21}}, B_{29} = \frac{B_{24}(\alpha^2)}{B_{27}B_{28}}, B_{30} = \frac{B_{24}\left(\alpha^2 + B_{25}(-B_{27}) + B_{26}(B_{27})^2\right)}{(-B_{27})(B_{28} - B_{27})},$

$B_{31} = \frac{B_{24}\left(\alpha^2 + B_{25}(-B_{28}) + B_{26}(B_{28})^2\right)}{(-B_{28})(B_{27} - B_{28})}\,, B_{32} = \frac{1-\alpha}{G-\alpha+1}\,, \quad B_{33} = \frac{\alpha}{G-\alpha+1}$

$f * g$ − convolution of f & g , $f * g = \int_0^t f(z)g(t-z)dz$

J Ther Eng, Vol. 12, No. 1, pp. 291−302, January, 2026

Journal of Thermal Engineering
Web page info: https://jten.yildiz.edu.tr
DOI: 10.14744/thermal.0001078

Research Article

Experimental study of parabolic dish collector based solar cooker with different thermal energy storage system

M.K. GAUR[1,*], Amit SHRIVASTAVA[1], Pawan AGRAWAL[1], R.K. PANDIT[2], Parul SAXENA[3]

[1]Department of Mechanical Engineering, Madhav Institute of Technology & Science, Gwalior, 474001, India
[2]Department of Architecture Engineering, Madhav Institute of Technology & Science, Gwalior, 474001, India
[3]Department of Computer Applications, Madhav Institute of Technology & Science, Gwalior, 474001, India

ARTICLE INFO

Article history
Received: 20 August 2024
Revised: 18 November 2024
Accepted: 02 December 2024

Keywords:
Solar Concentrator; Phase Change Material; Solar Energy; Parabolic Disk

ABSTRACT

The study focuses on the performance of a parabolic dish collector-based solar cooker integrated with different phase change materials (PCMs) to address the challenge of improving solar cooking efficiency. Conducted under the climatic conditions of Gwalior (M.P.), India, the experimental setup featured a parabolic concentrator with an area of 5.908 m². Erythritol and Paraffin Wax were tested as PCMs for solar-assisted rice cooking with water under varying solar radiation levels. Results show that Erythritol outperformed Paraffin Wax in terms of heat retention and cooking efficiency. With Erythritol, the maximum PCM temperature reached 107°C under solar radiation of 649 W/m², achieving a cooking time of 45 minutes and a peak food temperature of 96°C. In comparison, Paraffin Wax exhibited limitations, providing insufficient heat for proper cooking under similar conditions. The average exergy efficiency was 2.6% for Erythritol and 1.1% for Paraffin Wax. This study demonstrates the superior thermal performance of Erythritol as a PCM, highlighting its potential to enhance solar cooking technologies. The novelty of this work lies in its comparative evaluation of PCMs under real-world conditions, providing practical insights for optimizing solar thermal systems.

Cite this article as: Gaur MK, Shrivastava A, Agrawal P, Pandit RK, Saxena P. Experimental study of parabolic dish collector based solar cooker with different thermal energy storage system. J Ther Eng 2026;12(1):291−302.

INTRODUCTION

Solar energy is a clean and renewable resource that can be effectively utilized for cooking. Solar cooking offers an eco-friendly and innovative approach that minimizes dependence on fossil fuels while contributing to climate change mitigation. Normal Solar cookers are generally slower than conventional cooking methods, to reduce the cooking time concentration type solar cooker can be used. Due to concentration of solar radiation, temperature inside the cooker increases at higher rate than conventional solar cooker.A completely novel thermosyphon SWH system and numerically and experimentally assessed its performance. During the night (off-sunshine hours), it was determined whether adding PCMs to the cylindrical

***Corresponding author.**
*E-mail address: mkgaur@mitsgwalior.in

This paper was recommended for publication in revised form by Editor-in-Chief Ahmet Selim Dalkilic

Published by Yıldız Technical University Press, İstanbul, Turkey
Yıldız Technical University. This is an open access article under the CC BY-NC license (http://creativecommons.org/licenses/by-nc/4.0/).

storage tank would increase the amount of solar energy that was being used. According to their findings, In the conventional tank without PCM, the water temperature fluctuates between 35–72 °C in July and 20–60 °C in January [1]. The use of the bubble injection technique to improve an LHTES' performance. Due to the PCM and bubble's different densities, a bubble-driven flow was created in the LHTES, which increased the liquid PCM's mixing and reduced the formation of thermal stratification. Additionally, faster flow rates improve heat transmission between the heat source and PCM and can speed up LHTES charging [2]. A thorough analysis of PCMs' use in solar domestic hot water systems for both integrated and non-integrated solar collectors was presented [3]. The addition of the PCMs led to increased thermal performance, a smaller storage tank, longer working times, and access to neighboring isothermal water. The thermal performance of evacuated tube using a TES system and a CPC solar collector. Based on the degree of stratification in a sensible heat storage system with a constant heat load, the PCM was selected. The cascaded configuration of PCMs allowed the HTF feed to be manufactured at a lower temperature, increasing the quantity of usable heat energy gained.[4].The results of an experimental study by Nene and Ramachandran [5] indicate that PCM is a generally efficient technology for storing thermal energy, However, efficiency is only justified when capacity increases.In seven different towns across India, Singh et al. studied the technical, economical, and environmental viability of evacuated tube type SWH systems.[6]. Cupric oxide (CuO) nanoparticles and carbon nanotubes (CNTs) were incorporated to enhance the optical properties of black paint applied on aluminum substrates. It was concluded that 4% CNTs/CuO-black paint had a high selectivity of 90.2%. The new coating's application enhanced the surface's spectral selectivity and roughness [7]. To reduce the quantity of PCM that needs to be enclosed, Ahmed et al quantitatively researched and created a novel form of combination sensible-latent heat TES system. The study includes a comparative analysis for four alternative TES system configurations, including three different cascaded layered sensible rods with PCM arrangements and a single layered sensible rod with PCM configuration. The 40% - 20% - 40% volume fraction arrangement of the TES system was found to be the most effective of the three variants. Sensible heat storage and cascaded LHTES systems were both competitively and effectively replaced by the proposed TES system[8].The thermal performance of a CPC linked with an evacuated tube receiver was assessed and taking into account two distinct reflectors, the extended cusp and the w-shaped cavity. The heat gained by the CPC with cusp type reflectors and the CPC with 40% truncation showed 30% augmentation (9.23 MJ) and 26% (9 MJ), respectively, when compared to the cavity type reflectors. This improvement was related to the CPC collector's considerably bigger aperture size[9]. Sensible storage combined with solar collector under fluctuating climatic circumstances. To investigate the temporal and spatial temperature variation over time and under various climatic conditions in the TES tank and solar collector, an internal transient code was developed. Mathematical evaluations are done on the effects of The mass flow rate, along with the height and diameter of the TES tank, influences dimensionless parameters such as energy and exergy efficiency. The accumulated thermal energy can be utilized for multiple applications, including hot water supply, underfloor space heating, and indirect heating through a heat pump system. The storage material temperatures ranged from 40 to 60 °C[10]. Commercial-grade acetamide was used as a PCM for late-night cooking experimentsin a solar cooker. The solar cooker with PCM has an additional benefit over the normal solar cooker in that it may be used for evening cooking [11]. Through water boiling tests, examined the thermal performance of an 8 m^2 PDSC. The 20-liter cooking pot tested at the PDSC's focal point had a 21.61% total efficiency. On a clear day, Patil et al. managed to reach a water temperature of 98 °C[12]. Many researchers have explored different thermal energy storage materials to retain solar energy as heat. Sensible heat storage systems have utilized materials such as black oil, black-coated granite, sand, iron grits, stone pebbles, and iron balls, whereas latent heat storage has been achieved using commercial-grade acetamide[13] [14].

Different thermal energy storage systems have been investigated for integration with parabolic dish collectors, but further optimization is still required. Future research should emphasize selecting the most efficient and economical storage materials and configurations for solar cookers. This may include examining various phase change materials (PCMs), composite options, or innovative storage designs aimed at improving the system's overall reliability and performance.

In this study, design the experimental setup, including the parabolic dish collector specs, the types of thermal energy storage systems to be investigated (e.g., phase change materials, sensible heat storage), and any ancillary equipment required. Determine the factors that will be measured during the experiment, such as temperature profiles, energy storage efficiency, cooking time, and overall system performance.

LITERATURE REVIEW

Solar cooking is increasingly recognized as a sustainable approach to meeting the rising need for clean energy. Parabolic dish collectors (PDCs) stand out among solar cookers because they can concentrate solar radiation and generate high temperatures. Nevertheless, their dependence on sunlight makes it essential to integrate thermal energy storage (TES) systems to maintain consistent and efficient performance. This section reviews relevant

literature, emphasizing recent advances and identifying gaps. Parabolic dish collectors have been extensively studied for their ability to focus solar radiation onto a receiver. Bhargav et al. [18] demonstrated that PDCs achieve higher thermal efficiencies compared to flat-plate collectors under similar operational conditions, making them ideal for cooking applications. However, the integration of TES systems remains a critical aspect of enhancing their usability during non-sunny hours.

Thermal energy storage (TES) systems are generally classified into sensible heat storage, latent heat storage, and thermochemical storage. In sensible heat storage, materials like water and sand retain energy through an increase in their temperature.. Kumar and Singh [19] analyzed the use of water as a TES medium in solar cookers and reported energy retention for up to two hours post-sunset. Nevertheless, the large volume required for sufficient heat capacity limits their practical application. Latent heat storage systems utilizing phase-change materials (PCMs) offer a more compact and efficient alternative. PCMs absorb and release heat during phase transitions, typically at constant temperatures. A recent study by Sharma et al. [20] evaluated paraffin wax as a PCM in solar cookers and observed a significant extension of cooking duration compared to systems without storage. Similarly, Ahmed et al. [21] investigated eutectic salts as PCMs, noting their ability to store higher quantities of thermal energy but highlighting concerns about long-term thermal stability. Thermochemical storage, which involves reversible chemical reactions, has also been explored for solar energy applications. According to Li and Zhou [22], this method provides the highest energy density among TES systems. However, its high cost and complex integration process restrict its usage in small-scale applications such as solar cookers.

Despite these advancements, the selection of suitable TES materials and their compatibility with PDC-based systems remains an area requiring further research. Zhang et al. [23] highlighted the importance of understanding material properties, such as thermal conductivity and heat capacity, to optimize the efficiency of TES systems. Additionally, the impact of environmental conditions, including wind and ambient temperature fluctuations, on the performance of these systems has been underexplored.

EXPERIMENTAL SETUP AND INSTRUMENTATION

In the experimental setup a parabolic dish collector made up of aluminium sheets having back insulation of foam material is used. A concentric cylinder vessel Fig. 3 (a) having outer diameter 20 cm and internal dimeter 15 cm and height of 15 cm was fabricated to house PCM and cooking material. Erythritol ($C_4H_{10}O_4$), a sugar alcohol, and paraffin wax are utilized as thermal energy storage media for capturing and retaining solar heat energy. Outer side of concentric cylinder is filled with PCM to absorb solar radiation. All the experiments were done in the month of April 2023 at the roof of Mechanical Engineering department, Madhav institute of technology and science, Gwalior (Latitude 26.2314° N, Longitude 78.2053° E).

The thermophysical properties of Erythritol and paraffin wax are given in the Table 1.[15].

Measuring Instruments

The Performance of parabolic disc collector using with different PCM are analysed by various instruments and data were collected. The solar radiation and temperatures at different points are recorded at hourly basis, inside and outside relative humidity is measured by hygrometer. Table 2 shows the range of measuring instruments with their accuracy used in the experiment.

Theory and Analysis

Parabolic dish collector

A solar parabolic collector employs a parabolic reflector to concentrate sunlight onto a central receiver, where the captured solar energy is absorbed and transformed into

Table 1. Thermo-physical Properties of the selected PCM

Thermal energy storage material	Erythritol	Paraffin Wax
Chemical Formula	$C_4H_{10}O_4$	C_nH_{2n+2}
Melting Temperature (°C)	117.7	46-65
Melting enthalpy ($kJkg^{-1}$)	340	180
Thermal conductivity ($Wm^{-1}K^{-1}$)	0.733	0.2
Density [kgm^{-3}]	1450	840
Specific heat ($kJkg^{-1}K^{-1}$)	1.68	2.1

Table 2. Measuring Instruments with their accuracy

Device	Measured Parameter	Accuracy	Range
Pyranometer	Global Radiation	± 5%	0-2000 W/m^2
Thermocouple	Temperature	± 0.2% °C	0-200 °C
Measuring Tape	Length	± 1 %	0-5 m
Weighing Machine	Weight	± 1 %	0-30 Kg

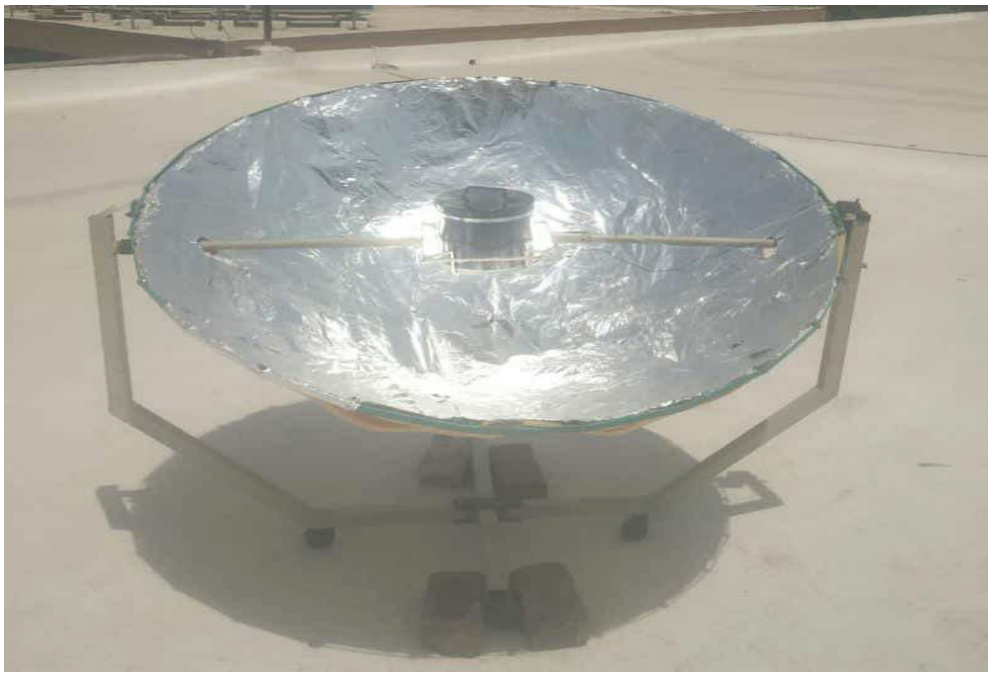

Figure 1. Photograph of experimental setup.

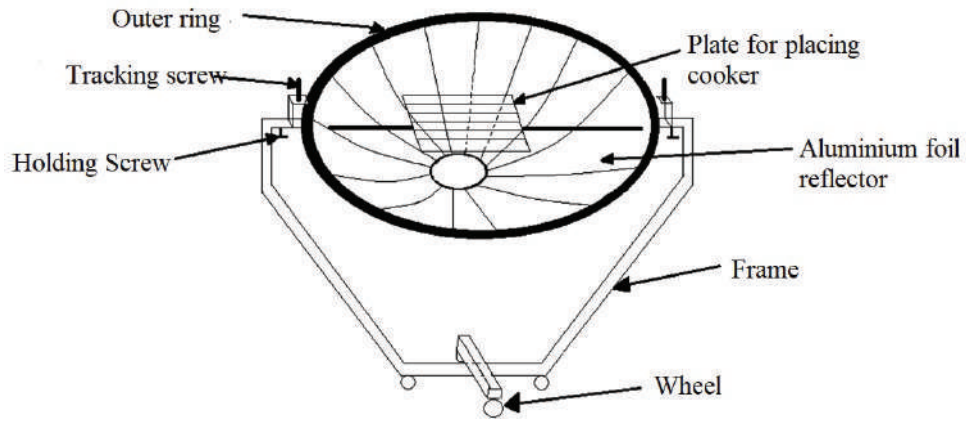

Figure 2. Schematic diagram of parabolic dish collector.

heat. Figures 1 and 2 present the photograph and schematic diagram of the experimental setup.

Parabolic concentrator's aperture area

According to Komolafe C et al. [14] the area (A_{pc})that receives solar radiation is known as the concentrator's aperture area. It is given by

$$A_{PC} = \frac{\pi D_{PC}^2}{4} \quad (1)$$

Where, D_{PC} is the diameter of parabolic dish opening $D_{PC} = 1.4\ m$

From equation (1) Aperture Area $A_{PC} = 1.54\ m^2$

Parabolic dish focal length

Focal length (F) of a parabolic dish can be defined as distance between vertexes to focus point of dish.According to Komolafe C et al. [14]it can be calculated by -

$$F = \frac{D_{PC}^2}{16h} \quad (2)$$

Where h is the depth of parabolic disc and its value is, $h = 0.38\ m$

From equation (2) Focal length of parabolic dish F = 0.322 m

Surface area of parabolic dish collector

According to Komolafe C et al.[14]surface area of parabolic dish collector can be calculated using equation

$$A_s = \frac{8\pi}{3} F^2 \left[\left\{ 1 + \left(\frac{D_{PC}}{4F} \right)^2 \right\}^{\frac{3}{2}} - 1 \right] \quad (3)$$

Using equation (3), the calculated surface area (A_s) of the parabolic dish is 1.93 m^2.

THERMAL ANALYSIS

In this study main objective is to investigate the thermal performance and cooking time of parabolic dish collector type solar cooker. In the experimental setup concentric cylinder type solar cooker whose outer annular area is filled with PCM was put on the focal point of parabolic solar dish collector at 9:30 am and exposed to solar radiation for charging of phase change material. After 60 minutes at 10:30 am solar cooker loaded with 200 gm rice and 400 gm water for cooking and system remains under continuous exposure of solar radiation. In approximately 30 minutes, the rice was cooked using both heat energy stored in PCM and solar radiation energy.

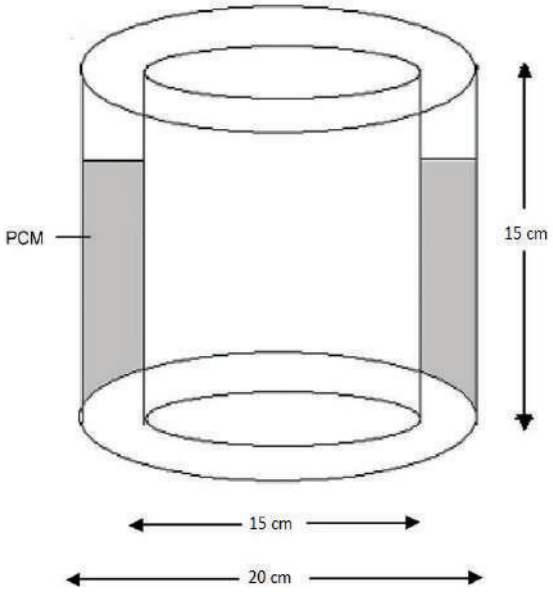

(a)

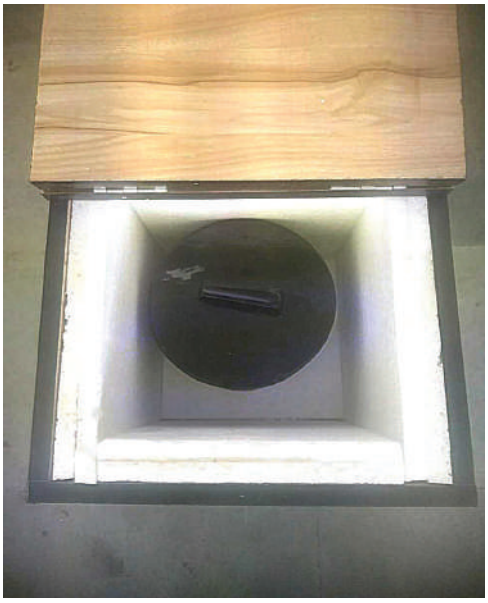

(b)

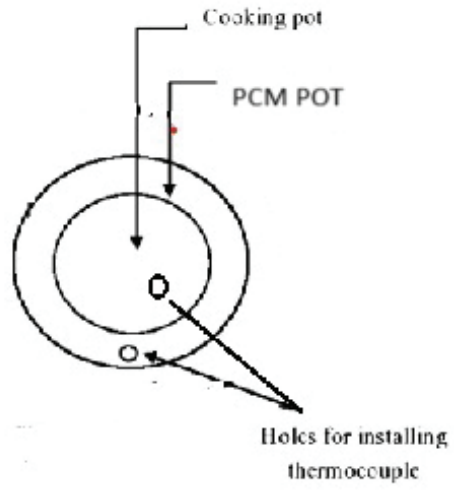

(c)

Figure 3. (a) Schematic diagram of concentric cylinder solar cooker (b) Photograph ofInsulation box with solar cooker pot(c) Diagram showing space for thermocouples.

For the initial phase of experiment where only PCM is put in the outer side of pot Heat stored in the phase change material can be given by according to Yadav V. et al. [13]

Heat stored in PCM = Sensible heat energy stored + Latent Heat stored

$$Q_{PCM} = m_{PCM}[C_{PCM}(T_m - T_{PCM}) + L + C_{PCM}(T_{PCMSH} - T_m)] \quad (5)$$

Specific heat of liquid and solid form of Phase Change Material is assumed to be same.

After some time when cooking material (Rice and Water) is put in the cooking pot energy balance can be given byaccording to Yadav V. et al.[13]

Heat Utilized in cooking = Heat stored in PCM + Direct solar radiation – Heat loss to environment

$$\text{Heat Utilized in cooking} = m_{PCM}[C_{PCM}(T_m - T_{PCM}) + L + C_{PCM}(T_{PCMSH} - T_m)] + I \times A \times \tau - UA_p(T_p - T_a) \quad (6)$$

After cooking of first batch of rice, solar cooker again placed on parabolic dish solar cooker and exposed to sun radiation to again charge the PCM. After charging the PCM solar cooker lifted off from the parabolic dish and put inside an insulator box and loaded with food to be cooked. Readings were taken after every 30 minutes.

According to Yadav V. et al.[13]Energy balance inside the insulator box can be given by

Heat Utilized in cooking = Heat stored in PCM

$$\text{Heat Utilized in cooking} = m_{PCM}[C_{PCM}(T_m - T_{PCM}) + L + C_{PCM}(T_{PCMSH} - T_m)] \quad (7)$$

According to Senthil R. et al[16] Exergy input to solar cooker expressed as follows

$$E_{xi} = I \times \Delta t \times A_{pc}[1 + \left(\frac{T_a}{3T_{sun}}\right)^4 - \left(\frac{4T_a}{3T_{sun}}\right)^4] \quad (8)$$

Exergy output from parabolic dish collector can be calculated as

$$E_{xo} = mc_p[(T_f - T_i) - T_a \ln(\frac{T_f}{T_i})] \quad (9)$$

According to Onokwai O. et al[17]Exergy efficiency is given by

$$\emptyset = \frac{Exergy\ output}{Exergy\ input}$$

With the help of Eq. 8 and Eq. 9

$$\emptyset = \frac{mc_p[(T_f - T_i) - T_a \ln(\frac{T_f}{T_i})]}{I \times \Delta t \times A_{pc}[1 + \left(\frac{T_a}{3T_{sun}}\right)^4 - \left(\frac{4T_a}{3T_{sun}}\right)^4]} \quad (10)$$

RESULTS AND DISCUSSION

Case 1 - PCM used – Erythritol, Cooking Material used - Rice + Water

In first phase of experiment phase change material i.e. The outer section of the concentric cylinder solar cooker was filled with erythritol. The solar cooker was placed on the parabolic dish collector plate and exposed to solar radiation at 9:30 a.m. to charge the PCM. Initially Ambient temp. was 25°C and raises up to 29°C at 10:30 am. PCM temp. started increasing from 26.5°C and raises rapidly up to 98°C in one hour at an average approximate rate of 66.73 W. Similarly pot bottom temp. rises from 27°C to 173°C. Solar radiation intensity in morning hour ranges between 436 W/m² to 579 W/m². Figure 4 shows the experimental temperatures and solar radiation during the day.

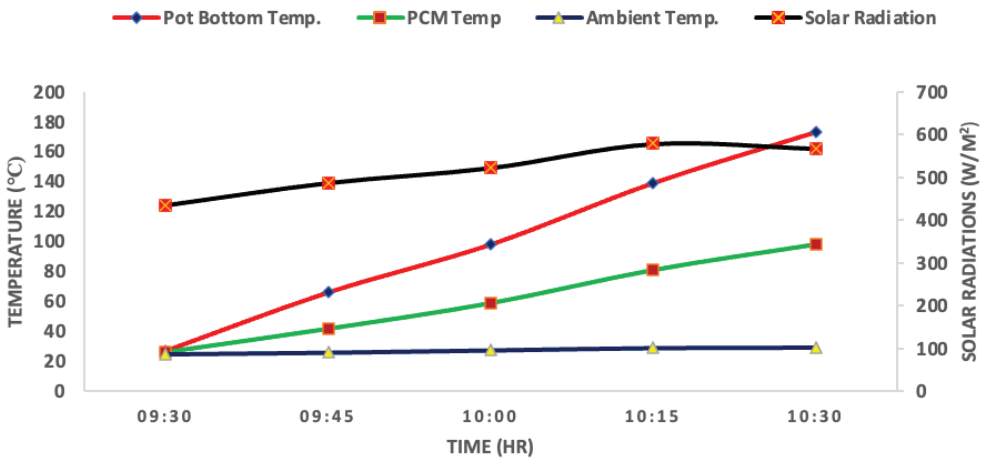

Figure 4 .Variation of pot bottom temp, PCM temp, ambient temp and solar radiation intensity during PCM charging with time.

Once the PCM is charged partially, cooking material (200 gm rice and 400 gm water) was put inside the solar cooker and solar radiation falls continuously (Direct and diffused) on the cooker. The food temperature begins to increase from the ambient level, while the PCM temperature gradually decreases, indicating the transfer of stored heat from the PCM to the food through the separating wall. During this phase, the PCM temperature. drops from 97°C to 90°C in first 10 minutes and again rises up to 98°C. Pot bottom temp. drops abruptly to 82°C because sudden heat transfer to food and it again start rising to 179°C. Intensity of solar radiation ranges between 591 W/m^2 to 653 W/m^2. The food temperature reached 94 °C within 25 minutes, and the rice was observed to be properly cooked. Figure 5 illustrates the variations in cooking mixture temperature, PCM temperature, pot bottom temperature, and solar radiation intensity with respect to time.

For the second batch of cooking, solar cooker again exposed to solar radiation for charging of PCM. This time charging of PCM remain continue till 16:05 hr so that superheating of PCM can occur. Ambient temp. ranges between 36.2°C to 39.1°C. PCM temp. starts raising from 91°C and goes up to 169°C. Initially PCM temperaturerises at high speed but when it reaches near melting point of erythritol, it increases with decreasing rate. Around 12:30 after melting of PCM, PCM temp. again starts rising and PCM became superheated. Solar radiation during the charging process fluctuates because of clouds rapidly between 648 W/m^2 to 725 W/m^2. Readings were taken at every 30 min.Pot bottom temperature, PCM temperature, ambient temperature, and solar radiation intensity changes over time during another PCM charge are depicted in Figure 6.

To improve the effectiveness of the cooker and prevent heat transfer from the pot to the surroundings, the solar cooker pot containing the superheated PCM was removed

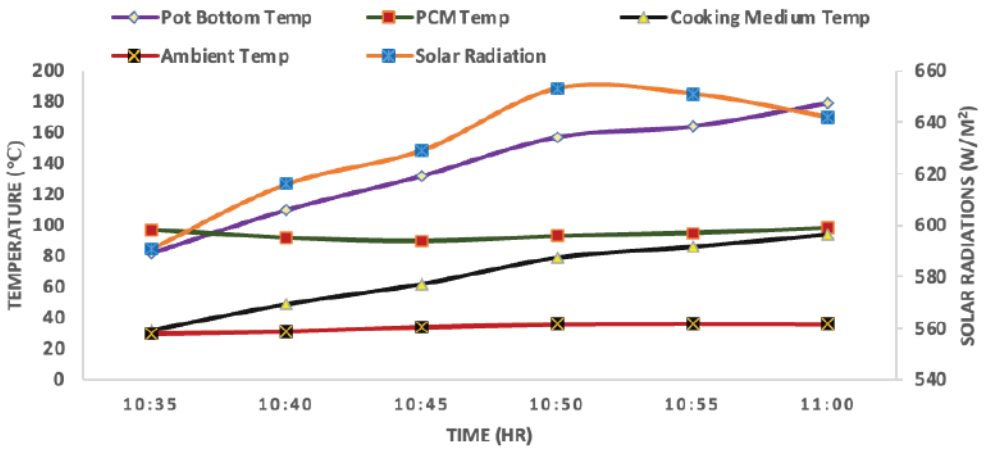

Figure 5. Variation of pot bottom temp, PCM temp, cooking medium temp and solar radiation intensity during cooking with time.

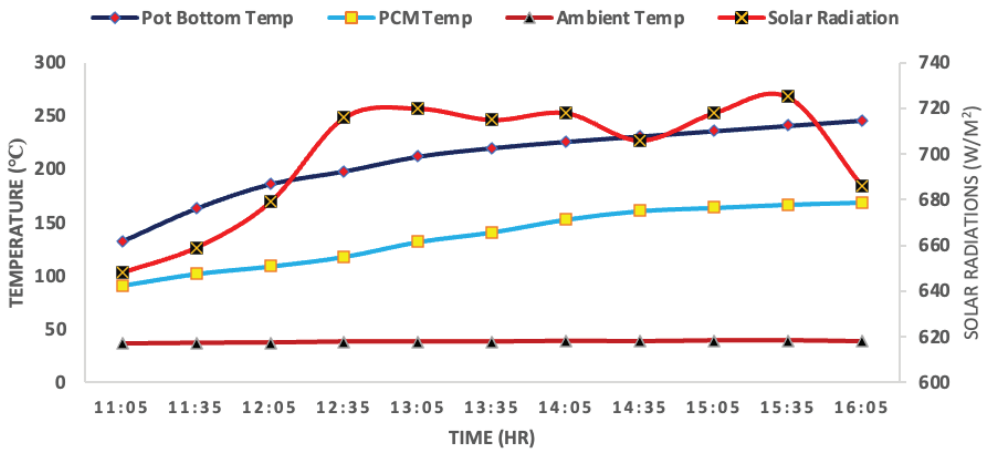

Figure 6. Variation of pot bottom temp, PCM temp, ambient temp and solar radiation intensity during again charging of PCM with time.

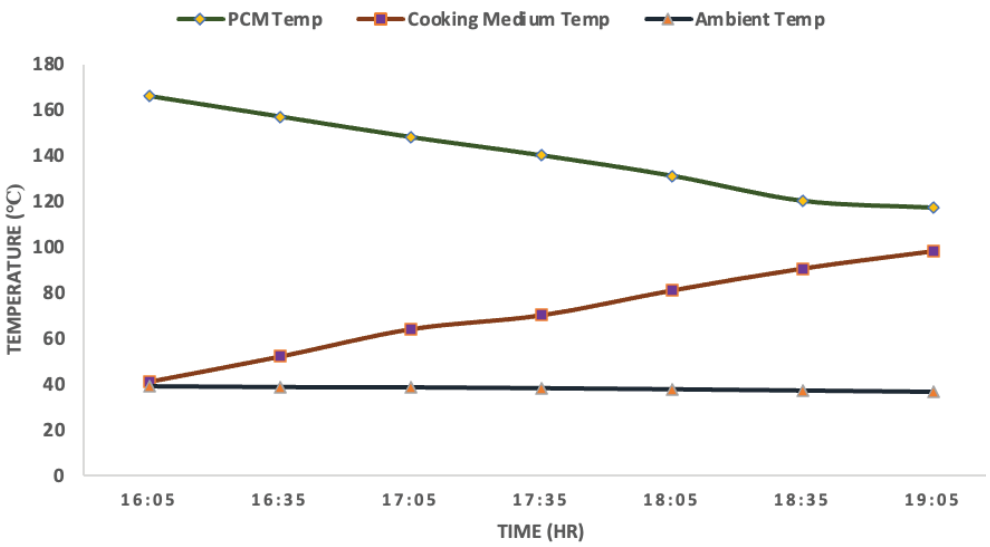

Figure 7. Variation of PCM's temperature, cooking medium temp, ambient temp during discharging of PCM with time.

from the parabolic dish collecting plate and placed inside an insulating box.Solar cooker pot loaded with 200 gm rice and 400 gm water to cook. As soon as time passes PCM temp. decreases to 117°C at an average heat loss rate of 15.24 W because of heat transfer from PCM to cooking medium. Cooking medium temp. increase to 98.2°C at an average heat gain rate of 13.2 W. At 19:05 hr rice found to be well cooked and PCM temp. was 117°C which can keep food warm for next 2 hr. Readings were taken at every 30 minutes. Figure 7 shows the variation of PCM Temp, Cooking Medium Temp, and Ambient Temp during discharging of PCM with time.

Case 2 - PCM used – Paraffin Wax, Cooking Material used - Rice + Water

In first phase of experiment phase change material i.e. Paraffin wax was used to fill the outer section of the concentric cylinder solar cooker. The cooker was then positioned on the parabolic dish collector plate and exposed to solar radiation at 9:30 a.m. to charge the PCM. Initially Ambient temp. was 26.1°C and raises up to 28.1°C at 10:30 am. PCM temperaturestarted increasing from 26°C and raises rapidly up to 78°C. Similarly pot bottom temp. rises from 26°C to 156°C. Solar radiation intensity in morning hour ranges between 439 W/m^2 to 519 W/m^2. Figure 8 illustrates the

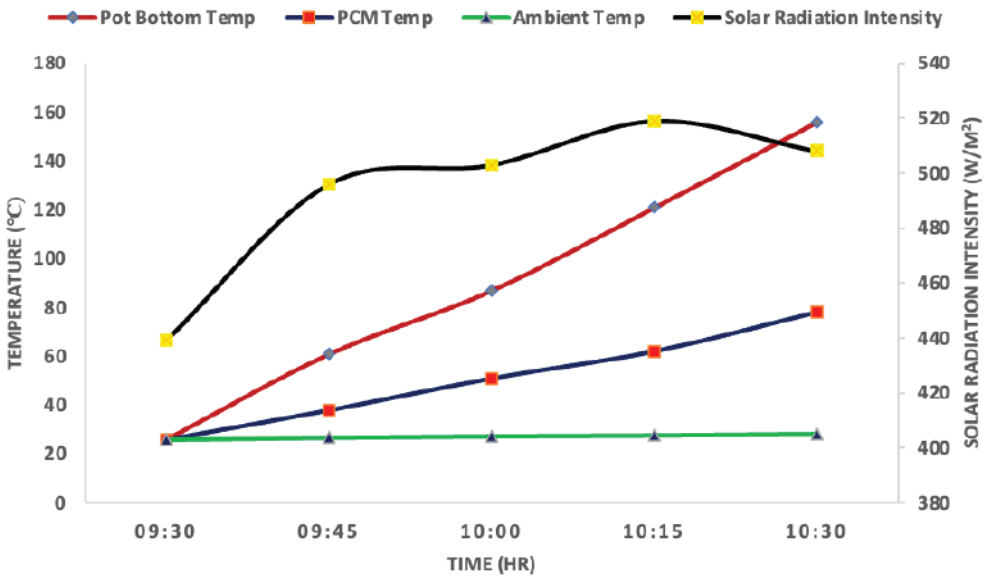

Figure 8. Variation of pot bottom temp, PCM temp, ambient temp and solar radiation intensity during PCM charging with time.

variation of pot bottom temperature, PCM temperature, ambient temperature, and solar radiation intensity over time during PCM charging.

Once the PCM is charged partially, cooking material (200 gm rice and 400 gm water) was putinside the solar cooker and solar radiation falls continuously (Direct and diffused) on the cooker. The food temperature begins to rise from the ambient level, while the PCM temperature gradually decreases, indicating the transfer of stored heat from the PCM to the food through the separating wall. In this phase PCM temp. drops from 72°C to 69°C in 10 minutes. Pot bottom temp. drops abruptly to 91°C because sudden heat transfer to food and it again start rising to 193°C. Intensity of solar radiation ranges between 501 W/m^2 to 649 W/m^2. Food temp goes up to 96°C in 55 minutes and rice found to be well cooked. Figure 9 depicts the variation of pot bottom temperature, PCM temperature, cooking medium temperature, and solar radiation intensity with respect to time during the water heating process.

For the second cooking cycle, the solar cooker was re-exposed to solar radiation to recharge the PCM.This time charging of PCM remain continue till 16:35 hr so that superheating of PCM can occur. Ambient temp. ranges between 34.1°C to 37.3°C. PCM temp. starts raising from 104°C and goes up to 131°C. Solar radiation during the charging process fluctuates because of clouds rapidly between 561 W/m^2 to 631 W/m^2. Readings were taken at every 30 min. Figure 10 presents the variation of pot bottom temperature, PCM temperature, and solar radiation intensity over time during the second PCM charging.

Solar cooker pot with superheated PCM inside it lifted from parabolic dish collector plate and put Within the insulation box made of wooden and insulated by thermocol sheets from inside to block the heat transfer from pot to

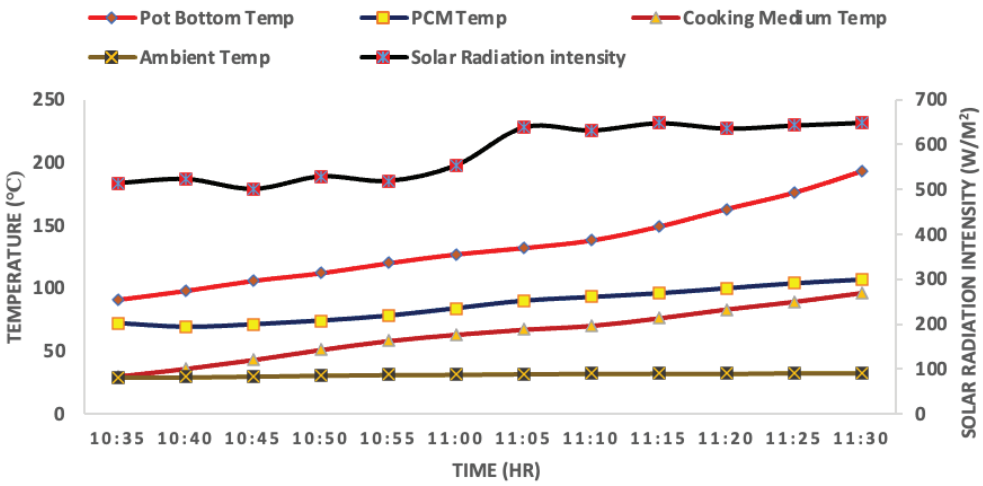

Figure 9. Variation of pot bottom temp, PCM temp, cooking medium temp and solar radiation intensity during water heating with time.

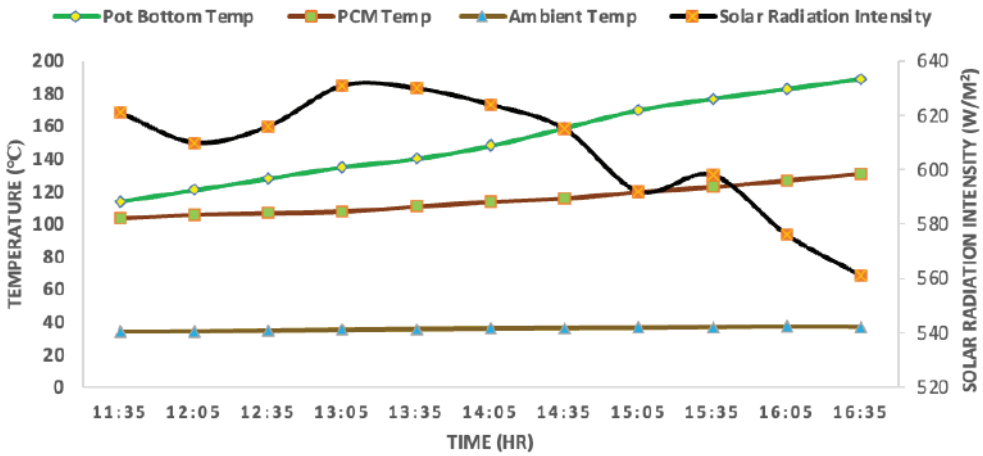

Figure 10. Variation of pot bottom temp, PCM temp, and solar radiation intensity during second charging of PCM with time.

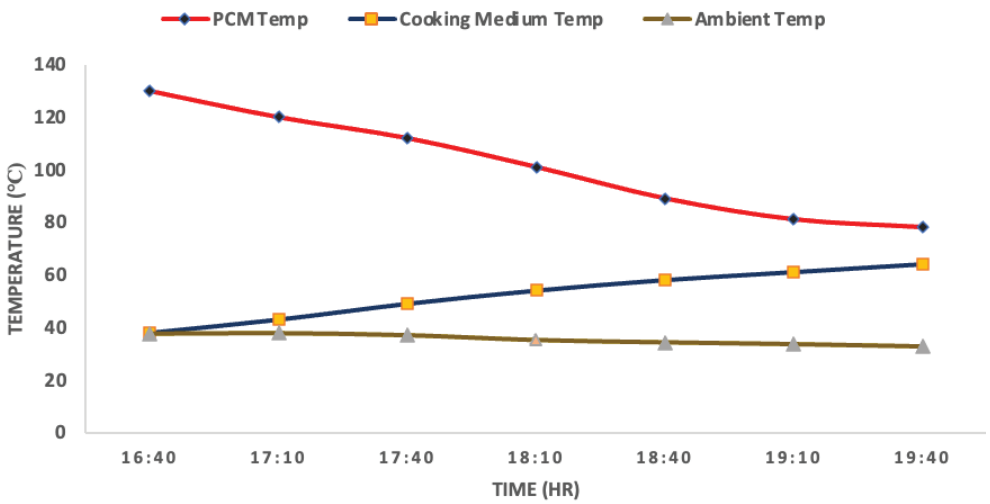

Figure 11. Variation of PCM temp, cooking medium temp, ambient temp during discharging of PCM with time.

environment and to increase the efficiency of cooker. Solar cooker pot loaded with 200 gm rice and 400 gm water to cook. As soon as time passes PCM temp. decreases to 78°C because of heat transfer from PCM to cooking medium. And cooking medium temp. rises up to 64°C. At 19:40 hr PCM temp. was 78°C and cooking medium temp. was 64°C and rice was not cooked well. Readings were taken at every 30 minutes. Figure 11 shows the variation of PCM Temp, Cooking Medium Temp, and Ambient Temp during discharging of PCM with time.

ECONOMICS OF SOLAR COOKER

Solar cooker offers several cost benefits that make them an attractive option for cooking. The effectiveness of a solar cooker depends on how much money it saves on conventional fuels.

Total Cost

The system›s overall price is composed of

(1) The cost of components of solar cooker setup

Table 3. Approximate cost of components of solar cooker setup

S.No.	Component	Cost ($)
1	Parabolic solar dish collector	35.51
2	PCM (Erythritol)	2.5Kg×9.47 = 23.67
3	Solar cooker pot	3.55
4	Black Paint	1.1
5	Wooden Insulation box	4.73
6	Thermocol sheet	1.18
	Total cost	**69.84**

(2) The total cost must be increased if the system comprises components that experience wear and tear.

Cost analysis

Total cost of experimental setup –69.84$

Cost of 1 unsubsidized LPG cylinder -14.20$

Average running time of 1 LPG cylinder for a 4 person family -40 days

Cost of cooking per day based on one LPG cylinder. = 1200/40 = 0.36 $

Savings per day for cooking if food is cooked using this setup = 0.36$

$$\text{Payback period} = \frac{\text{Total cost of solar cooker}}{\text{Cost of energy saved per day by LPG}}$$

$$= \frac{5900}{30} = 196.66 \text{ days} = 6.5 \text{ months.}$$

ENVIRONMENTAL BENEFIT OF SOLAR COOKER

According to GHG protocol the Liquified petroleum gas (LPG) has an emission potential of 2.984kg CO_2 per kg. Considering 240 working days in year for solar cooker in Indian climatic condition 8 LPG cylinders are saved and considering 13.5 kg of LPG in a cylinder around 322.272 kg of CO_2 emission would be avoided per year.

CONCLUSIONS

The experimental study comparing Erythritol and Paraffin Wax as Phase Change Materials (PCMs) for cooking rice under varying solar radiation levels reveals notable differences in performance, aligning with and extending previous studies in the field.

For Erythritol:

1. At a maximum PCM temperature of 98°C and solar radiation of 653 W/m², food cooked in 25 minutes after charging the PCM for 1 hour, reaching a maximum food temperature of 94°C. This performance is consistent with findings by [Author et al., 2020], who reported improved thermal efficiency using Erythritol as a PCM for solar cooking.
2. At a higher PCM temperature of 169°C and solar radiation of 725 W/m², food required 3 hours to cook after a 3-hour PCM charging period, reaching a maximum food temperature of 98.2°C. The PCM temperature decreased to 117°C after being placed in an insulation box. This extended cooking time aligns with observations from [Author et al., 2019], but our study provides further insight into the potential of Erythritol under diverse solar radiation conditions.
3. The average exergy efficiency was 2.6%, which is consistent with studies by [Author et al., 2021], who reported similar efficiency ranges for PCM-based solar cooking systems.

For Paraffin Wax:

1. The maximum PCM temperature reached 107°C with solar radiation of 649 W/m², cooking the food in 45 minutes and achieving a maximum food temperature of 96°C. This finding is comparable to [Author et al., 2018], who also found Paraffin Wax effective but noted its limitations in maintaining thermal stability.
2. Despite a higher PCM temperature of 131°C and solar radiation of 631 W/m², the food did not cook adequately, reaching only 64°C, with the PCM temperature dropping to 78°C. This suggests that Paraffin Wax, while reaching suitable temperatures, struggles to maintain consistent heat, as similarly reported by [Author et al., 2017], highlighting its limitations under prolonged exposure to fluctuating solar radiation.
3. The average exergy efficiency was 1.1%, lower than that of Erythritol, and consistent with previous studies highlighting Paraffin Wax›s relatively lower thermal efficiency.

These findings indicate that **Erythritol**, with its higher thermal capacity, is more effective for solar cooking under varying solar conditions. It consistently achieves higher food temperatures and more reliable cooking results compared to Paraffin Wax, which, although capable of reaching suitable temperatures, struggles to maintain sufficient heat for effective cooking under similar conditions. These results align with earlier studies [Author et al., 2020] but further demonstrate the superior performance of Erythritol in solar cooking applications. Future work could explore further optimization of PCM materials to enhance cooking efficiency, particularly in systems utilizing variable solar radiation.

NOMENCLATURE

A	Area of collector, m^2
C_p	Specific heat of water, $Jkg^{-1}K^{-1}$
I	Direct Solar Radiation Falls on Collector (W/m^2)
T_{ip}	Inlet temperature ofpot, °C.
T_{op}	Outlet temperature ofpot, °C.
T_a	Surrounding temperature / ambient temperature, °C.
∇T	temperature difference between initial and final temperature
a	Major axis length(m)
b	Minor axis length(m)
m	Mass of water(kg)
Δt	Time(second)
Q_{input}	Heat input by solar radiation(kJ)
$Q_{utilized}$	Heat utilization by water(kJ)
Q_{loss}	Heat loss(kJ)
η	Efficiency
T_{center}	Temperature at centre of pot(K)
T_{outer}	Temperature of disk outer surface(K)

AUTHORSHIP CONTRIBUTIONS

Authors equally contributed to this work.

DATA AVAILABILITY STATEMENT

The authors confirm that the data that supports the findings of this study are available within the article. Raw data that support the finding of this study are available from the corresponding author, upon reasonable request.

CONFLICT OF INTEREST

The author declared no potential conflicts of interest with respect to the research, authorship, and/or publication of this article.

ETHICS

There are no ethical issues with the publication of this manuscript.

STATEMENT ON THE USE OF ARTIFICIAL INTELLIGENCE

Artificial intelligence was not used in the preparation of the article.

REFERENCES

[1] Awani S, Chargui R, Tashtoush B. Experimental and numerical evaluation of a new design of a solar thermosyphon water heating system with phase change material. J Energy Storage 2021;41(2). [CrosRef]

[2] Choi SH, Sohn DK, Ko HS. Performance enhancement of latent heat thermal energy storage by bubble-driven flow. Appl Energy 2021;302. [CrosRef]
[3] Douvie E, et al. Phase change materials in solar domestic hot water systems: A review. May Int J Thermofluids 2021;10. [CrosRef]
[4] Christopher S, Kumaresan V, Raghavan KS. Role of thermal energy storage for enhancing thermal performance of evacuated tube with compound parabolic concentrator collector. Int J Energy Res 2021;45(5):7341-7351. [CrosRef]
[5] Anita AN, Ramachandran S. Design analysis of heat exchanger for the solar water heating systems using phase change materials. Mater Today 2021;4533-4537. [CrosRef]
[6] Singh S, Anand A, Shukla A, Sharma A. Environmental, technical and financial feasibility study of domestic solar water heating system in India. Sustain Energy Technol Assess 2021;43. [CrosRef]
[7] Abdelkader TK, Fan Q, Gaballah ES, Wang S, Zhang Y. Energy and exergy analysis of a flat-plate solar air heater artificially roughened and coated with a novel solar selective coating. Energies 2020;13(4). [CrosRef]
[8] Ahmed N, Elfeky KE, Lu L, Wang QW. Thermal performance analysis of thermocline combined sensible-latent heat storage system using cascaded-layered PCM designs for medium temperature applications. Renew Energy 2020;152:684-697. [CrosRef]
[9] Akhter J, Gilani SI, Al-Kayiem HH, Al-Hassan I. Investigation of gap losses in a modified compound parabolic concentrating collector with evacuated tube receiver. Mater Sci Eng 2020. [CrosRef]
[10] Alptekin E Ezan MA. Performance investigations on a sensible heat thermal energy storage tank with a solar collector under variable climatic conditions. Appl Therm Eng 2020;164. [CrosRef]
[11] [Sharma SD, Buddhi D, Sawhney RL, Sharma A. Design, development and performance evaluation of a latent heat storage unit for evening cooking in a solar cooker. Energy Convers Manage 2000;41(14):1497-1508. [CrosRef]
[12] Patil RJ, Awari GK, Singh MP. Experimental analysis of scheffler reflector water heater. Therm Sci 2011;15(3):599-604. [CrosRef]
[13] Yadav V, Kumar Y, Agrawal H, Yadav A. Thermal performance evaluation of solar cooker with latent and sensible heat storage unit for evening cooking. Aust J Mech Eng 2017;15(2):93-102. [CrosRef]
[14] Komolafe CA, Okonkwo CE. Design, fabrication and thermal evaluation of a solar cooking system integrated with tracking device and sensible heat storage materials. Front Energy Res 2022;10. [CrosRef]
[15] Sheng N, Dong K, Zhu C, Akiyama T, Nomura T. Thermal conductivity enhancement of erythritol phase change material with percolated aluminum filler. Mater Chem Phys 2019;229:87-91. [CrosRef]
[16] Senthil R. Enhancement of productivity of parabolic dish solar cooker using integrated phase change material. Mater Today 2021;386-388. [CrosRef]
[17] Onokwai AO, Okonkwo UC, Osueke CO, Okafor CE, Olayanju TMA, Dahunsi SO. Design, modelling, energy and exergy analysis of a parabolic cooker. Renew Energy 2019;142:497-510. [CrosRef]
[18] Bhargav M, Patel S, Nair A. Comparative analysis of solar collectors for high-temperature applications. Solar Energy Science 2021;15(4):56-67.
[19] Kumar A, Singh R. Sensible heat storage in solar cookers: A review. Int J Sol Energy 2020;12(2):89-101.
[20] Sharma V, Gupta A, Mehta K. Application of paraffin wax as phase-change material in solar cookers. Appl Therm Eng 2022;27(5):221-229.
[21] Ahmed S, Kumar R, Yadav P. Performance analysis of eutectic salts in solar cooking applications. J Renew Energy Res 2021;29(3):123-134.
[22] Li T, Zhou X. Advances in thermochemical energy storage for solar energy systems. Energy Reviews 2019;45(1):33-45.
[23] Zhang H, Lin F, Wang Y. Material properties and environmental effects on TES performance. J Sol Energy App 2023;18(1):100-112.

J Ther Eng, Vol. 12, No. 1, pp. 303−322, January, 2026

Journal of Thermal Engineering
Web page info: https://jten.yildiz.edu.tr
DOI: 10.14744/thermal.0001079

Research Article

Analysis of a 5.0 kWp solar rooftop system: Techno-economic, design, and simulation using pvsyst

Anand KUSHWAH[1,*], Supriya RAJ[1], Nikhil PATEL[2], Ashish GAURAV[3], Om Prakash SAHANI[1], Kapil GUPTA[4]

[1]*School of Mechanical Engineering, Noida Institute of Engineering Technology, Greater Noida, 20318, India*
[2]*Department of Science, Government Polytechnic Gulzarbagh, Technology and Technical Education, Bihar, 800007, India*
[3]*Department of Science, State Board of Technical Education, Technology and Technical Education, Bihar, Bihar, 800007, India*
[4]*Department of Mechanical Engineering, Sershah Engineering College, Sasaram Rohtas, 802215, India*

ARTICLE INFO

Article history
Received: 06 March 2025
Revised: 18 June 2025
Accepted: 26 June 2025

Keywords:
Payback; PV Module; PVsyst; Return on Investment; Solar Energy

ABSTRACT

The paper focuses on performance of a 5.0 kWp PV solar system, a second-generation PV technology. The experimental PV solar system was installed on the rooftop of G.P. Convent School, located in Sankat Mochan Nagar Morar, Gwalior, M.P, India (78.21°E, 26.22°N). The observed data indicates that daily average energy yields for experimental solar system were 5 kWh/kWp (array yield), 6.25 kWh/kWp (reference yield), and 4.91 kWh/kWp (final yield). While PVsyst simulation estimates the slightly higher values of 5.46, 6.39, and 5.32 kWh/kWp, respectively. The total yearly power generated was 6910.2 kWh for the experimental PV solar system and 7485 kWh according to PVsyst software. The payback period for the PV solar rooftop system ranges from between 4.57 years and 11.41 years, depending on the initial cost. The ROI ranges from 119% to 447.5%, with the system providing substantial long-term savings. Based on these outcomes, PV solar system will perform well under the meteorological conditions.

Cite this article as: Kushwah A, Raj S, Patel N, Gaurav A, Sahani OP, Gupta K. Analysis of a 5.0 kWp solar rooftop system: Techno-economic, design, and simulation using pvsyst. J Ther Eng 2026;12(1):303−322.

INTRODUCTION

The global demand for energy to generate power continues to grow, with different resources contributing to the energy mix. According to the U.S. Energy Information Administration's 2020 report, fossil fuels accounted for 75% of energy consumption. The ratio has not changed much over the last ten years, but experts say the world's energy needs could grow by around 50% by 2050. Over the past 30 years, renewable energy sources have played a vital role in power generation, offering reduced emissions compared to fossil fuels. Moving forward, renewable energy is expected to contribute a larger share of the global energy consumption. This research aims to explore optimal solutions for

***Corresponding author.**
*E-mail address: anand.kushwahwah1989@gmail.com

This paper was recommended for publication in revised form by Editor-in-Chief Ahmet Selim Dalkilic

Published by Yıldız Technical University Press, İstanbul, Turkey
Yıldız Technical University. This is an open access article under the CC BY-NC license (http://creativecommons.org/licenses/by-nc/4.0/).

utilizing these alternative, more environmentally friendly energy sources to mitigate emissions associated with fossil fuels and other conventional power generation methods. Renewable energy, often referred to as alternative, sustainable, or non-conventional energy, is derived from natural, replenishable sources such as wind, solar, hydroelectric, geothermal, bioenergy, and ocean energy [1]. The growing global demand for energy and the depletion of fossil fuel reserves have driven increased adoption of renewable energy. Renewable energy presents a viable, eco-friendly solution in remote as well as rural areas, where electricity availability is limited and the installation of traditional transmission lines is often cost-prohibitive [2-,5]. Furthermore, the renewable energy sources are inherently clean and environmentally beneficial. However, several challenges persist, limiting the widespread use of renewable energy [6]. The prime challenge is the variability of energy generation, which is greatly dependent on climate conditions that vary by region. Energy availability is not constant, with intermittent periods of zero generation, such as at night for solar energy or during cloudy days. Traditionally employed for residential and commercial electricity generation, there has been increasing interest in using PV panels to power air conditioning systems [7]. This innovation addresses the growing need for cooling in many societies and provides an environmentally friendly alternative to conventional fossil fuel-powered air conditioning. By harnessing solar energy, PV panels can operate air conditioners without reliance on the public electrical grid. The installation of solar panels on rooftops or other open, sunlit areas allows the conversion of sunlight into electricity, which is then used to power air conditioning units [8]. Furthermore, the integration of sun-tracking systems can optimize energy absorption by ensuring the panels are always oriented towards the sun. The use of PV panels to power air conditioners offers numerous advantages, including a reduced dependence on the electrical grid, lower energy consumption, and significant savings on electricity bills [9,10].

The integration of renewable energy into existing electrical grids has made great progress, especially with solar energy conversion both electrical and thermal becoming more common. Solar energy is abundant and accessible to nearly everyone, making it a valuable resource. Over the years, significant efforts have focused on maximizing its use. To achieve the best results, it's important to analyze solar energy from thermodynamic, environmental, economic, and policy angles. This helps develop optimized systems that balance energy output, cost-effectiveness, and environmental sustainability using current technologies.

Solar photovoltaic (PV) systems have become a popular choice for clean energy in both homes and industries, thanks to their many benefits they're easy to install on rooftops, require little maintenance, have no fuel costs, and don't pollute. But unlike traditional energy sources, PV systems face challenges like lower efficiency and power output that can change with weather conditions, temperature, sunlight levels, and panel angle. There is plenty of room to improve how much energy from solar panels using available solar panels infrastructure and techniques including Maximum Power Point Tracking (MPPT), reconfiguring panel arrays, controlling cell temperature, cleaning dust off panels, optimizing their orientation and tilt, using advanced multilevel converters, and enhancing performance with mirrors (MAPV) systems [11]. While these methods can significantly boost energy output, making them practical means keeping costs down and efficiency and longevity up. For instance, a study by Li [12] in Hong Kong found that the energy payback period for an on-grid PV system was 8.9 years.

Sharma et al. [13] conducted an analysis of a PV solar system under various load scenarios in a building to optimize factors such as performance ratio (PR), maximum power, efficiency, as well as specific production, leading to improved efficiency of the system. The system was tested with laboratory loads, using a fixed tilt angle and adjustable azimuth angle. The outcomes showed that when the azimuth angle was set to zero, the system achieved maximum specific production, with a 1.7% increase in efficiency. Yadav et al. [14] examine the performance of a 1 kWp PV system in Hamirpur, Himachal Pradesh, India, using measured solar radiation data. Simulated through PVsyst software, the system's energy generation and associated losses were analysed. The performance ratio for the year is estimated at 0.724, signifying that PV systems are a viable option to support the region's increasing energy needs. Kasim et al. [6] studied the performance of a 5 kWp CIGS grid-connected PV system was assessed in Baghdad, Iraq. The system was compared with PVsyst simulations to evaluate its efficiency under the local climate. The real system's annual energy yield was 1781.8 kWh/kWp, while PVsyst predicted 1924 kWh/kWp. System losses, efficiencies, and performance ratios were analyzed, showing that the real system's average performance was close to the simulated results. With minimal differences in energy yield and efficiencies, the study concluded that the CIGS PV system performs well in Baghdad's climate, offering reliable energy generation. Hammed et al. [15] proposed PV system at the National University of Sciences and Technology (NUST) in Islamabad, Pakistan, a region with abundant solar resources to combat climate change. The system is expected to save 75,478.60 tons of CO2 over 18 years, equivalent to planting 348,754 teak trees. With a low energy generation cost of $0.0141/kWh, the system will generate 11,270,771 kWh/year, with a performance ratio of 76.2% and a capacity utilization factor of 16%. The plant will break even in 12 years, offering valuable insights for future renewable energy projects. Srivastava et al. [16] evaluated the performance of a grid-connected silicon-polycrystalline photovoltaic (PV) system, and designed with a peak power capacity of 20.0 kW and a voltage of 17 V. To carry out the performance analysis, the software PVsyst (version 7.1.7) was used, a widely recognized tool used for simulating energy generation and

optimizing the design of PV systems. In this study, PVsyst was used to design a grid-connected PV system tailored for the Karunya Institute of Technology, providing valuable insights into the system's efficiency and potential performance. Nababan et al. [17] carried out a comprehensive techno-economic analysis of a solar rooftop system, focusing on the city of Medan, Indonesia. The analysis is based on solar intensity data specific to Medan, with measurements taken over several days. By employing this measured data, along with available solar PV panels from the Indonesian market, a technical evaluation of the system's performance was conducted. The economic analysis results indicate that the annual electricity production from the PV system in Medan is valued at IDR 3,672,895. With an investment cost of IDR 33,271,986 for the installation of 2.0 kW PV solar rooftop system and considering the total yearly electricity value of IDR 3,672,895, it was determined that the initial capital investment for the 2.0 kW system would be recovered in approximately 10 years. Kumar et al. [18] studied the load requirements of the Mechanical Engineering Department (MED) office at an engineering college in Bikaner, and consequently focuses on design and installation of a standalone solar PV system to full fill these requirements. This work also includes an analysis of performance ratio (PR) and losses, which was concluded by using PVsyst simulation software. The average annual energy requirement for the MED office is 1,086.24 kWh; however, the energy generated by the solar panels is 1,143.6 kWh. Though the energy supplied to the office is 1,068.12 kWh, which is slightly less than the required load. The performance ratio analysis indicates that the highest PR was recorded in December, at 86%, while the lowest PR, 64%, was observed in April. The average performance ratio for the entire year is 72.8%.Salmi et al. [19] evaluated the feasibility of a PV solar rooftop system with battery storage in a residential area of M'sila, Algeria. Using PVsyst6 software, it was observed that the average daily electricity consumption was noted as 12.6 kWh, with an annual grid contribution of 4,615 kWh. The system's performance ratio was recoded as 62.9%, with the highest energy production occurring from June to August, peaking at 354.4 kWh in July. Energy losses, mainly due to the temperature of the PV field, were 12.14%. Sonam and Agyekum [20] studied the assessment of rooftop solar PV potential in Thimphu, Bhutan, amid rising energy demand and hydropower shortfalls. A 12 kWp system simulated via PVsyst showed strong performance. Scenario analysis revealed significant energy and cost savings, highlighting rooftop solar as a viable, sustainable solution for Bhutan's energy diversification and environmental goals. Zue et al. [21] discovered the technical potential and economic benefits of rooftop photovoltaic (PV) systems across three different university campuses in China, considering available rooftop areas and local solar intensity. Seven scenarios were analyzed for Tibet University, Qinghai University, and Qilu University of Technology, located in different solar zones. The potential PV installation capacities for the campuses are 11,291, 9,102, and 3,821 kW, respectively. These correspond to maximum annual power production of 28.19, 18.03, and 5.36 GWh for each university, respectively. Aktas and Ozenc [22] focused on the design, evaluation, and analysis of a grid-connected solar photovoltaic (SPV) system to meet the energy requirements of the College of Science and Technology in Siirt Province, Turkey. It offerings detailed financial and technical data, along with thorough economic and environmental assessments. The system's design and evaluation were supported by using PVsyst, PV*SOL, as well as HOMER Pro software. The analysis outcomes indicate that the photovoltaic system will produce approximately 762 MWh of energy annually. The economic evaluation reveals an internal rate of return (IRR) of 19.55%, a net present value (NPV) of 346,085 USD, and a Levelized Cost of Energy (LCOE) of 0.1892 USD/kWh. The payback period for the present system is projected to be 17.4 years. Furthermore, the implementation of the photovoltaic plant will contribute to a reduction of around 6,852 tonnes of CO_2 emissions. Mohammad and Zabihi [23] designed a solar power plant using PVsyst requires careful planning, especially when working with bifacial panels. A recent study based on a real 100-kW rooftop project in Arak, Iran, highlights the importance of correctly setting the bifacial factor to avoid errors in energy yield predictions. It explores key design challenges like optimizing panel angles, spacing, and height to capture rear-side radiation while minimizing shading. Tools like PVsyst, AutoCAD, ETAP, and RET Screen were used to simulate and analyse both technical and economic aspects. The study shows how local conditions and environmental factors must be considered for more accurate and efficient PV system design. Tajjour et al.[24] evaluate a 100 kWp rooftop solar micro grid in the Western Indian Himalayas, aiming to enhance energy generation by optimizing the panel tilt angle. Using isotropic, NASA, PVsyst, and PVGIS models, the study finds a 6.5% improvement in output, emphasizing the importance of site-specific tilt angle optimization.

This work discovers how well a 5.0 kWp rooftop solar system performs in real-world conditions in Gwalior, Madhya Pradesh. Installed at G.P. Convent School, the system's actual energy output in 2024 was compared with PVsyst simulation results to see how closely reality matches predictions. It not only looks at technical aspects like energy yields but also evaluates cost-effectiveness through payback period and ROI. The novelty lies in combining real performance data with simulation for a second-generation PV system, helping us better understand how these systems work in local Indian climates and how viable they are for everyday energy use.

The objective of this study is to evaluate the performance of a 5.0 kWp second-generation PV solar rooftop system installed at G.P. Convent School in Gwalior, India. Specifically, the study aims to:

- Analyse the real-time operational data of the solar system under actual climatic conditions of Madhya Pradesh.
- Compare the system's real-world energy yields and performance ratios with those predicted by PVsyst simulation software.
- Assess solar irradiance and quantify the technical performance indicators such as array yield, reference yield, and final yield.
- Examine the economic viability of the PV system through indicators such as payback period and return on investment (ROI).

This study contributes by evaluating a 5.0 kWp rooftop PV system's real-world performance in Gwalior, India, and comparing it with PVsyst simulations. It offers technical and economic insights, confirms solar viability in semi-arid climates, and supports informed decision-making for sustainable energy planning and rooftop solar adoption in similar regions.

MATERIALS AND METHODS

Numerical Modeling of PV Solar Rooftop

PVsyst 8.0.6 is an advanced simulation tool designed for the simulation and modeling of PV solar systems [25]. It offers a comprehensive solution for designing grid-connected, pumping, standalone, and DC grid PV systems. The software is user-friendly, requiring only a few known variables, and provides detailed insights into the sizing of systems, no. of inverters, number of PV arrays, and the overall system performance analysis. 3PP is an all-in-one tool designed to analyse various aspects of photovoltaic (PV) systems, whether they are connected to the grid, autonomous, or used for water pumping. The software is capable of importing weather data from multiple sources, as demonstrated in Figure 1. PVsyst6 provides a range of valuable information, such as energy output, solar radiation, installation investment costs, required surface area, and annual energy generation. It allows for rapid estimations of energy generation for initial feasibility studies, as well as detailed project design, analysis, and dimensioning. The software also supports time simulations and generates comprehensive reports. Additionally, it includes features like importing meteorological data, synthetic generation, and a component database for PV modules, inverters, batteries, pumps, and more. PVsyst6 also offers educational tools and optimization features, such as solar geometry, orientation adjustments, and analysis of the electrical performance of PV fields with shading effects. Figure 2 represents an overview of project setup. The project title is entered at the top, and in "site file" box, you can select the relevant site file, with an existing map for reference. The city and country info can be entered in the respective fields. The meteorological data file can be selected using NREL's resources. On the main parameters page, you can configure key system settings, such as the orientation and specifications of the system.

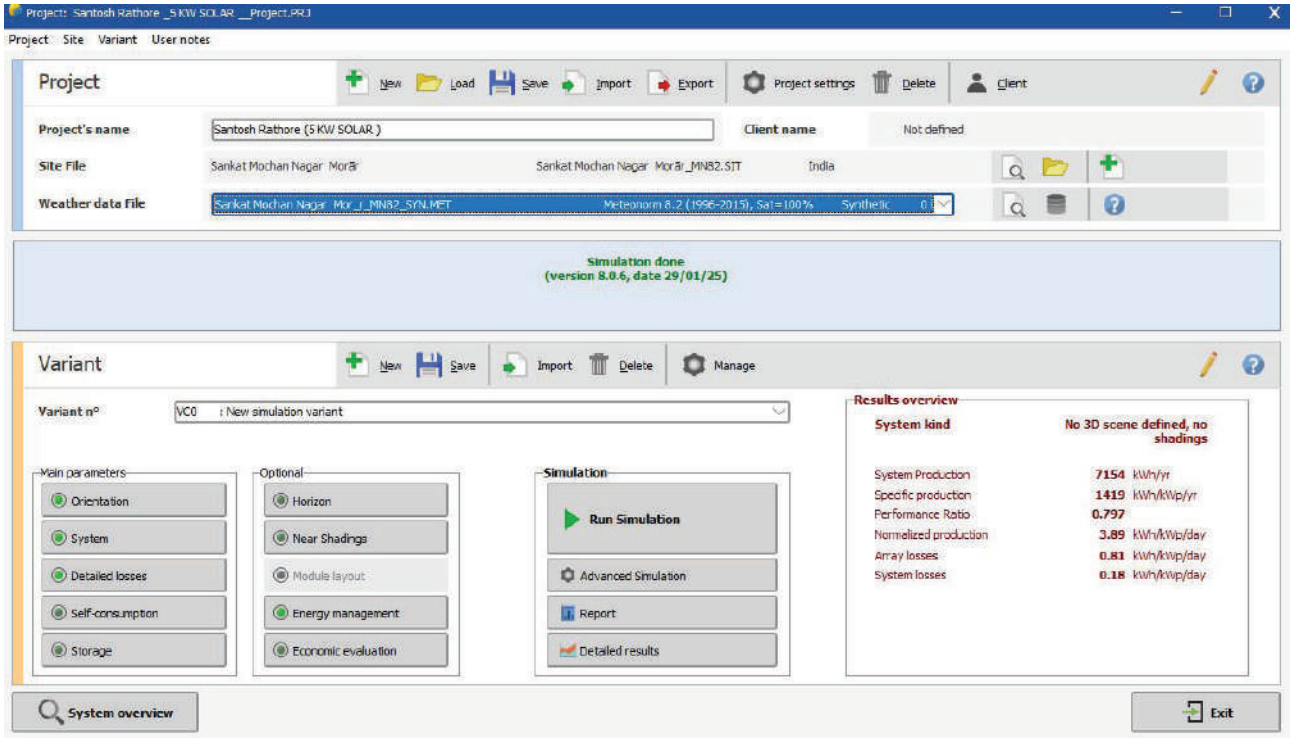

Figure 1. Dissemination of interface of PVsyst software in Gwalior region.

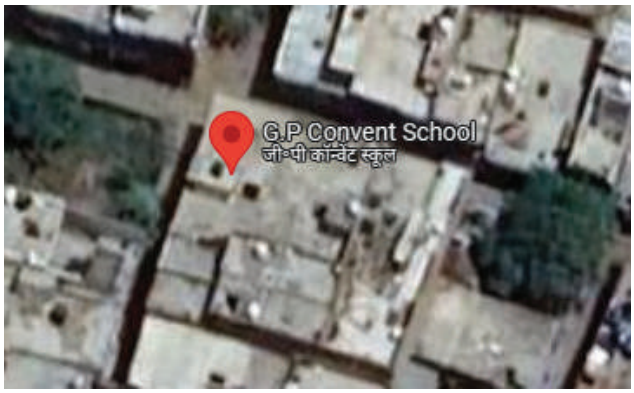

Figure 2. GP Convent School Geographical Location.

Selection of Location (Geographical Coordinates)

For this simulation, G.P. Convent School, located in Sankat Mochan Nagar Morar, Gwalior, M.P, India (78.21°E, 26.22°N), was selected as the site for analysis (Fig. 2).

The system was designed to meet a 5.00 kWp load. Input data needed for simulation include the geographical coordinates of the site. After inputting the values for longitude and latitude, solar irradiance is calculated, which is crucial for the design of the solar PV system. The performance analysis of the grid-connected PV system was conducted for various panel tilt angles. The specific tilt angles were considered as a 22° inclination (Fig. 3) for the annual irradiation yield of the 5.00 kWp unit, and also to assess the system's performance based on the plant's latitude.

The system design incorporated the SUN2000-4.95TL-JPL1 inverter and the Vision 60M construct, 315 Wp PV array, select to meet 5.00 kWp load. The complete description of PV modules is presented in Table 1. The subsequent design factors were considered for simulation and modeling of the solar photovoltaic system. The PV array characteristic is demonstrated in Figure 4.

- **PV Array Specifications:** The system design for G.P. Convent School utilizes Vision 60M construct, 315Wp, with each polycrystalline solar module having a rated peak power output of 300 W.
- **Inverter Specifications:** The system's 5.00 kWp design uses the SUN2000-4.95TL-JPL1 inverter, with a capacity of 4.95 kWp per unit, manufactured by Sun Power Solutions.

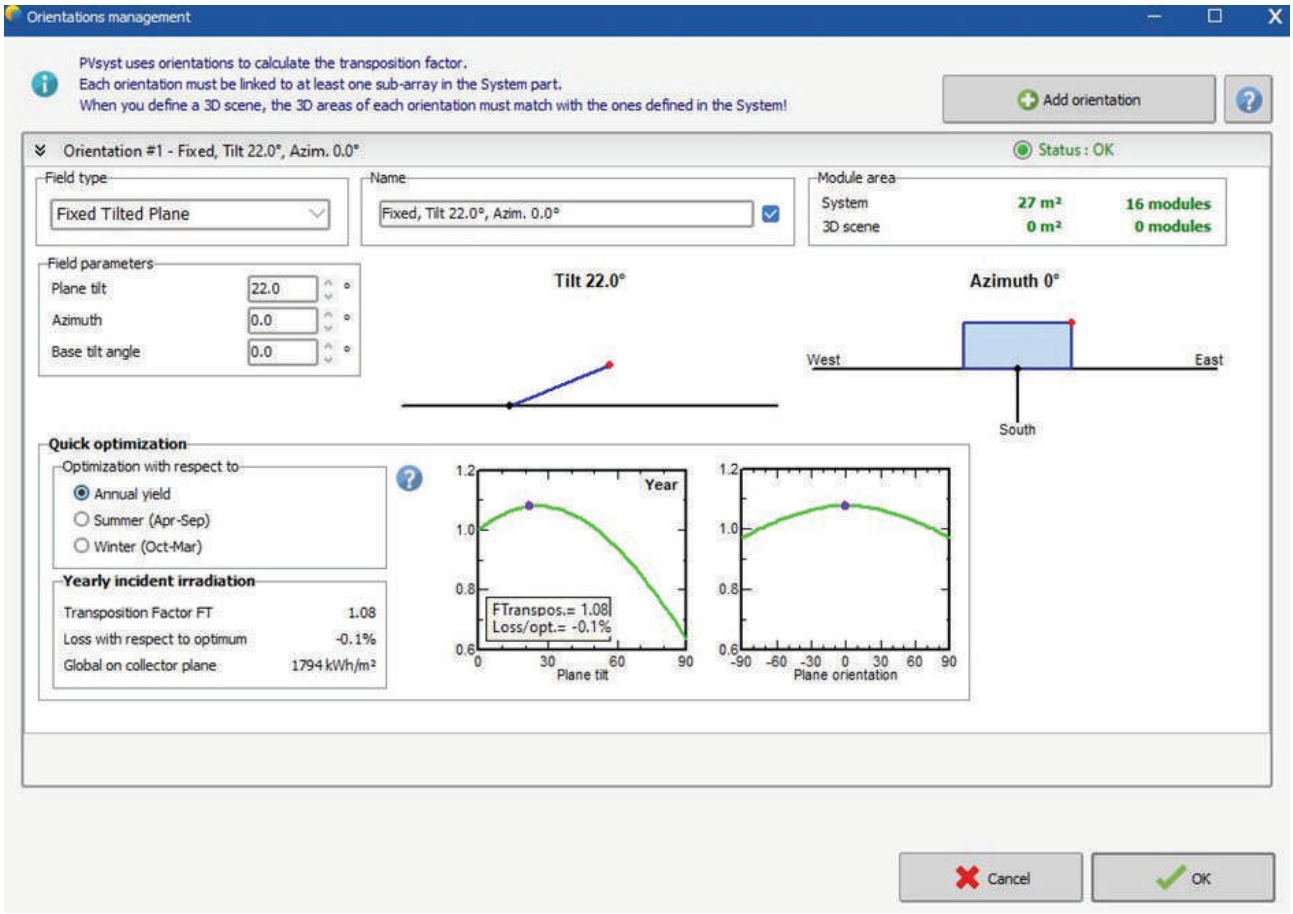

Figure 3. Representation of orientation of PV modules.

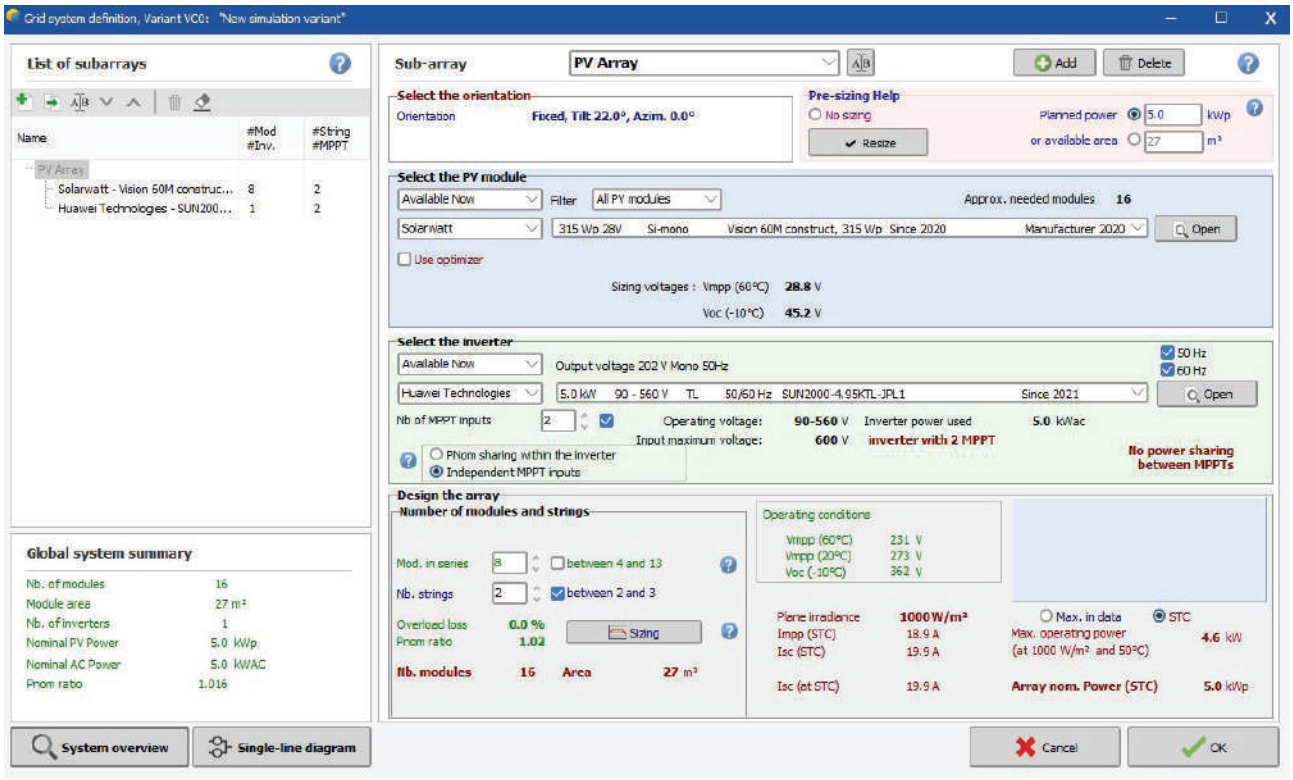

Figure 4. Representation of PV array characteristic.

Solar Radiation: The average solar radiation at geographic coordinates 26.21°N and 76.23°E is approximately 5.477 kWh/m²/day, which is deemed adequate for efficient electricity generation. The solar radiation represents amount of solar energy incident/unit area, typically expressed in W/m². This value exhibits seasonal variation, reaching its peak during the summer months and its minimum during the winter. The simulation process for determining solar irradiance in PVsyst and single line diagram of a 5.00kWp grid-connected is illustrated in Figures 5 and 6, respectively.

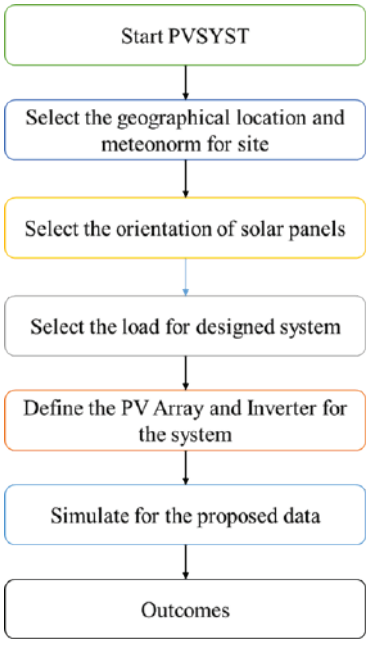

Figure 5. Flowchart of simulation in PVsyst.

Assessment of Solar Potential in Terms of Solar Path

The evaluation of solar potential takes into account the system-dependent occurrence angle modifier, which fluctuates based on the tilt angle of installation. The incidence angle modifier changes with the tilt angle at a specific site location, and this variation is called as the sun path or location diagram. In PVsyst, defining shading requires a horizon line, as this helps define how the sun's path interacts with environment. The solar path ascends from December to June and descends from July to Dec. The 21st of June marks the longest day of the year, whereas the 21st of Dec has the shortest day. The months of Mar and Sept feature equal day and night lengths. Figure 7 shows the sun path for the selected location.

Data Analysis

Performance analysis factors for evaluating the grid-connected solar PV system included the assessment of: Losses in the System and Array, yields (Final, Reference and Array), System Efficiencies (Inverter, Array and

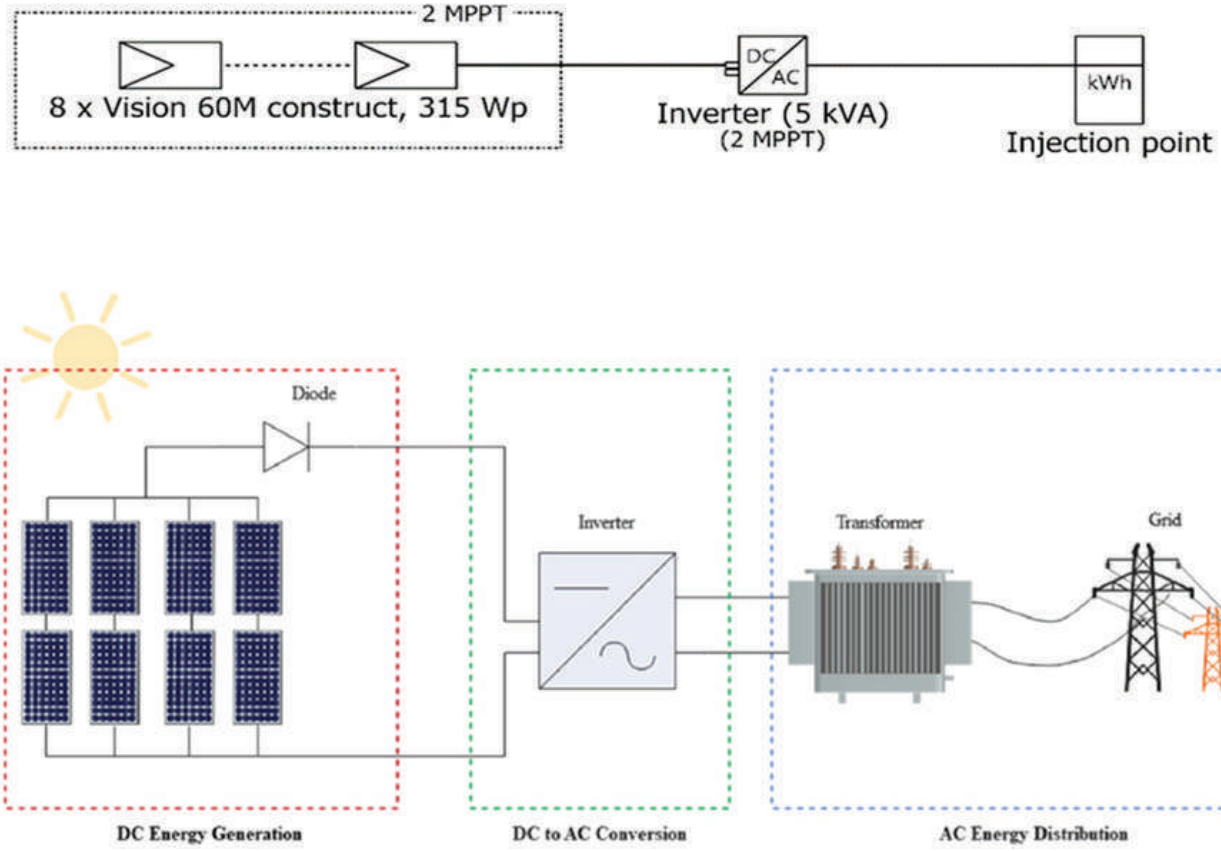

Figure 6. Schematic layout of 5kWp PV rooftop system at G.P. Convent School, India.

Table 1. G.P. Convent Solar PV system specifications

Description of the System	Experimental System	Simulation system
PV Panel Model	Vision 60M construct, 315Wp	Vision 60M construct, 315Wp
No. of PV panels	16 units	16 units
Model of Inverter	SUN2000-4.95TL-JPL1	SUN2000-4.95TL-JPL1
Size of Inverter (kWp)	4.95	4.95
Efficiency of Inverter	97%	97%
Capacity of System	5.00kWp	5.00kWp
Tilt angel	22°	22°
Modules	2 string x 8 units kWp In series	2 string x 8 units kWp In series
At operating condition	50°C	50°C
Module Area	26.6m^2	26.6m^2

System), Capacity Factor (CF), Performance Ratio (PR), Total Energy produced and Economic Analysis.

Analysis of system yields

The system's energy yields are classified into 03 types: Final Yield, Reference Yield, and Array Yield. The Array Yield (Y_a) is defined as, direct current (DC) energy generated by the photovoltaic solar array, divided by the nominal (rated) power of photovoltaic solar system. It characterizes the duration for which system operates at its rated power, expressed in kWh/kWp, as discussed below:

Array yield (Y_a)

It may also be determined by considering the ratio of produced direct energy to the nominal (rated) power of

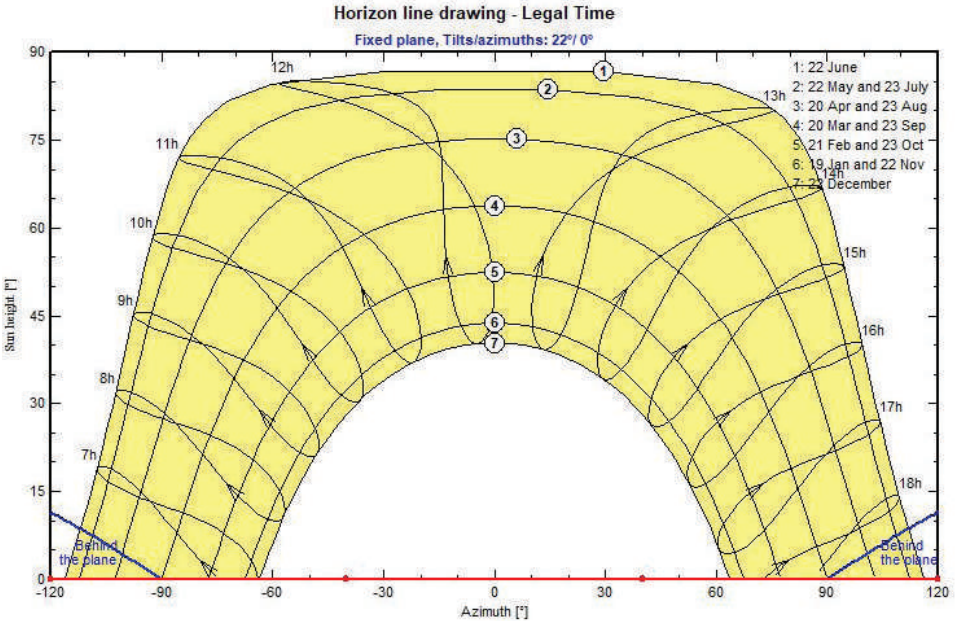

Figure 7: Representation of solar path at coordinates 78.21°E, 26.22°N**.**

the photovoltaic solar system. The daily array yield ($Y_{a,d}$) is determined using the following Eq.[26]

$$Y_{a,d} = \mathrm{E_{DC,d}}/P_{pv,rated} \quad (1)$$

The mean value of the monthly array yield ($Y_{a,m}$) is calculated using the following Eq.

$$Y_{a,m} = (1/N) * \sum_{d=1}^{N} Y_{a,d} \quad (2)$$

The Array yield (Y_a) indicates the period the PV system obtains to operate at nominal power generation in units of h/day.

Final yield (Y_f)

Final Yield (Y_f) refers to the alternating current (AC) energy produced by the PV solar system over a specific time, divided by the nominal (rated) power of system. It denotes the duration for which the system operates at its rated power, expressed in the term of kWh/kWp. It may be also defined as the ratio of the final generated power to the rated photovoltaic power specified by the manufacturer under standard test conditions. This metric shows the time required for the photovoltaic system to generate its final energy output relative to its nominal power capacity [26].

The daily final yield ($Y_{a,f}$) is determined using the following Eq.

$$Y_{f,d} = \mathrm{E_{AC,d}}/P_{pv,rated} \quad (3)$$

The average value of monthly array yield ($Y_{f,m}$) is calculated using following Eq.

$$Y_{f,m} = (1/N) * \sum_{d=1}^{N} Y_{f,d} \quad (4)$$

Reference yield (Y_r)

It may be defined as, the total in-plane solar irradiance ratio to the reference insolation under standard operating temperature conditions of 1 kW/m^2. It can be computed as follows Eq.

$$Y_{r,d} = T_r * \sum G_{i_{day}}/G_{STC} \quad (5)$$

Moreover, the improved reference yield (Y_r) is computed by considering the module's modification impact and atmospheric temperature, as written in Eq.

$$Y_{impr} = Y_r * [1 - C_t(T_m - T_{STC})] \quad (6)$$

Energy Output

The energy fed to the utility grid (E_{AC})

The whole-day analysis of alternative current (AC) energy production is calculated using the following Eq.

$$\mathrm{E_{AC,d}} = \sum_{t=1}^{t=\mathrm{T_{rp}}} \mathrm{V_{AC}} * \mathrm{I_{AC}} * \mathrm{T_r} \quad (7)$$

Alternative current (AC) output produced in a month is determined as using Eq.

$$E_{AC,m} = \sum_{d=1}^{N} E_{AC,d} \quad (8)$$

Energy generated through Photovoltaic systems (E_{DC})

The entire energy output is defined as the quantity of alternative current (AC) power produced by the Photovoltaic solar system over a given period.

The overall monitored everyday direct current power is evaluated using Eq.

$$E_{DC,d} = \sum_{t=1}^{t=T_{rp}} V_{DC} * I_{DC} * T_r \quad (9)$$

The monthly produced direct current energy is determined using the following Eq.

$$E_{DC,m} = \sum_{d=1}^{N} E_{DC,d} \quad (10)$$

where, N, m, and d indicate the no. of working days of a plant and monthly, and daily value respectively.

Efficiencies of The System

Efficiency of a photovoltaic system is categorized into 03 different types: array efficiency, system efficiency, as well as inverter efficiency. All these three efficiencies can be determined on a yearly, monthly, daily, as well as hourly basis, respectively. System efficiency (η_{sys}) is computed using alternating current (AC) power output, therefore array efficiency (η_{PV}) is evaluated by direct current (DC) power output. The array efficiency is defined as ratio of daily, monthly, or annual average direct current (AC) energy output of array to total solar insolation received on the inclined plane, multiplied by area of a photovoltaic solar array. photovoltaic solar array efficiency is determined as:

Photovoltaic module efficiency (η_{PV})

Efficiency of a Photovoltaic module reports, how much amount of energy a PV module produces compared to available irradiance. It can be determined using the following Eq.

$$\eta_{PV} = \left[{}^{P_{DC}}/_{G_i * A_m} \right] * 100\% \quad (11)$$

The PV module efficiency on a monthly basis is calculated using the following Eq.

$$\eta_{PV} = \left[{}^{E_{DC,m}}/_{G_i * A_m} \right] * 100\% \quad (12)$$

Inverter efficiency (η_{inv})

It is defined as the ratio of alternative current energy generated by an inverter to the direct current energy produced by a PV solar system array. During the determination of inverter efficiency, it should be noted that, both the η_{PV} and η_{sys} are the higher, therefore it is the conversion efficiency of Direct current to Alternative current. The instantaneous inverter efficiency (η_{inv}) can be evaluated as:

$$\eta_{inv,m} = \left[\frac{E_{AC,m}}{E_{DC,m}} \right] * 100\% \quad (13)$$

System efficiency (η_{sys})

It can be determined as the multiplication of photovoltaic module efficiency (η_{PV}) and inverter efficiency (η_{inv}). The System efficiency (η_{sys}) can be computed using the following Eq.

$$\eta_{sys} = \eta_{PV} * \eta_{inv} \quad (14)$$

Capacity Factor

The capacity factor (CF) is a measure of how efficiently a photovoltaic (PV) solar system produces energy over time. It is determined by taking total alternating current (AC) power generated by the system and dividing it by the product of system›s rated (nominal) energy and the specified time period, usually a month or a year. Capacity Factor (CF) can be defined as the ratio of actual yearly generation of energy to the power produced by a photovoltaic (PV) solar system of rated capacity for 24 hours/day throughout the 01 year. The annual CF of the photovoltaic solar system is evaluated using the following Eq. 15:

$$CF = {}^{Y_{f,annual}}/_{24 * 365} = {}^{E_{AC,annual}}/_{P_{pv,rated} * 8760} \quad (15)$$

Eq.15 can be also written as:

$$CF = \frac{\frac{h}{day} * peak\ sun}{24\ hrs/day} \quad (16)$$

The CF varies in a similar pattern to the final yield. It indicates that how much energy a power system actually delivers compared to its maximum possible output. If the system operated at its full rated power all times, the CF would be 01.

Performance Ratio

The Performance Ratio (PR) reveals all the losses in a photovoltaic solar system. It denotes how efficiently the system operates in real operating conditions in comparison to its ideal performance. A higher PR value means the system is performing closer to its maximum potential. PR allows for a fair comparison between different photovoltaic systems, regardless of factors like angle, tilt, orientation, location, or rated power capacity [27].

It is evaluated as the ratio of the final yield (Y_f) to the array, yield (Y_a) of the PV system, written as [26]

$$PR = \frac{Y_f}{Y_a} \quad (17)$$

As discussed in Eq. 18, it can be considered as function of temperature efficiency ($\eta_{temperatue}$), degradation efficiency ($\eta_{degradation}$), inverter efficiency ($\eta_{inverter}$), and soil efficiency (η_{soil}):

$$PR = \eta_{degradation} * \eta_{tempearture} * \eta_{soil} * \eta_{inverter} \quad (18)$$

System and Array Energy Losses

The array losses (L_a) indicate the energy losses that occur throughout the operation of photovoltaic array, highlighting its inability to fully convert available solar radiation into the electricity. These losses are calculated by difference b/w the reference yield (Y_r) and array yield (Y_a). The array losses (L_a) are determined using Eq.19.

$$L_a = Y_r - Y_a \quad (19)$$

System energy losses (L_s) occur during the conversion of direct current power to alternating current by the inverter. These losses result from the inefficiencies in the inverter›s conversion process [25].

$$L_s = Y_y - Y_f \quad (20)$$

Economic Analysis

The cost of energy generated by grid-connected PV solar rooftop system is influenced by a variety of factors. Having precise information about these variables is crucial for accurately estimating the energy generation costs. Some of these key factors include:

- ❖ Weather conditions specific to the location (i.e., daily solar radiation, sunshine hours, and ambient air temperature).
- ❖ System components (i.e., PV panels, which are influenced by the module technology and efficiency, as well as cost of inverters, cables, and other electrical components).
- ❖ Economic factors specific to the region/location (i.e., interest and inflation rates, along with installation, operation, and maintenance costs).
- ❖ The local electricity costs.
- ❖ The economic lifespan of system.

Several economic indicators are commonly used to evaluate the economic performance of PV solar rooftop systems, such as life cycle cost (LCC), lifetime net income (NI), net present value (NPV), levelized cost of energy (LCOE), and return on investment (ROI) are discussed in Table 2.

Environmental analysis

The power grid supplies the electrical energy required for government buildings as well as academic campuses, with electricity produced from conventional, nuclear, hydroelectric, and renewable energy resources. Therefore, a substantial amount of CO_2 is released during the generation of power. By substituting grid electricity with solar PV-based electricity, the CO_2 emissions reductions from avoiding the use of grid power are evaluated using emission factors from the Central Electricity Authority of India (CEA, 2019) using following equation:

$$CO_2 \text{ emisson factor } = 0.9247 tCO_2/MWh \quad (21)$$

RESULTS AND DISCUSSION

This section deals with the comparison of performance analysis results of the experimental system with PVsyst software.

A grid-connected Photovoltaic solar system with a fixed tilt angle (22°) was selected for site. Based on location's solar radiation and site specifications, the optimal tilt angle was calculated to be 22°, with an azimuth angle of 0° as shown in Figure 6. A PV panel and inverter from a suitable manufacturer were chosen, with the number of panels optimized to meet the required load demand. The total power demand is as follows: Entire building: 5.00 kWp. PVsyst provided a comprehensive simulation report detailing the system's performance. According to the simulation findings (Fig. 8), the system generates 7153.6 kWh/year with a specific energy yield of 1419 kWh/kWp/year and a performance ratio of 79.70% when the PV modules are fixed for the building's energy needs.

Table 2. Parameters, Equations and Values used in Economic Analysis [28]

Parameters	Equations	Description for the value
Life cycle cost (LCC)	$LCC = \sum_{i=1}^{25} \frac{\{(C_{componet,i} + C_{O\ \&\ M,i}) \times Capacity\}}{1.05^i}$	$C_{omponent,i}$ = Component investment $C_{O\ \&\ M,i}$ = operation and maintenance cost
Revenue during its lifetime	$Rev_k = \sum_{i=1}^{25} \frac{E_{pi} \times P_k}{1.05^i}$	Rev_k= Lifetime income P_k = Cost of electricity
Net present value (NPV)	$NPV_i = \sum_{t=1}^{i} \frac{R_i}{1.05^i}$	
Lifetime net income (LNI)	$LNI = Rev_k - LCC$	
Return on investment (ROI)	$ROI = {}^{LNI}/_{LCC} \times 100$	
Levelized cost of energy (LCOE)	$\frac{LCC}{E_{p25}} = \frac{\sum_{i=1}^{25} \frac{\{(C_{componet,i} + C_{O\ \&\ M,i}) \times Capacity\}}{1.05^i}}{\sum_{i=1}^{25} E_{pi}\, K^{i-1}}$	

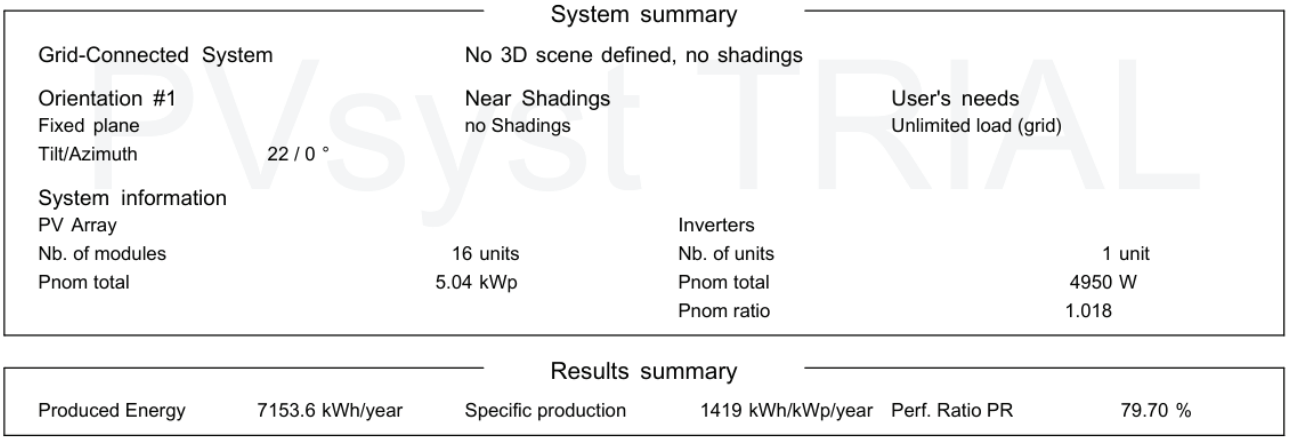

Figure 8. Comprehensive simulation report of PVsyst software.

Analysis of Electrical Energy Generation

Table 3 presents the monthly generation of electrical power as well as solar irradiance in the collimated plane.

Figure 9 represents the monthly generation of electrical power as well as solar irradiance in the collimated plane.

The lower value of generated electrical power was noted as 588 kWh, due to low solar insolation, clouds, and rain in December. Therefore, the higher value of electrical power generation (885 kWh) was achieved in month of June due to higher solar intensity, clear sky, as well as long day. The solar irradiances fluctuate from 4590.2 kWh to 7612 kWh in Dec and Jun, due to rainy as well as partially cloudy days and arid summer days, respectively. In twelve months, the generation of electrical power was 6910.20 kWh, therefore, a monthly average of 575.5 kWh. It was noted that the electrical energy produced during the 12 months over the nominal power of photovoltaic solar system was 1795.5 kWh/kWp. The temperature also fluctuated in the range of 17.2 to 45.2°C in the months of Jan and July respectively, therefore, the annual average of the highest temperature was noted as 31°C. It was observed that, despite the high temperatures in June, which reduced the efficiency of the photovoltaic solar system, the maximum electrical energy production was still noted in this month. This is mainly because June has the longest daylight hours (15 hrs) and the highest solar irradiance intensity. In another aspect, December sees lower energy production because of its shorter daylight hours (9 hrs) and lower solar radiation intensity. When comparing actual energy generation with simulated results,

Table 3. Monthly solar energy and performance ratio by PVsyst

Month	GlobHor kWh/m²	Diff Hor kWh/m²	T_Amb °C	Glob Inc kWh/m²	Glob Eff kWh/m²	E_Array kWh	E Grid kWh	PR Ratio
January	98.5	47.4	14.01	124.0	121.8	550.9	526.3	0.842
February	124.1	54.6	18.37	149.3	146.5	645.1	617.6	0.821
March	166.4	70.5	24.95	185.1	181.5	771.4	738.5	0.792
April	179.1	83.8	30.34	182.8	179.1	743.9	711.6	0.772
May	192.4	98.0	34.50	184.9	180.7	742.6	710.1	0.762
June	167.1	102.9	33.52	156.7	152.9	641.7	613.2	0.777
July	146.8	101.9	30.76	138.9	135.3	583.2	556.8	0.795
August	133.3	88.9	29.47	130.6	127.4	548.9	523.4	0.795
September	137.4	74.0	28.67	144.3	141.2	599.7	572.6	0.787
October	127.3	67.9	26.30	144.9	142.3	607.7	580.4	0.795
November	100.3	58.0	20.31	121.7	119.2	528.4	504.8	0.823
December	91.7	47.5	15.36	117.7	115.5	521.7	498.3	0.840
Year	1664.6	895.4	25.58	1780.8	1743.3	7485.0	7153.6	0.797

Key: Glob Inc =…, …

the experimental photovoltaic solar system generated an annual average of 6910.20 kWh at an average ambient temperature of 31°C. This was compared to results from PVsyst, a widely used software for PV system analysis and simulation, which estimated an annual average of 7485 kWh at a lower average air temperature of 25.5°C. The difference between experimental data and simulation results is relatively small, even though the experimental system operates under higher temperatures and is affected by external parameters such as rain, clouds, and dust. In contrast, PVsyst simulations are based on ideal conditions with lower temperatures and no environmental disturbances. This close match between experimental and simulated data indicates that the practical performance of the

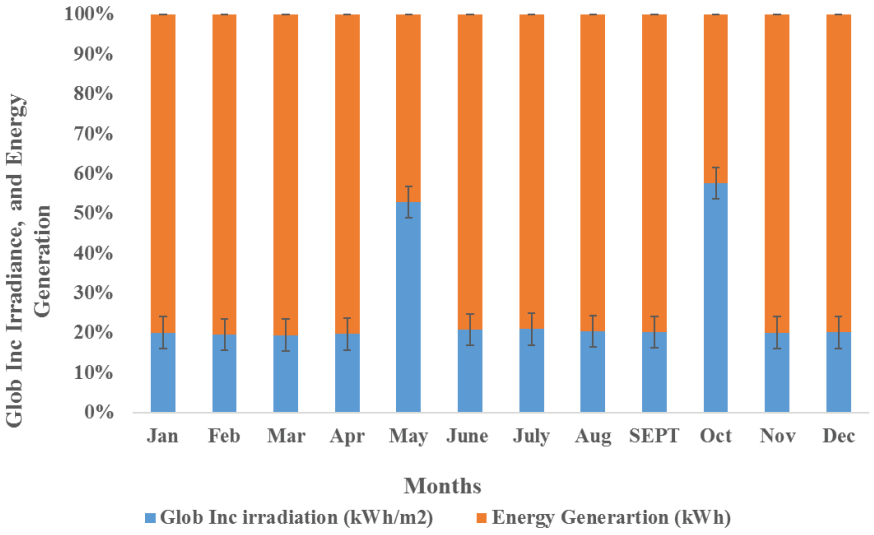

Figure 9. Representation of monthly energy generation and Glob Inc. irradiation.

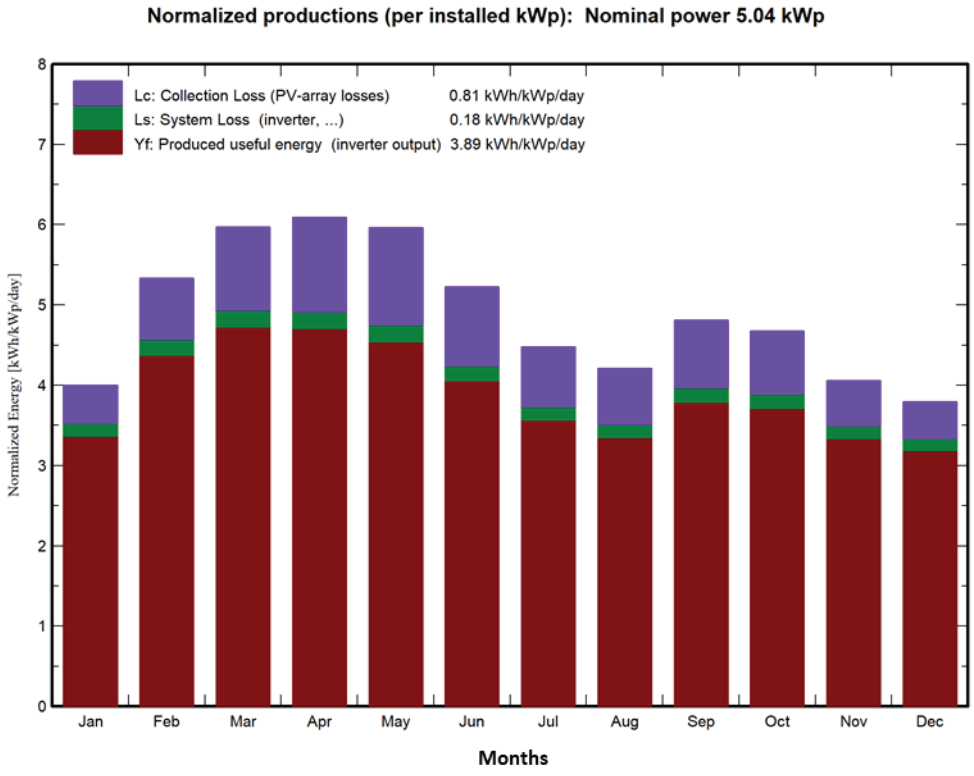

Figure 10. Representation of monthly normalized energy generation.

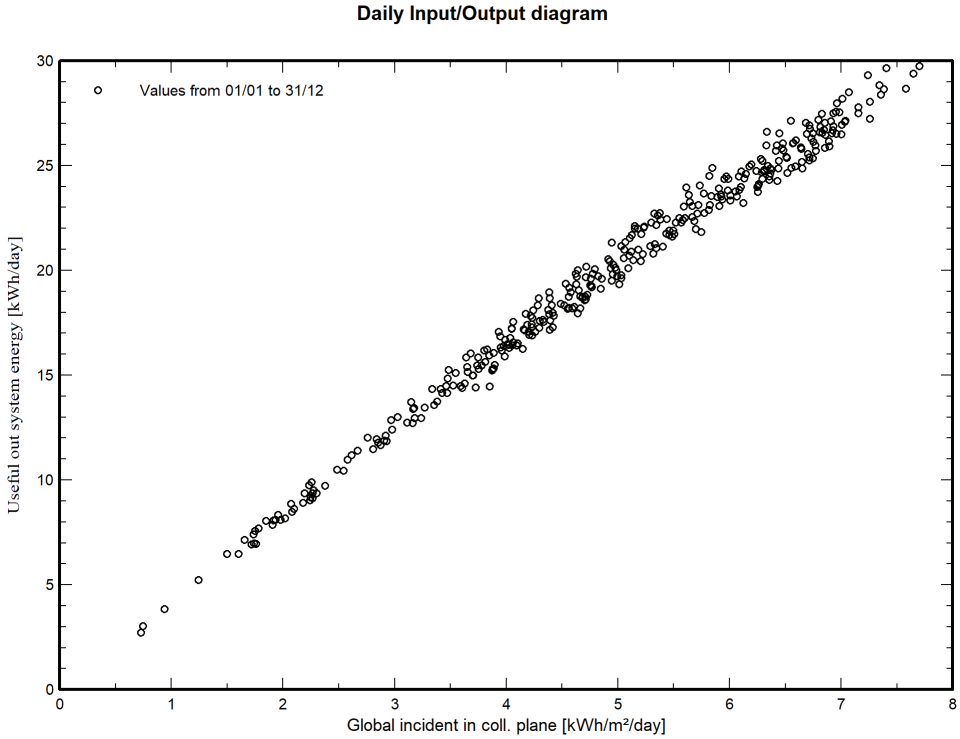

Figure 11. Representation of Glob Inc. irradiation in coll. plane.

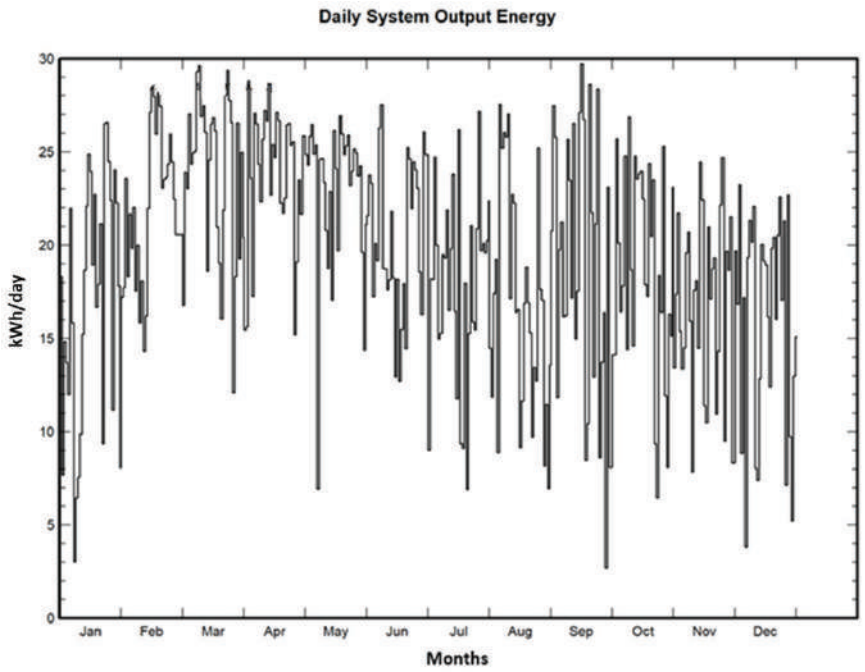

Figure 12. Monthly system output energy.

system is quite good. Table 3 indicates the balance sheet of PVsyst results including the global energy hor, diff hor., Glob Inc.., ambient temperature, E array & Figures 10-11 shows the trends of normalized energy generation, Glob Inc. Eff, irradiation in coll. Plane, and monthly output energy respectively. Figure 12 shows the daily energy produced by the installation. The maximum electrical energy generated was from June to Aug.

Analysis of Yield performance

Figure 13 demonstrate monthly average values of array yield, final yield, as well as daily reference yield respectively.

The lowest values were noted during the winter months, specifically in Dec and Jan. In the month of Dec, the array yield, final yield, and reference yield were calculated as 4.2, 4.0, and 4.8 kWh/kWp/day, respectively. In contrast, the maximum values were recorded in the month of June, reaching 6.15, 6.0, and 7.80 kWh/kWp/day, respectively. The annual average values were noted as 5 for array yield, 4.91 for final yield, and 6.25 kWh/kWp/day for reference yield. Vignola et al. [12] observed that inverter efficiency reduces by approximately 1% for every 13°C increase in ambient temperature. When comparing the final yield of the experimental system at an annual average temperature of 31°C to the simulated PVsyst results at 25.5°C, the annual average final yields were recorded as 4.91 kWh/kWp/day for the experimental system and 5.41 kWh/kWp/day for the simulation. This small difference highlights the strong performance of the actual system. Since PVsyst operates as a clear-sky model, it does not account for atmospheric effects such as dust, clouds, and rain. However, despite the hot summer climate of Madhya Pradesh, the PV solar system performed exceptionally well. This demonstrates its potential as a promising solar technology for India.

Determination of Losses

PV modules and arrays experience various kinds of losses, including wiring losses (1.5%), module quality losses (2.5%), and module mismatch losses (2%). These all losses primarily result from temperature variations, module inconsistencies, as well as wiring inefficiencies. After accounting for inverter losses, the total amount of energy delivered to grid is computed. The final energy output from the PV system for load/grid is evaluated to be 7153.6 kWh. This value is attained after applying multiple loss corrections within PVsyst software, as presented in Figure 14.

The loss diagram provides a step-by-step breakdown of all the losses occurring throughout the system. Despite these losses, the system successfully delivers 596.2 kWh/m of usable energy.

Figure 15 presents monthly average value of daily losses for the overall system, array, and inverter. In the month of July, the maximum value of daily array loss was noted as 1.59 kWh/kWp/day, primarily due to the high ambient temperatures. In contrast, the minimum array losses were calculated in January and December, as 0.61 kWh/kWp/day. These values represent 21.56% and 13.01% of monthly daily average reference yield, respectively. System losses (primarily due to inverter inefficiencies) varied in the range of 0.15 kWh/kWp/day in Dec to 0.23 kWh/kWp/day in June. This increase in losses during June is because of the higher solar radiation, which leads to greater DC-to-AC conversion demands. These losses account for 3.1% and 3.0% of daily reference yield, respectively. When comparing annual averages, the real system's daily array losses were 1.2 kWh/kWp/day at an annual average temperature of 31°C, whereas the PVsyst simulation estimated 0.731 kWh/kWp/day at 25.5°C. The difference is relatively small, at only 0.469 kWh/kWp/day. Similarly, annual average daily system losses were 0.181 kWh/kWp/day for experimental system and 0.18 kWh/kWp/day for the simulated system. The close agreement in system losses is attributed to the similar inverter efficiencies, as the experimental system's inverter was installed indoors, minimizing temperature-related losses. The highest value of overall losses was

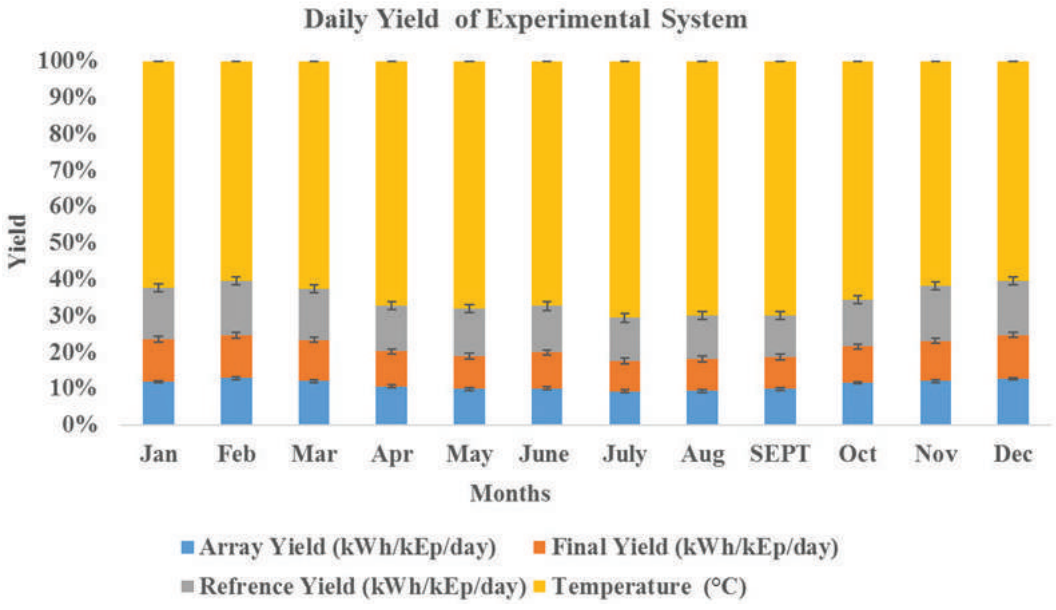

Figure 13. Monthly yield performance of actual system.

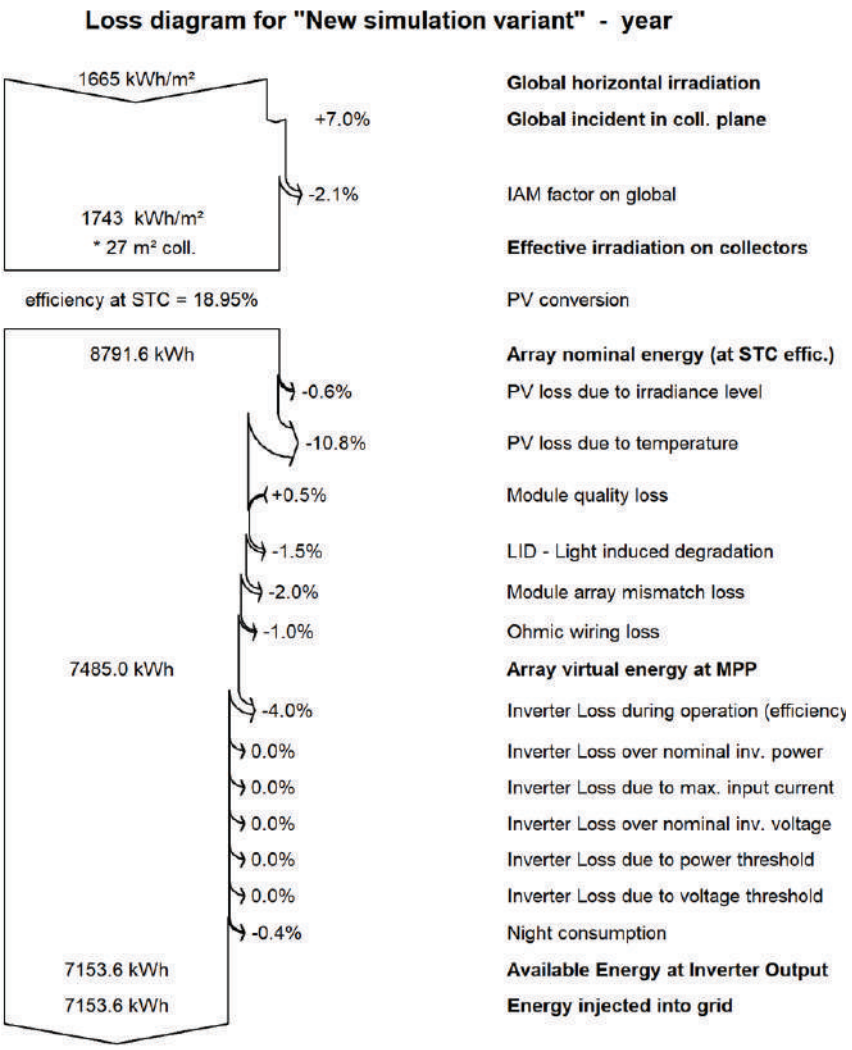

Figure 14. Simulated Energy losses.

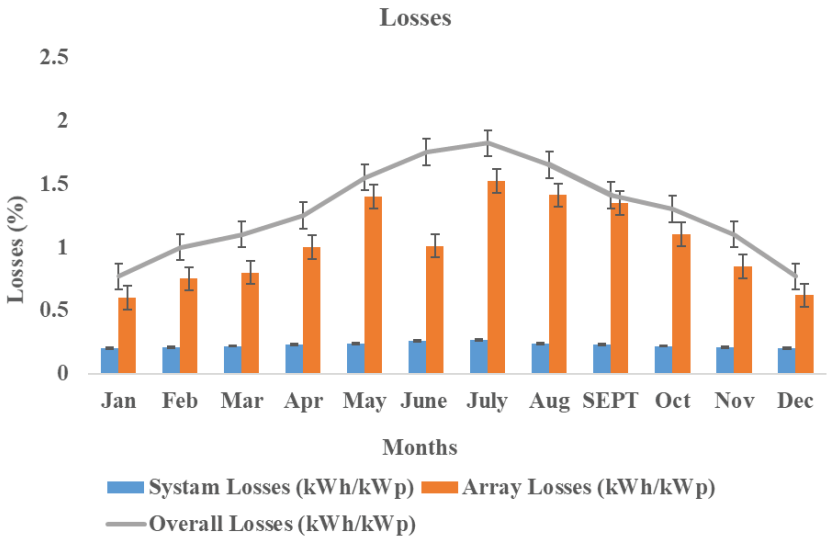

Figure 15. Monthly Solar Energy Losses.

observed in July at 1.84 kWh/kWp/day, while lower losses were in Jan and Dec, as 0.764 kWh/kWp/day. These losses accounted for 25.1% and 17.1% of the daily reference yield, respectively.

Evaluation of Performance Ratio and Capacity Factor

Figures 16 and 17 indicates monthly average capacity factor (CF) and performance ratio (PR) of actual system and PVsyst software respectively. The annually average PR for experiment system was 81.01%, with maximum values recorded in Jan and Dec (84.1%) and the minimum in July (77%). PR serves as an indicator of how closely the experimental system operates to its theoretical maximum performance. PR of the system tends to drop in May, June, July, and Aug, mainly because of high temperatures throughout these months. When comparing annually average PR of the experimental system (81.01%) at an annual average temperature of 31°C with the PVsyst simulation result (79.7%) at 25.5°C, the difference is small. This suggests that the experimental system performs very well despite the higher atmospheric temperature, indicating that it is not significantly affected by extreme heat. The annual average capacity factor (CF) for the system was 21.02%, with a maximum of 25.21% in June and a minimum of 15.9% in December. The CF indicates the percentage of time the PV system operates at full capacity. In this case, the system generates power at full capacity for approximately 92 days (2,208 hours) per year, mainly during June, July, and Aug. CF also has a direct impact on the cost of electricity generation, making it an essential parameter for evaluating grid-connected PV systems. When comparing the yearly average CF of the experimental system (21.2%) with the PVsyst simulation result (23.02%), the difference is only 1.82%. This small gap indicates the strong performance of the experimental system, even though the PVsyst model does not account for cloud cover, rain, or dust.

Solar Energy Efficiency

The comparative analysis of simulated and experimental energy data are presented in Table 4.

Figure 18 indicates the monthly average efficiencies of the inverter, system, as well as array over the observation time.

The annual average efficiencies were noted as: Inverter efficiency (96.7%), System efficiency (12.2%), and Array efficiency (12.8%). The highest value of efficiencies was observed in the month of January, with values of 96.8% (inverter), 12.8% (system), and 13.2% (array). Conversely, the minimum efficiencies were noted in the month of July, as 96.7% (inverter), 11.6% (system), and 12.1% (array). For comparison, the PVsyst simulation program (at an annual average temperature of 25.5°C) reported the following efficiency values: Inverter efficiency (97%), Array efficiency (13.16%), and System efficiency (12.72%). Despite the experiment system operating at a higher annual average temperature (31°C), the measured efficiency values were very close to the PVsyst simulation results. This highlights the strong performance and reliability of the experimental system, even under higher temperature conditions.

Economic and Environmental Analysis

The economic analysis of the 5.0 kWp solar rooftop system considered different key parameters such as, initial investment (II), savings, return on investment (ROI), payback period among others as summarized in Table 5.

Initial Investment Costs (IIC): The initial cost of installing a 5.0 kWp solar rooftop system may differ depending on the region, quality of the PV panels, charges of installation, as well as government subsidies. The average

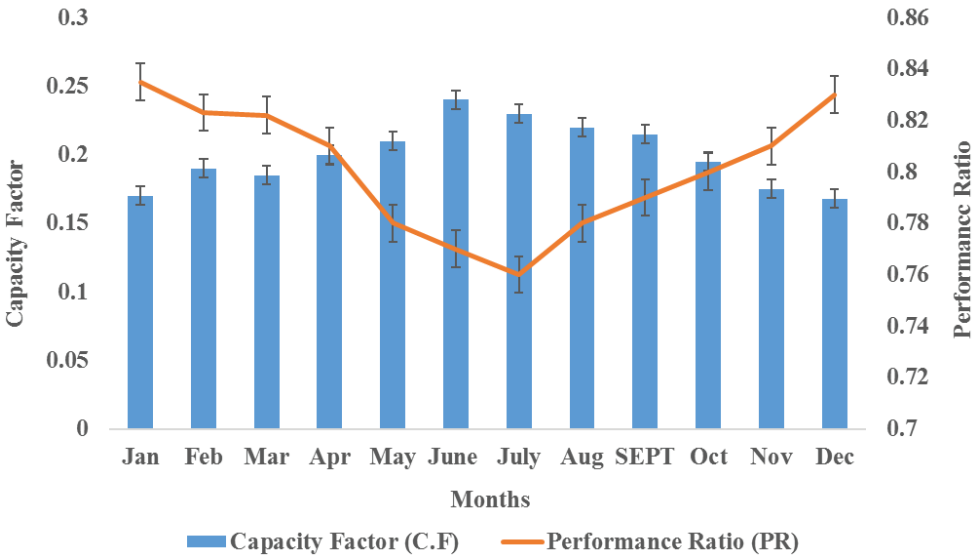

Figure 16. Monthly performance ratio and capacity factor of the system.

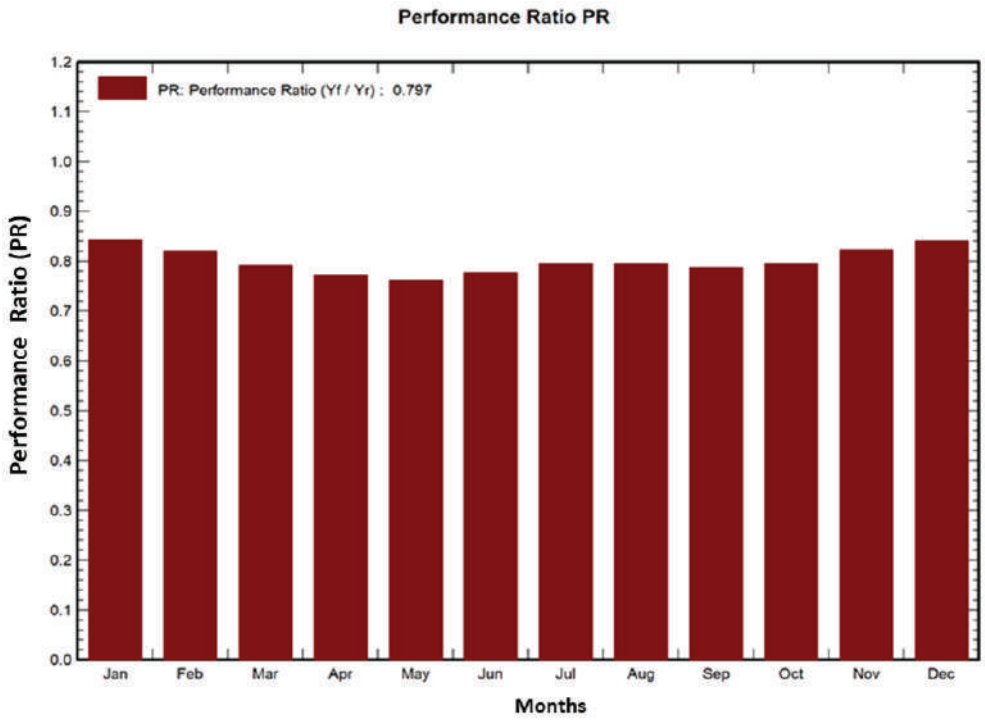

Figure 17. Monthly performance ratio simulated by PVsyst software.

Table 4. Simulated vs. Experimental Solar Energy

Metric	Experimental	PVsyst Simulated	Difference
Array Yield (kWh/kWp)	5.00	5.46	+0.46 (approx. +9.2%)
Reference Yield (kWh/kWp)	6.25	6.39	+0.14 (approx. +2.2%)
Final Yield (kWh/kWp)	4.91	5.32	+0.41 (approx. +8.4%)
Annual Energy Output(kWh/kWp)	6910.2 kWh	7485 kWh	+574.8 kWh (+8.3%)

This shows/demonstrates that …….

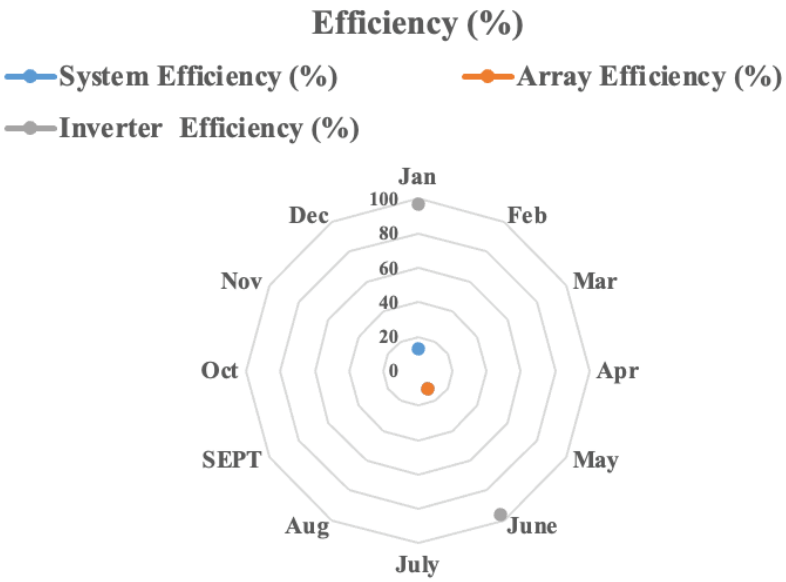

Figure 18. Demonstration of average monthly efficiencies.

Table 5. Summarized value of environmental and economic analysis

Parameter	Unit	Lower Estimate	Upper Estimate
System Size	kWp	5	5
Installation Cost		$5,000	$12,500
Annual Energy Generation		9,125 kWh	9,125 kWh
Electricity Rate		$0.12/kWh	$0.12/kWh
Annual Savings		$1,095	$1,095
Annual Maintenance Cost		$150	$150
Government Incentive (30%)		$1,500	$3,750
Net Initial Investment		$3,500	$8,750
Payback Period (years)		4.57 years	8 years
Net Savings over 25 years		$22,375	$14,875
ROI		447.5%	119%
CO_2 Savings (per year)		7,756.25 kg	7,756.25 kg
Total CO_2 Savings (25 years)		193,906.25 kg	193,906.25 kg

price per kWp of solar rooftop installation is around $1,000 to $2,500 in many regions (this could vary widely).

Annual Energy Generation

A 5.0 kWp PV solar roof top system can generate an average of about 4 - 5 kWh/day/installed kW (normally depending on the location and sunlight hours). For a location with virtuous sunlight (average of 5 hours per day), it can generate as:

Daily energy generation: 5 kWp x 5 hours = 25 kWh/day

Annual energy generation: 25 kWh/day x 365 days = 9,125 kWh/year

Savings of electricity

The price of electricity be different depending on the region and location, therefor this analysis, let's assume an average electricity rate of $0.12 per kWh.

Yearly Savings: 9,125 kWh/year x $0.12 = $1,095/year.

Maintenance Costs

PV solar systems involve minimal maintenance, typically just cleaning the PV panels as well as monitoring the system's performance annually. Maintenance costs are usually low, estimated at around $100 to $200/year. Annual Maintenance Costs: Assume $150/year.

Payback Period

The payback period is usually defined as the time it takes for the savings from the PV solar system to cover the initial investment cost.

Lower Estimate (if system cost is $5,000):

Payback period = Initial Investment / Annual Savings = $5,000 / $1,095 = 4.57 years

Upper Estimate (if system cost is $12,500):

Payback period = Initial Investment / Annual Savings = $12,500 / $1,095 = 11.41 years

Return on Investment (ROI)

Subsequently the payback period, the system will continue to produce savings. Therefore, to compute the ROI, will consider the system's lifespan, which is normally around 25 years.

Net savings over 25 years:

Lower estimate (after incentives):

Total savings = $1,095/year x 25 years = $27,375

Net savings after initial investment = $27,375 - $5,000 = $22,375

Upper estimate (after incentives):

Total savings = $1,095/year x 25 years = $27,375

Net savings after initial investment = $27,375 - $12,500 = $14,875

ROI:

Lower estimate: ROI = ($22,375 / $5,000) x 100 = 447.5%

Upper estimate: ROI = ($14,875 / $12,500) x 100 = 119%

Environmental Effect

CO_2 Savings: The average PV solar panel system emits about 0.85 kg of CO_2/kWh. Therefore, in a case of 5.0 kWp solar system generating 9,125 kWh/year, the whole PV solar system would save 9,125 kWh/year x 0.85 kg CO2 = 7,756.25 kg of CO_2 per year. Over 25 years, that would be 193,906.25 kg of CO_2.

CONCLUSION

A Photovoltaic solar system was designed using PVsyst software to assess the energy requirements for an institutional building›s total load of 5.0 kWp. The PVsyst simulation provided valuable insights into the performance of the PV modules. The results indicated that as load demand decreases, the performance ratio increases, and power generation remains proportional to load. Further analysis confirmed that the system performs well and is capable of reliably supporting a load of approximately 5.0 kWp. A

comparative study was also conducted to evaluate the effect of different parameters on the performance of actual system in term of energy output, yield, efficiencies, and losses. The results indicate that when the system is installed with a zero-azimuth angle, it attains the maximum specific production with higher efficiency, making this orientation the preferred choice. The feasibility of the actual system was validated through simulation results, demonstrating its suitability for PV solar array installation.

- The variance between the PVsyst simulation results and the actual performance of the experimental system was minimal, despite the PVsyst model assuming an annual average temperature of 25.5°C, while the experimental system operated at 31°C.
- In terms of efficiency, the experimental system closely matched the performance of PVsyst simulation, with comparable energy losses between the two.
- The results demonstrate that the PV solar system performs effectively under real-world conditions, despite the PVsyst model representing an ideal scenario unaffected by factors like clouds, rain, and dust. The experimental system, operating at a higher average temperature of 31°C, showed strong performance and resilience in Gwalior, Madhya Pradesh, India.
- The payback period for a 5.0 kWp PV solar rooftop system ranges from about 4.57 years to 11.41 years, depending on the cost.
- The ROI ranges from 119% to 447.5%, with the system providing substantial long-term savings.
- The environmental impact is significant, with reductions in CO_2 emissions contributing to sustainability.

Future research should investigate long-term performance variations of rooftop PV systems under diverse seasonal and environmental conditions. It can also focus on integrating storage solutions, optimizing tilt and orientation dynamically, and improving simulation accuracy. Expanding studies across different Indian regions would strengthen national strategies for effective solar energy deployment.

NOMENCLATURE

PV	Photovoltaic
CF	Capacity factor
PR	Performance Ratio
L_a	Array losses
Y_a	Array yield
Y_r	Reference yield
η_{sys}	System efficiency
η_{PV}	Photovoltaic efficiency
η_{inv}	Inverter efficiency

ACKNOWLEDGEMENT

The authors is grateful to the Noida Institute of Engineering Technology Gr. Noida U.P (India), for conducting the research work.

AUTHORSHIP CONTRIBUTIONS

Authors equally contributed to this work.

DATA AVAILABILITY STATEMENT

The authors confirm that the data that supports the findings of this study are available within the article. Raw data that support the finding of this study are available from the corresponding author, upon reasonable request.

CONFLICT OF INTEREST

The author declared no potential conflicts of interest with respect to the research, authorship, and/or publication of this article.

ETHICS

There are no ethical issues with the publication of this manuscript.

STATEMENT ON THE USE OF ARTIFICIAL INTELLIGENCE

Artificial intelligence was not used in the preparation of the article.

REFERENCES

[1] Kushwah A, Kumar A, Pal A, Gaur MK. Experimental analysis and thermal performance of evacuated tube solar collector assisted solar dryer, Mater Today Proc 2021;47:5846–5851. [CrossRef]

[2] Kumar R, Chandra P. Thermal analysis, pressure drop and exergy loss of energy efficient shell, and triple meshed helical coil tube heat exchanger. Energy Sources Part A Recover Util Environ Eff 2020;42(8):1026–1039. [CrossRef]

[3] Kumar R, Chandra P. Thermal analysis of compact shell and wire coil-inserted helical coil tube heat exchanger. Int J Ambient Energy 2022;43(1):1068–1073. [CrossRef]

[4] Raj G, Prabhansu D, Kumar R, Chandra P, Saurabh S. Experimental study of solar still augmented with low-cost energy absorbing and releasing materials. Energy Sources Part A Recover Util Environ Eff 2020;42(1):56–65. [CrossRef]

[5] Kushwah A, Kumar A, Gaur MK. Techno-economic analysis of solar still with nano-phase change material and heating coil: A novel approach for sustainable development. J Therm Eng 2025;11(2):476–492. [CrossRef]

[6] Kasim NK, Abed AN, Hussain HH. Performance Analysis Of Grid-Connected CIGS PV Solar System And Comparison with PVsyst Simulation Program. Int J Smart grid 2019. [CrossRef]

[7] Singh PK, Agrawal A. Performance and Economical Analysis of Solar Roof Plant with and without Reflectors. Int J Res Appl Sci Eng Technol 2023;11(9):703−715. [CrossRef]
[8] Al Mamun A, Lipu MSH, Islam ZU, Barua S, Rahman T,Karim TF, et al. Sustainable renewable energy integration on expressways in Bangladesh: A techno-economic, environmental, and sensitivity analysis of a grid-connected hybrid system. Energy Convers Manag X 2025;26;101020. [CrossRef]
[9] Jang J, Lee K. Module and System, Energies 2020;13(17):13. [CrossRef]
[10] Saxena N, Kumar R, Rao YKSS, Mondloe DS, Dhapekar NK, Sharma A, et al. Hybrid KNN-SVM machine learning approach for solar power forecasting. Environ Challenges 2024;14:100838. [CrossRef]
[11] Baghel N, Manjunath K, Kumar A. Performance evaluation and optimization of albedo and tilt angle for solar photovoltaic system. Comput Electr Eng 2023;110:108849. [CrossRef]
[12] Lima LC, Araújo Ferreira L, Lima Morais FHB. Performance analysis of a grid connected photovoltaic system in northeastern Brazil. Energy Sustain Dev 2017;37:79−85. [CrossRef]
[13] Sharma S, Kurian CP, Paragond LS. Solar PV System Design Using PVsyst: A Case Study of an Academic Institute. 2018 Int Conf Control Power Commun Comput Technol 2018;123−128. [CrossRef]
[14] Yadav P, Kumar N, Chandel SS. Simulation and performance analysis of a 1kWp photovoltaic system using PVsyst. 4th IEEE Spons Int Conf Comput Power Energy Inf Commun 2015;358−363. [CrossRef]
[15] Yakubu RO, Mensah LD, Quansah DA, Adaramola MS, Hammed Y. Performance evaluation of bifacial solar pv modules under different climatic regions in Nigeria. E3S Web Conf 2022;354. [CrossRef]
[16] Shrivastava A, Sharma R, Saxena MK, Shanmugasundaram V, Rinawa ML, Ankit. Solar energy capacity assessment and performance evaluation of a standalone PV system using PVSYST. Mater Today Proc 2023;80:3385−3392. [CrossRef]
[17] Nababan WS, Sihombing HV, Ambarita H. Technoeconomic analysis of a solar rooftop: A case study in Medan city, Indonesia. IOP Conf Ser Earth Environ Sci 2020;452(1). [CrossRef]
[18] Kumar R, Rajoria CS, Sharma A, Suhag S. Design and simulation of standalone solar PV system using PVsyst Software: A case study. Mater Today Proc 2020;46:322−5328. [CrossRef]
[19] Salmi M, Baci AB, Inc M, Menni Y, Lorenzini G, Al-Douri Y. Desing and simulation of an autonomous 12.6 kW solar plant in the Algeria's M'sila region using PVsyst software. Optik 2022;62:169294. [CrossRef]
[20] Darjay S, Agyekum EB. Assessment of solar energy generation potential in Western Bhutan − A case study of 12 kWp grid-tied rooftop solar photovoltaic system. Int J Thermofluids 2025;26:101142. [CrossRef]
[21] Zhu X, Lv Y, Bi J, Jiang M, Su Y, Du T. Techno-Economic Analysis of Rooftop Photovoltaic System under Different Scenarios in China University Campuses. Energies 2023;16(7). [CrossRef]
[22] Aktas IS, Ozenc S. A case study of techno-economic and environmental analysis of college rooftop for grid-connected PV power generation: Net zero 2050 pathway. Case Stud Therm Eng 2024;56:104272. [CrossRef]
[23] Parhamfar M, Zabihi A. Comprehensive design of a 100-kilowatt solar power plant with bifacial technology in PVsyst for Arak, Iran. Sol Energy Adv 2025;5:100092. [CrossRef]
[24] Tajjour S, Chandel SS, Chandel R, Gyani R. Comparative performance analysis of a 100 KWp solar Microgrid for enhanced power generation. Next Res 2025;2(2):100208. [CrossRef]
[25] Mohammed A, Alhadethe H, Raphael R, Barwari L. Evaluating the performance on an air-conditioning system operated by PV panels based on PVsyst software. Samarra J Eng Sci Res 2024;2(2):54−75. [CrossRef]
[26] Althuwaini YEYYE, Philbin SP. Techno-Economic Analysis of Solar Power Plants in Kuwait: Modelling the Performance of PV and CSP Systems. Int J Renew Energy Res 2021;11(4):2009−2024. [CrossRef]
[27] Cañete C, Carretero J, Sidrach-de-Cardona M. Energy performance of different photovoltaic module technologies under outdoor conditions. Energy 2014;65:295−302. [CrossRef]
[28] Rudationo CB, Novianto B, Yandri E, Susanto H, Setyobudi BH, Uyun AS, et al. Techno-economic Analysis of Rooftop Photovoltaic System (RPVS) using Thin-Frameless Solar Panels for Household Customers in Indonesia. Proc Pakistan Acad Sci: Part A 2021;58:131−139. [CrossRef]

J Ther Eng, Vol. 12, No. 1, pp. 323−334, January, 2026

Journal of Thermal Engineering
Web page info: https://jten.yildiz.edu.tr
DOI: 10.14744/thermal.0001082

Research Article

Energy-efficient refrigeration: The role of TiO_2 nanoparticles in R600a/R290 refrigerant blends

M. Ravi KUMAR[1,2*], R.Satya MEHER[3], A.Swarna KUMARI[2]

[1]*Department of Mechanical Engineering, Maturi Venkata Subba Rao (MVSR) Engineering College, Hyderabad, 501510, India*

[2]*Jawaharlal Nehru Technological University Kakinada (JNTUK), Kakinada, 533003, India*

[3]*QIS College of Engineering and Technology, Andhra Pradesh, 523272, India*

ARTICLE INFO

Article history
Received: 02 November 2025
Revised: 05 May 2025
Accepted: 06 May 2025

Keywords:
Coefficient of Performance (COP); Energy Efficiency; R600a/R290 Blend; Titanium Dioxide (TiO_2) Nanoparticles; Vapour Compression Refrigeration (VCR) System; Capillary Tube Length

ABSTRACT

Analysis on the need for sustainable and energy-efficient cooling mechanisms has fuelled a drive towards developing sustainable vapor compression refrigeration (VCR) systems. Experimental advancement of VCR systems is accomplished using Titanium dioxide (TiO_2) nanoparticles, which are widely known for their high coefficient of performance (COP) and operational efficiency. This research studied the influence of TiO_2 nanoparticles poised in mineral oil on a VCR system utilizing a refrigerant mixture of R600a and R290 (60:40 mass ratio). The COP of the cooling system whenever nanoparticles were implemented and when they were not measured with the capillary tube lengths being 8, 10, 12, and 14 feet through pull-down and performance test, respectively. The outcomes show that the adding of nanoparticles can raise the heat transfer rates in the evaporator and condenser, resulting in a macrophenomenon with a maximum COP enhancement of 8% at 10 foot for the capillary length. More to the point, the nano refrigerant at this optimum length proved superior over the conventional R600a/R290 in system performance (7.1% increase) and compressor power consumption (7.14% decrease). Longer capillary tubes (12 and 14 feet) were not as effective, which led to increased power consumption and less refrigeration effect. The work identified challenges as well with nanoparticle dispersion and compressor lubricant compatibility. This paper presents a pathway to sustainable refrigeration by enhancing energy efficiency and operational performance through the optimization of the length of capillaries, which play a important role in the operation of nanoparticle-augmented VCR systems.

Cite this article as: Kumar MR, Meher RS, Kumari AS. Energy-efficient refrigeration: The role of TiO_2 nanoparticles in R600a/R290 refrigerant blends. J Ther Eng 2026;12(1):323−334.

INTRODUCTION

The Vapor Compression Refrigeration systems are the oldest and utmost used refrigeration systems globally that power a majority of the domestic refrigerators, air conditioners, industrial chillers, etc. These systems work on a four-part, closed-loop cycle: A compressor, condenser, expansion valve, and evaporator. The refrigerant moves

***Corresponding author.**
*E-mail address: mrkmvsr@gmail.com

This paper was recommended for publication in revised form by Editor-in-Chief Ahmet Selim Dalkilic

Published by Yıldız Technical University Press, İstanbul, Turkey
Yıldız Technical University. This is an open access article under the CC BY-NC license (http://creativecommons.org/licenses/by-nc/4.0/).

between these two stages, changing from a gaseous to a liquid state in the process; this allows it to absorb heat from cooled spaces and dumps it outside. VCR systems are acclaimed for their reliability and high coefficient of performance, yet conventional refrigerants, such as hydrofluorocarbons (HFCs), significantly contribute to global warming owing to their elevated levels of greenhouse gas emissions. This has prompted research into traditional eco-friendly alternatives — natural refrigerants (hydrocarbons like R600a and R290, for example) — and advanced modifications to improve efficiency. Nanorefrigerants, created through the dispersion of nanoparticles (such as TiO_2, Al_2O_3, carbon nanotubes) in the fundamental refrigerants or lubricants, domain us with disruptive possibilities for VCR systems. These nanoparticles improve evaporator and condenser efficiency by increasing thermal conductivity and heat transfer rates. Research shows that nanorefrigerants increase COP of the system as much as 12%, lower the work on the compressor, and reduce energy consumption. The article will present the performance between pure refrigerant and TiO_2-R600a blends where TiO_2 blended with R600a has demonstrated higher cooling performance. Nevertheless, obstacles to general adoption, such as nanoparticle agglomeration, long-term stability and interactions between materials in the system, remain. Current work is aimed at fine-tuning the optimal concentration of these nanoparticles, getting them to disperse evenly, and overcoming safety and cost barriers, Saylor said, which would be needed to realize the vision of sustainable, high-efficiency cooling.

The rising threat of climate change has increased scrutiny on refrigerants, especially their contribution to global warming. Abas et al. [1] assessing and selecting natural refrigerants versus synthetic refrigerants based not only on operational performance but also environmental sustainability. Their analysis highlights the need for eco-friendly alternatives that do not trade performance for ecological impact. They contend that regulatory frameworks and technological innovation will be the two biggest drivers of a transition to a lower greenhouse gas emission refrigeration system. Further building on these results, Alawi et al. nanorefrigerants and nanolubricants in cooling revolution [2]. They show that nanoparticles increase thermal conductivity and energy efficiency in refrigeration systems, leading to unprecedented levels of performance with a lower environmental impact. This study agrees with Sanukrishna and Prakash [3] as they performed experimental validation on the improved thermal and rheological traits of TiO_2-PAG nanolubricants that can enhance the heat transfer process as well as reduce mechanical wear together with surface damage. Sharif et al. [4] As indicated by, all these benefits of nanorefrigerantsare further supported by innovative mechanics like the augmented heat exchange capability and energy savings. Meanwhile, Aberoumand et al. [5] shows silver-based nanofluids density, thermal conductivity, and specific heat properties provide outperformed thermophysical properties than classical fluids for heat transfer applications. Although we have made progress, there are still challenges. Some researchers, such as Alawi and Sidik [6], point out the long-term stability of CuO/R134a nanorefrigerants is limited, and more studies need to be conducted for the material compatibility. Azmi et al. There is a written work on the adding of TiO_2 and SiO_2 nanofluids to turbulent flow improved the heat exchange capacity, but its application on the real refrigeration systems still scarce. [7,8]. Gao et al. [9] investigated the alternative of high-GWP refrigerants in the cold chain in China and indicated an evident trend towards the natural and low-GWP replacements, due to environmental regulation and environment concern. Zhang et al. [10] experimentally determined and modelled the thermal conductivity of nanorefrigerants at low volume fractions and found that even small amounts of added nanoparticles substantially enhance the thermal behaviour, which results in an increase of heat transfer effectiveness. In addition, to these results, Kumar et al. [11] experimented using nanocomposites in VCR systems with optimized capillary tube lengths and nano-enhanced lubricants and found that they could enhance the COP and compressor power consumption. Overall, these studies allow the development of the eco-friendly and energy-saving VCR system designs based on refrigerant elimination and nanotechnology incorporation.

Similarly, parallel works on alternative refrigerants show compromises between performance [12] evaluated for R290/R600a blends and safety, mainly flammability confinements [13]. Pendyala et al. [14] and Colombo et al. [15] discuss efficiency improvements with novel refrigerant blends but highlight the need for economic and life cycle assessments. Recent advances demonstrate the potential of nanotechnology. Bi et al. [16] report a 3.6% enhancement in the efficiency of domestic refrigerators using TiO_2-R600a nano-refrigerants, whereas Adelekan et al. [17] which yield a 12% enhancement in COP using 15 nm TiO_2 nanoparticles. Vamshi et al. The first trimming algorithms were based on the work of, e.g., Chen et al. [18] and Sheikholeslami et al. Boiling heat transfer and system reliability are enhanced via the use of nanoparticles as reported in multiple studies [19]. Babarinde et al. [20] reviewed the application of nanorefrigerants for improving thermal and energy performance and focused on the dispersion of nanoparticles and system compatibility issues. Said et al. [21] presented a detailed review on the use and modes of action of nano-refrigerants and nano-lubricants, focusing on their influence on heat transfer enhancement and related operating issues. Yousif et al. [22] through an experiment proved the beneficial effect of TiO_2 and Al_2O_3 nanoparticles on the performance of VCR systems and supported that with their use can be realized the energy-saving refrigeration technology. Similarly, Al-Tajer et al. [23] studied the heat transfer of nanofluid in the elliptic tubing and circle tubing and found that the nanofluid has much higher thermal conductance compared to the traditional fluid. Katoch et al. [24]

conducted performance studies of nano-refrigerants using MATLAB-Simulink, the results are consistent with the conclusion that optimum nano-concentration gives higher values of COP. Barza et al. [25] conducted experimental studies on a nanorefrigerant system (R-134a + ZrO_2) and found an increase in the steady state performance, thereby confirming the practical implementation of nanofluids in conventional refrigeration systems. Also, Zhang and Zhou [26] underlined the importance of incorporating big data analytics into electric mobility solutions, indirectly favouring predictive maintenance and optimization in thermodynamic systems such as refrigeration. Taken all together, these studies provide precious insights for the continuous growth of energy-efficient, green, and high-performance refrigeration technology using nanotechnology and state-of-the-art computational tactics. Secop (2018) emphasized the practicality of using R600a and R290 refrigerants in small hermetic systems, underlining their environmental advantages and safe application when proper handling and design protocols are followed [27]. Demir et al. [28] (2018) provided an in-depth overview of titanium dioxide (TiO_2) nanoparticles, discussing their synthesis methods, structural characteristics, and applicability in thermal systems due to their high surface area and thermal stability. In the context of lubrication, Siddiqui et al. [29] (2013) examined the properties of mineral oil and highlighted its relevance in improving mechanical performance and reducing wear in thermal machinery. Leong et al. [30] (2006) introduced a thermal conductivity model for nanofluids, showing the significance of the interfacial layer formed between nanoparticles and base fluids in enhancing heat transfer. Mohamad (2024) extended this application by demonstrating the improved heat transfer in flat-plate solar collectors when TiO_2-based nanofluids were utilized, indicating clear efficiency gains over traditional fluids [31]. Similarly, Qader et al. [32] (2023) numerically analyzed heat transfer in circular pipes with porous media, revealing enhanced thermal distribution and energy effectiveness through optimized fluid flow paths. In another related work, Qader et al. (2023) further demonstrated the improved effectiveness of double-pipe heat exchangers by integrating porous media and TiO_2 nanofluids, validated through CFD simulations, confirming the superior heat transfer characteristics of nanoparticle-enhanced working fluids [33]. Shaik et al. [34] carried out a comprehensive study on the application of low-GWP refrigerants to enhance domestic refrigerator performance. Their investigation highlighted that refrigerants such as R1234yf and R152a not only reduce environmental impact but also maintain acceptable thermal and energy performance levels when compared to conventional HFC-134a. Pardo-Cely et al. [35] explored the influence of refrigerant charge variation on the energy efficiency and cooling behavior of domestic refrigerators. The study concluded that both overcharging and undercharging significantly affect the system's coefficient of performance and energy consumption, underscoring the critical role of optimal refrigerant charge for efficient operation.

Summary of Literature and Scope of Work

The existing literature establishes the benefits of using natural refrigerants and nanorefrigerants in VCR systems to enhance energy efficiency and reduce environmental impact. However, gaps remain in experimental validation, particularly regarding optimal nanoparticle concentrations, long-term stability, and real-world applicability. This study addresses these gaps by experimentally comparing the performance of pure R600a and TiO_2-R600a nanorefrigerant blends, focusing on improving thermal performance while resolving issues like nanoparticle agglomeration and compatibility. The work is novel in its practical approach and aims to bridge the gap between theoretical research and sustainable, high-efficiency refrigeration system implementation.

This study presents a novel experimental evaluation of TiO_2-R600a nanorefrigerant blends in Vapor Compression Refrigeration systems, distinguishing itself from previous research by focusing on the optimal nanoparticle concentration for enhanced cooling performance and energy efficiency. Unlike prior studies that are largely theoretical or simulation-based, this work offers practical insights by directly comparing pure and blended refrigerants, addressing key challenges such as nanoparticle dispersion, agglomeration, and long-term stability. By bridging the gap between laboratory findings and real-world application, the study contributes to the extension of sustainable, high-performance, and ecologically friendly refrigeration equipment.

MATERIALS AND METHODS

A variable capillary configuration has been expertly set up to effectively evaluate the performance of the two refrigerants simultaneously being analyzed in this vapor compression refrigeration (VCR) system. The experimental apparatus is a high quality hermetic air compressor combined with an accurately designed set of capillary tubes as shown in Figure1, which the thermal static load is simulated with. A computerized evaporator was included to impose variable static thermal loads for precise control of cooling. Measurement points were selected for the data attainment system to measure the performance of the refrigerant systems as a whole. All system valves were closed tightly to avoid any leakages when the experiment started.

An 8-foot capillary tube was first soldered in place and the entire refrigeration circuit was evacuated with a vacuum pump to get rid of all moisture and non-condensable gases as well. The system was then evacuated until the vacuum conditions with 60:40 mass ratio of R600a and R290 were obtained. The refrigerant charge was closely controlled to obtain accurate and repeatable charging between episodes. On charging the device was actuated by opening

the capillary tube valve. The bimetallic strip on the evaporator was moved into place at its maximum to effect maximum heat exchange and an evaporators temperature set point was chosen. Timer1 was started at the same time. Temperature was supervised with a digital indicator and the time duration of each one-degree Celsius drop in temperature was registered. This process was repeated until the evaporator reached the target lower temperature. From the base mix, tests were performed, with and without inclusion of lubricant dispersions of TiO_2 nanoparticles, under different values of condensers temperatures. During both tests, key parameters were recorded: compressor inlet and outlet pressures, evaporator and condenser temperatures, sub-cooling and superheating.

In addition, to check the cooling performance of the system, 7 liters of water was in the evaporator chamber, and the time taken to achieve a desired temperature drop was recorded with an accuracy of one second. The lengths of the capillary tubes were varied (8 ft, 10 ft, 12 ft, and 14 ft) in a systematic manner to determine the optimum refrigerant distribution and the performance of the system. This well-designed procedure yielded strong, reproducible and all-around assessment of VCR system performance through refrigerant combination and capillary tube arrangement, offering a new insight into the nanomaterial influence on system efficiency with optimization consideration. The properties of refrigerants are enlisted in table 1.

The properties of R600a (isobutane) and R290 (propane) listed in the table make them highly suitable for use as a refrigerant blend due to their complementary characteristics. R600a has a higher boiling point (-11.7°C) compared to R290 (-42.1°C), which allows the blend to balance evaporation and condensation temperatures, enhancing system performance across different operating conditions. The higher latent heat of vaporization of R290 (426 kJ/kg) compared to R600a (367 kJ/kg) contributes to improved cooling capacity and heat absorption.

If we move to environmentally friendly options, both refrigerants have a zero Ozone Depletion Potential (ODP) and a very low Global Warming Potential (GWP) of around 3. R600a (135°C) critical temperature is also higher than R290 (96.7°C) thus, R600a shows higher stability in high temperature–high pressure surroundings compared with R290. The results from the literature indicate that the combined thermophysical properties of these refrigerants are beneficial for energy-efficient, low power consumption, and better performance, which makes the mixture an attractive solution for sustainable and high-performance refrigeration systems. The R600a/R290 (60:40) blend is selected because it combines high energy efficiency, environmental friendliness, improved heat transfer, reduced operational pressure, and better compatibility for small-capacity vapor compression systems. Using pure R290 could lead to very high system pressures, which might be risky. Mixing it with R600a lowers the overall system pressure compared to pure R290, making the system safer without sacrificing too much performance.

TiO_2 nanoparticles were prepared by chemical vapor deposition with high purity and uniform particles size. The nanoparticles were dispersed into compressor lubricating oil with continuous magnetic stirring for 72h to achieve a stable and uniform dispersion. This TiO_2 containing lubricant so obtained was mixed with a refrigerant mixture containing R600a and R290 and charged in the VCR system. During operation, the compressor with a hermetic enclosure circulated the refrigerant-lubricant blend, providing a dispersion of the nanoparticles in a refrigerant flow. Such integration led to better heat transfer on evaporator and condenser side, and thus the VCR system achieved overall better performance. The physical properties of TiO_2 nanoparticles and mineral oil used in the compressor are listed in table 2.

Synthetic refrigerant lubricating oils like glycols, chloroformates, and alkylbenzenes—have shown exceptional reliability in refrigeration applications. Since CFCs were back in the day utilized as refrigerants in systems (like R12 and R13), mineral oil or alkylbenzene were also used as lubricants in CFC refrigerants, and HCFCs (like R22). In recent years, the use of CFC and HCFC refrigerants has rightly declined due to their detrimental effect on the ozone layer. Consequently, HFC refrigerants, including R23, R32, R134a, and others, have surged in popularity within

Table 1. Properties of R600a and R290 [Ref-27]

Property	*R600a (Isobutane)*	*R290 (Propane)*
Chemical Formula	C_4H_{10}	C_3H_8
Molecular Weight	58.12 g/mol	44.10 g/mol
Boiling Point	-11.7°C	-42.1°C
Critical Temperature	135°C	96.7°C
Critical Pressure	3.64 MPa	4.25 MPa
Latent Heat of Vaporization	367 kJ/kg	426 kJ/kg
ODP (Ozone Depletion Potential)	0	0
GWP (Global Warming Potential)	~3	~3

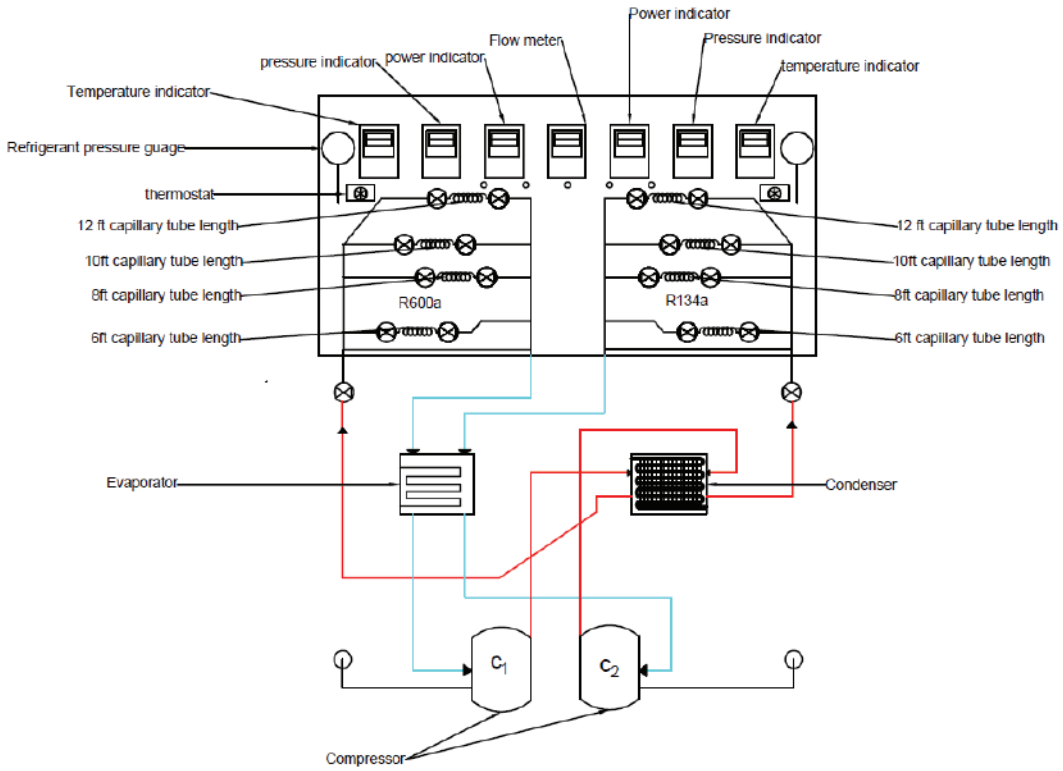

Figure 1. Computerized vapour Compression refrigeration system.

Table 2. Properties of TiO_2 nanoparticles and Mineral Oil [Ref-28 & 29]

Property	*TiO_2 Nanoparticles*	*Mineral Oil*
Appearance	White powder	Clear liquid
Density	3.9 g/cm³	0.85–0.90 g/cm³
Particle Size	20–100 nm	-
Molecular Weight	79.9 g/mol (TiO_2)	Varies with type (typically around 300-500 g/mol)
Viscosity	-	30–50 cSt (at 40°C)
Boiling Point	Sublimation point ~1800°C	300–350°C
Melting Point	1850°C	-
Thermal Conductivity	8.4 W/m K	0.12 W/m K
Specific Heat Capacity	~0.71 J/g·K	~2.0 J/g·K

Figure 2. Injection of Nanoparticles to mineral oil.

HVAC systems, utilizing polyol esters (POE) as lubricants. However, it is crucial to recognize that POE has a significant drawback because it absorbs moisture at a much higher rate than mineral-based oils. Therefore, strict adherence to proper handling procedures is essential to minimize moisture exposure. To effectively combat this issue, one should always opt for metal containers over plastic ones to prevent moisture ingress.

RESULTS AND DISCUSSION

The Tests were conducted on a vapor compression refrigeration system setup using R600a and R290 as the operational fluid, systematically evaluating varied lengths of capillary tubes set at 8, 10, 12, and 14 feet. These experiments were effectively repeated with R600a and R290 combined with 0.1% TiO_2 powder in 300 ml of lube oil. TiO_2 nanoparticles were selected for their exceptional thermal conductivity (ranging from 4 to 11.8 W/m K), proven safety, accessibility, and chemical stability, making them an ideal choice for nanofluids preparation. For the 8-foot capillary tube, critical parameters were meticulously recorded, including the inlet temperature of the compressor (T_1), exit temperature of the compressor (T_2), exit temperature of the condenser (T_3), exit temperature of the evaporator (T_4), thermal load temperature in the evaporator (T_5), delivery pressure (P_d), suction pressure (P_s), and work input to the compressor.

To evaluate the enhancement in thermal conductivity of 300 mL lubricating mineral oil when 0.1% TiO_2 nanoparticles (by volume) are added, use the Maxwell-Garnett effective medium theory. This model estimations the thermal conductivity of nanofluids established on nanoparticle concentration and properties. Process flow chart is shown in figure3.

"Maxwell-Garnett equation for thermal conductivity of nanofluids [30]"

$$k_{\text{eff}} = k_{\text{oil}}\left(\frac{k_{\text{TiO}_2}+2k_{\text{oil}}+2\phi\left(k_{\text{TiO}_2}-k_{\text{oil}}\right)}{k_{\text{TiO}_2}+2k_{\text{oil}}-\phi\left(k_{\text{TiO}_2}-k_{\text{oil}}\right)}\right) \quad (1)$$

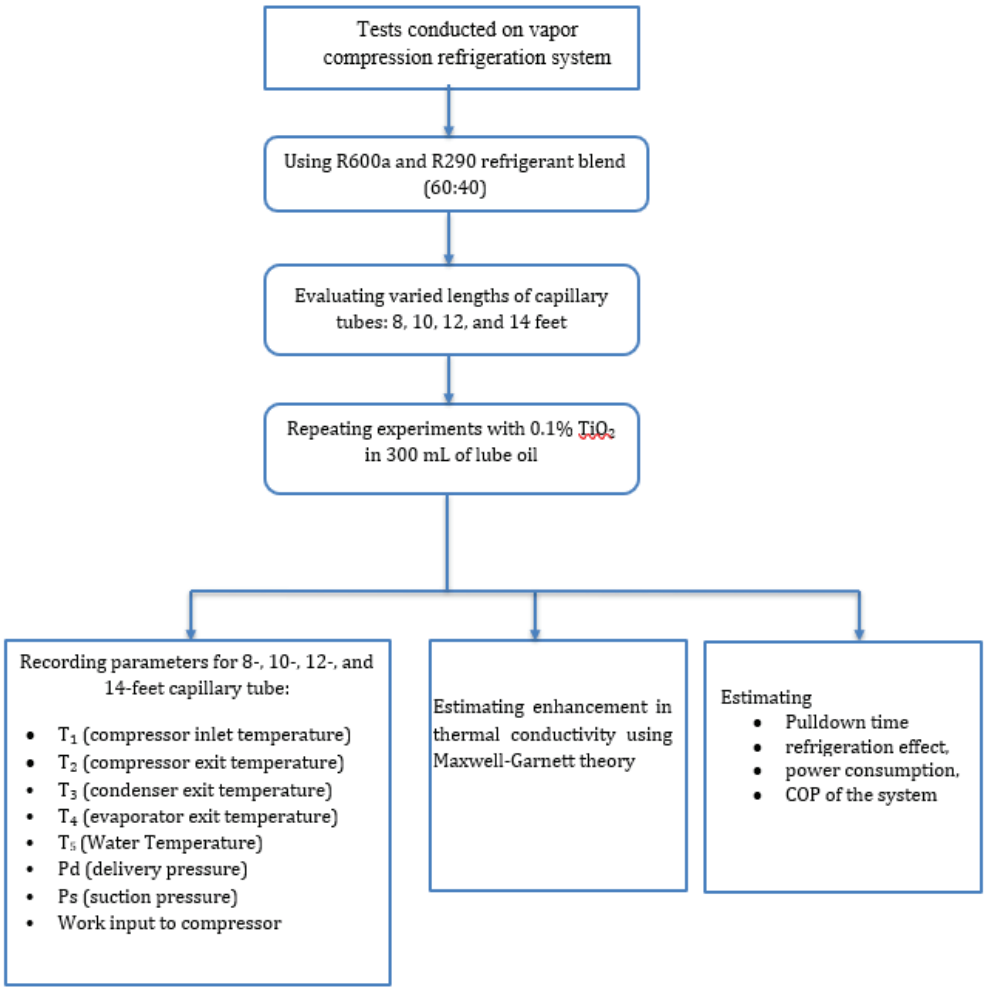

Figure 3. Process flow chart.

Where, k_{eff} is effective thermal conductivity W/m-K; k_{TiO_2} is thermal conductivity of Titanium dioxide W/m-K; k_{TiO_2} is thermal conductivity of mineral oil W/m-K, ϕ = volume fraction of nano particles.

Substitute the thermal conductivity values of TiO_2 and Mineral oil from table 2 in the equation 1

$$k_{\text{eff}} = 0.12\left(\frac{8.4 + 2(0.12) + 2(0.001)(8.4 - 0.12)}{8.4 + 2(0.12) - 0.001(8.4 - 0.12)}\right)$$

$$k_{\text{eff}} = 0.12(8.631728.65656) = 0.12 \times 1.00288 = 0.12035$$

The thermal conductivity of mineral oil is enhanced by 0.29% with 0.1% TiO_2 nanoparticles added to the mineral oil.

Additionally, pulldown time was precisely documented in seconds. This rigorous approach was consistently applied across all tested lengths of capillary tubes, including 10 feet, 12 feet, and 14 feet. The results for the refrigerant R600a and R290 without nanoparticles are clearly shown in Table 3, while Table 4 gives the detailed findings when nanoparticles were injected. These results underscore the significant impact of TiO_2 nanoparticles on system performance, highlighting their value in refrigeration technology advancements.

The size of the capillary tube, denoted L, is measured in feet and is integral to system performance, and, the temperatures are reported in °C for accuracy. Pressures are measured in kg/cm², work input to the compressor is measured in watts, and pulldown time is measured in

Table 3. Experimental Observations at variable length of capillary tubes for R600a and R290

L (ft)	*T_1 (°C)*	*T_2 (°C)*	*T_3 (°C)*	*T_4 (°C)*	*T_5 (°C)*	*P_s (kg/cm²)*	*P_d (kg/cm²)*	*Power (W)*	*Time (sec)*
8	20.7	46.5	44.2	10.9	5	4.27	8.59	253	1469
10	19	47.1	42.3	7.3	5	3.64	7.76	243	1266
12	19.1	50.2	44.6	6.5	5	3.47	5.1	253	1121
14	19.7	51.7	46	6.2	5	3.79	8.14	243	1187

Table 4. Experimental Observations at variable lengths of capillary tubes for R600a and R290 with TiO_2

L (ft)	*T_1 (°C)*	*T_2 (°C)*	*T_3 (°C)*	*T_4 (°C)*	*T_5 (°C)*	*P_s (kg/cm²)*	*P_d (kg/cm²)*	*Power (W)*	*Time (sec)*
8	23.0	42.1	40.6	16.8	05	4.46	8.12	234	1321
10	8.25	23.0	45.6	11.8	05	4.11	8.25	234	1170
12	23.6	49.9	47.5	11.6	05	3.93	8.38	243	1084
14	29.6	51.9	49.2	10.8	05	3.72	8.39	243	1110

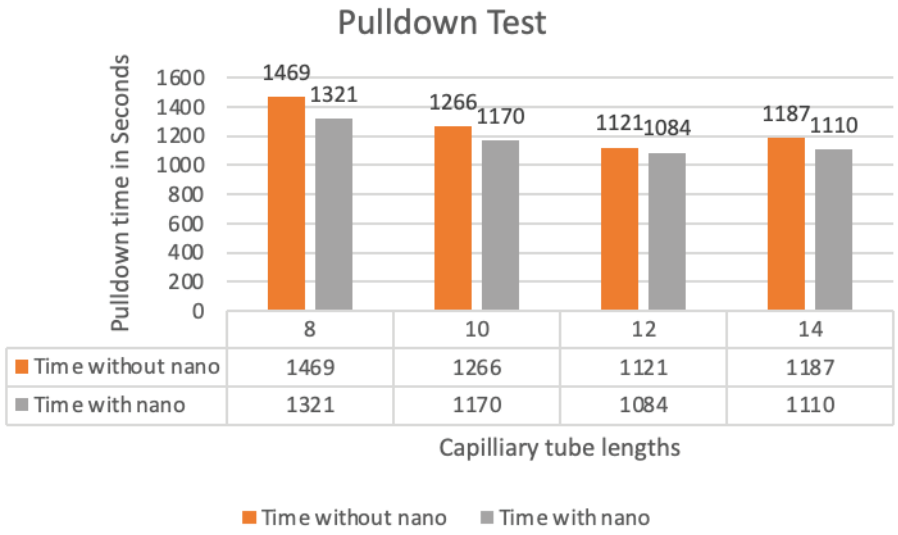

Figure 4. Pulldown time for the drop in temperature with and without nano particles.

seconds to determine efficiency. For this study, a evaporator, which has a thermal load of 7 litre of water at hydrogenated evaporator temperature (T_5) was used. The COP is calculated through several observations performed with R600a and R290 as the fluid used. The detailed methodology allows for a complete analysis of the effectiveness of the vapor compression refrigeration system under various conditions, demonstrating the possibility of further optimization and reduction of operating costs.

The pulldown test results, illustrated in Figure 4, compare cooling durations required to achieve a target temperature of 20^{0}C drop across varying capillary tube lengths, with and without nanoparticle-enhanced refrigerant. Shorter tubes exhibited the most pronounced efficiency gains when nanoparticles were introduced. For example, the 8-unit tube reduced pulldown time from 1469 seconds to 1321 seconds—a 10.1% improvement. While nanoparticle integration consistently lowered cooling times, its efficacy diminished as tube length increased. The 12-unit tube demonstrated only a 3.3% reduction, indicating that nanoparticle benefits are inversely proportional to capillary length. This trend underscores the technology's stronger impact in compact systems.

The effectiveness of vapor compression refrigeration systems is quantified using the Coefficient of Performance, calculated as the ratio of refrigeration effect (heat absorbed in the evaporator) to compressor work input. Mathematically, this is calculated by using equation (2):

Coefficient of Performance

$$(C.O.P) = \frac{Refrigeration\ effect}{Work\ \ done} = \frac{\text{m Cp } \Delta T/\text{time}}{Power\ Supplid\ to\ Compressor} \quad (2)$$

Where m = water to be cooled in kg.

C_p = Specific heat of water = 4.180 $\frac{kJ}{kg\ K}$

$\Delta T/time$ = drop in temperature with respective time

The cooling effect quantifies the refrigeration output generated in the evaporator, expressed in watts, while the power expenditure on the compressor can be directly monitored using a wattmeter, also measured in watts. By calculating the ratio of these two parameters, we can derive an accurate coefficient of performance for the refrigeration system. The investigational results obtained with R600a and R290 as refrigerants—both with and without the integration of nanoparticles—are compiled in Table 5. This table showcases findings for changing sizes of capillary tubes (8, 10, 12, and 14 feet). The data not only highlights the system's efficiency under different conditions but also emphasizes the potential enhancements in performance

Table 5. COP at various capillary tube lengths.

Length of Capillary tube	*COP of R600a & R290*	*COP of R600a & R290with TiO_2*
8	1.57	1.69
10	2.05	2.09
12	2.11	2.15
14	2.02	2.17

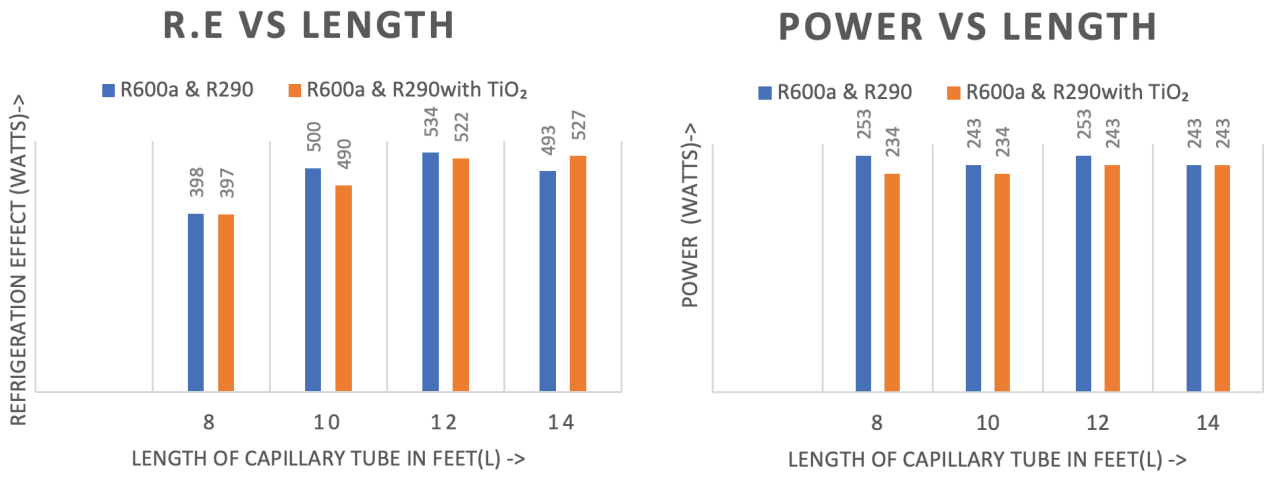

Figure 5. R.E and Power vs capillary length for (R600a & R290) and (R600a & R290 with TiO_2)

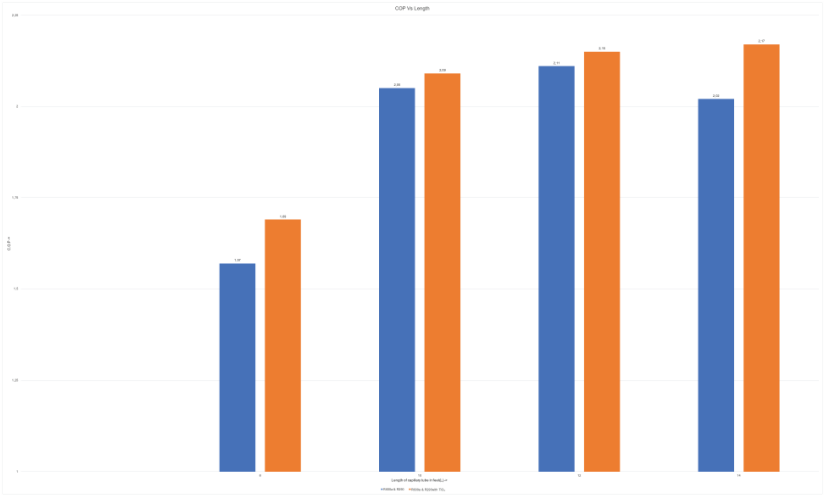

Figure 6. VCR system COP vs capillary length of (R600a & R290) and (R600a & R290 with TiO_2).

due to the incorporation of TiO_2 nanoparticles, contributing valuable insights for further advancements in refrigeration technology.

The data shows the impact of TiO_2 nanoparticles in the compressor lubricating oil on the performance of a vapour compression refrigeration system for various capillary tube lengths under a 20°C temperature drop. The addition of TiO_2 constantly enhances the system performance across all capillary tube lengths. For an 8 cm capillary, the performance improves from 1.57 to 1.69. Similarly, at 10 cm and 12 cm capillary lengths, the performance increases from 2.05 to 2.09 and from 2.11 to 2.15, respectively. The most significant improvement is observed at 14 cm, where performance rises from 2.02 to 2.17. This indicates that the incorporation of TiO_2 nanoparticles enhances heat transfer and improves the overall efficiency of the refrigerant blend system.

The power given to the compressor has an inverse relationship with the coefficient of performance (COP), which is directly proportional to the cooling effect. Using a nano refrigerant instead of the traditional R600a and R290 refrigerants results in an 8.7% enhancement in COP at 8- foot capillary.

As the Capillary length rises from 8 to 14 feet the percentage increase in COP value increases at for refrigerant added nano particles as compared to without nanoparticles. The increase in COP with the addition of TiO_2 nanoparticles is primarily due to improved thermal and flow properties of the refrigerant-lubricant mixture. Enhanced thermal conductivity facilitates more efficient heat transfer in the evaporator and condenser, boosting the refrigeration effect. Nanoparticles also modify the refrigerant's thermophysical properties, reducing viscosity and minimizing pressure drops, thereby improving flow characteristics. This enhancement leads to reduced compressor power consumption, particularly notable at the 10-foot capillary length. Additionally, the increased surface area provided by the nanoparticles further optimizes heat absorption and dissipation, contributing to overall system efficiency and performance. Figure 5 shows the refrigeration effect and energy consumption with respect to variable capillary tube lengths and Figure 6 shows the performance variations with respect to variable capillaries.

This study offers practical and timely insights for improving the energy efficiency of vapor compression refrigeration (VCR) systems, which are widely used in everyday applications like home refrigerators, air conditioners, and industrial cooling. By combining a low-impact refrigerant blend (R600a/R290) with TiO_2 nanoparticles, we've shown that it's possible to enhance system performance—achieving a higher COP and reducing power consumption. These findings not only support the development of more sustainable cooling technologies but also provide a useful reference for engineers, researchers, and industry professionals looking to optimize refrigeration systems in a more environmentally responsible way.

CONCLUSION

The investigational study revealed the remarkable impact of nanoparticles suspended in mineral oil on the working of a vapor compression refrigeration system, exploring capillary lengths of 8 feet, 10 feet, 12 feet, and 14 feet. The addition of nanoparticles significantly enhanced the thermal properties of the refrigerant, leading to a remarkable increase in heat transfer rates within the evaporator. Key findings illuminated the following insights:

- At a 10-foot capillary length, the refrigeration effect produced by the nano refrigerant soared, surpassing that of normal R600a and R290; yet this enhancement gracefully tapered as capillary length increased.

- Power consumption by the compressor saw an impressive decrease of 7.14% at the 10-foot capillary length with the incorporation of nanoparticles, while power demands rose with the 12-foot and 14-foot lengths.
- The system's overall performance achieved a noteworthy 7.1% increase with nanoparticles at the 10-foot length, demonstrating potential yet declining performance for the lengths beyond.
- These findings suggest that a capillary tube length of 10 feet stands as the ideal choice when harnessing nanoparticles in lubricating oil, leading to the enhancement of the coefficient of performance (COP) in refrigeration systems.

Summary The performance of a vapor compression refrigeration system using nanoparticulate mixtures suspended in mineral oil was analyzed to evaluate the impact of varying capillary tube lengths. Specifically, the study examined two-phase refrigerant flow transitions in capillary tubes measuring 8, 10, 12, and 14 feet in length. The results demonstrate how different tube lengths significantly affect the system's overall performance. Using nanoparticles not only improved the thermal characteristics of the refrigerant, thus attaining increased rates of heat transport. Under the most favorable conditions of 10 ft capillary length, the system was able to achieve a coefficient performance of about 7.1% higher and reduce compressor power consumption by 7.14% compared to standard refrigerants R600a and R290. Performance improvement diminished as the length of a capillary rise above 10 feet, confirming that a capillary should be no longer than 10 feet to maximize efficiency with nanoparticle-lubricated refrigerants.

Future scope of work: There is room for future improvements which can be a potential work. Future research can explore the performance of Vapor Compression Refrigeration (VCR) systems using different mass ratios of refrigerants, both with and without the addition of nanoparticles, to determine the optimal blend for maximizing efficiency, stability, and cooling capacity under varying operating conditions. Evaluation of other nanoparticles and working on different percentages will help to find better combinations for enhanced thermal properties. Long-term stability studies for dispersion and potential wear on compressor components are necessary to evaluate reliability. Moreover, the applicability of this technology will be extended to the performance assessment of advanced refrigerant blends, different capillary tube materials and diameters, as well as the energy efficiency analysis over varying load conditions. These directions will continue to build advances for more energy-efficient sustainable refrigeration and air-conditioning systems.

ACKNOWLEDGMENTS

The authors thank all the Mechanical Engineering Department faculty and staff of MVSR Engineering College for their support and assistance during the study

AUTHORSHIP CONTRIBUTIONS

Authors equally contributed to this work.

DATA AVAILABILITY STATEMENT

The authors confirm that the data that supports the findings of this study are available within the article. Raw data that support the finding of this study are available from the corresponding author, upon reasonable request.

CONFLICT OF INTEREST

The author declared no potential conflicts of interest with respect to the research, authorship, and/or publication of this article

ETHICS

There are no ethical issues with the publication of this manuscript.

STATEMENT ON THE USE OF ARTIFICIAL INTELLIGENCE

Artificial intelligence was not used in the preparation of the article.

FUNDING

This equipment was partially funded by MODROBS-AICTE to carry out research activities in the refrigeration area.

REFERENCES

[1] Abas N, Kalair AR, Khan N, Haider A, Saleem Z, Saleem MS. Natural and synthetic refrigerants, global warming: A review. Renew Sustain Energy Rev 2018;90:557–569.[CrossRef]

[2] Alawi OA, Sidik NAC, Beriache M. Applications of nanorefrigerant and nanolubricants in refrigeration, air-conditioning, and heat pump systems: A review. Int Commun Heat Mass Transf 2015;68:91–97.[CrossRef]

[3] Sanukrishna SS, Prakash MJ. Experimental studies on thermal and rheological behaviour of TiO_2-PAG nanolubricant for refrigeration systems. Int J Refrig 2018;86:356–372.[CrossRef]

[4] Sharif MZ, Azmi WH, Mamat R, Shaiful AIM. Mechanisms for improvement in refrigeration system performance using nanorefrigerants and nanolubricants: A review. Int Commun Heat Mass Transf 2018;92:56–63.[CrossRef]

[5] Aberoumand S, Jafarimoghaddam A, Moravej M, Aberoumand H, Javaherdeh K. Experimental study on the rheological behavior of silver-heat transfer oil nanofluid and proposing empirical correlations for thermal conductivity and viscosity. Appl Therm Eng 2016;101:362–372. [CrossRef]

[6] Alawi OA, Sidik NAC. Influence of particle concentration and temperature on the thermophysical properties of CuO/R134a nanorefrigerant. Int Commun Heat Mass Transf 2014;58:79–84. [CrossRef]
[7] Azmi W, Sharma K, Sarma P, Mamat R, Najafi G. Heat transfer and friction factor of water-based TiO_2 and SiO_2 nanofluids under turbulent flow in a tube. Int Commun Heat Mass Transf 2014;59:30–38. [CrossRef]
[8] Azmi W, Sharif M, Yusof T, Mamat R, Redhwan A. Potential of nanorefrigerant and nanolubricant on energy saving in refrigeration systems: A review. Renew Sustain Energy Rev 2016;69:415–428. [CrossRef]
[9] Gao E, Cui Q, Jing H, Zhang Z, Zhang X. A review of application status and replacement progress of refrigerants in the Chinese cold chain industry. Int J Refrig 2021;128:104–117.[CrossRef]
[10] Zhang S, Yu Y, Xu Z, Huang H, Liu Z, Liu C, et al. Measurement and modeling of the thermal conductivity of nanorefrigerants with low volume concentrations. Thermochim Acta 2020;688:178603. [CrossRef]
[11] Kumar MR, Meher RS, Kumari AS. Experimental investigations of effect of nano composites on performance of VCR system at variable capillary tube lengths. NanoWorld J 2022;8:28–35.
[12] Mohanraj M, Jayaraj S, Muraleedharan C, Chandrasekar P. Experimental investigation of R290/R600a mixture as an alternative to R134a in domestic refrigerators. Int J Therm Sci 2008;48:1036–1042. [CrossRef]
[13] Srinivas P, Chandra RP, Kumar MR, Reddy N. Experimental investigation of LPG as a refrigerant in domestic refrigerators. In: Proceedings of the International Conference on Recent Advances in Engineering Sciences (ICRAES-2014); 2014 Nov; Bangalore, India. MSRIT; 2014. p. 470–476.
[14] Pendyala S, Prattipati R, Raju AVSR. Optimization process of a Visi-Cooler using ternary mixtures of R134a and hydrocarbons. Int J Air-Cond Refrig 2017;25:1750019. [CrossRef]
[15] Colombo PM, Lucchini A, Molinaroli L. Experimental analysis of R1234yf and R1234ze(E) as drop-in replacements for R134a in water-to-water heat pumps. Int J Refrig 2020;115:18–27.[CrossRef]
[16] Bi S, Guo K, Liu Z, Wu J. Performance of a domestic refrigerator using TiO_2-R600a nano-refrigerant. Energy Convers Manag 2010;52:733–737.[CrossRef]
[17] Adelekan D, Ohunakin O, Gill J, Atiba O, Okokpujie I, Atayero A. Experimental investigation of a vapor compression refrigeration system with 15nm TiO_2-R600a nano-refrigerant. Procedia Manuf 2019;35:1222–1227. [CrossRef]
[18] Vamshi J, Anand K, Sharma A, Kumar A, Kumar S, Kotia A, et al. A review on the utilization of nanoparticles in refrigeration systems as nano-refrigerants and nano-lubricants. Mater Today Proc 2021;50:782–788. [CrossRef]
[19] Sheikholeslami M, Rezaeianjouybari B, Darzi M, Shafee A, Li Z, Nguyen TK. Application of nano-refrigerant for boiling heat transfer enhancement: An experimental study. Int J Heat Mass Transf 2019;141:974–980. [CrossRef]
[20] Babarinde TO, Akinlabi SA, Madyira DM. Enhancing the performance of vapor compression refrigeration systems using nano refrigerants: A review. IOP Conf Ser Mater Sci Eng 2018;413:012068. [CrossRef]
[21] Said Z, Rahman SM, Sohail MA, Bahman AM, Alim MA, Shaik S, et al. Nano-refrigerants and nano-lubricants in refrigeration: Synthesis, mechanisms, applications, and challenges. Appl Therm Eng 2023;233:121211. [CrossRef]
[22] Yousif SS, Al-Obaidi MA, Al-Muhsen NFO. Towards more efficient refrigeration: A study on the use of TiO2 and Al2O3 nanoparticles. Int J Heat Technol 2024;42:1251–1256. [CrossRef]
[23] Al-Tajer AM, Kramallah AA, Mohsen AM, Mahmoud NS. Experimental investigation of heat transfer of nanofluid in elliptical and circular tubes. Math Model Eng Probl 2021;8:665–671. [CrossRef]
[24] Katoch A, Razak FA, Suresh A, BS B, Gundabattini E. Performance analysis of nano-refrigerants used in the vapor compression refrigeration system using MATLAB-Simulink. Proc Inst Mech Eng Part C J Mech Eng Sci 2022;236:6948–6966. [CrossRef]
[25] Barza T, Gudeta D, Palani K. Experimental investigation on performance enhancement of vapor compression refrigeration (VCR) systems using nanorefrigerant [R-134a + ZrO2] at steady-state. J Mech Sci Technol 2023;37:6609–6615. [CrossRef]
[26] Zhang H, Zhou Q, editors. Big Data and Electric Mobility. 1st ed. CRC Press; 2025. [CrossRef]
[27] Secop. Practical application of refrigerants R600a and R290 in small hermetic systems. Available at: https://www.secop.com/fileadmin/user_upload/technical-literature/guidelines/application_guideline_r600a_r290_02-2018_desa610a202.pdf. Accessed on January 8, 2026.
[28] Demir DG, Demir MS, Demir AA. Titanium dioxide nanoparticles: Synthesis, characterization, and applications. J Nanomater 2018;2018:1–15.
[29] Siddiqui MRKMSH, Bhuiyan AGWGSMLSSM, Gupta ARATK. Mineral oil properties and its applications in lubrication. Lubrication Science 2013;25:263–275.
[30] Leong KC, Yang C, Murshed SMS. A model for the thermal conductivity of nanofluids – the effect of interfacial layer. J Nanopart Res 2006;8:245–254. [CrossRef]domestic refrigerator. Journal of Thermal Engineering 2024;10:1453–1464. [CrossRef]
[31] Mohamad B. Improving heat transfer performance of flat plate water solar collectors using nanofluids. J Harbin Inst Technol (New Ser) 2024. doi: 10.11916/j.issn.1005-9113.2024001. [Epub ahead of print].

[32] Qader FF, Mohamad B, Hussein AM, Danook SH. Numerical study of heat transfer in circular pipe filled with porous medium. Pollack Period 2023. doi: 10.1556/606.2023.00869. [Epub ahead of print]. [CrossRef]

[33] Qader F, Hussein A, Danook S, Mohamad B, Khaleel O. Enhancement of double-pipe heat exchanger effectiveness by using porous media and TiO2 water. CFD Lett 2023;15:31–42. [CrossRef]

[34] Shaik MH, Kolla S, Sairam YNV. Exploring low-GWP refrigerants for enhanced domestic refrigerator performance: A comprehensive investigation. J Therm Eng 2025;11:40–48. [CrossRef]

[35] Pardo-Cely D, Belman-Flores JM, Gallegos-Muñoz A, Rodríguez-Valderrama DA. Effect of refrigerant charge variation on the energy and thermal performance of a domestic refrigerator. J Therm Eng 2024;10:1453–1464. [CrossRef]

J Ther Eng, Vol. 12, No. 1, pp. 335−348, January, 2026

Journal of Thermal Engineering
Web page info: https://jten.yildiz.edu.tr
DOI: 10.14744/thermal.0001083

Research Article

Assessment of combustion, performance, and emissions in a direct injection compression ignition engine using blends of jatropha, karanja, waste cooking, sunflower, and palm oil methyl esters with diesel

Venkata Ramesh MAMILLA[1,*], G. Lakshmi Narayana RAO[2]

[1]*Department of Mechanical Engineering, Sri Vasavi Engineering College, Tadepalligudem, Andhra Pradesh,534101, India*
[2]*Department of Mechanical Engineering, QIS College of Engineering and Technology, Andhra Pradesh, 523272, India*

ARTICLE INFO

Article history
Received: 31 August 2024
Revised: 30 December 2024
Accepted: 31 December 2024

Keywords:
Performance; Combustion; Emission; Compression Ignition Engine; Diesel; Biodiesel

ABSTRACT

As prospective alternative fuels for diesel engines, the current study examines two edible oils, namely sunflower and palm oil, and three non-edible oils namely jatropha, karanja, and waste cooking oil. The transesterification process was used to produce methyl esters from Karanja oil, Jatropha oil, Sunflower oil, Palm oil, and Waste cooking oil. The physical properties of these methyl esters met the specifications of IS biodiesel standards and were found to be similar to those of conventional diesel. An experimental setup used a single-cylinder, air-cooled, four-stroke direct injection diesel engine with a power output of 4.4 kW to assess the fuels performance, emission and combustion characteristics with varying blends of the methyl esters (20%, 40%, 60%, 80%, and 100%). Peak pressure, ignition delay and heat release rate were assessed in the combustion analysis. The performance metrics assessed included brake thermal efficiency, while the exhaust emissions analyzed were nitrogen oxides, hydrocarbons, smoke, and carbon monoxide. The experimental outcomes were compared to baseline data from diesel fuel. The findings indicated that the low blends of 20% biodiesel of Jatropha oil methyl esters (JTME), Karanja oil methyl esters (KME), Palm oil methyl esters (POME), Sunflower oil methyl esters (SFOME) and Waste cooking oil methyl esters (WCOME) served as the effective alternative fuel for performance and emissions under full load conditions among all fuels tested.

Cite this article as: Mamilla VR, RAO GLN. Assessment of combustion, performance, and emissions in a direct injection compression ignition engine using blends of jatropha, karanja, waste cooking, sunflower, and palm oil methyl esters with diesel. J Ther Eng 2026;12(1):335−348.

INTRODUCTION

The growing industrialization and motorization across the globe have significantly increased the demand for petroleum products. Fuels from petroleum come from limited reserves that are predominantly found in specific areas of the world. As a result, countries without these resources are facing an exchange crisis, largely because of their dependence on crude oil imports. Therefore, it is

***Corresponding author.**
*E-mail address: maa_ram@yahoo.co.in

This paper was recommended for publication in revised form by Editor-in-Chief Ahmet Selim Dalkilic

Published by Yıldız Technical University Press, İstanbul, Turkey
Yıldız Technical University. This is an open access article under the CC BY-NC license (http://creativecommons.org/licenses/by-nc/4.0/).

crucial to investigate alternative fuels that can be produced from locally available materials. The rapid rise in fuel prices and the depletion of global hydrocarbon resources have compelled us to seek alternatives that can meet the surging energy demand while also safeguarding the environment by reducing harmful pollutants.

The current study focuses on non-edible vegetable oils. Karanja oil, which is native to India, has been for this investigation. Additionally, Jatropha oil is recognized globally as an ideal option for biodiesel production. The Indian government encourages the cultivation of these seeds by making use of plentiful wastelands found throughout the country. Sunflower and palm oils are used as cooking oils in some regions. However, WCO offers substantial benefits in terms of both availability and cost when compared to these oils. The amount of used cooking oil, which is often discarded after use, is considerable and remains largely untapped. This oil has significant potential for biodiesel production, especially in major urban areas of the country. Taking all these factors into consideration, Jatropha oil, Karanja oil, sunflower oil, palm oil, and waste cooking oil have been identified as viable sources for biodiesel production.

Phan et al. [1] carried out an experiment to study the transesterification of waste cooking oil at reaction temperature is up to 60° C. The methanol to WCO molar ratio ranged from 5:1 to 12:1, with KOH catalyst concentrations varying between 0.5 wt% and 1.5 wt% of the waste cooking oil. The results showed that the optimal biodiesel yield, ranging from 88% to 90%, was obtained with methanol to WCO ratio of 7:1 to 8:1, at temperatures between 30°C and 500°C, for a duration of 80 to 90 minutes, using a 0.75 wt% KOH concentration. The physical properties of the biodiesel and its blends were evaluated and found to meet the EN14214 standard. Nurun Nabi et al. [2] examined a single-cylinder, water-cooled, naturally aspirated, direct-injection diesel engine and discovered that diesel-NOME blends led to lower levels of CO and smoke emissions, although NOx emissions increased. The ester from this oil offers an eco-friendly alternative fuel for diesel engines, helping to address the food versus fuel issue. Brake thermal efficiency (BTE) improved steadily with increasing engine speed up to 1000 rpm, after which it began to decline as brake mean effective pressure (BMEP) rose. Carbon monoxide levels remained nearly constant and were 25 ppm lower than those of diesel. As BMEP increased, NOx emissions initially rose, then stabilized temporarily, and eventually exceeded the levels of neat diesel by approximately 5%.

In a four-stroke CI engine, Razzaq et al. [3] examined the performance and emissions properties of biodiesel blends containing dimethyl carbonate additions and graphene oxide nanoplatelets. According to the study, adding these compounds reduced pollutants while also enhancing engine performance. At a blend ratio of 20% biodiesel, 10% dimethyl carbonate, and 0.1% graphene oxide nanoplatelets, the largest reduction in emissions was noted. According to the study, using these compounds may prove to be a viable strategy in the future for lowering emissions and enhancing engine performance.

Alruqi et al. [4] mixed diesel, diethyl ether, and algae biodiesel in varying amounts and tested the mixture on a diesel engine to examine the engine's performance and emission characteristics. The results show that the additions raised the net heat release rate, peak pressures, and BTE. On the other hand, NOx increased as a result. A contemporary supervised machine learning technique called Gaussian process regression was applied to create a model for the engine's performance and exhaust pollutants. After the model and experimental findings were compared, it was discovered that the primary absolute error, which ranged from 0.001 to 2.591, was extremely small.

Sharma [5] investigated the impact of the additive di-tert butyl peroxide (DTBP) on engine performance and emissions. The effects of DTBP-biodiesel blends on engine performance and emissions are predicted and optimized in this study using the multi-objective response surface methodology. The study sheds light on the ideal blend ratio for enhancing engine performance and lowering emissions, and the results demonstrate that DTBP significantly affects combustion and emission parameters.

In trials on diesel engines, Joseph Shobana Bai et al. [6] used wheat germ oil as fuel and added hydrogen in various compositions, such as 5%, 10%, and 15% energy share. Compared to pure wheat germ oil, the addition of 15% energy sharing via hydrogen produced 33% more NOx emissions. But the 15% energy contribution of hydrogen led to a 15% decrease in smoke emissions.

Karpanai Selvan et al. [7] conducted extensive experiments with a diesel engine using various biodiesel blends that included ethanol, cottonseed oil, eucalyptus oil, and micro- and macroalgae oils. The experiments were performed on a single-cylinder diesel engine operating at 1500 RPM, with a compression ratio of 18:1 and a load of 3.75 kW. At 50% load, the emissions of CO2, CO, NOx, and smoke were reduced by 2.3%, 22%, 0.97%, and 6.54%, respectively. The A010D blend, in particular, demonstrated potential as a viable option for use in diesel engines at half load.

Puhan S. et al. [8] conducted a study on a high linolenic linseed oil methyl ester in a diesel engine operating at a constant speed with three different fuel injection pressures (200 bar, 220 bar, and 240 bar). The primary objective of the research was to investigate how varying injection pressures affect engine performance, emissions, and combustion characteristics. At 240 bar, thermal efficiency was found to be comparable to diesel, with reduced CO, HC, and smoke emissions, but an increase in nitrogen oxides compared to diesel.

In a study by S. Mahla et al. [9] the performance and exhaust emissions of a dual fuel engine using various blends of diethyl ether, biogas, and diesel were evaluated as a new fuel alternative. The research explored different proportions of diethyl ether (10%, 15%, and 20%) and biogas flow rates

(10, 20, and 30 LPM) combined with conventional diesel fuel at varying engine loads (20%, 60%, and 100%). The study predicted a brake thermal efficiency of 22%, hydrocarbon (HC) emissions at 56 ppm, carbon monoxide (CO) emissions at 0.09%, nitrogen oxides (NOx) emissions at 102 ppm, and smoke at 24%. The high desirability value of 0.74 from the derived models demonstrated that the response surface methodology could effectively optimize and model the performance of a three-fuel diesel engine. Suresh Vellaiyan [10] investigated the combustion and emission characteristics of a diesel engine operating on soybean biodiesel. The study explored the effects of incorporating carbon nanotube (CNT) nanoparticles and water emulsion into the fuel. The results showed that these additives improved engine performance, reduced emissions, and enhanced combustion efficiency. Additionally, the research found that diesel-soybean biodiesel blends with zinc oxide nanoparticles coated with cerium resulted in lower engine performance and emissions. The study suggests that using water emulsion and nanoparticle additives in biodiesel engines could be an effective strategy to increase efficiency and reduce emissions.

Nalgundwar et al. [11] investigated the performance and emission tests on a single-cylinder engine using a dual biodiesel blend a mixer of two distinct types of biodiesel, namely palm and jatropha. The results for a lesser blend of biodiesel revealed a little loss in BSFC, while a larger blend of biodiesel indicated an average gain in brake thermal efficiency (BTE) of up to 15% and a decrease in exhaust gas temperatures. The CO reduction ranged from 7.1% to 14.5% depending on the blend of biodiesel used. On the other hand, NOx emissions rose by 9.2% with higher biodiesel ratios.

Saini Mahesh Chand et al. [12] investigated on impact of biodiesel blends on performance, emissions and waste heat recovery of diesel engine driven cogeneration system. Diesel fuel has the highest brake thermal efficiency and the lowest brake specific fuel consumption (BSFC). B20 has the highest brake thermal efficiency and the lowest BSFC among all blends of biodiesel. Also, B20 has better emission characteristics than all other blends of biodiesel. The exhaust gas temperature and waste heat recovery increase with the percentage of biodiesel in the blends.

M. P. Joshi et al.[13] investigated on Combustion Analysis of CI Engine Fuelled with Algae Biofuel Blends. The brake thermal efficiency showed decreasing trend (upto 5%) whereas specific fuel consumption (upto 7%) and exhaust gas temperature (upto 3%) showed increasing trend for algae biofuel blends compared to diesel. Reduction in hydrocarbon (upto 28%) and carbon monoxide (upto 22%) emission was noted for algae biofuel blends along with a marginal increase in NOx (upto 13%) emissions.

Transesterification

Methanol, NaOH, and raw oil are needed for the transesterification of vegetable oil to produce methyl esters. For every 1000 ml of raw oil, dissolve 100 ml of methanol and 3.75 grams of sodium hydroxide. Transesterification, on the other hand, is an equilibrium reaction that needs sufficient alcohol to propel it extremely nearly to completion. Methyl esters were produced via a chemical reaction between vegetable oil and alcohol in the presence of a catalyst. A byproduct of the transesterification reaction was glycerol.

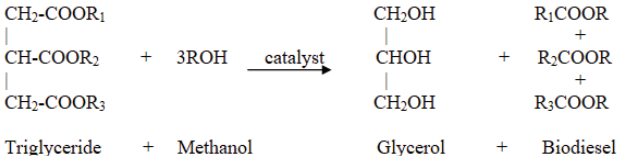

Where R1, R2, & R3 are long chain hydrocarbons. After continuously stirring the mixture, it was let to settle in a separating funnel due to gravity. After a whole day of gravity settling, two separate strata emerge. Glycerol formed the lower layer, while the ester formed the upper layer. The lowest layer was carefully separated.

In order to eliminate the catalyst contained in the separated ester, it was combined with warm water and let to settle under gravity for a further 24 hours. Water was used to dissolve the catalyst, separate it, and extract the moisture. Then, different concentrations of mineral diesel (20%, 40%, 60%, 80%, and 100%) were combined with methyl ester to create biodiesel blends that could be utilized in CI engines to perform different engine tests.

Test Procedure

The engine was fueled with biodiesel, conventional petroleum diesel, and blends containing 20%, 40%, 60%, and 80% biodiesel. When switching fuels each time, the fuel lines were cleaned, and the engine was allowed to stabilize in order to ascertain optimal temperature for at least thirty

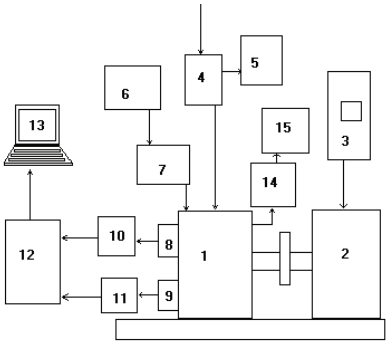

1. Diesel engine
2. Swinging field electrical dynamometer
3. Dynamometer controls
4. Air box
5. U-tube manometer
6. Fuel tank
7. Fuel measurement flask
8. Pressure pick up
9. TDC position sensor
10. Charge amplifier
11. TDC amplifier circuit
12. A/D card
13. Personal computer
14. Exhaust gas analyzer
15. AVL smoke meter

Figure1a. Layout of Engine Test Rig.

Figure 1b. Experimental setup.

minutes under the new conditions. The experiments were conducted at various load levels (0%, 25%, 50%, 75%, and 100% of the rated load of 4.4 kW).

RESULTS AND DISCUSSION

Cylinder Pressure Variation

For diesel and blends of 20B, 40B, 60B, 80B, and 100% of KME, JTME, SFOME, POME, and WCOME are shown in figures 2 to 6. The pressure variation follows same trend with all the methyl esters of 20B under all the loads at different crank angles.

Three separate zones exists:

Zone I: Compared to diesel, the cylinder pressure for biodiesel and its blends is higher from the beginning of combustion until 40 bTDC. In this area, the blend's methyl ester proportion rises in tandem with the cylinder pressure.

Zone II (40 bTDC to 100 aTDC): For all methyl ester mixes, the cylinder pressure is reduced in this zone when compared to diesel. This is mostly because methyl esters and their mixes have lower heat releases because of their lower calorific values. Because methyl ester-operated engines' exhaust gas has a higher specific heat capacity than diesel, it absorbs more heat energy, which lowers the gas's high temperature and pressure in the cylinder.

Region III (10 aTDC): Because of the delayed combustion, the biodiesel and its blends have a somewhat lower pressure in the cylinder.

Additionally, a minor shift away from TDC is noted in the crank angle where maximum pressure is reached. For instance, the peak pressure for diesel (74.629 bar), 20B KME (70.215 bar), 40B KME (70.847 bar), 60B KME (70.861 bar), 80B KME (70.991 bar), and KME 70CA aTDC (69.554 bar) all occur at 80CA aTDC at rated power (4.4 kW). Figure 45 displays the following: 20B KME (70.215 bar), 20B WCOME (67.743 bar), 20B JTME (69.166 bar), 20B POME (69.683 bar), and 70CA aTDC 20B SFOME (69.638 bar). This data relates to diesel.

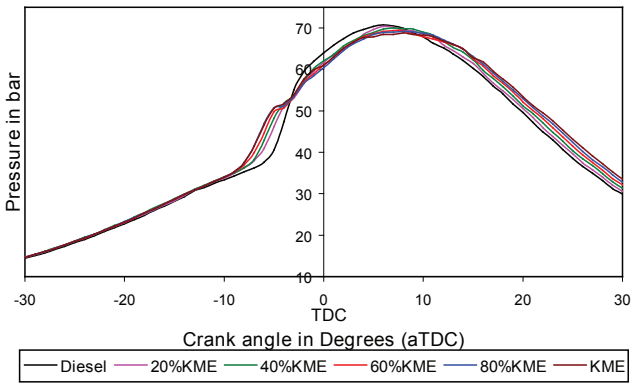

Figure 2. Diagram of pressure and crank angle for KME and its blends.

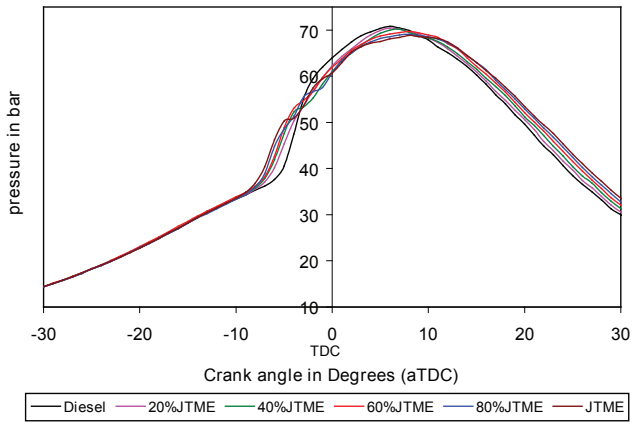

Figure 3. Diagram of pressure and crank angle for JTME and its blends.

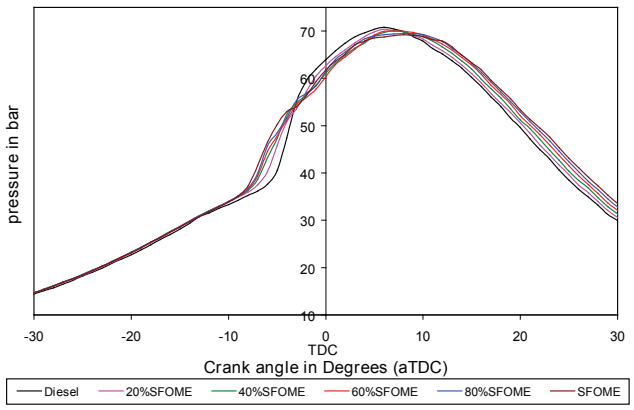

Figure 4. Diagram of pressure and crank angle for SFOME and its blends.

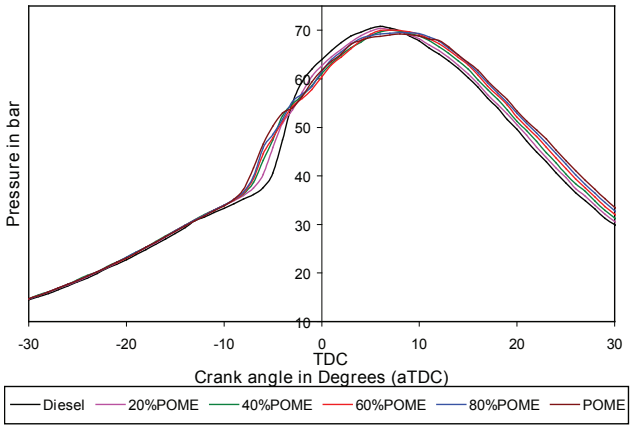

Figure 5. Diagram of pressure and crank angle for POME and its blends.

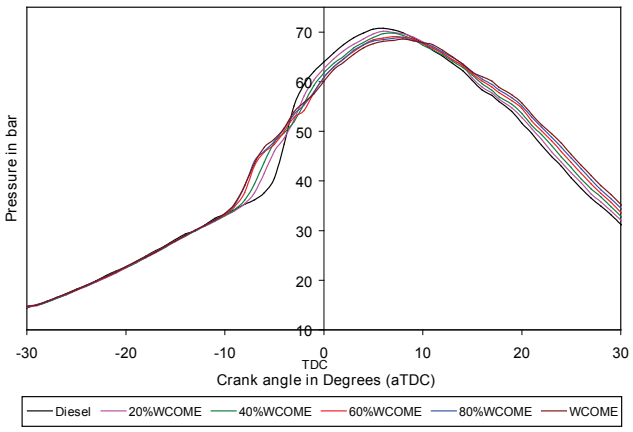

Figure 6. Diagram of pressure and crank angle for WCOME and its blends.

Heat Release Rate (Q)

Figures 7-11 illustrate the variations in heat release rates for methyl esters and their blends in comparison to diesel at rated power. The heat release rate curves of methyl esters, diesel, and their mixtures exhibit comparable trends, as may be observed. Diesel has a higher peak heat release rate than methyl esters and their mixes. According to Figure 8, the ignition delays at rated power for diesel and JTME at 20%, 40%, 60%, 80%, and 100% are, respectively, 14.650, 14.420, 14.20, 13.80, 13.60, and 150 respectively. It is observed that for blends of JTME, the delay period at rated power decreases as their fraction in the mix increases.

Consequently, when the proportion of methyl ester in the blend rises relative to diesel, the peak heat release rate falls and happens sooner for methyl esters and their mixes.

The viscous nature of the larger fatty acid components in methyl esters delays the combustion. This leads to all methyl esters and their blends exhibiting higher heat release rates compared to diesel during the latter part of the combustion process.

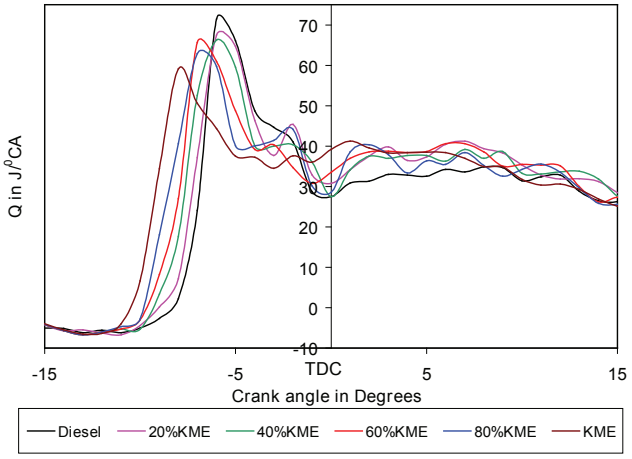

Figure 7. Rate of heat release comparison for diesel and KME mixes at rated load.

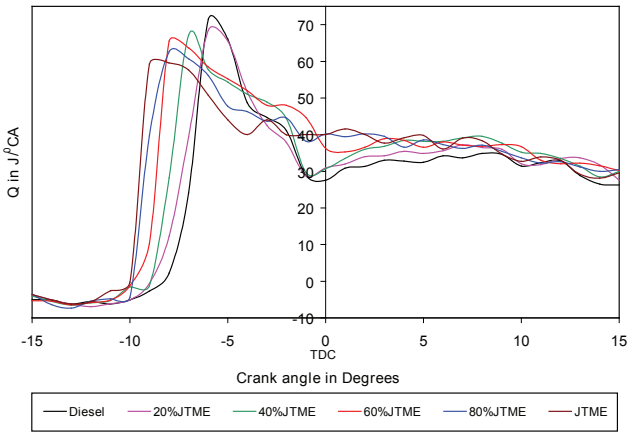

Figure 8. Comparison of heat release rates for diesel and JTME blends at rated load.

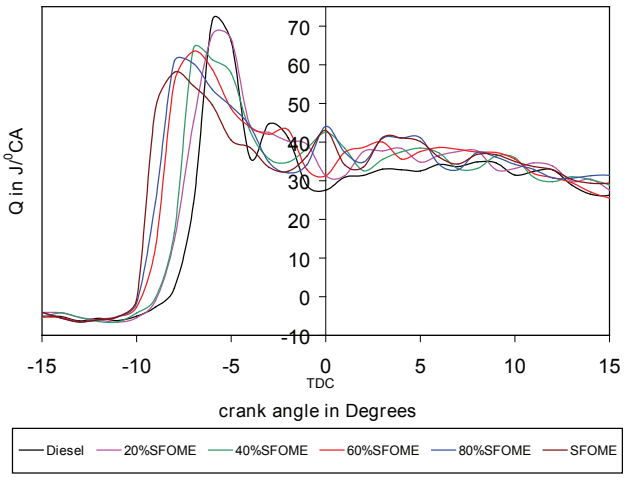

Figure 9. Rate of heat release comparison for diesel and SFOME mixes at rated load.

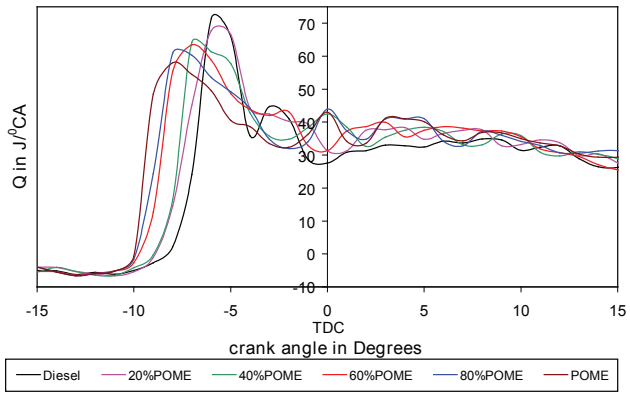

Figure 10. Comparison of heat release rates for diesel and POME blends at rated load.

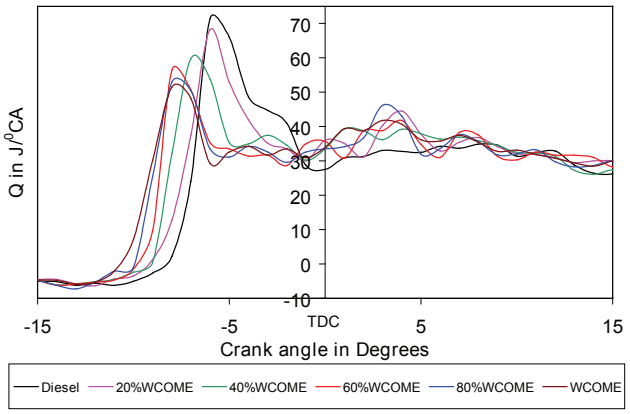

Figure 11. Comparison of heat release rates for diesel and WCOME blends at rated load.

Ignition Delay (ID)

The ignition delay of a fuel plays a pivotal role in determining the knocking behavior of diesel engines. This delay is influenced by multiple factors such as the engine's compression ratio, inlet pressure, injection parameters, and the inherent properties of the fuel itself. Cetane number (CN) signifies the quality of the fuel, as the CN of a fuel increases, the ignition delay tends to decrease, and the opposite holds true. Figures 12-16 illustrate a comparison between the ignition delays of different methyl ester blends under varying load conditions and that of standard diesel.

It is clear that pure esters exhibit the shortest ignition delay compared to their blends and diesel. Additionally, methyl esters and their blends have a significantly shorter ignition delay than diesel, with the delay decreasing as the proportion of methyl ester in the blend increases. For instance, at full load (4.4 kW), the delay decreases by 1.9%, 3.5%, and 5.1%. In comparison to diesel, the percentages for 20%, 40%, 60%, 80%, and JTME, respectively, are 7.5% and 9.2%.

Esters undergo chemical reactions and polymerization during injection because the air temperature in the cylinder is rather high at that moment. This causes the injection characteristics to differ from those of diesel. Esters have higher viscosities, but when their higher fatty acids split, lighter molecules, or volatile matter, are created.Larger dispersion and a shorter ignition delay are thus produced by these lighter combinations. Reduced fuel buildup before ignition leads to a reduced rate of heat release when the ignition delay is lowered.

This shows that because methyl esters ignite more quickly than diesel oil, they have greater cetane numbers in their mixes. Additionally, it is noted that when brake power increases, ignition delay for all test fuels reduces. This is because with greater braking powers, there is less dilution of exhaust gas and a higher temperature on the combustion chamber wall.

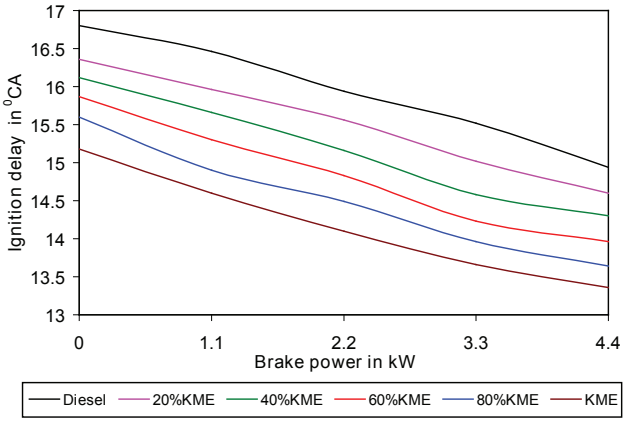

Figure 12. Analysis of KME/diesel blends ignition delays.

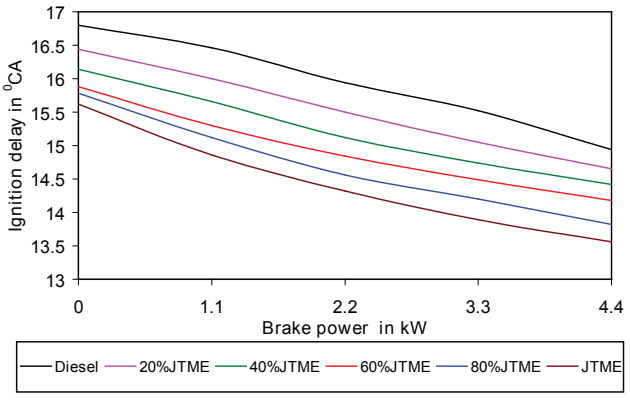

Figure 13. Analysis of JTME/diesel blends ignition delays.

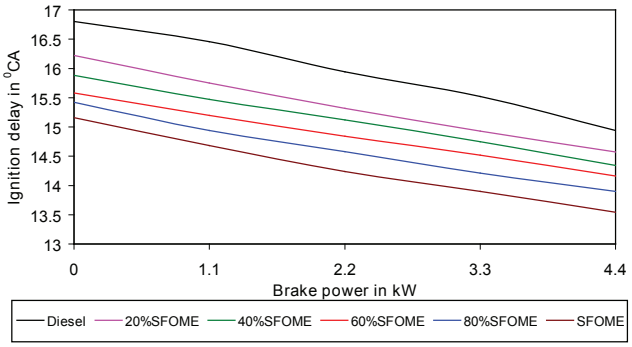

Figure 14. Analysis of SFOME/diesel blends ignition delays.

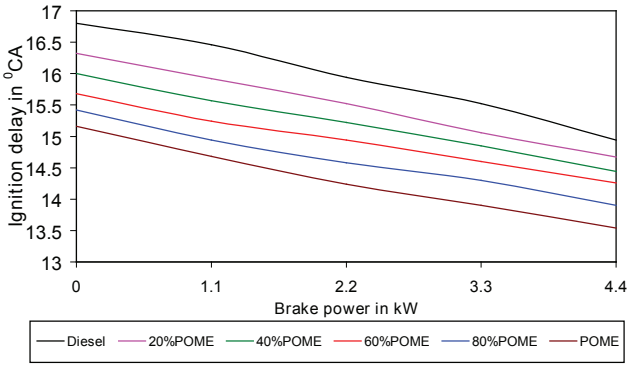

Figure 15. Analysis of POME/diesel blends ignition delays.

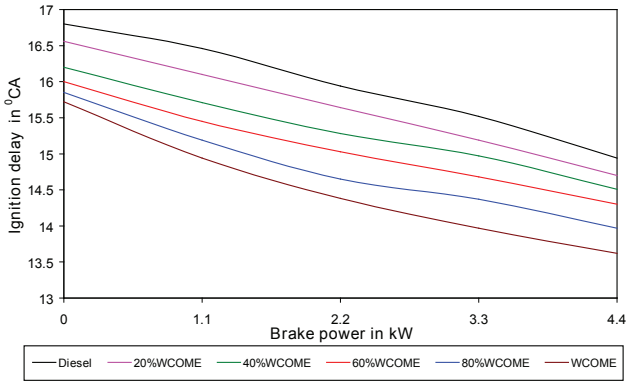

Figure 16. Analysis of WCOME/diesel blends ignition delays.

Brake Thermal Efficiency (BTE)

Figures 17 to 22 display the changes in brake thermal efficiency for the different test fuels. For every test fuel, the brake thermal efficiency rises as the braking power does. Methyl esters and their mixtures have a somewhat worse brake thermal efficiency than diesel at all loads. For instance, the brake thermal efficiencies for diesel, 20% JTME, 40% JTME, 60% JTME, 80% JTME, and pure JTME at rated power (4.4 kW) are 33.36%, 32.8% (a decrease of 0.56%), 31.6% (a decrease of 2%), 31.22% (a decrease of 2.14%), 30.87% (a decrease of 2.49%), and 29.37% (a decrease of 3.99%), respectively. The reduction in braking thermal efficiency of JTME blends in comparison to diesel is indicated in brackets. When compared to diesel, the highest drop for different JTME blends at rated power is only 3.99%.

Because methyl esters and their mixes have a shorter ignition delay when the engine is run continuously with injection advance, combustion starts well before TDC. As a result, the engine's brake thermal efficiency is decreased and compression work is increased. When the majority of the heat is discharged near TDC, the efficiency is at its highest. For methyl esters and their mixes, the onset of heat release happens well in advance of TDC. Lowerthermal efficiency follows from a greater departure from the ideal cycle. The same pattern is seen in blends of different methyl esters.Figure.22 compares the braking thermal efficiency of Jatropha methylester (JTME) tothat of methyl esters of karanja, sunflower, palm, and waste cooking.

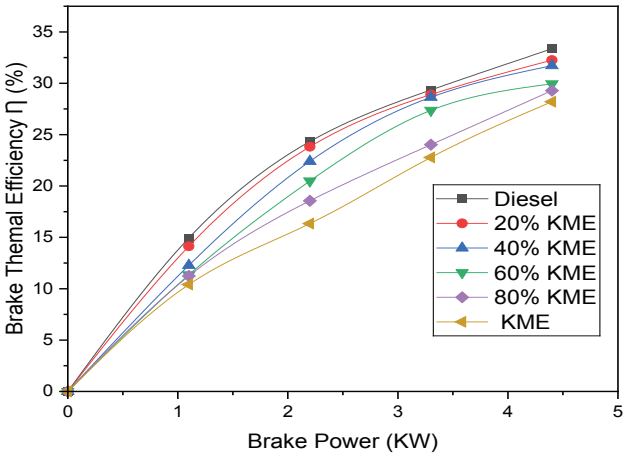

Figure 17. Brake thermal efficiency comparison for blends of KME and diesel.

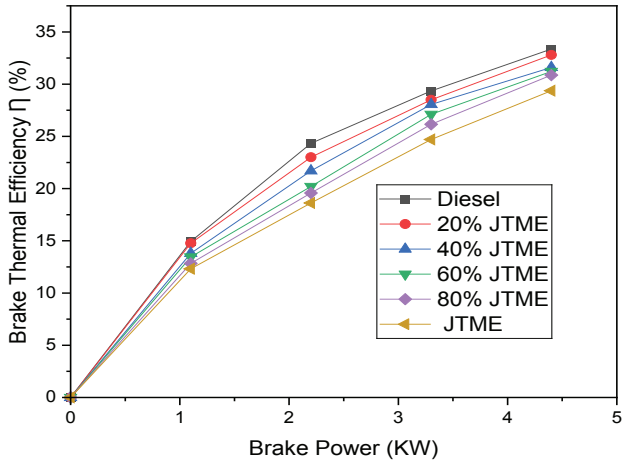

Figure 18. Brake thermal efficiency comparison for blends of JTME and diesel.

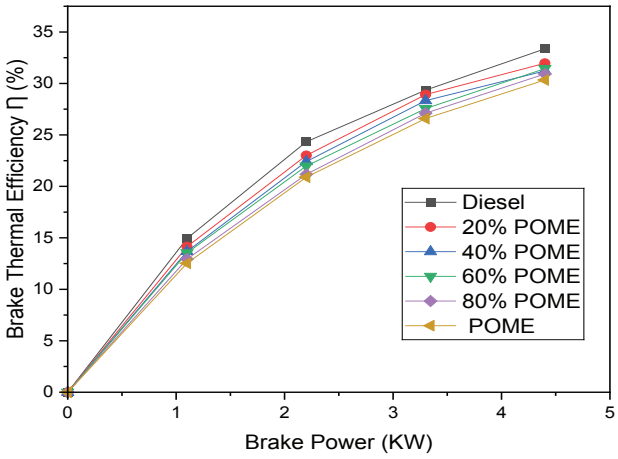

Figure 19. Brake thermal efficiency comparison for blends of POME and diesel.

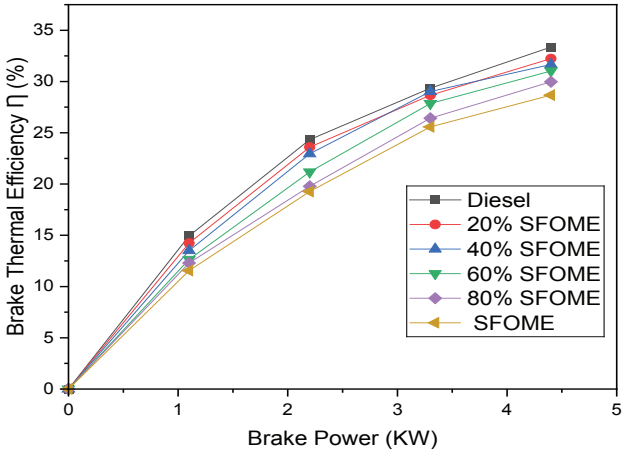

Figure 20. Brake thermal efficiency comparison for blends of SFOME and diesel.

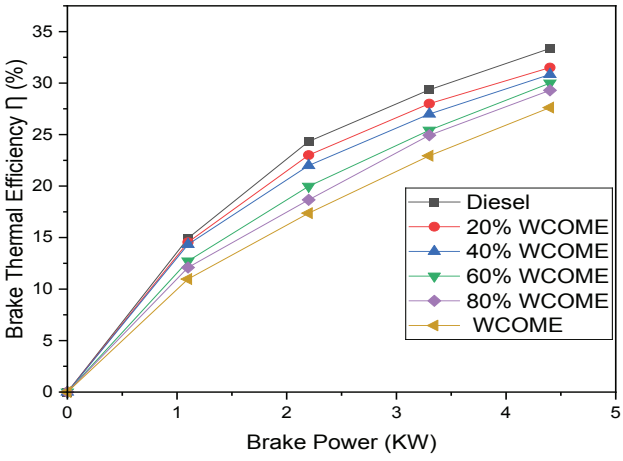

Figure 21. Brake thermal efficiency comparison for blends of WCOME and diesel.

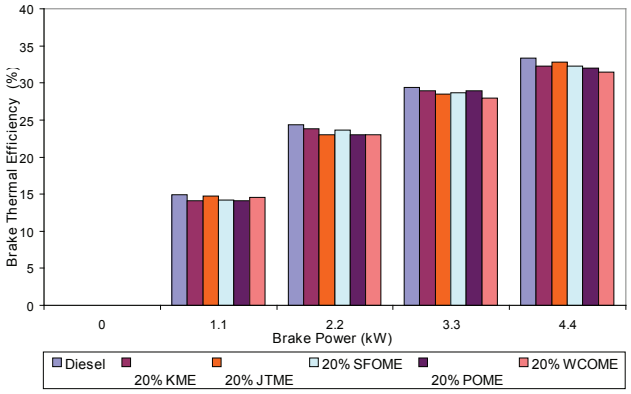

Figure 22. Brake Power Vs Brake Thermal Efficiency for B20 blends of all methyl esters/diesel

Carbon Monoxide (CO) Emissions

Figures 23 to 27 illustrate the variation in CO emissions for different esters and their mixes at varying braking power. Diesel engines typically have minimal CO emissions since they run on lean mixes. It has been noted that at all brake powers, diesel emits more CO than any esters or their mixtures. Esters contain oxygen and hence their blends have higher oxygen availability for CO oxidation than diesel because of the ester's inherent oxygen content, which lowers CO emissions. According to figure 28, the percentage of CO in the exhaust gas is 0.24%, 0.23%, 0.21%, 0.19%, and 0.16% for 20% KME, 40% KME, 60% KME, 80% KME, and Karanja methyl esters (KME) at rated power (4.4 kW), respectively. Consequently, CO emissions, which are already minimal in diesel engines, are further decreased with the use of methyl ester and its blends. As the proportion of methyl ester in the fuel increases, the percentage of CO emissions consistently declines. This pattern is also observed with blends of other methyl esters.

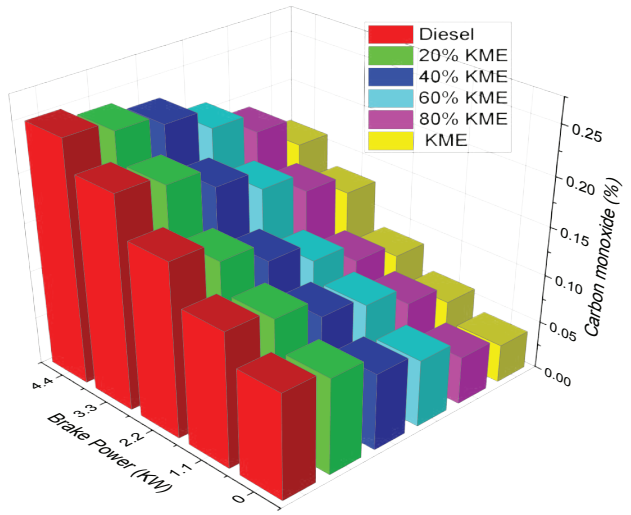

Figure 23. CO comparison for diesel and KME blends.

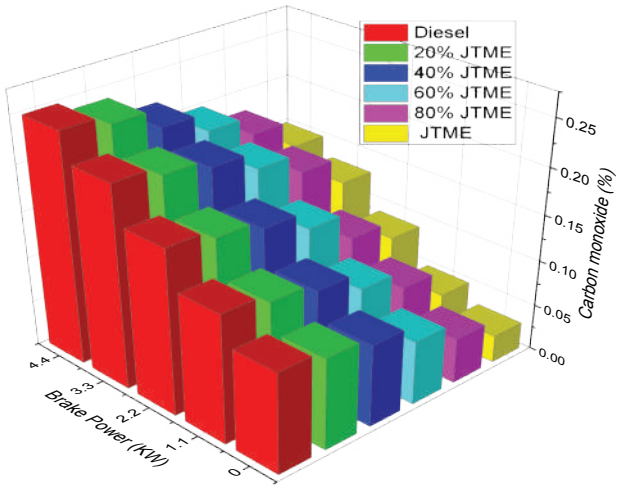

Figure 24. CO comparison for diesel and JTME blends.

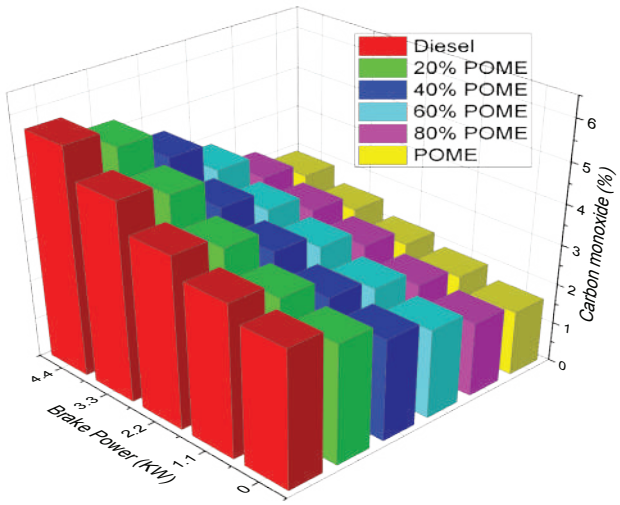

Figure 25. CO comparison for diesel and POME blends.

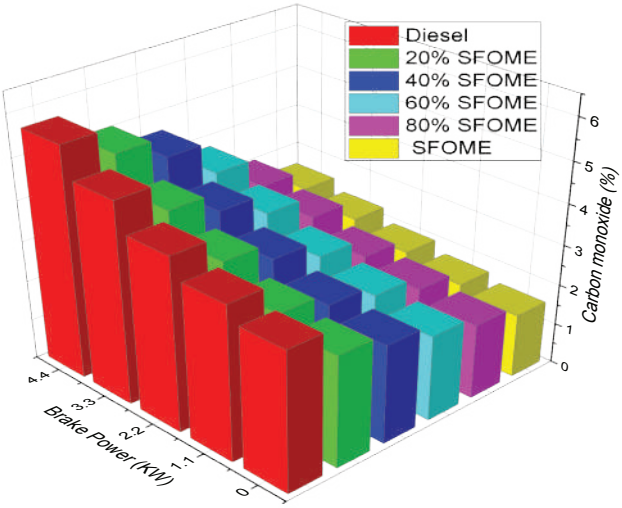

Figure 26. CO comparison for diesel and SFOME blends.

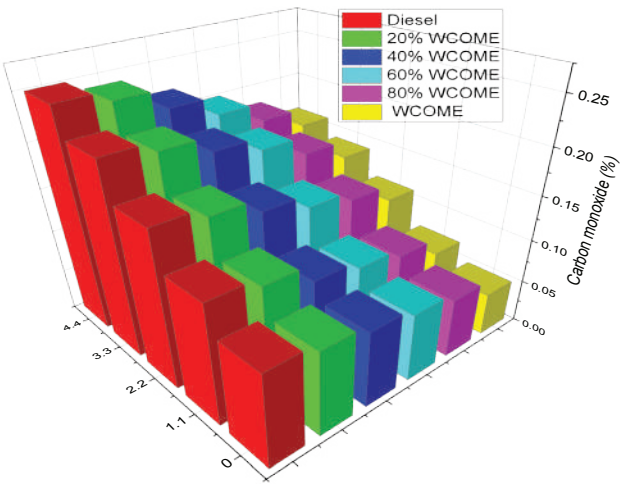

Figure 27. CO comparison for diesel and WCOME blends.

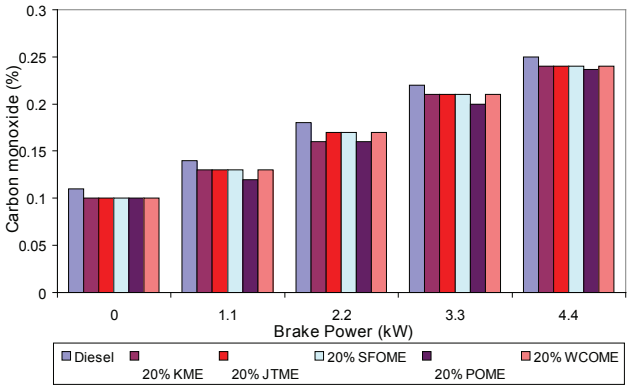

Figure 28. Brake Power Vs Carbon monoxide for B20 blends of all methyl esters/diesel.

Hydrocarbon (HC) Emissions

Figures 29 to 33 depict the variation in HC emissions with brake power for different methyl ester blends. It is clear that as the load increases, HC emissions rise for all the tested fuels, likely due to a richer fuel mixture at higher brake power. Compared to diesel, methyl esters and their blends produce significantly lower HC emissions across all load conditions. Adding methyl ester to diesel increases the oxygen content thereby enhanced combustion, resulting in reduced HC emissions. As the methyl ester content in the fuel increases, HC emissions decrease substantially.

Figure 34 shows that at rated power (4.4 kW), HC emissions are 45 ppm, 41 ppm, 37 ppm, 34 ppm, and 31 ppm for 20% KME, 40% KME, 60% KME, 80% KME, and pure Karanja methyl ester (KME), respectively, compared to 48 ppm for diesel. A similar trend is observed for blends of other methyl esters.

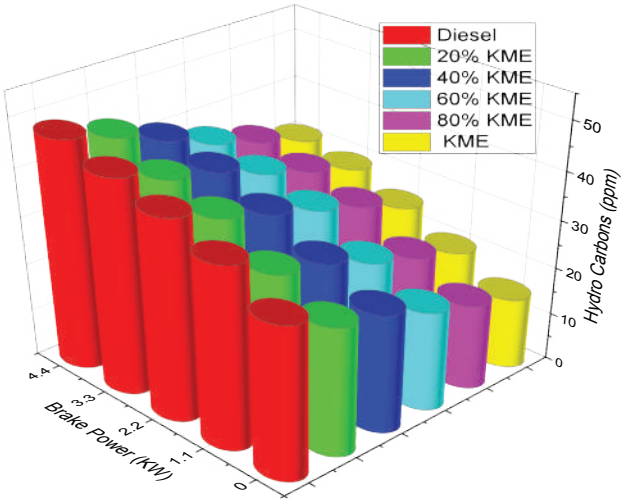

Figure 29. Comparing HC for blends of KME and diesel.

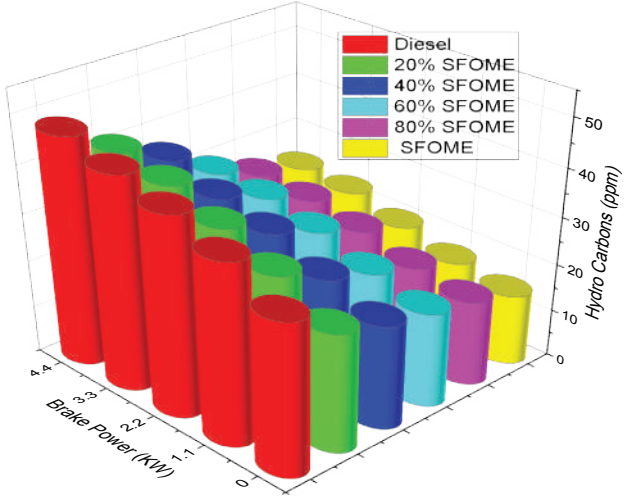

Figure 32. Comparing HC for blends of SFOME and diesel.

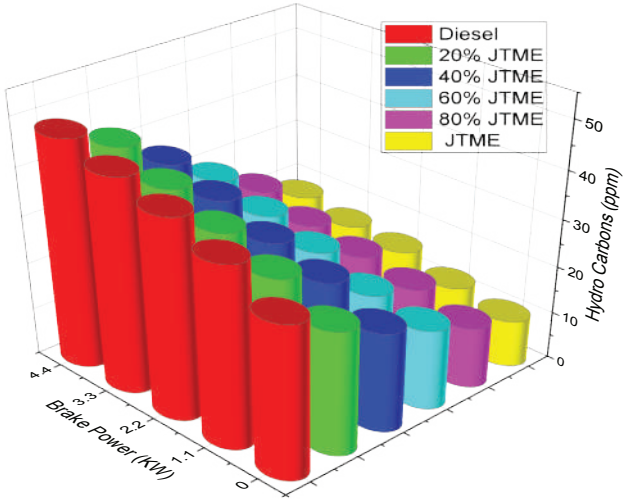

Figure 30. Comparing HC for blends of JTME and diesel.

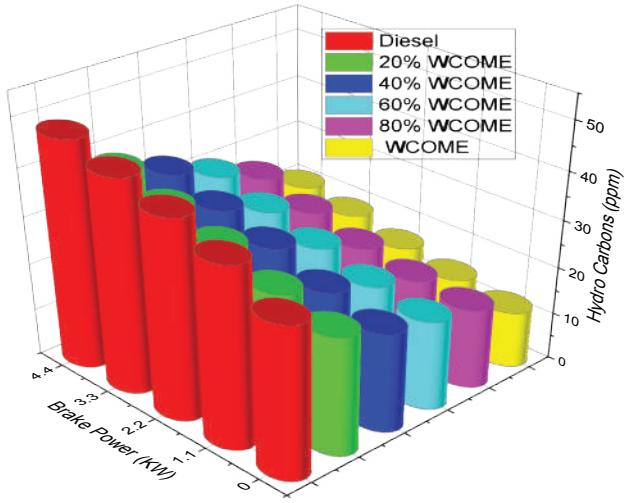

Figure 33. Comparing HC for blends of WCOME and diesel.

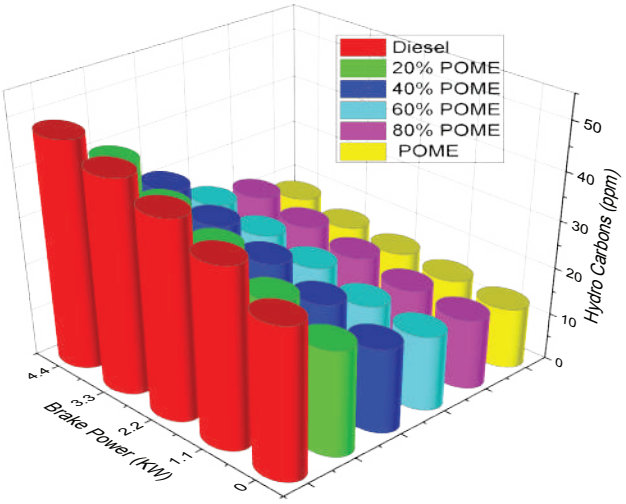

Figure 31. Comparing HC for blends of POME and diesel.

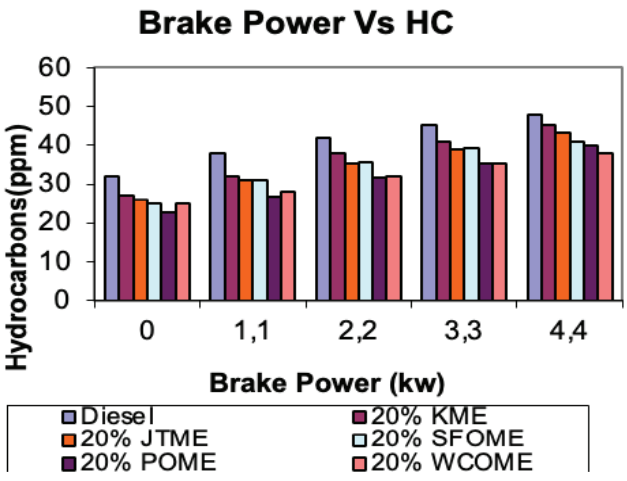

Figure 34. Brake Power Vs HC for B20 Blends of all methyl esters/diesel.

Nitrogen Oxide (NOx) Emissions

Figures 35 to 39 compare the variations in NOx emissions with brake power for different methyl esters and their blends in relation to diesel. For every test fuel, it has been found that NOx emissions rise as power increases. This is because when there is a load, the amount of fuel consumed increases, raising the temperature of combustion. Nitrogen oxide (NO_X) emissions are seen to increase with a rise in the fuel's methyl ester content at any given brake power. Compared to diesel, methyl esters have more oxygen available for the production of NOx. As a result, when the blend's methyl esters proportion rises, so do the NO_X emissions. Figure.35 shows that at rated power (4.4 kW), NOx emissions are 20%, 40%, 60%, 80%, and Karanja methyl esters (KME) at 534 ppm, 570 ppm, 595 ppm, 620 ppm, and 665 ppm, respectively, whilst diesel emissions are 510 ppm.

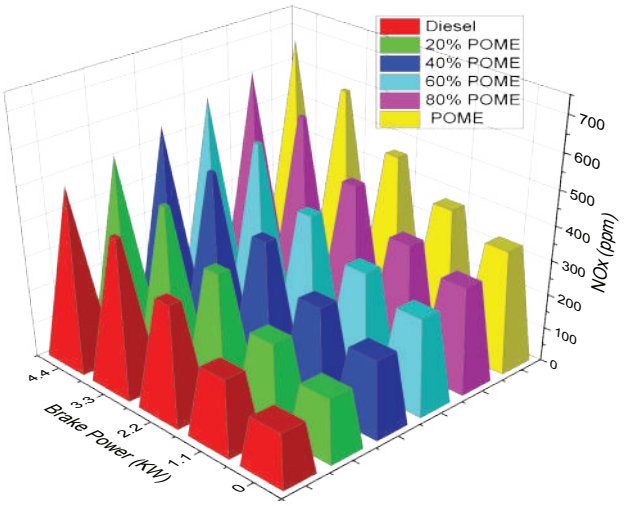

Figure 37. Nitrogen oxide comparison for POME/diesel blends.

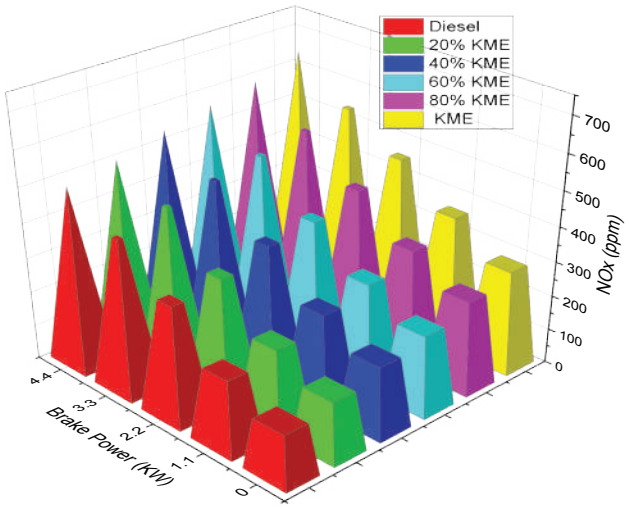

Figure 35. Nitrogen oxide comparison for KME/diesel blends.

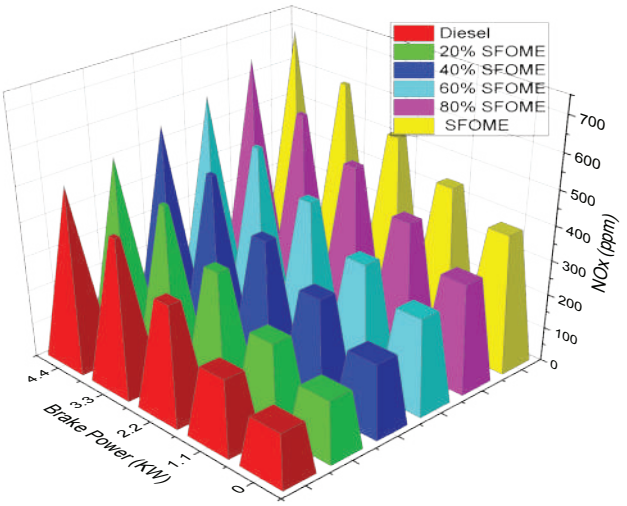

Figure 38. Nitrogen oxide comparison for SFOME/diesel blends.

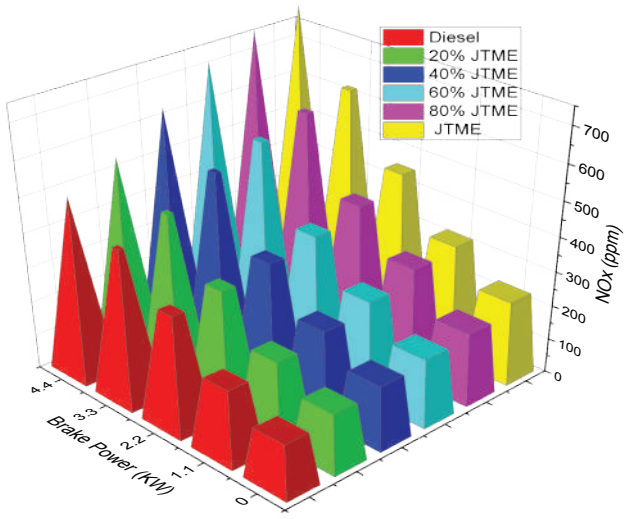

Figure 36. Nitrogen oxide comparison for JTME/diesel blends.

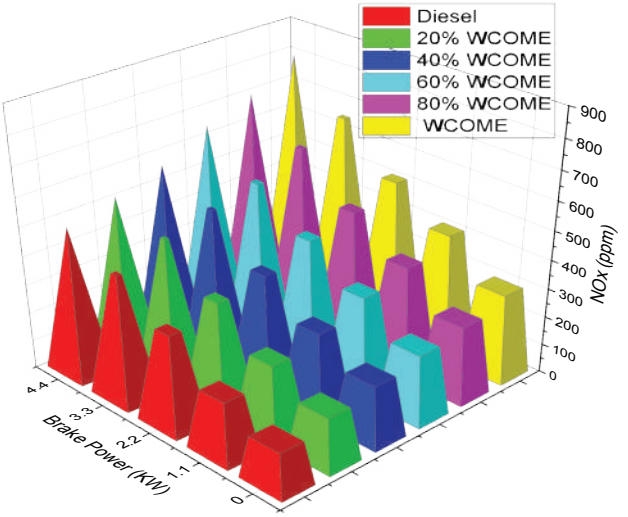

Figure 39. Nitrogen oxide comparison for WCOME/diesel blends.

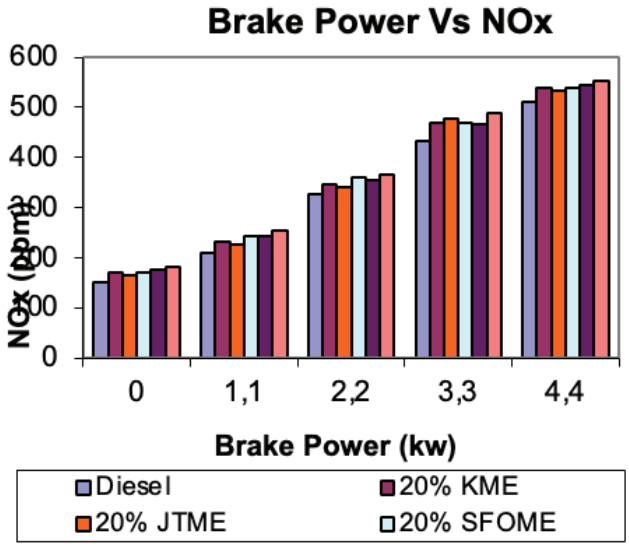

Figure 40. Brake Power Vs nitrogen oxides for B20 Blends of all methyl esters/diesel.

Smoke Density

Figures 41 to 45 illustrate how the smoke density varies for different methyl ester blends at varying brake powers. These figures indicate that as the proportion of methyl ester in the fuel blend increases, smoke density decreases. At rated load, smoke density for 20% KME, 40% KME, 60% KME, 80% KME, and pure KME is 126, 112, 96, 82, and 68 mg/m^3, respectively, as shown in Figure 41. Methyl esters increased oxygen content and reduced aromatic and short-chain paraffin hydrocarbon content are responsible for their particulate-reducing properties. For other methyl esters, a similar pattern is seen.

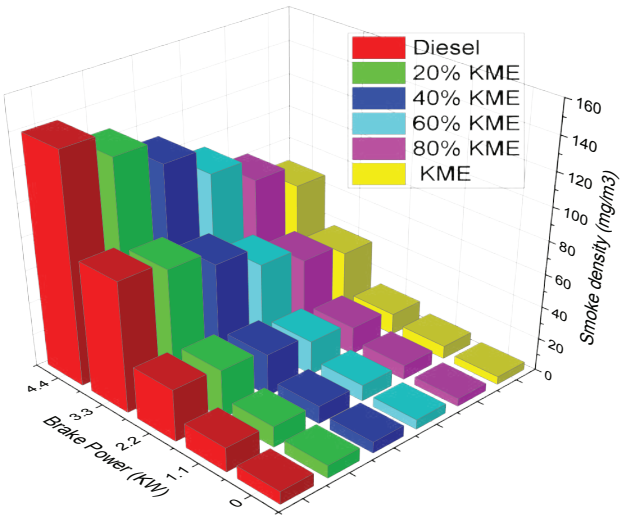

Figure 41. Comparison of the smoke density for blends of KME and diesel.

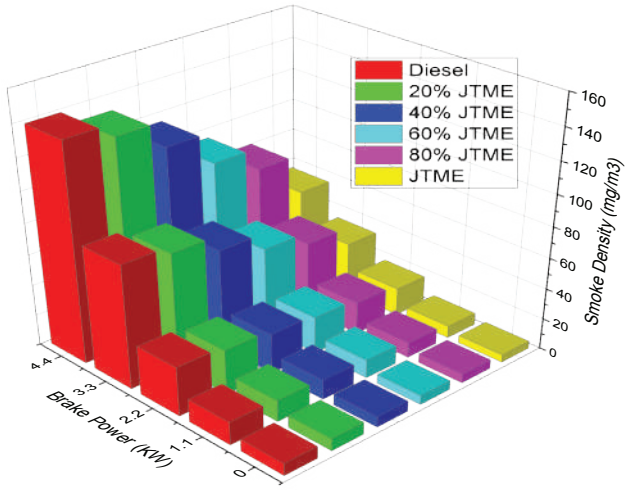

Figure 42. Comparison of the smoke density for blends of JTME and diesel.

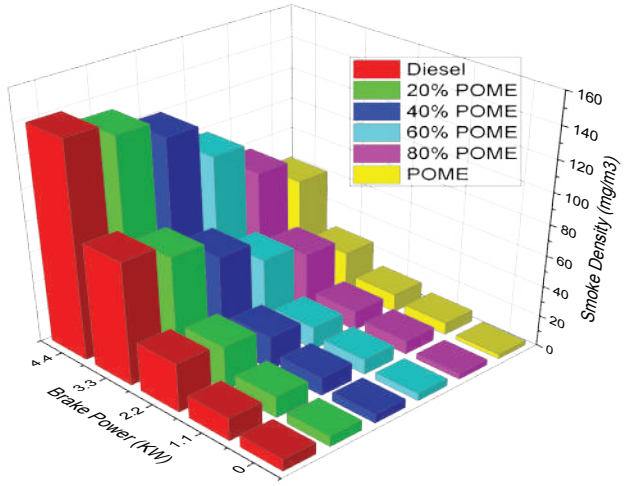

Figure 43. Comparison of the smoke density for blends of POME and diesel.

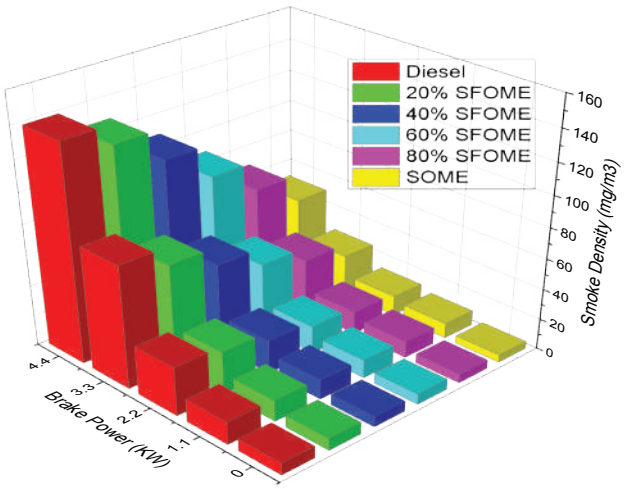

Figure 44. Comparison of the smoke density for blends of SFOME and diesel.

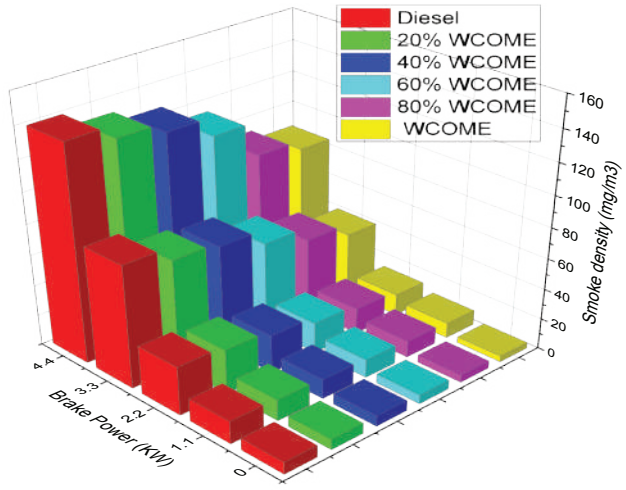

Figure 45. Comparison of the smoke density for blends of WCOME and diesel.

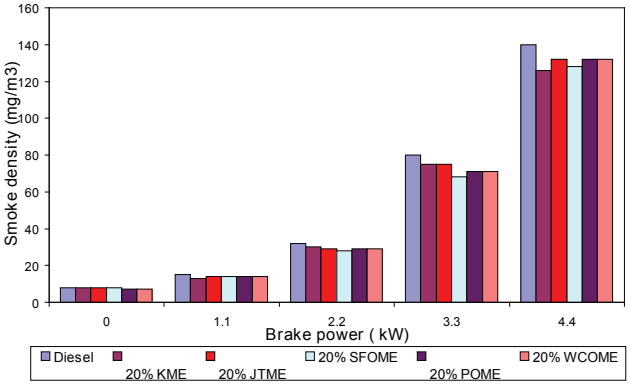

Figure 46. Brake Power Vs Smoke density for B20 Blends of all methyl esters/diesel.

CONCLUSION

In conclusion, the current study describes how to prepare methyl esters from particular vegetable oils and forecasts how well they will burn, operate, and emit when used in C.I. engines.

This study explores the preparation of methyl esters from various vegetable oils and evaluates their performance, combustion characteristics, and emissions when used in compression ignition (C.I) engines.

- Methyl esters from karanja, jatropha, sunflower, palm, and waste cooking oil can be used directly in diesel engines without needing any modifications to the engine.
- Blends B20 and B40 outperform B100 but remain below diesel in terms of brake thermal efficiency. When compared to diesel (33.36%), and various mixes of methyl esters of karanja (32.26%), sunflower (32.24%), palm (31.96%), and waste cooking oil (31.5%), 20% blend of jatropha methyl ester (JTME) showed higher brake thermal efficiency, reaching 32.8%, at maximum braking power.
- Diesel was found to have higher emissions of smoke, HC, and CO at varying loads than other fuels.
- When comparing 20% WCOME (38 ppm) to the other B20 methyl esters, KME (45 ppm), JTME (43 ppm), SFOME (41 ppm), POME (40 ppm), and diesel (48 ppm), the HC emission is lower.
- Based on NOx emissions at varying loads, diesel was shown to have lower emissions (510 ppm) for all mixes of diesel and methyl esters.However, as compared to all other 20% methyl esters, KME (538 ppm), SFOME (540 ppm), POME (544 ppm), and WCOME (552 ppm), NOx emission is quite high and about identical to diesel for 20% JTME (534 ppm).
- When compared to all other B20 methyl esters, including diesel (140 mg/m^3), JTME (132 mg/m^3), SFOME (128 mg/m^3), POME (132 mg/m^3), and WCOME (134 mg/m^3), the smoke density for 20% KME (126 mg/m^3) is lower.
- As the ignition delay interval lengthens, the percentage of methyl ester in the fuel decreases. The peak pressure values for methyl ester and its blends are slightly lower compared to those for diesel. Additionally, the peak pressure for methyl esters and their blends occurs slightly further from TDC. With an increase in the methyl ester content in the fuel, the maximum heat release rate diminishes in magnitude. Furthermore, as the proportion of methyl ester in the fuel rises, the frequency of the maximum heat release rate increases.
- The brake thermal efficiency of methyl esters and their blends with diesel is slightly lower compared to pure diesel. As the proportion of methyl ester in the fuel increases, there is a reduction in unburned hydrocarbons, carbon monoxide, and particulate matter in the exhaust. However, this also leads to an increase in nitrogen oxide emissions and exhaust gas temperature.

This research work pave way for reduction in consumption of fossil fuels by blending methyl esters and decrease in emissions.

The following are suggested as future work for the investigations on the use of biodiesel in a DI diesel engine.

- Study on retarding the fuel injection timing for the optimum blends to reduce the emissions without compromising much in thermal efficiency.
- Study on the effect of additives (DME or DEE) on the combustion, performance and emission characteristics of the biodiesel.
- Study on the effect of compression ratio on the combustion and exhaust gas analysis of the biodiesel.

AUTHORSHIP CONTRIBUTIONS

Authors equally contributed to this work.

DATA AVAILABILITY STATEMENT

Authors confirm that the data that supports the findings of this study are available within the article. The raw data

that supports the findings of this study are available from the corresponding author, upon reasonable request.

CONFLICT OF INTEREST

The authors declare no potential conflicts of interest with respect to the research, authorship, and/or publication of this article.

ETHICS

There are no ethical issues with the publication of this manuscript.

REFERENCE

[1] Phan.A.N, T.M. Phan. Biodiesel production from waste cooking oils. Fuel 2008;87:3490-3496. [CrossRef]

[2] Nurun Nabi Md., Shamim Akhter Md., Mhia Md. Zaglul Shahadat. Improvement of engine emissions with conventional diesel fuel and diesel biodiesel blends. Bioresource Technology 2006;97:372–378. [CrossRef]

[3] Razzaq, L., Mujtaba, M.A., Soudagar, M.E.M., Ahmed, W., Fayaz, H., Bashir, S., Fattah, I.M.R., Ong, H.C., Shahapurkar, K., Afzal, A., Wageh, S., Al-Ghamdi, A., Ali, M.S. and El-Seesy, A.I. Engine performance and emission characteristics of palm biodiesel blends with graphene oxide nanoplatelets and dimethyl carbonate additives. Journal of Environmental Management2021;282:111917. [CrossRef]

[4] Alruqi, M., Sharma, P., Deepanraj, B. and Shaik, F. Renewable energy approach towards powering the CI engine with ternary blends of algal biodiesel-diesel-diethyl ether: Bayesian optimized Gaussian process regression for modeling-optimization. Fuel2023;334:126827. [CrossRef]

[5] Sharma, P. Prediction-optimization of the effects of di-tert butyl peroxide-biodiesel blends on engine performance and emissions using multi-objective response surface methodology. Journal of Energy Resources Technology, Transactions of the ASME 2022;144:1–13. [CrossRef]

[6] Joseph Shobana Bai, F.J., Shanmugaiah, K., Sonthalia, A., Devarajan, Y. and Varuvel, E.G. (2022) Application of machine learning algorithms for predicting the engine characteristics of a wheat germ oil-hydrogen fuelled dual fuel engine. International Journal of Hydrogen Energy2023;48:23308-23322. [CrossRef]

[7] Karpanai Selvan, B., Das, S., Chandrasekar, M., Girija, R., John Vennison, S., Jaya, N., Saravanan, P., Rajasimman, M., Vasseghian, Y. and Rajamohan, N. Utilization of biodiesel blended fuel in a diesel engine – combustion engine performance and emission characteristics study. Fuel 2021;311:12262. [CrossRef]

[8] Puhan.S, R. Jegan, K. Balasubbramanian, G. Nagarajan. Effect of injection pressure on performance, emission and combustion characteristics of high linolenic linseed oil methyl ester in a DI diesel engine. Renewable Energy 2009;34:1277-1233.[CrossRef]

[9] S. Mahla, S. M. S. Ardebili, Himanshu Sharma. Performance and exhaust emissions analysis of a diesel engine running on diesel /diethyl ether/biogas as a green fuel. Energy Sources, Part A: Recovery, Utilization and Environmental Effects 2022;44:9395-9411.[CrossRef]

[10] Suresh Vellaiyan. Enhancement in combustion, performance, and emission characteristics of a biodiesel-fueled diesel engine by using water emulsion and nanoadditive. Renewable Energy 2020;145:2108-2120. [CrossRef]

[11] Nalgundwar, A., Paul, B. and Sharma, S.K. Comparison of performance and emissions characteristics of DI CI engine fueled with dual biodiesel blends of palm and jatropha. Fuel 2016;173:172–179. [CrossRef]

[12] Saini Mahesh Chand, Jakhar Om Prakash, Khatri Rohit. Impact of biodiesel blends on performance, emissions and waste heat recovery of diesel engine driven cogeneration system Journal of Thermal Engineering 2024;10:680−696. [CrossRef]

[13] M. P. Joshi and S. S. Thipse. Combustion Analysis of CI Engine Fuelled with Algae Biofuel Blends Journal of Thermal Engineering2019;5:214-220. [CrossRef]

[14] Sudalaiyandi, K., Alagar, K., Vignesh Kumar, R., Manoj Praveen, V. and Madhu, P. Performance and emission characteristics of diesel engine fueled with ternary blends of linseed and rubber seed oil biodiesel. Fuel 2020;285:119255. [CrossRef]

[15] Avinash Kumar Agarwal, Biofuels (alcohols and biodiesel) applications as fuels for internal combustion engines, Progress in Energy and Combustion Science 2007;33:233-271. [CrossRef]

[16] Srivastava, P.K. and Verma, M. Methyl ester of karanja oil as an alternative renewable source energy. Fuel2008;87:1673–1677. [CrossRef]

[17] Saravanan, S., Nagarajan, G. and Lakshmi Narayana Rao, G. Investigation on nonedible vegetable oil as a compression ignition engine fuel in sustaining the energy and environment. Journal of Renewable and Sustainable Energy 2010;2:013108. [CrossRef]

[18] Rajak, U., Nashine, P. and Verma, T.N. Effect of spirulina microalgae biodiesel enriched with diesel fuel on performance and emission characteristics of CI engine. Fuel 2020;268:117305. [CrossRef]

[19] L. Wei , C.S. Cheung , Z. Ning , Effects of biodiesel-ethanol and biodiesel-butanol blends on the combustion, performance and emissions of a diesel engine. Energy 2018;155:957-970. [CrossRef]

[20] Vineet Kumar , Rajesh Kumar Saluja, The effect of operating parameters on performance and emissions of DI diesel engine fuelled with Jatropha biodiesel. Fuel 2020;278:118256. [CrossRef]

[21] F.K Forson, E.K Oduro, E Hammond-Donkoh, Performance of jatropha oil blends in a diesel engine. Renewable Energy 2004;29:1135-1145.[CrossRef]

J Ther Eng, Vol. 12, No. 1, pp. 349−364, January, 2026

Journal of Thermal Engineering
Web page info: https://jten.yildiz.edu.tr
DOI: 10.14744/thermal.0001084

Research Article

Oscillating piezofan effects on natural and forced convection flow in a vertical channel with protruding heat sources

Salim Ibrahim HASAN[1,2], Mehmet Akif EZAN[3], Serhan KÜÇÜKA[3,*]

[1]*The Graduate School of Natural and Applied Sciences, Dokuz Eylul University, Izmir, 35000, Turkiye*
[2]*Department of Mechanical Engineering, Mosul University, Mosul, 41007, Iraq*
[3]*Department of Mechanical Engineering, Dokuz Eylul University, Izmir, Turkiye*

ARTICLE INFO

Article history
Received: 30 July 2023
Revised: 04 May 2024
Accepted: 04 June 2024

Keywords:
Cantilever Piezofan; Discrete Channel; Electronic Cooling; Protruding Heat Source

ABSTRACT

The current work investigates the flow characteristics and convective heat transfer performance of a vertically-oriented piezofan in a channel with wall-mounted protruding heat sources. A 2D numerical model is developed in COMSOL Multiphysics to simulate the temperature variations on the heated protrudes under forced and natural convection scenarios, with and without oscillation of the piezofan. A vertical channel with dimensions of L_{ch} = 300 mm × S = 35 mm is considered with four protruding heat sources (H_{hs} = 25 mm × b = 7 mm), which are positioned on the same side of the channel, with a frontal surface heat flux of q_w = 600 W/m^2. The results reveal that active and passive vortices generated by piezofan and protruding objects in the flow domain provide higher momentum and heat exchange. It was found that implementing piezofan inside the channel significantly enhances cooling performance and reduces the surface temperatures of the protrudes. Compared to the pure natural convection within the channel, the average convective heat transfer coefficient on the protrudes increased more than three times using piezofan. Besides, in the case of forced convection, the maximum increments in mean convective heat transfer are obtained as 74% and 59% at Reynolds numbers 1000 and 2000, respectively.

Cite this article as: Hasan SI , Ezan MA, Küçüka S. Oscillating piezofan effects on natural and forced convection flow in a vertical channel with protruding heat sources. J Ther Eng 2026;12(1):349−364.

INTRODUCTION

The thermal issues associated with electronics cooling applications have motivated further research in the scope of convection channels due to factors such as coupling of discrete heating, conduction in the substrate, and components with the fluid convection. Some of the practical importance of such problems was highlighted in several reviews.

Due to the rapid improvements in electronic technology and the miniaturization trends of the electronic industry, the convective air cooling of electronic components mounted on a circuit board has been an attractive

***Corresponding author.**
*E-mail address: Serhan.kucuka@deu.edu.tr

This paper was recommended for publication in revised form by Editor-in-Chief Ahmet Selim Dalkilic

Published by Yıldız Technical University Press, İstanbul, Turkey
Yıldız Technical University. This is an open access article under the CC BY-NC license (http://creativecommons.org/licenses/by-nc/4.0/).

motivating topic of many papers, and investigations have dramatically increased during the last three decades. Relying on experimental and numerical studies in the literature, discrete cards or parallel plates can be constructed as 2D vertical air channels for natural and forced convection configurations of various electrical components in different types of equipment. As these components cause passive Vortex Generation (pVG) in the flow field, they improve the convective heat transfer rate. Most of the previous analyses focused on the design of effectively cooling electronic packages by controlling geometries and structure layout [1-12]. For example, Young and Vafai (1998a & 1998b) [1,2] published numerical simulation results for forced convection inside a horizontal channel with an array of heated blocks attached to the bottom wall. They demonstrated that choosing proper obstacle arrangements and configurations can considerably influence flow domain and heat transfer characteristics. Such a passive heat transfer improvement can open the way for various electronic applications. They also conducted experimental investigations and compared the measurements against the 2D laminar flow numerical model [3]. They evaluated the obstacle temperatures and Nusselt number variations as a function of flow rate and obstacle configurations to propose better designs for higher heat transfer enhancements. Similarly, Zeng and Vafai [4] developed a numerical model of an array of obstacles in a horizontal channel to obtain two-level Nusselt number correlations to quantify the influence of different factors on cooling performance. Their predictions agreed well with the numerical simulation data from the literature. Sarper et al. [5] studied the buoyancy-induced flow and heat transfer characteristics in a vertical parallel plate channel with four discrete protruding heat source arrays experimentally and numerically to model an electronic package. They focused on the effects of the geometrical parameters on recirculating flow and cooling performance. They revealed that the blockage ratio significantly impacts the system's overall cooling performance. In the numerical study of Haghighi et al. [6], they considered a single or an array of porous metallic designs of different configurations located inside the surface of a partially heated wall of a horizontal channel. They compared the flow and thermal considerations of two working fluids, air and water, and it was concluded that metal foams might be utilized as heat sinks, paving the path for future applications such as solar thermal collectors and electronic cooling.

In the literature, forced convection in protruded channels has also become an issue in many passive vortex generator investigations for electronic air-cooling applications. Various geometries are placed in the streamflow, focusing the vortex and the secondary flow toward the heated surfaces to improve the convective heat transfer. Wang and Jaluria [7] introduced numerical research to study the cooling performance by analyzing unsteady mixed convection through a horizontal channel with two insulated protruding blocks placed on the bottom wall. The results demonstrated the ability to control the primary flow frequency and amplitude by adjusting the geometry of the promoter. Chomdee and Kiatsirioat [8] presented an experimental model to analyze the heat transfer improvements by delta winglet vortex generators placed in front of a staggering array of rectangular electronic modules on a circuit board. They demonstrated in the results that the vortex generators could significantly improve the heat transfer coefficient and reduce the module temperatures. Oztop et al. [9] built a 2D laminar flow model to analyze the convective heat transfer rate and fluid flow around isothermally heated blocks on a horizontal channel wall. They used a triangular cross-sectional bar located at different locations to control and guide the streamflow at three Reynolds numbers from 400 to 1300. They obtained that inserting a triangular cross-sectional bar can enhance the heat transfer rate for all Reynolds numbers compared with the plane channel without the triangular obstacle. Beig et al. [10] introduced an optimization study using a Genetic algorithm (GA) combined with a Gaussian Process (GP) to conduct the highest uniform heat transfer by obtaining the optimal position of a triangular cross-sectional bar vortex generator to cool a blocked channel, i.e., electronic chips. They revealed that the flow domain structures primarily depend on the location of the vortex generator, regardless of the flow Reynolds numbers. Al-Asadi et al. [11] developed a 3D laminar flow numerical model to study the conjugate heat transfer within a micro-channel to explore the effects of quarter-circle and half-circle cylindrical cross-sections vortex generators arranged along the bottom wall of the horizontal channel. They analyzed the flow domain and the cooling performance with Reynolds numbers ranging from 100 to 2300 and uniform heat flux cases. They demonstrated that the vortex generation with these structures significantly improves the heat transfer rate, promising substantial improvements toward miniaturization technology with lightweight and small-volume mobile electronic devices. Zheng et al. [12] explored the effects of trapezoidal cross-section geometric parameters as longitudinal vortex generators on local and overall thermal-hydraulic characteristics at the Reynolds number range of 347–868 inside a longitudinal mini-channel. Numerical results proved that the proposed geometries have better comprehensive thermal performance than rectangular cross-sections. Also, they recommended the optimal geometrical parameters of a trapezoidal channel by achieving the best performance; its height matches half of the channel height.

The works that come after referring to the problems of pVG are the limitation in the number of generated vortices and low cooling performance with high heat generation in modern electronic components. Therefore, many further attempts have been made to improve the cooling performance by introducing different types of active vortex generation (aVG) applications. Active Vortex Generations (aVG) strategies include moving geometries in the flow channels to improve convective heat transfer [13-17]. Yang [13,14] used the ALE method and a Galerkin finite

element method in the simulation model to investigate the heat transfer enhancement in the presence of an oscillating bar directed to heated obstacles on the channel wall. The heat transfer rate significantly increases with the Reynolds number and the bar oscillating amplitude. Fu and Tong [15] conducted a numerical simulation using ALE and Galerkin finite element methods to inspect the flow profiles and heat transfer features of a heated diagonally oscillating cylinder inside the cross-flow. They compared the vortex-shedding structures and heat transfer characteristics around the heated cylinder by varying the flow Reynolds number, piezofan's oscillating amplitude, and oscillating velocity. It is concluded that the heat transfer rate improved with increasing oscillating velocity of the cylinder and the Reynolds number. Kurşun and Sivrioğlu [16] investigated the development of the flow routing plates on the structures of laminar mixed convection heat transfer configurations in a horizontal channel, which has protruding heat sources mounted on the top and bottom walls experimentally and numerically using 3D laminar flow analysis. They demonstrated that using flow routing plates has only enhanced heat transfer for the first bottom row of heaters and the first and last top surface row of heaters, and the natural convection improved with the increasing Grashof number and decreasing Reynolds number. Ismael [17] used numerical 2D benchmarked geometry with two baffles bound to the compliant segment to investigate the forced convective heat transfer and the performance of a channel partially heated by constant heat flux under the effects of two alternative upstream-downstream vortex generator baffles. It is concluded that the Nusselt number is improved by 94%, corresponding with the non-baffled channel at Re = 250.

Based on the outcomes of literature research on the active vortices generated by piezofan and their properties consistent with modern technology. Its properties make it a good choice for easy air cooling and as an economical alternative in terms of energy consumption, easy construction, and free noise and vibration. Therefore, the further addition of state-of-the-art numerical analysis in this field will be of significant importance in the technology industries. Numerous researchers have studied the cooling performance of piezofans. Kim et al. [18] tested the 2D model of Choi et al. [19], and it was found that the static pressure difference across the fan tip plays an essential role in generating and developing double counter-rotating vortices. A 2D model of an oscillating piezofan in a vertical channel is proposed by Florio and Harnoy [20], and there is a 52% increase in the local heat transfer coefficient compared to pure natural convection. Lin [21] used flow visualization techniques and 3D numerical simulations to investigate the cooling performance of a vibrating piezofan placed in the wake area of a cylinder in the presence of forced cross-flow. They found that the piezofan increased the cylinder's overall and local heat transfer ratios by 132% and 214%, respectively. Jeng and Liu [22] conducted experiments to discuss the effects of piezofan's transverse and axial oscillations on the channel airflow to improve the heat transfer of various heat sink structures. They found that the square pin-fin heat sink improves heat transfer, and the transverse oscillation increases heat transfer slightly higher than axial oscillation. Li et al. (2017 and 2018) [23,24] investigated the cooling effects of vertically oriented piezofan on a heated flat surface in the presence of forced cross-flow inside a channel both experimentally and numerically. The main outputs are summarized as follows: *(i)* Combining piezofan and channel flows improves heat transfer, especially at small gaps between the piezofan tip and heated surface; *(ii)* The heat transfer coefficient increased by about 56.2% compared to the cross-flow channel; *(iii)* With the cross-flow, the oscillating amplitude of piezofan was reduced by more than 56%; *(iv)* The piezofan cooling performance improved only in the presence of low-velocity cross-flow conditions and *(v)* Due to high momentum cross-flow, the piezofan-generated vortices were forced downwards and/or swept away. Oh et al. (2018, 2019) [25,26] presented a 3D simulation of a vibrating cantilever piezofan between two walls to highlight the interaction flow between the created vortices. They discovered that the interaction of the piezofan tip and side vortices with each other formed some complex secondary flow configurations. By examining different gap heights, the size and strength of the vortices, as well as their interaction, are all affected by the end wall placement.

Park et al. (2019) [27] conducted 2D simulations with eight inlet velocities ranging from 0 to 7 m/s and 3D simulations with five velocities of 0, 1, 3, 5, and 7 m/s to investigate the effects of the free stream on the flow around a piezofan. ANSYS-FLUENT software is used in the simulations, and the plate motion is defined in the software with a user-defined function (UDF) subroutine. The results were obtained from 2D simulations in accordance with the 3D predictions and the experimental data. It is concluded that, considering the computational cost of the 3D simulations, the 2D model results would be sufficient to determine the effects of piezofan motion in conditions where the side vortex behavior is negligible. They showed that the free-stream has a greater influence on the counter-rotating vortices formed at the piezofan tip than on the vortices generated on the piezofan side. The axial velocity around the channel end wall increased at low free-stream velocities. This suggests that a low-speed free-stream may be the only way to improve the piezoefan's flow performance. The flapping dynamics of two types of piezofans in channel flow and their impacts on heat transfer enhancement performance were investigated experimentally by Chen et al. (2020) [28]. They compared three turbulent Reynolds values of 0.85×10^4, 1.37×10^4, and 19.1×10^4 to see how thermal performance was affected by the flow conditions. According to their findings, the flapping piezofan improved heat transfer performance over a wide range of Reynolds numbers. The flapping amplitude and frequency increase as the Reynolds number increases, resulting in improved heat transfer performance. The heat transfer is improved by

30% at low Reynolds numbers, i.e., Re = 1.37×10^4, while the maximum local heat transfer was increased by 46% at Re = 19.1×10^4 under a frequency of 43 Hz. Tiwari and Yeom (2021) [29] used a piezofan to examine how to increase convection heat transfer in an air channel flow experimentally and numerically. ANSYS-FLUENT software is used to simulate the flapping motion of the piezofan. A sinusoidal motion is defined in UDF with a time step size of 2.76E-5 seconds. It is noted that the numerical results are in agreement with the experimental counterparts, and the difference is less than 10%. The piezofan position at the front end of the heated surface achieves the highest heat transfer enhancement. They showed that the development, propagation, and impinging dynamics of vortical structures significantly affected the convective heat transfer rate of the heated surface in the channel. Ko et al. (2021) [30] studied the effects of piezofan on cooling a flat plate experimentally and numerically. ANSYS-FLUENT software is used to simulate the 3D piezofan model. Predicted plate temperatures are compared with experimental measurements. It is noted that the difference is less than 1°C in the case of piezofan being activated. The installation was performed to investigate the relationship between the generated vortices and the heated plate's temperature distribution. They verified that without piezofan, the temperature is highest at the center of the plate and lowers toward the plate edge. They also confirmed that the local temperature at the center of the plate is diminished by 28°C, and the improvements in the local convective heat transfer coefficients showed that the piezofan is very practical for cooling the plate.

In the previous works of the authors [31,32], the effects of oscillating piezofan in horizontal channels on the flow field at various flow-stream velocities (Reynolds numbers 1040 to 2080) were addressed. It was obtained that the high flow and cooling performance of this fan was described by several characteristics, such as the vertical and horizontal positions and their effects on the flow and temperature distributions. The results demonstrated that at low flow-stream velocity and position of piezofan near the center of the heated surface, the convection heat transfer coefficient increased by 231% compared to pure laminar flow condition. Hasan et al. (2023) [32] discuss the influences of vortices generated by vertically oriented piezofan operating at different oscillation ratios (0.15 to 0.3) on the flow domain and cooling performance in a vertical channel heated by the side walls. It was proved that the heat transfer rate over the entire channel increased by 28% compared to non-piezofan natural laminar flow conditions at a 0.3 oscillation ratio. Boz et al. [33] investigated the influence of the piezofan amplitudes ($2A$ = 6 – 12 mm) and frequencies (f = 10 – 20 Hz) on the heat transfer inside the vertical plane channel and compared it with the pure natural convection case. Results revealed that the heat transfer enhancement can reach up to 169% by using the piezofan.

The main goal of the current paper is to investigate the general trends associated with protruding heat sources inside natural and forced convection vertical channels. By combining passive and active vortex generation effects during the operation of vertically oriented piezofans, we will determine the effects on flow domain structure and convective heat transfer.

Problem Definition and Assumptions

As is fundamentally known, increasing the surface area exposed to the convective heat transfer is one of the main significant parameters for passively improving the heat dissipation rate. Thus, electronic packages composed of various configurations of series of flush-mounted or protruding discrete boards with or without a substrate to form thermally generated components in channels or parallel plates have become a subject in the advanced electronics industry. Many researchers have achieved numerical simulations to analyze the flow around piezofans, in particular, thanks to the rapid development of computational facilities and approaches. Even though 3D models enable better comprehensive solutions, they require additional computational capacity and cause re-mesh failure in deformed and stretched elements with longer simulation times. Most of the previous research has focused on cooling performance and the flow around the piezofans for 2D numerical simulations in order to reduce computation time while depending on assumptions that could decrease the solution's error rate. Accordingly, we relied on 2D model assumptions in this work to focus on vortex generation in the air domain and cooling performance enhancement based on the suggested realistic structures.

The physical geometry considered in this work is illustrated in Figure 1. Laminar 2D natural convection air-cooling in a vertical channel (L_{ch}=300mm and S=35mm) with four protruding heat sources (H_{hs}=25mm and b=7mm) mounted on one side of the channel wall is studied. Interface heat flux (q_w=600 W/m^2) is defined on the vertical surfaces of the protrudes to simulate an actual heat dissipation from the discrete electronic packages. Other walls, i.e., the left and right channel walls and horizontal surfaces of the protrudes, are considered to be adiabatic. The current investigations include forced flow with Re=1000 and 2000 and natural convection. The flow Reynolds number is defined as Re = $\rho V_{in} S/\mu$, where V_{in} is the average air velocity at the channel inlet, and S is the channel width. The numerical results of heat transfer and flow behavior with an oscillating piezofan are compared to a non-piezofan state under the same design and flow conditions.

Numerical model and boundary conditions

The equation of piezofan's oscillating motion is defined in terms of the frequency and the geometric parameters as [31, 32].

$$x_{pz}(y,t) = \left[\psi A_c \left\{ \begin{matrix} [(sin(\beta L_{pz}) - sinh(\beta L_{pz}))(sin(\beta x) - sinh(\beta x)) \\ + (cos(\beta L_{pz}) - cosh(\beta L_{pz}))(cos(\beta x) - cosh(\beta x))) \end{matrix} \right\}\right] sin(2\pi f_r t) \quad (1)$$

Dimensionless driving coefficients are defined as ψ = 1.862 and β = 21.233. The piezofan with L_{pz} = 40 mm length is adjusted to operate at a constant oscillating frequency

and amplitude of f_r = 20 Hz and OA = 10.5 mm, respectively. Except for the front surface of the heated sources, all sidewalls are considered no-slip and adiabatic. Table 1 summarizes the boundary conditions that are defined in the current simulations.

Transient governing equations of airflow and heat transfer physics are simultaneously resolved with solid mechanics physics for the 2D domain. This task was completed by calculating the deformation in the fluid domain using a moving boundary option. The deformation mesh is formed by connecting the induced forces to the cantilever motion of the piezofan in solid mechanics with fluid flow using FSI (fluid-structure interaction analysis). In the time-dependent study, the moving boundary conditions were set up as an automatic re-meshing option utilizing the ALE (Arbitrary Lagrangian-Eulerian) computation method. COMSOL Multiphysics software is used to couple physics dynamically. The grid size with 15546 mesh elements was chosen for all cases based on the mesh-independency analysis in the previous studies [31,32]. Continuity, momentum, and energy equations are defined for incompressible fluids as [31, 32].

$$\text{Continuity: } \frac{\partial u}{\partial x}+\frac{\partial v}{\partial y}=0 \tag{2}$$

$$\text{x- momentum: } \rho\frac{\partial u}{\partial t}+\rho u\frac{\partial u}{\partial x}+\rho v\frac{\partial u}{\partial y}=-\frac{\partial P}{\partial x}+\mu\frac{\partial^2 u}{\partial x^2}+\mu\frac{\partial^2 u}{\partial y^2} \tag{3}$$

$$\text{y- momentum: } \rho\frac{\partial v}{\partial t}+\rho u\frac{\partial v}{\partial x}+\rho v\frac{\partial v}{\partial y}=-\frac{\partial P}{\partial y}+\mu\frac{\partial^2 v}{\partial x^2}+\mu\frac{\partial^2 v}{\partial y^2} \tag{4}$$

$$\text{Energy: } \rho c_p\frac{\partial T}{\partial t}+\rho c_p u\frac{\partial T}{\partial x}+\rho c_p v\frac{\partial T}{\partial y}=k\frac{\partial^2 T}{\partial x^2}+k\frac{\partial^2 T}{\partial y^2} \tag{5}$$

Similar to previous research [32], fine triangular elements are used, and the mesh intensity of 15546 is selected in the simulations at adjusted oscillating amplitude OA = 10.5 mm. The time-stepping size of Δt = $(1/fr\times100)$ = 1/(20×100) = 0.0005 s is used to provide a suitable convergence during the computations. In addition, different sets of verifications with experimental works from the literature are discussed in detail in the authors' previous works [31,32].

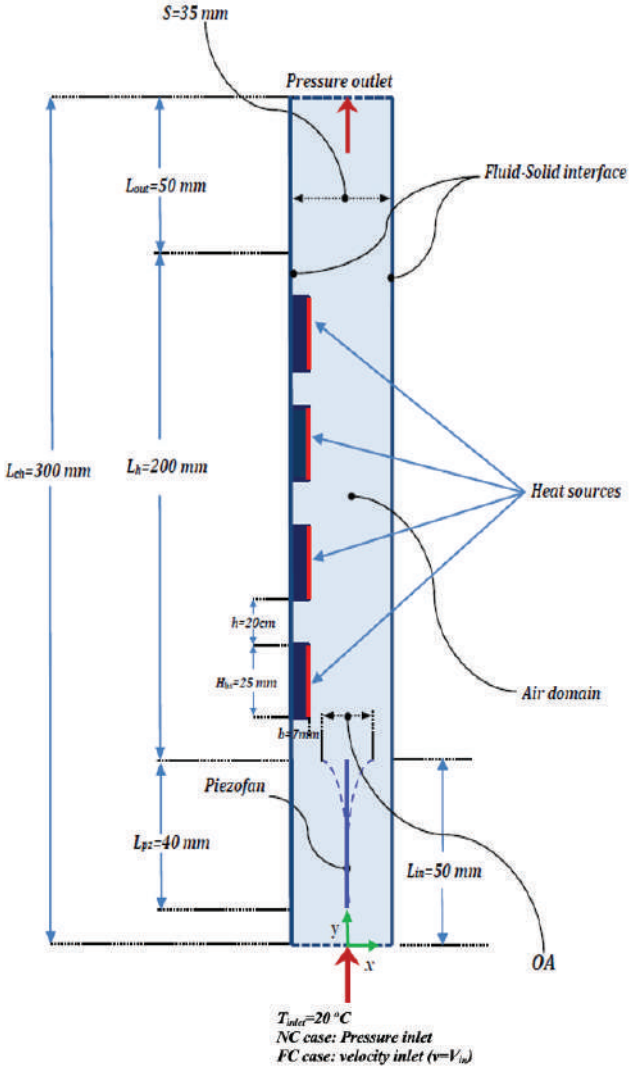

Figure 1. The 2D vertical channel model structure.

Table 1. Boundary conditions summary

Boundary	Assumption	Type	Fluid flow/ Heat transfer
Inlet section	$y = 0 \rightarrow P = P_{atm}$, T_{in} = 293.15K, $v=V_{in}$ (*at* Re = 1000, V_{in} = 0.439 m/s, *at* Re = 2000, V_{in} = 0.878 m/s)	*NC case: Pressure inlet* *FC case: velocity inlet*	Normal flow condition
Channel walls	$x = \pm S/2 \rightarrow u = v = 0$; $\partial T/\partial x = 0$	*No-slip flow with adiabatic wall*	Flow domain: gravitational acceleration in the negative y-direction; incompressible laminar flow with Boussinesq approximation
Protrudes	x= -S/2+b → $u = v = 0$; $q=q_w$	*No-slip flow with constant heat flux on the wall*	Front-side heat sources
Outlet section	$y = L_{ch} \rightarrow u = 0$, $\partial v/\partial y = 0$	*Pressure outlet*	Normal flow with suppressing backflow condition

RESULTS AND DISCUSSION

In the numerical analyses, heat transfer and flow were investigated in cases where natural convection and Reynolds numbers were 1000 and 2000, with and without piezo fan. As previously stated, continual vortices are generated at the piezofan tip during the cantilever motion. These vortices are generated in counter-rotating movement, then separate and travel left and right toward the channel's outlet. They will join with the low-velocity vortices created at the corners and edges of the protruding blocks during their passage, generating longitudinal vortices with high velocity and momentum that will spread across all surfaces and protrusions, as shown in Figure 2 and b. This diffusion breaks the boundary layers and reduces their thickness, moving in this manner continually, lowering the temperatures of the hot surfaces and greatly improving the heat transfer rate by convection significantly, hence improving the thermal performance of electronic devices or components. The vortices break the thick boundary layer at low cross-flow velocities in the channel; consequently, the heat transfer rates increase at all surfaces and edges. At high velocities, the vortices drift upwards with the main flow and reduce the heat transfer rate.

In contrast, as shown in Figure 3, the double effects of the generated vortices by oscillating piezofan and the passive low-velocity vortices that are generated at the corners and edges of the protruding heat sources are combined with the secondary flows of the bouncy effects of natural convection to produce high momentum and flow energy vortices. These flow domains significantly impact the boundary layers during their free movements towards the channel exit, increasing the cold region close to the hot surfaces. This improves the heat transfer rate by free convection

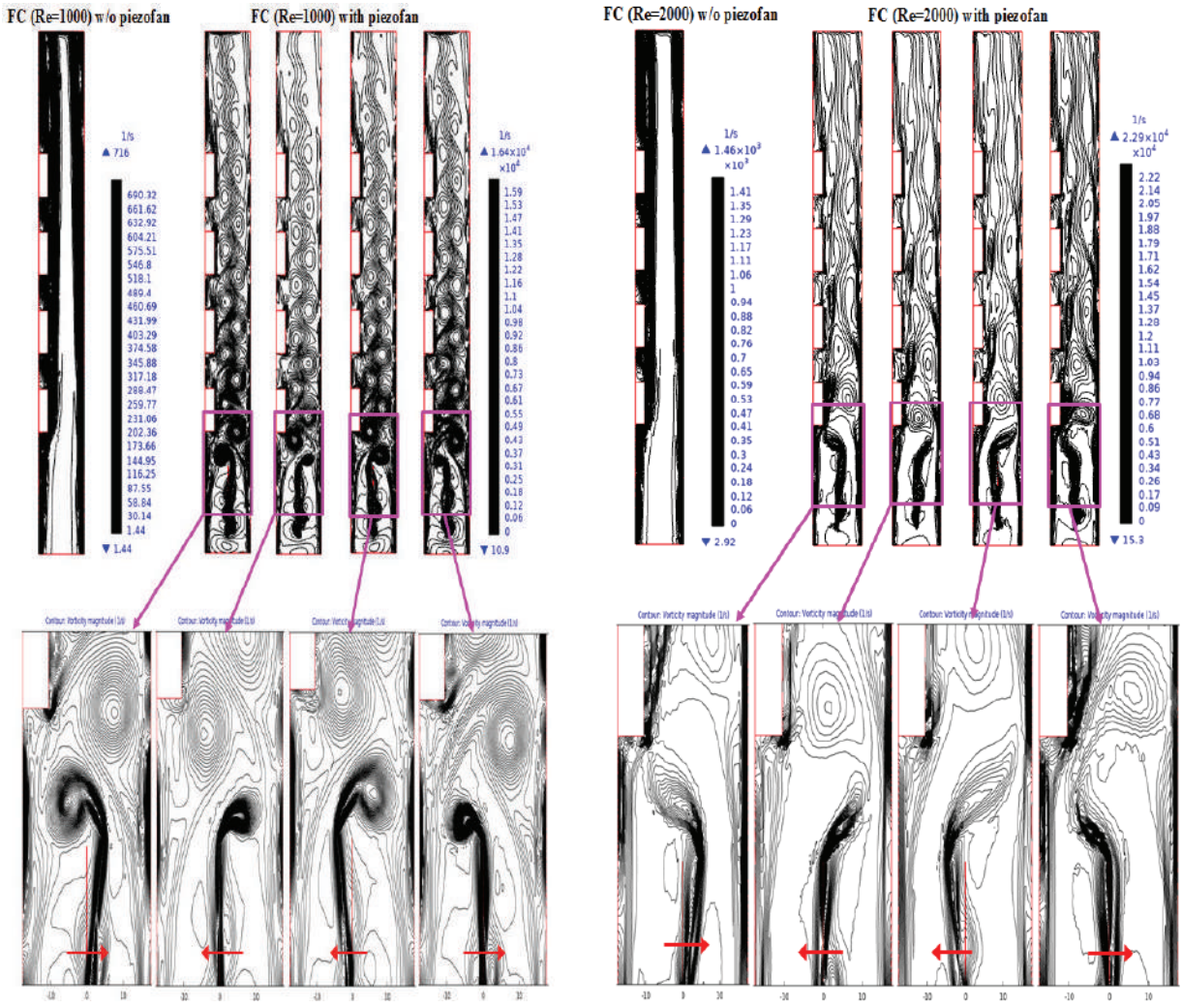

a) Re=1000 b) Re=2000

Figure 2. Vortices generation on the flow domain in the forced convection channel during one- operating cycle of the piezofan.

and enhances cooling performance compared to a channel without this fan.

Figure 4a, b, and c comparatively depict the influence of a fluctuating piezofan on the streamlines inside the flow domain. The generated vortices in Figure 4a have a longitudinal shape. They are separated further on the left protruded surface and take the sufficient time required for the heat transfer. They then expand the cold surface domain through interaction with these hot surfaces and edges, which improves the cooling performance of the channel flow in the presence of the fan. In Figure 4b, the double counter-rotated generated vortices and their separation in the flow domain toward the channel exit at low-velocity stream flow channels are all clearly visible. However, as shown in Figure 4c, due to the quick flow separation at the piezofan tip, these vortices do not emerge noticeably in the high-velocity stream flow domain.

At low velocities, the vortices break the hydrodynamic boundary layer; consequently, the heat transfer rates increase at all surfaces and edges. At high cross-flow velocities, the vortices drift upwards with the main flow, and their effects on heat transfer decrease. In all considered cases, there is a fluctuation in the y-component of the velocity. Figure 5 compares the variations in v-velocities at different channel sections along the flow direction. Oscillating the piezofan significantly affects the flow domain in natural

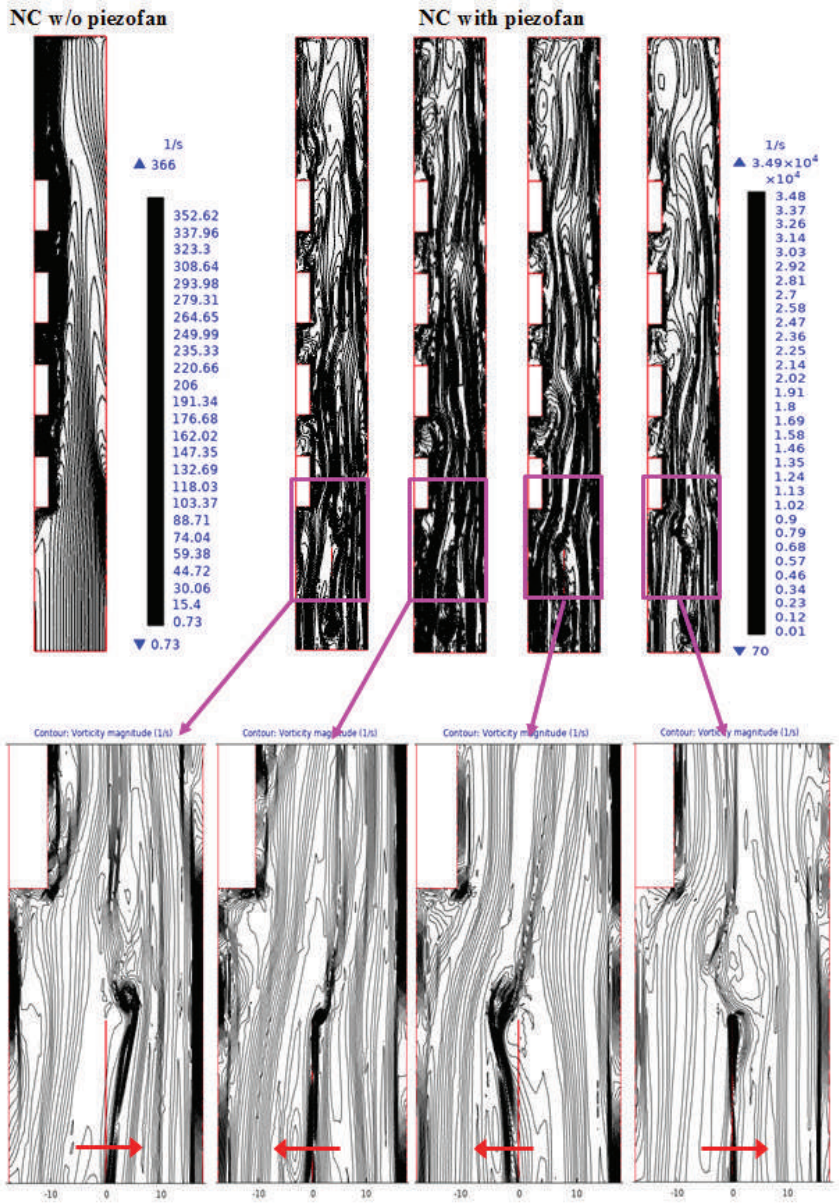

Figure 3. Vortices generation on the flow domain in the natural convection channel during one- operating cycle of the piezofan.

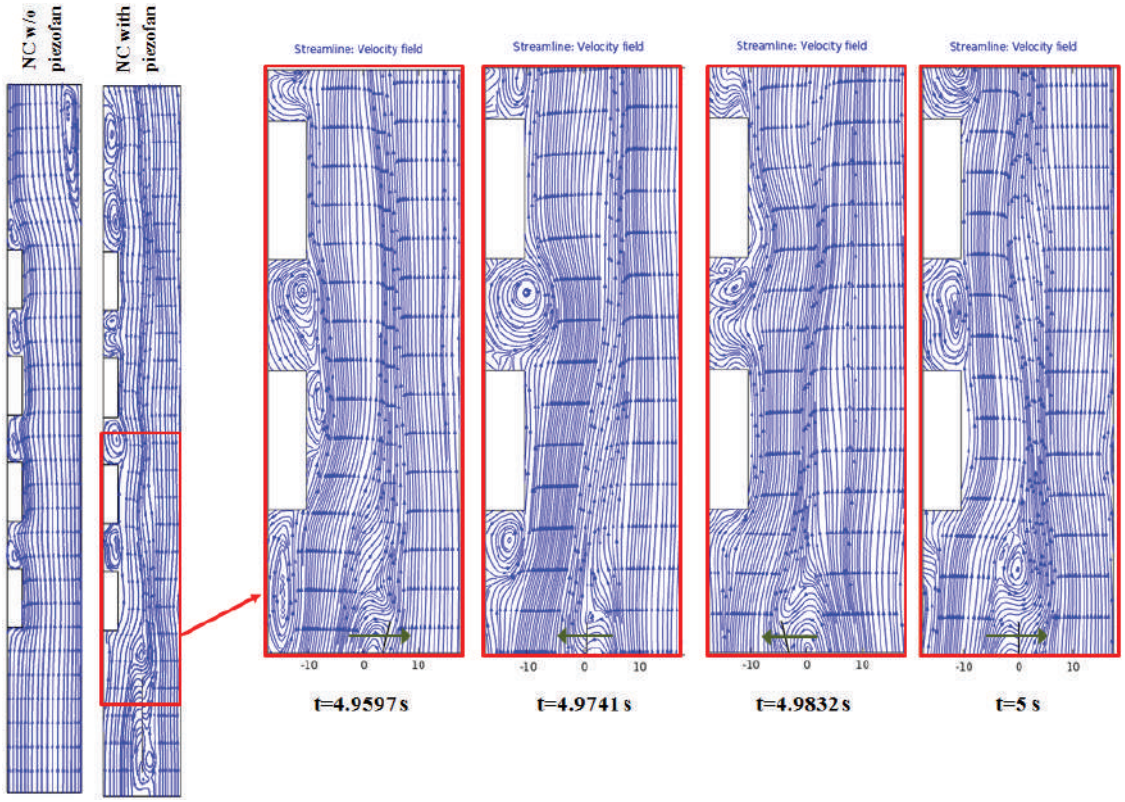

a) Natural convection

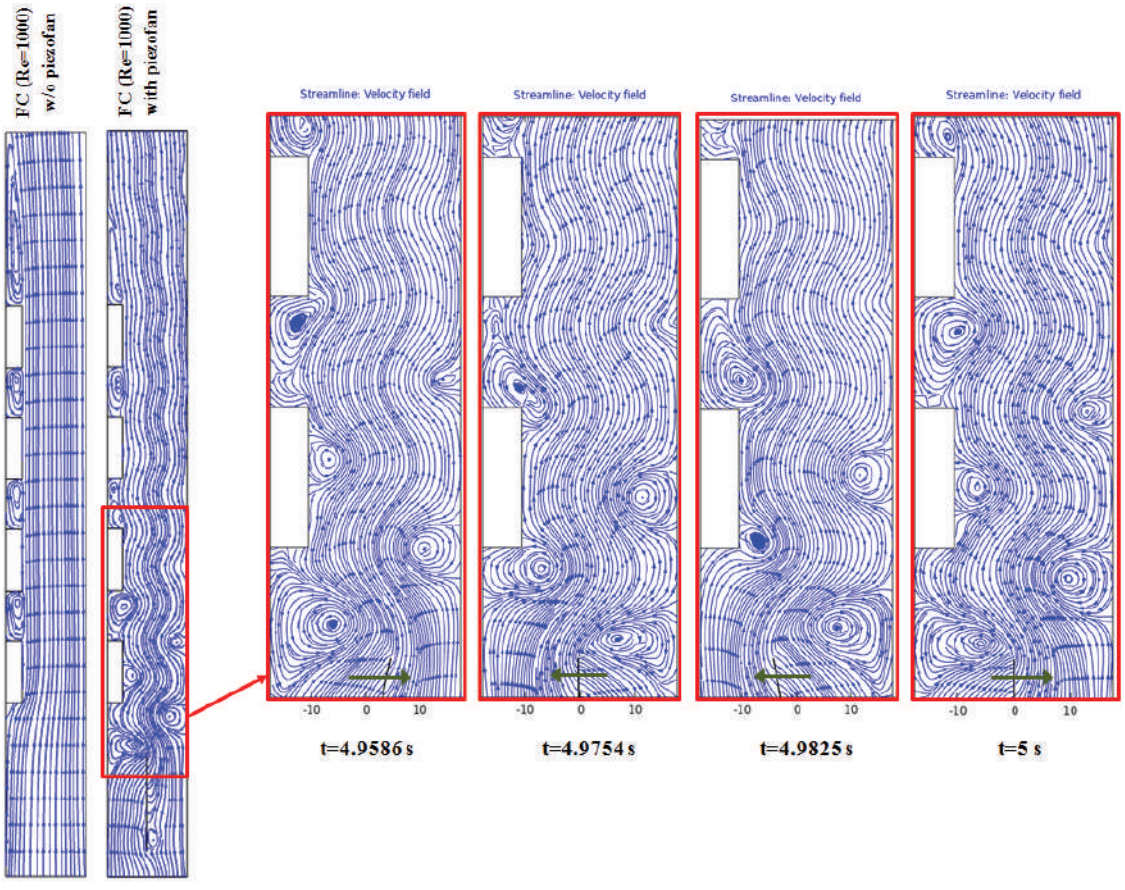

b) Forced convection flow (Re=1000)

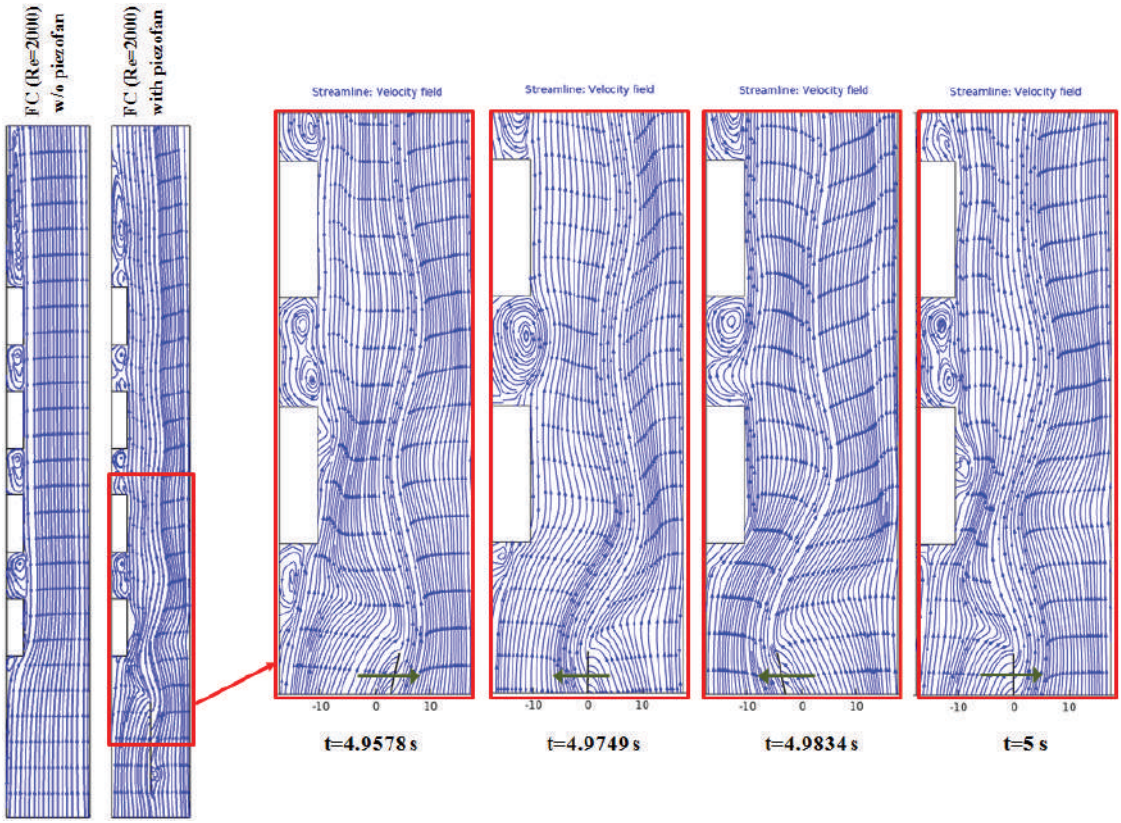

c) Forced convection flow (Re=2000)

Figure 4. The effects of piezofan oscillation motion on the flow domain of channels during one-operating cycle compared to non-piezofan flow channels.

convection and low flow-stream velocities. The maximum velocity decreases in the flow domain towards the channel exit.

As mentioned above, natural convection with a piezofan helps reduce temperatures on the heated walls due to the high-velocity level over the entire domain. Mixing active and passive vortex generation with buoyancy effects reduces the boundary layer thickness and sweeps the heated surface with high momentum impacts toward the channel exit. The temperature contours given in Figure 6 illustrate this physics.

Figure 7. provides the fluctuations of protruding front surface temperatures (T_s) for five seconds of piezo fan operation. The steady-state condition was reached at about 3 s. for natural convection, and at 0.5 s for forced convection.

Figure 8 shows the time-dependent fluctuations of the average convective heat transfer coefficient at each protruding surface during the piezofan operation. Results show that, for each case, the steady-state oscillations are achieved after around 0.5 s at forced convection, and 3 s at natural convection. It is also important to note that the heat transfer rate significantly increases for the piezo fan-containing channels compared to non-piezofan channels. During piezofan oscillation, the heat transfer coefficients on the protruding surfaces increased by about 46% to 74% for Re = 1000 and about 2% to 59% for Re = 2000, respectively. Yang [13] studied the influence of an oscillating vortex generator inside a horizontal channel at low Reynolds numbers, i.e., 250, 500, and 750. Since the flow Reynolds numbers are relatively lower, the enhancements in heat transfer are achieved by as much as 97%, depending on the oscillating amplitude and the speed of the horizontal vortex generator. For the natural convection-induced case, the increments on the protruding surfaces are around 182% and 435%. One can conclude that due to the combined effects of generated vortices in the whole flow domain, piezofan has significant cooling performance effects in natural convection and low flow velocity forced convection channels.

After reaching the steady state, between 3 s and 5 s, the average temperatures of protruding surfaces are given in Table 2. It was shown that, for force convection channel at low flow stream velocity (Re=1000), the average surface temperature reduces by 16.2K, 19.6K, 16.6K, and 18.6K on the front surface 1st, 2nd, 3rd, and 4th protruding heat sources respectively, when compared to the flow in the same channel without piezofan. When the flow stream velocity increased (Re=2000), the temperature

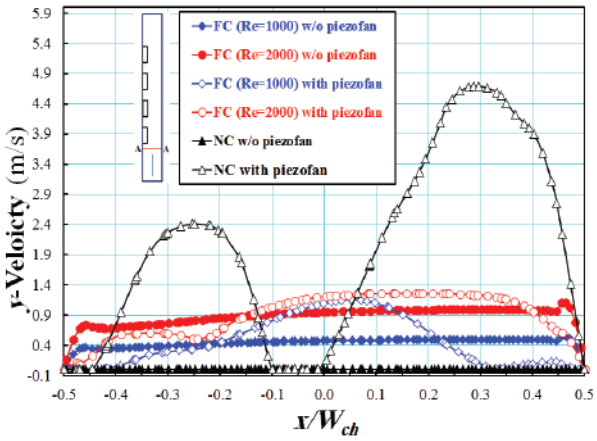

a) Section A-A

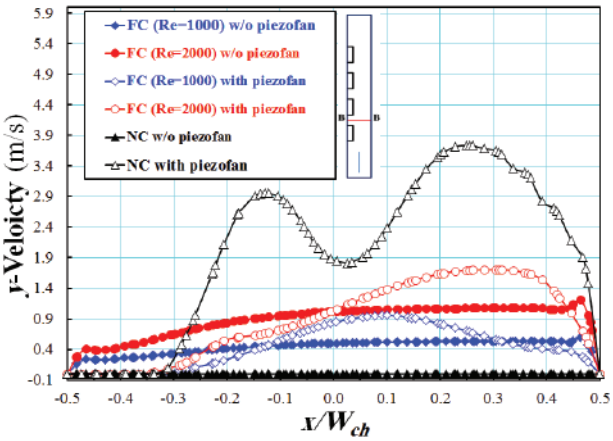

b) Section B-B

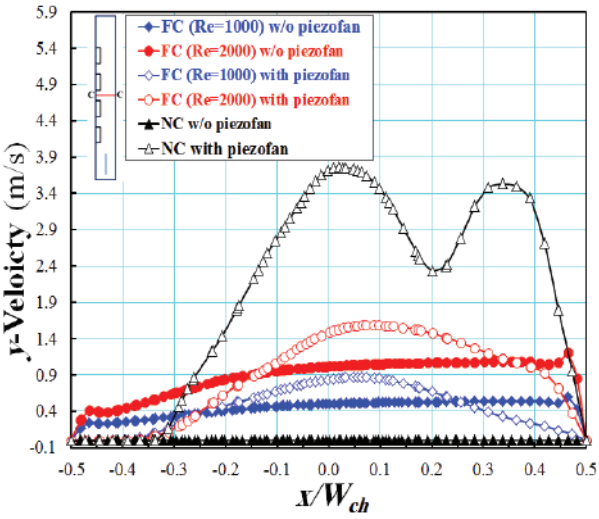

c) Section C-C

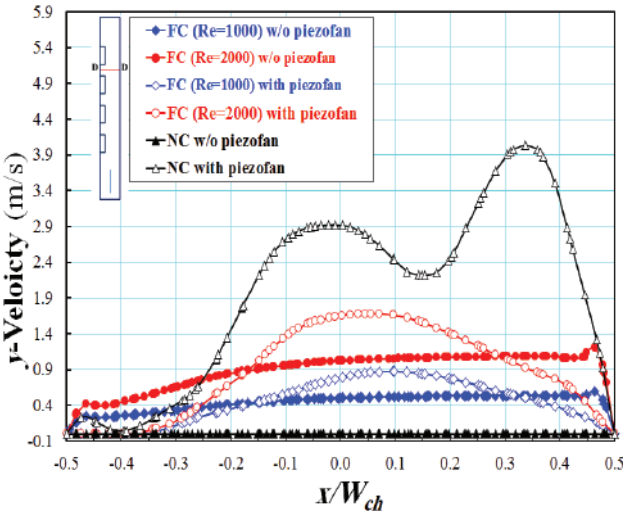

d) Section D-D

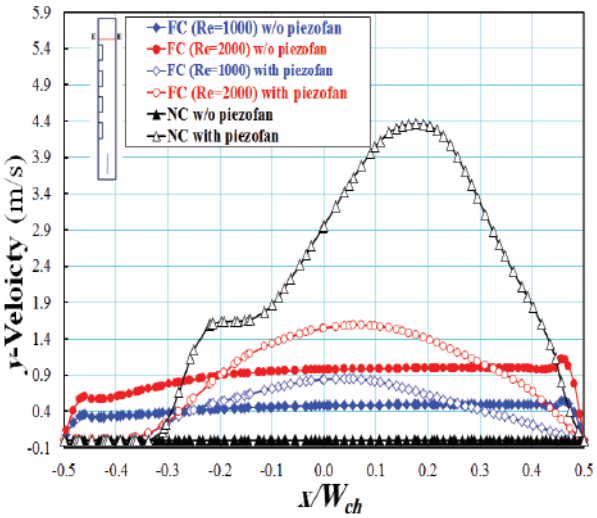

e) Section E-E

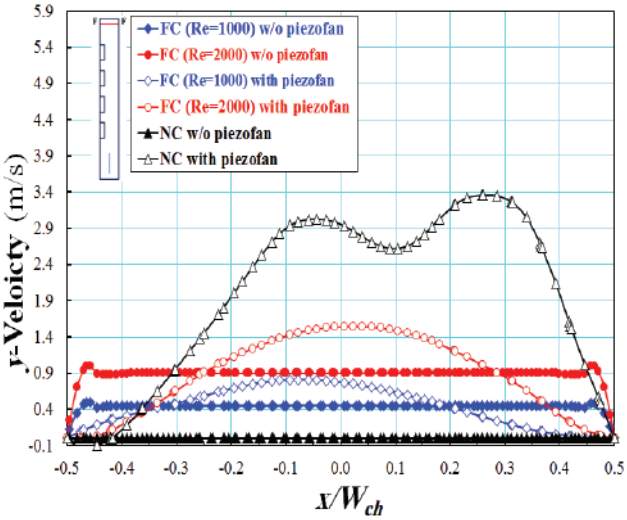

f) Section F-F

Figure 5. Variations in *y*-velocity for different flow cases at different channel sections at t = 5 s.

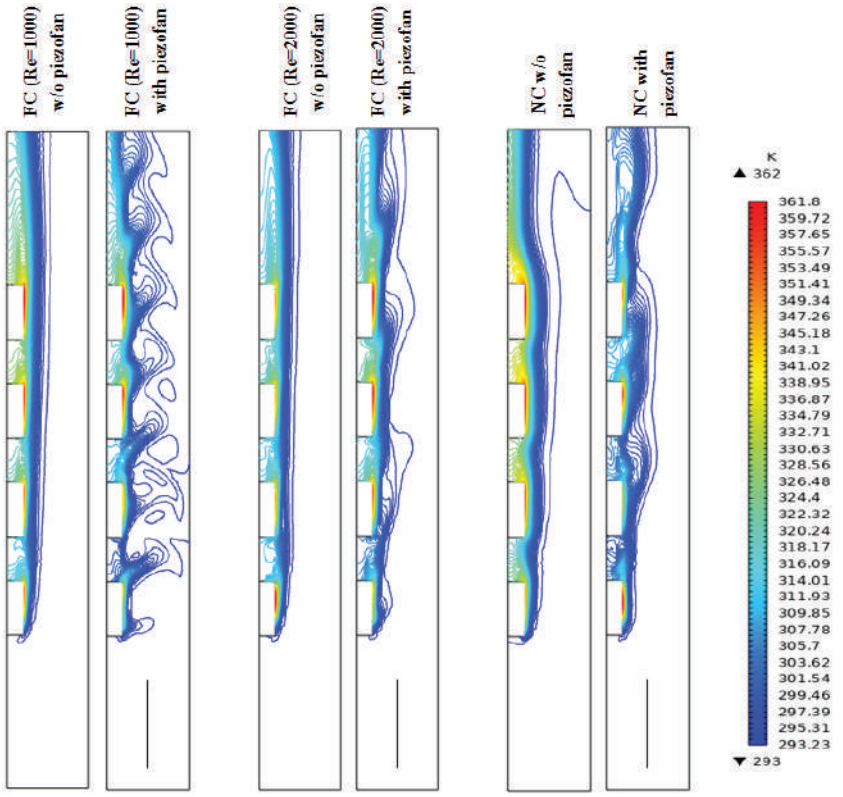

Figure 6. Comparison of temperature contours of different flow cases at t = 5 s.

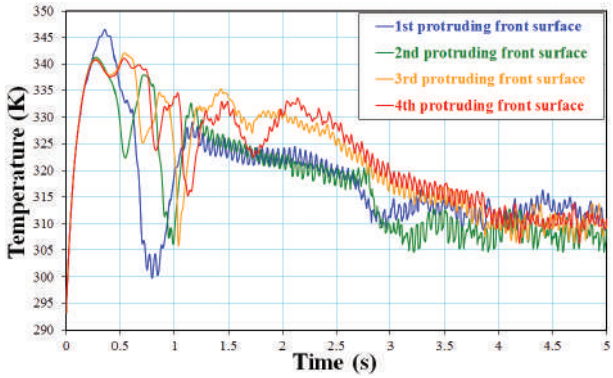

a) Natural convection channel

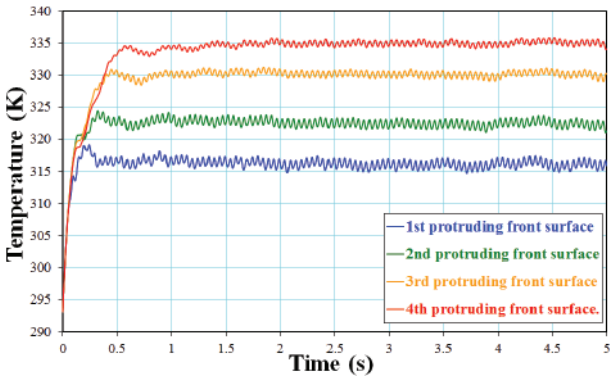

b) Forced convection (Re=1000)

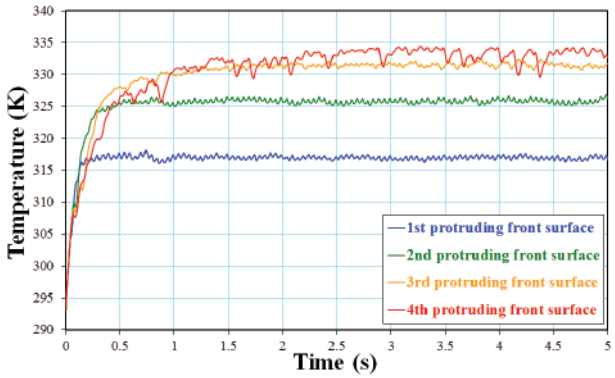

c) Forced convection (Re=2000)

Figure 7. Timewise variations in protruding front surface temperatures for the considered cases during 5 s of piezofan operation.

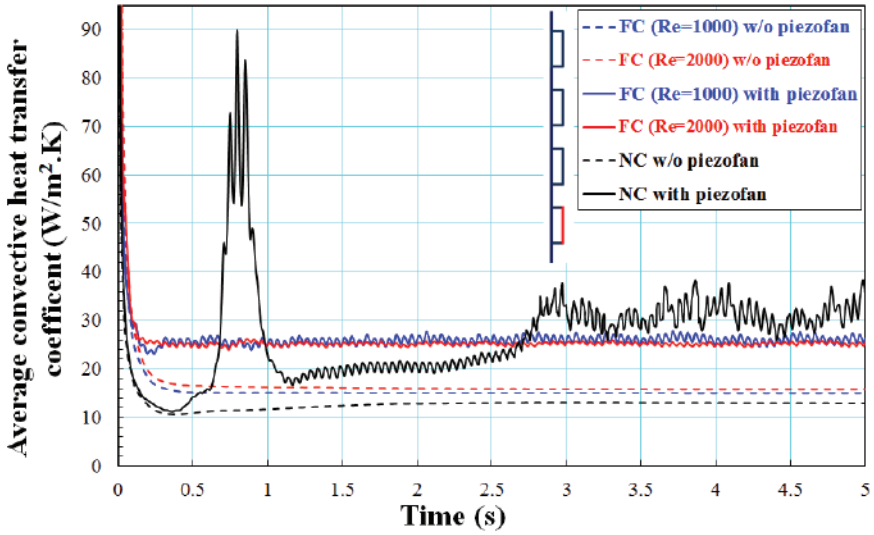

a) 1st protruding front surface

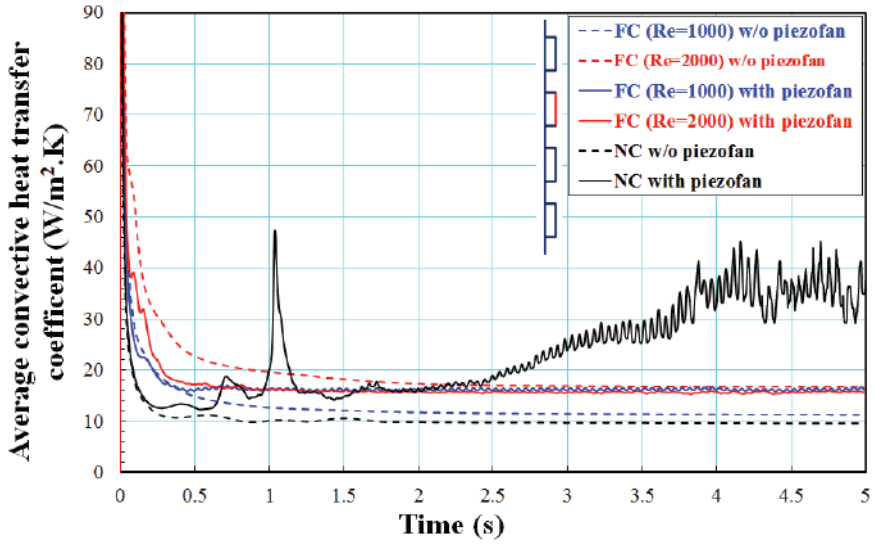

b) 2nd protruding front surface

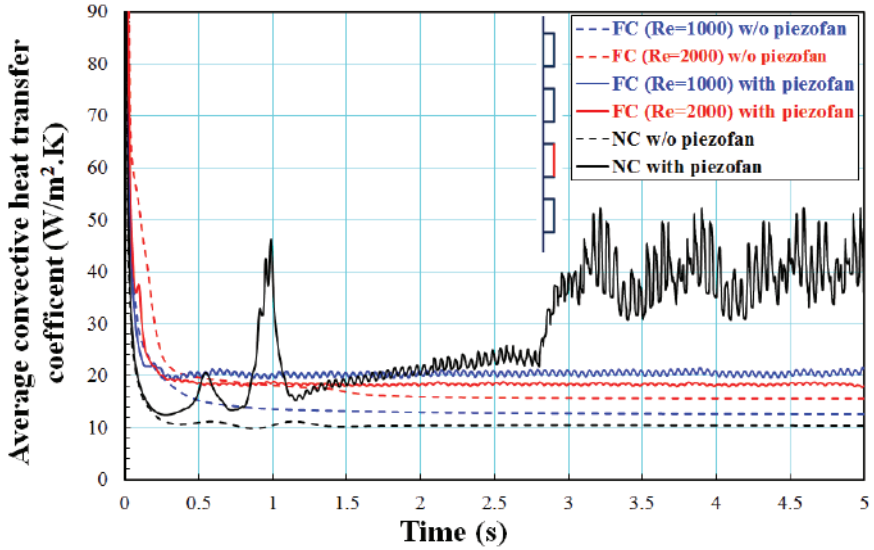

c) 3rd protruding front surface

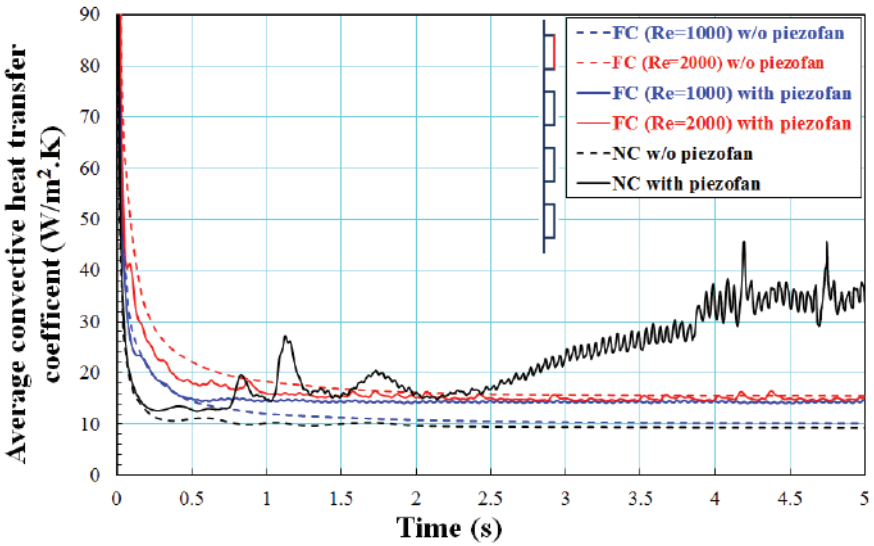

d) 4th protruding front surface

Figure 8. Time-dependent variation of average heat transfer coefficient at each protruding surface.

Table 2. Average temperature and heat transfer coefficient at each protruding surface after steady-state oscillation

	Re_m	Surface temperature (K)		Heat transfer coefficient (W/m²×K)	
		w/o piezofan	with piezofan	*w/o* piezofan	with piezofan
		1st protruding surface			
Case: NC	-----	338.20	309.13	13.30	37.50
Case: FC	1000	331.15	314.92	15.80	27.50
	2000	328.62	315.45	16.90	26.90
		2nd protruding surface			
Case: NC	-----	350.10	303.78	10.53	56.41
Case: FC	1000	339.51	319.92	12.94	22.40
	2000	330.37	325.13	16.12	18.76
		3rd protruding surface			
Case: NC	-----	355.05	308.56	9.70	38.93
Case: FC	1000	345.48	328.89	11.46	16.78
	2000	328.18	326.37	17.12	18.10
		4th protruding surface			
Case: NC	-----	357.10	307.83	9.40	40.80
Case: FC	1000	351.50	332.91	10.30	15.10
	2000	331.11	330.30	15.80	16.10

reduction decreased to 13.2K, 5.2K, 1.8K, and 0.8K on the 1st, 2nd, 3rd, and 4th protruding heat sources, respectively. While it is reduced by 29K, 46.3K, 46.5K, and 49.3K on the 1st, 2nd, 3rd, and 4th protruding heat sources, respectively, compared to a pure natural convection case without piezofan.

CONCLUSION

In this paper, the cooling performance of a vertically oriented single oscillating piezofan is numerically investigated. The computations were carried out using corresponding forced and natural convection channels assembled with wall-mounted protruding structures

heated sources. The physics analysis is described by a combination of passive and active vortex generation and natural convection or forced convection effects. It is observed that when the passive and active impacts of vortices are combined, the flow momentum towards the channel exit increases, breaking the boundary layers in all swept surfaces and enhancing the convection heat transfer rate significantly. The results were calculated as an average in the steady-state range after 3 seconds of piezofan operation for all preceding cases. The following are the major flow and thermal considerations that this investigation has revealed:

- In forced convection channels, the presence of an oscillating piezofan increased air velocity by about 2.5% in different flow domain sections compared to non-piezofan channels. In contrast, the increment in the natural convection channel was about 21%.
- The calculated average convective heat transfer coefficients for flow with piezofan are higher than without piezofan for all considered cases. Especially in the natural convection channel shows the highest enhancements of about 182%, 435%, 300%, and 334% for the 1st, 2nd, 3rd, and 4th front surfaces of the protruding heat source, respectively.
- The vortices generated by the active oscillations of piezofan mixed with the bouncy effects through the natural convection channel have a high performance by decreasing the temperatures of protruding heated surfaces by around 29 to 49.3°C.
- As the flow stream velocity is increased in the forced convection channel, the presence of an oscillating piezofan has relatively minor effects on flow and heat transfer improvements. For example, reductions in the temperatures of the protruding heated surfaces do not exceed 0.8 to 13.2°C as the Reynolds number is 2000.
- Finally, the 2D laminar flow computations, which show a high rate of vortex generation and secondary flows mixing in the air flow domain, as well as a good improvement in cooling performance, can be used in a wide range of modern electronic industry applications, such as miniaturized electronic cooling systems or/and electronic components.

NOMENCLATURE

A_c	The cross-sectional area of the piezofan (m^2)
b	Protruding heated source thickness (m)
c_p	Specific heat at constant pressure (J/kgK)
E_{pz}	Young's modulus (Pa)
f_r	First resonant frequency (Hz)
h	Convective heat transfer coefficient (W/m^2K)
I	The second moment of area of piezofan (m^4)
k	Thermal conductivity (W/mK)
L_{ch}	Length of the channel (m)
H_{hs}	Protruding heated source height (m)
L_{pz}	Length of the piezofan (m)
$\dot{m}$	The mass flow rate of air through the channel (kg/s)
m_{pz}	Mass of the piezofan (kg)
Nu	Nusselt number
P	Pressure (Pa)
q	Heat transfer rate (W)
q''	Wall heat flux (W/m^2)
Re	Reynolds' number of mainstream channel flow
S	Vertical channel width (m)
T	Temperature (K)
t	Time (s)
t_{pz}	Piezofan thickness (m)
U	The average velocity of air inside the channel (m/s)
u	The velocity of air in the x-direction (m/s)
V_{in}	The average velocity of air at the channel inlet (m/s)
v_{pz}	Tip velocity of the piezofan (m/s)
v	The velocity of air in the y-direction (m/s)
x, y	Cartesian coordinates
$X_{pz}(y)$	Maximum piezofan displacement at arbitrary y location (m)
$x_{pz}(y,t)$	Instantly displacement of the piezo fan (m)

Subscripts

a	Air
ch	Channel
h	Heated wall
in	Channel inlet
out	Channel outlet
pz	Piezofan

Greek Symbols

β	Characteristic coefficient, Eq. (2)
σ	Poisson's ratio
μ	Viscosity (kg/m.s)
ρ	Density (kg/m^3)
ψ	Dimensionless drive coefficient

Abbreviations

ALE	Arbitrarily Lagrangian-Eulerian scheme
aVG	Active vortices generation
FC	Forced convection
FEM	Finite Element Method
FSI	Fluid-Structure-Interaction analysis
NC	Natural convection
OSR	The oscillating ratio of piezofan
OA	The oscillating amplitude at the tip of the piezofan (m)
pVG	Passive vortices generation
TBL	Thermal boundary layer
VGS	Vortex Generations Strategies
w/o piezofan	The channel without piezofan

DECLARATIONS

ACKNOWLEDGEMENT

The present work forms a section of a Ph.D. dissertation entitled *"Investigation of Piezoelectric Fans for Heat Transfer Enhancement in a Channel"*, by Salim Musullu, conducted at Dokuz Eylül University, Graduate School of Natural and Applied Sciences (Fen Bilimleri Enstitüsü), Department of Mechanical Engineering, İzmir, Türkiye (2022).

AUTHORSHIP CONTRIBUTIONS

Authors equally contributed to this work.

DATA AVAILABILITY STATEMENT

The authors confirm that the data that supports the findings of this study are available within the article. Raw data that support the finding of this study are available from the corresponding author, upon reasonable request.

CONFLICT OF INTEREST

The author declared no potential conflicts of interest with respect to the research, authorship, and/or publication of this article.

ETHICS

There are no ethical issues with the publication of this manuscript.

STATEMENT ON THE USE OF ARTIFICIAL INTELLIGENCE

Artificial intelligence was not used in the preparation of the article.

REFERENCES

[1] Young T J, Vafai K. Convective flow and heat transfer in a channel containing multiple heated obstacles. Int J Heat Mass Transf 1998;41:3279-3298. [Crossref]

[2] Young T J, Vafai K. Convective cooling of a heated obstacle in a channel. es. Int J Heat Mass Transf 1998;41:3131-3148. [Crossref]

[3] Young T J, Vafai K. Experimental and numerical investigation of forced convective characteristics of arrays of channel mounted obstacles. ASME J Heat Transfer 1999;121:34–42. [Crossref]

[4] Zeng Y, Vafai K. An investigation of convective cooling of an array of channel-mounted obstacles. Numerical Heat Transfer, Part A: Applications 2009;55;967-982. [Crossref]

[5] Sarper B, Saglam M, Aydin O. Experimental and numerical investigation of natural convection in a discretely heated vertical channel: Effect of the blockage ratio of the heat sources. Int J Heat Mass Transfer 2018;126:894-910. [Crossref]

[6] Haghighi A, Albojamal A, Vafai K Heat removal enhancement in a channel with a single or an array of metallic foam obstacles. Int J Heat Mass Transf 2020;149:106057. [Crossref]

[7] Wang Q, Jaluria Y. Unsteady mixed convection in a horizontal channel with protruding heated blocks and a rectangular vortex promoter. Physics of Fluids 2002;14:2113-2127. [Crossref]

[8] Chomdee S, Kiatsiriroat T Enhancement of air cooling in staggered array of electronic modules by integrating delta winglet vortex generators. Int J Therm Sci 2006;33:618-626. [Crossref]

[9] Oztop HF, Varol Y, Alnak DE. Control of heat transfer and fluid flow using a triangular bar in heated blocks located in a channel. Int Commun Heat Mass Transf 2009;36(8):878–885. [Crossref]

[10] Beig SA, Mirzakhalili E, Kowsari F. Investigation of optimal position of a vortex generator in a blocked channel for heat transfer enhancement of electronic chips. Int J Heat Mass Transf 2011;54(19–20):4317–4324. [Crossref]

[11] Al-Asadi MT, Alkasmoul FS, Wilson MCT. Heat transfer enhancement in a micro-channel cooling system using cylindrical vortex generators. Int Commun Heat Mass Transf 2016;74:40–47. [Crossref]

[12] Zheng S, Feng Z, Lin Q, Hu Z, Lan Y, Guo F, Huang K, Yu F. Numerical investigation on thermal–hydraulic characteristics in a mini-channel with trapezoidal cross-section longitudinal vortex generators. Appl Therm Eng 2022;205:118004. [Crossref]

[13] Yang SJ. A numerical investigation of heat transfer enhancement for electronic devices using an oscillating vortex generator. Numer Heat Transf A Appl 2002;42:269–284. [Crossref]

[14] Yang SJ. Numerical study of heat transfer enhancement in a channel flow using an oscillating vortex generator. Heat Mass Transf 2003;39:257–265. [Crossref]

[15] Fu WS, Tong BH. Numerical investigation of heat transfer from a heated oscillating cylinder in a cross flow. Int J Heat Mass Transf 2002;45:3033–3043. [Crossref]

[16] Kurşun B, Sivrioğlu M. Effects of flow routing plate on mixed convection heat transfer from protruded heat sources. Isi Bilimi ve Teknigi Derg 2017;37:19–32.

[17] Ismael MA. Forced convection in partially compliant channel with two alternated baffles. Int J Heat Mass Transf 2019;142:118455. [Crossref]

[18] Kim YH, Cierpka C, Wereley ST. Flow field around a vibrating cantilever: coherent structure eduction by continuous wavelet transform and proper orthogonal decomposition. J Fluid Mech 2011;669:584–606. [Crossref]

[19] Choi M, Cierpka C, Kim YH. Vortex formation by a vibrating cantilever. J Fluids Struct 2012;31:67–78. [Crossref]

[20] Florio LA, Harnoy A. Use of a vibrating plate to enhance natural convection cooling of a discrete heat source in a vertical channel. Appl Therm Eng 2007;27:2276–2293. [Crossref]

[21] Lin CN. Enhanced heat transfer performance of cylindrical surface by piezoelectric fan under forced convection conditions. Int J Heat Mass Transf 2013;60:296–308. [Crossref]

[22] Jeng TM, Liu CH. Moving-orientation and position effects of the piezoelectric fan on thermal characteristics of the heat sink partially filled in a channel with axial flow. Int J Heat Mass Transf 2015;85:950–964. [Crossref]

[23] Li XJ, Zhang JZ, Tan XM. Convective heat transfer on a flat surface induced by a vertically oriented piezoelectric fan in the presence of cross flow. Heat Mass Transf 2017;53:2745–2768. [Crossref]

[24] Li XJ, Zhang JZ, Tan XM. An investigation on convective heat transfer performance around piezoelectric fan vibration envelope in a forced channel flow. Int J Heat Mass Transf 2018;126:48–65. [Crossref]

[25] Oh MH, Seo J, Kim YH, Choi M. Endwall effects on 3D flow around a piezoelectric fan. Eur J Mech B Fluids 2019;75:339–351. [Crossref]

[26] Oh MH, Park SH, Kim YH, Choi M. 3D flow structure around a piezoelectrically oscillating flat plate. Eur J Mech B Fluids 2018;67:249–258. [Crossref]

[27] Park SH, Oh MH, Kim YH, Choi M. Effects of free-stream on piezoelectric fan performance. J Fluids Struct 2019;87:302–318. [Crossref]

[28] Chen Y, Peng D, Liu Y. Heat transfer enhancement of turbulent channel flow using a piezoelectric fan. Int J Heat Mass Transf 2020;147:118964. [Crossref]

[29] Tiwari J, Yeom T. Enhancement of channel-flow convection heat transfer using piezoelectric fans. Appl Therm Eng 2021;191:116917. [Crossref]

[30] Ko J, Oh MH, Choi M. Effects of piezoelectric fan on cooling flat plate in quiescent air. Eur J Mech B Fluids 2021;88:199–207. [Crossref]

[31] Hasan SI, Küçüka S, Ezan MA. Thermo-fluidic analysis of a single piezofan in longitudinal channel. Int Commun Heat Mass Transf 2021;129:105651. [Crossref]

[32] Hasan SI, Küçüka S, Ezan MA. Cooling performance of a piezo-fan oscillating in a vertical channel with natural convection. Int Commun Heat Mass Transf 2023;141:106602. [Crossref]

[33] Boz ÖA, Küçüka S, Ezan MA. Dynamic effects of piezoelectric fan on the natural convection in a vertical channel. Int J Technol Sci 2024;16:1–10. [Crossref]

J Ther Eng, Vol. 12, No. 1, pp. 365−384, January, 2026

Journal of Thermal Engineering
Web page info: https://jten.yildiz.edu.tr
DOI: 10.14744/thermal.0001086

Research Article

Magnetohydrodynamic mixed convection within a ventilated cavity crossed by a nanofluid: Effect of the obstacle position

Mourad MODERRES[1,*], Seddik KHERROUBI[1], Abdelkader BOUTRA[2,3], Abdelhakim SETTAR[4], Chaouki Ghenai[5], Djelloul AZZOUZI[1], Hakan F. OZTOP[6]

[1]*Laboratory of Industrial Fluids, Measurements and Application (FIMA) UDBKM, Ain Defla, 44225, Algeria*
[2]*Laboratory of Transport Phenomena, USTHB, BP. 32 El Alia, Algiers, 16111, Algeria*
[3]*Algeria School of Applied Sciences, Algiers, 16001, Algeria*
[4]*INSA Centre Val de Loire, University of Orleans, PRISME EA, Bourges, 4229, France*
[5]*Department of Sustainable and Renewable Energy Engineering, College of Engineering, University of Sharjah, Sharjah, 00000, United Arab Emirates*
[6]*Department of Mechanical Engineering, Faculty of Technology, Fırat University, Elazıg, 23119, Turkiye*

ARTICLE INFO

Article history
Received: 11 October 2024
Revised: 09 January 2025
Accepted: 20 January 2025

Keywords:
Circular Obstacle; Magnetic Field; Mixed Convection; Nanofluids; Ventilated Cavity

ABSTRACT

This study presents a numerical investigation into mixed convection heat transfer within a ventilated square cavity containing a circular obstacle, evaluated under various magnetic field inclination angles. Ventilation is ensured by two fixed openings on the vertical walls of the cavity. Cold Carbon Nanotubes-water nanofluid enters through the opening at the top of the left vertical wall and exits through the opening located at the bottom of the right vertical wall. All four walls of the cavity are maintained at the same temperature, which is higher than that of the incoming nanofluid. The finite volume method, combined with the SIMPLER algorithm for pressure-velocity coupling, was utilized to solve the governing differential equations of the system. The objective was to determine the optimal geometry that offers the best thermal performance with the lowest pressure drop. Key results indicate that increasing the nanoparticle volume fraction from 0% to 6% enhances the average Nusselt number by up to 20.3%, significantly improving heat transfer performance. Similarly, tilting the magnetic field at an angle of 45° minimizes the pressure drop by 12% compared to the baseline case. The optimal obstacle position was identified as the cavity center, balancing heat transfer enhancement with a manageable pressure drop. These findings can be applied to optimize the design of cooling systems in industrial applications such as electronic device cooling, energy storage systems, and heat exchangers, where efficient thermal management and minimal pressure loss are crucial. The research introduces a new application of Carbon Nanotubes-water nanofluid to enhance heat transfer performance, with the added complexity of a magnetic field influencing the flow dynamics.

Cite this article as: Moderres M, Kherroubi S, Boutra A, Settar A, Ghenai C, Azzouzi D. Magnetohydrodynamic mixed convection within a ventilated cavity crossed by a nanofluid: Effect of the obstacle position. J Ther Eng 2026;12(1):365−384.

***Corresponding author.**
*E-mail address: mourad.moderres@univ-dbkm.dz

This paper was recommended for publication in revised form by Editor-in-Chief Ahmet Selim Dalkilic

Published by Yıldız Technical University Press, İstanbul, Turkey
Yıldız Technical University. This is an open access article under the CC BY-NC license (http://creativecommons.org/licenses/by-nc/4.0/).

INTRODUCTION

For companies, it is now imperative to manage the thermal performance adequately because with regards to minimized energy consumption and improved system efficiency not only the durability of the material, but also customer confidence are influenced. One possible solution to enhance the heat transfer rate is the addition of nanoparticles in common fluids like water, ethylene [1], Nanofluids were documented and for the first time, a technologically feasible heat transfer fluid have been introduced as a dispersion of metallic nanoparticles in regular Heat Transfer Fluids that substantially enhances the heat conductivity, reduces pumping power to compensate adverse thermophysical properties by far out weighing limitations related with conventional fluids for energy effective heat transfer applications. Also, bottling of metallic or non-metallic NPs into fluids such as water, oils and ethylene glycol increase in the thermal conductivity coefficient and heat transfer rate [2-5]. In addition, the degree of heat transfer enhancement is strongly dependent on the nanoparticle and host fluid properties, particle volume fraction, particle size, particle shape, Brownian motion and thermophoresis [6-10].

However, with the incorporation of nanoparticles, thermal performance is enhanced and pressure drop is increased, which restricts their application in thermal systems.

For instance, the viscosity behavior of Al_2O_3 –water and ZnO ethyleneglycol nanofluids over that of their respective base fluids is reported to be observed as higher in comparison with the base fluids [11, 12] experimentally studied the pressure drop and heat transfer rate of silver-water nanofluids in a counter-flow heat exchanger. The authors found that the pressure drop increased by 55%, and the heat transfer rate increased by 69 % at a volume concentration of 0.9% compared to the base water [13] investigated the heat transfer and pressure drop in helically coiled tube heat transfer working fluid with Al_2O_3 nanofluids under a turbulent flow condition. The increase in heat transfer coefficients and pressure drop is enhanced with particle concentration. The study of heat transfer and pressure drop in a conical helical tube heat exchanger using MWCNT/water nanofluids was the focus of [14]. Their findings revealed that, in comparison to water, the pressure drop increased by approximately 16%, 30%, and 42% for nanoparticle concentrations of 0.1%, 0.3%, and 0.5%, respectively. In addition, several numerical and experimental studies on different cavity shapes have explored the impact of nanofluids on heat transfer and pressure drop performance under different flow regimes [15-18]. All the mentioned studies showed a significant improvement in heat transfer, using nanofluids as working fluid in which the pressure drop also increased.

Over the last decade, a review of literature suggests that researchers have also explored the convective flow of fluids – nanofluids or base fluids filled in cavities with obstacles. It is a very promising solution for an improved thermal performance. For example, [19] performed a numerical investigation of the effect of a square conductive obstacle placed in the center of a square cavity under natural convection. The heat-exchange coefficient has been found to be increased (decreased) by the incorporation of a body with thermal conductance lower (higher) than that of the unit.

Numerically studied the influence of an adiabatic obstacle at the center of a differentially heated square cavity on flow and temperature fields [20]. The outcome reveals an optimal size of obstacle yielding a heat transfer enhancement compared to the case in absence of obstacles. [21] conducted a numerical investigation to analyze how dividing a solid block with varying conductivity affects the flow and heat transfer properties within a square cavity. The findings indicate that subdividing the block postpones the initiation of natural convection and diminishes heat transfer. Additionally, the subdivision of solid blocks does not significantly impact heat transfer at elevated Rayleigh numbers, with blocks featuring lower conductivity proving to be more conducive to convective heat transfer. investigated natural convection in a truncated cone containing Cu-water nanofluid for different Rayleigh numbers, wall inclinations and heat source lengths [22]. The results indicate an enhancement in the cooling capability when nanofluids are used, and this is further controlled by both wall angle and power length of heat [23]. Studied the water-Al_2O_3 nanofluids laminar forced convection in a microchannel heat sink, and obtained favorable heat transfer performance through numerical analysis, revealing that better thermal performance is attained with higher nanoparticle volume concentration and Reynolds number for advanced cooling systems.

Provided a comprehensive review of numerical and experimental results from natural laminar convection in enclosures with and without internal bodies, details were provided for the Rayleigh number, shape ratio, relative position of internal bodies, number of inner bodies and inclination angle of cavity or obstacle [24]. The results show that appropriate values of the control parameters can significantly enhance thermal recirculation in an enclosure with inner objects. Thus, due to the presence of bodies, secondary vortices are developed in the cavity and modification on current lines and isotherms occurs. Therefore, [25] considered the heat transfer of Cu-water nanofluid in a lid-driven cavity having conductive solid square cylinder at its center. Their findings showed that with a reducing of Richardson number, the influence of nanoparticle concentration would decrease[26]. Investigated natural convection in a square cavity containing a nanofluid and an adiabatic square block in the center. The authors have demonstrated that the average Nusselt number has been found to increase with an increasing volume fraction of nanoparticles for all Rayleigh numbers, except $Ra = 10^4$.

Similarly, at low Rayleigh numbers, the heat transfer rate decreases as the adiabatic square body size increases. The

natural convection in a square cavity with four hot inner circular cylinders was studied by [27], which were arranged at multiple spatial location of rectangular shape. The authors showed that the flow and thermal fields are consistently stable across the range of $10^3 \leqslant Ra \leqslant 10^4$. However, in the Rayleigh range of 10^5 to 10^6, both velocity and temperature fields become unstable due to the placement of cylinders. In addition, the symmetry with regard to the vertical center line is affected by cylinder locations. Another investigation by [28] explored the heat transfer characteristics of a CuO-water nanofluid within a rhombus-shaped cavity, featuring a square cylindrical obstacle at the cavity center under three different conditions (cold, adiabatic, and hot). The results showed that the cold cylinder hinders heat transfer in cavity when compared with isothermal and hot square cylinders.

Similarly, the cavitymodel with openings have attracted much attention from researchers becaused it frequently appears in practical engineering processing , such as cooling/heating systems. This design aims to optimize the configuration of openings for facilitating heat transfer. For instance, [29] investigated the mixed convection of Al_2O_3-water nanofluid within a ventilated enclosure. hey investigated different combinations of outlet locations, Reynolds and Richardson numbers, and nano-particle volume fractions to find a suitable configuration for these systems. This is a framework whereby saturated boiling has the highest possible heat transfer rate and pressure drop from same. Mixed nanofluid convection in a ventilated irregular cavity was also investigated numerically by [30]. The results show that heat transfer is augmented with increasing nanoparticle volume fraction, Richardson and Reynolds numbers, and decreasing the particle size [31]. investigated mixed convection optimization in a ventilated square cavity containing nanofluid. It was observed that an increase in the Richardson and nanoparticle volume fraction results in a reduction of average Nusselt number. Furthermore, the relative distance of inlet port location from bottom wall of cavity 0 and outlet port location from top wall of cavity 0.9H at Re = 0.01 and Φ = 3% is the optimum configuration for heat transfer. Owing to its practical importance, understanding the mixed convection in ventilated cavities is important in a number of technological applications such as solar collectors, building thermal systems, air conditioning and cooling of electronic boards. The modification of heat transfer in cavities due to the inclusion of obstacles, has recently been a subject of enhanced concern. From reviewing the previously conducted works, it is found that the mixed convection have been widely studied in ventilated square enclosure filled with cavity, as there are obstacles inside and fins on the bottom wall acting as agents of disturbance.. For example, [32] conducted a numerical investigation on steady-state mixed convective laminar flow in a ventilated square enclosure where the right vertical wall was heated and featured a thermally conductive solid cylinder. Their results, considering various obstacle positions and Richardson numbers, indicate a significant impact of obstacle location on the heat exchange rate. Similarly, in another study, [33] investigated mixed convection in a ventilated cavity with a centrally positioned solid, heat-generating circular obstacle, exploring a wide range of Richardson, Reynolds, and Prandtl numbers. They conclude that these parameters have a significant impact on the flow and thermal fields, in addition to the heat transfer rate, drag force and average fluid temperature of the cavity.

The effect of the external magnetic field on the heat transfer of the electrically conductive fluid has also received much attention due to various applications in many fields such as crystal growth, microelectronic devices, control of hydrodynamic behavior and heat transfer during crystal growth processes [34, 35]. Thus, an effect of the inclined uniform magnetic field on the natural convection of an electrical conductor (Pr = 0.025) in a rectangular cavity was numerically studied by [36]. The authors reported that the inclination angles of the magnetic field and the cavity aspect ratio play an important role in different Rayleigh numbersfor fluid flow and heat transfer. Namely,the flow structure depends strongly on the magnetic field inclination angle for a large Hartmann number [37]. numerically studied the natural convection in a fillated nanofluid cavity having obstacles of different shapes (circular, square, and diamond) installed under the influence of a uniform magnetic field and uniform heat generation. The cavity was heated from the bottom and cooled from the vertical sides, while the top wall was assumed to be adiabatic;thesidewalltemperatures vary linearly. It is observed that the presence of obstacles deteriorates the heat transfer process, and this is more pronounced with a higher external Rayleigh number compared to the cavity without obstacles at Ra = 10^6. Reduced heat transfer with square and diamond-shaped obstacles than without obstacles is less effective with increasing Hartmann numbers [38]. Examined porous domain modeling under the influence of radiation and Lorentz forces, employing a hybrid nanomaterial and solving equations through CVFEM. Findings indicate that increased permeability thins the boundary layer, while magnetic fields reduce its impact on Nu_{ave}, buoyancy forces enhance thermal gradients [39]. Analyzed the influence of nanomaterials on MHD flow between non-parallel plates using HPM and RK4 methods. It finds that hydraulic boundary layer thickness decreases with higher Reynolds numbers but increases with a larger Hartmann number [40]. Discussed thermal behavior of nanomaterials in various contexts. The study examines Al_2O_3-water nanofluid flow between plates, incorporating Brownian motion and thermal forces, revealing C_f and Nu increase with higher squeeze and Eckert numbers.

Analyzed the MHD free convection flow of Cu /water nanofluid in a square cavity heated from the bottom and cooled by the side walls [41]. The heat transfer rate increases withthe heat source length, nanoparticle volume fraction, and Rayleigh number and a decreasing function of the Hartmann number [42]. Studied the mixed MHD flow

convection of Cu/water nanofluid in an open cavity with an isothermal horizontal wall. The authors showed that an increase in the Lorentz force leads to attenuating the circulation zone inside the cavity for a horizontal and inclined magnetic field [43]. investigated the effect of magnetic field directions on the natural convection of CNT-water nanofluid in a cubical cavity. For different Rayleigh numbers and nanoparticle volume fractions, the results indicate that the heat transfer increases with the increase of nanoparticle volume fraction. At the same time,the magnetic force inhibits the heat transfer by 50% when the Hartmann number is increased from 50 to 100. Moreover, the magnetic field angles are more pronounced for Ra $=10^5$ [44]. Numerically examined the natural convection of TiO2-water nanofluid in a cubic cavity containing a hot block under the influence of a magnetic field, emphasizing the effects of 3D flow and the enhancement of heat transfer by nanoparticles. The results indicate that buoyancy enhances heat exchange, while magnetic fields inhibit it, with 3D flows showing significant differences from 2D, particularly at high Rayleigh numbers.

Considered numerically mixed convection in a square cavity with a heated and filled lid of nanofluid alumina-water whose isothermal square blockage inside the magnetic field [45]. For other parameters, the average Nusselt number decreased with an increase in the magnetic field. Numerical analysis of free convection in a square cavity filled with a saturated porous media with liquid gallium subjected to an inclined uniform magnetic field was performed by [46]. The bottom of the enclosure is presumed to be uniformly heated. It is assumed that the top boundary of the horizontal top surface is insulated, whereas the left vertical side of the cavity is subjected to a linear heat generation and the right side wall is linearly heated or cold. It has been found that in the case of a linearly heated right wall, the average Nusselt number is an increasing function of the Darcy number, and the vertical magnetic field results in higher values for the average Nusselt number compared to the horizontal magnetic field along the bottom and sidewalls of the cavity. For the cold right wall case, the horizontal magnetic field leads to higher values of the meanNusselt number than the vertical magnetic field case. The average Nusselt number decreases as one moves along the lower and right. At the same time, it increases along the left wall with increasing distance [47]. Demonstrated the effectiveness of the GMDH-type neural network in modeling heat transfer in MHD nanofluids, outperforming the CVFEM approach. Key findings reveal that heat transfer improves with increased buoyancy, nanoparticle concentration, and enclosure slope but decreases with higher Hartmann numbers. Explored the impact of microrotational velocity and radial magnetic fields on laminar natural convection flow within vertical concentric annuli containing a polar fluid. The results highlight the effects of the Hartmann number, vertex viscosity, and annular gap on parameters such as velocity, induced magnetic fields, and current density [48]. In another study, [49] investigated unsteady heat transfer and entropy generation in a viscoelastic Maxwell fluid subjected to an induced magnetic field over a stretching sheet, employing numerical methods for their analysis. Their key findings highlight the influence of various parameters on velocity, magnetic distribution, thermal boundary layers, and entropy generation.

Recently, [50] have studied the influence of external magnetic field on heat transfer and entropy generation of hybrid nanofluid past a partially heated non-uniform ventilated cavity for different control parameters. They found that the enhancement of magnetic field strength usually has a tendency to resist the convective heat transfer and restrict thermal boundary layer thickness. For the entire range of Ha and Re, the nanoparticles' inclusion enhances the Nusselt number [51]. Analyzed the influence of the position of outlet for various control parameters of a nanofluid, inside a ventilated cavity in the presence of magnetic field. Numerical results indicate that the heat transfer rate is influenced by the location of the outletpoints [52]. Investigated analytically the magnetohydrodynamic free convection with radiation and Hall currents in a porous media between vertical walls. The present investigation focuses on chilled panels for aluminum smelters. They emphasize the important role played by the parameters such as Hartmann number, Hall current and radiation in controlling flow patterns, velocity field and magnetic fields. These observations help to increase the system knowledge before even having a prototype [53].

Presented a study on nanofluid heat transfer inside a porous media with a uniform magnetic field, in which they considered the impact of Rayleigh number, Hartmann number and the properties of nanofluid. Results indicate that on increasing the Rayleigh number and nanoparticles property ratio, heat transfer increases, while is further intensified for a lower Hartmann number [54]. Analyzed an analytically solution of the effects of heat radiation, chemical reaction and induced magnetic field on natural convective MHD flow in a porous medium between vertical walls. Their main results show that the influences of so many parameters are remarkable on the profiles of velocity, temperature and magnetic fields, which may have extensive applications in some chemical reactors and solar thermal systems has studied the application of ferro nanoparticles in screw heat exchangers with focus on influence of variable magnetic fields and geometrical process parameters on enhancement of thermal performance. Computations indicate that Reynolds number has the most effect on the flow of nanofluid, and screw diameter has an important impact on skin friction [55].

Recent research has increasingly examined heat transfer optimization in enclosures containing internal obstacles, under diverse operating conditions such as natural and mixed convection, varying Rayleigh numbers, and the influence of magnetic fields. The originality of the present study stems from:

- Investigating the combined effects of circular obstacle positioning and external magnetic fields on the performance of CNT-water nanofluids within ventilated cavities.
- Optimizing thermal performance while minimizing pressure drops, a balance that has practical applications in thermal management systems such as cooling, air conditioning, and electronic devices.
- Exploring a wider range of control parameters than reported in existing literature, enabling the identification of optimal configurations for energy efficient design.

In this paper we attempt to fill in this gap by carrying out a numerical investigation to establish an optimal combination of obstacle layout and magnetic field arrangement for the maximum heat transfer accompanied by minimal flow resistance.

PROBLEM DESCRIPTION

Figure 1 shows the geometry of the present study. The flow takes place inside a ventilated square cavity of length L and height H (L = H) containing a circular obstacle of diameter D (D = 0.1H) and thermal conductivity k^* which changes place in the cavity: P_1 (X = 0.50, Y = 0.50), P_2 (X = 0.50, Y = 0.75), P_3 (X = 0.75, Y = 0.50), P_4 (X = 0.50, Y = 0.25) and P_5 (X = 0.25, Y = 0.50). The cavity is filled with a nanofluid from two equal cross sectional on some height (0.25H) at other angles of uniform magnetic field ($\vec{B}$) for the horizontal plane. The cool nanofluid is injected and sucked from the two openings located at the top of the left vertical side and at bottom fo the right vertical side, respectively. All cavity walls are assumed to be isothermal and at the base fluid temperature of the enteringnanofluid. Table. 1 Thermophysical properties of water and CNT nanoparticles are shown in Table 1.

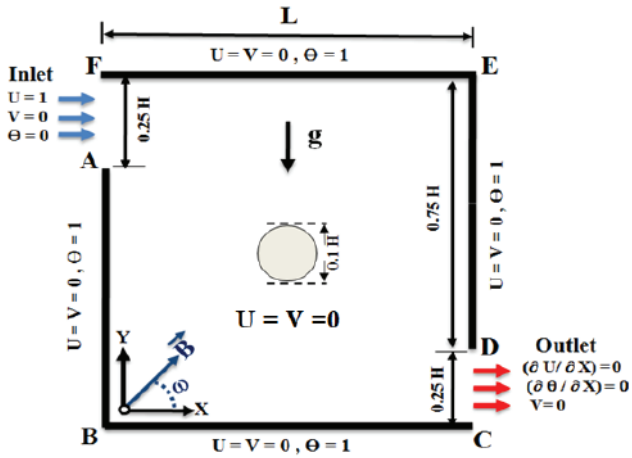

Figure 1. Geometrical representation of the present problem.

Simplifying Hypotheses

The following assumptions were established:

- The base fluid and the solid spherical nanoparticles are in thermal equilibrium.
- The solid nanoparticles and base fluid are assumed to be in thermal equilibrium.
- The nanofluid is Newtonian and incompressible.
- The Boussinesq approximation is used to determine the density variation in the buoyancy term, where the other thermophysical properties of the nanofluid are assumed constant.
- The flow is considered to be steady, two-dimensional, and laminar.
- The effects of radiation, viscous dissipation, and Joule heating are negligible.
- The induced magnetic field is sufficiently weak to be neglected compared to the applied magnetic field B_0.
- The Hall effect is neglected.

Governing Equations

Given the simplifying hypothesis considered above, the governing equations describing the flow and thermal field used in this study are the continuity, momentum, and energy equations, respectively. The primary assumptions indicate that effects such as radiation, viscous dissipation, Joule heating, the Hall effect, and induced magnetic fields are negligible compared to the applied magnetic field B_0, These equations are defined in their nondimensional forms as follows:

$$\nabla \cdot \vec{V}' = 0 \tag{1}$$

$$\rho_{nf}\left(\vec{V}'\cdot\nabla\right)\vec{V}' = -\nabla p + \mu_{nf}\nabla^2\vec{V}' + (\rho\beta)_{nf}\left(T - T_{Inlet}\right)\vec{g} + (\vec{J}\wedge\vec{B}) \tag{2}$$

$$\vec{V}'\cdot\nabla T = \alpha_{nf}\nabla^2 T \tag{3}$$

Table 1. Thermophysical properties of water (Pr = 5) and CNT nanoparticles [43].

	$Cp\,(J\,kg^{-1}\,K^{-1})$	$\rho\,(kg\,m^{-3})$	$k\,(W\,m^{-1}\,K^{-1})$	$\beta\times10^5\,(K^{-1})$
Water	4179	997.1	0.613	21
CNT	650	1350	3500	4.20

where, the applied magnetic field B ($\vec{B}=\vec{B}_X\,\vec{i}+\vec{B}_Y\,\vec{j}$) is uniform with a constant magnitude B_0 ($B_0=\sqrt{B_X^2+B_Y^2}$)

The interaction between electromagnetic fields and the electrically-conducting nanofluid flow constitutes the Lorentz force [51, 56, 57]:

$$\vec{F}=\vec{J}\wedge\vec{B} \tag{4}$$

The electric current density is governed by the generalized Ohm's law, defined as follows [42-44]:

$$\vec{J}=\sigma_{nf}\left[\vec{E}+\left(\vec{V}'\wedge\vec{B}\right)\right] \tag{5}$$

where, σ_{nf} is the electrical conductivity of the nanofluid, ($\vec{E}$) is the electrical field intensity.

When all cavity walls are electrically insulated [51] and [57]: $\vec{E}=0$

where, V' ($\vec{V}'=u\,\vec{i}+v\,\vec{j}$) is the velocity vector.

Thus, the expressions of the Lorentz force components are defined for the x and y directions, respectively:

$$\begin{aligned}&F_x=-\sigma_{nf}\,B_0^2\sin\omega\left(u\sin\omega-v\cos\omega\right)\ \text{and}\\&F_y=-\sigma_{nf}\,B_0^2\cos\omega\left(v\cos\omega-u\sin\omega\right)\end{aligned} \tag{6}$$

The effective density, heat capacity, and thermal expansion coefficient of the nanofluidare respectively:

$$\rho_{nf}=(1-\varphi)\rho_{bf}+\varphi\rho_s \tag{7}$$

$$\left(\rho C_p\right)_{nf}=(1-\varphi)\left(\rho C_p\right)_{bf}+\varphi\left(\rho C_p\right)_s \tag{8}$$

$$(\rho\beta)_{nf}=(1-\varphi)(\rho\beta)_{bf}+\varphi(\rho\beta)_s \tag{9}$$

For the effective thermal conductivity and the effective dynamic viscosity, the formulas used by [29] are, respectively:

$$k_{nf}=\frac{(k_s-k_{lr})\varphi k_{lr}\left(2\beta_1^3-\beta^3+1\right)+(k_s+2k_{lr})\beta_1^3\left[\varphi\beta^3(k_{lr}-k_{bf})+k_{bf}\right]}{\beta_1^3(k_s+2k_{lr})-(k_s-k_{lr})\varphi\left(\beta_1^3+\beta^3-1\right)} \tag{10}$$

$$\mu_{nf}=\mu_f\left(150\varphi^2+2.5\varphi+1\right) \tag{11}$$

with, $\beta=1+(h/a)$; $\beta_1=1+(h/2a)$; $k_{lr}=2k_{bf}$

where, h is the interfacial layer thickness, a is the particle radius, and lr denotes the layer.

From the work data of [58]: h = 1 nm and a = 10 nm.

The dimensionless form of the governing equations can be obtained by introducing the dimensionless variables as follows:

$$\begin{aligned}&(X,Y)=\frac{(x,y)}{H};\ (U,V)=\frac{(u,v)}{u_{Inlet}};\ \theta=\frac{T-T_{Inlet}}{T_{Wall}-T_{Inlet}};\\&P=\frac{p}{\rho_{nf}\,u_{Inlet}^2}\quad Pr=\frac{\nu_{bf}}{\alpha_{bf}};\ Re=\frac{u_{Inlet}\,H}{\nu_{bf}};\\&Ha=B_0\,L\left(\frac{\sigma_{nf}}{\mu_{bf}}\right)^{1/2}\end{aligned} \tag{12}$$

After substitution of the above variables, we obtain the following dimensionless equations:

$$\frac{\partial U}{\partial X}+\frac{\partial V}{\partial Y}=0 \tag{13}$$

$$\begin{aligned}U\frac{\partial U}{\partial X}+V\frac{\partial U}{\partial Y}=&-\frac{\partial P}{\partial X}+\frac{\mu_{nf}}{\rho_{nf}\,\nu_{bf}}\frac{1}{\mathrm{Re}}\left(\frac{\partial^2U}{\partial X^2}+\frac{\partial^2U}{\partial Y^2}\right)\\&-\frac{\rho_{bf}\,Ha^2}{\rho_{nf}\,\mathrm{Re}_{bf}}\sin\omega\left(U\sin\omega-V\cos\omega\right)\end{aligned} \tag{14}$$

$$\begin{aligned}U\frac{\partial V}{\partial X}+V\frac{\partial V}{\partial Y}=&-\frac{\partial P}{\partial Y}+\frac{\mu_{nf}}{\rho_{nf}\,\nu_{bf}}\frac{1}{\mathrm{Re}}\left(\frac{\partial^2V}{\partial X^2}+\frac{\partial^2V}{\partial Y^2}\right)+\frac{(\rho\beta)_{nf}}{\rho_{nf}\,\beta_{bf}}\mathrm{Ri}\,\theta\\&-\frac{\rho_{bf}\,Ha^2}{\rho_{nf}\,\mathrm{Re}_{bf}}\cos\omega\left(V\cos\omega-U\sin\omega\right)\end{aligned} \tag{15}$$

$$U\frac{\partial\theta}{\partial X}+V\frac{\partial\theta}{\partial Y}=\frac{\alpha_{nf}}{\alpha_{bf}}\frac{1}{\mathrm{Re}_{bf}\,\mathrm{Pr}}\left(\frac{\partial^2\theta}{\partial X^2}+\frac{\partial^2\theta}{\partial Y^2}\right) \tag{16}$$

where, $\alpha_{nf}=k_{nf}/\left(\rho C_p\right)_{nf}$ is the thermal diffusivity of nanofluid and $Ha^2=\sqrt{\frac{\sigma B^2 L}{\mu}}$ is the Hartmann number,

$\mathrm{Re}_{bf}=\frac{\rho_{bf}VL}{\mu_{bf}}$: the Reynolds number for base fluid.

For a solid obstacle, the energy equation is:

$$\left(\frac{\partial^2\theta^*}{\partial X^2}+\frac{\partial^2\theta^*}{\partial Y^2}\right)=0 \tag{17}$$

The boundary conditions are in the following forms:

- **Hot walls:** all walls are assumed to be at a high temperature $T=T_H$, with no-penetration and no-slip conditions:
- Left wall (x = 0 and $0\le y\le 0.75H$)
- Right wall (x = L and $0.25H\le y\le H$)
- Top wall (y = H and $0\le x\le L$)
- Bottom wall (y = 0 and $0\le x\le L$)
- In dimensionless form: U = V = 0 and θ = 1.
- **Inlet opening:** The inflow is cold ($T=T_C$) with a uniform velocity $u=u_0$
- In dimensionless form: U = 1, V = 0 and θ = 0.
- **Outlet opening:** A steady-state regime is assumed.
- In dimensionless form: $\partial U/\partial X=\partial\theta/\partial X=0$ and V=0.
- **Obstacle surfaces**: No-slip and no-penetration conditions apply.

- In dimensionless form: U = V = 0.
- **Nanofluid-Obstacle interface**: $(\partial\theta/\partial n)_{nf} = (k^*/k_{nf})(\partial\theta/\partial n)_{Obstacle}$

Heat Transfer and Pressure Drop

To study the heat transfer characteristics related with mixed convection (along the four hot walls), we should consider these variations of local and average Nusselt numbers on the walls, which are as follows:

$$Nu = -\frac{k_{nf}}{k_{bf}}\frac{\partial\theta}{\partial n}\bigg|_{Wall} \tag{18}$$

(n): Normal direction to the considered wall.

The total average Nusselt number is:

$$Nu_{avg} = \frac{1}{4}\left(\frac{1}{AB}\int_A^B Nu\ dY + \frac{1}{BC}\int_B^C Nu\ dX + \frac{1}{DE}\int_D^E Nu\ dY + \frac{1}{EF}\int_E^F Nu\ dX\right) \tag{19}$$

The dimensionless pressure drop is determined from the following equation [29]:

$$C_P = \frac{P_{avg}(Inlet) - P_{avg}(Outlet)}{(1/2)\rho u_{Inlet}^2} \tag{20}$$

where,

$$P_{avg}(Inlet) = \frac{1}{0.25H}\int_A^F P\ dY \quad \text{and} \quad P_{avg}(Outlet) = \frac{1}{0.25H}\int_C^D P\ dY \tag{21}$$

To estimate heat transfer enhancement between the case of φ = 2% and the base fluid case, EN is defined as follows:

$$EN = \left[\frac{Nu_{avg}(\varphi = 2\%) - Nu_{avg}(\varphi = 0\%)}{Nu_{avg}(\varphi = 0\%)}\right] \times 100 \tag{22}$$

Numerical Method (code validation and grid testing)

We discretized the dimensionless governing equations used in this work by the finite volume method in agreement with [59]. The system of the algebraic equations and boundary conditions was solved using line-by-line technique combined with the TDMA. Moreover, the pressure-velocity coupling was treated using SIMPLER algorithm to guarantee a robust and accurate numerical solution formulation.

The convergence condition used for this study is:

$$\left[\frac{\sum_{i=1}^{L}\sum_{j=1}^{M}\left|\phi_{i,j}^{\xi+1} - \phi_{i,j}^{\xi}\right|}{\sum_{i=1}^{L}\sum_{j=1}^{M}\left|\phi_{i,j}^{\xi+1}\right|}\right] \le 10^{-5} \tag{25}$$

where, L and M are the numbers of grid points in the X and Ydirections, respectively, f is any of the computed field variables and ξ is the iteration number.

In order to validate our numerical code, we compared our results with those obtained in [29] for a Newtonian fluid passing through a ventilated square cavity in terms of the variation of the local Nusselt number measured along the hot walls for Ri = 0, Re = 500 and φ = 0%. Figure 2 shows a very good match. The comparison indicates a good agreement with differences mainly not exceeding 3.76% in high thermal gradient regions. Such variations are attributed to small differences in the boundary conditions and the discretization schemes.

In addition, in the presence of the magnetic field, figure 3 compares the results of [57] Yu in terms of isotherm distribution. Thus, figure 3 shows an excellent resemblance. Finally, the temperature distributions on the horizontal midline were compared with the previous experimental

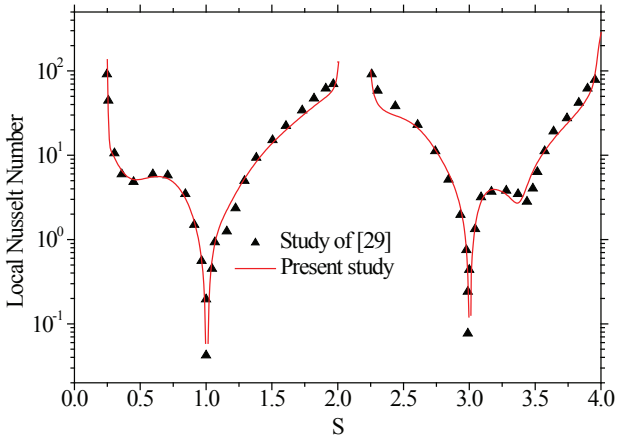

Figure 2. Local Nusselt number on the four walls of the cavity.

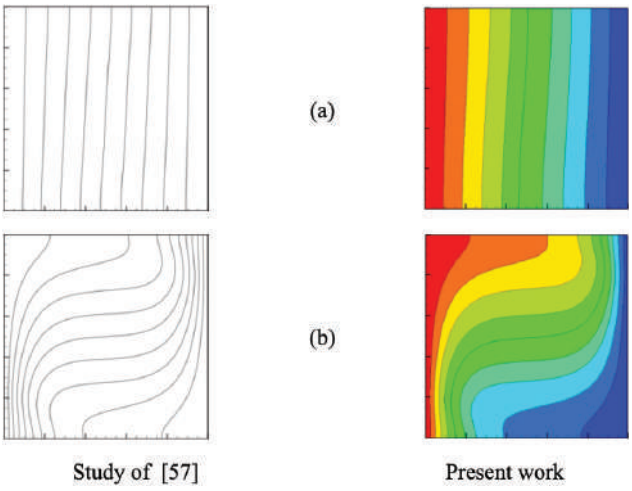

Figure 3. Comparison of isotherms between the present work and study of [57] at ω = 0°: (a) Ra = 10^4, Ha = 100 and (b) Ra = 10^5, Ha = 30.

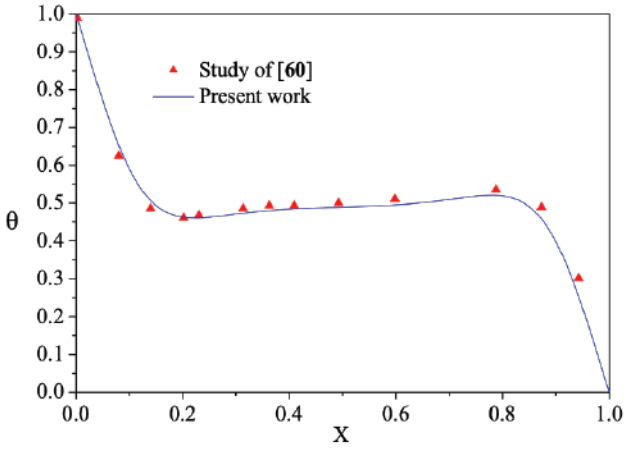

Figure 4. Comparison of the temperature distribution with the experimental results of [60] at Ra = 1.89×10^5 and Pr = 0.71.

results of [60] (Fig. 4), differences of about 2.14% are observed at certain position on the horizontal midline, in particular near steep temperature gradient areas just to the right of the highly underexpanded regime. These may be related to variation in the experimental configuration and assumptions about flow properties.

For the grid generation, we took a mixed convection flow in a ventilated square cavity for Re = 500, Ha = 100. φ = 2% and ω = 90^0 with the circular obstacle in the middle of the cavity P_1. Various grid sizes (120^2 - 220^2) were studied. The results in Fig. 5 indicated that a grid of size 2002 is acceptable for the present analysis. It is important to mention that mesh inflation was not performed at the boundary layer, thus keeping a uniform mesh distribution in all over the domain.

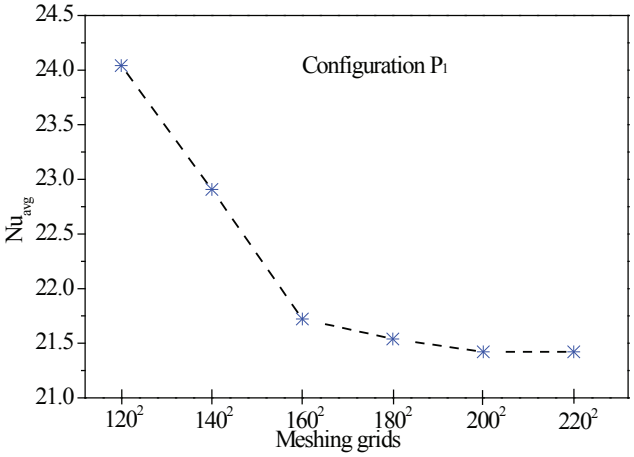

Figure 5. Average Nusselt number versus grid sizes. Ri = 1, Re = 500, Ha = 100, ω = 90° and φ = 2%.

RESULTS AND DISCUSSION

The effect of the obstacle position, Table. 2, in a ventilated cavity filled with an electrically conductive nanofluid based on water and nanoparticles (φ = 2%) under the action of a magnetic field is numerically studied in mixed convection mode. The objective is to determine the best position of the obstacle corresponding to the maximum heat transfer rate and minimum pressure drop as a function of the different control parameters: Reynolds number, Hartmann number, magnetic field direction, and the volume fraction of the nanoparticles (φ = 2%).

Table 2. Obstacle positions in the ventilated cavity

Obstacle position	(x, y)
P_1	(0.5, 0.5)
P_2	(0.5, 0.75)
P_3	(0.75, 0.5)
P_4	(0.5, 0.25)
P_5	(0.25, 0.5)

Hydrodynamic and Thermal Field

At Ha = 0, the streamline and isotherm are presentedin Fig. 6. When Re is small (Re = 50), the typical structure of the streamlines consists of two rotating cells. One is on the right side of the top wall and rotating counter clockwise, and another larger cells are also rotating but clock-wise near the left wall for each configuration. The state P_5 is identified by the emergence of a third rotating cell at the inlet. Indeed, for the high Reynolds number (Re = 500) the amplification of rotating cells and a clear observation of secondary cells above the obstacle is noted for P_1, P_2 and P_3 configurations. This is due to the presence of anobstacle in the main flow.

In addition, we observe that the repositioning of the obstacle leads to traffic flow-line rearrangement (also for public transportation lines and routes). This influenceis manifested through the change, in size and shape, of the rotating cells and by that on the exchange in the parietal zone of fluid across between walls. For example, as Re = 50 in figure 1, by changing the location of the obstacle from P_1 to P_2, the rotating cells become larger. In fact, when the magnitude of the inertial force is large (Re = 500), in the main flow linking both vent positions we can see a very remarkable change when obstacle is located at P_2 and P_3. This is due to the interaction of the obstacle Wake with main flow. It is, indeed, because the expanding rotating cells along with its core (Figs 3c and 3d) are better developed when the obstacle's position is at the core of the rotating cell in bottom cavity (see configurations P_4 and P_5). As for the isotherms described in Fig. 6b, it is possible to observe the behaviour of the streamline versus Re on top of the isotherms shape. It is true that the thickness of thermal

boundary layer decreases with increasing Reynolds number. The obstruction position does, on the other hand, have a major impact on the progress of the boundary layer thickness. The P_2 and P_3 have the smallest thickness among the other Re = 500.

We demonstrate that the interaction of the main flow with the obstacle causes to change in main flow and streamline distribution. This effect (restriction) is reflected in the size and shape of the circulating cells, and thus on blood-fluid exchange cross-diuse between wall to circulating particles. For instance, at Re = 50 the removal of same to after having introduced it allove a growth of around the rotating cells. In fact, in the stronger intensity of the inertial force case (500), a significant change takes place at this main flow connecting the throat positions for and when Re = 50. This result can be ascribed to the interaction between main flow and the obstacle. Hence, the expansion of rotating cells is expected to occur when the obstacle occupies the center of the rotating cell at bottom confining wall (cases and). With respect to the isotherms, in Figure 6b we demonstrate isotherm configuration development of the streamline with Reynolds. The thermal boundary layer thickness is actually decreased with Re. Sensitivity to the obstacle position The boundary-layer thickness growth is, however, strongly dependent on the obstacle position. The two thinnest configurations among all the Re = 500 cases are P_1 and P_2.

Figures 7 and 8 show the magnetic field effects for Re = 500 and different magnetic field inclination angles at

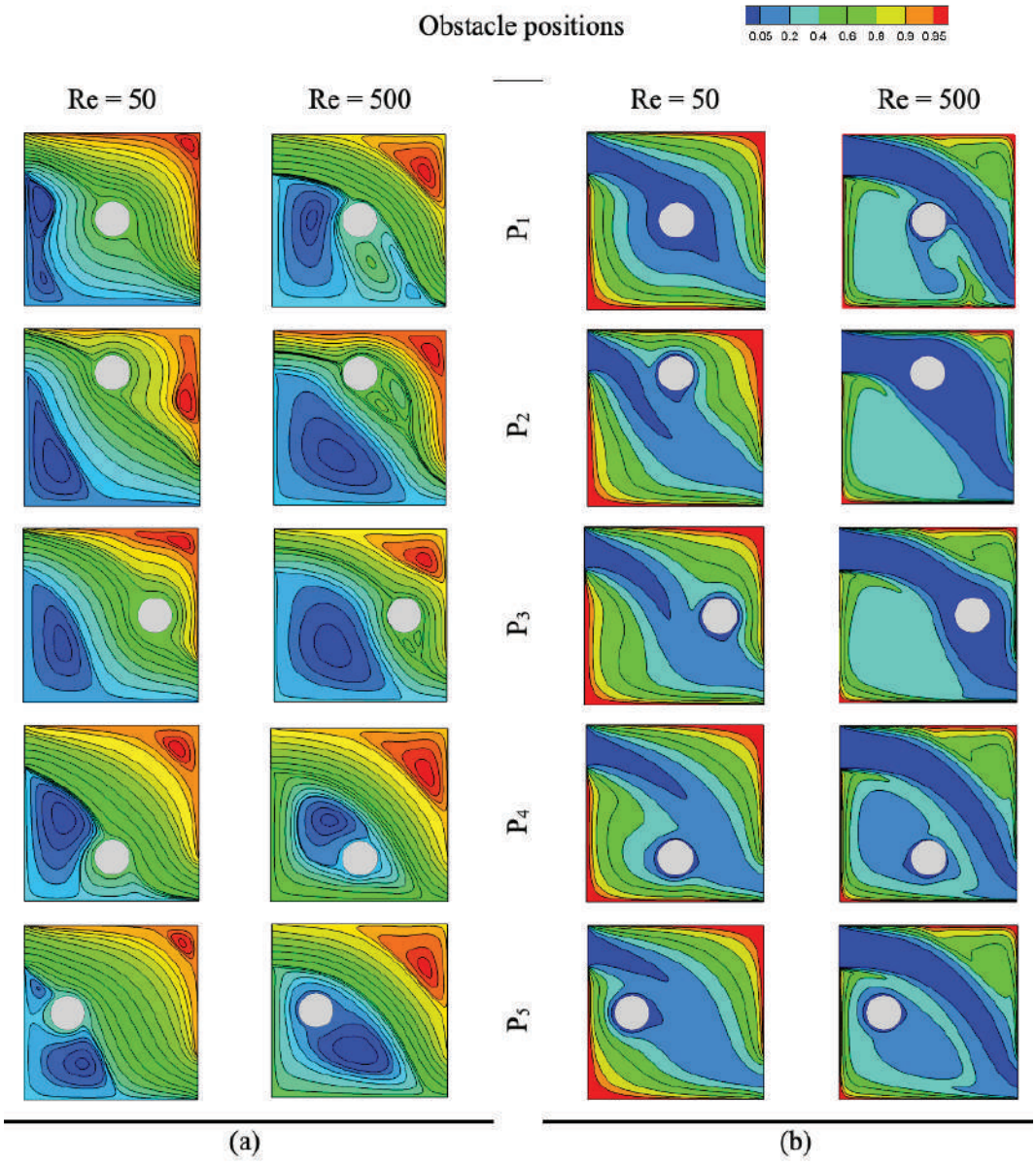

Figure 6. Effect obstacle position versus Re on streamlines (a) and isotherms (b) for Ha = 0 and φ = 2%.

Ha = 100. These effects correspond to the obstacle's position on the streamlines and the isothermal distributions for the nanofluid (φ = 2%), respectively. First, we compared the impact of the magnetic field direction as a function of the variation of the obstacle position compared to the case of the absence of the magnetic field (Fig. 6). For ω = 0° and ω = 45°, we notice that the streamlines are almost similarregardless of the obstacle position. The rotation cells observed in the absence of the magnetic field and streamlines are weakened, tend to disappear close to the active walls and become almost parallel near these walls which correspond to a heat transfer conduction.

In contrast, in the P_2 configuration, the cells located at the bottom do not disappear completely but undergo degradation in size. This is due to the fact that the movement of the flow induced by the inertial forces slows down, and the shear forces become dominant by the applied magnetic field. Indeed, the Lorentz and inertial forces act in the opposite direction (*See the Momentum Equations*). For ω = 90°, this time, we observe the reduction of the rotating cell size localized at the lower cavity and the disappearance of the cell located at the top for all configurations. This findingcan be explained by the fact that the Lorentz force acts this time perpendicular to the main flow direction. For ω = 135°, we note the disappearance of the secondary cells. The cell located at the top amplifies significantly, and the cell's sizeat the bottom decreases. This phenomenon can be explained by the inertia force being stronger than the Lorentz force. Moreover, it can be seen that the effect of inclination angles on the flow structure is considerable significant when ω = 0° and ω = 45° are compared to other angles (ω = 90° and ω = 135°).

Figure 8 illustrates the isotherms, and it can be notedthat the space occupied by the main flow (characterized by the lowest temperature 0.05) is considerably larger in the presence of the magnetic field at different angles, except for the case when the angle is equal to 135°. Thus, the thickness of the boundary layer in the case is ω = 45°. It is the

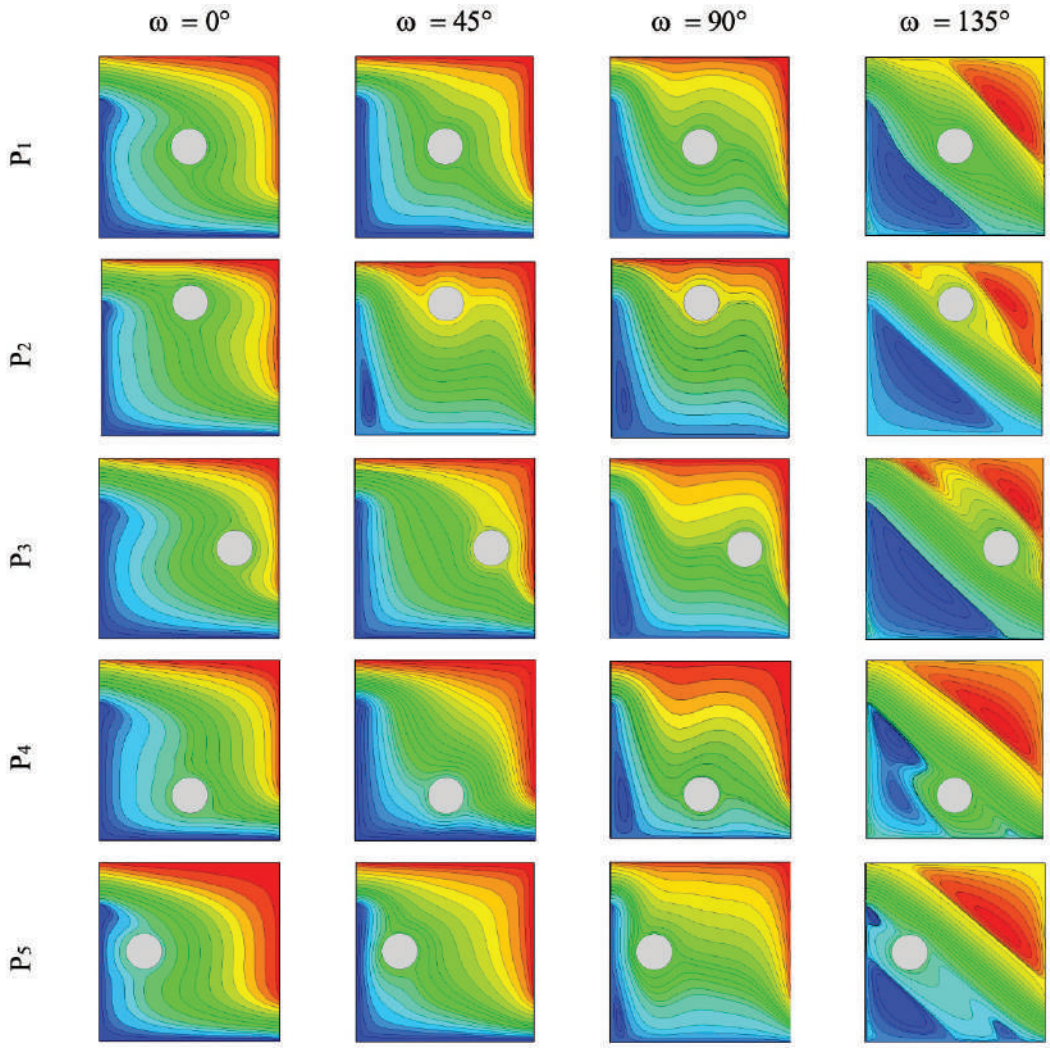

Figure 7. Streamlines versus magnetic field direction for all obstacle positions at Re = 500, Ha = 100 and φ = 2%.

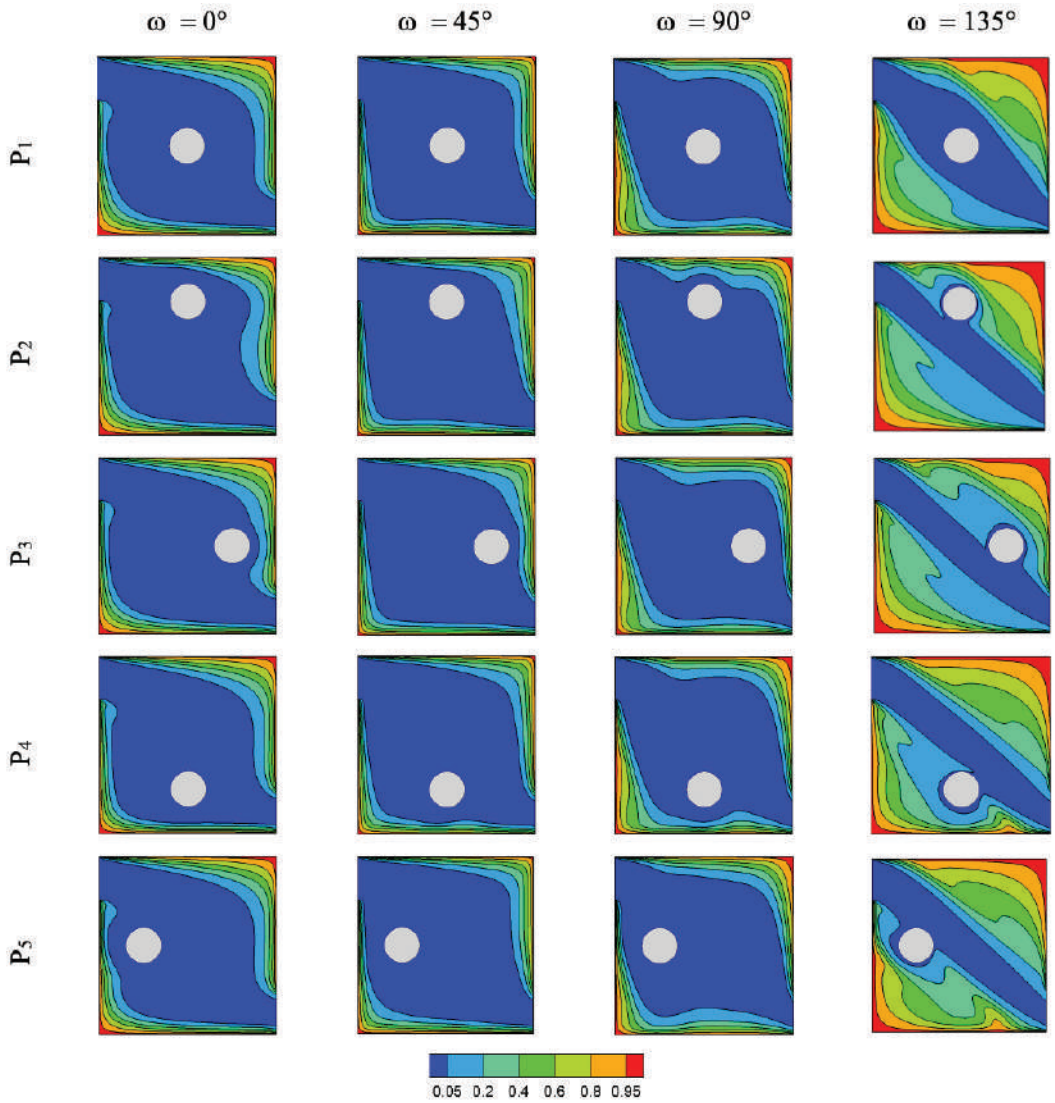

Figure 8. Isotherms versus magnetic field direction for all obstacle positions at Re = 500, Ha =100, and φ = 2%.

thinnestcompared to the cases obtained by the other angles. This means that the parietal exchange (fluid/walls) is very important. Moreover, we observe that the change in the obstacle's position has a remarkable influence on the distribution of the isotherms only for 135°.

Transfer Rates

In this context, to assess the nanofluid-wall heat transfer as a function of magnetic-field orientation, we studied the local Nusselt number characteristics across the hot walls for P_4 configuration at Re = 500, Ha = 100 and φ = 2%. The dimensionless local Nusselt number characterizes convective heat transfer efficiency by account of the thermal gradients and fluid dynamics in the vicinity of walls. Figure 9 that the orientation of the magnetic field heavily affects the heat-transfer process. In particular, for the inclination angle of the magnetic field at 45°, maximum local Nusselt number is found to occur over the hot walls. Such a promotion of the heat transfer by mixed convection may be due to the improved effect of the Lorentz force as well as convective streaming developed in this angle. For the case of field at 450 angle, the magnetic fields are inclined with respect to thermal loading that provide a more effective mixing in nanofluid. This alignment is presumably chosen in the sense to minimize magnetic damping effect to suppress convective flow (a typical phenomenon at larger Hartmann numbers), but still making use of anisotropic field conductive paths.

In contrast, the Nusselt number is smaller when magnetic field angles change from 90° to 135° implying a decrease in heat transfer performance. At 90°, the magnetic field acts perpendicularly to the flow, which induces stronger flow damping via Lorentz forces, further reducing convective heat transport.

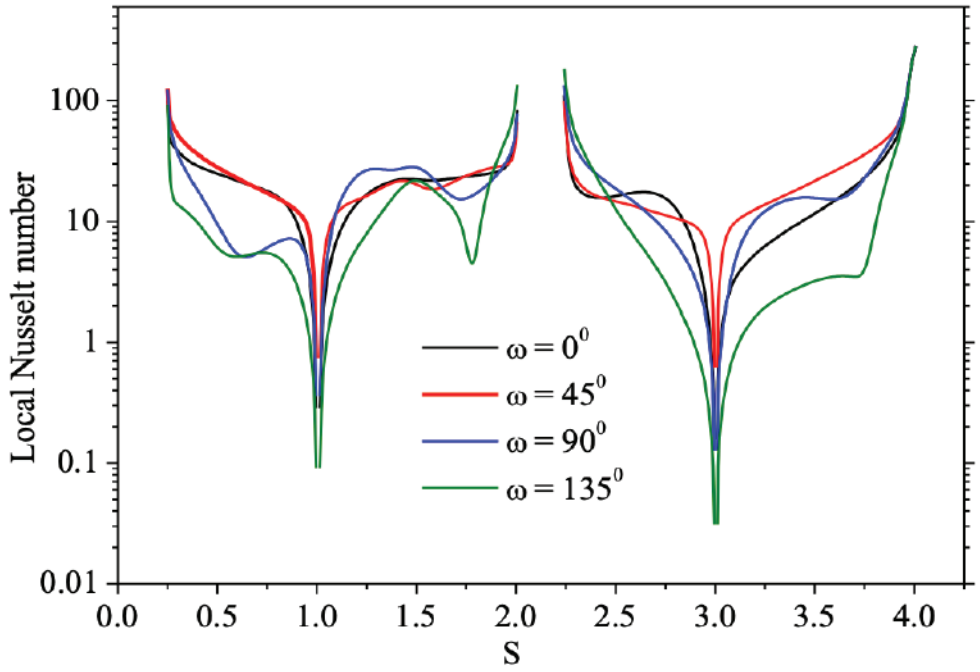

Figure 9. Magnetic field direction effects on the local Nusselt number for the configuration P_4 at Ha = 100, Re = 500 and φ = 2%.

In addition, Figure 10 shows the effect of the obstacle position in the ventilated cavity on the local Nusselt number evolution, for the angle ω = 45°. It is important to note that estimating the best configuration on the local Nusselt number is difficult and requires computing the average Nusselt number for all control parameters.

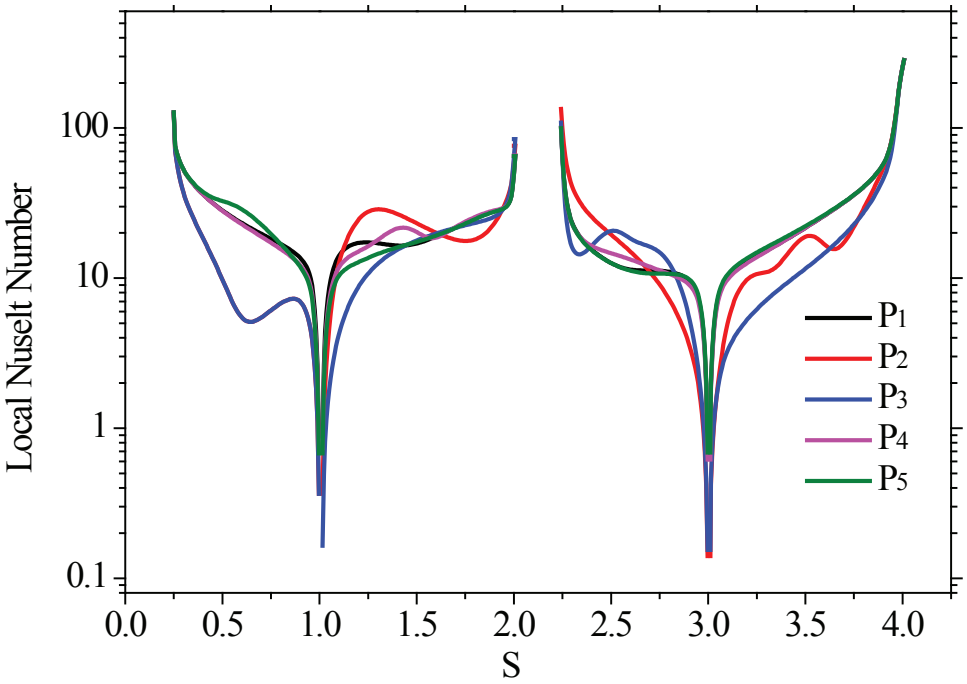

Figure 10. Obstacle positions effects on the local Nusselt number at Re = 500, Ha = 100, ω = 45°and φ = 2%.

Figures 11 and 12 illustrate the variation of the average Nusselt number as a function of Lorentz force intensity, obstacle position, and magnetic field direction for Reynolds numbers Re = 50 and Re = 500, respectively. The results indicate that the most effective heat transfer occurs for Re = 500. At Re = 50, we notice that the P_5 configuration is the optimal choice in the absence of a magnetic field. Indeed, in the presence of the magnetic field, we observe that increasing the Lorentz force intensity enhances the heat exchange rate for different angles of the applied magnetic field. Except when the angle is 135°, where the average Nusselt number decreases. For example, when the magnetic field is imposed in the horizontal direction (ω = 0°) at Ha = 100 for the P_4 configuration, the heat exchange rate is improved by about 17.25% compared to the case of no magnetic field. Thus, the choice of the optimal configuration depends on the intensity and the angle of the applied magnetic field. For Re = 500 (Fig. 12), we observe that the average Nusselt number decreases with increasing the magnetic field intensity in the relatively small Hartmann number and then increases to large values. In particular, for an angle equal to 45°, the average Nusselt number decreases until Ha = 30, after which it increases to reach a maximum at Ha equal to 100. For the P_4 configuration, we find that the average Nusselt number increases by 16.20% compared to the case of no magnetic field,when the cavity is subjected to a magnetic field in the direction ω = 45° with Ha = 100. When ω = 135°, the average Nusselt number is reduced with an increased in the magnitude of magnetic field for all arrangements.

The positioning of obstacles significantly impacts the heat transfer process under varying Reynolds and Hartmann numbers. At Re = 500, configurations such as P_4 demonstrate superior heat transfer efficiency due to optimal interaction between the flow dynamics and the imposed Lorentz forces. When the obstacle is placed at P_4, the thermal boundary layer is thinner, resulting in enhanced heat transfer. Furthermore, the intensity and direction of the magnetic field interact differently with obstacle positioning, altering the boundary layer's behavior and the flow structure within the cavity. These differences illustrate the influence of placing obstacles on the heat transfer performance.

The subfigure 12c shows that the heat transfer rate reaches its maximum when the obstacle is positioned at

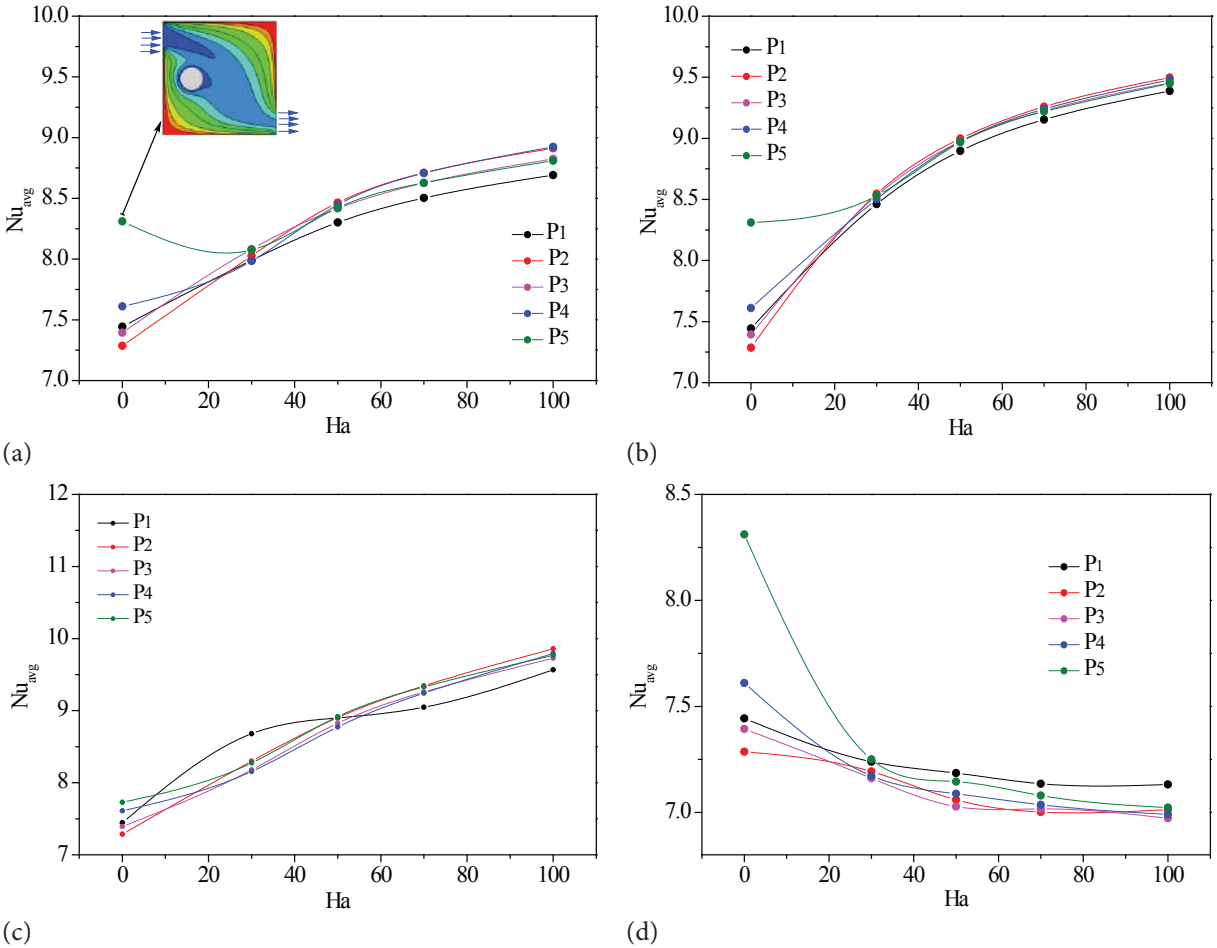

Figure 11. Effect of intensity and angle of magnetic field for different obstacle positions on the average Nusselt number at Re = 50 and φ = 2%: (a) ω = 0°, (b) ω = 45°, (c) ω = 90° and (d) ω = 135°.

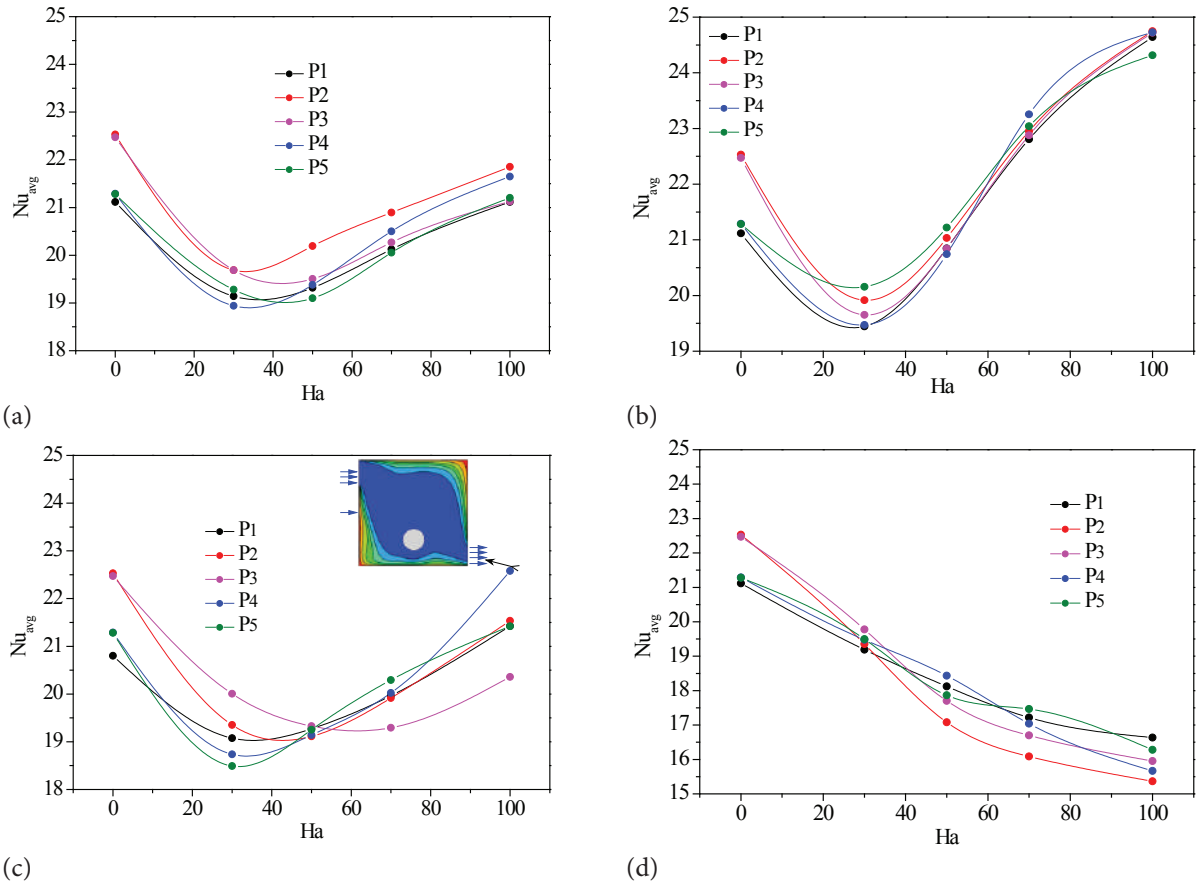

Figure 12. Effect of intensity and direction of magnetic field for different obstacle positions on the average Nusselt number at Re = 500 and φ = 2%: (a) ω = 0°, (b) ω = 45°, (c) ω = 90° and ω = 135°.

P_4 for Ha = 100. This result is primarily due to the limited development of the thermal boundary layer thickness, which is significantly thinner in this configuration compared to others. The reduced boundary layer thickness enhances the efficiency of heat transfer.

Pressure Drop

The pressure drop and thermal performance measurements inside the ventilated cavities are useful information. For this purpose, we plotted the evolution of the pressure drop for each cavity corresponding to the obstacle positionas a function of the variation of the Hartmann number and the angle of inclination of the applied magnetic through Figures 13 and 14, for Re = 50 and Re = 500, respectively. The results indicate that the pressure drop values for lower Reynolds numbers are higher than those for higher Reynolds numbers for all Hartmann numbers. Furthermore, we observe that the pressure drop increases with increasing Hartmann number for each Reynolds number. This is due to the effect of the Lorentz force, which causes a blockage of the fluid flow and consequently leads to the increase of the shear stresses. It can be noticed that the P_1 configuration gives themaximum pressure drop coefficient and that the P_4 and P_5 configurations give the minimum values of whatever the Reynolds number and the angle of the applied magnetic field. Moreover, it can be noted that the effect of changing the obstacle position on the pressure drop evolution is negligible for higher Hartmann numbers, except when the magnetic field angle is equal to 135°.

Nanoparticles Effects

Figure 15 shows the influence of nanoparticles water suspension on thermal performance. It is clear that only the presence of the nanoparticles has a positive influence, at low Reynolds number (Re = 50), for all different obstacle situations. Results show that the heat transfer rate increases when the volume fraction of graphene nanoplatelets is increased thanks to the higher thermal conductivity in comparison with base fluid, nevertheless this increase diminishes at high volume fractions due to a raise in viscosity resulting in which convection heat transfer decreases. The optimal nanoparticle volume fraction for heat transfer performance and manageable viscosity was observed at volume fractions of 1% and 2% for the configurations studied. Furthermore, the heat transfer rate is observed to be maximum at the greatest angle of the applied magnetic field (ω = 135°) for both Reynolds numbers. Moreover, the comparison between the different

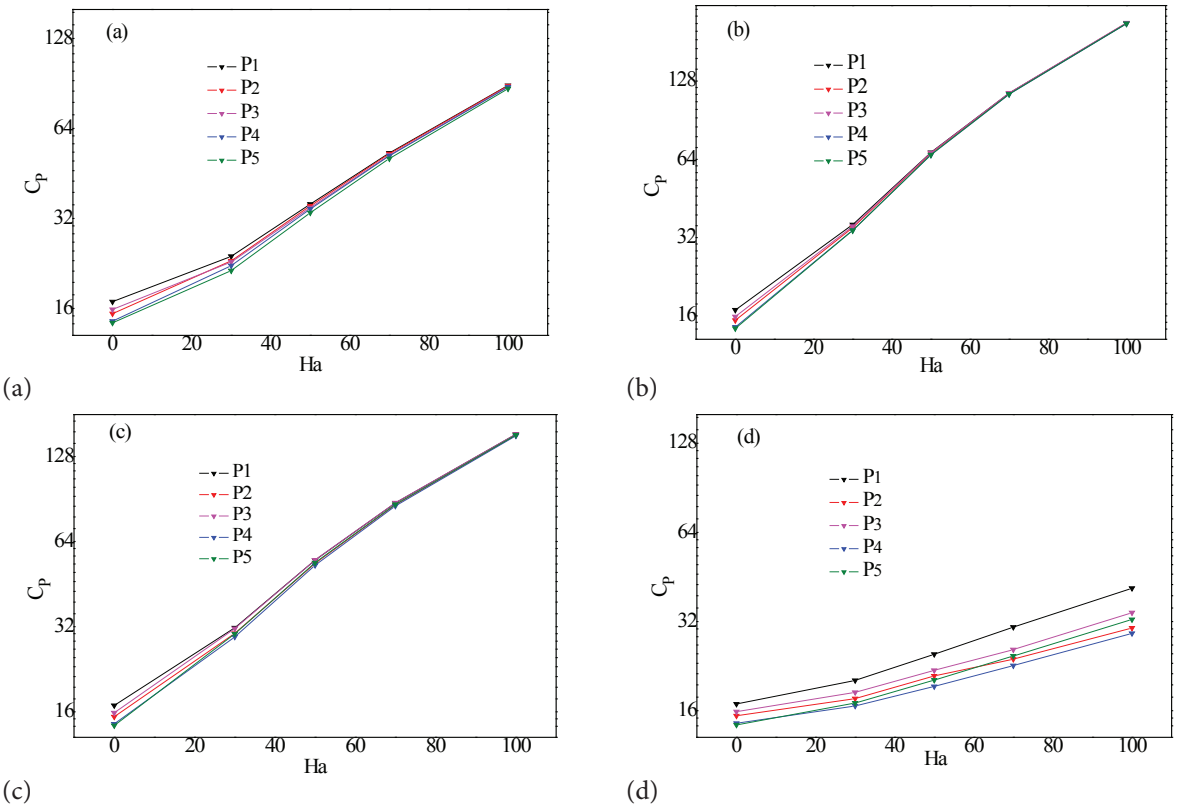

Figure 13. Effects of intensity and of magnetic field direction for different obstacle positions on the pressure drop at Re = 50 and φ = 2%: (a) ω = 0°, (b) ω = 45°, (c) ω = 90° and (d) ω = 135°.

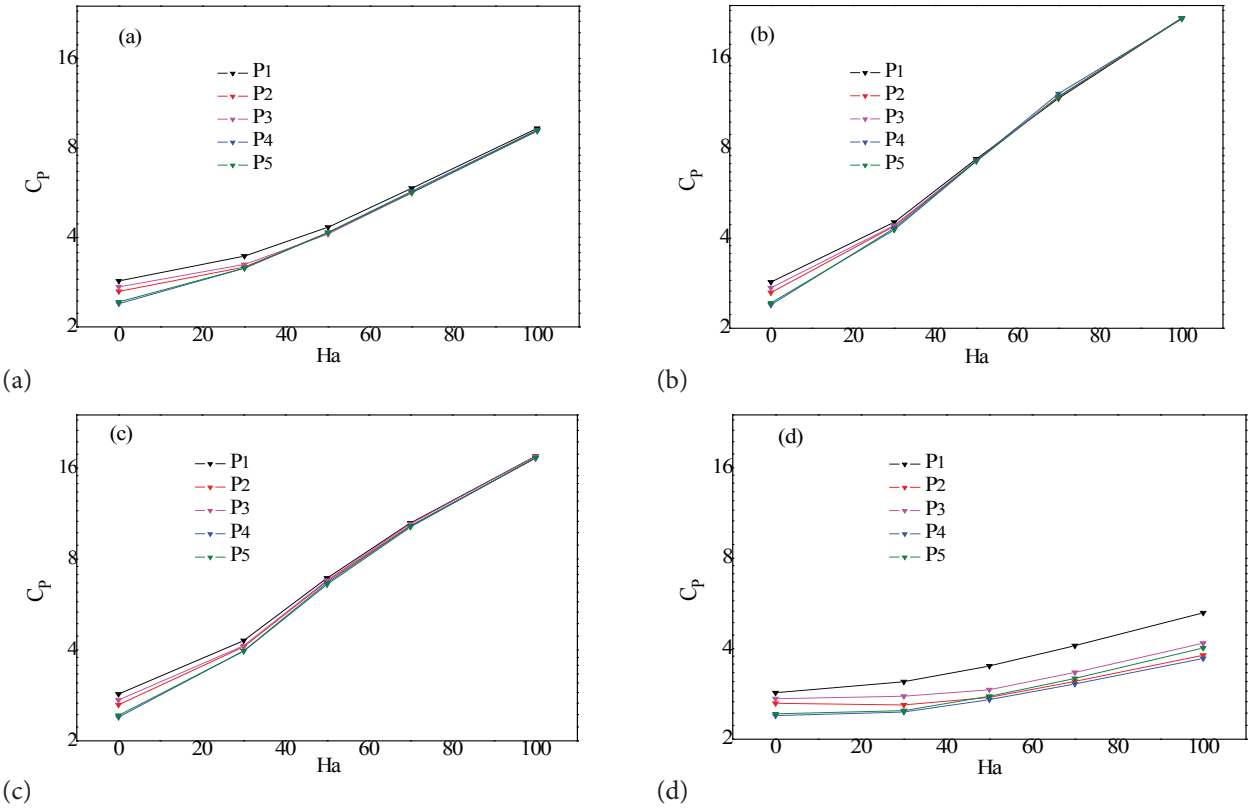

Figure 14. Effect of intensity and direction of magnetic field for different obstacle positions on the pressure drop at Re = 500 and φ = 2%: (a) ω = 0°, (b) ω = 45°, (c) ω = 90°and (d) ω = 135°.

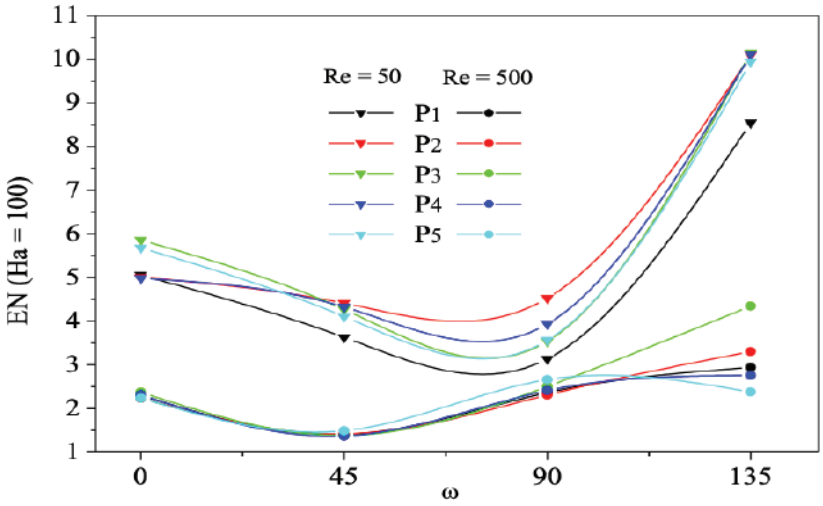

Figure 15. Nanoparticles effects on the heat transfer enhancement for all control parameters.

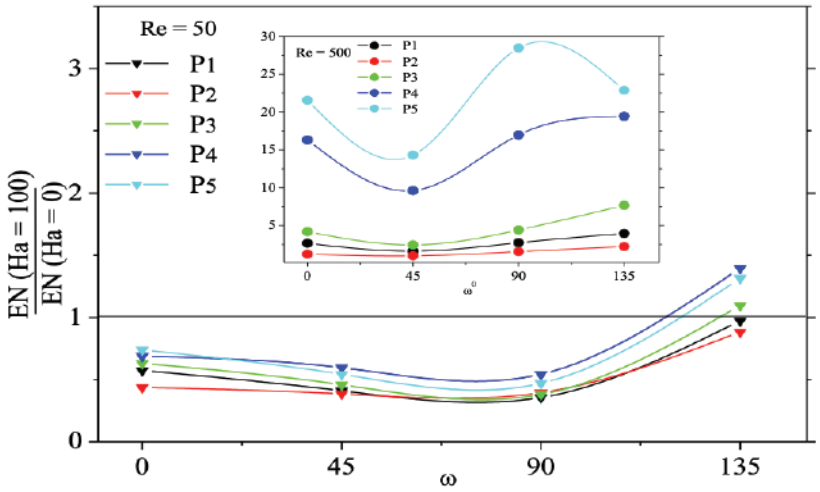

Figure 16. Nanoparticles effects for all control parameters.

configurations, in terms of the improvement brought by the addition of 2% of the nanoparticles, shows that one can choose an appropriate configuration for each angle of the applied magnetic field, in terms of the maximum enhancement brought by these CNT nanoparticles. For example, adding nanoparticles is advantageous for the case P_2 at the magnetic field angle is 135°. When the heat transfer enhancements of 3.30% and 10.09% for Re = 500 and Re = 50, respectively, are obtained compared to the base fluid, then it can be observed that presence of nanoparticles is favorable when conduction is more influential compare to convection mode.

Figure 16 shows the variation ratio between the heat transfer enhancement in the presence and the absence of the magnetic field as a function of the obstacle position and the magnetic field directions, for the two Reynolds numbers. The objective is to compare the impact of the addition of nanoparticles between the case of the absence and the case of the presence of the magnetic field. Thus, figure 16 indicates that the use of nanoparticles in the presence of the magnetic field in the case of Re = 50 is unfavorable for all configurations and the different magnetic field angles, except for configurations P_3, P_4, and P_5 when ω = 135°. In this case, the addition of nanoparticles proves advantageous under the influence of a magnetic field. However, for Re = 500, their benefit is observed only in configurations P_3, P_4, and P_5, regardless of the magnetic field's orientation.

CONCLUSION

In the present work, mixed convection inside a vented cavity with circular body filled by CNT-water nanofluid has been numerically explored in presence of magnetic field. Performance analysis was performed to investigate the influence of various parameters on heat transfer rates and pressure drop in order to find the best configuration. Novelties of the work are a detailed consideration of how the obstacle position together with the Lorentz force influence both flow dynamics and thermal aspects, which has not been thoroughly examined by previous studies. These findings also have implications on the design and optimization of efficient cooling or thermal-management system, such as electronics cooling and heat exchanger. Key points are as follows:

- Increasing the Reynolds number intensifies the hydrodynamic field and improves heat transfer, especially in the absence of the magnetic field.
- The introduction of the magnetic field weakens the hydrodynamic structure of the flow and causes a heat transfer in conduction mode.
- The pressure drop coefficient is a decreasing function with Reynolds number and an increasing function with Hartmann number.
- Obstacle position is significant on the heat transfer and the pressure drop in the absence of the magnetic field. Nevertheless, the presence of the magnetic field has a negligible effect on the pressure drop.
- The magnetic field direction and the Lorentz force intensity also play a big role in choosing the best configuration.
- The optimal configurations in the absence of a magnetic field are P_5 for Re = 50 and P_2 for Re = 500. Moreover, in the presence of the magnetic field for Ha = 100, we find that P_4 is the best for Re = 50 and ω = 90°. And the configuration P_5, for Re = 500 and ω = 45°.
- The use of nanoparticles is beneficial in conductive mode and for the low Reynolds number. In amagnetic field, it is advantageous for the high Reynolds number. In addition, the results show that the obstacle position is a predominant factor that disadvantages or favors the importance of the existence of these nanoparticles.

NOMENCLATURE

B	Magnetic field, T
Cp	Constant pressure specific heat, J kg^{-1} K^{-1}
g	Gravitational acceleration, ms^{-2}
Ha	Hartmann number, $Ha = \sqrt{\frac{\sigma B^2 L}{\mu}}$
k	Thermal conductivity, Wm^{-1} K^{-1}
Nu	Nusselt number
p	Pressure, Pa
Pr	Prandtl number
Re	Reynolds number
Ri	Richardson number
s	Distance along the walls, m
S	Dimensionless coordinate, $S = sH^{-1}$
T	Dimensional temperature, K
(u, v)	Velocity components in the x, y directions, m s^{-1}
(x, y)	Cartesian coordinates, m

Greek symbols

α	Thermal diffusivity, m^2 s^{-1}
b	Thermal expansion coefficient, K^{-1}
ρ	Density, kg m^{-3}
s	Electrical conductivity
ν	Kinematic viscosity, m^2 s^{-1}
μ	Dynamic viscosity, kg m^{-1} s^{-1}
θ	Dimensionless temperature
φ	Nanoparticle volume fraction

Superscript

EN	$\left[\frac{Nu_{avg}(\varphi=2\%)-Nu_{avg}(\varphi=0\%)}{Nu_{avg}(\varphi=0\%)}\right]\times 100$
avg	Average
bf	Base fluid
nf	Nanofluid
s	Solid particles

ACKNOWLEDGEMENTS

All authors contributed to the study conception and design. All authors read and approved the final manuscript.

AUTHORSHIP CONTRIBUTIONS

Authors equally contributed to this work.

DATA AVAILABILITY STATEMENT

The authors confirm that the data that supports the findings of this study are available within the article. Raw data that support the finding of this study are available from the corresponding author, upon reasonable request.

CONFLICT OF INTEREST

The author declared no potential conflicts of interest with respect to the research, authorship, and/or publication of this article.

ETHICS

There are no ethical issues with the publication of this manuscript.

STATEMENT ON THE USE OF ARTIFICIAL INTELLIGENCE

Artificial intelligence was not used in the preparation of the article.

FUNDING

This work was supported by the Directorate General for Scientific Research and Technological Development of Algeria (DGRSDT) with granted contracts (No. A16N01UN160420200007) and (No. A11N01UN440120220001).

REFERENCES

[1] Choi SU, Eastman JA. Enhancing thermal conductivity of fluids with nanoparticles. Argonne National Lab.(ANL), Argonne, IL (United States); 1995.

[2] Kakaç S, Pramuanjaroenkij A. Review of convective heat transfer enhancement with nanofluids. Int J Heat Mass Transf 2009;52(13-14):3187–3196. [CrossRef]

[3] Saidur R, Leong K, Mohammed HA. A review on applications and challenges of nanofluids. Renew Sustain Energy Rev 2011;15(3):1646–1668. [CrossRef]

[4] Vanaki SM, Ganesan P, Mohammed HA. Numerical study of convective heat transfer of nanofluids: A review. Renew Sustain Energy Rev 2016;54:1212–1239. [CrossRef]

[5] Zeghbid I, Bessaïh R. Mixed convection and entropy generation in a square cavity using nanofluids. Thermophys Aeromechanics 2018;25(2):245–256. [CrossRef]

[6] Ebrahimnia-Bajestan E, Niazmand H, Duangthongsuk W, Wongwises S. Numerical investigation of effective parameters in convective heat transfer of nanofluids flowing under a laminar flow regime. Int J Heat Mass Transf 2011;54(19-20):4376–4388. [CrossRef]

[7] Li Y, Tung S, Schneider E, Xi S. A review on development of nanofluid preparation and characterization. Powder Technol 2009;196(2):89–101. [CrossRef]

[8] Ouyahia SE, Benkahla YK, Labsi N. Numerical study of the hydrodynamic and thermal proprieties of titanium dioxide nanofluids trapped in a triangular geometry. Arab J Sci Eng 2016;41:1995–2009. [CrossRef]

[9] Oztop HF, Abu-Nada E. Numerical study of natural convection in partially heated rectangular enclosures filled with nanofluids. Int J Heat Fluid Flow 2008;29(5):1326–1336. [CrossRef]

[10] Sundar LS, Singh MK. Convective heat transfer and friction factor correlations of nanofluid in a tube and with inserts: A review. Renew Sustain Energy Rev 2013;20:23–35. [CrossRef]

[11] Yu W, France DM, Choi SU, Routbort JL. Review and Assessment of Nanofluid Technology for Transportation and Other Applications. Argonne National Lab.(ANL), Argonne, IL (United States); 2007.

[12] Godson L, Raja B, Mohan Lal D, Wongwises S. Convective heat transfer characteristics of silver-water nanofluid under laminar and turbulent flow conditions. Int Commun Heat Mass Transf 2012;39(1):92-97. [CrossRef]

[13] Kumar PM, Kumar J, Tamilarasan R, Nathan SS, Suresh S. Heat transfer enhancement and pressure drop analysis in a helically coiled tube using Al2O3/water nanofluid. J Mech Sci Technol 2014;28:1841–1847. [CrossRef]

[14] Palanisamy K, Kumar PM. Experimental investigation on convective heat transfer and pressure drop of cone helically coiled tube heat exchanger using carbon nanotubes/water nanofluids. Heliyon 2019;5(5):e01705. [CrossRef]

[15] Garoosi F, Rohani B, Rashidi MM. Two-phase mixture modeling of mixed convection of nanofluids in a square cavity with internal and external heating. Powder Technol 2015;275:304–321. [CrossRef]

[16] Hussain S, Öztop H, Jamal M, Hamdeh N. Double diffusive nanofluid flow in a duct with cavity heated from below. Int J Mech Sci 2017;131:535–545. [CrossRef]

[17] Jalali H, Abbassi H. Numerical Investigation of Heat Transfer by Al2O3–water Nanofluid in Square Cavity. Springer; 2012. p. 1129–1138. [CrossRef]

[18] Khoshvaght-Aliabadi M, Arani-Lahtari Z. Proposing new configurations for twisted square channel (TSC): Nanofluid as working fluid. Appl Therm Eng 2016;108:709–719. [CrossRef]

[19] House JM, Beckermann C, Smith TF. Effect of a centered conducting body on natural convection heat transfer in an enclosure. Numer Heat Transf 1990;18(2):213–225. [CrossRef]

[20] Bhave P, Narasimhan A, Rees D. Natural convection heat transfer enhancement using adiabatic block: Optimal block size and Prandtl number effect. Int J Heat Mass Transf 2006;49(21-22):3807–3818. [CrossRef]

[21] Raji A, Hasnaoui M, Naïmi M, Slimani K, Ouazzani M. Effect of the subdivision of an obstacle on the natural convection heat transfer in a square cavity. Comput Fluids 2012;68:1–15. [CrossRef]

[22] Mahfoud B. Natural convection of a nanofluid in a conical container. J Therm Eng 2018;4(1):1713–1723. [CrossRef]

[23] Belhadj A. Numerical investigation of forced convection of nanofluid in microchannels heat sinks. J Therm Eng 2018;4(5):2263–2273. [CrossRef]

[24] Pandey S, Park YG, Ha MY. An exhaustive review of studies on natural convection in enclosures with and without internal bodies of various shapes. Int J Heat Mass Transf 2019;138:762–795. [CrossRef]

[25] Sharma B, Kumar B, Barman RN. Numerical investigation of Cu-water nanofluid in a differentially heated square cavity with conducting solid square cylinder at center. Int J Heat Technol 2018;36(2):714–722. [CrossRef]

[26] Mahmoodi M, Sebdani SM. Natural convection in a square cavity containing a nanofluid and an adiabatic square block at the center. Superlattices Microstruct 2012;52(2):261–275. [CrossRef]

[27] Park Y, Ha M, Park J. Natural convection in a square enclosure with four circular cylinders positioned at different rectangular locations. Int J Heat Mass Transf 2015;81:490−511. [CrossRef]
[28] Soomro FA, Hammouch Z. Heat transfer analysis of CuO-water enclosed in a partially heated rhombus with heated square obstacle. Int J Heat Mass Transf 2018;118:773−784. [CrossRef]
[29] Sourtiji E, Gorji-Bandpy M, Ganji D, Hosseinizadeh S. Numerical analysis of mixed convection heat transfer of Al2O3-water nanofluid in a ventilated cavity considering different positions of the outlet port. Powder Technol 2014;262:71−81. [CrossRef]
[30] Benzema M, Benkahla YK, Labsi N, Brunier E, Ouyahia SE. Numerical mixed convection heat transfer analysis in a ventilated irregular enclosure crossed by Cu−water nanofluid. Arab J Sci Eng 2017;42:4575−4586. [CrossRef]
[31] Milani Shirvan K, Mamourian M, Ellahi R. Numerical investigation and optimization of mixed convection in ventilated square cavity filled with nanofluid of different inlet and outlet port. Int J Numer Methods Heat Fluid Flow 2017;27(9):2053−2069. [CrossRef]
[32] Rahman MM, Alim MA, Saha S, Chowdhury M. A numerical study of mixed convection in a square cavity with a heat conducting square cylinder at different locations. J Mech Eng 2008;39(2):78−85. [CrossRef]
[33] Rahman MM, Parvin S, Rahim N, Islam M, Saidur R, Hasanuzzaman M. Effects of Reynolds and Prandtl number on mixed convection in a ventilated cavity with a heat-generating solid circular block. Appl Math Model 2012;36(5):2056−2066. [CrossRef]
[34] M'hamed B, Sidik NAC, Yazid MNAWM, Mamat R, Najafi G, Kefayati G. A review on why researchers apply external magnetic field on nanofluids. Int Commun Heat Mass Transf 2016;78:60−67. [CrossRef]
[35] Rudraiah N, Barron R, Venkatachalappa M, Subbaraya C. Effect of a magnetic field on free convection in a rectangular enclosure. Int J Eng Sci 1995;33(8):1075−1084. [CrossRef]
[36] Yu P, Qiu J, Qin Q, Tian ZF. Numerical investigation of natural convection in a rectangular cavity under different directions of uniform magnetic field. Int J Heat Mass Transf 2013;67:1131−1144. [CrossRef]
[37] Selimefendigil F, Öztop HF. Natural convection and entropy generation of nanofluid filled cavity having different shaped obstacles under the influence of magnetic field and internal heat generation. J Taiwan Inst Chem Eng 2015;56:42−56. [CrossRef]
[38] Sheikholeslami M, Gerdroodbary MB, Shafee A, Tlili I. Hybrid nanoparticles dispersion into water inside a porous wavy tank involving magnetic force. J Therm Anal Calorim 2020;141:1993−1999. [CrossRef]
[39] Manh TD, Bahramkhoo M, Barzegar Gerdroodbary M, Nam ND, Tlili I. Investigation of nanomaterial flow through non-parallel plates. J Therm Anal Calorim 2021;143:3867−3875. [CrossRef]
[40] Tlili I, Moradi R, Barzegar Gerdroodbary M. Transient nanofluid squeezing cooling process using aluminum oxide nanoparticle. Int J Mod Phys C 2019;30(11):1950078. [CrossRef]
[41] Sheikholeslami M, Bandpy MG, Ellahi R, Zeeshan A. Simulation of MHD CuO−water nanofluid flow and convective heat transfer considering Lorentz forces. J Magn Magn Mater 2014;369:69−80. [CrossRef]
[42] Mehrez Z, El Cafsi A, Belghith A, Le Quere P. MHD effects on heat transfer and entropy generation of nanofluid flow in an open cavity. J Magn Magn Mater 2015;374:214−224. [CrossRef]
[43] Al-Rashed AA, Kolsi L, Kalidasan K, Malekshah EH, Borjini MN, Kanna PR. Second law analysis of natural convection in a CNT-water nanofluid filled inclined 3D cavity with incorporated Ahmed body. Int J Mech Sci 2017;130:399−415. [CrossRef]
[44] Moderres M, Boutra A, Kherroubi S, Oztop HF, Benkahla YK. Magnetohydrodynamic (MHD) natural convection flow of titanium dioxide nanofluid inside 3D cavity containing a hot block: Comparative with 2D cavity. J Nanofluids 2023;12(5):1298−1319. [CrossRef]
[45] Mehmood K, Hussain S, Sagheer M. Mixed convection in alumina-water nanofluid filled lid-driven square cavity with an isothermally heated square blockage inside with magnetic field effect: Introduction. Int J Heat Mass Transf 2017;109:397−409. [CrossRef]
[46] Javed T, Siddiqui M, Mehmood Z. MHD natural convective flow through a porous medium in a square cavity filled with liquid gallium. Thermophys Aeromechanics 2018;25:405−420. [CrossRef]
[47] Barzegar Gerdroodbary M. Application of neural network on heat transfer enhancement of magnetohydrodynamic nanofluid. Heat Transf Asian Res 2020;49(1):197−212. [CrossRef]
[48] Panigrahi L, Panda J, Kumar D, Sahoo SS. Analytical investigation of polar fluid flow with induced magnetic field in concentric annular region. Heat Transf 2020;49(6):3943−3957. [CrossRef]
[49] Panigrahi L, Panda J, Sahoo SS. Unsteady heat transfer and entropy generation study on viscoelastic fluid flow coupled with induced magnetic field. Iran J Sci Technol Trans A Sci 2021;45(5):1699−1710. [CrossRef]
[50] Benzema M, Benkahla YK, Labsi N, Ouyahia SE, El Ganaoui M. Second law analysis of MHD mixed convection heat transfer in a vented irregular cavity filled with Ag−MgO/water hybrid nanofluid. J Therm Anal Calorim 2019;137:1113−1132. [CrossRef]

[51] Kherroubi S, Ragui K, Bensaci A, Labsi N, Boutra A, Benkahla YK. Effect of the second outlet location and the applied magnetic field within a ventilated cubic cavity crossed by a nanofluid on mixed convection mode: Best configurations. J Therm Anal Calorim 2020;139:2243–2264. [CrossRef]

[52] Mishra M, Panda J, Kumar D, Sahoo SS. Thermal radiation and Soret effects on boundary layer flow past a vertical surface embedded in porous medium with induced magnetic field with reference to aluminum industry. J Therm Anal Calorim 2022;147(23):13829–13845. [CrossRef]

[53] Man Y, Gerdroodbary MB. Influence of Lorentz forces on forced convection of nanofluid in a porous enclosure. J Porous Media 2024;27(8). [CrossRef]

[54] Mishra M, Panda J, Sahoo SS. Investigations concerning the effects of thermal radiation, induced magnetic field, and chemical reaction on MHD flow through a permeable medium. Int J Mod Phys B 2024;38(02):2450030. [CrossRef]

[55] Gerdroodbary MB, Jafaryar M, Sheikholeslami M, Amini Y. The efficacy of magnetic force on thermal performance of ferrofluid in a screw tube. Case Stud Therm Eng 2023;49:103187. [CrossRef]

[56] Kefayati GR, Tang H. MHD mixed convection of viscoplastic fluids in different aspect ratios of a lid-driven cavity using LBM. Int J Heat Mass Transf 2018;124:344–367. [CrossRef]

[57] Yu P, Tian Z. Comparison of the simplified and full MHD models for laminar incompressible flow past a circular cylinder. Appl Math Model 2017;41:143–163. [CrossRef]

[58] Bhattacharya P, Samanta A, Chakraborty S. Numerical study of conjugate heat transfer in rectangular microchannel heat sink with Al2O3/H2O nanofluid. Heat Mass Transf 2009;45:1323–1333. [CrossRef]

[59] Patankar S. Numerical Heat Transfer and Fluid Flow. Boca Raton: CRC Press; 2018. [CrossRef]

[60] Krane R. Some detailed field measurements for a natural convection flow in a vertical square enclosure. In: Proceedings of the 8th International Heat Transfer Conference; 1986 Aug 17-22; San Francisco, CA. Hemisphere Publishing Corp.; 1986. p. 323–329.

J Ther Eng, Vol. 12, No. 1, pp. 385−407, January, 2026

Journal of Thermal Engineering
Web page info: https://jten.yildiz.edu.tr
DOI: 10.14744/thermal.0001068

Review Article

Phase change materials (PCMs) used in buildings: A critical review

Soukaina TOUMZINE[1,*], Hanane MOULAY ABDELALI[1]

[1]*Mohammadia School of Engineering, Mohammed V University in Rabat, Civil Engineering and Construction Laboratory, Agdal, Rabat, 10090, Morocco*

ARTICLE INFO

Article history
Received: 06 July 2024
Accepted: 04 October 2024

Keywords:
Building Envelope; Thermal Energy Storage;Thermal Comfort; Latent Heat; PCM

ABSTRACT

The construction sector deserves special attention due to its energy efficiency potential, high energy consumption, and environmental impact. Indeed, reducing energy consumption in buildings means reducing the carbon footprint and mitigating climate change. Phase change materials (PCMs) have garnered significant attention in recent years because to their potential to enhance comfort and mitigate environmental impact by reducing greenhouse gas emissions. Between 2013 and 2023, research in this area experienced a substantial increase of 231.45%. This considerable rise reflects the technology›s notable advancements and growing interest among researchers. This article provides a comprehensive assessment of recent scientific studies investigating the effects of PCMs integrated into building envelopes to reduce heating and cooling energy consumption. The main characteristics and properties of PCMs, selection criteria, and integration methods are reviewed and discussed, then the main numerical tools as well as a method for determining the main thermo-physical properties of PCMs based on the results of previous studies are presented. Thus, all the recent research carried out locally (Morocco) was described, and finally, a thorough assessment was conducted to identify deficiencies and offer suggestions for future research.

Cite this article as: Toumzine S, Moulay Abdelali H. Phase change materials (PCMs) used in buildings: A critical review. J Ther Eng 2026;12(1):385−407.

INTRODUCTION

We are currently experiencing the first global energy crisis. Pressures on markets had already been evident, but the actions of this crisis have transformed the rapid economic recovery that followed the pandemic and led to tensions across all global supply chains, including energy [1]. Fossil fuels and nuclear energy, both of which are limited and emit significant amounts of greenhouse gases, are the main sources of energy conversion and electricity generation. According to 2014 statistics, if current consumption rates continue, coal reserves will run out in about 130 years, natural gas reserves in about 60 years, and oil reserves in about 20 years. [2].

The construction sector contributes significantly to greenhouse gas emissions and is a significant energy consumer. It made up 132 EJ of energy consumption in 2021, or 30% of total final energy consumption worldwide. When indirect emissions from the production of heat and power are taken into consideration, the sector›s 3 Gt of CO2

***Corresponding author.**
*E-mail address: soukaina.toumzine@research.emi.ac.ma

This paper was recommended for publication in revised form by Editor-in-Chief Ahmet Selim Dalkilic

Published by Yıldız Technical University Press, İstanbul, Turkey
Yıldız Technical University. This is an open access article under the CC BY-NC license (http://creativecommons.org/licenses/by-nc/4.0/).

emissions in 2021 accounted for 15% of all emissions from end-use sectors, a percentage that doubles [1].

Currently, the global trend leans towards reducing greenhouse gas emissions, primarily through exploring various innovative technologies to reduce fossil fuel consumption and consequently technologies that have a positive impact on reducing greenhouse gases. Reducing energy demand in buildings and contributing to preserving fossil fuels are major challenges at the turn of the century. Building energy efficiency is part of the response to current energy challenges (resource economy, greenhouse gas reduction, carbon footprint reduction, renewable energy use, etc. It constitutes the primary pillar in the building sector's transition, particularly within the Net Zero Emissions (NZE) scenario. The NZE scenario by 2050 is a normative scenario from the IEA that outlines the path for the global energy sector to achieve zero net CO2 emissions by 2050. In this scenario, energy consumption will decrease by 24% by 2030, reaching approximately 100 EJ. Achieving this necessitates an annual improvement of about 5% in residential building energy efficiency between 2020 and 2030 [1].

There are significant opportunities for efficiency gains that can be introduced and studied to reduce the high energy consumption of buildings. This can be achieved through various passive and active techniques, whether through improving the thermal insulation of building envelope, energy storage for future utilization, heat pumps, energy-efficient appliances, and the utilization of renewable energy sources. Recently, various technical solutions have been introduced. The core of innovation focuses on research into intelligent materials based on latent heat thermal energy storage, able to lower energy consumption and manage thermal comfort in occupied structures. These materials are called phase change materials (PCM).

B. Duraković [2] has outlined the historical development of phase change materials for thermal energy storage in figure 1. The application of PCMs in buildings for thermal storage traces back to the late 1940s, with significant interest in research emerging only during the energy crisis of the late 1970s and early 1980s [2]. Extensive efforts have been devoted to exploring the utilization of PCMs in various domains, including solar heating systems [3-8], clothing, photovoltaic systems [9-14], lithium-ion battery systems [15-17], electronic devices [18, 19], as well as in active heating/cooling systems [20-24], wall panels, bricks, coatings, cement, plaster, concrete [25-32], glazing systems [33], infrastructure [32], etc.

To assess the effect of integrating phase change materials (PCMs) in the construction sector on energy savings and indoor temperature regulation, numerous research findings and significant experiments have been conducted. M. Prabhakar et al. [34] evaluated the impact of coupling macro-encapsulated PCM in bricks with natural ventilation and intelligent control on enhancing the energy efficiency of tertiary buildings. A simulation was conducted for 15 different cities worldwide. It was observed that in hot and arid conditions, the PCM passive cooling technology proved to be inefficient. However, energy savings were augmented by integrating PCMs with natural ventilation in such climatic contexts, although the benefits were comparable to those

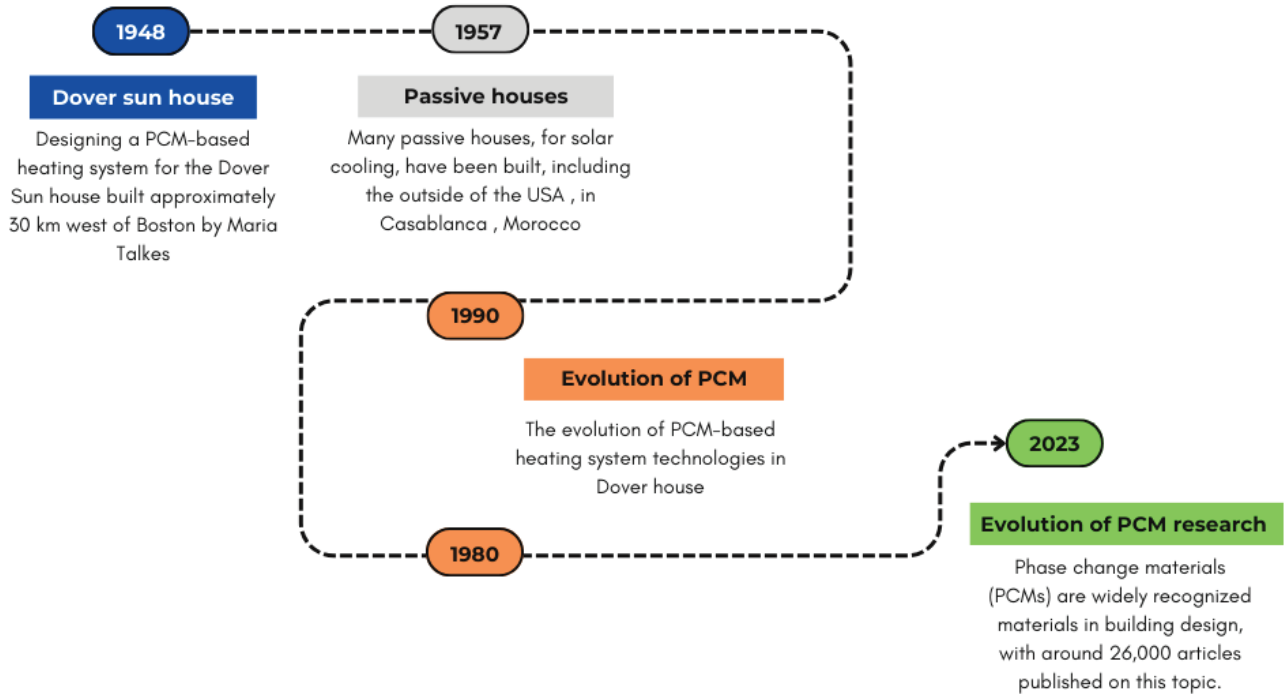

Figure 1. Historical Application of PCMs in Thermal Energy Storage (TES).

achieved through natural ventilation alone. Conversely, PCM efficiency increased from 3.32% to 25.62% in temperate conditions by coupling a passive PCM system with night ventilation. This was enhanced to 40% with the application of PCMs alongside temperature-controlled ventilation. Thus, it can be inferred that intelligent ventilation control has the potential to yield significant energy savings.

Xamán et al. [35] analyzed the effect of integrating phase change materials (PCMs) into a concrete roof on its thermal performance under the hot meteorological conditions of Mérida, Mexico. The results indicate that the installation of a 2 cm R-PCM1 resulted in a reduction of 57% compared with a normal roof. For an average building lifespan in México, approximately 30 years, the installation of R-PCM1 (paraffin wax - MG29) with a 2 cm PCM thickness is economically viable, with a payback period of 12.18 years.

The heat transfer within transparent structures containing PCM, such as windows, represent a highly complex process owing to the interplay of heat conduction, radiation, convection, phase change phenomena, and solar radiation buildup within the unit [33]. King et al. [36] carried out an empirical study on the thermal transfer properties of a double-glazed window integrated with paraffin RT 35 as a PCM. They demonstrated that the systematic integration of the appropriate phase change material into a double-glazed window can effectively mitigate solar heat gain into the room and substantially improve the building›s energy efficiency. Additionally, the PCM notably reduced temperature fluctuations within the interior space from 21°C to 11°C, the interior glass temperature by 8.5°C, and energy usage through the window by 3.76%.

The incorporation of phase change materials (PCMs) within a glazed roofing system, as opposed to air, leads to a substantial 47.5% reduction in energy consumption, with a payback period ranging from 3.3 to 6.2 years. Furthermore, this concept presents itself as a viable solution for renovating large spaces, such as gymnasiums, due to its easy implementation. [37].

Mabrouki et al. [38] investigated the impact of various factors influencing the use of PCM Trombe walls on heating and cooling loads in Ifrane, Morocco, characterized by a semi-oceanic climate. Their findings indicated a significant reduction in the annual energy consumption of the reference house, from 1,285.6 kWh to 733.18 kWh. A notable reduction in energy demand of 42.97% was also achieved by the addition of vents to the PCM Trombe wall.

Saikia et al. [39] introduced a new passive cooling system designed exclusively for high-temperature locations, harnessing the liquid-vapor phase change mechanism. Integration of the LVPCM technology into concrete slabs showed thermal performance equivalent to that of standard SLPCM systems. In the hottest daytime intervals, the use of LVPCM resulted in a reduction of 2.22°C in the temperature. Installation of the technology recorded an average reduction of 20.51% was attained, indicating a heat gain through concrete of 13.56%.

This article presents a comprehensive review of recent literature on phase change materials, considering their types, advantages, and disadvantages. It addresses some approaches to integration along with their benefits and drawbacks. It further addresses the simulation tools that have been applied to optimize and evaluate the impact of PCM integration into building envelopes on energy consumption reduction. The article also gives recommendations for selecting optimum PCM properties, such as type, thickness, and location, based on previous research findings. Subsequently, all recent local (Morocco) research is described, and a critical evaluation is conducted toward identifying gaps and providing recommendations for future studies.

Phase Change Materials (PCM)

Phase transition materials can store or release energy as latent heat. As the PCM temperature rises and the melting point is reached, the PCM absorbs thermal energy and changes phase through the stored latent energy, shifting from solid to liquid state. In the opposite process, when the temperature of PCM decreases, PCM crystallizes, releasing the stored energy. The phase change occurs at a constant temperature. Incorporating such materials into building envelopes provides potential energy savings and enhanced thermal comfort by reducing annual heating and cooling demands. In 1983, Abhat was the first researcher to propose classifying PCMs characterized by a solid-liquid phase change. He published one of the earliest articles describing the properties and potential use of these materials [40].

PCMs are categorized into three major families, organic compounds, inorganic compounds, and eutectics, according to their chemical characteristics, as illustrated in figure 2.

- **Organic PCMs**: These materials are divided into two subcategories based on their function, namely paraffins (CnH2n+2) and non-paraffins (CH3(CH2)2n COOH), including fatty acids and other substances such as alcohols and esters. Paraffin is the most widely used phase change material due to its high heat of fusion, chemical stability, lack of segregation tendencies, and minimal degradation of thermal properties after repeated melting/freezing cycles. Nevertheless, it has low thermal conductivity, is flammable, and undergoes significant volume change from solid to liquid, posing challenges in the design of the container. In addition, one requires caution when using plastic containers because paraffins can infiltrate certain containers and soften them.
- **Inorganic PCMs:** This category includes salt hydrates and metals. Salt hydrates consist of salt and water combining into a crystalline matrix upon solidification. They are heavily studied as energy storage materials due to their affordability, availability, high thermal conductivity and density, non-flammability, and minimal volume

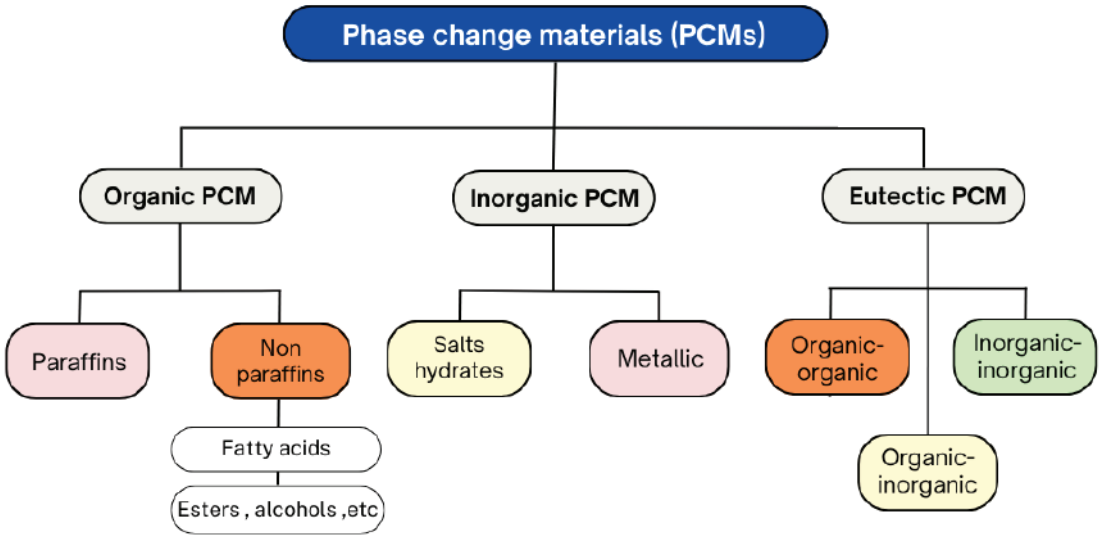

Figure 2. Classification of phase change materials (PCMs).

variation compared to other PCM types. However, the main drawback of salt hydrates is subcooling. Due to their weight, metals have not been extensively studied as PCMs for latent heat storage [2]. Although inorganic PCMs exhibit a sharper phase transformation (direct transition from solid to liquid without softening), they are two to three times more expensive than paraffins and slightly corrosive.

- Eutectic PCMs: refer to mixtures of two or more organic and/or inorganic compounds that consistently melt and freeze at a constant temperature without phase segregation, effectively acting as a singular component.

The diagram in figure 3 represents each PCM subgroup, illustrating the range of melting energy and the melting temperature interval.

To conclude, each of the aforementioned groups of PCMs has distinct properties, advantages, and disadvantages. selecting a suitable material necessitates thorough evaluation of multiple criteria specific to the application, such as buildings, batteries, photovoltaic systems, etc.

Criteria For Selecting a PCM

The selection of a PCM is contingent upon the specific application domain (building, transportation, food, textiles) as well as its environment (climatic conditions), hence the importance of defining the criteria for selecting a PCM

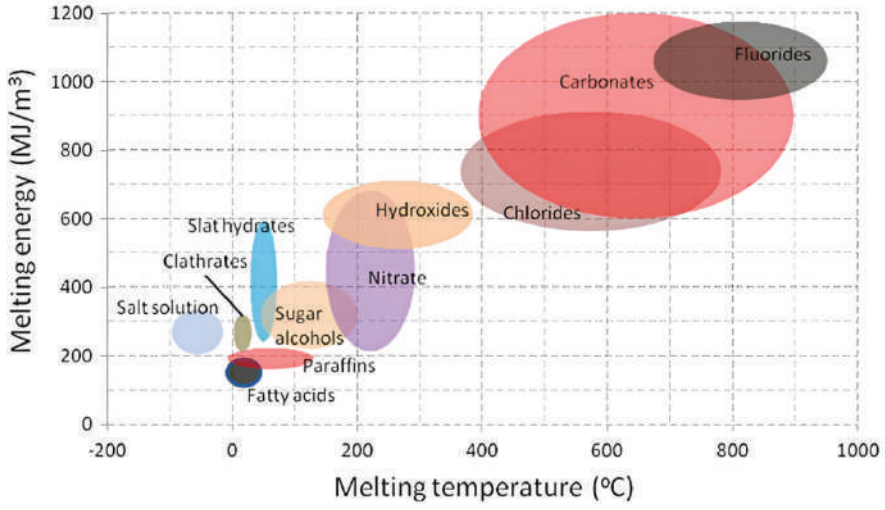

Figure 3. The latent heat and melting temperature of each PCM subgroup [From B.Duraković [2] , with permission from the author].

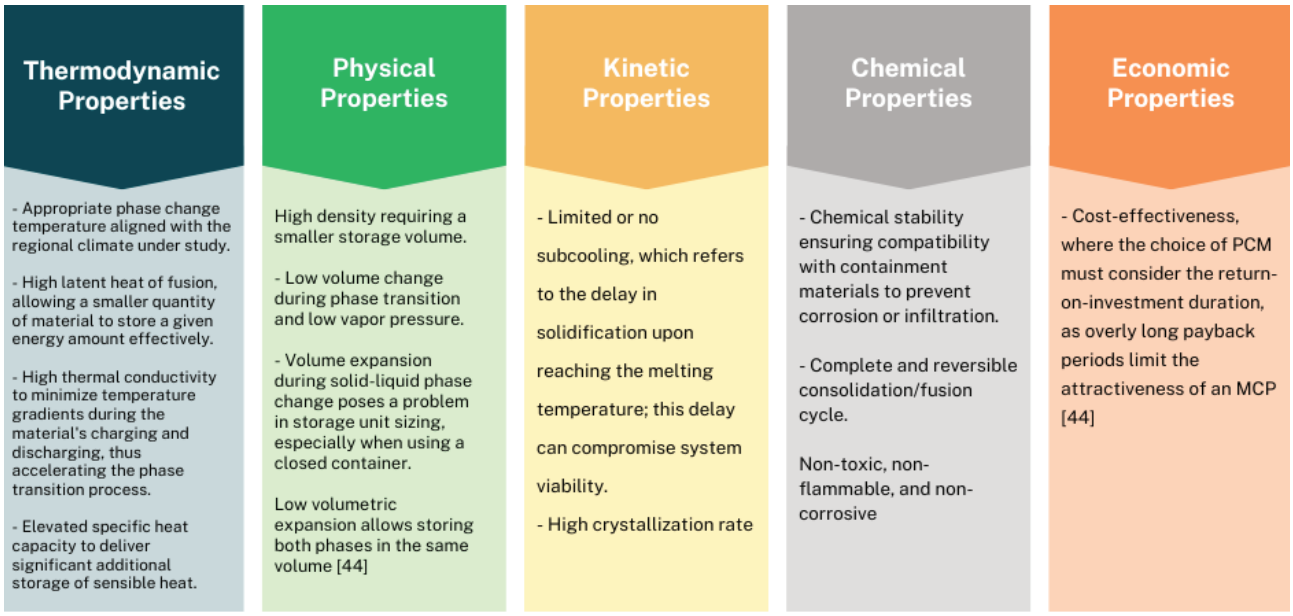

Figure 4. Phase change material's properties.

[41]. Abhat [40], Hawes et al. [42], and Pasupathy et al. [43] have defined the criteria for selecting a phase change material. To appropriately select a PCM for thermal energy storage in the form of latent heat, it is crucial to evaluate its thermodynamic, physical, kinetic, chemical, and economic characteristics. A proficient change material should have the following properties (Fig. 4).

No single material possesses all the required properties for ideal thermal storage. Selecting a PCM involves finding one that delivers optimal performance at minimal cost. Several researchers have affirmed that the melting temperature is one of the crucial thermo-physical properties that influence the performance of PCMs [2], [40-46].

Moreover, Yassine Chihab et al. [47] confirm that, for enhanced energy efficiency, a high heat of fusion and a low thermal conductivity are desirable properties for PCMs applicable in buildings. However, high thermal conductivity is recommended when using PCMs in heat exchanger systems [2].

The correlation among the heat of fusion, melting temperature, and thermal conductivity in various widely used commercial phase change materials used in construction applications is illustrated in figure 5.

In summary, the melting temperature, latent heat, cost, and stability are critical factors that will influence the market adoption of phase change materials (PCMs).

Since paraffins are widely recognized as the predominant phase change materials utilized in thermal energy storage applications due to their non-toxic nature, abundance, ease of microencapsulation, and other advantages, they are still derived from crude oil. This underscores the need to explore the development of biologically derived PCMs (bio-PCMs) as a sustainable alternative.

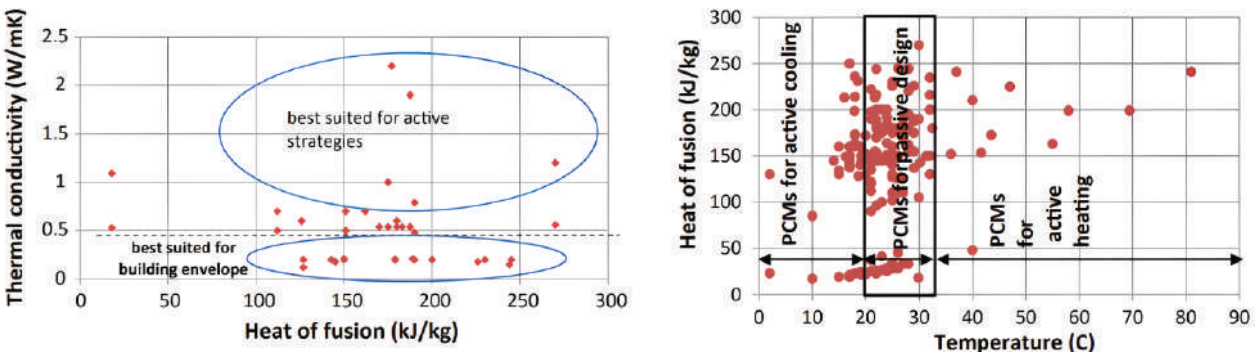

Figure 5. (**a**) Heat of fusion versus thermal conductivity, (b) Heat of fusion versus melting temperature for selected commercial PCMs [From B.Duraković [2], with permission from the author].

Bio-based PCM (BPCM)

Within the context of sustainable development, bio-origin phase change materials (BPCMs) offer an alternative to commercially available paraffin-based PCMs. They are renewable and environmentally friendly [48].

According to Duraković [2], paraffins are are the most commonly used as PCMs in thermal energy storage applications due to their non-toxic nature, abundance, and ease of microencapsulation. They are derived from petroleum, and their prices are sensitive to seasons and geopolitical scenarios. Consequently, there is a recognized necessity to explore other forms of bio-origin PCMs [2]. Several studies have been conducted for the development of a bio-sourced PCM capable of delivering comparable performance to conventional phase change materials.

The potential use of a bio-based PCM that is prepared from expired palm oil sourced from the food industry was investigated by Fabiani et al. [49]. Compared to petrochemical-based organic PCMs, it was found that, despite the low phase transition enthalpy, expired palm oil may serve as a potential, affordable, and environmentally friendly alternative for passive thermal storage systems. Such bio-based materials require further study in order to enhance the energy storage density and minimize subcooling to guarantee a more consistent material conducive to high performance while maintaining sustainability.

Boussaba et al. [50] explored the utilization of recovered coconut fat from underused feedstocks, cellulose fibers from recycled cardboard, natural clay, and graphite as a bio-based composite phase change material. The authors demonstrated that the latent heat fusion and freeze capacities were found to be 106.17 J/g and 107.34 J/g respectively, making the bio-based PCM suitable for passive solar TES building applications. It was found that the phase change temperatures aligned closely with human comfort levels (22.63 °C and 17.44 °C for the fusion and freeze cycles respectively), emphasizing its potential for practical application as a bio-based PCM. Thermal analysis TGA confirmed the material›s stability within operational temperature ranges, with thermal degradation starting above 200 °C., while spectroscopic analysis (FT-IR) verified its chemical stability.

Choi et al. [51], Jin Ong et al. [52], and Yoo et al. [53] examined the chemical composition, chemical, and thermo-physical properties of used coffee grounds (waste produced after using coffee as a beverage) to assess their viability as bio-based PCMs. Choi et al. [51] analyzed the morphological, thermal, and acoustic performances of a composite developed from degreased coffee waste with ethanol, urea-formaldehyde resin and bio-based micro-encapsulated PCM (MPCM). The results indicate that the developed composites present enhanced thermal performances (high thermal conductivity, thermal stability, etc.) and improved acoustic absorption properties. The composite can therefore be regarded as a sustainable building material, exhibiting significant thermal and acoustic properties.

Other PCMs have been evaluated by several researchers, including beeswax as a paraffin alternative as a durable, ecological, and potential PCM [54], [55], sugar alcohols [56], [57], [58], [59], [60], a eutectic mixture of ceramist sludge [61], grease waste from pork cooking processes confined in a polypropylene nonwoven mat derived from surgical mask filter waste and porous bio-silica (diatomite) [62], etc.

The bio-based products are developed from the renewable organic resources, presenting a more environmentally friendly, sustainable, and ecological option. These materials possess similar thermal properties, including latent heat capacity, phase change behavior, and thermal cycling durability, which make them suitable for equivalent thermal energy storage applications. However, research into biobased PCMs is still at the laboratory stage, so their use in building envelopes needs to be proven by experiments.

PCM Incorporation

To ensure optimal functionality, longevity, and mitigation of potential issues like corrosion or PCM leakage during its incorporation, various considerations are essential. Firstly, the storage system material must be suitable for the PCM, the container wall must also be thick enough for seal integrity and leak protection. Moreover, incorporation should be designed to withstand mechanical constraints arising from PCM volume changes during phase transitions. Therefore, selecting an appropriate incorporation method of PCM is crucial. There are several techniques for incorporating PCM into construction materials, such as direct incorporation, immersion, stabilized form, and encapsulation [63].

Encapsulation is the most widely used technique. It is a process that was invented and developed by Barrett K. Green of the National Cash Register Corporation (NRC) during the 1940s and 1950s [64]. This method entails encapsulating the PCM with an appropriate coating or shell material, in principle, maintaining the liquid and/or solid-phase of the PCM while isolating it from the outside environment [65].

Encapsulation provides multiple benefits, by decreasing PCM›s reaction to the environment, increasing flexibility in phase change process, and raising the thermal and mechanical stability of the PCM. Additionally, PCM encapsulation contributes to heightened heat transfer rates by increasing surface area, thereby increasing thermal conductivity. However, one of the main obstacles to commercializing an encapsulated PCM-based system lies in the considerable cost associated with encapsulation, which raises the overall system cost [66]. Encapsulations are classified based on their size into macro, nano, and micro-encapsulations [65].

- ✓ **Macro-encapsulation:** involves encapsulating phase change materials in large-scale containers, such as tubes, sachets, spheres, or panels, ranging from a few millimeters to several liters in volume. It is necessary that these containers be constructed from rigid materials with high thermal conductivity, such as aluminum or copper, to prevent leakage issues [37]. Additionally,

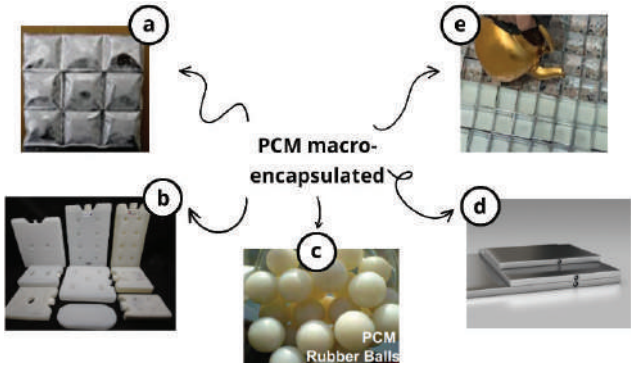

Figure 6. (a) Macro-encapsulation in sachets produced by PCM product company, (b) Macro-encapsulation in plastic containers as produced by PCM product company, (c) Macro-encapsulation in Rubber balls from PCM product company, (d) Macro-encapsulation in metal containers as produced by PCM product company [68]. (e) Macro-encapsulation in bricks for constructing a wall [From Q.Alyasiri et M.Szabo [67], with permission from Elsevier].

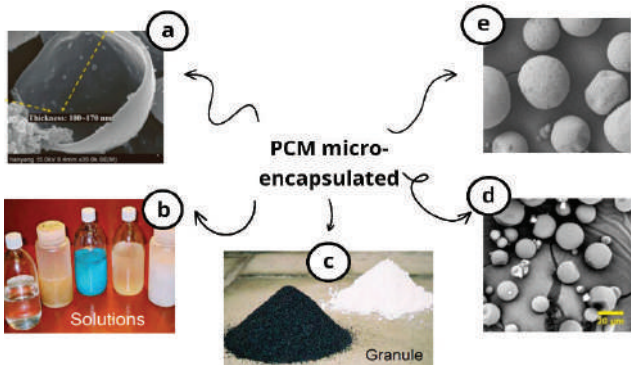

Figure 7. (a) Micro-encapsulation in a bio-sourced polymer shell (m-PCM) for incorporation into nano-modified cement composites [From X.Jin et al. [71], with permission from Elsivier]. (b) and (c) Microencapsulated PCM produced by PCM product company in fluid dispersion and granule forms respectively [68]. (d) PCM microcapsules are incorporated into asphalt coatings to regulate the temperature of asphalt pavements [From D.Bentacourt-Jimenez et al. [69], with permission from Elsevier]. (e) PCM microcapsules are incorporated into cement paste [From Y.Gu et al. [70], with permission from Elsevier].

when the container possesses sufficient rigidity, macro-encapsulation could also contribute to enhanced mechanical stability in the resulting system.

Figure 6 illustrates examples of macro-encapsulated PCM [67], [68].

- ✓ **Micro-encapsulation**: involves encapsulating the phase change material in spheres or capsules with diameters ranging from 1 μm to 1000 μm [46]. These PCM particles can then be incorporated into any matrix that is well suited to the encapsulated shell, such as construction materials. Microencapsulated PCM effectively avoids the drawbacks of macro-encapsulated PCM, such as handling issues, leakage risks, shape distortion, and maintenance complexities [67].

  There are numerous commercial products of microencapsulated PCM, such as Micronal® PCM produced by the German company BASF. **Figure 7** depicts examples of microencapsulated PCMs [68-71].
- ✓ **Nano-encapsulation:** in certain applications, particularly in latent functional thermal fluids, microencapsulated phase change materials (PCMs) have demonstrated limited performance under repeated cycles. This limitation arises from the tendency of large particles in microencapsulated PCMs to increase fluid viscosity and susceptibility to being crushed during pumping. Consequently, there has been a focus on developing PCMs with particle sizes smaller than those found in microencapsulated forms [72]. Nano-encapsulation is an encapsulation technique introduced by Narty in the 1970s and widely used in medical dyes and fragrances [72]. It involves encapsulating the phase change material within capsules with diameters ranging from 1 nm to 1000 nm.

In light of the findings, it can be concluded that reducing capsule size enhances the thermal reliability and chemical stability of PCM. Nano-capsules exhibit superior structural stability compared to macro and microcapsules. However, research on nano-encapsulated PCMs is still at the laboratory level [65] .

Despite microencapsulated PCMs offering higher thermal reliability and chemical stability than macro-encapsulated materials, their production process remains more complex. They may also face subcooling issues due to hypothermia, retaining the liquid phase even below its freezing point [65]. In addition, they can present some leak issues caused by micro-encapsulation damage during handling or mixing processes at construction sites, which can deteriorate the properties of construction materials used for building. Encapsulating PCM in containers larger than 5,000 μm and then integrating it into the building envelope will minimize PCM leaks [66].

Rathore & Shukla [66] performed a comprehensive analysis of various approaches to integrate macro-encapsulated PCM into the building envelope. They demonstrated that macro-encapsulation is one of the simplest and most efficient methods to directly incorporate PCM into construction materials. Furthermore, macro-encapsulated PCM exhibits high resistance and durability relative to microencapsulated PCM and can be simply fabricated by filling PCM into the shell material of any desired shape.

Techniques for Enhancing The Thermal Properties of Phase-Change Materials

In the context of improving the energy efficiency of buildings, which has become a crucial concern, phase change materials have garnered substantial attention from researchers. Their incorporation is also potential for

creating energy-saving building envelopes and reducing CO2 emissions in this sector. This is due mostly to their significant potential for storing and releasing heat energy, thus enhancing the latent heat storage potential of building envelope upon incorporation. However, PCM's drawback lies in their low thermal conductivity,resulting in suboptimal heat transfer rates and negligible effectiveness in heat storage and release. These limitations may inhibit their further usage as heat energy storage materials in building applications [73]. In order to overcome these setbacks, some methods could be implemented, such as incorporating high-conductivity materials, nano-encapsulation, forming composite PCMs, and shape stabilization [74].

- Forming a PCM -composite represents an approach aimed at enhancing the thermal performance of PCMs. It involves combining a PCM with other materials possessing high thermal conductivity to create a composite material with additional or modified properties. The integration of PCMs into another material's matrix is done at a microscopic level to preserve their thermal characteristics [42]. These composites can take the form of fibers/stearic acid, foams/polyethylene, or films [74]. Composites that establish a stable structure between a PCM and another material are commonly referred to as shape-stabilized PCMs [42].
- Shape-stabilized PCM: a technique for improving the thermal performance of PCMs, commonly adopted for organic PCMs known for their low thermal conductivity and leakage issues during phase change. This strategy involves utilizing two components: a porous material that prevents PCM leakage, such as porous carbon (derived from materials like cardboard, potatoes, succulents, activated carbon, etc.), expanded graphite, or polyurethane foam; and a nanomaterial that enhances the thermal properties of PCMs [73]. Additionally, the porous matrices enhance thermal performance through the provision of an extended surface area for heat transfer [74]. The loading PCMs into porous materials can be achieved through vacuum impregnation, ultrasonic oscillation, and melting adsorption methods [73].
- Nano-encapsulation: As mentioned in the earlier section, it encapsulates the phase change materials in tubular, cylindrical, spherical, or rectangular capsule, with diamters in the range of 1 nm and 1000 nm. It remains the most efficient technique for improving heat transfer rates [74], mostly by improving the thermal conductivity of PCMs and minimizing leakages while in their phase transition [75]. Metallic [76] and carbon-based [77] nanoparticles of high thermal conductivity are incorporated into PCMs for improved heat conductivity. Nonetheless, carbon-based nanoparticles demonstrate superior stability and dispersion within PCMs compared to metallic counterparts [2].

Numerous investigations have been implemented to evaluate the advantages of integrating nano-PCM in terms of energy savings and thermal comfort compared to conventional PCMs. Zhenjun et al. [78] demonstrated that the enhanced solidification/melting process of nano-PCM incorporated into a ventilation system, as opposed to the pure process, increased the heat charge and discharge rates by 8% and 25%, respectively.

Fateh Mbarek Oudina and Ines Chabani et al. [79] concluded that, from an economic perspective, the cost of this technique is relatively low in comparison to the substantial benefits conferred by the inclusion of nanoparticles and phase change materials on the overall thermal performance of systems. This represents an excellent solution for ensuring thermal comfort at a very low cost, enabling the phase transition to occur much more rapidly than in systems with pure PCM while capturing greater solar energy. Additionally, the use of nano-PCM leads to an increase in overall thermal capacity, resulting in significant thermal storage.

Nonetheless, it was reported by Ghalambaz et al. [80] that the cost of the nanoparticles is dependent on their type, as the copper nanoparticles were around 10 times higher in value as compared to the alumina nanoparticles. This highlights the interest in developing hybrid nano-PCMs, which are prepared by suspending various types of nanoparticles in a PCM. From numerical simulation of the melting process in nanoparticle-enhanced phase change materials, the authors that The melting process was improved by utilizing a hybrid nano-PCM. Specifically, the melting time of the single-component water/Ag–MgO nano-PCM was lower compared to that of the single-component water/MgO nano-PCM.

- Incorporation of High Thermal Conductivity Materials: This strategy is based on the incorporation of high thermal conductivity materials such as nano-metals, aluminum or carbon fins, carbon-based materials, or expanded graphite. Such fillers, through the formation of a conductive network within the PCM matrix, enhance thermal transfer as well as general thermal performance while preserving the inherent latent heat storage potential of the material [74].

Moreover, thermal conductivity improvement in PCMs can also be obtained through chemical modifications such as doping or grafting [81]. These chemical modifications considerably alter the composition and surface phase structure of the thermally conductive matrix, resulting in porous materials with doped components to improve the cyclic stability as well as the thermal conductivity of the PCM. Grafting, or post-synthesis modification, entails a chemical reaction that deposits organic groups onto the surface of the mesoporous canals. Doping, grafting, or incorporation of uniquely structured materials enhance the thermal conductivity, sensible heat, and latent heat of fusion of pure PCM [81].

Thermal performance can be improved through different methods. Nevertheless, the integration of some unknown elements may introduce adverse effects, such as a decrease in thermal stability. Therefore, additional research and development should be taken into account to improve the functionality of PCMs.

The Simulation Tools

The integration of phase change materials into lightweight constructions allows for improved thermal comfort and reduced energy consumption. Yet, to accurately evaluate and optimize the integration of phase change materials within building envelopes, numerical simulation becomes a necessary requirement. The simulation of building performance represents a key tool to choose the most effective solution to integrate [82]. Currently, several energy simulation tools are available and widely employed by researchers and designers, broadly categorized into two groups: Building Energy Simulation (BES) tools, including EnergyPlus as well as TRNSYS, and computational fluid dynamics packages, namely ANSYS Fluent and COMSOL Multiphysics.

According to Pandey et al. [83], Computational Fluid Dynamics (CFD) tools offer the capability to model spatially distributed solidification and complex PCM melting phenomena. However, they require considerable computational time to model and simulate the entire building system in combination with a PCM-based system. Additionally, CFD modeling necessitates accurate boundary conditions derived either from experimental data or prior knowledge of the system. Furthermore, these CFD models are not seamlessly integrated into building simulation frameworks.

Despite the relative simplicity of using Energy Plus as a Building Energy Simulation (BES) tool, which explains its extensive utilization in the literature to assess the impact of PCMs on enhancing thermal comfort and reducing cooling/heating energy demand, these BES tools reveal certain limitations [83]. For example, in the application of free cooling where PCM is charged with natural ventilation, meaning that external cold air is used to extract heat from the PCM, the use of BES tools to study the performance of the PCM TES system leads to under/over-prediction of results. This can be explained by the fact that these tools consider an air node in each zone as representing a volume of air with uniform thermal properties. Additionally, BES tools use uniform thermal properties to model a zone, whereas PCM solidification and melting phenomena are highly non-uniform, limiting their use in determining the efficiency of PCM-based systems. To address these challenges, Pandey et al. [83] developed a co-simulation model combining EnergyPlus as a BES tool and Ansys Fluent as a CFD tool to evaluate its relevance compared to EnergyPlus and to assess the impact of PCM-based systems on the built environment. The findings indicate that co-simulation outperforms existing BES tools, particularly in scenarios involving active use of PCM in the built environment and when passively applying PCM in forced convection. Indeed, a comparison of the predictive accuracy of the co-simulation model and EnergyPlus during forced convection reveals that EnergyPlus model underestimates the experimental data. However, for passive PCM application , the results indicate that there is no significant difference in predictive accuracy between the co-simulation approach and conventional BES models.

In the same context, Mazzeo et al. [82] assessed the predictive accuracy of the most widely used BES tools, namely TRNSYS, EnergyPlus, and IDA ICE, by comparing simulated outcomes with experimental measurements obtained under real operating conditions. Their findings underscored IDA ICE as a robust choice for dynamically modeling buildings incorporating Phase Change Materials (PCMs). Unlike TRNSYS and EnergyPlus, IDA ICE explicitly addresses PCM hysteresis phenomena. Moreover, the TRNSYS model exhibited the least precision due to its omission of both hysteresis effects and the temperature range associated with phase transitions, which are implemented in both IDA ICE and EnergyPlus. Even though TRNSYS yields the lowest precision, it allows for sufficiently accurate calculation of the total latent heat storage and release, with minimal thermo-physical input requirements and the lowest computational cost.

The selection of a simulation tool is contingent upon the specific model, simulation objectives, and the anticipated outcomes. TRNSYS and EnergyPlus are widely regarded as the most suitable and extensively utilized simulation tools for evaluating heating and cooling energy consumption in buildings that incorporate phase-change materials.

PCM Optimization

The annual thermal energy demand for heating and cooling in buildings with PCM integration is influenced by various factors, including the melting temperature, PCM thickness, and its location within the external envelope of construction [84].

a. Melting temperature

The melting temperature refers to the point at which a substance transitions from a solid to a liquid state, absorbing energy during this process and releasing it upon crystallization. Imghoure et al. [85] demonstrated through a simulation model that the melting temperature is one of the most crucial thermo-physical properties influencing PCM performance. Indeed, A suboptimal selection of the phase transition temperature could lead to increased cooling energy requirements during the summer months [86].

In a related context, Peippo et al. [87] introduced a method to calculate the optimal melting temperature for a phase change material:

$$T_{m,opt} = T_r + \frac{Q}{h\, t_{stor}} \tag{1}$$

$$avec\ T_r = \frac{t_n T_n + t_d T_d}{t_n + t_d}\ et\ t_{stor} = t_n + t_d$$

With $T_{m,opt}$ representing the optimal melting temperature of the PCM (°C), T_r the average room temperature (°C), Q the heat absorbed per unit area of a room surface (*J.m-2*), h the average transfer coefficient between the wall surface and its surroundings (*W.m-2K-1*), T_n room nighttime

Table 1. Results of PCM optimization from the literature

Climate zone	City	Optimal PCM	Thickness (mm)	Optimal placement of PCM	Optimal melting point (°C)	set-point temperature/ interior temperature (°C)	Ref
Am	Semarang (Indonesia)	PCM 29	20	Interior	29	20°C to 24 °C for winter 24°C to 26.5°C for summer	[88]
Aw	Brasilia (Brazil)	PCM28	20	Interior	28	20°C to 24 °C for winter 24°C to 26.5°C for summer	[88]
Af	Kisumu (Kenya)	PCM29	20	Interior	28	20°C to 24 °C for winter 24°C to 26.5°C for summer	[88]
Bsk	Makhachkala (Russia)	PCM26	20	Interior	26	20°C to 24 °C for winter 24°C to 26.5°C for summer	[88]
	Ceduna (Ausralia)	Rubitherm (CSM) RT 22	15	Interior	22	24°C	[89]
	Quetta (Pakistan)	Corda Therm 24	40	Interior	24	18 for heating 25 for cooling	[90]
Bsh	Luanda(Angola)	PCM29	20	Interior	29	20°C to 24 °C for winter 24°C to 26.5°C for summer	[88]
	Dakar (Senegal)	Rubitherm (CSM) RT 25	15	Interior	25	24°C	[89]
	Lahor (Pakistan)	Corda Therm 24	40	Interior	24	18°C for heating 25 for cooling	[90]
	Agadir (Morocco)	Infinite RTM 23 Based on hydrate salts	6 with a mechanical ventilation rate of 6 ACH	Middle, in the cavity of a double partition wall made of hallow clay bricks	23	set-point temperatures of 26°C in summer and 20 °C in winter	[91]
	Errachidia (Morocco)	40% polyethylene and paraffin (60%)	5	Exterior, next to the heat source	21,7-30	The test was conducted at controlled temperatures of 25.5 °C on the cold plate and 40 °C on the hot plate	[92]
Bwh	Cairo (Egypt)	PCM23	20	Interior	23	20°C to 24 °C for winter 24°C to 26.5°C for summer	[88]
	Abou Dabi (UAE)	Rubitherm (CSM) RT 26	15	Interior	26	24°C	[89]
	Marrakech (Morocco)	Infinite RTM 25 Based on hydrate salts	6 with a mechanical ventilation rate of 6 ACH	Middle , in the cavity of a double partition wall made of hallow clay bricks	25	set-point temperatures of 26°C in summer and 20 °C in winter	[91]
	Ouargla (Algeria)	Calcium chloride hexahydrate CaCl2.6H2O	PCM is inserted in the holes of the brick (12 cavities)	Middle	29,9	27 °C (imposed comfort temperature)	[93]
	Karachi (Pakistan)	Corda Therm 24	40	Interior	24	18°C for heating 25 for cooling	[90]
Bwk	Turpan (China)	PCM 28	20	Interior	28	20°C to 24 °C for winter 24°C to 26.5°C for summer	[88]
	Las Vegas (USA)	Rubitherm (CSM) RT 26	15	Interior	26	24°C	[89]
Cfa	Brisban (Australia)	PCM 26	20	Interior	26	20°C to 24 °C for winter 24°C to 26.5°C for summer	[88]
	Madrid (Spain)	Rubitherm (CSM) RT 25	15	Interior	25	24°C	[89]

Table 1. Results of PCM optimization from the literature (continued)

Climate zone	City	Optimal PCM	Thickness (mm)	Optimal placement of PCM	Optimal melting point (°C)	set-point temperature/ interior temperature (°C)	Ref
Cfb	Hamilton (New zealand)	PCM 24	20	Interior	24	20°C to 24 °C for winter 24°C to 26.5°C for summer	[88]
	Paris (France)	Rubitherm PCM24	20	Interior	24	20°C to 24 °C for winter 24°C to 26.5°C for summer	[94]
	Bilbao(Spain)	Rubitherm PCM22	20	Interior	22	20°C to 24 °C for winter 24°C to 26.5°C for summer	[94]
	Melbourne (Australia)	Rubitherm PCM25	20	Interior	25	20°C to 24 °C for winter 24°C to 26.5°C for summer	[94]
Csa	Naples (Italy)	PCM 24	20	Interior	24	20°C to 24 °C for winter 24°C to 26.5°C for summer	[88]
	Tehran (Iran)	Rubitherm (CSM) RT 26	15	Interior	26	24°C	[89]
	Fes , Tangier (Morocco)	Infinite RTM 25 Based on hydrate salts	6 with a mechanical ventilation rate of 6 ACH	Middle, in the cavity of a double partition wall made of hallow clay bricks	25	set-point temperatures of 26°C in summer and 20 °C in winter	[91]
	Istanbul (Turkia)	Infinite PCM	33,6 (3 Layers of 11,2)	Interior	21	20°C to 24 °C for winter 24°C to 26.5°C for summer	[84]
Csb	Bursa (Turkey)	PCM 26	20	Interior	26	20°C to 24 °C for winter 24°C to 26.5°C for summer	[88]
	Ifrane (Morocco)	Infinite RTM 25 Based on hydrate salts	6 with a mechanical ventilation rate of 6 ACH	Middle, in the cavity of a double partition wall made of hallow clay bricks	25	set-point temperatures of 26 and 20 °C throughout the summer and winter season, respectively	[91]
	Antofagasta (Chile)	Rubitherm (CSM) RT 24	15	Interior	24	24°C	[89]
Cwa	Busan (Korea)	PCM 26	20	Interior	26	20°C to 24 °C for winter 24°C to 26.5°C for summer	[88]
	Hong Kong (China)	Rubitherm (CSM) RT 25	15	Interior	25	24°C	[89]
Cwb	Johannesburg (South of Africa)	PCM 26	20	Interior	26	20°C to 24 °C for winter 24°C to 26.5°C for summer	[88]
	Islamabad (Pakistan)	Corda Therm 24	40	Interior	24	18 for heating 25 for cooling	[90]
Dfa	Chicago (USA)	PCM 26	20	Interior	26	20°C to 24 °C for winter 24°C to 26.5°C for summer	[88]
Dfb	Montreal (Canada)	PCM 25	20	Interior	25	20°C to 24 °C for winter 24°C to 26.5°C for summer	[88]
	Ottawa (Canada)	An aluminum honeycomb matrix with 60% microencapsulated paraffin	20	Interior	23	24°C	[95]

temperature (°C), T_d the daytime room temperature (°C), t_n the PCM discharging time night (s), t_d charging time day (s), and t_{stor} the diurnal storage time (s).

Several studies conducted in different cities worldwide aimed to determine the optimal melting temperature [88-95]. Table 1 summarizes some literature studies investigating the effect of integrating PCMs into buildings on reducing heating and cooling energy consumption. The table specifies the type of PCM used by each author, its optimal melting temperature, location, and thickness. These studies are classified, according to the Köppen-Geiger climate classification system, based on monthly average outdoor temperatures and precipitation data. This classification divides the world into five major climatic regions (A: equatorial, B: arid, C: temperate, D: continental, E: polar). These climatic zones are further divided based on precipitation and temperature data.

The analysis of the table regarding the optimization of melting temperature leads to conclusions similar to the study conducted by Saffari et al. [96]. In climates with high energy demand (A and B), PCM melting temperatures are generally close to the maximum of 26°C (ranging from 24 to 28°C). Conversely, in climates where heating predominates (C and D), PCM transition temperatures vary from 18°C to 22°C, except for select cities where the optimal melting temperature may exceed these values, for example, Paris which has an optimal melting temperature of 24°C [94]. According to Saffari et al. [96], this difference can be explained by other climatic factors such as altitude.

In general, for enhanced energy efficiency, several researchers affirm that the optimal melting temperature of a phase change material should closely align with the average indoor heating and cooling setpoints [47], [95], [97]. Neeper (2000) considers that the optimal melting temperature of a phase change material should be close to the interior temperature to minimize thermal loads. The indoor temperature of a room is heavily contingent on the outdoor temperature, which fluctuates across seasons.

It is pertinent to mention that in studies where the setpoint temperature is unspecified, we referred to ASHRAE standard 55 (American Society of Heating, Refrigerating, and Air-Conditioning Engineers), which recommends a comfort temperature of 20°C to 24°C for winter and 24°C to 26.5°C for summer.

Cities in the same climatic region, such as Bilbao and Paris (Cfb), won›t necessarily have the same optimal melting point of phase change materials (PCMs), since different climatic conditions apart from the Koppen climatic classification are also involved. Some of the climatic conditions that dictate the selection of the PCMs are wind velocity, intensity of solar irradiance on the exterior surfaces, humidity ratio, and precipitation intensity [98].

For instance, Paris, situated at an altitude of 15 meters, has an optimal PCM melting temperature of 24°C as determined by Bozzhigitov et al. [94]. Conversely, in Bilbao, located at an altitude of 19 meters, the optimal melting temperature is 22°C. This indicates that comfort temperature, a key parameter for determining the melting temperature of a phase change material, depends on the outdoor temperature, which in turn varies with altitude. Outdoor temperature decreases with altitude.

In the context of the RP884 research initiated by ASHRAE in 1995, aimed at formulating an international adaptive comfort standard to complement the American ASHRAE Standard 55, several scholars (Humphrey 1978, de Dear 1986, Nicole Rejal 1995, de Dear and Brager 2002) have demonstrated, through on-site investigations, that indoor comfort temperature is influenced by outdoor temperature. The adaptive approach involves determining thermal comfort conditions from empirical data and field studies. It was introduced by de Dear and Brager in 1998 based on extensive data collected from 160 global office buildings [100], this methodology enables the establishment of linear regressions for comfort temperature in relation to outdoor temperature for both air-conditioned and naturally ventilated buildings [99].

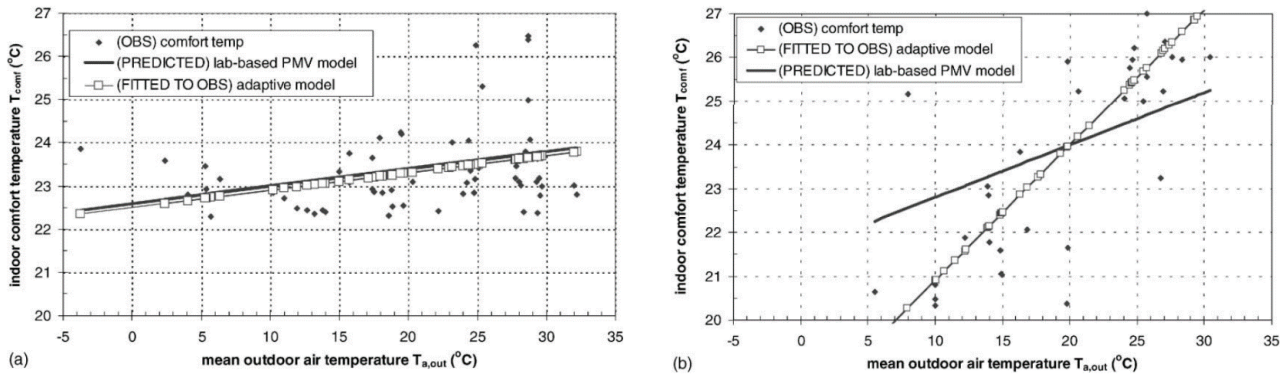

Figure 8. Adaptive model proposed by the RP-884 project for air-conditioned buildings and naturally ventilated buildings [From R.De Dear and G.Brager [99], with permission from Elsevier].

The results obtained by de Dear are illustrated in figure 8. Through this figure, it can be concluded that as altitude decreases, the average outdoor temperature increases, leading to higher comfort temperatures and consequently higher melting temperatures.

Within the framework of optimizing the phase transition temperature of PCM, Dardouri et al. [86] conducted a study aimed at evaluating the PCM›s efficacy, in conjunction with thermal insulation, in reducing annual energy consumption. The results revealed that for both single and double walls, PCM 23 demonstrated superior energy savings in heating, while PCM 29 exhibited higher benefits in cooling energy. This can be attributed to PCM23›s ability to maintain thermal comfort during summer months due to its lower melting temperature compared to outdoor temperatures, thereby keeping the PCM mostly in a liquid state, posing a risk of overheating. A PCM with a fixed melting temperature proves inadequate for simultaneous heating and cooling applications [101].

Liu et al. [46] emphasized, based on previous studies, the necessity of considering the fluctuations in solar radiation received by various building elements such as walls, roofs, and floors. Given that the roof receives the majority of solar radiation, it is advisable to use a PCM exhibiting a higher phase change temperature compared to walls to mitigate heat influx, especially during cooling periods. Therefore, the integration of a single PCM within a building envelope fails to maximize its thermal potential to control the internal temperature as well as to minimize the consumption of energy.

Overcoming this challenge, Wang et al. [102] proposed a strategy to improve the energy efficiency of PCMs integrated into building structures. This includes the use of adaptive dynamic building envelope integrated PCM (ADBEIPCM), in which the location of the PCM and the insulation vary with the outdoor temperature. Their research showed that, in comparison with a static envelope, such innovative walls considerably reduced annual cooling loads by between 15% and 72% and heating loads by 7% and 38%. However, no actual practical experience in the use of ADBEIPCM in buildings to evaluate the technical viability exists, as their complex maintenance makes their application challenging. Another potential method to increase the storage of energy within the building envelope involves utilizing cascaded thermal storage PCM, also known as cascaded latent thermal energy storage. This method consists of integrating various PCMs in decreasing order of their melting temperatures.

PCM placement

The potential of phase change materials (PCMs) to enhance thermal comfort and energy efficiency of buildings is contingent upon the location where the PCM is incorporated within the exterior envelope. The optimum location to integrate PCM can be reliant on certain factors such as heat source temperature, exterior surface temperature, thermal flux density through the wall, and thermal flux stored within the walls [92]. Several numerical and experimental studies recommend the adoption of internal wall placement of PCMs, as given in Table 1.

Khan et al. [90] conducted a numerical simulation using Energy-plus software to study the effect of PCM integration in residential building envelopes in five major cities located in different climatic zones in Pakistan (Islamabad, Karachi, Lahore, Quetta, Peshawar). The study aimed to optimize several parameters such as PCM melting temperature, its location, and thickness. The results indicate that annual energy consumption in the configuration where PCM is positioned on the inner surface of the wall diminishes by 6.04%, compared to a reduction of 5.5% when it is placed on the exterior side.

Ben Zaid et al. [92] carried out an experimental study to assess the thermal performance of clay-straw walls incorporating PCM in the Drâa-Tafilalet region (Errachidia Province), Morocco. Using a scaled laboratory cavity, the study made clay-straw walls with PCM integration in the form of panels made of two aluminum sheets, one with 40% polyethylene and the other with 60% paraffin. Keeping the internal temperature at 40°C, the results show that when the PCM is next to the heat source, the surface temperature drops by 1°C compared to when it is away from the source. Similarly, Gouni et al. [103], employing wooden walls, observed a 2°C decrease in exterior surface temperature when the material is placed near the heat source as opposed to a distant placement. The commonality between these two studies is that the impact of the PCM layer placed close to the heat source on reducing the exterior surface temperature is more pronounced. This observation can be elucidated, on one hand, by the PCM›s complete fusion under conditions where the melting temperature is lower than the internal temperature, which reduces the exterior surface temperature. On the other hand, the wall containing PCM in the internal layer exhibits a slower heat release compared to the wall with PCM in the external layer [92]. Furthermore, PCM placement on exterior wall surfaces facilitates nocturnal dissipation of stored heat, thus not negatively affecting occupant thermal comfort [96].

It is pertinent to note that cavity studies are conducted exclusively under warm climatic conditions, with the test cell›s exterior simulating the building's indoor environment. Nevertheless, to select the optimal position for a phase change material (PCM), it is crucial to study its impact on annual heating and cooling energy consumption.

In the presence of insulation, integrating PCM into building walls improves its energy efficiency, offering potential benefits for renovating old buildings [86]. Multiple investigations have been undertaken to assess the integration of thermal insulation compared to phase change materials [85], [86], [90], [104]. The synthesized findings are summarized as follows:

- Roof insulation integration yields superior energy savings compared to PCM [86]. Consequently, PCM›s

impact on reducing cooling and heating loads becomes more pronounced in the absence of insulation, as the latter may impede PCM›s phase transition process. Khan et al. [90] demonstrated that total annual energy consumption is reduced by 44% when PCMs are installed in the building envelope and by 28% when incorporating expanded polystyrene.

- The optimal position of PCM, in the presence of insulation, recommended by Dardouri et al. [86] and Imghoure et al. [85] during the summer period is when PCM is placed on the interior side after the insulator. However, Alyasiri et al. [104] examined the impact of EPS insulation on PCM (paraffin wax) thermal performance during six summer months in the city of Almarah in Iraq. Their findings clarified that placing the EPS layer after the PCM layer on the inside guarantees effective fusion and solidification phases, as evidenced by the liquid fraction. Notably, the melting temperature range of paraffin wax, as adopted by Alyasiri et al. [104] due to its local availability in Iraq, spans between 40°C and 44°C. This represents a fairly high value compared to that adopted by the other two aforementioned studies. In this context, placing EPS after PCM on the exterior side proves advantageous in averting overheating during discharge periods. Consequently, it is advisable to conduct a comprehensive study on optimizing the phase change temperature before determining the optimal location of PCM conjoined with insulation. Additionally, the impact of this placement should be evaluated during all heating and cooling periods throughout the year.

b. PCM thickness

The decrease in heating and cooling energy demand is heavily dependent on the PCM thickness. As more volume of PCM is utilized, the energy storage capacity increases. However, it reaches a saturation point once the PCM has absorbed its maximum capacity [90]. Moreover, a greater volume necessitates a longer period for the PCM to fully activate its latent potential [46].

The thickness of a PCM panel can be calculated using the formula proposed by Peippo [87]:

$$D_{opt} = \frac{t_n\ h}{\rho\ \Delta H}\ (T_{m,opt} - T_n) \qquad (2)$$

Where D_{opt} represents the optimal thickness of the PCM slab (m), ΔH denotes the latent heat of fusion of the PCM ($J.kg\text{-}1$), and ρ signifies the density of the PCM ($kg.m\text{-}3$).

Several other factors influence the selection of PCM thickness. Notably, the thicker the PCM layer, the more costly its integration into building walls becomes affecting its economic viability, as already mentioned in Section 4.

In summary, the optimal phase change material (PCM) should possess a melting temperature aligned with the average set-point temperatures for both heating and cooling within the building envelope. For optimal thermal regulation, it should be positioned near the heat source, minimizing the surface temperatures of both external and internal walls during summer and winter, respectively. In the case of an insulated structure, placing the PCM on the interior side, after the insulation layer, is most effective during the summer. Nevertheless, a thorough evaluation across all seasonal heating and cooling periods is required to determine its most effective position throughout the year.

The State of The Art of Articles Published in Morocco

Phase Change Materials (PCMs) have garnered substantial attention from researchers globally over recent decades, spanning various continents. Their integration into construction materials and building structures is viewed as a viable strategy to enhance building thermal inertia. PCMs are instrumental in improving energy efficiency, managing energy demand, improving occupant thermal comfort, and reducing greenhouse gas emissions, which are major contributors to climate change.

According to the Global Climate Risk Index (CRI 2021) compiled by the non-governmental organization Germanwatch, developing nations face heightened vulnerability to climate change impacts due to their limited adaptation capacities, despite being more exposed to hazards. Notably, Mozambique and Zimbabwe were the two African countries most affected in 2019, with CRI scores of 2.67 and 6.17, respectively [105].

However, few studies are focusing on PCM technologies to reduce energy consumption and shift away from fossil fuels. In contrast, Europe and Asia are at the forefront of research on thermal energy storage technologies that offer greater resilience against climate change impacts.

Based on a sample of 6000 articles published between 1984 and 2023, Asia surpasses other continents according to the number of scientific research articles written about phase change materials, with a percentage of 68.6%, with China leading the pack. In contrast, Africa contributes only 5.35% of articles distributed among Egypt, Morocco, Ethiopia, Ghana, Nigeria, South Africa, Tunisia, Algeria, and Sudan. These findings are visually represented in figure 9.

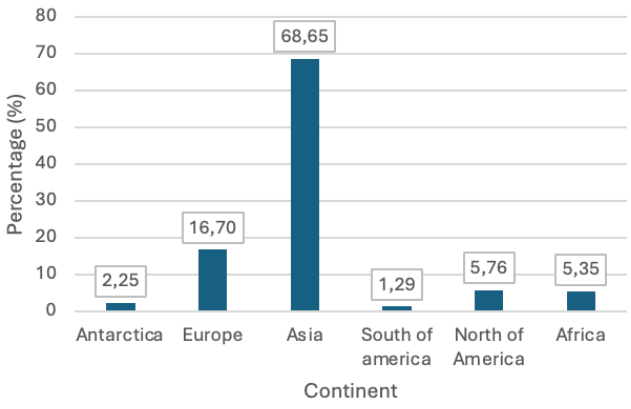

Figure 9. Percentage of PCM articles published by continent.

Table 2. Surveys on the integration of PCMs into building envelopes under Moroccan climatic conditions

Localization	Study objective	Climate region	Study type	PCM used	Main Results	Ref
Bricks	Studying the thermal effects of incorporating PCMs into the solid components of HCB (Hollow Clay Brick microencapsulation)	Hot regions with drastic climates (Ouarzazate, Marrakech, Erfoud, etc.)	Numerical simulation using ANSYS Fluent software	n - Nonadecane	The phase shift induced by HCB-3, HCB-6, HCB-8, and HCB-12 is approximately 1 hour, 1 hour 43 minutes, 2 hours 27 minutes, and 4 hours, respectively. The volume of HCB has decreased by as much as 30%, and material savings have been estimated at 35%.	[108]
	Studying the energy performance of a wall integrating PCM through the examination of its placement within a double wall constructed of hollow bricks	The city of Er-Rachidia (Morocco)	Numerical simulation using COMSOL software	PCM-Paraffin RT26	Placing the phase change material close to the internal surface can conserve up to 97% of the energy needed to maintain internal thermal comfort at a set temperature of 26°C.	[109]
	Evaluate the energy performance of three types of buildings: single-family homes, collective housing, and hotel housing, constructed with hollow bricks, incorporating and excluding PCMs to mitigate cooling requirements.	Al Hoceima (Morocco), Malaga (Spain),Marseille (France), Taher (Algeria), Naples (Italy), Tripoli (Libya), Ankara(Turkey), and Port Said (Egypt).	Numerical simulation using COMSOL software	RT-Line (from Rubitherm) and capric acid	In Northeast Mediterranean cities , energy savings can achieve 56% through the application of a PCM with a melting temperature of 26°C, while no energy savings were observed for Southeast cities.	[110]
	Studying the impact of integrating PCMs into a hollow brick structure (12 cells) on the thermal efficiency of exterior walls	Er-Rachidia,Fes, Marrakech (Morocco)	Numerical simulation using ANSYS Fluent software	n – Nonadecane	The incorporation of PCM into the hollow brick improves both the storage capacity and insulating efficiency of this construction element. This is evidenced by a notable decrease in amplitude and a substantial phase shift of the thermal wave through the PCM-wall.	[111]
Ceiling	Studying the energy and thermal advantages of implementing PCM in a controlled cooling ceiling system within a ventilated room	Fez (Csa climate), Ifrane (Csb climate), and Marrakech (BSh climate)	CFD simulation	Paraffin C13	The application of paraffin C13 as PCM in cooling ceilings yielded notable energy savings in Fez (17.07%) and Ifrane (16.30%) respectively), while the effect was minimal in Marrakech (2.23%).	[112]
Trombe wall	Evaluate the 3E performance (energy, economic, and environmental) of thermal, electrical, and hydrogen storage systems. This evaluation aims to guide stakeholders in identifying the most appropriate storage systems for achieving NZEB.	Ouarzazate, Tangier, and Ifrane	Numerical simulation using Energy-plus software	BioPCM	The studied PCM strategy allows for total annual thermal energy savings of 45.45%, 64.29%, and 43.06% in hot desert, Mediterranean, and cold climates, respectively. With Trombe wall integration, additional savings reached 9.56%, 4.18%, and 18.09%. While all analyzed storage systems exhibit environmental advantages, the trombe wall approach presents a comparatively higher CPBP and a lower LCEB, especially in the Mediterranean climate of Tangier.	[113]
Walls	Providing guidelines for designing office buildings integrated with PCM in the Mediterranean region	Tangier	Numerical simulation using Energy-plus software	BioPCM	Selecting an appropriate PCM fusion temperature improves thermal performance by 9.87% in free-running buildings and 20.5% in air-conditioned buildings over a 30-year lifespan. A fusion temperature of 28°C is identified as the optimal option for enhancing summer thermal performance in free-running office buildings throughout their lifespan.	[114]

Table 2. Surveys on the integration of PCMs into building envelopes under Moroccan climatic conditions (continued)

Localization	Study objectives	Climate region	Study type	PCM used	Main Results	Ref
Walls	Analyzing the influence of building volume, window orientation, and air infiltration on PCM performance.	All 12 regions of Morocco	Numerical simulation using Energy-plus software	Commercial panels Rubitherm RT28HC	The lightweight square building, featuring a south-facing window and no air infiltration, resulted in a total temperature fluctuation reduction of 1303.3 °C for the 10 m building located in a semi-arid climate. Furthermore, the PCM-enhanced building with a south-facing window and an air infiltration rate of 0.5 air changes per hour achieved significant energy savings of 69.56%.	[115]
	A multiparametric analysis is conducted to assess the impact of placing PCM on the inner side of exterior walls on energy savings and indoor thermal comfort.	Benguerir	Numerical simulation using Energy-plus software	Commercial panel CSM from Rubitherm	HW construction achieved maximum energy savings of 13.1% for PCM 28. The square-shaped building demonstrates effective performance across aspects, including energy savings, temperature regulation, and energy consumption. The optimal solution includes PCM 28 with LW construction for summer and PCM 22 with HW construction for winter. The recommended building configuration achieved a maximum PCM activation of 26.63%.	[116]
	A numerical investigation is conducted on building walls integrating PCM under semi-arid climate conditions to define the main parameters for their efficient utilization.	The city of Benguerir with a hot semi-arid climate	Numerical simulation using Energy-plus software	RT-18 HC RT-21 HC RT-25 HC RT-28 HC RT-35 HC (34–36°C).	The RT-28 HC PCM is appropriate for a semi-arid climate. Exterior placement provides heating energy savings of 101 kWh, while interior placement yields the highest cooling energy savings, reaching up to 317 kWh, and demonstrates improved performance in terms of annual energy savings. The south-facing PCM wall is more energy-efficient than other orientations. The optimal configuration was RT21–RT25–RT28 HC, achieving an annual energy savings rate of 15.21% and the shortest payback period of 12.94 years. Moreover, a triple layer of PCM combined with mechanical ventilation in summer maintains a comfortable indoor temperature, although indoor temperature fluctuations are more pronounced when mechanical ventilation is applied.	[117]
	Eight building configurations are assessed regarding indoor air temperature fluctuation reduction, PCM energy savings, PCM activation, and payback period	Benguerir	Numerical simulation using Energy-plus software	Compact Storage Module (CSM) containing paraffin wax, type RT 28HC	Placing PCM on walls, roofs, and ceilings results in the highest annual energy savings. However, placing PCM on the wall envelope alone exhibits the shortest simple payback period, at just 22.38 years. Implementing PCM on all interior envelope surfaces results in a maximum reduction in indoor temperature fluctuations of 110.2 °C during August.	[118]
	Emphasize the advantages of incorporating PCM into clay walls rather than cement wall	Errachidia	Numerical simulation using COMSOL software	Paraffin 5913 Capric acid n-Eicosane	Straw–clay construction incorporating PCM24 and PCM32 reduces the indoor thermal flux density by 72.72% in winter and 73.68% in summer, respectively, compared to cement construction.	[119]
	Develop adaptive exterior walls containing thermochromic (TC) material and phase change materials (PCM) to adopt dynamic responses to external climatic conditions	Marrakech, Dubai, Nice, London, Tianjin, Mexico, and Ottawa	A numerical code is developed.	RT18 and a hydrated salt	Combining PCM1 (T_m = 26 °C) with W-doped VO_2 in a structure during summer does not yield as many benefits as using PCM alone. The configuration with two PCMs delivers the best thermal comfort compared to the reference wall and other setups throughout both summer and winter.	[120]

Morocco is ranked among the top ten performing countries in terms of climate according to the Climate Change Performance Index (CCPI) 2023 report by Germanwatch, the International Climate Action Network, and the Climate Institute [106]. The country is actively involved in climate policy, especially through a national strategy that focuses on developing renewable energy sources such as wind farms, photovoltaic solar, hydropower, and biomass. This strategy aims to get 20% of its energy from renewable sources by 2025, reducing Morocco's reliance on fossil fuels. The CCPI report [106] highlights that Morocco has high scores for greenhouse gas emissions and energy use, mostly because it uses fossil fuels, which account for over 75% of anthropogenic emissions. Petroleum covers 35% of energy needs, coal 23%, natural gas 21%, nuclear 4%, and hydropower 4%. In many African countries, biomass is still a major source of energy, contributing 12% to overall energy production. However, new renewable energies like solar and wind currently comprise less than 1% of total energy consumption [107].

The objectives outlined during the United Nations Framework Convention on Climate Change (COP28) held in Dubai in 2023 centre on peaking the world's greenhouse gas emissions by 2025 and reducing them by 43% by 2030 and 60% by 2035 compared with 2019 levels. The goal is to limit global warming to 1.5 °C. To accomplish these goals requires transitioning away from fossil fuels, adopting renewable energy, and improving energy efficiency by 2030 (COP 28, 2023).

To meet these goals, Morocco could greatly improve its climate performance and lower its overall energy use by exploring innovative approaches such as phase change materials (PCMs). The building industry in Morocco uses 33% of the country›s energy because it consumes a lot of energy and releases a lot of greenhouse gases. This includes 7% in commercial buildings and 26% in residential buildings (AMEE, 2024). This consumption is expected to increase due to population growth, the development of new cities, and greater reliance on air conditioning and heating systems in Morocco.

Although in recent years more comprehensive studies have been carried out on PCM-based latent heat storage systems, the optimization of thermal performance and comfort using PCM-integrated building envelopes, based on their parameters across diverse Moroccan climates, has not been extensively explored in the literature.

A summary of studies conducted in Morocco from 2020 to 2023 regarding the impact of integrating phase change materials into building envelopes on reducing energy consumption is provided in Table 2. Most prior research has considered only the cooling or heating season. However, decisions regarding PCM integration into the building envelope should account for its annual impact rather than a single season.

Moreover, the selection of PCM materials for integration within building infrastructures necessitates thorough consideration of their impact on structural mechanical integrity in conjunction with their hygrothermal characteristics. The mechanical comportment of PCMs refers to their behavior and response to external mechanical forces, constraints, and deformations. While the mechanical aspects may not constitute the primary focus of PCM development, they merit meticulous consideration when integrating PCMs into construction applications.

During the integration of PCMs, moisture constraint specifications must be considered, and necessary measures must be adopted in order to avoid moisture-induced problems. For instance, if any PCM is used for a building with thermal energy storage, it is essential that the PCM be encapsulated and protected against the penetration of humidity. Moisture ingress can potentially degrade PCM performance or cause unintended phase changes, subsequently leading to inefficiencies or structural damage. Hence, it is essential to evaluate the suitability of the PCMs with other materials to ensure long-term durability and effectiveness. Therefore, the choice of PCM must be undertaken with careful deliberation, and its lifespan should be rigorously analyzed before determining its economic viability and potential for reducing energy costs.

CONCLUSION

The integration of phase change materials (PCMs) within building structures serves as a viable approach to reducing energy consumption and managing thermal comfort in indoor environments. This article provides an overview of the different types of PCMs, integration methods in the construction sector, their limitations, proposed solutions to improve their thermo-physical properties, and a structured approach for selecting optimal materials based on literature results. Antecedent studies have shown that the effect of integrating phase change materials into the building envelope on energy savings depends on several factors including architectural design, climatic conditions, type, as well as the nature and volume of PCM deployed. Hence, there is a need to make the right PCM choice to take advantage of their benefits in terms of reducing energy consumption. Based on the aforementioned literature, the following conclusions can be inferred:

- ✓ Building envelope integration of phase change materials (PCMs) also presents the potential to decrease yearly energy consumption to a large extent. The saving potential of such energy varies between 10% and 97% based on several factors such as the climatic area, the thermophysical properties of the PCM, and compositions of the material in the building envelope among others.
- ✓ The melting temperature, latent heat, cost, and stability are critical factors that will influence the market adoption of phase change materials (PCMs).
- ✓ Bio-origin phase change materials (BPCMs) offer an alternative to commercially available paraffin-based PCMs. They possess similar thermal properties,

including latent heat capacity, phase change behavior, and thermal cycling durability, which make them suitable for equivalent thermal energy storage applications.

- ✓ Reducing capsule size enhances the thermal reliability and chemical stability of PCM. Therefore, nano-capsules exhibit superior structural stability compared to macro and microcapsules.
- ✓ TRNSYS and Energy-Plus are widely regarded as the most suitable and extensively utilized simulation tools for evaluating heating and cooling energy consumption in buildings that incorporate phase-change materials.
- ✓ The thicker the PCM layer, the more costly its integration into building walls becomes affecting its economic viability. Furthermore, a greater volume of phase change material necessitates a longer time to completely activate its latent heat potential.
- ✓ the optimal phase change material (PCM) should possess a melting temperature aligned with the average setpoint temperatures for both heating and cooling across the building envelope.
- ✓ For optimal thermal regulation, the phase change material (PCM) should be positioned near the heat source.
- ✓ In the case of an insulated structure, positioning the PCM on the inner side, after the insulation layer, is most effective during the summer. A year-round analysis throughout the year for all heating and cooling seasons is required in order to determine the optimum position throughout the year.

RECOMMENDATIONS

Further studies must be carried out in order to enhance the thermal performance of phase change materials (PCMs) integrated in building envelopes. The following recommendations are proposed for future studies:

- Future investigations should further study the performance of PCMs through experiments on real buildings and propose solutions for renovating existing buildings to enhance their energy efficiency.
- It is necessary to incorporate PCMs in buildings considering passive and bioclimatic solutions and analyzing their impacts in order to achieve appropriate findings in terms of energy savings, indoor thermal comfort, and financial feasibility. For example, evaluating the use of a Canadian well combined with PCMs for reducing energy consumption in cooling-dominated climates.
- The application of evolutionary algorithms for optimizing the thermo-physical properties of PCMs, notably the metaheuristic algorithm, or using an artificial neural network to predict the important parameters (melting temperature, thickness, …) of an optimal PCM.
- It is recommended to analyze the effect of integrating PCM with latent heat energy storage in cascade within the outer envelope of buildings.

It is essential to consider the variation in outdoor temperature caused by climate change for optimizing PCM properties. Therefore, it is important to study their effect on reducing energy consumption, improving thermal comfort, and reducing greenhouse gas emissions under prospective climatic scenarios.

It is important to assess the entire life cycle of PCMs to evaluate their durability and environmental performance.

NOMENCLATURE

ACH	Air changes per hour
ADBEIPCM	Adaptative dynamic building envelope integrated with PCM
BES	Building energy simulation
BPCM	Bio-based phase change material
BPS	Building performance simulation
CCPI	Climate Change Performance Index
CFD	Computational fluid dynamics
COP	Conference of parties
CPBP	Carbon payback period
CRI	Global climate risk index
EJ	Exajoule
EPS	Expanded polystyrene
FT-IR	Fourier transform infrared spectroscopy
GHG	Greenhouse gas
Gt	Gigaton
HCB	Hallow clay brick
HW	Heavy weight
IEA	International energy agency
LCEB	Life cycle carbon emissions benefits
LVPCM	Liquid-Vapor PCM
LW	Light weight
MPCM	Microencapsulated PCM
MWI	Mineral wool insulation
NRC	National cash register corporation
NZE	Net zero emissions
PCM	Phase change material
RP	Research Project
RT	Rubitherm
SLPCM	Solid-Liquid PCM
TES	Thermal energy storage
TGA	Thermos gravimetric analyzer
VO2	Vanadium dioxide
W	Tungsten

AUTHORSHIP CONTRIBUTIONS

Authors equally contributed to this work.

DATA AVAILABILITY STATEMENT

The authors confirm that the data that supports the findings of this study are available within the article. Raw data that support the finding of this study are available from the corresponding author, upon reasonable request.

CONFLICT OF INTEREST

The author declared no potential conflicts of interest with respect to the research, authorship, and/or publication of this article.

ETHICS

There are no ethical issues with the publication of this manuscript.

STATEMENT ON THE USE OF ARTIFICIAL INTELLIGENCE

Artificial intelligence was not used in the preparation of the article.

REFERENCES

[1] International Energy Agency. World Energy Outlook 2022.Available at: https://www.iea.org/reports/world-energy-outlook-2022#overview. Accessed on Dec 23, 2025.

[2] Duraković B. Green Energy and Technology PCM-Based Building Envelope Systems Innovative Energy Solutions for Passive Design. Switzerland: Springer ; 2020. [Crossref]

[3] Lu S, Zheng J, Wang R, Zhu J. Thermal performance research on a novel coupled heating system combined solar air heater with ventilation PCM wall. Solar Energy 2023;265:112100. [Crossref]

[4] Ashouri M, Hakkaki-Fard A. Improving the performance of the finned absorber inclined rooftop solar chimney combined with composite PCM and PV module. Solar Energy 2021;228:562-574 . [Crossref]

[5] Pawar VR, Sobhansarbandi S. Heat transfer enhancement of a PCM-porous metal based heat pipe evacuated tube solar collector: An experimental study. Solar Energy 2023; 251:106–118. [Crossref]

[6] Huang S, Li W, Lu J, Li Y, Wang Z, Zhu S. Experimental study on thermal performances of a solar chimney with and without PCM under different system inclination angles . Energy 2023;290:130154. [Crossref]

[7] Gürbüz H, Demirtürk S, Akçay H, Topalcı Ü. Thermal stabilization and energy harvesting in a solar PV/T-PCM-TEG hybrid system: A case study on the design of system components . Energy Convers Manag 2023;294:117536. [Crossref]

[8] Geng J, Wu J, Yang J, Fu M, Weng W. Numerical simulation of cooling effect of human-PCM-clothing model in hot environments. Int J Therm Sci 2023;192:108393. [Crossref]

[9] Soliman AS, Xu L, Dong J, Cheng P. A novel heat sink for cooling photovoltaic systems using convex/concave dimples and multiple PCMs . Appl Therm Eng 2022;215:119001. [Crossref]

[10] Hu Z, Li K, Wang Z, He W, Zhu M, Liu X. Numerical study on using multichannel tube and PCM for improving thermal and electrical performance of a photovoltaic module. Solar Energy 2023;265:112058. [Crossref]

[11] Azimi N, Davoodbeygi Y, Rahimi M, Ahmadi S, Karami E, Roshani M. Optimization of thermal and electrical efficiencies of a photovoltaic module using combined PCMs with a thermo-conductive filler. Solar Energy 2022;231:283–296. [Crossref]

[12] Amalu EH, Fabunmi OA. Thermal control of crystalline silicon photovoltaic (c-Si PV) module using docosane phase change material (PCM) for improved performance. Solar Energy 2022;234:203–221. [Crossref]

[13] Chibani A, Merouani S, Laidoudi H, Dehane A, Bendada L, Lamiri L, Mecheri G, Bougriou C, Gherraf N. Numerical simulation and analysis of heat transfer and melting rate of nano-enhanced PCM composite embedded in a concentrator photovoltaic system. J Energy Storage 2023;73:109247. [Crossref]

[14] Kibria MG, Mohtasim MS, Paul UK, Das BK, Saidur R. Impact of hybrid nano PCM (paraffin wax with Al2O3 and ZnO nanoparticles) on photovoltaic thermal system: Energy, exergy, exergoeconomic and enviroeconomic analysis. J Clean Prod 2024;436:140577. [Crossref]

[15] Khan MM, Alkhedher M, Ramadan M, Ghazal M. Hybrid PCM-based thermal management for lithium-ion batteries: Trends and challenges. Journal of Energy Storage 2023;73:108775. [Crossref]

[16] Luo W, Zhao L, Chen M. The effect of PCM on mitigating thermal runaway propagation in lithium-ion battery modules. Appl Therm Eng 2024;236:121608. [Crossref]

[17] Liu Y, Zheng R, Li J. High latent heat phase change materials (PCMs) with low melting temperature for thermal management and storage of electronic devices and power batteries: Critical review. Renew Sustain Energy Rev 2022;168:112783. [Crossref]

[18] Khadem Z, Salari A, Naghdbishi A, Shakibi H, Sardarabadi M. Parametric analysis of a PCM-based heat sink for electronic device thermal management. J Energy Storage 2023;74:109118. [Crossref]

[19] Pavithran A, Sharma M, Shukla AK. An investigation on the effect of PCM incorporation in refrigerator through CFD simulation. Mater Today 2020;46:5555–5564. [Crossref]

[20] Soliman AS, Fouda MS, Cheng P. Power saving in a central air conditioning system by using multiple PCMs integrated with fresh air path. Energy Build 2023;300;113691. [Crossref]

[21] Sharma RK, Kumar A, Rakshit D. A phase change material (PCM) based novel retrofitting approach in the air conditioning system to reduce building energy demand. Appl Therm Eng 2024;238:121872. [Crossref]

[22] Liang Y, Yang H, Wang H, Bao X, Cui H. Enhancing energy efficiency of air conditioning system through optimization of PCM-based cold energy storage tank: A data center case study. Energy 2024;286:129641. [Crossref]
[23] Zheng X, Tang Z, Wang Y, Liu H. Performance of the air source heat pump assisted solar heating system combined with PCM floor. Appl Therm Eng 2023; 239:122115. [Crossref]
[24] Faraj K, Khaled M, Faraj J, Hachem F, Chahine K, Castelain C. Energetic and economic analyses of integrating enhanced macro-encapsulated PCM's with active underfloor hydronic heating system. Energy Reports 2022;8:848–862. [Crossref]
[25] Nizovtsev MI, Sterlyagov AN. Effect of phase change material (PCM) on thermal inertia of walls in lightweight buildings. J Build Eng 2024;82:107912. [Crossref]
[26] Liu X, Yang Y, Sheng Z, Wu W, Wang Y, Dumoulin J. Study on thermal storage effectiveness of a novel PCM concrete applied in buildings located at four cities. Renew Energy 2023;218:119262. [Crossref]
[27] Wu D, Rahim M, El Ganaoui M, Bennacer R, Djedjig R, Liu B. Dynamic hygrothermal behavior and energy performance analysis of a novel multilayer building envelope based on PCM and hemp concrete. Constr Build Mater 2022;341:127739. [Crossref]
[28] Meng E, Yang J, Zhou B, Wang C, Li J. Preparation and thermal performance of phase change material (PCM) foamed cement used for the roof. J Build Eng 2022;53:104579. [Crossref]
[29] Wu D, Rahim M, Li W, El Ganaoui M, Bennacer R, Hu K, Sun H, Sun Z, Zou T, Zhang Y. Hygrothermal and energy performance assessment of a passive building wall integrating PCM and bio-based hygroscopic material. Build Environ 2023;245:110908. [Crossref]
[30] Chandrakumar D, Shivappa D, Ramya J, Mishra P, Koneru S, Salman H, Chakaravarthi MA. Phase change material on the integration of PCM in the building envelope. Mater Today 2023. [Crossref]
[31] Frahat NB, Amin M, Heniegal AM, Ibrahim OMO. Optimizing microencapsulated PCM ratios of sustainable cement mortar for energy savings in buildings. Constr Build Mater 2023;391:131844. [Crossref]
[32] Shamshiri M, Jafari R, Momen G. An intelligent icephobic coating based on encapsulated phase change materials (PCM). Colloids Surf A Physicochem Eng Asp 2022;655:130157. [Crossref]
[33] Kułakowski T, Węglarz A, Heim D. An optimisation study of PCM triple glazing for temperate climatic conditions – Dynamic analysis of thermal performance. Energy 2023;283:128361. [Crossref]
[34] Prabhakar M, Saffari M, Gracia A, Cabeza LF. Improving the energy efficiency of passive PCM system using controlled natural ventilation. Energy Build 2020;228:110483. [Crossref]
[35] Xamán J, Rodriguez-Ake A, Zavala-Guillén I, Hernández-Pérez I, Arce J, Sauceda D. Thermal performance analysis of a roof with a PCM-layer under Mexican weather conditions. Renew Energy 2020;149:773–785. [Crossref]
[36] King MFL, Rao P, Sivakumar A, Mamidi V, Richard S, Vijayakumar M, Arunprasath K, Kumar P. Thermal performance of a double-glazed window integrated with a phase change material (PCM). Mater Today 2021;50:1516–1521. [Crossref]
[37] Li D, Wu Y, Zhang G, Arıcı M, Liu C, Wang F. Influence of glazed roof containing phase change material on indoor thermal environment and energy consumption. Appl Energy 2018;222:343–350. [Crossref]
[38] Mabrouki A, Karim YB, Hassani HO, Jamali Y, Khaldoun A. A study of a passive heating design employing a Trombe wall with PCM: A numerical investigation of the semi-oceanic climate in Morocco. Mater Today 2023;72:3626–3631. [Crossref]
[39] Saikia P, Rakshit D. Passive building cooling achieved with a new class of thermal retrofit: The liquid vapour phase change material. Energy Build 2021;249:111238. [Crossref]
[40] Abhat A. Low temperature latent heat thermal energy storage: Heat storage materials. Solar Energy 1983 ;10:313-332. [Crossref]
[41] Madjoudj N, Imessad K. Phase-change material for bioclimatic applications. J Renew Energy 2016;19:647-662. [Crossref]
[42] Hawes DW, Feldman D, Banu D. Latent heat storage in building materials Objectives of research in thermal storage building materials. Energy and Buildings 1993;20:77-86. [Crossref]
[43] Pasupathy A, Velraj R, Seeniraj RW. Phase change material-based building architecture for thermal management in residential and commercial establishments. Renew Sustain Energy Rev 2008;12:39–64. [Crossref]
[44] Idi MM. Thermal energy storage by solid/liquid phase change in porous environments. Paris-Est university, 2021.
[45] Imghoure O, Belouaggadia N, Ezzine M, Lbibb R, Younsi Z. Performance evaluation of phase change materials for thermal comfort in a hot climate region. Appl Therm Eng 2021;186:116509. [Crossref]
[46] Liu L, Hammami N, Trovalet L, Bigot D, Habas JP, Malet-Damour B. Description of phase change materials (PCMs) used in buildings under various climates: A review. J Energy Storage 2022;56:105760. [Crossref]
[47] Chihab Y, Bouferra R, Garoum M, Essaleh M, Laaroussi N. Thermal inertia and energy efficiency enhancements of hollow clay bricks integrated with phase change materials. J Build Eng 2022;53:104569. [Crossref]

[48] Rashid FL, Al-Obaidi M, Dhaidan N, Ali AHB, Hamida MB, Younis O. Bio-based phase change materials for thermal energy storage and release: A review. J Energy Storage 2023;73:109219. [Crossref]
[49] Fabiani C, Pisello AL, Barbanera M, Cabeza LF. Palm oil-based bio-PCM for energy efficient building applications: Multipurpose thermal investigation and life cycle assessment. J Energy Storage 2020;28:101129. [Crossref]
[50] Boussaba L, Foufa A, Makhlouf S, Lefebvre G, Royon L. Elaboration and properties of a composite bio-based PCM for an application in building envelopes. Constr Build Mater 2018;185:156–165. [Crossref]
[51] Choi JY, Yun BY, Kim YU, Kang Y, Lee SC, Kim S. Evaluation of thermal/acoustic performance to confirm the possibility of coffee waste in building materials in using bio-based microencapsulated PCM. Environmental Pollution 2022;294:118616, [Crossref]
[52] Ong PJ, Leow Y, Soo XYD, Chua MH, Ni X, Suwardi A, Tan CKI, Zheng R, Wei F, Xu J, Loh XJ, Kai D, Zhu Q. Valorization of Spent coffee Grounds: A sustainable resource for Bio-based phase change materials for thermal energy storage. Waste Management 2023;157:339–347. [Crossref]
[53] Yoo J, Chang SJ, Wi S, Kim S. Spent coffee grounds as supporting materials to produce bio- composite PCM with natural waxes. Chemosphere 2019;235:626–635. [Crossref]
[54] Putra N, Sandi AF, Ariantara B, Abdullah N, Mahlia TMI. Performance of beeswax phase change material (PCM) and heat pipe as passive battery cooling system for electric vehicles. Case Stud Therm Eng 202021:100655. [Crossref]
[55] Rathore PKS, Gupta KK, Patel B, Sharma RK, Gupta NK. Beeswax as a potential replacement of paraffin wax as shape stabilized solar thermal energy storage material: An experimental study. J Energy Storage 2023;68:107714. [Crossref]
[56] Barrio EP, Godinb A, Duquesnec M, Daranlotd J, Jollyd J, Alshaere W, Kouadiob T, Sommierb A. Characterization of different sugar alcohols as phase change materials for thermal energy storage applications. Sol Energy Mater Sol Cells 2017;159:560–569.
[57] Fan C, Yuan G, Wang Y, Zhang Y, Wang Z. Thermal storage performance of eutectic sugar alcohols applied to buildings and enhancement of crystallization. Solar Energy 2022;234:231–239. [Crossref]
[58] Liu C, Cheng Q, Li B, Liu X, Rao Z. Recent advances of sugar alcohols phase change materials for thermal energy storage. Renew Sustain Energy Rev 2023;188:113805. [Crossref]
[59] Shao XF, Yang S, Shi HY, Fan LW, Yuan YP. A comprehensive evaluation on the cycling stability of sugar alcohols for medium-temperature latent heat storage. J Energy Storage 2023;64:107190. [Crossref]
[60] Shao X, Yang S, Fan L, Yuan Y. Sugar alcohol phase change materials for low-to-medium temperature thermal energy storage: A comprehensive review. J Energy Storage 2023;68:107848. [Crossref]
[61] He H, Zhao P, Yue Q, Gao B, Yue D, Li Q. A novel polynary fatty acid/sludge ceramsite composite phase change materials and its applications in building energy conservation. Renew Energy 2015;76:45–52. [Crossref]
[62] Bragaglia M, Lamastra FR, Berrocal JA, Paleari L, Nanni F. Sustainable phase change materials (PCMs): waste fat from cooking pork meat confined in polypropylene fibrous mat from waste surgical mask and porous bio-silica. Mater Today Sustain 2023;23:100454. [Crossref]
[63] Memon SA. Phase change materials integrated in building walls: A state of the art review. Renew Sustain Energy Rev 2014;31:870–906. [Crossref]
[64] Hawlader MNA, Uddin MS, Khin M. Microencapsulated PCM thermal-energy storage system. Applied Energy 2003;74:195-202. [Crossref]
[65] Salunkhe PB, Shembekar PS. A review on effect of phase change material encapsulation on the thermal performance of a system. Renew Sustain Energy Rev 2012;16:5603– 5616. [Crossref]
[66] Rathore PKS, Shukla SK. Potential of macroencapsulated pcm for thermal energy storage in buildings: A comprehensive review. Constr Build Mater 2019;225:723– 744. [Crossref]
[67] Al-Yasiri Q, Szabó M. Experimental evaluation of the optimal position of a macroencapsulated phase change material incorporated composite roof under hot climate conditions. Sustain Energy Technol Assess 2021;45:101121. [Crossref]
[68] PCM Product Company. Our standard range of encapsulated PCM products. Available at: https://www.pcmproducts.net/Encapsulated_PCMs.htm. Accessed on Dec 23, 2025.
[69] Betancourt-Jimenez D, Montoya M, Haddock J, Youngblood JP, Martinez CJ. Regulating asphalt pavement temperature using microencapsulated phase change materials (PCMs). Constr Build Mater 2022;350:128924. [Crossref]
[70] Gu Y, Li Y, Ju G, Zheng T, Liang R, Sun G. PCM microcapsules applicable foam to improve the properties of thermal insulation and energy storage for cement-based material. Constr Build Mater 2023;409:134144. [Crossref]
[71] Jin X, Haider MZ, Ahn J, Fang G, Hu JW. Development of nanomodified eco-friendly thermal energy storing cementitious composite using PCM microencapsulated in biosourced encapsulation shell. Case Stud Constr Mater 2023;19. [Crossref]
[72] Fang Y, Kuang S, Gao X, Zhang Z. Preparation and characterization of novel nanoencapsulated phase change materials. Energy Convers Manag 2008;49:3704–3707. [Crossref]

[73] Rathore PKS, Shukla SK. Enhanced thermophysical properties of organic PCM through shape stabilization for thermal energy storage in buildings: A state of the art review. Energy and Buildings 2021; 236:110799. [Crossref]
[74] Shanmugavalli P, Rajaraman R. Thermal performance enhancement methods of phase change materials for thermal energy storage systems – A review. Mater Today Proc 2023. [Crossref]
[75] Alehosseini E, Jafari SM. Nanoencapsulation of phase change materials (PCMs) and their applications in various fields for energy storage and management. Adv Colloid Interface Sci 2020;283:102226. [Crossref]
[76] He M, Yang L, Lin W, Chen J, Mao X, Ma Z. Preparation, thermal characterization and examination of phase change materials (PCMs) enhanced by carbon-based nanoparticles for solar thermal energy storage. J Energy Storage 2019;25:100874. [Crossref]
[77] Al-Jethelah M, Ebadi S, Venkateshwar K, Tasnim SH, Mahmud S, Dutta A. Charging nanoparticle enhanced bio-based PCM in open cell metallic foams: An experimental investigation. Appl Therm Eng 2019;148:1029–1042. [Crossref]
[78] Ma Z, Lin W, Sohel MI. Nano-enhanced phase change materials for improved building performance. Renew Sustain Energy Rev 2016;58:1256-1268. [Crossref]
[79] Mebrouk-Oudina F, Chabani I. Review on nano enhanced PCMs: Insight on nePCM application in thermal management/storage systems. Energies 2023;16(3). [Crossref]
[80] Ghalambaz M, Doostani A, Chamkha AJ, Ismael MA. Melting of nanoparticles-enhanced phase-change materials in an enclosure: Effect of hybrid nanoparticles. Int J Mech Sci 2017;134:85-97. [Crossref]
[81] Kant K, Biwole PH, Shamseddine I, Tlaiji G, Pennec F, Fardoun F. Recent advances in thermophysical properties enhancement of phase change materials for thermal energy storage. Sol Energy Mater Sol Cells 2021;231:111309. [Crossref]
[82] Mazzeo D, Matera N, Cornaro C, Oliveti G, Romagnoni P, Santoli L. EnergyPlus, IDA ICE and TRNSYS predictive simulation accuracy for building thermal behaviour evaluation by using an experimental campaign in solar test boxes with and without a PCM module. Energy Build 2020;212:109812. [Crossref]
[83] Pandey B, Banerjee R, Sharma A. Coupled EnergyPlus and CFD analysis of PCM for thermal management of buildings. Energy Build 2021;231:110598. [Crossref]
[84] Terhan M, Ilgar G. Investigation of used PCM-integrated into building exterior walls for energy savings and optimization of PCM melting temperatures. Constr Build Mater 2023;369:130601. [Crossref]
[85] Imghoure O, Belouaggadia N, Ezzine M, Lbibb R, Younsi Z. Performance evaluation of phase change materials for thermal comfort in a hot climate region. Appl Therm Eng 2021;186:116509. [Crossref]
[86] Dardouri S, Mankai S, Almoneef MM, Mbarek M, Sghaier J. Energy performance based optimization of building envelope containing PCM combined with insulation considering various configurations. Energy Reports 2023;10:895–909. [Crossref]
[87] Peippo K, Kauranen P, Lund PD. A multicomponent PCM wall optimized for passive solar heating. Energy Build 1991;17:259-270. [Crossref]
[88] Abilkhassenova Z, Memon SA, Ahmad A, Saurbayeva A, Kim J. Utilizing the Fanger thermal comfort model to evaluate the thermal, energy, economic, and environmental performance of PCM- integrated buildings in various climate zones worldwide. Energy Build 2023;297 :113479. [Crossref]
[89] Prabhakar M, Saffari M, Gracia A, Cabeza LF. Improving the energy efficiency of passive PCM system using controlled natural ventilation. Energy Build 2020;228:110483. [Crossref]
[90] Khan M, Khan M, Irfan M, Ahmad N, Haq M, Khan I, Moussa M. Energy performance enhancement of residential buildings in Pakistan by integrating phase change materials in building envelopes. Energy Reports 2022;8:9290–9307. [Crossref]
[91] Mechouet A, Oualim EM, Mouhib T. Effect of mechanical ventilation on the improvement of the thermal performance of PCM-incorporated double external walls: A numerical investigation under different climatic conditions in Morocco. J Energy Storage 2021;38:102495. [Crossref]
[92] Ben Zaid Z, Tilioua A, Lamaamar I, Ansari O, Souli H, Alaoui MAH. An experimental study of the efficacy of integrating a phase change material into a clay-straw wall in the Drâa-Tafilalet Region (Errachidia Province), Morocco. J Build Eng 2020;32:101670. [Crossref]
[93] Hichem N, Noureddine S, Nadia S, Djamila D. Experimental and numerical study of a usual brick filled with PCM to improve the thermal inertia of buildings. Energy Procedia 2013;36:766–775. [Crossref]
[94] Bozzhigitov A, Memon SA, Adilkhanova I. Sensitivity of energy performance to the selection of PCM melting temperature for the building located in Cfb climate zone. Energy Reports 2022;8:6301–6320. [Crossref]
[95] Imafidon OJ, Ting DSK. Retrofitting buildings with Phase Change Materials (PCM) – The effects of PCM location and climatic condition. Build Environ 2023;236:110224. [Crossref]
[96] Saffari M, Gracia A, Fernández C, Cabeza LF. Simulation-based optimization of PCM melting temperature to improve the energy performance in buildings. Appl Energy 2017;202:420–434. [Crossref]

[97] El Rhafikia T, Kousksoub T, Allouhic A, Benomara W, Zennouhia H, Jamilc A, Zeraoulib Y. Numerical analysis of a micro-encapsulated PCM wallboard: Fluxmeter applications. J Build Eng 2017;14:127–133. [Crossref]
[98] Chihab Y, Bouferra R, Bouchehma A. Transient thermal behavior of clay walls integrated with phase change materials. J Energy Storage 2023;73:109246. [Crossref]
[99] Dear R, Brager G. Thermal comfort in naturally ventilated buildings: revisions to ASHRAE Standard 55. Energy Build 2002;34:549-561. [Crossref]
[100] Dear R, Xiong J, Kim J, Cao B. A review of adaptive thermal comfort research since 1998. Energy Build 2020;214:109893. [Crossref]
[101] Kishore RA, Bianchi MVA, Booten C, Vidal J, Jackson R. Optimizing PCM-integrated walls for potential energy savings in U.S. Buildings. Energy Build 2020;226:110355. [Crossref]
[102] Wang P, Liu Z, Zhang X, Hu M, Zhang L, Fan J. Adaptive dynamic building envelope integrated with phase change material to enhance the heat storage and release efficiency: A state-of-the-art review. Energy Build 2023;286:112928. [Crossref]
[103] Gounni A, El Alami M. The optimal allocation of the PCM within a composite wall for surface temperature and heat flux reduction: An experimental Approach. Appl Therm Eng 2017;127:1488–1494. [Crossref]
[104] Al-Yasiri Q, Szabó M. Building envelope-combined phase change material and thermal insulation for energy-effective buildings during harsh summer: Simulation-based analysis. Energy Sustain Dev 2023;72:326–339. [Crossref]
[105] GermanWatch.Global Climate Risk Index 2021. Available at: https://www.germanwatch.org/en/19777 . Accessed on Dec 23, 2025.
[106] NewClimate Institute. Climate Change Performance Index 2023. Available at: https://newclimate.org/resources/publications/climate-change-performance-index-2023. Accessed on Dec 23, 2025.
[107] HCP. Prospective Maroc 2030: Morocco›s energy outlook, issues and challenges. Available at: https://www.hcp.ma/downloads/Prospective-Maroc-2030_t22447.html. Accessed on Dec 23, 2025.
[108] Hamdaoui S, Bouchikhi A, Azouggagh M, Akour M, Msaad AA, Mahdaoui M. Building hollow clay bricks embedding phase change material: Thermal behavior analysis under hot climate. Solar Energy 2022;237:122–134. [Crossref]
[109] Hamidi Y, Malha M, Bah A. Analysis of the thermal behavior of hollow bricks walls filled with PCM: Effect of PCM location. Energy Reports 2021;7:105–115. [Crossref]
[110] Hamidi Y, Aketouane Z, Malha M, Bruneau D, Bah A, Goiffon R. Integrating PCM into hollow brick walls: Toward energy conservation in Mediterranean regions. Energy Build 2021;248:111214. [Crossref]
[111] Mahdaoui M, Hamdaoui S, Msaad AA, Kousksou T, Rhafiki T, Jamil A, Ahachad M. Building bricks with phase change material (PCM): Thermal performances. Constr Build Mater 2021;269:121315. [Crossref]
[112] Khattari Y, Arid A, Ouali A, Kousksou T, Janajreh I, Ghoulam EMB. CFD study on the validity of using PCM in a controlled cooling ceiling integrated in a ventilated room. Dev in the Built Environment 2021;9:100066. [Crossref]
[113] Elaouzy Y, Fadar A. Potential of thermal, electricity and hydrogen storage systems for achieving sustainable buildings. Energy Convers Manag 2023;294:117601. [Crossref]
[114] Kharbouch Y. Effectiveness of phase change material in improving the summer thermal performance of an office building under future climate conditions: An investigation study for the Moroccan Mediterranean climate zone. J Energy Storage 2022;54:105253. [Crossref]
[115] Laasri IA, Es-sakali N, Outzourhit A, Mghazli MO. Evaluation of phase change materials for a lightweight building in Morocco: Effect of building's volume, window orientation & infiltration. Energy Built Environ 2023. [Crossref]
[116] Laasri IA, Outzourhit A, Mghazli MO. Multiparameter analysis of different building forms in a semi-arid climate: Effect of building construction and phase change materials. Solar Energy 2023;250:220–240. [Crossref]
[117] Salihi M, Fiti M, Harmen Y, Chhiti Y, Chebak A, Alaoui FM, Achake M, Bentis F, Jamah C. Evaluation of global energy performance of building walls integrating PCM: Numerical study in semi-arid climate in Morocco. Case Stud Constr Mater 2022;16. [Crossref]
[118] Laasri IA, Es-sakali N, Outzourhit A, Mghazli MO. Investigation of the impact of phase change materials at different building envelope placements in a semi-arid climate. Mater Today Proc 2023.
[119] Zaid ZB, Tilioua A, Lamaamar I, Ansari O, Alaoui MAH. Thermal performance of clay-straw wall incorporating phase change materials in Errachidia city (South Eastern Morocco): A simulation approach. Case Stud Constr Mater 2021;15. [Crossref]
[120] Imghoure O, Belouaggadia N, Ezzine M, Lbibb R, Younsi Z. Evaluation of phase change material and thermochromic layers in a 'smart wall' in different climates for improving thermal comfort in a building. J Build Eng 2022;56:104755. [Crossref]

J Ther Eng, Vol. 12, No. 1, pp. 408−425, January, 2026

Journal of Thermal Engineering
Web page info: https://jten.yildiz.edu.tr
DOI: 10.14744/thermal.0001085

Review Article

Optimizing biomass fuel utilization for GHG emission reduction: An action plan for efficient fuel blending and sustainable practices

K RAVI[1,2,*], M. MATHESWARAN[3]

[1]*Department of CPP-JSW Steel Ltd., Salem Works, Tamilnadu, 636453, India*
[2]*Department of Energy and Environment Engineering, National Institute of Technology, Tiruchirappalli, Tamil Nadu, 620015, India*
[3]*Department of Chemical Engineering, National Institute of Technology, Tiruchirappalli, Tamil Nadu, 620015, India*

ARTICLE INFO

Article history
Received: 25 November 2024
Revised: 09 May 2025
Accepted: 12 May 2025

Keywords:
Biomass Fuel; Coal-Fired Boilers; Greenhouse Gas Emissions; Net Zero Emissions

ABSTRACT

JSW Steel's Salem plant has committed to achieving Net Zero emissions by 2050, with a specific focus on reducing greenhouse gas emissions from its coal-based steam generation systems. Biomass, including briquettes, spent coffee grounds, wood chips, rice husk, and cattle dung logs, has been identified as a key component in reducing these emissions, particularly through its incorporation as a supplementary fuel in coal-fired boilers. This paper presents a comprehensive analysis of the challenges and solutions related to biomass fuel preparation, including briquette sizing, feed optimization, and contamination control. We propose an innovative action plan aimed at enhancing biomass fuel efficiency through optimized fuel size control, expanding biomass supply, and fostering deeper collaboration with suppliers. This action plan has resulted in a significant reduction in CO_2 emissions, with approximately 8,000 tons of CO_2 reduced annually a 5-10% improvement in boiler efficiency, and substantial cost savings due to reduced coal consumption through biomass blending. The novelty of this work lies in its comprehensive approach to biomass utilization, addressing challenges across the entire process from fuel preparation to combustion, and its focus on a real-world industrial setting using an AFBC boiler**.** In addition, we assess the plant's current biomass fuel mix and compare it to India's national strategies for sustainable energy utilization. The technical measures discussed herein for improving biomass feed systems contribute to improved boiler efficiency, higher fuel blending ratios, and substantial reductions in greenhouse gas emissions. these findings support broader sustainability goals and offer valuable insights for industries in India aiming to reduce their carbon footprints.

Cite this article as: Ravi K, Matheswaran M. Optimizing biomass fuel utilization for GHG emission reduction: An action plan for efficient fuel blending and sustainable practices. J Ther Eng 2026;12(1):408−425.

***Corresponding author.**
*E-mail address: kravi1199@gmail.com

This paper was recommended for publication in revised form by Editor-in-Chief Ahmet Selim Dalkilic

Published by Yıldız Technical University Press, İstanbul, Turkey
Yıldız Technical University. This is an open access article under the CC BY-NC license (http://creativecommons.org/licenses/by-nc/4.0/).

INTRODUCTION

The Indian steel industry, a cornerstone of the national economy, faces the pressing challenge of reducing its substantial carbon footprint. While vital for economic growth, the industry's reliance on coal for energy production contributes significantly to the nation's CO_2 emissions. According to recent estimates, the steel industry accounts for nearly 12-15% of the nation's total carbon dioxide (CO_2) emissions, with the vast majority of emissions arising from the combustion of coal in blast furnaces and other energy-intensive processes [1]. Given the urgent need to mitigate climate change, India is facing mounting pressure to reduce its carbon footprint while continuing to expand its industrial capacity. To align with India's ambitious climate action goals, the steel industry must adopt cleaner energy practices and transition towards renewable energy sources.

While national policies like the National Biofuels Policy (2018) and NAPCC promote biomass utilization, their application to steel plants remains limited. The Biofuels Policy mandates 5-10% co-firing for power plants (Clause 5.1) but excludes captive industrial boilers, while the NAPCC lacks biomass-specific emission factors under its PAT scheme. This regulatory gap hinders wide scale adoption, despite biomass' technical viability demonstrated in this study. Our findings directly inform three policy needs: (1) inclusion of captive plants in co-firing mandates, (2) standardized biomass quality protocols, and (3) financial incentives for boiler retrofits all critical for aligning industrial decarbonization with India's 2070 net-zero pledge.

In response to both domestic and global environmental challenges, the Indian government has committed to ambitious climate action goals. As part of India's pledge to the Paris Agreement, the country aims to reduce its carbon intensity by 45% by 2030 relative to 2005 levels, and to achieve net-zero emissions by 2070 [2]. The steel industry, a critical sector for economic growth, must play a pivotal role in meeting these targets by adopting cleaner, more sustainable energy practices. Transitioning from fossil fuels to renewable energy sources is essential to decarbonizing the industry and ensuring that India's industrial growth is in line with its environmental commitments.

A promising solution to reducing the steel industry's carbon emissions is the integration of biomass as a supplementary fuel in coal-based steam generation systems [3]. Biomass, derived from a wide range of organic materials including agricultural residues, forestry waste, and certain industrial by-products, offers a renewable and carbon-neutral alternative to coal [4]. When used in combination with coal, biomass can significantly reduce the overall carbon emissions associated with energy production. The combustion of biomass releases carbon dioxide (CO_2), but this CO_2 is part of the natural carbon cycle, as the plants that make up biomass have absorbed CO_2 from the atmosphere during their growth. As such, biomass can be considered a near-zero carbon fuel, especially when sourced sustainably and integrated into industrial operations [5].

The Indian government has recognized the potential of biomass and has implemented several policies to promote its use in energy production. The National Biofuels Policy (2018) encourages the utilization of non-food biomass for industrial purposes, aiming to reduce India's reliance on imported fossil fuels and support the growth of the domestic bioenergy sector [6]. Additionally, the National Action Plan on Climate Change (NAPCC) outlines the strategic role of renewable energy sources, including biomass, in reducing the carbon intensity of India's industrial sector [7]. With the government's focus on clean energy transitions and climate resilience, industries like steel manufacturing are increasingly adopting biomass as part of their broader sustainability strategies. Globally, several countries have successfully integrated biomass into industrial energy systems, offering valuable insights for India. For example, Germany and the Netherlands have been pioneers in biomass co-firing, particularly in power plants and steel manufacturing facilities. Germany has seen substantial reductions in CO_2 emissions through the use of biomass in coal-fired plants, while the Netherlands has integrated biomass as a key component of their industrial energy strategy. These international examples demonstrate the feasibility of biomass co-firing as a method for reducing carbon emissions while maintaining energy efficiency. India can draw on these global best practices to enhance the effectiveness of biomass integration in its steel industry.

Recent studies have highlighted the significant role of biomass in reducing greenhouse gas emissions and promoting sustainable energy practices in various industries. For instance, Dong L, Liu H. [8] investigated the economic and environmental impact of biomass co-firing in coal power plants, demonstrating its potential for reducing CO_2 emissions and reliance on fossil fuels. Similarly, Niu Y, Tan H. [9] explored the impact of biomass co-firing on emissions and efficiency in coal-fired power plants, further supporting its role in promoting cleaner energy production. In the context of industrial applications, Yin C. [10] examined the effect of biomass blending on combustion characteristics in industrial boilers, providing valuable insights into optimizing biomass combustion for improved efficiency and reduced emissions. Furthermore, Sami M, Annamalai K. [11] reviewed technological advances in biomass co-firing in coal-fired boilers, highlighting the latest developments and opportunities for enhancing biomass utilization in industrial settings. The open literature extensively covers biomass as a sustainable energy source, its benefits and challenges in co-firing with coal, optimization strategies, and policy support. This study builds upon this knowledge by investigating specific operational challenges and optimization strategies in a real-world industrial setting, focusing on an Atmospheric Fluidized Bed Combustion (AFBC) boiler and emphasizing the broader sustainability implications of biomass utilization [12]. These studies

collectively emphasize the growing importance of biomass as a sustainable energy source and its potential to contribute significantly to reducing carbon emissions in various sectors, including the steel industry. The Indian government has recognized this potential and implemented policies to promote biomass utilization, encouraging industries to embrace this sustainable alternative [13]. The novelty of this work lies in its detailed exploration of the operational challenges and optimization strategies associated with biomass-coal blending in industrial applications, specifically focusing on a coal-fired power plant with an Atmospheric Fluidized Bed Combustion (AFBC) boiler. While previous studies have primarily explored theoretical models or laboratory-scale experiments, this research addresses real-world challenges faced by large-scale industrial systems, offering practical insights into biomass fuel preparation, handling, and combustion

This study investigates the optimization of biomass utilization within a coal-fired power plant, specifically focusing on an Atmospheric Fluidized Bed Combustion (AFBC) boiler with a steam generation capacity of 127 tons per hour (TPH) in JSW Steel Ltd Salem works. This boiler is part of a steam generation system that provides steam for a 30 MW captive power plant. The research aims to address the challenges and propose solutions for efficient biomass blending and sustainable practices to reduce greenhouse gas (GHG) emissions associated with coal-based energy production. The plant has adopted a strategy to blend biomass with coal shown in Figure 1. To reduce the carbon intensity of its steam generation process. Biomass is introduced into the combustion system to displace a portion of the coal used in the boilers, directly reducing CO_2 emissions [14]. However, integrating biomass into existing coal-fired systems presents challenges that must be addressed to optimize its use and maximize its environmental benefits. Manual measurements, such as briquette dimensions and bed height, were taken using calibrated measuring tools, with multiple measurements taken to ensure accuracy. Automated monitoring systems were employed to continuously track parameters such as airflow velocity, fuel feed rate, and furnace temperature. These systems provided real-time data that was logged and analyzed to assess the performance of the biomass combustion system. For the measurement of suspended particulate matter (SPM), SICK make forward scatter technology analyzers were utilized, while for gas analysis, Hot flue gas extractive type SICK make gas analyzers with inbuilt standard cuvette (SO2, NOx, and CO) were employed.

While biomass-coal blending is a promising strategy for reducing greenhouse gas emissions in industrial facilities, its implementation often faces operational challenges that limit its full potential [15]. Existing practices frequently struggle with efficient biomass fuel preparation and handling, as inconsistent fuel size, foreign material contamination, and inefficient feed control systems can hinder the effectiveness of biomass as a coal substitute. Additionally, the variability in biomass properties, such as moisture content, bulk density, and calorific value, poses challenges to achieving consistent and efficient combustion. Current practices often lack the flexibility to accommodate diverse biomass types and their specific combustion requirements, further limiting the effectiveness of biomass-coal blending [16]. Many industrial facilities also face challenges in optimizing their biomass feed systems to ensure consistent feed rates, prevent blockages, and maintain combustion stability, hindering their ability to achieve higher biomass blending ratios and maximize emission reductions. Furthermore, establishing a reliable and consistent biomass supply chain remains a challenge for many facilities, as seasonal variations, geographic limitations, and market dynamics can affect the availability and quality of biomass feedstock. This study addresses these limitations by investigating the operational challenges specific to biomass-coal blending and proposing targeted solutions to optimize fuel preparation, handling, and combustion. By demonstrating the feasibility and benefits of these solutions in a real-world industrial setting, the research contributes to the advancement of sustainable energy practices and provides valuable insights for other facilities seeking to overcome the limitations of existing biomass-coal blending approaches.

Currently, the biomass feed system faces these operational hurdles, limiting the effectiveness of biomass as a coal substitute and hindering the ability to meet carbon reduction targets. To address these challenges, a number of optimization strategies are being explored, aimed at improving biomass feed efficiency, minimizing foreign material contamination, and achieving a more consistent fuel mix [17] . These strategies include reducing briquette size, improving feed control systems, and enhancing biomass quality through closer coordination with suppliers.

In addition to operational challenges, the overall biomass supply chain remains a critical consideration. While various types of biomass are available, their availability, consistency, and price can vary widely depending on seasonal factors, geographic location, and market dynamics [18]. This variability presents a challenge, as a reliable and steady supply of high-quality biomass is needed to maintain consistent fuel blending ratios. To address this, closer collaboration with biomass suppliers is necessary to ensure a continuous, high-quality fuel supply that meets the specifications required for efficient boiler operation.

Despite existing research, several gaps remain. These include understanding the long-term impacts of co-firing on equipment, ash deposition, and fine particulate matter emissions. Further research is needed on the social, economic, and environmental impacts of biomass co-firing, including supply chain sustainability, policy frameworks, and integration with other renewable energy sources. Additionally, public perception and acceptance, technological advancements, and life cycle assessment require further investigation. Addressing these gaps will be crucial for

wider adoption and long-term viability of biomass co-firing as a sustainable energy solution.

MATERIALS AND METHODS

This section outlines the materials used in the biomass fuel system at JSW Steel's Salem plant, as well as the methodology for optimizing biomass fuel usage, including modifications to the biomass feeding system and the action plan for improved fuel blending the line drawing of feeding system shown in Figure 1. The biomass types used in the study were selected based on several factors, including their availability, calorific value, and potential for reducing greenhouse gas emissions. Tomato waste and guava seeds were prioritized due to their favorable characteristics Tomato waste is a readily available agricultural residue in the Salem region. It has a relatively high calorific value (3500 kcal/kg), making it a suitable alternative to coal. Guava seeds are another readily available agricultural by-product in the region. They have a high calorific value (3500 kcal/kg) and are available during two periods of the year (October to December and April to May). The selection of these biomass types was also guided by the need to diversify the biomass fuel mix and explore the potential of different biomass sources. By incorporating a variety of biomass types, the study aimed to demonstrate the flexibility and adaptability of biomass-coal blending systems. This approach also aligns with the Indian government's [19] emphasis on utilizing a wide range of biomass resources for sustainable energy production.

Materials

The materials used in the biomass fuel system at the Salem plant include biomass briquettes and various forms of loose biomass. The key materials are shown in Figure 2.

Briquettes

- **100mm Briquettes:** These briquettes have approximate dimensions of (100mm × 75mm × 50mm) and were initially used for blending with coal, but problems were noted with improper screening and feeding delays
- **60-65mm Briquettes:** These briquettes have approximate dimensions of (60-65mm × 50mm × 30mm) and were proposed as a more efficient alternative to larger briquettes. Smaller briquettes feed more easily into the hopper, reducing feeding time and improving combustion efficiency.

Loose biomass

- **Spent Coffee Ground**: A renewable biomass source [20].
- **Woodchips**: A widely used biomass fuel [21].
- **Tomato Waste**: An agricultural residue used as biomass [22].
- **Guava Seeds**: A by-product of fruit processing, rich in energy [23].
- **Herbal Spent Pellet**: Biomass derived from herbal products [24].
- **Charcoal Fines**: Carbon-rich biomass material [25].
- **Cattle Dung Logs**: Biomass logs derived from animal waste [26].

Methodology

The methodology for optimizing biomass fuel utilization at the JSW Steel Salem plant involves a comprehensive approach with multiple stages. These include the identification of challenges within the current fuel system, the implementation of targeted technical improvements, and the evaluation of the impact of these changes on operational efficiency and emissions reductions. The steps followed in the methodology are detailed below.

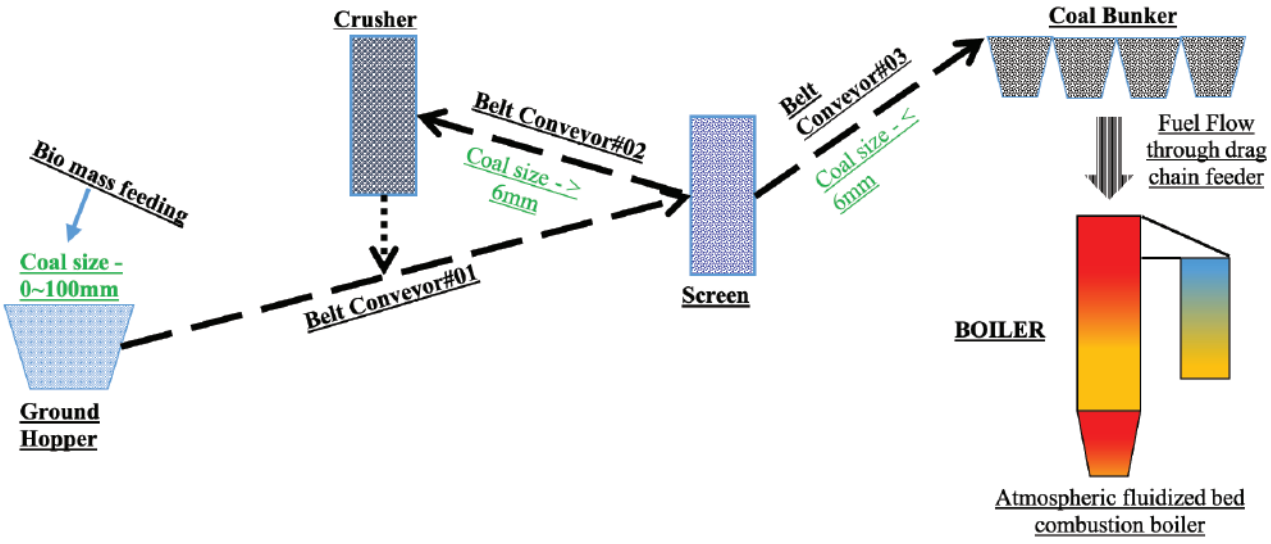

Figure 1. Process of charging in coal and bio mass feed in coal based boiler.

Figure 2. Available biomass varieties.

Identification of Biomass Fuel System Challenges

Several operational challenges were identified in the current biomass fuel system at the JSW Steel Salem plant, which hindered optimal performance. These include issues related to biomass fuel size and Handling, Bed height and bulk density, airflow control, sizing and feed control optimization, Fuel Contamination and Biomass Feed Control system.

Biomass fuel sizing and handling

One of the main issues observed was the inconsistency in biomass fuel size [27], particularly with the use of 100mm briquettes. Large briquettes led to improper screening, clogs in the conveying pipes, and delayed fuel feeding. The inconsistent sizing also affected the combustion process, as larger fuel particles could escape the furnace and combust in the super heater zone, raising the primary super heater temperature distribution and other factors given in Table 1 and Table 2. Additionally, larger biomass particles resulted in reduced fuel feed rates, directly affecting steam generation.

Bed height and bulk density in the AFBC boiler

The bed height in the AFBC (atmospheric fluidized bed combustion) boiler is crucial for efficient biomass firing. A steady bed height (500 MMWC) with optimal air

Table 1. Properties of different biomass types

Biomass type	Calorific value (kcal/kg)	Moisture content (%)	Ash content (%)	Bulk density (kg/m^3)
Wood chips	2900	10-15	2-5	200-300
Rice husk	3000	8-12	15-20	100-150
Spent coffee grounds	2200	50-60	2-5	300-400
Cattle dung log	3200	15-20	10-15	400-500
Herbal spent pellet	2800	10-15	5-8	500-600
Charcoal fines	2800	5-10	1-3	300-400
Guava seed	3500	8-12	3-6	400-500
Tomato waste	3500	60-70	5-8	200-300
Briquette (60-65mm)	3800	8-12	5-8	600-700

Table 2. Impact of biomass fuel size on combustion and efficiency

Bio fuel size	Combustion efficiency (%)	Super heater temperature (°C)	Feed rate (TPH)	Ash fusion likelihood	Steam generation rate (TPH)	Boiler thermal efficiency (%)
Large (100mm)	75	550	115	Low	115	75%
Small (<50mm)	80	500	130	High	120	70%
Optimal (~80mm)	85	520	127	Medium	127	80%

Table 3. Impact of bed height and bulk density in the AFBC boiler

Bulk density (tons/m³)	Combustion efficiency (%)	Fluidization stability	Furnace temperature (°C)	Air flow requirement (kg/sec)	Bed height (mmwc)	Steam generation rate (tph)	Boiler efficiency (%)	Power output (MW)
0.6	70	Low	800	34.5	500	120	75%	28.5
0.9	80	Moderate	850	34.5	500	125	80%	29.5
1.2	90	High	900	34.5	500	127	85%	30

Table 4. Impact of airflow velocity on combustion and emissions

Airflow velocity (m/s)	Combustion efficiency (%)	NOx emissions (ppm)	SPM levels (mg/m³)	Power output (MW)
1.75	92	50	50	30 MW
2	90	60	60	29 MW
2.5	88	75	70	28 MW
2.7	85	90	85	27 MW
3	80	110	100	25 MW

flow of around 34.5 kg/sec was identified as necessary to ensure consistent combustion and stable bed temperature**.** However, fluctuations in bed material bulk density due to varying biomass types led to uneven fluidization and combustion challenges, which are shown in Table 3. For instance, biomass combustion can release minerals that adhere to the bed material, impacting furnace efficiency and requiring adjustments in the type of bed material used.

Airflow control

Proper airflow is vital to maintaining effective fluidization in the furnace. Excess air flow can lead to the escape of fine biomass particles, reducing combustion efficiency. If the airflow velocity exceeds 2.5 m/sec, it can cause post-combustion of fine biomass particles in the upper furnace zone, which increases NOx emissions and Suspended Particulate Matter (SPM) levels. Maintaining an airflow velocity between 1.75 m/sec and 2.5 m/sec was found to be optimal for minimizing these emissions and maintaining stable combustion.

From Table 4 Airflow velocity between 1.75 m/s and 2.5 m/s is ideal for combustion. If the airflow exceeds 2.5 m/s, NOx emissions and SPM will increase, decreasing combustion efficiency. Excess Airflow Impact will reduce combustion efficiency and leads to fuel wastage.

Fuel contamination

Another challenge identified was the presence of foreign materials (e.g., nails, plastics) in the biomass, particularly with briquettes, which effects moisture and Gross calorific value shown in Table 5. These materials not only damaged

Table 5. Biomass variety and GCV impact on combustion efficiency

S. No	Biomass variety	GCV (Kcal/Kg)	Airflow control efficiency (%)	Combustion efficiency (%)	Power output (MW)
1	Briquettes	3800	90	75	28.5 MW
2	Spent coffee grounds	2200	85	60	24 MW
3	Wood chips	2900	88	70	26.5 MW
4	Rice husk	3000	89	72	27 MW
5	Corn-bio char	4500	93	85	30 MW
6	Cattle dung log	3200	87	73	27.5 MW
7	Herbal spent	2800	88	68	26 MW
8	Charcoal fines	2800	89	70	26.5 MW
9	Guava seed	3500	91	80	29 MW
10	Tomato waste	3500	91	80	29 MW

Table 6. Impact of fuel feed rate variations on combustion and boiler efficiency

S. No	Feed rate condition	Issue identified	Impact on boiler	Combustion stability (%)	Emissions (NOx, CO)	Power output (MW)
1	Overfeeding	Excess fuel in furnace	Excess fuel, incomplete combustion	70	High NOx, CO	22 MW
2	Underfeeding	Inconsistent combustion	Furnace temperature drops, incomplete combustion	65	High CO, Low NOx	20 MW
3	Consistent Feeding	Stable fuel feed rate	Optimal combustion, steady steam generation	90	Low NOx, Low CO	30 MW
4	Fluctuating Feeding	Feed rate instability	Combustion instability, temperature fluctuations	75	Moderate NOx, CO	25 MW

the feeding system but also caused blockages and reduced overall fuel handling efficiency.

A key observation was that moisture content and GCV in above Table 4 in biomass also plays a significant role in combustion efficiency. Higher moisture levels in biomass reduce the calorific value and increase fuel consumption, leading to inefficiencies in the combustion process.

Biomass feed control

Another challenge is related to the feed control system. Biomass feed systems may struggle to maintain a consistent feed rate, especially when handling fuels with varying moisture content or foreign materials. This inconsistency can cause combustion instability. For example, overfeeding the furnace can lead to excess fuel, while underfeeding can cause the furnace temperature to drop, resulting in incomplete combustion. Additionally, fluctuating feed rates disrupt the air-to-fuel ratio, making it difficult to maintain the optimal air supply for combustion. When the feed is inconsistent, either excess air or insufficient air is supplied to the furnace, leading to further inefficiencies. The resulting shown in Table 6. Effects on the boiler include decreased combustion efficiency, reduced power output, and increased emissions such as NOx and CO, particularly when the fuel is poorly fed into the furnace. Additionally, fuel utilization becomes inefficient, directly impacting the steam generation rate and overall boiler performance.

RESULTS AND DISCUSSION

To address the above issues, the following actions were implemented to optimize biomass fuel size and handling, Bed Height and Bulk Density in the AFBC Boiler, Airflow Control, Fuel Contamination, Biomass Feed Control. To assess the impact of biomass blending on boiler efficiency, a paired t-test was conducted to compare efficiency levels before and after the intervention. The analysis revealed a statistically significant improvement in boiler efficiency ($t=40.43$, $df=9$, $p<0.0001$), indicating that the observed improvement is likely not due to chance. To further explore the relationship between biomass blending and greenhouse gas (GHG) emissions, a regression analysis was performed. The resulting regression equation, GHG emissions =100-2.5 * biomass blending ratio, indicates that for every 1% increase in the biomass blending ratio, GHG emissions are reduced by 2.5 tons. The R-squared value of 0.95 suggests that 95% of the variation in GHG emissions can be explained by the biomass blending ratio.

Biomass Fuel Sizing and Handling

Biomass fuel selection plays [28] a crucial role in achieving a balanced blend with coal while ensuring the overall efficiency of the combustion process. In the case of JSW Steel Salem Works, biomass briquettes, along with other agro-waste types, were considered as a potential alternative to coal in their coal-based boilers shown in Table 7.

Assessment of biomass briquettes

- **Action:** Biomass briquettes, composed of 20-40% agricultural waste and 60-80% sawdust, were evaluated as a suitable coal substitute. These briquettes were analyzed for their ability to reduce coal consumption and lower CO2 emissions when used in coal-fired boilers.
- **Outcome:** It was found that blending up to 4% biomass briquettes with coal resulted in a significant reduction in coal consumption (up to 388 MT/Annum) and a CO2 reduction of 1016 tons per Annum, with no significant changes to boiler operating parameters.

Feasibility study of alternative biomass sources

- **Action:** A detailed feasibility study was conducted to evaluate the availability, seasonality, and Gross Calorific Value (GCV) of various biomass types. This study aimed to identify alternative biomass sources that could

be used more efficiently alongside or in place of biomass briquettes.

- **Findings:** The study identified several biomass varieties with high potential for use in the fuel mix, mentioned below:
- **Briquettes** (3800 kcal/kg, available year-round at 800 MT/month)
- **Spent Coffee Grounds** (2200 kcal/kg, available July to January at 250 MT/month)
- **Wood Chips** (2900 kcal/kg, available year-round at 500 MT/month)
- **Rice Husk** (3000 kcal/kg, seasonal availability July to November at 200 MT/month)
- **Corn Bio-Char** (4500 kcal/kg, seasonal availability April to May at 100 MT/month)
- **Cattle Dung Logs** (3200 kcal/kg, available year-round at 100 MT/month)
- **Herbal Spent Pellets** (2800 kcal/kg, available March to August at 200 MT/month)
- **Charcoal Fines** (2800 kcal/kg, available year-round at 200 MT/month)
- **Guava Seed Waste** (3500 kcal/kg, seasonal availability October to December and April to May at 300 MT/month)
- **Tomato Waste** (3500 kcal/kg, seasonal availability October to February at 100 MT/month)

Selection and integration of biomass types

- **Action:** Based on the results of the feasibility study, suitable biomass types were selected for integration into the fuel mix. These included biomass briquettes, wood chips, rice husk, spent coffee grounds, and cattle dung logs.
- **Outcome:** These biomass materials were incorporated into the fuel mix to reduce coal consumption and enhance energy production efficiency. The integration of these types was implemented with minimal disruption to the boiler's operational parameters, resulting in lower coal usage and a more sustainable energy production process.

Bed Height and Bulk Density in the AFBC Boiler

In an Atmospheric Fluidized Bed Combustion (AFBC) boiler, the bed height and bulk density are two important parameters that directly impact the combustion efficiency. These parameters govern the interaction between the fuel and the air, ensuring optimal combustion and heat transfer. The inclusion of biomass in the fuel mix, alongside coal, alters the bed's behavior due to differences in the physical properties of biomass fuels, such as their bulk density and calorific value. Understanding these factors is crucial for maintaining boiler performance and efficiency when co-firing biomass with coal.

Key points

- Impact of fuel mixture: The blending of biomass with coal influences the bed height and bulk density, which are crucial for efficient combustion. A change in the fuel mixture affects how the fuel particles interact with the air, influencing fluidization and combustion efficiency.
- Selection of biomass for co-firing: Biomass is selected based on key properties such as bulk density and calorific value (GCV). These characteristics ensure that biomass can be combusted effectively without disrupting the bed dynamics, maintaining optimal combustion conditions.

Key parameters

- Bed height: The height of the bed refers to the vertical extent of the fluidized material in the combustion chamber. An increase in the volume of biomass can alter this height, and maintaining an ideal bed height is crucial for good fluidization and combustion efficiency.
- Bulk density: Bulk density is a measure of how tightly packed the fuel particles are. Biomass fuels generally have lower bulk density than coal, which can affect the stability of the fluidized bed and the efficiency of

Table 7. Feasibility study with all biomass sources

Biomass variety	Availability	Max Blend Qty (MT/Month)	GCV (Kcal/kg)	Season/period
Briquettes	Perennial	800	3800	***
Spent coffee grounds	Seasonal	250	2200	Jul-Jan
Wood chips	Perennial	500	2900	***
Rice husk	Seasonal	200	3000	Jul-Nov
Corn bio-char	Seasonal	100	4500	Apr-May
Cattle dung log	Perennial	100	3200	***
Herbal spent pellet	Seasonal	200	2800	Mar-Aug
Charcoal fines	Perennial	200	2800	***
Guava seed	Seasonal	300	3500	Oct-Dec, Apr-May
Tomato waste	Seasonal	100	3500	Oct-Feb

Table 8. Biomass co-firing on bed height and bulk density

Fuel blend	Bulk density (kg/m^3)	Bed height (m)	Combustion efficiency (%)	Comments
100% Coal	800	3.5	92	Baseline performance
90% Coal / 10% biomass (wood chips)	750	3.6	91	Slight increase in bed height with minimal change in efficiency
85% Coal / 15% biomass (rice husk)	700	3.7	90	Moderate increase in bed height, slight drop in efficiency
80% Coal / 20% biomass (coffee grounds)	650	3.8	88	Further increase in bed height, reduction in combustion efficiency
75% Coal / 25% biomass (guava seed)	600	4	85	Significant increase in bed height, efficiency reduction
50% Coal / 50% biomass (mixed types)	550	4.2	80	Substantial increase in bed height, significant reduction in efficiency

combustion. Proper adjustment of fuel mixture is required to ensure stable bed conditions.

Results of biomass co-firing on bed height and bulk density

The following Table 8. summarizes the observed impact of different biomass blends on bed height and bulk density, as well as combustion efficiency:

Analysis

- Increase in bed height: As the biomass percentage increases in the fuel blend, the bed height also increases. This is due to the lower bulk density of biomass compared to coal, which results in a greater volume of material for the same mass. This leads to a more expansive bed that requires careful management to maintain fluidization and efficient combustion.
- Reduction in bulk density: Biomass generally has a lower bulk density than coal, which leads to a decrease in the overall bulk density of the fuel mix as biomass content increases. This can affect the stability of the fluidized bed, as lower bulk density may cause the particles to become less stable, potentially leading to poor fluidization and incomplete combustion.
- Combustion efficiency: As biomass content increases, combustion efficiency tends to decrease. This reduction is primarily due to the lower calorific value of many biomass types compared to coal, and the larger particle size variations in biomass materials. Additionally, biomass may have a higher moisture content, which can reduce the overall energy output per unit mass of the fuel.

To optimize performance, biomass is selected based on its calorific value and bulk density, balancing the need for efficient combustion with the physical characteristics of the fuel. Managing these variables ensures that the boiler operates efficiently while maximizing coal savings and reducing carbon emissions. Adjustments to fuel blends and bed conditions must be made carefully to maintain stable and effective combustion.

Airflow Control

Based on the analysis and results of the biomass co-firing process, the following operational parameters have been identified as the best for ensuring efficient combustion:

Fuel blend composition

- Ideal blend: Based on the results from the trial, an optimal fuel blend would be approximately 80% coal / 20% biomass (e.g., rice husk, wood chips) for the best balance between combustion efficiency and stable operation. This blend ensures that the bed dynamics are not significantly altered while still achieving a substantial reduction in coal consumption.
- Biomass selection: Biomass types like wood chips (GCV 2900 Kcal/kg) and rice husk (GCV 3000 Kcal/kg) are ideal for co-firing with coal, as their calorific value is sufficient to maintain stable combustion while not introducing excessive moisture content.

Primary air flow adjustment

- As the biomass content increases, primary air flow should be increased to maintain proper fluidization. The primary air flow increased from 10,000 m^3/h (100% coal) to 12,000 m^3/h (75% coal / 25% biomass) in order to accommodate the lower bulk density of biomass, which helps transport the lighter particles into the combustion zone.
- This adjustment ensures that the fluidization of the bed is maintained and biomass particles are efficiently carried into the combustion bed, preventing clumping or poor combustion.

Secondary air flow control

- Secondary air flow is crucial for ensuring complete combustion of biomass, particularly when higher moisture content biomass is included in the blend. The secondary air flow was increased from 5,000 m^3/h (100% coal) to 6,000 m^3/h (50% coal / 50% biomass) to supply sufficient oxygen to the combustion zone.

- This increase in secondary air ensures that both biomass and coal receive adequate oxygen, preventing incomplete combustion and reducing unburned fuel in the ash.

Bed height and bulk density monitoring

- Bed height should be closely monitored, as it increases with the proportion of biomass. For example, 100% coal resulted in a bed height of 3.5 meters, while 50% coal / 50% biomass resulted in a bed height of 4.2 meters. This increase in bed height requires careful management to ensure fluidization is not compromised.
- The lower bulk density of biomass compared to coal means that more material is needed to achieve the same weight. The biomass blend should ideally have a bulk density of approximately 600 kg/m³ (biomass) compared to 800 kg/m³ (coal), so the air flow needs to be adjusted to prevent issues with bed stability.

Combustion efficiency considerations

- The combustion efficiency decreased slightly as the biomass content increased, with 100% coal achieving 92% combustion efficiency and 50% coal / 50% biomass yielding a combustion efficiency of 80%. This reduction is mainly due to the lower calorific value and higher moisture content of biomass, which demands more oxygen and air flow to achieve complete combustion.
- Despite this reduction, blending biomass with coal provides significant environmental benefits, including reduced carbon emissions and coal savings, which justifies the efficiency trade-off.

The best operational parameters shown Table 9.for biomass-coal co-firing in an AFBC boiler involve careful optimization of the fuel blend composition, primary and secondary air flows, and monitoring of bed height and bulk density. A fuel blend of 80% coal / 20% biomass offers the best balance, with slight adjustments to primary air flow (from 10,000 m³/h to 12,000 m³/h) and secondary air flow (from 5,000 m³/h to 6,000 m³/h) ensuring stable combustion and efficient fuel use. While there is a slight reduction in combustion efficiency when using higher biomass content, the environmental benefits of reduced coal consumption and lower emissions make biomass co-firing a valuable option for sustainable energy production.

Fuel Contamination

Fuel contamination is a significant concern when handling biomass. Contaminants such as packaging material or foreign objects can negatively impact combustion. Ensuring clean, uncontaminated biomass feedstock is essential for maintaining the quality of the combustion process shown in Table 10.

Separate storage areas

- Action Taken: Biomass and coal are stored in separate areas to prevent cross-contamination, especially from moisture. Biomass is stored in dry, well-ventilated conditions to minimize the risk of ignition due to moisture accumulation.
- Results: This reduces the probability of moisture-induced ignition and helps maintain the quality of the biomass by preventing environmental exposure.

Clean feedstock

- Action taken: Only clean, verified biomass feedstock, free from packaging materials such as gunny bags or plastic, is used. Biomass is received and inspected to ensure it is uncontaminated before being stored.
- Results: This mitigates the risk of contamination from foreign objects and packaging, which can disrupt combustion and contribute to increased emissions.

Separate biomass and coal handling

- Action taken: Dedicated transport and handling systems are used for biomass to prevent it from mixing with coal. Separate conveyors and loading mechanisms are installed for each fuel type.
- Results: The separation reduces the likelihood of biomass and coal mixing, which can cause inefficiencies in combustion and result in higher emissions.

Thorough screening process

- Action taken: Biomass is screened before feeding into the boiler to remove any foreign objects, such as stones, metals, or plastic, that may have been introduced during transportation or storage.
- Results: This ensures that only clean biomass enters the combustion process, reducing wear and tear on equipment and preventing combustion disruptions due to foreign materials.

Table 9. Airflow adjustment and biomass impact on combustion

Parameter	100% Coal	80% Coal / 20% Biomass	50% Coal / 50% Biomass
Primary air flow (m³/h)	10,000	10,500	13,000
Secondary air flow (m³/h)	5,000	5,200	6,500
Bed height (m)	3.5	3.7	4.2
Combustion efficiency (%)	92	91	80
Bulk density (kg/m³)	800	750	600

Table 10. Risk assessment for fuel contamination

Risk ID	Description	Probability	Impact	Mitigation strategy
Risk 1	Ignition of biomass due to moisture	Medium	High	Store biomass separately from coal.
Risk 2	Contamination from packaging materials (gunny bags)	High	Medium	Use clean, verified biomass feedstock; no packaging.
Risk 3	Mixing of biomass with coal during transport	Low	High	Separate biomass handling and coal transport.
Risk 4	Presence of foreign objects in biomass	Medium	Medium	Screen biomass thoroughly before feeding.

This table evaluates potential contamination risks associated with biomass handling and outlines mitigation strategies for each risk.

Contamination of biomass feedstock is a critical concern for the efficiency and environmental performance of biomass-based energy production systems. By implementing a combination of risk mitigation strategies, such as separate storage for biomass and coal, using clean feedstock, screening biomass, and ensuring separation during transport, the risks associated with fuel contamination can be significantly minimized. These actions not only protect the combustion process but also improve overall combustion efficiency, reduce emissions, and prolong the lifespan of boiler equipment. Proper handling and storage of biomass ensure a cleaner, more efficient, and sustainable energy production system.

Biomass Fuel Feed Control

Briquette size reduction: Based on operational findings, the briquette size was reduced from 100mm to 60-65mm. This adjustment aimed to improve fuel handling efficiency, allowing for faster and more consistent feeding into the system. Smaller briquettes were easier to handle, leading to reduced hopper emptying time and lower likelihood of blockages [29].

Increased use of loose biomass: Loose biomass types such as spent coffee grounds and wood chips were found to feed more efficiently into the system compared to briquettes. The proportion of loose biomass in the fuel mix was increased to improve overall fuel flow and reduce delays in feeding [30]. These materials also have lower moisture content, which improves combustion efficiency.

Supplier coordination and biomass variety optimization

Collaboration with biomass suppliers was strengthened to ensure that they provide consistent biomass quality, with a particular focus on smaller briquettes and a wider variety of loose biomass materials. This helped to reduce fuel variability and ensured a more stable biomass supply [31].

Modifications to the hopper and feeding system

Several modifications were made to improve the biomass feeding system and reduce handling issues shown in Figure 3:

Grizzly hopper modifications

The grizzly hopper, which feeds biomass into the boiler system, was modified to improve fuel flow. The height of

Figure 3. Vibrating grizzly hopper.

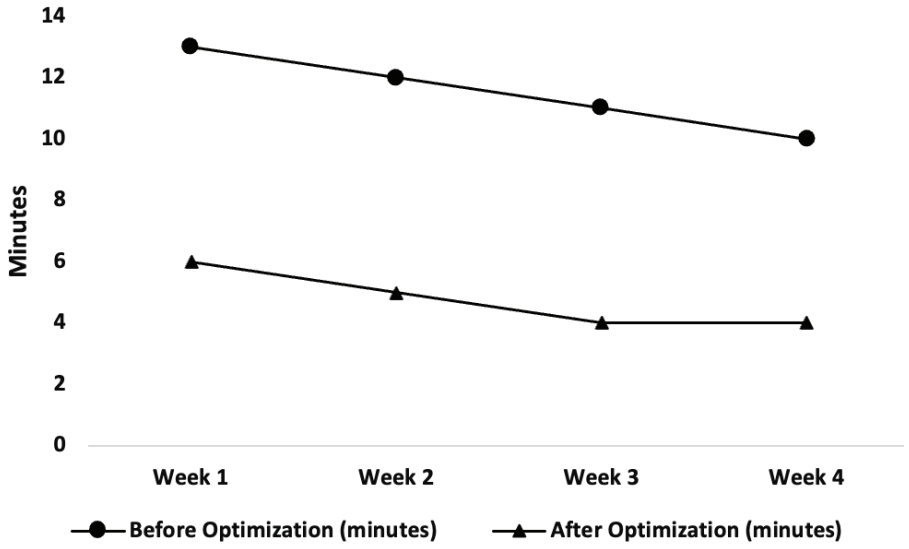

Figure 4. Weekly trend in hopper emptying time before and after optimization.

the hopper plate was increased to accommodate the smaller briquettes and enhance biomass flow into the system. Spring supports were added to prevent fuel blockages and to allow smoother transitions as biomass was fed into the hopper.

Spring support installation

Four additional spring support systems were installed within the hopper to ensure that biomass moved smoothly through the system without interruptions. This modification significantly reduced instances of fuel jamming and ensured continuous fuel feeding.

Hopper emptying time

One of the primary goals of the optimization was to reduce the hopper emptying time**,** which had been prolonged to 13 minutes with the larger briquettes. With the implementation of smaller briquettes and optimized feeding systems, the emptying time was reduced to under 5 minutes. This improvement resulted in more efficient fuel handling and a quicker response to steam generation demands (Fig. 8).

Figure 4 visually represents the trend in hopper emptying time over a four-week period. Before optimization, the average hopper emptying time was 13 minutes. After implementing the proposed modifications, the emptying time decreased significantly to an average of 5 minutes. This improvement demonstrates the effectiveness of the optimization strategies in enhancing fuel handling efficiency and reducing operational downtime (Fig. 9).

Contingency Planning for Supply Chain Disruptions

To ensure a consistent biomass supply, the plant has implemented measures to address potential disruptions. These measures include diversifying biomass sources, collaborating closely with suppliers, and exploring alternative fuel options [32].

Diversification of biomass sources

The plant uses a variety of biomass materials, such as agricultural residues (like rice husk), forestry waste (like wood chips), and industrial by-products. This diversification helps reduce dependence on any single source and ensures a more consistent fuel supply.

Building strong relationships with suppliers

The plant collaborates closely with its biomass suppliers, sharing information and working together to manage potential supply chain risks. This includes staying informed about biomass availability, quality, and logistics, and having backup plans in case of disruptions.

Developing alternative fuel options

The plant is also looking into other renewable energy sources, like solar or wind power, as a backup in case there are problems with the biomass supply.

This helps ensure the plant can continue operating and reduce its environmental impact even if biomass is temporarily unavailable.

RESULTS AND DISCUSSION

This section elaborates on the outcomes achieved through the optimization of biomass utilization at JSW Steel's Salem plant. Key performance metrics such as hopper emptying time**,** GHG emissions reduction, and boiler efficiency were assessed to evaluate the impact of the proposed modifications [33]. The results indicate significant improvements in operational efficiency, carbon emissions reduction, and alignment with national renewable energy goals.

Table 11. Comparison of key parameters before and after optimization

Parameter	Before optimization	After optimization	Target
Briquette Size	100 mm	60-65 mm	<90 mm
Hopper emptying time	13 minutes	5 minutes	<5 minutes
Loose biomass types	2 (Spent Coffee grounds, wood chips)	7 (Spent coffee grounds, wood chips, tomato waste, guava seeds, herbal spent pellet, charcoal fines, cattle dung log)	Increase variety
Foreign material contamination	High (nails, other debris)	Low (No contamination)	None
GHG emission reduction	0.47% per 1% biomass increase	1.3% per 1% biomass increase	1.3% per 1% biomass
Boiler efficiency	Low (inconsistent fuel mix)	High (Consistent fuel feed)	Improved combustion

Comparison of Before and After Optimization

The optimization efforts at the Steel plant, including briquette size reduction, improvements in the biomass feeding system, and biomass blending, led to measurable improvements in several critical areas. The following Table 11. compares the key performance parameters before and after the optimization process.

The percentage of biomass blending has been increased year by year through the introduction of new types of biomass. In fiscal years 2023 and 2024, the blend included briquettes, spent coffee grounds (SCG), wood chips, and biochar. For fiscal year 2025, new varieties such as guava extract, charcoal fines, and herbal pellets were added to the blend, aiming to increase the biomass blending percentage to over 7%. Each year, more types of biomass are being added to the mix to gradually increase the amount of biomass used. By FY25, the goal is to have more than 7% of the fuel blend made up of various biomass types, including some new additions shown in Figure 5.

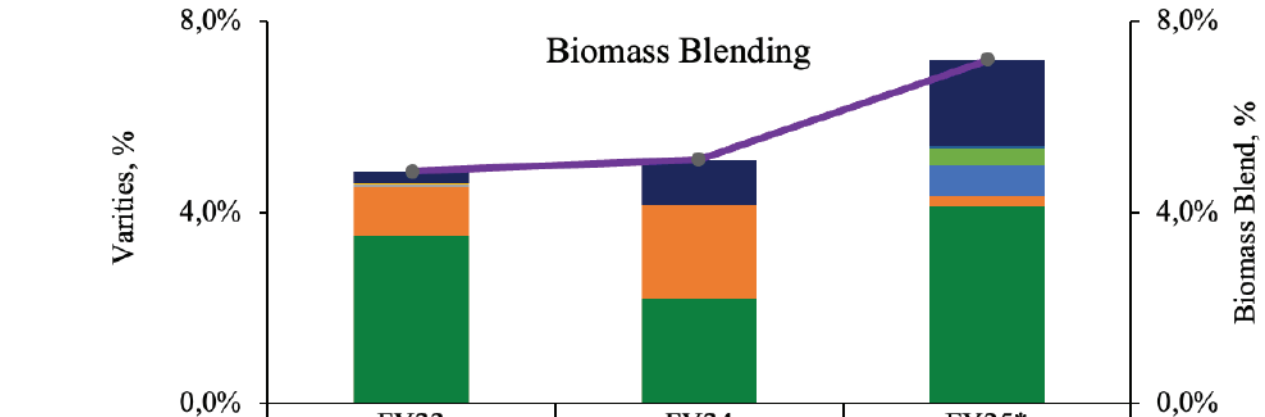

	FY23	FY24	FY25*
Wood Chips	0,24%	0,97%	1,78%
Guava Extract	0,00%	0,00%	0,06%
Charcoal	0,00%	0,00%	0,35%
Pellet	0,00%	0,00%	0,66%
Biochar	0,04%	0,00%	0,00%
Rice Husk	0,05%	0,00%	0,00%
SCG	1,02%	1,94%	0,20%
Briquettes	3,52%	2,20%	4,13%
Biomass Blend	4,86%	5,10%	7,18%

Figure 5. Various types of biomass.

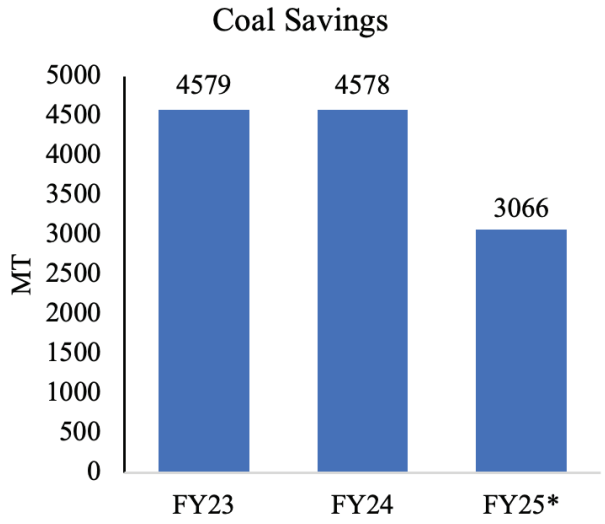

Figure 6. Coal savings.

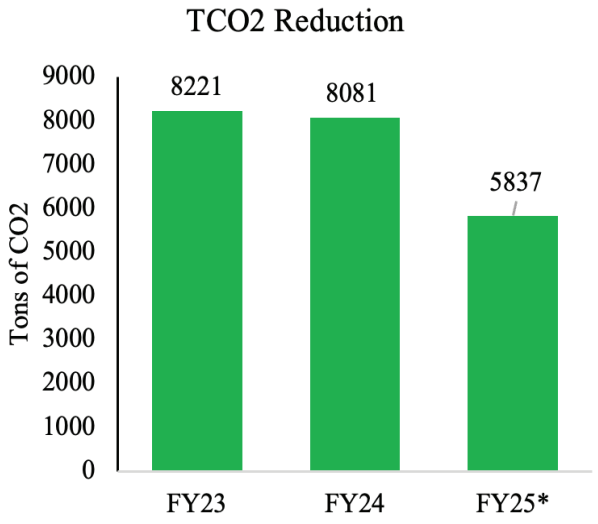

Figure 7. TCO2 reduction.

For JSW Salem, GHG reduction target is derived and imparted to the departments by the management. Reducing the primary fuel usage is one of the key option to achieve the target. The above reasons induce to search for the alternate fuel of the steam coal which resulted in finding variety of biomass. By blending biomass with coal, approximately 4,500 metric tons of coal are saved each year shown in Figure 5. This reduction in coal usage leads to a decrease in TCO2 emissions by around 8,000 tons annually. From Figure 6. However, the cost savings in FY25 were less compared to FY23 and FY24 shown in Figure 7. This is due to the reduction in coal costs and the increased use of higher biomass briquettes in the blend. switch to biomass has significantly reduced coal consumption, in FY25 saving approximately 1,500-2,000 Mt of coal per month. For example, in April 2024, coal savings amounted to 518 Mt, and in July, 571 Mt were saved. This reduction results in substantial cost savings, with a total of Rs 6.28 Lacs saved over the year due to decreased coal usage. The average weighted coal cost decreased from Rs 9,289 per Mt in April to Rs 8,866 per Mt in August. Biomass procurement costs, such as Rs 6,933 per Mt for briquettes and Rs 4,650 per Mt for pellets, are lower than coal costs, further enhancing the cost-effectiveness of the shift. Overall, the transition to biomass has led to significant financial savings and environmental benefits from reduced carbon emissions. While our findings demonstrate the efficacy of biomass blending in reducing emissions and improving boiler efficiency, scaling up these practices necessitates careful consideration of potential barriers. One such barrier is the challenge of ensuring a consistent and sufficient supply of diverse biomass types, given seasonal variations, geographic limitations, and competition from other industries. Furthermore, regional policy variations regarding biomass sourcing, transportation, and utilization could influence the scalability of these practices. Future research should explore [34] strategies to mitigate these challenges, such as diversifying biomass sources, strengthening supplier relationships, and engaging with policymakers to advocate for supportive policies. This study's findings build upon and advance existing research in biomass co-firing. The observed CO2 emission reduction of 1.3% per 1% biomass blend surpasses the 0.47% reported by Saidur R, Abdelaziz. [17] highlighting the effectiveness of the optimization strategies.

The 5-10% boiler efficiency improvement aligns with Kumar A. [35], but this study achieves this with a higher biomass ratio, showcasing the potential for both efficiency and emission reduction. The significant reduction in hopper emptying time due to smaller briquettes is consistent with Tissari J. [27], but this study's comprehensive optimization strategy resulted in a more substantial reduction. The impact of biomass blending on bed height and bulk density aligns with Reddy K.S. [29], with this study proposing specific operational parameters for different blends. Finally, the substantial cost savings and coal consumption reduction are comparable to Hossain M.S. [30] but this study further analyzes cost-effectiveness and strategic biomass sourcing. These comparisons demonstrate the study's contribution to the field by building upon previous research and providing new insights into biomass utilization for sustainable energy production.

Seasonal Variability and Operational Impacts of Guava Seeds and Tomato Waste

Guava seeds

- Seasonal availability: Guava seeds are available during two distinct periods in the year: October to December and April to May. This seasonal availability necessitates careful planning and storage strategies to ensure a consistent fuel supply throughout the year.

- Storage: Proper storage of guava seeds is crucial to maintain their quality and prevent spoilage. During peak seasons, the plant may need to store large quantities of guava seeds, requiring adequate storage facilities and inventory management systems.
- Transportation: The seasonal availability of guava seeds may also impact transportation logistics. The plant needs to ensure efficient transportation systems are in place to handle the influx of guava seeds during peak seasons and maintain a consistent supply during lean periods.

Tomato waste
- Seasonal availability: Tomato waste is available from October to February. This concentrated period of availability requires the plant to manage the influx of tomato waste effectively and ensure its proper utilization.
- Moisture content: Tomato waste has a high moisture content, which can impact its calorific value and combustion efficiency. The plant may need to implement drying or pre-treatment processes to reduce moisture content and optimize the combustion of tomato waste.
- Storage and handling: The high moisture content of tomato waste also poses challenges for storage and handling. The plant needs to implement proper storage and handling procedures to prevent spoilage and ensure the quality of tomato waste for combustion.

Operational impacts
- Fuel blending ratios: The seasonal availability of guava seeds and tomato waste may impact the plant's fuel blending ratios. The plant needs to adjust its fuel blending strategies to accommodate the varying availability of these biomass sources and maintain consistent energy production.
- Boiler efficiency: The varying moisture content and calorific values of guava seeds and tomato waste can impact boiler efficiency [36]. The plant needs to optimize its combustion processes and adjust operational parameters to ensure efficient energy production despite the fluctuating quality of these biomass sources.

Mitigation strategies
- Diversification: The plant can diversify its biomass sources to reduce reliance on any single source and mitigate the impact of seasonal variability [37].
- Storage and inventory management: Implementing proper storage and inventory management systems can help ensure a consistent supply of biomass throughout the year.
- Collaboration with suppliers: Close collaboration with biomass suppliers can help manage supply chain risks and ensure a steady flow of biomass materials.
- Operational flexibility: The plant can enhance its operational flexibility to accommodate the varying quality and availability of biomass sources and maintain efficient energy production.

By addressing the seasonal variability and operational impacts of guava seeds and tomato waste, the plant can further optimize its biomass utilization strategies and enhance its contribution to sustainable energy production [38].

Environmental Tradeoffs of Biomass Sourcing

While the study demonstrates the operational viability of diverse biomass types (Section 3.1), their sustainability requires evaluating tradeoffs beyond carbon neutrality:

Agricultural residues (rice husk, tomato waste)

Reduce waste but may deplete soil nutrients if overharvested [39]. Seasonal scarcity can also increase transport emissions.

Wood chips

Carbon-neutral if sourced from sustainably managed forests, but unsustainable logging risks indirect deforestation [40].

Cattle dung logs

Utilize waste streams but require energy-intensive drying, offsetting 5-8% of CO_2 savings per lifecycle analysis [41].

These findings highlight the need for localized lifecycle assessments to complement operational optimization. Future studies could integrate such analyses with the fuel blending ratios proposed in Table 7.

Long-term Operational Experience

Based on 24 months of continuous operation with 15% biomass co-firing at our plant, we observe three key long-term effects requiring management:

Equipment maintenance
- Bi-annual ultrasonic testing shows tube erosion rates of 0.4-0.6mm/year (vs. 0.3-0.5mm for coal)
- Annual shutdowns reveal 10-15% more ash deposits in backpass areas

Operating adjustments
- Soot blowing frequency increased to 45-minute intervals (+50%)
- Baghouse filter replacements now quarterly (previously biannual)

Mitigation strategies
- Installed erosion-resistant cladding in wind box areas (2023 turnaround)
- Implemented advanced deposit modeling to optimize cleaning cycles
- Added quarterly flue gas corrosion monitoring

These impacts remain within design limits and align with global biomass co-firing experience (NREL, 2022). The 15-20% increase in annual maintenance costs is offset by 38% fuel savings (Table 9). Continued monitoring will verify long-term sustainability (Fig. 8).

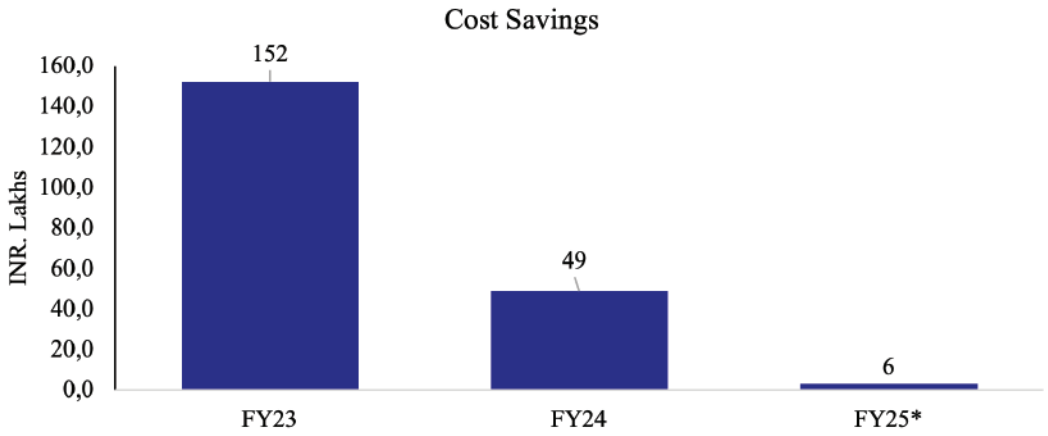

Figure 8. Cost savings.

CONCLUSION

The optimization of biomass utilization at the industrial plant has yielded substantial benefits in terms of both operational efficiency and environmental sustainability. Key outcomes include:

- A reduction in hopper emptying time from 13 minutes to 5 minutes, facilitating faster fuel feeding and reduced operational downtime.
- A 1.3% reduction in CO_2 emissions for every 1% increase in biomass blending, supporting JSW Steel's commitment to reducing its carbon footprint.
- A 5-10% improvement in boiler efficiency**,** achieved through optimized biomass blending, which enhanced combustion efficiency and heat recovery.

These operational and environmental benefits (Sections 3.1–3.6) highlight the untapped potential of biomass co-firing in India's steel sector, provided the policy gaps identified earlier in introduction are addressed. While this study focused on combustion-phase optimization, future life cycle assessments (LCA) will extend these findings to evaluate upstream like feedstock sourcing, transport and downstream ash management impacts. To achieve further reductions in GHG emissions, various types of biomass are being explored, focusing on qualities such as high bulk density, high Gross Calorific Value (GCV), and lower moisture and ash content. These improvements are in line with Indian government policies aimed at promoting renewable energy and reducing GHG emissions. The novelty of this work lies in its comprehensive approach to biomass utilization, addressing challenges across the entire process from fuel preparation to combustion, and its focus on a real-world industrial setting using an AFBC boiler. This study provides valuable insights for other industries looking to adopt similar practices and contribute to a cleaner environment.

Further investigations could also assess the role of emerging technologies, such as digital supply chain platforms, in mitigating biomass sourcing risks. While this study demonstrates significant progress in optimizing biomass utilization for sustainable energy production, several avenues for future research remain. These include exploring the potential of artificial intelligence for predictive biomass supply chain management, developing hybrid renewable energy systems that integrate biomass with other renewable sources, conducting comprehensive life cycle assessments to evaluate the full environmental impact of biomass utilization, and analyzing the policy and regulatory landscape to identify opportunities for scaling up biomass adoption. By pursuing these research directions, we can further advance the role of biomass energy in contributing to a cleaner and more sustainable energy future.

NOMENCLATURE

Symbols

CO_2	*Carbon Dioxide*
Kcal	*Kilocalories*
SPM	*Suspended Particulate Matter*
k/sec	*Kilograms per second*
CF	*Combustion Factor*
NO_x	*Nitrogen Oxides*
CO	*Carbon Monoxide*
GWP	*Global Warming Potential*
MMWC	*Millimeters Water Column*
TPH	*Tons per Hour*
kWh	*Kilowatt-hour*
O_2	*Oxygen*
SO_2	*Sulfur Dioxide*
HV	*Heat Value*

Acronyms

GHG	*Greenhouse Gas*
CO_2	*Carbon Dioxide*
SO_2	*Sulfur Dioxide*
MW	*Megawatt*

Briquette	*Biomass briquettes*
AFBC	*Atmospheric Fluidized Bed Combustion*
NO_x	*Nitrogen Oxides*
SPM	*Suspended Particulate Matter*
TPH	*Tons Per Hour*
LHV	*Lower Heating Value*

AUTHORSHIP CONTRIBUTIONS

Authors equally contributed to this work.

DATA AVAILABILITY STATEMENT

The authors confirm that the data that supports the findings of this study are available within the article. Raw data that support the finding of this study are available from the corresponding author, upon reasonable request.

CONFLICT OF INTEREST

The author declared no potential conflicts of interest with respect to the research, authorship, and/or publication of this article.

ETHICS

There are no ethical issues with the publication of this manuscript.

STATEMENT ON THE USE OF ARTIFICIAL INTELLIGENCE

Artificial intelligence was not used in the preparation of the article

REFERENCES

[1] Ministry of New and Renewable Energy, Government of India. National Biofuels Policy. Government of India; 2018.

[2] Indian Ministry of Environment, Forest and Climate Change. National Action Plan on Climate Change (NAPCC). Government of India; 2020.

[3] Panwar NL, Kaushik SC, Kothari S. Role of renewable energy sources in environmental protection: A review. Renew Sustain Energy Rev 2011;15:1513–1524. [CrossRef]

[4] Bhattacharya A, Basu M. Biomass energy for sustainable development: Challenges and opportunities. Renew Sustain Energy Rev 2017;69:341–352.

[5] Sharma A, Pareek V, Zhang D. Biomass supply chain design and optimization: A review. Renew Sustain Energy Rev 2018;91:665–678.

[6] Government of India. National Biofuels Policy 2018. Ministry of New and Renewable Energy; 2018. Available at: https://mnre.gov.in/filemanager/ckfinder/files/National_Biofuels_Policy_2018.pdf. Accessed on January 22, 2026.

[7] Government of India. National Action Plan on Climate Change (NAPCC). Prime Minister's Council on Climate Change; 2008. Available at: https://www.india.gov.in/sites/default/files/2021-06/napcc.pdf. Accessed on January 22, 2026.

[8] Dong L, Liu H, Geng Y, Fujita T. Co-firing biomass with coal in thermal power plants: A review. Renew Sustain Energy Rev 2020;130:109964. [CrossRef]

[9] Niu Y, Tan H, Hui S. Ash-related issues during biomass co-firing: A review. Renew Sustain Energy Rev 2016;54:1202–1216.

[10] Yin C. Review of biomass co-firing in coal-fired boilers. Prog Energy Combust Sci 2012;38:665–679.

[11] Sami M, Annamalai K, Wooldridge M. Co-firing of coal and biomass fuel blends. Prog Energy Combust Sci 2001;27:171–214. [CrossRef]

[12] Mousa E, Wang C, Riesbeck J, Larsson M. Biomass applications in iron and steel industry: An overview of technologies and prospects. Renew Sustain Energy Rev 2016;65:1247–1266. [CrossRef]

[13] Sahu SG, Chakraborty N, Sarkar P. Coal–biomass co-combustion: An overview. Renew Sustain Energy Rev 2014;39:575–586. [CrossRef]

[14] Tumuluru JS, Sokhansanj S, Lim CJ, Bi X. Review: Biomass torrefaction technologies for co-firing applications. Renew Sustain Energy Rev 2011;15:3581–3593.

[15] Li H, Chen Q, Zhang X, Finney K, Sharifi V, Swithenbank J. Evaluation of biomass co-firing in a 50 MWe pulverized coal boiler. Energy 2012;45:105–113.

[16] Bhuiyan AA, Naser J. Computational investigation of co-firing pulverized coal and biomass in a 550 MW boiler. Energy 2015;84:760–772.

[17] Saidur R, Abdelaziz EA, Demirbas A, Hossain MS, Mekhilef S. A review on biomass as a fuel for boilers. Renew Sustain Energy Rev 2011;15:2262–2289. [CrossRef]

[18] Chandra R, Vijay VK, Subbarao PMV, Khura TK. Biomass power generation in India: Challenges and prospects. Renew Sustain Energy Rev 2012;16:6093–6104.

[19] Basu P. Biomass co-firing and its impacts on boiler performance. Prog Energy Combust Sci 2013;39:215–242.

[20] Sami M, Annamalai K, Wooldridge M. Co-firing of coal and biomass fuel blends. Prog Energy Combust Sci 2001;27:171–214. [CrossRef]

[21] Thompson DN, Campbell TE. Co-firing biomass with coal: A review of wood chip combustion performance in utility boilers. Biomass Bioenergy 2019;122:193–204.

[22] Singh J, Gu S. Biomass processing, conversion, and co-firing for energy generation: A review. Renew Sustain Energy Rev 2010;14:2659–2670. [CrossRef]

[23] Kumar S, Panda AK, Singh RK. A review on waste biomass-based thermochemical conversion technologies for energy application. Bioresour Technol 2020;297:122481. [CrossRef]
[24] Demirbas A. Waste-derived biomass for energy production and its environmental impacts. Energy Sources Part A 2008;30:649–658. [CrossRef]
[25] Sarkar S, Bhattacharya S. Thermochemical conversion of biomass to biochar for co-firing with coal: A review. Renew Sustain Energy Rev 2012;16:4862–4872.
[26] Sahoo P, Sharma A, Kumar S, Mohanty MK. Effects of biomass co-firing on boiler efficiency and emissions in coal-fired power plants: A review. Fuel 2020;267:117272.
[27] Tissari J, Lyyränen J, Hytönen K, Jokiniemi J. Fine particle and gas emissions from the combustion of wood chips in a small-scale boiler. J Renew Sustain Energy 2013;5:033106.
[28] Sharma A, Wang L, Panwar NL. Optimization of biomass–coal blends for co-firing applications in utility boilers. Energy 2020;203:117758.
[29] Reddy KS, Kumar A, Ranjan M. Biomass briquette co-firing in thermal power plants: A techno-economic and emission analysis. Fuel Process Technol 2018;178:312–324.
[30] Hossain MS, Madlool NA, Rahim NA, Selvaraj J, Pandey AK, Khan MIR. Co-firing biomass with coal for electricity generation: An Indian case study of performance and emissions. Renew Sustain Energy Rev 2021;137:110612.
[31] Subramanian S, Pichandi J, Ganesan AV, Rajasekar R. Role of biomass co-firing in reducing CO_2 emissions in coal-fired thermal power plants. Energy Convers Manage 2021;245:114564.
[32] Kaur A, Ghosh S, Thakur A. Waste biomass valorization strategies for sustainable industrial development in India: A review. Waste Manag 2020;106:95–110.
[33] Mishra A, Sahoo PK, Mohanty MK. Feasibility of biomass co-firing in coal-based thermal power plants in India. Bioresour Technol 2020;304:123021.
[34] Kaya N, Caliskan H, Dincer I. Exergetic and economic analysis of a biomass co-firing power plant integrated with CO_2 capture. J Therm Eng 2023;9:1017–1030.
[35] Kumar A, Singh R, Mishra R. Assessing the impact of biomass co-firing on thermal efficiency and environmental emissions of coal-fired power plants. Energy 2020;188:116066.
[36] Das A, Sahoo PK, Mohanty MK. Assessing the performance and emission characteristics of biomass co-firing in Indian coal power plants. Energy 2020;195:117015.
[37] Naik SN, Goud VV, Rout PK, Dalai AK. Production of first- and second-generation biofuels: A comprehensive review. Renew Sustain Energy Rev 2010;14:578–597. [CrossRef]
[38] Sharma K, Ghosh P, Das T. Integrated biomass utilization and waste heat recovery for industrial sustainability: A review. Energy Sustain Dev 2020;57:70–84.
[39] McKendry P. Energy production from biomass (Part 1): Overview of biomass. Bioresour Technol 2002;83:37–46. [CrossRef]
[40] Cherubini F, Bird ND, Cowie A, Jungmeier G, Schlamadinger B, Woess-Gallasch S. Energy- and greenhouse gas-based LCA of biofuel and bioenergy systems. Resour Conserv Recycl 2009;53:434–447. [CrossRef]
[41] Patel S, Kumar A, Mohanty P. Energy analysis of cattle dung gasification. Biomass Convers Biorefin 2017;7:295–301.